



*pharmaceutics*

# Novel Anticancer Strategies (Volume II)

---

Edited by  
Hassan Bousbaa

Printed Edition of the Special Issue Published in *Pharmaceutics*

# **Novel Anticancer Strategies (Volume II)**



# Novel Anticancer Strategies (Volume II)

Editor

**Hassan Bousbaa**

MDPI • Basel • Beijing • Wuhan • Barcelona • Belgrade • Manchester • Tokyo • Cluj • Tianjin



*Editor*

Hassan Bousbaa  
UNIPRO–Oral Pathology and  
Rehabilitation Research Unit  
CESPU  
Gandra PRD  
Portugal

*Editorial Office*

MDPI  
St. Alban-Anlage 66  
4052 Basel, Switzerland

This is a reprint of articles from the Special Issue published online in the open access journal *Pharmaceutics* (ISSN 1999-4923) (available at: [www.mdpi.com/journal/pharmaceutics/special\\_issues/novel\\_anticancer\\_volume\\_II](http://www.mdpi.com/journal/pharmaceutics/special_issues/novel_anticancer_volume_II)).

For citation purposes, cite each article independently as indicated on the article page online and as indicated below:

LastName, A.A.; LastName, B.B.; LastName, C.C. Article Title. <i>Journal Name</i> <b>Year</b> , <i>Volume Number</i> , Page Range.
--

**ISBN 978-3-0365-7033-4 (Hbk)**

**ISBN 978-3-0365-7032-7 (PDF)**

© 2023 by the authors. Articles in this book are Open Access and distributed under the Creative Commons Attribution (CC BY) license, which allows users to download, copy and build upon published articles, as long as the author and publisher are properly credited, which ensures maximum dissemination and a wider impact of our publications.

The book as a whole is distributed by MDPI under the terms and conditions of the Creative Commons license CC BY-NC-ND.

# Contents

<b>About the Editor</b> . . . . .	<b>ix</b>
<b>Hassan Bousbaa</b> Novel Anticancer Strategies II Reprinted from: <i>Pharmaceutics</i> <b>2023</b> , <i>15</i> , 605, doi:10.3390/pharmaceutics15020605 . . . . .	<b>1</b>
<b>Yifeng Cao, Chuyang Chen, Yi Tao, Weifeng Lin and Ping Wang</b> Immunotherapy for Triple-Negative Breast Cancer Reprinted from: <i>Pharmaceutics</i> <b>2021</b> , <i>13</i> , 2003, doi:10.3390/pharmaceutics13122003 . . . . .	<b>7</b>
<b>Hualian Zha, Zhanxue Xu, Xichao Xu, Xingyu Lu, Peilin Shi and Youmei Xiao et al.</b> PD-1 Cellular Nanovesicles Carrying Gemcitabine to Inhibit the Proliferation of Triple Negative Breast Cancer Cell Reprinted from: <i>Pharmaceutics</i> <b>2022</b> , <i>14</i> , 1263, doi:10.3390/pharmaceutics14061263 . . . . .	<b>25</b>
<b>Shih-Cheng Pao, Mu-Tzu Chu and Shuen-Iu Hung</b> Therapeutic Vaccines Targeting Neoantigens to Induce T-Cell Immunity against Cancers Reprinted from: <i>Pharmaceutics</i> <b>2022</b> , <i>14</i> , 867, doi:10.3390/pharmaceutics14040867 . . . . .	<b>43</b>
<b>Dharambir Kashyap, Vivek Kumar Garg, Elise N. Sandberg, Neelam Goel and Anupam Bishayee</b> Oncogenic and Tumor Suppressive Components of the Cell Cycle in Breast Cancer Progression and Prognosis Reprinted from: <i>Pharmaceutics</i> <b>2021</b> , <i>13</i> , 569, doi:10.3390/pharmaceutics13040569 . . . . .	<b>63</b>
<b>Pedro Novais, Patrícia M. A. Silva, Isabel Amorim and Hassan Bousbaa</b> Second-Generation Antimitotics in Cancer Clinical Trials Reprinted from: <i>Pharmaceutics</i> <b>2021</b> , <i>13</i> , 1011, doi:10.3390/pharmaceutics13071011 . . . . .	<b>91</b>
<b>Bárbara Pinto, Pedro Novais, Ana C. Henriques, Juliana Carvalho-Tavares, Patrícia M. A. Silva and Hassan Bousbaa</b> Navitoclax Enhances the Therapeutic Effects of PLK1 Targeting on Lung Cancer Cells in 2D and 3D Culture Systems Reprinted from: <i>Pharmaceutics</i> <b>2022</b> , <i>14</i> , 1209, doi:10.3390/pharmaceutics14061209 . . . . .	<b>137</b>
<b>Patrícia M. A. Silva and Hassan Bousbaa</b> BUB3, beyond the Simple Role of Partner Reprinted from: <i>Pharmaceutics</i> <b>2022</b> , <i>14</i> , 1084, doi:10.3390/pharmaceutics14051084 . . . . .	<b>155</b>
<b>Carla S. S. Teixeira and Sérgio F. Sousa</b> Current Status of the Use of Multifunctional Enzymes as Anti-Cancer Drug Targets Reprinted from: <i>Pharmaceutics</i> <b>2021</b> , <i>14</i> , 10, doi:10.3390/pharmaceutics14010010 . . . . .	<b>167</b>
<b>Damiano Bartolucci, Andrea Pession, Patrizia Hrelia and Roberto Tonelli</b> Precision Anti-Cancer Medicines by Oligonucleotide Therapeutics in Clinical Research Targeting Undruggable Proteins and Non-Coding RNAs Reprinted from: <i>Pharmaceutics</i> <b>2022</b> , <i>14</i> , 1453, doi:10.3390/pharmaceutics14071453 . . . . .	<b>193</b>
<b>Surinder M. Soond, Lyudmila V. Savvateeva, Vladimir A. Makarov, Neonila V. Gorokhovets, Paul A. Townsend and Andrey A. Zamyatnin</b> Cathepsin S Cleaves BAX as a Novel and Therapeutically Important Regulatory Mechanism for Apoptosis Reprinted from: <i>Pharmaceutics</i> <b>2021</b> , <i>13</i> , 339, doi:10.3390/pharmaceutics13030339 . . . . .	<b>217</b>

<b>Antonio Fernando Leis-Filho, Patrícia de Faria Lainetti, Priscila Emiko Kobayashi, Carlos Eduardo Fonseca-Alves and Renée Laufer-Amorim</b> Effects of Lapatinib on HER2-Positive and HER2-Negative Canine Mammary Carcinoma Cells Cultured In Vitro Reprinted from: <i>Pharmaceutics</i> <b>2021</b> , <i>13</i> , 897, doi:10.3390/pharmaceutics13060897 . . . . .	<b>239</b>
<b>Adriana G. Quiroz-Reyes, Paulina Delgado-Gonzalez, Jose Francisco Islas, Juan Luis Delgado Gallegos, Javier Humberto Martínez Garza and Elsa N. Garza-Treviño</b> Behind the Adaptive and Resistance Mechanisms of Cancer Stem Cells to TRAIL Reprinted from: <i>Pharmaceutics</i> <b>2021</b> , <i>13</i> , 1062, doi:10.3390/pharmaceutics13071062 . . . . .	<b>253</b>
<b>Álvaro Javier Feliz Morel, Anida Hasanovic, Aurélie Morin, Chloé Prunier, Virginie Magnone and Kevin Lebrigand et al.</b> Persistent Properties of a Subpopulation of Cancer Cells Overexpressing the Hedgehog Receptor Patched Reprinted from: <i>Pharmaceutics</i> <b>2022</b> , <i>14</i> , 988, doi:10.3390/pharmaceutics14050988 . . . . .	<b>271</b>
<b>Yan Fu, Hongfei Ci, Wei Du, Qiongzhu Dong and Huliang Jia</b> CHRNA5 Contributes to Hepatocellular Carcinoma Progression by Regulating YAP Activity Reprinted from: <i>Pharmaceutics</i> <b>2022</b> , <i>14</i> , 275, doi:10.3390/pharmaceutics14020275 . . . . .	<b>299</b>
<b>Sarah I. Bukhari, Syed Sarim Imam, Mohammad Zaki Ahmad, Parameswara Rao Vuddanda, Sultan Alshehri and Wael A. Mahdi et al.</b> Recent Progress in Lipid Nanoparticles for Cancer Theranostics: Opportunity and Challenges Reprinted from: <i>Pharmaceutics</i> <b>2021</b> , <i>13</i> , 840, doi:10.3390/pharmaceutics13060840 . . . . .	<b>315</b>
<b>Shamama Javed, Sultan Alshehri, Ambreen Shoaib, Waquar Ahsan, Muhammad Hadi Sultan and Saad Saeed Alqahtani et al.</b> Chronicles of Nanoerythroosomes: An Erythrocyte-Based Biomimetic Smart Drug Delivery System as a Therapeutic and Diagnostic Tool in Cancer Therapy Reprinted from: <i>Pharmaceutics</i> <b>2021</b> , <i>13</i> , 368, doi:10.3390/pharmaceutics13030368 . . . . .	<b>339</b>
<b>Hanieh Montaseri, Cherie Ann Kruger and Heidi Abrahamse</b> Inorganic Nanoparticles Applied for Active Targeted Photodynamic Therapy of Breast Cancer Reprinted from: <i>Pharmaceutics</i> <b>2021</b> , <i>13</i> , 296, doi:10.3390/pharmaceutics13030296 . . . . .	<b>361</b>
<b>Jeffrey Stiltner, Kayla McCandless and Maliha Zahid</b> Cell-Penetrating Peptides: Applications in Tumor Diagnosis and Therapeutics Reprinted from: <i>Pharmaceutics</i> <b>2021</b> , <i>13</i> , 890, doi:10.3390/pharmaceutics13060890 . . . . .	<b>391</b>
<b>Shadab Md, Nabil A. Alhakamy, Shahid Karim, Gamal A Gabr, Mohammad Kashif Iqbal and Samar S. A. Murshid</b> Signaling Pathway Inhibitors, miRNA, and Nanocarrier-Based Pharmacotherapeutics for the Treatment of Lung Cancer: A Review Reprinted from: <i>Pharmaceutics</i> <b>2021</b> , <i>13</i> , 2120, doi:10.3390/pharmaceutics13122120 . . . . .	<b>405</b>
<b>Victoria R. Gabriele, Robabeh M. Mazhabi, Natalie Alexander, Purna Mukherjee, Thomas N. Seyfried and Njemuwa Nwaji et al.</b> Light- and Melanin Nanoparticle-Induced Cytotoxicity in Metastatic Cancer Cells Reprinted from: <i>Pharmaceutics</i> <b>2021</b> , <i>13</i> , 965, doi:10.3390/pharmaceutics13070965 . . . . .	<b>431</b>
<b>Baljinder Singh, Nutan Shukla, Junkee Kim, Kibeom Kim and Myoung-Hwan Park</b> Stimuli-Responsive Nanofibers Containing Gold Nanorods for On-Demand Drug Delivery Platforms Reprinted from: <i>Pharmaceutics</i> <b>2021</b> , <i>13</i> , 1319, doi:10.3390/pharmaceutics13081319 . . . . .	<b>445</b>

<b>Rebecca Alexandra Puiu, Paul Cătălin Balaure, Ema Constantinescu, Alexandru Mihai Grumezescu, Ecaterina Andronescu and Ovidiu-Cristian Oprea et al.</b> Anti-Cancer Nanopowders and MAPLE-Fabricated Thin Films Based on SPIONs Surface Modified with Paclitaxel Loaded $\beta$ -Cyclodextrin Reprinted from: <i>Pharmaceutics</i> <b>2021</b> , <i>13</i> , 1356, doi:10.3390/pharmaceutics13091356 . . . . .	463
<b>Simona Nistorescu, Ana-Maria Udrea, Madalina Andreea Badea, Iulia Lungu, Mihai Boni and Tatiana Tozar et al.</b> Low Blue Dose Photodynamic Therapy with Porphyrin-Iron Oxide Nanoparticles Complexes: In Vitro Study on Human Melanoma Cells Reprinted from: <i>Pharmaceutics</i> <b>2021</b> , <i>13</i> , 2130, doi:10.3390/pharmaceutics13122130 . . . . .	479
<b>Indra Van Zundert, Maria Bravo, Olivier Deschaume, Pierre Cybulski, Carmen Bartic and Johan Hofkens et al.</b> Versatile and Robust Method for Antibody Conjugation to Nanoparticles with High Targeting Efficiency Reprinted from: <i>Pharmaceutics</i> <b>2021</b> , <i>13</i> , 2153, doi:10.3390/pharmaceutics13122153 . . . . .	507
<b>Martin Studenovský, Anna Rumlerová, Jiřina Kovářová, Barbora Dvořáková, Ladislav Sivák and Libor Kostka et al.</b> HPMA Copolymer Mebendazole Conjugate Allows Systemic Administration and Possesses Antitumour Activity In Vivo Reprinted from: <i>Pharmaceutics</i> <b>2022</b> , <i>14</i> , 1201, doi:10.3390/pharmaceutics14061201 . . . . .	531
<b>Naoya Kondo, Fuko Hirano and Takashi Temma</b> Evaluation of 3-Borono-L-Phenylalanine as a Water-Soluble Boron Neutron Capture Therapy Agent Reprinted from: <i>Pharmaceutics</i> <b>2022</b> , <i>14</i> , 1106, doi:10.3390/pharmaceutics14051106 . . . . .	543
<b>Elena Domínguez-Jurado, Francisco J. Cimas, José Antonio Castro-Osma, Alberto Juan, Agustín Lara-Sánchez and Antonio Rodríguez-Diéguez et al.</b> Tuning the Cytotoxicity of Bis-Phosphino-Amines Ruthenium(II) Para-Cymene Complexes for Clinical Development in Breast Cancer Reprinted from: <i>Pharmaceutics</i> <b>2021</b> , <i>13</i> , 1559, doi:10.3390/pharmaceutics13101559 . . . . .	555
<b>Bárbara Costa and Nuno Vale</b> A Review of Repurposed Cancer Drugs in Clinical Trials for Potential Treatment of COVID-19 Reprinted from: <i>Pharmaceutics</i> <b>2021</b> , <i>13</i> , 815, doi:10.3390/pharmaceutics13060815 . . . . .	577
<b>Hirofumi Yamakawa, Shuichi Setoguchi, Shotaro Goto, Daisuke Watase, Kazuki Terada and Nami Nagata-Akaho et al.</b> Growth Inhibitory Effects of Ester Derivatives of Menahydroquinone-4, the Reduced Form of Vitamin K <sub>2(20)</sub> , on All-Trans Retinoic Acid-Resistant HL60 Cell Line Reprinted from: <i>Pharmaceutics</i> <b>2021</b> , <i>13</i> , 758, doi:10.3390/pharmaceutics13050758 . . . . .	599
<b>Zdeněk Kejík, Robert Kaplánek, Petr Dytrych, Michal Masařík, Kateřina Veselá and Nikita Abramenko et al.</b> Circulating Tumour Cells (CTCs) in NSCLC: From Prognosis to Therapy Design Reprinted from: <i>Pharmaceutics</i> <b>2021</b> , <i>13</i> , 1879, doi:10.3390/pharmaceutics13111879 . . . . .	615
<b>Alessandra Quarta, Nunzia Gallo, Daniele Vergara, Luca Salvatore, Concetta Nobile and Andrea Ragusa et al.</b> Investigation on the Composition of Agarose–Collagen I Blended Hydrogels as Matrices for the Growth of Spheroids from Breast Cancer Cell Lines Reprinted from: <i>Pharmaceutics</i> <b>2021</b> , <i>13</i> , 963, doi:10.3390/pharmaceutics13070963 . . . . .	667





# About the Editor

## **Hassan Bousbaa**

Hassan Bousbaa is a cancer researcher at the Oral Pathology and Rehabilitation Research Unit (UNIPRO) and associate professor of cellular and molecular biology at the Instituto Universitário de Ciências da Saúde –CESPU. Research interests include targeted anticancer therapy, targeting mitosis for cancer therapy, antimetabolic agents, biological evaluation of natural and synthetic compounds, and cancer biomarkers. He is acting as a Section Editor of the *Pharmaceutics* journal.



# Novel Anticancer Strategies II

Hassan Bousbaa <sup>1,2</sup> 

<sup>1</sup> UNIPRO-Oral Pathology and Rehabilitation Research Unit, Institute of Health Sciences (IUCS), Cooperativa de Ensino Superior Politécnico e Universitário (CESPU), Rua Central de Gandra 1317, 4585-116 Gandra, Portugal; hassan.bousbaa@iucs.cespu.pt

<sup>2</sup> Centro Interdisciplinar de Investigação Marinha e Ambiental (CIIMAR), Universidade do Porto, Terminal de Cruzeiros do Porto de Leixões, Av. General Norton de Matos s/n, 4450-208 Matosinhos, Portugal

Owing to the exceptional complexity of the development and progression of cancer, diverse cancer types are alarmingly increasing worldwide. Researchers and clinicians are facing a unique challenge. Radiotherapy and chemotherapy continue to be the main therapeutic options. However, these conventional therapies are associated with undesirable toxicity and resistance, and, as such, have proved unsuccessful in eradicating tumors completely. Consequently, the search for new anticancer drugs and novel drug delivery strategies are urgently needed to overcome conventional therapeutics' drawbacks and, hopefully, to offer more effective therapeutic options. This Special Issue ([https://www.mdpi.com/journal/pharmaceutics/special\\_issues/novel\\_anticancer\\_volume\\_II](https://www.mdpi.com/journal/pharmaceutics/special_issues/novel_anticancer_volume_II), (accessed on 31 January 2023)) was created after the successful first volume ([https://www.mdpi.com/journal/pharmaceutics/special\\_issues/novel\\_anticancer](https://www.mdpi.com/journal/pharmaceutics/special_issues/novel_anticancer), (accessed on 28 January 2023)), and is dedicated to innovative research on the development and validation of novel anticancer approaches, hopefully with relevant clinical value [1].

Sixteen original articles and fifteen reviews were published that provide the state-of-the-art of novel anticancer approaches. This editorial briefly summarizes the findings and highlights derived from the published articles.

Cancer immunotherapy deploys the immune system as a tool to treat neoplastic disease, and it is now firmly established as a novel pillar of cancer care. In this regard, Cao et al. nicely reviewed immunotherapy for triple-negative breast cancer [2]. The paper by Zha and colleagues used engineered cell membrane-derived programmed death-ligand 1 (PD-1) nanovesicles to encapsulate low-dose gemcitabine (PD-1&GEM NVs) to show that PD-1&GEM NVs could synergistically inhibit the proliferation of triple-negative breast cancer. The study highlighted the potential of the tested combination in the nanovesicles for triple-negative breast cancer therapy [3]. In their review paper, Pao et al. discussed recent progress in neoantigen identification and applications for cancer vaccines and summarized the results of ongoing trials [4].

Molecular-targeted therapies interfere with specific molecules to block cancer growth and progression, with the advantages of high efficiency, few side effects, and low drug resistance for patients. Cell signaling and cell cycle components are involved in many aspects of cancer cell proliferation and survival and, thus, are primary targets for cancer therapy [5]. As such, several inhibitors against mitotic regulation and surveillance components have been developed, with promising outcomes in preclinical assays. Unfortunately, these new antimitotics exhibited limited efficacy as monotherapy in clinical trials, as nicely reviewed in [6]. In a goal to give a second chance to these antimitotics, Pinto et al. combined the antimitotic BI2536, a potent inhibitor of Polo-like kinase 1 (PLK1), with Navitoclax, a BH3-mimetic and apoptosis inducer. The combination showed synergy in lung cancer cell-killing activity in 2D and 3D cell culture systems [7]. As to mitotic surveillance components, Silva and Bousbaa reviewed the structure and function of the spindle assembly checkpoint gene BUB3, its expression in cancer, its association with survival prognoses, and its potential as an anticancer target [8]. Other molecular targets are multifunctional enzymes, which have

**Citation:** Bousbaa, H. Novel Anticancer Strategies II. *Pharmaceutics* **2023**, *15*, 605. <https://doi.org/10.3390/pharmaceutics15020605>

Received: 6 February 2023  
Accepted: 10 February 2023  
Published: 10 February 2023



**Copyright:** © 2023 by the author. Licensee MDPI, Basel, Switzerland. This article is an open access article distributed under the terms and conditions of the Creative Commons Attribution (CC BY) license (<https://creativecommons.org/licenses/by/4.0/>).

been proposed as promising drug targets for cancer therapy. Teixeira and Sousa reviewed the structure and functions of four multifunctional enzymes, the inhibition of which has already demonstrated promising anti-cancer effects [9]. As a solution to undruggable targets, the review by Bartolucci et al. described the oligonucleotide therapeutics targeting RNA or DNA sequences as an emerging class of precision anticancer biotherapeutics [10]. Other papers reported molecular-targeted therapy strategies to block cancer growth and progression [11,12].

Cancer eradication is often compromised by a small population of Cancer Stem Cells (CSCs) within tumors, with capabilities of self-renewal, differentiation, and tumorigenicity, thereby causing tumor relapses. CSCs are also known for their therapy resistance. For instance, as reviewed by Quiroz-Reyes et al., CSCs can quickly develop adaptive evasion mechanisms for Tumor necrosis factor (TNF)-related apoptosis-inducing ligand (TRAIL) apoptosis [13]. Several CSC biomarkers have been identified with useful applications to diagnosis, therapy, and prognosis. The paper by Morel et al. described the isolation of a subpopulation of the adrenocortical carcinoma (ACC) cell line H295R overexpressing the cell surface Hedgehog receptor Patched (Ptch1) [14]. Ptch1 is overexpressed in many cancer types and was shown to contribute to the resistance to chemotherapy in ACC. The authors showed that this cell subpopulation is more tumorigenic than the parental cells, suggesting a cancer stem cell-like phenotype, which could be responsible for the therapy resistance, relapse, and metastases in ACC patients. In another paper by Fu et al., the  $\alpha 5$ -nicotinic acetylcholine receptor (CHRNA5), previously implicated in tumor progression, was reported to contribute to hepatocellular carcinoma (HCC) progression by regulating Yes-associated protein (YAP), the key transcription factor of the Hippo pathway [15]. Interestingly, CHRNA5 promoted the stemness of HCC by regulating stemness-associated genes, such as Nanog, Sox2, and OCT, suggesting a pivotal role in the progression and drug resistance of HCC.

Several drug-delivery systems have been successfully applied in cancer therapy. The rationale behind nanocarrier systems is to deliver cytotoxic drugs to the target cells in order to reduce their overall toxicity and increase their effectiveness and selectivity. Bukhari et al. provided a comprehensive and updated review of recent research in the field of lipidic nanocarriers loaded with theranostics (therapeutic and diagnostic agents), highlighting the main strengths and potential limitations of pretargeting theranostics. Simultaneous delivery of imaging (with contrasting agents), targeting (with biomarkers), and anticancer agents by one lipidic nanocarrier system (as cancer theranostics) are becoming popular, but significant hurdles in their clinical translation remain [16]. In another paper, Javet et al. reviewed the most recent advancements in the field of nanoerythrocytes [17]. Nanoerythrocytes are red blood cell-based nanocarrier systems and are viewed as excellent and biocompatible nanoplatforms for drug delivery of various drugs, particularly antineoplastic drugs. Montaseri et al. reviewed the application of inorganic nanoparticles in photodynamic therapy (PDT) [18]. PDT involves light-sensitive medicine and a light source to destroy a targeted tumor, with either a photosensitizer or photochemotherapeutic agent localized within it. Cell-penetrating peptides (CPPs) are short peptides with intrinsic properties to deliver therapeutic molecules to cells and tissues in a nontoxic manner. In their paper, Stiltner et al. provided a comprehensive state-of-the-art review of the role of these promising peptides in cancer diagnostics and therapeutics [19]. MicroRNA (miRNA) has been identified as a good target for cancer treatment. Shadab Md and colleagues discussed the potential use of miRNA in cancer therapy and provided a detailed description of nanocarrier-based drug delivery systems to deliver miRNAs [20]. Gabriele et al. showed that the coating of melanin nanoparticles, otherwise known to be biologically benign to human cells with glucose enhanced their uptake with cancer cells cultured in low glucose concentrations, making them more susceptible to killing by laser illumination [21]. Other original papers published in this Special Issue reported drug delivery systems that have been improved to potentially enhance the effectiveness of complex cancer treatments [22–26].

Improving the chemical and physical properties of anticancer drugs is key to improving treatment efficacy. In their study, Kondo et al. synthesized 3-borono-L-phenylalanine (3-BPA), a positional isomer of 4-BPA, with improved water solubility, making it a possible 4-BPA substitute in future boron neutron capture therapy (BNCT) [27]. BCCT is based on the nuclear reaction that results from boron-10 irradiation with neutrons of the appropriate energy to produce high-energy alpha particles and recoiling lithium-7 nuclei. Domínguez-Jurado et al. reported the synthesis of a ruthenium compound, namely *Ru3*, that showed cytotoxic activity against breast cancer cells, which might serve as the basis for the design of more active and less toxic antitumoral compounds [28]. Drug repurposing is an efficient and economical approach to identifying novel therapeutic agents from the existing FDA-approved clinically used drug molecules. Due to the similarities between cancer immune response and the coronavirus disease 2019 (COVID-19), a list of drugs that have been approved for cancer indication by the US FDA has entered clinical trials for COVID-19 treatments [29]. In the same line of thought, ester derivatives of menaquinone-4, used for osteoporosis treatment, were shown to exert strong growth-inhibitory effects on all-trans retinoic acid (ATRA)-resistant acute promyelocytic leukemia cells [30].

Diagnostic findings are critical for clinical decision-making in health care. In this regard, Kejík et al. discussed how circulating tumor cell count and targeting can influence the chemotherapeutic efficacy in non-small-cell lung carcinoma (NSCLC), providing a tool for prognosis and therapy design in NSCLC [31].

Three-dimensional (3D) cell culture systems (spheroids) have gained broader use in preclinical cancer research due to their ability to mimic the structural complexity of the tissue microenvironment of the real tumor. Quarta et al. presented a reliable 3D culture system based on collagen I-blended agarose hydrogel [32]. They showed that variation in the agarose percentage affects the physical and mechanical properties of the resulting hydrogel, making it a reliable biomimetic matrix for the growth of 3D cell structures.

Today, clinicians have a wide variety of effective cancer treatments at their disposal, which has translated into a steady increase in the survival of cancer patients. Yet, cancer incidence continues to rise, posing a continuous challenge to discovering and developing better anticancer treatments, stressing the need for more (focused) cancer research. Discovering new anticancer agents, refining our understanding of the old ones, and the main ways to target them should be thoroughly explored. The works published in this Special Issue have contributed to these goals by providing insights into some promising drugs, drug targets, drug combinations, and drug delivery.

**Funding:** H.B. received funding from CESPU—Cooperativa de Ensino Superior Politécnico e Universitário under the projects “SGA4Cancer-GI2-CESPU-2022”, “upPTXovcar-GI2-CESPU-2022”, and “Flav4Tumor-GI2-CESPU-2022”.

**Conflicts of Interest:** The author declares no conflict of interest.

## References

1. Bousbaa, H. Novel Anticancer Strategies. *Pharmaceutics* **2021**, *13*, 275. [CrossRef] [PubMed]
2. Cao, Y.; Chen, C.; Tao, Y.; Lin, W.; Wang, P. Immunotherapy for Triple-Negative Breast Cancer. *Pharmaceutics* **2021**, *13*, 2003. [CrossRef] [PubMed]
3. Zha, H.; Xu, Z.; Xu, X.; Lu, X.; Shi, P.; Xiao, Y.; Tsai, H.-I.; Su, D.; Cheng, F.; Cheng, X.; et al. PD-1 Cellular Nanovesicles Carrying Gemcitabine to Inhibit the Proliferation of Triple Negative Breast Cancer Cell. *Pharmaceutics* **2022**, *14*, 1263. [CrossRef] [PubMed]
4. Pao, S.-C.; Chu, M.-T.; Hung, S.-I. Therapeutic Vaccines Targeting Neoantigens to Induce T-Cell Immunity against Cancers. *Pharmaceutics* **2022**, *14*, 867. [CrossRef]
5. Kashyap, D.; Garg, V.K.; Sandberg, E.N.; Goel, N.; Bishayee, A. Oncogenic and Tumor Suppressive Components of the Cell Cycle in Breast Cancer Progression and Prognosis. *Pharmaceutics* **2021**, *13*, 569. [CrossRef]
6. Novais, P.; Silva, P.M.A.; Amorim, I.; Bousbaa, H. Second-Generation Antimitotics in Cancer Clinical Trials. *Pharmaceutics* **2021**, *13*, 1011. [CrossRef]
7. Pinto, B.; Novais, P.; Henriques, A.C.; Carvalho-Tavares, J.; Silva, P.M.A.; Bousbaa, H. Navitoclax Enhances the Therapeutic Effects of PLK1 Targeting on Lung Cancer Cells in 2D and 3D Culture Systems. *Pharmaceutics* **2022**, *14*, 1209. [CrossRef]
8. Silva, P.M.A.; Bousbaa, H. BUB3, beyond the Simple Role of Partner. *Pharmaceutics* **2022**, *14*, 1084. [CrossRef]

9. Teixeira, C.S.S.; Sousa, S.F. Current Status of the Use of Multifunctional Enzymes as Anti-Cancer Drug Targets. *Pharmaceutics* **2021**, *14*, 10. [CrossRef]
10. Bartolucci, D.; Pession, A.; Hrelia, P.; Tonelli, R. Precision Anti-Cancer Medicines by Oligonucleotide Therapeutics in Clinical Research Targeting Undruggable Proteins and Non-Coding RNAs. *Pharmaceutics* **2022**, *14*, 1453. [CrossRef]
11. Soond, S.M.; Savvateeva, L.V.; Makarov, V.A.; Gorokhovets, N.V.; Townsend, P.A.; Zamyatnin, A.A. Cathepsin S Cleaves BAX as a Novel and Therapeutically Important Regulatory Mechanism for Apoptosis. *Pharmaceutics* **2021**, *13*, 339. [CrossRef]
12. Leis-Filho, A.F.; de Faria Lainetti, P.; Emiko Kobayashi, P.; Fonseca-Alves, C.E.; Laufer-Amorim, R. Effects of Lapatinib on HER2-Positive and HER2-Negative Canine Mammary Carcinoma Cells Cultured In Vitro. *Pharmaceutics* **2021**, *13*, 897. [CrossRef]
13. Quiroz-Reyes, A.G.; Delgado-Gonzalez, P.; Islas, J.F.; Gallegos, J.L.D.; Martínez Garza, J.H.; Garza-Treviño, E.N. Behind the Adaptive and Resistance Mechanisms of Cancer Stem Cells to TRAIL. *Pharmaceutics* **2021**, *13*, 1062. [CrossRef]
14. Feliz Morel, Á.J.; Hasanovic, A.; Morin, A.; Prunier, C.; Magnone, V.; Lebrigand, K.; Aouad, A.; Cogoluegnes, S.; Favier, J.; Pasquier, C.; et al. Persistent Properties of a Subpopulation of Cancer Cells Overexpressing the Hedgehog Receptor Patched. *Pharmaceutics* **2022**, *14*, 988. [CrossRef]
15. Fu, Y.; Ci, H.; Du, W.; Dong, Q.; Jia, H. CHRNA5 Contributes to Hepatocellular Carcinoma Progression by Regulating YAP Activity. *Pharmaceutics* **2022**, *14*, 275. [CrossRef]
16. Bukhari, S.I.; Imam, S.S.; Ahmad, M.Z.; Vuddanda, P.R.; Alshehri, S.; Mahdi, W.A.; Ahmad, J. Recent Progress in Lipid Nanoparticles for Cancer Theranostics: Opportunity and Challenges. *Pharmaceutics* **2021**, *13*, 840. [CrossRef]
17. Javed, S.; Alshehri, S.; Shoaib, A.; Ahsan, W.; Sultan, M.H.; Alqahtani, S.S.; Kazi, M.; Shakeel, F. Chronicles of Nanoerythroosomes: An Erythrocyte-Based Biomimetic Smart Drug Delivery System as a Therapeutic and Diagnostic Tool in Cancer Therapy. *Pharmaceutics* **2021**, *13*, 368. [CrossRef]
18. Montaseri, H.; Kruger, C.A.; Abrahamse, H. Inorganic Nanoparticles Applied for Active Targeted Photodynamic Therapy of Breast Cancer. *Pharmaceutics* **2021**, *13*, 296. [CrossRef]
19. Stiltner, J.; McCandless, K.; Zahid, M. Cell-Penetrating Peptides: Applications in Tumor Diagnosis and Therapeutics. *Pharmaceutics* **2021**, *13*, 890. [CrossRef]
20. Md, S.; Alhakamy, N.A.; Karim, S.; Gabr, G.A.; Iqbal, M.K.; Murshid, S.S.A. Signaling Pathway Inhibitors, MiRNA, and Nanocarrier-Based Pharmacotherapeutics for the Treatment of Lung Cancer: A Review. *Pharmaceutics* **2021**, *13*, 2120. [CrossRef]
21. Gabriele, V.R.; Mazhabi, R.M.; Alexander, N.; Mukherjee, P.; Seyfried, T.N.; Nwaji, N.; Akinoglu, E.M.; Mackiewicz, A.; Zhou, G.; Giersig, M.; et al. Light- and Melanin Nanoparticle-Induced Cytotoxicity in Metastatic Cancer Cells. *Pharmaceutics* **2021**, *13*, 965. [CrossRef] [PubMed]
22. Singh, B.; Shukla, N.; Kim, J.; Kim, K.; Park, M.-H. Stimuli-Responsive Nanofibers Containing Gold Nanorods for On-Demand Drug Delivery Platforms. *Pharmaceutics* **2021**, *13*, 1319. [CrossRef] [PubMed]
23. Puiu, R.A.; Balaure, P.C.; Constantinescu, E.; Grumezescu, A.M.; Andronesu, E.; Oprea, O.-C.; Vasile, B.S.; Grumezescu, V.; Negut, I.; Nica, I.C.; et al. Anti-Cancer Nanopowders and MAPLE-Fabricated Thin Films Based on SPIONs Surface Modified with Paclitaxel Loaded  $\beta$ -Cyclodextrin. *Pharmaceutics* **2021**, *13*, 1356. [CrossRef] [PubMed]
24. Nistorescu, S.; Udrea, A.-M.; Badea, M.A.; Lungu, I.; Boni, M.; Tozar, T.; Dumitrache, F.; Maraloiu, V.-A.; Popescu, R.G.; Fleaca, C.; et al. Low Blue Dose Photodynamic Therapy with Porphyrin-Iron Oxide Nanoparticles Complexes: In Vitro Study on Human Melanoma Cells. *Pharmaceutics* **2021**, *13*, 2130. [CrossRef]
25. van Zundert, I.; Bravo, M.; Deschaume, O.; Cybulski, P.; Bartic, C.; Hofkens, J.; Uji-i, H.; Fortuni, B.; Rocha, S. Versatile and Robust Method for Antibody Conjugation to Nanoparticles with High Targeting Efficiency. *Pharmaceutics* **2021**, *13*, 2153. [CrossRef]
26. Studenovský, M.; Rumlerová, A.; Kovářová, J.; Dvořáková, B.; Sivák, L.; Kostka, L.; Berdár, D.; Etrych, T.; Kovář, M. HPMA Copolymer Mebendazole Conjugate Allows Systemic Administration and Possesses Antitumour Activity In Vivo. *Pharmaceutics* **2022**, *14*, 1201. [CrossRef]
27. Kondo, N.; Hirano, F.; Temma, T. Evaluation of 3-Borono-L-Phenylalanine as a Water-Soluble Boron Neutron Capture Therapy Agent. *Pharmaceutics* **2022**, *14*, 1106. [CrossRef]
28. Domínguez-Jurado, E.; Cimas, F.J.; Castro-Osma, J.A.; Juan, A.; Lara-Sánchez, A.; Rodríguez-Diéguez, A.; Shafir, A.; Ocaña, A.; Alonso-Moreno, C. Tuning the Cytotoxicity of Bis-Phosphino-Amines Ruthenium(II) Para-Cymene Complexes for Clinical Development in Breast Cancer. *Pharmaceutics* **2021**, *13*, 1559. [CrossRef]
29. Costa, B.; Vale, N. A Review of Repurposed Cancer Drugs in Clinical Trials for Potential Treatment of COVID-19. *Pharmaceutics* **2021**, *13*, 815. [CrossRef]
30. Yamakawa, H.; Setoguchi, S.; Goto, S.; Watase, D.; Terada, K.; Nagata-Akaho, N.; Toki, E.; Koga, M.; Matsunaga, K.; Karube, Y.; et al. Growth Inhibitory Effects of Ester Derivatives of Menahydroquinone-4, the Reduced Form of Vitamin K2(20), on All-Trans Retinoic Acid-Resistant HL60 Cell Line. *Pharmaceutics* **2021**, *13*, 758. [CrossRef]

31. Kejík, Z.; Kaplánek, R.; Dytrych, P.; Masařík, M.; Veselá, K.; Abramenko, N.; Hoskovec, D.; Vašáková, M.; Králová, J.; Martásek, P.; et al. Circulating Tumour Cells (CTCs) in NSCLC: From Prognosis to Therapy Design. *Pharmaceutics* **2021**, *13*, 1879. [CrossRef]
32. Quarta, A.; Gallo, N.; Vergara, D.; Salvatore, L.; Nobile, C.; Ragusa, A.; Gaballo, A. Investigation on the Composition of Agarose–Collagen I Blended Hydrogels as Matrices for the Growth of Spheroids from Breast Cancer Cell Lines. *Pharmaceutics* **2021**, *13*, 963. [CrossRef]

**Disclaimer/Publisher’s Note:** The statements, opinions and data contained in all publications are solely those of the individual author(s) and contributor(s) and not of MDPI and/or the editor(s). MDPI and/or the editor(s) disclaim responsibility for any injury to people or property resulting from any ideas, methods, instructions or products referred to in the content.





Review

# Immunotherapy for Triple-Negative Breast Cancer

Yifeng Cao <sup>1,\*</sup>,<sup>†</sup> , Chuayang Chen <sup>1,†</sup>, Yi Tao <sup>1</sup> , Weifeng Lin <sup>2</sup>  and Ping Wang <sup>1,\*</sup>

<sup>1</sup> College of Pharmaceutical Sciences, Zhejiang University of Technology, Hangzhou 310014, China; 2111907052@zjut.edu.cn (C.C.); taoyi1985@zjut.edu.cn (Y.T.)

<sup>2</sup> Department of Molecular Chemistry and Materials Science, Weizmann Institute of Science, Rehovot 76100, Israel; lin.weifeng@weizmann.ac.il

\* Correspondence: yifengcao@zjut.edu.cn (Y.C.); wangping45@zjut.edu.cn (P.W.)

† The authors contribute equally to this work.

**Abstract:** Triple-negative breast cancer (TNBC) is characterized by extensive tumor heterogeneity at both the pathologic and molecular levels, particularly accelerated aggressiveness, and terrible metastasis. It is responsible for the increased mortality of breast cancer patients. Due to the negative expression of estrogen receptors, progesterone receptors, and human epidermal growth factor receptor 2, the progress of targeted therapy has been hindered. Higher immune response in TNBCs than for other breast cancer types makes immunotherapy suitable for TNBC therapy. At present, promising treatments in immunotherapy of TNBC include immune checkpoints (ICs) blockade therapy, adoptive T-cell immunotherapy, and tumor vaccine immunotherapy. In addition, nanomedicines exhibit great potential in cancer therapy through the enhanced permeability and retention (EPR) effect. Immunotherapy-involved combination therapy may exert synergistic effects by combining with other treatments, such as traditional chemotherapy and new treatments, including photodynamic therapy (PTT), photodynamic therapy (PDT), and sonodynamic therapy (SDT). This review focuses on introducing the principles and latest development as well as progress in using nanocarriers as drug-delivery systems for the immunotherapy of TNBC.

**Citation:** Cao, Y.; Chen, C.; Tao, Y.; Lin, W.; Wang, P. Immunotherapy for Triple-Negative Breast Cancer. *Pharmaceutics* **2021**, *13*, 2003. <https://doi.org/10.3390/pharmaceutics13122003>

**Keywords:** TNBC; immunotherapy; immune checkpoint; nanocarrier; drug delivery; combinational immunotherapy

Academic Editors: James J. Moon and Chaoliang He

Received: 3 October 2021

Accepted: 23 November 2021

Published: 25 November 2021

**Publisher's Note:** MDPI stays neutral with regard to jurisdictional claims in published maps and institutional affiliations.



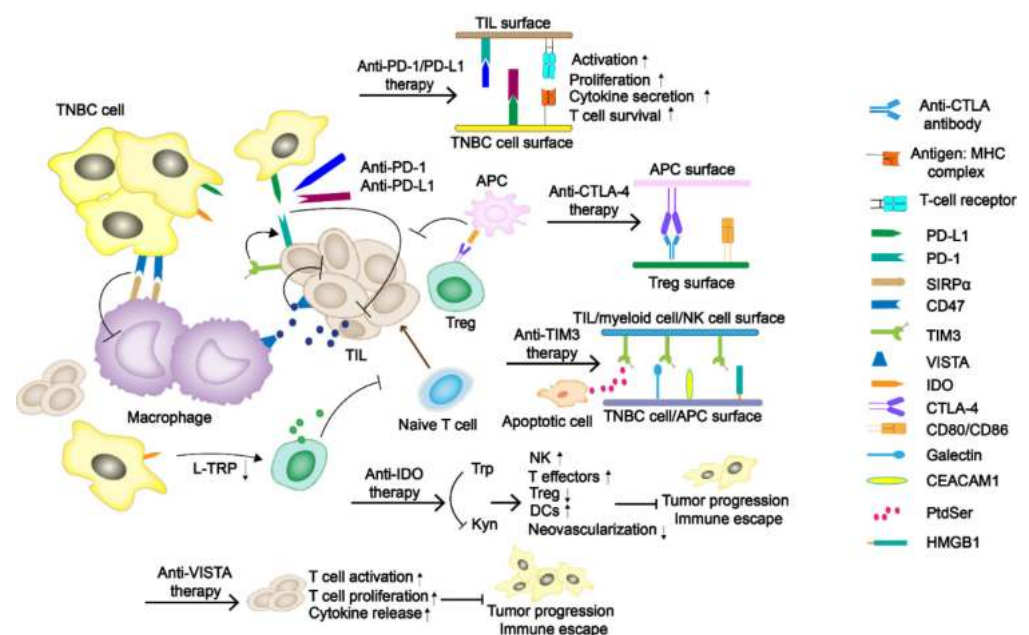
**Copyright:** © 2021 by the authors. Licensee MDPI, Basel, Switzerland. This article is an open access article distributed under the terms and conditions of the Creative Commons Attribution (CC BY) license (<https://creativecommons.org/licenses/by/4.0/>).

## 1. Immunotherapy in Triple-Negative Breast Cancer (TNBC)

Cancer constitutes the largest public health problem in the world. According to the data released by the American Cancer Society (ACS), there are about 4950 patients diagnosed with cancer and 1662 dying of it every day; Among them, breast cancer is the most popular female cancer type, which is estimated to be nearly 30% of the new cases and the death rate of which is as high as 15% in 2020 [1]. According to the expression of estrogen receptors (ER), progesterone receptors (PR), and human epidermal growth factor receptor 2 (HER2), breast cancer is defined as three major subtypes: hormone-receptor (HR) positive, HER2-enriched, and triple-negative breast cancer (TNBC). TNBC accounts for 15–20% of all breast cancers, particularly those in young women [2]. Compared with the other subtypes, TNBC does not respond well to hormonal therapy or medicines targeting HER2 protein receptors. It shows higher drug resistance and tumor heterogeneity and aggressiveness, and is often accompanied by lung or brain metastasis. Lacking therapeutic target is the main reason challenging the effective treatment of TNBC. Once the tumor metastasizes, the median overall survival of TNBC patients is only 12 to 18 months due to the limited therapeutic window [3]. Additionally, TNBC contains more immune cells [4], and is easily recognized by the immune system due to its high genetic instability and tumor mutational burden, making it one of the tumor types suitable for immunotherapy intervention [5]. Although there are limited options for its treatment, TNBC is the most immunogenic subtype of breast cancers. The robust antitumor responses of immunotherapy in hematologic and solid malignancies bring hope to TNBC patients [6].

Changes in the tumor microenvironment (TME), including tumor cell proliferation, tumor metastasis, tumor recurrence, and tumor resistance, play a critical role in the progression of tumors as well as in their response to treatment and prognosis. In fact, the success of immunotherapy links the TME with immunity [7,8]. In particular, tumor immune microenvironment (TIME) composed of various immune cells has also attracted much attention and exhibits significant importance to immunotherapy. Immune cells, scattered in the tumor center and infiltrating edge or adjacent tertiary lymphoid tissue, can be roughly divided into immunosuppressive cells and immune effector cells [9,10]. Similar to many other cancers, the antitumor immune killing effect in TNBC is performed by cytotoxic T cells CD8+ and helper T cells CD4+ [10]. Regulatory T cells (Tregs) is a major group of immunosuppressive cells, characterized by elevated Foxp3 expression and tumor-associated macrophages [11]. They inhibit the immune function mediated by CD8+ and CD4+ T cells by secreting TGF- $\beta$ , IL-10, and IL-35 in the process of immune escape. Meanwhile, they can kill T cells directly through producing granzymes and perforin [12]. When Tregs dominate the immune function of tumor, immune escape would occur [13].

Immune checkpoints (ICs) are molecules playing a protective role similar to brakes in the immune system. It can prevent inflammation damage and autoimmune diseases caused by excessive activation of T cells (Figure 1). Tumor cells use human immune system to over-express immune checkpoint molecules to inhibit the response of the human immune system and to escape immune surveillance and killing [14,15]. In particular, programmed cell death protein-1 (PD-1) and cytotoxic T-lymphocyte-associated protein-4 (CTLA-4), which weaken the immune function mediated by T cells, are of great importance to tumor immunosuppression [16]. More potential checkpoints have been discovered, and their value in immunotherapy is gradually being explored. Meanwhile, adoptive T-cell immunotherapy and tumor vaccine are also constantly being studied as promising treatments.



**Figure 1.** The regulatory mechanism of immune checkpoints (ICs) in TNBC tumor progress. The programmed cell death-1/programmed death-ligand 1 (PD-1/PD-L1) and cytotoxic T-lymphocyte-associated antigen-4 (CTLA-4) have been the primary immune checkpoint blockades. Some potentially new immune ICs, such as T-cell immunoglobulin and mucin domain-containing protein 3 (TIM-3), indoleamine 2,3-dioxygenase (IDO), as well as V domain Ig suppressor of T-cell activation (VISTA), are also demonstrated in the figure.

### 1.1. Immune Checkpoint Blockades PD-1/PD-L1 and CTLA-4

Immune checkpoint blockades PD-1/PD-L1 and CTLA-4 are currently the primary and most widely studied immunotherapy agents (Figure 1). PD-1 is a member of the CD28 superfamily and is mainly expressed in activated T and B lymphocytes, natural killer (NK) cells, and myeloid cells. The structure of PD-1 includes an extracellular immunoglobulin variable region (IGV), a hydrophobic transmembrane domain, and an intracellular domain. The tail of the intracellular region contains the immune receptor tyrosine-based inhibitory motif (ITIM) and the immune receptor tyrosine-based switch motif (ITSM) [17]. PD-L1 and PD-L2 are two ligands of PD-1. The inhibitory signals often appear upon PD-1/PD-L1 binding, tyrosine phosphorylation in ITSM causes dephosphorylation of downstream protein kinases Syk and PI3K, hinders downstream pathway activation, and inhibits transcription and translation of genes and cytokines required for T-cell activation. Studies have shown that PD-L1 expression is positive in about 20% of the TNBC patients, which is significantly higher than that in non-TNBC patients [18]. CTLA-4 is a transmembrane protein exclusively expressed on T cells and Tregs in tumor infiltrating lymphocytes (TILs). It has a similar domain structure to CD28 (sharing 31% identity) and binds to B7.1 (CD 80) and B7.2 (CD 86) with higher affinity [19]. Moreover, its engagement on Tregs could strengthen the suppressive effect.

Currently, PD-1/PD-L1 inhibitors are mainly monoclonal antibodies (mAbs) and some small molecules [20]. For example, pembrolizumab and emiplimab are humanized IgG4κ monoclonal antibodies binding to PD-1 [21], nivolumab is an all humanized genetically engineered monoclonal antibody against PD-1 [22,23], and atezolizumab and durvalumab are both humanized IgG1κ type monoclonal antibodies against PD-L1 [24]. There are many ongoing clinical trials in the treatment of TNBCs with mAbs (Table 1). Immune checkpoint blockade therapy has been proved for the treatment of multiple types of cancer; however, none of them has been approved for the treatment of TNBC so far. Some problems came along with the clinical trials. Demaria et al. [25] concluded that CTLA-4 antibody monotherapy could not inhibit the growth of metastatic tumor in mouse breast cancer cell 4T1. In the randomized phase II trial NCT02519322, grade III adverse events occurred in 8% of patients treated with nivolumab monotherapy and as high as 73% of patients treated with both nivolumab and ipilimumab [26]. In the phase II clinical trial NCT02536794, durvalumab combined with tremelimumab were administered, but was finally terminated due to objective response rate (ORR) did not match the required criteria [27]. Fortunately, the KEYNOTE-012 trial in Phase Ib and KEYNOTE-086 trial in phase II both revealed that pembrolizumab had controllable safety and persistent antitumor activity in TNBC with PD-L1 positive expression [28,29].

**Table 1.** Status of clinical trials with immune checkpoint blockade reagents for the treatment of TNBC [30].

Agent	Target	ClinicalTrials.Gov Identifier	Combinatorial Agent(s)	Phase	Recruitment Status
Atezolizumab	PD-L1	NCT02530489	Nab-paclitaxe	Phase II	Active, not recruiting
Pembrolizumab	PD-1	NCT02622074	Nab-paclitaxel + Doxorubicin + Cyclophosphamide, Nab-paclitaxel + Doxorubicin + Cyclophosphamide + Carboplatin, Doxorubicin + Cyclophosphamide + Carboplatin + Paclitaxel	Phase I	Completed
Pembrolizumab	PD-1	NCT02734290	Paclitaxel, Capecitabine	Phase I Phase II	Active, not recruiting
Pembrolizumab	PD-1	NCT02768701	Cyclophosphamide	Phase II	Active, not recruiting
Pembrolizumab	PD-1	NCT02977468	Intraoperative radiation therapy (IORT)	Phase I	Recruiting

Table 1. Cont.

Agent	Target	ClinicalTrials.Gov Identifier	Combinatorial Agent(s)	Phase	Recruitment Status
Pembrolizumab	PD-1	NCT02981303	Imprime PGG	Phase II	Completed
Pembrolizumab	PD-1	NCT03012230	Ruxolitinib Phosphate	Phase I	Recruiting
Pembrolizumab	PD-1	NCT03036488	Carboplatin + Paclitaxel + Doxorubicin or Epirubicin + Cyclophosphamide + Granulocyte colony-stimulating factor (G-CSF)	Phase III	Active, not recruiting
Atezolizumab	PD-L1	NCT03125902	Paclitaxel	Phase III	Active, not recruiting
Atezolizumab	PD-L1	NCT03164993	Pegylated liposomal doxorubicin, Cyclophosphamide	Phase II	Recruiting
Durvalumab	PD-L1	NCT03199040	Neoantigen DNA vaccine	Phase I	Active, not recruiting
Atezolizumab	PD-L1	NCT03206203	Carboplatin	Phase II	Active, not recruiting
Atezolizumab	PD-L1	NCT03281954	Paclitaxel + Carboplatin, Doxorubicin + Cyclophosphamide or Epirubicin + Cyclophosphamide	Phase III	Active, not recruiting
Atezolizumab	PD-L1	NCT03371017	Gemcitabine + Capecitabine or Carboplatin	Phase III	Recruiting
Atezolizumab	PD-L1	NCT03424005	Nab-paclitaxel, Nab-paclitaxel + Tocilizumab, Sacituzumab Govitecan, Ipatasertib, Landiratumab vedotin (SGN-LIV1A), Selicelumab + Bevacizumab, Chemo (Gemcitabine + Carboplatin or Eribulin)	Phase I Phase II	Recruiting
Nivolumab	PD-1	NCT03487666	Capecitabine	Phase II	Active, not recruiting
Atezolizumab	PD-L1	NCT03498716	Chemo (Paclitaxel, Dose-dense Doxorubicin or dose-dense Epirubicin), Cyclophosphamide	Phase III	Recruiting
Pembrolizumab	PD-1	NCT03639948	Carboplatin + Docetaxel + Pegfilgrastim	Phase II	Recruiting
Durvalumab	PD-L1	NCT03742102	Paclitaxel, Paclitaxel + Capivasertib, Paclitaxel + Oleclumab, Trastuzumab deruxtecan, Datopotamab deruxtecan	Phase I Phase II	Recruiting
Pembrolizumab	PD-1	NCT03752723	Cyclophosphamide + efineptakin alfa (GX-I7)	Phase I Phase II	Recruiting
Atezolizumab	PD-L1	NCT03756298	Capecitabine	Phase II	Recruiting
Durvalumab	PD-L1	NCT03801369	Olaparib	Phase II	Recruiting
Nivolumab	PD-1	NCT03818685	Ipilimumab	Phase II	Recruiting
Atezolizumab	PD-L1	NCT03853707	Ipatasertib + Carboplatin	Phase I Phase II	Suspended
Pembrolizumab	PD-1	NCT04095689	Docetaxel + Interleukin-12 gene therapy, Docetaxel + NG-monomethyl-L-arginine (L-NMMA)	Phase II	Recruiting
Camrelizumab	PD-1	NCT04129996	Nab-paclitaxel + famitinib	Phase II	Recruiting

Table 1. Cont.

Agent	Target	ClinicalTrials.Gov Identifier	Combinatorial Agent(s)	Phase	Recruitment Status
Atezolizumab	PD-L1	NCT04148911	Nab-paclitaxel	Phase III	Recruiting
Atezolizumab	PD-L1	NCT04177108	Ipatasertib	Phase III	Active, not recruiting
Pembrolizumab	PD-1	NCT04191135	Carboplatin + Gemcitabine, Carboplatin + Gemcitabine + Olaparib	Phase II Phase III	Active, not recruiting
Camrelizumab	PD-1	NCT04331067	Nivolumab + Paclitaxel + Carboplatin	Phase I Phase II	Recruiting
Camrelizumab	PD-1	NCT04335006	Nab-paclitaxel + Apatinib, Nab-paclitaxel	Phase III	Recruiting
Camrelizumab	PD-1	NCT04481763	Radiotherapy	Phase I Phase II	Recruiting
Tiragolumab and Atezolizumab	PD-L1	NCT04584112	Nab-paclitaxel, Nab-paclitaxel + Carboplatin + Doxorubicin + Cyclophosphamide + G-CSF or Granulocyte-macrophage colony-stimulating factor (GM-CSF), Nab-paclitaxel + Doxorubicin + Cyclophosphamide + G-CSF + GM-CSF	Phase I	Recruiting
Camrelizumab	PD-1	NCT04613674	Chemotherapy	Phase III	Recruiting
Camrelizumab	PD-1	NCT04676997	Nab-paclitaxel + Epirubicin + Cyclophosphamide	Phase II	Recruiting
Pembrolizumab	PD-1	NCT04683679	Olaparib + Radiation, Radiation	Phase II	Recruiting

### 1.2. T-Cell Immunoglobulin Domain and Mucin Domain-3 (TIM-3)

TIM-3, also known as HAVcr2 or CD366, is a type I cell-surface glycoprotein consisted of an amino-terminal immunoglobulin variable domain (V domain) with five noncanonical cysteines, a mucin-like stalk, a transmembrane domain, and an intracellular cytoplasmic tail [31]. It contains four different ligands, including galectin-9 (Gal-9), phosphatidylserine (PtdSer), carcinoembryonic antigen-related cell adhesion molecule-1 (CEACAM-1), and high mobility group protein B-1 (HMGB-1) [32]. TIM-3 is associated with tumor immune regulation and autoimmune diseases. Byun et al. [33] demonstrated that TIM-3 expression is a positive prognostic factor in TNBC. Due to the diversity of receptors causing the binding form to change under different situations, whether TIM-3 acts as a costimulatory receptor or a co-inhibitory receptor has not been fully determined. However, a recent study shows that TIM-3 mostly plays its role as an inhibitory receptor [34].

### 1.3. Indoleamine 2,3-Dioxygenase (IDO)

IDO is a rate-limiting enzyme in the catabolism of essential amino acid tryptophan (Trp) to kynurenine (Kyn). The downstream signal transduction of IDO includes the changes of general control non-derepressible-2 (GCN2), mammalian target of rapamycin (mTOR) and aryl hydrocarbon receptor (AhR) [35]. Research has proved that with the decrease of Trp followed by uncharged Trp tRNA accumulation, the GCN2 would be activated. Then, phosphorylation of eukaryotic initiation factor-2 $\alpha$  (eIF2 $\alpha$ ) induced by GNC2 would inhibit the proliferation of effector T cells. Moreover, its metabolite Kyn can bind to AhR, leading to an increase in the number of Tregs. The suppression of mTOR and the increase of IL-6 secretion are both reasons why IDO exerts its immunosuppressive effect [36]. In breast cancer therapy, it is closely related to poor prognosis and increased microvessel density [37]. Asghar et al. [38] conducted a study on 100 female breast cancer patients

in Pakistani (including triple-negative and non-triple-negative ones), linking the expression of IDO with median overall survival, proving that IDO plays a pivotal role in TNBCs. The overall survival of patients with low IDO expression is about  $91 \pm 41.9$  months, which is much higher than the intermediate and high levels,  $50 \pm 4.4$  and  $24 \pm 10.1$  months, respectively. Because of the potential effect of IDO in immunotherapy, some of the IDO inhibitors, including Epacadostat, BMS986205, PF-06840003, Navoximod, Indoximod, NLG802, and LY3381916, are under the latest ongoing clinical trials [39].

#### 1.4. V Domain Ig Suppressor of T-Cell Activation (VISTA)

VISTA, also referred to as PD-1H, is a newly discovered negative immune checkpoint related to immunotherapy resistance. VISTA is a type I transmembrane protein consisting of an N-terminal IgV domain, a stalk of about 30 amino acids, a transmembrane domain, and a cytoplasmic tail of 95 amino acids. Its molecule shares sequence homology with PD-L1 and PD-L2 [40,41]. Similar to PD-1, VISTA also serves as a negative regulatory agent for T cells by suppressing their activation, proliferation, and cytokine release. In breast cancer, it is expressed on TILs, macrophages, and other immune cells. Xue et al. [42] found that VISTA expression was higher in CD68+ tumor-associated macrophages (32.58%), CD4+ T cells (4.97%), CD8+ cytotoxic T cells (4.48%), and CD20+ B cells (1.46%). Gao et al. [43] proved that treating prostate cancer with ipilimumab can lead to a compensatory up-regulation of VISTA, indicating that VISTA may be related to the development of resistance to immune checkpoint blocking therapy. However, Cao et al. [44] evaluated the expression of VISTA in a cohort of 254 untreated TNBC patients, and found that VISTA was expressed in 87.8% (223/254) and 18.5% (47/254) of the immune cells and tumor cells, respectively. Meanwhile, the expression of VISTA in ICs is positively correlated with some TILs, especially CD4+ TIL. The information confirms the regulatory role of VISTA in antitumor immunity, but it has not been developed as a negative immune checkpoint so far.

#### 1.5. Adoptive T-Cell Immunotherapy

The adoptive T-cell immunotherapy starts with isolating T cells, which are afterwards genetically modified to express CRA, followed by proliferation, then are re injected to patients. The injected T cells combine with specific antigens, and ultimately eliminate targeted tumor cells [45]. Moreover, using genetic engineering technology, two types of engineered T cells, T cells with T-cell receptor (TCR) and Chimeric antigen receptor T-cell (CAR-T), were given higher recognition. CAR-T immunotherapy, started in the late 1980s, has been proved to play a key role in CD19 positive hematological malignancies [46]. CARs are synthesized receptors which consist of extra- and intracellular domains: the extracellular part is single chain fragment variable (scFv) domain composed of specific antibody, while the intracellular domain contains CD3 $\zeta$  and CD3 $\zeta$  co-stimulate with CD28, ICOS, 4-1BB (CD137), CD27, or OX40 signals domain. The main advantage of CAR-T technique is that it can recognize cancer cells without the presence of major histocompatibility complex (MHC) antigen.

To develop an effective CARs therapy for TNBCs, it is necessary to select a desired tumor cell-surface antigen, which can be expressed stably in most tumor cells, and has high tumor specificity [47]. For this purpose, Song et al. [48] designed a new folate receptor  $\alpha$  (FR $\alpha$ )-specific CAR-T, which was composed of MOv19 scFv and CD8a hinge in extracellular region, and of CD27 costimulatory domain and CD3 $\zeta$  signaling domain in the intracellular region. The FR $\alpha$ -specific CAR-T cells show a more robust immune effect in TNBCs with FR $\alpha$  protein overexpression. Zhou et al. [49] generated the MUC28z CAR-T cell consisted of TAB004 scFv coupled with CD28 and CD3 $\zeta$ , and demonstrated that MUC28z CAR-T cells have high tumor antigen specificity, and refrained recognition of normal tissues. Moreover, it is found that MUC28z CAR-T cells can lyse TNBCs and reduce the tumor growth both in vitro and in vivo. Moreover, the growth factor receptor (EGFR) is a potential tumor surface antigen, and EGFR-specific CAR-T has strong cytotoxicity. However, the emergence of drug resistance is an urgent problem. Lin et al. [50] combined

EGFR-specific CAR-T with THZ1, a CDK7 inhibitor, which together demonstrated a good effect on TNBCs proliferation, tumor metastasis and suppressed immune resistance in mice. Identically, Stuber et al. [51] combined ROR1-specific CAR-T cells to SD-208, a TGF- $\beta$  inhibitor, to weaken the immunosuppressive effects in therapy.

### 1.6. Tumor Vaccine Immunotherapy

In contrast to the traditional concept of vaccination, the definition of vaccine in modern medicine is not only limited to prevention of diseases, but expanded to target disease-specific antigens for the treatment of ongoing diseases. In the development of immune vaccines, tumor-associated antigens and delivery technology are the main considerations. The neoantigen is produced when gene coding contained non-synonymous mutations and only expressed in tumors [52]. However, tumor-associated antigens can be expressed in tumors and normal tissues at the same time. Studies have shown that neoantigens have a stronger affinity to human leukocyte antigen (HLA) and T-cell receptors, and are not limited by central tolerance and autoimmune problems [53]. Therefore, it has been regarded as one of the most potential tumor treatment targets since its discovery, and is the key to the development of personalized immunization vaccines.

Immunization vaccine also offers a viable option in the treatment of TNBCs. In the study by Liu et al. [54], an mRNA-based vaccine encoding tumor antigen MUC1 was delivered to dendritic cells (DCs) in lymph nodes using a nano-delivery system, and anti-CTLA-4 antibodies were used in combination to exert antitumor effects. Among them, the nano-delivery system can enhance the stability, persistence and expression level of the vaccine, and the vaccine that enters the body plays a role by activating and expanding tumor-specific T cells. Compared with other groups, the combination treatment group has the strongest effect of inhibiting tumor growth. Pack et al. [55] isolated tumor membrane vesicles (TMV) from 4T1 tumor, and glycosylphosphatidylinositol (GPI) anchored form of immunostimulatory B7-1 (CD80) and IL-12 molecules were combined to these TMVs to prepare TMV vaccine. Compared with monotherapy, tumor-bearing mice administrated with combined treatment of vaccine and anti-CTLA-4 antibody exhibited significantly improved survival rate and reduced lung metastasis.

### 1.7. Immunotherapy-Involved Combination Therapies

In the treatment with immune checkpoint inhibitors (ICIs), though mAbs show certain therapeutic effect, the response rate is generally low. For instance, the response rate of pembrolizumab monotherapy in TNBC is only 5.3% [29]. To solve this problem, combination therapy, combining mAbs with various chemotherapeutics, such as nab-paclitaxel, epirubicin, cyclophosphamide, with radiotherapy, or with some cytokines, has been intensively used in clinic trials. Table 1 summarizes such clinical trials that are being recruited or in progress. For example, the ongoing clinical phase II trial NCT02730130 was designed to assess the efficacy and safety of pembrolizumab with radiotherapy. Results show that the obtained ORR and progression-free survival (PFS) were dramatically higher than those for pembrolizumab monotherapy, increased from 3% to 17.6% and 1.9 to 2.6 months, respectively [56]. As for the phase III clinical trial KEYNOTE-355 using combined pembrolizumab, nab-paclitaxel, carboplatin, and paclitaxel/gemcitabine the combination therapy resulted in a remarkable and clinically meaningful improvement in median PFS (4.1 months longer) [57]. Similarly, phase III trial Impassion130 showed that atezolizumab plus nab-paclitaxel would induce significantly longer PFS in TNBCs [58]. As for CTLA-4, Bernier et al. [59] demonstrated that combining DZ-2384 with CTLA-4 antibody could slow down tumor growth and increase overall survival rate. Li et al. [60] demonstrated that compared with monotherapy in mice, matrix metalloproteinase inhibitor plus CTLA-4 antibody could delay tumor growth and reduce distant metastases.

It is worth noticing that the combination therapy has been designed mostly for locally advanced or metastatic TNBCs. Neoadjuvant therapy, which has been used in the treatment of melanoma or colon cancer, is a promising strategy for early TNBC. The KEYNOTE-522



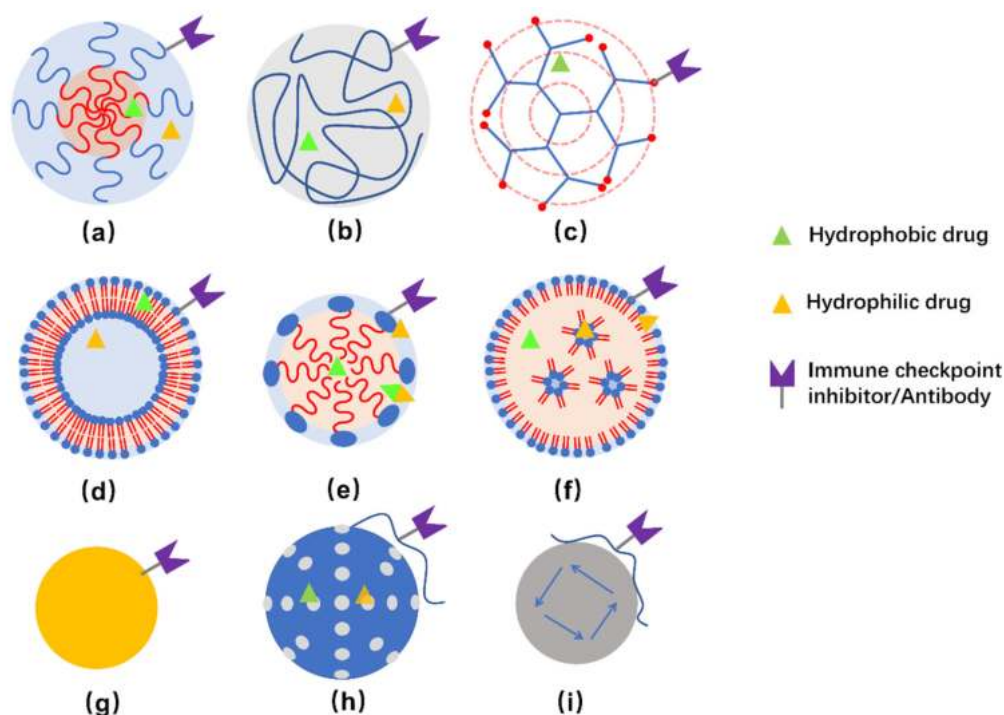
trial (NCT03036488, phase III) using a combination of pembrolizumab (MK-3475) and chemotherapy as adjuvant therapy for participants with early-stage TNBCs show that the rate of pathological complete response is significantly higher than in the placebo-chemotherapy group, even for patients with low PD-L1 expression [61].

## 2. Nanocarriers for the Immunotherapeutic Treatment of TNBC

The emergence of immunotherapy has shed light to the treatment of TNBC. However, due to the complex tumor microenvironment and complicated immunosuppressive mechanism, conventional drug administration methods are still limited to relatively low immune response and high adverse side effects. Thus, rational design of functional drug-delivery systems is necessary to improve drug targeting, control drug release, and obtain favorable pharmacokinetic behavior, enhanced drug absorption and more drug passing through biological barriers. In particular, using nanocarriers for the delivery of immune-responsive drugs can take advantage of the enhanced permeability and retention (EPR) effect, making more drug accumulate at the tumor site and a longer time circulation period [62–64]. The unique EPR effect and active targeting modification of drug-delivery systems play significant roles in the therapies for tumor in deep positions or metastasized. Therefore, nanocarrier-based immunotherapy may provide TNBC patients with safer and more effective treatment [65,66].

### 2.1. Nanomaterials for Delivering the Immunotherapeutic Agents of TNBC

Commonly studied NPs for delivering immunotherapeutic drugs to treat TNBC include polymeric micelles, dendrimers, liposomes, inorganic NPs, and so on [67]. Illustration of some representative NPs are presented in Figure 2.



**Figure 2.** Schemes of structure of polymeric nanocarriers (a–c), lipid-based nanocarriers (d–e), and inorganic NPs (g–i). (a) polymeric micelle, (b) polymeric NP, (c) dendrimer, (d) liposome, (e) lipid emulsion, (f) lipid NPs, (g) Au-NPs, (h) silica NPs, and (i) magnetic NPs. Hydrophobic, hydrophilic, as well as amphiphilic drugs can be embedded in corresponding regions. Meanwhile, it is possible to conjugate immune checkpoint inhibitors and/or antibodies to the surface of nanocarriers for therapeutic and/or targeting purposes. Usually, hybrid NPs are developed to obtain multiple function or improved properties for delivering the drugs.

The physiochemical properties of polymers, such as charge, hydrophobicity/hydrophilicity, as well as the features of the polymeric NPs, include size, shape, and rigidity, can be tuned for encapsulating specific immune-responsive drugs and be designed to improve the endocytic uptake, biodistribution, and body clearance properties as well [68–70]. Methods for preparing nano-sized polymeric particles include polymeric micelles prepared by self-assembling of co-polymer consisting of hydrophobic and hydrophilic sections, polymeric NPs prepared by solvent evaporation, emulsification/solvent diffusion, nanoprecipitation or emulsification/reverse salting-out, as well as dendrimers prepared by repetitive addition of monomers initiated from a polyfunctional center [71–73]. Poly(lactic-co-glycolic acid) (PLGA) and polylactic acid (PLA) are biocompatible and biodegradable polymers approved by FDA in drug-delivery systems [74,75]. Dendrimers are composed of a hydrophobic core, which favors the encapsulation of hydrophobic molecules, and the outer surface that provides sites for functionalization.

Lipids are amphiphilic molecules composed of hydrophilic headgroup and hydrophobic tail(s). Lipid-based nanocarriers for drug delivery include solid lipid nanoparticles, vesicular liposomes, nano-emulsions/nano-micelles, as well as non-spherical ones, such as nanotubes. The configuration of the nanocarriers strongly depends on the packing parameter of the lipids [76]. Phospholipids, being the major components of cell membranes, have attracted particular attention as drug-carrier materials due to their good biocompatible, low toxicity and higher permeation. Liposomes prepared from aggregated synthetic phospholipid(s) or even directly extracted from tumor cells are preferred as drug-delivery carriers [77,78]. Similar to polymeric micelles, liposomes, lipid emulsions as well as lipid NPs are composed of both hydrophobic and hydrophilic regions, which can be used to encapsulate hydrophobic and hydrophilic drugs, respectively. Amphiphilic drugs may also be encapsulated at the hydrophilic-hydrophobic interface.

Inorganic NPs are robust frameworks allowing encapsulation and incorporation of one or more drugs or therapeutic molecules. Several inorganic NPs, including gold NPs (Au-NPs), mesoporous silica NPs, magnetic NPs, and carbon nanotubes, have been investigated as nanocarriers for drug delivery [79]. In addition to the loaded therapeutic agents, some NPs exert specific functions by themselves. For example, Au-NPs can induce cell death [80], and can also adsorb light in the NIR region and dissipate heat to the surroundings. As for magnetic nanoparticles (MNPs), they not only generate nonuniform magnetic fields which affect the morphology, differentiation and function of cells by generating magnetically induced mechanical forces [81], but also activate anti-cancer immune responses through their own immunomodulatory effects [82]. Inorganic NPs coated with polymers or lipid bilayers, forming core-shell structures that enable surface modification and show enhanced biocompatibility, have also been widely studied [83].

## 2.2. Nanocarriers for the Delivery of Immune Checkpoint Blockade Molecules

IC blockade is the primary strategy for TNBC immunotherapy, but the effect of monotherapy is modest. Increasing the dose or choosing a combination of multiple ICIs is commonly used to overcome this problem. However, the increase in drug toxicity has led to the suspension of many clinical trials. For instance, in the randomized phase II trial NCT02519322, grade III adverse events occurred in 8% of patients treated with nivolumab monotherapy and in as high as 73% of patients treated with both nivolumab and ipilimumab [26].

Combining more than one ICIs can exert more effects than using one ICI. Considering there are more expressed CD155 and PD-L1 in TNBC than in other types of breast cancers, Chen et al. [84] designed mPEG-PLGA-PLL (PEAL) NPs loaded with CD155 siRNA (siCD155) by a double-emulsion method followed by coated with a PD-L1 blockade, termed as P/PEAL<sub>siCD155</sub>, for immunotherapy of TNBC. In CD8<sup>+</sup> TIL cells, CD155 can bind to different receptors, such as DNAM-1, TIGIT, and CD96 [85,86]. Based on the asynchronous expression of the above-mentioned receptors, this study shows that siCD155-mediated knockdown of CD155 by P/PEAL<sub>siCD155</sub> can achieve spatiotemporal targeting of surface

receptors and intracellular mRNA, making the antitumor effect take place in favorable periods, i.e., promoted CD155-mediated immune surveillance in the early stage and inhibited CD155-mediated immune evasion in the later stage. In the 4T1 TNBC tumor model, P/PEAL<sub>siCD155</sub> showed surprising biocompatibility, specific targeting, along with efficient inhibition of TNBC tumor progression and metastasis [84].

Discovering more efficient molecules is another option overcoming the problems along with monotherapy. NPs made of 100% BMS-200, a small-molecular inhibitor of PD-1/PD-L1 interaction, has also been developed as potential alternatives to anti-PD-L1 monoclonal antibody ( $\alpha$ -PD-L1) [87]. Compared with  $\alpha$ -PD-L1, BMS-202 NPs show equivalent immunotherapy effect by inhibiting >90% primary and distant tumors, and possible superior tumor penetration. The approach of using NPs for the delivery of immune checkpoint blockade molecules may provide an alternative nanomedicine for treating metastatic or advanced TNBC.

### 2.3. Nanoparticles for the Delivery of Combination Therapy Agents

The monotherapies of TNBC, including chemotherapy, radiotherapy, and immunotherapy based on ICs, all demonstrate limited therapeutic effect. Based on the low pH levels, endogenous H<sub>2</sub>O<sub>2</sub>, overexpressed enzymes, and other specific factors in the TME of TNBCs, combination therapy using immunotherapy with other specific treatment, such as chemotherapy, photothermal therapy (PTT), photodynamic therapy (PDT), and sonodynamic therapy (SDT), to overcome the insufficient efficacy by monotherapy and improve the therapeutic efficacy to TNBCs [88,89]. Combination therapy may also generate synergistic effect to the treatment of TNBC [90].

#### 2.3.1. Immunotherapy Combined with PTT

PTT is a process that converts light energy into heat to induce thermal ablation of the tumor. Near-infrared region (700–1350 nm) is the most commonly used wavelength, and recent studies have shown that light in the second near-infrared region (1000–1700 nm) has deeper tissue penetration and tolerance [91]. The conversion of electromagnetic energy into heat is achieved by photothermal agents (PAT). An excellent PAT is characterized by strong light absorption, strong photothermal conversion ability, stability, good biocompatibility, and the ability to turn off PTT in the non-treatment stage [92]. Near-infrared PAT include polyaniline [93], copper sulfides (CuS) NPs [94], as well as inorganic NPs, such as gold-based NPs [95]. Inorganic NPs show high photothermal conversion efficiency but relatively poor biocompatibility and toxicity [95], while liposome-based material and organic-conjugated polymers exhibit relatively better biocompatibility [96].

As PTT cannot directly kill tumor cells but acts as an adjuvant at about 45 °C, Huang et al. [97] developed a symbiotic mild photothermal-sensitized immunotherapy (SMPAI) and put forward a hypothesis of a synergistic effect by combining mild PTT with immunotherapy. They encapsulated a photothermal and photodynamic therapy agent (IR820) and an anti-PD-L1 antibody into a lipid gel composed of soybean phosphatidylcholine (SPC) and glycerol dioleate (GDO), which undergoes a reversible gel-to-sol transition for the controllable release of aPD-L1 and enhanced infiltration of T cells into tumor under manually controlled NIR irradiation. Overall, mild PTT can activate the systemic immune response, increase the number of TILs, and increase the expression of PD-L1 in tumor cells.

To specifically target CD44, Yasoathamani et al. [93] designed a conjugation of hyaluronan (HA)–polyaniline (PANi)–imiquimod (R837), denoted as HA-PANi/R837. The high photothermal conversion efficiency of PANi means that it has a significant thermal ablation effect in solid tumor. HA is a targeting ligand activating CD44 with high biosafety [98], which compensates for the poor targeting and low cellular uptake of PANi. R837 is a toll-like receptor 7 agonist, acting as an immunomodulator. In the TNBC model, HA-PANi/R837 directly killed a part of cancer cells through thermal ablation, induced the production of tumor-associated antigens, and activated immune response. Ultimately, the combination of HA-PANi/R837 and anti-CTLA-4 antibody shows enhanced immunother-

apy effect and played a synergistic antitumor effect. For research on PTT, it is clear that it has a certain tumor-killing effect, immunostimulatory effect, and NPs-based PTT can produce NPs-mediated antigen capture [99].

To suppress recurrence and metastasis of TNBC, Cheng et al. [94] designed a biomimetic nanopatform AM@DLMSN@CuS/R848, based on dendritic large-pore mesoporous silica nanoparticles (DLMSNs) loaded with CuS NPs, immune adjuvant R848 (resiquimod), TNBC cell membrane, and AUNP-12 (a PD-1/PD-L1 peptide inhibitor). AUNP-12 conjugated to the outer TNBC cell membrane by benzoic-imide bond readily released from the nanoparticle in the weakly acidic pH of tumor microenvironment. This nanocarrier exhibits targeted TNBC delivery, high photothermal efficiency of CuS NPs, photothermal-triggered release of R848, and pH-responsive release of AUNP-12, which together lead to strong antitumor efficacy and enhanced therapy against metastatic TNBC.

### 2.3.2. Immunotherapy Combined with PDT

PDT induces chemical cytotoxic effects to tumor cells on the generation of reactive oxygen species (ROS) [100]. Light, photosensitizer, and molecular oxygen are three indispensable elements for PDT. Light wavelengths in visible (400–700 nm) and near-infrared ranges (700–1350 nm) are commonly used. The photosensitizer absorbs photons and transforms from ground singlet state to excited singlet state, which afterwards generates excited triplet state and relaxation by undergoing intersystem crossing, accompanied by energy emitted as fluorescence, heat, and/or other photophysical energy [92]. The tetrapyrrole structure is extremely common in photosensitizer, and it is related to the photon absorption ability and the ability to convert the relatively low active triplet ground-state molecular oxygen ( $^3\text{O}_2$ ) into more active singlet oxygen ( $^1\text{O}_2$ ) [101]. Because oxygen content in TME is low (as TME is in a hypoxic state), it is challenging to provide enough molecular oxygen at tumor site for oxygen-dependent PDT.

Combining PDT with immunotherapy could play a synergistic effect. The release of ROS or PDT-induced exposure and/or release of damage-associated molecular patterns (DAMPs) would stimulate the body's immune system. The increase in immunogenicity induces the maturation of DCs and activation of cytotoxic T lymphocytes to increase the number of TILs [102]. In addition to the immune response caused by PDT itself, the combination of PDT with ICB also plays a synergistic effect in preclinical research. Zhang et al. [87] proved that BMS-202 NPs in combination with Ce6 NPs exhibited a better antitumor and antimetastatic effects. Chung et al. [103] designed smart multifunctional nanoparticle cluster, FM@VP, which combined co-assembly of a nanocomplex formed by a functional polysaccharide fucoidan and a bioreducible polyamidoamine dendrimer, and  $\text{MnO}_2$  NPs encapsulated with a photosensitizer verteporfin. It was able to target P-selectin-overexpressed TNBC. Moreover, due to the high concentration of glutathione, FM@VP clusters would rapidly disintegrate in tumor. The released verteporfin from the clusters enhanced PDT and inhibited yes-associated protein (involved in tumor development), which weakened tumor-mediated immunosuppression. Meanwhile,  $\text{MnO}_2$  NPs could efficiently convert  $\text{H}_2\text{O}_2$  into oxygen in TME, reducing the adverse impression caused by low-oxygen environments [104]. This discovery provided a powerful strategy for synergistic tumor targeting, PDT and immunotherapy.

### 2.3.3. Immunotherapy Combined with SDT

SDT is a non-invasive therapeutic modality based on ultrasound, which is more acceptable to patients than chemotherapy and radiotherapy. Low-intensity focused ultrasound is commonly used to activate sonosensitizers [105]. Compared with PTT and PDT, the tissue penetration ability of SDT is extremely powerful, thus therapeutic effect for tumors in deep positions is more significant [106,107]. Meanwhile, SDT generates many types of ROS, not only  $^1\text{O}_2$ , but also hydroxyl ( $\bullet\text{OH}$ ) and superoxide radicals ( $\bullet\text{O}_2^-$ ) [108]. Its functions include direct tumor cells killing, and indirect tumor-specific immunity activation through damaging blood vessels or inhibiting the regeneration of tumor tissues, et al. Sonosensitiz-

ers, including organic molecules (such as porphyrin derivatives), inorganic nanomaterials (such as TiO<sub>2</sub>, ZnO) as well as the hybrid ones, have been developed for SDT [109]. To better exert its immunomodulatory effect, the sonosensitizer was delivered through NPs drug-delivery system (DDS) when combined with immune adjuvants in some research.

In TNBC therapy, Chen et al. [110] designed a liposome-encapsulated anganese-protoporphyrin complex (MnP) and modified with folic acid (FA). In the 4T1 model, the multifunctional nanosensitizer FA-MnPs exhibited significant effect on both deep-state and superficial tumors. In addition to induce chemical damage to tumor cells, SDT could also exert an effect through immune regulation. For instance, M2 macrophages would develop towards the antitumor M1 phenotype. Similar to PDT, the damage-associated molecular patterns caused by SDT can also stimulate systemic immunity, including the maturation of DCs and the activation of cytotoxic T lymphocytes.

#### 2.3.4. Others

In addition to the direct delivery of immunomodulatory agent to the tumor site through the EPR effect, there are other studies focused on TME targeting. For example, although chemotherapy exert less efficacy to the treatment of TNBC, it also shows immunomodulatory effect on TME. Xu et al. [111] designed a peptide-based, structure-transformable NPs, 2-(Nap)-FFK<sub>Pt-2TPA-ADDGGGPLGVRG-WKYMVm-mPEG<sub>1000</sub></sub>, for contemporaneous delivery of chemotherapy agent for TNBC, cisplatin and adjuvant, as well as WKYMVm—an FPR-1 agonist functions as an immune adjuvant, which synergistically elicit and promote immunogenic cell death for TNBC immunotherapy. In another study, Xu et al. [112] prepared a puerarin nanoemulsion (nanoPue) surface modified with aminoethyl anisamide as targeting ligand to tumor-associated fibroblasts (TAFs). Together with improved solubility and bioavailability, the delivered puerarin significantly deactivate the stromal microenvironment, which synergistically enhances the activity of checkpoint blockade immunotherapy in a TNBC mode when combined with  $\alpha$ -PD-L1.

### 3. Conclusions and Perspective

In conclusion, immunotherapy has achieved many promising results in alleviating TNBC. In addition to the classic immune checkpoints PD-1/PD-L1 and CTLA-4, new immune checkpoints are constantly being discovered. At the same time, progress has been made in new treatments, including CAR-T and tumor immunization vaccines. ICIs are commonly used in combination with other therapy, such as chemotherapy, radiotherapy, CAR-T, and tumor vaccine, to obtain synergistic effects for more effective treatment of TNBCs. Moreover, the nano-delivery system integrated with TNBC immunotherapy provides strategy that can achieve precise targeting and reduce off-target effects. Immunotherapy has indeed brought hope to the treatment of TNBC. Although there are problems need to be solved, immunotherapy for TNBC is full of potential.

Finally, we may identify several issues and problems related to the immunotherapy of TNBC. These include: (1) The fundamental understanding of tumor heterogeneity, molecular changes, immunogenomics, and treatment resistance mechanisms in TNBC should be advanced to give better treatments to the patients. (2) The narrow therapeutic window is also a potential problem that needs to be resolved. Although the indication of drugs for monotherapy is clear, it still needs to be redefined in combination therapies. Most importantly, because the drug-delivery system of combination therapy is complex, it is more difficult to understand the mechanism. In particular, TME has changed tremendously when it comes to immunotherapy. Most of the research focus on DCs and TILs, but these are definitely not enough. Therefore, immune-regulatory mechanism needs to be further clarified when nanocarrier is involved in immunotherapy. (3) The discovery of new antigens specifically expressed in TNBC cells would facilitate the development of new immunotherapies. (4) For nanocarrier in immunotherapy of TNBC, the safety of nanomaterials is complicated. Particular attention should be paid to inorganic materials with poor biocompatibility and organic nanomaterials with good biocompatibility but

strong immunogenicity. (5) Immunoconjugates are effective with minimal toxicity, showing promise for clinical translation. Trodelvy (Sacituzumab govitecan), an antibody-drug conjugate consisting of an antibody Sacituzumab targeting the Trop-2 protein (found in more than 90% of TNBC), and coupled to chemotherapy drugs 7-ethyl-10-hydroxycamptothecin (SN-38, a topoisomerase I inhibitor to interfere with the replication of cancer cells) with a hydrolysable linker, is a first-in-class medicine for advanced TNBC therapy.

**Author Contributions:** Writing—original draft preparation, Y.C. and C.C.; writing—review and editing, Y.C., Y.T., W.L. and P.W.; funding acquisition, P.W. All authors have read and agreed to the published version of the manuscript.

**Funding:** This research was funded by the Science Technology Department of Zhejiang Province, China, Grant No. 2017C04009 and the Ministry of Science and Technology of the People’s Republic of China, Grant No. 2017YFE0130100.

**Institutional Review Board Statement:** Not applicable.

**Informed Consent Statement:** Not applicable.

**Data Availability Statement:** Not applicable.

**Conflicts of Interest:** The authors declare no conflict of interest.

## References

1. Siegel, R.L.; Miller, K.D.; Jemal, A. Cancer statistics, 2020. *CA Cancer J. Clin.* **2020**, *70*, 7–30. [CrossRef]
2. Carey, L.A.; Dees, E.C.; Sawyer, L.; Gatti, L.; Moore, D.T.; Collichio, F.; Ollila, D.W.; Sartor, C.I.; Graham, M.L.; Perou, C.M. The triple negative paradox: Primary tumor chemosensitivity of breast cancer subtypes. *Clin. Cancer Res.* **2007**, *13*, 2329–2334. [CrossRef]
3. Garrido-Castro, A.C.; Lin, N.U.; Polyak, K. Insights into molecular classifications of triple-negative breast cancer: Improving patient selection for treatment. *Cancer Discov.* **2019**, *9*, 176–198. [CrossRef]
4. Makhoul, I.; Atiq, M.; Alwbari, A.; Kieber-Emmons, T. Breast cancer immunotherapy: An update. *Breast Cancer (Auckl)* **2018**, *12*, 1–15. [CrossRef]
5. Yin, L.; Duan, J.J.; Bian, X.W.; Yu, S.C. Triple-negative breast cancer molecular subtyping and treatment progress. *Breast Cancer Res.* **2020**, *22*, 61. [CrossRef]
6. Emens, L.A. Breast cancer immunotherapy: Facts and hopes. *Clin. Cancer Res.* **2018**, *24*, 511–520. [CrossRef]
7. Deepak, K.G.K.; Vempati, R.; Nagaraju, G.P.; Dasari, V.R.; Nagini, S.; Rao, D.N.; Malla, R.R. Tumor microenvironment: Challenges and opportunities in targeting metastasis of triple negative breast cancer. *Pharmacol. Res.* **2020**, *153*, 104683. [CrossRef]
8. Belli, C.; Trapani, D.; Viale, G.; D’Amico, P.; Duso, B.A.; Della Vigna, P.; Orsi, F.; Curigliano, G. Targeting the microenvironment in solid tumors. *Cancer Treat. Rev.* **2018**, *65*, 22–32. [CrossRef]
9. Shihab, I.; Khalil, B.A.; Elemam, N.M.; Hachim, I.Y.; Hachim, M.Y.; Hamoudi, R.A.; Maghazachi, A.A. Understanding the role of innate immune cells and identifying genes in breast cancer microenvironment. *Cancers* **2020**, *12*, 2226. [CrossRef]
10. Gajewski, T.F.; Schreiber, H.; Fu, Y.X. Innate and adaptive immune cells in the tumor microenvironment. *Nat. Immunol.* **2013**, *14*, 1014–1022. [CrossRef]
11. Whiteside, T.L. FOXP3+ Treg as a therapeutic target for promoting anti-tumor immunity. *Expert Opin. Ther. Targets* **2018**, *22*, 353–363. [CrossRef]
12. Tanaka, A.; Sakaguchi, S. Targeting Treg cells in cancer immunotherapy. *Eur. J. Immunol.* **2019**, *49*, 1140–1146. [CrossRef]
13. Li, C.; Jiang, P.; Wei, S.; Xu, X.; Wang, J. Regulatory T cells in tumor microenvironment: New mechanisms, potential therapeutic strategies and future prospects. *Mol. Cancer* **2020**, *19*, 116. [CrossRef]
14. Topalian, S.L.; Taube, J.M.; Anders, R.A.; Pardoll, D.M. Mechanism-driven biomarkers to guide immune checkpoint blockade in cancer therapy. *Nat. Rev. Cancer* **2016**, *16*, 275–287. [CrossRef]
15. Wang, S.; Xie, K.; Liu, T. Cancer immunotherapies: From efficacy to resistance mechanisms—Not only checkpoint matters. *Front. Immunol.* **2021**, *12*, 690112. [CrossRef]
16. Hosseini, A.; Gharibi, T.; Marofi, F.; Babaloo, Z.; Baradaran, B. CTLA-4: From mechanism to autoimmune therapy. *Int. ImmunoPharmacol.* **2020**, *80*, 106221. [CrossRef]
17. Boussiotis, V.A.; Longo, D.L. Molecular and biochemical aspects of the PD-1 checkpoint pathway. *N. Engl. J. Med.* **2016**, *375*, 1767–1778. [CrossRef]
18. Gatalica, Z.; Snyder, C.; Maney, T.; Ghazalpour, A.; Holterman, D.; Nianqing, X.; Overberg, P.; Rose, I.; Basu, G.D.; Vranic, S.; et al. Programmed cell death 1 (PD-1) and its ligand (PD-L1) in common cancers and their correlation with molecular cancer type. *Cancer Epidemiol. Biomark. Prev.* **2014**, *23*, 2965–2970. [CrossRef]
19. Sharpe, A.H.; Freeman, G.J. The B7-CD28 superfamily. *Nat. Rev. Immunol.* **2002**, *2*, 116–126. [CrossRef]

20. Hargadon, K.M.; Johnson, C.E.; Williams, C.J. Immune checkpoint blockade therapy for cancer: An overview of FDA-approved immune checkpoint inhibitors. *Int. ImmunoPharmacol.* **2018**, *62*, 29–39. [CrossRef]
21. Markham, A.; Duggan, S. Cemiplimab: First global approval. *Drugs* **2018**, *78*, 1841–1846. [CrossRef]
22. Kwok, G.; Yau, T.C.; Chiu, J.W.; Tse, E.; Kwong, Y.L. Pembrolizumab (Keytruda). *Hum. Vaccin Immunother.* **2016**, *12*, 2777–2789. [CrossRef]
23. Zhao, X.; Shen, J.; Ivaturi, V.; Gopalakrishnan, M.; Feng, Y.; Schmidt, B.J.; Statkevich, P.; Goodman, V.; Gobburu, J.; Bello, A.; et al. Model-based evaluation of the efficacy and safety of nivolumab once every 4 weeks across multiple tumor types. *Ann. Oncol.* **2020**, *31*, 302–309. [CrossRef]
24. Lee, H.T.; Lee, J.Y.; Lim, H.; Lee, S.H.; Moon, Y.J.; Pyo, H.J.; Ryu, S.E.; Shin, W.; Heo, Y.S. Molecular mechanism of PD-1/PD-L1 blockade via anti-PD-L1 antibodies atezolizumab and durvalumab. *Sci. Rep.* **2017**, *7*, 5532. [CrossRef]
25. Demaria, S.; Kawashima, N.; Yang, A.M.; Devitt, M.; Babb, J.S.; Allison, J.P.; Formenti, S.C. Immune-mediated inhibition of metastases after treatment with local radiation and CTLA-4 blockade in a mouse model of breast cancer. *Clin. Cancer Res.* **2005**, *11*, 728–734.
26. Amaria, R.N.; Reddy, S.M.; Tawbi, H.A.; Davies, M.A.; Ross, M.I.; Glitza, I.C.; Cormier, J.N.; Lewis, C.; Hwu, W.J.; Hanna, E.; et al. Neoadjuvant immune checkpoint blockade in high-risk resectable melanoma. *Nat. Med.* **2018**, *24*, 1649–1654. [CrossRef]
27. Mediratta, K.; El-Sahli, S.; D’Costa, V.; Wang, L. Current progresses and challenges of immunotherapy in triple-negative breast cancer. *Cancers* **2020**, *12*, 3529. [CrossRef]
28. Nanda, R.; Chow, L.Q.; Dees, E.C.; Berger, R.; Gupta, S.; Geva, R.; Puzstai, L.; Pathiraja, K.; Aktan, G.; Cheng, J.D.; et al. Pembrolizumab in patients with advanced triple-negative breast cancer: Phase Ib KEYNOTE-012 study. *J. Clin. Oncol.* **2016**, *34*, 2460–2467. [CrossRef]
29. Adams, S.; Schmid, P.; Rugo, H.S.; Winer, E.P.; Loirat, D.; Awada, A.; Cescon, D.W.; Iwata, H.; Campone, M.; Nanda, R.; et al. Pembrolizumab monotherapy for previously treated metastatic triple-negative breast cancer: Cohort A of the phase II KEYNOTE-086 study. *Ann. Oncol.* **2019**, *30*, 397–404. [CrossRef]
30. ClinicalTrials.gov. Available online: <https://clinicaltrials.gov/ct2/home> (accessed on 2 November 2021).
31. Joller, N.; Kuchroo, V.K. Tim-3, Lag-3, and TIGIT. *Curr Top. Microbiol. Immunol.* **2017**, *410*, 127–156. [CrossRef]
32. Du, W.; Yang, M.; Turner, A.; Xu, C.; Ferris, R.L.; Huang, J.; Kane, L.P.; Lu, B. TIM-3 as a target for cancer immunotherapy and mechanisms of action. *Int. J. Mol. Sci.* **2017**, *18*, 645. [CrossRef]
33. Byun, K.D.; Hwang, H.J.; Park, K.J.; Kim, M.C.; Cho, S.H.; Ju, M.H.; Lee, J.H.; Jeong, J.S. T-cell immunoglobulin mucin 3 expression on tumor infiltrating lymphocytes as a positive prognosticator in triple-negative breast cancer. *J. Breast Cancer* **2018**, *21*, 406–414. [CrossRef]
34. Wolf, Y.; Anderson, A.C.; Kuchroo, V.K. TIM3 comes of age as an inhibitory receptor. *Nat. Rev. Immunol.* **2020**, *20*, 173–185. [CrossRef]
35. Iain, A.; Murray, A.D.P.; Gary, H. Perdew. AH receptor ligands in cancer: Friend and foe. *Nat. Rev. Cancer* **2014**, *14*, 801–814. [CrossRef]
36. Brochez, L.; Chevolet, I.; Kruse, V. The rationale of indoleamine 2,3-dioxygenase inhibition for cancer therapy. *Eur. J. Cancer* **2017**, *76*, 167–182. [CrossRef]
37. Wei, L.; Zhu, S.; Li, M.; Li, F.; Wei, F.; Liu, J.; Ren, X. High indoleamine 2,3-dioxygenase is correlated with microvessel density and worse prognosis in breast cancer. *Front. Immunol.* **2018**, *9*, 724. [CrossRef]
38. Asghar, K.; Loya, A.; Rana, I.A.; Tahseen, M.; Ishaq, M.; Farooq, A.; Bakar, M.A.; Masood, I. Indoleamine 2,3-dioxygenase expression and overall survival in patients diagnosed with breast cancer in Pakistan. *Cancer Manag. Res.* **2019**, *11*, 475–481. [CrossRef]
39. Tang, K.; Wu, Y.H.; Song, Y.; Yu, B. Indoleamine 2,3-dioxygenase 1 (IDO1) inhibitors in clinical trials for cancer immunotherapy. *J. Hematol. Oncol.* **2021**, *14*, 68. [CrossRef]
40. Wang, L.; Rubinstein, R.; Lines, J.L.; Wasiuk, A.; Ahonen, C.; Guo, Y.; Lu, L.F.; Gondek, D.; Wang, Y.; Fava, R.A.; et al. VISTA, a novel mouse Ig superfamily ligand that negatively regulates T cell responses. *J. Exp. Med.* **2011**, *208*, 577–592. [CrossRef]
41. Slater, B.T.; Han, X.; Chen, L.; Xiong, Y. Structural insight into T cell coinhibition by PD-1H (VISTA). *Proc. Natl. Acad. Sci. USA* **2020**, *117*, 1648–1657. [CrossRef]
42. Xie, X.; Zhang, J.; Shi, Z.; Liu, W.; Hu, X.; Qie, C.; Chen, W.; Wang, Y.; Wang, L.; Jiang, J.; et al. The expression pattern and clinical significance of the immune checkpoint regulator VISTA in human breast cancer. *Front. Immunol.* **2020**, *11*, 563044. [CrossRef]
43. Gao, J.; Ward, J.F.; Pettaway, C.A.; Shi, L.Z.; Subudhi, S.K.; Vence, L.M.; Zhao, H.; Chen, J.; Chen, H.; Efstathiou, E.; et al. VISTA is an inhibitory immune checkpoint that is increased after ipilimumab therapy in patients with prostate cancer. *Nat. Med.* **2017**, *23*, 551–555. [CrossRef]
44. Cao, X.; Ren, X.; Zhou, Y.; Mao, F.; Lin, Y.; Wu, H.; Sun, Q. VISTA expression on immune cells correlates with favorable prognosis in patients with triple-negative breast cancer. *Front. Oncol.* **2020**, *10*, 583966. [CrossRef]
45. Wei, H.; Wang, Z.; Kuang, Y.; Wu, Z.; Zhao, S.; Zhang, Z.; Li, H.; Zheng, M.; Zhang, N.; Long, C.; et al. Intercellular adhesion molecule-1 as target for CAR-T-cell therapy of triple-negative breast cancer. *Front. Immunol.* **2020**, *11*, 573823. [CrossRef]
46. Cummins, K.D.; Gill, S. Anti-CD123 chimeric antigen receptor T-cells (CART): An evolving treatment strategy for hematological malignancies, and a potential ace-in-the-hole against antigen-negative relapse. *Leuk. Lymphoma* **2018**, *59*, 1539–1553. [CrossRef]
47. Wei, J.; Han, X.; Bo, J.; Han, W. Target selection for CAR-T therapy. *J. Hematol. Oncol.* **2019**, *12*, 62. [CrossRef]

48. Song, D.G.; Ye, Q.; Poussin, M.; Chacon, J.A.; Figini, M.; Powell, D.J., Jr. Effective adoptive immunotherapy of triple-negative breast cancer by folate receptor-alpha redirected CAR T cells is influenced by surface antigen expression level. *J. Hematol. Oncol.* **2016**, *9*, 56. [CrossRef]
49. Zhou, R.; Yazdanifar, M.; Roy, L.D.; Whilding, L.M.; Gavrill, A.; Maher, J.; Mukherjee, P. CAR T cells targeting the tumor MUC1 glycoprotein reduce triple-negative breast cancer growth. *Front. Immunol.* **2019**, *10*, 1149. [CrossRef]
50. Xia, L.; Zheng, Z.; Liu, J.Y.; Chen, Y.J.; Ding, J.; Hu, G.S.; Hu, Y.H.; Liu, S.; Luo, W.X.; Xia, N.S.; et al. Targeting triple-negative breast cancer with combination therapy of EGFR CAR T cells and CDK7 inhibition. *Cancer Immunol. Res.* **2021**, *9*, 707–722. [CrossRef]
51. Stuber, T.; Monjezi, R.; Wallstabe, L.; Kuhnemundt, J.; Nietzer, S.L.; Dandekar, G.; Wockel, A.; Einsele, H.; Wischhusen, J.; Hudecek, M. Inhibition of TGF-beta-receptor signaling augments the antitumor function of ROR1-specific CAR T-cells against triple-negative breast cancer. *J. Immunother. Cancer* **2020**, *8*, e000676. [CrossRef]
52. Yarchoan, M.; Johnson, B.A., 3rd; Lutz, E.R.; Laheru, D.A.; Jaffee, E.M. Targeting neoantigens to augment antitumour immunity. *Nat. Rev. Cancer* **2017**, *17*, 209–222. [CrossRef]
53. Zhang, Z.; Lu, M.; Qin, Y.; Gao, W.; Tao, L.; Su, W.; Zhong, J. Neoantigen: A new breakthrough in tumor immunotherapy. *Front. Immunol.* **2021**, *12*, 672356. [CrossRef]
54. Liu, L.; Wang, Y.; Miao, L.; Liu, Q.; Musetti, S.; Li, J.; Huang, L. Combination immunotherapy of MUC1 mRNA nano-vaccine and CTLA-4 blockade effectively inhibits growth of triple negative breast cancer. *Mol. Ther.* **2018**, *26*, 45–55. [CrossRef]
55. Pack, C.D.; Bommireddy, R.; Munoz, L.E.; Patel, J.M.; Bozeman, E.N.; Dey, P.; Radhakrishnan, V.; Vartabedian, V.F.; Venkat, K.; Ramachandiran, S.; et al. Tumor membrane-based vaccine immunotherapy in combination with anti-CTLA-4 antibody confers protection against immune checkpoint resistant murine triple-negative breast cancer. *Hum. Vaccin Immunother.* **2020**, *16*, 3184–3193. [CrossRef]
56. Ho, A.Y.; Barker, C.A.; Arnold, B.B.; Powell, S.N.; Hu, Z.I.; Gucalp, A.; Lebron-Zapata, L.; Wen, H.Y.; Kallman, C.; D’Agnolo, A.; et al. A Phase 2 clinical trial assessing the efficacy and safety of pembrolizumab and radiotherapy in patients with metastatic triple-negative breast cancer. *Cancer* **2020**, *126*, 850–860. [CrossRef]
57. Cortes, J.; Cescon, D.W.; Rugo, H.S.; Nowecki, Z.; Im, S.-A.; Yusof, M.M.; Gallardo, C.; Lipatov, O.; Barrios, C.H.; Holgado, E.; et al. Pembrolizumab plus chemotherapy versus placebo plus chemotherapy for previously untreated locally recurrent inoperable or metastatic triple-negative breast cancer (KEYNOTE-355): A randomised, placebo-controlled, double-blind, phase 3 clinical trial. *Lancet* **2020**, *396*, 1817–1828. [CrossRef]
58. Schmid, P.; Rugo, H.S.; Adams, S.; Schneeweiss, A.; Barrios, C.H.; Iwata, H.; Diéras, V.; Henschel, V.; Molinero, L.; Chui, S.Y.; et al. Atezolizumab plus nab-paclitaxel as first-line treatment for unresectable, locally advanced or metastatic triple-negative breast cancer (IMpassion130): Updated efficacy results from a randomised, double-blind, placebo-controlled, phase 3 trial. *Lancet Oncol.* **2020**, *21*, 44–59. [CrossRef]
59. Bernier, C.; Soliman, A.; Gravel, M.; Dankner, M.; Savage, P.; Petrecca, K.; Park, M.; Siegel, P.M.; Shore, G.C.; Roulston, A. DZ-2384 has a superior preclinical profile to taxanes for the treatment of triple-negative breast cancer and is synergistic with anti-CTLA-4 immunotherapy. *Anticancer Drugs* **2018**, *29*, 774–785. [CrossRef]
60. Li, M.; Xing, S.; Zhang, H.; Shang, S.; Li, X.; Ren, B.; Li, G.; Chang, X.; Li, Y.; Li, W. A matrix metalloproteinase inhibitor enhances anti-cytotoxic T lymphocyte antigen-4 antibody immunotherapy in breast cancer by reprogramming the tumor microenvironment. *Oncol. Rep.* **2016**, *35*, 1329–1339. [CrossRef]
61. Schmid, P.; Cortes, J.; Pusztai, L.; McArthur, H.; Kummel, S.; Bergh, J.; Denkert, C.; Park, Y.H.; Hui, R.; Harbeck, N.; et al. Pembrolizumab for early triple-negative breast cancer. *N. Engl. J. Med.* **2020**, *382*, 810–821. [CrossRef]
62. Li, Y.; Zhang, X.; Liu, X.; Pan, W.; Li, N.; Tang, B. Designing and engineering of nanocarriers for bioapplication in cancer immunotherapy. *ACS Appl. Bio Mater.* **2020**, *3*, 8321–8337. [CrossRef]
63. Allen, T.M.; Cullis, P.R. Drug delivery systems: Entering the mainstream. *Science* **2004**, *303*, 1818–1822. [CrossRef]
64. Farokhzad, O.C.; Langer, R. Impact of nanotechnology on drug delivery. *ACS Nano* **2009**, *3*, 16–20. [CrossRef]
65. Gu, Z.; Da Silva, C.G.; Van der Maaden, K.; Ossendorp, F.; Cruz, L.J. Liposome-based drug delivery systems in cancer immunotherapy. *Pharmaceutics* **2020**, *12*, 1054. [CrossRef]
66. Johnson, R.; Sabnis, N.; McConathy, W.J.; Lacko, A.G. The potential role of nanotechnology in therapeutic approaches for triple negative breast cancer. *Pharmaceutics* **2013**, *5*, 353–370. [CrossRef]
67. Jain, V.; Kumar, H.; Anod, H.V.; Chand, P.; Gupta, N.V.; Dey, S.; Kesharwani, S.S. A review of nanotechnology-based approaches for breast cancer and triple-negative breast cancer. *J. Control. Release* **2020**, *326*, 628–647. [CrossRef]
68. Soppimath, K.S.; Aminabhavi, T.M.; Kulkarni, A.R.; Rudzinski, W.E. Biodegradable polymeric nanoparticles as drug delivery devices. *J. Control. Release* **2001**, *70*, 1–20. [CrossRef]
69. Bertrand, N.; Grenier, P.; Mahmoudi, M.; Lima, E.M.; Appel, E.A.; Dormont, F.; Lim, J.M.; Karnik, R.; Langer, R.; Farokhzad, O.C. Mechanistic understanding of in vivo protein corona formation on polymeric nanoparticles and impact on pharmacokinetics. *Nat. Commun.* **2017**, *8*, 777. [CrossRef]
70. Hickey, J.W.; Santos, J.L.; Williford, J.M.; Mao, H.Q. Control of polymeric nanoparticle size to improve therapeutic delivery. *J. Control. Release* **2015**, *219*, 536–547. [CrossRef]
71. Zielinska, A.; Carreiro, F.; Oliveira, A.M.; Neves, A.; Pires, B.; Venkatesh, D.N.; Durazzo, A.; Lucarini, M.; Eder, P.; Silva, A.M.; et al. Polymeric nanoparticles: Production, characterization, toxicology and ecotoxicology. *Molecules* **2020**, *25*, 3731. [CrossRef]



72. Jones, M.-C.; Leroux, J.-C. Polymeric micelles—A new generation of colloidal drug carriers. *Eur. J. Pharm. Biopharm.* **1999**, *48*, 101–111. [CrossRef]
73. Kesharwani, P.; Jain, K.; Jain, N.K. Dendrimer as nanocarrier for drug delivery. *Prog. Polym. Sci.* **2014**, *39*, 268–307. [CrossRef]
74. Makadia, H.K.; Siegel, S.J. Poly lactic-co-glycolic acid (PLGA) as biodegradable controlled drug delivery carrier. *Polymers* **2011**, *3*, 1377–1397. [CrossRef]
75. Tyler, B.; Gullotti, D.; Mangraviti, A.; Utsuki, T.; Brem, H. Polylactic acid (PLA) controlled delivery carriers for biomedical applications. *Adv. Drug Deliv. Rev.* **2016**, *107*, 163–175. [CrossRef]
76. Israelachvili, J.N. *Intermolecular and Surface Forces*, 3rd ed.; Academic Press: Cambridge, MA, USA, 2015.
77. Olusanya, T.O.B.; Haj Ahmad, R.R.; Ibegbu, D.M.; Smith, J.R.; Elkordy, A.A. Liposomal drug delivery systems and anticancer drugs. *Molecules* **2018**, *23*, 907. [CrossRef]
78. Park, J.W. Liposome-based drug delivery in breast cancer treatment. *Breast Cancer Res.* **2002**, *4*, 95–99. [CrossRef]
79. Huang, H.C.; Barua, S.; Sharma, G.; Dey, S.K.; Rege, K. Inorganic nanoparticles for cancer imaging and therapy. *J. Control. Release* **2011**, *155*, 344–357. [CrossRef]
80. Surapaneni, S.K.; Bashir, S.; Tikoo, K. Gold nanoparticles-induced cytotoxicity in triple negative breast cancer involves different epigenetic alterations depending upon the surface charge. *Sci. Rep.* **2018**, *8*, 12295. [CrossRef]
81. Wosik, J.; Chen, W.; Qin, K.; Ghobrial, R.M.; Kubiak, J.Z.; Kloc, M. Magnetic field changes macrophage phenotype. *Biophys. J.* **2018**, *114*, 2001–2013. [CrossRef]
82. Cheng, H.W.; Tsao, H.Y.; Chiang, C.S.; Chen, S.Y. Advances in magnetic nanoparticle-mediated cancer immune-theranostics. *Adv. Healthc. Mater.* **2021**, *10*, e2001451. [CrossRef]
83. Bayda, S.; Hadla, M.; Palazzolo, S.; Riello, P.; Corona, G.; Toffoli, G.; Rizzolio, F. Inorganic nanoparticles for cancer therapy: A transition from lab to clinic. *Curr. Med. Chem.* **2018**, *25*, 4269–4303. [CrossRef]
84. Chen, C.; Guo, Q.; Fu, H.; Yu, J.; Wang, L.; Sun, Y.; Zhang, J.; Duan, Y. Asynchronous blockade of PD-L1 and CD155 by polymeric nanoparticles inhibits triple-negative breast cancer progression and metastasis. *Biomaterials* **2021**, *275*, 120988. [CrossRef]
85. Manieri, N.A.; Chiang, E.Y.; Grogan, J.L. TIGIT: A key inhibitor of the cancer immunity cycle. *Trends Immunol.* **2017**, *38*, 20–28. [CrossRef]
86. O'Donnell, J.S.; Madore, J.; Li, X.Y.; Smyth, M.J. Tumor intrinsic and extrinsic immune functions of CD155. *Semin. Cancer Biol.* **2020**, *65*, 189–196. [CrossRef]
87. Zhang, R.; Zhu, Z.; Lv, H.; Li, F.; Sun, S.; Li, J.; Lee, C.S. Immune checkpoint blockade mediated by a small-molecule nanoinhibitor targeting the PD-1/PD-L1 pathway synergizes with photodynamic therapy to elicit antitumor immunity and antimetastatic effects on breast cancer. *Small* **2019**, *15*, e1903881. [CrossRef]
88. Sau, S.; Alsaab, H.O.; Bhise, K.; Alzhrani, R.; Nabil, G.; Iyer, A.K. Multifunctional nanoparticles for cancer immunotherapy: A groundbreaking approach for reprogramming malfunctioned tumor environment. *J. Control. Release* **2018**, *274*, 24–34. [CrossRef]
89. Hou, X.; Tao, Y.; Pang, Y.; Li, X.; Jiang, G.; Liu, Y. Nanoparticle-based photothermal and photodynamic immunotherapy for tumor treatment. *Int. J. Cancer* **2018**, *143*, 3050–3060. [CrossRef]
90. Feng, B.; Niu, Z.; Hou, B.; Zhou, L.; Li, Y.; Yu, H. Enhancing triple negative breast cancer immunotherapy by ICG-templated self-assembly of Paclitaxel nanoparticles. *Adv. Funct. Mater.* **2019**, *30*, 1906605. [CrossRef]
91. Zhang, Y.; Zhang, S.; Zhang, Z.; Ji, L.; Zhang, J.; Wang, Q.; Guo, T.; Ni, S.; Cai, R.; Mu, X.; et al. Recent progress on NIR-II photothermal therapy. *Front. Chem.* **2021**, *9*, 728066. [CrossRef]
92. Li, X.; Lovell, J.F.; Yoon, J.; Chen, X. Clinical development and potential of photothermal and photodynamic therapies for cancer. *Nat. Rev. Clin. Oncol.* **2020**, *17*, 657–674. [CrossRef]
93. Yasothamani, V.; Karthikeyan, L.; Shyamsivappan, S.; Haldorai, Y.; Seetha, D.; Vivek, R. Synergistic effect of photothermally targeted NIR-responsive nanomedicine-induced immunogenic cell death for effective triple negative breast cancer therapy. *Biomacromolecules* **2021**, *22*, 2472–2490. [CrossRef]
94. Cheng, Y.; Chen, Q.; Guo, Z.; Li, M.; Yang, X.; Wan, G.; Chen, H.; Zhang, Q.; Wang, Y. An intelligent biomimetic nanoplatfor for holistic treatment of metastatic triple-negative breast cancer via photothermal ablation and immune remodeling. *ACS Nano* **2020**, *14*, 15161–15181. [CrossRef]
95. Khafaji, M.; Zamani, M.; Golizadeh, M.; Bavi, O. Inorganic nanomaterials for chemo/photothermal therapy: A promising horizon on effective cancer treatment. *Biophys. Rev.* **2019**, *11*, 335–352. [CrossRef]
96. Lv, S.; Miao, Y.; Liu, D.; Song, F. Recent development of photothermal agents (PTAs) based on small organic molecular dyes. *ChemBioChem* **2020**, *21*, 2098–2110. [CrossRef]
97. Huang, L.; Li, Y.; Du, Y.; Zhang, Y.; Wang, X.; Ding, Y.; Yang, X.; Meng, F.; Tu, J.; Luo, L.; et al. Mild photothermal therapy potentiates anti-PD-L1 treatment for immunologically cold tumors via an all-in-one and all-in-control strategy. *Nat. Commun.* **2019**, *10*, 4871. [CrossRef]
98. Huang, G.; Huang, H. Application of hyaluronic acid as carriers in drug delivery. *Drug Deliv.* **2018**, *25*, 766–772. [CrossRef]
99. Balakrishnan, P.B.; Sweeney, E.E.; Ramanujam, A.S.; Fernandes, R. Photothermal therapies to improve immune checkpoint blockade for cancer. *Int. J. Hyperth.* **2020**, *37*, 34–49. [CrossRef]
100. Luby, B.M.; Walsh, C.D.; Zheng, G. Advanced photosensitizer activation strategies for smarter photodynamic therapy beacons. *Angew. Chem. Int. Ed. Engl.* **2019**, *58*, 2558–2569. [CrossRef]

101. Ming, L.; Cheng, K.; Chen, Y.; Yang, R.; Chen, D. Enhancement of tumor lethality of ROS in photodynamic therapy. *Cancer Med.* **2021**, *10*, 257–268. [CrossRef]
102. Yang, W.; Zhang, F.; Deng, H.; Lin, L.; Wang, S.; Kang, F.; Yu, G.; Lau, J.; Tian, R.; Zhang, M.; et al. Smart nanovesicle-mediated immunogenic cell death through tumor microenvironment modulation for effective photodynamic immunotherapy. *ACS Nano* **2020**, *14*, 620–631. [CrossRef]
103. Chung, C.-H.; Lu, K.-Y.; Lee, W.-C.; Hsu, W.-J.; Lee, W.-F.; Dai, J.-Z.; Shueng, P.-W.; Lin, C.-W.; Mi, F.-L. Fucoidan-based, tumor-activated nanoplatform for overcoming hypoxia and enhancing photodynamic therapy and antitumor immunity. *Biomaterials* **2020**, *257*, 120227. [CrossRef]
104. Shamay, Y.; Elkabets, M.; Li, H.; Shah, J.; Brook, S.; Wang, F.; Adler, K.; Baut, E.; Scaltriti, M.; Jena, P.V. P-selectin is a nanotherapeutic delivery target in the tumor microenvironment. *Sci. Transl. Med.* **2016**, *8*, 345ra87. [CrossRef]
105. Lafond, M.; Yoshizawa, S.; Umemura, S.I. Sonodynamic therapy: Advances and challenges in clinical translation. *J. Ultrasound. Med.* **2019**, *38*, 567–580. [CrossRef]
106. Canavese, G.; Ancona, A.; Racca, L.; Canta, M.; Dumontel, B.; Barbaresco, F.; Limongi, T.; Cauda, V. Nanoparticle-assisted ultrasound: A special focus on sonodynamic therapy against cancer. *Chem. Eng. J.* **2018**, *340*, 155–172. [CrossRef]
107. Wan, G.Y.; Liu, Y.; Chen, B.W.; Liu, Y.Y.; Wang, Y.S.; Zhang, N. Recent advances of sonodynamic therapy in cancer treatment. *Cancer Biol. Med.* **2016**, *13*, 325–338. [CrossRef]
108. Pan, X.; Bai, L.; Wang, H.; Wu, Q.; Wang, H.; Liu, S.; Xu, B.; Shi, X.; Liu, H. Metal-organic-framework-derived carbon nanostructure augmented sonodynamic cancer therapy. *Adv. Mater.* **2018**, *30*, e1800180. [CrossRef]
109. Son, S.; Kim, J.H.; Wang, X.; Zhang, C.; Yoon, S.A.; Shin, J.; Sharma, A.; Lee, M.H.; Cheng, L.; Wu, J.; et al. Multifunctional sonosensitizers in sonodynamic cancer therapy. *Chem. Soc. Rev.* **2020**, *49*, 3244–3261. [CrossRef]
110. Chen, H.; Liu, L.; Ma, A.; Yin, T.; Chen, Z.; Liang, R.; Qiu, Y.; Zheng, M.; Cai, L. Noninvasively immunogenic sonodynamic therapy with manganese protoporphyrin liposomes against triple-negative breast cancer. *Biomaterials* **2021**, *269*, 120639. [CrossRef]
111. Xu, C.; Yu, Y.; Sun, Y.; Kong, L.; Yang, C.; Hu, M.; Yang, T.; Zhang, J.; Hu, Q.; Zhang, Z. Transformable nanoparticle-enabled synergistic elicitation and promotion of immunogenic cell death for triple-negative breast cancer immunotherapy. *Adv. Funct. Mater.* **2019**, *29*, 1905213. [CrossRef]
112. Xu, H.; Hu, M.; Liu, M.; An, S.; Guan, K.; Wang, M.; Li, L.; Zhang, J.; Li, J.; Huang, L. Nano-puerarin regulates tumor microenvironment and facilitates chemo- and immunotherapy in murine triple negative breast cancer model. *Biomaterials* **2020**, *235*, 119769. [CrossRef]



## Article

# PD-1 Cellular Nanovesicles Carrying Gemcitabine to Inhibit the Proliferation of Triple Negative Breast Cancer Cell

Hualian Zha<sup>1,2,†</sup>, Zhanxue Xu<sup>1,†</sup>, Xichao Xu<sup>3,†</sup>, Xingyu Lu<sup>1</sup>, Peilin Shi<sup>1</sup>, Youmei Xiao<sup>1</sup>, Hsiang-I Tsai<sup>1</sup>, Dandan Su<sup>1</sup>, Fang Cheng<sup>1,4,\*</sup>, Xiaoli Cheng<sup>4,\*</sup> and Hongbo Chen<sup>1,\*</sup>

- <sup>1</sup> School of Pharmaceutical Sciences (Shenzhen), Shenzhen Campus of Sun Yat-sen University, Shenzhen 518107, China; zhahlian@mail2.sysu.edu.cn (H.Z.); 15602493072@163.com (Z.X.); luxy86@mail2.sysu.edu.cn (X.L.); shiplin@mail2.sysu.edu.cn (P.S.); xiaoy9@mail2.sysu.edu.cn (Y.X.); tsaihsangi88@163.com (H.-I.T.); sudd6@mail2.sysu.edu.cn (D.S.)
- <sup>2</sup> Department of Pharmacy, Guangzhou Institute of Respiratory Health, First Affiliated Hospital of Guangzhou Medical University, Guangzhou 510120, China
- <sup>3</sup> Endoscopy Center and Gastroenterology Department, Key Laboratory for Precision Diagnosis and Treatment of Pediatric Digestive System Diseases, Shenzhen Children's Hospital, Shenzhen 518036, China; xichaoxu0@163.com
- <sup>4</sup> Department of Pharmacy, Shenzhen Bao'an Maternal and Child Health Hospital, Shenzhen 518133, China
- \* Correspondence: chengf9@mail.sysu.edu.cn (F.C.); cattyh@126.com (X.C.); chenhb7@mail.sysu.edu.cn (H.C.)
- † These authors contribute equally to this work.

**Citation:** Zha, H.; Xu, Z.; Xu, X.; Lu, X.; Shi, P.; Xiao, Y.; Tsai, H.-I.; Su, D.; Cheng, F.; Cheng, X.; et al. PD-1 Cellular Nanovesicles Carrying Gemcitabine to Inhibit the Proliferation of Triple Negative Breast Cancer Cell. *Pharmaceutics* **2022**, *14*, 1263. <https://doi.org/10.3390/pharmaceutics14061263>

Academic Editors: Hassan Bousbaa and Carlos Alonso-Moreno

Received: 15 April 2022

Accepted: 3 June 2022

Published: 14 June 2022

**Publisher's Note:** MDPI stays neutral with regard to jurisdictional claims in published maps and institutional affiliations.



**Copyright:** © 2022 by the authors. Licensee MDPI, Basel, Switzerland. This article is an open access article distributed under the terms and conditions of the Creative Commons Attribution (CC BY) license (<https://creativecommons.org/licenses/by/4.0/>).

**Abstract:** PD-1 inhibitor Keytruda combined with chemotherapy for Triple-negative breast cancer (TNBC) has been approved for FDA, successfully representing the combination therapy of immunotherapy and chemotherapy for the first time in 2020. However, PD-L1 inhibitor Tecentriq combined with albumin paclitaxel using the similar strategy failed to achieve the expected effect. Therefore, it is still necessary to explore new effective immunotherapy and chemotherapy-based combined strategies. We developed a cell membrane-derived programmed death-ligand 1 (PD-1) nanovesicle to encapsulate low-dose gemcitabine (PD-1&GEM NVs) to study the effect on breast cancer in vitro and in vivo. We found that engineered PD-1&GEM NVs could synergistically inhibit the proliferation of triple-negative breast cancer, which interacted with PD-L1 in triple-negative breast cancer to disrupt the PD-L1/PD-1 immune inhibitory axis and promoted cancer cell apoptosis. Moreover, PD-1&GEM NVs had better tumor targeting ability for PD-L1 highly-expressed TNBC cells, contributing to increasing the drug effectiveness and reducing toxicity. Importantly, gemcitabine-encapsulated PD-1 NVs exerted stronger effects on promoting apoptosis of tumor cells, increasing infiltrated CD8<sup>+</sup> T cell activation, delaying the tumor growth and prolonging the survival of tumor-bearing mice than PD-1 NVs or gemcitabine alone. Thus, our study highlighted the power of combined low-dose gemcitabine and PD-1 in the nanovesicles as treatment to treat triple-negative breast cancer.

**Keywords:** PD-1; nanovesicles; immunotherapy; gemcitabine; breast cancer

## 1. Introduction

By 2020, the number of new cases and deaths of female breast cancer has surpassed that of lung cancer and it has become the most common cancer [1]. Triple-negative breast cancer (TNBC) is a highly heterogeneous disease that constitutes almost 20% of breast cancer cases, which is associated with poor overall survival and a high probability of distant recurrence and death [2,3]. In the past 10 years, surgical treatment is still the first-choice strategy for early breast cancer patients.

In addition to resection, chemotherapy is the cornerstone of systemic therapy for TNBC. Anthracycline, taxanes, and platinum drugs are still the most basic chemotherapy regimens. Meanwhile, the role of Gemcitabine has also been highlighted [4]. Gemcitabine,

a cell cycle-specific antimetabolite, is characterized by wide antitumor spectrum and few adverse reactions. In recent years, several large-scale phase III studies have shown that single or combined chemotherapy drugs are effective for advanced breast cancer. Many studies have shown that gemcitabine is effective in the treatment of advanced triple-negative breast cancer patients. The clinical remission rate of single drug is 15–20% and if combined anthracycline and taxanes, the overall remission rate can be increased to 20–79% [5], which makes it the first-choice chemotherapy drug as combination drug recommended for advanced breast cancer [6]. However, the increased toxic reaction and resistance of gemcitabine following the continuous implementation of the combined treatment have become obstacles that limit the in-depth application of gemcitabine in breast cancer. Therefore, exploring new effective combination therapy and reducing side effects through targeted administration are still of great clinical significance to expand the application of Gemcitabine.

Programmed death 1 (PD-1) is an immunosuppressive member on the surface of T cells and plays a vital role in regulating the immune system. PD-1 maintains immune homeostasis upon binding to its ligands, PD-L1 or PD-L2 [7]. However, tumors utilize this immune protective mechanism for their immune survival. In the tumor microenvironment, tumor cells and tumor-associated APCs highly express PD-L1, which combines with PD-1 of T cells to induce T cell exhaust, thereby inhibiting the anti-tumor function of CD8<sup>+</sup> T cells [8]. Therefore, destroying the interaction between PD-L1/PD-1 shows great potential in enhancing the lethality of the immune system to cancer cells [9,10]. In recent years, PD-1/PD-L1 blocking antibody drugs have made a breakthrough in tumor immunotherapy [11]. At present, several antibody drugs have been approved for clinical application in a variety of fields such as melanoma, non-small cell lung cancer, Hodgkin's lymphoma, and have achieved good results [12]. Excitedly, the FDA recently approved PD-1 inhibitor Pembrolizumab (Keytruda) combined chemotherapy (Albumin paclitaxel/paclitaxel with or without carboplatin) as a new adjuvant therapy for the unresectable or metastatic triple-negative breast cancer (TNBC) with PD-L1 expression in  $\geq 10\%$  tumor cells. In the final analysis of phase III keynote-355 trial, pembrolizumab plus chemotherapy significantly improved the progression-free survival (PFS) compared with chemotherapy alone, which suggests that chemotherapy combined with immunotherapy may be a promising treatment option for TNBC [13,14]. However, in contrast, because the clinical trials of PD-L1 monoclonal antibody inhibitor Atezolizumab (Tecentriq) are not enough to prove that the drug combined with other chemotherapeutic drugs is better than monotherapy [3], the European Drug Administration (EMA) withdrew Roche's application of the combination therapy of Atezolizumab with albumin paclitaxel or anthracyclines in the treatment of early or advanced TNBC [15]. These two contradictory results indicated that it is still very necessary to explore new combination therapies of different immune drugs and chemotherapeutic drugs.

Extracellular vesicles are important carriers for transferring information and substances between cells [16], and they play a significant role in tumor immune escape [17] and tumor metastasis [18]. Studies have shown that nucleic acid therapeutics can be transported to breast cancer tumors expressing EGFR (epidermal growth factor receptor) through extracellular vesicles [19] and may have anti-metastatic effects [20]. Importantly, cell membrane-derived nanovesicles (NVs) with serial extrusion have similar characteristics to the exosomes naturally secreted by cells and also inherit the characteristics of innate cells. NVs have several superiorities in large-scale preparation and expressing complex active proteins as a compound carrier to release the drug at target sites by the ways of co-incubation and electroporation [21,22].

Thus, we constructed an extracellular vesicle-like cell membrane nanovesicle (NVs) to co-deliver PD-1 and gemcitabine. NVs have the superior characteristics of excellent biocompatibility, large-scale preparation, and strong drug delivery capabilities [23,24]. They can not only carry targeted proteins or ligands stably through genetic modification strategies on the membrane of NVs, but also carry various traditional drugs inside the

NVs, which can increase the ability of NVs to target tumor and reduce the systemic side effects of drugs. The cell membrane vesicles have the promising potential to become an ideal nano-scale delivery system.

In this study, we established PD-1-expressing NVs carrying low-dose gemcitabine to suppress the immune escape pathway, thus inhibiting tumor growth. The combination of PD-1 NVs and gemcitabine significantly promoted the peripheral blood mononuclear cell (PBMC) activation, inhibited the proliferation of triple-negative breast cancer, induced the cancer cell apoptosis, increasing the infiltrated CD8<sup>+</sup> T cells, delaying the tumor growth, and prolonging the survival of tumor-bearing mice. Taken together, these data supported the idea that the power of combined low-dose gemcitabine and PD-1 in the nanovesicles presented a prospective strategy to treat triple-negative breast cancer.

## 2. Materials and Methods

### 2.1. Chemicals and Regents

Puromycin was supplied by Sigma-Aldrich (Merck, St. Louis, MO, USA). Na<sup>+</sup>/K<sup>+</sup> ATPase antibodies were obtained from Santa Cruz (Santa Cruz Biotechnology, Santa Cruz, CA, USA). Primary antibodies such as PD-1, GFP, and β-actin for western blotting were purchased from Cell Signaling Technology (Cell Signaling Technology, Danvers, MA, USA). Wheat germ agglutinin (WGA) Alexa Fluor 594 and 350 dyes were purchased from Thermo Scientific (ThermoFisher, Waltham, MA, USA). Staining antibodies including CD3, CD4, CD8, and CD25 for fluorescence activated cell sorting (FACS) analysis were purchased from Biolegend Inc. (BioLegend, San Diego, CA, USA), Ficoll Paque Plus was purchased from GE Healthcare (GE Healthcare, Chicago, IL, USA).

### 2.2. Plasmids

Human PD-1 lentivirus open reading fragment (ORF) cDNA expression plasmid with green fluorescent protein (C-GFP Spark tag) and mouse PD-1 lentivirus ORF cDNA expression plasmid (C-GFP Spark tag) were supplied by Sino Biological Inc (Sino Biological, Beijing, China).

### 2.3. Cell Lines

MDA-MB-231 cells (SCSP-5043), HEK293T cells (SCSP-502), MCF-7 cells (SCSP-531), 3T3L1 cells (SCSP-5038), and 4T1 cells (TCM32) were purchased from Chinese Academy of Sciences Cell Bank (Shanghai, China). MDA-MB-231 cells, MCF-7 cells and 4T1 cells, HEK293T cells and 3T3L1 cells were separately cultured in Leibovitz (L-15) (HyClone, Logan, UT, USA), minimum eagle's medium (MEM) (HyClone, Logan, UT, USA), Roswell Park Memorial Institute (RPMI-1640) (HyClone, Logan, UT, USA) and Dulbecco's modified eagle medium (DMEM) (HyClone, Logan, UT, USA) with 100 U/mL penicillin, 100 µg/mL streptomycin and 10% fetal bovine serum (FBS) (ExCell Bio, Canelones, Uruguay), at 37 °C with 5% CO<sub>2</sub>.

In order to obtain HEK293T/3T3L1 cell lines that stably overexpress PD-1, HEK293T cells ( $1.5 \times 10^7$ ) were firstly used to produce viral particles ( $10^7$  transducing units (TU)/mL) in the lentivirus packaging solution environment (phosphate buffer saline (HBS) solution 950 µL, packaging plasmid 10 µg, human/mouse PD1 gene lentiviral ORF cDNA expression plasmid 10 µg, 2.5 M CaCl<sub>2</sub> solution 50 µL). HEK293T/3T3L1 cells were then infected with collected viral particles at 12 h, 24 h, and 48 h post-transfection and co-incubated for 24 h at 37 °C. Under selection with puromycin, HEK293T/3T3-L1 cell lines with a high degree of overexpressing PD-1-GFP on the cell membrane was finally obtained.

### 2.4. Western Blotting

Cell samples and cell vesicles samples were lysed in radio immunoprecipitation assay lysis buffer (RIPA) solution, and then subjected to 10% SDS-PAGE for electrophoresis at 120 v and western transfer at 330 mA, 90 min. Primary antibodies of Na<sup>+</sup>/K<sup>+</sup> ATPase, PD-1, GFP and β-actin were co-incubated overnight at 4 °C. After incubation with horseradish

peroxidase (HRP) bounded anti-mouse or anti-rabbit secondary antibodies (Protein Tech, Wuhan, China), target proteins were detected by enhanced chemiluminescence (ECL) kit (Protein Tech, Wuhan, China).

### 2.5. Cell Membrane Vesicle Preparation

The collected HEK293T/3T3-L1 cells ( $3 \times 10^7$ ) were fully cracked in 2 mL homogenization medium buffer (1 mM EDTA, 0.25 M sucrose, 20 mM Hepes-NaOH, pH 7.4, and protease inhibitor cocktail), then thoroughly ground with a grinder, and centrifuged at different speeds of 5000 rpm (4 °C, 10 min) and 13,500 rpm (4 °C, 10 min), respectively. After filtration through 0.45 µm and 0.22 µm filters, the obtained vesicles were stored at −80 °C.

### 2.6. Size Distribution, Zeta-Potential Analysis, and Morphology

HEK293T/3T3-L1 cell membrane ( $3 \times 10^7$  cells) were dissolved with 0.5 mL PBS and filtered by 0.1 µm filter. The particle size distribution and zeta potential range of the samples were determined by a NanoBrook 90Plus PALS instrument (Brookhaven, NY, USA). The morphology of nanovesicles stained with uranium acetate on copper mesh were scanned by transmission electron microscopy (TEM) (JEOL, Tokyo, Japan).

### 2.7. Nanovesicle Cell Binding Assay

MDA-MB-231 cells were co-incubated with GFP-PD-1 NVs (25 mg/mL) for 2 h at 37 °C, and then stained with WGA Alexa594 for 10 min. After washing with phosphate buffer saline, images were captured using LSM880 confocal microscope (Zeiss, Jena, Germany) emitted by corresponding lasers 594.

### 2.8. Isolation of Peripheral Blood Mononuclear Cell (PBMC) from Human Peripheral Blood

Blood from healthy donors was collected into EDTA empty bottles, and then Ficoll Paque Plus (GE Healthcare, Chicago, IL, USA) separation solution was added. The blood was centrifuged at 1000 rpm for 30 min and PBMCs were obtained. PBMCs were washed twice with RPMI 1640, and lysed on ice for 2 min with 1 mL erythrocyte lysates. Finally, RPMI 1640 was added to neutralize and resuspend PBMCs.

### 2.9. Production of GEM&PD-1 NVs

The PD-1 NVs (0.5 mg protein weight) and 1 mg GEM were mixed gently in 1 mL electroporation liquid (1.15 mM potassium phosphate, pH 7.2, 25 mM potassium chloride), and electroporation was carried out in 0.4 cm electroporation cuvette by using bio-RAD electroporation instruments (Bio-Rad, Hercules, CA, USA). Parameters: 300 V, 150 µF, 3 s. The sample was then left on ice for 30 min. After washing with cold PBS solution and centrifuging at 12,000 rpm, GFP-PD-1 NVs carrying GEM (GEM&PD-1 NVs) were obtained.

### 2.10. Detection of Encapsulation Ratio

To obtain the GEM standard curve, standard solutions of different concentrations (50 µg/mL, 40 µg/mL, 30 µg/mL, 20 µg/mL, and 10 µg/mL of 2 mL standard solutions) were prepared and the absorbance values were measured at 268 nm by ultraviolet spectrophotometer. After measuring the absorbance of GEM in the sample, the concentration was calculated by substituting the GEM calibration curve.

Encapsulation Ratio% E.R. =  $\text{MG/MS} \times 100\%$  (MG is the mass of GEM in the supernatant and MS is the total mass of GEM in the sample).

### 2.11. Carboxyfluorescein Diacetate Succinimidyl Ester (CFSE) Staining

PBMCs were spread in 24-well plates with CD3 antibody, and then CFSE dye (5 µM) was added. The PBMCs were co-incubated at 37 °C in 5% CO<sub>2</sub> for 20 min under dark conditions, and then RPMI-1640 was added to stop response. After centrifugation (1000 rpm, 5 min) and repeated washing with RPMI-1640 medium, the stained cells were placed on

48-well plates with plate-bound anti-CD3 antibody (5 µg/mL) and allowed to grow for 2 days with the addition of the activating factor IL-2. MDA-MB-231 cells were co-incubated with PBMCs and vesicles of different groups (50 µg/mL). Then, apoptosis of MDA-MB-231 cells was detected by flow cytometry (Cytoflex, Beckman, Brea, CA, USA).

#### 2.12. Biodistribution

NVs labelled by sulfo-cyanine5.5 amine (cy5.5) (excitation/emission peaks, 680 nm/710 nm) (Lumiprobe Corporation, Hallandale Beach, FL, USA) were injected into BALB/c mice through the tail vein. After 4 h, the distribution of NVs in the main organs of mice was observed by NightOWL (LB983) imaging system (Berthold, Pforzheim, Germany).

#### 2.13. Breast Cancer Mouse Models

The use of laboratory animals and all experiments was reviewed and approved by the Animal Ethics Committee of Sun Yat-sen University, China, approval No. SYSU-IACUC-2021-000046.

Specific pathogen free (SPF) female BALB/C mice were purchased and adaptively fed at sterile room temperature for one week up to eight weeks for mouse models of breast cancer. Mice were firstly anesthetized by intraperitoneal injection of 1% pentobarbital, and the hair around the fourth pair of breasts were removed with shaving cream, and then disinfected with 75% alcohol. The prepared suspension of mouse breast cancer 4T1 cells ( $3 \times 10^6$ ) was injected to the mammary fat pad. Seven days later, the mouse models of breast cancer were established successfully. All 25 tumor-bearing mice were randomly divided into 5 groups and received different treatments: Control group (normal saline,  $n = 5$ ), Free nanovesicles group (Free NVs, 25 mg/kg,  $n = 5$ ), PD-1 nanovesicles group (PD-1 NVs, 25 mg/kg,  $n = 5$ ), single drug group (GEM, 10 mg/kg,  $n = 5$ ), PD-1 nanovesicles and GEM group (PD-1&GEM NVs, 10 + 25 mg/kg,  $n = 5$ ). In the first three days, mice were treated according to the above scheme every day. After three days, mice were treated every other day for continuous 10 days and sacrificed on the 10th day (on the 18th day from tumor inoculation). Tumor, spleens, and lymph nodes samples were collected and analyzed on the 18th day.

#### 2.14. Haematoxylin and Eosin Staining

Paraffin sections of tumor and spleen tissue samples were dewaxed, then placed in graded concentrations of alcohol (100%, 95%, 90%, 80%, 70%) for hydration. Tissue sections were stained with H&E, and inflammatory cell infiltration was observed by microscopy (Nikon, Tokyo, Japan) with 100× magnification.

#### 2.15. Cell Isolation from Spleen, Tumor, and Lymph Node and Flow Cytometry Assay

Spleens, tumors, and lymph nodes cells ( $10^6$ ) that were obtained after mouse dissection were infiltrated in PBS solution and the tissues were ground, washed in PBS solution, and passed through a 70 µm filter. All above operations were performed on ice to keep the cell activity. After 1000 rpm centrifugation for 5 min, the samples were co-incubated with 100 µL of the staining buffer and target antibodies of 1 µL, such as anti-CD3-FITC, anti-CD4-APC, and Anti-CD8-PB450, and shielded from light for 15 min at room temperature. After centrifugation and washing with PBS, samples should be performed by MoFlo XDP flow cytometer (Beckman Coulter, Miami, FL, USA).

#### 2.16. Annexin V/Propidium Iodide-Based Cell Apoptosis Assay

The cell samples treated under different conditions were collected, centrifuged, and re-suspended with 100 µL  $1 \times$  Annexin V Binding buffer. Then, 5 µL Annexin V-FITC and 5 µL PI were added according to the Apoptosis Detection Kit (BD Pharmingen, San Diego, CA, USA), and gently mixed and incubated for 15 min at room temperature, away from light. Samples should be detected within 1 h using the MoFlo XDP flow cytometer (Beckman Coulter, Miami, FL, USA).



### 2.17. Cell Viability and Colony Formation Assays

For the cell viability assay, MDA-MB-231 cells were seeded into 96-well plates ( $5 \times 10^4$ ) and incubated at 37 °C, 5% CO<sub>2</sub> overnight. The IC<sub>50</sub> analysis of GEM on MDA-MB-231 cells were treated with different doses of GEM for 48 h. The cell viability was assessed using CCK-8 according to the instructions. Experiments were repeated at least three times. For colony formation assay, MDA-MB-231 cells ( $1 \times 10^3$ /well) were seeded in 6-well plates and cultured in L-15 medium with various doses of GEM for 2 weeks. Then they were fixed by 4% paraformaldehyde (PFA) and stained with crystal violet for cell colony number count.

### 2.18. Quantitative Real-Time PCR

Total RNA from cells were isolated by 1 mL TRIZOL reagent (TaKaRa, Tokyo, Japan). Cells after washing with PBS were lysed in Trizol. Then, 200 µL trichloromethane, 550 µL isopropyl alcohol, and 1 mL 75% ethanol was added in turn, and 12,000 rpm centrifuge is required after each addition. Next, the 1 µg RNA was reversely transcribed into cDNA by using 4 µL HiScript III RT SuperMix for qPCR (+1 µL gDNA wiper) (Vazyme, Nanjing, China). Finally, RT-qPCR experiments were performed with 3-step amplification program (95 °C 10s, 60 °C 10s, 72 °C 10s) by using 2x SYBR Green qPCR Mix (TransGen Biotech, Beijing, China) with LightCycler<sup>®</sup> 96 (Roche, Basel, Switzerland). The quantitative calculation analysis of relative gene expression could be determined by  $2^{-\Delta\Delta C_t}$  method. Experiments were performed in triplicate.

### 2.19. Statistical Analysis

Data analysis was performed using GraphPad Prism version 7.0 software (GraphPad Software Inc., La Jolla, CA, USA) and Origin Pro 2021 software. One-way analysis of variance (ANOVA, R.A.Fisher) and Turkey's test were performed. All data were presented as mean  $\pm$  standard error (SEM). Statistical significance is indicated (\*  $p < 0.05$ , \*\*  $p < 0.01$ , \*\*\*  $p < 0.001$ ).

## 3. Results

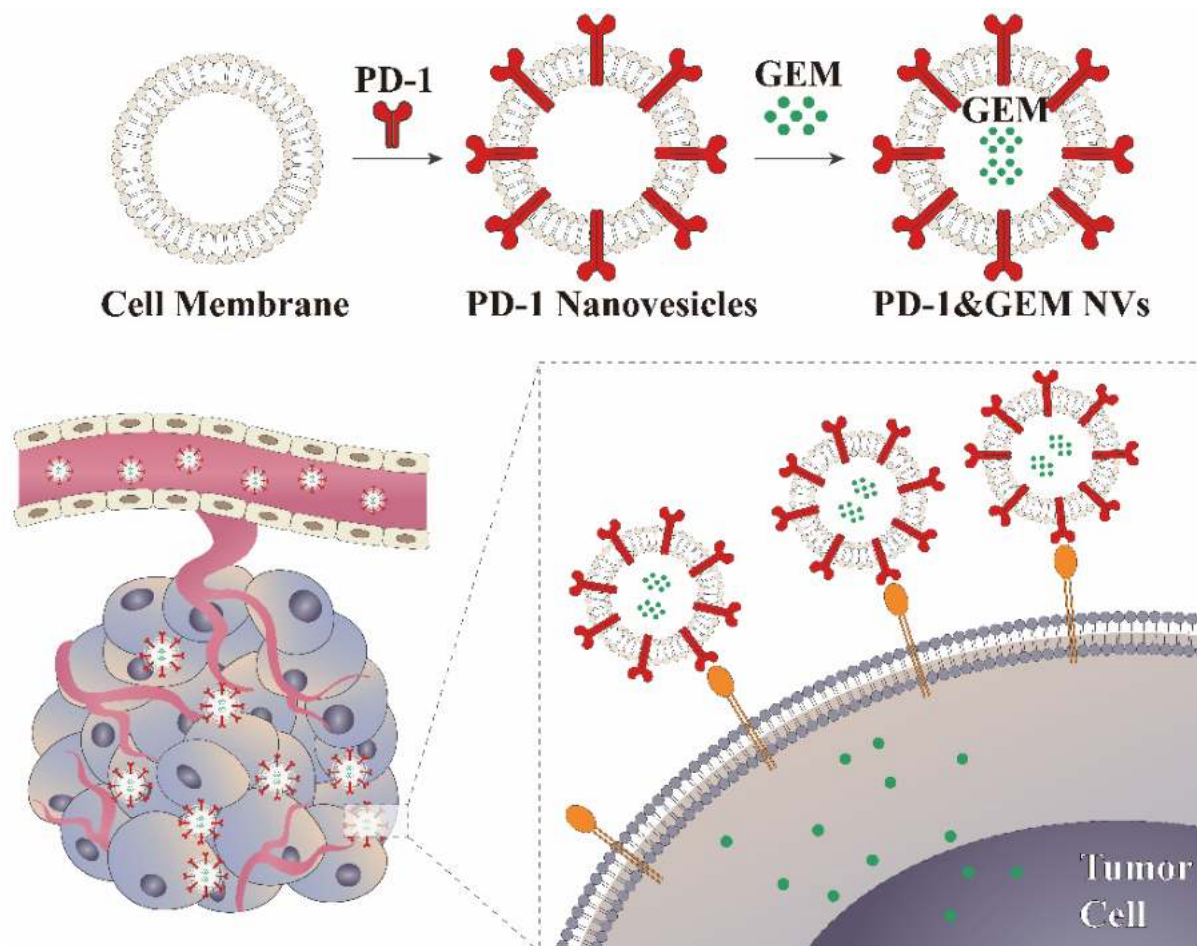
### 3.1. Construction of Stably Overexpressing PD-1 Cell Lines and Biological Behaviors of PD-1 NVs In Vitro

As shown in Figure 1, we designed membrane-derived nanovesicles to carry PD-1 protein. PD-1 can bind to PD-L1 on the surface of breast cancer cells. Therefore, PD-1 NVs could block PD-1/PD-L1 immunosuppressive signaling pathways. To inhibit the proliferation of breast cancer cells, we used PD-1 NVs to encapsulate low-dose GEM drugs (PD-1&GEM NVs).

To obtain PD-1 NVs, we firstly established PD-1-GFP stably overexpressing HEK293T cells using the lentiviral packaging system. HEK293 T cells were easy to proliferate with high transfection [21]. Thus, we constructed HEK293T cells derived PD-L1 NVs in vitro. Confocal microscopy showed the obvious cell membrane localization of PD-1-GFP (Figure 2B), while GFP as the control was mainly localized in the cytoplasm (Figure 2A). Furthermore, PD-1-GFP overexpression was confirmed in HEK293T stably cell lines by western blotting (Figure 2C). Compared with GFP control, the expression of PD-1-GFP mRNA was more than 600 times higher through the real-time quantitative PCR experiment (Figure 2D) (Table 1). At the same time, in order to meet the needs of subsequent treatment of transplanted tumors in mice to avoid cross-species reaction, we also constructed a mouse 3T3L1 cell line with high expression of PD-1-GFP, and confirmed its high expression by qPCR (Figure 2E) (Table 1).

To prepare HEK293T derived PD-1-GFP NVs and PD-1&GEM NVs, extruded nanovesicles were collected by cell lysis, differential centrifugation, and a serial extrusion as described in the Material and Method section. The cell vesicles were estimated by transmission electron microscope (TEM). The PD-1 NVs and PD-1&GEM NVs were found to be membrane-bound closed shape and about 100 nm (Figure 3A). In order to proof the expression of PD-1 in vesicles, we detected the PD-1 and Na<sup>+</sup>/K<sup>+</sup> ATPase expression via western

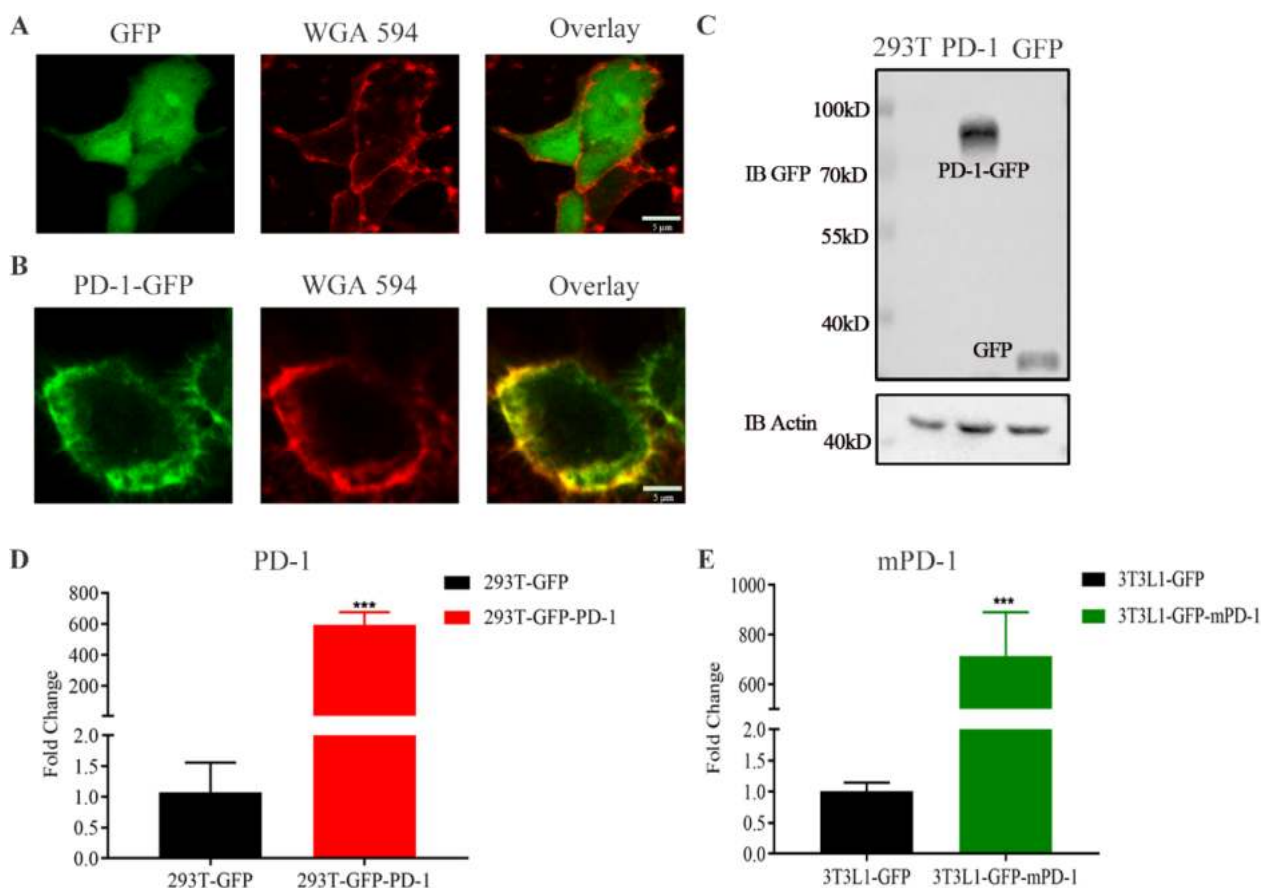
blotting. Results have shown that the PD-1 was expressed in cell vesicles (Figure 3B). Furthermore, dynamic light scattering (DLS) analysis also showed that PD-1-GFP NVs and PD-1&GEM NVs had a similar diameter with around 110 nm (Figure 3C), and the zeta potentials of PD-1-GFP NVs and PD-1&GEM NVs was around  $-22$  mv (Figure 3D), indicating that the PD-1-GFP NVs and PD-1&GEM NVs were a stable membrane structure. Therefore, all data showed that we have successfully prepared the PD-1-overexpressing cell membrane-based nanovesicle and the final product of PD-1&GEM NVs.



**Figure 1.** Schematic illustration of engineering PD-1 NVs carrying GEM for the treatment of triple-negative breast cancer.

### 3.2. PD-1-GFP NVs Specifically Bound to PD-L1 on the Surface of MDA-MB-231 Triple-Negative Breast Cancer Cells

We first assessed the expression of PD-L1 in the breast cancer cells MDA-MB-231 via FACS. PD-L1 was highly expressed in the MDA-MB-231 triple-negative breast cancer cell lines (TNBC) (Figure 4A), which was also in line with the results of previous reports. Compared to the MCF-7 as a non-TNBC cell line (control), we found that the expression of PD-L1 mRNA in MDA-MB-231 cells was 15 folds higher using RT-qPCR analysis, suggesting that the constructed PD-1&GEM NVs could target TNBC (Figure 4B) (Table 1). To test whether PD-1-GFP NVs can bind to PD-L1 on the surface of MDA-MB-231, we co-incubated the PD-1 NVs with MDA-MB-231 for 2 h and detected it by confocal microscopy. As shown in Figure 4C, PD-1-GFP NVs (green fluorescence) showed the obvious co-localization, suggesting that PD-1 NVs might competitively and specifically block the binding of PD-L1 on TNBC cell membrane to PD-1 of T cells, and restart the T cell immune killing effect.



**Figure 2.** Schematic illustration and characterization of HEK293T/3T3L1 stably overexpressing PD-1. (A,B) Confocal images indicated the establishment of HEK293T cell line stably expressing GFP and human PD-1. WGA Alexa-Fluor 594 dye was used to label cell membrane. Scale bar: 5  $\mu$ m. (C) Western blot assay verified the expression of PD-1 receptors on the whole cell lysate of the overexpressing PD-1 cell line.  $\beta$ -actin was used as a loading control. (D,E) RT-qPCR assay exhibited the expression of PD-1 on the whole cell lysate of the stable cell line including human cell (HEK293T) and mouse cell (3T3L1). Data were expressed as mean  $\pm$  SEM,  $n = 3$ . \*\*\*  $p < 0.001$ .

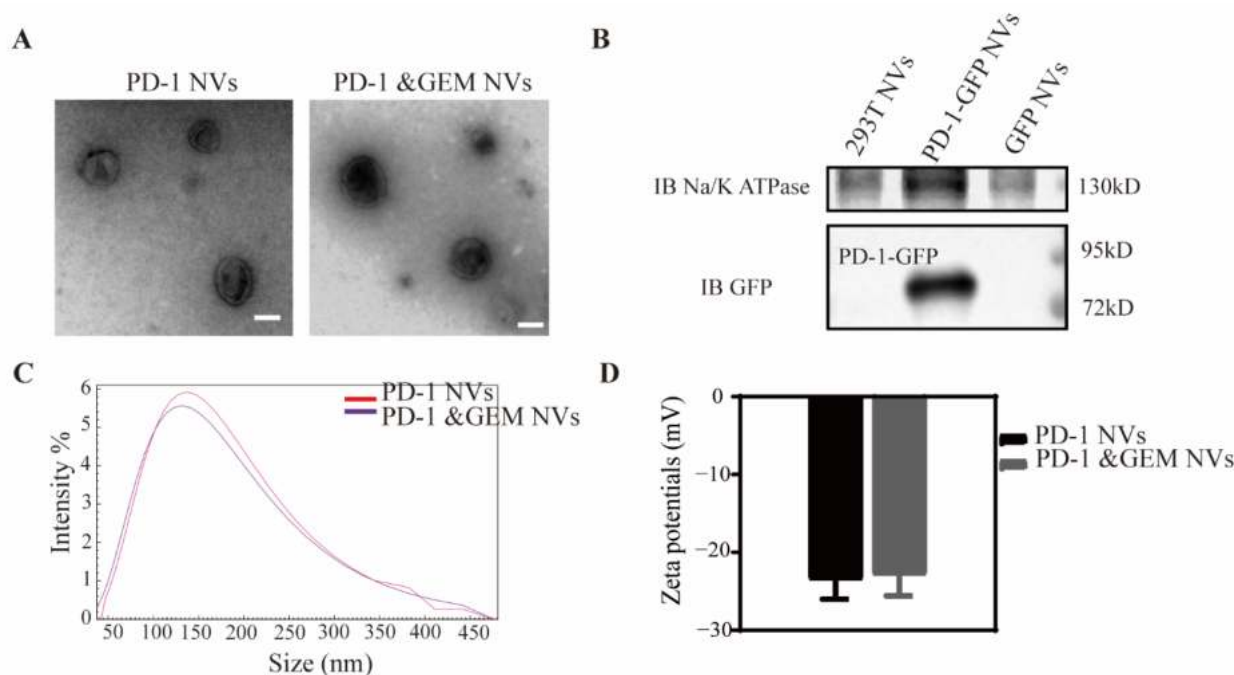
**Table 1.** qPCR primers sequences.

Genes	Forward Primer Sequence 5' $\rightarrow$ 3'	Reverse Primer Sequence 5' $\rightarrow$ 3'
Mouse- $\beta$ -Actin	GGCTGTATCCCCTCCATCG	CCAGTTGGTAACAATGCCATGT
Mouse-Pd-11	TCTGATCGTCGATTGGCAGC	CGTTGTTCCAGGCTCCTCTC
Human-Pd-1	CCCAAGGCGCAGATCAA	CTGGCGAGCCTTAGTTTGGAC
Human-Pd-11	GGTGAGGATGGTTCTACACAG	GAGAACTGCATGAGGTTGC
Human- $\beta$ -Actin	CCACACTGTGCCCATCTAC	AGGATCTTCATGAGGTAGTCAGTC

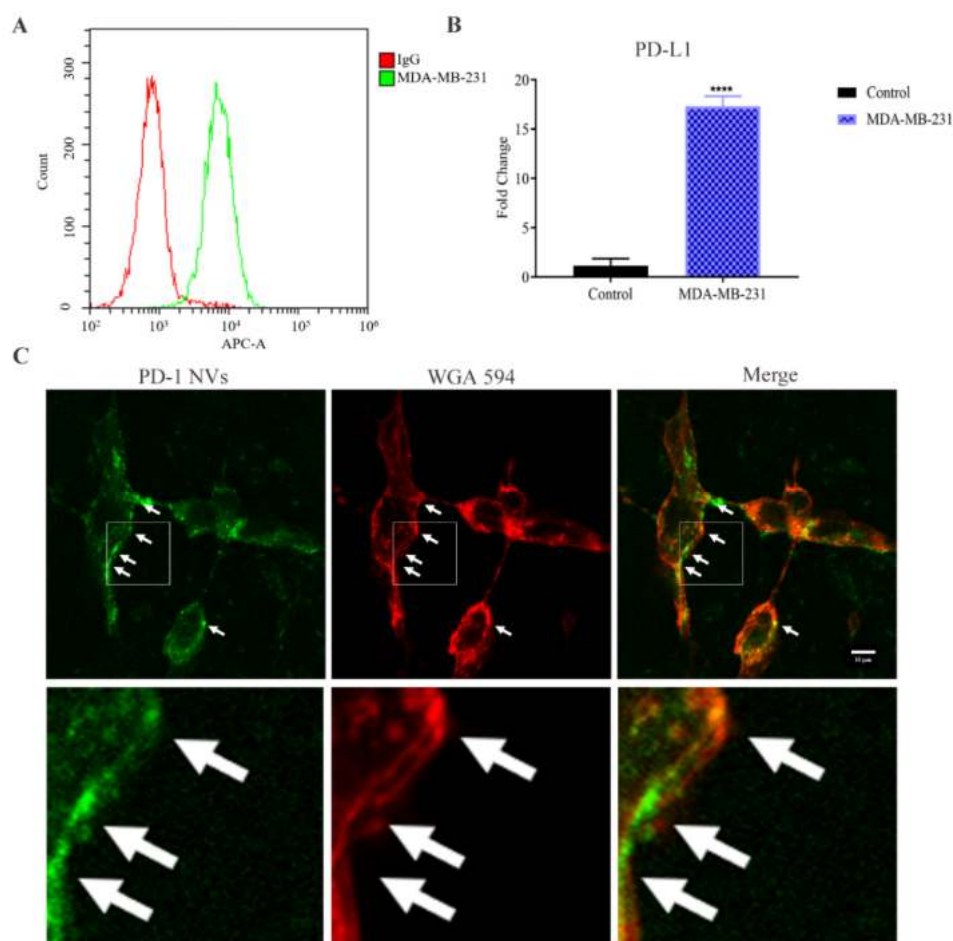
### 3.3. Gemcitabine Inhibited the Tumor Cell Growth and PD-1&GEM NVs Induced Cell Apoptosis of Breast Cancer In Vitro

At the beginning, the DNA-damaging chemotherapeutic drug including DNA-synthesis inhibitor gemcitabine and PARP (poly adenosine diphosphate ribose polymerase) inhibitor olaparib were both considered as a therapeutic drug. In order to verify the effect of gemcitabine and olaparib, cell activity and cell cloning experiments were performed in a dose-dependent manner. As shown in Figure 5A,B, we determined the effect of increasing concentrations of GEM (0.005  $\mu$ M, 0.01  $\mu$ M, 0.1  $\mu$ M, 1  $\mu$ M, and 10  $\mu$ M) on MDA-MB-231 breast cancer cells inhibition. Results indicated that 0.1  $\mu$ M, 1  $\mu$ M, and 10  $\mu$ M gemcitabine presented similar stronger inhibition on TNBC cells than low concentrations (0.005  $\mu$ M,

0.01  $\mu\text{M}$ ). Importantly, the effect of 0.1  $\mu\text{M}$  gemcitabine on MDA-MB-231 inhibition was comparable to the treatment with 1  $\mu\text{M}$  and 10  $\mu\text{M}$ , thus 0.1  $\mu\text{M}$  were chosen for suitable concentration. However, cell activation experiments showed that a larger olaparib dose (30  $\mu\text{M}$ ) was required to achieve the single drug-killing tumors (Figure 5A). Thus, low-dose 0.1  $\mu\text{M}$  gemcitabine was chosen for following experiments. Furthermore, research has revealed that gemcitabine possesses promising effects on chemotherapy in patients with breast cancer [25]. Afterwards, we developed a combined immunotherapy and chemotherapy therapy of PD-1 NVs carrying gemcitabine by the effect of targeting and carrier of NVs. Next, coated nanovesicles (PD-1&GEM NVs) were constructed by means of electroporation, and performed the experiments of GEM encapsulation and in-vitro drug release in PD-1 NVs. The result showed that gemcitabine was packaged into PD-1 nanovesicles by electroporation with an encapsulation efficiency of 21%, and the eventually released gemcitabine concentration was chosen to be 0.1  $\mu\text{M}$  in vitro, (Figure S1A). We also examined the release of encapsulated GEM from PD-1&GEM NVs at different times (1 h, 4 h, 8 h, 16 h, 24 h) by ultraviolet-visible spectroscopy (UV-Vis). The results suggested that with the increase of incubation time, GEM could be gradually released from NVs with a peak time at 24 h (Figure S1B). Many studies have shown that gemcitabine can inhibit tumor cells and induce apoptosis due to its blocking of the G/S phase of DNA [26,27]. Excitedly, the early apoptosis rate (Annexin V<sup>+</sup>/PI<sup>-</sup>) of MDA-MB-231 treated with PD-1&GEM NVs was 5.25%, 7.63%, 18.11%, 39.05%, and 46.74% at 12 h, 24 h, 48 h, 72 h, and 96 h, respectively. The late apoptosis rate (Annexin V<sup>+</sup>/PI<sup>+</sup>) of MDA-MB-231 was 3.75%, 7.67%, and 11.28%, and 14.49% at 12 h, 24 h, 72 h, and 96 h, respectively, indicating that PD-1&GEM NVs possessed a significant time-dependent pro-apoptotic effect (Figure 5C,D). In conclusion, the GEM could suppress the proliferation of MDA-MB-231 and PD-1&GEM NVs could promote the apoptosis of MDA-MB-231 breast cancer cells in vitro.



**Figure 3.** The preparation and characterization of PD-1 NVs and PD-1&GEM NVs. (A) The TEM image showed the shape and size of PD-1 NVs and PD-1&GEM NVs. Scale bar: 100 nm. (B) Western blot assay exhibited the expression of PD-1 receptors on the NVs of the stable cell line. Na, K-ATPase was used as a loading control. (C,D) The size distribution and zeta potentials of PD-1 NVs and PD-1&GEM NVs measured by dynamic light scattering (DLS) analysis. Data were expressed as mean  $\pm$  SEM,  $n = 3$ .



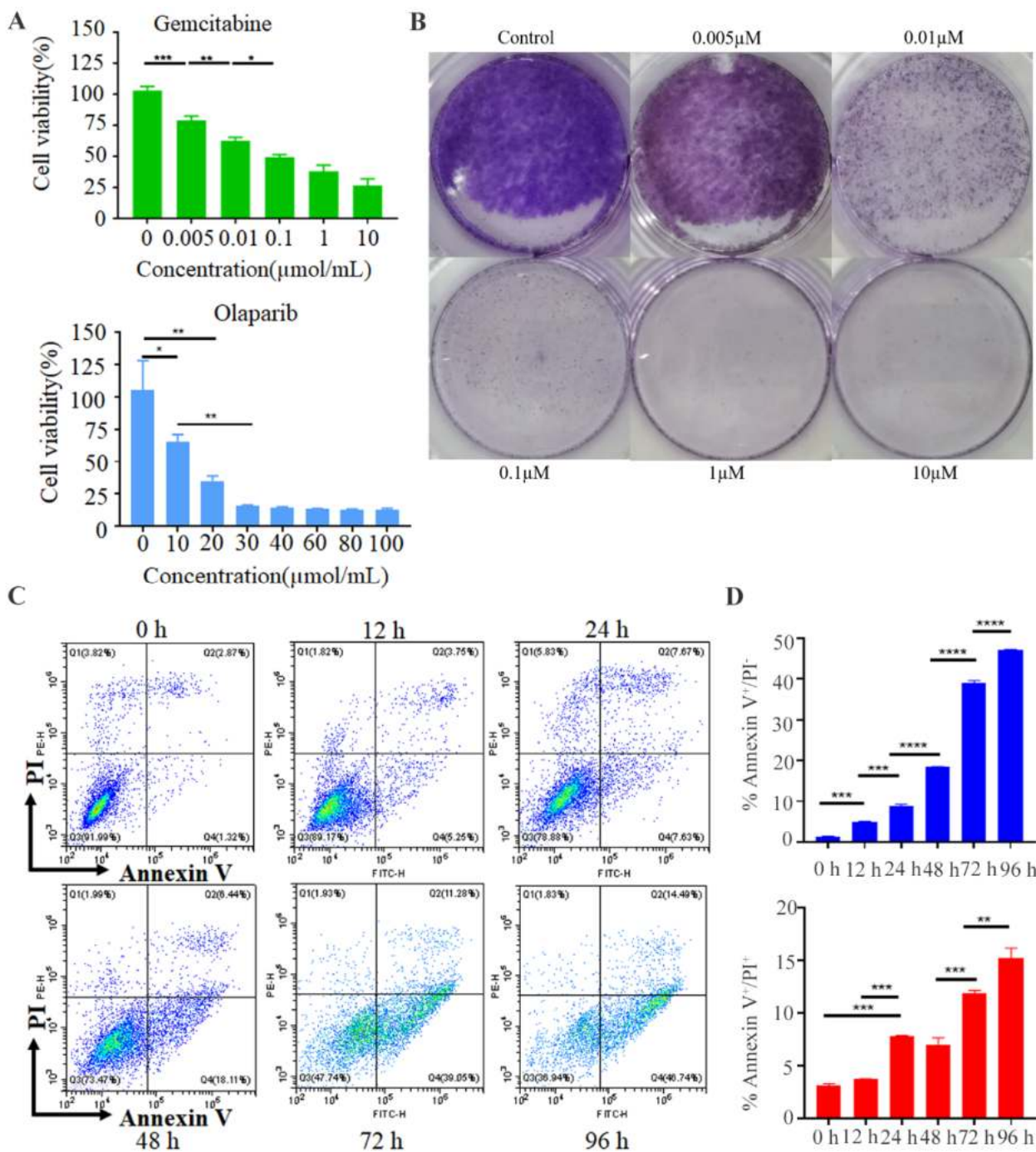
**Figure 4.** In vitro PD-1 NVs interacted with MDA-MB-231 cell. (A) FACS indicated the cell surface expression of PD-L1 in MDA-MB-231 cell line. (B) RT-qPCR assay exhibited the expression of PD-L1 in the MDA-MB-231 cell line and MCF-7 (non-TNBC cells). Data were expressed as mean  $\pm$  SEM,  $n = 3$ . \*\*\*\*  $p < 0.0001$ . (C) GFP-PD-1 NVs bound with the cell membrane of MDA-MB-231 cancer cell. PD-1 NVs (50  $\mu\text{g}/\text{mL}$ , protein weight) were incubated with MDA-MB-231 cancer cell for 2 h. Arrows pointed to PD-1 (on NVs), the MDA-MB-231 cell membrane (expressing PD-L1) and colocalization, respectively. WGA Alexa-Fluor 594 dye was used to detect MDA-MB-231 cell membrane (Scale bar: 10  $\mu\text{m}$ ).

#### 3.4. PD-1&GEM NVs Promoted PBMC Activation and MDA-MB-231 Cell Apoptosis When Co-Cultured

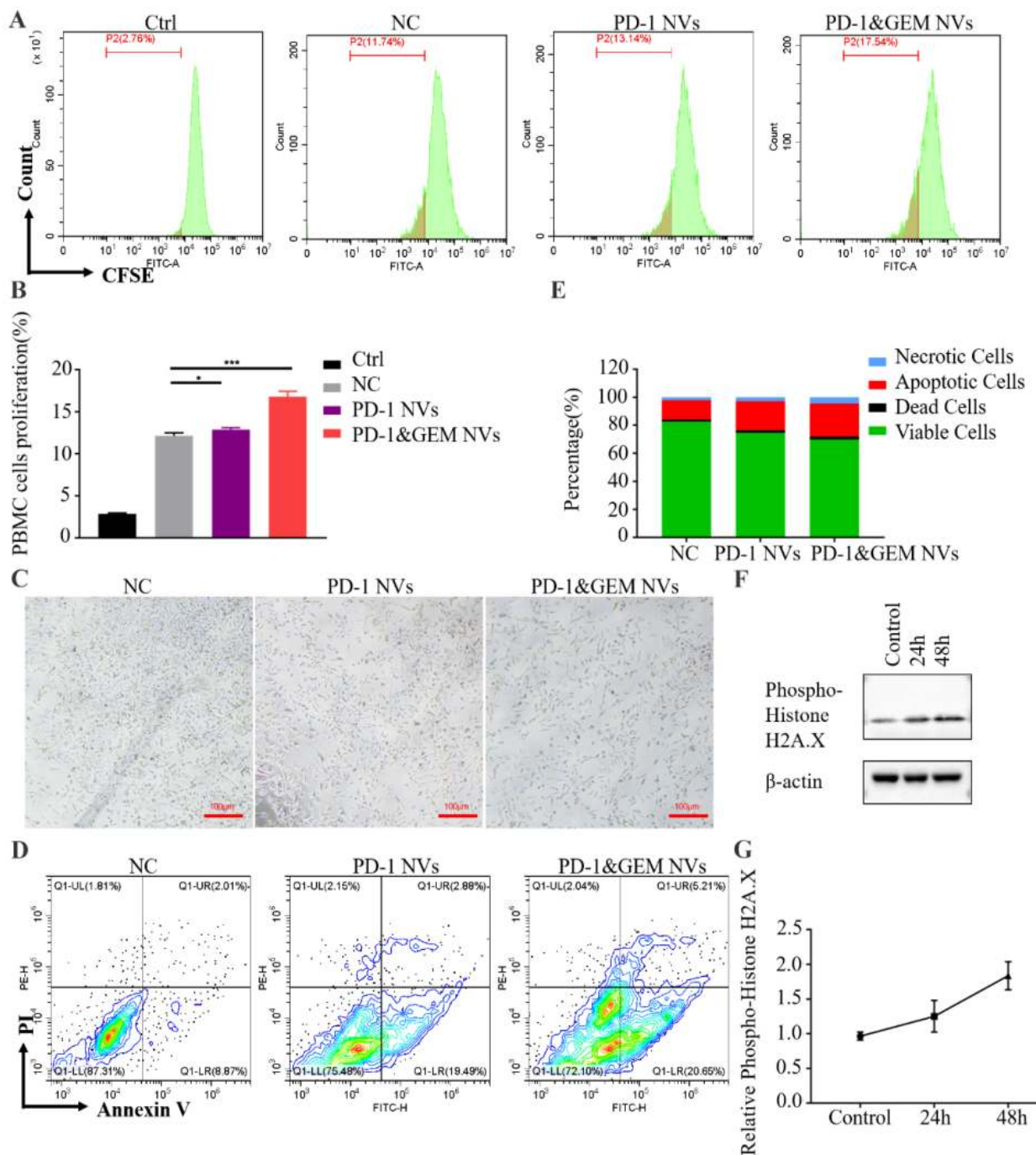
In order to further study the mechanism of PD-1&GEM NVs inhibiting tumor growth and whether it affected the activity of immune cells, we extracted PBMCs from peripheral blood mononuclear cells of healthy people. PBMCs were co-incubated with human MDA-MB-231 cells to simulate the tumor immune microenvironment. As shown in Figure 6A,B, compared to the control group, the degree of PBMC proliferation was significantly promoted by 10.38%, 14.78% in the PD-1 NVs, and PD-1&GEM NVs treatment groups, suggesting that PD-1 NVs effectively relieved the negative regulation of PD-L1 expressed by tumor cells on immune cells. It was worth noting that PD-1&GEM NVs induced the most significant proliferation of PBMC cells, and maybe PBMC was activated by released antigen when combined gemcitabine killed tumor cells. Expectedly, PD-1&GEM NVs produced a better inhibitory effect on the proliferation of MDA-MB-231 cells than only PD-1 NVs treatment in the co-culture of tumor and PBMC (Figure 6C). Correspondingly, we also observed more apoptotic and dead cells in the PD-1&GEM NVs than PD-1 NVs via flow cytometry analysis (Figure 6D,E). To further explore the role of gemcitabine in cell growth inhibition and apoptosis, we examined DNA damage marker  $\gamma$ -H2A.X expression

in MDA-MB-231 cells. Results showed that the expression of  $\gamma$ -H2A.X was significantly upregulated in a time-dependent manner after PD-1&GEM NVs treatment (Figure 6F,G).

Thus, these results suggest that PD-1&GEM NVs could enhance the activation of immune cells, inhibit tumor DNA synthesis, and promote tumor cell apoptosis of MDA-MB-231 cells in vitro.



**Figure 5.** GEM inhibited the proliferation of tumor cells and PD-1&GEM NVs promoted cell apoptosis. (A) Cell cytotoxicity of gemcitabine and olaparib on MDA-MB-231 breast cancer cell line. (B) The cell clone estimated the inhibition of gemcitabine on MDA-MB-231 cell line. (C) FACS assay exhibited PD-1&GEM NVs induced cell apoptosis. (D) Corresponding statistic data measured the proportion of PI<sup>+</sup>/PI<sup>-</sup> apoptosis cell. Data were expressed as mean  $\pm$  SEM,  $n = 3$ . \*  $p < 0.05$ , \*\*  $p < 0.01$ , \*\*\*  $p < 0.001$ , \*\*\*\*  $p < 0.0001$ .



**Figure 6.** PD-1&GEM NVs promoted the apoptosis of MDA-MB-231 and activated the proliferation of PBMC cells in vitro. (A) Flow cytometry analysis of the proliferation of PBMC when co-cultured with MDA-MB-231 in groups received different treatments (Ctrl, NC, PD-1 NVs, and PD-1&GEM NVs) for 3 days. Control group: PBMC at day 0, NC group: free NVs. (B) The corresponding quantitative analysis of PBMC from different treatment groups ( $n = 3$ ). (C) Microscopic examination estimated that the proliferation of MDA-MB-231 in groups received different treatments (NC, PD-1 NVs and PD-1&GEM NVs together with PBMC). (D) Flow cytometry analysis of the apoptosis of MDA-MB-231, which were co-cultured with PBMC. (E) Column data estimated the proportion of viable cell, apoptosis cell, necrotic cell, and dead cell. (F,G) Representative western blot plots and quantitative analysis of the effect of GEM at different time points on the expression of  $\gamma$ -H2AX,  $\beta$ -actin was used as a loading control. Data were expressed as mean  $\pm$  SEM,  $n = 3$ . NS: no significant, \*  $p < 0.05$ , \*\*\*  $p < 0.001$ .

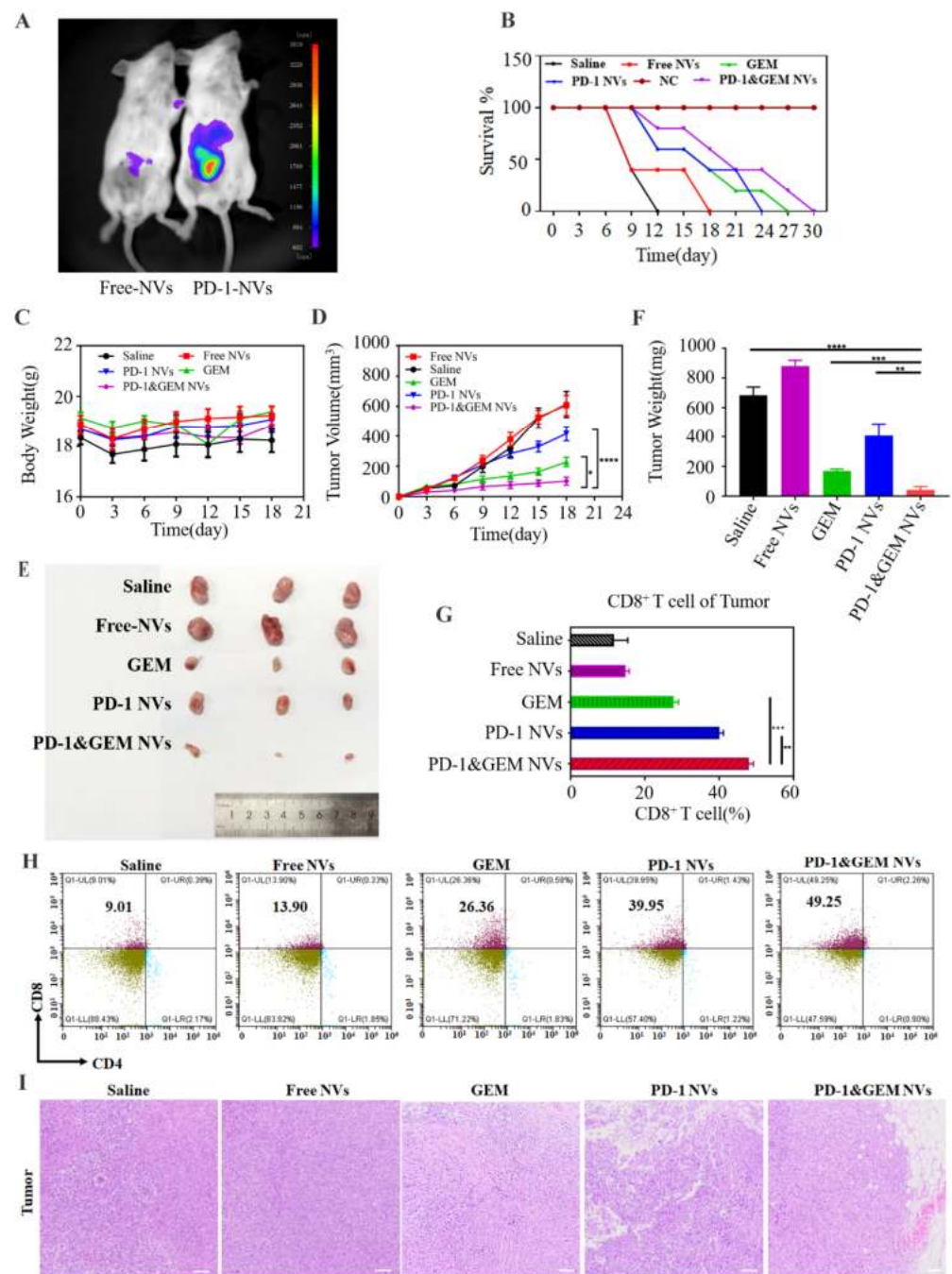
### 3.5. GEM&PD-1 NVs Inhibited the Growth of TNBC Breast Cancer In Vivo

The toxicity of Free NVs and PD-1 NVs in this study was evaluated. The result showed that heart, liver, spleen, lung, and kidney showed no pathological phenomena compared to the untreated group by hematoxylin-eosin (H&E) analysis (Figure S2).

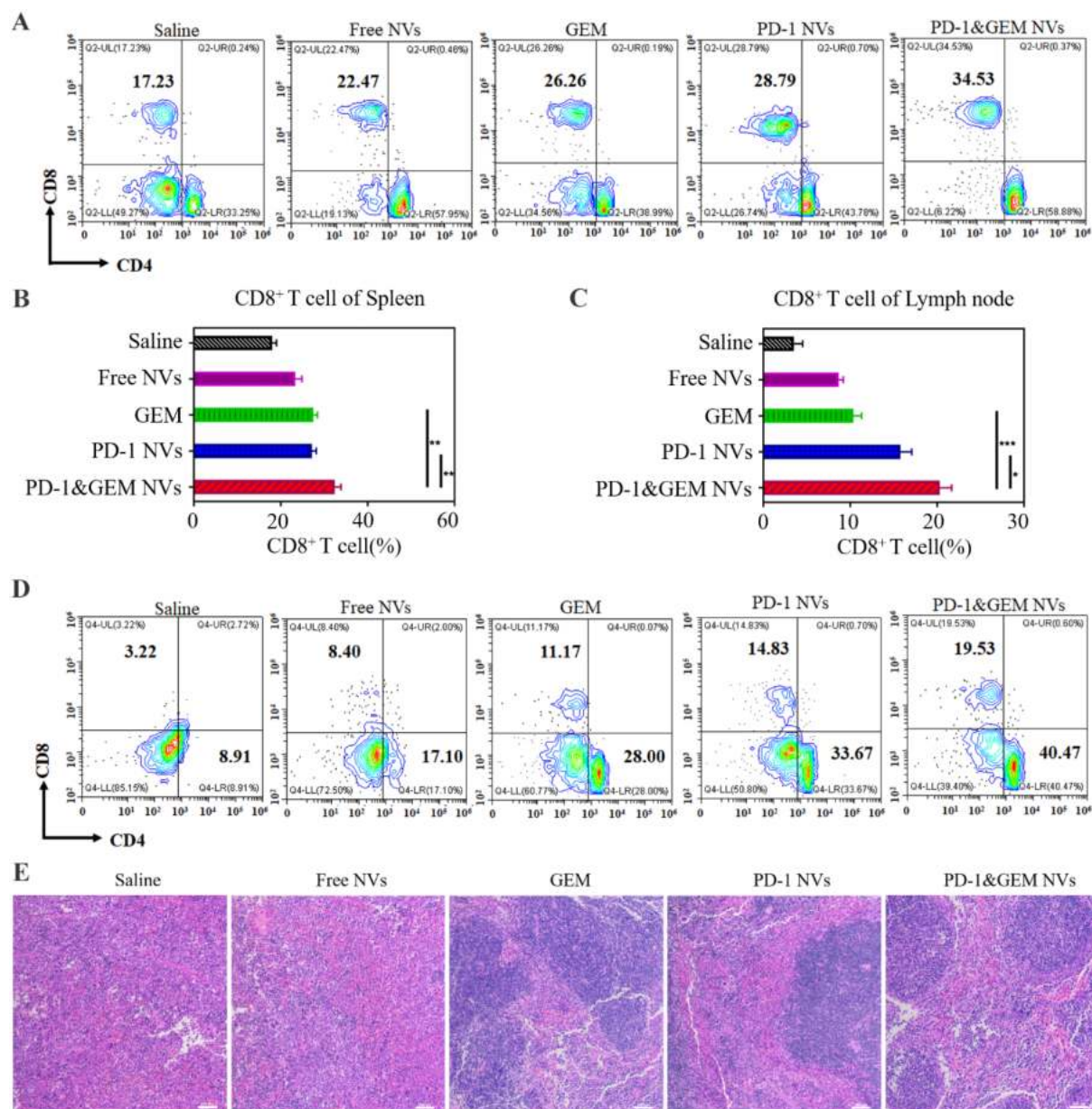
Next, to explore whether the GEM&PD-1 NVs promoted the immune response in the TNBC model, mice bearing-TNBC tumors were injected intravenously with PBS, Free NVs (25 mg/kg,  $n = 5$ ), PD-1 NVs (25 mg/kg,  $n = 5$ ), GEM (10 mg/kg,  $n = 5$ ), and GEM&PD-1 NVs (25 mg/kg,  $n = 5$ ). To avoid a cross-species immune response, we collected mouse 3T3 L1 cells-derived PD-L1 NVs [28]. The biological distribution of PD-L1 NVs was performed in tumor-bearing mice. Notably, we found cy5.5 labeled PD-1 NVs intensively accumulated in the tumor site compared to Free NVs (Figure 7A). The mouse models of breast cancer injected with 4T1 cells were established successfully after 7 days. Then, mice were received different treatments for 10 continuous days (on the 18th day from tumor inoculation). Tumor samples were collected on the 18th day following the performed experiments. However, after the treatment cycle, we stopped the injection to observe the survival days (considered the 1st day) among the different treatments. It was found that the PD-1&GEM NVs group significantly prolonged the survival time of mice for 30 days among different treatments after stopping the treatment, while saline delayed 12 days (Figure 7B). Moreover, there was no obvious weight loss in mice treated with different nanovesicles groups, indicating that the NVs were safe in mice (Figure 7C). Importantly, the growth of TNBC tumor was evidently delayed in the PD-1&GEM NVs group, which had better outcome than GEM and PD-1 NVs (Figure 7D–F). Next, treatment with GEM, PD-1 NVs, and PD-1&GEM NVs increased the proportion of CD8<sup>+</sup> T cell counts by 17.35%, 30.94%, and 40.24% in tumors treated with GEM, PD-1 NVs, and PD-1&GEM NVs compared to saline by flow cytometry analysis (Figure 7G,H). Moreover, hematoxylin-eosin (H&E) analysis also revealed more sparser tumor distribution in the PD-1&GEM NVs group than the saline group and the Free NVs group (Figure 7I). Therefore, these results demonstrated that PD-1&GEM NVs could inhibit TNBC tumor growth by increasing the infiltrated CD8<sup>+</sup> T cells.

To further assess the role of PD-1&GEM NVs in CD8<sup>+</sup> T cells, we also analyzed the activation of CD8<sup>+</sup> T cells in the mice spleens. Promisingly, compared with the saline, GEM single-drug group, PD-1 NVs group and PD-1&GEM NVs group significantly prompted the proportion of CD8<sup>+</sup> T cells by 9.03%, 11.56%, and 18.3%, suggesting that PD-1&GEM NVs had higher activation of CD8<sup>+</sup> T cells than GEM single-drug and PD-1 NVs in the spleens (Figure 8A). This was consistent with the corresponding statistical analysis (Figure 8B). Unsurprisingly, increased CD8<sup>+</sup> T cells in lymph nodes treated with GEM group, the PD-1 NVs group, and PD-1&GEM NVs group was also observed (Figure 8C,D). Similarly, hematoxylin-eosin (H&E) analysis also revealed that more normal cell morphologies were detected in spleens collected from mice received with the GEM group, the PD-1 NVs group, and the PD-1&GEM NVs treatments, compared with the pathological state in the normal saline group and the Free NVs group (Figure 8E). These results indicated that PD-1&GEM NVs restrained the proliferation of breast cancer and promoted CD8<sup>+</sup> T cell activation in vivo.





**Figure 7.** In vivo targeting ability and antitumor effect of PD-1&GEM NVs. (A) In vivo biodistribution imaging of PD-1 NVs that accumulate on the tumor compared to Free NVs. (B) Survival curves for the BALB/c mouse inoculated with TNBC received treatment of different groups ( $n = 5$ ). Saline (Group 1), Free NVs (Group 2), GEM (Group 3), PD-1 NVs (Group 4), PD-1&GEM NVs (Group 5). (C) Body weight of the BALB/c mouse inoculated with TNBC received treatment of different groups ( $n = 5$ ). Saline, Free NVs, GEM, PD-1 NVs, and PD-1&GEM NVs. (D) Average tumor volumes of mice inoculated with TNBC in different groups ( $n = 5$ ). (E) Representational tumor image collected from euthanized mice after different treatments. Saline, Free NVs, GEM, PD-1 NVs, and PD-1&GEM NVs. (F) Quantitative analysis of tumor weight of different groups ( $n = 3$ ). (G,H) Representative plots and quantitative analysis of CD8<sup>+</sup> T cells (gated on positive CD3<sup>+</sup> cells) in tumor in differently treated mice groups by flow cytometry ( $n = 3$ ). Error bar, mean  $\pm$  SEM. (I) Histological images for H&E staining obtained from the tumor of mice treated in different group. Data were expressed as mean  $\pm$  SEM,  $n = 3$ . \*  $p < 0.05$ , \*\*  $p < 0.01$ , \*\*\*  $p < 0.001$ , \*\*\*\*  $p < 0.0001$ .



**Figure 8.** In vivo PD-1&GEM NVs promoted the density of CD8<sup>+</sup> T cells in spleens and lymph nodes. (A,B) Representative plots and quantitative analysis of CD8<sup>+</sup> T cells (gated on positive CD3<sup>+</sup> cells) in spleens in different treated mice groups by flow cytometry ( $n = 3$ ). Error bar, mean  $\pm$  SEM. (C,D) Representative plots and quantitative analysis of CD8<sup>+</sup> T cells (gated on positive CD3<sup>+</sup> cells) in lymph nodes in different treated mice groups by flow cytometry ( $n = 3$ ). Error bar, mean  $\pm$  SEM. (E) Histological images for H&E staining obtained from the spleen of mice treated in different group. Data were expressed as mean  $\pm$  SEM,  $n = 3$ . \*  $p < 0.05$ , \*\*  $p < 0.01$ , \*\*\*  $p < 0.001$ . scale bar = 100  $\mu$ m.

#### 4. Discussion

TNBC is considered as an aggressive type of breast cancer because it grows and spreads quickly and lacks effective treatment options, thereby leading to a poor prognosis [29]. Recently, research has found that combination therapies displayed favorable efficacy of treatment [30]. Excitingly, combination with chemotherapy drugs and immunotherapies can improve clinical outcomes in patients [31,32]. In 14 November 2020, the FDA approved PD-1 inhibitor Keytruda combined with chemotherapy for TNBC. This is the first time that combination therapy of immunotherapy and chemotherapy has been approved by FDA for the treatment of breast cancer, representing an important milestone [13]. However,

another similar treatment scheme using PD-L1 inhibitor Tecentriq combined with albumin paclitaxel was rejected by EMA because it did not get the expected effect in the phase III clinical trial in January 2021 [33]. It is still very necessary to explore new combination therapies of different immune drugs and chemotherapeutic drugs. Therefore, exploring different combination therapies still has potential significance for the treatment of the triple-negative breast cancers.

Synergistic nanovesicles as a drug carrier could deliver anti-tumor drugs in a targeted manner, such as liposomes. Although liposomes have been applied in clinic trials by better compatibility and modifications, poor targeting, unstable morphology, immunogenicity, and their inability to cross the biological barrier have limited their therapeutic efficacy [34]. Recently, exosomes naturally released by different cells as drug carrier have become an alternative strategy by overcoming the abovementioned shortcomings of liposomes. However, complex purification processes and limited mass production are the obstacles of clinical translation. Strikingly, membrane-derived nanovesicles (NVs) share similar characteristics and function with exosomes, which have advantages in large-scale preparation, and can at the same time stably carry targeting ligands through genetic modification strategies and carry clinically chemotherapeutic drugs [21,22]. Noteworthy, it has been reported that NVs could retain structural stability for over 7 days at 4 °C as the storage condition, and the zeta and diameter of NVs still retain stability for over 24 h when in physiological conditions (PBS +10% serum) [35]. In this study, we proposed a protocol for cell-membrane derived PD-1 NVs as a GEM-targeted drug delivery system. PD-1 NVs could not only passively accumulate in the tumor due to the enhanced permeability and retention (EPR) effect [36,37], but also actively target overexpressing-PD-L1 TNBC, contributing to enrichment of PD-1 NVs. We also confirmed that the PD-1 NVs could efficiently bind to the PD-L1 receptor on breast cancer cells *in vitro* (Figure 4C). In addition, *in vivo* experiments also observed that the cell vesicles with high expression of PD-1 were more enriched in the transplanted tumor site of MDA-MB-231 than PD-1 free vesicles (Figure 7A). As we know that most chemotherapeutic drugs have low selectivity, long-term high-dose use will cause a great toxic effect and other side effects. Thus, wrapped gemcitabine in PD-1 NVs will improve the pharmacokinetics, increase the effective drug concentration at the tumor site, and significantly reduce the systemic toxicity of gemcitabine. Recent studies have emphasized that when cell-membrane derived NVs fused with cell membranes by means of lipid fusion, encapsulated contents in the NVs were delivered directly to the cytoplasm. In addition, NVs were also internalized by phagocytosis-based uptake pathway. After cellular uptake, NVs may be transported to endosomes and subsequently fused with lysosomes for degradation of NVs. Meanwhile, packaged drugs from NVs were gradually released into the cytoplasm, thus leading to enhanced drug delivery with better safety profiles [21,38]. Moreover, if gemcitabine within the NVs was released outside the tumor cells and subsequently penetrated into the tumor cytoplasm, they thereby improved the therapeutic target effect of the encapsulated drug at the tumor sites. It was noteworthy that our results demonstrated that gemcitabine from PD-1&GEM NVs released slowly with a peak of 24 h *in vitro* (Figure S1B). In brief, the combined NVs strategy outperformed the efficacy of gemcitabine when administered alone.

Of note, our study also verified that PD-1 NVs combined with gemcitabine has better therapeutic effect. PD-1&GEM NVs showed a better inhibition on the proliferation of TNBC tumor than PD-1 NVs alone, achieving a synergetic effect of immunotherapy and chemotherapy. Moreover, PD-1&GEM NVs significantly promoted the proliferation of PBMC, and perhaps PBMC was activated by released antigen when gemcitabine killed the tumor cells. For example, the proliferation of CFSE-staining PBMC treated with PD-1&GEM NVs was most significant among different treatment groups (Figure 6A). Consistent with *in vitro* experiments, *in vivo* PD-1&GEM NVs remarkably increased infiltrated CD8<sup>+</sup> T cell and delayed the tumor growth more than PD-1 NVs (Figure 7D,H). Therefore, our study highlighted the power of combining low-dose gemcitabine and PD-1 in the nanovesicles as treatment to inhibit the proliferation of triple-negative breast cancer.

**Supplementary Materials:** The following supporting information can be downloaded at: <https://www.mdpi.com/article/10.3390/pharmaceutics14061263/s1>.

**Author Contributions:** Conceptualization, H.Z., Z.X. and X.X.; methodology, H.Z., Z.X. and X.X.; software, H.-I.T.; validation, X.L., P.S. and Y.X.; formal analysis, H.Z., X.L. and P.S.; investigation, H.Z. and D.S.; resources, Z.X. and D.S.; data curation, Y.X. and H.-I.T.; writing—original draft preparation, H.Z., Z.X. and X.X.; writing—review and editing, H.Z., Z.X. and X.X.; visualization, Y.X. and D.S.; supervision, F.C., X.C. and H.C.; project administration, F.C., X.C. and H.C.; funding acquisition, F.C., X.C. and H.C. All authors have read and agreed to the published version of the manuscript.

**Funding:** This research was supported by the National Natural Science Foundation of China (81970145 and 82001698); Natural Science Foundation of Guangdong Province (2020A1515011465 and 2020A151501467); Science, Technology & Innovation Commission of Shenzhen Municipality (JCYJ20190807151609464, JCYJ20200109142605909, JCYJ20210324120007020 and JCYJ20180228175150018); Sun Yat-sen University (20ykzd17); International Collaboration of Science and Technology of Guangdong Province (2020A0505100031); and Guangdong Provincial Key Laboratory of Digestive Cancer Research (No. 2021B1212040006).

**Institutional Review Board Statement:** The study was conducted in accordance with the Declaration of Helsinki, and approved by the Institutional Review Board (or Ethics Committee) of Sun Yat-Sen University (protocol code: SYSU-IACUC-2021-000046, 19 January 2021).

**Informed Consent Statement:** Not applicable.

**Data Availability Statement:** All data generated or analyzed during this study are included in this published article and its Supplementary Information Files.

**Conflicts of Interest:** The authors declare no conflict of interest.

## References

1. Sung, H.; Ferlay, J.; Siegel, R.L.; Laversanne, M.; Soerjomataram, I.; Jemal, A.; Bray, F. Global Cancer Statistics 2020: GLOBOCAN Estimates of Incidence and Mortality Worldwide for 36 Cancers in 185 Countries. *Cancer J. Clin.* **2021**, *71*, 209–249. [CrossRef] [PubMed]
2. Pantelidou, C.; Sonzogno, O.; De Oliveria Taveira, M.; Mehta, A.K.; Kothari, A.; Wang, D.; Visal, T.; Li, M.K.; Pinto, J.; Castrillon, J.A.; et al. PARP Inhibitor Efficacy Depends on CD8(+) T-cell Recruitment via Intratumoral STING Pathway Activation in BRCA-Deficient Models of Triple-Negative Breast Cancer. *Cancer Discov.* **2019**, *9*, 722–737. [CrossRef] [PubMed]
3. Garrido-Castro, A.C.; Lin, N.U.; Polyak, K. Insights into Molecular Classifications of Triple-Negative Breast Cancer: Improving Patient Selection for Treatment. *Cancer Discov.* **2019**, *9*, 176–198. [CrossRef] [PubMed]
4. Harbeck, N.; Gnant, M. Breast cancer. *Lancet* **2017**, *389*, 1134–1150. [CrossRef]
5. Wengner, A.M.; Scholz, A.; Haendler, B. Targeting DNA Damage Response in Prostate and Breast Cancer. *Int. J. Mol. Sci.* **2020**, *21*, 8273. [CrossRef] [PubMed]
6. Paroha, S.; Verma, J.; Dubey, R.D.; Dewangan, R.P.; Molugulu, N.; Bapat, R.A.; Sahoo, P.K.; Kesharwani, P. Recent advances and prospects in gemcitabine drug delivery systems. *Int. J. Pharm.* **2021**, *592*, 120043. [CrossRef]
7. Zou, W.; Wolchok, J.D.; Chen, L. PD-L1 (B7-H1) and PD-1 pathway blockade for cancer therapy: Mechanisms, response biomarkers, and combinations. *Sci. Transl. Med.* **2016**, *8*, 328rv324. [CrossRef]
8. Sun, C.; Mezzadra, R.; Schumacher, T.N. Regulation and Function of the PD-L1 Checkpoint. *Immunity* **2018**, *48*, 434–452. [CrossRef]
9. Topalian, S.L.; Taube, J.M.; Anders, R.A.; Pardoll, D.M. Mechanism-driven biomarkers to guide immune checkpoint blockade in cancer therapy. *Nat. Rev. Cancer* **2016**, *16*, 275–287. [CrossRef]
10. Brahmer, J.R.; Tykodi, S.S.; Chow, L.Q.; Hwu, W.J.; Topalian, S.L.; Hwu, P.; Drake, C.G.; Camacho, L.H.; Kauh, J.; Odunsi, K.; et al. Safety and activity of anti-PD-L1 antibody in patients with advanced cancer. *N. Engl. J. Med.* **2012**, *366*, 2455–2465. [CrossRef]
11. Doroshow, D.B.; Bhalla, S.; Beasley, M.B.; Sholl, L.M.; Kerr, K.M.; Gnjjatic, S.; Wistuba, I.I.; Rimm, D.L.; Tsao, M.S.; Hirsch, F.R. PD-L1 as a biomarker of response to immune-checkpoint inhibitors. *Nat. Rev. Clin. Oncol.* **2021**, *18*, 345–362. [CrossRef] [PubMed]
12. Schmid, P.; Adams, S.; Rugo, H.S.; Schneeweiss, A.; Barrios, C.H.; Iwata, H.; Diéras, V.; Hegg, R.; Im, S.A.; Shaw Wright, G.; et al. Atezolizumab and Nab-Paclitaxel in Advanced Triple-Negative Breast Cancer. *N. Engl. J. Med.* **2018**, *379*, 2108–2121. [CrossRef] [PubMed]
13. Cortes, J.; Cescon, D.W.; Rugo, H.S.; Nowecki, Z.; Im, S.A.; Yusof, M.M.; Gallardo, C.; Lipatov, O.; Barrios, C.H.; Holgado, E.; et al. Pembrolizumab plus chemotherapy versus placebo plus chemotherapy for previously untreated locally recurrent inoperable or metastatic triple-negative breast cancer (KEYNOTE-355): A randomised, placebo-controlled, double-blind, phase 3 clinical trial. *Lancet* **2020**, *396*, 1817–1828. [CrossRef]

14. Salas-Benito, D.; Pérez-Gracia, J.L.; Ponz-Sarvisé, M.; Rodríguez-Ruiz, M.E.; Martínez-Forero, I.; Castañón, E.; López-Picazo, J.M.; Sanmamed, M.F.; Melero, I. Paradigms on Immunotherapy Combinations with Chemotherapy. *Cancer Discov.* **2021**, *11*, 1353–1367. [CrossRef] [PubMed]
15. Rosa, K. Roche Withdraws Application for Atezolizumab in Early or Locally Advanced TNBC in Europe. Available online: <https://www.onclive.com/view/roche-withdraws-application-for-atezolizumab-in-early-or-locally-advanced-tnbc-in-europe> (accessed on 27 July 2021).
16. Robbins, P.D.; Dorransoro, A.; Booker, C.N. Regulation of chronic inflammatory and immune processes by extracellular vesicles. *J. Clin. Investig.* **2016**, *126*, 1173–1180. [CrossRef]
17. Ma, J.; Zhang, Y.; Tang, K.; Zhang, H.; Yin, X.; Li, Y.; Xu, P.; Sun, Y.; Ma, R.; Ji, T.; et al. Reversing drug resistance of soft tumor-repopulating cells by tumor cell-derived chemotherapeutic microparticles. *Cell Res.* **2016**, *26*, 713–727. [CrossRef]
18. Bai, Y.; Guo, J.; Liu, Z.; Li, Y.; Jin, S.; Wang, T. The Role of Exosomes in the Female Reproductive System and Breast Cancers. *Oncotargets Ther.* **2020**, *13*, 12567–12586. [CrossRef]
19. Wang, X.; Xu, C.; Hua, Y.; Sun, L.; Cheng, K.; Jia, Z.; Han, Y.; Dong, J.; Cui, Y.; Yang, Z. Exosomes play an important role in the process of psoralen reverse multidrug resistance of breast cancer. *J. Exp. Clin. Cancer Res.* **2016**, *35*, 186. [CrossRef]
20. Lowry, M.C.; Gallagher, W.M.; O’Driscoll, L. The Role of Exosomes in Breast Cancer. *Clin. Chem.* **2015**, *61*, 1457–1465. [CrossRef]
21. Zhang, X.; Wang, C.; Wang, J.; Hu, Q.; Langworthy, B.; Ye, Y.; Sun, W.; Lin, J.; Wang, T.; Fine, J.; et al. PD-1 Blockade Cellular Vesicles for Cancer Immunotherapy. *Adv. Mater.* **2018**, *30*, e1707112. [CrossRef]
22. Zhang, X.; Wang, J.; Chen, Z.; Hu, Q.; Wang, C.; Yan, J.; Dotti, G.; Huang, P.; Gu, Z. Engineering PD-1-Presenting Platelets for Cancer Immunotherapy. *Nano Lett.* **2018**, *18*, 5716–5725. [CrossRef] [PubMed]
23. Wang, Y.; Xu, X.; Chen, X.; Li, J. Multifunctional Biomedical Materials Derived from Biological Membranes. *Adv. Mater.* **2021**, e2107406. [CrossRef]
24. Tan, S.; Wu, T.; Zhang, D.; Zhang, Z. Cell or cell membrane-based drug delivery systems. *Theranostics* **2015**, *5*, 863–881. [CrossRef] [PubMed]
25. de Gregorio, A.; Häberle, L.; Fasching, P.A.; Müller, V.; Schrader, I.; Lorenz, R.; Forstbauer, H.; Friedl, T.W.P.; Bauer, E.; de Gregorio, N.; et al. Gemcitabine as adjuvant chemotherapy in patients with high-risk early breast cancer—results from the randomized phase III SUCCESS-A trial. *Breast Cancer Res.* **2020**, *22*, 111. [CrossRef] [PubMed]
26. Zhu, J.; Chen, Y.; Ji, Y.; Yu, Y.; Jin, Y.; Zhang, X.; Zhou, J. Gemcitabine induces apoptosis and autophagy via the AMPK/mTOR signaling pathway in pancreatic cancer cells. *Biotechnol. Appl. Biochem.* **2018**, *65*, 665–671. [CrossRef] [PubMed]
27. Tripathy, D. Overview: Gemcitabine as single-agent therapy for advanced breast cancer. *Clin. Breast Cancer* **2002**, *3* (Suppl. S1), 8–11. [CrossRef]
28. Yang, M.; Xu, Z.; Yan, H.; Tsai, H.I.; Su, D.; Yan, F.; Lu, Q.; Feng, J.; Zeng, W.; Xi, L.; et al. PD-L1 cellular nanovesicles carrying rapamycin inhibit alloimmune responses in transplantation. *Biomater. Sci.* **2021**, *9*, 1246–1255. [CrossRef]
29. Loibl, S.; Poortmans, P.; Morrow, M.; Denkert, C.; Curigliano, G. Breast cancer. *Lancet* **2021**, *397*, 1750–1769. [CrossRef]
30. Bayat Mokhtari, R.; Homayouni, T.S.; Baluch, N.; Morgatskaya, E.; Kumar, S.; Das, B.; Yeger, H. Combination therapy in combating cancer. *Oncotarget* **2017**, *8*, 38022–38043. [CrossRef]
31. Nikanjam, M.; Patel, H.; Kurzrock, R. Dosing immunotherapy combinations: Analysis of 3,526 patients for toxicity and response patterns. *Oncimmunology* **2017**, *6*, e1338997. [CrossRef]
32. Rizvi, N.A.; Hellmann, M.D.; Brahmer, J.R.; Juergens, R.A.; Borghaei, H.; Gettinger, S.; Chow, L.Q.; Gerber, D.E.; Laurie, S.A.; Goldman, J.W.; et al. Nivolumab in Combination With Platinum-Based Doublet Chemotherapy for First-Line Treatment of Advanced Non-Small-Cell Lung Cancer. *J. Clin. Oncol.* **2016**, *34*, 2969–2979. [CrossRef] [PubMed]
33. Miles, D.; Gligorov, J.; André, F.; Cameron, D.; Schneeweiss, A.; Barrios, C.; Xu, B.; Wardley, A.; Kaen, D.; Andrade, L.; et al. Primary results from IMPassion131, a double-blind, placebo-controlled, randomised phase III trial of first-line paclitaxel with or without atezolizumab for unresectable locally advanced/metastatic triple-negative breast cancer. *Ann. Oncol.* **2021**, *32*, 994–1004. [CrossRef] [PubMed]
34. Srivastava, A.; Rathore, S.; Munshi, A.; Ramesh, R. Organically derived exosomes as carriers of anticancer drugs and imaging agents for cancer treatment. In *Seminars in Cancer Biology*; Academic Press: Cambridge, MA, USA, 2022. [CrossRef]
35. Ramesh, A.; Kumar, S.; Nandi, D.; Kulkarni, A. CSF1R- and SHP2-Inhibitor-Loaded Nanoparticles Enhance Cytotoxic Activity and Phagocytosis in Tumor-Associated Macrophages. *Adv. Mater.* **2019**, *31*, e1904364. [CrossRef] [PubMed]
36. Caro, C.; Avasthi, A.; Paez-Muñoz, J.M.; Pernia Leal, M.; García-Martín, M.L. Passive targeting of high-grade gliomas via the EPR effect: A closed path for metallic nanoparticles? *Biomater. Sci.* **2021**, *9*, 7984–7995. [CrossRef] [PubMed]
37. Islam, W.; Fang, J.; Imamura, T.; Etrych, T.; Subr, V.; Ulbrich, K.; Maeda, H. Augmentation of the Enhanced Permeability and Retention Effect with Nitric Oxide-Generating Agents Improves the Therapeutic Effects of Nanomedicines. *Mol. Cancer Ther.* **2018**, *17*, 2643–2653. [CrossRef]
38. Donahue, N.D.; Acar, H.; Wilhelm, S. Concepts of nanoparticle cellular uptake, intracellular trafficking, and kinetics in nanomedicine. *Adv. Drug Deliv. Rev.* **2019**, *143*, 68–96. [CrossRef]

Review

# Therapeutic Vaccines Targeting Neoantigens to Induce T-Cell Immunity against Cancers

Shih-Cheng Pao <sup>1,2</sup> , Mu-Tzu Chu <sup>1</sup>  and Shuen-Iu Hung <sup>1,2,\*</sup> 

<sup>1</sup> Cancer Vaccine & Immune Cell Therapy Core Lab, Department of Medical Research, Chang Gung Memorial Hospital, Linkou Branch, No. 5, Fuxing St., Taoyuan 333, Taiwan; bigan818@gmail.com (S.-C.P.); clairechuymu@gmail.com (M.-T.C.)

<sup>2</sup> Institute of Pharmacology, School of Medicine, National Yang Ming Chiao Tung University, No. 155, Sec. 2, Linong Street, Taipei 112, Taiwan

\* Correspondence: sihung@cgmh.org.tw or hungshueniu@gmail.com; Tel.: +886-3-328-1200 (ext. 7806)

**Abstract:** Cancer immunotherapy has achieved multiple clinical benefits and has become an indispensable component of cancer treatment. Targeting tumor-specific antigens, also known as neoantigens, plays a crucial role in cancer immunotherapy. T cells of adaptive immunity that recognize neoantigens, but do not induce unwanted off-target effects, have demonstrated high efficacy and low side effects in cancer immunotherapy. Tumor neoantigens derived from accumulated genetic instability can be characterized using emerging technologies, such as high-throughput sequencing, bioinformatics, predictive algorithms, mass-spectrometry analyses, and immunogenicity validation. Neoepitopes with a higher affinity for major histocompatibility complexes can be identified and further applied to the field of cancer vaccines. Therapeutic vaccines composed of tumor lysates or cells and DNA, mRNA, or peptides of neoantigens have revoked adaptive immunity to kill cancer cells in clinical trials. Broad clinical applicability of these therapeutic cancer vaccines has emerged. In this review, we discuss recent progress in neoantigen identification and applications for cancer vaccines and the results of ongoing trials.

**Keywords:** cancer therapy; neoantigens; immunotherapy; vaccine

**Citation:** Pao, S.-C.; Chu, M.-T.; Hung, S.-I. Therapeutic Vaccines Targeting Neoantigens to Induce T-Cell Immunity against Cancers. *Pharmaceutics* **2022**, *14*, 867. <https://doi.org/10.3390/pharmaceutics14040867>

Academic Editor: Hassan Bousbaa

Received: 16 March 2022

Accepted: 13 April 2022

Published: 15 April 2022

**Publisher's Note:** MDPI stays neutral with regard to jurisdictional claims in published maps and institutional affiliations.



**Copyright:** © 2022 by the authors. Licensee MDPI, Basel, Switzerland. This article is an open access article distributed under the terms and conditions of the Creative Commons Attribution (CC BY) license (<https://creativecommons.org/licenses/by/4.0/>).

## 1. Introduction

Cancers are driven by genetic instabilities that rapidly accumulate somatic mutations and eventually alter cell properties. Excellent progression has resulted from understanding the mechanisms of genetic mutations, immune recognition of tumor antigens, tumor-mediated immunosuppression, immune surveillance, and tumor escape. Genome sequencing has revealed the heterogeneity of cancer cells, as evidenced by the Cancer Genome Atlas [1–4]. Neoantigens are a group of tumor-specific antigens (TSAs) arising from genetic variations or retroelements and are considered one of the vital characteristics and derivations of cancers. They have aberrant residues caused by gene alterations that are only expressed on tumor cells and serve as ideal foreign targets for recognition by T cells with high-affinity T-cell receptors (TCRs) [3,5,6]. Theoretically, targeting neoantigens avoids unwanted off-target effects and can precisely guide effector cells to tumor cells. Neoantigen vaccination could be an active immunotherapy and provide immunogens to the immune system to elicit an antitumor immune response. Cancer vaccines have been rapidly developed as a practical method to boost target-specific humoral and cellular immunity and induce long-lasting immune protection [7]. Various vaccination approaches are under investigation and are broadly categorized based on their design methods, including tumor lysates, cell-based vaccines, gene-based vaccines, and peptide-based vaccines. This review summarizes the current knowledge, development, and challenges associated with immunotherapeutics targeting neoantigens by assessing current cancer clinical tri-

als of vaccines to provide insights into the clinical development of personalized cancer immunotherapy.

## 2. Types of Cancer Antigens

Tumor cells have a wide range of protein-expression profiles that differ from those of normal cells. There are different types of tumor antigens: tumor-associated antigens (TAAs), TSAs, and unconventional antigens (UCAs) [8].

Compared to normal cells, TAAs are unmodified self-proteins that are abnormally expressed in cancerous cells due to oncogenic signaling processes. The upregulated expression of these wild-type proteins or glycoproteins enables TAAs to act as self-antigens on tumor cells. Most TAAs refer to overexpressed tumor antigens, for example, the receptor for advanced glycation endproducts-1 (RAGE-1), human telomerase reverse transcriptase (hTERT), human epidermal growth factor receptor 2 (HER2), mesothelin, and mucin 1 (MUC1) [9–14]. In addition, TAAs can be cell-lineage-differentiation antigens (e.g., prostate-specific antigen (PSA) and prostatic-acid phosphatase (PAP), which are typically not expressed in adult tissues [15,16], and cancer/germline antigens (also known as cancer/testis) (e.g., melanoma-associated antigen 1 (MAGE-A1), melanoma-associated antigen 3 (MAGE-A3), New York esophageal squamous-cell carcinoma 1 (NY-ESO-1), and preferentially expressed antigen of melanoma (PRAME), which are typically only expressed in immune-privileged germline cells [17–21]. These TAAs may represent universal targets for chimeric-antigen-receptor-T (CAR-T) therapy in patients with the same malignancy.

In comparison, TSAs are neoantigens expressed by cancer cells. The uniqueness of the mutant epitopes makes them more likely to be identified by the diverse TCRs of T cells, which are not depleted during clonal selection in the thymus. The degraded peptide fragments of mutant proteins become tumor antigens that play essential roles in T-cell-mediated immunity against cancer. Neoantigens could represent the differences between the peptide repertoires of the major-histocompatibility-complex (MHC) presentations of cancer cells and normal cells. Most TSAs arise from somatic mutations of non-synonymous single-nucleotide variants, frameshifts, insertion or deletion (INDEL) mutations, gene fusion, splice variants, and retroelements [22]. Unlike TAAs, which are self-antigens not recognized by T cells, TSAs are aberrant proteins absent in T-cell clonal selection during thymus education and are, therefore, more likely to escape the central tolerance mechanism.

Unconventional antigens (UCAs) originate from aberrant transcription, translation, or post-translational modifications in tumor cells. Some UCAs may be completely tumor specific, whereas others may also occur in normal cells.

## 3. Neoantigen-Induced Antitumor Immunity

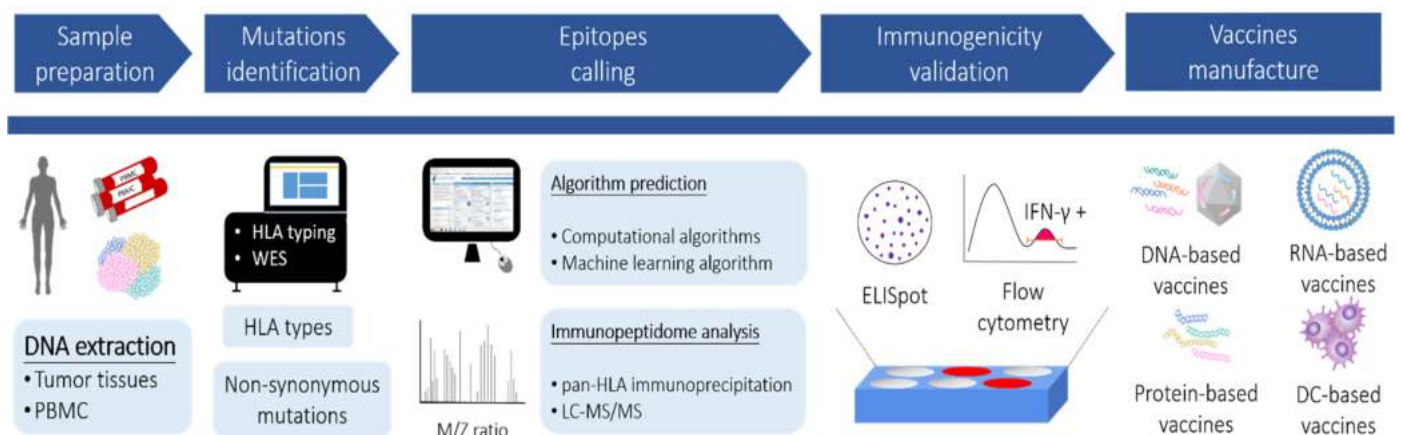
Regarding the molecular mechanism, neoantigens are proposed to enhance their immunogenicity by modulating immune synapses in several ways: (1) Compared to wild epitopes, neoepitopes strengthen the TCR–MHC-I stability with higher levels of binding affinities and then result in a robust immune response [23]. (2) The absence of neoepitopes in MHC presentation during T-cell selection in thymus education improves TCR recognition [24]. (3) Flanking residues of neoepitopes interfere with and compete with endogenous peptides on the MHC binding groove [25].

In the tumor microenvironment (TME), abundant tumor antigens can be secreted via tumor-derived exosomes, which are further enhanced through tumor-cell death caused by immune modulation, radiotherapy, or chemotherapy [26–28]. Tumor-infiltrating antigen-presenting cells (APCs) capture tumor antigens and migrate to regional lymph nodes. The epitopes of the captured antigens presented on human-leukocyte-antigen (HLA) molecules of APCs can initiate the activation and differentiation of tumor-specific CD4<sup>+</sup> and CD8<sup>+</sup> T cells in the draining lymph node, resulting in the expansion of effector T cells in secondary lymphoid organs [29]. Many effector cells then travel through the bloodstream to the tumor site by involving various chemokines (e.g., C-C motif chemokine ligand 2 (CCL2), C-X-C motif chemokine ligand 2 (CXCL2), and C-X-C motif chemokine ligand 16 (CXCL16)) [30,31].

Activated CD8<sup>+</sup> T cells can recognize the expressed neoepitope–HLA complexes on tumor cells and then kill cancer cells through the degranulation of cytotoxic proteins, such as perforin, granzyme, and granulysin. CD4<sup>+</sup> T cells indirectly modulate antitumor cellular and humoral immune responses. Released tumor antigens prime more tumor-reactive immune cells into the TME and trigger adaptive-immune memory responses [29]. However, these immune reactions can be inhibited by an immunosuppressive microenvironment.

#### 4. Neoantigen Identification

Approaches for identifying neoantigens and proceeding to vaccine manufacture are illustrated in Figure 1, which involve the discovery of the mutanome by next-generation sequencing (NGS), prediction of HLA epitopes by algorithms or mass spectrometry (MS), and functional validation by immunological assays.



**Figure 1.** Schematic representation of neoantigen selection for therapeutic cancer vaccines. The DNA samples are extracted from cancer tissues and peripheral blood mononuclear cells (PBMC), respectively. Non-synonymous mutations and HLA types are obtained through whole-exome sequencing (WES) and HLA genotyping following bioinformatic analyses. The potential neoepitopes derived from the identified mutations are prioritized according to (1) algorithm prediction or (2) immunopeptidome analysis. Afterward, each prioritized neoepitope is examined by immunological assays (e.g., ELISpot or flow cytometry) to validate the immunogenicity. Vaccines encoding the selected neoepitopes are then generated in various formats, including DNA-based, RNA-based, peptide-based, and dendritic-cell (DC)-based vaccines.

##### 4.1. Discovery of the Mutanome by Next-Generation Sequencing

Practitioners and researchers used to have technical restrictions until the advent of advanced high-throughput NGS technologies. Reliable sequencing data are generated at a lower price with greater accuracy to identify individual gene variations in tumor samples. Identifying the entirety of somatic cancer mutations in an individual tumor, referred to as variant calling of the mutanome, yields potential neoantigens. Typically, a small fraction of tumor biopsies is required for DNA and RNA sequencing to obtain the variation profile of the tumor. For SNVs, INDELs, and gene fusions, variants of the mutanome could be detected by comparing WES data from tumor tissue and healthy samples (e.g., PBMC) of the same individual to exclude germline variants [32]. Endogenous retroelement-derived antigens were identified from RNA-expression data. For splicing variants, tools such as SplAdder [33], SpliceGrapher [34], and ASGAL mainly compare the spliced alignments of RNA-seq data to genome references and then generate splicing graphs to predict alternative cleaving events [35]. In addition, these tools integrate proteomic databases to analyze cancer-specific germline and somatic mutations that are rapidly developing. A recently reported proteogenomic tool called QUILTS can be used to generate variants including SNVs, INDELs, fusions, and junctions from RNA-seq data [36].



#### 4.2. HLA-Epitope Calling by Computational Algorithms

Only a small portion of expressed neoantigens can fit perfectly into the binding pockets of HLA molecules and possess adequate immunogenicity to elicit immune responses. Selecting neoepitopes with the highest probability of increasing tumor-specific immune responses is critical for designing neoantigen vaccines [6]. The prediction of neoepitopes using computational algorithms is a commonly applied methodology. These programs (e.g., NetMHCpan [37], MULTIPRED [38], IEDB [39], and EpitoolKit [40]) simulate the binding affinity of antigen epitopes with the MHC alleles of subjects and predict potential neoantigens.

The MHC-I-epitope-prediction algorithms have gained greater attention because hypotheses assume that CD8<sup>+</sup> T-cell-mediated immune responses play a more vital role in antitumor immunity [41]. CD8<sup>+</sup> T cells infiltrating the tumors has correlated with a better prognosis of the disease [42]. Furthermore, CD4<sup>+</sup> T cells also play essential roles in cancer immunity. Kreiter et al. reported that mutant MHC-class-II epitopes could drive CD4<sup>+</sup> T-cell-mediated therapeutic immune responses to cancer [43]. Trans et al. reported that the application of adoptive cell therapy (ACT) using neoantigen ERBB2 (HER2) interaction protein-specific CD4<sup>+</sup> tumor-infiltrating lymphocytes (TILs) achieved tumor regression in a patient with metastatic cholangiocarcinoma [44]. Due to these clinical findings indicating that CD4<sup>+</sup> T-cell-mediated antitumor immunity is indispensable for cancer immunotherapy, MHC-II-epitope predictors have been recently improved. For instance, NetMHCIIpan adapted the NN-align algorithms, which add the influence of the core structure of epitopes and the flanking-region characteristics, thereby substantially facilitating MHC-II-binding-prediction performance [45,46].

#### 4.3. Identification of HLA Epitopes by Mass Spectrometry (MS)

Recent developments in MS-based sequencing technology have expanded the detection of peptide epitopes on MHC molecules [47,48]. For MS detection, HLA molecules from harvested cell lines or resected tumors can be isolated by pan-HLA immunoprecipitation (IP). After several washes to remove the unwanted mixture, binding epitopes of HLA molecules can be dissociated, purified, and subsequently analyzed by liquid chromatography–tandem MS (LC–MS/MS) [49]. Algorithms have been developed for immunogenic antigen discovery and the establishment of high-resolution, raw quantitative MS data for the patient-customized peptide repertoire, such as MaxQuant [50], SWATH-MS [51], Proteome discovery [52], and PEAKS studio [53]. MS-based sequencing enables researchers to directly identify clinically relevant neoepitopes in human cancer tissues. MS-based HLA-immunopeptidome profiling is also practical for spotting epitopes from post-translational modification [54]. For instance, a study revealed 11 epitopes from gene variants of over 90,000 immunopeptides identified from melanoma patients. Through MS analysis, phosphorylated immune epitopes were identified, and positions 4 and 6 of the 9–12-mer HLA-binding peptide were the major phosphorylation sites [55].

#### 4.4. Prediction of HLA Epitopes by Machine Learning Algorithms

By combining it with experimental HLA-immunopeptidome profiling, machine learning in silicon algorithms was developed to provide a rapid and accurate prediction platform. Abelin et al. developed a neural-network prediction algorithm using an extensive dataset collected via MS profiling of HLA-associated peptidomes and found that it outperformed the experimentally measured epitope affinities [56]. GibbsCluster, another machine-learning model built on MS-analysis data integrated with in vitro binding-affinity results, showed an outstanding performance for predicting antigen-restricted epitopes [57,58]. In addition, Bulik-Sullivan et al. launched a computational model named EDGE for epitope prediction, which was trained using a dataset of HLA–MS neoantigen peptides and genomic data of 74 patients. EDGE validation showed a nine-fold-higher positive predictive value than that obtained from tumor test sets using binding-affinity data [59]. The in silico ligand-prediction algorithms ameliorated the previously high false-discovery rate of

predicted ligands of specific HLA alleles. Nevertheless, considerable experimental data are required to train the algorithms, especially for the less prevalent HLA alleles for which there are not enough data on epitope affinity or MS results. The sensitivity of algorithms varied among different types of gene alterations and committed bioinformatics tools to optimize HLA-molecule-binding epitope prediction. The Human Immuno-Peptidome Project Consortium aims to establish a repertoire of peptides presented by HLA molecules to facilitate data collection [60]. With more disclosure of epitope sequences, a steadier immunopeptidome database will provide reliable and trustworthy predictions. Table 1 lists the methods and platforms that are commonly used to predict neoantigens.

**Table 1.** Methods and platforms commonly used for predicting neoantigens.

Method [Ref]	Principle	Year
NetMHCpan [37]	Comparison of epitope sequences by artificial neural networks that provide peptide–MHC-I-affinity predictions	2016
NetMHCIIpan [61]	Pan-specific predictor able to predict binding affinities for all HLA-class-II molecules based on neural networks	2013
MHCflurry [62]	Neutral networks including mass-spectrometry datasets for predicting peptide–MHC-I affinities	2018
ConvMHC [63]	peptide–MHC interactions encoded into image-like array data and analyzed by deep convolutional neural network	2017
PLAtEAU [64]	Defines shared consensus epitopes arising from a series of eluted nested peptides and quantified by mass spectrometry	2018
MuPeXI [65]	Integration of somatic mutation calls, list of HLA types, an optional gene-expression profile, and NetMHCpan 3.0 to provide immunogenicity score based on similarity to non-mutated wild-type peptide	2017
NeoPrepPipe [66]	Predicts neoantigen burdens and provide insights into the tumor heterogeneity, somatic mutation calls, and patient HLA haplotypes	2019
EpitopeHunter [67]	Integrates expression of RNA with artificial neural networks of immunogenicity-prediction algorithm based on the hydrophobicity of the TCR contact residues	2015
Neopepsee [68]	Integrates sequence and amino-acid-immunogenicity information, including antigen processing and presentation to reduce the false-discovery rate	2018

## 5. Neoantigen-Derived Cancer Vaccines

### 5.1. Tumor Lysates and Allogeneic Tumor-Cell-Based Vaccine

Autologous tumor lysates or allogeneic tumor cells obtained from patients were the earliest developed cancer vaccines. By administering either inactivated resected tumor lysates or allogeneic tumor-cell lysates with additional components such as adjuvants and cytokines, these cancer vaccines could present epitopes of tumor antigens to activate both CD4<sup>+</sup> and CD8<sup>+</sup> T cells in the human body [69–71].

An autologous tumor-lysate vaccine from Vaccinogen Inc, OncoVax, which uses Bacillus Calmette–Guerin (BCG) as an adjuvant, was shown to extend the recurrence-free period and reduce the risk for recurrences in surgically resected patients with stage II colon cancer. Their phase III trial (NTC02448173) evaluating further clinical benefits of OncoVax is ongoing [72]. GVAX (Cell Genesys, Inc., South San Francisco, CA, USA) is an allogeneic whole-tumor-cell vaccine that consists of two prostate-cancer cell lines, LNCaP and PC-3, transfected with a human granulocyte-macrophage-stimulating factor (GM-CSF) gene. Phase I/II studies demonstrated its safety and clinical activity; however, it failed to reach clinical efficacy in a phase III trial of advanced prostate cancer [73]. To improve the overall survival rate, GVAX was recently used with chemotherapy agents and ipilimumab to treat metastatic pancreatic cancer in the trial stage [74]. Other studies on tumor-cell vaccines include melacine (an allogeneic melanoma tumor-cell-lysate vaccine) [75], canvaxin (an

antigen-rich allogeneic whole-cell vaccine developed from three melanoma cell lines) [76], and TRIMELVax (a heat-shocked melanoma-cell-lysate vaccine) [77]. Although all epitopes are included in this type of vaccine, the contents of neoantigens are quite low, and most are wild-type endogenous peptides, which might dilute the expected immune responses and increase the risk of adverse reactions. Research on optimizing this approach, such as combination therapy and optimized carriers to transport the cells, might address the current limitations of tumor lysates or allogeneic tumor-cell-based vaccines.

## 5.2. DNA-Based Vaccines

DNA vaccines can be introduced into cells and tissues via non-viral or viral gene-delivery systems. After being introduced into the cytoplasm, DNA migrates to the nucleus and initiates the production of antigens. Physical forces mainly represent the non-viral methods of facilitating intracellular gene transfection by transiently loosening the cell-membrane structure. These systems include electroporation, microinjection, and a gene gun to transfect plasmid DNA into the tissue [78]. Although the physical delivery system offers highly efficient gene transfection, tissue damage resulting from the applied physical forces may cause low activity [79]. GNOS-PV02, a neoantigen-DNA vaccine with plasmid-encoded IL-12 administered by electroporation and intradermal injection, entered a phase I/II clinical study with the combination of pembrolizumab for the treatment of advanced hepatocellular carcinoma. The up-to-date result revealed that the objective response rate (ORR) was 25% without reported dose-limiting toxicities (DLTs). Post-vaccination TCR-repertoire analysis identified novel expanded T-cell clones in both peripheral blood and tumor tissue, which potentially mediated the observed regression of tumors [80].

DNA vaccines can also be delivered by viral carriers such as adenoviruses, modified vaccinia viruses, lentiviruses, and retroviruses. The adenovirus is a non-envelope, double-stranded DNA virus commonly used as a viral vector among these viruses. Adenoviral-vector vaccines replace genes that enable replication of transgenes or other genes of interest, making the vector unable to generate their genome copies after delivery. This property also provides the virus with a higher package capacity to incorporate large transgene sequences [81]. Compared to other virus-based vectors, adenoviral vectors have less potential genotoxicity and have been applied to infectious diseases such as COVID-19 [82], Ebola virus [83], and malaria [84]. Nous-209 is a virus-based cancer vaccine encoding 209 commonly shared frameshift mutations of microsatellite instability tumors and uses the Great Ape Adenoviruses vectors for priming and Modified Vaccinia Ankara vectors for boosting. The preliminary results of the phase I study combined with pembrolizumab showed no DLTs. Seven out of the twelve enrolled patients had confirmed partial responses (PRs), and two patients had stable disease (SD), suggesting that Nous-209 is safe and immunogenic and may contribute to early clinical outcomes [85]. PRGN-2009, a human papillomavirus (HPV) therapeutic vaccine encoding 35 non-HLA-restricted epitopes of HPV 16 and 18 by a novel gorilla adenoviral vector, increased the number of T cells targeting HPV 16 or HPV 18 after vaccination in all six recruited patients in a phase I study without observed DLTs [86]. However, pre-existing immunity against particular virus serotypes prevents the efficacy of virus-based vaccines [87]. This problem may be overcome using viral vectors derived from other species [88]. Nonetheless, it remains to be determined whether existing immunity will decrease the immunization potential for a repeated dose of vaccine constructed in the same or similar serotype virus.

In addition to viral vectors, microbes are also candidates for carrying target antigens. Lm-platform technology is an antigen delivery platform via *Listeria monocytogenes* developed by ADVAXIS. Attenuated *Listeria monocytogenes* carrying the bacterial vector expresses fusion proteins containing adjuvant parts and target antigens to T cells after phagocytosis. ADXS-503 is a phase I study of pembrolizumab plus the Lm vaccine targeting 11 common hotspot mutations and 11 TAAs of metastatic non-small-cell lung carcinoma (NSCLC). Antigen-specific T cells were found in all patients with a transient release of pro-inflammatory cytokines. Seven of the nine recruited patients also showed antigen

spreading. The ORR was 11%, and the disease-control rate (DCR) was 44%, with one achieving a PR and three achieving SD. The vaccine was well-tolerated without reported immune-related adverse events (irAEs) [89]. Another phase I study, ADXS-NEO-2, targeted personalized neoantigens for each cancer patient. Preliminary findings included immune-cell proliferation, antigen-specific T-cell response, and antigen spreading in one patient at 108 colony-forming units (CFUs). However, two patients had manageable DLTs at an initial dose of 109 CFUs, and the current state of this trial remains unclear [90]. The neoantigen-DNA-vaccine trials currently in the active or completed stages are listed in Table 2.

**Table 2.** Clinical trials of neoantigen-DNA vaccines.

Trial No. (Brand Name)	Target	Indication	Format/Route of Administration	Combination Therapy	Status
NCT03122106	Personalized NeoAg + Mesothelin	Pancreatic Cancer	Plasmid DNA/Electroporation + IM injection	N/A	Phase 1, Active, Not Recruiting
NCT04015700 (GNOS-PV01)	Personalized NeoAg	Unmethylated Glioblastoma	Plasmid DNA/Electroporation + IM injection	Pembrolizumab, Plasmid encoded IL-12 (INO-9012)	Phase 1, Recruiting
NCT04251117 (GNOS-PV02)	Personalized NeoAg + Mesothelin	HCC	Plasmid DNA/Electroporation + IM injection	Pembrolizumab, Plasmid encoded IL-12 (INO-9012)	Phase 1/2a, Recruiting
NCT04990479 (Nous-PEV)	Personalized NeoAg	Melanoma, NSCLC	Adenovirus vector + Vaccinia virus vector/IM injection	Pembrolizumab	Phase 1, Recruiting
NCT04041310 (Nous-209)	Personalized NeoAg	MSI-H CRC, gastric, G-E junction tumors	Adenovirus vector + vaccinia virus vector/IM injection	Pembrolizumab	Phase 1/2, Active, Not Recruiting
NCT05018273 (VB10.NEO)	Personalized NeoAg	Solid Tumors	Plasmid DNA/IM injection	Atezolizumab	Phase 1b, Recruiting
NCT02348320	Personalized NeoAg	Triple-Negative Breast Cancer	Plasmid DNA/Electroporation + IM injection	N/A	Phase 1, Completed
NCT03953235 (SLATE)	Shared Neoantigen	Shared neoantigen positive tumors	Adenovirus vector + RNA vector/Not specific	Nivolumab, Ipilimumab	Phase 1/2, Recruiting
NCT03265080 (ADXS-NEO)	Personalized NeoAg	Colon Cancer, Head & Neck Cancer, NSCLC, Urothelial Carcinoma, Melanoma	<i>Lm</i> -based vector/I.V. infusion	Pembrolizumab (selectively)	Phase 1, Active, Not Recruiting
NCT03847519 (ADXS-503)	Personalized NeoAg	NSCLC, Metastatic SCC, Metastatic NSCLC	<i>Lm</i> -based vector/I.V. infusion	Pembrolizumab (selectively)	Phase 1/2, Recruiting

Abbreviations: CRC, colorectal cancer. HCC, hepatocellular carcinoma. I.V., intravascular infusion. I.M., intramuscular injection. *Lm*, *Listeria monocytogenes*. MSI-H, high microsatellite instability. NSCC, small-cell lung cancer. NSCLC, non-small-cell lung cancer.

### 5.3. mRNA-Based Vaccines

Additionally, mRNA vaccines have shown substantial potential against diseases during the COVID-19 pandemic [91]. Theoretically, mRNA vaccines are internalized in the cytoplasm, and antigens of interest can be translated without mutagenesis concerns. The magnitude and rate of mRNA translation are typically higher than those of DNA vaccines. Currently, mRNA can be rapidly produced using in vitro transcription (IVT) methods, making it feasible for scale-up manufacturing. These characteristics make mRNA vaccines powerful tools for responding to emergent needs.

The significant clinical breakthrough of the application of mRNA cancer vaccines was first published by Sahin et al. [92]. Thirteen patients with stage III and IV melanoma

received at least eight doses of personalized neoantigen vaccines percutaneously into the inguinal lymph nodes. Each patient's five–ten mutations were selected based on the predicted high-affinity binding to autologous HLA class I and HLA class II. Not only were de novo immune responses observed, but pre-existing immune responses against predicted neoantigens were also augmented in all patients. Eight patients remained recurrence-free during the follow-up period. One patient experienced a complete response of metastases, which contributed to neoantigen-vaccine monotherapy. Another patient had a rapid, complete response within two months with PD1-blockade combination therapy. These results translated into sustained progression-free survival (PFS) and significantly reduced the cumulative sum of metastatic events compared to those before vaccine treatment. Notably, immune escape was observed in one patient who initially had a PR but suffered from metastasis two months after 12 vaccinations and follow-up surgeries. Loss of  $\beta$ -2 microglobulin was observed in autologous tumor cells, leading to HLA-class-I dysfunction [92].

Additionally, mRNA-4157 is the neoantigen-mRNA-vaccine trial of Moderna and is currently under phase I evaluation for solid tumors. From the updated outcome, the vaccine's safety was acceptable, with only mild-related adverse events reported [93]. Remarkably, the response rate was 50% for HPV-negative head and neck squamous-cell carcinoma combined with pembrolizumab, and the median PFS was compared favorably to pembrolizumab monotherapy. In addition, 14 of 16 patients with resected solid tumors receiving vaccine monotherapy remained disease free. The trial is ongoing for efficacy analysis [94]. However, the other trial of neoantigen-mRNA vaccines, mRNA-4650, did not proceed because no clinical response was observed. In this study, neoepitopes for each patient were selected by HLA-I prediction and validated by TIL-APC coculture, plus any mutations in the hot driver genes of Kirsten rat sarcoma virus (KRAS), tumor protein p53 (TP53), and phosphatidylinositol-4,5-bisphosphate 3-kinase catalytic subunit alpha (PIK3CA). Despite the suboptimal clinical results, T-cell reactivity against several predicted neoepitopes was found in the post-vaccination PBMC of some patients. TCR analysis revealed neoantigen-specific clonotypes capable of recognizing designed neoantigens, suggesting that a combination of immune-checkpoint inhibitors (ICIs) or immune-cell therapy could have clinical benefits [95].

Naked RNA is vulnerable to extracellular RNase and can undergo rapid degradation that limits the internalization of the vaccine. Improved mRNA-delivery systems facilitate vaccine protection, distribution, and release. For instance, ionizable lipid nanoparticles (LNPs) are self-assembled particles commonly used for RNA delivery. LNPs are stable at physiological pH, but the ionizable coated lipid can interact with the ionic endosomal membrane in an acidic endosomal microenvironment, thus promoting membrane fusion and RNA release. Moreover, mRNA has intrinsic immunogenicity, recognized mostly by toll-like receptor-7 and -8, and activates downstream interferon pathways and pro-inflammatory cytokine release. Although this might augment adaptive-immune responses, it could also dampen the antigen presentation. Unwanted double-stranded RNA (dsRNA) produced during IVT can activate RNA-dependent protein kinase, phosphorylate eukaryotic elongation factor-2, and block mRNA translation [96]. Several strategies have been investigated to overcome this limitation. Baidersdörfer et al. presented a dsRNA-removal method using cellulose in an ethanol-containing buffer. Up to 90% of dsRNA contaminants can be removed, resulting in better translation efficacy in vivo [97]. CureVax AG developed an RNA/protamine complex that serves as a toll-like receptor 7/8 (TLR7/8) adjuvant, increasing antitumor immunity after vaccination [98]. Luo et al. reported a formulation of synthetic polymeric nanoparticles with an intrinsic activating property for the stimulator of interferon genes (STING), leading to the inhibition of tumor progression in three types of cancer models [99]. In addition, BioNTech developed an RNA-lipoplex cancer-vaccine platform, Lipo-MERIX, which can precisely target dendritic cells (DC) in the lymphoid compartment by systematic administration (intravenous injection) to induce a potent immune response [100]. Several trials evaluating Lipo-MERIX carrying TAA or TSA for different types of solid tumors are ongoing. A relative trial targeting TAA for advanced melanoma,

BNT-111, has recently received FDA fast-track designation [101]. Active and completed neoantigen-mRNA-vaccine trials are listed in Table 3.

**Table 3.** Clinical trials of neoantigen RNA vaccines.

Trial No. (Brand Name)	Target	Indication	Format/Route of Administration	Combination Therapy	Status
RO7198457					
NCT03289962	Personalized NeoAg	Solid tumors	RNA-Lipoplex/I.V.	Atezolizumab	Phase 1a/1b, Recruiting
NCT03815058	Personalized NeoAg	Advanced Melanoma	RNA-Lipoplex/I.V.	Pembrolizumab	Phase 2, Recruiting
NCT04486378	Personalized NeoAg	Colorectal Cancer Stage II, III	RNA-Lipoplex/I.V.	N/A	Phase 2, Recruiting
NCT04161755	Personalized NeoAg	Pancreatic Cancer	RNA-Lipoplex/I.V.	Atezolizumab, mFOLFIRINOX	Phase 1, Recruiting
IVAC mutanome					
NCT02035956	Personalized NeoAg	Melanoma	Not specific/Intra-nodal	RBL001/RBL002 (TAA RNA Vaccine)	Phase 1, Completed
NCT02316457	Personalized NeoAg	Breast Cancer (TNBC)	Nanoparticulate lipoplex RNA/I.V.	IVAC_W_bre1_uID (TAA RNA vaccine)	Phase 1, Active, Not Recruiting
mRNA-4157					
NCT03897881	Personalized NeoAg	Melanoma	lipid encapsulated RNA/I.M.	Pembrolizumab	Phase 2, Active, Not Recruiting
NCT03313778	Personalized NeoAg	Solid tumors	lipid encapsulated RNA/I.M.	Pembrolizumab	Phase 1, Recruiting
mRNA-5671					
NCT03948763	KRAS common mutations	Solid Tumors	lipid encapsulated RNA/I.M.	Pembrolizumab (selectively)	Phase 1, Recruiting

Abbreviations: I.V., intravascular infusion. I.M., intramuscular injection. TAA, tumor-associated antigens. TNBC, triple-negative breast cancer.

#### 5.4. Protein and Peptide Vaccines

Peptide-based vaccines use synthetic peptides to trigger peptide-specific immune responses against cancer. It is intuitive and cost-effective, and no intricate logistics are required for transport and restoration. As reviewed by Shemesh et al., neoantigen vaccines derived from peptides, along with mRNA, have undergone the most ongoing clinical trials [102]. The primary outcomes of peptide vaccines showed promising results in treating melanoma and brain malignancies in multiple trials [103,104].

Hilf et al. conducted the GAPVAC trial for glioblastoma by administering peptide vaccines containing the predicted neoantigens and glioma-related TAAs. Notably, Th1 cells were induced in 11 of 13 patients receiving the neoepitope vaccine. In one patient who had a complete response after vaccination but experienced recurrence two years afterward, high infiltration by T cells was found, with a favorable ratio of CD8<sup>+</sup>/FOXP3<sup>+</sup> (forkhead box P3+) Treg cells from the re-resected tumor [105]. Similar results were reported by Keskin et al., who demonstrated that neoantigen-specific CD4<sup>+</sup> and CD8<sup>+</sup> T cells enriched in the memory phenotype were found after neoantigen-peptide administration. This study further proved that neoantigen-specific T cells triggered by the vaccine could migrate into intracranial glioblastoma tumors [103].

Recently, Platten et al. tested the safety and efficacy of a mutated isocitrate dehydrogenase 1 (IDH1) peptide vaccine in a phase I trial. Mutations in IDH1 are molecular characteristics of certain gliomas that contribute to the early stages of tumor development. Patients with the IDH1 R132H variant were recruited and treated with a 20-mer peptide containing a mutated spot. A mutant-specific T-cell response was found in over 90% of

recruited patients with appropriate safety profiles [106]. In recent years, elongated CD8<sup>+</sup> T-cell epitopes have been thought to enhance epitope-specific anticancer immunity. Unlike the predicted short epitopes, long peptides are believed to only be processed and presented by professional APC, leading to robust T-cell induction. In the mutant IDH1 trial, a single LSP (long synthetic peptide) was presented across various MHC alleles and, therefore, could be applied as an off-the-shelf product.

Moreover, the combination of neoantigen-peptide vaccines and ICIs has been validated in several trials. The NEO-PV-01 phase Ib clinical trial of a personalized peptide vaccine plus anti-PD1 (anti-programmed death-1) agent was evaluated for safety and efficacy in patients with advanced melanoma, NSCLC, and bladder cancer. Persistent cytotoxic T-cell responses were identified post-vaccination, without severe adverse reactions, in all three cancer cohorts. The median ORR and PFS were favorably compared with historical results for anti-PD-1 monotherapy but could not firmly attribute these outcomes to the vaccine because it was a single-arm investigation [107]. The comparison of neoantigen-peptide-vaccine monotherapy or in combination with ICIs was validated in an ongoing trial, GEN-009 [108].

NeoVax is a personalized long-peptide vaccine plus poly-ICLC (polyinosinic-polycytidylic acid stabilized with polylysine and carboxymethylcellulose) (i.e., a TLR-3 and MDA5 (melanoma differentiation-associated protein 5) agonist) [104,107]. A long-term follow-up study revealed that all patients with resected metastatic melanoma who had previous NeoVax treatment were still alive up to four years after treatment. Six of the eight patients had no evidence of disease. T cells with reactivity against certain vaccinated neoantigens persisted in the circulating blood of patients during the priming, boosting, and post-vaccination stages (up to 4.5 years). After the vaccination period, these functional T cells shifted to the less exhausted memory phenotype. Encouragingly, T cells able to target non-vaccinated TAAs or neoantigens were identified only in the post-vaccination sample, suggesting that the neoantigen-peptide vaccine could induce epitope spreading [108]. Epitope spreading has also been observed in several neoantigen-peptide-vaccine trials, including the NEO-PV-01, GEN-009, and glioblastoma trials [103,105,107,108]. In the NeoVax follow-up study, enhanced epitope spreading was observed in one patient experiencing recurrence in the post-vaccination period, but no evidence of disease after pembrolizumab therapy was shown, indicating that the combination of the neoantigen vaccine and ICIs could further improve clinical outcomes [108]. More neoantigen-peptide-vaccine trials in the active and completed stages are summarized in Table 4.

### 5.5. DC-Based Vaccines

The cell-based-vaccine approach exploits autologous DCs loaded with tumor antigens in various formats, including tumor lysates, DNA, mRNA, or peptides. Encouraging results, including Sipuleucel-T, an autologous DC vaccine targeting prostatic-acid phosphatase (PAP), a TAA, have demonstrated a significant improvement in overall survival for men with metastatic castration-resistant prostate cancer and was approved by the FDA [109]. For the neoantigen-pulsed DC vaccine, Carreno et al. conducted a trial applying an in vitro matured autologous DC vaccine stimulated by personalized neoantigen peptides in three patients with advanced melanoma. TCR-sequencing results indicated diverse neoantigen-specific clonotypes induced by personalized DC vaccines, and increased immunity was observed in all patients [110]. Moreover, a patient with metastatic pancreatic cancer experienced regression of multiple metastatic lesions 2.5 months after DC-based-vaccine treatment. In this case, the selected neoepitope was an HLA-A\*0201-restricted KRAS-G12D epitope, and the patient received a vaccine containing a neoantigen plus DC and neoantigen-reactive CD8<sup>+</sup>CD137<sup>+</sup> T cells [111]. Similar research on patients with heavily treated lung cancer by administering a neoantigen-peptide-loaded DC vaccine demonstrated a 25% ORR and 75% DCR. Although none of the recruited patients achieved CR, the results were auspicious considering the initially poor prognosis of the study population. In addition, they noticed that the neoantigen-loaded DC vaccine could re-induce objective

responses to ICIs in patients who had a relapse after previous ICI treatment. This finding corresponds to that mentioned in the peptide-vaccine section, namely that the combination of cancer vaccines and ICMs could further provide synergetic therapeutic benefits [112].

**Table 4.** Clinical trials of neoantigen-peptide vaccines.

Trial No. (Brand Name)	Target	Indication	Format/Route of Administration	Combination Therapy	Status
NCT04799431	Personalized NeoAg	MMR-p Colon Cancer Pancreatic Ductal Cancer	Peptide + poly- ICLC/subcutaneous	Retifanlimab	Phase 1, Not Yet Recruiting
NCT03956056	Personalized NeoAg + Mesothelin	Pancreatic Cancer	Peptide + poly-ICLC/ subcutaneous	N/A	Phase 1, Recruiting
NCT04248569	DNAJB1- PRKACA fusion	Fibrolamellar Hepatocellular Carcinoma	Peptide + poly-ICLC	Nivolumab, Ipilimumab	Phase 1, Recruiting
NCT04117087	Common mutant KRAS	Colorectal Cancer Pancreatic Cancer	Peptide + poly-ICLC	Nivolumab, Ipilimumab	Phase 1, Recruiting
NCT04749641	Histone H3.3-K27M mutant	Diffuse Intrinsic Pontine Glioma	Peptide + poly- ICLC/subcutaneous	N/A	Phase 1, Recruiting
NCT03715985 (NeoPepVac)	Personalized NeoAg	Melanoma, NSCLC, Bladder, Urothelial Carcinoma,	Peptide + CAF09b/I.P. + I.M.	N/A	Phase 1, Recruiting
NCT03359239 (PGV-001)	Personalized NeoAg	Urothelial/Bladder Cancer	Peptide + poly-ICLC	Atezolizumab	Phase 1, Recruiting
NCT02149225 (GAPVAC)	Personalized NeoAg	Glioblastoma	Peptide + poly-ICLC/not specific	TAA peptide vaccine, GM-CSF	Phase 1, Completed
NeoVax					
NCT01970358	Personalized NeoAg	Melanoma	Peptide + poly- ICLC/subcutaneous	N/A	Phase 1, Completed
NCT02950766	Personalized NeoAg	Kidney cancer	Peptide + poly- ICLC/subcutaneous	Nivolumab, Ipilimumab	Phase 1, Recruiting
NCT02287428	Personalized NeoAg	Glioblastoma	Peptide + poly-ICLC	Pembrolizumab Temozolomide (Both selectively)	Phase 1, Recruiting
NCT03929029	Personalized NeoAg	Melanoma	Peptide + poly-ICLC + Montanide	Nivolumab Ipilimumab	Phase 1b, Recruiting
NCT0402487	Personalized NeoAg	Ovarian Cancer	Peptide + poly-ICLC	Nivolumab	Phase 1, Recruiting
NCT03219450	Personalized NeoAg	Lymphocytic Leukemia	Peptide + poly-ICLC	Pembrolizumab Cyclophosphamide (both selectively)	Phase 1, Recruiting
Neo-PV-01					
NCT03380871	Personalized NeoAg	Lung cancer	Peptide + poly- ICLC/subcutaneous	Pembrolizumab Carboplatin Pemetrexed	Phase 1, Completed
NCT02897765	Personalized NeoAg	Urinary Bladder Cancer Melanoma Lung Cancer	Peptide + poly- ICLC/subcutaneous	Nivolumab	Phase 1, Completed

Abbreviations: I.V., intravenous infusion. I.M., intramuscular injection. MMR-p, mismatch repair protein deficiency. NSCLC, non-small-cell lung cancer. poly-ICLC, polyinosinic-polycytidylic acid. TAA, tumor-associated antigens.

## 6. Opinions and Future Perspectives

Therapeutic cancer vaccines have several promising clinical outcomes. However, all vaccines are still in the early stages of clinical trials (phases I and II). This may reflect



difficulties in inducing a robust immune response to kill aggressive cancer cells in immunosuppressed patients. In addition, the variation in neoantigens in different individuals makes large-scale applications more challenging than targeting commonly shared antigens. Whether therapeutic vaccines can be applied and used in clinical practice depends on different factors, such as (1) the ability to yield sufficient numbers of T cells to overcome the suppressive TME, (2) augmented immune cells that can penetrate and infiltrate the tumors, (3) the use of adequate adjuvants and carriers, and (4) optimal selection of target antigens [113,114].

Moreover, T-cell exhaustion has been reported in numerous studies where vaccine-elicited T lymphocytes often express several inhibitory receptors [92,103–105]. A combination of ICIs or other immunotherapies is necessary to achieve synergistic efficacy. In addition to cytotoxic T cells, the importance of CD4<sup>+</sup> T cells in cancer immunity has been well established. Notably, MHC-II-restricted tumor epitopes also play a crucial role in immunotherapy efficacy. Activated CD4<sup>+</sup> cells could give rise to the induction of CD8<sup>+</sup> T cells with less inhibitory profiles and strengthened effector functions. At the beginning of cancer-vaccine treatment, priming of the immunization determines the phenotype and magnitude of the vaccine-elicited immune response. Ideally, a subset of neoantigen-specific T cells with memory phenotypes is generated after antigen clearance. Continuous exposure to antigens can induce functional profiles of T cells, including memory T cells [115–117]. The expression of MHC-II epitopes by tumors can recruit more intratumoral T cells and inducible nitric-oxide-synthase-positive macrophages [118]. Including MHC-II epitopes and stimulants to activate CD4<sup>+</sup> cells in cancer vaccines has been suggested to improve efficacy. Therefore, optimized priming and boosting regimens for vaccination should be carefully determined. Applying advanced technologies to identify TSAs and generate vaccines with potent adjuvants is the key to developing successful anticancer therapeutics.

Immunoengineering, the field that integrates nanotechnology, bioengineering, material sciences, drug delivery, and immunology, aims to elicit a robust antitumor immune response. In particular, nanoparticles provide better delivery efficiency and T-cell priming for gene-based and peptide-based vaccines. By loading or conjugating adjuvants, innate-immunity agonists, and target receptors to nanoparticles, co-delivery can enhance the magnitude of antitumor responses [119,120]. For instance, a "nanodiscs" mixing synthetic high-density lipoprotein, cysteine-modified antigens, and cholesterol-modified CpG adjuvant successfully promoted antigen presentation and eliminated established mouse tumors when combined with ICIs [121]. In addition, a biodegradable matrix loaded with small molecules and biologics implanted near the tumor or post-resection sites can reverse the immunosuppressive conditions. The matrix provides artificial immune niches that enable the *in situ* manipulation of cells [122]. Implantation of a biopolymer-based scaffold loaded with tumor-reactive T cells and agonists enhances antigen presentation and T-cell response to eradicate inoperable orthotopic tumors in mice [123,124]. Moreover, protein-based gels loaded with nanoparticles containing anti-CD47, an inhibitory ligand on cancerous cells, polarized macrophages to M1 phenotypes, and prolonged survival in mice with incomplete resection [125]. Further exploration using matrix-coated tumor neoantigens as cancer vaccines is required. These advanced methods aim to provide the best formulation and dosage of tumor antigens and adjuvants to induce the immune cells and improve the efficacy of therapeutic cancer vaccines.

The immune system is intricate and highly coordinated; the absence of specific cytokines or subsets of immune cells could substantially alter the subsequent cascade of responses, indicating that *ex vivo* immunostimulatory experiments may not precisely interpret the real circumstances *in vivo*. Emerging tools such as the three-dimensional modeling system and immune organ/tumor "on a chip" system could foster sophisticated examination of immune-organ function and immune-cell interaction [126]. For example, a microfluidic chip containing hepatocellular carcinoma cells was built to evaluate the time-dependent migration and cytotoxicity of TCR-engineered T cells. The device allowed the investigation of T-cell ability under different inflammatory conditions [127]. In addition,

the microphysiological 3D cancer model used to test the efficacy of receptor-engineered cells was validated in lung-, breast-, and ovarian-cancer models [128,129].

Regarding the different types of formulations, mRNA vaccines have the advantage of a cost-effective and straightforward manufacturing procedure. On the other hand, favorable clinical outcomes were also observed in patients who received protein and peptide vaccines, such as NeoVax, Neo-PV-01, GAPVAC, and the IDH1 peptide vaccine for glioma. Targeting neoantigens through integrating immunotherapeutics, including vaccines, cell-based therapy, ICIs, and immunoengineering may provide opportunities to overcome the unmet needs of cancer immunotherapy.

## 7. Conclusions

The development of therapeutic cancer vaccines is a promising prospect for improving the safety and efficacy of the currently used immunotherapeutics. This is a ready-to-produce procedure with an extensive selection of formats. Targeting neoantigens and other TSAs enables immunogens to induce tumor-specific adaptive-immune responses. High-throughput sequencing, epitope-identified mass spectrometry, and predictive algorithms have enabled neoantigen epitopes to be disclosed and subsequently used to design vaccines. Two primary tactics for neoantigen vaccines are evolving. One harnesses personalized vaccines for personalized therapy, and the other utilizes shared neoantigens or viral oncoproteins as off-the-shelf therapeutics. The clinical results summarized in this review indicate encouraging progress in disease control and favorable immune responses. However, several hurdles remain, including on-target distribution, conversion of immunosuppressive environments, and antigen selection. By investigating adequate delivery systems, carriers, adjuvants, and new immunology research tools, these endeavors could gradually reach new heights. Numerous studies using various formats, therapeutic regimens, delivery systems, and combination therapies are still in progress. Targeting neoantigens could be a path to success for significant clinical improvement in cancer treatment.

**Author Contributions:** Writing-original draft preparation, S.-C.P.; writing-review and editing, M.-T.C. and S.-I.H.; funding acquisition, S.-I.H. All authors have read and agreed to the published version of the manuscript.

**Funding:** This work was supported by grants from Chang Gung Memorial Hospital (CIRPG3I0041~43, CIRPG3I0021~23, CIRPG3I0031~33, CIRPG2I0011~13) and Ministry of Science and Technology of Taiwan (MOST 108-2320-B-182A-023 -MY3, MOST 109-2320-B-182A-008-MY3).

**Institutional Review Board Statement:** Not applicable.

**Informed Consent Statement:** Not applicable.

**Data Availability Statement:** Not applicable.

**Acknowledgments:** We thank the support of members of the Cancer Vaccine and Immune Cell Therapy core lab, Chang Gung Memorial Hospital.

**Conflicts of Interest:** The authors declare no conflict of interest.

## References

1. Genomic Classification of Cutaneous Melanoma. *Cell* **2015**, *161*, 1681–1696. [CrossRef] [PubMed]
2. Lawrence, M.S.; Stojanov, P.; Mermel, C.H.; Robinson, J.T.; Garraway, L.A.; Golub, T.R.; Meyerson, M.; Gabriel, S.B.; Lander, E.S.; Getz, G. Discovery and saturation analysis of cancer genes across 21 tumour types. *Nature* **2014**, *505*, 495–501. [CrossRef] [PubMed]
3. Lawrence, M.S.; Stojanov, P.; Polak, P.; Kryukov, G.V.; Cibulskis, K.; Sivachenko, A.; Carter, S.L.; Stewart, C.; Mermel, C.H.; Roberts, S.A.; et al. Mutational heterogeneity in cancer and the search for new cancer-associated genes. *Nature* **2013**, *499*, 214–218. [CrossRef] [PubMed]
4. Wood, L.D.; Parsons, D.W.; Jones, S.; Lin, J.; Sjoblom, T.; Leary, R.J.; Shen, D.; Boca, S.M.; Barber, T.; Ptak, J.; et al. The genomic landscapes of human breast and colorectal cancers. *Science* **2007**, *318*, 1108–1113. [CrossRef] [PubMed]
5. Ciriello, G.; Miller, M.L.; Aksoy, B.A.; Senbabaoglu, Y.; Schultz, N.; Sander, C. Emerging landscape of oncogenic signatures across human cancers. *Nat. Genet.* **2013**, *45*, 1127–1133. [CrossRef] [PubMed]

6. Tran, E.; Robbins, P.F.; Rosenberg, S.A. ‘Final common pathway’ of human cancer immunotherapy: Targeting random somatic mutations. *Nat. Immunol.* **2017**, *18*, 255–262. [CrossRef] [PubMed]
7. Hollingsworth, R.E.; Jansen, K. Turning the corner on therapeutic cancer vaccines. *NPJ Vaccines* **2019**, *4*, 7. [CrossRef]
8. Coulie, P.G.; Van den Eynde, B.J.; van der Bruggen, P.; Boon, T. Tumour antigens recognized by T lymphocytes: At the core of cancer immunotherapy. *Nat. Rev. Cancer* **2014**, *14*, 135–146. [CrossRef]
9. Van den Eynde, B.J.; van der Bruggen, P. T cell defined tumor antigens. *Curr. Opin. Immunol.* **1997**, *9*, 684–693. [CrossRef]
10. Oesterling, J.E. Prostate specific antigen: A critical assessment of the most useful tumor marker for adenocarcinoma of the prostate. *J. Urol.* **1991**, *145*, 907–923. [CrossRef]
11. Hollingsworth, M.A.; Swanson, B.J. Mucins in cancer: Protection and control of the cell surface. *Nat. Rev. Cancer* **2004**, *4*, 45–60. [CrossRef] [PubMed]
12. Vonderheide, R.H.; Hahn, W.C.; Schultze, J.L.; Nadler, L.M. The telomerase catalytic subunit is a widely expressed tumor-associated antigen recognized by cytotoxic T lymphocytes. *Immunity* **1999**, *10*, 673–679. [CrossRef]
13. Chang, K.; Pastan, I. Molecular cloning of mesothelin, a differentiation antigen present on mesothelium, mesotheliomas, and ovarian cancers. *Proc. Natl. Acad. Sci. USA* **1996**, *93*, 136–140. [CrossRef] [PubMed]
14. Finn, O.J.; Gantt, K.R.; Lepisto, A.J.; Pejaward-Gaddy, S.; Xue, J.; Beatty, P.L. Importance of MUC1 and spontaneous mouse tumor models for understanding the immunobiology of human adenocarcinomas. *Immunol. Res.* **2011**, *50*, 261–268. [CrossRef] [PubMed]
15. Correale, P.; Walmsley, K.; Nieroda, C.; Zaremba, S.; Zhu, M.; Schlom, J.; Tsang, K.Y. In vitro generation of human cytotoxic T lymphocytes specific for peptides derived from prostate-specific antigen. *J. Natl. Cancer Inst.* **1997**, *89*, 293–300. [CrossRef] [PubMed]
16. Muniyan, S.; Chaturvedi, N.K.; Dwyer, J.G.; LaGrange, C.A.; Chaney, W.G.; Lin, M.-F. Human Prostatic Acid Phosphatase: Structure, Function and Regulation. *Int. J. Mol. Sci.* **2013**, *14*, 10438–10464. [CrossRef] [PubMed]
17. Karbach, J.; Neumann, A.; Atmaca, A.; Wahle, C.; Brand, K.; von Boehmer, L.; Knuth, A.; Bender, A.; Ritter, G.; Old, L.J.; et al. Efficient in vivo priming by vaccination with recombinant NY-ESO-1 protein and CpG in antigen naive prostate cancer patients. *Clin. Cancer Res.* **2011**, *17*, 861–870. [CrossRef]
18. Simpson, A.J.; Caballero, O.L.; Jungbluth, A.; Chen, Y.T.; Old, L.J. Cancer/testis antigens, gametogenesis and cancer. *Nat. Rev. Cancer* **2005**, *5*, 615–625. [CrossRef]
19. Hofmann, O.; Caballero, O.L.; Stevenson, B.J.; Chen, Y.T.; Cohen, T.; Chua, R.; Maher, C.A.; Panji, S.; Schaefer, U.; Kruger, A.; et al. Genome-wide analysis of cancer/testis gene expression. *Proc. Natl. Acad. Sci. USA* **2008**, *105*, 20422–20427. [CrossRef]
20. De Smet, C.; Lurquin, C.; van der Bruggen, P.; De Plaen, E.; Brasseur, F.; Boon, T. Sequence and expression pattern of the human MAGE2 gene. *Immunogenetics* **1994**, *39*, 121–129. [CrossRef]
21. Gnjatic, S.; Cao, Y.; Reichelt, U.; Yekebas, E.F.; Nölker, C.; Marx, A.H.; Erbersdobler, A.; Nishikawa, H.; Hildebrandt, Y.; Bartels, K.; et al. NY-CO-58/KIF2C is overexpressed in a variety of solid tumors and induces frequent T cell responses in patients with colorectal cancer. *Int. J. Cancer* **2010**, *127*, 381–393. [CrossRef] [PubMed]
22. Smith, C.C.; Selitsky, S.R.; Chai, S.; Armistead, P.M.; Vincent, B.G.; Serody, J.S. Alternative tumour-specific antigens. *Nat. Rev. Cancer* **2019**, *19*, 465–478. [CrossRef] [PubMed]
23. Fritsch, E.F.; Rajasagi, M.; Ott, P.A.; Brusica, V.; Hacohen, N.; Wu, C.J. HLA-binding properties of tumor neoepitopes in humans. *Cancer Immunol. Res.* **2014**, *2*, 522–529. [CrossRef] [PubMed]
24. Duan, F.; Duitama, J.; Al Seesi, S.; Ayres, C.M.; Corcelli, S.A.; Pawashe, A.P.; Blanchard, T.; McMahon, D.; Sidney, J.; Sette, A.; et al. Genomic and bioinformatic profiling of mutational neoepitopes reveals new rules to predict anticancer immunogenicity. *J. Exp. Med.* **2014**, *211*, 2231–2248. [CrossRef] [PubMed]
25. Milicic, A.; Price, D.A.; Zimbwa, P.; Booth, B.L.; Brown, H.L.; Easterbrook, P.J.; Olsen, K.; Robinson, N.; Gileadi, U.; Sewell, A.K.; et al. CD8+ T cell epitope-flanking mutations disrupt proteasomal processing of HIV-1 Nef. *J. Immunol.* **2005**, *175*, 4618–4626. [CrossRef]
26. Wolfers, J.; Lozier, A.; Raposo, G.; Regnault, A.; Thery, C.; Masurier, C.; Flament, C.; Pouzieux, S.; Faure, F.; Tursz, T.; et al. Tumor-derived exosomes are a source of shared tumor rejection antigens for CTL cross-priming. *Nat. Med.* **2001**, *7*, 297–303. [CrossRef]
27. Zitvogel, L.; Casares, N.; Pequignot, M.O.; Chaput, N.; Albert, M.L.; Kroemer, G. Immune response against dying tumor cells. *Adv. Immunol.* **2004**, *84*, 131–179. [CrossRef]
28. Green, D.R.; Ferguson, T.; Zitvogel, L.; Kroemer, G. Immunogenic and tolerogenic cell death. *Nat. Rev. Immunol.* **2009**, *9*, 353–363. [CrossRef]
29. Boon, T.; Cerottini, J.C.; Van den Eynde, B.; van der Bruggen, P.; Van Pel, A. Tumor antigens recognized by T lymphocytes. *Annu. Rev. Immunol.* **1994**, *12*, 337–365. [CrossRef]
30. Bacon, K.; Baggiolini, M.; Broxmeyer, H.; Horuk, R.; Lindley, I.; Mantovani, A.; Maysushima, K.; Murphy, P.; Nomiyama, H.; Oppenheim, J.; et al. Chemokine/chemokine receptor nomenclature. *J. Interferon Cytokine Res.* **2002**, *22*, 1067–1068. [CrossRef]
31. Dubinett, S.M.; Lee, J.M.; Sharma, S.; Mule, J.J. Chemokines: Can effector cells be redirected to the site of the tumor? *Cancer J.* **2010**, *16*, 325–335. [CrossRef] [PubMed]
32. Tureci, O.; Vormehr, M.; Diken, M.; Kreiter, S.; Huber, C.; Sahin, U. Targeting the Heterogeneity of Cancer with Individualized Neoepitope Vaccines. *Clin. Cancer Res.* **2016**, *22*, 1885–1896. [CrossRef] [PubMed]

33. Kahles, A.; Ong, C.S.; Zhong, Y.; Ratsch, G. SplAdder: Identification, quantification and testing of alternative splicing events from RNA-Seq data. *Bioinformatics* **2016**, *32*, 1840–1847. [CrossRef] [PubMed]
34. Rogers, M.F.; Thomas, J.; Reddy, A.S.; Ben-Hur, A. SpliceGrapher: Detecting patterns of alternative splicing from RNA-Seq data in the context of gene models and EST data. *Genome Biol.* **2012**, *13*, R4. [CrossRef]
35. Denti, L.; Rizzi, R.; Beretta, S.; Vedova, G.D.; Previtali, M.; Bonizzoni, P. ASGAL: Aligning RNA-Seq data to a splicing graph to detect novel alternative splicing events. *BMC Bioinform.* **2018**, *19*, 444. [CrossRef]
36. Ruggles, K.V.; Tang, Z.; Wang, X.; Grover, H.; Askenazi, M.; Teubl, J.; Cao, S.; McLellan, M.D.; Clauser, K.R.; Tabb, D.L.; et al. An Analysis of the Sensitivity of Proteogenomic Mapping of Somatic Mutations and Novel Splicing Events in Cancer. *Mol. Cell. Proteom.* **2016**, *15*, 1060–1071. [CrossRef]
37. Jurtz, V.; Paul, S. NetMHCpan-4.0: Improved Peptide-MHC Class I Interaction Predictions Integrating Eluted Ligand and Peptide Binding Affinity Data. *J. Immunol.* **2017**, *199*, 3360–3368. [CrossRef]
38. Zhang, G.L.; Khan, A.M.; Srinivasan, K.N.; August, J.T.; Brusica, V. MULTIPRED: A computational system for prediction of promiscuous HLA binding peptides. *Nucleic Acids Res.* **2005**, *33*, W172–W179. [CrossRef]
39. Vita, R.; Overton, J.A.; Greenbaum, J.A.; Ponomarenko, J.; Clark, J.D.; Cantrell, J.R.; Wheeler, D.K.; Gabbard, J.L.; Hix, D.; Sette, A.; et al. The immune epitope database (IEDB) 3.0. *Nucleic Acids Res.* **2015**, *43*, D405–D412. [CrossRef]
40. Schubert, B.; Brachvogel, H.P.; Jurges, C.; Kohlbacher, O. EpiToolKit—A web-based workbench for vaccine design. *Bioinformatics* **2015**, *31*, 2211–2213. [CrossRef]
41. Fridman, W.H.; Pagès, F.; Sautès-Fridman, C.; Galon, J. The immune contexture in human tumours: Impact on clinical outcome. *Nat. Rev. Cancer* **2012**, *12*, 298–306. [CrossRef] [PubMed]
42. Galon, J.; Costes, A.; Sanchez-Cabo, F.; Kirilovsky, A.; Mlecnik, B.; Lagorce-Pagès, C.; Tosolini, M.; Camus, M.; Berger, A.; Wind, P.; et al. Type, density, and location of immune cells within human colorectal tumors predict clinical outcome. *Science* **2006**, *313*, 1960–1964. [CrossRef] [PubMed]
43. Kreiter, S.; Vormehr, M.; van de Roemer, N.; Diken, M.; Lower, M.; Diekmann, J.; Boegel, S.; Schrors, B.; Vascotto, F.; Castle, J.C.; et al. Mutant MHC class II epitopes drive therapeutic immune responses to cancer. *Nature* **2015**, *520*, 692–696. [CrossRef] [PubMed]
44. Tran, E.; Turcotte, S.; Gros, A.; Robbins, P.F.; Lu, Y.C.; Dudley, M.E.; Wunderlich, J.R.; Somerville, R.P.; Hogan, K.; Hinrichs, C.S.; et al. Cancer immunotherapy based on mutation-specific CD4+ T cells in a patient with epithelial cancer. *Science* **2014**, *344*, 641–645. [CrossRef]
45. Nielsen, M.; Lund, O. NN-align. An artificial neural network-based alignment algorithm for MHC class II peptide binding prediction. *BMC Bioinform.* **2009**, *10*, 296. [CrossRef]
46. Andreatta, M.; Karosiene, E.; Rasmussen, M.; Stryhn, A.; Buus, S.; Nielsen, M. Accurate pan-specific prediction of peptide-MHC class II binding affinity with improved binding core identification. *Immunogenetics* **2015**, *67*, 641–650. [CrossRef]
47. Hunt, D.F.; Henderson, R.A.; Shabanowitz, J.; Sakaguchi, K.; Michel, H.; Sevilir, N.; Cox, A.L.; Appella, E.; Engelhard, V.H. Characterization of peptides bound to the class I MHC molecule HLA-A2.1 by mass spectrometry. *Science* **1992**, *255*, 1261–1263. [CrossRef]
48. Cravatt, B.F.; Simon, G.M.; Yates Iii, J.R. The biological impact of mass-spectrometry-based proteomics. *Nature* **2007**, *450*, 991–1000. [CrossRef]
49. Kasuga, K. Comprehensive analysis of MHC ligands in clinical material by immunoaffinity-mass spectrometry. *Methods Mol. Biol.* **2013**, *1023*, 203–218. [CrossRef]
50. Mommen, G.P.M.; Frese, C.K.; Meiring, H.D.; van Gaans-van den Brink, J.; de Jong, A.P.J.M.; van Els, C.A.C.M.; Heck, A.J.R. Expanding the detectable HLA peptide repertoire using electron-transfer/higher-energy collision dissociation (ET<sub>h</sub>CD). *Proc. Natl. Acad. Sci. USA* **2014**, *111*, 4507–4512. [CrossRef]
51. Cox, J.; Mann, M. MaxQuant enables high peptide identification rates, individualized p.p.b.-range mass accuracies and proteome-wide protein quantification. *Nat. Biotechnol.* **2008**, *26*, 1367–1372. [CrossRef] [PubMed]
52. Rosenberger, G.; Koh, C.C.; Guo, T.; Röst, H.L.; Kouvonen, P.; Collins, B.C.; Heusel, M.; Liu, Y.; Caron, E.; Vichalkovski, A.; et al. A repository of assays to quantify 10,000 human proteins by SWATH-MS. *Sci. Data* **2014**, *1*, 140031. [CrossRef] [PubMed]
53. Veit, J.; Sachsenberg, T.; Chernev, A.; Aichele, F.; Urlaub, H.; Kohlbacher, O. LFQProfiler and RNP(xl): Open-Source Tools for Label-Free Quantification and Protein-RNA Cross-Linking Integrated into Proteome Discoverer. *J. Proteome Res.* **2016**, *15*, 3441–3448. [CrossRef] [PubMed]
54. Bassani-Sternberg, M.; Bräunlein, E.; Klar, R.; Engleitner, T.; Sinitcyn, P.; Audehm, S.; Straub, M.; Weber, J.; Slotta-Huspenina, J.; Specht, K.; et al. Direct identification of clinically relevant neoepitopes presented on native human melanoma tissue by mass spectrometry. *Nat. Commun.* **2016**, *7*, 13404. [CrossRef] [PubMed]
55. Regnier, M.; Goubeyre, P.; Pinton, P.; Napper, S.; Laffite, J.; Cossalter, A.M.; Bailly, J.D.; Lippi, Y.; Bertrand-Michel, J.; Bracarense, A.; et al. Identification of Signaling Pathways Targeted by the Food Contaminant FB1: Transcriptome and Kinome Analysis of Samples from Pig Liver and Intestine. *Mol. Nutr. Food Res.* **2017**, *61*, 1700433. [CrossRef] [PubMed]
56. Abelin, J.G.; Keskin, D.B.; Sarkizova, S.; Hartigan, C.R.; Zhang, W.; Sidney, J.; Stevens, J.; Lane, W.; Zhang, G.L.; Eisenhaure, T.M.; et al. Mass Spectrometry Profiling of HLA-Associated Peptidomes in Mono-allelic Cells Enables More Accurate Epitope Prediction. *Immunity* **2017**, *46*, 315–326. [CrossRef] [PubMed]

57. Nielsen, M.; Connelley, T.; Ternette, N. Improved Prediction of Bovine Leucocyte Antigens (BoLA) Presented Ligands by Use of Mass-Spectrometry-Determined Ligand and in Vitro Binding Data. *J. Proteome Res.* **2018**, *17*, 559–567. [CrossRef]
58. Andreatta, M.; Lund, O.; Nielsen, M. Simultaneous alignment and clustering of peptide data using a Gibbs sampling approach. *Bioinformatics* **2013**, *29*, 8–14. [CrossRef]
59. Bulik-Sullivan, B.; Busby, J.; Palmer, C.D.; Davis, M.J.; Murphy, T.; Clark, A.; Busby, M.; Duke, F.; Yang, A.; Young, L.; et al. Deep learning using tumor HLA peptide mass spectrometry datasets improves neoantigen identification. *Nat. Biotechnol.* **2019**, *37*, 55–63. [CrossRef]
60. Caron, E.; Aebersold, R.; Banaei-Esfahani, A.; Chong, C.; Bassani-Sternberg, M. A Case for a Human Immuno-Peptidome Project Consortium. *Immunity* **2017**, *47*, 203–208. [CrossRef]
61. Karosiene, E.; Rasmussen, M.; Blicher, T.; Lund, O.; Buus, S.; Nielsen, M. NetMHCIIpan-3.0, a common pan-specific MHC class II prediction method including all three human MHC class II isotypes, HLA-DR, HLA-DP and HLA-DQ. *Immunogenetics* **2013**, *65*, 711–724. [CrossRef] [PubMed]
62. O'Donnell, T.J.; Rubinsteyn, A.; Bonsack, M.; Riemer, A.B.; Laserson, U.; Hammerbacher, J. MHCflurry: Open-Source Class I MHC Binding Affinity Prediction. *Cell Syst.* **2018**, *7*, 129–132.e4. [CrossRef] [PubMed]
63. Han, Y.; Kim, D. Deep convolutional neural networks for pan-specific peptide-MHC class I binding prediction. *BMC Bioinform.* **2017**, *18*, 585. [CrossRef] [PubMed]
64. Alvaro-Benito, M.; Morrison, E.; Abualrous, E.T.; Kuropka, B.; Freund, C. Quantification of HLA-DM-Dependent Major Histocompatibility Complex of Class II Immunopeptidomes by the Peptide Landscape Antigenic Epitope Alignment Utility. *Front. Immunol.* **2018**, *9*, 872. [CrossRef]
65. Bjerregaard, A.M.; Nielsen, M.; Hadrup, S.R.; Szallasi, Z.; Eklund, A.C. MuPeXI: Prediction of neo-epitopes from tumor sequencing data. *Cancer Immunol. Immunother.* **2017**, *66*, 1123–1130. [CrossRef]
66. Schenck, R.O.; Lakatos, E.; Gatenbee, C.; Graham, T.A.; Anderson, A.R.A. NeoPredPipe: High-throughput neoantigen prediction and recognition potential pipeline. *BMC Bioinform.* **2019**, *20*, 264. [CrossRef]
67. Chowell, D.; Krishna, S.; Becker, P.D. TCR contact residue hydrophobicity is a hallmark of immunogenic CD8+ T cell epitopes. *Proc. Natl. Acad. Sci.* **2015**, *112*, E1754–E1762. [CrossRef] [PubMed]
68. Kim, S.; Kim, H.S.; Kim, E.; Lee, M.G.; Shin, E.C.; Paik, S.; Kim, S. Neopepsee: Accurate genome-level prediction of neoantigens by harnessing sequence and amino acid immunogenicity information. *Ann. Oncol.* **2018**, *29*, 1030–1036. [CrossRef]
69. Chan, A.D.; Morton, D.L. Active immunotherapy with allogeneic tumor cell vaccines: Present status. *Semin. Oncol.* **1998**, *25*, 611–622.
70. Simons, J.W.; Mikhak, B. Ex-vivo gene therapy using cytokine-transduced tumor vaccines: Molecular and clinical pharmacology. *Semin. Oncol.* **1998**, *25*, 661–676.
71. Phan, V.; Errington, F.; Cheong, S.C.; Kottke, T.; Gough, M.; Altmann, S.; Brandenburger, A.; Emery, S.; Strome, S.; Bateman, A.; et al. A new genetic method to generate and isolate small, short-lived but highly potent dendritic cell-tumor cell hybrid vaccines. *Nat. Med.* **2003**, *9*, 1215–1219. [CrossRef] [PubMed]
72. Vermorken, J.B.; Claessen, A.M.; van Tinteren, H.; Gall, H.E.; Ezinga, R.; Meijer, S.; Scheper, R.J.; Meijer, C.J.; Bloemena, E.; Ransom, J.H.; et al. Active specific immunotherapy for stage II and stage III human colon cancer: A randomised trial. *Lancet* **1999**, *353*, 345–350. [CrossRef]
73. Arlen, P.M.; Mohebtash, M.; Madan, R.A.; Gulley, J.L. Promising novel immunotherapies and combinations for prostate cancer. *Future Oncol.* **2009**, *5*, 187–196. [CrossRef] [PubMed]
74. Wu, A.A.; Bever, K.M.; Ho, W.J.; Fertig, E.J.; Niu, N.; Zheng, L.; Parkinson, R.M.; Durham, J.N.; Onners, B.; Ferguson, A.K.; et al. A Phase II Study of Allogeneic GM-CSF-Transfected Pancreatic Tumor Vaccine (GVAX) with Ipilimumab as Maintenance Treatment for Metastatic Pancreatic Cancer. *Clin. Cancer Res.* **2020**, *26*, 5129–5139. [CrossRef] [PubMed]
75. Sondak, V.K.; Sosman, J.A. Results of clinical trials with an allogeneic melanoma tumor cell lysate vaccine: Melacine. *Semin. Cancer Biol.* **2003**, *13*, 409–415. [CrossRef] [PubMed]
76. Hsueh, E.C.; Morton, D.L. Antigen-based immunotherapy of melanoma: Canvaxin therapeutic polyvalent cancer vaccine. *Semin. Cancer Biol.* **2003**, *13*, 401–407. [CrossRef]
77. Gleisner, M.A.; Pereda, C.; Tittarelli, A. A heat-shocked melanoma cell lysate vaccine enhances tumor infiltration by prototypic effector T cells inhibiting tumor growth. *J. Immunother. Cancer* **2020**, *8*, e000999. [CrossRef]
78. Nayerossadat, N.; Maedeh, T.; Ali, P. Viral and nonviral delivery systems for gene delivery. *Adv. Biomed. Res.* **2012**, *1*, 27. [CrossRef]
79. Xiang, S.D.; Selomulya, C.; Ho, J.; Apostolopoulos, V.; Plebanski, M. Delivery of DNA vaccines: An overview on the use of biodegradable polymeric and magnetic nanoparticles. *Wiley Interdiscip. Rev. Nanomed. Nanobiotechnol.* **2010**, *2*, 205–218. [CrossRef]
80. Yarchoan, M.; Gane, E.; Marron, T.; Rochestie, S.; Cooch, N.; Peters, J.; Csiki, I.; Perales-Puchalt, A.; Sardesai, N. 453 Personalized DNA neoantigen vaccine (GNOS-PV02) in combination with plasmid IL-12 and pembrolizumab for the treatment of patients with advanced hepatocellular carcinoma. *J. Immunother. Cancer* **2021**, *9*, A481. [CrossRef]
81. He, T.C.; Zhou, S.; da Costa, L.T.; Yu, J.; Kinzler, K.W.; Vogelstein, B. A simplified system for generating recombinant adenoviruses. *Proc. Natl. Acad. Sci. USA* **1998**, *95*, 2509–2514. [CrossRef] [PubMed]

82. Falsey, A.R.; Sobieszczyk, M.E.; Hirsch, I.; Sproule, S.; Robb, M.L.; Corey, L.; Neuzil, K.M.; Hahn, W.; Hunt, J.; Mulligan, M.J.; et al. Phase 3 Safety and Efficacy of AZD1222 (ChAdOx1 nCoV-19) COVID-19 Vaccine. *N. Engl. J. Med.* **2021**, *385*, 2348–2360. [CrossRef] [PubMed]
83. Tapia, M.D.; Sow, S.O.; Mbaye, K.D.; Thiongane, A.; Ndiaye, B.P.; Ndour, C.T.; Mboup, S.; Keshinro, B.; Kinge, T.N.; Vernet, G.; et al. Safety, reactogenicity, and immunogenicity of a chimpanzee adenovirus vectored Ebola vaccine in children in Africa: A randomised, observer-blind, placebo-controlled, phase 2 trial. *Lancet Infect. Dis.* **2020**, *20*, 719–730. [CrossRef]
84. Shiratsuchi, T.; Rai, U.; Kaneko, I.; Zhang, M.; Iwanaga, S.; Yuda, M.; Tsuji, M. A potent malaria vaccine based on adenovirus with dual modifications at Hexon and pVII. *Vaccine* **2017**, *35*, 6990–7000. [CrossRef]
85. Overman, M.; Fakih, M.; Le, D.; Shields, A.; Pedersen, K.; Shah, M.; Mukherjee, S.; Faivre, T.; Leoni, G.; D’Alise, A.M.; et al. 410 Phase I interim study results of Nous-209, an off-the-shelf immunotherapy, with pembrolizumab, for the treatment of tumors with a deficiency in mismatch repair/microsatellite instability (dMMR/MSI). *J. Immunother. Cancer* **2021**, *9*, A441. [CrossRef]
86. Floudas, C.; Strauss, J.; Allen, C.; Donahue, R.; Jochems, C.; Steinberg, S.; Cordes, L.; Brough, D.; Lankford, A.; McMahon, S.; et al. 483 Initial safety results and immune responses induced by a novel human papillomavirus (HPV)-specific gorilla adenovirus immunotherapy vaccine, PRGN-2009, in patients with advanced HPV-associated cancers. *J. Immunother. Cancer* **2021**, *9*, A513. [CrossRef]
87. Barouch, D.H.; Pau, M.G.; Custers, J.H.; Koudstaal, W.; Kostense, S.; Havenga, M.J.; Truitt, D.M.; Sumida, S.M.; Kishko, M.G.; Arthur, J.C.; et al. Immunogenicity of recombinant adenovirus serotype 35 vaccine in the presence of pre-existing anti-Ad5 immunity. *J. Immunol.* **2004**, *172*, 6290–6297. [CrossRef]
88. Guo, J.; Mondal, M.; Zhou, D. Development of novel vaccine vectors: Chimpanzee adenoviral vectors. *Hum. Vaccines Immunother.* **2018**, *14*, 1679–1685. [CrossRef]
89. Haigentz, M.; Ramalingam, S.S.; Gerstner, G.J.; Halmos, B.; Morganstein, N.; Vangala, S.; Parsi, M.; Kabala, V.; Simkhada, D.; Metran, C.; et al. A phase 1 study of an off-the shelf, multi-neoantigen vector (ADXS-503) in subjects with metastatic non-small cell lung cancer (NSCLC) progressing on pembrolizumab as last therapy. *J. Clin. Oncol.* **2021**, *39*, 2616. [CrossRef]
90. Hecht, J.R.; Goldman, J.W.; Hayes, S.; Balli, D.; Princiotta, M.F.; Dennie, J.G.; Heyburn, J.; Sands, T.; Sheeri, S.; Petit, R.; et al. Abstract CT007: Safety and immunogenicity of a personalized neoantigen—*Listeria* vaccine in cancer patients. *Cancer Res.* **2019**, *79*, CT007. [CrossRef]
91. Pilishvili, T.; Gierke, R.; Fleming-Dutra, K.E.; Farrar, J.L.; Mohr, N.M.; Talan, D.A.; Krishnadasan, A.; Harland, K.K.; Smithline, H.A.; Hou, P.C.; et al. Effectiveness of mRNA COVID-19 Vaccine among U.S. Health Care Personnel. *N. Engl. J. Med.* **2021**, *385*, e90. [CrossRef] [PubMed]
92. Sahin, U.; Derhovannessian, E.; Miller, M.; Kloke, B.-P.; Simon, P.; Löwer, M.; Bukur, V.; Tadmor, A.D.; Luxemburger, U.; Schrörs, B.; et al. Personalized RNA mutanome vaccines mobilize poly-specific therapeutic immunity against cancer. *Nature* **2017**, *547*, 222–226. [CrossRef] [PubMed]
93. Burris, H.A.; Patel, M.R.; Cho, D.C.; Clarke, J.M.; Gutierrez, M.; Zaks, T.Z.; Frederick, J.; Hopson, K.; Mody, K.; Binanti-Berube, A.; et al. A phase I multicenter study to assess the safety, tolerability, and immunogenicity of mRNA-4157 alone in patients with resected solid tumors and in combination with pembrolizumab in patients with unresectable solid tumors. *J. Clin. Oncol.* **2019**, *37*, 2523. [CrossRef]
94. Bauman, J.; Burris, H.; Clarke, J.; Patel, M.; Cho, D.; Gutierrez, M.; Julian, R.; Scott, A.; Cohen, P.; Frederick, J.; et al. 798 Safety, tolerability, and immunogenicity of mRNA-4157 in combination with pembrolizumab in subjects with unresectable solid tumors (KEYNOTE-603): An update. *J. Immunother. Cancer* **2020**, *8*, A477. [CrossRef]
95. Cafri, G.; Gartner, J.J.; Zaks, T.; Hopson, K.; Levin, N.; Paria, B.C.; Parkhurst, M.R.; Yossef, R.; Lowery, F.J.; Jafferji, M.S.; et al. mRNA vaccine-induced neoantigen-specific T cell immunity in patients with gastrointestinal cancer. *J. Clin. Invest.* **2020**, *130*, 5976–5988. [CrossRef]
96. Sahin, U.; Karikó, K.; Türeci, Ö. mRNA-based therapeutics—Developing a new class of drugs. *Nat. Rev. Drug Discov.* **2014**, *13*, 759–780. [CrossRef]
97. Baiersdörfer, M.; Boros, G.; Muramatsu, H.; Mahiny, A.; Vlatkovic, I.; Sahin, U.; Karikó, K. A Facile Method for the Removal of dsRNA Contaminant from In Vitro-Transcribed mRNA. *Mol. Ther. Nucleic Acids* **2019**, *15*, 26–35. [CrossRef]
98. Rauch, S.; Lutz, J.; Kowalczyk, A.; Schlake, T.; Heidenreich, R. RNActive® Technology: Generation and Testing of Stable and Immunogenic mRNA Vaccines. *Methods Mol. Biol.* **2017**, *1499*, 89–107. [CrossRef]
99. Luo, M.; Wang, H.; Wang, Z.; Cai, H.; Lu, Z.; Li, Y.; Du, M.; Huang, G.; Wang, C.; Chen, X.; et al. A STING-activating nanovaccine for cancer immunotherapy. *Nat. Nanotechnol.* **2017**, *12*, 648–654. [CrossRef]
100. Kranz, L.M.; Diken, M.; Haas, H.; Kreiter, S.; Loquai, C.; Reuter, K.C.; Meng, M.; Fritz, D.; Vascotto, F.; Hefesha, H.; et al. Systemic RNA delivery to dendritic cells exploits antiviral defence for cancer immunotherapy. *Nature* **2016**, *534*, 396–401. [CrossRef]
101. BioNTech Receives FDA Fast Track Designation for Its FixVac Candidate BNT111 in Advanced Melanoma. Available online: <https://investors.biontech.de/news-releases/news-release-details/biontech-receives-fda-fast-track-designation-its-fixvac> (accessed on 19 November 2021).
102. Shemesh, C.S.; Hsu, J.C.; Hosseini, I.; Shen, B.Q.; Rotte, A.; Twomey, P.; Girish, S.; Wu, B. Personalized Cancer Vaccines: Clinical Landscape, Challenges, and Opportunities. *Mol. Ther.* **2021**, *29*, 555–570. [CrossRef] [PubMed]

103. Keskin, D.B.; Anandappa, A.J.; Sun, J.; Tirosch, I.; Mathewson, N.D.; Li, S.; Oliveira, G.; Giobbie-Hurder, A.; Felt, K.; Gjini, E.; et al. Neoantigen vaccine generates intratumoral T cell responses in phase Ib glioblastoma trial. *Nature* **2019**, *565*, 234–239. [CrossRef] [PubMed]
104. Ott, P.A.; Hu, Z.; Keskin, D.B.; Shukla, S.A.; Sun, J.; Bozym, D.J.; Zhang, W.; Luoma, A.; Giobbie-Hurder, A.; Peter, L.; et al. An immunogenic personal neoantigen vaccine for patients with melanoma. *Nature* **2017**, *547*, 217–221. [CrossRef] [PubMed]
105. Hilf, N.; Kuttruff-Coqui, S.; Frenzel, K.; Bukur, V.; Stevanović, S.; Gouttefangeas, C.; Platten, M.; Tabatabai, G.; Dutoit, V.; van der Burg, S.H.; et al. Actively personalized vaccination trial for newly diagnosed glioblastoma. *Nature* **2019**, *565*, 240–245. [CrossRef] [PubMed]
106. Platten, M.; Bunse, L.; Wick, A.; Bunse, T.; Le Cornet, L.; Harting, I.; Sahm, F.; Sanghvi, K.; Tan, C.L.; Poschke, I.; et al. A vaccine targeting mutant IDH1 in newly diagnosed glioma. *Nature* **2021**, *592*, 463–468. [CrossRef] [PubMed]
107. Ott, P.A.; Hu-Lieskovan, S.; Chmielowski, B.; Govindan, R.; Naing, A.; Bhardwaj, N.; Margolin, K.; Awad, M.M.; Hellmann, M.D.; Lin, J.J.; et al. A Phase Ib Trial of Personalized Neoantigen Therapy Plus Anti-PD-1 in Patients with Advanced Melanoma, Non-small Cell Lung Cancer, or Bladder Cancer. *Cell* **2020**, *183*, 347–362.e24. [CrossRef] [PubMed]
108. Gillison, M.L.; Awad, M.M.; Twardowski, P.; Sukari, A.; Johnson, M.L.; Stein, M.N.; Hernandez, R.; Price, J.; Mancini, K.J.; Shainheit, M.; et al. Long term results from a phase 1 trial of GEN-009, a personalized neoantigen vaccine, combined with PD-1 inhibition in advanced solid tumors. *J. Clin. Oncol.* **2021**, *39*, 2613. [CrossRef]
109. Nabhan, C. Sipuleucel-T immunotherapy for castration-resistant prostate cancer. *N. Engl. J. Med.* **2010**, *363*, 1966–1967. [CrossRef]
110. Carreno, B.M.; Magrini, V.; Becker-Hapak, M.; Kaabinejadian, S.; Hundal, J.; Petti, A.A.; Ly, A.; Lie, W.-R.; Hildebrand, W.H.; Mardis, E.R.; et al. A dendritic cell vaccine increases the breadth and diversity of melanoma neoantigen-specific T cells. *Science* **2015**, *348*, 803–808. [CrossRef]
111. Chen, F.; Zou, Z.; Du, J.; Su, S.; Shao, J.; Meng, F.; Yang, J.; Xu, Q.; Ding, N.; Yang, Y.; et al. Neoantigen identification strategies enable personalized immunotherapy in refractory solid tumors. *J. Clin. Invest.* **2019**, *129*, 2056–2070. [CrossRef]
112. Ding, Z.; Li, Q.; Zhang, R.; Xie, L.; Shu, Y.; Gao, S.; Wang, P.; Su, X.; Qin, Y.; Wang, Y.; et al. Personalized neoantigen pulsed dendritic cell vaccine for advanced lung cancer. *Signal Transduct. Target. Ther.* **2021**, *6*, 26. [CrossRef] [PubMed]
113. Tran, T.; Blanc, C.; Granier, C.; Saldmann, A.; Tanchot, C.; Tartour, E. Therapeutic cancer vaccine: Building the future from lessons of the past. *Semin. Immunopathol.* **2019**, *41*, 69–85. [CrossRef] [PubMed]
114. van der Burg, S.H. Correlates of immune and clinical activity of novel cancer vaccines. *Semin. Immunol.* **2018**, *39*, 119–136. [CrossRef] [PubMed]
115. Masopust, D.; Ha, S.J.; Vezys, V.; Ahmed, R. Stimulation history dictates memory CD8 T cell phenotype: Implications for prime-boost vaccination. *J. Immunol.* **2006**, *177*, 831–839. [CrossRef]
116. Wirth, T.C.; Xue, H.H.; Rai, D.; Sabel, J.T.; Bair, T.; Harty, J.T.; Badovinac, V.P. Repetitive antigen stimulation induces stepwise transcriptome diversification but preserves a core signature of memory CD8(+) T cell differentiation. *Immunity* **2010**, *33*, 128–140. [CrossRef]
117. Fraser, K.A.; Schenkel, J.M.; Jameson, S.C.; Vezys, V.; Masopust, D. Preexisting high frequencies of memory CD8+ T cells favor rapid memory differentiation and preservation of proliferative potential upon boosting. *Immunity* **2013**, *39*, 171–183. [CrossRef]
118. Alspach, E.; Lussier, D.M.; Miceli, A.P.; Kizhvatov, I.; DuPage, M.; Luoma, A.M.; Meng, W.; Lichti, C.F.; Esaulova, E.; Vomund, A.N.; et al. MHC-II neoantigens shape tumour immunity and response to immunotherapy. *Nature* **2019**, *574*, 696–701. [CrossRef]
119. Nembrini, C.; Stano, A.; Dane, K.Y.; Ballester, M.; van der Vlies, A.J.; Marsland, B.J.; Swartz, M.A.; Hubbell, J.A. Nanoparticle conjugation of antigen enhances cytotoxic T-cell responses in pulmonary vaccination. *Proc. Natl. Acad. Sci. USA* **2011**, *108*, E989–E997. [CrossRef]
120. Li, A.V.; Moon, J.J.; Abraham, W.; Suh, H.; Elkhader, J.; Seidman, M.A.; Yen, M.; Im, E.J.; Foley, M.H.; Barouch, D.H.; et al. Generation of effector memory T cell-based mucosal and systemic immunity with pulmonary nanoparticle vaccination. *Sci. Transl. Med.* **2013**, *5*, 204ra130. [CrossRef]
121. Kuai, R.; Ochyl, L.J.; Bahjat, K.S.; Schwendeman, A.; Moon, J.J. Designer vaccine nanodiscs for personalized cancer immunotherapy. *Nat. Mater.* **2017**, *16*, 489–496. [CrossRef]
122. Spranger, S.; Gajewski, T.F. Impact of oncogenic pathways on evasion of antitumour immune responses. *Nat. Rev. Cancer* **2018**, *18*, 139–147. [CrossRef] [PubMed]
123. Smith, T.T.; Moffett, H.F.; Stephan, S.B.; Opel, C.F.; Dumigan, A.G.; Jiang, X.; Pillarisetty, V.G.; Pillai, S.P.S.; Wittrup, K.D.; Stephan, M.T. Biopolymers codelivering engineered T cells and STING agonists can eliminate heterogeneous tumors. *J. Clin. Invest.* **2017**, *127*, 2176–2191. [CrossRef] [PubMed]
124. Stephan, S.B.; Taber, A.M.; Jileeva, I.; Pegues, E.P.; Sentman, C.L.; Stephan, M.T. Biopolymer implants enhance the efficacy of adoptive T-cell therapy. *Nat. Biotechnol.* **2015**, *33*, 97–101. [CrossRef] [PubMed]
125. Chen, Q.; Wang, C.; Zhang, X.; Chen, G.; Hu, Q.; Li, H.; Wang, J.; Wen, D.; Zhang, Y.; Lu, Y.; et al. In situ sprayed bioresponsive immunotherapeutic gel for post-surgical cancer treatment. *Nat. Nanotechnol.* **2019**, *14*, 89–97. [CrossRef] [PubMed]
126. Gosselin, E.A.; Eppler, H.B.; Bromberg, J.S.; Jewell, C.M. Designing natural and synthetic immune tissues. *Nat. Mater.* **2018**, *17*, 484–498. [CrossRef] [PubMed]
127. Pavesi, A.; Tan, A.T.; Koh, S.; Chia, A.; Colombo, M.; Antonicchia, E.; Miccolis, C.; Ceccarello, E.; Adriani, G.; Raimondi, M.T.; et al. A 3D microfluidic model for preclinical evaluation of TCR-engineered T cells against solid tumors. *JCI Insight* **2017**, *2*, e89762. [CrossRef] [PubMed]

128. Ando, Y.; Siegler, E.L.; Ta, H.P.; Cinay, G.E.; Zhou, H.; Gorrell, K.A.; Au, H.; Jarvis, B.M.; Wang, P.; Shen, K. Evaluating CAR-T Cell Therapy in a Hypoxic 3D Tumor Model. *Adv. Healthc. Mater.* **2019**, *8*, e1900001. [CrossRef]
129. Wallstabe, L.; Göttlich, C.; Nelke, L.C.; Kühnemundt, J.; Schwarz, T.; Nerreter, T.; Einsele, H.; Walles, H.; Dandekar, G.; Nietzer, S.L.; et al. ROR1-CAR T cells are effective against lung and breast cancer in advanced microphysiologic 3D tumor models. *JCI Insight* **2019**, *4*, e126345. [CrossRef]







Review

# Oncogenic and Tumor Suppressive Components of the Cell Cycle in Breast Cancer Progression and Prognosis

Dharambir Kashyap <sup>1</sup>, Vivek Kumar Garg <sup>2</sup>, Elise N. Sandberg <sup>3</sup>, Neelam Goel <sup>4,\*</sup> and Anupam Bishayee <sup>3,\*</sup>

<sup>1</sup> Department of Histopathology, Postgraduate Institute of Medical Education and Research, Chandigarh 160 012, Punjab, India; make.must@gmail.com

<sup>2</sup> Punjab Biotechnology Incubator, Mohali 160 059, Punjab, India; garg.vivek85@gmail.com

<sup>3</sup> Lake Erie College of Osteopathic Medicine, Bradenton, FL 34211, USA; Elise.sandberg@gmail.com

<sup>4</sup> University Institute of Engineering and Technology, Panjab University, Chandigarh 160 014, Punjab, India

\* Correspondence:erneelam@pu.ac.in (N.G.); abishayee@lecom.edu or abishayee@gmail.com (A.B.)

**Abstract:** Cancer, a disease of inappropriate cell proliferation, is strongly interconnected with the cell cycle. All cancers consist of an abnormal accumulation of neoplastic cells, which are propagated toward uncontrolled cell division and proliferation in response to mitogenic signals. Mitogenic stimuli include genetic and epigenetic changes in cell cycle regulatory genes and other genes which regulate the cell cycle. This suggests that multiple, distinct pathways of genetic alterations lead to cancer development. Products of both oncogenes (including cyclin-dependent kinase (CDKs) and cyclins) and tumor suppressor genes (including cyclin-dependent kinase inhibitors) regulate cell cycle machinery and promote or suppress cell cycle progression, respectively. The identification of cyclins and CDKs help to explain and understand the molecular mechanisms of cell cycle machinery. During breast cancer tumorigenesis, cyclins A, B, C, D1, and E; cyclin-dependent kinase (CDKs); and CDK-inhibitor proteins p16, p21, p27, and p53 are known to play significant roles in cell cycle control and are tightly regulated in normal breast epithelial cells. Following mitogenic stimuli, these components are deregulated, which promotes neoplastic transformation of breast epithelial cells. Multiple studies implicate the roles of both types of components—oncogenic CDKs and cyclins, along with tumor-suppressing cyclin-dependent inhibitors—in breast cancer initiation and progression. Numerous clinical studies have confirmed that there is a prognostic significance for screening for these described components, regarding patient outcomes and their responses to therapy. The aim of this review article is to summarize the roles of oncogenic and tumor-suppressive components of the cell cycle in breast cancer progression and prognosis.

**Keywords:** cell cycle; cyclin-dependent kinase; p16; p21; p27; breast cancer; prognosis

**Citation:** Kashyap, D.; Garg, V.K.; Sandberg, E.N.; Goel, N.; Bishayee, A. Oncogenic and Tumor Suppressive Components of the Cell Cycle in Breast Cancer Progression and Prognosis. *Pharmaceutics* **2021**, *13*, 569. <https://doi.org/10.3390/pharmaceutics13040569>

**Academic Editors:**  
Carlos Alonso-Moreno and  
Hassan Bousbaa

Received: 10 March 2021

Accepted: 13 April 2021

Published: 17 April 2021

**Publisher's Note:** MDPI stays neutral with regard to jurisdictional claims in published maps and institutional affiliations.

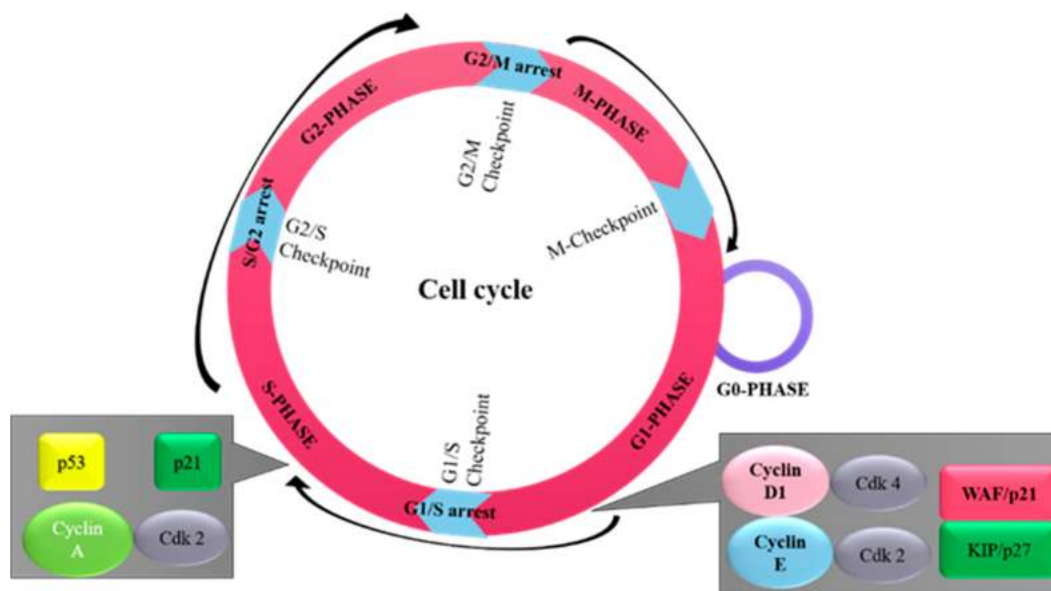


**Copyright:** © 2021 by the authors. Licensee MDPI, Basel, Switzerland. This article is an open access article distributed under the terms and conditions of the Creative Commons Attribution (CC BY) license (<https://creativecommons.org/licenses/by/4.0/>).

## 1. Introduction

Cancer, a disease of uncontrolled cell division, is known to exhibit a series of changes in the activity of cell cycle regulators [1]. All cancer types arise from a single cell that has transformed due to genetic or regulatory alterations, resulting in uncontrolled cell division in response to mitogenic signals [2]. Mitogenic signals include genetic and epigenetic aberrations in cell cycle regulatory genes. These mitogenic stimuli make oncogenic changes, resulting in cell transformation [3]. The gain-of-function mutations cause the activation of proto-oncogenes, which are normally present in the suppressed state in differentiated cells under epigenetic control [4]. Oncogenic stimuli have the potential to induce transformation of the differentiated cells, causing alterations in genetic material and therefore stimulating the development of certain cancers [5–7]. Loss-of-function mutations lead to a decreased expression of tumor suppressor genes, resulting in the diminishment of tumor-protective functions [8–11]. The collective data obtained suggest that distinct pathways of genetic alteration lead to cancer [11]. Products of both oncogenes and tumor suppressor genes regulate cell cycle machinery [8,12]. There are different phases of the

cell cycle, and progression through these phases requires many regulatory components, which include oncogenic genes (CDKs (cyclin-dependent kinases) and cyclins) and tumor suppressor genes (cyclin-dependent kinase inhibitors) [13]. The identification and subsequent functional analysis of cyclins and CDKs enable us to understand the molecular mechanism of cell-cycle machinery [14]. In the pathogenesis of breast cancer, cyclins A, B, C, D1, and E; CDKs; and CDK-inhibitors, such as p21 (Waf1/Cip1), p27 (Kip1), p16 and 53, are known to play important roles in cell cycle control [15] (Figure 1). Each cell cycle phase is tightly regulated in normal cells [15]. After exposure to mitogenic stimuli, however, these regulatory components become deregulated, which predisposes the cellular transformation of breast epithelial cells. Numerous studies implicate the roles of oncogenic and tumor-suppressive components in various human cancer types, including the initiation and development of breast cancer, more specifically [9,16,17]. In addition, several research bodies have confirmed the prognostic significance of oncogenic and tumor suppressor components in regard to therapy or clinical outcomes [18]. Significant information exists on the regulation and roles of the cell cycle components in breast cancer cells, and previous studies may be utilized for therapeutic purposes. Findings from experimental studies also support that alterations in these components are clinically significant [19]. The aim of this review article is to summarize the role of various oncogenic and tumor suppressor components of the cell cycle that are involved in breast cancer progression and prognosis.

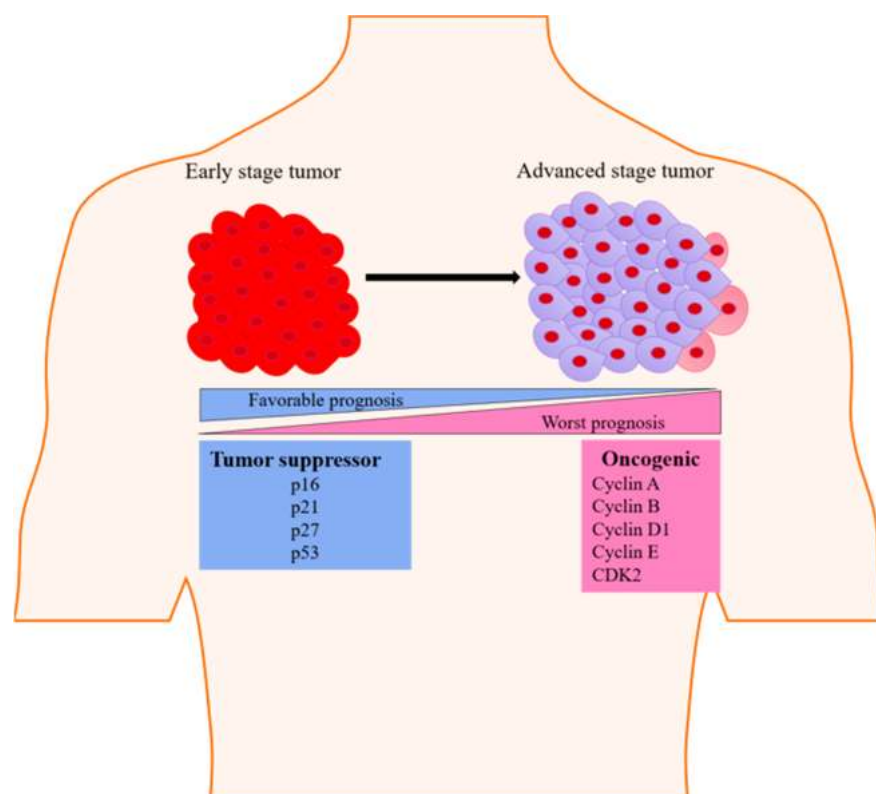


**Figure 1.** The sequential order of cell cycle events. The cell cycle progresses through four sequential phases: G1-phase (cell increases in size), S-phase (DNA synthesis), G2-phase (prepares to divide), and M-phase (cell division). The phases G1, S, and G2 make up the interphase stage, and span between cell division. There are special proteins and checkpoint systems for the proper progression of the cell cycle. First: G1 checkpoint (at G1/S transition) is the main irreversible decision point for cell division, which assesses for adequate cell size, availability of nutrients, positive molecular signals, and DNA integrity. Second: G2 checkpoint (at G2/M transition) ensures smooth cell division and assesses DNA integrity and successful DNA replication before division. In the case of error, cellular progression will become paused at the G2 checkpoint for repair. Third: the spindle checkpoint (metaphase to anaphase transition), ensures correct attachment of sister chromatids to the spindle microtubules.

## 2. Overview of Cell Cycle

The cell cycle is composed of several phases (Figure 1), including a phase for the preparation of DNA synthesis—G1 phase; a phase for DNA synthesis—S phase; a second preparation phase—G2 phase; and mitosis—M phase. These phases are tightly controlled under physiological conditions [20]. Quiescence (G0) is another phase of the cell cycle found in some differentiated cells, in which the cell undergoes its own distinct biochemical

or molecular changes [21]. Under certain pathological stimuli, differentiated cells can leave the G0 phase and re-enter the cell cycle [21]. The transitions between these cell cycle phases are controlled by the function of specific CDKs. This includes CDK1/CDK2, which causes the transition from G2 to mitosis, and CDK2/CDK4/CDK6, which causes the G1 to S phase transition [22]. During cellular division, another group of proteins called cyclins form complexes with specific CDK molecules in their respective phases [22]. The G1 cell cycle phase transition is identified by the activity of CDK4/6-cyclin D and CDK2-cyclin E complexes, S cell cycle phase transition by cyclin A-CDK1/2 complex, and G2-mitosis phase transition by cyclin A-CDK and cyclin B-CDK1 complexes [23]. Many genetic alterations can affect the functional activities of oncogenes or tumor suppressors, including alterations in cyclin E, cyclin D1, and p27. These alterations have been shown to induce a transition from the quiescent state into the active state in breast epithelial cells, subsequently leading to breast epithelial cell transformation (Figure 2) [24].



**Figure 2.** Illustration showing the change in the expression status of genes serving as tumor-suppressive and oncogenic markers during tumorigenesis. These changes in expression impact progression into advanced-staged cancer and overall breast cancer prognosis.

### 3. Oncogenic Components of Cell Cycle

#### 3.1. Cyclin D

The proto-oncogene cyclin D is a crucial regulator for the transition from the G1 to S phase during the cell cycle. It binds with CDK4 and CDK6 and forms an active cyclin D-CDK4/6 complex, which then phosphorylates the retinoblastoma protein (Rb) to promote cell cycle progression [25,26]. Cyclin D may also modulate the activity of various transcription factor proteins and histone deacetylase enzyme [27]. Having a half-life of ~24 min, cyclin D is degraded inside the cell mainly via the activity of 26S proteasome in a ubiquitin-dependent and Skp2 F-box protein-dependent manner [28,29]. In addition, D1-CDK4/6 complex can also impair the functions of mitochondria through the phosphorylation and repression of nuclear respiratory factor 1 (NRF1) and mitochondrial transcription factor A (mtTFA). An earlier report established a molecular link between cyclin D1 and control of mitochondrial function through the inhibition of nuclear respiratory factor 1 [30].

Previously accumulated data underscore the role of cyclin D1 in the tumorigenesis of mammary cancer [31,32]. Overexpression and gene amplification of cyclin D has also been linked to a worsened prognosis and the development of resistance against endocrine therapy in breast cancer (Tables 1 and 2) [33,34]. A study documented cyclin D1 gene overexpression and copy number amplification in 20% and 50% of human breast cancer cases, respectively [35–37]. Furthermore, an enhanced expression of cyclin D1 was also observed in 67.5% of invasive ductal carcinoma cases, where it was strongly correlated with estrogen receptor (ER) and progesterone receptor (PR) expression [38]. Similarly, a study analyzed the immunohistochemical (IHC) positivity of cyclin D1 in invasive ductal and moderately differentiated breast cancer cases, which was associated with significantly poorer prognoses in these patients [39]. Additionally, research data based on in vitro and clinical studies implicated an increased cyclin D1 gene expression and amplification in ~45–50% of breast cancer cases [40]. In another in vitro study, genetic alterations in the cyclin D1 gene and mRNA expression were found in the ER-negative MDA-MB-453 cell line (Table 3), which may be related to malignant transformation [41]. Similarly, cyclin D1 protein expression was examined in infiltrating mammary carcinoma with ER/PR positivity [42]. An abnormal expression of cyclin D1 was displayed in 66% of mammary infiltrating duct carcinomas, suggesting its role in breast tumor metastasis [43]. Zhang et al. [44] determined that enhanced expression of the cyclin D gene was found in ~82% of human breast tumors, and gene amplification was present in ~17% of cases.

**Table 1.** Clinical relevance of oncogenic and tumor suppressive cell cycle components in breast cancer patients with different molecular subtypes.

Marker	Expression	Consequences	Receptor Status	Ref
	Overexpression	High risk of replace, Local recurrence, Metastasis	ER+/ER-	[45]
	Overexpression	High tumor grade	ER+/ER-/PR+/PR-/HER2+	[35]
	Overexpression	High proliferation	ER+/ER-/PR+/PR-/TNBC	[38]
	Overexpression	High proliferation	ER+/ER-/PR+/PR-	[39]
	Overexpression	High proliferation	ER+/ER-	[40]
	Overexpression	High proliferation	ER+/ER-/PR+/PR-	[42]
	Overexpression	Metastasis		[43]
	Gene amplification Overexpression	High proliferation		[44]
	Overexpression	High proliferation	ER+	[46]
	Gene amplification	High risk for recurrence	ER+/ER-	[47]
	Overexpression, Gene amplification	High proliferation	ER+/ER-/PR+/PR-	[48]
	Overexpression	High proliferation, Short overall survival, Large tumor size, Lymph node metastasis	ER+/ER-/PR+/PR-	[49]
	Overexpression, Gene amplification	High proliferation	ER+/ER-/Basal like	[50]
	Overexpression	Reduce relapse-free survival	ER+/PR+	[51]
	Overexpression	High proliferation	ER+/PR+/ER-/PR-/HER2+	[52]
	Overexpression	High proliferation	ER+/PR+/ER-/PR-/HER2+	[53]
	Overexpression	High proliferation	ER+/ER-	[54]
	Overexpression	High risk of recurrence	ER+ER-/HER2+/HER2-	[55]
	Gene amplification	High proliferation	ER+/ER-	[56]

Cyclin D

Table 1. Cont.

Marker	Expression	Consequences	Receptor Status	Ref
	Gene amplification	Reduce patient survival time, therapy resistance	ER+	[57]
	Overexpression	Poor prognosis	ER+/PR+/ER-/PR-/HER2+/Basal like	[58]
	Overexpression	Invasiveness, metastasis	TNBC	[59]
	Overexpression	High proliferation	ER+	[60]
	Reduce expression	High tumor grade, Nodal positive status, Invasion	ER+/PR+/ER-/PR-/HER2+/HER2-	[61]
	Overexpression, Gene amplification	Poor prognosis		[62]
	Overexpression	Relapse, Shorter disease-free survival	ER+/ER-	[63]
	Overexpression	Worst prognosis	ER+/ER-	[64]
	Overexpression	Shorter relapse time	ER+/ER-	[65]
	Overexpression	Less survival rate, High relapse rate	ER+/PR+/ER-/PR-	[66]
	Overexpression	Short distant metastasis-free survival	ER+/PR+/ER-/PR-	[67]
	Overexpression	Poor prognosis	ER+/ER-	[68]
	Overexpression	High tumor grade, High proliferation index	HER2+/HER2-	[69]
	Overexpression	Poor survival	ER+/ER-	[70]
	Overexpression	Poor prognosis, Decrease survival rate	ER+/PR+/ER-/PR-/HER2+	[71]
	Overexpression	Decrease survival	ER+/PR+/ER-/PR-/HER2+/HER2-	[72]
Cyclin B1	Overexpression	Reduce overall survival, Disease free survival, Lymphatic invasion	ER+/PR+/ER-/PR-/HER2+/HER2-	[73]

Table 1. Cont.

Marker	Expression	Consequences	Receptor Status	Ref
p21(WAF1/Cip1)	Overexpression	High tumor grade, Large tumor size, Positive lymph node, High Ki-67 expression	ER+/PR+/ER-/PR- /HER2+/HER2-	[74]
	Overexpression	Favorable prognosis	ER+/PR+/ER-/PR-	[75]
	Overexpression	Better survival	ER+/PR+/ER-/PR-/HER2+	[76]
	Overexpression	Better survival	ER+/PR+/ER-/PR- /HER2+/HER2-	[77]
	Overexpression	Large tumor size, High tumor grade, Lymph node metastasis	ER+/PR+/ER-/PR- /HER2+/HER2-	[78]
	Reduced expression	High tumor grade, Lack of tumor differentiation, Poor prognosis	ER+/PR+/ER-/PR- /HER2+/HER2-	[79]
	Overexpression	Better prognosis	ER+/ER-	[80]
p27 (Kip1)	Overexpression	Favorable prognosis	ER+/PR+/HER2+	[81]
	Reduced expression	Poor prognosis	ER+/PR+/ER-/PR- /HER2+/HER2-	[82]
	Overexpression	Long disease-free survival, overall survival	ER+/PR+/ER-/PR-	[83]
	Reduced expression	Poor prognosis	ER+/PR+/ER-/PR-	[84]
	Reduced expression	Large tumor size, high tumor grade, lymph node metastasis	ER+/ER-	[85]
	Overexpression	Long relapse-free survival, Overall survival	ER+/PR+	[86]
	Reduced expression	Poor prognosis	ER+/PR+	[87]
	Reduced expression	Increase proliferation	ER+/PR+/ER-/PR- /HER2+/HER2-	[88]
	Overexpression	Favorable prognosis	ER+/PR+/ER-/PR- /HER2+/HER2-	[89]



Table 1. Cont.

Marker	Expression	Consequences	Receptor Status	Ref
p16 (ink4a)	Lower expression	Worst overall survival, Worst disease-free survival	ER+/PR+/ER-/PR-	[90]
	Lower expression	Worst overall survival	ER+/PR+/ER-/PR-	[91]
	Overexpression	High proliferation index	ER+/PR+/ER-/PR- /HER2+/HER2-	[92]
	Overexpression	Favorable prognosis	ER+/PR+/ER-/PR-	[93]
	Overexpression	Favorable prognosis	ER-/PR-/HER2-	[94]
	Overexpression	Favorable prognosis	ER+/PR+/ER-/PR-	[95]
	Overexpression	Disease progression	ER+/PR+/ER-/PR-	[96]
	Overexpression	Lung and brain metastasis	ER+/PR+/ER-/PR- /HER2+/HER2-	[97]
	Reduced expression	Metastasis	ER+/PR+/ER-/PR- /HER2+/HER2-	[98]
	Overexpression	Favorable prognosis	ER+/PR+/ER-/PR- /HER2+/HER2-	[99]
p53 (wild type)	Overexpression	Better disease-free survival	ER+/PR+/ER-/PR-	[100]
	Overexpression	Favorable prognosis	ER+/PR+/ER-/PR- /HER2+/HER2-/Basal like	[101]
	Overexpression	Favorable prognosis	ER+/PR+/ER-/PR-	[102]
	Overexpression	Worst prognosis	ER-/PR-/HER2-	[103]
	Overexpression	Worst prognosis	ER+/PR+/ER-/PR- /HER2+/HER2-	[104]
	Overexpression	Worst prognosis associated with ER expression	ER+/PR+/ER-/PR-	[105]
	Overexpression	Worst prognosis associated with HER2+/TNBC subtypes	ER+/PR+/ER-/PR- /HER2+/HER2-	[106]

Table 1. Cont.

Marker	Expression	Consequences	Receptor Status	Ref
	Overexpression	Worst prognosis, High tumor grade, Lymph vascular invasion, Lymphocyte infiltration	ER+/PR+/ER-/PR-	[107]
	Overexpression	Better overall survival in TNBC	ER-/PR-/HER2-	[108]
	Overexpression	Correlated with HER2 overexpression, High tumor grade	ER+/PR+/ER-/PR- /HER2+/HER2-	[109]
	Overexpression	Worst overall survival, Reoccurrence free survival	ER+/PR+/ER-/PR-	[110]
	Overexpression	Early relapse	ER+/PR+/ER-/PR- /HER2+/HER2-	[111]
	Overexpression	Poor prognosis	ER+/PR+/ER-/PR-	[112]
	Overexpression	Less 5-years reoccurrence free survival	ER+/PR+/ER-/PR-	[113]

ER: estrogen receptor; PR: progesterone receptor; Her2+: human epidermal growth factor receptor-2 positive.

**Table 2.** Clinical relevance of oncogenic and tumor suppressive cell cycle components in breast cancer cell lines with different molecular subtypes.

Marker	Expression	Consequences	Model	Histology	Ref
Cyclin D	Gene amplification mRNA Overexpression	Proliferation	MCF-7	ER+	[33]
	Overexpression	Malignant transformation	MDA-MB-453	HER2+	[41]
	Overexpression	Increase proliferation	T-47D, MCF-7	ER+/HER2+	[34]
	Overexpression	Increase proliferation	MCF-7	ER+	[114]
	Overexpression	Increase proliferation	MCF-7, T-47D, MDA-MB-468, BT-549	ER+/ER-/PR-/HER2-	[115]
	Overexpression	Increase proliferation	HBL-100, MDA-MB-231, T-47D, MCF-7, MDA-MB-134, HMEC-184	ER+/PR+/ER-/PR-/HER2- /HER2+	[52]
	Overexpression	Increase proliferation	MCF-7I,	Tamoxifen-resistant	[116]
	Downregulation	Cell death, Growth arrest	MCF-7, MDA-MB-231, MDA-MB-435, HCC-1937, CAL-148	ER+/ER-/PR-/HER2-	[117]
	Overexpression	Invasiveness, metastasis	MDA-MB-231	ER-/PR-/HER2-	[59]
	Overexpression	Increase proliferation	MCF-7	ER+	[118]
Overexpression	Increase proliferation	MCF-7	ER+	[60]	
Overexpression	Increase proliferation	MCF-7	ER+	[119]	

Table 2. Cont.

Marker	Expression	Consequences	Model	Histology	Ref
	Overexpression	Increase proliferation	ZR75-1-2, ZR-75-1, MDAMB-157, MDA-MB-231, MDA-MB-436, T-47D, BT-20, HBL-100, Hs578T, SK-BR3	ER+/ER-/PR+/PR-/HER2- /HER2+	[120]
Cyclin E	Overexpression, Gene amplification Downregulation	Increase proliferation Suppression of cell cycle progression	BT-474, BT-474R MCF-7	HER2+ ER+	[121] [122]
	Overexpression	Associated with ER+ status	MCF-7, MDA-MB-231, MDA-MB-436, Hs578 T	ER+/PR+/ER-/PR-/HER2- /HER2+	[123,124]
Cyclin B	Downregulation	Apoptosis, Anti-proliferation	MCF-7, BT-474, SK-BR-3, MDA-MB-231	ER+/ER-/PR+/PR-/HER2- /HER2+	[125]
p16(WAF1/Cip1)	Reduced expression	Therapy resistance	HCC-1428, T-47D, MCF-7, MDA-MB-436, BT-549, MDA-MB-157, MDA-MB-231, MDA-MB-435S, Hs578T, HCC-1937, BT-20, SK-BR-3	ER+/PR+/ER-/PR-/HER2- /HER2+	[126]

Table 2. Cont.

Marker	Expression	Consequences	Model	Histology	Ref
	Overexpression	Good survival	MCF-7, BT-549, MDA-MB-134, MDA-MB-157, MDA-MB-231, MDA-MB-453, MDA-MB-468, ZR-75-1, BT-20, SK-BR-3, T-47D	ER+/PR+/ER-/PR-/HER2- /HER2+	[76]
	Overexpression	High proliferation rate	ZR75-1, ZR75-30, MCF-7, MDA-MB-453, T-47D, Cal51, SK-BR-5, SK-BR-7, CAMA-1, BT-20	ER+/PR+/ER-/PR-/HER2+	[127]
p21(WAF1/Cip1)	Reduced expression	Trastuzumab resistance	SK-BR-3	HER2+	[128]
	Overexpression	Cell cycle arrest	MCF-7	ER+	[129]
	Reduced expression	Acquired resistance to docetaxel	MCF-7, MDA-MB-231	ER+/ER-/PR-/HER2-	[130]
	Overexpression	Associated with ER+ status	MCF-7, MDA-MB-231, MDA-MB-436, Hs578T	ER+/PR+/ER-/PR-/HER2- /HER2+	[123,124]

**Table 3.** Characteristics of breast cancer cell lines with different molecular subtypes (adopted from Dai, X et al. 2017) [131].

Cell Line	ER	PR	HER2/neu+	Subtype	BRCA1 Mutation	p53 Mutation	Tumor
CAMA-1	+	+/-	-	LA	WT	MU	AC
HCC1428	+	+	-	LA	ND	ND	AC
MCF-7	+	-	-	LA	ND	WT	IDC
MDA-MB-134	+	-	-	LA	ND	MU	IDC
T-47D	+	+	-	LA	WT	MU	IDC
ZR75-1	+	+/-	-	LA	WT	WT	IDC
BT-474	+	+	+	LB	WT	MU	IDC
ZR75-30	+	-	+	LB	WT	WT	IDC
MDA-MB-453	-	-	+	Her2+	WT	MU	AC
SK-BR-3	-	-	+	Her2+	WT	MU	AC
SK-BR-5	-	-	+	Her2+	WT	MU	AC
BT-20	-	-	-	TNBC	WT	MU	IDC
BT-549	-	-	-	TNBC	WT	MU	IDC
CAL-51	-	-	-	TNBC	WT	MU	AC
CAL-148	-	-	-	TNBC	WT	MU	AC
HCC1937	-	-	-	TNBC	MU	MU	DC
Hs578T	-	-	-	TNBC	WT	MU	IDC
MDA-MB-157	-	-	-	TNBC	WT	MU	MC
MDA-MB-231	-	-	-	TNBC	WT	MU	AC
MDA-MB-435	-	-	-	TNBC	WT	MU	AC
MDA-MB-436	-	-	-	TNBC	MU	MU	AC
MDA-MB-468	-	-	-	TNBC	WT	MU	AC
SK-BR-7	-	-	-	TNBC	WT	WT	AC

WT: wild type; ND: not decided; MU: BRCA1 mutation; AC: adenocarcinoma; DC: ductal carcinoma; LA: luminal A; LB: luminal B; HER2+: human epidermal growth factor receptor 2-positive; TNBC: triple-negative breast cancer.

A study using a mouse mammary tumor virus model of breast cancer identified CCND1 gene amplification with positive IHC staining in 40% of breast cancer samples [132]. Further, the study identified ectopic overexpression of cyclin D1 and a reversed growth-inhibitory outcome after anti-hormonal therapy in ER-positive breast cancer cases, which provided a potential antitumor mechanism [46]. Kenny et al. [43] showed that ER-positive breast cancer patients had cyclin D1 high expression, and at the same time, also displayed more risk of relapse, metastasis, and early death [34]. Moreover, the data also showed that CCND1 gene amplification alone is a strong predictor of anti-hormonal therapy response in young-age breast cancer patients [47]. Moreover, data from another study indicated amplification of the cyclin D1 gene and noted its correlation with ER-positive invasive lobular breast carcinoma with lymph node metastasis, suggesting a sign of poorer prognosis [48]. An additional study suggested overexpression of cyclin D1 gene in the ER-positive MCF-7 breast tumor cell line, which was responsible for hyperproliferation under growth factor-deprived conditions [114]. Another study identified overexpression of cyclin D1 in ER-positive and ER-negative breast cancer samples; however, both shorter overall survival and relapse-free survival were associated only with the ER-negative subgroup [49].

Correlation of high cyclin D1-related elevation with Rb phosphorylation was also observed in >100 high-grade breast carcinomas [115]. Furthermore, a separate study also demonstrated a strong positive correlation between cyclin D gene amplification and higher expression in basal-like and ER-positive breast cancer subtypes, and suggested that cyclin D1 was an independent predictor for prognosis in ER-positive breast cancers [50]. The ABCSG Trial 05 and 06 documented an increased expression of cyclin D1, which was associated with the poorer clinical outcome and shorter overall survival of breast cancer patients [51]. A separate investigation determined the cyclin D1 positivity in proliferative disease without atypia, atypical ductal hyperplasia, low-grade ductal carcinoma in situ (DCIS), high-grade DCIS, and invasive carcinoma. The results showed that cyclin D1 was significantly higher in proliferative disease than normal breast epithelium, and even higher in DCIS than proliferative disease [52]. Additionally, another research group demonstrated an association between high cyclin D1 gene expression and high-grade tumor development, increased Ki-67 expression, and poorer survival in the ER-positive breast cancer group [53].

The majority of invasive lobular carcinomas showed cyclin D1 overexpression at the protein levels, suggesting its role in the progression of invasive lobular carcinoma [54]. Another study showed that ER-positive patients with moderate cyclin D1 expression had benefited from anti-hormonal therapy (tamoxifen), whereas those with high cyclin D1 expression had not benefited from tamoxifen, suggesting its role as a predictive marker for tamoxifen resistance [55]. Further results suggest that the silencing of cyclin D1 expression may reduce the development and progression of tamoxifen-resistant tumors [116]. Cisplatin drug targets cyclin D1, and treatment of ER-positive MCF-7 breast cancer cells with cisplatin increased cell death or growth arrest by decreasing the cyclin D in MCF-7 cells [117]. Using techniques fluorescent in situ hybridization (FISH) and IHC, researchers observed that CCND1 had increased amplification in high-grade infiltrating ductal carcinoma in comparison to low-grade infiltrate ductal carcinoma [56]. Cyclin D1 overexpression has been found to have a strong correlation with receptor status, suggesting that cyclin D1 expression could be a biomarker for good prognoses [57,58].

Additionally, expression of cyclin D2 was found to be very rare in breast cancer cases, in comparison to normal human mammary epithelial cells [47,59]; its role in cancer is yet to be elucidated [133]. Cyclin D3 has also been reported to be overexpressed in breast cancer samples, but there are limited research data on its relationship to disease outcomes [118,133,134]. Furthermore, experimental evidence has also shown elevated cyclin D1 protein levels and deposition of cyclin D3 in breast cancer samples [60]. Another study identified that 64 breast cancer cases out of 82 had cyclin D1 gene amplification, and 36 out of 86 cases had cyclin D3 gene amplification [62]. Expression of cyclin D1 was evaluated in different molecular breast cancer subtypes, and results showed a stronger

intensity of positive cyclin D1 staining in the ER positive/PR positive subtype than in triple-negative breast cancer (TNBC) cases, and negative cyclin D1 staining was seen in human epidermal growth factor receptor 2-positive (HER2-positive) molecular subtypes. Further, TNBC cases with a low amount of cyclin D1 expression had higher tumor grade, tumor stage, and more positive lymph nodes with lymphovascular invasion, proposing that cyclin D1 expression may be a key factor to consider for aid in breast cancer management [61]. Lundberg et al. [135] determined CCND1 amplification and its association with worst 15-year survival with ER+/LN−/HER2− (1.66; 1.14–2.41), luminal A (HR = 1.68; 95% CI, 1.15–2.46), and luminal B (1.37; 1.01–1.86) breast cancer subtypes [135]. Overexpressed cyclin D1 induced Dicer expression in luminal A and basal-like breast cancer subtypes [136]. In another study, lower levels of cyclin D led to a decrease in MDA-MB-231 cells' motility which resulted due to the decrease in phosphorylation of filamin A protein [137]. These studies found that cyclin D1 can also contribute to cellular proliferation and migration through non-canonical functions.

### 3.2. Cyclin A

Cyclin A protein forms complexes with both CDK1 and CDK2, which functions in both the S to G2 phase transition and the G2 to M phase transition of the cell cycle [51]. In the S phase, the cyclin-A-CDK complexes phosphorylate the components of the DNA replication machinery, subsequently initiating replication [51]. While in the mitosis phase, cyclin A/CDK2 coordinates centrosomal and nuclear mitotic events. However, it is thought to contribute to the stability of other cyclin molecules [51]. The increased expression of cyclin A gene has been found in different types of human tumors, including breast cancer, which suggests that cyclin A may potentially serve as a prognosis marker for the disease (Tables 1 and 2). Studies have shown that microinjection of cyclin A into *Xenopus* oocytes and mammalian cells stimulates the breast tumor epithelial cells and induce the transition into M phase of the cell cycle [46,58,119,138,139]. A great number of tumors have shown a strong statistical correlation between cyclin A gene amplification and cyclin A protein levels [62]. Findings suggested that assessment of cyclin A and/or E2-promoter binding factor 1 (E2F1) expression levels associated with Ki-67 might be a useful tool for improved prognostic evaluation in negative lymph node breast cancer patients [63]. Another study showed that cyclin A is an independent prognostic factor and predictor of both breast cancer recurrence and response to tamoxifen therapy [64]. Lastly, overexpressed cyclin A was observed to be significantly correlated with breast cancer patients with earlier relapse, higher risk, and shorter overall survival rate, when compared to the breast cancer patients with better prognoses. Therefore, cyclin A may potentially be an accurate marker for tumor proliferation and prognosis in breast cancer [65].

### 3.3. Cyclin E

Cyclin E protein, a regulatory subunit for CDK-2, is thought to be a rate-limiting factor for the G1 to S phase cell cycle transition [140]. Cyclin E protein and its associated kinase (CDK2) experience well-regulated activation in normal cells. In actively-dividing tumor epithelial cells, however, the cyclin E and CDK complex remains activated throughout the cell cycle [141]. The deregulation in the expression of the cyclin E gene was found responsible for breast cancer tumorigenesis [46,60,114]. Previous data have demonstrated that higher levels of cyclin E gene amplification have been found in breast cancer tissues (Table 1) [62]. Another study observed an 8-fold amplification of the cyclin E gene and a 64-fold overexpression of its mRNA in human breast cancer cells, which provides evidence for aberrant cyclin E expression during tumorigenesis [120]. Further, a multivariate analysis correlated an elevated cyclin E level with poor patient outcome and showed that patients with elevated levels of cyclin E had a greater hazard ratio, as compared to those with low levels of cyclin E [142]. In addition, a relation between cyclin E gene expression and an ER-positive status was also observed in patients with breast cancer. In additional studies [89–91], cyclin E expression was greater in the ER-negative group and correlated



with increased risks of death and relapse, suggesting that cyclin E may be responsible for ER-independent tumor growth. Similarly, cyclin E overexpression in breast cancer cells was associated with ER-negative tumors, HER2-positive tumors, and high-grade tumors with increased proliferation indexes [68,69]. A cohort study performed on 34 HER2-positive patients subjected to trastuzumab (Herceptin)-based therapy observed that the cyclin E gene copy number or mRNA overexpression was associated with diminished therapeutic benefits and lower rates of progression-free survival, as compared to non-overexpressing cyclin E patients [121]. Moreover, cyclin E expression was associated with a poor prognosis and closely related with cyclin D1 and p27Kip1 expression [70]. Similarly, high expression of cyclin E measured by IHC was a significant factor of poor prognosis and associated with a higher risk of death in the node-positive breast cancer group, as illustrated in a separate multivariate analysis [71].

### 3.4. Cyclin B

Two types of mammalian cyclin B regulate the G2-to-mitosis phase progression in the cell cycle, which do so by forming complexes with CDK1 kinase [143]. The available data suggest that breast cancer patients experience cyclin B gene amplification and overexpression at both the mRNA level and protein level (Tables 1 and 2) [62]. Its increased expression has been correlated with a large tumor size, a high tumor grade, lymph node involvement, an ER-negative/PR-negative status, and a HER2-positive status [74]. Its overexpression has also been linked with younger age at diagnosis and higher expression levels of cyclin A, cyclin E, and Ki-67 [144]. Both univariate and multivariate analyses significantly identified an increased breast cancer death rate correlated with cyclin B1 overexpression, suggesting that it serves as a remarkable prognostic factor [72].

A meta-analysis investigated the significance between cyclin B protein and clinicopathological characteristics in breast cancer patients. Observations showed that overexpressed cyclin B was associated with poorer rates in disease-free survival (DFS), disease-specific survival (DSS), and overall survival (OS), along with a positive association with lymphatic invasion [73]. Androic et al. [100] observed apoptosis induction and growth reduction in different breast cancer cell lines, namely MCF-7, MDA-MB-231, BT-474, and SK-BR-3 (Table 3), in the absence of cyclin B. The suppression of cyclin B via small interfering RNA (siRNA) caused G2/M cell cycle phase arrest in breast cancer cell lines [73,125]. The HER2-positive invasive breast cancer samples used for the determination of cyclin B1 expression showed a direct correlation between positive cyclin B1 staining and higher tumor grade, large tumor size, positive lymph node counts, younger age, and higher Ki-67 expression. Thus, due to its relation with an aggressive phenotype, cyclin B1 might be considered a strong independent prognostic factor in breast cancer [74].

### 3.5. CDK2

Cyclin-dependent kinase 2 binds and forms complexes with cyclin E or cyclin A proteins and exclusively promotes the G1 to S and G2 to M phase transition within the cell cycle [145,146]. It has been observed that fulvestrant inhibited cyclin E-CDK2 activity, which in turn promoted the arrest of MCF-7 cells in quiescence (G<sub>0</sub>) [147]. Similarly, the findings suggest that the suppression of the cell-cycle progression through the G1 cell cycle phase by pentagalloylglucose (5GG) treatment in MCF-7 cells was mediated by blocking cyclin E/CDK2 activity [122].

## 4. Tumor Suppressive Components of Cell Cycle

### 4.1. p16(*INK4A/MTS-1/CDKN2A*)

The tumor suppressor p16, also known as *INK4A/MTS-1/CDKN2A*, has widespread importance in oncology due to its CDK-inhibitory function [148]. The frequently occurring SNP (single nucleotides polymorphism) mutations and deletions of the p16 gene in breast cancer cells suggest an important role in tumorigenesis [149]. The p16 protein molecule binds to and inactivates the cyclin D-CDK4/6 complexes, leads to subsequent Rb protein

inactivation, and consequently results in cell cycle arrest [149]. Archived breast tumors of different histological subtypes provided evidence that aberrant p16 gene expression is the most common abnormality in human breast cancer (Table 1) [150]. Furthermore, an abnormal expression of p16 was found in ER-negative, pre-menopause breast cancer patients, in comparison to ER-positive patients. The abnormal p16 expression these researchers observed was closely associated with a high proliferative index [108]. An earlier study suggests that abnormal p16 expression may act as a predictor of poor response to hormonal therapy [92]. Another study found p16 protein-positive expression in the luminal A subtype of breast cancer patients, and higher expression was associated with breast cancer progression from DCIS to invasive ductal carcinoma (IDC) [96]. Abou-Bakr et al. [110] investigated the p16 expression in basal-like breast carcinoma grade III with histopathological findings in line with IDC. Results suggested that the p16 protein demonstrated high IHC intensity in basal-like carcinoma, which subsequently was associated with brain and lung metastasis [97]. A study by Arima et al. [126] found low p16 expression in resistant TNBC carcinoma [126]. Both p16-positive and p16-negative cells in the stromal cells of invasive lobular carcinoma reflected high nodal involvement, early recurrence, and metastatic propensity. Additionally, restoration of p16 expression in stromal fibroblasts suppressed cancer cell migration and invasion. Thus, these findings proposed positive stromal p16 expression as a treatment strategy to prevent nodal or distant metastasis [98].

#### 4.2. p21 (WAF1/CIP1/SDI1/MDA-6)

The CDK-inhibitor p21 (also known as WAF1/CIP1/SDI1/MDA-6) activates the CDK4 and proliferating cell nuclear antigen, which results in G1 phase arrest [151]. Both in vivo and in vitro experimental models demonstrated that overexpression of p21WAF1/CIP1 resulted in G1 cell cycle phase arrest and effectively suppressed tumor growth (Tables 1 and 2) [151]. Data on lymph node-negative breast cancer patients suggested that detection of p21 indicates the presence of a parameter that may act as a tumor suppressor and benefit patient survival [75]. Another study identified p21-positive tumor cell nuclei in more than 30% of the breast carcinomas, which was remarkably associated with a low histological grade and node-negative status [76]. The findings strongly suggested that p21WAF1/CIP1 gene expression might be used as a key prognostic biomarker for breast cancer, allowing therapy options to be adjusted more appropriately for individual cancer patients [77]. Breast cancer mastectomy used for measuring p21WAF1/CIP1 expression showed its upregulation in larger tumors in patients who presented with higher tumor dedifferentiation grades, more lymph node metastases, and shorter disease-free survival rates [78]. Moreover, an in vitro study where ER-positive or ER-negative breast cancer cell lines were immunostained for evaluation of p21 found a direct correlation between p21WAF1/CIP1 and ER expression [123,124].

In addition, p21WAF1/CIP1 also plays multifaceted roles in breast cancer. For instance, p21WAF1/CIP1 expression induced cell invasion and had correlation with OS and distant metastasis-free survival in breast cancer patients mediated via controlling TGF $\beta$ /Smad signaling [152]. A study measured high p21WAF1/CIP1 levels in the cytoplasm of metastatic breast cancer cells where it was associated with elevated p53 levels and poor prognoses [153]. Multiple studies identified that phosphorylation of p21WAF1/CIP1 by AKT1 disrupted its binding with proliferating cell nuclear antigen (PCNA) and induced its cytoplasmic accumulation. Accumulated p21WAF1/CIP1 regulates the ERBB2-mediated proliferation of breast cancer cells and breast carcinogenesis [154,155]. Further, downregulation of p21WAF1/CIP1 promoted EMT, enhanced the cell viability and migration potential in response to long non-coding RNA plasmacytoma variant translocation 1 (PVT1) in distinct MDA-MB-231, MDA-BA-468 breast cancer cell lines [156]. Similarly, another study using breast cancer mouse models has shown that invasion is accompanied by an upregulation of p21WAF1/CIP1, indicating its oncogenic role [157]. The overexpression of p21WAF1/CIP1 has also been found to be associated with a poor response to tamoxifen treatment in MCF-7 cells [158]. Similarly, Akt-dependent phosphorylated p21WAF1/CIP1

enhanced doxorubicin resistance in SUM159 TNBC cells [159]. Another study demonstrated that p21WAF1/CIP1 inhibited apoptosis in breast cancer. The overexpression of p21WAF1/CIP1 in breast cancer decreased cell sensitivity to infrared-induced apoptosis through inhibition of CDKs [160].

#### 4.3. p27 (Kip1)

Tumor suppressor p27, an important regulator for the G1 to S transition in the cell cycle, is known to coordinate the activation of the cyclin E-CDK2 complex with the accumulation of cyclin D-CDK4, which initiates the exit of cells from the cell cycle in response to anti-mitogenic signals [161]. The downregulation of p27 gene expression is strongly correlated with higher tumor grade and phenotypes with lower tumor differentiation (Table 1) [79]. Reduced levels of p27 protein is also an indicator of poor clinical outcomes in a majority of lymph node-negative breast cancer patients [79].

Multiple sources of evidence suggest that p27 induced G1 cell cycle phase arrest, mediated by transforming growth factor- $\beta$  (TGF- $\beta$ ), rapamycin, and cyclic adenosine monophosphate (cAMP) [48,60,114,127]. Previous studies also demonstrated that high expression levels of p27 in human breast cancer cells inversely correlated with the degree of malignancy in the human breast [127]. Moreover, a high expression of p27 was noticed in breast cancer patients, which was significantly correlated with an ER-positive status and inversely associated with shorter survival [80]. A univariate Kaplan–Meier analysis indicated that the decreased expression of p27 was significantly correlated with a worse clinical course [81]. A flow cytometry study using resistant breast tumor cells demonstrated a higher S-phase fraction and increased CDK2 activity in low p27-expressed cells, which was reversed after an exogenous addition of p27 [128].

Immunostaining of breast tumor indicated that downregulation of p27 correlated with HER2 gene overexpression in primary breast carcinomas, which may be significant in selecting patients for HER2-positive/neu antibody therapy in the future [82]. A separate study found that tamoxifen treatment caused MCF-7 cell cycle arrest due to an upregulation of p27 levels [129]. Another evaluation of p27 expression observed that it was a significant predictor for 5-year breast cancer survival, and that reduced p27 expression correlated with a high histologic grade, an advanced TNM stage (tumor size, lymph node status, metastatic status), and negative hormone receptor status [83,84]. A reduced expression of p27 was also observed in docetaxel-resistant breast cancer cells (MCF-7 and MDA-MB-231 cell lines) [130]. Another univariate analysis showed a remarkable relationship between low p27 expression and increased tumor grade, nuclear pleomorphism, and mitosis, along with decreased tubule formation in ER-negative and ductal/no special type tumor status [85].

High p27 expression independently predicted superior relapse-free survival and overall survival, and subsequently suggested its use as an independent predictor in hormonal therapy response [86]. An immunohistochemically retrospective investigation of 216 breast carcinomas found that p27-negative patients had a poorer prognosis than those in other categories, highlighting that the examination of p27 expression may identify breast carcinoma patients who would benefit from adjuvant therapy [87]. Further, in the lymph node-negative population, decreased p27 immunoreactivity was associated with higher tumor grade, more HER2-positive overexpression, greater lymph node positive populations, lower expression of thymidylate synthase, higher Ki-67 expression, and poorer disease-free survival [88]. In hormonal receptor- positive carcinoma, lower p27Kip1 was correlated with decreased overall survival [hazard ratio (HR) = 1.42; 95% confidence intervals (CI) = 1.05 to 1.94; disease-free survival HR = 1.27; and 95% CI = 0.99 to 1.63], as compared to carcinoma with higher p27Kip1 expression treated with adjuvant therapy (doxorubicin and cyclophosphamide) [90]. An inverse correlation was also observed between p27Kip1 expression and the degree of breast tumor malignancy [162]. Breast cancer patients in Taiwan were evaluated for the expression of p27Kip1, and both univariate and multivariate analyses showed that lower p27Kip1 expression correlated with OS in ER/PR positive

tumors. Therefore, p27Kip1 may be considered an independent prognosis marker for breast cancer in Taiwan [91].

Another meta-analysis study showed a significant association between high p27 expression and OS, DFS, and RFS in lymph node-negative and lymph node-positive breast cancer patients [163]. In addition, Austrian Breast and Colorectal Cancer Study Group Trial 06 enrolled early-stage breast cancer patients with an ER/PR hormonal-positive status for evaluation of p27Kip1 expression and observed its impact on the clinicopathological features of women receiving adjuvant tamoxifen for 5 years. Observations confirmed that high p27Kip1 expression was significantly associated with longer disease-free survival (0.22; 95% CI, 0.11–0.42;  $p < 0.001$ ) and overall survival (0.39; 95% CI, 0.21–0.72;  $p = 0.002$ ) as compared to women with low p27 expression [164].

#### 4.4. p53 (Wild Type)

Tumor suppressor p53 protein plays a key role in coordinating the response of cells to several stress conditions, including oncogenic activation, hypoxia, and DNA damage [165]. In response to mitogenic stress, p53 activates apoptosis in normal cells. This same activation of apoptosis by p53 has also been observed in anticancer therapy response. A mutated version of p53 protein that does not respond appropriately during oncogenic stress allows cell transformation, resulting in tumor initiation [165]. After immunohistochemical evaluation of p53 expression in primary breast cancer specimens, it was assessed that p53 overexpression was associated with an advanced-stage tumor, metastatic spread, and lower concentrations of progesterone receptors (Table 1) [89]. An increased cytoplasmic accumulation of p53 was observed in breast cancer patients as well. These patient samples demonstrated high proliferative activity with median Ki-67 fractions increased by up to 75%, along with a 74% increase in median S-phase fraction compared to the control group [93].

Utilizing invasive ductal carcinoma samples, Yang et al. (2013) [143] calculated DFS and its correlation with p53 expression. The Cox regression and multivariate analysis showed that p53 expression acted as a predictive factor of DFS [100]. Additionally, several studies also associated positive p53 expression with worsened prognoses. For instance, a Kaplan–Meier analysis of TNBC invasive ductal carcinoma samples showed that a positive p53 expression was correlated with worse overall survival (79.6% vs. 89.6%, log-rank test  $p = 0.025$ ) and the patients had a 2.2 times higher mortality risk than that of p53-negative patients (HR: 2.222; 95% CI: 1.147–4.308) [102]. Similarly, p53 overexpression tested by IHC on modified radical mastectomy samples obtained from TNBC patients also showed lower overall survival rates ( $p = 0.021$ , log-rank test) compared to the patient group with low p53 expression. Moreover, the multivariate analysis proposed p53 overexpression as having the strongest prognostic significance in TNBC patients (<50 years) [103].

In a retrospective study of a large number of luminal/HER2-negative breast cancer patients, the data demonstrated that a p53 expression of  $\geq 50\%$  (present in 9% patients) was associated with shorter disease-free survival, in comparison to patients with p53 expression of  $< 50\%$ . Therefore, p53 overexpression was classified as a prognostic marker for unfavorable characteristics [104]. Another study performed on ER-positive and ER-negative invasive breast cancer determined an association of p53 overexpression with ER status. Results showed that in ER-negative breast tumors, a higher p53 expression was associated with DFS and OS than in ER-positive breast tumors [105].

Expression of the p53 gene was also evaluated in all breast cancer subtypes, i.e., luminal A, luminal B, HER2-positive, TNBC, and basal-like, and the findings suggested that p53 had a higher expression within HER2-positive and TNBC subtypes than in luminal A and luminal B subtypes. The overexpression of p53 in HER2-positive and TNBC subtypes also had significance in early-onset, high-grade tumors, and an increased proliferative index [106]. In invasive breast carcinoma grade II and III samples, positive p53 expression was significantly related with increased tumor grade ( $p < 0.006$ ), lymphovascular invasion ( $p < 0.003$ ), and lymphocytic infiltration ( $p < 0.004$ ). These results indicate that p53 overex-

pression is a marker for a poor prognosis and a compromised immune response in more aggressive breast cancer types [107].

Better overall survival was observed in p53-overexpressed TNBC cases than in p53-negative TNBC patients who underwent neoadjuvant chemotherapy [108]. Another study concluded that p53 overexpression was inversely correlated with ER/PR expression and positively correlated with HER2-positive overexpression in high-grade tumors with nodal metastasis [109]. In a randomized stage II clinical trial on lymph node-positive patients who received four cycles of cyclophosphamide and one dose of doxorubicin adjuvant therapy, epithelial p53 expression was evaluated (using monoclonal antibodies DO7 and 1801). After univariate analysis, this study stated that positive p53 IHC was associated with worse OS and RFS in lymph node-positive patients [110].

#### 4.5. p53 (Mutant)

A study performed by Marchetti et al. [154] found an “Arg72Pro” p53 variant in 23% of primary breast cancer patients. The patients positive for the Arg72Pro variant had relapsed within 10 months of the median DFS, compared to those that showed a wild-type p53 status [111]. Lenora W.M. et al. [155] also found a higher nuclear expression of mutant p53 using PAb1801 monoclonal antibody in young breast cancer patients. Kaplan–Meier curves and a log-rank test analysis correlated mutant p53 expression with a poor prognosis among distinct ethnic populations. Similarly, TNBC patients with abnormal mRNA expression of mutant p53 in a separate study were more likely to experience less 5-year recurrence-free survival. Mutant p53, therefore, may be considered a potential prognostic marker in TNBC patients [113].

### 5. Future Perspectives

Aside from great improvements in diagnostic tools and the increased availability of multiple therapeutic options, breast cancer cure rates remain poor. In the GLOBOCAN-2018 report, 2.1 million new breast cancer cases (11% of all total cancer types) were diagnosed in 185 countries [166]. In India, 144,000 breast cancer cases with a 5-year prevalence of 396,000 and 70,000 deaths were reported in 2012 [166,167]. As per the GLOBOCAN-2018 report, 162,000 breast cancer cases (27.7% of all new cancers), a 5-year prevalence of 405,000 breast cancer cases, and 87,000 deaths were observed in the Indian population [166]. Knowledge of reliable biomarkers related to disease prognosis and therapy decisions can improve cancer management. In this regard, the oncogenic and tumor suppressor components of the cell cycle may serve as such markers. Data from the multiple studies provided above support this notation.

Although these markers are detectable by expression-profiling experiments, the lack of reproductivity of the described results from various studies delays their use in the clinical setting. In addition to technique sensitivity issues, the non-reproducibility of the results might be due to the variation in sample selection methods or variations in study designs. Studies having a smaller number of patients, different-aged patients, varying tumor grades, varying tumor sizes or metastatic potential, and different patient ethnicities can also lead to non-reproducible results. Therefore, larger-scale validation studies involving greater demographic, ethnic, and clinicopathological variabilities are required in the future, before we can apply their suggestive use in patient management. High throughput technologies, such as next-generation RNA sequencing [168–170] and single-cell RNA sequencing [171,172], give results with high coverage and depth, and cover potential sensitivity issues. The use of these technologies may help to identify reliable biomarkers for cancer management. Thus, the data presented in the review article propose the use of cell cycle components as biomarkers in breast cancer management.

### 6. Conclusions

Previous experimental studies have described several oncogenic and tumor-suppressive genes involved in cell cycle regulation and progression among various subtypes of hu-

man breast cancer. It is well-established that multiple genetic alterations are required for tumorigenesis, yet continued research regarding the specific and sequential mechanisms involved—and how they affect clinical outcomes—may continue to guide new therapeutic strategies for more effective cancer treatments. Current research supports the notion that these regulatory cell cycle genes are useful prognostic biomarkers in breast cancer tumorigenesis, and the clinical relevance of these suggestive biomarkers has been established by several studies, as described above. The accurate measurement of cell cycle component expression and their correlation with clinical symptoms and prognoses may provide valuable insight for the future of both breast cancer management and anti-cancer therapeutics.

**Author Contributions:** N.G. conceived the study; D.K. designed the study design and wrote the first draft; V.K.G. performed literature search and collection. E.N.S. performed language editing and suggested for quality improvement. A.B. supervised the project and performed the final editing. All authors have read and agreed to the published version of the manuscript.

**Funding:** This research received no external funding.

**Institutional Review Board Statement:** Not applicable.

**Informed Consent Statement:** Not applicable.

**Data Availability Statement:** Not applicable.

**Acknowledgments:** The authors (D.K., N.G., and V.K.G.) would like to gratefully acknowledge the Department of Histopathology, Post Graduate Institute of Medical Education and Research and University Institute of Engineering and Technology, Panjab University, Chandigarh, Punjab for providing platform support to compile this manuscript.

**Conflicts of Interest:** There exists no conflict of interest amongst authors regarding the publication of this manuscript.

## Abbreviations

5GG	Pentagalloylglucose
ABCSG	Austrian breast and colorectal cancer study group
AC	Adenocarcinoma
c-AMP	Cyclic adenosine monophosphate
CCND1	Cyclin D1
CDC2 kinase	Cell division control 2 kinase
CDKs	Cyclin-dependent kinases
CI	Confidence interval
DC	Ductal carcinoma
DCIS	Ductal carcinoma in situ
DFS	Disease-free survival
DSS	Disease-specific survival
E2F1	E2 promoter factor 1
ER	Estrogen receptor
FISH	Fluorescent in situ hybridization
GLOBOCAN	Global cancer observatory
HDAC3	Histone deacetylase 3
HER2+	Human epidermal growth factor receptor2+
HR	Hazard ratio
IDC	Invasive ductal carcinoma
IHC	Immunohistochemistry
ILC	Invasive lobular carcinoma
LA	Luminal A

MU	Mutation
NBE	Normal breast epithelium
ND	Not decided
OS	Overall survival
PD	Proliferative disease
PR	Progesterone receptor
Rb	Retinoblastoma
RFS	Recurrence free survival
siRNA	Small interfering RNA
TGF- $\beta$	Transforming growth factor- $\beta$
TNBC	Triple negative breast cancer
WT	Wild type

## References

- Zhivotovsky, B.; Orrenius, S. Cell cycle and cell death in disease: Past, present and future. *J. Intern. Med.* **2010**, *268*, 395–409. [CrossRef]
- Witsch, E.; Sela, M.; Yarden, Y. Roles for Growth Factors in Cancer Progression. *Physiology* **2010**, *25*, 85–101. [CrossRef] [PubMed]
- You, J.S.; Jones, P.A. Cancer Genetics and Epigenetics: Two Sides of the Same Coin? *Cancer Cell* **2012**, *22*, 9–20. [CrossRef] [PubMed]
- Baylin, S.B.; Jones, P.A. Epigenetic Determinants of Cancer. *Cold Spring Harb. Perspect. Biol.* **2016**, *8*, a019505. [CrossRef]
- Singh, A.; Goel, N. Yogita Integrative Analysis of Multi-Genomic Data for Kidney Renal Cell Carcinoma. *Interdiscip. Sci. Comput. Life Sci.* **2020**, *12*, 12–23. [CrossRef] [PubMed]
- Goel, N.; Khandnor, P. TCGA: A multi-genomics material repository for cancer research. In *Materials Today: Proceedings*; Elsevier: Amsterdam, The Netherlands, 2020; pp. 1492–1495.
- Lee, S.Y.; Ju, M.K.; Jeon, H.M.; Lee, Y.J.; Kim, C.H.; Park, H.G.; Han, S.I.; Kang, H.S. Oncogenic Metabolism Acts as a Prerequisite Step for Induction of Cancer Metastasis and Cancer Stem Cell Phenotype. *Oxidative Med. Cell. Longev.* **2018**, *2018*, 1–28. [CrossRef]
- Kashyap, D.; Tuli, H.S.; Garg, V.K.; Goel, N.; Bishayee, A. Oncogenic and Tumor-Suppressive Roles of MicroRNAs with Special Reference to Apoptosis: Molecular Mechanisms and Therapeutic Potential. *Mol. Diagn. Ther.* **2018**, *22*, 179–201. [CrossRef]
- Kashyap, D.; Kaur, H. Cell-free miRNAs as non-invasive biomarkers in breast cancer: Significance in early diagnosis and metastasis prediction. *Life Sci.* **2020**, *246*, 117417. [CrossRef]
- Mitra, S.; Bal, A.; Kashyap, D.; Kumar, S.; Shrivastav, S.; Das, A.; Singh, G. Tumour angiogenesis and c-Met pathway activation—implications in breast cancer. *APMIS* **2020**, *128*, 316–325. [CrossRef]
- Wang, L.-H.; Wu, C.-F.; Rajasekaran, N.; Shin, Y.K. Loss of Tumor Suppressor Gene Function in Human Cancer: An Overview. *Cell. Physiol. Biochem.* **2018**, *51*, 2647–2693. [CrossRef] [PubMed]
- Lee, E.Y.H.P.; Muller, W.J. Oncogenes and Tumor Suppressor Genes. *Cold Spring Harb. Perspect. Biol.* **2010**, *2*, a003236. [CrossRef]
- Velez, A.M.A.; Howard, M.S. Tumor-suppressor genes, cell cycle regulatory checkpoints, and the skin. *N. Am. J. Med. Sci.* **2015**, *7*, 176–188. [CrossRef] [PubMed]
- Deshpande, A.; Sicinski, P.; Hinds, P.W. Cyclins and cdks in development and cancer: A perspective. *Oncogene* **2005**, *24*, 2909–2915. [CrossRef]
- Law, M.E.; Corsino, P.E.; Narayan, S.; Law, B.K. Cyclin-Dependent Kinase Inhibitors as Anticancer Therapeutics. *Mol. Pharmacol.* **2015**, *88*, 846–852. [CrossRef]
- Yixiao, F.; Mia, S.; Shifeng, H.; Chengfu, Y.; Zongyue, Z.; Linghuan, Z.; Xiaojuan, J.; Wei, L.; Bo, H.; Wenping, L.; et al. Breast cancer development and progression: Risk factors, cancer stem cells, signaling pathways, genomics, and molecular pathogenesis. *Genes Dis.* **2018**, *5*, 77–106. [CrossRef]
- Aggarwal, V.; Kashyap, D.; Sak, K.; Tuli, H.S.; Jain, A.; Chaudhary, A.; Garg, V.K.; Sethi, G.; Yerer, M.B. Molecular Mechanisms of Action of Tocotrienols in Cancer: Recent Trends and Advancements. *Int. J. Mol. Sci.* **2019**, *20*, 656. [CrossRef]
- Mehta, S.; Shelling, A.; Muthukaruppan, A.; Lasham, A.; Blenkiron, C.; Laking, G.; Print, C. Predictive and prognostic molecular markers for cancer medicine. *Ther. Adv. Med. Oncol.* **2010**, *2*, 125–148. [CrossRef] [PubMed]
- Caldon, C.E.; Daly, R.J.; Sutherland, R.L.; Musgrove, E.A. Cell cycle control in breast cancer cells. *J. Cell. Biochem.* **2005**, *97*, 261–274. [CrossRef]
- Haase, S.B.; Wittenberg, C. Topology and Control of the Cell-Cycle-Regulated Transcriptional Circuitry. *Genetics* **2014**, *196*, 65–90. [CrossRef]
- Cheung, T.H.T.; Rando, T.A. Molecular regulation of stem cell quiescence. *Nat. Rev. Mol. Cell Biol.* **2013**, *14*, 329–340. [CrossRef] [PubMed]
- Enders, G.H. Mammalian Interphase Cdks: Dispensable Master Regulators of the Cell Cycle. *Genes Cancer* **2012**, *3*, 614–618. [CrossRef] [PubMed]
- Bertoli, C.; Skotheim, J.M.; De Bruin, R.A.M. Control of cell cycle transcription during G1 and S phases. *Nat. Rev. Mol. Cell Biol.* **2013**, *14*, 518–528. [CrossRef]

24. Cynthia, O.; Paschal, W.; Debu, T. Oncogenes and tumor suppressor genes in breast cancer: Potential diagnostic and therapeutic applications. *Oncologist*. **2004**, *9*, 361–377. [CrossRef]
25. Kato, J.; Matsushima, H.; Hiebert, S.W.; Ewen, E.M.; Sherr, C.J. Direct binding of cyclin D to the retinoblastoma gene product (pRb) and pRb phosphorylation by the cyclin D-dependent kinase CDK4. *Genes Dev.* **1993**, *7*, 331–342. [CrossRef] [PubMed]
26. Wiman, K.G. The retinoblastoma gene: Role in cell cycle control and cell differentiation. *FASEB J.* **1993**, *7*, 841–845. [CrossRef]
27. Coqueret, O. Linking cyclins to transcriptional control. *Gene* **2002**, *299*, 35–55. [CrossRef]
28. Diehl, A.J.; Zindy, F.; Sherr, C.J. Inhibition of cyclin D1 phosphorylation on threonine-286 prevents its rapid degradation via the ubiquitin-proteasome pathway. *Genes Dev.* **1997**, *11*, 957–972. [CrossRef]
29. Yu, Z.-K.; Gervais, J.L.M.; Zhang, H. Human CUL-1 associates with the SKP1/SKP2 complex and regulates p21CIP1/WAF1 and cyclin D proteins. *Proc. Natl. Acad. Sci. USA* **1998**, *95*, 11324–11329. [CrossRef]
30. Wang, C.; Li, Z.; Lu, Y.; Du, R.; Katiyar, S.; Yang, J.; Fu, M.; Leader, J.E.; Quong, A.; Novikoff, P.M.; et al. Cyclin D1 repression of nuclear respiratory factor 1 integrates nuclear DNA synthesis and mitochondrial function. *Proc. Natl. Acad. Sci. USA* **2006**, *103*, 11567–11572. [CrossRef]
31. Hall, M.; Peters, G. Genetic Alterations of Cyclins, Cyclin-Dependent Kinases, and Cdk Inhibitors in Human Cancer. In *Advances in Cancer Research*; Elsevier: Amsterdam, The Netherlands, 1996; pp. 67–108.
32. Yamamoto, M.; Tamakawa, S.; Yoshie, M.; Yaginuma, Y.; Ogawa, K. Neoplastic hepatocyte growth associated with cyclin D1 redistribution from the cytoplasm to the nucleus in mouse hepatocarcinogenesis. *Mol. Carcinog.* **2006**, *45*, 901–913. [CrossRef]
33. Hodges, L.C.; Cook, J.D.; Lobenhofer, E.K.; Li, L.; Bennett, L.; Bushel, P.R.; Aldaz, C.M.; Afshari, A.C.; Walker, C.L. Tamoxifen functions as a molecular agonist inducing cell cycle-associated genes in breast cancer cells. *Mol. Cancer Res.* **2003**, *1*, 300–311.
34. Kenny, F.S.; Hui, R.; Musgrove, E.A.; Gee, J.M.; Blamey, R.W.; Nicholson, R.I.; Sutherland, R.L.; Robertson, J.F. Overexpression of cyclin D1 messenger RNA predicts for poor prognosis in estrogen receptor-positive breast cancer. *Clin Cancer Res.* **1999**, *5*, 2069–2076. [PubMed]
35. Mohammadzadeh, F.; Hani, M.; Ranaee, M.; Bagheri, M. Role of cyclin D1 in breast carcinoma. *J. Res. Med Sci.* **2013**, *18*, 1021–1025. [PubMed]
36. Barnes, D.M.; Gillett, C.E. Cyclin D1 in Breast Cancer. *Breast Cancer Res. Treat.* **1998**, *52*, 1–15. [CrossRef] [PubMed]
37. A Velasco-Velázquez, M.; Li, Z.; Casimiro, M.; Loro, E.; Homsí, N.; Pestell, R.G. Examining the role of cyclin D1 in breast cancer. *Futur. Oncol.* **2011**, *7*, 753–765. [CrossRef] [PubMed]
38. Ravikumar, G.; Ananthamurthy, A. Cyclin D1 expression in ductal carcinoma of the breast and its correlation with other prognostic parameters. *J. Cancer Res. Ther.* **2014**, *10*, 671–675. [PubMed]
39. Assem, M.; Youssef, E.A.; Rashad, R.M.; Yahia, M.A.-H. Immunohistochemical Expression of Cyclin D1 in Invasive Ductal Carcinoma of Human Breast. *Oncomedicine* **2017**, *2*, 80–87. [CrossRef]
40. Buckley, M.F.; Sweeney, K.J.; Hamilton, A.J.; Sini, R.L.; Manning, D.L.; Nicholson, I.R.; DeFazio, A.; Watts, C.K.; Musgrove, A.E.; Sutherland, R.L. Expression and amplification of cyclin genes in human breast cancer. *Oncogene* **1993**, *8*, 2127–2133.
41. Lebowitz, E.D.; Muise-Helmericks, R.; Sepp-Lorenzino, L.; Serve, S.; Timaul, M.; Bol, R.; Borgen, P.; Rosen, N. A truncated cyclin D1 gene encodes a stable mRNA in a human breast cancer cell line. *Oncogene* **1994**, *9*, 1925–1929.
42. Zukerberg, L.R.; Yang, I.W.; Gadd, M.; Thor, A.D.; Koerner, F.C.; Schmidt, E.V.; Arnold, A. Cyclin D1 (PRAD1) protein expression in breast cancer: Approximately one-third of infiltrating mammary carcinomas show overexpression of the cyclin D1 oncogene. *Mod. Pathol.* **1995**, *8*, 560–567.
43. Khan, N.; Syed, D.N.; Ahmad, N.; Mukhtar, H. Fisetin: A Dietary Antioxidant for Health Promotion. *Antioxid. Redox Signal.* **2013**, *19*, 151–162. [CrossRef]
44. Rosendahl, A.H.; Perks, C.M.; Zeng, L.; Markkula, A.; Simonsson, M.; Rose, C.; Ingvar, C.; Holly, J.M.; Jernström, H. Caffeine and Caffeic Acid Inhibit Growth and Modify Estrogen Receptor and Insulin-like Growth Factor I Receptor Levels in Human Breast Cancer. *Clin. Cancer Res.* **2015**, *21*, 1877–1887. [CrossRef] [PubMed]
45. Zhang, S.-Y.; Caamano, J.; Cooper, F.; Guo, X.; Klein-Szanto, A.J. Immunohistochemistry of Cyclin D1 in Human Breast Cancer. *Am. J. Clin. Pathol.* **1994**, *102*, 695–698. [CrossRef]
46. Wilcken, N.R.; Prall, O.W.; Musgrove, A.E.; Sutherland, R.L. Inducible overexpression of cyclin D1 in breast cancer cells reverses the growth-inhibitory effects of antiestrogens. *Clin. Cancer Res.* **1997**, *3*, 849–854. [PubMed]
47. Jirstrom, K.; Stendahl, M.; Rydén, L.; Kronblad, A.; Bendahl, P.-O.; Stal, O.; Landberg, G. Adverse Effect of Adjuvant Tamoxifen in Premenopausal Breast Cancer with Cyclin D1 Gene Amplification. *Cancer Res.* **2005**, *65*, 8009–8016. [CrossRef]
48. Courjal, F.; Louason, G.; Speiser, P.; Katsaros, D.; Zeillinger, R.; Theillet, C. Cyclin gene amplification and overexpression in breast and ovarian cancers: Evidence for the selection of cyclin D1 in breast and cyclin E in ovarian tumors. *Int. J. Cancer* **1996**, *69*, 247–253. [CrossRef]
49. Umekita, Y.; Ohi, Y.; Sagara, Y.; Yoshida, H. Overexpression of cyclinD1 predicts for poor prognosis in estrogen receptor-negative breast cancer patients. *Int. J. Cancer* **2002**, *98*, 415–418. [CrossRef] [PubMed]
50. Elsheikh, S.; Green, A.R.; Aleskandarany, M.A.; Grainge, M.; Paish, C.E.; Lambros, M.B.K.; Reis-Filho, J.S.; Ellis, I.O. CCND1 amplification and cyclin D1 expression in breast cancer and their relation with proteomic subgroups and patient outcome. *Breast Cancer Res. Treat.* **2007**, *109*, 325–335. [CrossRef] [PubMed]



51. Rudas, M.; Lehnert, M.; Huynh, A.; Jakesz, R.; Singer, C.; Lax, S.; Schippinger, W.; Dietze, O.; Greil, R.; Stiglbauer, W.; et al. Cyclin D1 Expression in Breast Cancer Patients Receiving Adjuvant Tamoxifen-Based Therapy. *Clin. Cancer Res.* **2008**, *14*, 1767–1774. [CrossRef]
52. Alle, K.M.; Henshall, S.M.; Field, A.S.; Sutherland, R.L. Cyclin D1 protein is overexpressed in hyperplasia and intraductal carcinoma of the breast. *Clin. Cancer Res.* **1998**, *4*, 847–854. [PubMed]
53. Heiss, C.; Schanz, A.; Amabile, N.; Jahn, S.; Chen, Q.; Wong, M.L.; Rassaf, T.; Heinen, Y.; Cortese-Krott, M.; Grossman, W.; et al. Nitric Oxide Synthase Expression and Functional Response to Nitric Oxide Are Both Important Modulators of Circulating Angiogenic Cell Response to Angiogenic Stimuli. *Arter. Thromb. Vasc. Biol.* **2010**, *30*, 2212–2218. [CrossRef] [PubMed]
54. Oyama, T.; Kashiwabara, K.; Yoshimoto, K.; Arnold, A.; Koerner, F. Frequent overexpression of the cyclin D1 oncogene in invasive lobular carcinoma of the breast. *Cancer Res.* **1998**, *58*, 2876–2880. [PubMed]
55. Ahnström, M.; Nordenskjöld, B.; Rutqvist, L.E.; Skoog, L.; Stål, O. Role of cyclin D1 in ErbB2-positive breast cancer and tamoxifen resistance. *Breast Cancer Res. Treat.* **2005**, *91*, 145–151. [CrossRef] [PubMed]
56. Simpson, J.F.; Quan, D.E.; O'Malley, F.; Odom-Maryon, T.; Clarke, P.E. Amplification of CCND1 and expression of its protein product, cyclin D1, in ductal carcinoma in situ of the breast. *Am. J. Pathol.* **1997**, *151*, 161–168.
57. Tobin, N.P.; Bergh, J. Analysis of Cyclin D1 in Breast Cancer: A Call to Arms. *Curr. Breast Cancer Rep.* **2012**, *4*, 171–173. [CrossRef]
58. Boström, P.; Söderström, M.; Palokangas, T.; Vahlberg, T.; Collan, Y.; Carpén, O.; Hirsimäki, P. Analysis of cyclins A, B1, D1 and E in breast cancer in relation to tumour grade and other prognostic factors. *BMC Res. Notes* **2009**, *2*, 140. [CrossRef]
59. Dai, M.; Al-Odaini, A.A.; Fils-Aimé, N.; Villatoro, A.M.; Guo, J.; Arakelian, A.; Rabbani, A.S.; Ali, S.; Lebrun, J.J. Cyclin D1 cooperates with p21 to regulate TGF $\beta$ -mediated breast cancer cell migration and tumor local invasion. *Breast Cancer Res.* **2013**, *15*, R49. [CrossRef]
60. Russell, A.F.; Thompson, A.M.; Hendley, J.; Trute, L.; Armes, E.J.; Germain, D.S. Cyclin D1 and D3 associate with the SCF complex and are coordinately elevated in breast cancer. *Oncogene* **1999**, *18*, 1983–1991. [CrossRef]
61. Khandeparkar, S.G.S.; Lengare, P.V.; Joshi, A.R.; Gogate, B.P.; Solanke, S.G.; Gore, S.H. Immunohistochemical expression of cyclin D1 in invasive breast carcinoma and its correlation with clinicopathological parameters. *Indian J. Pathol. Microbiol.* **2020**, *63*, 376. [CrossRef]
62. Husdal, A.; Bukholm, G.; Bukholm, I.R.K. The Prognostic Value and Overexpression of Cyclin A Is Correlated with Gene Amplification of both Cyclin A and Cyclin E in Breast Cancer Patient. *Cell. Oncol.* **2006**, *28*, 107–116. [CrossRef]
63. Baldini, E.; Camerini, A.; Sgambato, A.; Prochilo, T.; Capodanno, A.; Pasqualetti, F.; Orlandini, C.; Resta, L.; Bevilacqua, G.; Collecchi, P. Cyclin A and E2F1 overexpression correlate with reduced disease-free survival in node-negative breast cancer patients. *Anticancer. Res.* **2007**, *26*, 4415–4421.
64. Michalides, R.; Van Tinteren, H.; Balkenende, A.; Vermorken, J.B.; Benraadt, J.; Huldij, J.; Van Diest, P. Cyclin A is a prognostic indicator in early stage breast cancer with and without tamoxifen treatment. *Br. J. Cancer* **2002**, *86*, 402–408. [CrossRef] [PubMed]
65. Poikonen, P.; Sjöström, J.; Amini, R.-M.; Villman, K.; Ahlgren, J.; Blomqvist, C. Cyclin A as a marker for prognosis and chemotherapy response in advanced breast cancer. *Br. J. Cancer* **2005**, *93*, 515–519. [CrossRef] [PubMed]
66. Nielsen, N.; Arnerlöv, C.; Emdin, S.; Landberg, G. Cyclin E overexpression, a negative prognostic factor in breast cancer with strong correlation to oestrogen receptor status. *Br. J. Cancer* **1996**, *74*, 874–880. [CrossRef]
67. Sieuwerts, A.M.; Look, M.P.; Gelder, M.E.M.-V.; Timmermans, M.; Trapman, A.M.; Garcia, R.R.; Arnold, M.; Goedheer, A.J.; De Weerd, V.; Portengen, H.; et al. Which Cyclin E Prevails as Prognostic Marker for Breast Cancer? Results from a Retrospective Study Involving 635 Lymph Node-Negative Breast Cancer Patients. *Clin. Cancer Res.* **2006**, *12*, 3319–3328. [CrossRef]
68. Donnellan, R.; Kleinschmidt, I.; Chetty, R. Cyclin E immunorexpression in breast ductal carcinoma: Pathologic correlations and prognostic implications. *Hum. Pathol.* **2001**, *32*, 89–94. [CrossRef]
69. Potemski, P.; Kusinska, R.; Watala, C.; Pluciennik, E.; Bednarek, A.K.; Kordek, R. Cyclin E expression in breast cancer correlates with negative steroid receptor status, HER2 expression, tumor grade and proliferation. *J. Exp. Clin. Cancer Res.* **2006**, *25*, 59–64. [PubMed]
70. Han, S.; Park, K.; Bae, B.-N.; Kim, K.H.; Kim, H.-J.; Kim, Y.-D. Prognostic implication of cyclin E expression and its relationship with cyclin D1 and p27Kip1 expression on tissue microarrays of node negative breast cancer. *J. Surg. Oncol.* **2003**, *83*, 241–247. [CrossRef] [PubMed]
71. Potemski, P.; Kusińska, R.; Pasz-Walczak, G.; Piekarski, J.H.; Watała, C.; Płuciennik, E.; Bednarek, A.K.; Kordek, R. Prognostic relevance of cyclin E expression in operable breast cancer. *Med Sci. Monit.* **2009**, *15*, 34–40.
72. Niméus-Malmström, E.; Koliadi, A.; Ahlin, C.; Holmqvist, M.; Holmberg, L.; Amini, R.-M.; Jirstrom, K.; Wärnberg, F.; Blomqvist, C.; Fernö, M.; et al. Cyclin B1 is a prognostic proliferation marker with a high reproducibility in a population-based lymph node negative breast cancer cohort. *Int. J. Cancer* **2009**, *127*, 961–967. [CrossRef]
73. Sun, X.; Zhangyuan, G.; Shi, L.; Wang, Y.; Sun, B.; Ding, Q. Prognostic and clinicopathological significance of cyclin B expression in patients with breast cancer. *Medicine* **2017**, *96*, e6860. [CrossRef] [PubMed]
74. Aaltonen, K.; Amini, R.-M.; Heikkilä, P.; Aittomäki, K.; Tamminen, A.; Nevanlinna, H.; Blomqvist, C. High cyclin B1 expression is associated with poor survival in breast cancer. *Br. J. Cancer* **2009**, *100*, 1055–1060. [CrossRef] [PubMed]
75. Göhring, U.-J.; Schöndorf, T.; Kiecker, V.R.; Becker, M.; Kurbacher, C.; Scharl, A. Immunohistochemical detection of H-ras protooncprotein p21 indicates favorable prognosis in node-negative breast cancer patients. *Tumor Biol.* **1999**, *20*, 173–183. [CrossRef]

76. Domagala, W.; Welcker, M.; Chosia, M.; Karbowniczek, M.; Harezga, B.; Bartkova, J.; Bartek, J.; Osborn, M. p21/WAF1/Cip1 expression in invasive ductal breast carcinoma: Relationship to p53, proliferation rate, and survival at 5 years. *Virchows Arch.* **2001**, *439*, 132–140. [CrossRef]
77. Fayed, Y.M.; El-Sheikh, S.A.-M.; Abulkheir, I.L.H.; Khorshed, I.N.A.-H. Immunohistochemical expression of p27 in ductal carcinoma of breast and its correlation with HER2/neu expression and hormonal status. *Egypt. J. Pathol.* **2012**, *32*, 33–41. [CrossRef]
78. Wei, C.-Y.; Tan, Q.-X.; Zhu, X.; Qin, Q.-H.; Zhu, F.-B.; Mo, Q.-G.; Yang, W.-P. Expression of CDKN1A/p21 and TGFBR2 in breast cancer and their prognostic significance. *Int. J. Clin. Exp. Pathol.* **2015**, *8*, 14619–14629.
79. Alkarain, A.; Jordan, R.; Slingerland, J. p27 Deregulation in Breast Cancer: Prognostic Significance and Implications for Therapy. *J. Mammary Gland. Biol. Neoplasia* **2004**, *9*, 67–80. [CrossRef]
80. Tsuchiya, A.; Zhang, G.J.; Kanno, M. Prognostic impact of cyclin-dependent kinase inhibitor p27kip1 in node-positive breast cancer. *J. Surg. Oncol.* **1999**, *70*, 230–234. [CrossRef]
81. Traub, F.; Mengel, M.; Lück, H.J.; Kreipe, H.H.; Von Wasielewski, R. Prognostic impact of Skp2 and p27 in human breast cancer. *Breast Cancer Res. Treat.* **2006**, *99*, 185–191. [CrossRef]
82. Newman, L.; Xia, W.; Yang, H.-Y.; Sahin, A.; Bondy, M.; Lukmanji, F.; Hung, M.-C.; Lee, M.-H. Correlation of p27 protein expression with HER-2/neu expression in breast cancer. *Mol. Carcinog.* **2001**, *30*, 169–175. [CrossRef]
83. Deepu, M.; Daniel, F.R.; Giorgio, I.; Anne, Z.J.; Joan, C.; Amber, G.; Rachael, A.S.; Silvia, C.F.; Michele, P.; Franco, M. Loss of p27KIP1 expression in fully-staged node-negative breast cancer: Association with lack of hormone receptors in T1a/b, but not T1c infiltrative ductal carcinoma. *Anticancer Res.* **2011**, *12*, 4401–4405.
84. Leivonen, M.; Nordling, S.; Lundin, J.; Von Boguslawski, K.; Haglund, C. p27 expression correlates with short-term, but not with long-term prognosis in breast cancer. *Breast Cancer Res. Treat.* **2001**, *67*, 15–22. [CrossRef] [PubMed]
85. Barnes, A.; Pinder, S.; Bell, J.; Paish, E.; Wencyk, P.; Robertson, J.; Elston, C.; Ellis, I. Expression of p27kip1 in breast cancer and its prognostic significance. *J. Pathol.* **2003**, *201*, 451–459. [CrossRef]
86. Pohl, G.; Rudas, M.; Dietze, O.; Lax, S.; Markis, E.; Pirker, R.; Zielinski, C.C.; Hausmaninger, H.; Kubista, E.; Samonigg, H.; et al. High p27Kip1 Expression Predicts Superior Relapse-Free and Overall Survival for Premenopausal Women With Early-Stage Breast Cancer Receiving Adjuvant Treatment With Tamoxifen Plus Goserelin. *J. Clin. Oncol.* **2003**, *21*, 3594–3600. [CrossRef] [PubMed]
87. Nohara, T.; Ryo, T.; Iwamoto, S.; Gon, G.; Tanigawa, N. Expression of Cell-Cycle Regulator p27 Is Correlated to the Prognosis and ER Expression in Breast Carcinoma Patients. *Oncology* **2001**, *60*, 94–100. [CrossRef]
88. Spataro, V.J.; Litman, H.; Viale, G.; Maffini, F.; Masullo, M.; Golouh, R.; Martínez-Tello, F.J.; Grigolato, P.; Shilkin, K.B.; Gusterson, B.A.; et al. Decreased immunoreactivity for p27 protein in patients with early-stage breast carcinoma is correlated with HER-2/neu overexpression and with benefit from one course of perioperative chemotherapy in patients with negative lymph node status. *Cancer* **2003**, *97*, 1591–1600. [CrossRef]
89. Davidoff, A.M.; Herndon, E.J.; Glover, N.S.; Kerns, B.J.; Pence, J.C.; Iglehart, J.D.; Marks, J.R. Relation between p53 overexpression and established prognostic factors in breast cancer. *Surgery* **1991**, *110*, 259–264.
90. Porter, P.L.; Barlow, W.E.; Yeh, I.-T.; Lin, M.G.; Yuan, X.P.; Donato, E.; Sledge, G.W.; Shapiro, C.L.; Ingle, J.N.; Haskell, C.M.; et al. p27 Kip1 and Cyclin E Expression and Breast Cancer Survival After Treatment With Adjuvant Chemotherapy. *J. Natl. Cancer Inst.* **2006**, *98*, 1723–1731. [CrossRef]
91. Chu, J.-S.; Huang, C.-S.; Chang, K.-J. p27 expression as a prognostic factor of breast cancer in Taiwan. *Cancer Lett.* **1999**, *141*, 123–130. [CrossRef]
92. Cui, S.-P.; Wang, H.-L.; Peng, W.; Liu, H.-J.; Hou, L.; Zhang, B. Aberrant expression and correlative analysis of P16 in breast cancers. *Beijing da xue xue bao. Yi xue ban = J. Peking Univ. Heal. Sci.* **2012**, *44*, 755–759.
93. Emig, R.; Magener, A.; Ehemann, V.; Meyer, A.; Stilgenbauer, F.; Volkmann, M.; Wallwiener, D.; Sinn, H.P. Aberrant cytoplasmic expression of the p16 protein in breast cancer is associated with accelerated tumour proliferation. *Br. J. Cancer* **1998**, *78*, 1661–1668. [CrossRef]
94. Pan, Y.; Yuan, Y.; Liu, G.; Wei, Y. P53 and Ki-67 as prognostic markers in triple-negative breast cancer patients. *PLoS ONE* **2017**, *12*, e0172324. [CrossRef] [PubMed]
95. Al-Joudi, F.S.; Iskandar, A.Z.; Rusli, J. The expression of p53 in invasive ductal carcinoma of the breast: A study in the North-East States of Malaysia. *Med. J. Malays.* **2008**, *63*, 96–99.
96. Shan, M.; Zhang, X.; Liu, X.; Qin, Y.; Liu, T.; Liu, Y.; Wang, J.; Zhong, Z.; Zhang, Y.; Geng, J.; et al. P16 and P53 Play Distinct Roles in Different Subtypes of Breast Cancer. *PLoS ONE* **2013**, *8*, e76408. [CrossRef] [PubMed]
97. Abou-Bakr, A.A.; Eldweny, I.H. P16 expression correlates with basal-like triple-negative breast carcinoma. *Ecancermedicalscience* **2013**, *7*, 317. [CrossRef] [PubMed]
98. Harbhajanka, A.; Lamzabi, I.; Bitterman, P.; Reddy, V.B.; Ghai, R.; Gattuso, P. Correlation of p16 Expression on Cancer and Stromal Cells With Clinicopathologic and Immunohistochemical Features of Lobular Breast Carcinoma. *Appl. Immunohistochem. Mol. Morphol.* **2019**, *27*, 658–662. [CrossRef] [PubMed]
99. Salmani, H.; Hosseini, A.; Azarnezhad, A.; Ahmad, H. PTEN and p53 gene expressions in breast cancer specimens and their clinicopathological significance. *Middle East J. Cancer* **2018**, *9*, 105–111. [CrossRef]

100. Yang, P.; Du, C.W.; Kwan, M.; Liang, S.X.; Zhang, G.J. The impact of p53 in predicting clinical outcome of breast cancer patients with visceral metastasis. *Sci. Rep.* **2013**, *3*, srep02246. [CrossRef] [PubMed]
101. Bertheau, P.; Lehmann-Che, J.; Varna, M.; Dumay, A.; Poirot, B.; Porcher, R.; Turpin, E.; Plassa, L.-F.; De Roquancourt, A.; Bourstyn, E.; et al. p53 in breast cancer subtypes and new insights into response to chemotherapy. *Breast* **2013**, *22*, S27–S29. [CrossRef]
102. Li, J.-P.; Zhang, X.-M.; Zhang, Z.; Zheng, L.-H.; Jindal, S.; Liu, Y.-J. Association of p53 expression with poor prognosis in patients with triple-negative breast invasive ductal carcinoma. *Medicine* **2019**, *98*, e15449. [CrossRef]
103. Lee, D.-S.; Kim, S.H.; Suh, Y.J.; Kim, H.K.; Shim, B.Y. Clinical Implication of p53 Overexpression in Breast Cancer Patients Younger than 50 Years with a Triple-negative Subtype Who Undergo a Modified Radical Mastectomy. *Jpn. J. Clin. Oncol.* **2011**, *41*, 854–866. [CrossRef] [PubMed]
104. Kikuchi, S.; Nishimura, R.; Osako, T.; Okumura, Y.; Nishiyama, Y.; Toyozumi, Y.; Arima, N. Definition of p53 overexpression and its association with the clinicopathological features in luminal/HER2-negative breast cancer. *Anticancer. Res.* **2013**, *33*, 3891–3898. [PubMed]
105. Coates, A.S.; Millar, E.K.; O’Toole, S.A.; Molloy, T.J.; Viale, G.; Goldhirsch, A.; Regan, M.M.; Gelber, R.D.; Sun, Z.; Castiglione-Gertsch, M.; et al. Prognostic interaction between expression of p53 and estrogen receptor in patients with node-negative breast cancer: Results from IBCSG Trials VIII and IX. *Breast Cancer Res.* **2012**, *14*, R143. [CrossRef] [PubMed]
106. Abubakar, M.; Guo, C.; Koka, H.; Sung, H.; Shao, N.; Guida, J.; Deng, J.; Li, M.; Hu, N.; Zhou, B.; et al. Clinicopathological and epidemiological significance of breast cancer subtype reclassification based on p53 immunohistochemical expression. *NPJ Breast Cancer* **2019**, *5*. [CrossRef]
107. Muhammad, E.M.S.; Ahmad, A.N.; Guirguis, M.N.; Ali, A.-E.M. Immunohistochemical P53 Expression in Breast Carcinoma with Correlation to Clinico-Pathological Parameters. *Med. J. Cairo Univ.* **2012**, *80*, 179–189.
108. Bae, S.Y.; Lee, J.H.; Bae, J.W.; Jung, S.P. Differences in prognosis by p53 expression after neoadjuvant chemotherapy in triple-negative breast cancer. *Ann. Surg. Treat. Res.* **2020**, *98*, 291–298. [CrossRef] [PubMed]
109. Nema, S.; Mehta, P.; Narang, S. Role of p53 and Ki-67 in prognostication of carcinoma breast. *Indian J. Pathol. Oncol.* **2019**, *6*, 261–265. [CrossRef]
110. Lara, J.F.; Thor, A.D.; Dressler, L.G.; Broadwater, G.; Bleiweiss, I.J.; Edgerton, S.; Cowan, D.; Goldstein, L.J.; Martino, S.; Ingle, J.N.; et al. p53 Expression in Node-Positive Breast Cancer Patients: Results from the Cancer and Leukemia Group B 9344 Trial (159905). *Clin. Cancer Res.* **2011**, *17*, 5170–5178. [CrossRef]
111. Marchetti, P.; Cannita, K.; Ricevuto, E.; De Galitiis, F.; Di Rocco, Z.C.; Tessitore, A.; Bisegna, R.; Porzio, G.; De Rubeis, G.P.; Ventura, T.; et al. Prognostic value of p53 molecular status in high-risk primary breast cancer. *Ann. Oncol.* **2003**, *14*, 704–708. [CrossRef]
112. Loo, L.W.M.; Gao, C.; Shvetsov, Y.B.; Okoro, D.R.; Hernandez, B.Y.; Bargonetti, J. MDM2, MDM2-C, and mutant p53 expression influence breast cancer survival in a multiethnic population. *Breast Cancer Res. Treat.* **2018**, *174*, 257–269. [CrossRef]
113. Kim, J.-Y.; Park, K.; Jung, H.H.; Lee, E.; Cho, E.Y.; Lee, K.H.; Bae, S.Y.; Lee, S.K.; Kim, S.W.; Lee, J.E.; et al. Association between Mutation and Expression of TP53 as a Potential Prognostic Marker of Triple-Negative Breast Cancer. *Cancer Res. Treat.* **2016**, *48*, 1338–1350. [CrossRef] [PubMed]
114. Zwijsen, R.M.; Klomp maker, R.; Wientjens, E.B.; Kristel, P.M.; Van Der Burg, B.; Michalides, R.J. Cyclin D1 triggers autonomous growth of breast cancer cells by governing cell cycle exit. *Mol. Cell. Biol.* **1996**, *16*, 2554–2560. [CrossRef] [PubMed]
115. Lodén, M.; Stighall, M.; Nielsen, N.H.; Roos, G.; Emdin, S.O.; Östlund, H.; Landberg, G. The cyclin D1 high and cyclin E high subgroups of breast cancer: Separate pathways in tumorigenesis based on pattern of genetic aberrations and inactivation of the pRb node. *Oncogene* **2002**, *21*, 4680–4690. [CrossRef]
116. Kilker, R.L.; Planas-Silva, M.D. Cyclin D1 Is Necessary for Tamoxifen-Induced Cell Cycle Progression in Human Breast Cancer Cells. *Cancer Res.* **2006**, *66*, 11478–11484. [CrossRef]
117. Yde, C.W.; Issinger, O.-G. Enhancing cisplatin sensitivity in MCF-7 human breast cancer cells by down-regulation of Bcl-2 and cyclin D1. *Int. J. Oncol.* **2006**, *29*, 1397–1404. [CrossRef]
118. Kilker, R.L.; Hartl, M.W.; Rutherford, T.M.; Planas-Silva, M.D. Cyclin D1 expression is dependent on estrogen receptor function in tamoxifen-resistant breast cancer cells. *J. Steroid Biochem. Mol. Biol.* **2004**, *92*, 63–71. [CrossRef]
119. Joung, Y.H.; Lim, E.J.; Lee, M.Y.; Park, J.-H.; Ye, S.-K.; Park, E.U.; Kim, S.Y.; Zhang, Z.; Lee, K.J.; Park, N.K.; et al. Hypoxia activates the cyclin D1 promoter via the Jak2/STAT5b pathway in breast cancer cells. *Exp. Mol. Med.* **2005**, *37*, 353–364. [CrossRef] [PubMed]
120. Keyomarsi, K.; Pardee, A.B. Redundant cyclin overexpression and gene amplification in breast cancer cells. *Proc. Natl. Acad. Sci. USA* **1993**, *90*, 1112–1116. [CrossRef]
121. Scaltriti, M.; Eichhorn, P.J.; Cortés, J.; Prudkin, L.; Aura, C.; Jiménez, J.; Chandarlapaty, S.; Serra, V.; Prat, A.; Ibrahim, Y.H.; et al. Cyclin E amplification/overexpression is a mechanism of trastuzumab resistance in HER2+breast cancer patients. *Proc. Natl. Acad. Sci. USA* **2011**, *108*, 3761–3766. [CrossRef]
122. Chen, W.-J.; Chang, C.-Y.; Lin, J.-K. Induction of G1 phase arrest in MCF human breast cancer cells by pentagalloylglucose through the down-regulation of CDK4 and CDK2 activities and up-regulation of the CDK inhibitors p27(Kip) and p21(Cip). *Biochem. Pharmacol.* **2003**, *65*, 1777–1785. [CrossRef]

123. Chen, X.; Danes, C.; Lowe, M.; Herliczek, T.W.; Keyomarsi, K. Activation of the Estrogen-Signaling Pathway by p21WAF1/CIP1 in Estrogen Receptor-Negative Breast Cancer Cells. *J. Natl. Cancer Inst.* **2000**, *92*, 1403–1413. [CrossRef]
124. Fritah, A.; Saucier, C.; Mester, J.; Redeuilh, G.; Sabbah, M. p21WAF1/CIP1 Selectively Controls the Transcriptional Activity of Estrogen Receptor  $\alpha$ . *Mol. Cell. Biol.* **2005**, *25*, 2419–2430. [CrossRef]
125. Androic, I.; Krämer, A.; Yan, R.; Rödel, F.; Gätje, R.; Kaufmann, M.; Strebhardt, K.; Yuan, J. Targeting cyclin B1 inhibits proliferation and sensitizes breast cancer cells to taxol. *BMC Cancer* **2008**, *8*, 391. [CrossRef]
126. Arima, Y.; Hayashi, N.; Hayashi, H.; Sasaki, M.; Kai, K.; Sugihara, E.; Abe, E.; Yoshida, A.; Mikami, S.; Nakamura, S.; et al. Loss of p16 expression is associated with the stem cell characteristics of surface markers and therapeutic resistance in estrogen receptor-negative breast cancer. *Int. J. Cancer* **2012**, *130*, 2568–2579. [CrossRef] [PubMed]
127. Maria, K.; Vassilis, G.G.; George, Z.R.; Petros, L.; Christos, M.; John, G.; Christos, K. High expression levels of p27 correlate with lymph node status in a subset of advanced invasive breast carcinomas: Relation to E-cadherin alterations, proliferative activity, and ploidy of the tumors. *Cancer*. **2002**, *94*, 2454–2465. [CrossRef]
128. Nahta, R.; Takahashi, T.; Ueno, N.T.; Hung, M.-C.; Esteva, F.J. P27kip1 Down-Regulation Is Associated with Trastuzumab Resistance in Breast Cancer Cells. *Cancer Res.* **2004**, *64*, 3981–3986. [CrossRef] [PubMed]
129. Cariou, S.; Donovan, J.C.H.; Flanagan, W.M.; Milic, A.; Bhattacharya, N.; Slingerland, J.M. Down-regulation of p21WAF1/CIP1 or p27Kip1 abrogates antiestrogen-mediated cell cycle arrest in human breast cancer cells. *Proc. Natl. Acad. Sci. USA* **2000**, *97*, 9042–9046. [CrossRef] [PubMed]
130. Brown, I.; Shali, K.; McDonald, S.L.; Moir, E.S.; Hutcheon, A.W.; Heys, S.D.; Schofield, A.C. Reduced expression of p27 is a novel mechanism of docetaxel resistance in breast cancer cells. *Breast Cancer Res.* **2004**, *6*, 1–7. [CrossRef]
131. Dai, X.; Cheng, H.; Bai, Z.; Li, J. Breast Cancer Cell Line Classification and Its Relevance with Breast Tumor Subtyping. *J. Cancer* **2017**, *8*, 3131–3141. [CrossRef]
132. Dickson, C.; Fäntl, V.; Gillett, C.; Brookes, S.; Bartek, J.; Smith, R.; Fisher, C.; Barnes, D.; Peters, G. Amplification of chromosome band 11q13 and a role for cyclin D1 in human breast cancer. *Cancer Lett.* **1995**, *90*, 43–50. [CrossRef]
133. Zhang, P. The cell cycle and development: Redundant roles of cell cycle regulators. *Curr. Opin. Cell Biol.* **1999**, *11*, 655–662. [CrossRef]
134. Sutherland, R.L.; Musgrove, E.A. Cyclins and Breast Cancer. *J. Mammary Gland. Biol. Neoplasia* **2004**, *9*, 95–104. [CrossRef]
135. Lundberg, A.; Lindström, L.S.; Li, J.; Harrell, J.C.; Darai-Ramqvist, E.; Sifakis, E.; Foukakis, T.; Perou, C.M.; Czene, K.; Bergh, J.; et al. The long-term prognostic and predictive capacity of cyclin D1 gene amplification in 2305 breast tumours. *Breast Cancer Res.* **2019**, *21*, 34. [CrossRef] [PubMed]
136. Yu, Z.; Wang, L.; Wang, C.; Ju, X.; Wang, M.; Chen, K.; Loro, E.; Li, Z.; Zhang, Y.; Wu, K.; et al. Cyclin D1 induction of Dicer governs microRNA processing and expression in breast cancer. *Nat. Commun.* **2013**, *4*, 1–10. [CrossRef] [PubMed]
137. Zhong, Z.; Yeow, W.-S.; Zou, C.; Wassell, R.; Wang, C.; Pestell, R.G.; Quong, J.N.; Quong, A.A. Cyclin D1/Cyclin-Dependent Kinase 4 Interacts with Filamin A and Affects the Migration and Invasion Potential of Breast Cancer Cells. *Cancer Res.* **2010**, *70*, 2105–2114. [CrossRef]
138. Ravazoula, P.; Batistatou, A.; Aletra, C.; Ladopoulos, J.; Kourounis, G.; Tzigounis, B. Immunohistochemical expression of glucose transporter Glut1 and cyclin D1 in breast carcinomas with negative lymph nodes. *Eur. J. Gynaecol. Oncol.* **2003**, *24*, 544–546.
139. Ates, C.; Sevinçli, S.; Pohl, T. Electromagnetically induced transparency in strongly interacting Rydberg gases. *Phys. Rev. A* **2011**, *83*, 6380–6385. [CrossRef]
140. Leng, X.; Connell-Crowley, L.; Goodrich, D.; Harper, J. S-Phase entry upon ectopic expression of G1 cyclin-dependent kinases in the absence of retinoblastoma protein phosphorylation. *Curr. Biol.* **1997**, *7*, 709–712. [CrossRef]
141. Hwang, H.C.; Clurman, E.B. Cyclin E in normal and neoplastic cell cycles. *Oncogene* **2005**, *24*, 2776–2786. [CrossRef]
142. Keyomarsi, K.; Tucker, S.L.; Buchholz, T.A.; Callister, M.; Ding, Y.; Hortobagyi, G.N.; Bedrosian, I.; Knickerbocker, C.; Toyofuku, W.; Lowe, M.; et al. Cyclin E and Survival in Patients with Breast Cancer. *N. Engl. J. Med.* **2002**, *347*, 1566–1575. [CrossRef]
143. Dorée, M.; Galas, S. The cyclin-dependent protein kinases and the control of cell division. *FASEB J.* **1994**, *8*, 1114–1121. [CrossRef]
144. Singhai, R.; Patil, A.V.; Patil, V.W.; Gurav, P.D. Triple-negative (ER, PgR, HER-2/neu) breast cancer in Indian women. *Breast Cancer Targets Ther.* **2011**, *3*, 9–19. [CrossRef]
145. Kaldis, P.; Aleem, E. Cell Cycle Sibling Rivalry: Cdc2 Versus Cdk2. *Cell Cycle* **2005**, *4*, 1491–1494. [CrossRef] [PubMed]
146. Hakem, A.; Sasaki, T.; Kozieradzki, I.; Penninger, J.M. The Cyclin-dependent Kinase Cdk2 Regulates Thymocyte Apoptosis. *J. Exp. Med.* **1999**, *189*, 957–968. [CrossRef]
147. Carroll, J.S.; Prall, O.W.J.; Musgrove, E.A.; Sutherland, R.L. A Pure Estrogen Antagonist Inhibits Cyclin E-Cdk2 Activity in MCF-7 Breast Cancer Cells and Induces Accumulation of p130-E2F4 Complexes Characteristic of Quiescence. *J. Biol. Chem.* **2000**, *275*, 38221–38229. [CrossRef] [PubMed]
148. Li, J.; Poi, M.J.; Tsai, M.-D. Regulatory Mechanisms of Tumor Suppressor P16INK4A and Their Relevance to Cancer. *Biochemistry* **2011**, *50*, 5566–5582. [CrossRef] [PubMed]
149. Baker, S.J.; Reddy, E.P. CDK4: A Key Player in the Cell Cycle, Development, and Cancer. *Genes Cancer* **2012**, *3*, 658–669. [CrossRef]
150. Geradts, J.; Wilson, P. High frequency of aberrant p16(INK4A) expression in human breast cancer. *Am. J. Pathol.* **1996**, *149*, 15–20.
151. Gartel, A.L.; Serfas, M.S.; Tyner, A.L. p21–Negative Regulator of the Cell Cycle. *Exp. Biol. Med.* **1996**, *213*, 138–149. [CrossRef]

152. Dai, M.; Al-Odaini, A.A.; Arakelian, A.; Rabbani, A.S.; Ali, S.; Lebrun, J.-J. A novel function for p21Cip1 and acetyltransferase p/CAF as critical transcriptional regulators of TGF $\beta$ -mediated breast cancer cell migration and invasion. *Breast Cancer Res.* **2012**, *14*, R127. [CrossRef] [PubMed]
153. Winters, Z.; Hunt, N.; Bradburn, M.; Royds, J.; Turley, H.; Harris, A.; Norbury, C. Subcellular localisation of cyclin B, Cdc2 and p21WAF1/CIP1 in breast cancer: Association with prognosis. *Eur. J. Cancer* **2001**, *37*, 2405–2412. [CrossRef]
154. Li, Y.; Dowbenko, D.; Lasky, L.A. AKT/PKB Phosphorylation of p21Cip/WAF1 Enhances Protein Stability of p21Cip/WAF1 and Promotes Cell Survival. *J. Biol. Chem.* **2002**, *277*, 11352–11361. [CrossRef]
155. Rossig, L.; Jadidi, A.S.; Urbich, C.; Badorff, C.; Zeiher, A.M.; Dimmeler, S. Akt-Dependent Phosphorylation of p21Cip1 Regulates PCNA Binding and Proliferation of Endothelial Cells. *Mol. Cell. Biol.* **2001**, *21*, 5644–5657. [CrossRef] [PubMed]
156. Wang, L.; Wang, R.; Ye, Z.; Wang, Y.; Li, X.; Chen, W.; Zhang, M.; Cai, C. PVT1 affects EMT and cell proliferation and migration via regulating p21 in triple-negative breast cancer cells cultured with mature adipogenic medium. *Acta Biochim. Biophys. Sin.* **2018**, *50*, 1211–1218. [CrossRef]
157. Qian, X.; Hulit, J.; Suyama, K.; Eugenin, A.E.; Belbin, T.J.; Loudig, O.; Smirnova, T.; Zhou, Z.N.; Segall, J.; Locker, J.; et al. p21CIP1 mediates reciprocal switching between proliferation and invasion during metastasis. *Oncogene* **2012**, *32*, 2292–2303. [CrossRef]
158. Pérez-Tenorio, G.; Berglund, F.; Merca, A.E.; Nordenskjöld, B.; Rutqvist, L.E.; Skoog, L.; Stål, O. Cytoplasmic p21WAF1/CIP1 correlates with Akt activation and poor response to tamoxifen in breast cancer. *Int. J. Oncol.* **2006**, *28*, 1031–1042. [CrossRef]
159. Vincent, A.J.; Ren, S.; Harris, L.G.; Devine, D.J.; Samant, R.S.; Fodstad, O.; Shevde, L.A. Cytoplasmic translocation of p21 mediates NUPR1-induced chemoresistance. *FEBS Lett.* **2012**, *586*, 3429–3434. [CrossRef]
160. Sohn, D.; Essmann, F.; Schulze-Osthoff, K.; Jänicke, R.U. p21 Blocks Irradiation-Induced Apoptosis Downstream of Mitochondria by Inhibition of Cyclin-Dependent Kinase-Mediated Caspase-9 Activation. *Cancer Res.* **2006**, *66*, 11254–11262. [CrossRef] [PubMed]
161. Neganova, I.; Lako, M. G1 to S phase cell cycle transition in somatic and embryonic stem cells. *J. Anat.* **2008**, *213*, 30–44. [CrossRef] [PubMed]
162. Fredersdorf, S.; Burns, J.; Milne, A.M.; Packham, G.; Fallis, L.; Gillett, C.E.; Royds, J.A.; Peston, D.; Hall, P.A.; Hanby, A.M.; et al. High level expression of p27kip1 and cyclin D1 in some human breast cancer cells: Inverse correlation between the expression of p27kip1 and degree of malignancy in human breast and colorectal cancers. *Proc. Natl. Acad. Sci. USA* **1997**, *94*, 6380–6385. [CrossRef]
163. Guan, X.; Wang, Y.; Xie, R.; Chen, L.; Bai, J.; Lu, J.; Kuo, M.T. p27Kip1 as a prognostic factor in breast cancer: A systematic review and meta-analysis. *J. Cell. Mol. Med.* **2009**, *14*, 944–953. [CrossRef]
164. Filipits, M.; Rudas, M.; Heinzl, H.; Jakesz, R.; Kubista, E.; Lax, S.; Schippinger, W.; Dietze, O.; Greil, R.; Stiglbauer, W.; et al. Low p27 Expression Predicts Early Relapse and Death in Postmenopausal Hormone Receptor-Positive Breast Cancer Patients Receiving Adjuvant Tamoxifen Therapy. *Clin. Cancer Res.* **2009**, *15*, 5888–5894. [CrossRef] [PubMed]
165. Zilfou, J.T.; Lowe, S.W. Tumor Suppressive Functions of p53. *Cold Spring Harb. Perspect. Biol.* **2009**, *1*, a001883. [CrossRef]
166. Sung, H.; Ferlay, J.; Siegel, R.L.; Laversanne, M.; Soerjomataram, I.; Jemal, A.; Bray, F. Global cancer statistics 2020: GLOBOCAN estimates of incidence and mortality worldwide for 36 cancers in 185 countries. *CA A Cancer J. Clin.* **2018**, *68*, 394–424. [CrossRef]
167. Mathur, P.; Sathishkumar, K.; Chaturvedi, M.; Das, P.; Sudarshan, K.L.; Santhappan, S.; Nallasamy, V.; John, A.; Narasimhan, S.; Roselind, F.S.; et al. Cancer Statistics, 2020: Report From National Cancer Registry Programme, India. *JCO Glob. Oncol.* **2020**, *6*, 1063–1075. [CrossRef] [PubMed]
168. Chen, F.; Li, Y.; Qin, N.; Wang, F.; Du, J.; Wang, C.; Du, F.; Jiang, T.; Jiang, Y.; Dai, J.; et al. RNA-seq analysis identified hormone-related genes associated with prognosis of triple negative breast cancer. *J. Biomed. Res.* **2020**, *34*, 129–138. [CrossRef]
169. Yu, Z.; Wang, Z.; Yu, X.; Zhang, Z. RNA-Seq-Based Breast Cancer Subtypes Classification Using Machine Learning Approaches. *Comput. Intell. Neurosci.* **2020**, *2020*, 1–13. [CrossRef] [PubMed]
170. Pennock, N.D.; Jindal, S.; Horton, W.; Sun, D.; Narasimhan, J.; Carbone, L.; Fei, S.S.; Searles, R.; Harrington, C.A.; Burchard, J.; et al. RNA-seq from archival FFPE breast cancer samples: Molecular pathway fidelity and novel discovery. *BMC Med Genom.* **2019**, *12*, 1–18. [CrossRef]
171. Zhou, S.; Huang, Y.-E.; Liu, H.; Zhou, X.; Yuan, M.; Hou, F.; Wang, L.; Jiang, W. Single-cell RNA-seq dissects the intratumoral heterogeneity of triple-negative breast cancer based on gene regulatory networks. *Mol. Ther.-Nucleic Acids* **2021**, *23*, 682–690. [CrossRef]
172. Karaayvaz, M.; Cristea, S.; Gillespie, S.M.; Patel, A.P.; Mylvaganam, R.; Luo, C.C.; Specht, M.C.; Bernstein, B.E.; Michor, F.; Ellisen, L.W. Unravelling subclonal heterogeneity and aggressive disease states in TNBC through single-cell RNA-seq. *Nat. Commun.* **2018**, *9*, 1–10. [CrossRef]



Review

# Second-Generation Antimitotics in Cancer Clinical Trials

Pedro Novais <sup>1,2,3</sup> , Patrícia M. A. Silva <sup>1</sup> , Isabel Amorim <sup>4</sup> and Hassan Bousbaa <sup>1,\*</sup>

<sup>1</sup> CESPU, Institute of Research and Advanced Training in Health Sciences and Technologies (IINFACTS), Rua Central de Gandra, 1317, 4585-116 Gandra, Portugal; pedro.ha.novais@gmail.com (P.N.); patricia.silva@cespu.pt (P.M.A.S.)

<sup>2</sup> Faculty of Sciences, University of Porto, Rua do Campo Alegre, s/n, 4169-007 Porto, Portugal

<sup>3</sup> ICBAS, Instituto de Ciências Biomédicas Abel Salazar, University of Porto, 4050-313 Porto, Portugal

<sup>4</sup> GreenUPorto (Sustainable Agrifood Production) Research Center, Faculty of Sciences, University of Porto, Rua do Campo Alegre, s/n, 4169-007 Porto, Portugal; mpamorim@fc.up.pt

\* Correspondence: hassan.bousbaa@iucs.cespu.pt

**Abstract:** Mitosis represents a promising target to block cancer cell proliferation. Classical antimetotics, mainly microtubule-targeting agents (MTAs), such as taxanes and vinca alkaloids, are amongst the most successful anticancer drugs. By disrupting microtubules, they activate the spindle assembly checkpoint (SAC), which induces a prolonged delay in mitosis, expected to induce cell death. However, resistance, toxicity, and slippage limit the MTA's effectiveness. With the desire to overcome some of the MTA's limitations, mitotic and SAC components have attracted great interest as promising microtubule-independent targets, leading to the so-called second-generation antimetotics (SGAs). The identification of inhibitors against most of these targets, and the promising outcomes achieved in preclinical assays, has sparked the interest of academia and industry. Many of these inhibitors have entered clinical trials; however, they exhibited limited efficacy as monotherapy, and failed to go beyond phase II trials. Combination therapies are emerging as promising strategies to give a second chance to these SGAs. Here, an updated view of the SGAs that reached clinical trials is here provided, together with future research directions, focusing on inhibitors that target the SAC components.

**Citation:** Novais, P.; Silva, P.M.A.; Amorim, I.; Bousbaa, H. Second-Generation Antimitotics in Cancer Clinical Trials. *Pharmaceutics* **2021**, *13*, 1011. <https://doi.org/10.3390/pharmaceutics13071011>

Academic Editor: Sanjay Garg

Received: 24 May 2021

Accepted: 29 June 2021

Published: 2 July 2021

**Publisher's Note:** MDPI stays neutral with regard to jurisdictional claims in published maps and institutional affiliations.

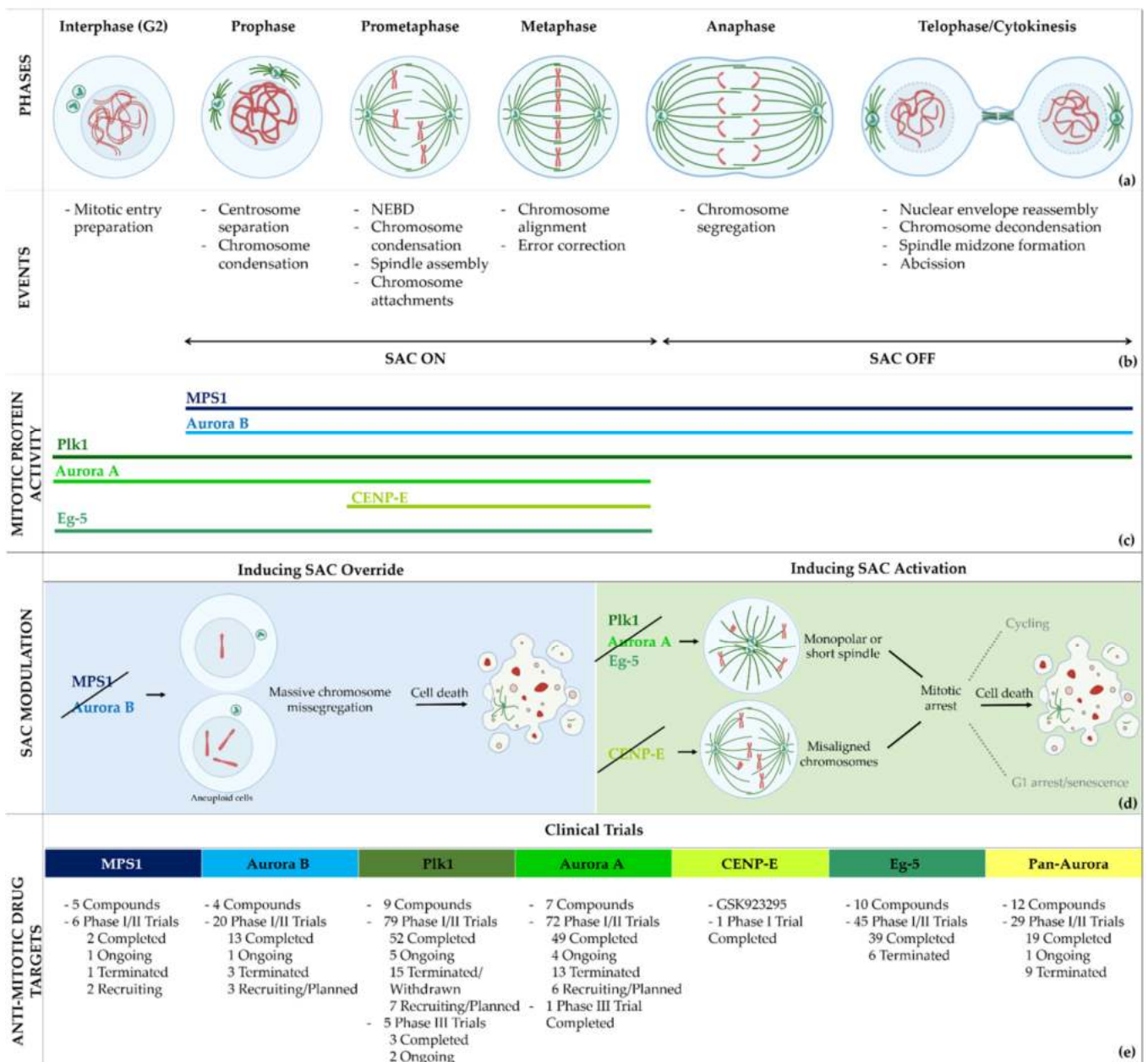


**Copyright:** © 2021 by the authors. Licensee MDPI, Basel, Switzerland. This article is an open access article distributed under the terms and conditions of the Creative Commons Attribution (CC BY) license (<https://creativecommons.org/licenses/by/4.0/>).

**Keywords:** cancer; antimetotics; mitotic slippage; spindle assembly checkpoint; clinical trials

## 1. Introduction

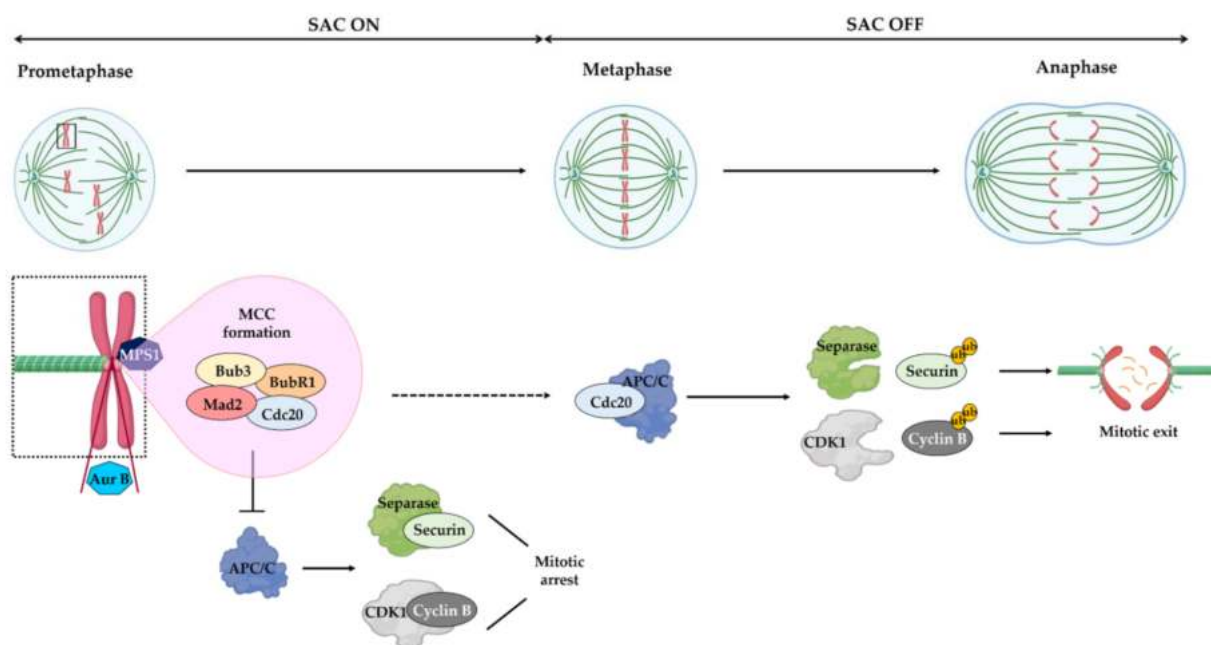
The cell cycle is a tightly regulated process in which a parental cell gives rise to two genetically identical daughter cells. Cell cycle progression is under the control of the family of serine/threonine kinases cyclin-dependent kinases (Cdk 1, 2, 4, and 6) and their regulatory subunits cyclins (A, B, D, and E). While Cdks' concentration is constant throughout the cell cycle, their activation depends on the oscillation of cyclin levels at different phases of the cell cycle [1]. The cell cycle is divided into two phases, interphase and mitosis. Interphase is a time of synthesis and growth, occurring according to the consecutive phases G1, S, and G2, during which the DNA is replicated. Mitosis consists of five active phases: prophase, prometaphase, metaphase, anaphase, and telophase, followed by cytokinesis. During prophase, chromosomes start to condense and the centrosomes start to migrate to the opposite sides of the mitotic cell. After nuclear envelope breakdown (NEBD), at the onset of prometaphase, microtubules emanating from centrosomes grow to assemble the mitotic spindle and capture the chromosomes by attaching to their kinetochores. Chromosomes then align at the spindle equator, forming the metaphase plate. When all chromosomes are bipolarly attached to spindle microtubules, sister chromatids are separated and segregate at the anaphase. The nuclear envelope reassembles at the telophase and the cytoplasm divides (cytokinesis), giving rise to two genetically equal daughter cells (Figure 1a,b).



**Figure 1.** Targeting mitosis for cancer treatment. (a,b) Representation of G2 interphase and the stages of mitosis. A description of the main cellular changes at each stage is presented. The progression throughout mitosis is monitored by the spindle assembly checkpoint activity (SAC ON and SAC OFF). (c) Activity of mitotic proteins during G2 and mitotic phases. MPS1, Aurora B, and PLK1 kinases are involved in several processes, being activated from G2 of interphase to telophase/cytokinesis. Aurora A and Eg-5 proteins ensure proper bipolar spindle shape, remaining activated from G2 to metaphase. CENP-E is required for accurate kinetochore–microtubule attachments, operating from prometaphase to metaphase. (d) SAC modulation by targeting mitotic proteins. MPS1 and Aurora B inhibition leads to SAC override, followed by massive chromosome missegregation and cell death. PLK1, Aurora A and Eg-5 inhibition induces spindle defects, while CENP-E inhibition promotes chromosome misalignment, leading to SAC activation, which in turn arrests cells in mitosis. Under mitotic arrest, the cell undergoes death or alternative pathways, namely G1 arrest/senescence, or continues cycling. (e) Second-generation antimetotics in clinical trials. Summary of antimetotic drug targets in different phases of clinical trials and current status. Created in BioRender.

A successful mitosis relies on equal chromosome segregation at the transition from metaphase to anaphase. Kinetochore–microtubule attachment defects lead to the missegregation of chromosomes resulting in genome instability, a hallmark of cancer [2,3]. Fortunately,

the fidelity of chromosome segregation is ensured by the spindle assembly checkpoint (SAC) (Figure 2). The SAC consists of a protein network that delays the anaphase in the presence of erroneous kinetochore–microtubule attachments or the absence of attachments [4]. SAC activation is mediated by the orderly orchestrated recruitment to the unattached kinetochores of the SAC proteins monopolar spindle 1 (Mps1), Aurora kinase B, budding uninhibited by benomyl 1 (Bub1), and mitotic arrest deficiency 1 (Mad1). Consequently, the mitotic checkpoint complex (MCC) is assembled, which is formed by Mad2, Bub1-related 1 (BubR1), Bub3 and Cdc20. By sequestering Cdc20, the MCC inhibits the ultimate target of SAC, the anaphase promoting complex/cyclosome (APC/C), an E3 ubiquitin ligase. When all kinetochores are correctly attached to microtubules, the SAC is turned off and APC/C becomes active, targeting securin and cyclin B for proteolysis. The degradation of securin releases the protease separase, which thus cleaves the cohesin rings, allowing sister chromatids to separate, whereas the proteolysis of cyclin B triggers mitotic exit [4].



**Figure 2.** Spindle assembly checkpoint mechanism. In response to unattached or improperly attached kinetochores (Prometaphase), the SAC is turned ON and promotes the assembly of the mitotic checkpoint complex (MCC), made of Mad2, Bub3, BubR1 and Cdc20. At these kinetochores, MPS1 recruits Bub3, Bub1 and BubR1. The MCC inhibits the activity of anaphase-promoting complex/cyclosome (APC/C), leading to the stabilization of separase/securin and CDK1/cyclin B complexes, and consequent mitotic arrest. The Aurora B kinase (Aur B), associated with centromere heterochromatin, promotes proper kinetochore–microtubule attachments. Once all chromosomes are properly attached to spindle microtubules and are aligned at the metaphase plate (metaphase), the SAC is turned OFF, through MCC disassembly, and consequently Cdc20 can bind and activates the APC/C, resulting in the ubiquitylation (ub) of cyclin B and securin mitotic substrates. In turn, separase can cleave cohesins to promote sister chromatid separation (anaphase), while Cdk1 inactivation promotes exit from mitosis. Created in BioRender.

Based on the uncontrolled proliferation of many cancers, anticancer drugs have been developed to block the cell cycle, particularly mitosis. In this review, we will briefly discuss the current antimetabolic approaches, and focus on the new generation of promising antimetotics that have reached clinical trials, with particular emphasis on their clinical efficacy. These so-called second-generation antimetotics (SGAs) target the mitotic kinases and spindle motor proteins. Possible research directions will be discussed.



## 2. Limitations of Current Microtubule-Targeting Agents

Microtubule-targeting agents (MTAs) are the main current antimitotic drugs in the clinic, and are widely used for the treatment of several cancers [5]. MTAs are divided into two groups, based on their action mechanism: microtubule destabilizers, such as the vinca alkaloids, that inhibit microtubule polymerization; and microtubule stabilizers, such as taxanes, that enhance microtubule polymerization [6]. Both classes impair a functional mitotic spindle, leading to SAC activation and subsequent mitotic arrest, which usually results in cell death by apoptosis [7]. However, other outcomes are possible after MTA treatment. After a prolonged mitotic arrest, cells may exit mitosis without undergoing cytokinesis, originating tetraploid cells, a process known as mitotic slippage, which results from a constant and slow degradation of cyclin B even when SAC is on [8]. The slipped cells can follow three possible fates: become senescent, undergo post-mitotic death, or continue dividing [9]. Therefore, mitotic slippage, together with efflux pumps, mutations in tubulin genes, and deficient apoptotic signaling, represent the main reasons for the therapeutic failure of MTAs [10]. Additionally, MTAs treatment is also frequently associated with neurological and myeloid toxicity [10].

## 3. Second-Generation Antimitotics in Clinical Trials

Due to the aforementioned limitation of MTAs, alternative approaches to directly targeting microtubules were developed to block cells in mitosis. These new strategies consist of inhibiting the activity of mitotic proteins, especially kinases and motor proteins, that play crucial roles in different processes during mitosis, such as mitotic entry, spindle assembly, chromosome congression, or SAC regulation. The inhibition of these proteins is made possible through small molecules or small interfering RNAs (siRNAs), known as the second-generation antimitotics (SGAs), with promising outcomes in preclinical assays [11]. Here, we will focus on those SGAs that reached clinical trials, namely, inhibitors of Mps1, polo-like kinase 1 (Plk1), Aurora kinases, Eg-5, and centromeric protein E (CENP-E), review their clinical outcomes, and provide future research directions.

### 3.1. *Mps1*

Mps1, also known as TKK, is a dual-specificity protein kinase phosphorylating serine/threonine and tyrosine residues [12]. Mps1 is recruited early in mitosis to unattached kinetochores, where it is responsible for SAC activation through the recruitment of several SAC components to kinetochores and subsequent MCC formation [13]. It has also been involved in DNA damage checkpoint response, chromosome alignment, meiosis, cytokinesis, centrosome duplication, and error-correction of kinetochore–microtubule attachment [14–16]. Mps1 is overexpressed in various tumors, correlating with poor prognosis [17]. The inhibition of Mps1 activity compromises the SAC, which leads to premature mitotic exit, resulting in massive aberrant chromosome segregation and subsequent cell death [18,19]. Furthermore, inhibition of Mps1 has been shown to sensitize cancer cells to Paclitaxel [18,20]. Hence, Mps1 became an attractive target for cancer therapy, and a variety of small molecules that inhibit Mps1 have been developed. As with most kinases, Mps1 inhibitors are ATP competitive molecules. So far, five Mps1 inhibitors have been approved to begin clinical trials, namely, BOS 172722, BAY 1217389, BAY1161909, CFI-402257 and S 81694. Six phase I/II studies have been undertaken: two have been completed, one has been terminated, two are recruiting participants and another one is ongoing (Figure 1 and Table 1).

#### 3.1.1. BAY 1217389 and BAY1161909

BAY 1217389, an Imidazopyridazine, and BAY1161909, a Triazolopyridine, inhibit Mps1 with an  $IC_{50}$  of 0.34 nM and 0.63 nM, respectively, in vitro [21]. Both compounds were developed by Bayer and showed similar behavior in vivo, with modest efficacy as single agents. However, both compounds demonstrate synergistic effects when combined with Paclitaxel on the growth inhibition of human tumor xenografts in immunocompromised

mice [21]. In the clinical trial involving BAY1161909 (NCT02138812) for the treatment of advanced solid malignancies, in a combinational treatment with 75 mg/m<sup>2</sup> and 90 mg/m<sup>2</sup> of Paclitaxel, five (14%) and four (14%) partial responses (PRs) were reported, respectively [22]. However, Bayer decided to interrupt clinical trials with BAY1161909 in favor of BAY 1217389, which was being developed in parallel. The BAY 1217389 phase I study (NCT02366949) in combination with Paclitaxel was completed in March 2018, but the outcomes are not available yet.

### 3.1.2. S 81694

S 81694 inhibits Mps1 with an IC<sub>50</sub> of 3 nM in vitro, and was first discovered by Nerviano Medical Sciences (NMS-P153), and thereafter acquired and further developed by Servier [23]. S 81694 pre-clinical studies demonstrated that triple-negative breast cancer cell lines were particularly sensitive to S 81694 and, in an MDA-MB-231 xenograft and orthotopic model of tumor regression, the curing of animals and metastasis reduction were observed [24]. A phase I/II trial with S 81694 (NCT03411161) for the treatment of breast cancer was completed in June of 2020, the outcomes of which are not published yet.

### 3.1.3. BOS 172722

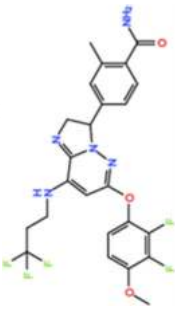
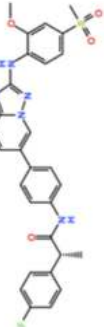
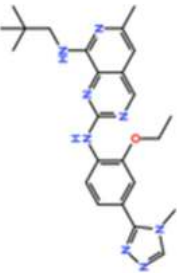

BOS 172722 is a pyrido[3,4-d]pyrimidine, developed by Boston Pharmaceuticals, and was shown to inhibit Mps1 with an IC<sub>50</sub> of 11 nM, in vitro [25]. It exhibited modest efficacy as a monotherapy in xenograft studies, but exerted strong synergistic effects in combination with Paclitaxel in triple-negative breast cancer (TNBC) cell lines [26]. A phase I trial (NCT03328494) is currently ongoing with patients with advanced nonhematologic malignancies.

### 3.1.4. CFI-402257

CFI-402257, a pyrazolo[1,5-a]pyrimidine, is a potent Mps1 inhibitor with an IC<sub>50</sub> of 1.2 nM in vitro, and it induced tumor regression in murine colon and lung cancer models [27,28]. Currently, two phase I/II trials are recruiting participants: one for the treatment of advanced solid tumors, including breast cancer, as a monotherapy and in combination with Fulvestrant (NCT02792465), and one in combination with Paclitaxel for breast cancer (NCT03568422).

Based on the promising results of in vivo preclinical studies that have demonstrated a synergistic effect between Mps1 inhibitors and taxanes, all small molecules that entered clinical trials were combined with Paclitaxel. However, it is too early to draw a conclusion on the clinical efficacy and safety of these combinations, as only the outcomes of BAY 1161909 have been published to date. Nevertheless, in this trial, the combinational treatment was generally well tolerated, with the most common AEs being gastrointestinal and hematological. Objective responses were observed with BAY 1161909. The rationale behind these combinations is interesting: silencing the SAC by Mps1 inhibition leads to premature mitotic exit with chromosome missegregation, while the affecting of microtubule dynamics by the taxanes further enhances chromosome misalignment and chromosome missegregation, culminating in massive cell death [20]. Inhibition of Mps1 also demonstrated a synergic effect with cisplatin in malignant mesothelioma cisplatin-resistant cell lines in vitro. Therefore, it will be interesting to evaluate the clinical efficacy of Mps1 inhibitors combined with anti-cancer drugs other than taxanes, in particular with platinum-based agents [29]. It should be noted that all clinical trials enrolled patients with solid tumors. Recently, the inhibition of Mps1 was shown to induce apoptosis in multiple myeloma cell lines, but further research is required to evaluate the potential effectiveness of Mps1 inhibitors in hematological tumors [30].

Table 1. Mps1 inhibitors in clinical trials <sup>1</sup>.

Compound	Clinical Trials	Current Status	Conditions	Interventions	Outcomes <sup>2</sup>	Ref.
BAY 1217389 	NCT02366949	Phase I Completed	Advanced Solid Malignancies	Combination with Paclitaxel	Not published	-
BAY 1161909 (Empesertib) 	NCT02138812	Phase I Terminated	Advanced Solid Malignancies	Combination with Paclitaxel	Best response was PR	[22]
S 81694 Structure Undisclosed	NCT03411161	Phase I Phase II Completed	Metastatic Breast Cancer, Metastatic Triple-Negative Breast Cancer	Combination with Paclitaxel	Not published	-
BOS 172722 	NCT03328494	Phase I Ongoing	Advanced Nonhematologic Malignancies	Combination with Paclitaxel	-	-
CFI-402257 	NCT03568422	Phase I Phase II Recruiting	Breast Cancer	Combination with Paclitaxel	-	-
	NCT02792465	Phase I, Recruiting	Breast Cancer, Advanced Solid Malignancies	Monotherapy Combination with Fulvestrant	-	-

<sup>1</sup> Data collected from clinicaltrials.gov. <sup>2</sup> PR, partial response.

### 3.2. Plk1

Plk1 is a cell cycle-regulating serine/threonine kinase implicated in centrosome maturation and separation, mitotic entry, spindle assembly, kinetochore–microtubule attachment, the SAC, DNA damage checkpoint activation, and cytokinesis [31–33]. Knockdown or inhibition through small molecules of Plk1 leads to monopolar spindle formation, G2/M arrest, and polyploidy, which ultimately leads to cell death [34–36]. Plk1 is overexpressed in several tumors, associated with poor prognosis, and has been associated with resistance to chemotherapeutics such as Doxorubicin, Gemcitabine, and Paclitaxel [37,38]. Taken together, these facts led to the development of several small molecules that target Plk1 for cancer therapy. Nine Plk1 inhibitors have already entered clinical trials: CYC 140, GSK461364, TAK-960, NMS-1286937 (Onvansertib), BI 6727 (Volasertib), BI 2536, Rigosertib, MK-1496, and lipid nanoparticles carrying the siRNA TKM-080301 (Figure 1 and Table 2). Seventy-nine phase I/II clinical trials with solid and hematological tumor patients have been initiated: fifty-two completed, five ongoing, fifteen terminated/withdrawn, and seven are recruiting participants. Additionally, three phase III studies with metastatic pancreatic adenocarcinoma and myelodysplastic syndrome (MDS) patients have been completed, and two studies with acute myeloid leukemia (AML) and MDS patients are ongoing.

#### 3.2.1. BI 2536 and BI6727 (Volasertib)

BI 2536 and Volasertib are two similar molecules developed by Boehringer Ingelheim. BI2536 is a potent ATP-competitive Plk1 inhibitor with an  $IC_{50}$  of 0.83 nM in vitro [39]. Several studies have been undertaken with this compound. Overall, the most common AEs were neutropenia and leukopenia. PR were reported in non-small-cell lung cancer patients as monotherapy (2.1%, NCT00376623) and in combination with pemetrexed (5.2%, NCT02211833), and in pancreatic cancer patients (2.3%, NCT00710710) as a monotherapy [40–42]. Nevertheless, the greatest efficacy was observed in AML patients (NCT00701766), in which two complete remissions (CRs, 3.7%) and three PRs (5.5%) were reported, and in non-Hodgkin's lymphoma patients (NCT00243087), also as monotherapy, in which three CR (17.7%) and one PR (5.9%) were achieved [43,44]. However, clinical trials with BI 2536 have been terminated as single agent, and the second-generation inhibitor Volasertib has been chosen for further clinical development.

Volasertib is a dihydropteridinone derivative that inhibits the Plk1 with an  $IC_{50}$  of 0.84 nM in vitro [45]. The first-in-human trial of Volasertib was initiated in 2005 against solid tumors as monotherapy (NCT02273388) [46]. The most common AEs were predominantly hematological, and the main dose-limiting toxicities (DLT) were thrombocytopenia, neutropenia, and febrile neutropenia. The MTD was established as 400 mg. However, due to overall tolerability, 300 mg was set as the recommended dose for further development [46]. Three PRs (4.6%) were reported in patients with melanoma, ovarian and urothelial cancer, and 40% of patients had the best response of SD [46]. Since then, at least twenty-four more phase I/II trials (twelve completed, six withdrawn, four terminated and two ongoing) have begun against solid and hematological tumors. Several PRs have been reported with Volasertib as a single agent or in combination with other drugs against many solid tumors. In two phase I trials with Volasertib as the single agent against solid tumors, three PRs (3.3%) were reported in patients with melanoma, ureteral cancer (NCT00969553), and gastric cancer (6.7%, NCT01348347) [47,48]. Based on this phase I result of Volasertib as a monotherapy, two phase II trials were conducted in patients with urothelial cancer (NCT01023958) and platinum-resistant/refractory ovarian cancer (NCT01121406). In the study with urothelial cancer patients, seven PRs (14%) were reported and 26% of patients had SD. The safety profile was considered acceptable, but Volasertib demonstrated insufficient antitumor activity for further evaluation as a monotherapy in these patients [49]. Additionally, in the trial with platinum-resistant/refractory ovarian cancer patients, seven PRs (13%) were reported and 44.4% of patients had SD. The expression of Plk1 was evaluated in 47.3% of patients, but the results demonstrated no relationship between Plk1 levels and Volasertib response. In this regard, it was suggested that further clinical development

of Volasertib as a single agent in these patients should only be performed after biomarker analysis, in order to select patients with higher chances of response [50]. Another phase II trial was conducted in patients with non-small-cell lung cancer treated with Volasertib as a single agent, in combination with pemetrexed, or pemetrexed alone (NCT00824408). The combinational regimen did not increase toxicity compared to pemetrexed as a single agent. Three PRs (8.1%) were reported with Volasertib as a single agent, and ten (21.3%) in the combinational arm; however, the combination treatment did not demonstrate an efficacy improvement [51]. More objective responses were reported in other studies with solid tumor patients treated with Volasertib in combination with several drugs. In a phase I trial in combination with Nintedanib (NCT01022853), one CR (3.3%) in a breast cancer patient and one PR (3.3%) in a patient with non-small-cell lung cancer were reported [52]. In another phase I study in combination with Afatinib (NCT01206816), two PRs (3.3%) were observed in patients with non-small-cell lung cancer and head and neck cancer of the tongue [53]. Additionally, in a phase I trial, Volasertib was combined with platinum agents (Cisplatin or Carboplatin, NCT00969761); two PRs (6.7%) were reported with Volasertib plus cisplatin in patients with follicular dendritic reticulum cell carcinoma of the palatine tonsil and follicular dendritic reticulum cell retroperitoneal sarcoma, and two additional PRs (6.5%) were also reported with Volasertib plus Carboplatin in patients with non-small-cell lung cancer and hypopharynx carcinoma [54]. Still, the best response was achieved in patients with AML, in which three CRs (15.8%) and another three CRs with incomplete blood count remission (15.8%, CRi) were reported as monotherapy (NCT01662505) [55]. In this trial, the MTD was established as 450 mg, administered intravenously on days 1 and 15 in a 28-day cycle, and grade 3 or higher AEs were mainly hematological (neutropenia and thrombocytopenia). However, the safety profile was considered acceptable and could be managed through the supportive care of granulocyte colony-stimulating factor (G-CSF) [55]. These results prompted the use of Volasertib in a phase II (NCT00804856) and a phase III (NCT01721876) trial against AML, both in combination with cytarabine, which are currently ongoing.

### 3.2.2. ON 01910.Na (Rigosertib)

Rigosertib inhibits Plk1 with an  $IC_{50}$  of 9 nM *in vitro* [56]. At least thirty-two phase I/II trials have begun (twenty-four completed, one terminated, two withdrawn, three planned/recruiting participants and two ongoing) as monotherapy and in combinational treatments against solid and hematological tumors. Three PRs (9.3%) were reported in Hodgkin lymphoma, thymic cancer and pancreatic ductal adenocarcinoma patients in combination with Gemcitabine (NCT01125891) [57]. These led Rigosertib to a phase III trial against pancreatic adenocarcinoma in combination with Gemcitabine (NCT01360853), which was completed in 2015. In this study the best response was PR in 19% of patients, and SD in 50% of patients; however, the combinational treatment did not demonstrate an improvement in survival compared to Gemcitabine as a single agent [58]. Nevertheless, the phase I/II outcomes in patients with myelodysplastic syndrome (MDS) were the most promising, and Rigosertib was approved for three phase III trials as monotherapy. One is ongoing (NCT02562443), and two have been completed (NCT01241500 and NCT01928537), in which the best overall response was marrow complete remission (mCR) in 20% and 22% of patients, respectively [59,60]. Additionally, in a phase I/II trial in combination with Azacitidine in patients with MDS (NCT01926587), two CRs (12.5%) were reported and the phase II trial is ongoing [61]. Currently, two phase I/II trials with Rigosertib as monotherapy are planned, recruiting participants against recessive dystrophic epidermolysis bullosa (NCT03786237 and NCT04177498), and also a phase I study in patients with non-small-cell lung cancer with Rigosertib in combination with nivolumab is recruiting participants (NCT04263090).

### 3.2.3. GSK461364

GSK461364 is a thiophene amide that inhibits Plk1 with an  $IC_{50}$  of 7 nM in vitro, and it was developed by GlaxoSmithKline [62]. GSK461364 entered a phase I trial for the treatment of advanced solid malignancies as monotherapy (NCT00536835). No objective responses were reported, and only six stable diseases (SD, 15%) were observed in patients with esophageal, endometrial carcinoma, and ovarian cancers, all treated with doses at or above the MTD [63]. The most common AEs were infusion site reactions and phlebitis, and due to the high incidence of venous thromboembolism (20%) no further development is planned.

### 3.2.4. MK-1496

MK-1496, developed by Merck Sharp & Dohme Corp., has completed a phase I trial as monotherapy for the treatment of advanced solid tumors in 2009 (NCT00880568). The MTD was determined as 80 mg/m<sup>2</sup>, and reversible hematotoxicity was the main side effect [64]. Two PRs (11.8%) were reported in patients with parotid gland carcinoma and small-cell lung cancer, but no further development is planned for MK-1496.

### 3.2.5. TAK-960

TAK-960, developed by Millennium Pharmaceuticals, inhibits Plk1 with an  $IC_{50}$  of 2 nM in vitro [65]. TAK-960 has demonstrated substantial antitumor activity in various human cancer models [66]. A phase I trial was started in 2010 with TAK-960 as monotherapy for the treatment of advanced nonhematologic malignancies (NCT01179399), but has been terminated early due to lack of efficacy, and further development has been halted.

### 3.2.6. NMS-1286937 (Onvansertib)

Onvansertib, from Nerviano Medical Sciences, is another potent Plk1 inhibitor with an  $IC_{50}$  of 2 nM in vitro [67]. In a phase I trial as monotherapy, the best response was SD (26%) in patients with colorectal cancer, pancreatic carcinoma with a K-RAS mutation, head and neck squamous cell carcinoma, and basal cell carcinoma (NCT01014429) [68]. Despite the lack of efficacy as a monotherapy, three phase I/II studies are currently recruiting participants: one for AML in combination with decitabine or cytarabine (NCT03303339), one for metastatic prostate cancer in combination with FOLFIRI (folinic acid, fluorouracil, and irinotecan) and bevacizumab (NCT03829410), and one for metastatic colorectal cancer with a KRAS mutation in combination with abiraterone and prednisone (NCT03414034).

### 3.2.7. TKM-080301

TKM-080301 is distinctive among the anti-Plk1 since it is a lipid nanoparticle formulation of an siRNA targeting the Plk1 gene transcript. Phase I/II studies on TKM-080301 as monotherapy in patients with advanced hepatocellular carcinomas (HCC, NCT02191878), adrenocortical cancer (ACC, NCT01262235) and other solid tumors (NCT01437007) were completed. TKM-080301 was generally well tolerated, but did not demonstrate clinical antitumor activity against HCC. However, it showed a better response against ACC with a PR (12.5%) reported, and further clinical evaluation is warranted [69,70].

### 3.2.8. CYC 140

CYC 140, from Cyclacel Pharmaceuticals, inhibits Plk1 with an  $IC_{50}$  of 3 nM in vitro, and has demonstrated antitumor activity in human tumor xenografts at non-toxic doses [71]. CYC 140 is the most recent Plk1 inhibitor in clinical trials, and a phase I study using it against hematological malignancies as monotherapy is currently recruiting participants (NCT03884829).

Table 2. PI3K inhibitors in clinical trials <sup>1</sup>.

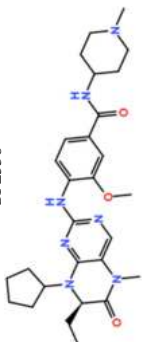
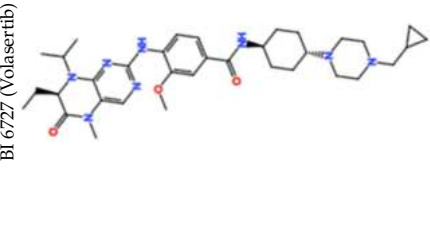
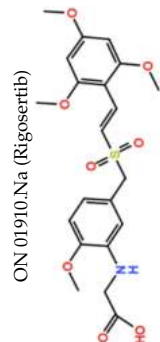
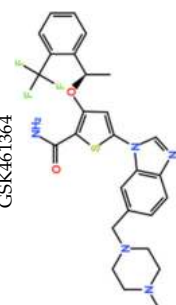
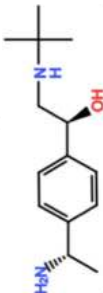
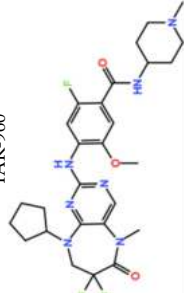
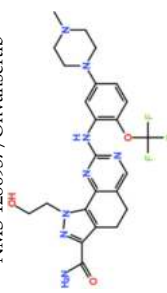
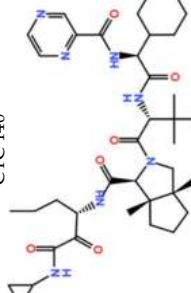
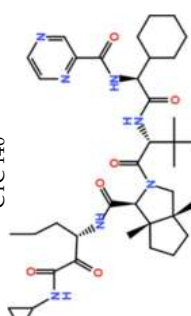
Compound	Clinical Trials	Current Status	Conditions	Interventions	Outcomes <sup>2</sup>	Refs.
 BI 2536	11 Clinical trials	Phase I/II 10 Completed 1 Terminated	Advanced Solid Tumors, Acute Myeloid Leukemia, Non-Hodgkin's Lymphoma	Monotherapy  Combination with Pemtrexed and Gemcitabine	Best responses were CR for acute myeloid leukemia and non-Hodgkin's lymphoma; PR for non-small-cell lung cancer, pancreatic cancer, acute myeloid leukemia, and non-Hodgkin's lymphoma  Best response was PR for adenocarcinoma and squamous cell carcinoma	[40–44]
 BI 6727 (Volasertib)	26 Clinical trials	25 Phase I/II 12 Completed 4 Terminated 6 Withdrawn 3 Ongoing	Acute Myeloid Leukemia Pediatric Patients with Advanced Cancers, Myelodysplastic Syndromes, Non-Hodgkin's Lymphoma, Urothelial, Ovarian, Lung Pancreatic, Colorectal and Prostate Cancer	Monotherapy  Combination with Cytarabine, Pemtrexed, Azacitidine, Afatinib, Decitabine, Daunorubicin, Nintedanib, Mitoxantrone and Itraconazole	Best responses were CR for breast cancer in combination with Nintedanib, PR for non-small-lung cancer in combination with Pemtrexed, Nintedanib, Afatinib, and Carboptatin, PR for head and neck carcinoma in combination with Afatinib, PR for undifferentiated follicular dendritic reticulum cell sarcoma and differentiated follicular dendritic reticulum cell retroperitoneal sarcoma in combination with Cisplatin, PR for differentiated hypopharynx carcinoma in combination with Carboptatin	[46–55]
 ON 01910.Na (Rigosertib)	36 Clinical trials	1 Phase III Ongoing  32 Phase I/II 24 Completed 1 Terminated 2 Withdrawn 3 Recruiting/ Planned 2 Ongoing  4 Phase III 3 Completed 1 Ongoing	Acute Myeloid Leukemia  Refractory Leukemia, Myelodysplastic Syndrome, Squamous Cell Carcinoma Acute/Chronic Myeloid Leukemia, Ovarian and Lung Cancer, Advanced Solid Tumors  Metastatic Pancreatic Adenocarcinoma, Myelodysplastic Syndromes	Combination with Cytarabine  Monotherapy  Combination with Nivolumab, Cisplatin, Azacitidine, Oxaplatin, Gemcitabine and Irinotecan  Monotherapy  Combination with Gemcitabine	Best response was PR for non-Hodgkin's lymphoma, thymic cancer, and pancreatic ductal adenocarcinoma  Best responses were CR and mCR for myelodysplastic syndrome in combination with Azacitidine  Best responses were SD and mCR for myelodysplastic syndromes Best response was PR for pancreatic adenocarcinoma	[57–61,72,73]
 GSK461364	NCT00536835	Phase I Completed	Non-Hodgkin Lymphoma, Advanced Solid Malignancies	Monotherapy	Best response was SD for esophageal and ovarian cancers and endometrial carcinoma	[63]

Table 2. Cont.

Compound	Clinical Trials	Current Status	Conditions	Interventions	Outcomes <sup>2</sup>	Refs.
MK-1496 	NCT00880568	Phase I Completed	Advanced Solid Tumors	Monotherapy	Best response was PR for parotid gland carcinoma and small cell lung cancer	[64]
TAK-960 	NCT01179399	Phase I Terminated	Advanced Nonhematologic Malignancies	Monotherapy	Discontinued strategically by sponsor due to lack of efficacy	-
NMS-1286937/Onvansertib 	4 Clinical trials	Phase I/II 1 Completed 3 Recruiting	Advanced or Metastatic Solid Tumors  Acute Myeloid Leukemia, Metastatic Prostate Cancer, Metastatic Colorectal Cancer with a KRAS mutation	Monotherapy  Combination with Decitabine, Cytarabine, Abiraterone, Prednisone, FOLFIRI and Bevacizumab	Best response was SD for colorectal cancer, pancreatic carcinoma with a K-RAS mutation, head and neck squamous cell carcinoma, and basal cell carcinoma	[68]
TKM-080301 (siRNA) 	3 Clinical trials	Phase I/II Completed	Hepatocellular Carcinoma, Colorectal, Pancreas, Breast and Ovarian Cancer with Hepatic Metastases, Adrenocortical Carcinoma, Neuroendocrine Tumors	Monotherapy	Best response was PR for adrenocortical carcinoma	[69,70]
CYC 140 	NCT03884829	Phase I Recruiting	Acute Myeloid Leukemia, Myelodysplastic Syndromes, Acute Lymphoblastic Leukemia	Monotherapy	-	-

<sup>1</sup> Data collected from clinicaltrials.gov. <sup>2</sup> CR, complete remission; mCR, marrow complete remission; PR, partial response; SD, stable disease.



The AEs associated with Plk1 inhibitors were mainly hematological, namely, neutropenia and thrombocytopenia, but the safety profile of most molecules was considered acceptable and manageable. The efficacy outcomes in patients with solid tumors were modest, either as monotherapy or in combinational treatments. Inhibition of Plk1 has been suggested to be more effective in tumors with high levels of Plk1 and mutated p53, thus selection of patients with these tumor characteristics may improve the clinical outcomes of Plk1 inhibitors against solid tumors [74,75]. Interestingly, better responses were achieved in patients with hematological tumors, especially against AML and MDS, with Volasertib and Rigosertib, respectively, representing the most promising molecules among Plk1 inhibitors. Both inhibitors have demonstrated antitumor activity as a monotherapy, which was improved when combined with other chemotherapeutic drugs. Therefore, future efforts should focus on combinational treatments in order to increase efficacy while reducing drug dosage, DLTs, and development of resistance. Additionally, further investigation of biomarkers that predict small molecule efficiency towards inhibiting Plk1 is needed.

#### 4. Aurora Kinases

Aurora kinases A, B, and C (AurA, AurB, and AurC) are a family of serine/threonine kinases that play critical functions during mitosis. AurA is implicated in centrosome maturation and separation, cytokinesis, and bipolar spindle assembly, whereas AurB is involved in chromosome condensation and alignment, kinetochore–microtubule attachments, SAC activation, and cytokinesis [76,77]. All Aurora family members are overexpressed in several tumors, and have been related to improving the survival and proliferation of tumor cells [77]. The inhibition of AurA and AurB results in cell death through different mechanisms. AurB inhibition leads to defects in kinetochore–microtubule attachments that override the SAC, resulting in extensive aneuploidy and cell death [78,79]. In contrast, inhibition of AurA provokes a shortened and disorganized microtubule spindle, inducing a transient SAC activation and subsequent mitotic arrest, followed by mitotic exit and apoptosis [80,81]. For these reasons, Aurora kinases were seen as attractive targets for cancer therapy. Therefore, several small molecules with broad-spectrum inhibition activity against Aurora kinases have been developed in pre-clinical studies, known as pan-Aurora inhibitors. Twelve compounds have reached clinical trials: VX-680 (Tozasertib), CYC 116, PHA739358 (Danusertib), SNS-314 Mesylate, PF-03814735, AS703569 (Cenisertib), TAK-901, ABT-348 (Ilorasertib), AMG-900, GSK1070916 (NIM-900), AT9283, and BI-847325 (Figure 1 and Table 3).

##### 4.1. Pan-Aurora Inhibitors

###### 4.1.1. ABT-348 (Ilorasertib)

Ilorasertib was reported to inhibit AurA with an  $IC_{50}$  of 120 nM, AurB with an  $IC_{50}$  of 7 nM, and AurC with an  $IC_{50}$  of 1nM, *in vitro*, and is also able to inhibit the VEGF [82]. At least four phase I/II trials have been initiated with Ilorasertib against solid and hematological tumors. A phase I trial was conducted with patients with solid tumors in which Ilorasertib was administered as single agent, or in combination with Docetaxel or Carboplatin (NCT01110486). However, only the outcomes as monotherapy were published. In total, 10% of patients experienced a total of ten DLTs, and the study was terminated by strategic decision of the sponsor without establishment of MTD. Nevertheless, two PRs (2.4%) were reported in patients with basal cell carcinoma and adenocarcinoma [83]. In a phase I trial in patients with hematological tumors, Ilorasertib was administered in combination with Azacitidine (NCT01110473). The DLTs observed were pancreatitis, acute kidney injury, and hypertension. Among the fifty-two patients, twelve had SD as the best response, and three objective responses (CR, CRi, and PR) were reported in patients with AML [84]. Currently, a phase II trial is ongoing with Ilorasertib as a single agent (NCT02478320).

###### 4.1.2. AS703569/MSK1992371A (Cenisertib)

Cenisertib displays a broad inhibitory activity against a number of kinases, including AurA and B [85]. A phase I trial using it as monotherapy was conducted in patients with

solid tumors (NCT00391521). Neutropenia, febrile neutropenia, and thrombocytopenia were the most common DLTs observed, and no objective responses were observed [86]. In another phase I trial with patients with solid tumors, Cenisertib was administered in combination with Gemcitabine (NCT01097512). The MTD was 37 mg/m<sup>2</sup> of Cenisertib with the standard 1000 mg/m<sup>2</sup> of Gemcitabine, and neutropenia was the main DLT reported. The best response observed was two PRs (3%) in patients with non-small-cell lung cancer and hepatocellular carcinoma [87]. A phase I trial was also conducted with patients with hematological malignancies with Cenisertib as single agent in two schedules (NCT01080664). In the first schedule, Cenisertib was given on days 1–3 and 8–10, and in the second schedule on days 1–6, both in a 21-day cycle. The MTDs were established as 37 mg/m<sup>2</sup> and 28 mg/m<sup>2</sup> for the first and second schedules, respectively. The DLTs reported were severe neutropenia with infection and sepsis, mucositis, and diarrhea. Overall, two CRs (2.7%) were observed in patients with AML, and a CRi (1.3%) was reported in a patient with acute lymphoid leukemia with Philadelphia chromosome [88].

#### 4.1.3. VX-680 (Tozasertib)

Tozasertib, also known as VX-680 or MK-0457, was developed by Merck Sharp & Dohme Corp., and was shown to inhibit AurA with an IC<sub>50</sub> of 0.6 nM, AurB with an IC<sub>50</sub> of 18 nM, and AurC with an IC<sub>50</sub> of 4.6 nM, *in vitro* [89]. Tozasertib has entered five trials as monotherapy against solid and hematological tumors, and in combination with Dasatinib in patients with chronic myeloid leukemia and Philadelphia chromosome-positive acute lymphoblastic leukemia (NCT00500006). In the first-in-human study in patients with solid tumors (NCT02532868), the MTD was identified as 64 mg/m<sup>2</sup>, and Tozasertib was generally well tolerated, with neutropenia and a herpes zoster reactivation being the DLTs observed. No objective responses were reported, and twelve patients (44.4%) had SD as best response [90]. The best response to Tozasertib treatment was observed in a trial with patients with leukemia (NCT00111683), in which a CR (1.3%) was reported in a patient with chronic myeloid leukemia [91].

#### 4.1.4. BI-847325

BI-847325, from Boehringer Ingelheim, is a potent inhibitor of all Aurora family members as well as MEK1/2 kinases [92]. A phase I study with BI-847325 as the single agent in patients with solid tumors was initiated in 2011 (NCT01324830). The DLTs observed were primarily hematological (neutropenia, febrile neutropenia, and thrombocytopenia) and gastrointestinal (vomiting and diarrhea). In total, 45% of patients had SD as the best response, and one PR (1.4%) was reported in a patient with squamous cell carcinoma of the esophagus [93].

#### 4.1.5. AT9283

AT9283, from Astex Pharmaceuticals, inhibits AurA and AurB with an IC<sub>50</sub> of 3 nM *in vitro*. Additionally, AT9283 was also found to inhibit other kinases including JAK2, Flt3, and Abl (T315I) [94]. At least five trials have been completed with AT9283 as monotherapy. A phase I trial in patients with solid tumors or non-Hodgkin's lymphoma was started in 2007 (NCT00443976). The MTD was determined to be 47 mg/m<sup>2</sup>/day, and febrile neutropenia and wound infection were the DLTs observed. Four patients (12.5%) achieved SD as best response and one PR (3.1%) was reported in a patient with squamous cell carcinoma of the anal canal [95]. In a phase II trial with patients with leukemia or myelofibrosis (NCT00522990), the MTD was established as 324 mg/m<sup>2</sup>/72h, and tolerability was strongly dose-dependent. No CR or PR were observed [96]. A phase I trial was conducted in children and adolescents with solid tumors (NCT00985868). The MTD was 18.5 mg/m<sup>2</sup>/day, and the most common DLTs observed were neutropenia and febrile neutropenia. The best response reported was a PR (4.3%) in a patient with central nervous system-primitive neuroectodermal tumor [97].

#### 4.1.6. AMG-900

AMG-900, developed by Amgen, inhibits Aurora A, B, and C in vitro, with  $IC_{50}$  values of 5 nM, 4 nM, and 1 nM, respectively [98]. The first-in-human trial of AMG-900 was conducted in patients with solid tumors (NCT00858377). The MTD was 25 mg/day, and neutropenia was the most common DLT observed. Consequently, G-CSF support was included in treatment regimen, and the MTD was established as a higher dose of 40 mg/day. In total, 56% of the patients had SD and one PR (2.4%) was reported in a patient with clear-cell endometrial cancer [99]. In a phase I trial against AML (NCT01380756) with AMG-900 as monotherapy, the most common AEs were nausea, diarrhea, and febrile neutropenia. Three patients had a best response of CRi (9%) and no other responses were observed [100].

#### 4.1.7. PHA739358 (Danusertib)

Danusertib is a pyrrolo-pyrazole developed by Nerviano Medical Sciences, and inhibits AurA with an  $IC_{50}$  of 13 nM, AurB with an  $IC_{50}$  of 79 nM, and AurC with an  $IC_{50}$  of 61 nM, in vitro [101]. A phase II trial in patients with multiple myeloma was terminated earlier due to low recruitment rate (NCT00872300). Another phase II trial with Danusertib as single agent against metastatic hormone-refractory prostate cancer was completed (NCT00766324). Danusertib was generally well tolerated with neutropenia and fatigue being the most common AEs observed. No objective responses were observed, and 21 (25.9%) patients achieved SD as the best response [102].

#### 4.1.8. SNS-314 Mesylate

SNS-314 Mesylate, from Sunesis Pharmaceuticals, inhibits AurA with an  $IC_{50}$  of 9 nM, AurB with an  $IC_{50}$  of 31 nM, and AurC with an  $IC_{50}$  of 3 nM, in vitro [103]. SNS-314 Mesylate entered a phase I trial (NCT00519662) in patients with solid tumors as a single agent. It was generally well tolerated, with nausea, fatigue, vomiting, constipation, and pain being the most AEs commonly observed. In total, 18.8% of patients had SD as the best response, and no objective responses were reported [104].

#### 4.1.9. TAK-901

TAK-901 was developed by Millennium Pharmaceuticals (Takeda) and inhibits AurA and B in vitro, with  $IC_{50}$  values of 21 nM and 15 nM, respectively [105]. TAK-901 entered two phase I trials for solid and hematological malignancies (NCT00935844 and NCT00807677). Both trials were completed but no data are available yet.

#### 4.1.10. CYC116

CYC116, from Cyclacel Pharmaceuticals, inhibits AurA with a  $K_i$  of 8 nM and AurB with a  $K_i$  of 9.2 nM, and showed antitumor activity in vivo [106]. CYC116 entered a phase I trial in patients with solid tumors as monotherapy (NCT00560716); however, the study was terminated early by sponsor decision.

#### 4.1.11. GSK1070916 (NIM-900)

GSK1070916, also known as NIM-900, is a potent Aurora B and C inhibitor, with  $IC_{50}$  values of 5 nM and 6.5 nM, respectively, in vitro [107]. A phase I trial in patients with advanced solid tumors was completed in 2013 with GSK1070916 as monotherapy (NCT01118611), but the outcomes are not published yet.

#### 4.1.12. PF-03814735

PF-03814735, developed by Pfizer, is a potent Aurora A and B inhibitor with  $IC_{50}$  values of 0.8 nM and 5 nM, respectively, in vitro [108]. PF-03814735 entered a phase I trial against solid tumors as a single agent (NCT00424632). The DLTs observed were neutropenia, febrile neutropenia, increase in aspartate amino transferase, and left ventricular dysfunction. No objective responses were reported, with 35.5% of patients achieving SD as the best response [109].

Table 3. Pan-Aurora inhibitors in clinical trials <sup>1</sup>.

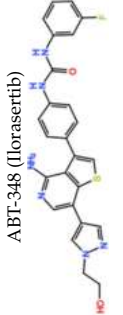

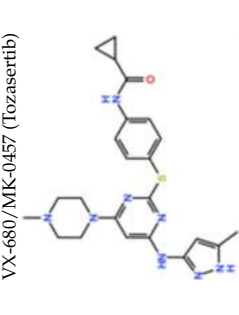
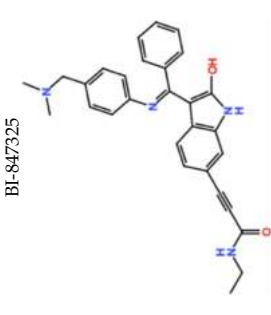
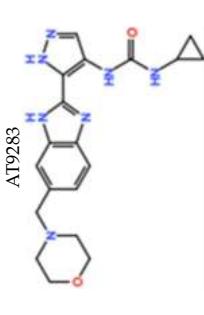
Compound	Clinical Trials	Current Status	Conditions	Interventions	Outcomes <sup>2</sup>	Refs.
<p>ABT-348 (Ilorasertib)</p> 	4 Clinical trials	Phase I/II 3 Completed 1 Ongoing	Solid Tumors, Advanced Hematological Malignancies	<p>Monotherapy</p> <p>Combination with Carboplatin, Docetaxel and Azacitidine</p>	<p>Best response was PR for basal cell carcinoma, and adenocarcinoma</p> <p>Best responses were CR, PR, and CRi for acute myeloid leukemia in combination with Azacitidine</p>	[83,84]
<p>AS703569 /MSC1992371A (Cenisertib)</p> 	3 Clinical trials	Phase I/II 2 Completed 1 Terminated	Solid Tumors, Advanced Malignancies	<p>Monotherapy</p> <p>Combination with Gemcitabine</p>	<p>Best response was CR for acute myeloid leukemia and CRi for acute lymphoid leukemia with Philadelphia chromosome</p> <p>Best response was PR for non-small-cell lung cancer and hepatocellular carcinoma</p>	[86–88]
<p>VX-680/MK-0457 (Tozasertib)</p> 	6 Clinical trials	Phase I/II 1 Completed 5 Terminated	Chronic Myeloid Leukemia, Philadelphia Chromosome-Positive, Acute Lymphoblastic Leukemia, Non-Small-Cell Lung Carcinoma, Advanced Solid Tumors	<p>Monotherapy</p> <p>Combination with Dasatinib</p>	Best response was one CR for chronic myeloid leukemia with BCR-ABL T315I mutation phenotype as monotherapy	[90,91,110]
<p>BI-847325</p> 	NCT01324830	Phase I Completed	Solid Tumors	Monotherapy	Best response was PR for esophageal cancer	[93]
<p>AT9283</p> 	5 Clinical trials	Phase I/II 4 Completed 1 Terminated	Multiple Myeloma, Acute Leukemia, Myelofibrosis, Advanced or metastatic solid tumors, Non-Hodgkin's lymphoma, Solid Tumors	Monotherapy	Best response was PR for nervous system primitive neuroectodermal tumor and squamous cell carcinoma	[95–97]

Table 3. Cont.

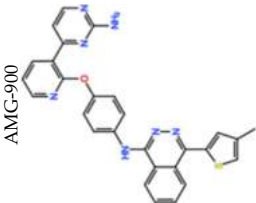
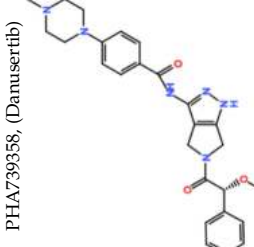
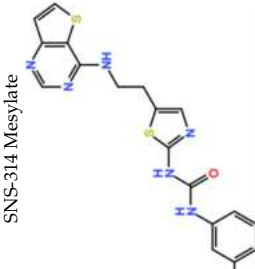
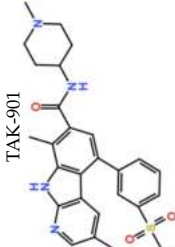

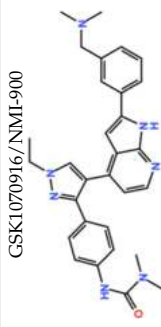
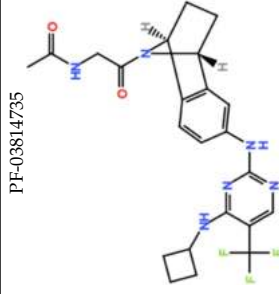
Compound	Clinical Trials	Current Status	Conditions	Interventions	Outcomes <sup>2</sup>	Refs.
 AMC-900	NCT00858377	Phase I Completed	Advanced Solid Tumors	Monotherapy	Best response was PR for clear-cell endometrial cancer	[99]
 PHA739358, (Danusertib)	NCT01380756	Phase I Completed	Acute Myeloid Leukemia	Monotherapy	Best response was CRi	[100]
 SNS-314 Mesylate	NCT00766324	Phase II Completed	Metastatic Hormone Refractory Prostate Cancer	Monotherapy	The best response was SD	[102]
 TAK-901	NCT00872300	Phase II Terminated	Multiple Myeloma	Monotherapy	-	-
	NCT00519662	Phase I Completed	Advanced Solid Tumors	Monotherapy	Best response was SD	[104]
	NCT00935844	Phase I Completed	Advanced Solid Tumors Lymphoma	Monotherapy	Not published	-
	NCT00807677	Phase I Completed	Advanced Hematologic Malignancies	Monotherapy	Not published	-

Table 3. Cont.

Compound	Clinical Trials	Current Status	Conditions	Interventions	Outcomes <sup>2</sup>	Refs.
 <p>CYC116</p>	NCT00560716	Phase I Terminated	Advanced Solid Tumors	Monotherapy	-	-
 <p>GSK1070916/NMI-900</p>	NCT01118611	Phase I Completed	Advanced Solid Tumors	Monotherapy	Not published	-
 <p>PF-03814735</p>	NCT00424632	Phase I Completed	Advanced Solid Tumors	Monotherapy	Best response was SD for non-small-cell lung cancer, melanoma, renal cell carcinoma, and neuroendocrine tumor	[109]

<sup>1</sup> Data collected from clinicaltrials.gov. <sup>2</sup> CR, complete remission; Cri, complete remission with incomplete blood count remission; PR, partial response; SD, stable disease.

## 4.2. Aurora B inhibitors

In addition to inhibitors with a broad-spectrum for Aurora kinases, several small molecules have been developed with selectivity to each Aurora family member. Four AurB-specific inhibitors (Chiauranib, AZD1152 or Barasertib, BI-811283, and BI-831266) have entered clinical trials for the treatment of solid and hematological tumors (Figure 1 and Table 4).

### 4.2.1. AZD1152 (Barasertib)

Barasertib, from AstraZeneca, is a potent AurB inhibitor with an  $IC_{50}$  of 0.37 nM *in vitro* [111]. Barasertib entered at least ten clinical trials for the treatment of solid and hematological tumors. A phase I trial as single agent was conducted in patients with solid tumors (NCT00338182). Fatigue, neutropenia, and nausea were the most common AEs, and neutropenia was the main DLT observed. No objective responses were reported, and 26.5% of patients had SD as the best response [112]. In another phase I trial with patients with solid tumors (NCT00497731), the outcomes were similar to the previous study, in which neutropenia was the main DLT observed and the best response reported was SD in 25.5% of patients [113]. Despite the lack of efficacy in solid tumors, Barasertib demonstrated better antitumor activity in patients with AML. In a phase I/II trial (NCT00497991) using it as a single agent, the MTD was established as 1200 mg, with febrile neutropenia and stomatitis/mucosal inflammation being the most common AEs observed. Sixteen (25%) objective responses were observed, including three CRs, six CRi, and seven PRs [114]. Furthermore, additional responses (CR, CRi, or PR) were reported in other trials (NCT00530699, NCT00952588, and NCT01019161) with Barasertib as a single agent in patients with AML [115–117]. Another phase I trial was conducted in AML patients in combination with low doses of Cytarabine (NCT00926731). The MTD was established as 1000 mg of Barasertib and 400 mg of Cytarabine, with the most common AEs being febrile neutropenia, nausea, diarrhea, peripheral edema, and stomatitis. Ten patients (45%) had a response to treatment, including six CR, two CRi, and two PRs [118]. A phase I/II trial with AML patients is currently recruiting participants with Barasertib as a single agent, or in combination with Venetoclax and Azacitidine (NCT03217838). A phase II trial was also conducted with patients with diffuse large B-cell lymphoma (NCT01354392) with Barasertib as a single agent. Patients received up to six cycles of 800 mg of Barasertib starting on day 1 of the 21-day cycle, and G-CSF support was added to the regimen if grade 3 or higher neutropenia occurred. The most common AEs were neutropenia, nausea, diarrhea, anemia, fatigue, and mucositis. In total, 33% of patients had SD and three PRs (20%) were reported [119].

### 4.2.2. BI-831266

BI-831266 inhibits AurB with an  $IC_{50}$  of 42 nM *in vitro* and has demonstrated antitumor activity in murine xenograft tumor models [120]. A phase I trial as monotherapy was conducted with patients with solid tumors (NCT00756223). The most common AEs were fatigue, neutropenia, and alopecia, with febrile neutropenia being the only DLT observed. In total, 16% of patients had SD, and one PR (4%) was reported in a patient with cervical cancer [121].

### 4.2.3. BI-811283

BI-811283 is another small molecule developed by Boehringer Ingelheim that inhibits AurB with an  $IC_{50}$  of 9 nM *in vitro* [122]. A phase I study with patients with solid tumors was completed with BI-811283 as a single agent (NCT00701324). The DLTs observed were mainly hematological, including neutropenia and thrombocytopenia. No objective responses were reported, and 37% of patients had SD as the best response [123]. Better results were observed in a phase II trial with BI-811283 in combination with a low dose of cytarabine in AML patients (NCT00632749). MTD was established as 100 mg of BI-811283, with anemia, nausea, pyrexia, and febrile neutropenia being the most common

AEs observed. In total, 14% of patients showed treatment responses, including seven CR, one CRi, and one PR [124].

#### 4.2.4. Chiauranib

Chiauranib, developed by Chipscreen Biosciences, is a potent AurB inhibitor with an IC<sub>50</sub> of 9 nM in vitro. Chiauranib also exerts an inhibitory activity against VEGF receptors and the colony-stimulating receptor 1 (CSF-1R), and is the most recent AurB inhibitor tested in trials [125]. A phase I trial monotherapy was conducted with patients with solid tumors (NCT02122809). Chiauranib was generally well tolerated, with fatigue, proteinuria, hematuria, hypothyroidism, hypertriglyceridemia, and hypertension being the most common AEs observed. No objective responses were observed, with 66.7% of patients achieving SD as best response [126]. Currently, a phase II trial is ongoing with ovarian cancer patients (NCT03901118), and another three phase I/II studies are planned, recruiting participants with hepatocellular carcinoma (NCT03245190), non-Hodgkin's lymphoma (NCT03974243), and small-cell lung cancer (NCT03216343).

#### 4.3. Aurora A inhibitors

Inhibitors with selectivity to AurA were also developed. In fact, more AurA inhibitors have reached clinical trials than AurB inhibitors, including MLN8237 (Alisertib), LY3295668 (Erbumine), TAS-119, ENMD-2076, MK-5108/VX-689, KW-2449, and MLN8054. At least seventy-three trials involving these compounds have been initiated for the treatment of solid and hematological tumors (Figure 1 and Table 5).

##### 4.3.1. MLN8237 (Alisertib)

Alisertib is a potent oral AurA inhibitor with an IC<sub>50</sub> of 1.2 nM in vitro [127]. Alisertib has been extensively tested in clinical trials, with at least fifty-four trials initiated as monotherapy, and in several combinational treatments against solid and hematological tumors.

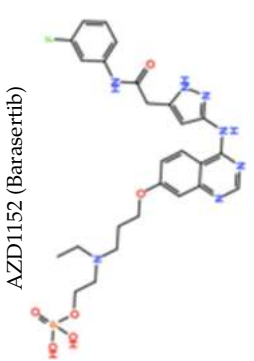
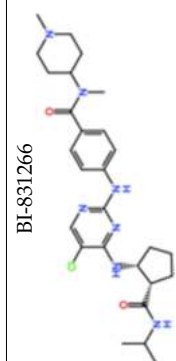
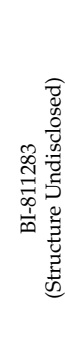
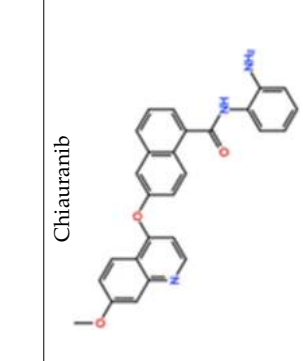
The first-in-human trial was conducted in patients with solid tumors with Alisertib as a single agent (NCT00500903). Patients were administered orally with Alisertib for 7, 14, or 21 consecutive days, followed by a 14-day recovery period. MTD was established as 50 mg twice a day for 7 consecutive days, and the main DLTs observed were neutropenia and thrombocytopenia. Alisertib was generally well tolerated, with 38% of patients achieving SD as the best response, and one PR (1.1%) was reported in a patient with platinum- and radiation-refractory ovarian cancer lasting for more than one year [128]. These results prompted the undertaking of more trials with Alisertib as a single agent in patients with solid tumors. Objective responses were reported. In a phase II trial in patients with ovarian, fallopian tube, or peritoneal carcinoma (NCT00853307), two (6%) PRs were reported in patients with ovarian carcinoma [129]. In two phase II trials in patients with metastatic sarcoma (NCT01653028) and metastatic castrate-resistant and neuroendocrine prostate cancer (NCT01799278), two PRs in each study (2.7% and 3.3%, respectively) were reported [130,131]. Additionally, several studies tested the combination of Alisertib with taxane drugs (Paclitaxel and Docetaxel) in patients with solid tumors. A phase I/II trial was conducted in patients with breast or ovarian carcinoma, who received Alisertib in combination with Paclitaxel or Paclitaxel alone (NCT01091428). The MTD was established as 10 mg of Alisertib twice a day plus 80 mg/m<sup>2</sup> of Paclitaxel. Febrile neutropenia, neutropenia, stomatitis, and diarrhea were the DLTs observed, although this combination has demonstrated a manageable safety profile. Seven CRs (11%) and 23 PRs (37%) were reported in the combinational treatment schedule, representing a 10% improvement in the ORR, in comparison to Paclitaxel as single agent (30% vs. 20%) [132]. More objective responses with Alisertib in combination with Paclitaxel were also reported in other solid tumors. For instance, in a phase II trial for the treatment of small-cell lung cancer (NCT02038647), nineteen PRs (21%) and one CR were reported (1.1%), and in a phase II with urothelial cancer patients (NCT02109328), two PRs (9.1%) were observed [133,134]. The efficacy outcomes of a phase



I trial which combined Alisertib with Docetaxel in solid tumor patients (NCT01094288) were similar to those for the combination with Paclitaxel, in which seven PRs (25%) were reported in patients with angiosarcoma and castration-resistant prostate cancer, and a CR (3,6%) was observed in a patient with bladder cancer [135]. Furthermore, additional PRs in patients with solid tumors were reported with Alisertib in combination with other drugs, such as Pazopanib against breast cancer and mesothelioma (7%, NCT01639911), Irinotecan and Temozolomide against neuroblastoma (12.5%, NCT01601535), Oxaliplatin, Leucovorin, and Fluorouracil against colorectal cancer (8.3%, NCT02319018), and Fulvestrant against lobular ER+/PR+/HER2-breast cancer (22.2%, NCT02219789) [136–139]. Currently, several phase I/II trials are ongoing, namely, with lung cancer and mesothelioma patients treated with Alisertib as single agent (NCT02293005), with solid tumor patients in combination with Gemcitabine (NCT01924260), with breast cancer patients in combination with Paclitaxel (NCT02187991), and with solid tumor and breast cancer patients in combination with MLN0128 (NCT02719691). Additionally, other trials are recruiting participants for the treatment of head and neck squamous cell carcinoma and malignant solid neoplasm with Alisertib in combination with Pembrolizumab (NCT04555837), and non-small-cell lung cancer (NCT04479306) and EGFR-mutant lung cancer (NCT04085315) with Alisertib in combination with Pembrolizumab.

The clinical trial results of Alisertib against hematological tumors were also very promising. A phase I monotherapy study was conducted (NCT00697346). The recommended phase II dose was 50 mg twice a day for 7 days, followed by a recovery period of 14 days, in a 21-day cycle. The DLTs observed were mainly hematological, including neutropenia, febrile neutropenia, and thrombocytopenia, with 9% of patients who had their treatment discontinued due to AEs. However, Alisertib was generally well tolerated at the recommended phase II dose. In total, 27.6% of patients had SD as the best response, and six PRs (12.8%) were reported in patients with follicular lymphoma, multiple myeloma, peripheral T-cell lymphoma, and diffuse large B-cell lymphoma [140]. These results encouraged the use of Alisertib in a phase II study in patients with T-cell lymphoma as monotherapy (NCT01466881). Patients received the recommended phase II dose established in the previous study. The most common grade 3 or higher AEs were neutropenia, anemia, and thrombocytopenia. In total, 18.9% of patients had SD, and the best responses observed were two CRs (5.4%) and seven PRs (18.9%) [141]. Based on the efficacy results observed in this study, a phase III trial (NCT01482962) was conducted in patients with peripheral T-cell lymphoma, in which Alisertib efficacy as a single agent was evaluated and compared to a comparator (Pralatrexate, Gemcitabine, or Romidepsin). Despite the ORR with Alisertib being 33% (18 CRs and 16 PRs), it was not statistically significantly superior to the comparator arm [142]. However, objective responses were reported in other hematological tumors too. In a phase II trial with non-Hodgkin lymphoma patients treated with Alisertib as a single agent (NCT00807495), 10% of patients had CR and 17% had PR [143]. In a phase I/II trial conducted in patients with non-Hodgkin lymphomas (NCT01397825), treated with Alisertib in combination with Rituximab or with Rituximab plus Vincristine, 38% ORR was observed, including seven CRs and seven PRs [144]. Additionally, six PRs (23%) were observed in a phase I/II trial with multiple myeloma patients (NCT01034553) treated with Alisertib in combination with Bortezomib [145]. In a phase II trial in patients with AML (NCT02560025), treated with Alisertib combined with induction chemotherapy (Daunorubicin or Idarubicin plus Cytarabine), 51% of patients had CR and five CRi (13%) were also reported [146]. Currently, a phase I trial is ongoing in patients with non-Hodgkin lymphomas, with Alisertib in combination with Bortezomib and Rituximab (NCT01695941).

Table 4. Aurora B inhibitors in clinical trials <sup>1</sup>.

Compound	Clinical Trials	Current Status	Conditions	Interventions	Outcomes <sup>2</sup>	Refs.
 AZD1152 (Barasertib)	10 Clinical trials	Phase I/II 8 Completed 2 Terminated	Lymphoma, Advanced Solid Tumors, Acute Myeloid Leukemia	Monotherapy	Best response was CR for acute myeloid leukemia, and PR for lymphoma and acute myeloid leukemia	[112–119]
 BI-831266	NCT00756223	Phase I Completed	Advanced Solid Tumors	Monotherapy	Best response was CR and PR for acute myeloid leukemia in combination with low dose of Cytarabine, Venetoclax, Azacitidine	[121]
 BI-811283 (Structure Undisclosed)	NCT00701324 NCT00632749	Phase I Completed Phase II Completed	Solid Tumors Acute Myeloid Leukemia	Monotherapy Combination with Cytarabine	Best response was SD Best responses were CR, PR, and CRi	[123] [124]
 Chiauranib	7 Clinical trials	Phase I/II 2 Completed 1 Terminated 3 Recruiting/Planned 1 Ongoing	Ovarian Cancer, Non-Hodgkin's Lymphoma, Hepatocellular Carcinoma, Small Cell Lung Cancer, Other Advanced Solid Tumors	Monotherapy	Best response was SD	[126]

<sup>1</sup> Data collected from clinicaltrials.gov. <sup>2</sup> CR, complete remission; Cri, complete remission with incomplete blood count remission; PR, partial response; SD, stable disease.

Alisertib was also evaluated in children with solid and hematological tumors. A phase I trial was conducted in pediatric patients with solid tumors, with Alisertib as single agent (NCT02444884). Neutropenia was the most common DLT observed, and the MTD was established as 80 mg/m<sup>2</sup> once daily for 7 days followed by 2 weeks rest in a 21-day cycle. In total, 18% of patients had SD and one PR (3%) was reported in a patient with hepatoblastoma [147]. A phase II trial combined Alisertib with Paclitaxel in patients with solid tumors or leukemia (NCT01154816). The most common AEs were neutropenia, anemia, leukopenia, and thrombocytopenia. One CR (0.7%) and two PRs (1.5%) were observed in patients with neuroblastoma and another patient with Wilms tumor also had a CR [148]. Currently, a phase II trial using Alisertib as a single agent against rhabdoid tumor is recruiting participants (NCT02114229).

#### 4.3.2. ENMD-2076

ENMD-2076 is an orally administered AurA inhibitor with an IC<sub>50</sub> of 14 nM, and is also capable of inhibiting multiple tyrosine kinases in vitro [149]. ENMD-2076 entered eight phase I/II trials for the treatment of solid and hematological tumors, all as monotherapy. The first-in-human trial was conducted in patients with solid tumors (NCT00658671). MTD was established as 160 mg/m<sup>2</sup>, and the DLTs observed were neutropenia and hypertension. In total, 85% of patients achieved SD as the best response, and two PRs (3%) were reported in patients with platinum-refractory/resistant ovarian cancer [150]. These results prompted the conduction of two phase II studies with ENMD-2076 in patients with ovarian cancer. Overall, ENMD-2076 was well tolerated, with hypertension and diarrhea being the most common AEs in both studies. In the first trial (NCT01104675), with patients with platinum-refractory/resistant ovarian cancer, the majority of patients (52%) had progressive diseases, although five PRs (8%) were reported [151], whereas in the other study (NCT01914510), with patients with clear-cell ovarian cancer, 55% of patients achieved SD and two PRs (7.9%) were observed [152]. Additional objective responses were also observed in other tumors. A phase II trial was conducted in patients with soft tissue sarcoma (NCT01719744), in which 35% of patients had SD and two PRs (9%) were reported in patients with angiosarcoma and undifferentiated pleomorphic sarcoma [153]. In a phase II trial with triple-negative breast cancer patients (NCT01639248), 38.9% of patients had SD and two PRs (5.2%) were reported [154]. Furthermore, in a phase II trial with fibrolamellar carcinoma patients (NCT02234986), one PR (3%) was reported and 57% of patients had SD [155]. Additionally, ENMD-2076 entered two trials against hematological tumors. A phase I trial with patients with AML or chronic myelomonocytic leukemia was completed in 2011 (NCT00904787). MTD was established as 225 mg once a day, with typhilitis, fatigue, syncope, and QTc prolongation being the DLTs observed. The best response was observed in three patients who had CRi (19%) [156].

#### 4.3.3. LY3295668 (Erbumine)

LY3295668 is a potent AurA inhibitor with an IC<sub>50</sub> of 1.12 nM in vitro, and it has demonstrated antitumor activity in xenograft cancer models [80]. LY3295668 is the most recently tested inhibitor in clinical trials, with two trials completed. The first-in-human trial with LY3295668 as monotherapy was conducted in patients with solid tumors (NCT03092934). MTD was 25 mg twice a day, with diarrhea, corneal deposits, and mucositis being the DLTs observed. The best response was SD achieved in 69% of patients [157]. The other phase I/II study, with metastatic breast cancer patients, was completed in 2020; the results are yet to be announced (NCT03955939). Currently, a phase I trial is ongoing for the treatment of small-cell lung cancer (NCT03898791) with LY3295668 as monotherapy, and another phase I study with LY3295668 in combination with Topotecan and Cyclophosphamide in patients with neuroblastoma is recruiting participants (NCT04106219).

#### 4.3.4. MLN8054

MLN8054, from Millennium Pharmaceuticals, inhibits AurA with an  $IC_{50}$  of 4 nM in vitro [158]. The first-in-human trial was conducted with patients with solid tumors (NCT00249301), in which MLN8054 was given orally for 7, 14, or 21 days, followed by a 14-day recovery period. The MTD was 60 mg, with the most common DLT observed being somnolence. No objective responses were observed, and 15% of patients had SD as the best response [159]. In another phase I trial with patients with solid tumors (NCT00652158), the efficacy outcomes were similar, in which the best response observed was SD [160].

#### 4.3.5. MK-5108 (VX-689)

MK-5108, from Merck Sharp & Dohme, is a highly potent AurA inhibitor with an  $IC_{50}$  of 0.064 nM in vitro [161]. A phase I trial was conducted in patients with solid tumors, in which MK-5108 was given as single agent and in combination with Docetaxel (NCT00543387). Its MTD as a single agent was not established because no patients experienced a DLT, whereas the MTD of the combinational treatment was 300 mg/day. Overall, the drug-related AEs were mainly blood and lymphatic system disorders. No objective responses were reported with MK-5108 as a single agent. However, a PR (5.9%) was observed in a patient who received 450mg/day and a standard dose of Docetaxel [162].

#### 4.3.6. TAS-119

TAS-119, developed by Taiho Oncology, is a potent AurA inhibitor with an  $IC_{50}$  of 1 nM in vitro [163]. The first-in-human phase I study with TAS-119 as monotherapy was conducted in patients with solid tumors (NCT02448589). The MTD was established as 250 mg twice a day, with fatigue, pain, and diarrhea being the most common AEs observed. No objective responses were observed, and 35% of patients had SD as the best response [164]. In a phase I trial for the treatment of solid tumors, TAS-119 was given in combination with Paclitaxel (NCT02134067). The MTD was established as 80 mg/m<sup>2</sup> of Paclitaxel with 75 mg of TAS-119 twice a day. Neutropenia and elevated AST were the DLTs observed. In total, 45% of patients had SD, and four PRs (15.4%) were reported in patients with ovarian/fallopian tube cancers [165].

#### 4.3.7. KW-2449

KW-2449, developed by Kyowa Kirin Pharmaceutical Development, is a multikinase inhibitor, active against AurA with an  $IC_{50}$  of 48 nM in vitro [166]. KW-2449 entered two phase I trials with patients with hematological tumors. However, both were terminated due to a suboptimal dosing schedule and failure to identify a tolerable dose that had potential efficacy (NCT00346632 and NCT00779480).

Table 5. Aurora A kinase-specific inhibitors in clinical trials <sup>1</sup>.

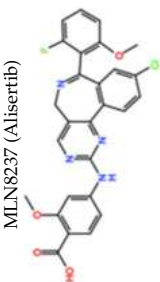
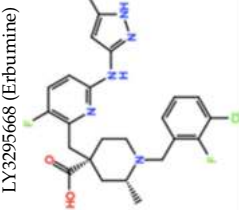
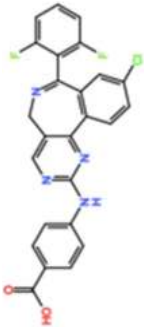
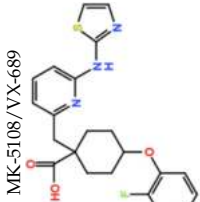
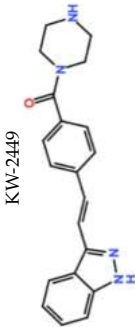
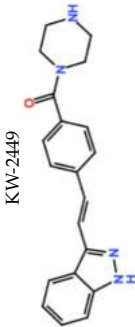
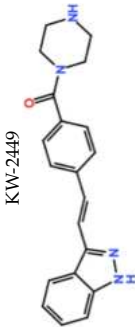
Compound	Clinical Trials	Current Status	Conditions	Interventions	Outcomes <sup>2</sup>	Refs.
 MLN8237 (Alisertib)	53 Clinical trials	Phase I/II 38 completed 7 terminated 4 ongoing 4 recruiting	Advanced Hematological Malignancies, Advanced Solid Tumors, Lymphoma, Prostate Cancer, Ovarian, Fallopian Tube and Peritoneal Carcinoma, Leiomyosarcoma, Neuroblastoma, Acute Myeloid Leukemia, Mantle Cell Lymphoma, Burkitt's Lymphoma, Breast Carcinoma, Glioma, Non-Hodgkin's Lymphoma, Bladder Cancer, Non-Small-Cell Lung Cancer, Mesothelioma, Small-Cell Lung Cancer, Adenocarcinoma, Melanoma, Head and Neck Squamous Cell Carcinoma, EGFR-mutant Lung Cancer, Rhabdoid Tumor	Monotherapy  Combination with Pazopanib, Bortezomib, Docetaxel, Irinotecan, Temozolomide, Daunorubicin, Idarubicin, Cytarabine, Rituximab, Vincristine, Paclitaxel, Oxaliplatin, Leucovorin, Fluorouracil, Etoposide, Rifampin, Fulvestrant, Itraconazole, Idarubicin, Cytarabine, Vorinostat, MLN0128, Abiraterone Acetate, Prednisone, Erlotinib, Gemcitabine, Pembrolizumab, Osimertinib, Romidepsin, Bortezomib	Best responses were CR for neuroblastoma, Wilms tumor, non-Hodgkin's lymphoma, and acute myeloid leukemia; PR for lymphoma, multiple myeloma, angiosarcoma, ovarian cancer, prostate cancer, hepatoblastoma, neuroblastoma, non-Hodgkin's lymphoma, and acute myeloid leukemia  Best responses were CR for multiple myeloma in combination with Bortezomib, ovarian cancer in combination with Paclitaxel acute myeloid leukemia in combination with Daunorubicin, Idarubicin, and Cytarabine, refractory aggressive B-cell lymphoma in combination with Rituximab and Vincristine, small-cell lung cancer in combination with Paclitaxel; PR for urothelial cancer in combination with Paclitaxel, breast cancer in combination with Pazopanib, Fulvestrant and Paclitaxel, mesothelioma in combination with Pazopanib, multiple myeloma in combination with Bortezomib, angiosarcoma in combination with Docetaxel, castration-resistant prostate cancer in combination with Docetaxel, neuroblastoma in combination with Temozolomide, acute myeloid leukemia in combination with Daunorubicin, Idarubicin, and Cytarabine, refractory aggressive B-cell lymphoma in combination with Rituximab and Vincristine, ovarian cancer in combination with Paclitaxel, colon and Fluorouracil, small-cell lung cancer in combination with Paclitaxel	[128–141,143,144,144–148]
 MLN8237 (Alisertib)	NCT01482962	Phase III Completed	Relapsed/Refractory Peripheral T-Cell Lymphoma	Monotherapy	Best responses were CR and PR	[142]
 ENMD-2076	8 Clinical trials	Phase I/II Completed	Soft Tissue Sarcoma, Ovarian Cancer, Triple-Negative Breast Cancer, Relapsed or Refractory Hematological Malignancies, Advanced Fibrolamellar Carcinoma, Multiple Myeloma, Advanced Malignancies	Monotherapy	Best response was PR for ovarian cancer, triple-negative breast cancer, advanced fibrolamellar carcinoma, undifferentiated pleomorphic sarcoma, and angiosarcoma; and CR for relapsed or refractory hematological malignancies	[150–156,167]

Table 5. Cont.

Compound	Clinical Trials	Current Status	Conditions	Interventions	Outcomes <sup>2</sup>	Refs.
 LY3295668 (Eribudine)	4 Clinical trials	Phase I/II 2 Completed 1 Recruiting 1 Planned	Small-Cell Lung Cancer, Metastatic Breast Cancer, Neuroblastoma, Solid Tumors	Monotherapy Combination with Topotecan and Cyclophosphamide	Best response was SD	[157]
 MLN8054	NCT00249301	Phase I Terminated	Solid Tumors	Monotherapy	Best response was SD	[159]
 MK-5108/VX-689	NCT00652158	Phase I Terminated	Advanced Malignancies	Monotherapy	Best response was SD	[160]
 TAS-119 (Structure Undisclosed)	NCT00543387	Phase I Completed	Solid Tumors	Monotherapy	Best response was SD	[162]
 KW-2449	NCT02448589	Phase I Terminated	Advanced Solid Tumors	Monotherapy	Best response was SD	[164]
	NCT02134067	Phase I Terminated	Advanced Solid Tumors	Combination with Docetaxel	Best response was PR	[165]
 KW-2449	NCT00346632	Phase I Terminated	Acute Leukemias Myelodysplastic Syndromes—Chronic Myelogenous Leukemia	Monotherapy	Terminated due to suboptimal dosing schedule	-
	NCT00779480	Phase I Terminated	Acute Myelogenous Leukemia	Monotherapy	Failure to demonstrate a tolerable dose that had potential for efficacy	-

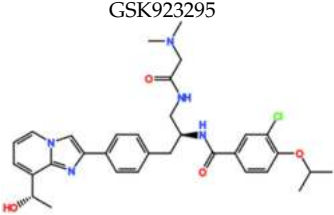
<sup>1</sup> Data collected from clinicaltrials.gov. <sup>2</sup> CR, complete remission; Cri, complete remission with incomplete blood count remission; PR, partial response; SD, stable disease.

In summary, considering all Aurora inhibitors, either those with broad-spectrum or with selective activity, the AEs observed were mainly hematological, primarily neutropenia, which was manageable through G-CSF support. As to pan-Aurora inhibitors, the majority of small molecules were used as monotherapy and demonstrated a poor or modest efficacy in solid and hematological tumors, except for the clinical trials with Cenisertib and Tozasertib, in which CRs were reported in patients with leukemia. CRs in leukemia patients were also observed with Ilorasertib in combination with Azacitidine. Similar efficacy results were observed with the AurB-selective inhibitors. The best responses were achieved in patients with AML with Barasertib as monotherapy and in combination with Cytarabine, while in patients with solid tumors, all inhibitors showed modest efficacy. AurA inhibitors have demonstrated better responses in patients with solid tumors comparatively to AurB and pan-Aurora inhibitors, especially with Alisertib. Even so, the efficacy outcomes of AurA inhibitors were better in hematological tumors than in solid tumors. There is a substantial debate as to whether it is more efficient to inhibit AurA, AurB, or both simultaneously. A pre-clinical study in pancreatic cancer cells has pointed to AurA as a better target than AurB [168]. However, another pre-clinical study has demonstrated that colon cancer cells were more sensitive to AurB inhibition compared to AurA [78]. In fact, the molecule with better efficacy outcomes in trials was the AurA inhibitor Alisertib, but both strategies have demonstrated antitumor activity, especially against hematological tumors. Perhaps, some tumors may be more sensitive to inhibition of one of the two kinases, but further studies are required to address this question. An important aspect of Aurora kinase inhibition is the existence of biomarkers that permit access to its cellular activity, such as histone H3 phosphorylation or autophosphorylation on T288 of AurA, enabling one to verify whether the inhibitors are efficiently targeting the kinases [169]. In sum, either AurA or AurB inhibition seem to be sustainable approaches for cancer therapy that could be improved in combination with other drugs.

## 5. CENP-E Kinesin

Centromere-associated protein E (CENP-E) is a plus end-directed motor protein that plays a crucial role in cytokinesis, chromosome congression and alignment, and in SAC signaling through modulation of BubR1 function [170–172]. Inhibition of CENP-E results in mitotic arrest due to unaligned chromosomes, which activates the SAC and has demonstrated antitumor activity in human cancer models [173–175]. Some CENP-E inhibitors have been tested in pre-clinical studies, but only one small molecule, GSK923295, has reached clinical trials (Figure 1 and Table 6). GSK923295 is an allosteric inhibitor of CENP-E with an  $IC_{50}$  of 1.6 nM in vitro [176]. In the phase I trial (NCT00504790), the MTD was established as 190 mg/m<sup>2</sup> [177]. GSK923295 was generally well tolerated; the most common AEs were fatigue, diarrhea, and decreased appetite. Five patients (12.8%) experienced DLTs such as increase in aspartate aminotransferase (AST), fatigue, hypoxia, and hypokalemia [177]. Antitumor activity was modest, and the best response was one PR (3%) in a patient with urothelial carcinoma treated with a dose above the MTD (250 mg/m<sup>2</sup>), and 33% had SD [177]. More studies are needed to overcome the challenges of using the CENP-E inhibition approach, in order to develop novel CENP-E inhibitors and to test combinational treatments with other drugs for possible synergistic effects.

**Table 6.** CENP-E inhibitors in clinical trials <sup>1</sup>.

Compound	Clinical Trials	Current Status	Conditions	Interventions	Outcomes <sup>2</sup>	Ref.
 GSK923295	NCT00504790	Phase I Completed	Refractory Cancer	Monotherapy	Best response was PR for urothelial carcinoma	[177]

<sup>1</sup> Data collected from clinicaltrials.gov. <sup>2</sup> PR, partial response.

## 6. Eg-5 Kinesin

Eg-5 kinesin is a plus end-directed motor protein that plays a critical role in bipolar spindle assembly [178,179]. The inhibition of Eg-5 results in monopolar spindles, which leads to SAC activation and mitotic arrest, and has demonstrated antitumor activity in human xenografts models [180–182]. Together with its overexpression in several tumors, this makes Eg-5 an attractive target for cancer therapy [183–186]. Conversely to the kinesin CENP-E, ten Eg-5 inhibitors have reached clinical trials: 4SC-205, ARRY-520 (Filanesib), AZD4877, MK-0731, SB-715992 (Ispinesib), LY2523355 (Litronesib), SB-743921, EMD 534085, ARQ 621, and ALN-VSP02 (Figure 1 and Table 7). Forty-five phase I/II trials against solid and hematological tumors, in monotherapy or in combinational treatments, have been completed or terminated.

### 6.1. SB-715992 (Ispinesib) and SB-743921

Ispinesib, developed by Cytokinetics and GlaxoSmithKline, was the first Eg-5 inhibitor to enter clinical trials. Thirteen studies have been completed or terminated as monotherapy against solid and hematological tumors, and three phase I/II trials in combination with Docetaxel (NCT00169520), Capecitabine (NCT00119171), and Carboplatin (NCT00136578) against solid tumors have also been completed [187–189]. In the phase I study in combination with Docetaxel, the MTD was established as 10 mg/m<sup>2</sup> of Ispinesib and 60 mg/m<sup>2</sup> of Docetaxel; prolonged neutropenia and febrile neutropenia were the DLTs observed, although the safety profile was considered acceptable and manageable [187]. Similar results were obtained with Carboplatin and Capecitabine, in which the best response was SD, and the DLTs observed were thrombocytopenia and neutropenia, respectively [188,189]. The efficacy outcomes with Ispinesib as monotherapy in patients with liver cancer (NCT00095992), metastatic prostate cancer (NCT00096499), recurrent or metastatic squamous cell carcinoma of the head and neck (NCT00095628), melanoma (NCT00095953), and metastatic kidney cancer (NCT00354250) were also disappointing, with SD being the best response [190–194]. Better results, although modest, were reported from trials against ovarian cancer (NCT00097409) and breast cancer (NCT00607841), in which PRs were observed in 5% and 6.7% of patients, respectively [195,196]. Additionally, a phase I trial on pediatric patients with relapsed or refractory solid tumors has also been initiated with Ispinesib as monotherapy (NCT00363272). Similarly to the previous studies, Ispinesib was well tolerated, but no objective responses were observed, and only three SDs (12.5%) were reported [197].

Meanwhile, another small molecule derived from Ispinesib, SB-743921, was discovered, which exhibited a five-fold increase in potency against Eg-5 compared to Ispinesib, and reached two phase I/II trials, both already completed [198]. In the first-in-human trial (NCT00136513) in patients with solid tumors as monotherapy, the MTD was established as 4 mg/m<sup>2</sup>, and neutropenia was the most common DLT registered. Six patients (15%) showed SD as the best response and a PR was reported in a patient (2.3%) with cholangiocarcinoma [199]. In another phase I/II trial with non-Hodgkin lymphoma and Hodgkin lymphoma patients (NCT00343564), it was reported that DLT and MTD were significantly increased when SB-743921 was co-administered with G-CSF [200]. In this study, four PRs (7.1%) were reported: in three patients with Hodgkin lymphoma, and in one patient with non-Hodgkin lymphoma [200].

### 6.2. ARRY-250 (Filanesib)

Filanesib is a potent Eg-5 inhibitor with an IC<sub>50</sub> of 6 nM in vitro [201]. Eight phase I/II studies have been completed in patients with solid and hematological tumors. In the phase I trial (NCT00462358) with patients with solid tumors as monotherapy or with G-CSF support (Filgrastim), the MTD was defined as 1.25 mg/m<sup>2</sup> without prophylactic Filgrastim, and as 1.60 mg/m<sup>2</sup> in combination with Filgrastim [202]. Filanesib was observed to cause myelosuppression, with the most common treatment-related AEs being febrile neutropenia, neutropenia, leukopenia, and thrombocytopenia [202]. No objective responses were



reported and 18% of patients achieved SD as best response [202]. In another monotherapy phase I/II trial in AML patients (NCT00637052), hematological toxicities were the most common AEs. SD was observed in 10% of patients and one PR (3%) was reported [203]. The most promising outcomes were reported in patients with multiple myeloma. The first phase I/II trial with patients with multiple myeloma started in 2009 (NCT00821249) to assess the safety profile and efficacy of Filanesib. Based on the myelosuppression reported in previous studies, G-CSF (Filgrastim) was added to the treatment regimen during phase I and II [204]. In phase II, patients were treated with Filanesib as monotherapy (including G-CSF support), or in combination with low doses of Dexamethasone. As a single agent, 39% of patients had SD and five PRs (16%) were reported, whereas in combination with Dexamethasone, 41% of patients achieved SD and eight PRs (15%) were observed [204]. These results prompted the use of Filanesib in more trials in patients with multiple myeloma in combination with the proteasome inhibitors Bortezomib and Carfilzomib. In a phase I trial (NCT01248923), Filanesib was administered in combination with Bortezomib and Dexamethasone (including G-CSF support). The safety profile was considered favorable and the hematological toxicities were manageable through G-CSF support [205]. The overall response rate (ORR) was 20%, including one CR (2%) and ten PRs (18%) [205]. In another phase I trial (NCT01372540), Filanesib was administered in combination with Carfilzomib and Dexamethasone, and G-CSF support was also included. Overall, no CR was reported, although twenty-three PRs (37%) were observed [206]. Additionally, in another phase I/II trial (NCT02384083), Filanesib was combined with Pomalidomide and Dexamethasone, and G-CSF support was also included. Despite the G-CSF support, more than 60% of the patients developed grade 3/4 neutropenia; nevertheless, the efficacy results were promising with an ORR of 51%, including two CRs (4%) and twenty-one PRs (47%) [207]. Considering these good results, Filanesib will likely enter a phase III trial against multiple myeloma.

### 6.3. ALN-VSP02

ALN-VSP02 is unique among the anti-Eg-5 as it is an siRNA lipid nanoparticle formulation targeting the expression of Eg-5 and vascular endothelial growth factor (VEGF) [208]. Two phase I trials were completed with patients with solid tumors as monotherapy (NCT01158079 and NCT00882180). Patients were enrolled sequentially on one of seven dose levels, ranging from 0.1 to 1.5 mg/kg. ALN-VSP02 demonstrated a safety profile at multiple doses, with fatigue, asthenia, nausea, vomiting, and fever being the most common AEs. The best response was a CR (2.7%) observed in a patient with endometrial cancer with multiple hepatic metastases [209].

### 6.4. Litronesib

Litronesib, developed by Kyowa Kirin and Eli Lilly and Company, was demonstrated to inhibit Eg-5 with an  $IC_{50}$  of 26 nM in vitro [210]. At least seven phase I/II trials were completed, involving solid tumor patients treated with Litronesib as monotherapy or with G-CSF support (Pegfilgrastim and Filgrastim). Generally, the efficacy results were disappointing. In two phase I trials in advanced tumor patients (NCT01214629 and NCT01214642), Litronesib was administered as single agent or in combination with Pegfilgrastim. In the first-in-human study with Litronesib (NCT01214629), the MTD was 4 mg/m<sup>2</sup> for Litronesib without G-CSF support, and 6 mg/m<sup>2</sup> with Pegfilgrastim. Neutropenia and leukopenia were the most common AEs observed. In total, 26% of patients had SD as the best response, and two PRs (3.7%) were reported in patients with platinum-sensitive ovarian carcinoma and neuroendocrine carcinoma [211], whereas in the other trial (NCT01214642), the safety profile was similar, but no objective responses were observed, with 36.5% of patients achieving SD as the best response [211]. Additionally, another study with Litronesib as monotherapy in patients with solid tumors was initiated in 2011 (NCT01358019). Again, the best response was SD observed in two patients (16.7%) [212].

No further development is planned for this Eg-5 inhibitor, since Kyowa Kirin and Eli Lilly and Company decided to discontinue Litronesib.

#### 6.5. EMD 534085

EMD 534085 was developed by Merck-KGaA and was shown to inhibit Eg-5 with an  $IC_{50}$  of 8 nM in vitro [213]. EMD 534085 entered a phase I trial in patients with solid tumors or lymphoma as a single agent. The MTD was defined as 108 mg/m<sup>2</sup> and neutropenia was the most common DLT observed. No objective responses were reported, with 52% of patients achieving SD [214]. No further development is planned with this inhibitor.

#### 6.6. SC-205

4SC-205, developed by 4SC, has entered a phase I study against advanced malignancies as monotherapy (NCT01065025). Patients received 4SC-205 once a week or twice weekly. The MTD was defined as 150 mg/m<sup>2</sup> (once weekly) and 75 mg/m<sup>2</sup> (twice weekly). Neutropenia was the most common DLT, similarly to the results obtained with the other Eg-5 inhibitors. No CR or PR were reported, and 28% of patients had SD as the best response [215].

#### 6.7. AZD4877

AZD4877, from AstraZeneca, inhibits Eg-5 with an  $IC_{50}$  of 2 nM in vitro, and has entered six phase I/II trials against solid and hematological tumors [216]. Overall, the results were disappointing. In the phase I trials in solid tumor patients (NCT00613652 and NCT00389389), neutropenia was the most common DLT [217,218]. No objective responses were observed, with 31% and 27% of patients achieving SD, respectively [217,218]. Other trials with AML (NCT00486265) and urothelial cancer (NCT00661609) patients demonstrated similar efficacy. In the phase I trial, all AML patients had treatment failure, whereas in the phase II study with urothelial cancer patients, 18% of patients had SD, and no objective responses were reported [219,220]. No further development is planned for AZ4877.

#### 6.8. ARQ 621

ARQ 621, from ArQule, demonstrated a broad spectrum toxicity against a panel of human cancer cell lines [221]. In 2009, ARQ 621 entered a phase I trial with solid tumor patients as monotherapy (NCT00825487). ARQ 621 appeared to be well tolerated at a dose of 280 mg/m<sup>2</sup>, with the most common AEs being fatigue, nausea, and anemia. No objective responses were observed, with 12.5% of patients achieving SD as the best response [222]. No further development is planned for this compound.

#### 6.9. MK-0731

MK-0731, developed by Merck Sharp & Dohme, inhibits Eg-5 with an  $IC_{50}$  of 2.2 nM in vitro [223]. MK-0731 has entered a phase I trial against advanced solid tumors as monotherapy in 2005 (NCT00104364). The MTD was determined as 17 mg/m<sup>2</sup>, neutropenia being the major DLT observed [224]. No objective responses were reported and only four patients (4.3%) achieved SD [224]. Development of MK-0731 has been halted.

The safety outcomes of the Eg-5 inhibitors were similar to those of Mps1, Plk1, and Aurora kinase inhibitors, with neutropenia as the most common AE. Generally, Eg-5 inhibitors exhibited poor or modest efficacy in patients with solid tumors, either as monotherapy or in combinational treatments, except for a CR observed with ALN-VSP02 as a single agent in a patient with endometrial cancer with multiple hepatic metastases. The most promising efficacy results were achieved with Filanesib in multiple myeloma patients, especially when combined with the proteasome inhibitors Bortezomib and Carfilzomib. It is expected that Filanesib will enter phase III trials. One possible explanation for the promising results of Filanesib is its better pharmacokinetic profile, primarily a higher half-life compared to the other Eg-5 inhibitors. More studies must be performed to assess which drugs demonstrate synergistic effects with Eg-5 inhibitors, as well as to identify novel and more potent inhibitors with a better pharmacokinetic profile, in order to improve the efficacy of the Eg-5 inhibition-based therapeutic approach.

Table 7. Eg-5 inhibitors in clinical trials <sup>1</sup>.

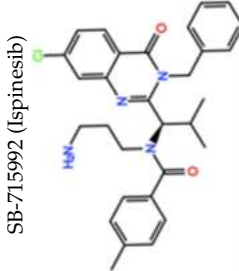
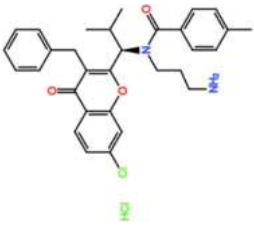
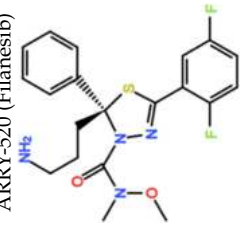
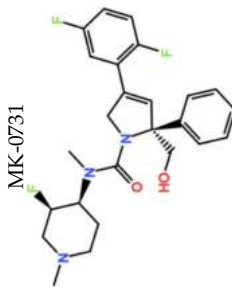
Compound	Clinical Trials	Current Status	Conditions	Interventions	Outcomes <sup>2</sup>	Refs.
SB-715992 (Ispinesib) 	16 Clinical trials	Phase I/II 14 Completed 2 Terminated	Metastatic Prostate, Kidney and Colorectal Cancer, Recurrent or Metastatic Squamous Cell Carcinoma of the Head and Neck, Breast, Ovarian and Liver Cancer, Melanoma, Hodgkin's or Non-Hodgkin's Lymphoma, Acute Leukemia Advanced Myelodysplastic Syndromes	Monotherapy  Combination with Docetaxel, Capecitabine and Carboplatin	Best response was a PR for ovarian and breast cancer  Best response was SD	[190–197]
SB-743921 	NCT00136513	Phase I Completed	Solid Tumors	Monotherapy	Best response was PR for cholangiocarcinoma	[199]
ARRY-520 (Filanesib) 	8 Clinical trials	Phase I/II Completed	Non-Hodgkin Lymphoma and Hodgkin Lymphoma  Multiple Myeloma, Advanced/Refractory Myeloid Leukemia, Advanced Solid Tumors	Monotherapy  Combination with Pomalidomide, Dexamethasone, Carfilzomib, Filgrastim, Bortezomib, Carfilzomib	Best response was PR for non-Hodgkin lymphoma  Best responses were a PR for multiple myeloma in combination with Pomalidomide, Bortezomib, Dexamethasone, and Filgrastim; PR for multiple myeloma in combination with Bortezomib, Pomalidomide, Dexamethasone, Filgrastim, and Carfilzomib	[200]  [202–207]
ALN-VSP02 (siRNA)	NCT01158079  NCT00882180	Phase I Completed  Phase I Completed	Solid Tumors	Monotherapy	Best response was CR for endometrial cancer with multiple hepatic metastases	[209]

Table 7. Cont.

Compound	Clinical Trials	Current Status	Conditions	Interventions	Outcomes <sup>2</sup>	Refs.
LY2523355 (Litronesib) 	7 Clinical trials	Phase I/II 6 Completed 1 Terminated	Metastatic Breast Cancer, Metastatic and/or Advanced Cancer, Acute Leukemia, Small Cell Lung Cancer	Monotherapy, Combination with Pegfilgrastim, and Filgrastim	Best response was PR for non-small-cell lung cancer, ovarian and neuroendocrine carcinomas, and breast cancer in combination with Pegfilgrastim	[211,212]
EMD 534085 	Unknown	Phase I	Advanced Solid Tumors, Lymphoma	Monotherapy	Best response was SD	[214]
4SC-205 (Structure Undisclosed) AZD4877 	NCT01065025  6 Clinical trials	Phase I Completed  Phase I/II 3 Completed 3 Terminated	Advanced Malignancies  Bladder Cancer, Transitional Cell Bladder Cancer, Urethra Cancer, Ureter Cancer, Renal Pelvis Cancer, Acute Myelogenous Leukemia, Non-Hodgkin Lymphoma	Monotherapy  Monotherapy	Best response was SD  Best response was SD for non-Hodgkin lymphoma, acute myeloid leukemia, and urothelial cancer	[215]  [217–220,225]
ARQ 621 	NCT00825487	Phase I Completed	Metastatic Solid Tumors, Refractory/Relapsed Hematologic Malignancies	Monotherapy	Best response was SD	[222]

Table 7. Cont.

Compound	Clinical Trials	Current Status	Conditions	Interventions	Outcomes <sup>2</sup>	Refs.
 <p>MK-0731</p>	NCT00104364	Phase I Completed	Advanced Solid Malignancies	Monotherapy	Best response was SD for non-small-cell lung cancer, cervical and ovarian cancer	[224]

<sup>1</sup> Data collected from [clinicaltrials.gov](http://clinicaltrials.gov). <sup>2</sup> CR, complete remission; PR, partial response; SD, stable disease.

## 7. Conclusions and Perspectives

MTAs were the first class of antimetabolites that demonstrated clinical benefits in cancer patients. However, several tumors have developed resistance, which, together with the neurological and myeloid toxicity provoked by these agents, has led to the search for and development of alternative approaches to block mitosis. Our increased knowledge on mitotic events has provided an opportunity to identify key mitotic proteins that could be targeted for cancer therapy. As described in this review, several inhibitors, known as second-generation antimetabolites (SGAs), were identified for Mps1, Aurora kinases, Plk1, Eg-5, and, to a lesser extent, CENP-E, and these have reached clinical trials.

Among all SGAs tested, the most promising molecules are (i) the Plk1 inhibitors Volasertib and Rigosertib, which demonstrated good efficacy results in AML and MDS patients, respectively; (ii) the AurB inhibitor Barasertib for patients with AML; (iii) the AurA inhibitor Alisertib, which has demonstrated antitumor activity against several solid and hematological tumors; (iv) the pan-Aurora inhibitors Ilorasertib and Cenisertib for patients with AML; and (v) the Eg-5 inhibitor Filanesib for patients with multiple myeloma. However, many AEs were reported. The most common AEs associated with these SGAs were hematological, primarily neutropenia. These results were somehow expected given the high proliferation rate of the bone marrow cells [226]. In the same line of thought, better responses were achieved in patients with hematological tumors than in those with solid cancers, in concordance with the lower proliferation rate observed in solid tumors, compared to hematological cancers [226].

Until now, no small molecule has been approved for clinical use, and MTAs still remain the antimetabolite agents with the best therapeutic benefit. While SGAs target individual proteins, MTAs destabilize the huge microtubule/cytoskeleton network involved in the dynamics of several proteins and organelles, thereby indirectly affecting their function. This could be a plausible explanation for the MTAs' therapeutic success, compared to SGAs. Interestingly, better responses were achieved in combinational treatments than with SGAs as monotherapy. Several studies reported the synergistic effects of different SGAs with many drugs such as MTAs or platinum-based agents. Therefore, combinational treatment represents a solid strategy for achieving better therapeutic effectiveness, while decreasing drug dosage and minimizing AEs and resistance.

From an SAC response point of view, the SGAs are divided into two groups [11,227]. The mitotic blockers, which include the inhibitors of CENP-E, Eg-5, and Plk1, activate the SAC, thereby inducing a prolonged mitotic delay that is expected to culminate in cell death. The mitotic drivers, which include the inhibitors of Mps1 and Aurora B kinase, override the SAC and induce premature mitotic exit with extensive chromosome missegregation, resulting in chromosome aberrations that are incompatible with the cell viability of daughter cells. Thus, it seems reasonable to use both approaches for cancer therapy. Yet, some challenges need to be overcome. There is profound inter- and an intra-variability in terms of cell fates following the prolonged mitotic arrest of cancer cells treated with mitotic blockers [228]. Prolonged mitotic arrest can result in cell death in mitosis, or mitotic slippage (also known as checkpoint adaptation), in which cells exit mitosis without cell division and return to the interphase as tetraploid cells. These cells can undergo cell cycle arrest, die, or re-replicate their genomes and endocycle [228]. Slippage is one of the resistance mechanisms against antimetabolite drugs.

On the other hand, mitotic drivers can fuel genomic instability. In case of the incomplete inhibition of mitotic driver targets, which is more likely to occur *in vivo* than *in vitro*, chromosome segregation errors may be generated below the threshold required to kill cancer cells, which, theoretically, increases genomic instability, thereby fueling malignancy. This may explain the general failure of both mitotic blockers and mitotic drivers in clinical trials when used as monotherapy. Nonetheless, despite their poor clinical activity as single agents, SGAs may be valuable for synthetic lethal combinations intended to selectively target cancer cells, thus decreasing the risk of mitotic slippage, while enhancing the therapeutic window.

SGAs exhibited promising antitumor activity in pre-clinical studies, but failed in clinical trials. A possible reason for this differential antitumor activity is that two-dimensional (2D) cultures lack cell–cell contacts and a natural tumor microenvironment, which are important in tumor signaling and drug response [229]. Using preclinical models that better mimic the tumor microenvironment, such as patient-derived 3D tumors, should increase the predictive value of pre-clinical antimetabolic research, helping in anticipating clinical outcomes [230].

The most common AEs observed in patients treated with SGA were related to hematologic dysfunction. The development of drug-delivery systems could be a valuable approach to overcome this issue, facilitating better targeting towards cancer cells and in-tumor drug retention, while increasing the therapeutic window [231].

Patients with the same tumor type respond differently to the same agents, probably due to different genetic and/or epigenetic modifications that alter the sensitivity to a specific drug [232,233]. Thus, patient stratification using predictive biomarkers, together with an in-depth understanding of the mechanisms by which SGAs kill cancer cells, should pave the way to their effective clinical use.

**Author Contributions:** Review topic and general structure, H.B.; data collection, P.N., writing the review draft, P.N. and H.B.; discussions, revising of text and generation of final version, P.N., P.M.A.S., I.A., and H.B.; preparation of the figures and tables, P.N. and P.M.A.S.; funding acquisition, H.B. All authors have read and agreed to the published version of the manuscript.

**Funding:** This work was funded by CESP—Cooperativa de Ensino Superior Politécnico e Universitário, under the projects “AntiMitoSphere\_APSFCT\_IINFACTS\_2021” and “ActivCHIRAL\_PI2RL\_IINFACTS\_2021”.

**Institutional Review Board Statement:** Not applicable.

**Informed Consent Statement:** Not applicable.

**Data Availability Statement:** Publicly available datasets were analyzed in this study. The data can be found here: [https://clinicaltrials.gov/].

**Conflicts of Interest:** The authors declare no conflict of interest.

## References

1. Lim, S.; Kaldis, P. Cdks, cyclins and CKIs: Roles beyond cell cycle regulation. *Development* **2013**, *140*, 3079–3093. [CrossRef] [PubMed]
2. Hanahan, D.; Weinberg, R.A. Hallmarks of Cancer: The Next Generation. *Cell* **2011**, *144*, 646–674. [CrossRef] [PubMed]
3. Compton, D.A. Mechanisms of Aneuploidy. *Curr. Opin. Cell Biol.* **2011**, *23*, 109–113. [CrossRef] [PubMed]
4. Silva, P.; Barbosa, J.; Nascimento, A.V.; Faria, J.; Reis, R.; Bousbaa, H. Monitoring the fidelity of mitotic chromosome segregation by the spindle assembly checkpoint. *Cell Prolif.* **2011**, *44*, 391–400. [CrossRef]
5. Van Vuuren, R.J.; Visagie, M.H.; Theron, A.E.; Joubert, A.M. Antimitotic drugs in the treatment of cancer. *Cancer Chemother. Pharm.* **2015**, *76*, 1101–1112. [CrossRef]
6. Jordan, M.A.; Wilson, L. Microtubules as a target for anticancer drugs. *Nat. Rev. Cancer* **2004**, *4*, 253–265. [CrossRef]
7. Matson, D.R.; Stukenberg, P.T. Spindle Poisons and Cell Fate: A Tale of Two Pathways. *Mol. Interv.* **2011**, *11*, 141. [CrossRef]
8. Brito, D.A.; Rieder, C.L. Mitotic Checkpoint Slippage in Humans Occurs via Cyclin B Destruction in the Presence of an Active Checkpoint. *Curr. Biol.* **2006**, *16*, 1194–1200. [CrossRef]
9. Nakayama, Y.; Inoue, T. Antiproliferative fate of the tetraploid formed after mitotic slippage and its promotion; a novel target for cancer therapy based on microtubule poisons. *Molecules* **2016**, *21*, 663. [CrossRef]
10. Dumontet, C.; Jordan, M.A. Microtubule-binding agents: A dynamic field of cancer therapeutics. *Nat. Rev. Drug Discov.* **2010**, *9*, 790–803. [CrossRef]
11. Henriques, A.C.; Ribeiro, D.; Pedrosa, J.; Sarmento, B.; Silva, P.M.A.; Bousbaa, H. Mitosis inhibitors in anticancer therapy: When blocking the exit becomes a solution. *Cancer Lett.* **2019**, *440*, 64–81. [CrossRef]
12. Lauzé, E.; Stoelcker, B.; Luca, F.C.; Weiss, E.; Schutz, A.R.; Winey, M. Yeast spindle pole body duplication gene MPS1 encodes an essential dual specificity protein kinase. *EMBO J.* **1995**, *14*, 1655–1663. [CrossRef]
13. Ji, Z.; Gao, H.; Jia, L.; Li, B.; Yu, H. A sequential multi-target Mps1 phosphorylation cascade promotes spindle checkpoint signaling. *Elife* **2017**, *6*. [CrossRef]
14. Liu, X.; Winey, M. The MPS1 family of protein kinases. *Annu. Rev. Biochem.* **2012**, *81*, 561–585. [CrossRef]

15. Yang, H.; Zhang, F.; Huang, C.-J.; Liao, J.; Han, Y.; Hao, P.; Chu, Y.; Lu, X.; Li, W.; Yu, H.; et al. Mps1 regulates spindle morphology through MCRS1 to promote chromosome alignment. *Mol. Biol. Cell* **2019**, *30*, 1060–1068. [CrossRef]
16. Maciejowski, J.; Drechsler, H.; Grundner-Culemann, K.; Ballister, E.R.; Rodriguez-Rodriguez, J.-A.; Rodriguez-Bravo, V.; Jones, M.J.K.; Foley, E.; Lampson, M.A.; Daub, H.; et al. Mps1 Regulates Kinetochores-Microtubule Attachment Stability via the Ska Complex to Ensure Error-Free Chromosome Segregation. *Dev. Cell* **2017**, *41*, 143–156. [CrossRef]
17. Xie, Y.; Wang, A.; Lin, J.; Wu, L.; Zhang, H.; Yang, X.; Wan, X.; Miao, R.; Sang, X.; Zhao, H. Mps1/TTK: A novel target and biomarker for cancer. *J. Drug Target.* **2017**, *25*, 112–118. [CrossRef]
18. Jemaà, M.; Galluzzi, L.; Kepp, O.; Senovilla, L.; Brands, M.; Boemer, U.; Koppitz, M.; Lienau, P.; Prechtel, S.; Schulze, V.; et al. Characterization of novel MPS1 inhibitors with preclinical anticancer activity. *Cell Death Differ.* **2013**, *20*, 1532–1545. [CrossRef]
19. Kwiatkowski, N.; Jelluma, N.; Filippakopoulos, P.; Soundararajan, M.; Manak, M.S.; Kwon, M.; Choi, H.G.; Sim, T.; Deveraux, Q.L.; Rottmann, S.; et al. Small-molecule kinase inhibitors provide insight into Mps1 cell cycle function. *Nat. Chem. Biol.* **2010**, *6*, 359–368. [CrossRef]
20. Janssen, A.; Kops, G.J.P.L.; Medema, R.H. Elevating the frequency of chromosome mis-segregation as a strategy to kill tumor cells. *Proc. Natl. Acad. Sci. USA* **2009**, *106*, 19108–19113. [CrossRef]
21. Wengner, A.M.; Siemeister, G.; Koppitz, M.; Schulze, V.; Kosemund, D.; Klar, U.; Stoeckigt, D.; Neuhaus, R.; Lienau, P.; Bader, B.; et al. Novel Mps1 Kinase Inhibitors with Potent Antitumor Activity. *Mol. Cancer Ther.* **2016**, *15*, 583–592. [CrossRef]
22. Lorusso, P.; Chawla, S.P.; Bendell, J.; Shields, A.F.; Shapiro, G.; Rajagopalan, P.; Cyrus, C.; Bruns, I.; Mei, J.; Souza, F.; et al. First-in-human study of the monopolar spindle 1 (Mps1) kinase inhibitor BAY 1161909 in combination with paclitaxel in subjects with advanced malignancies. *Ann. Oncol.* **2018**, *29*, viii138. [CrossRef]
23. Colombo, R.; Caldarelli, M.; Giorgini, M.L.; Degrossi, A.; Ciomei, M.; Pezzetta, D.; Ballinari, D.; Montagnoli, A.; Pesenti, E.; Donati, D.; et al. Abstract 2097: Targeting aneuploidy with NMS-P153, a tight binder inhibitor of the spindle assembly checkpoint MPS1 (TTK) kinase. *Cancer Res.* **2013**, *73*, 2097. [CrossRef]
24. Colombo, R.; Burbridge, M.; Rodriguez, M.; Cantero, F.; Caldarelli, M.; Giorgini, M.L.; Sola, F.; Ballinari, D.; Ciomei, M.; Bosotti, R.; et al. Abstract 1638: Preclinical characterization of the novel TTK kinase inhibitor S81694 for the treatment of triple negative breast cancer. *Cancer Res.* **2015**, *75*, 1638. [CrossRef]
25. Woodward, H.L.; Innocenti, P.; Cheung, K.-M.J.; Hayes, A.; Roberts, J.; Henley, A.T.; Faisal, A.; Mak, G.W.-Y.; Box, G.; Westwood, I.M.; et al. Introduction of a Methyl Group Curbs Metabolism of Pyrido[3,4- d]pyrimidine Monopolar Spindle 1 (MPS1) Inhibitors and Enables the Discovery of the Phase 1 Clinical Candidate N 2-(2-Ethoxy-4-(4-methyl-4 H-1,2,4-triazol-3-yl)phenyl)-6-methyl- N 8-neopentylp. *J. Med. Chem.* **2018**, *61*, 8226–8240. [CrossRef]
26. Anderhub, S.J.; Mak, G.W.-Y.; Gurden, M.D.; Faisal, A.; Drosopoulos, K.; Walsh, K.; Woodward, H.L.; Innocenti, P.; Westwood, I.M.; Naud, S.; et al. High Proliferation Rate and a Compromised Spindle Assembly Checkpoint Confers Sensitivity to the MPS1 Inhibitor BOS172722 in Triple-Negative Breast Cancers. *Mol. Cancer Ther.* **2019**, *18*, 1696–1707. [CrossRef]
27. Mason, J.M.; Wei, X.; Fletcher, G.C.; Kiarash, R.; Brokx, R.; Hodgson, R.; Beletskaya, I.; Bray, M.R.; Mak, T.W. Functional characterization of CFI-402257, a potent and selective Mps1/TTK kinase inhibitor, for the treatment of cancer. *Proc. Natl. Acad. Sci. USA* **2017**, *114*, 3127–3132. [CrossRef] [PubMed]
28. Zheng, L.; Chen, Z.; Kawakami, M.; Chen, Y.; Roszik, J.; Mustachio, L.M.; Kurie, J.M.; Villalobos, P.; Lu, W.; Behrens, C.; et al. Tyrosine threonine kinase inhibition eliminates lung cancers by augmenting apoptosis and polyploidy. *Mol. Cancer Ther.* **2019**, *18*, 1775–1786. [CrossRef] [PubMed]
29. Szymiczek, A.; Carbone, M.; Pastorino, S.; Napolitano, A.; Tanji, M.; Minaai, M.; Pagano, I.; Mason, J.M.; Pass, H.I.; Bray, M.R.; et al. Inhibition of the spindle assembly checkpoint kinase Mps-1 as a novel therapeutic strategy in malignant mesothelioma. *Oncogene* **2017**, *36*, 6501–6507. [CrossRef] [PubMed]
30. de Bousac, H.; Bruyer, A.; Jourdan, M.; Maes, A.; Robert, N.; Gourzones, C.; Vincent, L.; Seckinger, A.; Cartron, G.; Hose, D.; et al. Kinome expression profiling to target new therapeutic avenues in multiple myeloma. *Haematologica* **2020**, *105*, 784–795. [CrossRef] [PubMed]
31. Bruinsma, W.; Raaijmakers, J.A.; Medema, R.H. Switching Polo-like kinase-1 on and off in time and space. *Trends Biochem. Sci.* **2012**, *37*, 534–542. [CrossRef]
32. Colicino, E.G.; Hehnl, H. Regulating a key mitotic regulator, polo-like kinase 1 (PLK1). *Cytoskeleton* **2018**, *75*, 481–494. [CrossRef]
33. Combes, G.; Alharbi, I.; Braga, L.G.; Elowe, S. Playing polo during mitosis: PLK1 takes the lead. *Oncogene* **2017**, *36*, 4819–4827. [CrossRef]
34. Wang, H.; Tao, Z.; Feng, M.; Li, X.; Deng, Z.; Zhao, G.; Yin, H.; Pan, T.; Chen, G.; Feng, Z.; et al. Dual PLK1 and STAT3 inhibition promotes glioblastoma cells apoptosis through MYC. *Biochem. Biophys. Res. Commun.* **2020**, *533*, 368–375. [CrossRef]
35. Ueda, A.; Oikawa, K.; Fujita, K.; Ishikawa, A.; Sato, E.; Ishikawa, T.; Kuroda, M.; Kanekura, K. Therapeutic potential of PLK1 inhibition in triple-negative breast cancer. *Lab. Invest.* **2019**, *99*, 1275–1286. [CrossRef]
36. Pajtler, K.W.; Sadowski, N.; Ackermann, S.; Althoff, K.; Schönbeck, K.; Batzke, K.; Sch, S.; Odersky, A.; Heukamp, L.; Astrahantseff, K.; et al. The GSK461364 PLK1 inhibitor exhibits strong antitumoral activity in preclinical neuroblastoma models. *Oncotarget* **2016**, *8*, 6730–6741. [CrossRef]
37. Gutteridge, R.E.A.; Ndiaye, M.A.; Liu, X.; Ahmad, N. Plk1 inhibitors in cancer therapy: From laboratory to clinics. *Mol. Cancer Ther.* **2016**, *15*, 1427–1435. [CrossRef]
38. Liu, Z.; Sun, Q.; Wang, X. PLK1, A Potential Target for Cancer Therapy. *Transl. Oncol.* **2016**, *10*, 22–32. [CrossRef]



39. Lénárt, P.; Petronczki, M.; Steegmaier, M.; Di Fiore, B.; Lipp, J.J.; Hoffmann, M.; Rettig, W.J.; Kraut, N.; Peters, J.-M. The Small-Molecule Inhibitor BI 2536 Reveals Novel Insights into Mitotic Roles of Polo-like Kinase 1. *Curr. Biol.* **2007**, *17*, 304–315. [CrossRef]
40. Sebastian, M.; Reck, M.; Waller, C.F.; Kortsik, C.; Frickhofen, N.; Schuler, M.; Fritsch, H.; Gaschler-Markefski, B.; Hanft, G.; Munzert, G.; et al. The efficacy and safety of BI 2536, a novel Plk-1 inhibitor, in patients with stage IIIB/IV non-small cell lung cancer who had relapsed after, or failed, chemotherapy: Results from an open-label, randomized phase ii clinical trial. *J. Thorac. Oncol.* **2010**, *5*, 1060–1067. [CrossRef]
41. Ellis, P.M.; Chu, Q.S.; Leighl, N.; Laurie, S.A.; Fritsch, H.; Gaschler-Markefski, B.; Gyorffy, S.; Munzert, G. A phase i open-label dose-escalation study of intravenous BI 2536 together with pemetrexed in previously treated patients with non-small-cell lung cancer. *Clin. Lung Cancer* **2013**, *14*, 19–27. [CrossRef]
42. Mross, K.; Dittrich, C.; Aulitzky, W.E.; Strumberg, D.; Schutte, J.; Schmid, R.M.; Hollerbach, S.; Merger, M.; Munzert, G.; Fleischer, F.; et al. A randomised phase II trial of the Polo-like kinase inhibitor BI 2536 in chemo-naïve patients with unresectable exocrine adenocarcinoma of the pancreas—a study within the Central European Society Anticancer Drug Research (CESAR) collaborative network. *Br. J. Cancer* **2012**, *107*, 280–286. [CrossRef]
43. Müller-Tidow, C.; Bug, G.; Lübbert, M.; Krämer, A.; Krauter, J.; Valent, P.; Nachbaur, D.; Berdel, W.E.; Ottmann, O.G.; Fritsch, H.; et al. A randomized, open-label, phase I/II trial to investigate the maximum tolerated dose of the Polo-like kinase inhibitor BI 2536 in elderly patients with refractory/relapsed acute myeloid leukaemia. *Br. J. Haematol.* **2013**, *163*, 214–222. [CrossRef]
44. Vose, J.M.; Friedberg, J.W.; Waller, E.K.; Cheson, B.D.; Juvvigunta, V.; Fritsch, H.; Petit, C.; Munzert, G.; Younes, A. The Plk1 inhibitor BI 2536 in patients with refractory or relapsed non-Hodgkin lymphoma: A phase I, open-label, single dose-escalation study. *Leuk. Lymphoma* **2013**, *54*, 708–713. [CrossRef]
45. Rudolph, D.; Steegmaier, M.; Hoffmann, M.; Grauert, M.; Baum, A.; Quant, J.; Haslinger, C.; Garin-Chesa, P.; Adolf, G.R. BI 6727, a polo-like kinase inhibitor with improved pharmacokinetic profile and broad antitumor activity. *Clin. Cancer Res.* **2009**, *15*, 3094–3102. [CrossRef]
46. Schöffski, P.; Awada, A.; Dumez, H.; Gil, T.; Bartholomeus, S.; Wolter, P.; Taton, M.; Fritsch, H.; Glomb, P.; Munzert, G. A phase I, dose-escalation study of the novel Polo-like kinase inhibitor volasertib (BI 6727) in patients with advanced solid tumours. *Eur. J. Cancer* **2012**, *48*, 179–186. [CrossRef]
47. Nokihara, H.; Yamada, Y.; Fujiwara, Y.; Yamamoto, N.; Wakui, H.; Nakamichi, S.; Kitazono, S.; Inoue, K.; Harada, A.; Taube, T.; et al. Phase I trial of volasertib, a Polo-like kinase inhibitor, in Japanese patients with advanced solid tumors. *Investig. New Drugs* **2016**, *34*, 66–74. [CrossRef]
48. Lin, C.-C.; Su, W.-C.; Yen, C.-J.; Hsu, C.-H.; Su, W.-P.; Yeh, K.-H.; Lu, Y.-S.; Cheng, A.-L.; Huang, D.C.-L.; Fritsch, H.; et al. A phase I study of two dosing schedules of volasertib (BI 6727), an intravenous polo-like kinase inhibitor, in patients with advanced solid malignancies. *Br. J. Cancer* **2014**, *110*, 2434–2440. [CrossRef]
49. Stadler, W.M.; Vaughn, D.J.; Sonpavde, G.; Vogelzang, N.J.; Tagawa, S.T.; Petrylak, D.P.; Rosen, P.; Lin, C.-C.; Mahoney, J.; Modi, S.; et al. An open-label, single-arm, phase 2 trial of the polo-like kinase inhibitor volasertib (BI 6727) in patients with locally advanced or metastatic urothelial cancer. *Cancer* **2014**, *120*, 976–982. [CrossRef]
50. Pujade-Lauraine, E.; Selle, F.; Weber, B.; Ray-Coquard, I.-L.; Vergote, I.; Sufliarisky, J.; Del Campo, J.M.; Lortholary, A.; Lesoin, A.; Follana, P.; et al. Volasertib Versus Chemotherapy in Platinum-Resistant or -Refractory Ovarian Cancer: A Randomized Phase II Groupe des Investigateurs Nationaux pour l’Etude des Cancers de l’Ovaire Study. *J. Clin. Oncol. Off. J. Am. Soc. Clin. Oncol.* **2016**, *34*, 706–713. [CrossRef]
51. Ellis, P.M.; Leighl, N.B.; Hirsh, V.; Reaume, M.N.; Blais, N.; Wierzbiicki, R.; Sadrolhefazi, B.; Gu, Y.; Liu, D.; Pilz, K.; et al. A Randomized, Open-Label Phase II Trial of Volasertib as Monotherapy and in Combination With Standard-Dose Pemetrexed Compared With Pemetrexed Monotherapy in Second-Line Treatment for Non-Small-Cell Lung Cancer. *Clin. Lung Cancer* **2015**, *16*, 457–465. [CrossRef] [PubMed]
52. De Braud, F.; Cascinu, S.; Spitaleri, G.; Pilz, K.; Clementi, L.; Liu, D.; Sikken, P.; De Pas, T. A phase I, dose-escalation study of volasertib combined with nintedanib in advanced solid tumors. *Ann. Oncol. Off. J. Eur. Soc. Med. Oncol.* **2015**, *26*, 2341–2346. [CrossRef] [PubMed]
53. Machiels, J.-P.; Peeters, M.; Herremans, C.; Surmont, V.; Specenier, P.; De Smet, M.; Pilz, K.; Strelkowa, N.; Liu, D.; Rottey, S. A phase I study of volasertib combined with afatinib, in advanced solid tumors. *Cancer Chemother. Pharm. Ther.* **2015**, *76*, 843–851. [CrossRef] [PubMed]
54. Awada, A.; Dumez, H.; Aftimos, P.G.; Costermans, J.; Bartholomeus, S.; Forceville, K.; Berghmans, T.; Meeus, M.-A.; Cescutti, J.; Munzert, G.; et al. Phase I trial of volasertib, a Polo-like kinase inhibitor, plus platinum agents in solid tumors: Safety, pharmacokinetics and activity. *Investig. New Drugs* **2015**, *33*, 611–620. [CrossRef]
55. Kobayashi, Y.; Yamauchi, T.; Kiyoi, H.; Sakura, T.; Hata, T.; Ando, K.; Watabe, A.; Harada, A.; Taube, T.; Miyazaki, Y.; et al. Phase I trial of volasertib, a Polo-like kinase inhibitor, in Japanese patients with acute myeloid leukemia. *Cancer Sci.* **2015**, *106*, 1590–1595. [CrossRef]
56. Gumireddy, K.; Reddy, M.V.R.; Cosenza, S.C.; Nathan, R.B.; Baker, S.J.; Papathi, N.; Jiang, J.; Holland, J.; Reddy, E.P. ON01910 a non-ATP-competitive small molecule inhibitor of Plk1, is a potent anticancer agent. *Cancer Cell* **2005**, *7*, 275–286. [CrossRef]

57. Ma, W.W.; Messersmith, W.A.; Dy, G.K.; Weekes, C.D.; Whitworth, A.; Ren, C.; Maniar, M.; Wilhelm, F.; Eckhardt, S.G.; Adjei, A.A.; et al. Phase I study of Rigosertib, an inhibitor of the phosphatidylinositol 3-kinase and Polo-like kinase 1 pathways, combined with gemcitabine in patients with solid tumors and pancreatic cancer. *Clin. Cancer Res.* **2012**, *18*, 2048–2055. [CrossRef]
58. O’Neil, B.H.; Scott, A.J.; Ma, W.W.; Cohen, S.J.; Aisner, D.L.; Menter, A.R.; Tejani, M.A.; Cho, J.K.; Granfortuna, J.; Coveler, L.; et al. A phase II/III randomized study to compare the efficacy and safety of rigosertib plus gemcitabine versus gemcitabine alone in patients with previously untreated metastatic pancreatic cancer. *Ann. Oncol.* **2015**, *26*, 1923–1929. [CrossRef]
59. Garcia-Manero, G.; Fenaux, P.; Al-Kali, A.; Baer, M.R.; Sekeres, M.A.; Roboz, G.J.; Gaidano, G.; Scott, B.L.; Greenberg, P.; Platzbecker, U.; et al. Rigosertib versus best supportive care for patients with high-risk myelodysplastic syndromes after failure of hypomethylating drugs (ONTIME): A randomised, controlled, phase 3 trial. *Lancet Oncol.* **2016**, *17*, 496–508. [CrossRef]
60. Al-Kali, A.; Hiwase, D.; Baer, M.R.; Greenberg, P.; Shortt, J.; Collins, R.; Steensma, D.P.; Verma, A.; Roboz, G.J.; Shammo, J.M.; et al. Relationship of bone marrow blast (BMBl) response to overall survival (OS) in a multicenter study of rigosertib (Rigo) in patients (pts) with myelodysplastic syndrome (MDS) with excess blasts progressing on or after treatment with a hypomethylating agent. *JCO* **2017**, *35*, 7056. [CrossRef]
61. Navada, S.C.; Garcia-Manero, G.; Odchimar-Reissig, R.; Pemmaraju, N.; Alvarado, Y.; Ohanian, M.N.; John, R.B.; Demakos, E.P.; Zbyszewski, P.S.; Maniar, M.; et al. Rigosertib in combination with azacitidine in patients with myelodysplastic syndromes or acute myeloid leukemia: Results of a phase 1 study. *Leuk Res.* **2020**, *94*, 106369. [CrossRef]
62. Gilmartin, A.G.; Bleam, M.R.; Richter, M.C.; Erskine, S.G.; Kruger, R.G.; Madden, L.; Hassler, D.F.; Smith, G.K.; Gontarek, R.R.; Courtney, M.P.; et al. Distinct concentration-dependent effects of the polo-like kinase 1-specific inhibitor GSK461364A, including differential effect on apoptosis. *Cancer Res.* **2009**, *69*, 6969–6977. [CrossRef]
63. Olmos, D.; Barker, D.; Sharma, R.; Brunetto, A.T.; Yap, T.A.; Taegtmeier, A.B.; Barriuso, J.; Medani, H.; Degenhardt, Y.Y.; Allred, A.J.; et al. Phase I study of GSK461364, a specific and competitive Polo-like kinase 1 inhibitor, in patients with advanced solid malignancies. *Clin. Cancer Res. An. Off. J. Am. Assoc. Cancer Res.* **2011**, *17*, 3420–3430. [CrossRef]
64. Doi, T.; Murakami, H.; Wan, K.; Miki, M.; Kotani, H.; Sakamoto, N.; Yamamoto, N.; Ohtsu, A. A first-in-human phase I dose-escalation study of MK-1496, first-in-class orally available novel PLK1 inhibitor, in patients with advanced solid tumors. *JCO* **2011**, *29*, 3012. [CrossRef]
65. Nie, Z.; Feher, V.; Natala, S.; McBride, C.; Kiryanov, A.; Jones, B.; Lam, B.; Liu, Y.; Kaldor, S.; Stafford, J.; et al. Discovery of TAK-960: An orally available small molecule inhibitor of polo-like kinase 1 (PLK1). *Bioorganic. Med. Chem. Lett.* **2013**, *23*, 3662–3666. [CrossRef]
66. Hikichi, Y.; Honda, K.; Hikami, K.; Miyashita, H.; Kaieda, I.; Murai, S.; Uchiyama, N.; Hasegawa, M.; Kawamoto, T.; Sato, T.; et al. TAK-960, a novel, orally available, selective inhibitor of polo-like kinase 1, shows broad-spectrum preclinical antitumor activity in multiple dosing regimens. *Mol. Cancer Ther.* **2012**, *11*, 700–709. [CrossRef]
67. Valsasina, B.; Beria, I.; Alli, C.; Alzani, R.; Avanzi, N.; Ballinari, D.; Cappella, P.; Caruso, M.; Casolaro, A.; Ciavolella, A.; et al. NMS-P937, an orally available, specific small-molecule polo-like kinase 1 inhibitor with antitumor activity in solid and hematologic malignancies. *Mol. Cancer Ther.* **2012**, *11*, 1006–1016. [CrossRef]
68. Weiss, G.J.; Jameson, G.; Von Hoff, D.D.; Valsasina, B.; Davite, C.; Di Giulio, C.; Fiorentini, F.; Alzani, R.; Carpinelli, P.; Di Sanzo, A.; et al. Phase I dose escalation study of NMS-1286937, an orally available Polo-Like Kinase 1 inhibitor, in patients with advanced or metastatic solid tumors. *Investig. New Drugs* **2018**, *36*, 85–95. [CrossRef]
69. Demeure, M.J.; Armaghany, T.; Ejadi, S.; Ramanathan, R.K.; Elfiky, A.; Strosberg, J.R.; Smith, D.C.; Whitsett, T.; Liang, W.S.; Sekar, S.; et al. A phase I/II study of TKM-080301, a PLK1 -targeted RNAi in patients with adrenocortical cancer (ACC). *JCO* **2016**, *34*, 2547. [CrossRef]
70. El Dika, I.; Lim, H.Y.; Yong, W.P.; Lin, C.-C.; Yoon, J.-H.; Modiano, M.; Freilich, B.; Choi, H.J.; Chao, T.-Y.; Kelley, R.K.; et al. An Open-Label, Multicenter, Phase I, Dose Escalation Study with Phase II Expansion Cohort to Determine the Safety, Pharmacokinetics, and Preliminary Antitumor Activity of Intravenous TKM-080301 in Subjects with Advanced Hepatocellular Carcinoma. *Oncologist* **2019**, *24*, 747. [CrossRef]
71. Available online: [https://cyclacel.com/research\\_programs\\_oncology\\_cyc140.shtml](https://cyclacel.com/research_programs_oncology_cyc140.shtml) (accessed on 8 May 2021).
72. Navada, S.C.; Fruchtman, S.M.; Odchimar-Reissig, R.; Demakos, E.P.; Petrone, M.E.; Zbyszewski, P.S.; Holland, J.F.; Silverman, L.R. A phase 1/2 study of rigosertib in patients with myelodysplastic syndromes (MDS) and MDS progressed to acute myeloid leukemia. *Leuk Res.* **2018**, *64*, 10–16. [CrossRef]
73. Komrokji, R.S.; Raza, A.; Lancet, J.E.; Ren, C.; Taft, D.; Maniar, M.; Wilhelm, F.; List, A.F. Phase I clinical trial of oral rigosertib in patients with myelodysplastic syndromes. *Br. J. Haematol.* **2013**, *162*, 517–524. [CrossRef]
74. King, S.I.; Purdie, C.A.; Bray, S.E.; Quinlan, P.R.; Jordan, L.B.; Thompson, A.M.; Meek, D.W. Immunohistochemical detection of Polo-like kinase-1 (PLK1) in primary breast cancer is associated with TP53 mutation and poor clinical outcome. *Breast Cancer Res.* **2012**, *14*, R40. [CrossRef]
75. Guan, R.; Tapang, P.; Levenson, J.D.; Albert, D.; Giranda, V.L.; Luo, Y. Small Interfering RNA-Mediated Polo-Like Kinase 1 Depletion Preferentially Reduces the Survival of p53-Defective, Oncogenic Transformed Cells and Inhibits Tumor Growth in Animals. *Cancer Res.* **2005**, *65*, 2698–2704. [CrossRef]
76. Bolanos-Garcia, V.M. Aurora kinases. *Int. J. Biochem. Cell Biol.* **2005**, *37*, 1572–1577. [CrossRef]
77. Willems, E.; Dedobbeleer, M.; Digregorio, M.; Lombard, A.; Lumapat, P.N.; Rogister, B. The functional diversity of Aurora kinases: A comprehensive review. *Cell Div.* **2018**, *13*, 7. [CrossRef]

78. Girdler, F.; Gascoigne, K.E.; Eyers, P.A.; Hartmuth, S.; Crafter, C.; Foote, K.M.; Keen, N.J.; Taylor, S.S. Validating Aurora B as an anti-cancer drug target. *J. Cell Sci.* **2006**, *119*, 3664–3675. [CrossRef] [PubMed]
79. Hauf, S.; Cole, R.W.; LaTerra, S.; Zimmer, C.; Schnapp, G.; Walter, R.; Heckel, A.; van Meel, J.; Rieder, C.L.; Peters, J.-M. The small molecule Hesperadin reveals a role for Aurora B in correcting kinetochore-microtubule attachment and in maintaining the spindle assembly checkpoint. *J. Cell Biol.* **2003**, *161*, 281–294. [CrossRef] [PubMed]
80. Du, J.; Yan, L.; Torres, R.; Gong, X.; Bian, H.; Marugán, C.; Boehnke, K.; Baquero, C.; Hui, Y.-H.; Chapman, S.C.; et al. Aurora A-Selective Inhibitor LY3295668 Leads to Dominant Mitotic Arrest, Apoptosis in Cancer Cells, and Shows Potent Preclinical Antitumor Efficacy. *Mol. Cancer Ther.* **2019**, *18*, 2207–2219. [CrossRef] [PubMed]
81. Kaestner, P.; Stolz, A.; Bastians, H. Determinants for the efficiency of anticancer drugs targeting either Aurora-A or Aurora-B kinases in human colon carcinoma cells. *Mol. Cancer Ther.* **2009**, *8*, 2046–2056. [CrossRef]
82. Glaser, K.B.; Li, J.; Marcotte, P.A.; Magoc, T.J.; Guo, J.; Reuter, D.R.; Tapang, P.; Wei, R.-Q.; Pease, L.J.; Bui, M.H.; et al. Preclinical characterization of ABT-348, a kinase inhibitor targeting the aurora, vascular endothelial growth factor receptor/platelet-derived growth factor receptor, and Src kinase families. *J. Pharm. Exp. Ther.* **2012**, *343*, 617–627. [CrossRef]
83. Maitland, M.L.; Piha-Paul, S.; Falchook, G.; Kurzrock, R.; Nguyen, L.; Janisch, L.; Karovic, S.; McKee, M.; Hoening, E.; Wong, S.; et al. Clinical pharmacodynamic/exposure characterisation of the multikinase inhibitor ilorasertib (ABT-348) in a phase 1 dose-escalation trial. *Br. J. Cancer* **2018**, *118*, 1042–1050. [CrossRef]
84. Garcia-Manero, G.; Tibes, R.; Kadia, T.; Kantarjian, H.; Arellano, M.; Knight, E.A.; Xiong, H.; Qin, Q.; Munasinghe, W.; Roberts-Rapp, L.; et al. Phase 1 dose escalation trial of ilorasertib, a dual Aurora/VEGF receptor kinase inhibitor, in patients with hematologic malignancies. *Investig. New Drugs* **2015**, *33*, 870–880. [CrossRef]
85. Peter, B.; Bibi, S.; Eisenwort, G.; Wingelhofer, B.; Berger, D.; Stefanzl, G.; Blatt, K.; Herrmann, H.; Hadzijusufovic, E.; Hoermann, G.; et al. Drug-induced inhibition of phosphorylation of STAT5 overrides drug resistance in neoplastic mast cells. *Leukemia* **2018**, *32*, 1016–1022. [CrossRef]
86. Mita, M.; Gordon, M.; Rejeb, N.; Gianella-Borradori, A.; Jegu, V.; Mita, A.; Sarantopoulos, J.; Sankhala, K.; Mendelson, D. A phase I study of three different dosing schedules of the oral aurora kinase inhibitor MSC1992371A in patients with solid tumors. *Target. Oncol.* **2014**, *9*, 215–224. [CrossRef]
87. Raymond, E.; Alexandre, J.; Faivre, S.; Goldwasser, F.; Besse-Hammer, T.; Gianella-Borradori, A.; Jegu, V.; Trandafir, L.; Rejeb, N.; Awada, A. A phase I schedule dependency study of the aurora kinase inhibitor MSC1992371A in combination with gemcitabine in patients with solid tumors. *Investig. New Drugs* **2014**, *32*, 94–103. [CrossRef]
88. Graux, C.; Sonet, A.; Maertens, J.; Duyster, J.; Greiner, J.; Chalandon, Y.; Martinelli, G.; Hess, D.; Heim, D.; Giles, F.J.; et al. A phase I dose-escalation study of MSC1992371A, an oral inhibitor of aurora and other kinases, in advanced hematologic malignancies. *Leuk Res.* **2013**, *37*, 1100–1106. [CrossRef]
89. Harrington, E.A.; Bebbington, D.; Moore, J.; Rasmussen, R.K.; Ajose-Adeogun, A.O.; Nakayama, T.; Graham, J.A.; Demur, C.; Hercend, T.; Diu-Hercend, A.; et al. VX-680, a potent and selective small-molecule inhibitor of the Aurora kinases, suppresses tumor growth in vivo. *Nat. Med.* **2004**, *10*, 262–267. [CrossRef]
90. Traynor, A.M.; Hewitt, M.; Liu, G.; Flaherty, K.T.; Clark, J.; Freedman, S.J.; Scott, B.B.; Leighton, A.M.; Watson, P.A.; Zhao, B.; et al. Phase I dose escalation study of MK-0457, a novel Aurora kinase inhibitor, in adult patients with advanced solid tumors. *Cancer Chemother. Pharm.* **2011**, *67*, 305–314. [CrossRef]
91. Giles, F.J.; Swords, R.T.; Nagler, A.; Hochhaus, A.; Ottmann, O.G.; Rizzieri, D.A.; Talpaz, M.; Clark, J.; Watson, P.; Xiao, A.; et al. MK-0457, an Aurora kinase and BCR-ABL inhibitor, is active in patients with BCR-ABL T315I leukemia. *Leukemia* **2013**, *27*, 113–117. [CrossRef]
92. Sini, P.; Gürtler, U.; Zahn, S.K.; Baumann, C.; Rudolph, D.; Baumgartinger, R.; Strauss, E.; Haslinger, C.; Tontsch-Grunt, U.; Waizenegger, I.C.; et al. Pharmacological profile of BI 847325, an orally bioavailable, ATP-competitive inhibitor of MEK and Aurora kinases. *Mol. Cancer Ther.* **2016**, *15*, 2388–2398. [CrossRef]
93. Schöffski, P.; Aftimos, P.; Dumez, H.; Deleporte, A.; De Block, K.; Costermans, J.; Billiet, M.; Meeus, M.-A.; Lee, C.; Schnell, D.; et al. A phase I study of two dosing schedules of oral BI 847325 in patients with advanced solid tumors. *Cancer Chemother. Pharm.* **2016**, *77*, 99–108. [CrossRef]
94. Howard, S.; Berdini, V.; Boulstridge, J.A.; Carr, M.G.; Cross, D.M.; Curry, J.; Devine, L.A.; Early, T.R.; Fazal, L.; Gill, A.L.; et al. Fragment-based discovery of the pyrazol-4-yl urea (AT9283), a multitargeted kinase inhibitor with potent aurora kinase activity. *J. Med. Chem.* **2009**, *52*, 379–388. [CrossRef]
95. Dent, S.F.; Gelmon, K.A.; Chi, K.N.; Jonker, D.J.; Wainman, N.; Capier, C.A.; Chen, E.X.; Lyons, J.F.; Seymour, L. NCIC CTG IND.181: Phase I study of AT9283 given as a weekly 24 hour infusion in advanced malignancies. *Investig. New Drugs* **2013**, *31*, 1522–1529. [CrossRef] [PubMed]
96. Foran, J.; Ravandi, F.; Wierda, W.; Garcia-Manero, G.; Verstovsek, S.; Kadia, T.; Burger, J.; Yule, M.; Langford, G.; Lyons, J.; et al. A phase I and pharmacodynamic study of AT9283, a small-molecule inhibitor of aurora kinases in patients with relapsed/refractory leukemia or myelofibrosis. *Clin. Lymphoma Myeloma Leuk.* **2014**, *14*, 223–230. [CrossRef] [PubMed]
97. Moreno, L.; Marshall, L.V.; Pearson, A.D.J.; Morland, B.; Elliott, M.; Campbell-Hewson, Q.; Makin, G.; Halford, S.E.R.; Acton, G.; Ross, P.; et al. A phase I trial of AT9283 (a selective inhibitor of aurora kinases) in children and adolescents with solid tumors: A cancer research UK study. *Clin. Cancer Res.* **2015**, *21*, 267–273. [CrossRef] [PubMed]

98. Payton, M.; Bush, T.L.; Chung, G.; Ziegler, B.; Eden, P.; McElroy, P.; Ross, S.; Cee, V.J.; Deak, H.L.; Hodous, B.L.; et al. Preclinical evaluation of AMG 900, a novel potent and highly selective pan-aurora kinase inhibitor with activity in taxane-resistant tumor cell lines. *Cancer Res.* **2010**, *70*, 9846–9854. [CrossRef]
99. Carducci, M.; Shaheen, M.; Markman, B.; Hurvitz, S.; Mahadevan, D.; Kotasek, D.; Goodman, O.B.; Rasmussen, E.; Chow, V.; Juan, G.; et al. A phase 1, first-in-human study of AMG 900, an orally administered pan-Aurora kinase inhibitor, in adult patients with advanced solid tumors. *Investig. New Drugs* **2018**, *36*, 1060–1071. [CrossRef]
100. Kantarjian, H.M.; Schuster, M.W.; Jain, N.; Advani, A.; Jabbour, E.; Gamelin, E.; Rasmussen, E.; Juan, G.; Anderson, A.; Chow, V.F.; et al. A phase 1 study of AMG 900, an orally administered pan-aurora kinase inhibitor, in adult patients with acute myeloid leukemia. *Am. J. Hematol.* **2017**, *92*, 660–667. [CrossRef]
101. Carpinelli, P.; Ceruti, R.; Giorgini, M.L.; Cappella, P.; Gianellini, L.; Croci, V.; Degrassi, A.; Texido, G.; Rocchetti, M.; Vianello, P.; et al. PHA-739358, a potent inhibitor of Aurora kinases with a selective target inhibition profile relevant to cancer. *Mol. Cancer Ther.* **2007**, *6*, 3158–3168. [CrossRef]
102. Meulenbeld, H.J.; Bleuse, J.P.; Vinci, E.M.; Raymond, E.; Vitali, G.; Santoro, A.; Dogliotti, L.; Berardi, R.; Cappuzzo, F.; Tagawa, S.T.; et al. Randomized phase II study of danusertib in patients with metastatic castration-resistant prostate cancer after docetaxel failure. *BJU Int.* **2013**, *111*, 44–52. [CrossRef]
103. Oslob, J.D.; Romanowski, M.J.; Allen, D.A.; Baskaran, S.; Bui, M.; Elling, R.A.; Flanagan, W.M.; Fung, A.D.; Hanan, E.J.; Harris, S.; et al. Discovery of a potent and selective aurora kinase inhibitor. *Bioorg. Med. Chem. Lett.* **2008**, *18*, 4880–4884. [CrossRef]
104. Robert, F.; Verschraegen, C.; Hurwitz, H.; Uronis, H.; Advani, R.; Chen, A.; Taverna, P.; Wollman, M.; Fox, J.; Michelson, G. A phase I trial of sns-314, a novel and selective pan-aurora kinase inhibitor, in advanced solid tumor patients. *JCO* **2009**, *27*, 2536. [CrossRef]
105. Farrell, P.; Shi, L.; Matuszkiewicz, J.; Balakrishna, D.; Hoshino, T.; Zhang, L.; Elliott, S.; Fabrey, R.; Lee, B.; Halkowycz, P.; et al. Biological characterization of TAK-901, an investigational, novel, multitargeted Aurora B kinase inhibitor. *Mol. Cancer Ther.* **2013**, *12*, 460–470. [CrossRef]
106. Wang, S.; Midgley, C.A.; Scaërou, F.; Grabarek, J.B.; Griffiths, G.; Jackson, W.; Kontopidis, G.; McClue, S.J.; McInnes, C.; Meades, C.; et al. Discovery of N-Phenyl-4-(thiazol-5-yl)pyrimidin-2-amine aurora kinase inhibitors. *J. Med. Chem.* **2010**, *53*, 4367–4378. [CrossRef]
107. Adams, N.D.; Adams, J.L.; Burgess, J.L.; Chaudhari, A.M.; Copeland, R.A.; Donatelli, C.A.; Drewry, D.H.; Fisher, K.E.; Hamajima, T.; Hardwicke, M.A.; et al. Discovery of GSK1070916, a potent and selective inhibitor of aurora B/C kinase. *J. Med. Chem.* **2010**, *53*, 3973–4001. [CrossRef]
108. Jani, J.P.; Arcari, J.; Bernardo, V.; Bhattacharya, S.K.; Briere, D.; Cohen, B.D.; Coleman, K.; Christensen, J.G.; Emerson, E.O.; Jakowski, A.; et al. PF-03814735, an orally bioavailable small molecule aurora kinase inhibitor for cancer therapy. *Mol. Cancer Ther.* **2010**, *9*, 883–894. [CrossRef]
109. Schöffski, P.; Jones, S.F.; Dumez, H.; Infante, J.R.; Van Mieghem, E.; Fowst, C.; Gerletti, P.; Xu, H.; Jakubczak, J.L.; English, P.A.; et al. Phase I, open-label, multicentre, dose-escalation, pharmacokinetic and pharmacodynamic trial of the oral aurora kinase inhibitor PF-03814735 in advanced solid tumours. *Eur. J. Cancer* **2011**, *47*, 2256–2264. [CrossRef]
110. Seymour, J.F.; Kim, D.W.; Rubin, E.; Haregewoin, A.; Clark, J.; Watson, P.; Hughes, T.; Dufva, I.; Jimenez, J.L.; Mahon, F.-X.; et al. A phase 2 study of MK-0457 in patients with BCR-ABL T315I mutant chronic myelogenous leukemia and philadelphia chromosome-positive acute lymphoblastic leukemia. *Blood Cancer J.* **2014**, *4*, e238. [CrossRef]
111. Yang, J.; Ikezoe, T.; Nishioka, C.; Tasaka, T.; Taniguchi, A.; Kuwayama, Y.; Komatsu, N.; Bandobashi, K.; Togitani, K.; Koeffler, H.P.; et al. AZD1152, a novel and selective aurora B kinase inhibitor, induces growth arrest, apoptosis, and sensitization for tubulin depolymerizing agent or topoisomerase II inhibitor in human acute leukemia cells in vitro and in vivo. *Blood* **2007**, *110*, 2034–2040. [CrossRef]
112. Schwartz, G.K.; Carvajal, R.D.; Midgley, R.; Rodig, S.J.; Stockman, P.K.; Ataman, O.; Wilson, D.; Das, S.; Shapiro, G.I. Phase I study of barasertib (AZD1152), a selective inhibitor of Aurora B kinase, in patients with advanced solid tumors. *Investig. New Drugs* **2013**, *31*, 370–380. [CrossRef] [PubMed]
113. Boss, D.S.; Witteveen, P.O.; van der Sar, J.; Lolkema, M.P.; Voest, E.E.; Stockman, P.K.; Ataman, O.; Wilson, D.; Das, S.; Schellens, J.H. Clinical evaluation of AZD1152, an i.v. inhibitor of Aurora B kinase, in patients with solid malignant tumors. *Ann. Oncol.* **2011**, *22*, 431–437. [CrossRef] [PubMed]
114. Löwenberg, B.; Muus, P.; Ossenkoppele, G.; Rousselot, P.; Cahn, J.-Y.; Ifrah, N.; Martinelli, G.; Amadori, S.; Berman, E.; Sonneveld, P.; et al. Phase 1/2 study to assess the safety, efficacy, and pharmacokinetics of barasertib (AZD1152) in patients with advanced acute myeloid leukemia. *Blood* **2011**, *118*, 6030–6036. [CrossRef] [PubMed]
115. Tsuboi, K.; Yokozawa, T.; Sakura, T.; Watanabe, T.; Fujisawa, S.; Yamauchi, T.; Uike, N.; Ando, K.; Kihara, R.; Tobinai, K.; et al. A phase I study to assess the safety, pharmacokinetics and efficacy of barasertib (AZD1152), an Aurora B kinase inhibitor, in Japanese patients with advanced acute myeloid leukemia. *Leuk. Res.* **2011**, *35*, 1384–1389. [CrossRef]
116. Kantarjian, H.M.; Martinelli, G.; Jabbour, E.J.; Quintás-Cardama, A.; Ando, K.; Bay, J.-O.; Wei, A.; Gröpper, S.; Papayannidis, C.; Owen, K.; et al. Stage I of a phase 2 study assessing the efficacy, safety, and tolerability of barasertib (AZD1152) versus low-dose cytosine arabinoside in elderly patients with acute myeloid leukemia. *Cancer* **2013**, *119*, 2611–2619. [CrossRef]

117. Dennis, M.; Davies, M.; Oliver, S.; D'Souza, R.; Pike, L.; Stockman, P. Phase I study of the Aurora B kinase inhibitor barasertib (AZD1152) to assess the pharmacokinetics, metabolism and excretion in patients with acute myeloid leukemia. *Cancer Chemother. Pharm.* **2012**, *70*, 461–469. [CrossRef]
118. Kantarjian, H.M.; Sekeres, M.A.; Ribrag, V.; Rousselot, P.; Garcia-Manero, G.; Jabbour, E.J.; Owen, K.; Stockman, P.K.; Oliver, S.D. Phase I study assessing the safety and tolerability of barasertib (AZD1152) with low-dose cytosine arabinoside in elderly patients with AML. *Clin. Lymphoma Myeloma Leuk.* **2013**, *13*, 559–567. [CrossRef]
119. Collins, G.P.; Eyre, T.A.; Linton, K.M.; Radford, J.; Vallance, G.D.; Soilleux, E.; Hatton, C. A phase II trial of AZD1152 in relapsed/refractory diffuse large B-cell lymphoma. *Br. J. Haematol.* **2015**, *170*, 886–890. [CrossRef]
120. Available online: <https://opnme.com/molecules/aurb-bi831266> (accessed on 1 July 2021).
121. Dittrich, C.; Fridrik, M.A.; Koenigsberg, R.; Lee, C.; Goeldner, R.-G.; Hilbert, J.; Greil, R. A phase I dose escalation study of BI 831266, an inhibitor of Aurora kinase B, in patients with advanced solid tumors. *Investig. New Drugs* **2015**, *33*, 409–422. [CrossRef]
122. Tontsch-Grunt, U.; Gürtler, U.; Zahn, S.K.; Boehmelt, G.; Jarvis, M.; Adolf, G.R.; Solca, F. Abstract 1080: Molecular and cellular pharmacology of BI 811283, a potent inhibitor of Aurora B kinase. *Cancer Res.* **2010**, *70*, 1080. [CrossRef]
123. Mross, K.; Richly, H.; Frost, A.; Scharf, D.; Nokay, B.; Graeser, R.; Lee, C.; Hilbert, J.; Goeldner, R.-G.; Fietz, O.; et al. A phase I study of BI 811283, an Aurora B kinase inhibitor, in patients with advanced solid tumors. *Cancer Chemother. Pharm.* **2016**, *78*, 405–417. [CrossRef]
124. Döhner, H.; Müller-Tidow, C.; Lübbert, M.; Fiedler, W.; Krämer, A.; Westermann, J.; Bug, G.; Schlenk, R.F.; Krug, U.; Goeldner, R.-G.; et al. A phase I trial investigating the Aurora B kinase inhibitor BI 811283 in combination with cytarabine in patients with acute myeloid leukaemia. *Br. J. Haematol.* **2019**, *185*, 583–587. [CrossRef]
125. Zhou, Y.; Shan, S.; Li, Z.; Xin, L.; Pan, D.; Yang, Q.; Liu, Y.; Yue, X.; Liu, X.; Gao, J.; et al. CS2164, a novel multi-target inhibitor against tumor angiogenesis, mitosis and chronic inflammation with anti-tumor potency. *Cancer Sci.* **2017**, *108*, 469–477. [CrossRef]
126. Sun, Y.; Yang, L.; Hao, X.; Liu, Y.; Zhang, J.; Ning, Z.; Shi, Y. Phase I dose-escalation study of chiauranib, a novel angiogenic, mitotic, and chronic inflammation inhibitor, in patients with advanced solid tumors. *J. Hematol. Oncol.* **2019**, *12*, 9. [CrossRef]
127. Manfredi, M.G.; Ecsedy, J.A.; Chakravarty, A.; Silverman, L.; Zhang, M.; Hoar, K.M.; Stroud, S.G.; Chen, W.; Shinde, V.; Huck, J.J.; et al. Characterization of alisertib (MLN8237), an investigational small-molecule inhibitor of Aurora A kinase using novel in vivo pharmacodynamic assays. *Clin. Cancer Res.* **2011**, *17*, 7614–7624. [CrossRef]
128. Dees, E.C.; Cohen, R.B.; von Mehren, M.; Stinchcombe, T.E.; Liu, H.; Venkatakrisnan, K.; Manfredi, M.; Fingert, H.; Burris, H.A.; Infante, J.R. Phase I study of aurora A kinase inhibitor MLN8237 in advanced solid tumors: Safety, pharmacokinetics, pharmacodynamics, and bioavailability of two oral formulations. *Clin. Cancer Res.* **2012**, *18*, 4775–4784. [CrossRef]
129. Matulonis, U.A.; Sharma, S.; Ghamande, S.; Gordon, M.S.; Del Prete, S.A.; Ray-Coquard, I.; Kutarska, E.; Liu, H.; Fingert, H.; Zhou, X.; et al. Phase II study of MLN8237 (alisertib), an investigational Aurora A kinase inhibitor, in patients with platinum-resistant or -refractory epithelial ovarian, fallopian tube, or primary peritoneal carcinoma. *Gynecol. Oncol.* **2012**, *127*, 63–69. [CrossRef]
130. Dickson, M.A.; Mahoney, M.R.; Tap, W.D.; D'Angelo, S.P.; Keohan, M.L.; Van Tine, B.A.; Agulnik, M.; Horvath, L.E.; Nair, J.S.; Schwartz, G.K. Phase II study of MLN8237 (Alisertib) in advanced/metastatic sarcoma. *Ann. Oncol.* **2016**, *27*, 1855–1860. [CrossRef]
131. Beltran, H.; Oromendia, C.; Danila, D.C.; Montgomery, B.; Hoimes, C.; Szmulewitz, R.Z.; Vaishampayan, U.; Armstrong, A.J.; Stein, M.; Pinski, J.; et al. A Phase II Trial of the Aurora Kinase Inhibitor Alisertib for Patients with Castration-resistant and Neuroendocrine Prostate Cancer: Efficacy and Biomarkers. *Clin. Cancer Res.* **2019**, *25*, 43–51. [CrossRef]
132. Falchook, G.; Coleman, R.L.; Roszak, A.; Behbakht, K.; Matulonis, U.; Ray-Coquard, I.; Sawrycki, P.; Duska, L.R.; Tew, W.; Ghamande, S.; et al. Alisertib in Combination with Weekly Paclitaxel in Patients With Advanced Breast Cancer or Recurrent Ovarian Cancer: A Randomized Clinical Trial. *JAMA Oncol.* **2019**, *5*, e183773. [CrossRef]
133. Necchi, A.; Lo Vullo, S.; Mariani, L.; Raggi, D.; Giannatempo, P.; Calareso, G.; Togliardi, E.; Crippa, F.; Di Genova, N.; Perrone, F.; et al. An open-label, single-arm, phase 2 study of the Aurora kinase a inhibitor alisertib in patients with advanced urothelial cancer. *Investig. New Drugs* **2016**, *34*, 236–242. [CrossRef]
134. Owonikoko, T.K.; Niu, H.; Nackaerts, K.; Csoszi, T.; Ostoros, G.; Mark, Z.; Baik, C.; Joy, A.A.; Chouaid, C.; Jaime, J.C.; et al. Randomized Phase II Study of Paclitaxel plus Alisertib versus Paclitaxel plus Placebo as Second-Line Therapy for SCLC: Primary and Correlative Biomarker Analyses. *J. Thorac. Oncol.* **2020**, *15*, 274–287. [CrossRef]
135. Graff, J.N.; Higano, C.S.; Hahn, N.M.; Taylor, M.H.; Zhang, B.; Zhou, X.; Venkatakrisnan, K.; Leonard, E.J.; Sarantopoulos, J. Open-label, multicenter, phase 1 study of alisertib (MLN8237), an aurora A kinase inhibitor, with docetaxel in patients with solid tumors. *Cancer* **2016**, *122*, 2524–2533. [CrossRef]
136. Haddad, T.C.; D'Assoro, A.; Suman, V.; Opyrchal, M.; Peethambaram, P.; Liu, M.C.; Goetz, M.P.; Ingle, J.N. Phase I trial to evaluate the addition of alisertib to fulvestrant in women with endocrine-resistant, ER+ metastatic breast cancer. *Breast Cancer Res. Treat.* **2018**, *168*, 639–647. [CrossRef] [PubMed]
137. Goff, L.W.; Azad, N.S.; Stein, S.; Whisenant, J.G.; Koyama, T.; Vaishampayan, U.; Hochster, H.; Connolly, R.; Weise, A.; LoRusso, P.M.; et al. Phase I study combining the aurora kinase a inhibitor alisertib with mFOLFOX in gastrointestinal cancer. *Investig. New Drugs* **2019**, *37*, 315–322. [CrossRef] [PubMed]

138. DuBois, S.G.; Mosse, Y.P.; Fox, E.; Kudgus, R.A.; Reid, J.M.; McGovern, R.; Groshen, S.; Bagatell, R.; Maris, J.M.; Twist, C.J.; et al. Phase II Trial of Alisertib in Combination with Irinotecan and Temozolomide for Patients with Relapsed or Refractory Neuroblastoma. *Clin. Cancer Res.* **2018**, *24*, 6142–6149. [CrossRef] [PubMed]
139. Shah, H.A.; Fischer, J.H.; Venepalli, N.K.; Danciu, O.C.; Christian, S.; Russell, M.J.; Liu, L.C.; Zacny, J.P.; Dudek, A.Z. Phase I Study of Aurora A Kinase Inhibitor Alisertib (MLN8237) in Combination With Selective VEGFR Inhibitor Pazopanib for Therapy of Advanced Solid Tumors. *Am. J. Clin. Oncol.* **2019**, *42*, 413–420. [CrossRef] [PubMed]
140. Kelly, K.R.; Shea, T.C.; Goy, A.; Berdeja, J.G.; Reeder, C.B.; McDonagh, K.T.; Zhou, X.; Danaee, H.; Liu, H.; Ecsedy, J.A.; et al. Phase I study of MLN8237—investigational Aurora A kinase inhibitor—in relapsed/refractory multiple myeloma, non-Hodgkin lymphoma and chronic lymphocytic leukemia. *Investig. New Drugs* **2014**, *32*, 489–499. [CrossRef]
141. Barr, P.M.; Li, H.; Spier, C.; Mahadevan, D.; LeBlanc, M.; Ul Haq, M.; Huber, B.D.; Flowers, C.R.; Wagner-Johnston, N.D.; Horwitz, S.M.; et al. Phase II Intergroup Trial of Alisertib in Relapsed and Refractory Peripheral T-Cell Lymphoma and Transformed Mycosis Fungoides: SWOG 1108. *J. Clin. Oncol.* **2015**, *33*, 2399–2404. [CrossRef]
142. O'Connor, O.A.; Özcan, M.; Jacobsen, E.D.; Roncero, J.M.; Trotman, J.; Demeter, J.; Masszi, T.; Pereira, J.; Ramchandren, R.; Beaven, A.; et al. Randomized phase III study of alisertib or investigator's choice (selected single agent) in patients with relapsed or refractory peripheral T-cell lymphoma. *J. Clin. Oncol.* **2019**, *37*, 613–623. [CrossRef]
143. Friedberg, J.W.; Mahadevan, D.; Cebula, E.; Persky, D.; Lossos, I.; Agarwal, A.B.; Jung, J.; Burack, R.; Zhou, X.; Leonard, E.J.; et al. Phase II study of alisertib, a selective Aurora A kinase inhibitor, in relapsed and refractory aggressive B- and T-cell non-Hodgkin lymphomas. *J. Clin. Oncol.* **2014**, *32*, 44–50. [CrossRef]
144. Kelly, K.R.; Friedberg, J.W.; Park, S.I.; McDonagh, K.; Hayslip, J.; Persky, D.; Ruan, J.; Puvvada, S.; Rosen, P.; Iyer, S.P.; et al. Phase I Study of the Investigational Aurora A Kinase Inhibitor Alisertib plus Rituximab or Rituximab/Vincristine in Relapsed/Refractory Aggressive B-cell Lymphoma. *Clin. Cancer Res.* **2018**, *24*, 6150–6159. [CrossRef]
145. Rosenthal, A.; Kumar, S.; Hofmeister, C.; Laubach, J.; Vij, R.; Dueck, A.; Gano, K.; Stewart, A.K. A Phase Ib Study of the combination of the Aurora Kinase Inhibitor Alisertib (MLN8237) and Bortezomib in Relapsed Multiple Myeloma. *Br. J. Haematol.* **2016**, *174*, 323–325. [CrossRef]
146. Brunner, A.M.; Blonquist, T.M.; DeAngelo, D.J.; McMasters, M.; Fell, G.; Hermance, N.M.; Winer, E.S.; Lindsley, R.C.; Hobbs, G.S.; Amrein, P.C.; et al. Alisertib plus induction chemotherapy in previously untreated patients with high-risk, acute myeloid leukaemia: A single-arm, phase 2 trial. *Lancet Haematol.* **2020**, *7*, e122–e133. [CrossRef]
147. Mossé, Y.P.; Lipsitz, E.; Fox, E.; Teachey, D.T.; Maris, J.M.; Weigel, B.; Adamson, P.C.; Ingle, M.A.; Ahern, C.H.; Blaney, S.M. Pediatric phase I trial and pharmacokinetic study of MLN8237, an investigational oral selective small-molecule inhibitor of Aurora kinase A: A Children's Oncology Group Phase I Consortium study. *Clin. Cancer Res.* **2012**, *18*, 6058–6064. [CrossRef]
148. Mossé, Y.P.; Fox, E.; Teachey, D.T.; Reid, J.M.; Safgren, S.L.; Carol, H.; Lock, R.B.; Houghton, P.J.; Smith, M.A.; Hall, D.; et al. A Phase II Study of Alisertib in Children with Recurrent/Refractory Solid Tumors or Leukemia: Children's Oncology Group Phase I and Pilot Consortium (ADVL0921). *Clin. Cancer Res.* **2019**, *25*, 3229–3238. [CrossRef]
149. Fletcher, G.C.; Brokx, R.D.; Denny, T.A.; Hembrough, T.A.; Plum, S.M.; Fogler, W.E.; Sidor, C.F.; Bray, M.R. ENMD-2076 is an orally active kinase inhibitor with antiangiogenic and antiproliferative mechanisms of action. *Mol. Cancer Ther.* **2011**, *10*, 126–137. [CrossRef]
150. Diamond, J.R.; Bastos, B.R.; Hansen, R.J.; Gustafson, D.L.; Eckhardt, S.G.; Kwak, E.L.; Pandya, S.S.; Fletcher, G.C.; Pitts, T.M.; Kulikowski, G.N.; et al. Phase I safety, pharmacokinetic, and pharmacodynamic study of ENMD-2076, a novel angiogenic and aurora kinase inhibitor, in patients with advanced solid tumors. *Clin. Cancer Res.* **2011**, *17*, 849–860. [CrossRef]
151. Matulonis, U.A.; Lee, J.; Lasonde, B.; Tew, W.P.; Yehwalashet, A.; Matei, D.; Behbakht, K.; Grothusen, J.; Fleming, G.; Lee, N.K.; et al. ENMD-2076, an oral inhibitor of angiogenic and proliferation kinases, has activity in recurrent, platinum resistant ovarian cancer. *Eur. J. Cancer* **2013**, *49*, 121–131. [CrossRef]
152. Lheureux, S.; Tinker, A.; Clarke, B.; Ghatage, P.; Welch, S.; Weberpals, J.I.; Dhani, N.C.; Butler, M.O.; Tonkin, K.; Tan, Q.; et al. A Clinical and Molecular Phase II Trial of Oral ENMD-2076 in Ovarian Clear Cell Carcinoma (OCCC): A Study of the Princess Margaret Phase II Consortium. *Clin. Cancer Res.* **2018**, *24*, 6168–6174. [CrossRef]
153. Veitch, Z.; Zer, A.; Loong, H.; Salah, S.; Masood, M.; Gupta, A.; Bradbury, P.A.; Hogg, D.; Wong, A.; Kandel, R.; et al. A phase II study of ENMD-2076 in advanced soft tissue sarcoma (STS). *Sci. Rep.* **2019**, *9*. [CrossRef] [PubMed]
154. Diamond, J.R.; Eckhardt, S.G.; Pitts, T.M.; van Bokhoven, A.; Aisner, D.; Gustafson, D.L.; Capasso, A.; Sams, S.; Kabos, P.; Zolman, K.; et al. A phase II clinical trial of the Aurora and angiogenic kinase inhibitor ENMD-2076 for previously treated, advanced, or metastatic triple-negative breast cancer. *Breast Cancer Res.* **2018**, *20*, 82. [CrossRef] [PubMed]
155. Abou-Alfa, G.K.; Mayer, R.; Venook, A.P.; O'Neill, A.F.; Beg, M.S.; LaQuaglia, M.; Kingham, P.T.; Kobos, R.; Basturk, O.; Brennan, C.; et al. Phase II Multicenter, Open-Label Study of Oral ENMD-2076 for the Treatment of Patients with Advanced Fibrolamellar Carcinoma. *Oncologist* **2020**, *25*, e1837–e1845. [CrossRef] [PubMed]
156. Yee, K.W.L.; Chen, H.-W.T.; Hedley, D.W.; Chow, S.; Brandwein, J.; Schuh, A.C.; Schimmer, A.D.; Gupta, V.; Sanfelice, D.; Johnson, T.; et al. A phase I trial of the aurora kinase inhibitor, ENMD-2076, in patients with relapsed or refractory acute myeloid leukemia or chronic myelomonocytic leukemia. *Investig. New Drugs* **2016**, *34*, 614–624. [CrossRef]
157. Chu, Q.; Bouganin, N.; Fortier, C.; Zaknoen, S.; Stille, J.R.; Kremer, J.D.; Yuen, E.; Hui, Y.-H.; Peña, A.; de la Lithio, A.; et al. Abstract CT083: A Phase I/II study of aurora kinase A inhibitor, LY3295668 erbumine (AK-01): Safety as monotherapy in patients with locally advanced or metastatic solid tumors. *Cancer Res.* **2019**, *79*, CT083. [CrossRef]

158. Manfredi, M.G.; Ecsedy, J.A.; Meetze, K.A.; Balani, S.K.; Burenkova, O.; Chen, W.; Galvin, K.M.; Hoar, K.M.; Huck, J.J.; LeRoy, P.J.; et al. Antitumor activity of MLN8054, an orally active small-molecule inhibitor of Aurora A kinase. *Proc. Natl. Acad. Sci. USA* **2007**, *104*, 4106–4111. [CrossRef]
159. Dees, E.C.; Infante, J.R.; Cohen, R.B.; O’Neil, B.H.; Jones, S.; von Mehren, M.; Danaee, H.; Lee, Y.; Ecsedy, J.; Manfredi, M.; et al. Phase 1 study of MLN8054, a selective inhibitor of Aurora A kinase in patients with advanced solid tumors. *Cancer Chemother. Pharm.* **2011**, *67*, 945–954. [CrossRef]
160. Macarulla, T.; Cervantes, A.; Elez, E.; Rodríguez-Braun, E.; Baselga, J.; Roselló, S.; Sala, G.; Blasco, I.; Danaee, H.; Lee, Y.; et al. Phase I study of the selective Aurora A kinase inhibitor MLN8054 in patients with advanced solid tumors: Safety, pharmacokinetics, and pharmacodynamics. *Mol. Cancer Ther.* **2010**, *9*, 2844–2852. [CrossRef]
161. Shimomura, T.; Hasako, S.; Nakatsuru, Y.; Mita, T.; Ichikawa, K.; Kodera, T.; Sakai, T.; Nambu, T.; Miyamoto, M.; Takahashi, I.; et al. MK-5108, a highly selective Aurora-A kinase inhibitor, shows antitumor activity alone and in combination with docetaxel. *Mol. Cancer Ther.* **2010**, *9*, 157–166. [CrossRef]
162. Amin, M.; Minton, S.E.; LoRusso, P.M.; Krishnamurthi, S.S.; Pickett, C.A.; Lunceford, J.; Hille, D.; Mauro, D.; Stein, M.N.; Wang-Gillam, A.; et al. A phase I study of MK-5108, an oral aurora kinase inhibitor, administered both as monotherapy and in combination with docetaxel, in patients with advanced or refractory solid tumors. *Investig. New Drugs* **2016**, *34*, 84–95. [CrossRef]
163. Miura, A.; Sootome, H.; Fujita, N.; Suzuki, T.; Fukushima, H.; Mizuarai, S.; Masuko, N.; Ito, K.; Hashimoto, A.; Uto, Y.; et al. TAS-119, a novel selective Aurora A and TRK inhibitor, exhibits antitumor efficacy in preclinical models with deregulated activation of the Myc,  $\beta$ -Catenin, and TRK pathways. *Investig. New Drugs* **2021**. [CrossRef]
164. Robbrecht, D.G.J.; Lopez, J.; Calvo, E.; He, X.; Hiroshi, H.; Soni, N.; Cook, N.; Dowlati, A.; Fasolo, A.; Moreno, V.; et al. A first-in-human phase 1 and pharmacological study of TAS-119, a novel selective Aurora A kinase inhibitor in patients with advanced solid tumours. *Br. J. Cancer* **2020**, 1–8. [CrossRef]
165. Cardin, D.B.; Park, H.; Diamond, J.R.; Drilon, A.E.; VerMeulen, W.L.; He, X.; Hirai, H.; Soni, N.; Berlin, J. Phase I study of the Aurora A kinase (AurA) inhibitor TAS-119 with paclitaxel (P) in advanced solid tumors. *JCO* **2019**, *37*, 3031. [CrossRef]
166. Shiotsu, Y.; Kiyoi, H.; Ishikawa, Y.; Tanizaki, R.; Shimizu, M.; Umehara, H.; Ishii, K.; Mori, Y.; Ozeki, K.; Minami, Y.; et al. KW-2449, a novel multikinase inhibitor, suppresses the growth of leukemia cells with FLT3 mutations or T315I-mutated BCR/ABL translocation. *Blood* **2009**, *114*, 1607–1617. [CrossRef]
167. Farag, S.; Zhang, S.; Suvannasankha, A.; Liang, J.; O’Byrant, R.; Lisa, W.; Gupta, S.; Bray, M.; Sidor, C.F.; Abonour, R. Clinical Activity of a Novel Multiple Tyrosine Kinase and Aurora Kinase Inhibitor, ENMD-2076, Against Multiple Myeloma: Interim Phase I Trial Results. *Blood* **2010**, *116*, 1957. [CrossRef]
168. Warner, S.L.; Munoz, R.M.; Stafford, P.; Koller, E.; Hurley, L.H.; Hoff, D.D.; Von Han, H. Comparing Aurora A and Aurora B as molecular targets for growth inhibition of pancreatic cancer cells. *Mol. Cancer Ther.* **2006**, *5*, 2450–2458. [CrossRef]
169. Carpinelli, P.; Moll, J. Aurora kinase inhibitors: Identification and preclinical validation of their biomarkers. *Expert Opin. Targets* **2008**, *12*, 69–80. [CrossRef]
170. Ohashi, A.; Otori, M.; Iwai, K. Motor activity of centromere-associated protein-E contributes to its localization at the center of the midbody to regulate cytokinetic abscission. *Oncotarget* **2016**, *7*, 79964–79980. [CrossRef]
171. Yu, K.-W.; Zhong, N.; Xiao, Y.; She, Z.-Y. Mechanisms of kinesin-7 CENP-E in kinetochore-microtubule capture and chromosome alignment during cell division. *Biol. Cell* **2019**, *111*, 143–160. [CrossRef]
172. Mao, Y.; Desai, A.; Cleveland, D.W. Microtubule capture by CENP-E silences BubR1-dependent mitotic checkpoint signaling. *J. Cell Biol.* **2005**, *170*, 873–880. [CrossRef]
173. Kung, P.-P.; Martinez, R.; Zhu, Z.; Zager, M.; Blasina, A.; Rymer, I.; Hallin, J.; Xu, M.; Carroll, C.; Chionis, J.; et al. Chemogenetic evaluation of the mitotic kinesin CENP-E reveals a critical role in triple-negative breast cancer. *Mol. Cancer Ther.* **2014**, *13*, 2104–2115. [CrossRef]
174. Ohashi, A.; Otori, M.; Iwai, K.; Nambu, T.; Miyamoto, M.; Kawamoto, T.; Okaniwa, M. A novel time-dependent CENP-E inhibitor with potent antitumor activity. *PLoS ONE* **2015**, *10*. [CrossRef]
175. Tanudji, M.; Shoemaker, J.; L’Italien, L.; Russell, L.; Chin, G.; Schebye, X.M. Gene silencing of CENP-E by small interfering RNA in HeLa cells leads to missegregation of chromosomes after a mitotic delay. *Mol. Biol. Cell* **2004**, *15*, 3771–3781. [CrossRef]
176. Wood, K.W.; Lad, L.; Luo, L.; Qian, X.; Knight, S.D.; Nevins, N.; Brejc, K.; Sutton, D.; Gilmartin, A.G.; Chua, P.R.; et al. Antitumor activity of an allosteric inhibitor of centromere-associated protein-E. *Proc. Natl. Acad. Sci. USA* **2010**, *107*, 5839–5844. [CrossRef]
177. Chung, V.; Heath, E.I.; Schelman, W.R.; Johnson, B.M.; Kirby, L.C.; Lynch, K.M.; Botbyl, J.D.; Lampkin, T.A.; Holen, K.D. First-time-in-human study of GSK923295, a novel antimitotic inhibitor of centromere-associated protein e (CENP-E), in patients with refractory cancer. *Cancer Chemother. Pharm.* **2012**, *69*, 733–741. [CrossRef]
178. Sawin, K.E.; LeGuellec, K.; Philippe, M.; Mitchison, T.J. Mitotic spindle organization by a plus-end-directed microtubule motor. *Nature* **1992**, *359*, 540–543. [CrossRef]
179. Blangy, A.; Lane, H.A.; D’Hérin, P.; Harper, M.; Kress, M.; Nigg, E.A. Phosphorylation by p34cdc2 regulates spindle association of human Eg5, a kinesin-related motor essential for bipolar spindle formation in vivo. *Cell* **1995**, *83*, 1159–1169. [CrossRef]
180. Weil, D.; Garçon, L.; Harper, M.; Duménil, D.; Dautry, F.; Kress, M. Targeting the kinesin Eg5 to monitor siRNA transfection in mammalian cells. *Biotechniques* **2002**, *33*, 1244–1248. [CrossRef]

181. Nakai, R.; Iida, S.; Takahashi, T.; Tsujita, T.; Okamoto, S.; Takada, C.; Akasaka, K.; Ichikawa, S.; Ishida, H.; Kusaka, H.; et al. K858, a novel inhibitor of mitotic kinesin Eg5 and antitumor agent, induces cell death in cancer cells. *Cancer Res.* **2009**, *69*, 3901–3909. [CrossRef] [PubMed]
182. Liu, M.; Yu, H.; Huo, L.; Liu, J.; Li, M.; Zhou, J. Validating the mitotic kinesin Eg5 as a therapeutic target in pancreatic cancer cells and tumor xenografts using a specific inhibitor. *Biochem. Pharm. Ther.* **2008**, *76*, 169–178. [CrossRef]
183. Liu, L.; Liu, X.; Mare, M.; Dumont, A.S.; Zhang, H.; Yan, D.; Xiong, Z. Overexpression of Eg5 correlates with high grade astrocytic neoplasm. *J. Neurooncol* **2016**, *126*, 77–80. [CrossRef]
184. Liu, C.; Zhou, N.; Li, J.; Kong, J.; Guan, X.; Wang, X. Eg5 Overexpression Is Predictive of Poor Prognosis in Hepatocellular Carcinoma Patients. *Dis. Markers* **2017**, 2017. [CrossRef]
185. Ding, S.; Xing, N.; Lu, J.; Zhang, H.; Nishizawa, K.; Liu, S.; Yuan, X.; Qin, Y.; Liu, Y.; Ogawa, O.; et al. Overexpression of Eg5 predicts unfavorable prognosis in non-muscle invasive bladder urothelial carcinoma. *Int. J. Urol.* **2011**, *18*, 432–438. [CrossRef]
186. Liu, M.; Wang, X.; Yang, Y.; Li, D.; Ren, H.; Zhu, Q.; Chen, Q.; Han, S.; Hao, J.; Zhou, J. Ectopic expression of the microtubule-dependent motor protein Eg5 promotes pancreatic tumorigenesis. *J. Pathol.* **2010**, *221*, 221–228. [CrossRef]
187. Blagden, S.P.; Molife, L.R.; Seebaran, A.; Payne, M.; Reid, A.H.M.; Protheroe, A.S.; Vasist, L.S.; Williams, D.D.; Bowen, C.; Kathman, S.J.; et al. A phase I trial of ispinesib, a kinesin spindle protein inhibitor, with docetaxel in patients with advanced solid tumours. *Br. J. Cancer* **2008**, *98*, 894–899. [CrossRef]
188. Rodon, J.; Till, E.; Patnaik, A.; Takimoto, C.; Beeram, M.; Williams, D.; Bowen, C.; Hodge, J.; Dar, M.; Tochner, A. 640 POSTER Phase I study of ispinesib (SB-715992), a kinesin spindle protein inhibitor, in combination with capecitabine in patients with advanced solid tumors. *Eur. J. Cancer Suppl.* **2006**, *4*, 193. [CrossRef]
189. Jones, S.F.; Plummer, E.R.; Burris, H.A.; Razak, A.R.; Meluch, A.A.; Bowen, C.J.; Williams, D.H.; Hodge, J.P.; Dar, M.M.; Calvert, A.H. Phase I study of ispinesib in combination with carboplatin in patients with advanced solid tumors. *JCO* **2006**, *24*, 2027. [CrossRef]
190. Beer, T.M.; Goldman, B.; Synold, T.W.; Ryan, C.W.; Vasist, L.S.; Van Veldhuizen, P.J.; Dakhil, S.R.; Lara, P.N.; Drelichman, A.; Hussain, M.H.A.; et al. Southwest Oncology Group phase II study of ispinesib in androgen-independent prostate cancer previously treated with taxanes. *Clin. Genitourin Cancer* **2008**, *6*, 103–109. [CrossRef]
191. Tang, P.A.; Siu, L.L.; Chen, E.X.; Hotte, S.J.; Chia, S.; Schwarz, J.K.; Pond, G.R.; Johnson, C.; Colevas, A.D.; Synold, T.W.; et al. Phase II study of ispinesib in recurrent or metastatic squamous cell carcinoma of the head and neck. *Investig. New Drugs* **2008**, *26*, 257–264. [CrossRef]
192. Lee, C.W.; Bélanger, K.; Rao, S.C.; Petrella, T.M.; Tozer, R.G.; Wood, L.; Savage, K.J.; Eisenhauer, E.A.; Synold, T.W.; Wainman, N.; et al. A phase II study of ispinesib (SB-715992) in patients with metastatic or recurrent malignant melanoma: A National Cancer Institute of Canada Clinical Trials Group trial. *Investig. New Drugs* **2008**, *26*, 249–255. [CrossRef]
193. Knox, J.J.; Gill, S.; Synold, T.W.; Biagi, J.J.; Major, P.; Feld, R.; Cripps, C.; Wainman, N.; Eisenhauer, E.; Seymour, L. A phase II and pharmacokinetic study of SB-715992, in patients with metastatic hepatocellular carcinoma: A study of the National Cancer Institute of Canada Clinical Trials Group (NCIC CTG IND.168). *Investig. New Drugs* **2008**, *26*, 265–272. [CrossRef]
194. Lee, R.T.; Beekman, K.E.; Hussain, M.; Davis, N.B.; Clark, J.I.; Thomas, S.P.; Nichols, K.F.; Stadler, W.M. A University of Chicago consortium phase II trial of SB-715992 in advanced renal cell cancer. *Clin. Genitourin. Cancer* **2008**, *6*, 21–24. [CrossRef]
195. Shahin, M.S.; Braly, P.; Rose, P.; Malpass, T.; Bailey, H.; Alvarez, R.D.; Hodge, J.; Bowen, C.; Buller, R. A phase II, open-label study of ispinesib (SB-715992) in patients with platinum/taxane refractory or resistant relapsed ovarian cancer. *JCO* **2007**, *25*, 5562. [CrossRef]
196. Gomez, H.L.; Philco, M.; Pimentel, P.; Kiyan, M.; Monsalvo, M.L.; Conlan, M.G.; Saikali, K.G.; Chen, M.M.; Seroogy, J.J.; Wolff, A.A.; et al. Phase I dose-escalation and pharmacokinetic study of ispinesib, a kinesin spindle protein inhibitor, administered on days 1 and 15 of a 28-day schedule in patients with no prior treatment for advanced breast cancer. *Anticancer Drugs* **2012**, *23*, 335–341. [CrossRef]
197. Soud, A.-K.; Dubowy, R.L.; Ingle, A.M.; Conlan, M.G.; Sun, J.; Blaney, S.M.; Adamson, P.C. A pediatric phase I trial and pharmacokinetic study of ispinesib: A Children’s Oncology Group phase I consortium study. *Pediatr. Blood Cancer* **2010**, *55*, 1323–1328. [CrossRef]
198. Jackson, J.R.; Gilmartin, A.; Dhanak, D.; Knight, S.; Parrish, C.; Luo, L.; Sutton, D.; Caulder, E.; Diamond, M.; Giardinieri, M.; et al. A second generation KSP inhibitor, SB-743921, is a highly potent and active therapeutic in preclinical models of cancer. *Clin. Cancer Res.* **2006**, *12*, B11.
199. Holen, K.D.; Belani, C.P.; Wilding, G.; Ramalingam, S.; Volkman, J.L.; Ramanathan, R.K.; Vasist, L.S.; Bowen, C.J.; Hodge, J.P.; Dar, M.M.; et al. A first in human study of SB-743921, a kinesin spindle protein inhibitor, to determine pharmacokinetics, biologic effects and establish a recommended phase II dose. *Cancer Chemother. Pharm.* **2011**, *67*, 447–454. [CrossRef]
200. O’Connor, O.A.; Gerecitano, J.; Van Deventer, H.; Hainsworth, J.; Zullo, K.M.; Saikali, K.; Seroogy, J.; Wolff, A.; Escandón, R. The addition of granulocyte-colony stimulating factor shifts the dose limiting toxicity and markedly increases the maximum tolerated dose and activity of the kinesin spindle protein inhibitor SB-743921 in patients with relapsed or refractory lymphoma: R. *Leuk. Lymphoma* **2015**, *56*, 2585–2591. [CrossRef]
201. Lemieux, C.; Dewolf, W.; Voegtli, W.; Delisle, R.; Laird, E.; Wallace, E.; Woessner, R.; Corrette, C.; Allen, S.; Hans, J.; et al. ARRY-520, a novel, highly selective KSP inhibitor with potent anti-proliferative activity. *Proc. Am. Assoc. Cancer Res.* **2007**, *48*, 5590.



202. LoRusso, P.M.; Goncalves, P.H.; Casetta, L.; Carter, J.A.; Litwiler, K.; Roseberry, D.; Rush, S.; Schreiber, J.; Simmons, H.M.; Ptaszynski, M.; et al. First-in-human phase 1 study of filanesib (ARRY-520), a kinesin spindle protein inhibitor, in patients with advanced solid tumors. *Investig. New Drugs* **2015**, *33*, 440–449. [CrossRef]
203. Khoury, H.J.; Garcia-Manero, G.; Borthakur, G.; Kadia, T.; Foudray, M.C.; Arellano, M.; Langston, A.; Bethelmie-Bryan, B.; Rush, S.; Litwiler, K.; et al. A phase 1 dose-escalation study of ARRY-520, a kinesin spindle protein inhibitor, in patients with advanced myeloid leukemias. *Cancer* **2012**, *118*, 3556–3564. [CrossRef]
204. Shah, J.J.; Kaufman, J.L.; Zonder, J.A.; Cohen, A.D.; Bensinger, W.I.; Hilder, B.; Rush, S.; Walker, D.; Tunquist, B.; Litwiler, K.; et al. A Phase 1/2 study of filanesib alone and in combination with low-dose dexamethasone in relapsed/refractory multiple myeloma. *Cancer* **2017**, *123*, 4617–4630. [CrossRef]
205. Chari, A.; Htut, M.; Zonder, J.A.; Fay, J.W.; Jakubowiak, A.J.; Levy, J.B.; Lau, K.; Burt, S.M.; Tunquist, B.J.; Hilder, B.W.; et al. A phase 1 dose-escalation study of filanesib plus bortezomib and dexamethasone in patients with recurrent/refractory multiple myeloma. *Cancer* **2016**, *122*, 3327–3335. [CrossRef]
206. Lee, H.C.; Shah, J.J.; Feng, L.; Manasanch, E.E.; Lu, R.; Morphey, A.; Crumpton, B.; Patel, K.K.; Wang, M.L.; Alexanian, R.; et al. A phase 1 study of filanesib, carfilzomib, and dexamethasone in patients with relapsed and/or refractory multiple myeloma. *Blood Cancer J.* **2019**, *9*, 80. [CrossRef]
207. Ocio, E.M.; Motlló, C.; Rodríguez-Otero, P.; Martínez-López, J.; Cejalvo, M.J.; Martín-Sánchez, J.; Bladé, J.; García-Malo, M.D.; Dourdil, M.V.; García-Mateo, A.; et al. Filanesib in combination with pomalidomide and dexamethasone in refractory MM patients: Safety and efficacy, and association with alpha 1-acid glycoprotein (AAG) levels. Phase Ib/II Pomdefil clinical trial conducted by the Spanish MM group. *Br. J. Haematol.* **2021**, *192*, 522–530. [CrossRef]
208. Toudjarska, I.; Judge, A.; Buck, T.; McClintock, K.; Jong, S.; de Ambegia, E.; Brodsky, J.; Akinc, A.; Racie, T.; Jeffs, L.; et al. Abstract B204: Development of ALN-VSP: An RNAi therapeutic for liver malignancies. *Mol. Cancer Ther.* **2009**, *8*, B204. [CrossRef]
209. Taberero, J.; Shapiro, G.I.; LoRusso, P.M.; Cervantes, A.; Schwartz, G.K.; Weiss, G.J.; Paz-Ares, L.; Cho, D.C.; Infante, J.R.; Alsina, M.; et al. First-in-humans trial of an RNA interference therapeutic targeting VEGF and KSP in cancer patients with liver involvement. *Cancer Discov.* **2013**, *3*, 406–417. [CrossRef]
210. Ye, X.S.; Fan, L.; Van Horn, R.D.; Nakai, R.; Ohta, Y.; Akinaga, S.; Murakata, C.; Yamashita, Y.; Yin, T.; Credille, K.M.; et al. A novel Eg5 inhibitor (LY2523355) causes mitotic arrest and apoptosis in cancer cells and shows potent antitumor activity in xenograft tumor models. *Mol. Cancer Ther.* **2015**, *14*, 2463–2472. [CrossRef]
211. Infante, J.R.; Patnaik, A.; Verschraegen, C.F.; Olszanski, A.J.; Shaheen, M.; Burris, H.A.; Tolcher, A.W.; Papadopoulos, K.P.; Beeram, M.; Hynes, S.M.; et al. Two Phase 1 dose-escalation studies exploring multiple regimens of litronesib (LY2523355), an Eg5 inhibitor, in patients with advanced cancer. *Cancer Chemother. Pharm.* **2017**, *79*, 315–326. [CrossRef]
212. Wakui, H.; Yamamoto, N.; Kitazono, S.; Mizugaki, H.; Nakamichi, S.; Fujiwara, Y.; Nokihara, H.; Yamada, Y.; Suzuki, K.; Kanda, H.; et al. A phase 1 and dose-finding study of LY2523355 (litronesib), an Eg5 inhibitor, in Japanese patients with advanced solid tumors. *Cancer Chemother. Pharm.* **2014**, *74*, 15–23. [CrossRef]
213. Schiemann, K.; Finsinger, D.; Zenke, F.; Amendt, C.; Knöchel, T.; Bruge, D.; Buchstaller, H.-P.; Emde, U.; Stähle, W.; Anzali, S. The discovery and optimization of hexahydro-2H-pyrano[3,2-c]quinolines (HHPQs) as potent and selective inhibitors of the mitotic kinesin-5. *Bioorg. Med. Chem. Lett.* **2010**, *20*, 1491–1495. [CrossRef]
214. Hollebecque, A.; Deutsch, E.; Massard, C.; Gomez-Roca, C.; Bahleda, R.; Ribrag, V.; Bourgier, C.; Lazar, V.; Lacroix, L.; Gazzah, A.; et al. A phase I, dose-escalation study of the Eg5-inhibitor EMD 534085 in patients with advanced solid tumors or lymphoma. *Investig. New Drugs* **2013**, *31*, 1530–1538. [CrossRef]
215. Mross, K.B.; Scharf, D.; Richly, H.; Frost, A.; Bauer, S.; Krauss, B.; Krauss, R.; Mais, A.; Hauns, B.; Hentsch, B.; et al. First-in-human study of 4SC-205 (AEGIS), a novel oral inhibitor of Eg5 kinesin spindle protein. *JCO* **2014**, *32*, 2564. [CrossRef]
216. Theoclitou, M.-E.; Aquila, B.; Block, M.H.; Brassil, P.J.; Castriotta, L.; Code, E.; Collins, M.P.; Davies, A.M.; Deegan, T.; Ezhuthachan, J.; et al. Discovery of (+)-N-(3-aminopropyl)-N-[1-(5-benzyl-3-methyl-4-oxo-[1,2]thiazolo[5,4-d]pyrimidin-6-yl)-2-methylpropyl]-4-methylbenzamide (AZD4877), a kinesin spindle protein inhibitor and potential anticancer agent. *J. Med. Chem.* **2011**, *54*, 6734–6750. [CrossRef]
217. Esaki, T.; Seto, T.; Ariyama, H.; Arita, S.; Fujimoto, C.; Tsukasa, K.; Kometani, T.; Nosaki, K.; Hirai, F.; Yagawa, K. Phase I study to assess the safety, Tolerability and pharmacokinetics of AZD4877 in Japanese patients with solid tumors. *Arch. Drug Inf.* **2011**, *4*, 23–31. [CrossRef]
218. Infante, J.R.; Kurzrock, R.; Spratlin, J.; Burris, H.A.; Eckhardt, S.G.; Li, J.; Wu, K.; Skolnik, J.M.; Hylander-Gans, L.; Osmukhina, A.; et al. A Phase I study to assess the safety, tolerability, and pharmacokinetics of AZD4877, an intravenous Eg5 inhibitor in patients with advanced solid tumors. *Cancer Chemother. Pharm.* **2012**, *69*, 165–172. [CrossRef]
219. Jones, R.; Vuky, J.; Elliott, T.; Mead, G.; Arranz, J.A.; Chester, J.; Chowdhury, S.; Dudek, A.Z.; Müller-Mattheis, V.; Grimm, M.-O.; et al. Phase II study to assess the efficacy, safety and tolerability of the mitotic spindle kinesin inhibitor AZD4877 in patients with recurrent advanced urothelial cancer. *Investig. New Drugs* **2013**, *31*, 1001–1007. [CrossRef]
220. Kantarjian, H.M.; Padmanabhan, S.; Stock, W.; Tallman, M.S.; Curt, G.A.; Li, J.; Osmukhina, A.; Wu, K.; Huszar, D.; Borthukar, G.; et al. Phase I/II multicenter study to assess the safety, tolerability, pharmacokinetics and pharmacodynamics of AZD4877 in patients with refractory acute myeloid leukemia. *Investig. New Drugs* **2012**, *30*, 1107–1115. [CrossRef]
221. Jeay, S.; Ali, S.; Chen, C.-R.; Uppalapati, U.; Senator, D.; Chan, T.; France, D.; Ashwell, M. Discovery of a novel Eg5 kinesin inhibitor, ARQ 621, with potent antitumor activity while sparing bone marrow-derived cells. *Cancer Res.* **2008**, *68*, 656.

222. Chen, L.C.; Rosen, L.S.; Iyengar, T.; Goldman, J.W.; Savage, R.; Kazakin, J.; Chan, T.C.K.; Schwartz, B.E.; Abbadessa, G.; Von Hoff, D.D. First-in-human study with ARQ 621, a novel inhibitor of Eg5: Final results from the solid tumors cohort. *JCO* **2011**, *29*, 3076. [CrossRef]
223. Cox, C.D.; Garbaccio, R.M. Discovery of allosteric inhibitors of kinesin spindle protein (KSP) for the treatment of taxane-refractory cancer: MK-0731 and analogs. *Anticancer Agents Med. Chem.* **2010**, *10*, 697–712. [CrossRef] [PubMed]
224. Holen, K.; DiPaola, R.; Liu, G.; Tan, A.R.; Wilding, G.; Hsu, K.; Agrawal, N.; Chen, C.; Xue, L.; Rosenberg, E.; et al. A phase I trial of MK-0731, a kinesin spindle protein (KSP) inhibitor, in patients with solid tumors. *Investig. New Drugs* **2012**, *30*, 1088–1095. [CrossRef] [PubMed]
225. Gerecitano, J.F.; Stephenson, J.J.; Lewis, N.L.; Osmukhina, A.; Li, J.; Wu, K.; You, Z.; Huszar, D.; Skolnik, J.M.; Schwartz, G.K. A Phase I trial of the kinesin spindle protein (Eg5) inhibitor AZD4877 in patients with solid and lymphoid malignancies. *Investig. New Drugs* **2013**, *31*, 355–362. [CrossRef] [PubMed]
226. Mitchison, T.J. The proliferation rate paradox in antimetabolic chemotherapy. *Mol. Biol. Cell* **2012**, *23*, 1–6. [CrossRef] [PubMed]
227. Bennett, A.; Sloss, O.; Topham, C.; Nelson, L.; Tighe, A.; Taylor, S.S. Inhibition of Bcl-xL sensitizes cells to mitotic blockers, but not mitotic drivers. *Open Biol.* **2016**, *6*, 160134. [CrossRef] [PubMed]
228. Gascoigne, K.E.; Taylor, S.S. Cancer Cells Display Profound Intra- and Interline Variation following Prolonged Exposure to Antimitotic Drugs. *Cancer Cell* **2008**, *14*, 111–122. [CrossRef]
229. Fitzgerald, K.A.; Malhotra, M.; Curtin, C.M.; O' Brien, F.J.; O' Driscoll, C.M. Life in 3D is never flat: 3D models to optimise drug delivery. *J. Control. Release* **2015**, *215*, 39–54. [CrossRef]
230. Pinto, B.; Henriques, A.C.; Silva, P.M.A.; Bousbaa, H. Three-Dimensional Spheroids as In vitro Preclinical Models for Cancer Research. *Pharmaceutics* **2020**, *12*, 1186. [CrossRef]
231. Sgorla, D.; Bunhak, É.J.; Cavalcanti, O.A.; Fonte, P.; Sarmiento, B. Exploitation of lipid-polymeric matrices at nanoscale for drug delivery applications. *Expert Opin. Drug. Deliv.* **2016**, *13*, 1301–1309. [CrossRef]
232. Lv, J.-F.; Hu, L.; Zhuo, W.; Zhang, C.-M.; Zhou, H.-H.; Fan, L. Epigenetic alternations and cancer chemotherapy response. *Cancer Chemother. Pharm.* **2016**, *77*, 673–684. [CrossRef]
233. Mountzios, G.; Dimopoulos, M.-A.; Soria, J.-C.; Sanoudou, D.; Papadimitriou, C.A. Histopathologic and genetic alterations as predictors of response to treatment and survival in lung cancer: A review of published data. *Crit. Rev. Oncol. Hematol.* **2010**, *75*, 94–109. [CrossRef]



## Article

# Navitoclax Enhances the Therapeutic Effects of PLK1 Targeting on Lung Cancer Cells in 2D and 3D Culture Systems

Bárbara Pinto <sup>1,2,†</sup>, Pedro Novais <sup>1,3,4,†</sup> , Ana C. Henriques <sup>1</sup>, Juliana Carvalho-Tavares <sup>2</sup>,  
Patrícia M. A. Silva <sup>1,5,\*</sup>  and Hassan Bousbaa <sup>1,6,\*</sup> 

<sup>1</sup> UNIPRO—Oral Pathology and Rehabilitation Research Unit, University Institute of Health Sciences (IUCS), Cooperativa de Ensino Superior Politécnico e Universitário (CESPU), Rua Central de Gandra, 1317, 4585-116 Gandra, Portugal; barbara\_fernandes\_pinto@hotmail.com (B.P.); pedro.ha.novais@gmail.com (P.N.); a24955@alunos.cespu.pt (A.C.H.)

<sup>2</sup> Departamento de Fisiologia e Biofísica, Instituto de Ciências Biológicas, Universidade Federal de Minas Gerais, Belo Horizonte 31270-901, Brazil; julianact@ufmg.br

<sup>3</sup> Faculty of Sciences, University of Porto, Rua do Campo Alegre, s/n, 4169-007 Porto, Portugal

<sup>4</sup> Instituto de Ciências Biomédicas Abel Salazar (ICBAS), University of Porto, 4050-313 Porto, Portugal

<sup>5</sup> TOXRUN—Toxicology Research Unit, University Institute of Health Sciences (IUCS), Cooperativa de Ensino Superior Politécnico e Universitário (CESPU), Rua Central de Gandra, 1317, 4585-116 Gandra, Portugal

<sup>6</sup> Centro Interdisciplinar de Investigação Marinha e Ambiental (CIIMAR), Universidade do Porto, Terminal de Cruzeiros do Porto de Leixões, Av. General Norton de Matos s/n, 4450-208 Matosinhos, Portugal

\* Correspondence: patricia.silva@cespu.pt (P.M.A.S.); hassan.bousbaa@iucs.cespu.pt (H.B.); Tel.: +351-224157189 (P.M.A.S.); +351-224157186 (H.B.)

† These authors contributed equally to this work.

**Citation:** Pinto, B.; Novais, P.; Henriques, A.C.; Carvalho-Tavares, J.; Silva, P.M.A.; Bousbaa, H. Navitoclax Enhances the Therapeutic Effects of PLK1 Targeting on Lung Cancer Cells in 2D and 3D Culture Systems. *Pharmaceutics* **2022**, *14*, 1209. <https://doi.org/10.3390/pharmaceutics14061209>

Academic Editor: Tomáš Etrych

Received: 23 May 2022

Accepted: 4 June 2022

Published: 6 June 2022

**Publisher's Note:** MDPI stays neutral with regard to jurisdictional claims in published maps and institutional affiliations.

**Abstract:** The efficacy of antimetotics is limited by slippage, whereby treated cells arrested in mitosis exit mitosis without cell division and, eventually, escape apoptosis, constituting a serious resistance mechanism to antimetotics. Strategies to overcome slippage should potentiate the cancer cell killing activity of these antimetotics. Such strategies should accelerate cell death in mitosis before slippage. Here, we undertook a mechanistic analysis to test whether the apoptosis activator Navitoclax potentiates apoptosis triggered by the antimetotic BI2536, a potent inhibitor of Polo-like kinase 1 (PLK1) with the goal of overcoming slippage. We found that cancer cells in 2D cultures treated with BI2536 alone accumulate in mitosis, but a significant fraction of arrested cells undergo slippage and survive. Remarkably, combining BI2536 with Navitoclax dramatically reduces slippage, shifting the cell fate to accelerated death in mitosis. The results are confirmed in 3D spheroids, a preclinical system that mimics in vivo tumor drug responses. Importantly, in 3D spheroids, the effect of the BI2536/Navitoclax combination requires a lower therapeutic dosage of each drug, underlying its potential to improve the therapeutic index. Our results highlight the relevance of apoptosis potentiators to circumvent slippage associated with antimetotics. The combination of BI2536 with Navitoclax shows in vitro synergy/additive effect, which warrants further clinical research.

**Keywords:** PLK1; BI2536; Navitoclax; slippage; antimetotics; cancer therapy; mitosis; apoptosis



**Copyright:** © 2022 by the authors. Licensee MDPI, Basel, Switzerland. This article is an open access article distributed under the terms and conditions of the Creative Commons Attribution (CC BY) license (<https://creativecommons.org/licenses/by/4.0/>).

## 1. Introduction

Lung cancer is the leading cause of cancer-related mortality worldwide, being one of the major challenges to public health [1]. Non-small cell lung cancer (NSCLC) remains the most common lung cancer type, corresponding to 85% of all lung cancer cases [2]. Most NSCLC patients have advanced disease at diagnosis. Platinum-based chemotherapy doublet, including antimicrotubule agents (e.g., paclitaxel/carboplatin and docetaxel/cisplatin), is the standard of care for first-line treatment of advanced NSCLC [3–5]. However, only partial responses were achieved with this approach in 30% to 40% of patients [6]. Thus, there is a strong interest in developing more efficacious and safer therapies, thereby improving health management.

The classic antimitotic agents, known as microtubule-targeting agents (MTAs), have been widely used for cancer therapy and remain one of the most successful approaches [7]. MTAs impair a functional mitotic spindle by binding to  $\beta$ -tubulin subunits, leading to spindle assembly checkpoint (SAC) activation and consequent mitotic arrest, which is expected to result in cancer cell death by apoptosis [8]. The SAC is a surveillance mechanism that ensures correct chromosome segregation by monitoring kinetochore–microtubule attachments and chromosome alignment at the metaphase plate [9,10]. SAC operates through the assembly of the mitotic checkpoint complex (MCC) at unattached kinetochores, which diffuses throughout the cell and inhibits the anaphase-promoting complex/cyclosome (APC/C), a ubiquitin ligase that targets securin and cyclin B for proteasomal degradation, resulting in mitotic arrest [11]. When all chromosomes are correctly attached to microtubules, emanating from opposite spindle poles, and aligned at the cell equator, the SAC is silenced, leading to APC/C activation and mitosis progression [9,10].

Despite the therapeutic success of MTAs against several tumor types, including lung cancer, they face some challenges that compromise their efficacy, namely resistance mechanisms developed by tumor cells and the associated toxicity, mainly neurological, gastrointestinal, and myeloid [12,13]. To overcome these drawbacks, the development of alternative strategies to block cells in mitosis without directly targeting microtubules has been gaining more attention. These new approaches consist of inhibiting proteins that play crucial roles during mitosis, especially kinases and kinesins, through small molecules or small interfering RNAs (siRNA), known as second-generation antimitotics (SGAs) [8,14]. One of the targeted proteins is the Polo-like kinase 1 (PLK1), which participates in several mitotic events, including mitotic entry, spindle assembly, kinetochore–microtubule attachment, SAC signaling, and cytokinesis [15]. Several PLK1 inhibitors have been developed that exhibited promising antitumor activity in preclinical models; however, they failed in human clinical trials as monotherapy, stressing the need for the development of strategies to improve their efficacy [14,16,17].

Tumor cells display many cell fate variations after exposure to antimitotic agents, including PLK1 inhibitors [18,19]. Consequently, tumor cells arrested in mitosis could die in mitosis by apoptosis, undergo unequal cell division generating aneuploid daughter cells, or undertake slippage whereby cells exit mitosis without dividing. Slippage occurs due to the slow and gradual degradation of cyclin B even when SAC is on, triggering mitotic exit. What dictates whether the cell dies in mitosis or undergoes slippage is the rate of cyclin B degradation versus the accumulation rate of the apoptotic signal [20]. According to these two competitive network models, if cyclin B levels reach the mitotic exit threshold before the levels of death signals reach the threshold to trigger apoptosis, slippage occurs. Conversely, if death signals reach the threshold to trigger cell death before cyclin B levels fall below the threshold that dictates mitotic exit, cells die in mitosis [19]. Slipped cells can follow three different pathways: they can undergo post slippage death, become senescent, or continue dividing, fueling tumor growth [8,19,21]. Therefore, slippage has been pointed out to be a major resistance mechanism to antimitotics [20].

The efficacy of chemotherapeutics that induce mitotic arrest relies on the intrinsic (or mitochondrial) apoptosis response of the treated cancer cells [22]. The Bcl2 family is essential for this intrinsic apoptosis and consists of three groups of proteins, including anti-apoptotic proteins (BCL-2, BCL-W, BCL-XL, and MCL-1), pro-apoptotic proteins (BAX and BAK), and BH3-only proteins (e.g., BAD, BIK, BIM, BID, and NOXA) [22]. BH3 only members inhibit the anti-apoptotic BCL-2-like proteins (pro-survivals), thereby enabling activation of the pro-apoptotic effectors BAX and BAK, necessary for the mitochondrial pathway of apoptosis, through mitochondrial outer membrane permeabilization. BH3 mimetics have been developed as novel anticancer agents and have shown promise in pre-clinical studies and clinical trials, particularly in patients with lymphoid malignancies [23].

Since antimitotics, including those that target PLK1, rely on apoptosis to kill cancer cells and given the aforementioned two competitive networks that determine whether mitosis-arrested cells will die or undergo slippage, here, we investigated whether the inhi-

bition of the anti-apoptotic BCL-2 family members can enhance cell death during mitotic arrest caused by a PLK1 inhibitor and, thus, identify a relevant strategy to improve the efficacy of PLK1 targeting, when it is combined with targeted apoptosis potentiators. For this purpose, we used BI2536, a highly selective and potent inhibitor of PLK1, and Navitoclax, a BCL-2 family inhibitor with high affinity toward BCL-2 anti-apoptotic proteins, including BCL-2, BCL-W, and BCL-XL [24–27]. The strategy was tested on cancer cells in 2D cultures and also in a three-dimensional (3D) cancer model used as a preclinical system to mimic physiologic drug responses. The cellular mechanism by which Navitoclax enhances cancer cell killing by the antimetabolic BI2536 was also investigated.

## 2. Materials and Methods

### 2.1. Compounds

BI2536, Navitoclax, Volasertib, and ABT-737 (MedChem Express, Shanghai, China) were reconstituted in sterile dimethyl sulfoxide (DMSO, Sigma-Aldrich Co., Ltd., St. Louis, MO, USA) to a stock concentration of 10 mM. To avoid physicochemical changes and to maintain their integrity and activity, the drugs were stored as small volume aliquots at  $-20\text{ }^{\circ}\text{C}$ . On the day of the experiment, all compounds were diluted in fresh culture medium at desired concentrations.

### 2.2. Cell Lines and Culture Conditions

NCI-H460 (Non-Small Cell Lung Cancer) cell line was obtained from the European Collection of Cell Culture and was grown in RPMI-1640 culture medium (Roswell Park Memorial Institute, Biochrom, Buffalo, NY, USA) supplemented with 5% heat-inactivated fetal bovine serum (FBS, Biochrom, Berlin, Germany). A549 (Human Lung Adenocarcinoma Epithelial Cells) were obtained from American Type Culture Collection, and HPAEpiC (Human Pulmonary Alveolar Epithelial Cells) was obtained from ScienCell Research Laboratories; both cell lines were grown in DMEM medium (Dulbecco's Modified Eagle's, Biochrom), supplemented with 10% heat-inactivated FBS and 1% of non-essential amino acids (Sigma-Aldrich Co., Ltd.). Cell lines were cultured in 25 cm<sup>2</sup> cell culture flasks (VWR) with complete respective growth culture medium and maintained in a humidified incubator at 37 °C with 5% CO<sub>2</sub> (Hera Cell, Heraeus, Hanau, Germany).

### 2.3. RNA Isolation and Real-Time PCR Analysis

Total RNA was isolated using the PureZOL<sup>TM</sup> RNA Isolation Reagent (Bio-Rad Laboratories, Inc. Hercules, Hercules, CA, USA) according to the manufacturer's instructions and quantified through spectrophotometry (NanoDrop 2000, Thermo Scientific, Waltham, MA, USA). cDNA was synthesized using the iScript<sup>TM</sup> cDNA Synthesis Kit (Bio-Rad, Hercules, CA, USA) according to the supplier's instructions, and was amplified using iQ<sup>TM</sup> SYBR Green Supermix Kit (Bio-Rad) on iQ Thermal Cycler (Bio-Rad), according to the following program: initial denaturing step at 95.0 °C for 3 min; 40 cycles at 94.0 °C for 20 s; 54.0 °C for 30 s and 72.0 °C for 30 s. The primers, used at a final concentration of 10 μM, were: PLK1: forward 5'-CCCCTCACAGTCCTCAATAA-3' and reverse 5'-TGTCGAATAGTCCACCC-3'; GAPDH: forward 5'-ACAGTCAGCCGCATCTTC-3' and reverse 5'-GCCCAATACGACCAATCC-3'; Actin: forward 5'-AATCTGGCACCACACCTTCTA-3' and reverse 5'-ATAGCACAGCCTGGATAGCAA-3'. Experiments were performed in triplicate, and the data were acquired using CFX Manager<sup>TM</sup> Software (version 1.0, Bio-Rad). The results were analyzed according to  $\Delta\text{CT}$  and normalized against Actin and GAPDH expression levels, which were used as control templates. A fold value of mRNA level  $\geq$  or  $\leq 1.5$  relative to that of normal cells was considered as over- or underexpression, respectively.

### 2.4. MTT Assay

The cell viability was determined by tetrazolium salt 3-(4, 5-dimethylthiazol-2-yl)-2, 5-diphenyltetrazolium bromide (MTT) assay. Briefly, A549 and NCI-H460 cells were seeded

in 96-well plates at a density of  $0.05 \times 10^6$  cells/well. After 24 h, the culture medium was replaced with fresh medium containing 2-fold serial dilutions of BI2536, or Navitoclax, or Volasertib, or ABT-737 ranging from 0 to 16,000 nM. Then, 48 hours later, the medium was replaced with 200  $\mu$ L of fresh medium, and then 20  $\mu$ L of tetrazolium salt MTT (5 mg/mL PBS) was added to each well. Following 4 h of incubation at 37 °C under darkness, the resulting formazan crystals were solubilized in 100  $\mu$ L of DMSO. The optical density of the solubilized MTT formazan product was measured at 570 nm using a microplate reader (Biotek Synergy 2, Winooski, VT, USA) coupled with Gen5 software (version 1.07.5, Biotek, Winooski, VT, USA). The percentage of cell viability was expressed as a mean  $\pm$  standard deviation relative to the control group from three independent experiments performed in triplicate. The mean 50% inhibition concentration ( $IC_{50}$ ) values were calculated using GraphPad Prism version 8 (GraphPad software Inc., San Diego, CA, USA). To analyze the combination treatment effects, a dual-drug crosswise concentration matrix was made for each combination, using concentrations ranging from 0 to 250 nM. The results were analyzed by Combenefit Software (version 2.021, Cancer Research UK Cambridge Institute, Cambridge, UK).

### 2.5. Mitotic Index Determination

A total of  $9.0 \times 10^4$  A549 and NCI-H460 tumor cells were plated in 6-well plates with complete culture medium and allowed to adhere for 24 h. Then, cells were treated with BI2536 (125 nM for A549 and 62.5 nM for NCI-H460) and Navitoclax (62.5 nM for A549 and 125 nM for NCI-H460), alone or in combination, for 24 h. A549 cells were also treated with 62.5 nM of Volasertib and/or 125 nM of ABT-737. Cells treated with 1  $\mu$ M of Nocodazole (Sigma-Aldrich Co., Ltd.) were used as a positive control. Additionally, DMSO-treated cells, up to 0.25% concentration, were included as compound solvent control. The mitotic index (MI) was determined by cell-rounding under phase-contrast microscopy using a Nikon TE 2000-U microscope (Nikon, Tokyo, Japan), coupled to a DXM1200F digital camera with Nikon ACT-1 software (Melville, NY, USA). At least 3000 cells were counted from random microscope fields. MI (%) was determined as the ratio between the number of mitotic cells and the total number of cells  $\times$  100.

### 2.6. Flow Cytometry Analysis for Apoptosis Detection

Cells from 2D cultures were treated as described for mitotic index determination. After 24 h of treatment, A549 floating and adherent cells were collected and processed with the “Annexin V-FITC Apoptosis Detection Kit” (eBioscience), according to the manufacturer’s instructions. Fluorescence was assessed by BD Accuri™ C6 Plus Flow cytometer (BD Biosciences), and data were analyzed with BD Accuri™ C6 Plus software (version 1.0.27.1, San Jose, CA, USA). At least 20,000 events per sample were collected.

To analyze apoptotic cell death in 3D cultures, 48 h after exposure to BI2536 and/or Navitoclax, or to Volasertib and/or ABT-737, alone or in combination, approximately 32 spheroids were collected from a 96-well ultra-low attachment plate and transferred to a 15 mL centrifuge tube. After precipitation of the spheroids, the supernatants were carefully removed and washed with PBS. Then, 200  $\mu$ L of trypsin (GIBCO, Invitrogen) was added, and the cells were incubated at 37 °C for 25 min to ensure complete dissociation of spheroids into single cells. Finally, 500  $\mu$ L of culture medium was added, and the cell suspension was centrifuged at 1000 rpm for 4 min and washed with PBS. The samples were treated with “Annexin V-FITC Apoptosis Detection Kit” according to the manufacturer’s instructions. At least 20,000 events per sample were collected.

### 2.7. Death Fluorometric TUNEL Assay

A total of  $9.0 \times 10^4$  of A549 cells were grown on poly-L-lysine-coated coverslips for 24 h, and cells were treated as described for mitotic index determination. Immediately after the treatment, cells were fixed in 4% paraformaldehyde (*w/v*, Sigma-Aldrich Co., Ltd.) in PBS for 10 min. Then, cells were washed in PBS and permeabilized with 0.2% (*v/v*) Triton

X-100 (Sigma-Aldrich Co., Ltd.) in PBS for 5 min. The DeadEnd Fluorometric TUNEL System (Promega, Madison, WI, USA) was used according to the manufacturer's instructions. The 4',6-diamidino-2-phenylindole (DAPI, Sigma-Aldrich Co., Ltd.) was used to stain DNA at 2 µg/mL in Vectashield mounting medium (Vector, Newark, CA, USA). Images were acquired with an Axio Observer Z.1 SD microscope (Carl Zeiss, Oberkochen, Germany), with the Plan Aplanachromatic 63×/NA 1.4 objective, coupled to an AxioCam MR3. The images were then processed using ImageJ (version 1.51, Rasband, W.S., ImageJ, U.S. National Institutes of Health, Bethesda, MD, USA). TUNEL-positive cells were counted from a total of approximately 500 cells from 10 random fields under a fluorescence microscope. Then, the apoptotic index (the percentage of positively TUNEL-stained cells over the total of cells) was determined.

### 2.8. Live-Cell Imaging

For live-cell imaging experiments,  $9.0 \times 10^4$  A549 cells were plated onto LabTek II chambered cover glass (Nunc) with complete culture medium and maintained for 24 h at 37 °C with 5% CO<sub>2</sub>. Then, cells were treated with 125 nM of BI2536, or with 62.5 nM of Navitoclax, or with a combination of both compounds. A differential interference contrast (DIC) optics, with a 63× objective on an Axio Observer Z.1 SD inverted microscope, equipped with an incubation chamber with a temperature of 37 °C in a 5% CO<sub>2</sub> atmosphere, was used to capture images at 5 min intervals up to 48 h. The time-lapse images were used to generate movies using ImageJ software (version 1.51). Cell fate was followed since the first mitosis. Dead cells were classified as death in mitosis (DiM), when cells died in mitosis; as post-mitotic death (PMD), when cells died after complete cell division; or as post slippage death (PSD), when cells died following mitotic exit without cell division. Cells that exited mitosis without dying and survived were classified as post slippage survival (PSS).

### 2.9. 3D Spheroid Formation and Drug Treatment

A549 cells were seeded at 4000 cells/well into the 96-well ultra-low attachment plates (Corning 7007, Fisher Scientific, Pittsburgh, PA, USA) in order to promote the self-assembly of cells into three-dimensional (3D) cellular spheroids. After 4 days, the spheroids were treated with BI2536 and Navitoclax, or with Volasertib and ABT-737, in a dual-drug cross-wise concentration matrix, using concentrations ranging from 0 to 16,000 nM. Then, 48 h later, 3D spheroids viability and apoptosis were determined.

### 2.10. CellTiter-Glo Viability Assay

Spheroid viability, based on ATP measurement, was determined by CellTiter-Glo 3D cell viability assay (Promega) according to the manufacturer's instructions. Briefly, A549 spheroids in 96-well ultra-low attachment culture plate were exposed for 48 h to BI2536 and/or Navitoclax, or to Volasertib and/or ABT-737. Then, they were transferred separately into single wells of a 96-well opaque culture plate (Fisher Scientific), and after exposure to CellTiter-Glo<sup>®</sup> 3D reagent for 10 min, the luminescence signal was measured using a microplate reader. The results were expressed as the percentage of cell viability relative to the control group. The BI2536, Navitoclax, Volasertib, and ABT-737 IC<sub>50</sub> values were calculated using GraphPad Prism version 8.

### 2.11. Statistical Analysis

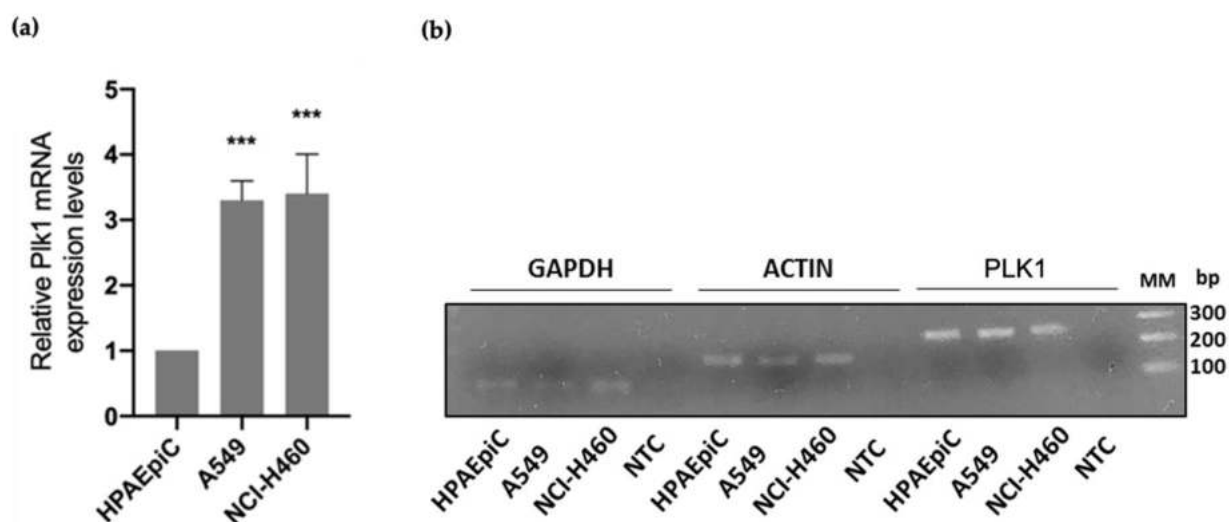
Statistical analysis was performed using one-way ANOVA followed by the Tukey's post-test or unpaired *t*-test in GraphPad Prism version 8. Experiments were performed in triplicate, and the data expressed as the mean ± standard deviation (SD). *p*-values of \* *p* < 0.05, \*\* *p* < 0.01, \*\*\* *p* < 0.001, and \*\*\*\* *p* < 0.0001 defined the level of statistical significance.



### 3. Results

#### 3.1. *PLK1 Is Upregulated in Lung Cancer Cells*

To assess the relevance of PLK1 as a potential target for cancer therapy, we analyzed its expression in A549 and NCI-H460 non-small cell lung cancer (NSCLC) cell lines (Figure 1). Analysis of PLK1 mRNA levels by qRT-PCR demonstrated that PLK1 was overexpressed in both cancer cell lines tested when compared to the non-tumor cell line HPAEpic. There was a  $3.3 \pm 0.3$  and  $3.4 \pm 0.6$ -fold increase in PLK1 expression in A549 and NCI-H460 cell lines, respectively, compared to the lung non-tumor cell line. These results are in concordance with previous studies that reported a PLK1 overexpression in NSCLC, highlighting the relevance of PLK1 targeting [28,29].

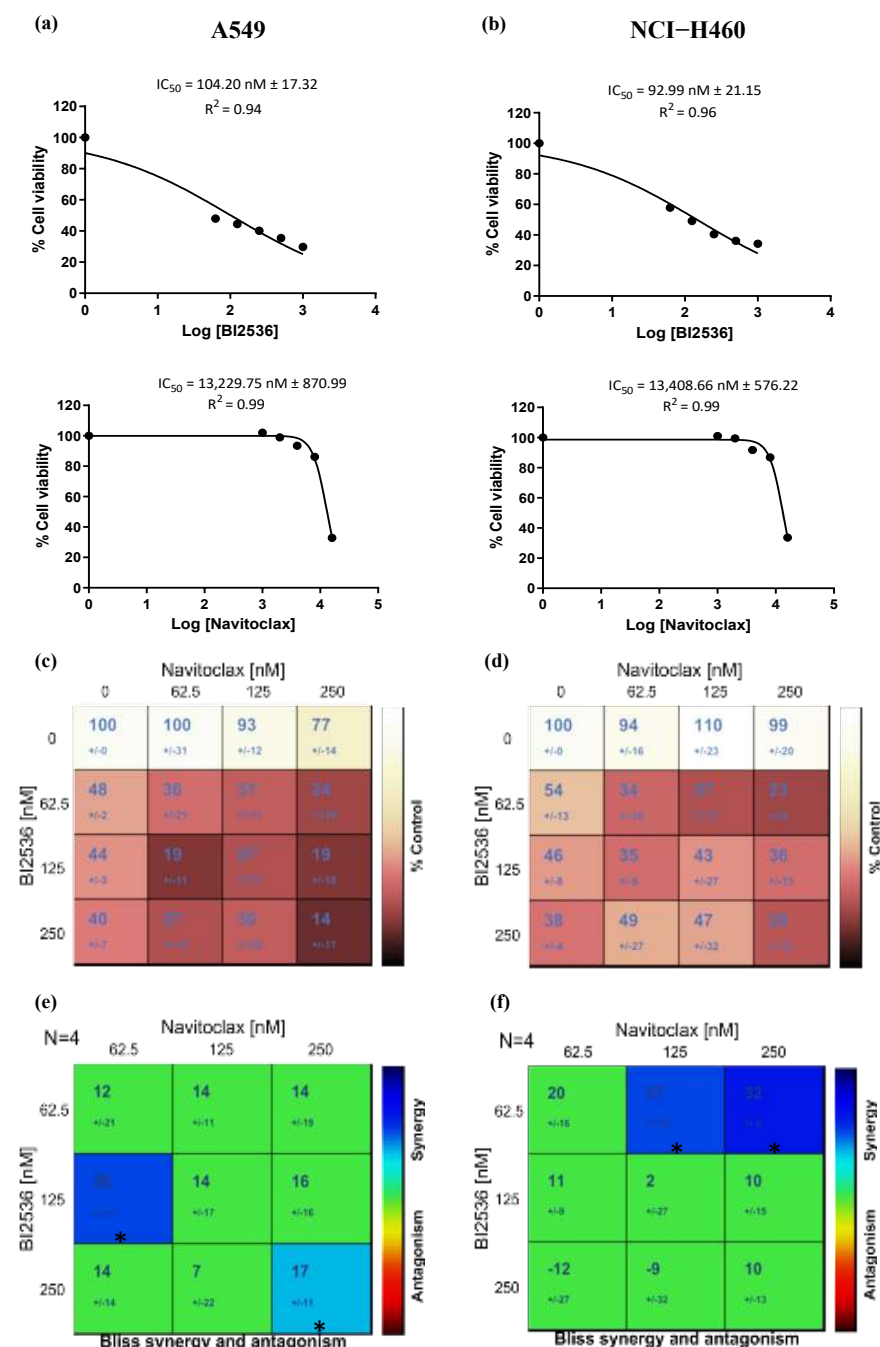


**Figure 1.** PLK1 is overexpressed in NSCLC cell lines. (a) Relative mRNA expression of PLK1 was determined by qRT-PCR in NCI-H460 and A549 cancer cell lines, and compared to non-tumor HPAEpic cell line, showing PLK1 overexpression in tumor cell lines with statistical relevance of \*\*\*  $p < 0.001$  by unpaired *t*-test from three independent experiments. (b) Representative 1% agarose gel image of PCR products is shown. MM-molecular marker; bp-base pair; NTC-Non-Template Control.

#### 3.2. *Navitoclax Enhances the Antiproliferative Effect of BI2536-Mediated PLK1 Inhibition in Lung Cancer Cells*

To explore the antiproliferative effect of PLK1 inhibition in combination with an apoptotic potentiator, we first determined the concentration of the PLK1 inhibitor BI2536 and the BH3-mimetic Navitoclax, able to cause 50% cell viability inhibition ( $IC_{50}$ ), after 48 h exposure, in the two lung cancer cell lines, A549 and NCI-H460. Figure 2a,b summarizes the  $IC_{50}$  values of the single agents on both cell lines. BI2536 showed dose-dependent antiproliferative effects on both cell lines, with an  $IC_{50}$  of  $104.20 \pm 17.32$  nM and  $92.99 \pm 21.15$  nM for A549 and NCI-H460 cells, respectively (Figure 2c,d). Navitoclax had little antitumor effect on both cancer cell lines, showing cytotoxicity only at concentrations higher than 13,000 nM (Figure 2c,d). Remarkably, in all the BI2536/Navitoclax combinations tested, cell viability was severely affected, and in many cases, the decrease associated with the dual-drug combination was higher than the sum of the decrease induced by each of the matching single-agent treatments (Figure 2c,d). Interestingly, such a potentially synergistic effect was also observed with the combinations where the concentrations of the single agents were low, which is very relevant, from a therapeutic perspective, to minimize toxicity and side effects reported in clinical trials for both drugs [14,30]. Based on these results, synergy matrices were created (Figure 2e,f). The synergy matrix of A549 showed that 125 nM BI2536 was the first concentration where synergism was detected in combination with 62.5 nM Navitoclax. The synergy matrix of NCI-H460 showed that 62.5 nM BI2536 was the first concentration where synergism was detected in combination with 125 nM

Navitoclax. We selected these synergy points for subsequent experiments to investigate the cellular mechanistic underlying the enhanced cytotoxicity of the combinations.

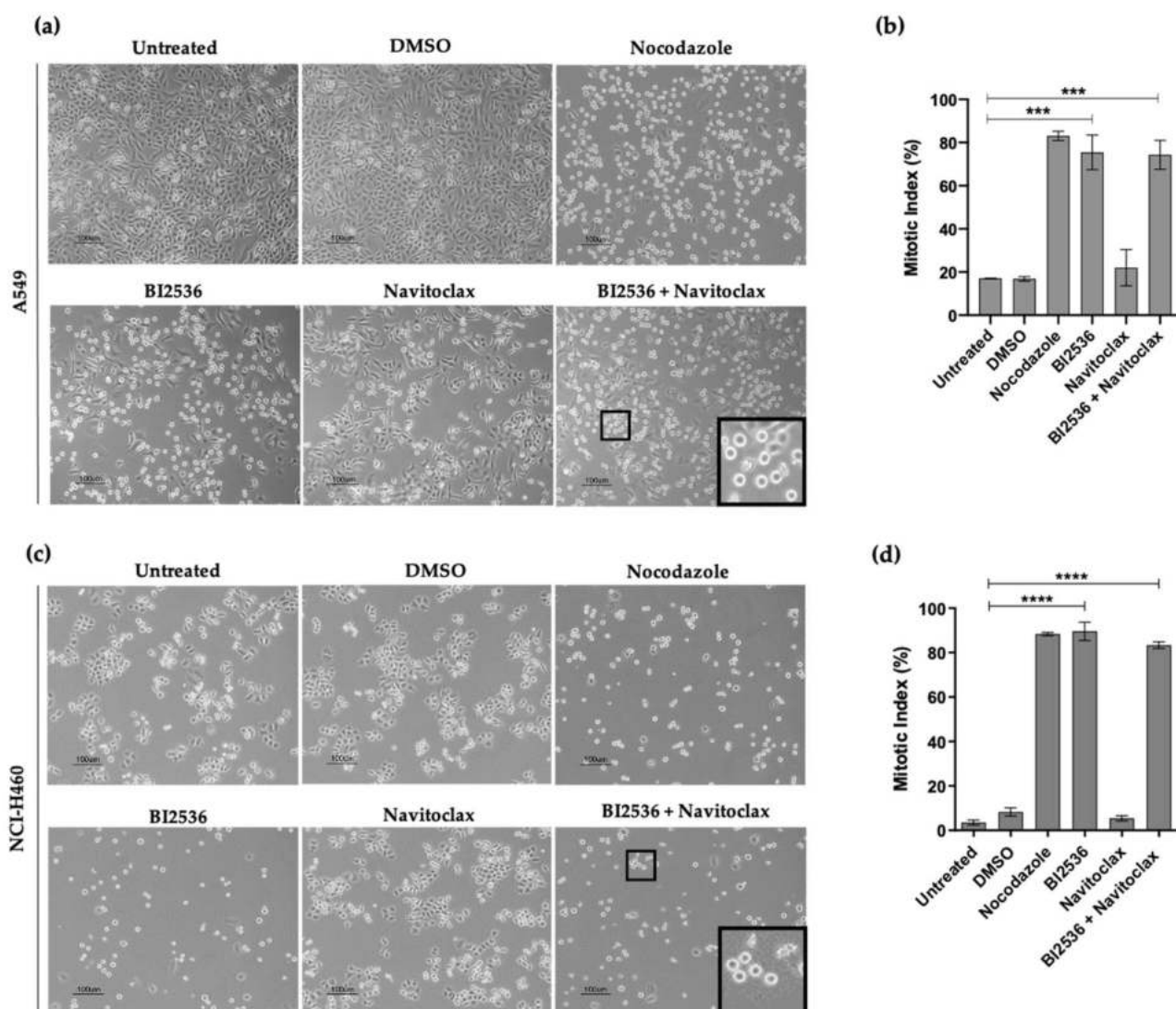


**Figure 2.** BI2536/Navitoclax combination exacerbates cytotoxicity of lung cancer cells. Dose–response curve of BI2536 and Navitoclax in A549 (a) and NCI–H460 (b) cell lines. Cell viability (%) of mono or dual–drug combinations after 48 h of treatment in A549 (c) and NCI–H460 (d) cells, from four independent experiments, as determined by MTT assay. Synergy scores calculated by the Bliss model of Combenefit software with statistical relevance of  $p < 0.05$  in A549 (e) and NCI–H460 (f).

### 3.3. Combining BI2536-Mediated PLK1 Inhibition with Navitoclax Overcomes Slippage and Shifts the Cancer Cell Fate to Accelerated Death in Mitosis

In order to unveil the cellular mechanistic associated with the enhanced antiproliferative effect induced by BI2536 in combination with Navitoclax, A549 and NCI–H460 cells

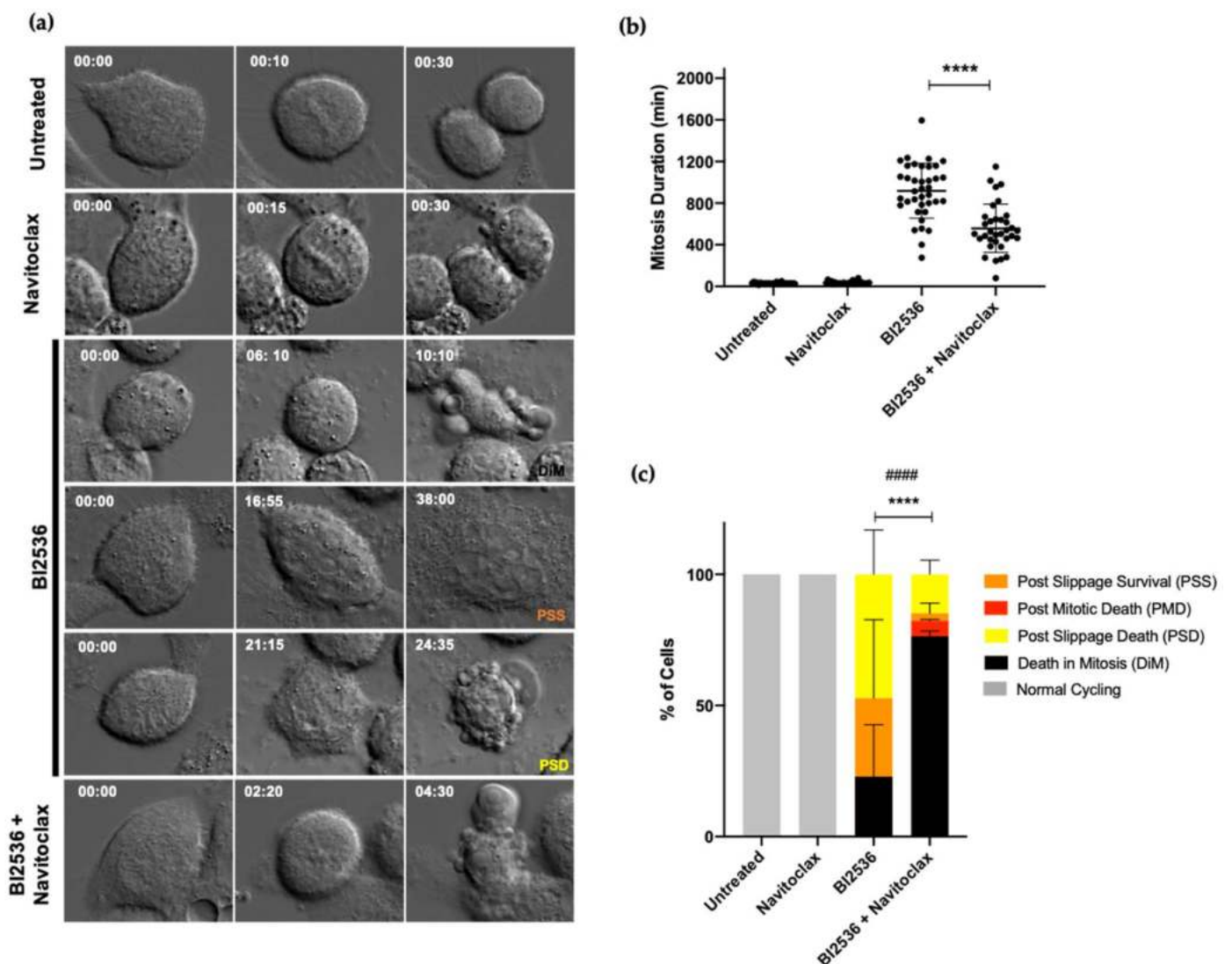
were treated for 24 h with the above combinations with single agents or with medium or DMSO (controls) and then examined by phase-contrast microscopy. For BI2536 single treatment, and as expected, we observed an accumulation of bright and round cells reminiscent of cells arrested in mitosis, similarly to Nocodazole, a known antimetabolic agent, used here as a positive control (Figure 3a,c). This observation was confirmed by the calculation of the mitotic index (MI), which was significantly increased in both BI2536-treated cancer cell lines ( $75.4 \pm 8.0\%$  and  $89.6 \pm 4.1\%$  in A549 and NCI-H460, respectively) compared to untreated ( $17.1 \pm 0.2\%$  and  $3.3 \pm 1.4\%$  for A549 and NCI-H460 cells, respectively) and DMSO-treated cells ( $16.9 \pm 1.0\%$  and  $8.3 \pm 1.8\%$  for A549 and NCI-H460 cells, respectively) (Figure 3b,d). Treatment with Navitoclax alone did not affect normal cell cycling, apart from a few dead cells. As mitosis is not supposed to be affected by Navitoclax, the increase in the mitotic index observed in the BI2536/Navitoclax combinations should be attributed to BI2536. This result confirms the previously reported antimetabolic activity of BI2536-mediated PLK1 inhibition, thereby validating the use of PLK1 inhibitor in our study for the subsequent studies to unveil the cellular mechanism of the enhanced cell toxicity in combination with Navitoclax.



**Figure 3.** BI2536, but not Navitoclax, induces mitotic arrest of lung cancer cells. Representative phase-contrast microscopy images of untreated BI2536 (125 nM in A549 and 62.5 nM in NCI-H460), and Navitoclax (62.5 nM in A549 and 125 nM in NCI-H460) co-treated cells, for 24 h, showing accumulation of rounded and bright cells (mitotic cells) in A549 (a) and NCI-H460 (c) cell lines. Cells

treated with up to 0.25% DMSO (compound solvent) and 1 $\mu$ M Nocodazole (antimitotic agent) were used as controls. Mitotic index graph showing accumulation of A549 (b) and NCI-H460 (d) mitotic cells with statistical relevance of \*\*\*  $p < 0.001$  and \*\*\*\*  $p < 0.0001$  by one-way ANOVA with Tukey's multiple comparisons test from three independent experiments. Bar, 100  $\mu$ m. Data were expressed as mean  $\pm$  SD.

Antimitotic agents induce prolonged mitotic arrest through activation of the SAC [31]. Then, treated cells either die in mitotic arrest or slip out of mitosis, without cell division, into an abnormal G1 state in which they may die, arrest in a tetraploid G1 state, or continue to proliferate [19]. Slippage is a major mechanism contributing to drug resistance [20]. Therefore, an ideal strategy should shift the fate of antimitotic-treated cells to death instead of slippage. To this end, we analyzed the cell fates after treatment with the BI2536/Navitoclax combination, taking advantage of time-lapse microscopy, which allows monitoring the spatiotemporal dynamics of live cells (Figure 4a).



**Figure 4.** Navitoclax prevents slippage and accelerates cell death in mitosis in lung cancer cells treated with BI2536. (a) Representative time-lapse sequences of untreated, BI2536-, Navitoclax- and BI2536/Navitoclax-treated cells. Untreated ( $n = 27$ ) and Navitoclax-treated cells ( $n = 25$ ) undertake mitosis for about 30 min. BI2536-treated cells ( $n = 38$ ) arrest in mitosis during several hours ( $918.2 \pm 263.5$  min) and die in mitosis (top) or undergo slippage followed by death (bottom) or remain alive (middle). BI2536/Navitoclax-treated cells ( $n = 34$ ) spend less time in mitosis ( $558.3 \pm 232.0$  min)

than BI2526-treated cells. Numbers indicate time in 00 h:00 min. **(b)** Quantification of mitosis duration in the different treatments, as determined by time-lapse microscopy, with statistical relevance of \*\*\*\*  $p < 0.0001$  by one-way ANOVA with Tukey's multiple comparisons test. Each dot represents one cell. **(c)** Quantification of cell fate under the indicated treatments. Percentage of cells undergoing death in mitosis (DiM), post-mitotic death (PMD), post slippage death (PSD), cells that remain alive after slippage (post slippage survival, PSS), and cells with normal cycling, with statistical relevance of \*\*\*\*  $p < 0.0001$  (DiM) and #####  $p < 0.0001$  (Slippage [PSD +PSS]) by two-way ANOVA with Tukey's multiple comparisons test. The error bars represent mean  $\pm$  SD of three independent experiments.

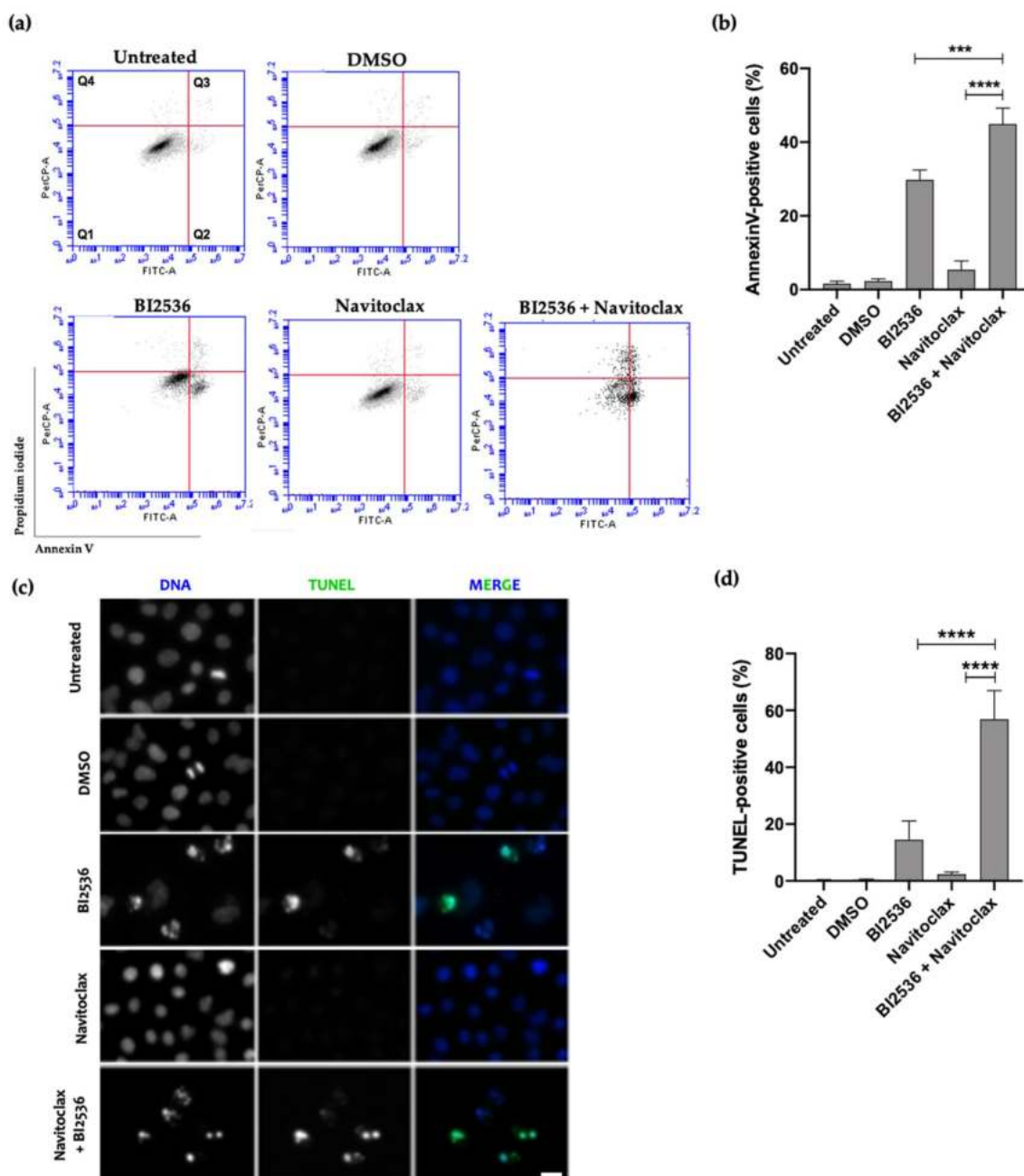
A549 tumor cells were treated with BI2536 and Navitoclax, alone or in combination, and each cell was followed over 48 h live-cell time-lapse analysis. As expected, BI2536-treated cells lasted in mitosis for several hours ( $918.2 \pm 263.5$  min) (Figure 4b), while untreated and Navitoclax-treated cells undertook mitosis for about 30 min ( $30.5 \pm 7.3$  min and  $36.0 \pm 14.1$  min, respectively) (Figure 4b, Video S1 and Video S2, respectively). Interestingly, the addition of Navitoclax to BI2536-treated cells shortened the duration of mitotic arrest ( $558.2 \pm 232.0$  min) as compared to cells treated with BI2536 only, suggesting that the time from mitotic arrest to death was shortened (Figure 4b). Concerning cell fates, all Navitoclax-treated cells were able to divide normally, indicating that Navitoclax alone is not toxic to tumor cells, at least at the concentration used (Figure 4c and Video S2). As to BI2536-treated cells, different fates were observed:  $22.9 \pm 19.8\%$  died in mitosis (DiM), and  $77.1 \pm 18.8\%$  underwent slippage, of which  $64.8 \pm 31.3\%$  died after slippage (post slippage death, PSD) and  $35.2 \pm 31.3\%$  survived (post slippage survival, PSS) during the recorded time (Figure 4c, Video S3, Video S5, and Video S4, respectively). In cells treated with the BI2536/Navitoclax combination,  $76.4 \pm 2.0\%$  of cells died in mitosis (Figure 4c and Video S6),  $5.9 \pm 0.5\%$  of cells divided but died in the following interphase (post-mitotic death, PMD), and, remarkably, only  $17.7 \pm 1.5\%$  underwent slippage (of which  $83.3 \pm 23.6\%$  PSD and  $16.7 \pm 23.6\%$  PSS) (Figure 4c). Taken together, the results show that combining BI2536-mediated PLK1 inhibition with an apoptosis potentiator minimizes slippage and, thus, drug resistance by shifting the cell fate to accelerated death in mitosis, likely through accelerating the accumulation of apoptotic signals.

Cell death in the BI2536/Navitoclax combination was mainly by apoptosis, as revealed both by Annexin V/PI and TUNEL assays (Figure 5). Indeed, flow cytometry analysis of Annexin V/PI-stained cells showed that the percentage of apoptotic cells in the BI2536/Navitoclax combination was significantly higher than that of BI2536-only treatment ( $44.9 \pm 4.3\%$  vs.  $29.8 \pm 2.7\%$ , respectively), being residual in untreated, DMSO- or Navitoclax-treated cells ( $1.6 \pm 0.7\%$ ,  $5.4 \pm 2.4\%$ , and  $2.3 \pm 0.6\%$ , respectively). This result was corroborated by the TUNEL assay (Figure 5c,d).

### 3.4. Co-Treatment with BI2536 and Navitoclax Decrease 3D Cancer Spheroid Viability

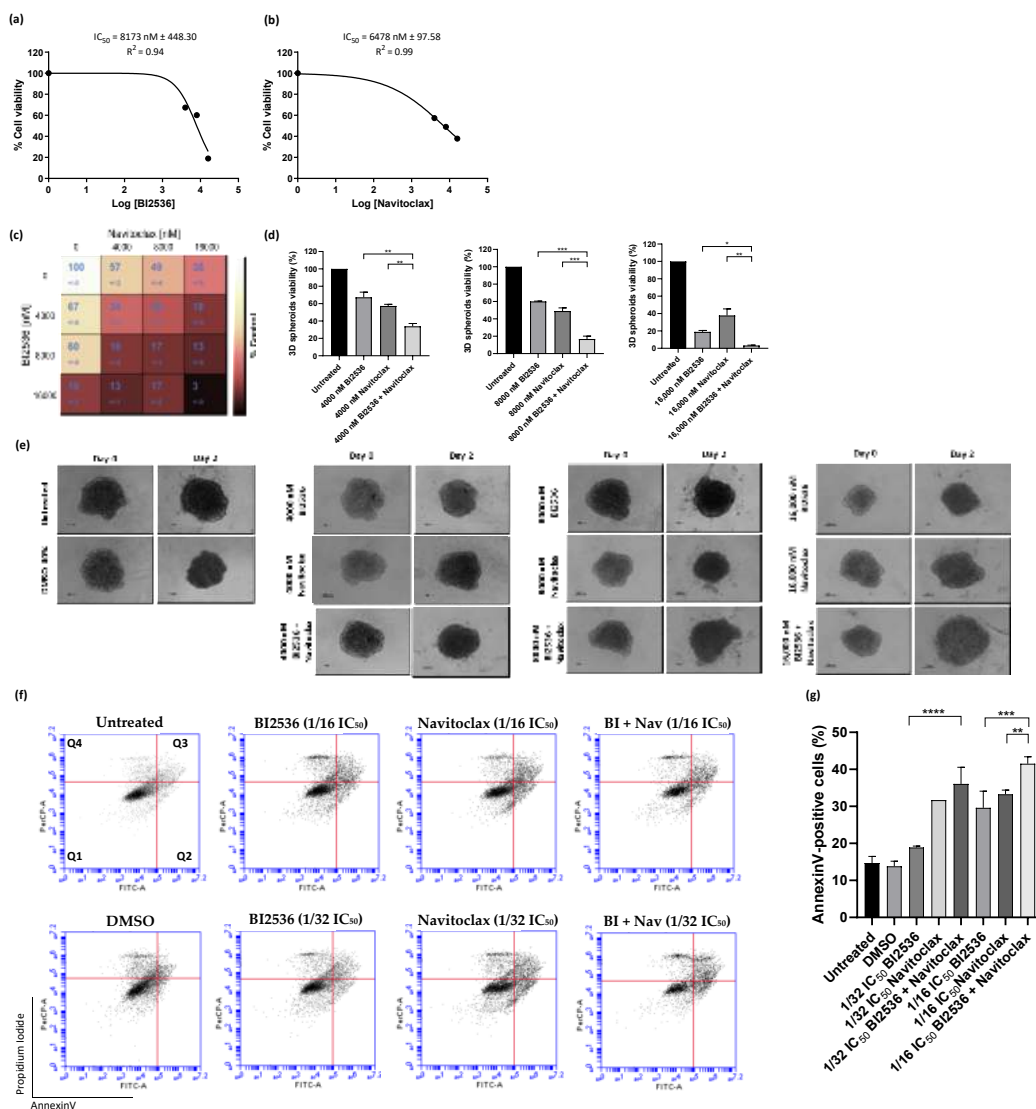
Three-dimensional (3D) spheroid cell cultures exhibit several characteristics of in vivo tumor tissues, such as cell–cell interaction, hypoxia, pH gradient, drug penetration, response and resistance, and production/deposition of extracellular matrix [32]. Therefore, the spheroids can be used to closely mimic a solid in vivo tumor. We, thus, established spheroids of A549 cells and evaluated the cytotoxic activity of 48 h BI2536 treatment, individually or in combination with Navitoclax, by CellTiter-Glo assay (Figure 6). Both BI2536 and Navitoclax showed dose-dependent antiproliferative effects on A549 spheroids, with an  $IC_{50}$  of  $8173.0 \pm 448.3$  nM and  $6478.0 \pm 97.58$  nM (Figure 6a,b). The BI2536  $IC_{50}$  was much higher than its corresponding  $IC_{50}$  in the 2D cultures, probably due to the aforementioned characteristics of the 3D cultures. We also performed a spheroid viability matrix containing 16 different combinations at concentrations of 0, 4000, 8000, and 16,000 nM of BI2536 and Navitoclax (Figure 6c). In all the BI2536/Navitoclax combinations tested, cell viability was severely affected, being the decrease at least equal to the sum of the decrease induced by each of the matching single-agent treatments (Figure 6d). Interestingly, we still observed an additive effect of the BI2536/Navitoclax combination when spheroids

were treated with 4000 nM concentration of each agent, a concentration much lower than the respective IC<sub>50</sub> (33.95 ± 2.3% viability with the combination, 67.4 ± 4.2% with BI2536, and 57.4 ± 1.3% with Navitoclax). From macroscopic observations, the spheroids of A549 cells treated with BI2536 or Navitoclax individual agents were loosely compacted and partially fragmented, with many cells that lost adhesion to the spheroid surface, indicative of cytotoxicity, as compared to the intact control spheroids (Figure 6e). This phenotype was exacerbated after treatment with the BI2536/Navitoclax combinations, leading to even more flattened and loosely compacted spheroids. Annexin V/PI co-staining followed by flow cytometry analysis showed exacerbation of cell death by apoptosis in spheroids treated with BI2536/Navitoclax combinations, even at concentrations as low as 1/32 or 1/16 × IC<sub>50</sub> of each agent (Figure 6f,g).



**Figure 5.** Combination of BI2536 and Navitoclax potentiates cancer cell death by apoptosis. **(a,b)** Flow cytometry analysis of apoptosis, in A549 cell line, by Annexin V/PI co-staining, after 48 h treatment.

The quadrants Q were defined as Q1 = live (Annexin V- and PI-negative), Q2 = early stage of apoptosis (Annexin V-positive/PI-negative), Q3 = late stage of apoptosis (Annexin V- and PI-positive), and Q4 = necrosis (Annexin V-negative/PI-positive). (b,d) Quantification of A549 (b) Annexin V-positive cells are shown with statistical relevance of \*\*\*  $p < 0.001$  and \*\*\*\*  $p < 0.0001$  by one-way ANOVA with Tukey’s multiple comparisons test. (c) Representative images of A549 apoptotic cells after 48 hours’ treatment, revealed by TUNEL assay to detect DNA fragmentation (green). DNA (blue) was stained with DAPI. Bar, 5  $\mu\text{m}$ . (d) Quantification of A549 TUNEL-positive cells. \*\*\*\*  $p < 0.0001$ , by one-way ANOVA with Tukey’s multiple comparisons test. The error bars represent mean  $\pm$  SD of three independent experiments.



**Figure 6.** BI2536/Navitoclax combination potentiates 3D spheroid cytotoxicity and cell death. Dose–response curve of BI2536 (a) and Navitoclax (b) in A549 spheroids. (c) Cell viability (%) of single or dual–drug combinations after 48 h of treatment, using the Combenefit software package. (d) The combinatory therapy significantly reduced the 3D spheroid viability at the indicated concentrations. (e) Representative images of A549 3D spheroids at days 0 and 2 post-treatment with mono– or BI2536/Navitoclax combinations (100  $\mu\text{m}$ ). Representative cytograms (f) and quantification (g) of Annexin V–positive cells are shown for A549 cancer cell line. The quadrants Q were defined as Q1 = live (Annexin V– and PI–negative), Q2 = early stage of apoptosis (Annexin V–positive/PI–negative), Q3 = late stage of apoptosis (Annexin V– and PI–positive), and Q4 = necrosis (Annexin V–negative/PI–positive). Data represent the mean  $\pm$  SD, one-way ANOVA followed by Tukey’s multiple comparisons test, \*  $p < 0.05$ ; \*\*  $p < 0.01$ ; \*\*\*  $p < 0.001$  and \*\*\*\*  $p < 0.0001$ .

Overall, and similarly to the effect on 2D cancer cultures, combining the antimetabolic BI2536 with the apoptosis activator Navitoclax potentiates cancer cell death in a model that mimics a solid *in vivo* tumor. The required cytotoxic concentration of BI2536 is higher for 3D cancer cultures, but a lower therapeutic dosage of each individual drug is required in the combination regimen. Such BI2536/Navitoclax combination therapy may be able to prevent the toxic effects on non-cancer cells while simultaneously producing cytotoxic effects on cancer cells.

#### 4. Discussion

Inhibition of PLK1 has been extensively explored as a therapeutic strategy against cancer [33–36]. Several PLK1 inhibitors entered clinical trials and globally demonstrated poor efficacy [14]. Mitotic slippage has been pointed out as one of the reasons for the therapeutic failure of antimetabolic agents, including PLK1 inhibitors [18,20,37]. In this study, we showed that the efficacy of the PLK1 inhibitor BI2536 was significantly improved when combined with Navitoclax, an inhibitor of the anti-apoptotic proteins of the BCL-2 family, as a strategy to overcome slippage and accelerate apoptosis. Similar results were observed when alternative small molecule inhibitors of PLK and BCL-2 family members, namely Volasertib and ABT-737, respectively, were used; therefore, excluding potential off-target effects (Figures S1 and S2).

Since what dictates whether cells die in mitosis or undergo slippage in response to antimetabolic agents is the relative rate of cyclin B degradation and the accumulation of death signals, our results suggest that Navitoclax favors the accumulation of death signals in cancer cells arrested in mitosis by BI2536, thereby, accelerating apoptosis in these cells, before slippage occurs. These results are in agreement with previous studies that reported increased cell death when apoptosis was targeted in cells treated with paclitaxel or an inhibitor of kinesin-5 in 2D cultures [38–41]. Therefore, targeting apoptosis could be a general strategy to increase the antitumor efficacy of antimetabolics. This is particularly relevant given that many cancers develop resistance to antimetabolics, exhibit deficient SAC or acquire resistance to apoptosis [42,43]. For instance, patients whose ovarian tumor tissue expresses high BCL-XL levels are less sensitive to taxane treatment, highlighting further the relevance of the addition of BCL-XL inhibitors, such as Navitoclax, to improve taxane-based therapy [44]. Importantly, we showed that the BI2536/Navitoclax combination enhances tumor cell death by apoptosis at concentrations significantly lower than their respective  $IC_{50}$ . Thus, the combination provides an opportunity to reduce the dosage of both compounds, which is expected to minimize their toxicity and other side effects. At the same time, this result is particularly relevant to overcoming possible resistance to Navitoclax. Indeed, the anti-apoptotic BCL-2 and BCL-XL are frequently expressed at high levels in a variety of cancers, and also in NCI-H460 and A549, which may contribute to chemoresistance of cancer cells [45–47].

Navitoclax, as a single agent, has demonstrated limited outcomes in clinical trials on particular cancer types, namely acute lymphocytic leukemia (ALL) and advanced small cell lung cancer (SCLC), probably due to different expression levels of the BCL-2 family proteins, being thrombocytopenia and neutropenia the most adverse events [48,49]. Compared to its potent antitumor efficacy in preclinical studies, the efficacy of BI2536 as a single agent in clinical studies was moderate, namely in patients with NSCLC, advanced exocrine adenocarcinoma of the pancreas, and different types of lymphoma [14,50,51]. In this context, the synergistic efficacy, at low doses, demonstrated by the BI2536/Navitoclax combination in the present study is encouraging and highlights its potential to overcome the disappointing outcomes and adverse effects reported for both compounds in clinical trials as monotherapy.

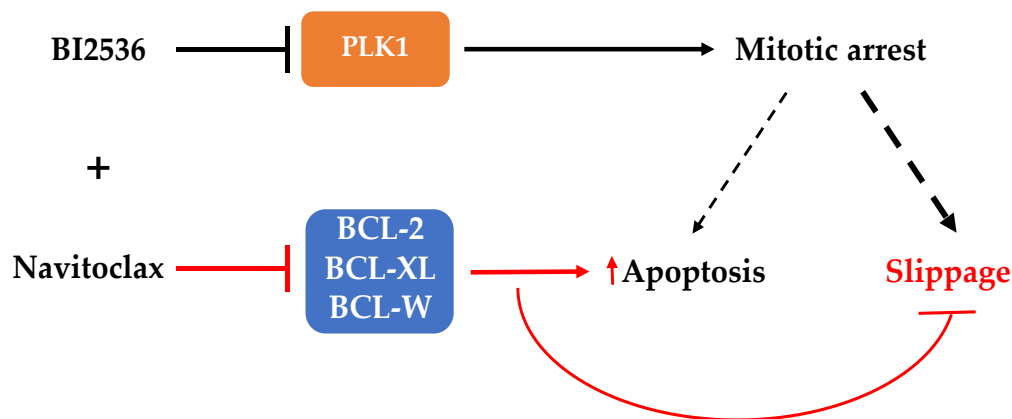
3D cell cultures have been widely used due to their capacity to reproduce the *in vivo* tumor microenvironment, including oxygen and nutrient gradients, cell heterogeneity, gene expression, and cell-to-cell and cell-to-extracellular matrix interactions [32,52]. To validate the findings observed in 2D monolayer cell cultures, 3D models were used as an alternative



to recapitulate the real tumor. We showed that the BI2536/Navitoclax combination was also significantly cytotoxic to 3D spheroids, even at lower concentrations of the single agents. This suggests that our strategy to overcome slippage subsequent to antimitotic treatment could be applied to the complex environment of the real tumor, with an efficacy that is similar to that observed in 2D monolayer cultures, presumably with reduced toxicity to non-cancer cells. A previous study also demonstrated that the combination of Navitoclax with Carfilzomib (a proteasome inhibitor) potentiated apoptotic induction in 3D spheroids of pancreatic tumor cells (PANC1) [53].

Our results present, however, some limitations that deserve to be addressed. The 3D spheroid cell cultures used in this study consisted of an avascular system, with only lung tumor cells, while the tumor microenvironment encompasses other cell types such as tumor-associated fibroblasts, immune, and endothelial cells, which affect drug efficacy [32]. Therefore, further research with heterotypic and vascular spheroids, as well as with xenograft models of human lung cancer, is required to validate the synergistic interaction between BI2536 and Navitoclax in an environment that is close to the real in vivo tumor. PLK1 is overexpressed in several cancers, including NSCLC [54]. Notwithstanding, it remains to be elucidated if these cancers are more sensitive to PLK1 inhibition than cancers with normal expression levels of PLK1. In the same line of thought, it remains to be addressed whether the efficacy of the combinational treatment is determined by the expression levels of the anti-apoptotic proteins (BCL-2, BCL-XL, BCL-W, and MCL-1). Answering these questions should clarify whether the expression levels of the anti-apoptotic proteins and PLK1 can be used to help clinicians to select those cancer patients who may benefit from combination treatments.

In conclusion, we showed that the efficacy of the antimitotic BI2536 could be improved, either in 2D or 3D culture systems, if apoptosis is accelerated by the use of an apoptosis potentiator such as Navitoclax to prevent slippage (Figure 7). This finding is relevant as it gives BI2536, which previously entered clinical trials but unsuccessfully, a second chance to be used to fight cancer, hopefully with successful outcomes.



**Figure 7.** Model for the effects of the combination of PLK1 inhibition and Navitoclax in human lung cancer cells. Cancer cells arrested in mitosis under individual treatment with PLK1 inhibitor BI2536 can die in mitosis by apoptosis, or exit mitosis by slippage, the most frequent cell fate (larger dashed line). The addition of Navitoclax (+), an inhibitor of the indicated BCL-2 family members, can synergistically potentiate BI2536-mediated apoptosis during the mitotic arrest and, thus, prevents mitotic slippage, highlighting the therapeutic potential of targeting PLK1 in combination with an apoptotic inducer. Black and red lines represent the BI2536 and Navitoclax effects, respectively.

**Supplementary Materials:** The following supporting information can be downloaded at: <https://www.mdpi.com/article/10.3390/pharmaceutics14061209/s1>. Video S1: Time-lapse imaging (DIC microscopy) of a normal mitosis in untreated A549 cell, time is shown in hours:minutes, available online at <https://youtu.be/vITdWvAr16U>. Video S2: Time-lapse imaging (DIC microscopy) of a A549 cell treated with Navitoclax undergoing a normal mitosis, time is shown in hours:minutes,

available online at <https://youtu.be/zZSR-kfCzfQ>. Video S3: Time-lapse imaging (DIC microscopy) of a A549 cell treated with BI2536 undergoing death in mitosis after spending more than 13 h in mitosis, time is shown in hours:minutes, available online at [https://youtu.be/EjwSWnHe0\\_s](https://youtu.be/EjwSWnHe0_s). Video S4: Time-lapse imaging (DIC microscopy) of a A549 cell treated with BI2536 undergoing slippage and remaining alive, time is shown in hours:minutes, available online at <https://youtu.be/EjLqOKQ4cHo>. Video S5: Time-lapse imaging (DIC microscopy) of a A549 cell treated with BI2536 undergoing slippage followed by death, time is shown in hours:minutes, available online at <https://youtu.be/nARMNfPHCXY>. Video S6: Time-lapse imaging (DIC microscopy) of a A549 cell treated with BI2536 and Navitoclax undergoing cell death in mitosis after arresting in mitosis for less than 3 h, time is shown in hours:minutes, available online at <https://youtu.be/2q1w1-J47j0>. Figure S1: Volasertib/ABT-737 combination exacerbates cytotoxicity of lung cancer cells. Dose-response curve of Volasertib and ABT-737 in A549 cell line (a). Cell viability (%) of mono or dual-drug combinations after 48 hours of treatment in A549 cells (b), from two independent experiments, as determined by MTT assay. Synergy scores calculated by the Bliss model of Combenefit software with statistical relevance of \*  $p < 0.05$  in A549 cells (c). Volasertib, but not ABT-737, induces mitotic arrest of lung cancer cells. Representative phase contrast microscopy images of untreated, Volasertib (62.5 nM), and ABT-737 (125 nM) co-treated cells, for 24 h, showing accumulation of rounded and bright cells (mitotic cells). Cells treated with up to 0.25% DMSO (compound solvent), and 1  $\mu$ M Nocodazole (antimitotic agent) were used as controls (d). Mitotic index graph showing accumulation of A549 mitotic cells (e) with statistical relevance of \*\*\*\*  $p < 0.0001$  by one-way ANOVA with Tukey's multiple comparisons test from three independent experiments. Bar, 10  $\mu$ m. Data were expressed as mean  $\pm$  SD; Figure S2: Volasertib/ABT-737 combination potentiates 3D spheroid cytotoxicity and cell death. Dose-response curve of Volasertib (a) and ABT-737 (b) in A549 spheroids. (c) Cell viability (%) of single or dual-drug combinations after 48 hours of treatment, using the Combenefit software package. (d) The combinatory therapy reduced significantly the 3D spheroid viability at the indicated concentrations. (e) Representative images of A549 3D spheroids at days 0 and 2 post-treatment with mono- or Volasertib/ABT-737 combinations (100  $\mu$ m). Representative cytograms (f) and quantification (g) of Annexin V-positive cells are shown for A549 cancer cell line. The quadrants Q were defined as Q1 = live (Annexin V- and PI-negative), Q2 = early stage of apoptosis (Annexin V-positive/PI-negative), Q3 = late stage of apoptosis (Annexin V- and PI-positive) and Q4 = necrosis (Annexin V-negative/PI-positive). Data represent the mean  $\pm$  SD, One-way ANOVA followed by Tukey's multiple comparisons test, \*  $p < 0.05$ ; \*\*\*  $p < 0.001$  and \*\*\*\*  $p < 0.0001$ .

**Author Contributions:** Conceptualization, H.B. and P.M.A.S.; methodology, B.P., P.N., A.C.H., P.M.A.S. and H.B.; formal analysis, B.P., P.N., A.C.H., J.C.-T., P.M.A.S. and H.B.; investigation, B.P., P.N., A.C.H. and P.M.A.S.; data curation, B.P., P.N., A.C.H. and P.M.A.S.; writing—original draft preparation, B.P., P.N., P.M.A.S. and H.B.; writing—review and editing, B.P., P.N., A.C.H., J.C.-T., P.M.A.S. and H.B.; supervision, P.M.A.S. and H.B.; project administration, H.B.; funding acquisition, H.B. All authors have read and agreed to the published version of the manuscript.

**Funding:** This work was funded by CESPU—Cooperativa de Ensino Superior Politécnico e Universitário under the project “AntiMitoSphere\_APSFCT\_IINFACTS\_2021” to Hassan Bousbaa. Bárbara Fernandes Pinto is a PhD fellowship holder from CESPU (grant BD/CBAS/CESPU/01/2020). Ana C. Henriques acknowledges FCT—Fundação para a Ciência e a Tecnologia for financial support (grant SFRH/BD/116167/2016).

**Conflicts of Interest:** The authors declare no conflict of interest.

## References

1. Siegel, R.L.; Miller, K.D.; Jemal, A. Cancer statistics, 2020. *CA. Cancer J. Clin.* **2020**, *70*, 7–30. [CrossRef] [PubMed]
2. Howlader, N.; Noone, A.M.; Krapcho, M.; Miller, D.; Brest, A.; Yu, M.; Ruhl, J.; Tatalovich, Z.; Mariotto, A.; Lewis, D.R.; et al. (Eds.) *SEER Cancer Statistics Review, 1975–2016*; National Cancer Institute: Bethesda, MD, USA, 2020. Available online: [https://seer.cancer.gov/csr/1975\\_2016/](https://seer.cancer.gov/csr/1975_2016/) (accessed on 15 November 2021).
3. Ashrafizadeh, M.; Mirzaei, S.; Hushmandi, K.; Rahmanian, V.; Zabolian, A.; Raei, M.; Farahani, M.V.; Goharrizi, M.A.S.B.; Khan, H.; Zarrabi, A.; et al. Therapeutic potential of AMPK signaling targeting in lung cancer: Advances, challenges and future prospects. *Life Sci.* **2021**, *278*, 119649. [CrossRef]
4. Ashrafizadeh, M.; Najafi, M.; Makvandi, P.; Zarrabi, A.; Farkhondeh, T.; Samarghandian, S. Versatile role of curcumin and its derivatives in lung cancer therapy. *J. Cell. Physiol.* **2020**, *235*, 9241–9268. [CrossRef] [PubMed]

5. Schiller, J.H.; Harrington, D.; Belani, C.P.; Langer, C.; Sandler, A.; Krook, J.; Zhu, J.; Johnson, D.H. Comparison of Four Chemotherapy Regimens for Advanced Non-Small-Cell Lung Cancer. *N. Engl. J. Med.* **2002**, *346*, 92–98. [CrossRef]
6. Peters, S.; Adjei, A.A.; Gridelli, C.; Reck, M.; Kerr, K.; Felip, E. Metastatic non-small-cell lung cancer (NSCLC): ESMO Clinical Practice Guidelines for diagnosis, treatment and follow-up. *Ann. Oncol.* **2012**, *23*, vii56–vii64. [CrossRef]
7. Perez, E.A. Microtubule inhibitors: Differentiating tubulin-inhibiting agents based on mechanisms of action, clinical activity, and resistance. *Mol. Cancer Ther.* **2009**, *8*, 2086–2095. [CrossRef] [PubMed]
8. Henriques, A.C.; Ribeiro, D.; Pedrosa, J.; Sarmento, B.; Silva, P.M.A.; Bousbaa, H. Mitosis inhibitors in anticancer therapy: When blocking the exit becomes a solution. *Cancer Lett.* **2019**, *440–441*, 64–81. [CrossRef]
9. Lara-Gonzalez, P.; Pines, J.; Desai, A. Spindle assembly checkpoint activation and silencing at kinetochores. *Semin. Cell Dev. Biol.* **2021**, *117*, 86–98. [CrossRef]
10. Silva, P.; Barbosa, J.; Nascimento, A.V.; Faria, J.; Reis, R.; Bousbaa, H. Monitoring the fidelity of mitotic chromosome segregation by the spindle assembly checkpoint. *Cell Prolif.* **2011**, *44*, 391–400. [CrossRef]
11. Marques, S.; Fonseca, J.; Silva, P.; Bousbaa, H. Targeting the Spindle Assembly Checkpoint for Breast Cancer Treatment. *Curr. Cancer Drug Targets* **2015**, *15*, 272–281. [CrossRef] [PubMed]
12. Dumontet, C.; Jordan, M.A. Microtubule-binding agents: A dynamic field of cancer therapeutics. *Nat. Rev. Drug Discov.* **2010**, *9*, 790–803. [CrossRef]
13. Čermák, V.; Dostál, V.; Jelínek, M.; Libusová, L.; Kovář, J.; Rösel, D.; Brábek, J. Microtubule-targeting agents and their impact on cancer treatment. *Eur. J. Cell Biol.* **2020**, *99*, 151075. [CrossRef]
14. Novais, P.; Silva, P.M.A.; Amorim, I.; Bousbaa, H. Second-Generation Antimitotics in Cancer Clinical Trials. *Pharmaceutics* **2021**, *13*, 1011. [CrossRef]
15. Colicino, E.G.; Hehnl, H. Regulating a key mitotic regulator, polo-like kinase 1 (PLK1). *Cytoskeleton* **2018**, *75*, 481–494. [CrossRef]
16. Wu, M.; Wang, Y.; Yang, D.; Gong, Y.; Rao, F.; Liu, R.; Danna, Y.; Li, J.; Fan, J.; Chen, J.; et al. A PLK1 kinase inhibitor enhances the chemosensitivity of cisplatin by inducing pyroptosis in oesophageal squamous cell carcinoma. *EBioMedicine* **2019**, *41*, 244–255. [CrossRef] [PubMed]
17. Pajtler, K.W.; Sadowski, N.; Ackermann, S.; Althoff, K.; Schönbeck, K.; Batzke, K.; Schäfers, S.; Odersky, A.; Heukamp, L.; Astrahantseff, K.; et al. The GSK461364 PLK1 inhibitor exhibits strong antitumoral activity in preclinical neuroblastoma models. *Oncotarget* **2017**, *8*, 6730–6741. [CrossRef]
18. Raab, M.; Krämer, A.; Hehlgans, S.; Sanhaji, M.; Kurunci-Csacsko, E.; Dötsch, C.; Bug, G.; Ottmann, O.; Becker, S.; Pachel, F.; et al. Mitotic arrest and slippage induced by pharmacological inhibition of Polo-like kinase 1. *Mol. Oncol.* **2015**, *9*, 140–154. [CrossRef] [PubMed]
19. Gascoigne, K.E.; Taylor, S.S. Cancer Cells Display Profound Intra- and Interline Variation following Prolonged Exposure to Antimitotic Drugs. *Cancer Cell* **2008**, *14*, 111–122. [CrossRef] [PubMed]
20. Sinha, D.; Duijf, P.H.G.; Khanna, K.K. Mitotic slippage: An old tale with a new twist. *Cell Cycle* **2019**, *18*, 7–15. [CrossRef]
21. Silva, P.M.A.; Ribeiro, N.; Lima, R.T.; Andrade, C.; Diogo, V.; Teixeira, J.; Florindo, C.; Tavares, Á.; Vasconcelos, M.H.; Bousbaa, H. Suppression of spindle delays mitotic exit and exacerbates cell death response of cancer cells treated with low doses of paclitaxel. *Cancer Lett.* **2017**, *394*, 33–42. [CrossRef]
22. Czabotar, P.E.; Lessene, G.; Strasser, A.; Adams, J.M. Control of apoptosis by the BCL-2 protein family: Implications for physiology and therapy. *Nat. Rev. Mol. Cell Biol.* **2014**, *15*, 49–63. [CrossRef] [PubMed]
23. Cang, S.; Iragavarapu, C.; Savooji, J.; Song, Y.; Liu, D. ABT-199 (venetoclax) and BCL-2 inhibitors in clinical development. *J. Hematol. Oncol.* **2015**, *8*, 129. [CrossRef]
24. Lénárt, P.; Petronczki, M.; Steegmaier, M.; Di Fiore, B.; Lipp, J.J.; Hoffmann, M.; Rettig, W.J.; Kraut, N.; Peters, J.-M. The Small-Molecule Inhibitor BI 2536 Reveals Novel Insights into Mitotic Roles of Polo-like Kinase 1. *Curr. Biol.* **2007**, *17*, 304–315. [CrossRef]
25. Mross, K.; Frost, A.; Steinbild, S.; Hedbom, S.; Rentschler, J.; Kaiser, R.; Rouyre, N.; Trommeshauser, D.; Hoesl, C.E.; Munzert, G. Phase I Dose Escalation and Pharmacokinetic Study of BI 2536, a Novel Polo-Like Kinase 1 Inhibitor, in Patients With Advanced Solid Tumors. *J. Clin. Oncol.* **2008**, *26*, 5511–5517. [CrossRef] [PubMed]
26. Vogler, M.; Dinsdale, D.; Dyer, M.J.S.; Cohen, G.M. Bcl-2 inhibitors: Small molecules with a big impact on cancer therapy. *Cell Death Differ.* **2009**, *16*, 360–367. [CrossRef]
27. Tse, C.; Shoemaker, A.R.; Adickes, J.; Anderson, M.G.; Chen, J.; Jin, S.; Johnson, E.F.; Marsh, K.C.; Mitten, M.J.; Nimmer, P.; et al. ABT-263: A potent and orally bioavailable Bcl-2 family inhibitor. *Cancer Res.* **2008**, *68*, 3421–3428. [CrossRef] [PubMed]
28. Wolf, G.; Elez, R.; Doermer, A.; Holtrich, U.; Ackermann, H.; Stutte, H.J.; Altmannsberger, H.M.; Rübsamen-Waigmann, H.; Strebhardt, K. Prognostic significance of polo-like kinase (PLK) expression in non-small cell lung cancer. *Oncogene* **1997**, *14*, 543–549. [CrossRef]
29. Zeng, Y.; Li, N.; Liu, W.; Zeng, M.; Cheng, J.; Huang, J. Analyses of expressions and prognostic values of Polo-like kinases in non-small cell lung cancer. *J. Cancer Res. Clin. Oncol.* **2020**, *146*, 2447–2460. [CrossRef] [PubMed]
30. Mohamad Anuar, N.N.; Nor Hisam, N.S.; Liew, S.L.; Ugasman, A. Clinical Review: Navitoclax as a Pro-Apoptotic and Anti-Fibrotic Agent. *Front. Pharmacol.* **2020**, *11*, 1817. [CrossRef]
31. Gascoigne, K.E.; Taylor, S.S. How do anti-mitotic drugs kill cancer cells? *J. Cell Sci.* **2009**, *122*, 2579–2585. [CrossRef]

32. Pinto, B.; Henriques, A.C.; Silva, P.M.A.; Bousbaa, H. Three-Dimensional Spheroids as In Vitro Preclinical Models for Cancer Research. *Pharmaceutics* **2020**, *12*, 1186. [CrossRef]
33. Liu, N.; Hu, G.; Wang, H.; Li, Z.; Guo, Z. PLK1 inhibitor facilitates the suppressing effect of temozolomide on human brain glioma stem cells. *J. Cell. Mol. Med.* **2018**, *22*, 5300–5310. [CrossRef]
34. Steegmaier, M.; Hoffmann, M.; Baum, A.; Lénárt, P.; Petronczki, M.; Krššák, M.; Gürtler, U.; Garin-Chesa, P.; Lieb, S.; Quant, J.; et al. BI 2536, a Potent and Selective Inhibitor of Polo-like Kinase 1, Inhibits Tumor Growth In Vivo. *Curr. Biol.* **2007**, *17*, 316–322. [CrossRef] [PubMed]
35. Deng, Z.; Chen, G.; Liu, S.; Li, Y.; Zhong, J.; Zhang, B.; Li, L.; Huang, H.; Wang, Z.; Xu, Q.; et al. Discovery of methyl 3-((2-((1-(dimethylglycyl)-5-methoxyindolin-6-yl)amino)-5-(trifluoro-methyl) pyrimidin-4-yl)amino)thiophene-2-carboxylate as a potent and selective polo-like kinase 1 (PLK1) inhibitor for combating hepatocellular carcinoma. *Eur. J. Med. Chem.* **2020**, *206*, 112697. [CrossRef] [PubMed]
36. Mao, F.; Li, J.; Luo, Q.; Wang, R.; Kong, Y.; Carlock, C.; Liu, Z.; Elzey, B.D.; Liu, X. Plk1 inhibition enhances the efficacy of BET epigenetic reader blockade in castration-resistant prostate cancer. *Mol. Cancer Ther.* **2018**, *17*, 1554–1565. [CrossRef] [PubMed]
37. De Martino, D.; Yilmaz, E.; Orlacchio, A.; Ranieri, M.; Zhao, K.; Di Cristofano, A. PI3K blockage synergizes with PLK1 inhibition preventing endoreduplication and enhancing apoptosis in anaplastic thyroid cancer. *Cancer Lett.* **2018**, *439*, 56–65. [CrossRef] [PubMed]
38. Shi, J.; Zhou, Y.; Huang, H.C.; Mitchison, T.J. Navitoclax (ABT-263) accelerates apoptosis during drug-induced mitotic arrest by antagonizing Bcl-xL. *Cancer Res.* **2011**, *71*, 4518–4526. [CrossRef] [PubMed]
39. Tan, N.; Malek, M.; Zha, J.; Yue, P.; Kassees, R.; Berry, L.; Fairbrother, W.J.; Sampath, D.; Belmont, L.D. Navitoclax enhances the efficacy of taxanes in non-small cell lung cancer models. *Clin. Cancer Res.* **2011**, *17*, 1394–1404. [CrossRef]
40. Henriques, A.C.; Silva, P.M.A.; Sarmiento, B.; Bousbaa, H. Antagonizing the spindle assembly checkpoint silencing enhances paclitaxel and Navitoclax-mediated apoptosis with distinct mechanistic. *Sci. Rep.* **2021**, *11*, 4139. [CrossRef]
41. Henriques, A.C.; Silva, P.M.A.; Sarmiento, B.; Bousbaa, H. The Mad2-Binding Protein p31comet as a Potential Target for Human Cancer Therapy. *Curr. Cancer Drug Targets* **2021**, *21*, 401–415. [CrossRef] [PubMed]
42. Wong, R.S.Y. Apoptosis in cancer: From pathogenesis to treatment. *J. Exp. Clin. Cancer Res.* **2011**, *30*, 87. [CrossRef]
43. Barbosa, J.; Nascimento, A.V.; Faria, J.; Silva, P.; Bousbaa, H. The spindle assembly checkpoint: Perspectives in tumorigenesis and cancer therapy. *Front. Biol.* **2011**, *6*, 147–155. [CrossRef]
44. Wong, M.; Tan, N.; Zha, J.; Peale, F.V.; Yue, P.; Fairbrother, W.J.; Belmont, L.D. Navitoclax (ABT-263) Reduces Bcl-x L –Mediated Chemoresistance in Ovarian Cancer Models. *Mol. Cancer Ther.* **2012**, *11*, 1026–1035. [CrossRef] [PubMed]
45. Borgovan, T.; Bellistri, J.P.S.; Slack, K.N.; Kopelovich, L.; Desai, M.; Joe, A.K. Inhibition of BCL2 expression and activity increases H460 sensitivity to the growth inhibitory effects of polyphenon E. *J. Exp. Ther. Oncol.* **2009**, *8*, 129–144.
46. Bojes, H. Bcl-2 and Bcl-xLin Peroxide-Resistant A549 and U87MG Cells. *Toxicol. Sci.* **1998**, *42*, 109–116. [CrossRef]
47. Amundson, S.A.; Myers, T.G.; Scudiero, D.; Kitada, S.; Reed, J.C.; Fornace, A.J. An Informatics Approach Identifying Markers of Chemosensitivity in Human Cancer Cell Lines. *Cancer Res.* **2000**, *60*, 6101–6110. [PubMed]
48. Nor Hisam, N.S.; Ugusman, A.; Rajab, N.F.; Ahmad, M.F.; Fenech, M.; Liew, S.L.; Mohamad Anuar, N.N. Combination Therapy of Navitoclax with Chemotherapeutic Agents in Solid Tumors and Blood Cancer: A Review of Current Evidence. *Pharmaceutics* **2021**, *13*, 1353. [CrossRef]
49. de Vos, S.; Leonard, J.P.; Friedberg, J.W.; Zain, J.; Dunleavy, K.; Humerickhouse, R.; Hayslip, J.; Pesko, J.; Wilson, W.H. Safety and efficacy of navitoclax, a BCL-2 and BCL-X L inhibitor, in patients with relapsed or refractory lymphoid malignancies: Results from a phase 2a study. *Leuk. Lymphoma* **2021**, *62*, 810–818. [CrossRef]
50. Mross, K.; Dittrich, C.; Aulitzky, W.E.; Strumberg, D.; Schutte, J.; Schmid, R.M.; Hollerbach, S.; Merger, M.; Munzert, G.; Fleischer, F.; et al. A randomised phase II trial of the Polo-like kinase inhibitor BI 2536 in chemo-naïve patients with unresectable exocrine adenocarcinoma of the pancreas—A study within the Central European Society Anticancer Drug Research (CESAR) collaborative network. *Br. J. Cancer* **2012**, *107*, 280–286. [CrossRef]
51. Yim, H. Current clinical trials with polo-like kinase 1 inhibitors in solid tumors. *Anticancer Drugs* **2013**, *24*, 999–1006. [CrossRef] [PubMed]
52. Bousbaa, H. Novel Anticancer Strategies. *Pharmaceutics* **2021**, *13*, 275. [CrossRef] [PubMed]
53. Mathews Griner, L.A.; Zhang, X.; Guha, R.; McKnight, C.; Goldlust, I.S.; Lal-Nag, M.; Wilson, K.; Michael, S.; Titus, S.; Shinn, P.; et al. Large-scale pharmacological profiling of 3D tumor models of cancer cells. *Cell Death Dis.* **2016**, *7*, e2492. [CrossRef] [PubMed]
54. Liu, Z.; Sun, Q.; Wang, X. PLK1, A Potential Target for Cancer Therapy. *Transl. Oncol.* **2016**, *10*, 22–32. [CrossRef] [PubMed]





Review

# BUB3, beyond the Simple Role of Partner

Patrícia M. A. Silva <sup>1,2</sup> and Hassan Bousbaa <sup>1,3,\*</sup>

- <sup>1</sup> UNIPRO—Oral Pathology and Rehabilitation Research Unit, University Institute of Health Sciences (IUCS), University Polytechnic Higher Education Cooperative (CESPU), Rua Central de Gandra, 4585-116 Gandra, Portugal; patricia.silva@cespu.pt
- <sup>2</sup> TOXRUN—Toxicology Research Unit, University Institute of Health Sciences (IUCS), University Polytechnic Higher Education Cooperative (CESPU), Rua Central de Gandra, 4585-116 Gandra, Portugal
- <sup>3</sup> Centro Interdisciplinar de Investigação Marinha e Ambiental (CIIMAR), Universidade do Porto, Terminal de Cruzeiros do Porto de Leixões, Av. General Norton de Matos s/n, 4450-208 Matosinhos, Portugal
- \* Correspondence: hassan.bousbaa@iucs.cespu.pt

**Abstract:** The BUB3 protein plays a key role in the activation of the spindle assembly checkpoint (SAC), a ubiquitous surveillance mechanism that ensures the fidelity of chromosome segregation in mitosis and, consequently, prevents chromosome mis-segregation and aneuploidy. Besides its role in SAC signaling, BUB3 regulates chromosome attachment to the spindle microtubules. It is also involved in telomere replication and maintenance. Deficiency of the BUB3 gene has been closely linked to premature aging. Upregulation of the BUB3 gene has been found in a variety of human cancers and is associated with poor prognoses. Here, we review the structure and functions of BUB3 in mitosis, its expression in cancer and association with survival prognoses, and its potential as an anticancer target.

**Keywords:** BUB3; spindle assembly checkpoint; mitosis; cancer; senescence; anticancer target

**Citation:** Silva, P.M.A.; Bousbaa, H. BUB3, beyond the Simple Role of Partner. *Pharmaceutics* **2022**, *14*, 1084. <https://doi.org/10.3390/pharmaceutics14051084>

Academic Editor: Carlo Irace

Received: 31 March 2022

Accepted: 16 May 2022

Published: 18 May 2022

**Publisher's Note:** MDPI stays neutral with regard to jurisdictional claims in published maps and institutional affiliations.



**Copyright:** © 2022 by the authors. Licensee MDPI, Basel, Switzerland. This article is an open access article distributed under the terms and conditions of the Creative Commons Attribution (CC BY) license (<https://creativecommons.org/licenses/by/4.0/>).

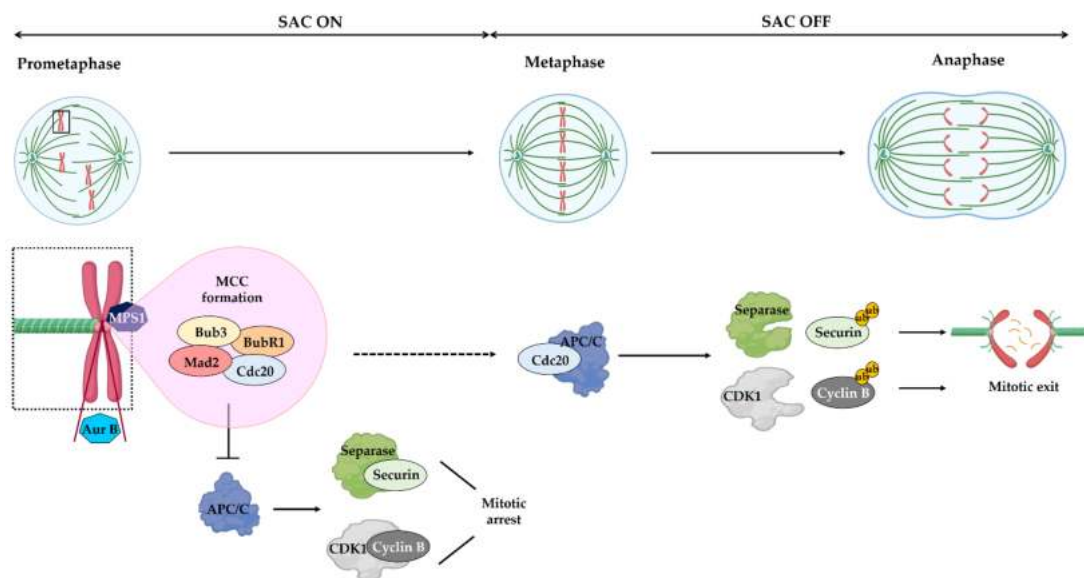
## 1. Introduction

BUB3 belongs to the conserved budding uninhibited by benomyl (BUB) protein family, which is known to function in the spindle assembly checkpoint (SAC) pathway, from yeast to mammals [1,2]. The SAC monitors and ensures appropriate attachments of spindle microtubules to kinetochores, delaying anaphase onset until all chromosomes have been attached to the mitotic spindle in a bi-oriented manner, thereby preventing chromosome mis-segregation and aneuploidy, a driving force of tumorigenesis [1,2]. BUB3 is also involved in establishing kinetochore–microtubule attachment [3–6]. It recruits BUBR1 to kinetochores to form functional complexes which, together with MAD2 and CDC20, form the mitotic checkpoint complex (MCC), in charge of inhibiting the anaphase-promoting complex (APC) [7]. When all kinetochores are attached to microtubules and aligned at the metaphase plate, the MCC is dissociated, and no more MCC is formed, which releases the SAC to promote exit from mitosis. Besides its role in SAC signaling, BUB3 has been implicated in proper telomere replication and maintenance, as well as in the regulation of aging [8–10]. In addition, a number of studies have reported deregulated expression of the *BUB3* gene in human cancers; however, its role in carcinogenesis is still controversial [11–13]. Here, we reviewed BUB3's functions in cell cycle progression, its roles in human cancers, and its potential as a target for cancer treatment.

## 2. The Structure of BUB3 and Its Functions in Mitosis

*BUB3* belongs to a series of genes (*BUB1*, *BUB2*, *BUB3*, *MAD1*, *MAD2*, *MAD3*, and *MPS1*) identified in a genetic screen in the budding yeast *Saccharomyces cerevisiae* that failed to arrest in response to spindle damage [14–16]. Mutants of these genes prematurely exit mitosis in the presence of microtubule-depolymerizing drugs, thereby accumulating severe mitotic errors. Functional orthologs of these genes were also identified in higher

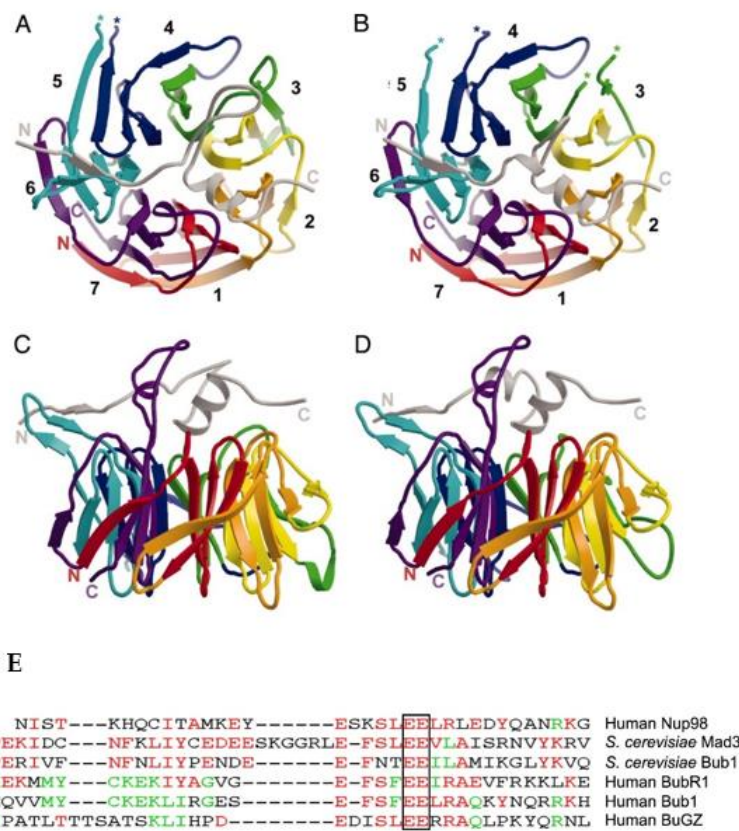
eukaryotes, including humans [17–20]. After nuclear envelope breakdown at the prophase to prometaphase transition, each of the two kinetochores formed at the centromeric regions of paired sister chromatids initiates attachment to spindle microtubules, with the goal of achieving bi-orientation with sister kinetochores oriented toward opposite poles of the spindle. However, in response to unattached kinetochores, the SAC is activated, through hierarchical recruitment of SAC proteins, including MAD1, MAD2, BUB3, BUBR1, and CENP-E, at the unattached kinetochores [21,22]. Consequently, MAD2, BUBR1, and BUB3 form a complex with CDC20, known as the mitotic checkpoint complex (MCC) [7] (Figure 1). This way, CDC20 is sequestered and prevented from activating the anaphase-promoting complex/cyclosome (APC/C), which is a ubiquitin E3 ligase that promotes proteolysis of securin and cyclin B and subsequent mitotic exit. Proper bipolar attachments of all chromosomes to the mitotic spindle leads to SAC inactivation, allowing CDC20 release and APC/C activation, which promotes anaphase entry.



**Figure 1.** Spindle assembly checkpoint mechanism. In response to unattached or improperly attached kinetochores (prometaphase), the SAC is turned ON and promotes the assembly of the mitotic checkpoint complex (MCC), made of MAD2, BUB3, BUBR1 and CDC20. At these kinetochores, the SAC kinase MPS1 recruits BUB3, BUB1 and BUBR1. The MCC inhibits the activity of anaphase-promoting complex/cyclosome (APC/C), leading to the stabilization of separase/securin and CDK1/cyclin B complexes and, consequently, mitotic arrest. The Aurora B kinase (AUR B), associated with centromere heterochromatin, promotes proper kinetochore–microtubule attachments. Once all chromosomes are properly attached to spindle microtubules and are aligned at metaphase plate (metaphase), the SAC is turned OFF, through MCC disassembly, and, consequently, CDC20 can bind and activate the APC/C, resulting in ubiquitylation (ub) of cyclin B and securin mitotic substrates. In turn, separase can cleave cohesins to promote sister chromatid separation (anaphase), while CDK1 inactivation promotes exit from mitosis. Reprinted from [23], MDPI 2021.

BUB3 is a fundamental piece in SAC activation. At the molecular level, BUB3 is a WD40-repeat protein with a seven-blade  $\beta$ -propeller structure forming a symmetric circular wall around a central pore, giving it a donut-like shape [24–26] (Figure 2A–D). BUB3 binds to phosphorylated MELT repeats (Met-Glu-Leu-Thr(P)) on the outer kinetochore subunit Kn1 (also known as Spc7, BLINKIN, CASC5 in different organisms), resulting in the recruitment of its binding partners BUBR1 and BUB1 to kinetochores [27–30]. The BUB3–BUB1 and BUB3–BUBR1 interactions involve the BUB3 central pore region and the respective Gle2 binding sequence (GLEBS) motif of BUBR1/BUB1 (Figure 2E) [31]. Specifically, the interaction of BUB3 with the BUBR1 GLEBS motif is essential for the integrity of the human MCC, as mutations that disrupt this interaction interface result in

SAC deficiency and chromosome instability in yeast and human cells [24,32]. Interestingly, specific disruption of endogenous BUBR1–BUB3 complexes in cancer cells phenocopies the effects observed in gene-targeting experiments [33]. Besides its role in SAC signaling, BUB3 promotes the establishment of correct kinetochore–microtubule (K-MT) attachments, in concert with BUB1 and BUBR1, probably through an antagonistic interaction between BUB3 and the motor protein dynein [5,6,34,35]. For this purpose, BuGZ, a GLEBS domain-containing and kinetochore-binding protein, interacts with and stabilizes BUB3 to facilitate its kinetochore targeting and function in K-MT attachment [36]. This interaction was disrupted when the highly conserved EE to AA of the BuGZ GLEBS motif was mutated (see the outlined EE in Figure 2E) [37]. The specific contribution of each BUB protein in the regulation of K-MT attachments remains difficult to assign, given the dependency of BUB1 and BUBR1 on BUB3 for kinetochore localization [6]. We previously addressed the specific contribution of BUB3 to K-MT attachment in human cells, and compared it to that of BUB1 and BUBR1, using an RNA interference (RNAi) approach and high-resolution microscopy [5,6]. We found that BUB3-depleted cells exhibited microtubules running past the kinetochore pairs, similarly to BUB1-depleted cells, suggesting side-on binding to the walls of microtubules. In addition, chromosome alignment defects in the BUB3/BUB1 double depletion were worse than in BUB3 and BUB1 single RNAi, which is expected for proteins with specific and parallel functions in K-MT regulation, suggesting a cooperative role. In contrast, BUBR1-depleted cells exhibited misaligned chromosomes, which, despite being detached from microtubules, have kinetochore pairs parallel to the spindle axis, suggesting that BubR1 is involved in K-MT stability rather than in microtubule binding. Thus, in our view, BUB1 and BUB3 seem to regulate the switching from lateral to end-on attachment, while BUBR1 is required for stabilization of K-MT attachments.



**Figure 2.** Top overview of Bub3 bound to GLEBS motif determined in yeast. (A) Top view of Bub3 bound to the GLEBS motif from Mad3 (BUBR1 in higher eukaryotes). The GLEBS peptide is colored



in gray and lies along the top face of the propeller. N and C termini are labeled, and breaks in main-chain density are denoted with asterisks (\*). (B) Top view of Bub3 bound to GLEBS motif from Bub1. Overall, the structures are quite similar, except that the Bub1 GLEBS motif has a shorter loop between helices  $\alpha 1$  and  $\alpha 2$ . (C,D) Side views of Bub3 bound to Mad3/BUBR1 (C) and Bub1 (D) GLEBS motifs. The three-stranded  $\beta$ -sheet that includes the DA loop between blades 5 and 6 of Bub3 projects leftward in these views. Numbers indicate blades. Reprinted with permission from [24]. Copyright 2021, National Academy of Sciences, U.S.A. (E) The conserved GLEBS motif in BUB1 and BUBR1 that binds BUB3; alignment of GLEBS motifs from hNUP98, scMad3, scBub1, hBUBR1, mBUB1, and hBuGZ; the completely conserved amino acids, EE, are boxed. Reprinted with permission from [37]. Copyright 2022, Elsevier.

### 3. BUB3 in Aging

BUB3 shares extensive sequence homology with each of the four WD repeat motifs, and over the entire length of the RAE1 protein, indicative of functional similarity [31,38]. While BUB3 functions in the SAC pathway, RAE1 (also called Gle2 or mrnp41) is involved in mRNA export in interphase [38–42]. Binding to RAE1 is mediated by a GLEBS motif present in the nucleoporin Nup98 [41]. Strikingly, RAE1 also binds to the GLEBS motif of BUB1 [43]. The discovery that BUB3 also binds to the GLEBS motifs of the SAC proteins BUB1 and BUBR1 has led to the hypothesis that RAE1 might have a role as an SAC protein [43]. Homologous recombination-mediated mouse *Rae1* gene disruption showed that the loss of a single *Rae1* allele causes a SAC defect and chromosome mis-segregation. Besides the 34% identity and 52% similarity of the human RAE1 and BUB3, *Bub3* haploinsufficient cells exhibit a strikingly similar mitotic phenotype, suggesting that RAE1 and BUB3 are functionally analogous, namely, by playing a specific or perhaps a redundant role in BUB1 targeting to unattached kinetochores and subsequent SAC activation [26,44]. Interestingly, double *Rae1/Bub3* haploinsufficiency causes a much more severe chromosomal instability phenotype than single haploinsufficiencies, suggesting a cooperative role of RAE1 and BUB3 in regulating the SAC activities to prevent chromosomal mis-segregation [44]. Long-term phenotype analysis showed a reduced lifespan of mice harboring the combined *Bub3* and *Rae1* haploinsufficiency, with phenotypes associated with aging appearing early in double haploinsufficient mice, while mice with single *Bub3* or *Rae1* haploinsufficiency were viable and had a normal appearance [9,10,44]. Aneuploidy in single haploinsufficient *Bub3* or *Rae1* mice increased dramatically with age, and increased further in double *Bub3/Rae1* haploinsufficient mice [10,44,45]. Curiously, mice with single or combined disruption of *Bub3* and *Rae1* were not predisposed to spontaneous tumorigenesis. Instead, *Bub3/Rae1* haploinsufficiency caused early onset of cellular senescence, which was due to SAC weakening, rather than to aneuploidy itself. Since the age-associated phenotypes exhibited by haploinsufficient *Bub3/Rae1* mice also occur in very old wild-type mice, then *Rae1* and *Bub3* were proposed to accelerate the aging process. Molecularly, haploinsufficient *Bub3/Rae1* mice embryonic fibroblasts (MEFs) accumulate high levels of cellular senescence inducers, including p16, p19, p21, and p53, but, surprisingly, no major signs of apoptosis, suggesting that haploinsufficiency of *Bub3* and *Rae1* accelerates aging through induction of cellular senescence [9,10,44,45]. Significantly, and similarly to haploinsufficient *Bub3/Rae1* mice, hypomorphic *BubR1* mice develop several aging-associated phenotypes at a very young age, including cataracts, lordokyphosis, loss of subcutaneous fat, and impaired wound healing [46]. However, hypomorphic *BubR1* mice had a much earlier onset of aging phenotypes, with many more senescent cells, than haploinsufficient *Bub3/Rae1* mice, indicating that the rate of premature aging is correlated with the level of induction of senescence. Therefore, in addition to oncogenic transformation, accelerated aging seems to be another major biological manifestation of a weakened SAC [10,46]. What determines if it is oncogenic transformation or accelerated aging that will take place in a deficient SAC background is unknown. It might depend on the extent of SAC deficiency and/or SAC component depletion.

#### 4. BUB3 in Cancer

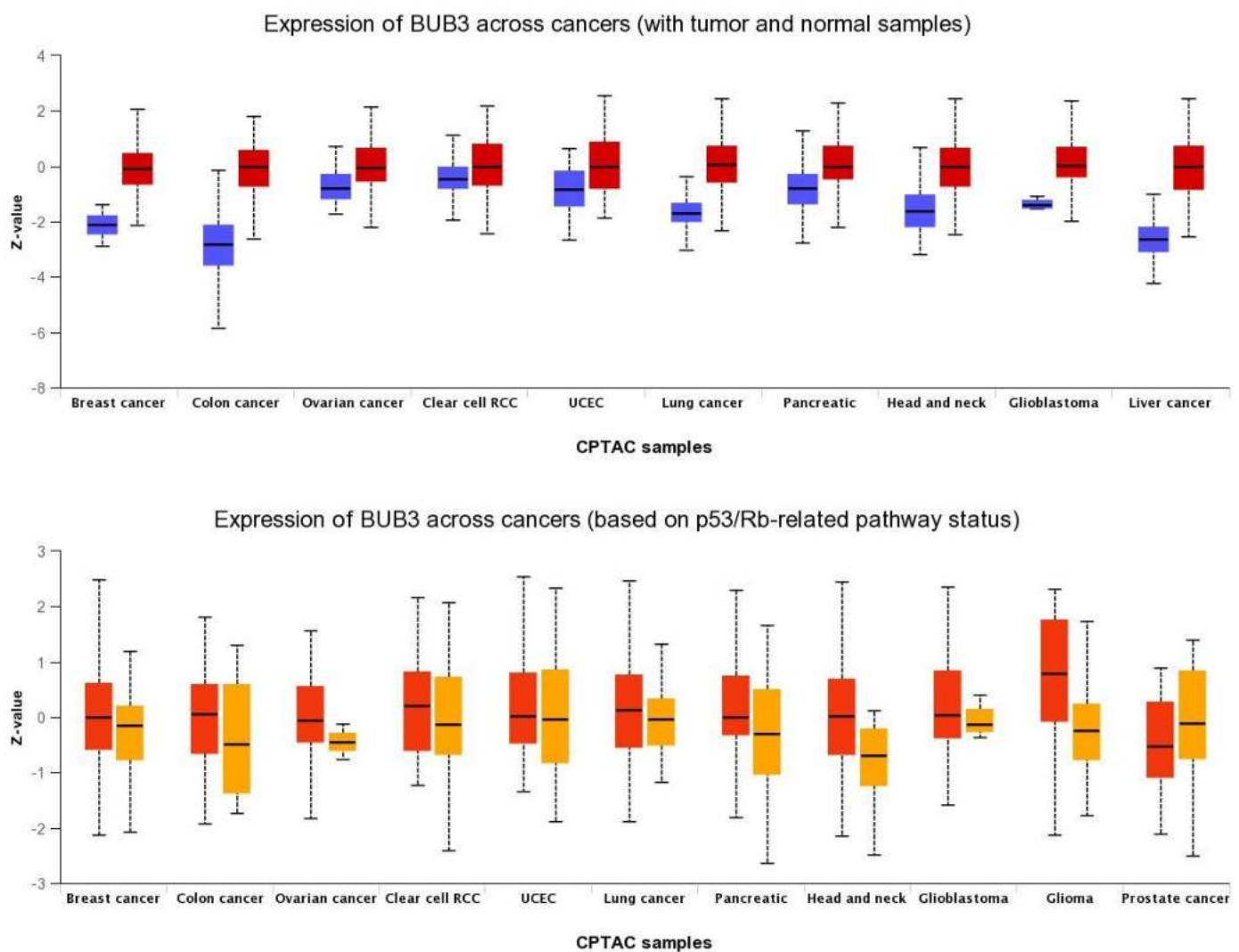
Defects in SAC activity lead to chromosome mis-segregation, which is thought to be responsible, at least in part, for aneuploidy generation in human malignancies [1,47–50]. SAC deficiency is often associated with deregulated SAC genes [1,48,50]. We examined the expression of *BUB3* in various human cancer types. To this end, *BUB3* gene expression and clinical data for 35 cancer types retrieved from the UALCAN data portal (<http://ualcan.path.uab.edu/index.html>, accessed on 24 December 2021) were analyzed [51]. *BUB3* transcript levels were compared between cancers and normal tissue in 18 cancer types; 17 cancer types were excluded from the analysis due to lack of normal samples. We found *BUB3* to be significantly overexpressed in cancers compared to normal tissue in 16 of the 18 cancer types analyzed (Table 1).

**Table 1.** Comparison of *BUB3* expression between cancers and normal tissue.

Cancer Type	Fold Change <sup>1</sup>	<i>p</i> Value <sup>2</sup>
Bladder urothelial carcinoma	1.68	$1.68 \times 10^{-12}$
Breast invasive carcinoma	1.79	$1.11 \times 10^{-16}$
Cervical squamous cell carcinoma	2.24	$3.72 \times 10^{-3}$
Cholangiocarcinoma	3.96	$5.06 \times 10^{-14}$
Colon adenocarcinoma	1.51	$1.62 \times 10^{-12}$
Esophageal carcinoma	2.62	$3.50 \times 10^{-8}$
Glioblastoma multiforme	1.43	$2.73 \times 10^{-1}$
Head and neck squamous cell carcinoma	1.82	$<1 \times 10^{-12}$
Kidney chromophobe	0.38	$<1 \times 10^{-12}$
Liver hepatocellular carcinoma	2.16	$<1 \times 10^{-12}$
Lung adenocarcinoma	1.51	$<1 \times 10^{-12}$
Lung squamous cell carcinoma	1.86	$<1 \times 10^{-12}$
Prostate adenocarcinoma	1.11	$6.02 \times 10^{-3}$
Rectum adenocarcinoma	1.43	$1.62 \times 10^{-12}$
Sarcoma	2.00	$1.36 \times 10^{-1}$
Stomach adenocarcinoma	2.17	$1.62 \times 10^{-12}$
Thyroid carcinoma	0.93	$3.43 \times 10^{-9}$
Uterine corpus endometrial carcinoma	1.43	$<1 \times 10^{-12}$

<sup>1</sup> Mean *BUB3* expression in cancers/mean *BUB3* expression in normal tissue; <sup>2</sup> Student's *t* test, *p* value < 0.05.

*BUB3* protein levels are also elevated in a wide variety of human cancers compared to normal tissue (Figure 3). We analyzed *BUB3* protein levels in TP53-mutant cancers, as TP53-dependent SAC has been described [52–54]. TP53 is a transcription factor that acts as a tumor suppressor by inducing cell cycle arrest, cellular senescence, or apoptosis in response to cellular stresses, such as hypoxia, DNA and spindle damage [55]. *TP53* gene mutations are universal across cancer types, and this contributes to human cancers in different ways [56]. The TP53 pathway regulates the expression of a network of genes that are targeted to respond to a variety of intrinsic and extrinsic stress signals to ensure, among other things, accurate DNA replication, chromosome segregation, and cell division [57]. Interestingly, in most of the cancer types analyzed, *BUB3* levels are significantly higher in TP53-mutant cancers than in TP53-wild-type cancers, suggesting that wild-type TP53 represses *BUB3* gene expression in physiological conditions, and that the TP53–*BUB3* pathway may play an important role in carcinogenesis (Figure 3).



**Figure 3.** Pan-cancer view of expression of BUB3 protein across cancers. (**Upper panel**) Comparison between normal (blue) and primary tumors (red); (**lower panel**) Comparison between TP53-mutant (red) and TP53-non-mutant (orange) tumor samples. RCC: renal cell carcinoma; UCEC: Uterine corpus endometrial carcinoma; CPTAC: Clinical Proteomic Tumor Analysis Consortium. Data were retrieved from UALCAN portal (<http://ualcan.path.uab.edu/index.html>) on 24 December 2021.

Previous studies have reported *BUB3* overexpression, at both RNA and protein levels, in a variety of human cancers compared with normal tissue. In most cancers, this upregulation was associated with poor prognoses. We reported that *BUB3* is upregulated and is associated with poor prognosis in oral squamous cell carcinoma [11]. The positive expression of cytoplasmic *BUB3*, together with that of cyclin B1 and the pituitary tumor-transforming gene 1, was significantly correlated with recurrence in prostate cancer [58]. *BUB3* was upregulated in 79% of gastric cancers, being a proliferation-dependent phenomenon in gastric cancer [13]. *BUB3* levels were reported to be higher in sarcoma samples, and higher expression levels of *BUB3* were associated with lower overall and disease-free survival in patients with sarcomas [59]. High expression of *BUB3* was associated with increased mortality in hepatocellular carcinoma [60]. In other studies, however, high protein expression of *BUB3* in low-grade breast cancers was associated with longer overall survival, whereas lower expression resulted in poorer outcomes [61]. Upregulated *BUB3* was also reported in breast cancer samples [62]. Polymorphism in the *BUB3* gene was associated with the worst survival outcomes in early-stage non-small-cell lung cancer [63]. As with other SAC genes, epigenetic deregulation remains the most common alteration in the *BUB3*

gene, while mutations at the sequence levels are rather rare and confer no increased cancer risk [1]. For instance, genetic variation in the *BUB3* gene did not affect familial breast cancer risk, and mutations in the *BUB3* gene were shown to be rare in bladder tumors and glioblastomas [64–66]. Overall, these studies confirm that the overexpression of the *BUB3* gene and protein is a common feature of human cancers, being associated with poor prognosis.

Why is *BUB3* overexpressed in cancer cells? This question still remains unanswered. *BUB3* and other SAC genes are frequently overexpressed in cancer, and such overexpression is correlated with chromosomal instability [67]. It was reported that loss of major tumor suppressor pathways, such as RB and TP53 pathways, can lead to transcriptional upregulation of SAC genes through E2F promoters and, subsequently, to chromosome mis-segregation [68–70]. As suggested by our analysis (Figure 3), TP53 loss could also lead to *BUB3* upregulation, which should fuel chromosomal instability in cancer cells.

The role of *BUB3* in carcinogenesis is still unclear. Contradictory results have been reported from animal models. For instance, haploinsufficiency of *Bub3* causes an increase in chromosome instability in mice, but is not clearly associated with the frequency or the rate at which tumors appear in the animal [71]. Analysis of mice with reduced levels of *Bub3* has shown that mice have significant increases in the number of aneuploid fibroblasts, and are predisposed to chemical-induced lung tumorigenesis rather than spontaneous tumor development [44]. A tumor suppressor role has been suggested for *Bub3* in a *Drosophila melanogaster* tumorigenesis model derived from knocking down SAC genes [72]. Indeed, when transplanted into adult flies, *Bub3*-deficient tumors displayed neoplastic growth, widespread chromosomal aneuploidy, and high proliferative potential. Overall, these studies reveal that aneuploidy induced by *BUB3* downregulation might not be sufficient to initiate tumorigenesis but might still facilitate it.

### 5. *BUB3* as an Anticancer Therapeutic Target

For many years, the role of *BUB3* has been reduced to the recruitment of its partners *BUB1* and *BUBR1* to unattached kinetochores. Probably for this reason, *BUB3* has not been regarded as a potential anticancer target. Nevertheless, and as referred to above, *BUB3* itself has a specific role in regulating kinetochore–microtubule attachments, and is involved in telomere replication maintenance and premature aging [5,8,10]. Importantly, the *BUB3* gene is upregulated in most cancers studied, which is generally associated with poor outcomes. Thus, *BUB3* is not just a simple partner, and its targeting deserves attention. Today, there are no small molecules against *BUB3*, and the unique attempt to target *BUB3* makes use of RNAi [11]. In this study, we have shown that RNAi-mediated inhibition of *BUB3* was cytotoxic to OSCC cells and enhanced their chemosensitivity to cisplatin [11]. This antiproliferative activity of *BUB3* inhibition against OSCC cells was recently confirmed by another group [73]. Very recently, we showed that inhibition of *BUB3* compromises glioblastoma cell proliferation, mainly through senescence induction rather than by apoptosis, suggesting that premature senescence can be a viable approach to restrain cancer propagation [74]. Thus, oligonucleotide-based targeting of *BUB3* could be a viable therapeutic approach. However, small-molecule inhibitors should be a better option due to RNAi security and stability issues. As *BUB3* is a non-enzyme protein, and, thus, an “undruggable target”, the development of an anti-*BUB3* drug may be a challenging task. To circumvent this, one should design small molecules that target protein–protein interactions to interfere with biological processes by modulating the formation of protein–protein complexes. In this sense, targeting the interaction of *BUB3* with *BUB1* and *BUBR1* is an attractive option. This would prevent MCC formation, leading to SAC inactivation, which is expected to kill cancer cells as a consequence of massive chromosome mis-segregation. Strategies to mimic *Bub3/Rae1* haploinsufficiency in order to induce premature senescence of cancer cells should be explored. Indeed, cellular senescence has also been considered a suppressive mechanism of tumorigenesis, making therapy-induced senescence a plausible approach for cancer treatment, by irreversibly arresting the cell cycle [75].

## 6. Conclusions and Perspectives

Proteins of the SAC signaling pathway have been investigated as targets for the development of new antimitotic strategies for cancer treatment. Here, we have reviewed the role of BUB3 in mitosis and highlighted its potential as an anticancer therapeutic target. Besides its key role in K-MT attachment and SAC activation, BUB3 has a role in telomere replication and maintenance. Its upregulation is a common feature of human cancers, with higher expression in *TP53*-mutant cancers, and this could be a prognosis biomarker. Importantly, decreased levels of BUB3, either through genetic recombination or RNAi, accelerate aging through induction of senescence. Therefore, BUB3 could be a promising target for cancer treatment, namely, to increase sensitivity to radiotherapy and chemotherapy.

Some challenging issues need to be addressed to allow progress to clinical application. For instance, we need to know whether *BUB3* upregulation in cancer is a cause or just a consequence of the carcinogenesis process. Additionally, understanding how *TP53* regulates *BUB3* expression is important to explore the impact of BUB3 targeting, namely, for the treatment of *TP53*-mutant cancers. Elucidating the crosstalk between the SAC pathway and the senescence pathway is crucial for understanding the cellular mechanism of BUB3 targeting. These lines of study would provide additional insights into the role of BUB3 in carcinogenesis, which in turn might be useful for a rational drug design. Overall, we believe that BUB3 targeting could be a promising strategy for anticancer therapy that deserves to be explored.

**Author Contributions:** H.B. conceived the work, collected the data, acquired and managed the funding, and wrote the original draft; P.M.A.S. collected the data and wrote the original draft. All authors have read and agreed to the published version of the manuscript.

**Funding:** This research was funded by CESPU—Cooperativa de Ensino Superior Politécnico e Universitário, grant number (AntiMitoSphere\_APSFCT\_IINFACTS\_2021), and partially by FCT—Fundação para a Ciência e a Tecnologia, grant number (PTDC/BIA-CEL/30014/2017; POCI-01-0145-FEDER-030014).

**Institutional Review Board Statement:** Not applicable.

**Informed Consent Statement:** Not applicable.

**Data Availability Statement:** Not applicable.

**Acknowledgments:** We are grateful to Ana Henriques, Bárbara Pinto and João Silva from Hassan Bousbaa's lab for their critical discussion of the present work.

**Conflicts of Interest:** The authors declare no conflict of interest.

## References

1. Silva, P.; Barbosa, J.; Nascimento, A.V.; Faria, J.; Reis, R.; Bousbaa, H. Monitoring the fidelity of mitotic chromosome segregation by the spindle assembly checkpoint. *Cell Prolif.* **2011**, *44*, 391–400. [CrossRef] [PubMed]
2. Musacchio, A.; Salmon, E.D. The spindle-assembly checkpoint in space and time. *Nat. Rev. Mol. Cell Biol.* **2007**, *8*, 379–393. [CrossRef] [PubMed]
3. Foley, E.A.; Kapoor, T.M. Microtubule attachment and spindle assembly checkpoint signalling at the kinetochore. *Nat. Rev. Mol. Cell Biol.* **2013**, *14*, 25–37. [CrossRef] [PubMed]
4. Lara-Gonzalez, P.; Westhorpe, F.G.; Taylor, S.S. The spindle assembly checkpoint. *Curr. Biol.* **2012**, *22*, R966–R980. [CrossRef] [PubMed]
5. Logarinho, E.; Resende, T.; Torres, C.; Bousbaa, H. The human spindle assembly checkpoint protein Bub3 is required for the establishment of efficient kinetochore-microtubule attachments. *Mol. Biol. Cell* **2008**, *19*, 1798–1813. [CrossRef] [PubMed]
6. Logarinho, E.; Bousbaa, H. Kinetochore-microtubule interactions “in check” by Bub1, Bub3 and BubR1: The dual task of attaching and signalling. *Cell Cycle* **2008**, *7*, 1763–1768. [CrossRef] [PubMed]
7. Sudakin, V.; Chan, G.K.; Yen, T.J. Checkpoint inhibition of the APC/C in HeLa cells is mediated by a complex of BUBR1, BUB3, CDC20, and MAD2. *J. Cell Biol.* **2001**, *154*, 925–936. [CrossRef]
8. Li, F.; Kim, H.; Ji, Z.; Zhang, T.; Chen, B.; Ge, Y.; Hu, Y.; Feng, X.; Han, X.; Xu, H.; et al. The BUB3-BUB1 Complex Promotes Telomere DNA Replication. *Mol. Cell* **2018**, *70*, 395–407.e4. [CrossRef]
9. Dai, W.; Wang, X. Aging in check. *Sci. Aging Knowl. Environ.* **2006**, *2006*, pe9. [CrossRef]

10. Baker, D.J.; Jeganathan, K.B.; Malureanu, L.; Perez-Terzic, C.; Terzic, A.; van Deursen, J.M.A. Early aging-associated phenotypes in Bub3/Rae1 haploinsufficient mice. *J. Cell Biol.* **2006**, *172*, 529–540. [CrossRef]
11. Silva, P.M.A.; Delgado, M.L.; Ribeiro, N.; Florindo, C.; Tavares, Á.A.; Ribeiro, D.; Lopes, C.; do Amaral, B.; Bousbaa, H.; Monteiro, L.S. Spindly and Bub3 expression in oral cancer: Prognostic and therapeutic implications. *Oral Dis.* **2019**, *25*, 1291–1301. [CrossRef] [PubMed]
12. Mur, P.; De Voer, R.M.; Olivera-Salguero, R.; Rodríguez-Perales, S.; Pons, T.; Setién, F.; Aiza, G.; Valdés-Mas, R.; Bertini, A.; Pineda, M.; et al. Germline mutations in the spindle assembly checkpoint genes BUB1 and BUB3 are infrequent in familial colorectal cancer and polyposis. *Mol. Cancer* **2018**, *17*, 23. [CrossRef] [PubMed]
13. Grabsch, H.; Takeno, S.; Parsons, W.J.; Pomjanski, N.; Boecking, A.; Gabbert, H.E.; Mueller, W. Overexpression of the mitotic checkpoint genes BUB1, BUBR1, and BUB3 in gastric cancer—Association with tumour cell proliferation. *J. Pathol.* **2003**, *200*, 16–22. [CrossRef] [PubMed]
14. Hoyt, M.A.; Totis, L.; Roberts, B.T.S. *Cerevisiae* genes required for cell cycle arrest in response to loss of microtubule function. *Cell* **1991**, *66*, 507–517. [CrossRef]
15. Li, R.; Murray, A.W. Feedback control of mitosis in budding yeast. *Cell* **1991**, *66*, 519–531. [CrossRef]
16. Weiss, E.; Winey, M. The *Saccharomyces cerevisiae* spindle pole body duplication gene MPS1 is part of a mitotic checkpoint. *J. Cell Biol.* **1996**, *132*, 111–123. [CrossRef]
17. Chen, R.H.; Waters, J.C.; Salmon, E.D.; Murray, A.W. Association of spindle assembly checkpoint component X MAD2 with unattached kinetochores. *Science* **1996**, *274*, 242–246. [CrossRef]
18. Taylor, S.S.; McKeon, F. Kinetochores localization of murine Bub1 is required for normal mitotic timing and checkpoint response to spindle damage. *Cell* **1997**, *89*, 727–735. [CrossRef]
19. Basu, J.; Logarinho, E.; Herrmann, S.; Bousbaa, H.; Li, Z.; Chan, G.K.; Yen, T.J.; Sunkel, C.E.; Goldberg, M.L. Localization of the *Drosophila* checkpoint control protein Bub3 to the kinetochore requires Bub1 but not Zw10 or Rod. *Chromosoma* **1998**, *107*, 376–385. [CrossRef]
20. Basu, J.; Bousbaa, H.; Logarinho, E.; Li, Z.; Williams, B.C.; Lopes, C.; Sunkel, C.E.; Goldberg, M.L. Mutations in the essential spindle checkpoint gene bub1 cause chromosome missegregation and fail to block apoptosis in *Drosophila*. *J. Cell Biol.* **1999**, *146*, 13–28. [CrossRef]
21. Sacristan, C.; Kops, G.J.P.L. Joined at the hip: Kinetochores, microtubules, and spindle assembly checkpoint signaling. *Trends Cell Biol.* **2015**, *25*, 21–28. [CrossRef] [PubMed]
22. Chen, C.; Whitney, I.P.; Banerjee, A.; Sacristan, C.; Sekhri, P.; Kern, D.M.; Fontan, A.; Kops, G.J.P.L.; Tyson, J.J.; Cheeseman, I.M.; et al. Ectopic Activation of the Spindle Assembly Checkpoint Signaling Cascade Reveals Its Biochemical Design. *Curr. Biol.* **2019**, *29*, 104–119.e10. [CrossRef] [PubMed]
23. Novais, P.; Silva, M.A.; Amorim, I.; Bousbaa, H. Second-Generation Antimitotics in Cancer Clinical Trials. *Pharmaceutics* **2021**, *13*, 1011. [CrossRef] [PubMed]
24. Larsen, N.A.; Al-Bassam, J.; Wei, R.R.; Harrison, S.C. Structural analysis of Bub3 interactions in the mitotic spindle checkpoint. *Proc. Natl. Acad. Sci. USA* **2007**, *104*, 1201–1206. [CrossRef]
25. Wilson, D.K.; Cerna, D.; Chew, E. The 1.1-angstrom structure of the spindle checkpoint protein Bub3p reveals functional regions. *J. Biol. Chem.* **2005**, *280*, 13944–13951. [CrossRef]
26. Larsen, N.A.; Harrison, S.C. Crystal structure of the spindle assembly checkpoint protein Bub3. *J. Mol. Biol.* **2004**, *344*, 885–892. [CrossRef]
27. Kiyomitsu, T.; Obuse, C.; Yanagida, M. Human Blinkin/AF15q14 is required for chromosome alignment and the mitotic checkpoint through direct interaction with Bub1 and BubR1. *Dev. Cell* **2007**, *13*, 663–676. [CrossRef]
28. Krenn, V.; Wehenkel, A.; Li, X.; Santaguida, S.; Musacchio, A. Structural analysis reveals features of the spindle checkpoint kinase Bub1-kinetochore subunit Knl1 interaction. *J. Cell Biol.* **2012**, *196*, 451–467. [CrossRef]
29. Yamagishi, Y.; Yang, C.-H.; Tanno, Y.; Watanabe, Y. MPS1/Mph1 phosphorylates the kinetochore protein KNL1/Spc7 to recruit SAC components. *Nat. Cell Biol.* **2012**, *14*, 746–752. [CrossRef]
30. Primorac, I.; Weir, J.R.; Chirolì, E.; Gross, F.; Hoffmann, I.; van Gerwen, S.; Ciliberto, A.; Musacchio, A. Bub3 reads phosphorylated MELT repeats to promote spindle assembly checkpoint signaling. *eLife* **2013**, *2*, e01030. [CrossRef]
31. Taylor, S.S.; Ha, E.; McKeon, F. The human homologue of Bub3 is required for kinetochore localization of Bub1 and a Mad3/Bub1-related protein kinase. *J. Cell Biol.* **1998**, *142*, 1–11. [CrossRef] [PubMed]
32. Han, J.S.; Vitre, B.; Fachinetti, D.; Cleveland, D.W. Bimodal activation of BubR1 by Bub3 sustains mitotic checkpoint signaling. *Proc. Natl. Acad. Sci. USA* **2014**, *111*, E4185–E4193. [CrossRef] [PubMed]
33. Prinz, F.; Puetter, V.; Holton, S.J.; Andres, D.; Stegmann, C.M.; Kwiatkowski, D.; Prechtel, S.; Petersen, K.; Beckmann, G.; Kreft, B.; et al. Functional and Structural Characterization of Bub3-BubR1 Interactions Required for Spindle Assembly Checkpoint Signaling in Human Cells. *J. Biol. Chem.* **2016**, *291*, 11252–11267. [CrossRef] [PubMed]
34. Silva, P.M.A.; Reis, R.M.; Bolanos-Garcia, V.M.; Florindo, C.; Tavares, Á.A.; Bousbaa, H. Dynein-dependent transport of spindle assembly checkpoint proteins off kinetochores toward spindle poles. *FEBS Lett.* **2014**, *588*, 3265–3273. [CrossRef] [PubMed]
35. Silva, P.M.A.; Tavares, Á.A.; Bousbaa, H. Co-silencing of human Bub3 and dynein highlights an antagonistic relationship in regulating kinetochore-microtubule attachments. *FEBS Lett.* **2015**, *589*, 3588–3594. [CrossRef] [PubMed]

36. Toledo, C.M.; Herman, J.A.; Olsen, J.B.; Ding, Y.; Corrin, P.; Girard, E.J.; Olson, J.M.; Emili, A.; DeLuca, J.G.; Paddison, P.J. BuGZ is required for Bub3 stability, Bub1 kinetochore function, and chromosome alignment. *Dev. Cell* **2014**, *28*, 282–294. [CrossRef]
37. Jiang, H.; He, X.; Wang, S.; Jia, J.; Wan, Y.; Wang, Y.; Zeng, R.; Yates, J.; Zhu, X.; Zheng, Y. A Microtubule-Associated Zinc Finger Protein, BuGZ, Regulates Mitotic Chromosome Alignment by Ensuring Bub3 Stability and Kinetochore Targeting. *Dev. Cell* **2014**, *28*, 268–281. [CrossRef]
38. Martinez-Exposito, M.J.; Kaplan, K.B.; Copeland, J.; Sorger, P.K. Retention of the BUB3 checkpoint protein on lagging chromosomes. *Proc. Natl. Acad. Sci. USA* **1999**, *96*, 8493–8498. [CrossRef]
39. Brown, J.A.; Bharathi, A.; Ghosh, A.; Whalen, W.; Fitzgerald, E.; Dhar, R. A mutation in the *Schizosaccharomyces pombe* rae1 gene causes defects in poly(A)<sup>+</sup> RNA export and in the cytoskeleton. *J. Biol. Chem.* **1995**, *270*, 7411–7419. [CrossRef]
40. Murphy, R.; Watkins, J.L.; Wente, S.R. GLE2, a *Saccharomyces cerevisiae* homologue of the *Schizosaccharomyces pombe* export factor RAE1, is required for nuclear pore complex structure and function. *Mol. Biol. Cell* **1996**, *7*, 1921–1937. [CrossRef]
41. Pritchard, C.E.; Fornerod, M.; Kasper, L.H.; van Deursen, J.M. RAE1 is a shuttling mRNA export factor that binds to a GLEBS-like NUP98 motif at the nuclear pore complex through multiple domains. *J. Cell Biol.* **1999**, *145*, 237–254. [CrossRef] [PubMed]
42. Bailer, S.M.; Siniossoglou, S.; Podtelejnikov, A.; Hellwig, A.; Mann, M.; Hurt, E. Nup116p and nup100p are interchangeable through a conserved motif which constitutes a docking site for the mRNA transport factor gle2p. *EMBO J.* **1998**, *17*, 1107–1119. [CrossRef] [PubMed]
43. Wang, X.; Babu, J.R.; Harden, J.M.; Jablonski, S.A.; Gazi, M.H.; Lingle, W.L.; de Groen, P.C.; Yen, T.J.; van Deursen, J.M. The mitotic checkpoint protein hBUB3 and the mRNA export factor hRAE1 interact with GLE2p-binding sequence (GLEBS)-containing proteins. *J. Biol. Chem.* **2001**, *276*, 26559–26567. [CrossRef] [PubMed]
44. Babu, J.R.; Jeganathan, K.B.; Baker, D.J.; Wu, X.; Kang-Decker, N.; van Deursen, J.M. Rae1 is an essential mitotic checkpoint regulator that cooperates with Bub3 to prevent chromosome missegregation. *J. Cell Biol.* **2003**, *160*, 341–353. [CrossRef]
45. Kalitsis, P.; Earle, E.; Fowler, K.J.; Choo, K.H. Bub3 gene disruption in mice reveals essential mitotic spindle checkpoint function during early embryogenesis. *Genes Dev.* **2000**, *14*, 2277–2282. [CrossRef]
46. Baker, D.J.; Jeganathan, K.B.; Cameron, J.D.; Thompson, M.; Juneja, S.; Kopecka, A.; Kumar, R.; Jenkins, R.B.; de Groen, P.C.; Roche, P.; et al. BubR1 insufficiency causes early onset of aging-associated phenotypes and infertility in mice. *Nat. Genet.* **2004**, *36*, 744–749. [CrossRef]
47. Marques, S.; Fonseca, J.; Silva, P.M.A.; Bousbaa, H. Targeting the spindle assembly checkpoint for breast cancer treatment. *Curr. Cancer Drug Targets* **2015**, *15*, 272–281. [CrossRef]
48. Diogo, V.; Teixeira, J.; Silva, P.M.A.; Bousbaa, H. Spindle Assembly Checkpoint as a Potential Target in Colorectal Cancer: Current Status and Future Perspectives. *Clin. Colorectal Cancer* **2017**, *16*, 1–8. [CrossRef]
49. Danielsen, H.E.; Pradhan, M.; Novelli, M. Revisiting tumour aneuploidy—The place of ploidy assessment in the molecular era. *Nat. Rev. Clin. Oncol.* **2016**, *13*, 291–304. [CrossRef]
50. Kops, G.J.P.L.; Weaver, B.A.A.; Cleveland, D.W. On the road to cancer: Aneuploidy and the mitotic checkpoint. *Nat. Rev. Cancer* **2005**, *5*, 773–785. [CrossRef]
51. Chandrashekar, D.S.; Bashel, B.; Balasubramanya, S.A.H.; Creighton, C.J.; Ponce-Rodriguez, I.; Chakravarthi, B.V.S.K.; Varambally, S. UALCAN: A Portal for Facilitating Tumor Subgroup Gene Expression and Survival Analyses. *Neoplasia* **2017**, *19*, 649–658. [CrossRef] [PubMed]
52. Chun, A.C.S.; Jin, D.-Y. Transcriptional regulation of mitotic checkpoint gene MAD1 by p53. *J. Biol. Chem.* **2003**, *278*, 37439–37450. [CrossRef] [PubMed]
53. Polyak, K.; Xia, Y.; Zweier, J.L.; Kinzler, K.W.; Vogelstein, B. A model for p53-induced apoptosis. *Nature* **1997**, *389*, 300–305. [CrossRef] [PubMed]
54. Schvartzman, J.-M.; Duijf, P.H.G.; Sotillo, R.; Coker, C.; Benezra, R. Mad2 is a critical mediator of the chromosome instability observed upon Rb and p53 pathway inhibition. *Cancer Cell* **2011**, *19*, 701–714. [CrossRef]
55. Chen, J. The Cell-Cycle Arrest and Apoptotic Functions of p53 in Tumor Initiation and Progression. *Cold Spring Harb. Perspect. Med.* **2016**, *6*, a026104. [CrossRef]
56. Olivier, M.; Hollstein, M.; Hainaut, P. TP53 mutations in human cancers: Origins, consequences, and clinical use. *Cold Spring Harb. Perspect. Biol.* **2010**, *2*, a001008. [CrossRef]
57. Vogelstein, B.; Lane, D.; Levine, A.J. Surfing the p53 network. *Nature* **2000**, *408*, 307–310. [CrossRef]
58. Ersvær, E.; Kildal, W.; Vlatkovic, L.; Cyll, K.; Pradhan, M.; Kleppe, A.; Hveem, T.S.; Askautrud, H.A.; Novelli, M.; Wæhre, H.; et al. Prognostic value of mitotic checkpoint protein BUB3, cyclin B1, and pituitary tumor-transforming 1 expression in prostate cancer. *Mod. Pathol.* **2020**, *33*, 905–915. [CrossRef]
59. Long, Z.; Wu, T.; Tian, Q.; Carlson, L.A.; Wang, W.; Wu, G. Expression and prognosis analyses of BUB1, BUB1B and BUB3 in human sarcoma. *Aging* **2021**, *13*, 12395–12409. [CrossRef]
60. Liping, X.; Jia, L.; Qi, C.; Liang, Y.; Dongen, L.; Jianshuai, J. Cell Cycle Genes Are Potential Diagnostic and Prognostic Biomarkers in Hepatocellular Carcinoma. *BioMed Res. Int.* **2020**, *2020*, 6206157. [CrossRef]
61. Mukherjee, A.; Joseph, C.; Craze, M.; Chrysanthou, E.; Ellis, I.O. The role of BUB and CDC proteins in low-grade breast cancers. *Lancet* **2015**, *385*, S72. [CrossRef]

62. Yuan, B.; Xu, Y.; Woo, J.-H.; Wang, Y.; Bae, Y.K.; Yoon, D.-S.; Wersto, R.P.; Tully, E.; Wilsbach, K.; Gabrielson, E. Increased expression of mitotic checkpoint genes in breast cancer cells with chromosomal instability. *Clin. Cancer Res.* **2006**, *12*, 405–410. [CrossRef] [PubMed]
63. Kang, H.G.; Yoo, S.S.; Choi, J.E.; Hong, M.J.; Do, S.K.; Jin, C.C.; Kim, S.; Lee, W.K.; Choi, S.H.; Lee, S.Y.; et al. Polymorphisms in mitotic checkpoint-related genes can influence survival outcomes of early-stage non-small cell lung cancer. *Oncotarget* **2017**, *8*, 61777–61785. [CrossRef] [PubMed]
64. Vaclavicek, A.; Bermejo, J.L.; Wappenschmidt, B.; Meindl, A.; Sutter, C.; Schmutzler, R.K.; Kiechle, M.; Bugert, P.; Burwinkel, B.; Bartram, C.R.; et al. Genetic variation in the major mitotic checkpoint genes does not affect familial breast cancer risk. *Breast Cancer Res. Treat.* **2007**, *106*, 205–213. [CrossRef]
65. Hernando, E.; Orlow, I.; Liberal, V.; Nohales, G.; Benezra, R.; Cordon-Cardo, C. Molecular analyses of the mitotic checkpoint components hMAD2, hBUB1 and hBUB3 in human cancer. *Int. J. Cancer* **2001**, *95*, 223–227. [CrossRef]
66. Reis, R.M.; Nakamura, M.; Masuoka, J.; Watanabe, T.; Colella, S.; Yonekawa, Y.; Kleihues, P.; Ohgaki, H. Mutation analysis of hBUB1, hBUBR1 and hBUB3 genes in glioblastomas. *Acta Neuropathol.* **2001**, *101*, 297–304. [CrossRef]
67. Carter, S.L.; Eklund, A.C.; Kohane, I.S.; Harris, L.N.; Szallasi, Z. A signature of chromosomal instability inferred from gene expression profiles predicts clinical outcome in multiple human cancers. *Nat. Genet.* **2006**, *38*, 1043–1048. [CrossRef]
68. Schvartzman, J.-M.; Sotillo, R.; Benezra, R. Mitotic chromosomal instability and cancer: Mouse modelling of the human disease. *Nat. Rev. Cancer* **2010**, *10*, 102–115. [CrossRef]
69. Hernando, E.; Nahlé, Z.; Juan, G.; Diaz-Rodriguez, E.; Alaminos, M.; Hemann, M.; Michel, L.; Mittal, V.; Gerald, W.; Benezra, R.; et al. Rb inactivation promotes genomic instability by uncoupling cell cycle progression from mitotic control. *Nature* **2004**, *430*, 797–802. [CrossRef]
70. Kabeche, L.; Compton, D.A. Checkpoint-Independent Stabilization of Kinetochore-Microtubule Attachments by Mad2 in Human Cells. *Curr. Biol.* **2012**, *22*, 638–644. [CrossRef]
71. Kalitsis, P.; Fowler, K.J.; Griffiths, B.; Earle, E.; Chow, C.W.; Jamsen, K.; Choo, K.H.A. Increased chromosome instability but not cancer predisposition in haploinsufficient Bub3 mice. *Genes Chromosom. Cancer* **2005**, *44*, 29–36. [CrossRef] [PubMed]
72. da Silva, S.M.; Moutinho-Santos, T.; Sunkel, C.E. A tumor suppressor role of the Bub3 spindle checkpoint protein after apoptosis inhibition. *J. Cell Biol.* **2013**, *201*, 385–393. [CrossRef] [PubMed]
73. Zheng, J.; Li, T.-K.; Bao, Y.; Zhang, S.-X. Expression and clinical significance of Spindly and Bub3 in oral squamous cell carcinoma. *Shanghai Kou Qiang Yi Xue* **2020**, *29*, 528–532. [PubMed]
74. Silva, P.M.A.; Nascimento, V.A.; Marinho, O.; Reis, R.M.; Bousbaa, H. Targeting BUB3 in combination with paclitaxel inhibits proliferation of glioblastoma cells by enhancing cellular senescence. *Sci. Lett.* **2022**, *1*, 1. [CrossRef]
75. Lee, S.; Lee, J.-S. Cellular senescence: A promising strategy for cancer therapy. *BMB Rep.* **2019**, *52*, 35–41. [CrossRef] [PubMed]





Review

# Current Status of the Use of Multifunctional Enzymes as Anti-Cancer Drug Targets

Carla S. S. Teixeira <sup>1,2</sup>  and Sérgio F. Sousa <sup>1,2,\*</sup> 

<sup>1</sup> Associate Laboratory i4HB, Faculty of Medicine, Institute for Health and Bioeconomy, University of Porto, 4050-313 Porto, Portugal; carla.s.silva.teixeira@gmail.com

<sup>2</sup> UCIBIO—Applied Molecular Biosciences Unit, BioSIM—Department of Biomedicine, Faculty of Medicine, University of Porto, 4051-401 Porto, Portugal

\* Correspondence: sergiofsousa@med.up.pt

**Abstract:** Fighting cancer is one of the major challenges of the 21st century. Among recently proposed treatments, molecular-targeted therapies are attracting particular attention. The potential targets of such therapies include a group of enzymes that possess the capability to catalyze at least two different reactions, so-called multifunctional enzymes. The features of such enzymes can be used to good advantage in the development of potent selective inhibitors. This review discusses the potential of multifunctional enzymes as anti-cancer drug targets along with the current status of research into four enzymes which by their inhibition have already demonstrated promising anti-cancer effects in vivo, in vitro, or both. These are PFK-2/FBPase-2 (involved in glucose homeostasis), ATIC (involved in purine biosynthesis), LTA<sub>4</sub>H (involved in the inflammation process) and Jmjd6 (involved in histone and non-histone posttranslational modifications). Currently, only LTA<sub>4</sub>H and PFK-2/FBPase-2 have inhibitors in active clinical development. However, there are several studies proposing potential inhibitors targeting these four enzymes that, when used alone or in association with other drugs, may provide new alternatives for preventing cancer cell growth and proliferation and increasing the life expectancy of patients.

**Citation:** Teixeira, C.S.S.; Sousa, S.F.

Current Status of the Use of Multifunctional Enzymes as Anti-Cancer Drug Targets.

*Pharmaceutics* **2022**, *14*, 10. <https://doi.org/10.3390/pharmaceutics14010010>

Academic Editor: Hassan Bousbaa

Received: 5 November 2021

Accepted: 17 December 2021

Published: 21 December 2021

**Publisher's Note:** MDPI stays neutral with regard to jurisdictional claims in published maps and institutional affiliations.



**Copyright:** © 2021 by the authors. Licensee MDPI, Basel, Switzerland. This article is an open access article distributed under the terms and conditions of the Creative Commons Attribution (CC BY) license (<https://creativecommons.org/licenses/by/4.0/>).

**Keywords:** cancer; molecular-targeted therapies; multifunctional enzymes

## 1. Introduction

Cancer has become one of the greatest barriers to the increase of life expectancy in almost every country in the world, and is one of the biggest medical challenges of the 21st century. According to GLOBOCAN, in 2020 there were a record 19.3 million new cases and 10 million deaths caused by cancer worldwide [1]. Cancer is a multifactorial disease developed when normal cells acquire mutations or alterations that provide them a growth and/or survival advantage, enabling them to multiply and form a tumor. The extraordinary capability of cancer cells to divide and proliferate is highly associated with their metabolic reprogramming [2,3].

One of the biggest challenges in cancer research is the complexity of cancer's genomic landscape [4], which results in an enormous heterogeneity: there are more than 200 different recorded types of cancers, affecting as many as 60 human organs [5]. Over the years, several different approaches to fighting cancer have emerged including surgery, hormone therapy, radiation therapy, immunotherapy, chemotherapy, and more recently molecular-targeted therapy (reviewed in [6]). Although there have been significant advances in cancer survival, there are still many issues associated with the existing cancer therapies, including the existence of severe side effects, the acquisition of multidrug resistance, relapse, or even the possibility of developing new cancers caused by the treatment.

In recent years, molecular-targeted therapies have been gaining particular attention. Unlike the standard chemotherapies, which are cytotoxic (killing the cancer cells) and act on both rapidly dividing normal and on cancerous cells, molecular-targeted drugs

are cytostatic (stopping cancer cell growth and/or proliferation) and only inhibit specific molecular targets that are involved in the growth and spread of cancer cells [7]. Therefore, molecular-targeted drugs are less prone to causing secondary effects [7]. Among the potential anti-cancer drug targets are the proteins abnormally expressed in some tumors. To date, a panoply of proteins have been identified as potential targets, including some enzymes that belong to special class generally designated as “multifunctional enzymes”. These enzymes share a common characteristic: they possess the capability to catalyze at least two different reactions in the same or in different overlapping or distant active sites.

In this review, we focus on four multifunctional enzymes that are abnormally expressed in different cancer cells, and that have been previously proposed as good drug targets for cancer treatment.

First, 6-phosphofructo-2-kinase (PFK-2)/fructose-2,6-bisphosphatase (FBPase-2) is involved in glucose homeostasis and encompasses two independent domains in the same monomer, each possessing an independent active site.

Second, 5-aminoimidazole-4-carboxamide ribonucleotide formyltransferase/inosine monophosphate cyclohydrolase (ATIC) is involved in purine biosynthesis and also encompasses two independent domains in the same monomer, each possessing an independent active site.

Third, Leukotriene A<sub>4</sub> hydrolase (LTA<sub>4</sub>H) is involved in the inflammation process; its distinct catalytic activities occur in two distinct but overlapping active sites.

Fourth, Jumonji domain-containing protein 6 (Jmjd6) is involved in histone and non-histone posttranslational modifications, and uses the same active site to catalyze at least two different reactions.

In general, multifunctional enzymes are promising drug targets because they can be inhibited in multiple ways depending on their characteristics.

The most specific type of enzymatic inhibition relies on the use of inhibitors that are transition state analogs. The design of these inhibitors is based on the structure of the transition state of the rate-limiting step of a catalytic reaction, and their development therefore depends on a deep knowledge of the enzyme’s mechanism that can only be accomplished by combining experimental and computational data [8]. However, the design of such inhibitors is not always possible, either because there is no atomistic description of the transition state structures or because the molecules obtained cannot be used as therapeutic drugs due to their pharmacokinetic properties or toxicity. The choice of multifunctional enzymes as drug targets is advantageous because their complexity enables inhibition using multiple different approaches.

We start this review with a global description of the biological role of each enzyme, followed by a description of its tertiary and quaternary structure; we then provide evidence about its role in cancer development and/or survival; finally, we describe the most promising inhibitors proposed to date targeting each enzyme.

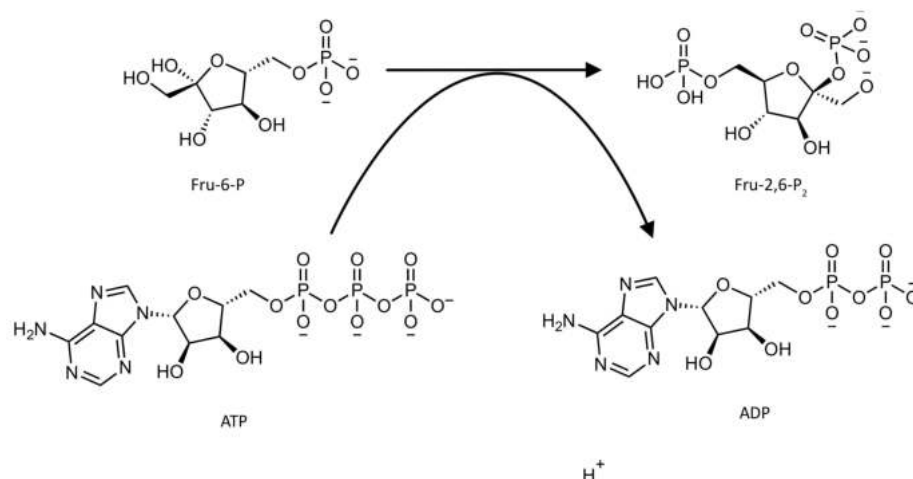
## 2. 6-phosphofructo-2-kinase/fructose 2,6-bisphosphatase (PFK-2/FBPase-2)

### 2.1. Biological Role

Fructose 2,6-bisphosphate (Fru-2,6-P<sub>2</sub>) is an important signal molecule that can be found in all mammalian tissues [9–11]. In the liver, Fru-2,6-P<sub>2</sub> plays an important role in the control of glucose homeostasis by allowing the liver to switch from glycolysis to gluconeogenesis through the inhibition of FBPase-1 (fructose-1,6-bisphosphatase), a regulatory enzyme of gluconeogenesis [12]. When mammals are experiencing fasting conditions, the α-cells of the pancreas secrete a linear peptide hormone called glucagon, which decreases the concentration of hepatic Fru-2,6-P<sub>2</sub> and thereby relieves the inhibition of FBPase-1, allowing gluconeogenesis to prevail [9]. In most mammalian tissues, which do not contain FBPase-1, Fru-2,6-P<sub>2</sub> acts as a potent positive allosteric effector of 6-phosphofructo-1-kinase (PFK-1), an enzyme that catalyzes one of the most critical steps of glycolysis—the conversion of fructose 6-phosphate (Fru-6-P) and ATP to fructose 1,6-bisphosphate and ADP [9,11,13,14]. The levels of Fru-2,6-P<sub>2</sub> are controlled by a family of

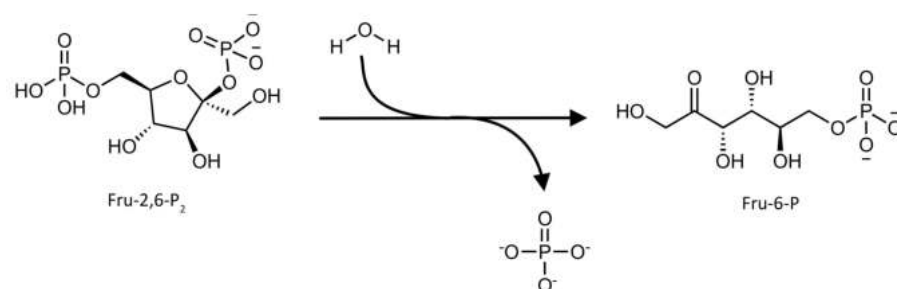
bifunctional enzymes that possess in the same peptide a 6-phosphofructo-2-kinase (PFK-2) and a fructose-2,6-bisphosphatase (FBPase-2) domain.

The PFK-2 domain (E.C. 2.7.1.105) synthesizes Fru-2,6-P<sub>2</sub> from fructose-6-phosphate (Fru-6-P) and ATP (Figure 1).



**Figure 1.** Schematic representation of the reaction catalyzed by the PFK-2 domain of the PFK-2/FBPase-2 enzyme.

The FBPase-2 domain (E.C. 3.1.3.46) hydrolyzes Fru-2,6-P<sub>2</sub> into Fru-6-P and inorganic phosphate (Figure 2) [15,16].



**Figure 2.** Schematic representation of the reaction catalyzed by the FBPase-2 domain of the PFK-2/FBPase-2 enzyme.

The balance between the activity of the two catalytic domains ultimately determines the concentration of Fru-2,6-P<sub>2</sub>. This important regulatory function of Fru-2,6-P<sub>2</sub> in carbohydrate metabolism requires tight regulation of its concentration as a function of the cell needs. This is accomplished by the existence of different PFK-2/FBPase-2 isoenzymes [17] with different kinetic and regulatory mechanisms, which regulate the glycolysis and gluconeogenesis pathways in different tissues under various physiological conditions [18].

Mammals express four PFK-2/FBPase-2 isoenzymes, which are encoded by four different genes, *PFKFB1* to *PFKFB4* [19]. Although the different isoenzymes were initially named according to the tissue from which they were first purified (*PFKFB1* in the liver, *PFKFB2* in the heart, *PFKFB3*, in the brain and placenta, and *PFKFB4* in the testes), more recent evidence has demonstrated that they are expressed in other tissues as well, and they are now classified according to their coding gene [9]. Each isozyme has several isoforms that share the same catalytic core as the parent isoenzyme but differ in the flanking sequences. These variable sites in each isoform are subject to different post-translational modifications, usually phosphorylation by different protein kinases, that modulate the relative activities of their catalytic domains under the control of cellular signaling pathways. This complex

regulation allows the cell to adapt the carbohydrate metabolism in response to extracellular stimuli (e.g., hormones, growth factors, nutritional state) [18].

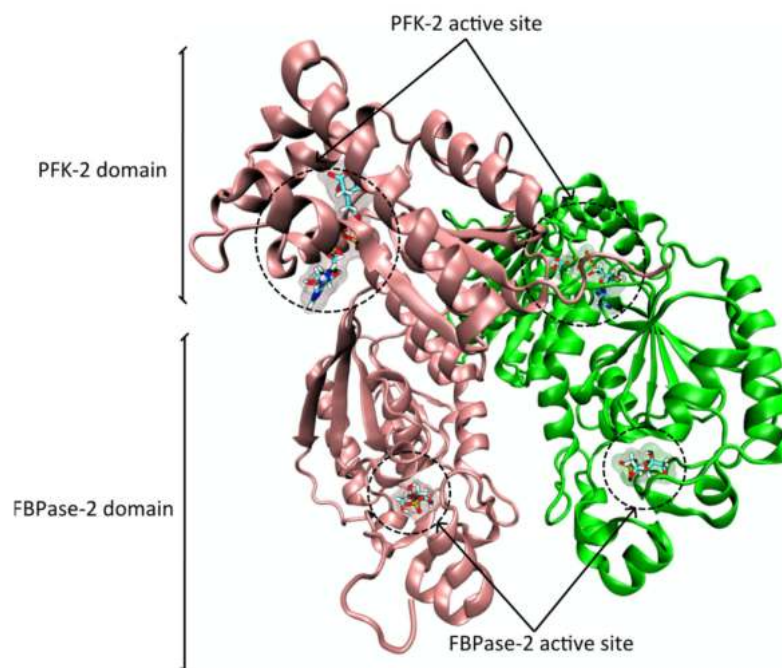
## 2.2. Protein Structure

The different PFK-2/FBPase-2 isoenzymes differ in the sequence of their bifunctional catalytic core, while their various isoforms conserve the catalytic core of the parent isoenzyme but differ in their N- and C-terminal ends where the post translation modifications take place. Although those sequence variations result in relevant conformational differences among the different proteins, their overall 3D structure is quite similar.

The PFK-2/FBPase-2 is a homodimer composed of two 55-kDa monomers. Each monomer possesses a kinase domain (E.C. 2.7.1.105) at the N-terminal and a bisphosphatase domain at the C-terminal end of the protein (Figure 3) [9,16,20]. Observation of the global 3D structure of the homodimer shows that the PFK-2 domains come together in a head-to-head fashion while the FBPase-2 domains are almost independent, with few dimeric point interactions the number and nature of which (e.g., hydrogen bridges) vary among the different isoenzymes [9,16,20]. These observations are in line with experimental data showing that when expressed independently, the PFK-2 domain forms inactive aggregates [21], while the FBPase-2 domain retains its catalytic activity [22].

The differences in the binding pockets (where catalysis occurs) in the N- and C-terminal flanking sequences (where the post translation modifications take place) and in the dimeric interface contacts among the different isoenzymes and respective isoforms affects both the conformational stability and affinity for the substrate of Fru-2,6-P<sub>2</sub>, ultimately resulting in enzymes with different kinetics [9]. The kinase/phosphatase activity ratio is above 2.5/1 for PFKFB1 and PFKFB2, 730/1 for PFKFB3 and about 4.6/1 for PFKFB4 [23–25].

The advantage of expressing two independent catalytic domains encoded by a fused gene in the same monomer is the simplicity of both short-term control (by regulating the activity of the two domains through post translation modifications and allosteric modulation) and long-term control (through the expression of two catalytic domains from a single mRNA molecule) [9].



**Figure 3.** Ribbon representation of the human PFK-2/FBPase-2 (PFKFB2) enzyme with the PDB ID 5HTK [26], obtained with VMD. The PFK-2 active site harbors an ATP and a citrate molecule (inside the Fru-6-P binding pocket) and the FBPase-2 active site harbors a fructose-6-phosphate molecule inside the F-2,6-P<sub>2</sub> binding pocket. All ligands are represented in licorice.

### 2.3. Role in Cancer

To support their continuous growth and proliferation under challenging conditions, most cancer cells have a markedly modified energy metabolism in comparison with normal cells [27–29]. Both normal and cancer cells predominantly use glucose, the most abundant nutrient in the blood, to generate ATP [30]. The overexpression of several glycolytic genes in many tumors [27–29] allows them to change from respiration to a glycolytic phenotype even in aerobic conditions, a phenomenon known as the Warburg effect [31].

Several studies have shown that the Fru-2,6-P<sub>2</sub> concentration is significantly higher in cancer cells with a glycolytic phenotype than in normal cells [32–34]. The increased levels of Fru-2,6-P<sub>2</sub> allows the transformed cells to maintain a high glycolytic flux despite the presence of the PFK-1 inhibitor, ATP.

ATP inhibits PFK-1 activity as part of the negative feedback loop that limits glycolytic flux under aerobic conditions, the so-called Pasteur effect [35]. The presence of high levels of Fru-2,6-P<sub>2</sub>, which is a positive allosteric effector of PFK-1, relieves the ATP inhibition [14] and allows the cancer cells to maintain a high glycolytic flux. This is advantageous for the transformed cells because the maintenance a high glycolytic flux allows them to produce higher ATP rates when compared with oxidative phosphorylation, and provides them with intermediates that are vital for other important biosynthetic pathways, (for example, ribose sugars for nucleotide synthesis; hexose sugar derivatives, glycerol and citrate for lipid synthesis; non-essential amino acids and NADPH, which are important for nucleotide and fatty acid biosynthesis and for the maintenance of cellular redox balance [18].

Due to their role in the modulation of Fru-2,6-P<sub>2</sub> levels, the PFK-2/FBPase-2 enzymes have been pointed out as key players in the glycolytic phenotype of cancer cells and consequently in the regulation of these cells' metabolic activity [18]. This observation is supported by the fact that PFK-2/FBPase-2 mRNAs are overexpressed in human lung cancers [36] and by the fact that PFK-2/FBPase-2 enzymes are induced in hypoxia [37–39], an important component of the tumor microenvironment that regulates, for example, tumor angiogenesis and metastasization [18]. It has been suggested that cancer cells may express variable levels of different PFK-2/FBPase-2 enzymes and modulate their relative kinase and/or bisphosphatase activity according to their temporal and spatial metabolic needs [18].

All evidence suggests that PFK-2/FBPase-2 is a potential good target for cancer therapy.

To date, efforts have been focused on inhibition of the PFK-2 activity of PFKFB3 [40].

The choice of this isoenzyme as a target is justified by the fact that its expression is induced by several oncogenes and by hypoxia, as well as by the suggestion that it may contribute to the high glycolytic activity of cancer cells [18].

Recently, it has been shown that PFKFB4 regulates transcriptional reprogramming by enhancing the transcriptional activity of the oncogenic steroid receptor coactivator-3 (SRC-3), deregulation of which is frequently associated with aggressive metastatic tumors [41].

The phosphorylation of SRC-3 at Ser857 by PFKFB4 increases its transcriptional activity and promotes the synthesis of genes that direct the glucose flux towards purine synthesis. This so-called PFKFB4–SRC-3 axis is enriched in oestrogen receptor-positive breast tumors [41].

Additionally, by affecting the SRC3/Akt/mTOR pathway (that regulates autophagy) PFKFB4 functions as a bridge between glycolysis and autophagy. Although autophagy can be involved in both tumor suppression and tumor promotion, it has been proposed that the downregulation of PFKFB4 (or the inhibition of its kinase activity) can help inhibit the SRC3/Akt/mTOR pathway, and hence direct autophagy to promote apoptosis of tumor cells [42].

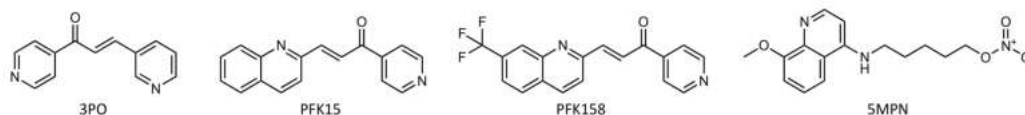
There is also evidence showing that the FBPase-2 domain of PFKFB4 is important for cancer cell survival, which indicates the phosphatase domain as a new potential therapeutic target for cancer [43]. The selective inhibition of the FBPase-2 activity of the PFKFB4 isoenzyme could ultimately lead to irreversible cellular damage caused by the

accumulation of reactive oxygen species as a result of simultaneous high glycolytic flux and depletion of metabolites from the pentose phosphate [18].

The major limitation in the discovery of specific inhibitors of the PFK-2/FBPase-2 phosphatase domains lies in the lack of unique topological features among the different isozymes [18]. The simultaneous inhibition of the FBPase-2 activity of other isozymes, particularly in the liver, impairs the organism's normal metabolic homeostasis and originates secondary effects [18]. One possible way to overcome this limitation is through the use of computer-aided drug design, a strategy that has been gaining particular relevance in recent years due to the large increase in high-performance computing resources and the development of new *in silico* approaches [44].

#### 2.4. Inhibitors

To date, many PFKFB3 inhibitors have been designed, synthesized, and tested *in vitro* and/or *in vivo* to evaluate their potential in anti-cancer therapy [45]. Among the different proposed molecules, the charcolones derived from the 3-(3-pyridinyl)-1-(4-pyridinyl)-2-propen-1-one (3PO) molecule (Figure 4) have gained particular attention [46]. The 3PO was the first PFKFB3 inhibitor proposed; however, its poor solubility and selectivity together with the high dose required to achieve potency limited its potential use in clinical trials [47]. To overcome those limitations a large number of 3PO derivatives were synthesized, including PFK15 (Figure 4), which showed increased selectivity and inhibitory effectiveness when compared with 3PO [48]. Further structural optimizations led to PFK158 (Figure 4), a PFK15 derivative that demonstrated a favorable preclinical therapeutic index and superior efficacy and pharmaceutical properties to 3PO and PFK15 both *in vitro* and *in vivo* [49]. Its characteristics turned PFK158 into the first-in-man and first-in-class PFKFB3 inhibitor to be evaluated in a phase I clinical trial in patients with advanced solid malignancies (NCT02044861) [50].



**Figure 4.** Chemical structure of PFKFB3 (3PO, PFK15 and PFK158) and PFKFB4 (5MPN) inhibitors.

Although the great majority of the studies were focused on the inhibition of PFKFB3, there is record of at least one promising PFKFB4 inhibitor, 5-(n-(8-methoxy-4-quinoly)amino)pentyl nitrate (5MPN) (Figure 4), that demonstrated an anti-proliferative effect of cancer cells both *in vitro* as *in vivo* [51]; 5MPN is a PFKFB4 specific inhibitor that binds competitively to its F6P binding site, suppressing kinase activity and consequently reducing the intracellular concentration of F-2,6-BP [51]. Recently, 5MPN was tested in combination therapy with Sunitinib, a receptor tyrosine kinase inhibitor used as a chemotherapeutic agent, showing promising results [52].

### 3. 5-aminoimidazole-4-carboxamide Ribonucleotide Formyltransferase/Inosine Monophosphate Cyclohydrolase (ATIC)

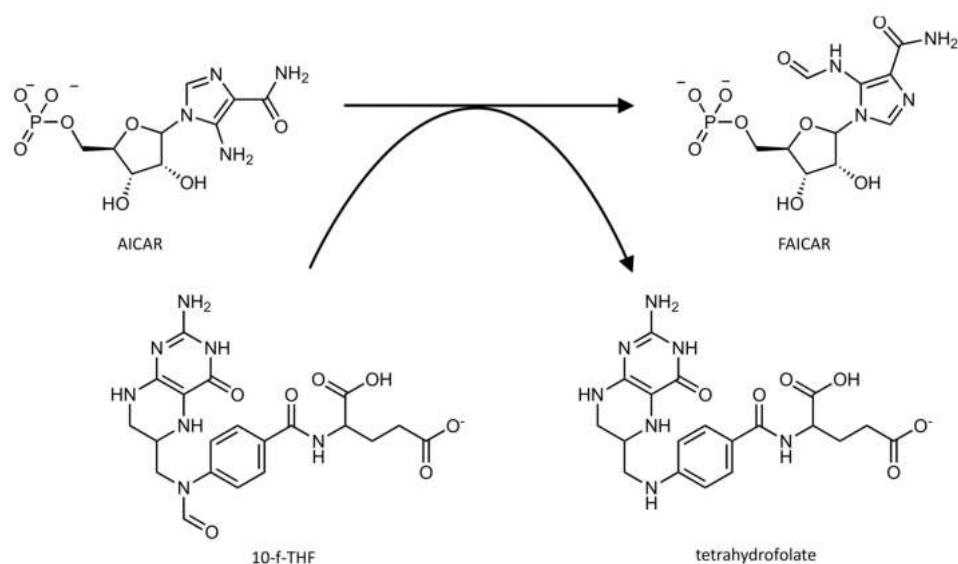
#### 3.1. Biological Role

The purine bases are a group of heterocyclic aromatic organic compounds composed of a pyrimidine ring fused to an imidazole molecule. Two of the most common purines are adenine and guanine, which are constituents of vital biomolecules including ATP, GTP, cAMP, DNA, RNA, NADH, FAD, and coenzyme A among others. The purine nucleotides can be obtained by two biosynthetic pathways: the salvage pathway, in which nucleotides are retrieved after the breakdown of nucleic acids or coenzymes, and the *de novo* biosynthetic pathway, a highly conserved pathway in which phosphoribosyl pyrophosphate (PRPP) is converted into inosine 5'-monophosphate (IMP), the departing nucleotide for the posterior synthesis of AMP and GMP [53].

In humans, the purine requirement for normal cellular growth can be largely maintained through the salvage pathway. However, in the case of rapidly dividing cells, like cancer cells, there is an enormous increase in RNA production and DNA replication. Additionally, the metabolic demand of those cells is so high that they are reprogrammed to increase the use of the anabolic pathways. This metabolic change generates elevated purine requirements that can only be supported through the maintenance of the de novo purine synthesis pathway at high levels [54,55].

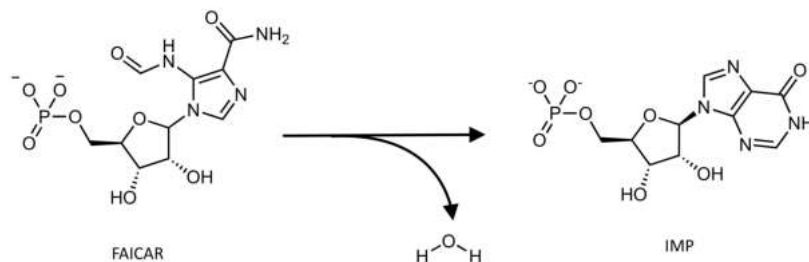
In humans, the de novo purine biosynthetic pathway requires six enzymes and ten successive steps to convert PRPP into IMP [56]. The 5-aminoimidazole-4-carboxamide ribonucleotide formyltransferase/inosine monophosphate (IMP) cyclohydrolase (ATIC) enzyme is a cytosolic bifunctional enzyme that catalyzes the final two steps of the pathway.

Its AICAR formyltransferase (AICAR TFase) domain (EC 2.1.2.3) catalyzes the transfer of the one-carbon formyl group from the cofactor  $N^{10}$ -formyl-tetrahydrofolate (10-f-THF) to the substrate 5'-phosphoribosyl-5-aminoimidazole-4-carboxamide (AICAR) in order to produce the products 5'-phosphoribosyl-5-formaminoimidazole-4-carboxamide (FAICAR) and tetrahydrofolate (Figure 5).



**Figure 5.** Schematic representation of the reaction catalyzed by the AICAR TFase domain of the ATIC enzyme.

Its IMP cyclohydrolase domain (IMPCHase) (E.C. 3.5.4.10) enhances the intramolecular cyclization of the product of the AICAR TFase domain (FAICAR) to the final product of the de novo purine biosynthesis pathway, IMP (Figure 6).



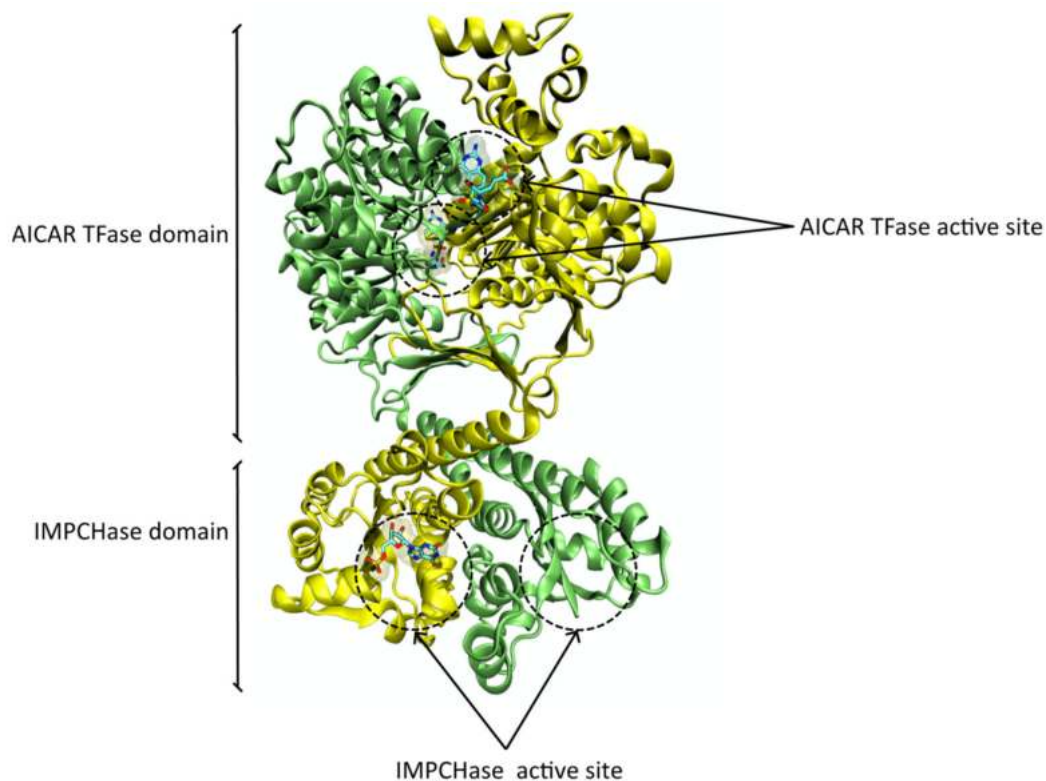
**Figure 6.** Schematic representation of the reaction catalyzed by the IMPCHase domain of the ATIC enzyme.

### 3.2. Protein Structure

The human ATIC enzyme is an intertwined homodimer with 64 kDa composed by two polypeptide chains with 592 residues each [57]. Each monomer contains a C-terminal



AICAR TFase domain composed by residues 199 to 592 and an N-terminal IMPCHase domain composed by residues 1 to 198 [57] (Figure 7). The active sites of each domain are separated by  $\sim 50$  Å [57] and are not interconnected by any intramolecular tunnel [58].



**Figure 7.** Ribbon representation of the human ATIC enzyme with the PDB ID 1P4R [57] obtained with VMD. The AICAR TFase active site harbors the folate-based inhibitor BW1540U88UD, and the IMPCHase active site (of the ATIC monomer colored in yellow) harbors a xanthosine 5'->monophosphate molecule. All ligands are represented in licorice.

There is evidence that the human ATIC exists in a monomer/dimer equilibrium [59]. The AICAR TFase active site is located in a long, narrow cleft at the dimer interface where AICAR interacts primarily with one subunit and the folate co-factor with the opposing subunit [60]. Since both subunits are required for AICAR TFase catalytic activity, this domain is only active in the dimer form [59].

The IMPCHase substrate binding site is localized in one monomeric unit away from the dimeric interface, and there is evidence that the IMPCHase domain possesses catalytic activity in both the monomeric and dimeric forms, although the dimeric form is more active [59]. In this case, the obvious advantage of bringing together two different domains in the same enzyme is to place the two catalytic sites in close proximity, avoiding the dilution effects caused by diffusion through solvent. Additionally, there is evidence that the AICAR TFase reaction favors the reverse direction [61]; therefore, the proximity between the two domains raises the high local concentration of FAICAR, favoring its conversion to the final product, IMP, and avoiding its conversion back to AICAR.

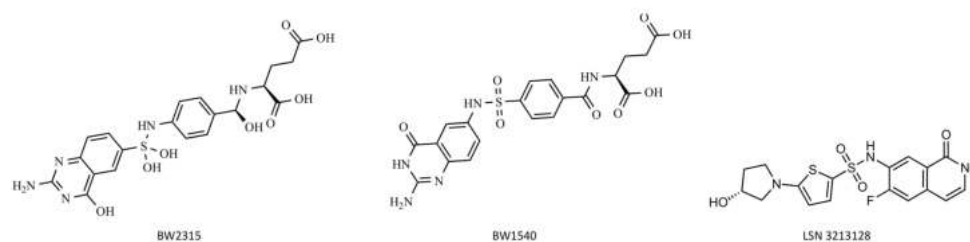
### 3.3. Role in Cancer

Attending to the evidence that normal cells preferentially utilize the salvage pathway for the synthesis of purines while tumor cells favor the de novo pathway, it can be expected that the inhibition of enzymes exclusively involved in the de novo pathway represents a good strategy to effectively inhibit cancer growth with minimal damage to normal cells [62]. Although the significance of ATIC in human cancer requires further investigation, there are several studies strongly suggesting that ATIC is a good target against several

different cancers [63–65]. One such study demonstrated that the inhibition of the AICAR TFase activity of ATIC and the subsequent rise in intracellular levels of 5-Aminoimidazole-4-carboxamide ribonucleotide plays a significant role in the anti-tumorigenic effects of pemetrexed, a drug used in the treatment of non-small cell lung cancer [63,64]. A recent study also showed that ATIC is upregulated in Hepatocellular carcinoma (HCC) tissues, and high levels of ATIC are correlated with poor survival in HCC patients. The inhibition of ATIC expression in cancer cells resulted in a dramatic decrease of cell proliferation and migration and in the increase of cell apoptosis [65].

### 3.4. Inhibitors

The first ATIC inhibitors developed were two sulfamido-bridged 5,8-dideazafolate analogs, designated BW1540 and BW2315 [57] (Figure 8). They are anti-folate inhibitors specific for the AICAR TFase active site; however, they have never been tested in vitro or in vivo. Recently, a potent new ATIC inhibitor designated LSN3213128 (Figure 8) has been proposed. It is a folate competitive non-classical anti-folate inhibitor selective for AICAR TFase relative to other folate dependent enzymes [66]. In vivo studies have shown that LSN3213128 is orally bioavailable and that it demonstrates anti-tumor activity in murine models [66,67].



**Figure 8.** Chemical structure of AICAR TFase inhibitors.

To date there are no records of any specific ATIC inhibitors in active clinical development.

## 4. Leukotriene A<sub>4</sub> Hydrolase (LTA<sub>4</sub>H)

### 4.1. Biological Role

Inflammation is a major pathological characteristic of a wide array of severe endemic illnesses potentially affecting almost all tissues and organ systems of the human body. The development and maintenance of inflammation are governed by a complex network of cellular and soluble factors. Among these are the eicosanoids, a class of structurally related paracrine hormones derived from the metabolism of arachidonic acid, which include the prostaglandins, leukotrienes and lipoxins. During inflammation, the cytosolic enzyme phospholipase A<sub>2</sub> releases arachidonic acid from cell membrane phospholipids; the free arachidonic acid can then be converted to prostaglandins by cyclooxygenase or to leukotrienes by the lipoxygenase pathway [68].

The leukotrienes (LTs) are lipid mediators that act during the first phase of inflammation triggered by injury or pathogen invasion [69]. As the name indicates, they are primarily formed in leukocytes and can be divided into two major classes: dihydroxy acid leukotriene B<sub>4</sub> (LTB<sub>4</sub>), which is a potent chemotactic agent, and the cysteinyl leukotrienes (CysLTs), which are a group of three (LTC<sub>4</sub>, LTD<sub>4</sub>, LTE<sub>4</sub>) potent spasmogenic agents [69].

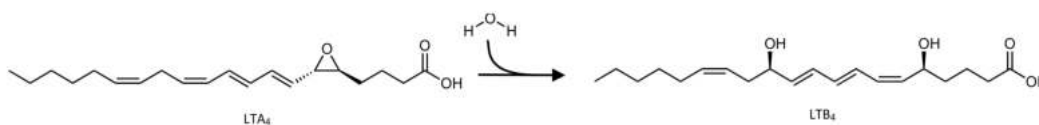
The most important leukotriene synthesized during acute inflammatory responses is LTB<sub>4</sub>. It is derived from cell membrane phospholipids by the sequential actions of phospholipase A<sub>2</sub>, 5-lipoxygenase (5-LO) and LTA<sub>4</sub> hydrolase [68]. It operates its pro-inflammatory functions through the activation of leukocytes and the extension of their survival, acting as a chemoattractant (which induce directed movement of their targets in a concentration-dependent manner) for macrophages and neutrophils, and through the stimulation of leukocyte adhesion to vascular endothelium by the upregulation of integrin expression [68,70]

The chemotactic activity of  $\text{LTB}_4$  is mediated through its binding to two specific G-protein-coupled receptors (GPCR), BLT1 (high affinity and specific for  $\text{LTB}_4$ ) and BLT2 (non-specific and low affinity for  $\text{LTB}_4$ ) [71].

Among the panoply of molecules that are supposed to intervene directly or indirectly in the inflammatory process is the tripeptide Pro-Gly-Pro (PGP). It is derived from the extracellular matrix collagen through a multistep proteolytic pathway involving matrix metalloproteases 8 and 9 and the serine protease prolyl endopeptidase [72]. It has been proposed that the PGP peptide functions as a neutrophil chemoattractant by binding to the GPCR chemokine receptors CXCR1/2 [73]. Although there are many studies reporting the presence of significant quantities of PGP in patients with chronic neutrophilic lung diseases (e.g., chronic obstructive pulmonary disease, cystic fibrosis, and bronchiolitis obliterans syndrome) [72–77], a recent study did not find evidence of PGP's role as a chemoattractant of human and mouse neutrophils [78]. Further studies are required to elucidate the effective biological role of PGP.

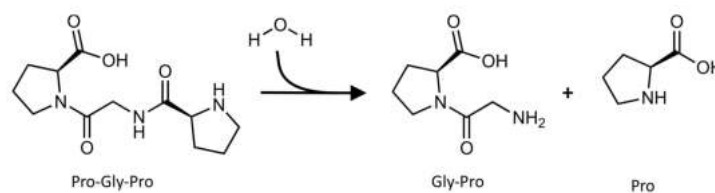
Interestingly, the levels of these two chemically unrelated molecules ( $\text{LTB}_4$  and PGP) are inversely controlled by the same enzyme, Leukotriene A4 hydrolase ( $\text{LTA}_4\text{H}$ ).  $\text{LTA}_4\text{H}$  is a bifunctional enzyme that has been detected in almost all mammalian cells, organs, and tissues [79]. In a common active center, it catalyzes the final rate limiting step in the biosynthesis of  $\text{LTB}_4$  through its epoxide hydrolase activity, and catalyzes the hydrolysis of the tripeptide Pro-Gly-Pro (though not the *N*-acetyl PGP) through its aminopeptidase activity [78]

The epoxide hydrolase activity of  $\text{LTA}_4\text{H}$  (EC 3.3.2.6) converts the transient epoxide  $\text{LTA}_4$  (5*S*-5,6-epoxy-7,9-*trans*-11,14-*cis*-eicosatetraenoic acid) into the dihydroxy acid  $\text{LTB}_4$  (5*S*,12*R*-dihydroxy-6,14-*cis*-8,10-*trans*-eicosatetraenoic acid) [80–82] (Figure 9).



**Figure 9.** Schematic representation of the reaction catalyzed by the epoxide hydrolase activity of the  $\text{LTA}_4\text{H}$  enzyme.

The aminopeptidase activity of  $\text{LTA}_4\text{H}$  (EC 3.4.11.6) catalyzes the *N*-terminal cleavage of the Pro-Gly-Pro tripeptide into the Pro-Gly dipeptide and the amino acid proline [81–83] (Figure 10).

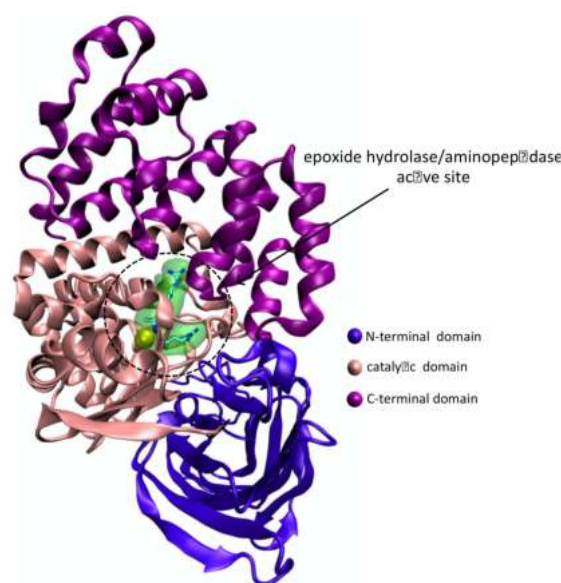


**Figure 10.** Schematic representation of the reaction catalyzed by the aminopeptidase activity of the  $\text{LTA}_4\text{H}$  enzyme.

Mechanistic proposals show that the residues Glu296 and Tyr383 are specifically required for the aminopeptidase reaction, and Asp375 is only required for the epoxide hydrolase reaction. However,  $\text{Zn}^{2+}$  Glu-271 and Arg-563 are necessary for both catalytic mechanisms [81,82]. Interestingly, it has been suggested that the  $\text{LTA}_4\text{H}$  developed from an ancestral aminopeptidase which initially possessed an allosteric lipid binding site, and that the enzyme's architecture has evolved into an active site capable of accommodating  $\text{LTA}_4$ . Subsequent structural optimizations have further improved the substrate alignment, culminating in the establishment of an efficient catalytic mechanism for the conversion of  $\text{LTA}_4$  into  $\text{LTB}_4$  [81].

#### 4.2. Protein Structure

The LTA<sub>4</sub>H is a monomeric 69-kDa cytosolic bifunctional zinc metalloenzyme with 611 amino acids and which is folded into three domains, the N-terminal, catalytic, and C-terminal domains. These domains are packed in a flat triangular arrangement, with an L-shaped cavity between them [84] (Figure 11). The two distinct catalytic activities of LTA<sub>4</sub>H occur in two distinct but overlapping active sites located in that deep L-shaped cavity (Figure 11). One arm of the cavity is wider and highly hydrophilic; it starts near the protein's surface, where the substrates enter the cleft, then bends and narrows at the site of the catalytic Zn<sup>2+</sup> into another arm that is predominantly a hydrophobic tunnel that penetrates deeper into the protein [84]. The LTA<sub>4</sub> occupies the entire cavity, with its epoxide coordinating with the zinc and its long hydrophobic tail buried into the narrow and hydrophobic tunnel [85]. The Pro-Gly-Pro is confined to the wide hydrophilic arm of the cavity that contains the catalytic zinc [85].



**Figure 11.** Ribbon representation of the human LTA<sub>4</sub>H enzyme with the PDB ID 3B7T [86] obtained with VMD. The LTA<sub>4</sub>H active site harbors a catalytic Zn<sup>2+</sup> ion (colored in yellow) and an Arg-Ala-Arg substrate. All ligands are represented in licorice.

#### 4.3. Role in Cancer

LTA<sub>4</sub>H is overexpressed in several cancers including colorectal [87], lung and esophageal [88,89], skin squamous cell carcinoma [90], and oral squamous cell carcinoma [91], and several studies have shown that its hydrolase function is implicated in cancer development [87,90–94].

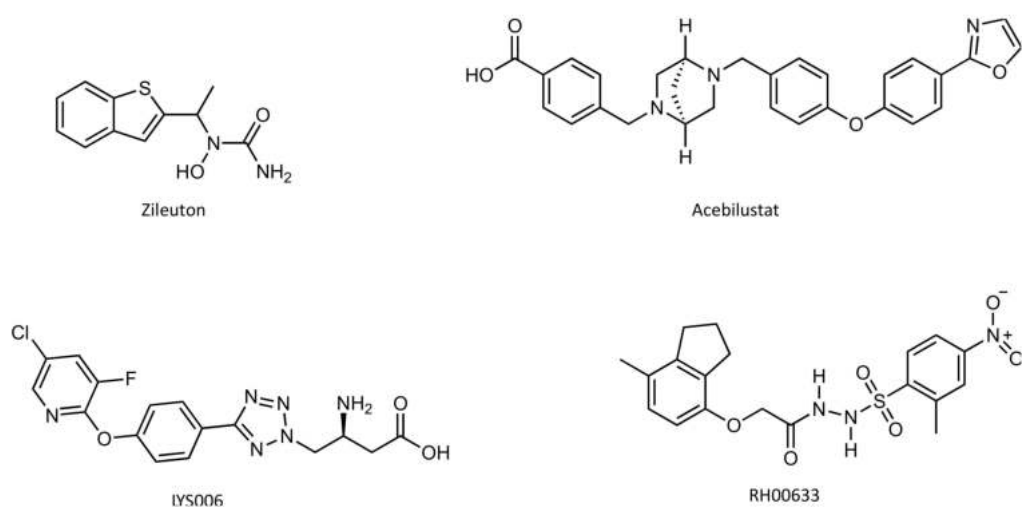
It has been proposed that LTA<sub>4</sub>H and the product of its epoxide hydrolase activity, LTB<sub>4</sub>, may play an important role in chronic inflammation-associated carcinogenesis via several mechanisms, including the autocrine and paracrine growth-stimulatory effect of LTB<sub>4</sub> (produced respectively in epithelial cells and inflammatory cells) on precancerous and cancer cells, and the inflammation–augmentation effect on inflammatory cells through positive feedback mediated by its BLT1 receptor and downstream signaling molecules [89].

A recent study has suggested that LTA<sub>4</sub>H is a key modulator of the cell cycle through its negative effect on the expression of the tumor suppressor p27 protein [90]. The Cyclin-dependent kinase inhibitor 1B (CDKN1B, p27<sup>Kip1</sup>), known as p27 protein, controls the transition from the G1 phase into the S phase of the cell cycle [95]. The inactivation of p27 is generally accomplished post-transcriptionally by the oncogenic activation of various pathways that accelerate the proteolysis of the p27 protein and allow cancer cells to undergo rapid division and uncontrolled proliferation. The absence or reduction of p27

protein expression is also reported to be associated with a poor prognosis in several human cancers [95–100]. The depletion of LTA<sub>4</sub>H enhances p27 protein stability by mediating the downregulation of its ubiquitination. This ultimately leads to a decrease in cancer cell growth by inducing cell cycle arrest at the G<sub>0</sub>/G<sub>1</sub> phase [90]. Taken together, all of the evidence suggests that inhibiting LTA<sub>4</sub>H epoxide hydrolase activity is a promising strategy for cancer prevention.

#### 4.4. Inhibitors

The only compound currently available on the market that interferes with LTB<sub>4</sub> biosynthesis is Zileuton (Figure 12), a 5-LO inhibitor and a very weak inhibitor of LTB<sub>4</sub> biosynthesis [101]. It has only been approved in the United States for the treatment of asthma, and has some disadvantages, for example dose-limiting toxicity and unfavorable pharmacokinetic properties [102].



**Figure 12.** Chemical structure of one 5-LO inhibitor (Zileuton) and three LTA<sub>4</sub>H inhibitors (Acebilustat, LYS006 and RH00633).

The development of an inhibitor specifically targeting LTA<sub>4</sub>H would be advantageous because it would allow the inhibition of LTB<sub>4</sub> synthesis without affecting the biosynthesis of other lipids that depend on the upstream enzymes (e.g., 5-LO) [103]. Researchers and the pharmaceutical industry have been actively searching for selective and potent LTA<sub>4</sub>H inhibitors for over ten years (see [103] for review). During this time, several inhibitors of LTA<sub>4</sub>H have been proposed, and five of those molecules have reached the early clinical development stage, although none of the clinical trials has targeted cancer patients [102]. Of these, only two, Acebilustat from CeltaSys [104] and LYS006 from Novartis [105] (Figure 12), remain in active clinical development. Acebilustat completed Phase 2 clinical trials for cystic fibrosis (NCT02443688 [106]) and for Acne Vulgaris (NCT02385760 [107]). LYS006 is in ongoing Phase 2 clinical trials for hidradenitis suppurativa (NCT03827798 [108]), inflammatory acne (NCT03497897 [109]), ulcerative colitis (NCT04074590 [110]), nonalcoholic steatohepatitis and non-alcoholic Fatty Liver Disease (NCT04147195 [111]).

All five proposed molecules inhibit both epoxide hydrolase and aminopeptidase catalytic activities of the enzyme [102].

Recently, a research group has used computer-aided drug design to search for new effective and selective LTA<sub>4</sub>H inhibitors. In the last stage of the study, they experimentally evaluated the epoxide hydrolase inhibitory activities of the five best scored hits found *in silico*. Among the tested compounds, the one designated RH00633 (Figure 12) stands out with 73.6% inhibition of the basal epoxide hydrolase activity of LTA<sub>4</sub>H. RH00633 binds to the enzyme's active site and interacts with the catalytic Zn<sup>2+</sup>, along with several other important catalytic residues [112].

Several studies have suggested an association between the difficulties in the discovery of a potent and selective LTA4H and the simultaneous inhibition of both catalytic activities of the enzyme [113,114]. These studies suggested that a good LTA4H inhibitor should be epoxide hydrolase selective and aminopeptidase sparing, in order to reduce the production of LTB4 while retaining the ability to reduce PGP levels.

The fact that the Pro-Gly-Pro binding site is confined to the wide hydrophilic arm of the cavity while the LTA<sub>4</sub> occupies the entire cavity suggests that the selective blockade of the hydrophobic tunnel where the long hydrophobic tail of LTA<sub>4</sub> is buried without interfering with the aminopeptidase active site would be a good strategy for the selective inhibition of the epoxide hydrolase activity of LTA4H [83,85]. However, all the aminopeptidase-sparing LTA4H inhibitors proposed to date have shown very low potency in inhibiting the epoxide hydrolase activity of LTA4H when compared to general LTA4H inhibitors [78,85]. Because there are no solid data to date about the true physiological role of PGP, the physiological relevance of sparing the aminopeptidase function of LTA4H remains questionable [102].

## 5. Jumonji Domain-Containing Protein 6 (Jmjd6)

### 5.1. Biological Role

Posttranslational modifications (PTMs) are a variety of covalent processing events that change the properties of a protein through proteolytic cleavage or the addition of a modifying group, such as hydroxyl, acetyl, phosphoryl, glycosyl, methyl, etc., to one or more amino acids [115]. To date, more than 400 different PTM have been identified [116]. They can be reversible or irreversible, and inevitably affect the structure and the dynamics of the proteins that play key roles in a panoply of biological processes [116–118].

Protein hydroxylation is a reversible post-translational modification that occurs with more frequency in proline, and can occur in lysine, asparagine, aspartate or histidine as well, among other amino acids [119]. Although for a long time it was mainly considered a specialized post-translational modification of the extracellular collagens and proteins with collagen-like sequences, the recent discovery of new hydroxylation substrates demonstrates that protein hydroxylation can extensively influence cell signaling pathways. In general, protein hydroxylation can modify protein stability, affect the enzymatic activity of certain proteins through the perturbation of their interaction with direct activators, and influence the occurrence of other post-translational modifications that affect their activity in turn [119].

Methylation is one of the most common post-translational modifications, and has been implicated in the regulation of transcription [120], signal transduction [121], nuclear transport [122], T-cell activation [123], protein trafficking, and protein repair [124] among many other cellular processes [125]. It usually occurs at the nitrogen atom of arginine or lysine side chains or at the terminal  $\alpha$ -amino group of polypeptides.

About 0.5% of all arginine residues in mammalian tissues are methylated [126]. Arginine is the most basic of all amino acids, with a  $pK_a$  of ~13.8. It contains a guanidinium group that is protonated at physiological pH, generating a positive charge that is very important for the establishment of several intramolecular and intermolecular interactions, including hydrogen bonds (it has five hydrogen donors) and cation- $\pi$  interactions with aromatic rings or salt bridges (it can mediate the formation of two salt bridges simultaneously).

The methylation of the guanidinium group of arginine delocalizes its positive charge, raising its hydrophobicity and consequently increasing its affinity to aromatic rings in cation- $\pi$  interactions [127]. It removes one potential hydrogen bond for each methyl group added, and it increases its side chain bulkiness [126,128]. These chemical changes of the arginine side chain regulate its binding to certain protein domains that are “readers” of methylarginine marks (e.g., Tudor domains) [126]. Ultimately, arginine methylation can both positively and negatively regulate protein-protein interactions [125].

Posttranslational arginine methylation occurs in hundreds of proteins, usually affecting protein-protein interaction or protein stability [129]. In the case of histones, the methylation of arginine plays an important role in the epigenetic regulation of gene ex-

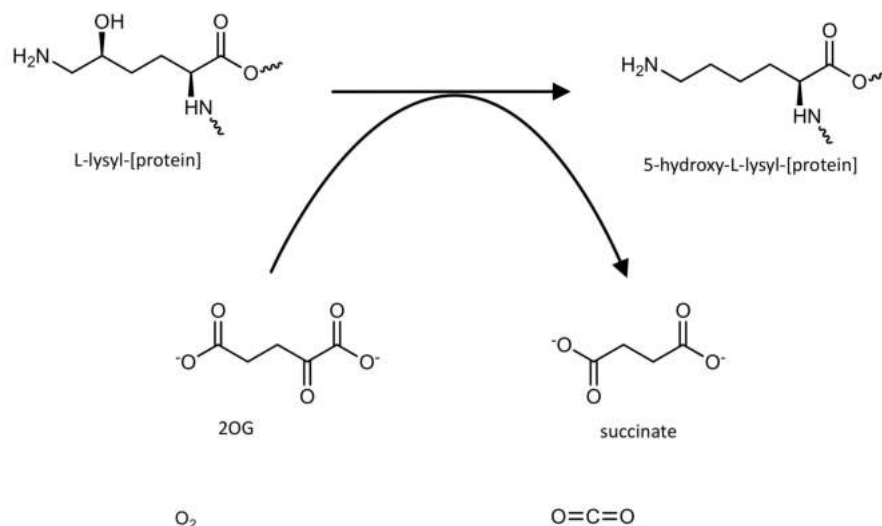
pression by altering chromatin structure [125]. There are three different types of arginine methylation that occur in mammalian cells, monomethylarginine, asymmetric dimethylarginine, and symmetric dimethylarginine, and they are all catalyzed by a family of nine protein arginine methyltransferases [126].

Although there is evidence that arginine methylation is reversible, to date only one enzyme, Fe(II) and 2-oxoglutarate-dependent dioxygenase Jumonji domain-containing protein 6 (Jmjd6) (EC 1.14.11.-), has been reported to have potential arginine demethylation activity *in vivo* [130,131].

Jmjd6 is a bifunctional enzyme that also catalyzes the hydroxylation of lysine in a wide variety of target molecules [131–133].

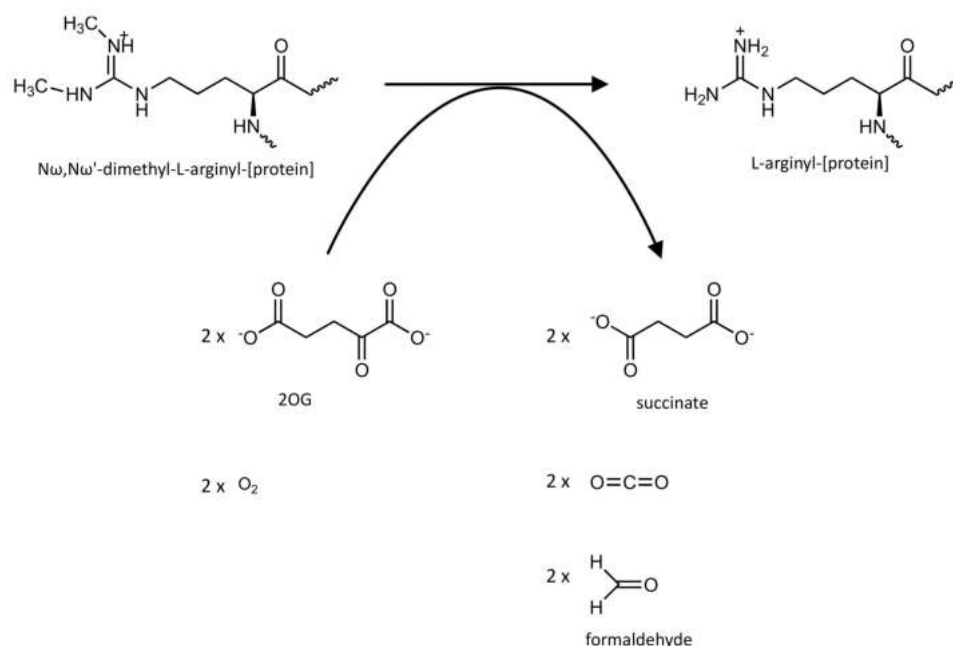
Both the demethylation and hydroxylation mechanisms catalyzed by Jmjd6 require the presence of Fe (II) as a cofactor and 2-oxoglutarate (2-OG) as a co-substrate [134,135].

The hydroxylation mechanism starts with the sequential binding of 2OG, the substrate and dioxygen, to the active site containing a Fe (II) ion. Then, the oxidative decarboxylation of 2OG results in the carbon dioxide, succinate and a ferryl intermediate that mediate substrate oxidation. Hydroxylation can occur via a radical rebound mechanism or via direct insertion of oxygen from the ferryl intermediate into the requisite C–H bond [135] (Figure 13).



**Figure 13.** Schematic representation of the reaction catalyzed by the lysine hydroxylase activity of the Jmjd6 enzyme.

The demethylation catalytic mechanism is thought to be preceded by a hydroxylation reaction that produces an unstable hydroxymethyl-lysine intermediate, succinate, and CO<sub>2</sub>. The hydroxymethyl group of the hydroxymethyl-lysine intermediate is then spontaneously lost as formaldehyde, releasing the methyl group and producing an unmodified arginine residue [134] (Figure 14).



**Figure 14.** Schematic representation of the reaction catalyzed by the arginine demethylation activity of the Jmjd6 enzyme.

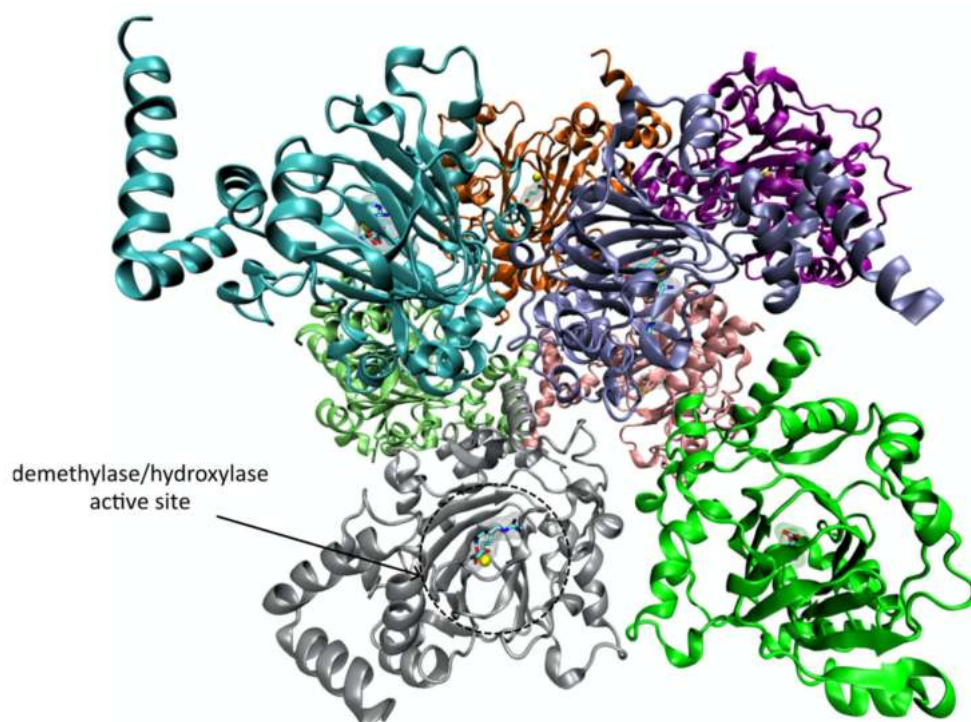
Recent studies suggest that in addition to its demethylase and hydroxylase activities, this enzyme may also have a kinase [136] and a protease function [137].

### 5.2. Protein Structure

JMJD6 is a 47.5 kDa protein with 403 amino acids that belongs to a family of Jumonji domain (JmjC)-containing proteins which are non-haeme iron (II) and 2-oxoglutarate (2OG or  $\alpha$ -ketoglutarate)-dependent oxygenases. JMJD6 can exist as a monomer, but in solution adopts an oligomeric form, which can be a trimeric, pentameric or larger oligomeric form [138] (Figure 15), organized in ring like structures that upon deletion of its poly-Ser sequence turn into a fibril form [119,139].

Its structure comprises a double-stranded  $\beta$ -helix (DSBH) fold, characteristic of the 2OG-dependent oxygenases, which is surrounded by characteristic secondary structure elements [139]. The Fe(II) binding site of the catalytic center is located in the opening end of the barrel-like structure formed by the strands  $\beta$ 1 and  $\beta$ 2 of the typical DSBH fold (Figure 15). The Fe(II) is coordinated with the side chain of His187, Asp189 and His273, which form a conserved HXD/E(X)nH motif that is essential for the enzyme's catalytic activity [119,139,140]. Structural analysis of JMJD6 shows that in addition to its Jumonji domain, it also possesses other motifs, namely a DNA binding motif (AT-hook), five nuclear localization signals, a nuclear export signal, a SUMOylating site, and a C-terminal polyserine (poly-Ser) domain (residues 340–359) that is involved in regulating its oligomerization and cellular localization [119,138,139].





**Figure 15.** Ribbon representation of the human Jmjd6 enzyme with the PDB ID 6MEV [137] obtained with VMD. The Jmjd6 active site harbors a catalytic Fe (II) ion (colored in yellow), one molecule of mono-Methyl Arginine and one molecule of 2-oxoglutaric acid. All ligands are represented in licorice.

### 5.3. Role in Cancer

Epigenetics is a term used to describe heritable changes in gene expression without alteration in DNA sequences. The key processes responsible for epigenetic regulation include DNA methylation, histone modification (e.g., methylation, hydroxylation, acetylation, ubiquitination, etc.) nucleosome remodeling, and alterations in non-coding RNA profiles [141]. The deregulation of the epigenetic processes leads to altered gene functions and ultimately to wide variety of pathologies including cancer, metabolic diseases, autoimmune diseases and neurological disorders, among others [138]. The activities of JMJD6 as arginine demethylase [130], lysyl hydroxylase [142] and eventually as tyrosine kinase [136] of histones suggests that this enzyme may have an important role in the epigenetic regulation of chromosomal rearrangement and gene transcription.

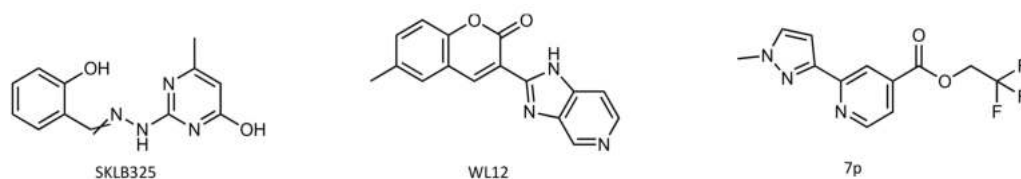
The involvement of JMJD6 in many developmental processes including embryogenesis [143], angiogenesis [144] and tumorigenesis has been demonstrated [145]. Recently, Yang and colleagues compiled a series of studies relating the abnormal overexpression of JMJD6 in several different cancers (e.g., Breast cancer, Melanoma, Oral cancer, Glioblastoma, Hepatocellular carcinoma, Colon carcinoma, Ovarian cancer, Neuroglioma, etc.) to increased cancer cell proliferation and invasion leading to aggressive tumors and poor prognosis [138].

Both the histone arginine demethylase and lysyl hydroxylase activities of JMJD6 have been associated with tumorigenesis. In glioblastoma and neuroblastoma, JMJD6 upregulates target gene transcription by forming a complex with Bromodomain-containing protein 4 (BRD4)—a transcriptional and epigenetic regulator associated with cell cycle control—and demethylating the histone H4 at arginine 3 (H4R3) target gene antipause enhancers, leading to RNA polymerase II release from promoter-proximal pause regions and consequently to aberrant gene expression [146–148]. In colon carcinoma, JMJD6 complexes with the tumor suppressor protein p53 and catalyzes its hydroxylation, resulting in the repression of its transcriptional activity. It has been demonstrated that the knockdown of JMJD6 represses p53-dependent cell proliferation and tumorigenesis in vivo [149].

Overall, the existing evidence suggests that the simultaneous inhibition of both the demethylase and hydroxylase activities of JMJD6 may be a promising strategy for effective cancer therapy.

#### 5.4. Inhibitors

To date, only three molecules have been proposed as drug candidates targeting JMJD6, and none of them has reached an early clinical development stage. SKLB325 (Figure 16) was designed, synthesized, and tested to evaluate its antitumor activity against ovarian cancer cells in vivo and in vitro [150]. The results demonstrated that it suppresses ovarian cancer growth through inhibition of proliferation and induction of apoptosis and cell death. In vivo tests demonstrated that the administration of SKLB325 to tumor-bearing mice prolonged survival without obvious side effects [150].



**Figure 16.** Chemical structure of the JMJD6 inhibitors.

WL12 (Figure 16) was designed to bind to the 2OG-binding site of JMJD6 and inhibit its demethylase activity. It was tested in vitro and demonstrated the ability to suppress the JMJD6-dependent proliferation of cervical and liver cancer cells [151]. A new potent and selective JMJD6 inhibitor, 7p (Figure 16), was recently proposed; however, it still requires in vitro and in vivo validation [152].

## 6. Current and Future Developments

The four enzymes described here possess different biological functions and different structural and functional characteristics; however, they all share two characteristics: they are promising drug targets against cancer, and they are multifunctional.

Multifunctionality is an advantage that must be exploited for the development of new potent and selective inhibitors. Depending on an enzyme's particular features, such as the number and location of active sites, possession or not of allosteric regulation, provenience of the substrates, etc., its catalytic activity can be inhibited using multiple approaches.

In the case of the PFK-2/FBPase-2 enzyme, there is evidence of the anti-cancer benefits accomplished by the inhibition of both its kinase [45] and phosphatase activities [18]. Considering that the PFK-2 domain is only active in the dimer form, there are three different strategies that can be used to target this enzyme for anti-cancer treatment: (1) selective inhibition of PFK-2 activity; (2) selective inhibition of FBPase-2 activity; and (3) the inhibition of PFK-2 activity by preventing monomeric dimerization.

In the case of ATIC, the product of the IMPCHase domain is the substrate of the AICAR TFase domain. Hence, the inhibition of the former prevents the activity of the latter through the elimination of its substrate. Additionally, there is also evidence that AICAR TFase catalytic activity is only active in the dimeric form [59]. Because both catalytic activities are essential for purine biosynthesis in cancer cells, three different strategies can be used to target ATIC for anti-cancer treatment: (1) selective inhibition of IMPCHase activity; (2) selective inhibition of AICAR TFase activity; and (3) the inhibition of AICAR TFase activity by preventing monomeric dimerization.

LTA<sub>4</sub>H catalyzes two distinct catalytic activities that occur in two distinct but overlapping active sites. This means that both activities will be inhibited independently of the transition state or substrate analog used to selectively inhibit the enzyme. Although only the inhibition of LTA<sub>4</sub>H epoxide hydrolase activity has been related to anti-cancer effects, there is no evidence that the inhibition of aminopeptidase would bring any beneficial effects; therefore, three strategies can be used to inhibit this enzyme: (1) selective inhibition

of epoxide hydrolase; (2) selective inhibition of aminopeptidase; and (3) aminopeptidase-sparing LTA<sub>4</sub>H inhibitors that bind to the hydrophobic tunnel where the long hydrophobic tail of LTA<sub>4</sub> is buried.

In the case of the Jmjd6, both demethylation and hydroxylation mechanisms catalyzed by Jmjd6 require the presence of Fe (II) as a cofactor and 2-oxoglutarate (2-OG) as a co-substrate, which means that both mechanisms occur in the same active site. Since both histone arginine demethylase and lysyl hydroxylase activities of JMJD6 has been associated with tumorigenesis it is possible to target the enzyme by using either: (1) arginine demethylase selective inhibitors; or (2) lysyl hydroxylase selective inhibitors.

The current status of the development of inhibitors targeting the four enzymes described in this review is summarized in Table 1.

**Table 1.** Current status of the development of inhibitors targeting PFK-2/FBPase-2, ATIC, LTA<sub>4</sub>H and Jmjd6.

Enzyme	Specific Target	Inhibitors	Evaluated in vitro	Evaluated in vivo	Clinical Trials in Cancer Patients
PFK-2/FBPase-2	PFK-2 activity of PFKB3	3PO [46]	yes [46]	yes [46]	no
		PFK15 [48]	yes [48]	yes [48]	no
		PFK158 [48]	yes [49]	yes [49]	NCT02044861 [50]
	PFK-2 activity of PFKFB4	5MPN [51]	yes [51]	yes [51]	no
ATIC	AICAR TFase	BW1540 [57]	no	no	no
	AICAR TFase	BW2315 [57]	no	no	no
	AICAR TFase	LSN3213128 [66]	yes [66,67]	yes [66,67]	no
LTA <sub>4</sub> H	epoxide hydrolase and aminopeptidase activities	Acebilustat	no available data	no available data	no <sup>(1)</sup>
	epoxide hydrolase and aminopeptidase	LYS006 [105]	yes [105]	yes [105]	no <sup>(1)</sup>
	epoxide hydrolase	RH00633 [112]	yes [112]	no	no
Jmjd6	Demethylase and hydroxylase	SKLB325 [150]	yes [150]	yes [150]	no
	Demethylase and hydroxylase	WL12 [151]	yes [151]	no	no
	Demethylase and hydroxylase	7p [152]	no	no	no

<sup>(1)</sup> Currently in Phase 2 clinical trials for other inflammatory conditions.

## 7. Conclusions

Multifunctionality is an extraordinary capability restricted to a small number of enzymes. PFK-2/FBPase-2, ATIC, LTA<sub>4</sub>H and Jmjd6 are four multifunctional enzymes with a proven relevant role in the proliferation and/or survival of cancer cells, and their inhibition can increase the life expectancy of some cancer patients.

Although there are studies reporting the identification of potential inhibitors targeting each of the four described enzymes, to date only LTA<sub>4</sub>H and PFK-2/FBPase-2 have inhibitors in active clinical development, and only the PFK-2/FBPase-2 inhibitor (PFK158) is being tested in cancer patients. However, all evidence points to these four enzymes as promising targets for the development of new anti-cancer drugs, and it is our belief that these enzymes' extraordinary capability to perform different catalytic reactions could be

used as an advantage in the development of efficient new molecular-targeted therapies against cancer.

**Author Contributions:** Conceptualization, C.S.S.T. and S.F.S.; investigation, C.S.S.T. and S.F.S.; writing—original draft preparation, C.S.S.T.; writing—review and editing, S.F.S.; supervision, S.F.S.; funding acquisition, S.F.S. All authors have read and agreed to the published version of the manuscript.

**Funding:** This work was supported by the Applied Molecular Biosciences Unit—UCIBIO, which is financed by national funds from FCT (UIDP/04378/2020 and UIDB/04378/2020). S.F.S. acknowledges FCT funding, 2020.01423.CEECIND/CP1596/CT0003.

**Institutional Review Board Statement:** Not applicable.

**Informed Consent Statement:** Not applicable.

**Conflicts of Interest:** The authors declare no conflict of interest.

## References

- Sung, H.; Ferlay, J.; Siegel, R.L.; Laversanne, M.; Soerjomataram, I.; Jemal, A.; Bray, F. Global Cancer Statistics 2020: GLOBOCAN Estimates of Incidence and Mortality Worldwide for 36 Cancers in 185 Countries. *CA Cancer J. Clin.* **2021**, *71*, 209–249. [CrossRef] [PubMed]
- Martínez-Reyes, I.; Chandel, N.S. Cancer metabolism: Looking forward. *Nat. Rev. Cancer* **2021**, *21*, 669–680. [CrossRef] [PubMed]
- Counihan, J.L.; Grossman, E.A.; Nomura, D.K. Cancer Metabolism: Current Understanding and Therapies. *Chem. Rev.* **2018**, *118*, 6893–6923. [CrossRef] [PubMed]
- Salk, J.J.; Fox, E.J.; Loeb, L.A. Mutational Heterogeneity in Human Cancers: Origin and Consequences. *Annu. Rev. Pathol. Mech. Dis.* **2010**, *5*, 51–75. [CrossRef]
- Kumar, B.; Singh, S.; Skvortsova, I.; Kumar, V. Promising Targets in Anti-cancer Drug Development: Recent Updates. *Curr. Med. Chem.* **2018**, *24*, 4729–4752. [CrossRef]
- Arruebo, M.; Vilaboa, N.; Sáez-Gutiérrez, B.; Lambea, J.; Tres, A.; Valladares, M.; González-Fernández, Á. Assessment of the Evolution of Cancer Treatment Therapies. *Cancers* **2011**, *3*, 3279–3330. [CrossRef]
- Zhong, L.; Li, Y.; Xiong, L.; Wang, W.; Wu, M.; Yuan, T.; Yang, W.; Tian, C.; Miao, Z.; Wang, T.; et al. Small molecules in targeted cancer therapy: Advances, challenges, and future perspectives. *Signal. Transduct. Target. Ther.* **2021**, *6*, 201. [CrossRef]
- Schramm, V.L. Transition States, Analogues, and Drug Development. *ACS Chem. Biol.* **2013**, *8*, 71–81. [CrossRef]
- Rider, M.H.; Bertrand, L.; Vertommen, D.; Michels, P.A.; Rousseau, G.G.; Hue, L. 6-Phosphofructo-2-kinase/fructose-2,6-bisphosphatase: Head-to-head with a bifunctional enzyme that controls glycolysis. *Biochem. J.* **2004**, *381*, 561–579. [CrossRef]
- Hue, L.; Rider, M.H. Role of fructose 2,6-bisphosphate in the control of glycolysis in mammalian tissues. *Biochem. J.* **1987**, *245*, 313–324. [CrossRef]
- Okar, D.A.; Lange, A.J. Fructose-2,6-bisphosphate and control of carbohydrate metabolism in eukaryotes. *BioFactors* **1999**, *10*, 1–14. [CrossRef]
- Pilkis, S.J.; El-Maghrabi, M.R.; Claus, T.H. Hormonal Regulation of Hepatic Gluconeogenesis and Glycolysis. *Annu. Rev. Biochem.* **1988**, *57*, 755–783. [CrossRef]
- Uyeda, K.; Furuya, E.; Luby, L.J. The effect of natural and synthetic D-fructose 2,6-bisphosphate on the regulatory kinetic properties of liver and muscle phosphofructokinases. *J. Biol. Chem.* **1981**, *256*, 8394–8399. [CrossRef]
- Wu, C.; Khan, S.A.; Peng, L.-J.; Lange, A.J. Roles for fructose-2,6-bisphosphate in the control of fuel metabolism: Beyond its allosteric effects on glycolytic and gluconeogenic enzymes. *Adv. Enzym. Regul.* **2006**, *46*, 72–88. [CrossRef]
- Pilkis, S.J.; Claus, T.H.; Kurland, I.J.; Lange, A.J. 6-Phosphofructo-2-Kinase/Fructose-2,6-Bisphosphatase: A Metabolic Signaling Enzyme. *Annu. Rev. Biochem.* **1995**, *64*, 799–835. [CrossRef]
- Okar, D.A.; Lange, A.J.; Manzano, Á.; Navarro-Sabatè, A.; Riera, L.S.; Bartrons, R. PFK-2/FBPase-2: Maker and breaker of the essential biofactor fructose-2,6-bisphosphate. *Trends Biochem. Sci.* **2001**, *26*, 30–35. [CrossRef]
- Darville, M.I.; Crepin, K.M.; Hue, L.; Rousseau, G.G. 5' flanking sequence and structure of a gene encoding rat 6-phosphofructo-2-kinase/fructose-2,6-bisphosphatase. *Proc. Natl. Acad. Sci. USA* **1989**, *86*, 6543–6547. [CrossRef]
- Ros, S.; Schulze, A. Balancing glycolytic flux: The role of 6-phosphofructo-2-kinase/fructose 2,6-bisphosphatases in cancer metabolism. *Cancer Metab.* **2013**, *1*, 8. [CrossRef]
- Manzano, A.; Rosa, J.L.; Ventura, F.; Pérez, J.X.; Nadal, M.; Estivill, X.; Ambrosio, S.; Gil, J.; Bartrons, R. Molecular cloning, expression, and chromosomal localization of a ubiquitously expressed human 6-phosphofructo-2-kinase/fructose-2,6-bisphosphatase gene (PFKFB3). *Cytogenet. Genome Res.* **1998**, *83*, 214–217. [CrossRef]
- Hasemann, C.A.; Istvan, E.S.; Uyeda, K.; Deisenhofer, J. The crystal structure of the bifunctional enzyme 6-phosphofructo-2-kinase/fructose-2,6-bisphosphatase reveals distinct domain homologies. *Structure* **1996**, *4*, 1017–1029. [CrossRef]
- Tauler, A.; Lange, A.J.; el-Maghrabi, M.R.; Pilkis, S.J. Expression of rat liver 6-phosphofructo-2-kinase/fructose-2,6-bisphosphatase and its kinase domain in *Escherichia coli*. *Proc. Natl. Acad. Sci.* **1989**, *86*, 7316–7320. [CrossRef]

22. Tauler, A.; Rosenberg, A.H.; Colosia, A.; Studier, F.W.; Pilakis, S.J. Expression of the bisphosphatase domain of rat liver 6-phosphofructo-2-kinase/fructose-2,6-bisphosphatase in *Escherichia coli*. *Proc. Natl. Acad. Sci. USA* **1988**, *85*, 6642–6646. [CrossRef]
23. Sakakibara, R.; Kato, M.; Okamura, N.; Nakagawa, T.; Komada, Y.; Tominaga, N.; Shimojo, M.; Fukasawa, M. Characterization of a Human Placental Fructose-6-Phosphate, 2-Kinase/Fructose-2,6-Bisphosphatase. *J. Biochem.* **1997**, *122*, 122–128. [CrossRef]
24. Kotowski, K.; Rosik, J.; Machaj, F.; Supplitt, S.; Wiczew, D.; Jabłońska, K.; Wiechec, E.; Ghavami, S.; Dzięgiel, P. Role of PFKFB3 and PFKFB4 in Cancer: Genetic Basis, Impact on Disease Development/Progression, and Potential as Therapeutic Targets. *Cancers* **2021**, *13*, 909. [CrossRef]
25. Yi, M.; Ban, Y.; Tan, Y.; Xiong, W.; Li, G.; Xiang, B. 6-Phosphofructo-2-kinase/fructose-2,6-bisphosphatase 3 and 4: A pair of valves for fine-tuning of glucose metabolism in human cancer. *Mol. Metab.* **2019**, *20*, 1–13. [CrossRef]
26. Crochet, R.B.; Kim, J.-D.; Lee, H.; Yim, Y.-S.; Kim, S.-G.; Neau, D.; Lee, Y.-H. Crystal structure of heart 6-phosphofructo-2-kinase/fructose-2,6-bisphosphatase (PFKFB2) and the inhibitory influence of citrate on substrate binding. *Proteins: Struct. Funct. Bioinform.* **2017**, *85*, 117–124. [CrossRef]
27. Flier, J.; Mueckler, M.; Usher, P.; Lodish, H. Elevated levels of glucose transport and transporter messenger RNA are induced by ras or src oncogenes. *Science* **1987**, *235*, 1492–1495. [CrossRef]
28. Osthus, R.C.; Shim, H.; Kim, S.; Li, Q.; Reddy, R.; Mukherjee, M.; Xu, Y.; Wonsley, D.; Lee, L.A.; Dang, C.V. Deregulation of Glucose Transporter 1 and Glycolytic Gene Expression by c-Myc. *J. Biol. Chem.* **2000**, *275*, 21797–21800. [CrossRef]
29. Hockel, M.; Vaupel, P. Biological consequences of tumor hypoxia. *Semin. Oncol.* **2001**, *28*, 36–41. [CrossRef]
30. Ahn, C.S.; Metallo, C.M. Mitochondria as biosynthetic factories for cancer proliferation. *Cancer Metab.* **2015**, *3*, 1. [CrossRef]
31. Warburg, O. On the Origin of Cancer Cells. *Science* **1956**, *123*, 309–314. [CrossRef] [PubMed]
32. Nissler, K.; Petermann, H.; Wenz, I.; Brox, D. Fructose 2,6-bisphosphate metabolism in Ehrlich ascites tumour cells. *J. Cancer Res. Clin. Oncol.* **1995**, *121*, 739–745. [CrossRef] [PubMed]
33. Mojena, M.; Bosca, L.; Hue, L. Effect of glutamine on fructose 2,6-bisphosphate and on glucose metabolism in HeLa cells and in chick-embryo fibroblasts. *Biochem. J.* **1985**, *232*, 521–527. [CrossRef] [PubMed]
34. Miralpeix, M.; Azcon-Bieto, J.; Bartrons, R.; Argiles, J.M. The impairment of respiration by glycolysis in the Lewis lung carcinoma. *Cancer Lett.* **1990**, *50*, 173–178. [CrossRef]
35. Barker, J.; Khan, M.A.A.; Solomos, T. Mechanism of the Pasteur Effect. *Nature* **1964**, *201*, 1126–1127. [CrossRef]
36. Minchenko, O.H.; Ogura, T.; Opentanova, I.L.; Minchenko, D.O.; Ochiai, A.; Caro, J.; Komisarenko, S.V.; Esumi, H. 6-Phosphofructo-2-kinase/fructose-2,6-bisphosphatase gene family overexpression in human lung tumor. *Ukr. Biokhim. Zh.* **2005**, *77*, 46–50.
37. Obach, M.; Navarro-Sabaté, À.; Caro, J.; Kong, X.; Duran, J.; Gómez, M.; Perales, J.C.; Ventura, F.; Rosa, J.L.; Bartrons, R. 6-Phosphofructo-2-kinase (pfkfb3) Gene Promoter Contains Hypoxia-inducible Factor-1 Binding Sites Necessary for Transactivation in Response to Hypoxia. *J. Biol. Chem.* **2004**, *279*, 53562–53570. [CrossRef]
38. Minchenko, O.; Opentanova, I.; Minchenko, D.; Ogura, T.; Esumi, H. Hypoxia induces transcription of 6-phosphofructo-2-kinase/fructose-2,6-bisphosphatase-4 gene via hypoxia-inducible factor-1 $\alpha$  activation. *FEBS Lett.* **2004**, *576*, 14–20. [CrossRef]
39. Minchenko, O.; Opentanova, I.; Caro, J. Hypoxic regulation of the 6-phosphofructo-2-kinase/fructose-2,6-bisphosphatase gene family (PFKFB-1-4) expression in vivo. *FEBS Lett.* **2003**, *554*, 264–270. [CrossRef]
40. Hirata, T.; Watanabe, M.; Miura, S.; Ijichi, K.; Fukasawa, M.; Sakakibara, R. Inhibition of Tumor Cell Growth by A Specific 6-Phosphofructo-2-kinase Inhibitor, N-Bromoacetyethanolamine Phosphate, and Its Analogues. *Biosci. Biotechnol. Biochem.* **2014**, *64*, 2047–2052. [CrossRef]
41. Dasgupta, S.; Rajapakshe, K.; Zhu, B.; Nikolai, B.C.; Yi, P.; Putluri, N.; Choi, J.M.; Jung, S.Y.; Coarfa, C.; Westbrook, T.F.; et al. Metabolic enzyme PFKFB4 activates transcriptional coactivator SRC-3 to drive breast cancer. *Nature* **2018**, *556*, 249–254. [CrossRef]
42. Guo, Q.; Chen, Q.; Zhang, Y.; Zhou, W.; Li, X.; Li, C.; Zhang, Y.; Chen, H.; Liu, P.; Chu, Y.; et al. Click-Nucleic-Acid-Containing Codelivery System Inducing Collapse of Cellular Homeostasis for Tumor Therapy through Bidirectional Regulation of Autophagy and Glycolysis. *ACS Appl. Mater. Interfaces* **2020**, *12*, 57757–57767. [CrossRef]
43. Ros, S.; Santos, C.R.; Moco, S.; Baenke, F.; Kelly, G.; Howell, M.; Zamboni, N.; Schulze, A. Functional Metabolic Screen Identifies 6-Phosphofructo-2-Kinase/Fructose-2,6-Bisphosphatase 4 as an Important Regulator of Prostate Cancer Cell Survival. *Cancer Discov.* **2012**, *2*, 328–343. [CrossRef]
44. Anwar, T.; Kumar, P.; Khan, A.U. Modern Tools and Techniques in Computer-Aided Drug Design. In *Molecular Docking for Computer-Aided Drug Design*; Elsevier: Amsterdam, The Netherlands, 2021; pp. 1–30. [CrossRef]
45. Wang, Y.; Qu, C.; Liu, T.; Wang, C. PFKFB3 inhibitors as potential anticancer agents: Mechanisms of action, current developments, and structure-activity relationships. *Eur. J. Med. Chem.* **2020**, *203*, 112612. [CrossRef]
46. Clem, B.; Telang, S.; Clem, A.; Yalcin, A.; Meier, J.; Simmons, A.; Rasku, M.A.; Arumugam, S.; Dean, W.L.; Eaton, J.; et al. Small-molecule inhibition of 6-phosphofructo-2-kinase activity suppresses glycolytic flux and tumor growth. *Mol. Cancer Ther.* **2008**, *7*, 110–120. [CrossRef]
47. Houddane, A.; Bultot, L.; Novellasdemunt, L.; Johanns, M.; Gueuning, M.-A.; Vertommen, D.; Coulie, P.G.; Bartrons, R.; Hue, L.; Rider, M.H. Role of Akt/PKB and PFKFB isoenzymes in the control of glycolysis, cell proliferation and protein synthesis in mitogen-stimulated thymocytes. *Cell. Signal.* **2017**, *34*, 23–37. [CrossRef]

48. Clem, B.F.; O'Neal, J.; Tapolsky, G.; Clem, A.L.; Imbert-Fernandez, Y.; Kerr, D.A.; Klarer, A.C.; Redman, R.; Miller, D.M.; Trent, J.O.; et al. Targeting 6-Phosphofructo-2-Kinase (PFKFB3) as a Therapeutic Strategy against Cancer. *Mol. Cancer Ther.* **2013**, *12*, 1461–1470. [CrossRef]
49. Mondal, S.; Roy, D.; Sarkar Bhattacharya, S.; Jin, L.; Jung, D.; Zhang, S.; Kalogera, E.; Staub, J.; Wang, Y.; Xuyang, W.; et al. Therapeutic targeting of PFKFB3 with a novel glycolytic inhibitor PFK158 promotes lipophagy and chemosensitivity in gynecologic cancers. *Int. J. Cancer* **2019**, *144*, 178–189. [CrossRef]
50. Phase 1 Safety Study of ACT-PFK-158, 2HCl in Patients with Advanced Solid Malignancies. Available online: <https://clinicaltrials.gov/> (accessed on 5 December 2021).
51. Chesney, J.; Clark, J.; Lanceta, L.; Trent, J.O.; Telang, S. Targeting the sugar metabolism of tumors with a first-in-class 6-phosphofructo-2-kinase (PFKFB4) inhibitor. *Oncotarget* **2015**, *6*, 18001–18011. [CrossRef]
52. Feng, C.; Li, Y.; Li, K.; Lyu, Y.; Zhu, W.; Jiang, H.; Wen, H. PFKFB4 is overexpressed in clear-cell renal cell carcinoma promoting pentose phosphate pathway that mediates Sunitinib resistance. *J. Exp. Clin. Cancer Res.* **2021**, *40*, 308. [CrossRef]
53. Zhang, Y.; Morar, M.; Ealick, S.E. Structural biology of the purine biosynthetic pathway. *Cell. Mol. Life Sci.* **2008**, *65*, 3699–3724. [CrossRef]
54. Yamaoka, T.; Kondo, M.; Honda, S.; Iwahana, H.; Moritani, M.; Ii, S.; Yoshimoto, K.; Itakura, M. Amidophosphoribosyltransferase Limits the Rate of Cell Growth-linked de Novo Purine Biosynthesis in the Presence of Constant Capacity of Salvage Purine Biosynthesis. *J. Biol. Chem.* **1997**, *272*, 17719–17725. [CrossRef]
55. Martinez-Outschoorn, U.E.; Peiris-Pagés, M.; Pestell, R.G.; Sotgia, F.; Lisanti, M.P. Cancer metabolism: A therapeutic perspective. *Nat. Rev. Clin. Oncol.* **2016**, *14*, 11–31. [CrossRef]
56. Pareek, V.; Pedley, A.M.; Benkovic, S.J. Human de novo purine biosynthesis. *Crit. Rev. Biochem. Mol. Biol.* **2020**, *56*, 1–16. [CrossRef]
57. Cheong, C.-G.; Wolan, D.W.; Greasley, S.E.; Horton, P.A.; Beardsley, G.P.; Wilson, I.A. Crystal Structures of Human Bifunctional Enzyme Aminoimidazole-4-carboxamide Ribonucleotide Transformylase/IMP Cyclohydrolase in Complex with Potent Sulfonyl-containing Antifolates. *J. Biol. Chem.* **2004**, *279*, 18034–18045. [CrossRef]
58. Greasley, S.E.; Horton, P.; Ramcharan, J.; Beardsley, G.P.; Benkovic, S.J.; Wilson, I.A. Crystal structure of a bifunctional transformylase and cyclohydrolase enzyme in purine biosynthesis. *Nat. Struct. Biol.* **2001**, *8*, 402–406. [CrossRef]
59. Vergis, J.M.; Bullock, K.G.; Fleming, K.G.; Beardsley, G.P. Human 5-Aminoimidazole-4-carboxamide Ribonucleotide Transformylase/Inosine 5'-Monophosphate Cyclohydrolase. *J. Biol. Chem.* **2001**, *276*, 7727–7733. [CrossRef]
60. Wolan, D.W.; Greasley, S.E.; Wall, M.J.; Benkovic, S.J.; Wilson, I.A. Structure of Avian AICAR Transformylase with a Multisubstrate Adduct Inhibitor  $\beta$ -DADF Identifies the Folate Binding Site. *Biochemistry* **2003**, *42*, 10904–10914. [CrossRef]
61. Wall, M.; Shim, J.H.; Benkovic, S.J. Human AICAR Transformylase: Role of the 4-Carboxamide of AICAR in Binding and Catalysis. *Biochemistry* **2000**, *39*, 11303–11311. [CrossRef]
62. Pedley, A.M.; Benkovic, S.J. A New View into the Regulation of Purine Metabolism: The Purinosome. *Trends Biochem. Sci.* **2017**, *42*, 141–154. [CrossRef] [PubMed]
63. Rothbart, S.B.; Racanelli, A.C.; Moran, R.G. Pemetrexed Indirectly Activates the Metabolic Kinase AMPK in Human Carcinomas. *Cancer Res.* **2010**, *70*, 10299–10309. [CrossRef] [PubMed]
64. Racanelli, A.C.; Rothbart, S.B.; Heyer, C.L.; Moran, R.G. Therapeutics by Cytotoxic Metabolite Accumulation: Pemetrexed Causes ZMP Accumulation, AMPK Activation, and Mammalian Target of Rapamycin Inhibition. *Cancer Res.* **2009**, *69*, 5467–5474. [CrossRef] [PubMed]
65. Li, M.; Jin, C.; Xu, M.; Zhou, L.; Li, D.; Yin, Y. Bifunctional enzyme ATIC promotes propagation of hepatocellular carcinoma by regulating AMPK-mTOR-S6 K1 signaling. *Cell Commun. Signal.* **2017**, *15*, 52. [CrossRef]
66. Fales, K.R.; Njoroge, F.G.; Brooks, H.B.; Thibodeaux, S.; Torrado, A.; Si, C.; Toth, J.L.; Mc Cowan, J.R.; Roth, K.D.; Thrasher, K.J.; et al. Discovery of N-(6-Fluoro-1-oxo-1,2-dihydroisoquinolin-7-yl)-5-[(3R)-3-hydroxypyrrolidin-1-yl]thiophene-2-sulfonamide (LSN 3213128), a Potent and Selective Nonclassical Antifolate Aminoimidazole-4-carboxamide Ribonucleotide Formyltransferase (AICARFT) Inhibitor Effective at Tumor Suppression in a Cancer Xenograft Model. *J. Med. Chem.* **2017**, *60*, 9599–9616. [CrossRef]
67. Brooks, H.B.; Meier, T.I.; Geeganage, S.; Fales, K.R.; Thrasher, K.J.; Konicek, S.A.; Spencer, C.D.; Thibodeaux, S.; Foreman, R.T.; Hui, Y.-H.; et al. Characterization of a novel AICARFT inhibitor which potently elevates ZMP and has anti-tumor activity in murine models. *Sci. Rep.* **2018**, *8*, 15458. [CrossRef]
68. Furie, M.B. Recruitment of Leukocytes: Adhesion Molecules and Chemoattractants. In *Pathobiology of Human Disease*; Elsevier: Amsterdam, The Netherlands, 2014; pp. 275–288. [CrossRef]
69. Di Gennaro, A.; Haeggström, J.Z. The Leukotrienes: Immune-Modulating Lipid Mediators of Disease. *Adv. Immunol.* **2012**, *116*, 51–92. [CrossRef]
70. Abeles, A.M.; Pillinger, M.H.; Abramson, S.B. Inflammation and its mediators. In *Rheumatology*; Elsevier: Amsterdam, The Netherlands, 2015; pp. 169–182. [CrossRef]
71. Tager, A.M.; Luster, A.D. BLT1 and BLT2: The leukotriene B4 receptors. *Prostagland. Leukot. Essent. Fat. Acids* **2003**, *69*, 123–134. [CrossRef]

72. Gaggar, A.; Jackson, P.L.; Noerager, B.D.; O'Reilly, P.J.; McQuaid, D.B.; Rowe, S.M.; Clancy, J.P.; Blalock, J.E. A Novel Proteolytic Cascade Generates an Extracellular Matrix-Derived Chemoattractant in Chronic Neutrophilic Inflammation. *J. Immunol.* **2008**, *180*, 5662–5669. [CrossRef]
73. Weathington, N.M.; van Houwelingen, A.H.; Noerager, B.D.; Jackson, P.L.; Kraneveld, A.D.; Galin, F.S.; Folkerts, G.; Nijkamp, F.P.; Blalock, J.E. A novel peptide CXCR ligand derived from extracellular matrix degradation during airway inflammation. *Nat. Med.* **2006**, *12*, 317–323. [CrossRef]
74. O'Reilly, P.; Jackson, P.L.; Noerager, B.; Parker, S.; Dransfield, M.; Gaggar, A.; Blalock, J.E. N- $\alpha$ -PGP and PGP, potential biomarkers and therapeutic targets for COPD. *Respir. Res.* **2009**, *10*, 38. [CrossRef]
75. Wells, J.M.; O'Reilly, P.J.; Szul, T.; Sullivan, D.I.; Handley, G.; Garrett, C.; McNicholas, C.M.; Roda, M.A.; Miller, B.E.; Tal-Singer, R.; et al. An Aberrant Leukotriene A4Hydrolase–Proline-Glycine-Proline Pathway in the Pathogenesis of Chronic Obstructive Pulmonary Disease. *Am. J. Respir. Crit. Care Med.* **2014**, *190*, 51–61. [CrossRef]
76. Wells, J.M.; Jackson, P.L.; Viera, L.; Bhatt, S.P.; Gautney, J.; Handley, G.; King, R.W.; Xu, X.; Gaggar, A.; Bailey, W.C.; et al. A Randomized, Placebo-controlled Trial of Roflumilast. Effect on Proline-Glycine-Proline and Neutrophilic Inflammation in Chronic Obstructive Pulmonary Disease. *Am. J. Respir. Crit. Care Med.* **2015**, *192*, 934–942. [CrossRef]
77. Hardison, M.T.; Galin, F.S.; Calderon, C.E.; Djekic, U.V.; Parker, S.B.; Wille, K.M.; Jackson, P.L.; Oster, R.A.; Young, K.R.; Blalock, J.E.; et al. The Presence of a Matrix-Derived Neutrophil Chemoattractant in Bronchiolitis Obliterans Syndrome after Lung Transplantation. *J. Immunol.* **2009**, *182*, 4423–4431. [CrossRef]
78. Numao, S.; Hasler, F.; Laguerre, C.; Srinivas, H.; Wack, N.; Jäger, P.; Schmid, A.; Osmont, A.; Röthlisberger, P.; Houguenade, J.; et al. Feasibility and physiological relevance of designing highly potent aminopeptidase-sparing leukotriene A4 hydrolase inhibitors. *Sci. Rep.* **2017**, *7*, 13591. [CrossRef]
79. Haeggström, J.Z.; Wetterholm, A. Enzymes and receptors in the leukotriene cascade. *Cell. Mol. Life Sci.* **2002**, *59*, 742–753. [CrossRef]
80. Stsiapanava, A.; Samuelsson, B.; Haeggström, J.Z. Capturing LTA4 hydrolase in action: Insights to the chemistry and dynamics of chemotactic LTB4 synthesis. *Proc. Natl. Acad. Sci. USA* **2017**, *114*, 9689–9694. [CrossRef]
81. Haeggström, J.Z. Leukotriene A4 Hydrolase/Aminopeptidase, the Gatekeeper of Chemotactic Leukotriene B4 Biosynthesis. *J. Biol. Chem.* **2004**, *279*, 50639–50642. [CrossRef]
82. Haeggström, J.Z.; Tholander, F.; Wetterholm, A. Structure and catalytic mechanisms of leukotriene A4 hydrolase. *Prostaglandins Other Lipid Mediat.* **2007**, *83*, 198–202. [CrossRef]
83. Stsiapanava, A.; Olsson, U.; Wan, M.; Kleinschmidt, T.; Rutishauser, D.; Zubarev, R.A.; Samuelsson, B.; Rinaldo-Matthis, A.; Haeggstrom, J.Z. Binding of Pro-Gly-Pro at the active site of leukotriene A4 hydrolase/aminopeptidase and development of an epoxide hydrolase selective inhibitor. *Proc. Natl. Acad. Sci. USA* **2014**, *111*, 4227–4232. [CrossRef]
84. Thunnissen, M.M.G.M.; Nordlund, P.; Haeggström, J.Z. Crystal structure of human leukotriene A(4) hydrolase, a bifunctional enzyme in inflammation. *Nat. Struct. Biol.* **2001**, *8*, 131–135. [CrossRef]
85. Low, C.M.; Akthar, S.; Patel, D.F.; Löser, S.; Wong, C.-T.; Jackson, P.L.; Blalock, J.E.; Hare, S.A.; Lloyd, C.M.; Snelgrove, R.J. The development of novel LTA4H modulators to selectively target LTB4 generation. *Sci. Rep.* **2017**, *7*, 44449. [CrossRef] [PubMed]
86. Tholander, F.; Muroya, A.; Roques, B.-P.; Fournié-Zaluski, M.-C.; Thunnissen, M.M.G.M.; Haeggström, J.Z. Structure-Based Dissection of the Active Site Chemistry of Leukotriene A4 Hydrolase: Implications for M1 Aminopeptidases and Inhibitor Design. *Chem. Biol.* **2008**, *15*, 920–929. [CrossRef] [PubMed]
87. Jeong, C.-H.; Bode, A.M.; Pugliese, A.; Cho, Y.-Y.; Kim, H.-G.; Shim, J.-H.; Jeon, Y.-J.; Li, H.; Jiang, H.; Dong, Z. [6]-Gingerol Suppresses Colon Cancer Growth by Targeting Leukotriene A4Hydrolase. *Cancer Res.* **2009**, *69*, 5584–5591. [CrossRef] [PubMed]
88. Chen, X.; Li, N.; Wang, S.; Wu, N.; Hong, J.; Jiao, X.; Krasna, M.J.; Beer, D.G.; Yang, C.S. Leukotriene A4 Hydrolase in Rat and Human Esophageal Adenocarcinomas and Inhibitory Effects of Bestatin. *JNCI J. Natl. Cancer Inst.* **2003**, *95*, 1053–1061. [CrossRef]
89. Chen, X.; Wang, S.; Wu, N.; Yang, C. Leukotriene A4 Hydrolase as a Target for Cancer Prevention and Therapy. *Curr. Cancer Drug Targets* **2004**, *4*, 267–283. [CrossRef]
90. Oi, N.; Yamamoto, H.; Langfald, A.; Bai, R.; Lee, M.-H.; Bode, A.M.; Dong, Z. LTA4H regulates cell cycle and skin carcinogenesis. *Carcinogenesis* **2017**, *38*, 728–737. [CrossRef]
91. El-Hakim, I.E.; Langdon, J.D.; Zakrzewski, J.T.; Costello, J.F. Leukotriene B4 and oral cancer. *Br. J. Oral Maxillofac. Surg.* **1990**, *28*, 155–159. [CrossRef]
92. Tong, W.-G.; Ding, X.-Z.; Talamonti, M.S.; Bell, R.H.; Adrian, T.E. LTB4 stimulates growth of human pancreatic cancer cells via MAPK and PI-3 kinase pathways. *Biochem. Biophys. Res. Commun.* **2005**, *335*, 949–956. [CrossRef]
93. Ihara, A.; Wada, K.; Yoneda, M.; Fujisawa, N.; Takahashi, H.; Nakajima, A. Blockade of Leukotriene B4 Signaling Pathway Induces Apoptosis and Suppresses Cell Proliferation in Colon Cancer. *J. Pharmacol. Sci.* **2007**, *103*, 24–32. [CrossRef]
94. Yang, P.; Sun, Z.; Chan, D.; Cartwright, C.A.; Vijjeswarapu, M.; Ding, J.; Chen, X.; Newman, R.A. Zyflamend<sup>®</sup> reduces LTB 4 formation and prevents oral carcinogenesis in a 7,12-dimethylbenz[ $\alpha$ ]anthracene (DMBA)-induced hamster cheek pouch model. *Carcinogenesis* **2008**, *29*, 2182–2189. [CrossRef]
95. Polyak, K.; Kato, J.Y.; Solomon, M.J.; Sherr, C.J.; Massague, J.; Roberts, J.M.; Koff, A. p27Kip1, a cyclin-Cdk inhibitor, links transforming growth factor-beta and contact inhibition to cell cycle arrest. *Genes Dev.* **1994**, *8*, 9–22. [CrossRef]
96. Shapira, M.; Ben-Izhak, O.; Linn, S.; Futerman, B.; Minkov, I.; Hershko, D.D. The prognostic impact of the ubiquitin ligase subunits Skp2 and Cks1 in colorectal carcinoma. *Cancer* **2005**, *103*, 1336–1346. [CrossRef]

97. He, W.; Wang, X.; Chen, L.; Guan, X. A Crosstalk Imbalance Between p27Kip1 and Its Interacting Molecules Enhances Breast Carcinogenesis. *Cancer Biother. Radiopharm.* **2012**, *27*, 399–402. [CrossRef]
98. Tian, Y.-F.; Chen, T.-J.; Lin, C.-Y.; Chen, L.-T.; Lin, L.-C.; Hsing, C.-H.; Lee, S.-W.; Sheu, M.-J.; Lee, H.-H.; Shiue, Y.-L.; et al. SKP2 overexpression is associated with a poor prognosis of rectal cancer treated with chemoradiotherapy and represents a therapeutic target with high potential. *Tumor Biol.* **2013**, *34*, 1107–1117. [CrossRef]
99. Hershko, D.D. Oncogenic properties and prognostic implications of the ubiquitin ligase Skp2 in cancer. *Cancer* **2008**, *112*, 1415–1424. [CrossRef]
100. Timmerbeul, I.; Garrett-Engele, C.M.; Kossatz, U.; Chen, X.; Firpo, E.; Grunwald, V.; Kamino, K.; Wilkens, L.; Lehmann, U.; Buer, J.; et al. Testing the importance of p27 degradation by the SCFskp2 pathway in murine models of lung and colon cancer. *Proc. Natl. Acad. Sci. USA* **2006**, *103*, 14009–14014. [CrossRef]
101. Israel, E. The Effect of Inhibition of 5-Lipoxygenase by Zileuton in Mild-to-Moderate Asthma. *Ann. Intern. Med.* **1993**, *119*, 1059–1066. [CrossRef]
102. Röhn, T.A.; Numao, S.; Otto, H.; Loesche, C.; Thoma, G. Drug discovery strategies for novel leukotriene A4 hydrolase inhibitors. *Expert Opin. Drug Discov.* **2021**, *16*, 1483–1495. [CrossRef]
103. Haeggström, J.Z. Leukotriene biosynthetic enzymes as therapeutic targets. *J. Clin. Investig.* **2018**, *128*, 2680–2690. [CrossRef]
104. Elborn, J.S.; Horsley, A.; MacGregor, G.; Bilton, D.; Grosswald, R.; Ahuja, S.; Springman, E.B. Phase I Studies of Acebilustat: Biomarker Response and Safety in Patients with Cystic Fibrosis. *Clin. Transl. Sci.* **2017**, *10*, 28–34. [CrossRef]
105. Markert, C.; Thoma, G.; Srinivas, H.; Bollbuck, B.; Luond, R.M.; Miltz, W.; Walchli, R.; Wolf, R.; Hinrichs, J.; Bergsdorf, C.; et al. Discovery of LYS006, a Potent and Highly Selective Inhibitor of Leukotriene A4 Hydrolase. *J. Med. Chem.* **2021**, *64*, 1889–1903. [CrossRef]
106. EMPIRE CF: A Phase 2 Study to Evaluate the Efficacy, Safety, and Tolerability of CTX-4430 in Adult Cystic Fibrosis (CF) Patients. Available online: <https://clinicaltrials.gov/ct2/show/NCT02443688> (accessed on 5 December 2021).
107. CTX-4430 for the Treatment of Moderate to Severe Facial Acne Vulgaris. Available online: <https://clinicaltrials.gov/ct2/show/NCT02385760> (accessed on 5 December 2021).
108. Study of Efficacy and Safety of Investigational Treatments in Patients with Moderate to Severe Hidradenitis Suppurativa. Available online: <https://clinicaltrials.gov/ct2/show/NCT03827798> (accessed on 5 December 2021).
109. Study to Assess the Efficacy and Safety of LYS006 in Patients with Moderate to Severe Inflammatory Acne. Available online: <https://clinicaltrials.gov/ct2/show/NCT03497897> (accessed on 5 December 2021).
110. Study of Efficacy, Safety, and Tolerability of LYS006, in Patients with Mild to Moderate Ulcerative Colitis. Available online: <https://clinicaltrials.gov/ct2/show/NCT04074590> (accessed on 5 December 2021).
111. Study of Various Treatments in Non-alcoholic Fatty Liver Disease (NAFLD) Patients Who Have Aspects of Non-alcoholic Steatohepatitis (NASH) (NEXSCOT). Available online: <https://clinicaltrials.gov/ct2/show/NCT04147195> (accessed on 5 December 2021).
112. Audat, S.A.; Al-Shar'i, N.A.; Al-Oudat, B.A.; Bryant-Friedrich, A.; Bedi, M.F.; Zayed, A.L.; Al-Balas, Q.A. Identification of Human Leukotriene A4 Hydrolase Inhibitors Using Structure-Based Pharmacophore Modeling and Molecular Docking. *Molecules* **2020**, *25*, 2871. [CrossRef]
113. Snelgrove, R.J.; Jackson, P.L.; Hardison, M.T.; Noerager, B.D.; Kinloch, A.; Gaggar, A.; Shastry, S.; Rowe, S.M.; Shim, Y.M.; Hussell, T.; et al. A Critical Role for LTA<sub>4</sub>H in Limiting Chronic Pulmonary Neutrophilic Inflammation. *Science* **2010**, *330*, 90–94. [CrossRef]
114. Akthar, S.; Patel, D.F.; Beale, R.C.; Peiró, T.; Xu, X.; Gaggar, A.; Jackson, P.L.; Blalock, J.E.; Lloyd, C.M.; Snelgrove, R.J. Matrikines are key regulators in modulating the amplitude of lung inflammation in acute pulmonary infection. *Nat. Commun.* **2015**, *6*, 8423. [CrossRef]
115. Ramazi, S.; Allahverdi, A.; Zahiri, J. Evaluation of post-translational modifications in histone proteins: A review on histone modification defects in developmental and neurological disorders. *J. Biosci.* **2020**, *45*, 135. [CrossRef]
116. Ramazi, S.; Zahiri, J. Post-translational modifications in proteins: Resources, tools and prediction methods. *Database* **2021**, *2021*, baab012. [CrossRef]
117. Mann, M.; Jensen, O.N. Proteomic analysis of post-translational modifications. *Nat. Biotechnol.* **2003**, *21*, 255–261. [CrossRef]
118. Xu, Y.; Chou, K.-C. Recent Progress in Predicting Posttranslational Modification Sites in Proteins. *Curr. Top. Med. Chem.* **2015**, *16*, 591–603. [CrossRef]
119. Zurlo, G.; Guo, J.; Takada, M.; Wei, W.; Zhang, Q. New Insights into Protein Hydroxylation and Its Important Role in Human Diseases. *Biochim. Biophys. Acta Rev. Cancer* **2016**, *1866*, 208–220. [CrossRef]
120. Lee, D.Y.; Teyssier, C.; Strahl, B.D.; Stallcup, M.R. Role of Protein Methylation in Regulation of Transcription. *Endocr. Rev.* **2005**, *26*, 147–170. [CrossRef]
121. Aletta, J.M.; Cimato, T.R.; Ettinger, M.J. Protein methylation: A signal event in post-translational modification. *Trends Biochem. Sci.* **1998**, *23*, 89–91. [CrossRef]
122. Smith, W.A.; Schurter, B.T.; Wong-Staal, F.; David, M. Arginine Methylation of RNA Helicase A Determines Its Subcellular Localization. *J. Biol. Chem.* **2004**, *279*, 22795–22798. [CrossRef] [PubMed]
123. Mowen, K.A.; Schurter, B.T.; Fathman, J.W.; David, M.; Glimcher, L.H. Arginine methylation of NIP45 modulates cytokine gene expression in effector T lymphocytes. *Mol. Cell* **2004**, *15*, 559–571. [CrossRef] [PubMed]



124. McBride, A.E.; Silver, P.A. State of the Arg. *Cell* **2001**, *106*, 5–8. [CrossRef]
125. Guccione, E.; Richard, S. The regulation, functions and clinical relevance of arginine methylation. *Nat. Rev. Mol. Cell Biol.* **2019**, *20*, 642–657. [CrossRef]
126. Gayatri, S.; Bedford, M.T. Readers of histone methylarginine marks. *Biochim. Biophys. Acta Gene Regul. Mech.* **2014**, *1839*, 702–710. [CrossRef]
127. Hughes, R.M.; Waters, M.L. Arginine Methylation in a  $\beta$ -Hairpin Peptide: Implications for Arg– $\pi$  Interactions,  $\Delta C_p^\circ$ , and the Cold Denatured State. *J. Am. Chem. Soc.* **2006**, *128*, 12735–12742. [CrossRef]
128. Wu, Q.; Schapira, M.; Arrowsmith, C.H.; Baryte-Lovejoy, D. Protein arginine methylation: From enigmatic functions to therapeutic targeting. *Nat. Rev. Drug Discov.* **2021**, *20*, 509–530. [CrossRef]
129. Zhang, X.; Huang, Y.; Shi, X. Emerging roles of lysine methylation on non-histone proteins. *Cell. Mol. Life Sci.* **2015**, *72*, 4257–4272. [CrossRef]
130. Chang, B.; Chen, Y.; Zhao, Y.; Bruick, R.K. JMJD6 Is a Histone Arginine Demethylase. *Science* **2007**, *318*, 444–447. [CrossRef]
131. Wesche, J.; Kühn, S.; Kessler, B.M.; Salton, M.; Wolf, A. Protein arginine methylation: A prominent modification and its demethylation. *Cell. Mol. Life Sci.* **2017**, *74*, 3305–3315. [CrossRef]
132. Webby, C.J.; Wolf, A.; Gromak, N.; Dreger, M.; Kramer, H.; Kessler, B.; Nielsen, M.L.; Schmitz, C.; Butler, D.S.; Yates, J.R.; et al. Jmjd6 Catalyses Lysyl-Hydroxylation of U2AF65, a Protein Associated with RNA Splicing. *Science* **2009**, *325*, 90–93. [CrossRef]
133. Vangimalla, S.S.; Ganesan, M.; Kharbanda, K.K.; Osna, N.A. Bifunctional Enzyme JMJD6 Contributes to Multiple Disease Pathogenesis: New Twist on the Old Story. *Biomolecules* **2017**, *7*, 41. [CrossRef]
134. Meng, Y.; Li, H.; Liu, C.; Zheng, L.; Shen, B. Jumonji domain-containing protein family: The functions beyond lysine demethylation. *J. Mol. Cell Biol.* **2018**, *10*, 371–373. [CrossRef]
135. Hewitson, K.S.; Granatino, N.; Welford, R.W.D.; McDonough, M.A.; Schofield, C.J. Oxidation by 2-oxoglutarate oxygenases: Non-haem iron systems in catalysis and signalling. *Philos. Trans. R. Soc. A Math. Phys. Eng. Sci.* **2005**, *363*, 807–828. [CrossRef]
136. Liu, Y.; Long, Y.-H.; Wang, S.-Q.; Zhang, Y.-Y.; Li, Y.-F.; Mi, J.-S.; Yu, C.-H.; Li, D.-Y.; Zhang, J.-H.; Zhang, X.-J. JMJD6 regulates histone H2A.X phosphorylation and promotes autophagy in triple-negative breast cancer cells via a novel tyrosine kinase activity. *Oncogene* **2018**, *38*, 980–997. [CrossRef]
137. Lee, S.; Liu, H.; Hill, R.; Chen, C.; Hong, X.; Crawford, F.; Kingsley, M.; Zhang, Q.; Liu, X.; Chen, Z.; et al. JMJD6 cleaves MePCE to release positive transcription elongation factor b (P-TEFb) in higher eukaryotes. *eLife* **2020**, *9*, e53930. [CrossRef]
138. Yang, J.; Chen, S.; Yang, Y.; Ma, X.; Shao, B.; Yang, S.; Wei, Y.; Wei, X. Jumonji domain-containing protein 6 protein and its role in cancer. *Cell Prolif.* **2020**, *53*. [CrossRef]
139. Mantri, M.; Krojer, T.; Bagg, E.A.; Webby, C.J.; Butler, D.S.; Kochan, G.; Kavanagh, K.L.; Oppermann, U.; McDonough, M.A.; Schofield, C.J. Crystal Structure of the 2-Oxoglutarate- and Fe(II)-Dependent Lysyl Hydroxylase JMJD6. *J. Mol. Biol.* **2010**, *401*, 211–222. [CrossRef]
140. Clifton, I.J.; McDonough, M.A.; Ehrismann, D.; Kershaw, N.J.; Granatino, N.; Schofield, C.J. Structural studies on 2-oxoglutarate oxygenases and related double-stranded  $\beta$ -helix fold proteins. *J. Inorg. Biochem.* **2006**, *100*, 644–669. [CrossRef]
141. Dawson, M.A.; Kouzarides, T. Cancer Epigenetics: From Mechanism to Therapy. *Cell* **2012**, *150*, 12–27. [CrossRef] [PubMed]
142. Unoki, M.; Masuda, A.; Dohmae, N.; Arita, K.; Yoshimatsu, M.; Iwai, Y.; Fukui, Y.; Ueda, K.; Hamamoto, R.; Shirakawa, M.; et al. Lysyl 5-Hydroxylation, a Novel Histone Modification, by Jumonji Domain Containing 6 (JMJD6). *J. Biol. Chem.* **2013**, *288*, 6053–6062. [CrossRef] [PubMed]
143. Böse, J.; Gruber, A.D.; Helming, L.; Schiebe, S.; Wegener, I.; Hafner, M.; Beales, M.; Köntgen, F.; Lengeling, A. The phosphatidylserine receptor has essential functions during embryogenesis but not in apoptotic cell removal. *J. Biol.* **2004**, *3*, 15. [CrossRef] [PubMed]
144. Boeckel, J.N.; Guarani, V.; Koyanagi, M.; Roexe, T.; Lengeling, A.; Schermuly, R.T.; Gellert, P.; Braun, T.; Zeiher, A.; Dimmeler, S. Jumonji domain-containing protein 6 (Jmjd6) is required for angiogenic sprouting and regulates splicing of VEGF-receptor 1. *Proc. Natl. Acad. Sci. USA* **2011**, *108*, 3276–3281. [CrossRef]
145. Liu, X.; Si, W.; Liu, X.; He, L.; Ren, J.; Yang, Z.; Yang, J.; Li, W.; Liu, S.; Pei, F.; et al. JMJD6 promotes melanoma carcinogenesis through regulation of the alternative splicing of PAK1, a key MAPK signaling component. *Mol. Cancer* **2017**, *16*, 175. [CrossRef]
146. Donati, B.; Lorenzini, E.; Ciarrocchi, A. BRD4 and Cancer: Going beyond transcriptional regulation. *Mol. Cancer* **2018**, *17*, 164. [CrossRef]
147. Miller, T.E.; Liau, B.B.; Wallace, L.C.; Morton, A.R.; Xie, Q.; Dixit, D.; Factor, D.C.; Kim, L.J.Y.; Morrow, J.J.; Wu, Q.; et al. Transcription elongation factors represent in vivo cancer dependencies in glioblastoma. *Nature* **2017**, *547*, 355–359. [CrossRef]
148. Wong, M.; Sun, Y.; Xi, Z.; Milazzo, G.; Poulos, R.C.; Bartenhagen, C.; Bell, J.L.; Mayoh, C.; Ho, N.; Tee, A.E.; et al. JMJD6 is a tumorigenic factor and therapeutic target in neuroblastoma. *Nat. Commun.* **2019**, *10*, 3319. [CrossRef]
149. Manfredi, J.; Wang, F.; He, L.; Huangyang, P.; Liang, J.; Si, W.; Yan, R.; Han, X.; Liu, S.; Gui, B.; et al. JMJD6 Promotes Colon Carcinogenesis through Negative Regulation of p53 by Hydroxylation. *PLoS Biol.* **2014**, *12*, e1001819. [CrossRef]
150. Zheng, H.; Tie, Y.; Fang, Z.; Wu, X.; Yi, T.; Huang, S.; Liang, X.; Qian, Y.; Wang, X.; Pi, R.; et al. Jumonji domain-containing 6 (JMJD6) identified as a potential therapeutic target in ovarian cancer. *Signal. Transduct. Target. Ther.* **2019**, *4*, 24. [CrossRef]

151. Ran, T.; Xiao, R.; Huang, Q.; Yuan, H.; Lu, T.; Liu, W. In Silico Discovery of JMJD6 Inhibitors for Cancer Treatment. *ACS Med. Chem. Lett.* **2019**, *10*, 1609–1613. [CrossRef]
152. Wang, T.; Zhang, R.; Liu, Y.; Fang, Z.; Zhang, H.; Fan, Y.; Yang, S.; Xiang, R. Discovery of a new class of JMJD6 inhibitors and structure–activity relationship study. *Bioorganic Med. Chem. Lett.* **2021**, *44*, 128109. [CrossRef]



Review

# Precision Anti-Cancer Medicines by Oligonucleotide Therapeutics in Clinical Research Targeting Undruggable Proteins and Non-Coding RNAs

Damiano Bartolucci <sup>1</sup>, Andrea Pession <sup>2</sup>, Patrizia Hrelia <sup>3</sup> and Roberto Tonelli <sup>3,\*</sup>

<sup>1</sup> R&D Department, BIOGENERA SpA, 40064 Bologna, Italy; damiano.bartolucci@biogenera.com

<sup>2</sup> Pediatric Unit, IRCCS, Azienda Ospedaliero-Universitaria di Bologna, 40138 Bologna, Italy; andrea.pession@unibo.it

<sup>3</sup> Department of Pharmacy and Biotechnology, University of Bologna, 40126 Bologna, Italy; patrizia.hrelia@unibo.it

\* Correspondence: roberto.tonelli@unibo.it

**Abstract:** Cancer incidence and mortality continue to increase, while the conventional chemotherapeutic drugs confer limited efficacy and relevant toxic side effects. Novel strategies are urgently needed for more effective and safe therapeutics in oncology. However, a large number of proteins are considered undruggable by conventional drugs, such as the small molecules. Moreover, the mRNA itself retains oncological functions, and its targeting offers the double advantage of blocking the tumorigenic activities of the mRNA and the translation into protein. Finally, a large family of non-coding RNAs (ncRNAs) has recently emerged that are also dysregulated in cancer, but they could not be targeted by drugs directed against the proteins. In this context, this review describes how the oligonucleotide therapeutics targeting RNA or DNA sequences, are emerging as a new class of drugs, able to tackle the limitations described above. Numerous clinical trials are evaluating oligonucleotides for tumor treatment, and in the next few years some of them are expected to reach the market. We describe the oligonucleotide therapeutics targeting undruggable proteins (focusing on the most relevant, such as those originating from the MYC and RAS gene families), and for ncRNAs, in particular on those that are under clinical trial evaluation in oncology. We highlight the challenges and solutions for the clinical success of oligonucleotide therapeutics, with particular emphasis on the peculiar challenges that render it arduous to treat tumors, such as heterogeneity and the high mutation rate. In the review are presented these and other advantages offered by the oligonucleotide as an emerging class of biotherapeutics for a new era of precision anti-cancer medicine.

**Citation:** Bartolucci, D.; Pession, A.; Hrelia, P.; Tonelli, R. Precision Anti-Cancer Medicines by Oligonucleotide Therapeutics in Clinical Research Targeting Undruggable Proteins and Non-Coding RNAs. *Pharmaceutics* **2022**, *14*, 1453. <https://doi.org/10.3390/pharmaceutics14071453>

Academic Editor: Hassan Bousbaa

Received: 30 May 2022

Accepted: 8 July 2022

Published: 12 July 2022

**Publisher's Note:** MDPI stays neutral with regard to jurisdictional claims in published maps and institutional affiliations.



**Copyright:** © 2022 by the authors. Licensee MDPI, Basel, Switzerland. This article is an open access article distributed under the terms and conditions of the Creative Commons Attribution (CC BY) license (<https://creativecommons.org/licenses/by/4.0/>).

**Keywords:** cancer therapy; new anti-cancer drugs; precision medicine; undruggable targets; non-coding RNAs; oligonucleotide therapeutics

## 1. Introduction

Cancer is a disease of uncontrolled cell growth caused by various genetic (i.e., mutations, amplifications, deletions, and translocations) and epigenetic alterations (i.e., hypo- or hypermethylation), and characterized by dysregulation in multiple cellular signaling pathways involved in processes, including cellular proliferation, survival, cell death, differentiation, energy metabolism, genomic stability, DNA repair, and escape from immune surveillance [1]. Both intra-/inter-tumoral heterogeneities caused by genetic, epigenetic, and regional adaptive patterns are extremely high in some cancers. The molecular heterogeneity is considered as one of the major failures of cancer therapeutics, radiotherapy, and chemotherapy, and various responses range from no response due to intrinsic resistance to a complete response [2]. In addition, conventional untargeted chemotherapeutic strategies often increase the rate of cancer mutations, and impose a selection of tumor cells that become resistant to the chemotherapy, which could also create new mutations in the

healthy cells, in addition to the toxicities and adverse side effects on healthy organs, such as bone marrow, kidneys, heart, brain, liver, eyes, and other normal tissues [3]. Cancer incidence and mortality continue to increase rapidly worldwide [4,5]. The conventional cancer chemotherapeutic drugs confer relevant toxic side effects [6–8], while their clinical efficacy is often obtained for limited periods of time, because drug resistance emerges and the tumors evolve [9,10]. Therefore, the development and discovery of novel therapeutic strategies are urgently needed to offer more effective and safe therapeutic options. Novel cancer therapy strategies emerged in the recent years with the potential to selectively detect and eradicate malignant cells, with minimal damage to the healthy tissue. In this context, many mutated genes that play a causative role in tumorigenesis have been identified and characterized in many cases, and could constitute the starting point for targeted and effective precision medicine therapies. However, it is estimated that a large number of proteins (about 70–85%) are considered undruggable, or difficult to be targeted by conventional drug discovery approaches, such as the small molecules [11–13]. These traditional approaches could not generate new drugs that enable a precision medicine that maximizes specificity against the target, while minimizing or eliminating the potential side effects and toxicity. The limitation of other relevant classes of drugs, such as the monoclonal antibodies, is the localization of the target protein in the cells, with cytoplasmic or nuclear proteins that are difficult to be reached and targeted by this approach [14]. Moreover, the mRNA itself could retain the oncological functions before it is translated in the protein. For instance, it was demonstrated that the mRNA could act as a sponge, by recruiting and so neutralizing the other regulatory elements (mostly microRNAs) critical for the maintenance of normal function in the cell, as reported for the MYCN mRNA to the let-7 microRNA [14,15]; therefore, if the drug acts only at the level of the protein, this oncogenic effect would remain, while when the drug acts at the mRNA level, it has the double advantage of blocking the translation into protein and blocking the specific pro-tumor activities of the mRNA.

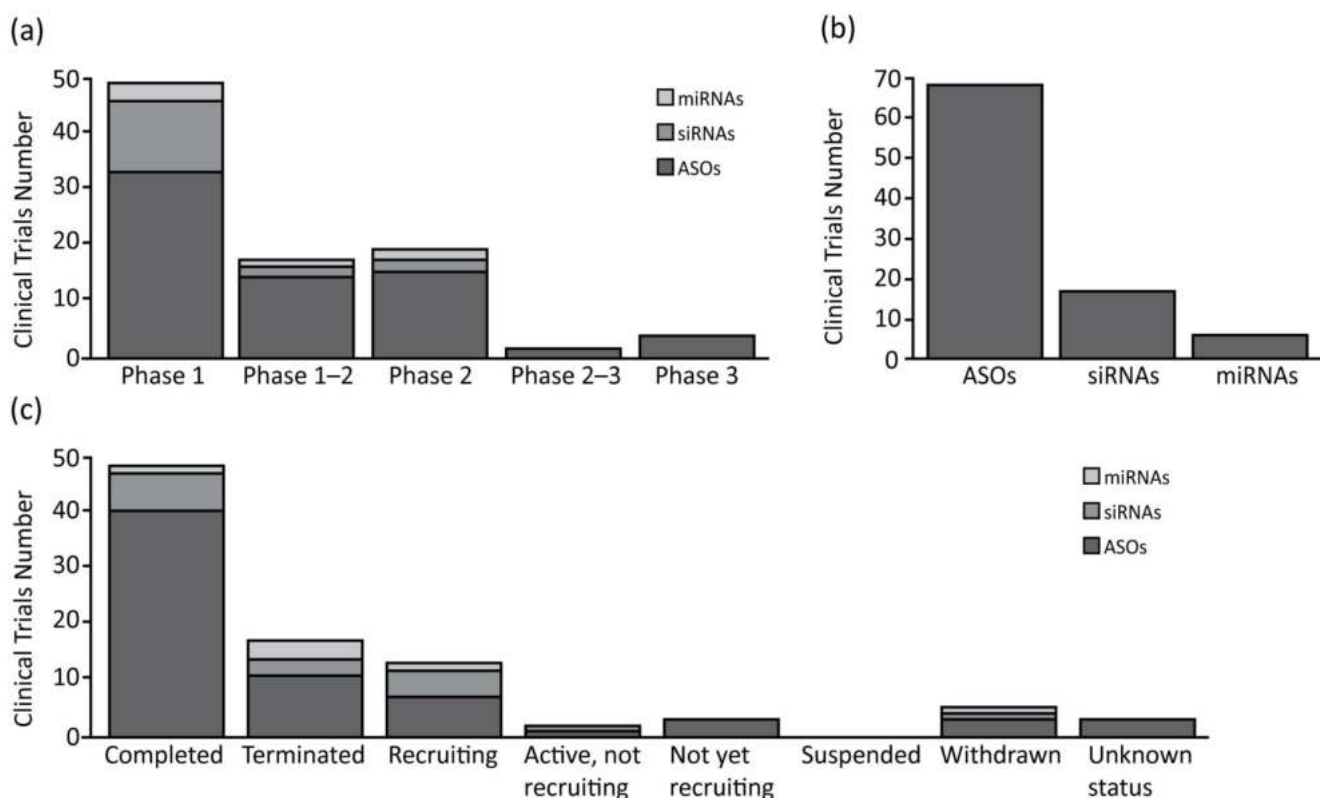
Finally, in the recent years emerged a large part of the genome containing genes whose transcription generate a large family of different non-coding RNAs (ncRNAs). This ncRNAs plays key regulatory roles in both normal cellular activity and disease, including cancer, but because ncRNAs are not translated into proteins, they could not be targeted by conventional drug discovery approaches directed against the proteins [16,17]. In this context, nucleic acid therapeutics by oligonucleotides that target RNA or DNA sequences, are emerging as a new and highly promising class of drugs, able to tackle the limitations described above, and to open a new era of tailored drugs and precision medicine also in cancer therapy [18–20]. Indeed, oligonucleotides showed the ability to also specifically target the so-called undruggable proteins and ncRNAs. Currently, oligonucleotide therapeutics have been only approved for the treatment of different rare diseases [21], but none is yet available for cancer therapy. However, many clinical trials with oligonucleotides are ongoing for tumor treatment, and, in the next few years, some of them are expected to reach the market.

## **2. Oligonucleotide Therapeutics as New Targeted Anti-Cancer Drugs for Challenging or Undruggable Proteins**

The molecular targets for therapy could be divided in two major categories, namely, druggable and undruggable. “Druggability” implies that the target molecule must have structures that should allocate the specific binding and inhibition by low-molecular-weight compounds. Typically, a protein is considered druggable if it contains a cavity, usually a well-defined catalytic cleft. It is estimated that almost 70% of the human proteins [22] are considered difficult to be targeted, including the transcription factors that are widely thought to be undruggable due to the lack of catalytic clefts and the much-sought drug-binding pockets. To date, targeting the relevant transcription factors with small molecular compounds remains challenging. In particular, relevant examples are the members of the MYC family and RAS family of oncogenes, that account for amongst the highest rate of mutations in cancers and define aggressive tumor behaviors [23,24]. The strategies that propose the indirect blocking of transcription factors by targeting their upstream or

downstream pathway genes could result in less efficacy and also specific side effects in healthy cells. New strategies are urgently needed to generate drugs able to tackle the undruggable targets in cancer. In this respect, oligonucleotide therapeutics enable a direct targeting of the gene by acting at the level of the RNA or at the level of the DNA, based on the Watson-Crick complementary rule of binding. Different classes of oligonucleotides have been developed since the first use in clinical was proposed in the 1970s, but, in particular, antisense oligonucleotides (ASOs), small interfering RNAs (siRNAs), and microRNAs (miRNAs) imposed their presence as the most representative for clinical development and therapeutic application [25,26]. For a better understanding of the impact and the relevance of each group, we performed a research study in clinicaltrials.gov (accessed on 1 May 2022) using “Cancer” as the keyword and focusing our attention on clinical trials available for each class of oligonucleotide in analysis.

As expected, the ASOs are the most represented oligonucleotides, accounting for 66% of all of the compounds analyzed (75% of clinical trials), and are the only class with some compounds in clinical phase II or III (Figure 1 and Table 1). Interestingly, only 12% of the clinical studies are recruiting or active, and the majority are completed (59%), or in other status (29%). From a structural point of view, the ASOs range in size from 12 to 30 nucleotides, are single stranded, and work through the classic Watson-Crick base pairing and can act as both gene expression inhibitors or splicing modulators [27,28].



**Figure 1.** Summary of clinical trials therapies using oligonucleotide in oncology. (a) Antisense oligonucleotides (ASOs), small interfering RNAs (siRNAs) and microRNAs (miRNAs) number of clinical trials divided for clinical phases; (b) Total clinical trials number for each class of oligonucleotide analyzed; (c) ASOs, siRNAs and miRNAs number of clinical trials divided for clinical status condition.

**Table 1.** Summary of oligonucleotides in clinical trials for oncology.

Oligonucleotide	Target	Drug Type	Cancer Type	Clinical Phase	Clinical Trials ID
WGI-0301	AKT1	ASO	Advanced Solid Tumors	Phase 1	NCT05267899
AZD5312	AR	ASO	Advanced Solid Tumors with Androgen Receptor Pathway as a Potential Factor	Phase 1	NCT02144051
BP1002 (L-Bcl-2 antisense oligonucleotide)	BCL-2	ASO	Mantle Cell Lymphoma   Peripheral T-cell Lymphoma (PTCL)   Cutaneous T-cell Lymphoma (CTCL)   Chronic Lymphocytic Leukemia (CLL)   Small Lymphocytic Lymphoma (SLL)   Follicular Lymphoma   Marginal Zone Lymphoma   Hodgkin Lymphoma   Waldenström Macroglobulinemia   DLBCL	Phase 1	NCT04072458
PNT2258	BCL-2	ASO	Cancer   Lymphoma   Prostate Cancer   Melanoma	Phase 1	NCT01191775
LErafAON	CRAF	ASO	Neoplasms	Phase 1	NCT0024648   NCT0024661   NCT00100672
AZD8701	FOXP3	ASO	Clear Cell Renal Cell Cancer   Non-Small-Cell Lung Cancer   Triple Negative Breast Neoplasms   Squamous Cell Cancer of Head and Neck   Small-Cell Lung Cancer   Gastroesophageal Cancer   Melanoma   Cervical Cancer   Advanced Solid Tumors	Phase 1	NCT04504669
BP1001-A (Liposomal Grb2 Antisense Oligonucleotide)	GRB-2	ASO	Solid Tumor, Adult   Carcinoma, Ovarian Epithelial   Fallopian Tube Neoplasms   Endometrial Cancer   Peritoneal Cancer   Solid Tumor	Phase 1	NCT04196257
EZN-2968	HIF-1 $\alpha$	ASO	Neoplasms   Liver Metastases   Carcinoma   Lymphoma	Phase 1	NCT01120288   NCT00466583
AZD4785	KRAS	ASO	Non-Small-Cell Lung Cancer   Advanced Solid Tumors	Phase 1	NCT03101839
TASO-001	TGF- $\beta$ 2	ASO	Solid Tumor	Phase 1	NCT04862767
SD-101 (CpG Oligonucleotide)	TLR9	ASO	Advanced Malignant Solid Neoplasm   Extracranial Solid Neoplasm   Metastatic Malignant Solid Neoplasm	Phase 1	NCT038831295
CpG7909 (PF3512676)	TLR9	ASO	Intraocular Melanoma   Malignant Conjunctival Neoplasm   Melanoma (Skin)	Phase 1	NCT00471471
ISS 1018 (CpG ODN)	TLR9	ASO	Colorectal Neoplasms	Phase 1	NCT00403052
IONIS-STAT3Rx (AZD9150)	STAT3	ASO	Hepatocellular Carcinoma   Ovarian Cancer   Ascites   Gastrointestinal Cancer   Advanced Cancers   DLBCL   Lymphoma	Phase 1   2	NCT01839604   NCT02417753   NCT01563302   NCT02549651
ISIS 183750	eIF4E	ASO	Colorectal Neoplasms   Colorectal Carcinoma   Colorectal Tumors	Phase 1   Phase 2	NCT01675128

Table 1. Cont.

Oligonucleotide	Target	Drug Type	Cancer Type	Clinical Phase	Clinical Trials ID
Apatorsen (OGX-427)	HSP-27	ASO	Squamous Cell Lung Cancer   Bladder Cancer   Urothelial Carcinoma   Prostate Cancer	Phase 1   Phase 2	NCT02423590   NCT00959868   NCT00487786   NCT01780545   NCT01120470
GTI-2040	R2 subunit of RNR	ASO	Carcinoma, Renal Cell   Metastases, Neoplasm	Phase 1   Phase 2	NCT00056173
Aezea (Cenersen)	TP53	ASO	Myelodysplastic Syndromes   Acute Myelogenous Leukemia	Phase 1   Phase 2	NCT02243124   NCT00967512
VEGF-Antisense Oligonucleotide	VEGF	ASO	Mesothelioma	Phase 1   Phase 2	NCT00668499
AEG35156	XIAP	ASO	Human Mammary Carcinoma   Carcinoma   Pancreas   Non-Small-Cell Lung	Phase 1   Phase 2	NCT00385775   NCT00558545   NCT00557596   NCT00558922
XIAP Antisense	XIAP	ASO	Leukemia, Myelomonocytic, Acute	Phase 1   Phase 2	NCT00363974
Oblimersen (G3139)	BCL-2	ASO	Lymphoma   Prostate Cancer   Lung Cancer   Melanoma (Skin)   Colorectal Cancer   Breast Cancer	Phase 1   Phase 2   Phase 3	NCT00070083   NCT00080847   NCT00017251   NCT00070343   NCT00016263   NCT00017602   NCT00085228   NCT00030641   NCT00063934   NCT00004870   NCT00005032   NCT00054548   NCT00543231   NCT00543205   NCT00636545   NCT00078234   NCT00021749   NCT00024440   NCT00059813



Table 1. Cont.

Oligonucleotide	Target	Drug Type	Cancer Type	Clinical Phase	Clinical Trials ID
Apatorsen (OGX-427)	HSP-27	ASO	Squamous Cell Lung Cancer   Bladder Cancer   Urothelial Carcinoma   Prostate Cancer	Phase 1   Phase 2	NCT02423590   NCT00959868   NCT00487786   NCT01780545   NCT01120470
GTI-2040	R2 subunit of RNR	ASO	Carcinoma, Renal Cell   Metastases, Neoplasm	Phase 1   Phase 2	NCT00056173
Aezea (Cenersen)	TP53	ASO	Myelodysplastic Syndromes   Acute Myelogenous Leukemia	Phase 1   Phase 2	NCT02243124   NCT00967512
G4460 (c-myc antisense oligonucleotide)	C-MYB	ASO	Hematologic Malignancies	Phase 2	NCT00780052   NCT00002592
ISIS 5132	CRAF	ASO	Breast Cancer	Phase 2	NCT00003236
BP1001 (Liposomal Grb2 Antisense Oligonucleotide)	GRB-2	ASO	Recurrent Adult Acute Myeloid Leukemia   Acute Lymphoblastic Leukemia   Myelodysplastic Syndrome   Ph1 Positive CML	Phase 2	NCT02923986   NCT02781883   NCT01159028
IGV-001 Cell Immunotherapy	IGF type 1 receptor	ASO	Glioblastoma Multiforme   Glioblastoma	Phase 2	NCT04485949
ISIS 3521	PKC $\alpha$	ASO	Breast Cancer	Phase 2	NCT00003236
STP705	TGF- $\beta$ 1 and COX-2	ASO	Squamous Cell Carcinoma in Situ	Phase 2	NCT04844983
CpG-ODN	TLR9	ASO	Glioblastoma   Lung Cancer   Hepatocellular Carcinoma   Solid Tumor	Phase 2	NCT00190424   NCT04952272
Custirsen (OGX-011)	clusterin	ASO	Prostate Cancer   Bladder Cancer   Breast Cancer   Kidney Cancer   Lung Cancer   Ovarian Cancer   Unspecified Adult Solid Tumor	Phase 2   Phase 3	NCT00054106   NCT00258375   NCT00471432   NCT01083615
INT-1B3	JNK1	miRNA	Solid Tumor	Phase 1	NCT04675996

Table 1. Cont.

Oligonucleotide	Target	Drug Type	Cancer Type	Clinical Phase	Clinical Trials ID
TargomiRs	Multiple oncogenes, including BCL2, MCL1, CCND1, and WNT3A	miRNA	Malignant Pleural Mesothelioma   Non-Small-Cell Lung Cancer	Phase 1	NCT02369198
MRX34	30 unique oncogenes, including but not limited to MET, MYC, PDGFR- $\alpha$ , CDK4/6 and BCL2	miRNA	Melanoma	Phase 1   Phase 2	NCT01829971   NCT02862145
Cobomarsen (MRG-106)	mir-155	miRNA	Cutaneous T-Cell Lymphoma / Mycosis Fungoides	Phase 2	NCT03837457   NCT03713320
siRNA-transfected peripheral blood mononuclear cells APN401	CBLB	siRNA	Metastatic Malignant Neoplasm in the Brain   Metastatic Solid Neoplasm   Recurrent Colorectal Carcinoma   Recurrent Melanoma   Recurrent Pancreatic Cancer   Recurrent Renal Cell Cancer	Phase 1	NCT03087591   NCT02166255
EphA2-targeting DOPC-encapsulated siRNA	EPHA2	siRNA	Advanced Malignant Solid Neoplasm	Phase 1	NCT01591356
NBF-006	GSTP	siRNA	Non-Small-Cell Lung Cancer   Pancreatic Cancer   Colorectal Cancer	Phase 1	NCT03819387
Mesenchymal Stromal Cells-derived Exosomes with KRAS G12D siRNA	KRASG12D	siRNA	Metastatic Pancreatic Adenocarcinoma   Pancreatic Ductal Adenocarcinoma	Phase 1	NCT03608631
Proteasome siRNA and tumor antigen RNA-transfected dendritic cells	LMP2, LMP7, MECL1	siRNA	Metastatic Melanoma   Absence of CNS Metastases	Phase 1	NCT00672542
CALAA-01	M2 subunit of ribonucleotide reductase (R2)	siRNA	Cancer   Solid Tumor	Phase 1	NCT00689065

Table 1. Cont.

Oligonucleotide	Target	Drug Type	Cancer Type	Clinical Phase	Clinical Trials ID
TKM-080301	PLK1	siRNA	Colorectal Cancer with Hepatic Metastases   Pancreas Cancer with Hepatic Metastase   Gastric Cancer With Hepatic Metastases   Breast Cancer With Hepatic	Phase 1	NCT01437007
SLN124	TMPRSS6	siRNA	Non-transfusion-dependent Thalassemia   Low Risk Myelodysplastic Syndrome	Phase 1	NCT04176653
DCR-MYC	MYC	siRNA	Solid Tumors   Multiple Myeloma   Non-Hodgkins Lymphoma   Pancreatic Neuroendocrine Tumors   PNET   NHL   Hepatocellular Carcinoma	Phase 1   Phase 2	NCT02110563   NCT02314052
Atu027	PNK3	siRNA	Advanced Solid Tumors   Carcinoma, Pancreatic Ductal	Phase 1   Phase 2	NCT00938574   NCT01808638
siG12D LODER	KRASG12D	siRNA	Pancreatic Ductal Adenocarcinoma   Pancreatic Cancer	Phase 2	NCT01188785   NCT01676259
STP705	TGF- $\beta$ 1, COX-2 mRNA	siRNA	Squamous Cell Carcinoma in Situ	Phase 2	NCT04844983
CpG-STAT3 siRNA CAS3/SS3	TLR9 and STAT3	siRNA	B-Cell Non-Hodgkin Lymphoma   Diffuse Large B-Cell Lymphoma   Follicular Lymphoma   Mantle Cell Lymphoma   Marginal Zone Lymphoma   Small Lymphocytic Lymphoma	Phase 1	NCT04995536

The second most common oligonucleotide class is represented by the siRNAs, accounting for 25% of the compounds. The analysis shows how they are the subject of almost the same number of clinical trials as the miRNAs, but with a higher number of trials in Phase I (76% of total siRNAs' clinical trials). In relation to the clinical trial status, the siRNAs show 35% active/recruiting trials, and 18% of the trials terminated with no suspension (Figure 1 and Table 1). The siRNAs are the longest oligonucleotides in size (20–25 nt), they are double stranded, and work in complex with RISC to post-transcriptionally silence the target gene expressions [29]. These compounds can be chemically synthesized, maintaining the characteristics needed for the proper activation of the enzymatic mRNA degradation, allowing their use as therapeutic compounds [30].

Finally, the miRNAs represent the smallest class with only four compounds in clinical trial (9%). Despite their number, these compounds are well represented in clinical trials, as mentioned before, and are equally distributed among phases 1 and 2. Furthermore, a relevant number of clinical trials are recruiting (17%), while others are now terminated (50%), or withdrawn (17%) (Figure 1 and Table 1). The miRNAs are small (18–25 nt) single stranded non-coding RNAs, containing usually sequences complementary to one or more of the target RNAs [31]. They work similarly to the siRNAs, activating the RISC complex after formation of miRNAs duplex [32]. The miRNAs can also be synthesized by mimicking their normal biological function, to be redirected against specific targets for therapeutic purposes [33].

### 2.1. Oligonucleotide Therapeutics Targeting the MYC Gene Family

The MYC family is composed of c-MYC, MYCN, and MYCL [34]. The MYC gene family encodes for the basic helix-loop-helix-leucine zipper (bHLH-LZ) transcription factor proteins which exhibit a high-structural homology, including highly conserved Myc boxes (MB) and a basic region (BR), helix-loop-helix (HLH) and leucine zipper (LZ) motifs [35,36]. The MYC gene family is highly involved in tumors in which they are often dysregulated and mutated (mainly by translocations or gene amplification), resulting in overexpression and association with tumor aggressiveness and poor prognosis [37]. The proteins that originate from the MYC gene family are mainly considered undruggable with the conventional approaches that rely on small molecules.

#### 2.1.1. Oligonucleotide Therapeutics Targeting MYC

MYC has been proposed as an important oncogenic target for its role in cell proliferation and survival, angiogenesis, metastasis, drug resistance, and poor patient prognosis [38,39]. MYC-targeted oligonucleotide therapeutics, based on a small interfering RNA lipid-based nanoparticle (DCR-MYC, Dicerna Pharmaceuticals), to inhibit the oncogene MYC at the level of the mRNA, was developed to treat various cancer types, including hepatocellular carcinoma (HCC), solid tumors, lymphoma, or multiple myeloma. The liposomal delivery system of the DCR-MYC is based on EnCore Dicerna's proprietary technology, due to its specific Envelope and Core lipid contents. For targeting MYC, Dicer-substrate small interfering RNA (DsiRNA) was used in the drug formulation. DsiRNAs, longer duplex RNAs, are Dicer substrates to be subsequently processed into small interfering RNAs (siRNAs), and have an increased potency in RNA interfering processing [40]. The data from the Phase I—dose-escalation study indicated that DCR-MYC presents good clinical and metabolic responses in patients at a variety of dose levels [41]. However, Phase I (clinicaltrials.gov (accessed on 1 May 2022) NCT02110563) and Phase Ib/2 trials (clinicaltrials.gov (accessed on 1 May 2022) NCT02314052) were terminated on the sponsor's decision, due to a lack of the gene-silencing effectiveness that was anticipated by the company [42].

#### 2.1.2. Oligonucleotide Therapeutics Targeting MYCN

The MYCN oncogene is a well-known driver of different, highly aggressive tumors (including Neuroblastoma, Small-Cell Lung Cancer, Rhabdomyosarcoma), where it is

dysregulated and amplified and is strongly associated with poor survival prognosis [43,44]. MYCN overexpression reprograms the tumor cells towards a stem-like phenotype that promotes proliferation and cell growth, while inhibiting cell differentiation and apoptosis. It also favors immune escape, invasion, metastases, and angiogenesis [45,46]. Interestingly, MYCN is expressed during embryogenesis and has a highly restricted pattern of expression in normal cells after birth [47]. All of these factors make the N-Myc protein a promising target for a tumor-specific therapy. However, inhibitors against the N-Myc protein have, to date, largely failed and have led to N-Myc being currently considered to be an undruggable target [48].

It has been demonstrated that an alternative approach concerns specific gene expression inhibition at the level of DNA through a MYCN-specific antigene peptide nucleic acid (agPNA) oligonucleotide [49,50]. The antigene oligonucleotide approach (via persistent blocking at the level of transcription) has shown advantages in blocking translation by the antisense oligonucleotide strategies. The peptide nucleic acids (PNAs) have shown promising results as antigenes, due to their resistance to proteases and nucleases and their ability to potently and specifically bind the target DNA [51,52]. Differing from the use of antisense oligonucleotides, which inhibit mRNA translation, the antigene approach involves binding to the chromosomal DNA, resulting in the inhibition of transcription. By persistently blocking the transcription, the antigene oligonucleotides showed higher efficacy compared with antisense oligonucleotides [49,51]. Antigene therapy by targeting MYCN transcription has great potential in treating MYCN-expressing tumors, as was previously demonstrated in the preclinical treatment of neuroblastoma and rhabdomyosarcoma by MYCN-specific agPNA [50,51]. Neuroblastoma (NB) is the deadliest pediatric tumor. Approximately 25% of patients with a NB diagnosis present with MYCN amplification (MNA), which is linked to a poor prognosis, metastasis, and recurrence [53,54]. It has been shown that BGA002, a new and highly improved agPNA oligonucleotide, is able to specifically target a unique sequence on the human MYCN gene [55]. BGA002 showed a specific, dose-dependent decrease in the MYCN mRNA and protein, while decreasing the viability in a panel of 20 NB cell lines, followed by the block of different MYCN tumorigenic alterations, and to the anti-tumor efficacy of BGA002 in vivo in a MNA NB mouse model [55]. Moreover, while MYCN drives a tumor immunosuppressive environment, which impacts survival in several MYCN-positive tumors, the block of MYCN by the anti-MYCN BGA002 is able to reactivate and restore the effectiveness of the natural killer immune cells against NB [56]. It has been also found that BGA002 restores the retinoic acid (RA) response, leading to a differentiation or apoptosis in the MNA NB and also to a significant increase in survival in a mouse model of MNA-NB [57]. This study shows that it is possible to realize precision medicine by the identification of optimal combined drugs that can achieve a potent and selective block of cancer pathways only in tumor cells, preserving the impact of side effects on normal cells. MNA is not restricted to NB, and the restoration of RA treatment could be beneficial in different MNA tumors. BGA002 has received orphan drug designation from the Food and Drug Administration (orphan registry: DRU-2017-6085) and from the European Medicines Agency (orphan registry: EU/3/12/1016). Based upon its well-tolerated regulatory safety profile package, BGA002 is now moving to Phase I clinical trials in neuroblastoma patients.

## 2.2. Oligonucleotide Therapeutics Targeting the RAS Gene Family

Ras proteins regulate the activation of different patterns strongly involved in cancer, such as cell proliferation, differentiation, and survival [58]. This family of proteins is encoded by three ubiquitously expressed genes, HRAS, KRAS, and NRAS, that share most of their sequence and function [59]. In normal conditions, they act as the activator of more than 20 different proteins from different effectors' families [60], so their constitutive activation may cause a deregulation of many cell functions and lead to cancer. In particular, the frequency and the pattern of the gene mutations can associate different Ras genes with different cancer types [61]. While each Ras member is involved in cancer, KRAS is surely the major cancer-causing isoform, accounting for 75% of all Ras-associated tumors [62].

The other isoforms NRAS (17%) and HRAS (7%) account for only a small subset of cancer types [62]. In the past years, many attempts were performed to develop direct Ras gene family inhibitors, but the protein structure showed characteristics that were not very compatible with the small molecules' approach [63]. As the same post-translational approach was ineffective, due to isoform-specific differences [64], so a more specific approach was needed in consideration of the relevance of the KRAS specific isoform to the others. In particular, the oligonucleotides have a promising therapeutic potential as mutant-specific RAS inhibitors, active against any major mutation.

### Oligonucleotide Therapeutics Targeting KRAS

The KRAS-targeted siRNA-polymeric nanoparticles for local therapy, siG12D-LODER, were designed by Silenseed Ltd. for patients with locally advanced pancreatic cancer. The biodegradable polymer matrix, Local Drug EluteR (LODER), was used to release the G12D-mutated KRAS-targeted siRNA locally within a pancreatic tumor microenvironment for controlled and prolonged delivery [65]. The LODER matrix consists of a copolymer of poly lactic-co-glycolic acid (PLGA) of a high molecular weight greater than 50 kD. The siG12D-LODER was designed to be properly inserted and placed into the tumor using a standard biopsy procedure [66,67]. A slow and stable release of siRNA from siG12D-LODER over a few months was demonstrated when incubated in PBS. The siG12D-LODER remarkably suppressed the growth of pancreatic tumors in both subcutaneous and orthotopic, xenograft, and syngraft mouse models, without causing any toxicity [65]. In another preclinical study, following subcutaneous implantation of the siG12D-LODER, all of the rats exhibited local and systemic safety and tolerability, without any adverse effects or deaths [67]. A Phase I clinical trial was conducted by injection of the siG12D-LODER drug into patients via the endoscopic ultrasound (EUS) biopsy needle (clinicaltrials.gov (accessed on 1 May 2022) NCT01188785). The patients received a combination treatment of siG12D-LODER with gemcitabine or FOLFIRINOX in the phase II study, reporting an enhanced therapeutic effect [66]. phase II trials of siG12D-LODER with gemcitabine + nab-paclitaxel are currently underway (clinicaltrials.gov (accessed on 1 May 2022) NCT01676259).

The ASO strategy has also been proposed for the treatment of the KRAS mutation in cancer. AZD4785 is a cEt-modified ASO [68], complementary to a KRAS mRNA sequence, developed by Ionis in collaboration with Astra Zeneca. Interestingly, the advanced chemistry of this compound and the resulting potency, allowed its use without any delivery agent in the first preclinical studies. As expected, AZD4785 is able to directly downregulate KRAS mRNA at the nM level in vitro (IC<sub>50</sub> 10 nM), and is also able to increase survival and reduce tumor growth in a mouse model of lung cancer [69]. From the clinical point of view, only one Phase I study is reported (NCT03101839) as completed in 2017, without any recent advancement.

### 2.3. Oligonucleotide Therapeutics Targeting STAT3

STAT3 is a protein activated by members of the JAK family through phosphorylation [70]. In its phosphorylated form, STAT3 dimerizes and works in the nucleus as a transcription factor involved in cell proliferation, development, differentiation, inflammation, and apoptosis. Constitutive activation can be found in several types of human cancer [71,72], and it is able to increase the level of different cancer-related molecules, such as surviving, Bcl-XL, cyclin D1/D2, C-Myc, Mcl-1, and vascular endothelial growth factor (VEGF), favoring tumorigenic progression [73,74]. For this reason, STAT3 represents one of the most interesting targets for therapeutics in oncology, and in the past years many strategies were developed to effectively inhibit STAT3 expression. For example, synthetic inhibitors, such as CDDO-Me or FLLL32, can reduce the activity of the protein downstream, blocking the JAK/STAT3 interaction or inhibiting the DNA binding process but cannot overcome the issue related to the overall aspect of STAT3 overexpression [75,76]. In a different way, oligonucleotide compounds are able to specifically target STAT3 reducing the protein

expression, directly downregulating the mRNA. A new compound, such as AZD9150 (ISIS 481464), a 16-nucleotide next generation chemistry antisense oligonucleotide [77], or CpG-Stat3 siRNA, a conjugate of an oligonucleotide TLR9 agonist linked to a STAT3 siRNA [78], are, in fact, designed to specifically reach this aim. In particular, the combined use of synthetic oligonucleotide agonists for TLRs and siRNA target-specific, is a novel and potent strategy that can achieve both target delivery enhancement of siRNA to immune cells and antitumor immune response activation [78]. Furthermore, this strategy can target a broad spectrum of TLRs, including TLR3, TLR7, TLR8 and TLR9, allowing the selection of the best combination of oligonucleotides and receptors [79,80]. The TLR9-specific oligodeoxynucleotides, containing an unmethylated CpG-motif (CpG ODN), represent the first choice, because they are already in clinical testing [81]. Additionally, CpG ODN are efficiently internalized by various antigen-presenting cells (APC), such as macrophages, B cells, and dendritic cells (DCs), and their binding to TLR-9 can initiate immune response cascade, effectively providing the immuno-stimulation [81,82]. Obviously, the interest in these new compounds is high, and preclinical Phase I and/or 2 clinical studies are still ongoing and promising.

#### 2.4. Oligonucleotide Therapeutics Targeting BCL-2

BCL-2 is one of the first-discovered regulators of the apoptosis process. This gene is overexpressed by the translocation  $t(14;18)$  in B-cell lymphoma and is implicated in many different cancers, such as melanoma, breast, and lung carcinoma [83]. BCL-2 is not only involved in the neoplastic development, but also in the resistance mechanism to cancer treatment [84]. In this context, the therapies pointed at BCL-2 inhibition can be considered crucial to overcome resistance to the common strategies for cancer treatments [85]. Oblimersen (G3139) is certainly the most studied BCL-2 inhibitor and was involved in many clinical studies (Table 1). Unfortunately, despite its high efficacy *in vitro* and *in vivo* preclinical studies [86,87], the clinical studies showed how it is important to administer this compound in combination to achieve significant results. Phase 3 clinical studies (data not shown) are indeed available, but only for this form of application. It is important to underline that other BCL-2 inhibitors have been developed, such as BP1002 [88] and PNT2258 [89]. Both of them are still in clinical Phase I trials; the first active, and the second successfully completed, and they represent promising compounds for the future of the Bcl-2 inhibitor.

### 3. Oligonucleotide Therapeutics as New Targeted Anti-Cancer Drugs for Non-Coding RNAs

The only function of RNA in cells was thought to be as a template for protein synthesis, but extensive research in the last few decades proved otherwise [90]. For many years, scientists have called the non-protein-coding part of the human genome as “junk DNA”. Approximately 80% of the genome is biologically active and transcribed to RNA, while only 2% is transcribed to protein-coding mRNA [91], as groundbreaking projects on the human genome, such as the FANTOM [92] and ENCODE [93], have contributed, revealed and elucidated. Non-coding RNAs (ncRNAs) constitute a large part of the genome and are transcribed from DNA but not translated into protein [94]. The ncRNAs can be classified in consideration of their function and/or dimension in many different ways [95,96]. Normally, ncRNA are conventionally divided into two major groups, based on the threshold of 200 nucleotides (nt) of length, namely short non-coding RNA (sncRNA) and long non-coding RNA (lncRNA) [90,97]. The sncRNAs (<200 nt) include both structural and regulatory RNA [97,98]. The structural sncRNAs include the RNAs involved in fundamental housekeeping functions. For example, the ribosomal RNAs (rRNA) and transfer RNAs (tRNAs) are involved in the mRNA translation process to protein, while the small nuclear RNAs (snRNAs) and small nucleolar RNAs (snoRNAs) resemble other fundamental functions concerning rRNA modification and/or mRNA maturation [95,99]. In addition to these conventional RNAs, the sncRNAs include several regulatory RNAs, such as microRNAs

(miRNAs), small interference RNAs (siRNAs) and Piwi-interacting RNAs (piRNAs), all of which are able to regulate gene expression through different mechanisms [100,101]. The lncRNAs (>200 nt) are a group of more heterogeneous ncRNAs, with an unknown function. Interestingly, the lncRNAs show many characteristics in common with the coding RNA, having the possibility of expressing differentially, using splice variants [102], and including many different types of RNA with a great variety of mechanisms of action, mostly used to term and classify it [103].

The expression of some ncRNAs is dysregulated and contributes to the development and progression of various diseases, including cancer [104]. The ncRNAs have been shown to have great potential as therapeutic targets, drugs, and diagnostic markers [105,106]. Therefore, the ncRNA-based therapies by oligonucleotides have gained great interest for use with the targets considered “undruggable”, and for their potential use as a part of precision or personalized medicine in the treatment of a wide range of diseases, including cancer [107]. With the growing body of evidence on the biology and clinical significance of ncRNA, a number of investigators in academia, biotechnology, and pharmaceutical companies are currently working on developing oligonucleotide therapeutics to regulate the pathogenic ncRNA gene expression in various diseases [105,108]. miRNA and siRNA are the most studied ncRNAs and, over the past decade, 23 clinical trials (Figure 1 and Table 1) have been initiated for testing the efficacy of miRNA and siRNA in cancer therapeutics. Several miRNA-based therapeutics recently moved to phase II clinical trials for advanced cancers, including TargomiR (miR-16 mimic-based therapy) in mesothelioma [109], Cobomarsen (anti-miR-155) in T-cell leukemia/lymphoma [110], and Miravirsen (anti-miR-122) in individuals with hepatitis C infection [111].

### 3.1. microRNA Therapeutics

Two types of oligonucleotides are currently being used as miRNA therapeutics: miRNA mimetics to restore the levels of miRNAs downregulated in cancer; and antagomiRs to inhibit overexpressed miRNAs [112]. Thus far, six clinical trials have been investigating miRNA therapeutics’ potential as oncology drugs. Of these, three were terminated and one withdrawn, leaving one Phase I trial completed and one still recruiting patients. The termination of NCT01829971 and the withdrawal of NCT02862145 were due to frequently related serious adverse events reported by the investigators, while the NCT03837457 and NCT03713320 trials were terminated due to business reasons and patients placed in other trials, according to the comments on clinicaltrials.gov (accessed on 1 May 2022) [113].

#### 3.1.1. Cobomarsen

Cobomarsen, or MRG-106 (anti-miR-155, miRagen Therapeutics, Inc, Boulder, Colorado), is a locked nucleic acid (LNA)-modified oligonucleotide inhibitor of miR-155. miR-155 is found at high levels and is related to a worse prognosis in lymphoma and leukemia. It plays an important role in the progression of mycosis fungoides (MF), the most common type of cutaneous T-cell lymphoma (CTCL) [114]. The preclinical studies of cobomarsen in NSG mice carrying B-cell lymphoma (ABC-DLBCL) xenografts indicated that by intravenous injection, the tumor volume was reduced, apoptosis was induced, and the expression of direct target of miR-155 was upregulated. In addition, it was emphasized that the drug did not exhibit any toxic effects [115]. Phase I clinical studies evaluated the safety, tolerability, pharmacokinetics, and potential efficacy of the drug in patients with a subset of lymphomas and leukemias. The patients received the drug by subcutaneous or intravenous injection for six dosages in the first 26 days, later once a week. The results showed that the treatments sustained a reduction in the lesion burden accompanied by an inhibited miR-155 level. Moreover, it displayed an efficient clinical activity without serious adverse effects (clinicaltrials.gov (accessed on 1 May 2022) NCT02706886) [116]. phase II clinical trials began to compare the efficacy and safety of cobomarsen with vorinostat, the Food and Drug Administration (FDA) approved the drug for CTCL (clinicaltrials.gov (accessed on 1 May 2022) NCT03713320), and to study its efficacy and safety in subjects



who have confirmed disease progression after treatment with vorinostat (clinicaltrials.gov (accessed on 1 May 2022) NCT03837457) [117]. However, phase II studies were terminated on the company's decision, without any safety or efficacy issues [118]. In the Phase I trial (NCT02580552), the patients showed acceptable toxicity and drug responses in all four of the patients recruited for the intra-tumoral injection, with decreased neoplastic cell density and depth [110]. The FDA granted Orphan Drug Designation to cobomarsen for mycosis fungoides type cutaneous T-cell lymphoma in 2017.

### 3.1.2. TargomiRs (a miR-16 Mimic and a MIR16-Based miRNA Mimetic)

TargomiRs is a miRNA replacement therapy and is the first technology to complete Phase I trials of carrier-based miRNA therapeutics in cancer patients [119]. It consists of three components: (I) a miR-16 mimic that acts as a tumor suppressor in a range of cancer types; (II) an EnGeneIC Delivery Vehicle (EDV); and (III) a targeting ligand; anti-epidermal growth factor (EGFR) bispecific antibody. EDVs are non-living bacterial minicells of a 400 nm diameter that have the ability to deliver chemotherapeutic drugs, nucleic acids, and proteins [120]. Bcl-2 and CCND1 genes, which promote cancer progression, have been reported to be important targets of miR-16. In vitro studies indicate that depleted miR-16 levels could be restored with MIR16 mimetics in malignant pleural mesothelioma cell lines, which led to growth inhibition [121]. In vivo delivery of the miR-16 mimic via EDV to nude mice with malignant pleural mesothelioma (MPM) xenografted tumors significantly inhibited the tumor growth without any safety concerns from the minicells. Additionally, the miR-16 mimic, at doses less than 1 lg, had a powerful tumor inhibitory effect in vivo [121]. An open-label, dose-escalation Phase I study of TargomiRs (also called MesomiR-1) was conducted in patients with MPM. The results demonstrated that TargomiRs was well tolerated, together with early signs of antitumor efficacy and encouraging survival in patients. In addition, the phase II trial, in which TargomiRs will be added to standard chemotherapy, will begin soon (clinicaltrials.gov (accessed on 1 May 2022) NCT02369198) [109].

### 3.1.3. MRX34 (MiR-34a Mimic)

Phase I trials of MRX34, a MiR-34a mimic, were initiated in 2013 in patients with multiple solid tumors, including primary liver cancer, renal cell carcinoma, multiple myeloma, lymphoma, or small-cell lung cancer, with the strategy of restoring endogenous miR-34 using miRNA mimics. The liposome formulation is comprised of amphoteric lipids which are anionic at neutral or higher pH and cationic at lower pH values. This technology facilitates liposome formation, mixing lipids and miRNA in an acid environment, and increasing the specific tumor targeting. In fact, in normal biological fluids (at pH7–7.5), the nanoparticles may prevent an unwanted interaction with the negative charge of cellular membrane, but at the same time they can improve adhesion to tumor cells, in consideration of the lower pH normally found in tumor areas [122]. MRX34 was reported to directly regulate 24 oncogenes carrying essential roles in proliferation, cell cycle, metastasis, anti-apoptosis, the cancer cell self-renewal process, oncogenic transcription, and chemoresistance [123]. The systemic delivery of MRX34 into mice with orthotopic Hep3B and HuH7 liver cancer xenografts resulted in dramatic tumor growth reduction, and even tumor regression. The therapeutic doses used had no harmful side effects or immune stimulation in mice. Following a single administration of MRX34, multiple oncogenes of the key cancer pathways were inhibited, including Wnt/b-Catenin, MapK, c-Met, Hedgehog, and vascular endothelial growth factor (VEGF), while multiple genes of the p53 pathway were stimulated [124]. However, despite its very high therapeutic performance in preclinical studies, in 2016, Mirna Therapeutics discontinued the Phase I trials, due to immune-related severe adverse effects (SAEs) observed in five patients that resulted in four of their deaths (clinicaltrials.gov (accessed on 1 May 2022) NCT01829971). Further Phase I and II studies of MRX34 for melanoma treatment were also withdrawn because of SAE (clinicaltrials.gov (accessed on 1 May 2022) NCT02862145). Nevertheless, a recently published study reported that MRX34 treatment with dexamethasone premedication exhibited clinical activity and a

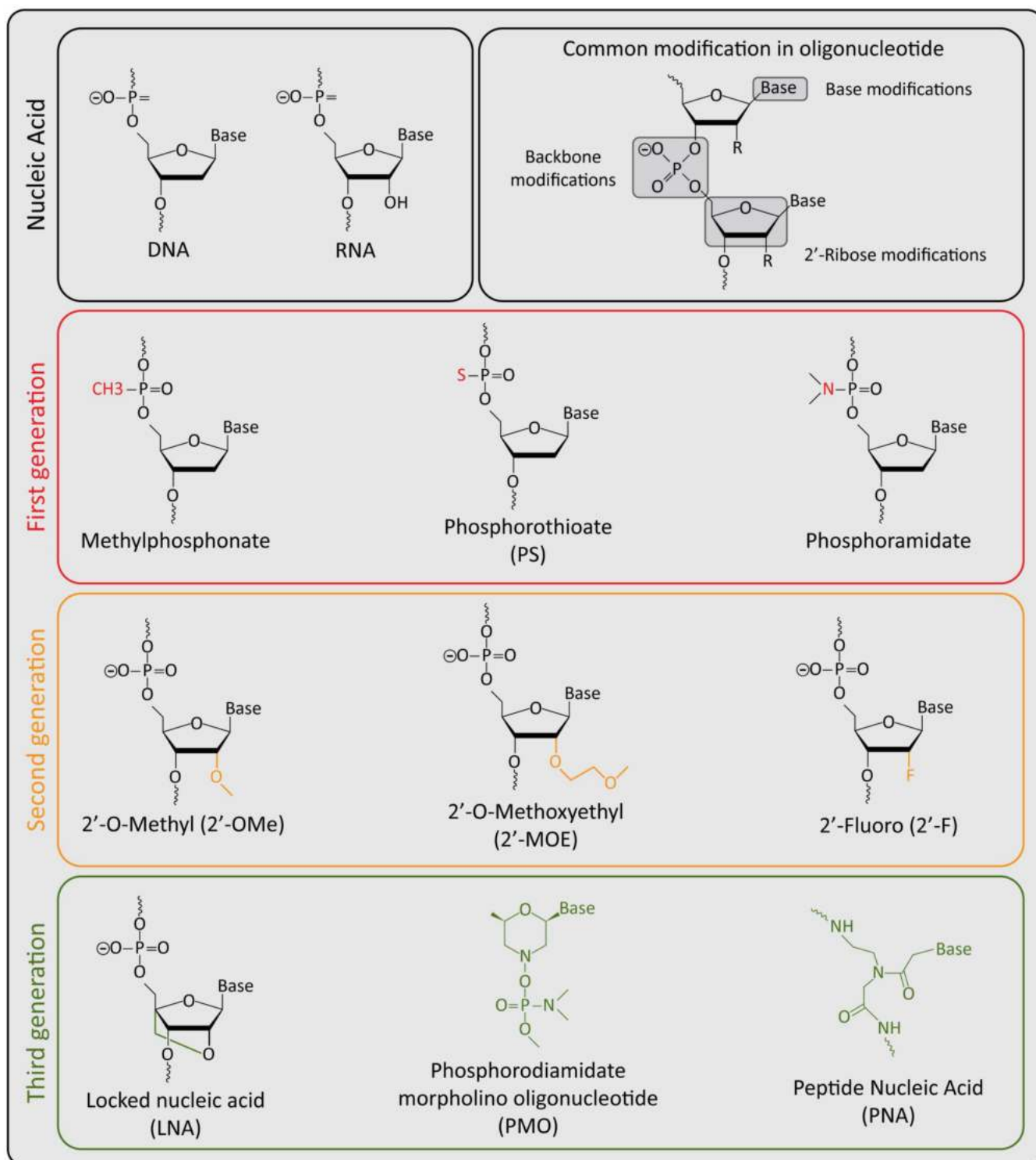
manageable toxicity profile in most of the patients [125]. All of the miRNA therapeutics across indications are still in clinical trials, with some positive outcomes thus far. Studies on miRNAs for cancer diagnosis have also exponentially increased in the last few years, and miRNA-based diagnostic tools are being developed [112].

#### 4. Challenges and Solutions for the Clinical Success of Oligonucleotide Therapeutics

The pharmacokinetic properties of oligonucleotides have been extensively characterized. Oligonucleotides show a wide tissue biodistribution in several organs, and the kidney, liver and spleen are the principal target organs [126,127]. In general, oligonucleotides are negatively charged and this chemical characteristic limits the cross of the blood-brain barrier, and consequently the localization to the brain and spinal cord. Thus, the treatment of brain tumors or of brain metastases of tumors that arise in other organs is not feasible by systemic treatment, but should require a route of administration that delivers the drug into the central nervous system [128]. Another possibility is the use of delivery systems, such as liposomes that could cross the blood-brain barrier [129]. The phosphorothioate modification of the backbone greatly improved the binding of the oligonucleotides to the plasma proteins, increasing the time of the oligonucleotides in the circulation, while reducing their elimination. *In vivo* stability and resistance to degradation by DNases or RNases have been greatly improved by the different chemical modifications introduced in the nucleotides and in the backbone [130,131]. Regarding the delivery to the target cells, oligonucleotides are hydrophilic molecules and cannot passively cross the plasma membrane in the same way as the small molecule lipophilic drugs. The delivery of oligonucleotides is mainly mediated by the formation of endosomes, but then they should be released to the cytoplasm before the fusion of the endosome with the lysosome triggers their degradation. In this respect, several systems of oligonucleotide delivery have focused on their endosomal escape to avoid their degradation [132–134]. Oligonucleotides are used without the delivery systems, or formulated with liposomes, nanoparticles, or conjugated with carriers, such as peptides, small molecules, and cell surface receptors. These delivery systems confer improved pharmacokinetic and pharmacodynamic *in vivo* properties, but should be carefully evaluated for their potential side effects, and the overall therapeutic index that should respect the means of the oligonucleotides when used, without any carrier. Many tumors are highly vascularized, and several reports indicate that cancer cells can be accessible and targeted by oligonucleotides [135–137].

Regarding the safety profile of the oligonucleotides, these could be related to the potential inhibition of the expression of off-target genes. However, performing a robust process of bioinformatic prediction of the complementary target sequences, and by the selection of optimal unique sequences only present in the target gene, followed by the experimental evaluation of potential off-target genes, means that it is possible to identify potent and specific drug-candidate oligonucleotides that maximize the on-target effects and greatly minimize the potential for off-target effects at a level that do not impact healthy cells [138–140]. Moreover, the introduction of the different chemical modifications to the oligonucleotide is reported to confer different improved characteristics. First generation ASOs, for example, are able to efficiently recruit RNase H (methylphosphonate and phosphorothioate); however, they show limited clinical application due to their sensibility for endo- and exonucleases as well as their limited binding affinity for the target and potential cytotoxic side effects [141,142]. Second generation ASOs introduce the first important improvement in oligonucleotides in overall stability and target engagement, reducing at the same time the off-target toxic effects [143,144]. Finally, the third generation ASOs shows the most enhanced resistance against nucleases and the best target affinity, compared to the previous generations [144–146]. The last generation is also potentially considered the most safe, thanks to its high specificity, affinity, and very limited off-target effects that can be avoided with many bioinformatic tools [131]. Thus, the chemical modification introduced into DNA or RNA oligonucleotides (Figure 2) have allowed an improvement in the specificity, stability, safety and pharmacokinetic/pharmacodynamic profiles, making

this class of compounds more reliable for clinical purposes [131,144]. Other potential toxic effects of oligonucleotides that are reported in preclinical and clinical studies could be related to a stimulation of the immune system [147], liver inflammation, or accumulation in the proximal tubule of the kidney [148–150]. However, these phenomena are usually not serious events and could be recovered after cessation of the oligonucleotide administration.



**Figure 2.** Graphic representation of chemical specific characteristics for each generation ASOs. Main chemical differences from common shared structure are marked with colors.

Regarding the potential stimulation of the immune system, in DNA-based oligonucleotides this phenomenon is related to the presence of CGs in the oligonucleotide that are recognized by the TLR9, followed by cytokine release and activation of the innate immunity [151,152]. In RNA-based oligonucleotides, the immune system stimulation is related to the activation of TLR3 and TLR7 [152,153]. Nevertheless, in the context of a cancer therapy, the activation of the immune system could not necessarily be considered a side effect, but rather an advantage and a potential dual anti-tumor effect of the oligonucleotide, in addition to the on-target inhibition of its specific cancer gene.

## 5. Challenges and Solutions Related to the Oligonucleotides for Cancer Therapy

Because of the high rate of new mutations that occur in the tumors, the new targeted drugs based on small molecules could also result in being ineffective, especially if the mutations fall in the functional domains (most often catalytic domains) of the proteins that are the most relevant target sites of these class of drugs [154,155]. For these reasons, new targeted cancer therapeutics are needed to enhance the efficacy and reduce the side effects. For a successful use of oligonucleotides for cancer therapy, many critical aspects and challenges have to be considered and solved. An optimal cancer treatment should employ a sustained therapeutic schedule, able to counteract the continuous growth of the tumor, especially those with aggressive characteristics. The most relevant and causative target genes in cancer present the challenge that they are often overexpressed. Therefore, to reach a therapeutic response, the oligonucleotide should exert a pharmacological inhibitory activity by contrasting its target gene, that is often constitutively activated at a high level of expression. However, a relevant level of inhibition of the target gene expression is not always required, because the cancer cells, following the downregulation of the critical key oncogenes, could become vulnerable and susceptible to elimination by other drugs or by the immune system, even if high levels of targeted gene expression inhibition are not reached.

## 6. Conclusions and Future Perspectives

Oligonucleotide therapeutics appear particularly adequate to respond to the challenges mentioned above. They could also expand the range of targets for a specific therapy for challenging or undruggable targets. Moreover, the drug discovery process to identify a new lead candidate oligonucleotide drug is, in general, shorter than the time required to identify a conventional lead drug based on a small molecule compound. This aspect is relevant to adapting and responding in a specific manner to the high rate of tumor mutations and heterogeneity. The numerous advantages offered by the oligonucleotide position them as an emerging and promising class of biotherapeutics for a new era of precision and personalized medicine in cancer therapy.

**Author Contributions:** D.B. conducted data acquisition and statistical analysis, figure assembling, and manuscript writing and design; A.P. and P.H. participated in manuscript revision and study supervision; R.T. performed study design and conceptualization, funding acquisition, manuscript revision and study supervision. All authors have read and agreed to the published version of the manuscript.

**Funding:** A. Pession, P. Hrelia and R. Tonelli are funded by the University of Bologna (ECOITONELL.). D. Bartolucci is funded by Biogenera SpA.

**Institutional Review Board Statement:** Not applicable.

**Informed Consent Statement:** Not applicable.

**Data Availability Statement:** Publicly available datasets at <https://www.clinicaltrials.gov/> were analyzed in this study.

**Conflicts of Interest:** R. Tonelli and A. Pession are Biogenera shareholders. D. Bartolucci is employed at Biogenera SpA. The authors declare no potential conflict of interest. The company had no role in the design of the study; in the collection, analyses, or interpretation of data; in the writing of the manuscript; or in the decision to publish the results.

## References

- Hanahan, D.; Weinberg, R.A. Hallmarks of Cancer: The Next Generation. *Cell* **2011**, *144*, 646–674. [CrossRef] [PubMed]
- Guo, M.; Peng, Y.; Gao, A.; Du, C.; Herman, J.G. Epigenetic Heterogeneity in Cancer. *Biomark. Res.* **2019**, *7*, 23. [CrossRef] [PubMed]
- Padma, V.V. An Overview of Targeted Cancer Therapy. *BioMedicine* **2015**, *5*, 19. [CrossRef]
- Siegel, R.L.; Miller, K.D.; Fuchs, H.E.; Jemal, A. Cancer Statistics, 2022. *CA Cancer J. Clin.* **2022**, *72*, 7–33. [CrossRef]
- Dalmartello, M.; La Vecchia, C.; Bertuccio, P.; Boffetta, P.; Levi, F.; Negri, E.; Malvezzi, M. European Cancer Mortality Predictions for the Year 2022 with Focus on Ovarian Cancer. *Ann. Oncol.* **2022**, *33*, 330–339. [CrossRef] [PubMed]
- Printezi, M.I.; Kilgallen, A.B.; Bond, M.J.G.; Štibler, U.; Putker, M.; Teske, A.J.; Cramer, M.J.; Punt, C.J.A.; Sluijter, J.P.G.; Huitema, A.D.R.; et al. Toxicity and Efficacy of Chronomodulated Chemotherapy: A Systematic Review. *Lancet Oncol.* **2022**, *23*, e129–e143. [CrossRef]
- Lowenthal, R.M.; Eaton, K. Toxicity of Chemotherapy. *Hematol. Oncol. Clin. N. Am.* **1996**, *10*, 967–990. [CrossRef]
- van den Boogaard, W.M.C.; Komninos, D.S.J.; Vermeij, W.P. Chemotherapy Side-Effects: Not All DNA Damage Is Equal. *Cancers* **2022**, *14*, 627. [CrossRef]
- Vasan, N.; Baselga, J.; Hyman, D.M. A View on Drug Resistance in Cancer. *Nature* **2019**, *575*, 299–309. [CrossRef]
- Bukowski, K.; Kciuk, M.; Kontek, R. Mechanisms of Multidrug Resistance in Cancer Chemotherapy. *Int. J. Mol. Sci.* **2020**, *21*, 3233. [CrossRef]
- Bakan, A.; Nevins, N.; Lakdawala, A.S.; Bahar, I. Druggability Assessment of Allosteric Proteins by Dynamics Simulations in the Presence of Probe Molecules. *J. Chem. Theory Comput.* **2012**, *8*, 2435–2447. [CrossRef] [PubMed]
- Schmidtke, P.; Barril, X. Understanding and Predicting Druggability. A High-Throughput Method for Detection of Drug Binding Sites. *J. Med. Chem.* **2010**, *53*, 5858–5867. [CrossRef] [PubMed]
- Neklesa, T.K.; Winkler, J.D.; Crews, C.M. Targeted Protein Degradation by PROTACs. *Pharmacol. Ther.* **2017**, *174*, 138–144. [CrossRef] [PubMed]
- Powers, J.T.; Tsanov, K.M.; Pearson, D.S.; Roels, F.; Spina, C.S.; Ebricht, R.; Seligson, M.; de Soysa, Y.; Cahan, P.; Theißen, J.; et al. Multiple Mechanisms Disrupt the Let-7 MicroRNA Family in Neuroblastoma. *Nature* **2016**, *535*, 246–251. [CrossRef]
- Perini, G.; Milazzo, G.; Narayan, N.; Ekert, P.G. Letting the Breaks off MYCN. *Cell Death Differ.* **2016**, *23*, 1904–1905. [CrossRef]
- Anastasiadou, E.; Jacob, L.S.; Slack, F.J. Non-Coding RNA Networks in Cancer. *Nat. Rev. Cancer* **2018**, *18*, 5–18. [CrossRef]
- Slack, F.J.; Chinnaiyan, A.M. The Role of Non-Coding RNAs in Oncology. *Cell* **2019**, *179*, 1033–1055. [CrossRef]
- Dai, H.; Abdullah, R.; Wu, X.; Li, F.; Ma, Y.; Lu, A.; Zhang, G. Pancreatic Cancer: Nucleic Acid Drug Discovery and Targeted Therapy. *Front. Cell Dev. Biol.* **2022**, *10*, 855474. [CrossRef]
- Le, B.T.; Raguraman, P.; Kosbar, T.R.; Fletcher, S.; Wilton, S.D.; Veedu, R.N. Antisense Oligonucleotides Targeting Angiogenic Factors as Potential Cancer Therapeutics. *Mol. Ther.-Nucleic Acids* **2019**, *14*, 142–157. [CrossRef]
- Tian, Z.; Liang, G.; Cui, K.; Liang, Y.; Wang, Q.; Lv, S.; Cheng, X.; Zhang, L. Insight into the Prospects for RNAi Therapy of Cancer. *Front. Pharmacol.* **2021**, *12*, 644718. [CrossRef]
- Igarashi, J.; Niwa, Y.; Sugiyama, D. Research and Development of Oligonucleotide Therapeutics in Japan for Rare Diseases. *Future Rare Dis.* **2022**, *2*, FRD19. [CrossRef]
- Wang, C.; Fang, H.; Zhang, J.; Gu, Y. Targeting “Undruggable” c-Myc Protein by Synthetic Lethality. *Front. Med.* **2021**, *15*, 541–550. [CrossRef] [PubMed]
- Huang, L.; Guo, Z.; Wang, F.; Fu, L. KRAS Mutation: From Undruggable to Druggable in Cancer. *Signal Transduct. Target. Ther.* **2021**, *6*, 386. [CrossRef]
- Duffy, M.J.; O’Grady, S.; Tang, M.; Crown, J. MYC as a Target for Cancer Treatment. *Cancer Treat. Rev.* **2021**, *94*, 102154. [CrossRef]
- Moumné, L.; Marie, A.-C.; Crouvezier, N. Oligonucleotide Therapeutics: From Discovery and Development to Patentability. *Pharmaceutics* **2022**, *14*, 260. [CrossRef] [PubMed]
- Stephenson, M.L.; Zamecnik, P.C. Inhibition of Rous Sarcoma Viral RNA Translation by a Specific Oligodeoxyribonucleotide. *Proc. Natl. Acad. Sci. USA* **1978**, *75*, 285–288. [CrossRef]
- Quemener, A.M.; Bachelot, L.; Forestier, A.; Donnou-Fournet, E.; Gilot, D.; Galibert, M. The Powerful World of Antisense Oligonucleotides: From Bench to Bedside. *WIREs RNA* **2020**, *11*, e1594. [CrossRef]
- Deleavey, G.F.; Damha, M.J. Designing Chemically Modified Oligonucleotides for Targeted Gene Silencing. *Chem. Biol.* **2012**, *19*, 937–954. [CrossRef]
- Bernstein, E.; Caudy, A.A.; Hammond, S.M.; Hannon, G.J. Role for a Bidentate Ribonuclease in the Initiation Step of RNA Interference. *Nature* **2001**, *409*, 363–366. [CrossRef]
- Thompson, J.D. Clinical Development of Synthetic SiRNA Therapeutics. *Drug Discov. Today Ther. Strateg.* **2013**, *10*, e133–e138. [CrossRef]

31. MacFarlane, L.-A.; Murphy, P.R. MicroRNA: Biogenesis, Function and Role in Cancer. *Curr. Genom.* **2010**, *11*, 537–561. [CrossRef] [PubMed]
32. Ha, M.; Kim, V.N. Regulation of MicroRNA Biogenesis. *Nat. Rev. Mol. Cell Biol.* **2014**, *15*, 509–524. [CrossRef]
33. Matsuyama, H.; Suzuki, H.I. Systems and Synthetic MicroRNA Biology: From Biogenesis to Disease Pathogenesis. *Int. J. Mol. Sci.* **2019**, *21*, 132. [CrossRef]
34. Ryan, K.M.; Birnie, G.D. *Myc* Oncogenes: The Enigmatic Family. *Biochem. J.* **1996**, *314*, 713–721. [CrossRef] [PubMed]
35. Sammak, S.; Hamdani, N.; Gorrec, F.; Allen, M.D.; Freund, S.M.V.; Bycroft, M.; Zinzalla, G. Crystal Structures and Nuclear Magnetic Resonance Studies of the Apo Form of the C-MYC:MAX BHLHZip Complex Reveal a Helical Basic Region in the Absence of DNA. *Biochemistry* **2019**, *58*, 3144–3154. [CrossRef]
36. Beaulieu, M.-E.; Castillo, F.; Soucek, L. Structural and Biophysical Insights into the Function of the Intrinsically Disordered Myc Oncoprotein. *Cells* **2020**, *9*, 1038. [CrossRef] [PubMed]
37. Dang, C.V. MYC on the Path to Cancer. *Cell* **2012**, *149*, 22–35. [CrossRef]
38. Knies-Bamforth, U.E.; Fox, S.B.; Poulsom, R.; Evan, G.I.; Harris, A.L. C-Myc Interacts with Hypoxia to Induce Angiogenesis *In Vivo* by a Vascular Endothelial Growth Factor-Dependent Mechanism. *Cancer Res.* **2004**, *64*, 6563–6570. [CrossRef] [PubMed]
39. Ma, L.; Young, J.; Prabhala, H.; Pan, E.; Mestdagh, P.; Muth, D.; Teruya-Feldstein, J.; Reinhardt, F.; Onder, T.T.; Valastyan, S.; et al. MiR-9, a MYC/MYCN-Activated MicroRNA, Regulates E-Cadherin and Cancer Metastasis. *Nat. Cell Biol.* **2010**, *12*, 247–256. [CrossRef]
40. Doré-Savard, L.; Roussy, G.; Dansereau, M.-A.; Collingwood, M.A.; Lennox, K.A.; Rose, S.D.; Beaudet, N.; Behlke, M.A.; Sarret, P. Central Delivery of Dicer-Substrate siRNA: A Direct Application for Pain Research. *Mol. Ther.* **2008**, *16*, 1331–1339. [CrossRef]
41. Tolcher, A.W.; Papadopoulos, K.P.; Patnaik, A.; Rasco, D.W.; Martinez, D.; Wood, D.L.; Fielman, B.; Sharma, M.; Janisch, L.A.; Brown, B.D.; et al. Safety and Activity of DCR-MYC, a First-in-Class Dicer-Substrate Small Interfering RNA (DsiRNA) Targeting MYC, in a Phase I Study in Patients with Advanced Solid Tumors. *J. Clin. Oncol.* **2015**, *33*, 11006. [CrossRef]
42. Whitfield, J.R.; Beaulieu, M.-E.; Soucek, L. Strategies to Inhibit Myc and Their Clinical Applicability. *Front. Cell Dev. Biol.* **2017**, *5*, 10. [CrossRef]
43. Brodeur, G.M.; Seeger, R.C.; Schwab, M.; Varmus, H.E.; Bishop, J.M. Amplification of N-Myc in Untreated Human Neuroblastomas Correlates with Advanced Disease Stage. *Science* **1984**, *224*, 1121–1124. [CrossRef]
44. Seeger, R.C.; Brodeur, G.M.; Sather, H.; Dalton, A.; Siegel, S.E.; Wong, K.Y.; Hammond, D. Association of Multiple Copies of the N-Myc Oncogene with Rapid Progression of Neuroblastomas. *N. Engl. J. Med.* **1985**, *313*, 1111–1116. [CrossRef]
45. Huang, M.; Weiss, W.A. Neuroblastoma and MYCN. *Cold Spring Harb. Perspect. Med.* **2013**, *3*, a014415. [CrossRef]
46. Dang, C.V.; Kim, J.; Gao, P.; Yustein, J. The Interplay between MYC and HIF in Cancer. *Nat. Rev. Cancer* **2008**, *8*, 51–56. [CrossRef]
47. Zimmerman, K.A.; Yancopoulos, G.D.; Collum, R.G.; Smith, R.K.; Kohl, N.E.; Denis, K.A.; Nau, M.M.; Witte, O.N.; Toran-Allerand, D.; Gee, C.E.; et al. Differential Expression of Myc Family Genes during Murine Development. *Nature* **1986**, *319*, 780–783. [CrossRef]
48. Fletcher, J.I.; Ziegler, D.S.; Trahair, T.N.; Marshall, G.M.; Haber, M.; Norris, M.D. Too Many Targets, Not Enough Patients: Rethinking Neuroblastoma Clinical Trials. *Nat. Rev. Cancer* **2018**, *18*, 389–400. [CrossRef]
49. Janowski, B.A.; Kaihatsu, K.; Huffman, K.E.; Schwartz, J.C.; Ram, R.; Hardy, D.; Mendelson, C.R.; Corey, D.R. Inhibiting Transcription of Chromosomal DNA with Antigene Peptide Nucleic Acids. *Nat. Chem. Biol.* **2005**, *1*, 210–215. [CrossRef]
50. Tonelli, R.; Purgato, S.; Camerin, C.; Fronza, R.; Bologna, F.; Alboresi, S.; Franzoni, M.; Corradini, R.; Sforza, S.; Faccini, A.; et al. Anti-Gene Peptide Nucleic Acid Specifically Inhibits MYCN Expression in Human Neuroblastoma Cells Leading to Cell Growth Inhibition and Apoptosis. *Mol. Cancer Ther.* **2005**, *4*, 779–786. [CrossRef]
51. Tonelli, R.; McIntyre, A.; Camerin, C.; Walters, Z.S.; Di Leo, K.; Selfe, J.; Purgato, S.; Missiaglia, E.; Tortori, A.; Renshaw, J.; et al. Antitumor Activity of Sustained N-Myc Reduction in Rhabdomyosarcomas and Transcriptional Block by Antigene Therapy. *Clin. Cancer Res.* **2012**, *18*, 796–807. [CrossRef]
52. Nielsen, P.E.; Egholm, M.; Berg, R.H.; Buchardt, O. Sequence-Selective Recognition of DNA by Strand Displacement with a Thymine-Substituted Polyamide. *Science* **1991**, *254*, 1497–1500. [CrossRef]
53. Campbell, K.; Gastier-Foster, J.M.; Mann, M.; Naranjo, A.H.; Van Ryn, C.; Bagatell, R.; Matthay, K.K.; London, W.B.; Irwin, M.S.; Shimada, H.; et al. Association of MYCN Copy Number with Clinical Features, Tumor Biology, and Outcomes in Neuroblastoma: A Report from the Children’s Oncology Group: MYCN Copy Number in Neuroblastoma. *Cancer* **2017**, *123*, 4224–4235. [CrossRef]
54. Qing, G.; Li, B.; Vu, A.; Skuli, N.; Walton, Z.E.; Liu, X.; Mayes, P.A.; Wise, D.R.; Thompson, C.B.; Maris, J.M.; et al. ATF4 Regulates MYC-Mediated Neuroblastoma Cell Death upon Glutamine Deprivation. *Cancer Cell* **2012**, *22*, 631–644. [CrossRef]
55. Montemurro, L.; Raieli, S.; Angelucci, S.; Bartolucci, D.; Amadesi, C.; Lampis, S.; Scardovi, A.L.; Venturelli, L.; Nieddu, G.; Cerisoli, L.; et al. A Novel MYCN-Specific Antigene Oligonucleotide Deregulates Mitochondria and Inhibits Tumor Growth in MYCN-Amplified Neuroblastoma. *Cancer Res.* **2019**, *79*, 6166–6177. [CrossRef]
56. Raieli, S.; Di Renzo, D.; Lampis, S.; Amadesi, C.; Montemurro, L.; Pession, A.; Hrelia, P.; Fischer, M.; Tonelli, R. MYCN Drives a Tumor Immunosuppressive Environment Which Impacts Survival in Neuroblastoma. *Front. Oncol.* **2021**, *11*, 625207. [CrossRef] [PubMed]
57. Lampis, S.; Raieli, S.; Montemurro, L.; Bartolucci, D.; Amadesi, C.; Bortolotti, S.; Angelucci, S.; Scardovi, A.L.; Nieddu, G.; Cerisoli, L.; et al. The MYCN Inhibitor BGA002 Restores the Retinoic Acid Response Leading to Differentiation or Apoptosis by the MTOR Block in MYCN-Amplified Neuroblastoma. *J. Exp. Clin. Cancer Res.* **2022**, *41*, 160. [CrossRef]

58. Simanshu, D.K.; Nissley, D.V.; McCormick, F. RAS Proteins and Their Regulators in Human Disease. *Cell* **2017**, *170*, 17–33. [CrossRef]
59. Mo, S.P.; Coulson, J.M.; Prior, I.A. RAS Variant Signalling. *Biochem. Soc. Trans.* **2018**, *46*, 1325–1332. [CrossRef]
60. Hobbs, G.A.; Der, C.J.; Rossman, K.L. RAS Isoforms and Mutations in Cancer at a Glance. *J. Cell Sci.* **2016**, *129*, 1287–1292. [CrossRef]
61. Prior, I.A.; Lewis, P.D.; Mattos, C. A Comprehensive Survey of Ras Mutations in Cancer. *Cancer Res.* **2012**, *72*, 2457–2467. [CrossRef] [PubMed]
62. Prior, I.A.; Hood, F.E.; Hartley, J.L. The Frequency of Ras Mutations in Cancer. *Cancer Res.* **2020**, *80*, 2969–2974. [CrossRef] [PubMed]
63. Wang, W.; Fang, G.; Rudolph, J. Ras Inhibition via Direct Ras Binding—Is There a Path Forward? *Bioorg. Med. Chem. Lett.* **2012**, *22*, 5766–5776. [CrossRef] [PubMed]
64. Whyte, D.B.; Kirschmeier, P.; Hockenberry, T.N.; Nunez-Oliva, I.; James, L.; Catino, J.J.; Bishop, W.R.; Pai, J.-K. K- and N-Ras Are Geranylgeranylated in Cells Treated with Farnesyl Protein Transferase Inhibitors. *J. Biol. Chem.* **1997**, *272*, 14459–14464. [CrossRef] [PubMed]
65. Zorde Khvalevsky, E.; Gabai, R.; Rachmut, I.H.; Horwitz, E.; Brunschwig, Z.; Orbach, A.; Shemi, A.; Golan, T.; Domb, A.J.; Yavin, E.; et al. Mutant KRAS Is a Druggable Target for Pancreatic Cancer. *Proc. Natl. Acad. Sci. USA* **2013**, *110*, 20723–20728. [CrossRef]
66. Golan, T.; Khvalevsky, E.Z.; Hubert, A.; Gabai, R.M.; Hen, N.; Segal, A.; Domb, A.; Harari, G.; David, E.B.; Raskin, S.; et al. RNAi Therapy Targeting KRAS in Combination with Chemotherapy for Locally Advanced Pancreatic Cancer Patients. *Oncotarget* **2015**, *6*, 24560–24570. [CrossRef]
67. Ramot, Y.; Rotkopf, S.; Gabai, R.M.; Zorde Khvalevsky, E.; Muravnik, S.; Marzoli, G.A.; Domb, A.J.; Shemi, A.; Nyska, A. Preclinical Safety Evaluation in Rats of a Polymeric Matrix Containing an siRNA Drug Used as a Local and Prolonged Delivery System for Pancreatic Cancer Therapy. *Toxicol. Pathol.* **2016**, *44*, 856–865. [CrossRef]
68. Seth, P.P.; Siwkowski, A.; Allerson, C.R.; Vasquez, G.; Lee, S.; Prakash, T.P.; Wanciewicz, E.V.; Wittchell, D.; Swayze, E.E. Short Antisense Oligonucleotides with Novel 2′–4′ Conformationally Restricted Nucleoside Analogues Show Improved Potency without Increased Toxicity in Animals. *J. Med. Chem.* **2009**, *52*, 10–13. [CrossRef]
69. Ross, S.J.; Revenko, A.S.; Hanson, L.L.; Ellston, R.; Staniszewska, A.; Whalley, N.; Pandey, S.K.; Revill, M.; Rooney, C.; Buckett, L.K.; et al. Targeting KRAS-Dependent Tumors with AZD4785, a High-Affinity Therapeutic Antisense Oligonucleotide Inhibitor of KRAS. *Sci. Transl. Med.* **2017**, *9*, eaal5253. [CrossRef]
70. Zhong, Z.; Wen, Z.; Darnell, J.E. Stat3: A STAT Family Member Activated by Tyrosine Phosphorylation in Response to Epidermal Growth Factor and Interleukin-6. *Science* **1994**, *264*, 95–98. [CrossRef]
71. Liu, Y.; Li, P.-K.; Li, C.; Lin, J. Inhibition of STAT3 Signaling Blocks the Anti-Apoptotic Activity of IL-6 in Human Liver Cancer Cells. *J. Biol. Chem.* **2010**, *285*, 27429–27439. [CrossRef] [PubMed]
72. Azare, J.; Leslie, K.; Al-Ahmadie, H.; Gerald, W.; Weinreb, P.H.; Violette, S.M.; Bromberg, J. Constitutively Activated Stat3 Induces Tumorigenesis and Enhances Cell Motility of Prostate Epithelial Cells through Integrin B6. *Mol. Cell. Biol.* **2007**, *27*, 4444–4453. [CrossRef] [PubMed]
73. Masuda, M.; Suzui, M.; Yasumatu, R.; Nakashima, T.; Kuratomi, Y.; Azuma, K.; Tomita, K.; Komiyama, S.; Weinstein, I.B. Constitutive Activation of Signal Transducers and Activators of Transcription 3 Correlates with Cyclin D1 Overexpression and May Provide a Novel Prognostic Marker in Head and Neck Squamous Cell Carcinoma. *Cancer Res.* **2002**, *62*, 3351–3355. [PubMed]
74. Danoch, H.; Kalechman, Y.; Albeck, M.; Longo, D.L.; Sredni, B. Sensitizing B- and T-Cell Lymphoma Cells to Paclitaxel/Abraxane—Induced Death by AS101 via Inhibition of the VLA-4—IL10—Survivin Axis. *Mol. Cancer Res.* **2015**, *13*, 411–422. [CrossRef] [PubMed]
75. Ryu, K.; Susa, M.; Choy, E.; Yang, C.; Hornicek, F.J.; Mankin, H.J.; Duan, Z. Oleanane Triterpenoid CDDO-Me Induces Apoptosis in Multidrug Resistant Osteosarcoma Cells through Inhibition of Stat3 Pathway. *BMC Cancer* **2010**, *10*, 187. [CrossRef]
76. Fossey, S.L.; Bear, M.D.; Lin, J.; Li, C.; Schwartz, E.B.; Li, P.-K.; Fuchs, J.R.; Fenger, J.; Kisseberth, W.C.; London, C.A. The Novel Curcumin Analog FLLL32 Decreases STAT3 DNA Binding Activity and Expression, and Induces Apoptosis in Osteosarcoma Cell Lines. *BMC Cancer* **2011**, *11*, 112. [CrossRef]
77. Reilly, M.J.; McCoon, P.; Cook, C.; Lyne, P.; Kurzrock, R.; Kim, Y.; Woessner, R.; Younes, A.; Nemunaitis, J.; Fowler, N.; et al. STAT3 Antisense Oligonucleotide AZD9150 in a Subset of Patients with Heavily Pretreated Lymphoma: Results of a Phase 1b Trial. *J. Immunother. Cancer* **2018**, *6*, 119. [CrossRef]
78. Kortylewski, M.; Swiderski, P.; Herrmann, A.; Wang, L.; Kowolik, C.; Kujawski, M.; Lee, H.; Scuto, A.; Liu, Y.; Yang, C.; et al. In Vivo Delivery of siRNA to Immune Cells by Conjugation to a TLR9 Agonist Enhances Antitumor Immune Responses. *Nat. Biotechnol.* **2009**, *27*, 925–932. [CrossRef]
79. Kanzler, H.; Barrat, F.J.; Hessel, E.M.; Coffman, R.L. Therapeutic Targeting of Innate Immunity with Toll-like Receptor Agonists and Antagonists. *Nat. Med.* **2007**, *13*, 552–559. [CrossRef]
80. Barchet, W.; Wimmenauer, V.; Schlee, M.; Hartmann, G. Accessing the Therapeutic Potential of Immunostimulatory Nucleic Acids. *Curr. Opin. Immunol.* **2008**, *20*, 389–395. [CrossRef]
81. Krieg, A.M. Toll-like Receptor 9 (TLR9) Agonists in the Treatment of Cancer. *Oncogene* **2008**, *27*, 161–167. [CrossRef] [PubMed]

82. Klinman, D.M.; Currie, D.; Gursel, I.; Verthelyi, D. Use of CpG Oligodeoxynucleotides as Immune Adjuvants. *Immunol. Rev.* **2004**, *199*, 201–216. [CrossRef] [PubMed]
83. Tsujimoto, Y.; Finger, L.R.; Yunis, J.; Nowell, P.C.; Croce, C.M. Cloning of the Chromosome Breakpoint of Neoplastic B Cells with the t(14;18) Chromosome Translocation. *Science* **1984**, *226*, 1097–1099. [CrossRef] [PubMed]
84. Vaux, D.L.; Cory, S.; Adams, J.M. Bcl-2 Gene Promotes Haemopoietic Cell Survival and Cooperates with c-Myc to Immortalize Pre-B Cells. *Nature* **1988**, *335*, 440–442. [CrossRef]
85. García-Aranda, M.; Pérez-Ruiz, E.; Redondo, M. Bcl-2 Inhibition to Overcome Resistance to Chemo- and Immunotherapy. *Int. J. Mol. Sci.* **2018**, *19*, 3950. [CrossRef]
86. Cotter, F.E.; Johnson, P.; Hall, P.; Pocock, C.; al Mahdi, N.; Cowell, J.K.; Morgan, G. Antisense Oligonucleotides Suppress B-Cell Lymphoma Growth in a SCID-Hu Mouse Model. *Oncogene* **1994**, *9*, 3049–3055.
87. Raynaud, F.I.; Orr, R.M.; Goddard, P.M.; Lacey, H.A.; Lancashire, H.; Judson, I.R.; Beck, T.; Bryan, B.; Cotter, F.E. Pharmacokinetics of G3139, a Phosphorothioate Oligodeoxynucleotide Antisense to Bcl-2, after Intravenous Administration or Continuous Subcutaneous Infusion to Mice. *J. Pharmacol. Exp. Ther.* **1997**, *281*, 420–427.
88. Gagliardi, M.; Ashizawa, A.T. Making Sense of Antisense Oligonucleotide Therapeutics Targeting Bcl-2. *Pharmaceutics* **2022**, *14*, 97. [CrossRef]
89. Ebrahim, A.S.; Kandouz, M.; Liddane, A.; Sabbagh, H.; Hou, Y.; Li, C.; Al-Katib, A. PNT2258, a Novel Deoxyribonucleic Acid Inhibitor, Induces Cell Cycle Arrest and Apoptosis via a Distinct Mechanism of Action: A New Class of Drug for Non-Hodgkin's Lymphoma. *Oncotarget* **2016**, *7*, 42374–42384. [CrossRef]
90. Qadir, M.I.; Bukhat, S.; Rasul, S.; Manzoor, H.; Manzoor, M. RNA Therapeutics: Identification of Novel Targets Leading to Drug Discovery. *J. Cell. Biochem.* **2020**, *121*, 898–929. [CrossRef]
91. Romano, G.; Veneziano, D.; Acunzo, M.; Croce, C.M. Small Non-Coding RNA and Cancer. *Carcinogenesis* **2017**, *38*, 485–491. [CrossRef] [PubMed]
92. The FANTOM Consortium and the RIKEN PMI and CLST (DGT) A Promoter-Level Mammalian Expression Atlas. *Nature* **2014**, *507*, 462–470. [CrossRef] [PubMed]
93. The ENCODE Project Consortium an Integrated Encyclopedia of DNA Elements in the Human Genome. *Nature* **2012**, *489*, 57–74. [CrossRef] [PubMed]
94. Ning, B.; Yu, D.; Yu, A.-M. Advances and Challenges in Studying Noncoding RNA Regulation of Drug Metabolism and Development of RNA Therapeutics. *Biochem. Pharmacol.* **2019**, *169*, 113638. [CrossRef] [PubMed]
95. Hombach, S.; Kretz, M. Non-Coding RNAs: Classification, Biology and Functioning. In *Non-Coding RNAs in Colorectal Cancer*; Slaby, O., Calin, G.A., Eds.; Advances in Experimental Medicine and Biology; Springer International Publishing: Cham, Switzerland, 2016; Volume 937, pp. 3–17. ISBN 978-3-319-42057-8.
96. Dahariya, S.; Paddibhatla, I.; Kumar, S.; Raghuvanshi, S.; Palapati, A.; Gutti, R.K. Long Non-Coding RNA: Classification, Biogenesis and Functions in Blood Cells. *Mol. Immunol.* **2019**, *112*, 82–92. [CrossRef]
97. Srijyothi, L.; Ponne, S.; Prathama, T.; Ashok, C.; Baluchamy, S. Roles of Non-Coding RNAs in Transcriptional Regulation. In *Transcriptional and Post-Transcriptional Regulation*; Ghedira, K., Ed.; InTech: London, UK, 2018; ISBN 978-1-78923-791-7.
98. Kwok, Z.H.; Ni, K.; Jin, Y. Extracellular Vesicle Associated Non-Coding RNAs in Lung Infections and Injury. *Cells* **2021**, *10*, 965. [CrossRef]
99. Slaby, O.; Laga, R.; Sedlacek, O. Therapeutic Targeting of Non-Coding RNAs in Cancer. *Biochem. J.* **2017**, *474*, 4219–4251. [CrossRef]
100. Dozmorov, M.G.; Giles, C.B.; Koelsch, K.A.; Wren, J.D. Systematic Classification of Non-Coding RNAs by Epigenomic Similarity. *BMC Bioinform.* **2013**, *14*, S2. [CrossRef]
101. Rasool, M.; Malik, A.; Zahid, S.; Basit Ashraf, M.A.; Qazi, M.H.; Asif, M.; Zaheer, A.; Arshad, M.; Raza, A.; Jamal, M.S. Non-Coding RNAs in Cancer Diagnosis and Therapy. *Non-Coding RNA Res.* **2016**, *1*, 69–76. [CrossRef]
102. Guttman, M.; Amit, I.; Garber, M.; French, C.; Lin, M.F.; Feldser, D.; Huarte, M.; Zuk, O.; Carey, B.W.; Cassady, J.P.; et al. Chromatin Signature Reveals over a Thousand Highly Conserved Large Non-Coding RNAs in Mammals. *Nature* **2009**, *458*, 223–227. [CrossRef]
103. Geisler, S.; Collier, J. RNA in Unexpected Places: Long Non-Coding RNA Functions in Diverse Cellular Contexts. *Nat. Rev. Mol. Cell Biol.* **2013**, *14*, 699–712. [CrossRef]
104. Suzuki, H.; Maruyama, R.; Yamamoto, E.; Niinuma, T.; Kai, M. Relationship Between Noncoding RNA Dysregulation and Epigenetic Mechanisms in Cancer. *Adv. Exp. Med. Biol.* **2016**, *927*, 109–135. [CrossRef]
105. Bajan, S.; Hutvagner, G. RNA-Based Therapeutics: From Antisense Oligonucleotides to MiRNAs. *Cells* **2020**, *9*, 137. [CrossRef]
106. Harries, L.W. RNA Biology Provides New Therapeutic Targets for Human Disease. *Front. Genet.* **2019**, *10*, 205. [CrossRef]
107. Wang, T.; Shigdar, S.; Shamaileh, H.A.; Gantier, M.P.; Yin, W.; Xiang, D.; Wang, L.; Zhou, S.-F.; Hou, Y.; Wang, P.; et al. Challenges and Opportunities for siRNA-Based Cancer Treatment. *Cancer Lett.* **2017**, *387*, 77–83. [CrossRef]
108. Matsui, M.; Corey, D.R. Non-Coding RNAs as Drug Targets. *Nat. Rev. Drug Discov.* **2017**, *16*, 167–179. [CrossRef]
109. van Zandwijk, N.; Pavlakis, N.; Kao, S.C.; Linton, A.; Boyer, M.J.; Clarke, S.; Huynh, Y.; Chrzanowska, A.; Fulham, M.J.; Bailey, D.L.; et al. Safety and Activity of MicroRNA-Loaded Minicells in Patients with Recurrent Malignant Pleural Mesothelioma: A First-in-Man, Phase 1, Open-Label, Dose-Escalation Study. *Lancet Oncol.* **2017**, *18*, 1386–1396. [CrossRef]





110. Foss, F.M.; Querfeld, C.; Porcu, P.; Kim, Y.H.; Pacheco, T.; Halwani, A.S.; DeSimone, J.; William, B.M.; Seto, A.G.; Ruckman, J.; et al. Phase 1 Trial Evaluating MRG-106, a Synthetic Inhibitor of MicroRNA-155, in Patients with Cutaneous t-Cell Lymphoma (CTCL). *J. Clin. Oncol.* **2017**, *35*, 7564. [CrossRef]
111. Janssen, H.L.A.; Reesink, H.W.; Lawitz, E.J.; Zeuzem, S.; Rodriguez-Torres, M.; Patel, K.; van der Meer, A.J.; Patick, A.K.; Chen, A.; Zhou, Y.; et al. Treatment of HCV Infection by Targeting MicroRNA. *N. Engl. J. Med.* **2013**, *368*, 1685–1694. [CrossRef]
112. Bonneau, E.; Neveu, B.; Kostantin, E.; Tsongalis, G.J.; De Guire, V. How Close Are MiRNAs from Clinical Practice? A Perspective on the Diagnostic and Therapeutic Market. *EJIFCC* **2019**, *30*, 114–127.
113. Xiong, H.; Veedu, R.N.; Diermeier, S.D. Recent Advances in Oligonucleotide Therapeutics in Oncology. *Int. J. Mol. Sci.* **2021**, *22*, 3295. [CrossRef] [PubMed]
114. Seto, A.G.; Beatty, X.; Lynch, J.M.; Hermreck, M.; Tetzlaff, M.; Duvic, M.; Jackson, A.L. Cobomarsen, an Oligonucleotide Inhibitor of MiR-155, Co-Ordinately Regulates Multiple Survival Pathways to Reduce Cellular Proliferation and Survival in Cutaneous T-Cell Lymphoma. *Br. J. Haematol.* **2018**, *183*, 428–444. [CrossRef] [PubMed]
115. Anastasiadou, E.; Seto, A.G.; Beatty, X.; Hermreck, M.; Gilles, M.-E.; Stroopinsky, D.; Pinter-Brown, L.C.; Pestano, L.; Marchese, C.; Avigan, D.; et al. Cobomarsen, an Oligonucleotide Inhibitor of MiR-155, Slows DLBCL Tumor Cell Growth *In Vitro* and *In Vivo*. *Clin. Cancer Res.* **2021**, *27*, 1139–1149. [CrossRef] [PubMed]
116. Witten, L.; Slack, F.J. MiR-155 as a Novel Clinical Target for Hematological Malignancies. *Carcinogenesis* **2020**, *41*, 2–7. [CrossRef]
117. Fuertes, T.; Ramiro, A.R.; de Yébenes, V.G. MiRNA-Based Therapies in B Cell Non-Hodgkin Lymphoma. *Trends Immunol.* **2020**, *41*, 932–947. [CrossRef]
118. Winkle, M.; El-Daly, S.M.; Fabbri, M.; Calin, G.A. Noncoding RNA Therapeutics—Challenges and Potential Solutions. *Nat. Rev. Drug Discov.* **2021**, *20*, 629–651. [CrossRef]
119. Hanna, J.; Hossain, G.S.; Kocerha, J. The Potential for MicroRNA Therapeutics and Clinical Research. *Front. Genet.* **2019**, *10*, 478. [CrossRef]
120. Rupaimoole, R.; Slack, F.J. MicroRNA Therapeutics: Towards a New Era for the Management of Cancer and Other Diseases. *Nat. Rev. Drug Discov.* **2017**, *16*, 203–222. [CrossRef]
121. Reid, G.; Pel, M.E.; Kirschner, M.B.; Cheng, Y.Y.; Mugridge, N.; Weiss, J.; Williams, M.; Wright, C.; Edelman, J.J.B.; Vallely, M.P.; et al. Restoring Expression of MiR-16: A Novel Approach to Therapy for Malignant Pleural Mesothelioma. *Ann. Oncol.* **2013**, *24*, 3128–3135. [CrossRef]
122. Bader, A.G. MiR-34—A MicroRNA Replacement Therapy Is Headed to the Clinic. *Front. Genet.* **2012**, *3*, 120. [CrossRef]
123. Bouchie, A. First MicroRNA Mimic Enters Clinic. *Nat. Biotechnol.* **2013**, *31*, 577. [CrossRef] [PubMed]
124. Daige, C.L.; Wiggins, J.F.; Priddy, L.; Nelligan-Davis, T.; Zhao, J.; Brown, D. Systemic Delivery of a MiR34a Mimic as a Potential Therapeutic for Liver Cancer. *Mol. Cancer Ther.* **2014**, *13*, 2352–2360. [CrossRef] [PubMed]
125. Hong, D.S.; Kang, Y.-K.; Borad, M.; Sachdev, J.; Ejadi, S.; Lim, H.Y.; Brenner, A.J.; Park, K.; Lee, J.-L.; Kim, T.-Y.; et al. Phase 1 Study of MRX34, a Liposomal MiR-34a Mimic, in Patients with Advanced Solid Tumours. *Br. J. Cancer* **2020**, *122*, 1630–1637. [CrossRef] [PubMed]
126. Geary, R.S.; Norris, D.; Yu, R.; Bennett, C.F. Pharmacokinetics, Biodistribution and Cell Uptake of Antisense Oligonucleotides. *Adv. Drug Deliv. Rev.* **2015**, *87*, 46–51. [CrossRef]
127. Herkt, M.; Thum, T. Pharmacokinetics and Proceedings in Clinical Application of Nucleic Acid Therapeutics. *Mol. Ther.* **2021**, *29*, 521–539. [CrossRef]
128. Boursereau, R.; Donadieu, A.; Dabertrand, F.; Dubayle, D.; Morel, J.-L. Blood Brain Barrier Precludes the Cerebral Arteries to Intravenously-Injected Antisense Oligonucleotide. *Eur. J. Pharmacol.* **2015**, *747*, 141–149. [CrossRef]
129. Mendonça, M.C.P.; Kont, A.; Aburto, M.R.; Cryan, J.F.; O’Driscoll, C.M. Advances in the Design of (Nano)Formulations for Delivery of Antisense Oligonucleotides and Small Interfering RNA: Focus on the Central Nervous System. *Mol. Pharm.* **2021**, *18*, 1491–1506. [CrossRef]
130. Klabenkova, K.; Fokina, A.; Stetsenko, D. Chemistry of Peptide-Oligonucleotide Conjugates: A Review. *Molecules* **2021**, *26*, 5420. [CrossRef]
131. Quemener, A.M.; Centomo, M.L.; Sax, S.L.; Panella, R. Small Drugs, Huge Impact: The Extraordinary Impact of Antisense Oligonucleotides in Research and Drug Development. *Molecules* **2022**, *27*, 536. [CrossRef]
132. Crooke, S.T.; Wang, S.; Vickers, T.A.; Shen, W.; Liang, X.-H. Cellular Uptake and Trafficking of Antisense Oligonucleotides. *Nat. Biotechnol.* **2017**, *35*, 230–237. [CrossRef]
133. Bost, J.P.; Barriga, H.; Holme, M.N.; Gallud, A.; Maugeri, M.; Gupta, D.; Lehto, T.; Valadi, H.; Esbjörner, E.K.; Stevens, M.M.; et al. Delivery of Oligonucleotide Therapeutics: Chemical Modifications, Lipid Nanoparticles, and Extracellular Vesicles. *ACS Nano* **2021**, *15*, 13993–14021. [CrossRef] [PubMed]
134. Wan, Y.; Moyle, P.M.; Toth, I. Endosome Escape Strategies for Improving the Efficacy of Oligonucleotide Delivery Systems. *Curr. Med. Chem.* **2015**, *22*, 3326–3346. [CrossRef] [PubMed]
135. Nuzzo, S.; Roscigno, G.; Affinito, A.; Ingenito, F.; Quintavalle, C.; Condorelli, G. Potential and Challenges of Aptamers as Specific Carriers of Therapeutic Oligonucleotides for Precision Medicine in Cancer. *Cancers* **2019**, *11*, 1521. [CrossRef] [PubMed]
136. Gagliardi, M.; Ashizawa, A.T. The Challenges and Strategies of Antisense Oligonucleotide Drug Delivery. *Biomedicines* **2021**, *9*, 433. [CrossRef]

137. Roberts, T.C.; Langer, R.; Wood, M.J.A. Advances in Oligonucleotide Drug Delivery. *Nat. Rev. Drug Discov.* **2020**, *19*, 673–694. [CrossRef]
138. Chi, X.; Gatti, P.; Papoian, T. Safety of Antisense Oligonucleotide and siRNA-Based Therapeutics. *Drug Discov. Today* **2017**, *22*, 823–833. [CrossRef]
139. Jackson, A.L.; Linsley, P.S. Recognizing and Avoiding siRNA Off-Target Effects for Target Identification and Therapeutic Application. *Nat. Rev. Drug Discov.* **2010**, *9*, 57–67. [CrossRef]
140. Andersson, P. Preclinical Safety Assessment of Therapeutic Oligonucleotides. *Methods Mol. Biol.* **2022**, *2434*, 355–370. [CrossRef]
141. Koziolkiewicz, M.; Gendaszewska, E.; Maszewska, M.; Stein, C.A.; Stec, W.J. The Mononucleotide-Dependent, Nonantisense Mechanism of Action of Phosphodiester and Phosphorothioate Oligonucleotides Depends upon the Activity of an Ecto-5'-Nucleotidase. *Blood* **2001**, *98*, 995–1002. [CrossRef]
142. Dias, N.; Stein, C.A. Antisense Oligonucleotides: Basic Concepts and Mechanisms. *Mol. Cancer Ther.* **2002**, *1*, 347–355.
143. Sproat, B.S.; Lamond, A.I.; Beijer, B.; Neuner, P.; Ryder, U. Highly Efficient Chemical Synthesis of 2'-O-Methyloligoribonucleotides and Tetrabiotinylated Derivatives; Novel Probes That Are Resistant to Degradation by RNA or DNA Specific Nucleases. *Nucleic Acids Res.* **1989**, *17*, 3373–3386. [CrossRef] [PubMed]
144. Khvorova, A.; Watts, J.K. The Chemical Evolution of Oligonucleotide Therapies of Clinical Utility. *Nat. Biotechnol.* **2017**, *35*, 238–248. [CrossRef] [PubMed]
145. Moulton, J.D.; Yan, Y. Using Morpholinos to Control Gene Expression. *Curr. Protoc. Mol. Biol.* **2008**, *83*, 26.8.1–26.8.29. [CrossRef]
146. Larsen, H.J.; Bentin, T.; Nielsen, P.E. Antisense Properties of Peptide Nucleic Acid. *Biochim. Biophys. Acta* **1999**, *1489*, 159–166. [CrossRef]
147. Hartmann, G. Nucleic Acid Immunity. *Adv. Immunol.* **2017**, *133*, 121–169. [CrossRef] [PubMed]
148. Levin, A.A. A Review of Issues in the Pharmacokinetics and Toxicology of Phosphorothioate Antisense Oligonucleotides. *Biochim. Biophys. Acta-Gene Struct. Expr.* **1999**, *1489*, 69–84. [CrossRef]
149. Lindow, M.; Vornlocher, H.-P.; Riley, D.; Kornbrust, D.J.; Burchard, J.; Whiteley, L.O.; Kamens, J.; Thompson, J.D.; Nochur, S.; Younis, H.; et al. Assessing Unintended Hybridization-Induced Biological Effects of Oligonucleotides. *Nat. Biotechnol.* **2012**, *30*, 920–923. [CrossRef]
150. Hagedorn, P.H.; Yakimov, V.; Ottosen, S.; Kammler, S.; Nielsen, N.F.; Høg, A.M.; Hedtjærn, M.; Meldgaard, M.; Møller, M.R.; Ørum, H.; et al. Hepatotoxic Potential of Therapeutic Oligonucleotides Can Be Predicted from Their Sequence and Modification Pattern. *Nucleic Acid Ther.* **2013**, *23*, 302–310. [CrossRef]
151. Lange, M.J.; Burke, D.H.; Chaput, J.C. Activation of Innate Immune Responses by a CpG Oligonucleotide Sequence Composed Entirely of Threose Nucleic Acid. *Nucleic Acid Ther.* **2019**, *29*, 51–59. [CrossRef]
152. Ouattara, D.A.; Remolue, L.; Becker, J.; Perret, M.; Bunescu, A.; Hennig, K.; Biliaut, E.; Badin, A.; Giacomini, C.; Reynier, F.; et al. An Integrated Transcriptomics and Metabolomics Study of the Immune Response of Newly Hatched Chicks to the Cytosine-Phosphate-Guanine Oligonucleotide Stimulation. *Poult. Sci.* **2020**, *99*, 4360–4372. [CrossRef]
153. Schlee, M.; Hornung, V.; Hartmann, G. siRNA and IsRNA: Two Edges of One Sword. *Mol. Ther.* **2006**, *14*, 463–470. [CrossRef] [PubMed]
154. Nussinov, R.; Tsai, C.-J.; Jang, H. Anticancer Drug Resistance: An Update and Perspective. *Drug Resist. Updates* **2021**, *59*, 100796. [CrossRef] [PubMed]
155. Feizabadi, M.S. Modeling Multi-Mutation and Drug Resistance: Analysis of Some Case Studies. *Theor. Biol. Med. Model.* **2017**, *14*, 6. [CrossRef] [PubMed]



## Article

# Cathepsin S Cleaves BAX as a Novel and Therapeutically Important Regulatory Mechanism for Apoptosis

Surinder M. Soond<sup>1,\*</sup>, Lyudmila V. Savvateeva<sup>1</sup>, Vladimir A. Makarov<sup>1</sup>, Neonila V. Gorokhovets<sup>1</sup>, Paul A. Townsend<sup>2,3</sup> and Andrey A. Zamyatnin Jr.<sup>1,4,5,\*</sup>

<sup>1</sup> Institute of Molecular Medicine, Sechenov First Moscow State Medical University, Trubetskaya Str. 8-2, 119991 Moscow, Russia; ludmilasl@yandex.ru (L.V.S.); known.sir@yandex.ru (V.A.M.); gorokhovets\_n\_v@staff.sechenov.ru (N.V.G.)

<sup>2</sup> Division of Cancer Sciences and Manchester Cancer Research Centre, Faculty of Biology, Medicine and Health, University of Manchester, Manchester M13 9PL, UK; paul.townsend@manchester.ac.uk

<sup>3</sup> Faculty of Health and Medical Sciences, University of Surrey, Guildford, Surrey GU2 7X, UK

<sup>4</sup> Belozersky Institute of Physico-Chemical Biology, Lomonosov Moscow State University, 119992 Moscow, Russia

<sup>5</sup> Department of Biotechnology, Sirius University of Science and Technology, 1 Olympic Ave, 354340 Sochi, Russia

\* Correspondence: surinder.soond@yandex.ru (S.M.S.); zamyat@belozersky.msu.ru (A.A.Z.J.)

**Citation:** Soond, S.M.; Savvateeva, L.V.; Makarov, V.A.; Gorokhovets, N.V.; Townsend, P.A.; Zamyatnin, A.A., Jr. Cathepsin S Cleaves BAX as a Novel and Therapeutically Important Regulatory Mechanism for Apoptosis. *Pharmaceutics* **2021**, *13*, 339. <https://doi.org/10.3390/pharmaceutics13030339>

Academic Editors: Hassan Bousbaa and Tihomir Tomašić

Received: 17 January 2021

Accepted: 1 March 2021

Published: 5 March 2021

**Publisher's Note:** MDPI stays neutral with regard to jurisdictional claims in published maps and institutional affiliations.



**Copyright:** © 2021 by the authors. Licensee MDPI, Basel, Switzerland. This article is an open access article distributed under the terms and conditions of the Creative Commons Attribution (CC BY) license (<https://creativecommons.org/licenses/by/4.0/>).

**Abstract:** Certain lysosomal cathepsin proteins have come into focus as being good candidates for therapeutic targeting, based on them being over-expressed in a variety of cancers and based on their regulation of the apoptotic pathway. Here, we report novel findings that highlight the ability of cathepsin S expression to be up-regulated under Paclitaxel-stimulatory conditions in kidney cell lines and it being able to cleave the apoptotic p21 BAX protein in intact cells and in vitro. Consistent with this, we demonstrate that this effect can be abrogated in vitro and in mammalian cells under conditions that utilize dominant-inhibitory cathepsin S expression, cathepsin S expression-knockdown and through the activity of a novel peptide inhibitor, CS-PEP1. Moreover, we report a unique role for cathepsin S in that it can cleave a polyubiquitinated-BAX protein intermediate and is a step that may contribute to down-regulating post-translationally-modified levels of BAX protein. Finally, CS-PEP1 may possess promising activity as a potential anti-cancer therapeutic against chemotherapeutic-resistant Renal Clear Cell Carcinoma kidney cancer cells and for combined uses with therapeutics such as Paclitaxel.

**Keywords:** cathepsins; BAX; MOMP; ubiquitination; apoptosis; chemotherapy; cancer

## 1. Introduction

The lysosomal cathepsin proteases are emerging as being quite pleiotropic concerning the regulatory role they play in a number of key cellular processes that are central to disease progression [1]. From this family of proteins, the cysteine cathepsins have gained considerable attention due to their ability to be auto-activated, remain catalytically active at lysosomally-acidic [2] and cytoplasmically-neutral pHs and include cathepsins -B, -C, -F, -H, -K, -L, -O, -S, -V, -X, -W and -Z [1,3]. More recently, cathepsin proteases have gained in importance based on their contributions to cancer progression and angiogenesis, when expressed extracellularly or intracellularly, and have been evaluated for their candidacy as therapeutic targets [1,3–8]. One such member from this hopeful family of targets is cathepsin S (CS), particularly in the context of cardiovascular disease or gastric- and colon-cancers [9].

Mechanistically, the cathepsins gained importance following the seminal studies, which demonstrated the ability of cathepsins -B, -K, -L, -H, -D and possibly -S to cleave and activate the Bcl-2 family member BID or caspase-8, resulting in their respective activation of the intrinsic and extrinsic arms of the apoptosis pathway [10,11]. Briefly, the Bcl-2

family of proteins can be divided into 3 sub-families: pro-apoptotic (for example BAX and BAK), anti-apoptotic (which include Bcl-2 and Bcl-xl), and the BH3-only proteins (such as BID, BAD and BIM) [12,13]. Of importance is the p21 BAX protein, which is structurally composed of 9  $\alpha$ -helices [14], is predominantly monomeric [15] and is activated through two possible mechanisms upon stimulation of cells with cytotoxic agents [16]. Firstly, binding of BH3-only proteins to helices  $\alpha$ 1– $\alpha$ 6 (the ‘rear pocket’ of p21 BAX) can displace the  $\alpha$ -helix 9 *trans*-membrane (TM) domain from the hydrophobic groove (composed of helices  $\alpha$ 2– $\alpha$ 5), thus allowing the insertion of the TM domain into the outer mitochondrial membrane leading to mitochondrial outer membrane permeabilization (MOMP) [17]. Secondly, displacement of the  $\alpha$ 1– $\alpha$ 2 helices by activator BH3-proteins can expose the BH3 domain [18] and permit the oligomerization of BAX [18,19], which is a key step in activating MOMP and apoptosis through the intrinsic pathway [20].

The BH3 domain of p21 BAX can also bind the hydrophobic groove of the inhibitory Bcl-2 protein (through helices  $\alpha$ 2– $\alpha$ 5 [21]), which reduces the ability of p21 BAX to oligomerize to 80-, 96-, 160- or 260-kD complexes [22], thus limiting BAX-mediated MOMP activation [23]. Therapeutically, targeting this *pro*-apoptotic BH3 domain protein-*anti*-apoptotic Bcl-2 protein hydrophobic groove interaction using ‘BH3 mimetics’ has yielded a number of very promising *anti*-cancer drugs such as Venetoclax [24,25] and WEHI539 [26].

Based on the importance of cathepsin-mediated cleavage of BH3-domain containing pro-apoptotic proteins, albeit an area of controversy [27,28], we questioned the regulatory dynamics that exist between the CS and p21 BAX proteins in the context of kidney cancer. Here, we report that cathepsin S (CTSS) and BAX gene expression through Paclitaxel stimulation or cellular stress are inducible in kidney cell lines. We also report that p21 BAX is a novel substrate for CS, which may be a step that is important in regulating apoptosis as it has the effect of depleting cells of the p21 BAX protein. Moreover, we show that this cleavage event can be inhibited in the presence of a novel Bcl-xl protein-derived inhibitory peptide (named CS-PEP1) and which can induce apoptosis of HEK293 and 769P cancer cells through mechanisms that involve p21 BAX protein stabilization and Bcl-xl protein destabilization. Collectively, our novel findings offer good potential for Paclitaxel-resistant Renal Clear Cell Carcinoma (RCCC) cancer cells [29] to be sensitized to the apoptosis-inducing effects of CS-PEP1 alone or in combination with Paclitaxel therapy.

## 2. Materials and Methods

### Reagents, Antibodies and cells

Paclitaxel (Pac, in DMSO), hydrogen peroxide (HP), z-VAD-FMK (in DMSO), MG132 (in DMSO) and 100 mM cycloheximide (in DMSO) were purchased from (Sigma-Aldrich, Moscow, Russia). Mouse *anti*-human Cathepsin S (E-3) was purchased from Santa Cruz Biotechnology (Santa Cruz, CA, USA), and *anti*-HA tag (SG77) or goat *anti*-Cathepsin S (PA5-47088) were purchased from Invitrogen (Carlsbad, CA, USA). *Anti*-Bcl-xl (Ab15274) and -BAX (Ab3154) were purchased from Abcam (Cambridge, UK). An *anti*-active caspase-3 specific antibody was purchased from Abcam (Ab13847) to detect the cleaved 17 kD form of caspase-3 by Western blotting. Protein AG agarose was purchased from Pierce (Waltham, MA, USA). HEK293 (RRID:CVCL\_0045) and 769-P (RRID:CVCL\_1050) kidney cells lines were sourced originally from ATCC and respectively maintained in DMEM (Invitrogen, Carlsbad, CA, USA) and RPMI 1640 (Invitrogen, Carlsbad, CA, USA) medium containing 10% FBS and antibiotics, as recommended by the supplier (Invitrogen, CA, USA). All human cell lines were authenticated using Short Tandem Repeat (STR) profiling within the last three years. All experiments were performed with mycoplasma-free cells. The Bcl-xl-derived peptide CS-PEP1 (of sequence FFSFGGAL) was synthesized by Peptech (Saint Petersburg, Russia) and dissolved in sterile DMSO as a stock solution of 10 mM.

### Expression Plasmids and Primers

Cathepsin S-FLAG (pCS-FLAG) and cathepsin S C25A-FLAG (pCS-C25A-FLAG) mammalian expression plasmids were gifts from Dr Yun-Sin Lee [30]. BID, BAX, Bcl-xl coding sequences were PCR cloned into pCDNA3.1+/HA for carboxyl-terminal HA-

epitope tagging. Bcl-xl-HA was difficult to detect using Western blotting, possibly due to c-terminal processing of the protein. Plasmid pBAX was made by cleaving pBAX-HA with *Xho* I, T<sub>4</sub> DNA polymerase fill-in reaction, and auto-ligation (to remove in-frame HA-tag expression). The coding sequences for BAX and Bcl-xl were respectively sub-cloned into pET28A and pGEX5x-1 for bacterial expression. Bcl-2 protein and CS PCR primers:

BAX-GCTAGCTGAATTCATGGACGGGTCCGGGGAGCAG and CCGCTCGAGGCCATCTTCTTCCAGATGG;

BID-GCTAGCTGAATTCATGGACTGTGAGGTCAACAACGGTTCC and CCGCTC-GAGGTCCATCCCATTCTGGCTAAGCTCC;

Bcl-xl-GCTAGCTGAATTCATGTCTCAGAGCAACCGGGAGCTGGTGG and CCGCTCGAGTTTCCGACTGAAGAGTGAGCCC.

The human cathepsin s coding sequence was PCR cloned into pET15b using: CATHS-TATACATATGCAGTTGCATAAAGATCCTACC and CATH-AS TTCTCGAGCTAGATTTCTGGTAAGAGG.

#### 5' CTS gene reporter construction

The -1048 bp and -564 bp fragments upstream of the cathepsin S (CS) gene sequence were PCR cloned using: -1048 bp (CTCGAGTGCCTCCAGCATGGGAGACAAA with GTCAATTGAACTGAAATAAGCTT); and -564 bp (CTCGAGTACAAGGAGCTGGGATTGGGG with GTCAATTGAACTGAAATAAGCTT). DNA fragments were subcloned into *Xho* I/*Hind* III digested pTurbo-GFP PRL, giving pCS-1048 and pCS-564. Mammalian cells were transfected with 1 µg of plasmid for 24 h and stimulated with Pac (5 µg/mL) for a further 24 hr, lysed and equal volumes analyzed by Western blotting for GFP expression, using an *anti*-GFP antibody (Evrogen, Moscow, Russia).

#### Semi-Quantitative RT-PCR

Cells seeded on 100 mm tissue culture plates were stimulated as outlined and total RNA isolated using Trizol reagent (Invitrogen, CA, USA). 1 µg of total RNA was reverse transcribed MMLV Reverse Transcriptase kit (Evrogen, Moscow, Russia). 2.5 ng of cDNA template was used in the qPCRmix-SH system (Evrogen, Moscow, Russia) for each reaction, at an annealing temperature of 55 °C and equal volumes (10 µL) analyzed on 1% agarose gels. Primers used to quantify CS, BAX and GAPDH transcripts were: CS-F (TCAACTGAAAATATGGAA), CS-R (CCTTCTTACCAAAGTTGTGGCC), BAX-F (ATGTTTTCTGACGGCAACTTC), BAX-R (AGTCCAATGTCCAGCCCAT), GAPDH-F (CTTCGCTCTCTGCTCCTGTTTCG) and GAPDH-R (ACCAGGCGCCCAATACGACCAAAT), and gave 390, 133, and 140 bp products, respectively.

#### Primers for CS knockdown plasmid construction

The pCS-shRNA expression plasmid was made by annealing the two primers of the sequence; GATCGGGAGACATGACCAGTGAAGATCAAGAGTCTTCACTGGTCATGTCTCC and GATCGGGAGACATGACCAGTGAAGACTCTTGATCTTCACTGGTCATGTCTCC, followed by their ligation into *Bgl* II digested plasmid pTER (as outlined in [31]). Insert integrity was confirmed by DNA sequencing, and approximately 3 µg plasmid was used to transfect HEK293 or 769P cells for 24 h, before cells were lysed and equal volumes of cleared lysates analyzed by reducing SDS-PAGE/Western blotting.

#### Bacterial expression and purification of proteins

Bacterial strain BL-21 (DE3) Lys-S was used for expression of bacterial BAX-His<sub>6</sub> and GST-Bcl-xl fusion proteins. GST-Bcl-xl protein was purified as outlined previously [32] and the BAX-His<sub>6</sub> was bacterially expressed, batch purified using the method outlined previously [31] and the protein kept immobilized on NTA agarose (Pierce, Waltham MA, USA) for subsequent CS-mediated cleavage assays. Cathepsin S protein was expressed in BL-21 cells, sonicated and inclusion bodies solubilized in 4 mL 20 mM Tris-HCl, 6 M Guanidine hydrochloride (Gnd-HCl), 0.5 M NaCl and 10 mM imidazole (Im), pH 8.0 (Buffer A). Cleared lysates were applied to an IMAC column, washed in Buffer A and eluted using 6 M Gnd-HCl, 0.5 M NaCl, 0.3 M Im, pH 8.0 (Buffer B). DTT was added to a final concentration of 10 mM to eluted fractions, which were dialyzed against refolding buffer (1 M Tris-HCl, 1 M Arg-HCl, 1 mM reduced L-Glutathione, 2 mM oxidized L-

Glutathione, 2 mM EDTA, pH 8.0). Cleared protein solution was concentrated using a 10 kD cut-off Amicon protein concentrating cell and protein concentration was determined.

#### **Transfection of mammalian cells**

HEK293 or 769P cells were seeded at  $1.5 \times 10^5$  cells per 35 mm well and transfected using the recommended amount of plasmid DNA with Turbofect reagent (Thermo Fisher Scientific, Carlsbad, CA, USA). Generally, pBAX-HA (or other Bcl-2 protein encoding plasmids) were co-transfected at 0.5 µg with 1.5 µg pCS-FLAG (or pCS-C25A-FLAG) or at a respective ratio of 1:3 per transfection of HEK293 or 769P cells. Plasmid pCDNA3.1+ was used in negative control transfections and to keep plasmid amounts consistent between differing transfection conditions. Transfected cells were lysed in equal volumes of 1% NP40LB (as described in [33]) and equal volumes of cleared whole cell lysates used in subsequent procedures.

#### **Cycloheximide Pulse Chase Studies**

Cells were transfected for 24 h with 0.25 µg BAX-HA and CS-FLAG-derived expression plasmids (0.75 µg) for 6 h and left either untreated or treated with 10 µM CS-PEP1 for a further 18 h. Cells were then treated with 20 µM cycloheximide (in medium containing 10% serum) for 1 h and the cells washed in PBS, lysed in 1% NP40LB buffer at the indicated time points and 10% *v/v* of cleared whole cell lysate analyzed by reducing SDS-PAGE and Western blotting.

#### **Immunoprecipitation of Proteins**

These were carried out overnight as described previously [31,33], with 0.25 µg of *anti*-HA antibody and 30 µL of protein AG agarose beads (Pierce).

#### **Cathepsin S-Ni-NTA Co-precipitations**

30 µL of Ni-NTA agarose (Pierce) were incubated with 5 µg of CS protein diluted in 1 mL 1% NP40LB (lacking EDTA) and incubated with gentle rotation overnight at 4 °C. The resulting CS-NTA agarose was washed six times with 1% NP40LB (-EDTA) using cycles of microcentrifugation and after the last wash, equal volumes of 100 mM sodium acetate pH 4.0 buffer (50 µL) added and the mix incubated at 37 °C for 5 min. 50 µL of 100 mM Na<sub>2</sub>PO<sub>4</sub>, pH 7.2 were added, followed by cleared lysate prepared from mammalian cells expressing BAX-HA and the resulting mixtures incubated at 4 °C overnight with gentle rotation. As a negative control, Ni-NTA alone was also incubated with equal volumes of lysate. Precipitates were washed using 1 mL 1% NP40LB (-EDTA) six times and then 20 µL of 2× Laemmli buffer/DTT added followed by heating to 95 °C for 5 min. Samples were analyzed by Western blotting using the *anti*-HA antibody to detect BAX-HA. 5% *v/v* of the cleared lysate expressing BAX-HA was also analyzed by Western blotting.

#### **Isolation of ubiquitinated BAX intermediates**

p21 BAX protein (pBAX-3.1+, 0.25 µg) was co-expressed with HA-tagged ubiquitin (0.5 µg) or cathepsin S-FLAG derivatives (0.75 µg) in mammalian cells and cleared soluble lysates prepared using 1% NP40LB containing protease inhibitors. Immune complexes were purified using *anti*-HA antibody overnight, washed and 50 µL of 2× Laemmli buffer added to the beads before samples were boiled for 5 min. 950 µL of 1% NP40LB were added to each sample, centrifuged and the soluble fraction removed and immunoprecipitated again, overnight using the *anti*-HA antibody (as outlined above) before being washed six times with 1% NP40LB and equal volumes analyzed by reducing SDS-PAGE and Western blotting, as described [31] (either before or after being subjected to cathepsin S-mediated cleavage, *in vitro*).

#### **In vitro cathepsin S cleavage assays**

Purified immune complexes (as described in [31]) were washed in 1 mL of 100 mM Na<sub>2</sub>PO<sub>4</sub>, pH 7.2 buffer and resuspended in 20 µL of the same buffer. An equal volume of 100 mM sodium acetate (pH 4.0) buffer was added to 0.5 µg of purified cathepsin S and the mixture incubated at 37 °C for 10 min to auto-activate the cathepsin S protein. An equal volume of 100 mM Na<sub>2</sub>PO<sub>4</sub> pH 7.2 buffer was added to this enzyme mix giving a final concentration of cathepsin S of 0.125 µg/µL. For pH 7 cleavage assays, 4 µL of this mix (0.5 µg cathepsin S) were added to the immunoprecipitated complexes, 100 ng BAX-Ni-NTA

agarose beads or 0.5 µg GST-BCI-xI agarose beads that had been previously washed twice in 1 mL of 100 mM Na<sub>2</sub>PO<sub>4</sub>, pH 7.2 and then resuspended in 20 µL of 100 mM Na<sub>2</sub>PO<sub>4</sub>, pH 7.2, 2 mM DTT. The reactions were incubated at 37 °C for 50 min and the reaction terminated upon the addition of 20 µL of 2× Laemmli Buffer (containing 100 mM DTT), followed by a 5 min incubation at 94 °C. For cleavage assays conducted at pH 5, immobilized substrate proteins (in 20 µL of 100 mM Na<sub>2</sub>PO<sub>4</sub> buffer, pH 7.2) were resuspended in 20 µL of 100 mM sodium acetate (pH 4.0), prior to the addition of 0.5 µg (4 µL) of activated cathepsin S mix, followed by incubation at 37 °C for 50 min and termination with 2× Laemmli Buffer/DTT and heating to 95 °C for 5 min. Reaction mixtures were scaled up so that their pH could be determined with greater accuracy using a pH electrode (Millipore). Equal reaction volumes were analyzed by SDS PAGE or Western blotting.

#### Laser Scanning Confocal Microscopy

HEK293 cells were seeded on glass coverslips, transfected for 24 h and then stimulated with Pac (or HP) for an additional 24 h. Coverslips were fixed in 4% PFA/PBS pH 7.4, permeabilized in 0.1% Triton X-100/PFA/PBS, washed and treated with 100 mM Glycine PBS/pH 8.2 for 30 min and incubated in primary antibody (at the recommended dilution) for 1 h. Incubation in secondary antibody-fluorophore conjugate (Molecular probes, Eugene, OR, USA) was for 1 h and coverslips mounted in Mounting Mix Gold-with or without DAPI stain (Invitrogen). Images were recorded on a Zeiss LSM880 Airyscan microscope using Zeiss Zen Black software.

#### Apoptosis Assays

HEK293 or 769P cell lines were treated as outlined in the Click-IT TUNEL Alexa-Fluor 594 Imaging Assay kit (Molecular Probes) and coverslips mounted on microscope slides in the presence of DAPI staining. Between 200–1000 cells were visualized using 20x and 40x objectives on a Zeiss LSM 880 Airyscan laser scanning confocal microscopy and apoptotic cells (stained in red) scored. Results from one series of experiments are presented where consistency was seen between duplicated experiments. Experiments were repeated identically in the absence of seeding cells on coverslips and cells lysed in 200 µL of 1% NP40LB and 2× Laemmli buffer/DTT before samples were heated at 95 °C for 10 min for Western blot analysis.

#### Statistical Analysis and Densitometry

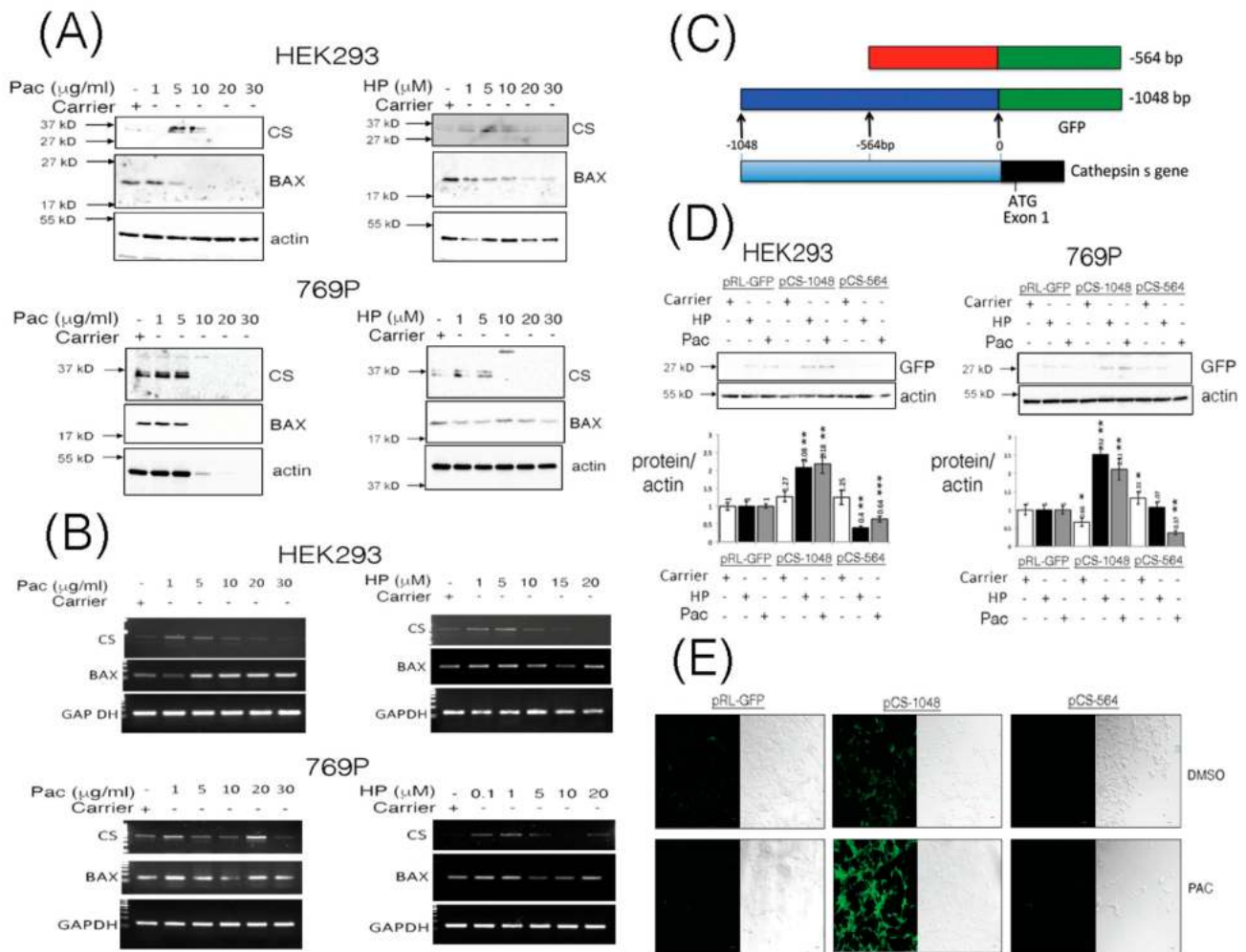
Experiments were performed independently with an  $n = 3$ . The results representative of one experiment are highlighted within the figures, where consistency was seen at least twice. Western blot images were analyzed using Adobe Photoshop CS4 to quantify and record the intensity of bands (using technical repetitions of  $n = 3$ , which were generally all normalized for β-actin protein levels as observed for unstimulated HEK293 or 769P cells (and negative control samples) using Excel (Microsoft, Moscow, Russia). For statistical analyses, the intensity of bands (or apoptotic cell numbers) were calculated from the mean between three readings and the Standard Error around the Mean ( $\pm$ SEM). These results were plotted using Excel (Microsoft, Moscow, Russia). The two-tails unpaired student *t*-test (Excel) was performed to test for significance of  $\pm$ SEM values (Excel). Source data are available for all figures.

### 3. Results

#### 3.1. The CTTS Gene Is Induced under Paclitaxel or Hydrogen Peroxide Stimulatory Conditions

While the classical approach to defining a direct relationship between cathepsins and cancer have emerged through characterizing deregulated expression of cathepsins in tumor progression [1], relatively less is understood about the inducible nature of cathepsin gene expression under normal conditions or during chemotherapy. We stimulated Human Embryonic Kidney (HEK293) cells and the human RCCC cell line 769P with increasing doses of Paclitaxel (Pac) and hydrogen peroxide (HP) and observed steady-state levels of *pro*-cathepsin S protein (CS, 37 kD) to be enhanced in a dose-dependent manner (Figure 1A), while p21 BAX protein levels were observed to diminish (Figure 1A, Supplementary Figure S1A,B).





**Figure 1.** Cathepsin S (CS) protein expression levels are induced through the -1048 promoter fragment from the *CTTS* gene upon Paclitaxel or hydrogen peroxide stimulation. HEK293 and 769P cells were stimulated with increasing doses of Paclitaxel (Pac) and hydrogen peroxide (HP) and soluble lysates prepared after 24 h and equal volumes analyzed by Western blotting for cathepsin S (CS), BAX and actin expression (Panel A). Similarly, total RNA was isolated from cells stimulated for 24 h with increasing doses of Pac or HP and equal quantities of template cDNA analyzed for transcriptional expression of CS, BAX and Glyceraldehyde-3-phosphate dehydrogenase (GAP-DH, Panel B). Promoter fragments, derived from the transcriptional start site of the *CTTS* gene to -1048 and -564, were PCR cloned and fused to a promoter-less GFP encoding plasmid (Panel C) and evaluated for GFP expression in equal volumes of HEK293 and 769P cleared whole cell lysates (WCLs) under Pac (10 µg/mL and 5 µg/mL, respectively) or HP (5 µM) stimulatory conditions. GFP expression was also quantified, standardized and corrected against GFP expression from cells stimulated with carrier alone and is shown as a fold change over basal GFP expression (Panel D). HEK293 cells transfected with pCS-1048 or pCS-564 and stimulated with Pac (5 µg/mL) for 24 h were also fixed and visualized for GFP expression using laser scanning confocal microscopy (Panel E). The red bar indicates 1 micron. Quantified data are presented as the mean ± SEM and its significance (where  $p < 0.05$ ) determined, using a two-way Student's *t*-test (\*  $p < 0.05$ , \*\*  $p < 0.01$  and \*\*\*  $p < 0.001$ ).

In order to ascertain whether the changes in levels of CS (or even p21 BAX) proteins were due to transcriptional modulation of their genes, we performed quantitative RT-PCR analysis on total RNA isolated from cells stimulated in a dose-dependent manner using Pac or HP. CS and BAX transcripts were basally- or inducibly-expressed in HEK293 cells upon treatment with Pac (1–20 µg/mL) and HP (1–5 µM) (Figure 1B, Supplementary Figure S1C). In 769P cells, cathepsin S gene (*CTSS*) expression was induced with 1 µg/mL PAC and 0.1–5 µM HP (Figure 1B, Supplementary Figure S1D). *BAX* gene expression was also in-

duced in 769P cells through stimulation with Pac at 1  $\mu\text{g}/\text{mL}$  or HP at 0.1–1  $\mu\text{M}$  (Figure 1B, Supplementary Figure S1D).

To confirm some of these effects, we embarked on analyzing the promoter region of the *CTSS* gene to ascertain whether it is amenable to inducible regulation under Pac or HP stimulatory conditions (Figure 1C). Using a GFP-protein reporter assay, the upstream -1048 bp fragment of the *CTSS* gene was inducibly responsive to stimulation of HEK293 or 769P cells with Pac or HP, as a respective 2–3 fold increase in GFP-reporter gene expression was observed (Figure 1D). Moreover, enhanced GFP-reporter expression could be clearly visualized under Pac stimulatory conditions in HEK293 cells (Figure 1E).

### 3.2. Expressed Cathepsin S Protein Destabilizes p21 BAX Protein Levels in Mammalian Cells

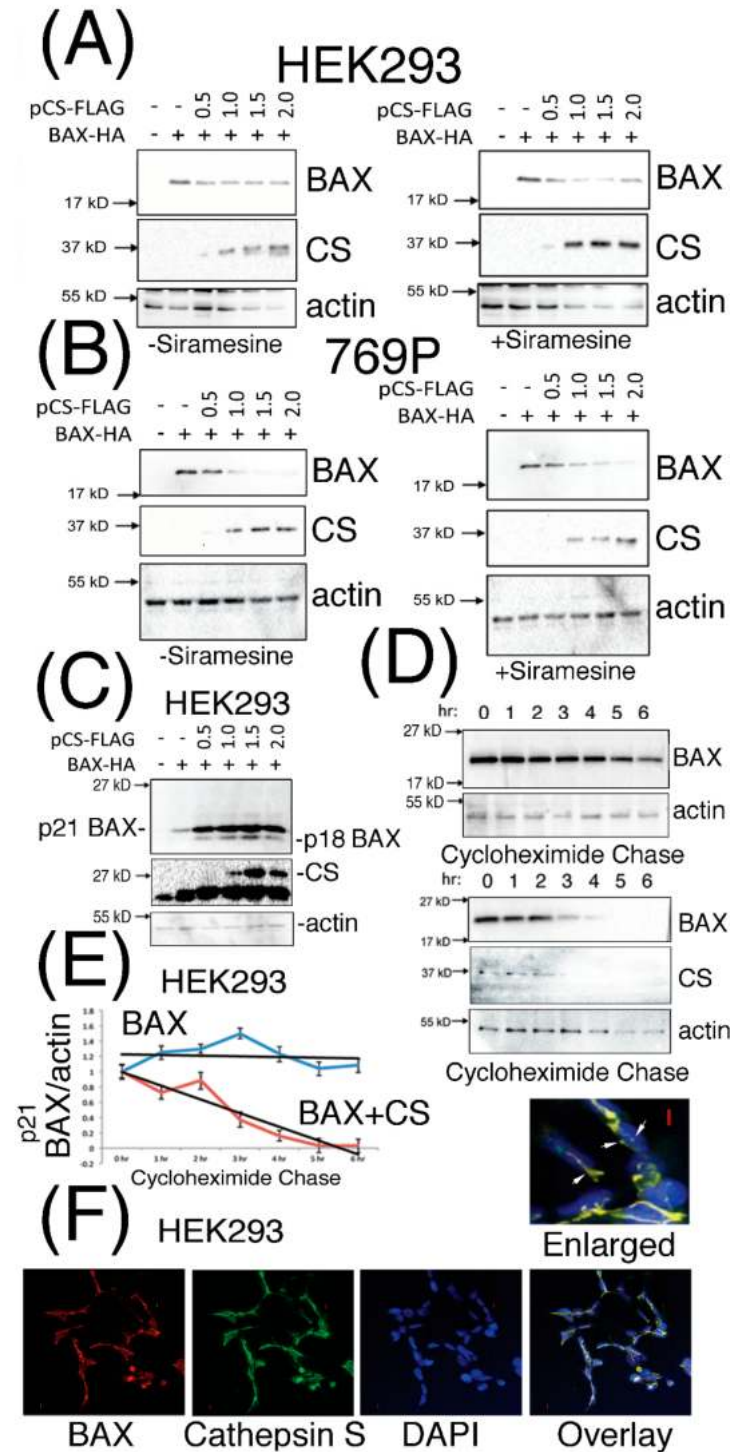
Previously published findings have proposed that destabilization of the p21 BAX protein can occur in a cathepsin protease-dependent manner in A-549, U-937, K-562 and HL-60 cells, and for which a cathepsin protease had not been identified and characterized [27]. Taken with our *in silico* analyses [34], we investigated the effect of co-expressing p21 BAX protein with increasing doses of CS protein expression in mammalian cells. Diminished steady state levels of p21 BAX protein were observed upon increasing levels of CS expression in HEK293 (Figure 2A) and 769P cells (Figure 2B), which were slightly reduced further upon the treatment of cells with the lysosomorphogenic agent Siramesine (Supplementary Figure S2A,B). Interestingly, under identical transfection conditions, an estimated p21 BAX-derived protein derivative of 18 kD was clearly visible following the incubation of transfected HEK293 for 48 h (Figure 2C). Moreover, CS-mediated destabilization of p21 BAX could be confirmed by performing cycloheximide pulse chase experiments in the presence or absence of CS with p21 BAX co-expression in HEK293 cells (Figure 2D,E). Moreover, CS and BAX proteins were observed to co-localize within distinct unidentified cytoplasmic and peri-nuclear filamentous structures (Figure 2F).

### 3.3. Cathepsin S-Mediated Cleavage of p21 BAX is Inhibited by the Novel CS Antagonist CS-PEP1 *In Vitro* and in Mammalian Cells

The approach for developing ‘BH3-mimetics’ through disrupting the interaction of the BH3 domain (from the *pro*-apoptotic BH3-only proteins) with the hydrophobic pocket of *anti*-apoptotic proteins does have demonstrated potential in effective and selective therapeutic design [35,36]. Being mindful of this approach, we identified a novel peptide (of sequence FFSFGAL, called CS-PEP1) derived from the  $\alpha$ 5-helix from within the hydrophobic pocket of the Bcl-xl protein, based on the presence of this sequence in the fungal papain-like protease inhibitor, Pit2 [37]. We reasoned that such a peptide may exhibit three potentially useful qualities in that it may be inhibitory towards CS, while offering some degree of hindrance against inhibitory Bcl-xl interacting with p21 BAX (or other BH3-only proteins), in addition to it simultaneously blocking Bcl-xl homodimer formation through blocking the BH3-hydrophobic pocket interaction.

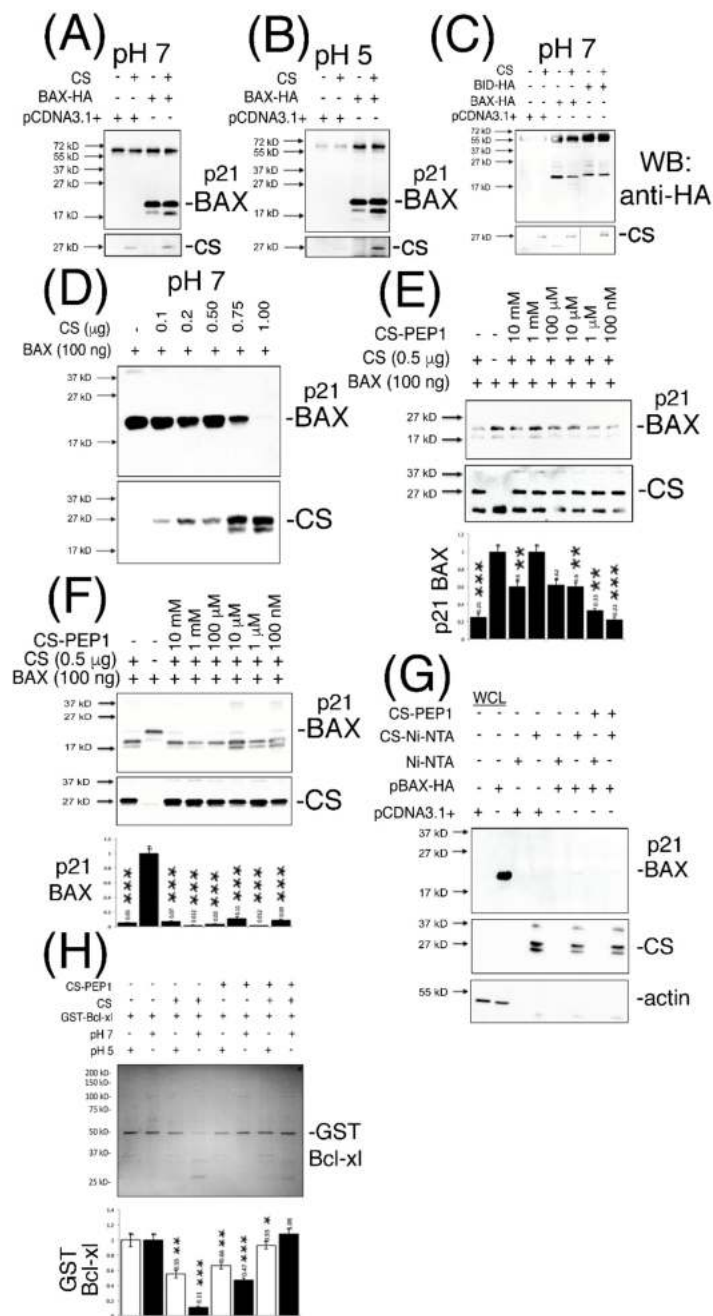
In striving towards addressing some of these key points, we firstly developed a CS-mediated ‘*in vitro* cleavage assay’ which confirmed that our bacterially expressed CS protein activated *in vitro* (and of size 27 kD) was catalytically-active against immunoprecipitated p21 BAX (Figure 3A,B) and BID protein substrates (Figure 3C) at pHs 7 and 5. Interestingly, enhanced p21 BAX-derived cleavage products of size 18- and 17-kD were readily discernable from cleavage reactions performed at pHs 7 and 5 (Figure 3A–C). As a novel substrate for CS, recombinant p21 BAX could also be cleaved in a CS dose-dependent manner at pH 7, as seen from (Figure 3D), and which could be inhibited by CS-PEP1 in the range of 10 mM–1  $\mu\text{M}$  *in vitro* (Figure 3E, lanes 3–7). Similarly, CS-mediated cleavage of immunoprecipitated p21 BAX protein was significantly inhibited; through detection of the p21 BAX substrate or the accumulation of its 17- and 18-kD cleavage products (Figure 3F, lanes 3, 6, 8). Furthermore, CS-PEP1 dependent inhibition of CS-mediated p21 BAX cleavage did not appear to occur through the disruption of the CS-BAX protein interaction, as p21 BAX-HA could still interact with CS-Ni-NTA agarose beads in the presence of CS-PEP1 co-incubation (Figure 3G, lanes 6 and 8). As an important regulatory step for BAX protein

activation, we also observed CS-PEP1 to exhibit inhibitory activity towards CS-mediated Bcl-xl cleavage in vitro (Figure 3H) at pH 7 (lane 8) significantly better than at pH 5 (lane 7). Of note, was the marginal destabilizing effects on GST-Bcl-xl protein at pH 5, and which may occur due to reductions in thermodynamic stability at this pH, as previously reported for the Bcl-xl $\Delta$ TM protein derivative at pH 4.9, in vitro [38].



**Figure 2.** CS expression can destabilize the p21 BAX protein and co-localize with it in distinct cytoplasmic and peri-nuclear compartments. (Panels A and B), HEK293 and 769P cells were co-transfected with pBAX-HA and increasing doses of pCS-FLAG ( $\mu$ g) expression plasmids for 24 h, stimulated with carrier (left panels) or 2  $\mu$ M Siramesine (right panels) for 1 h and equal volumes of

soluble cell extracts analyzed for p21 BAX, CS and actin expression levels. (Panel C), HEK293 cells transfected for 48 h with the indicated  $\mu\text{g}$  amounts of plasmid DNA, were lysed and equal volumes of soluble extracts analyzed for BAX protein expression. (Panel D), Protein levels of p21 BAX were analyzed following cycloheximide pulse chase after HEK293 cells were transfected for 24 h with pBAX-HA (0.25  $\mu\text{g}$ ) alone or with pCS-FLAG (0.75  $\mu\text{g}$ ). p21 BAX expression levels were quantified, standardized for actin expression levels from cells treated with cycloheximide at T = 0 h. (Panel E), The blue and red curves indicate p21 BAX or p21 BAX levels upon co-expression with CS (respectively) and trend lines are shown in black. (Panel F), HEK293 cells co-expressing BAX-HA and CS for 24 h were stained for BAX and CS expression using *anti*-HA and -CS antibodies (SCB). BAX and CS co-localization is highlighted by white arrows and the red bars represent 1 micron. Quantified data is presented as the mean  $\pm$  SEM and its significance (where  $p < 0.05$ ) determined.

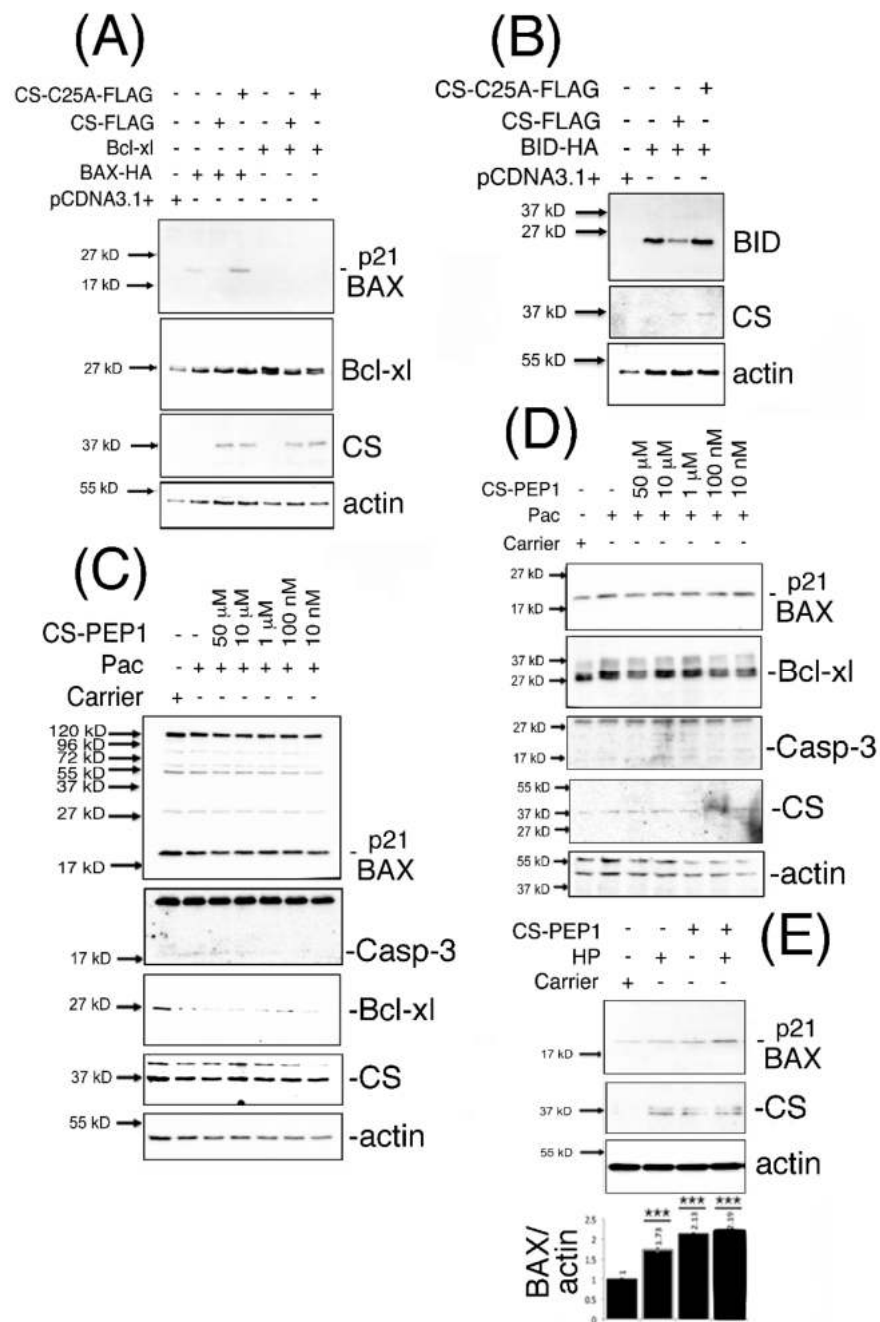


**Figure 3.** Active CS cleaves p21 BAX and GST-Bcl-xl in vitro and is inhibited by peptide CS-PEP1

in a pH-dependent manner. (Panels A–C), Equal cleared cell lysate volumes from HEK293 cells expressing BAX-HA or BID-HA for 24 h were immunoprecipitated using an *anti*-HA antibody, and washed immunoprecipitates exposed to active CS at pHs 7 and 5. Cleavage products were detected by Western blotting (top panels) and filters were re-probed to detect CS (lower panels). (Panel D), Equal quantities of bacterially expressed p21 BAX protein were exposed to active CS at pH 7 and the reactions analyzed for BAX cleavage using Western blotting using an *anti*-BAX antibody (Abcam). Filters were re-probed to detect CS (lower panels, SCB). (Panel E) BAX cleavage reactions at pH 7 were co-incubated in the presence of decreasing doses of CS-PEP1 and equal reaction volumes analyzed for p21 BAX cleavage products (top panel) and CS levels (middle panel), using an *anti*-BAX (Abcam) or *anti*-CS (SCB) antibody. p21 BAX substrate levels were quantified, standardized against BAX alone (lane 2) and are displayed in the lower panel. (Panel F), Equal amounts of immunoprecipitated p21 BAX-HA protein, derived from 0.25 µg BAX-HA expression in HEK293 cells, were co-exposed to active CS and decreasing amounts of CS-PEP1 at pH 7, and p21 BAX cleavage products (or CS) detected by Western blotting with an *anti*-BAX or -CS antibody (top and middle panels). p21 BAX substrate levels were quantified, standardized against BAX alone (lane 2) and are displayed in the lower panel. (Panel G), Cells expressing p21 BAX-HA were stimulated with carrier or CS-PEP1 (10 µM) for 24 h, lysed and equal volumes of soluble lysates (WCLs) incubated with activated CS-Ni-NTA agarose beads overnight (in the presence of 10 µM CS-PEP1), washed and analyzed for BAX-HA binding using an *anti*-HA antibody (top panel). CS (middle panel) and actin (lower panel) proteins were also revealed. (Panel H), In vitro CS-mediated cleavage assays were performed at pH 7 and 5 (top panel) using equal quantities of GST-Bcl-xl as a substrate in the presence of 100 µM CS-PEP1 (or carrier). Cleavage products were detected using Coomassie blue staining and substrate levels were quantified as shown in the lower panel (pH 7-white bars and pH 5-black bars). Quantified data are presented as the mean ± SEM and its significance (where  $p < 0.05$ ) determined, using a two-way Student's *t*-test (\*  $p < 0.05$ , \*\*  $p < 0.01$  and \*\*\*  $p < 0.001$ ).

#### 3.4. Dominant-Inhibitory Cathepsin S Expression and CS-PEP1-Mediated Cathepsin S Inhibition Rescues p21 BAX Destabilization

We next sought to address whether CS-mediated effects on BAX destabilization in mammalian cells could be mechanistically reversed, using the approaches of expressing dominant-inhibitory CS-C25A or stimulation of cells with CS-PEP1. Steady state levels of monomeric expressed p21 BAX, Bcl-xl and BID proteins (Figure 4A,B) were enhanced in the presence of expressed CS-C25A (Supplementary Figure S3A). Upon co-stimulation of HEK293 (Figure 4C) or 769P cells (Figure 4D) with CS-PEP1 and Pac, endogenous p21 BAX protein levels were enhanced between CS-PEP1 concentrations of 10 µM–10 nM (Supplementary Figure S3B,C). Interestingly, under Pac stimulatory conditions in HEK293 cells, Bcl-xl protein levels (in relation to p21 BAX protein levels) were observed to diminish (Supplementary Figure S3B). As reported in previous studies, this may be due to dose- and time-dependent responsiveness of cells to Pac, as seen with 8305C cells [39]. Moreover, down-regulation of Bcl-xl, has been reported upon the treatment of prostate cells with Docetaxel [40,41] or under oxidative stress conditions, in a Keap1 adaptor protein-dependent manner [42], and cannot be excluded as contributory factors. However, enhanced active caspase-3 (and diminished β-actin levels) levels were also evident in the presence of CS-PEP1 concentrations as low as 10 nM when stimulating HEK293 and 769P cells (Supplementary Figure S3C). Such findings are suggestive of apoptosis activation, in the presence of CS-PEP1 treatment of cells, and which can have the effect of masking gene regulatory events of importance. Consequently, co-treatment of 769P cells with the caspase inhibitor z-VAD (with Pac and CS-PEP1) did offer a more reliable alternative for visualizing enhanced CS-PEP1 mediated endogenous p21 BAX stabilization effects (Figure 4E), in the presence of β-actin stabilization and due possibly to effective cell death inhibition.



**Figure 4.** p21 BAX protein is stabilized in the presence of CS-C25A expression and in the presence of cell stimulation of HEK293 or 769P cells with CS-PEP1. HEK293 cells co-expressing BID-HA, Bcl-xl or BAX-HA with CS-FLAG or CS-C25A-FLAG for 24 h were lysed and equal volumes of soluble cellular extracts analyzed for p21 BAX, Bcl-xl or BID expression using Western blotting with *anti*-HA or *anti*-Bcl-xl antibodies (Panels A and B). HEK293 cells (Panel C) or 769P cells (Panel D) were co-stimulated with decreasing doses of CS-PEP1 in the presence of carrier or 5 μg/mL Pac for 24 h and equal volumes of cleared lysates analyzed for p21 BAX (Abcam), active Caspase-3 (Abcam), Bcl-xl (Abcam), CS (Invitrogen) and actin (Abcam) expression. 769P cells (Panel E) were co-stimulated with carrier or 5 μg/mL Pac, 10 μM zVAD-fmk and 10 μM CS-PEP1 for 24 h. Equal volumes of soluble whole cell lysates (WCLs) were analyzed for endogenous p21 BAX (Abcam), CS (Abcam) and actin (Abcam) expression. p21 BAX protein levels were quantified, standardized for actin expression and are represented by black bars as fold changes over stimulations with carrier alone. Quantified data are presented as the mean ± SEM and its significance (where  $p < 0.05$ ) determined, using a two-way Student’s *t*-test (\*\* $p < 0.01$ ).

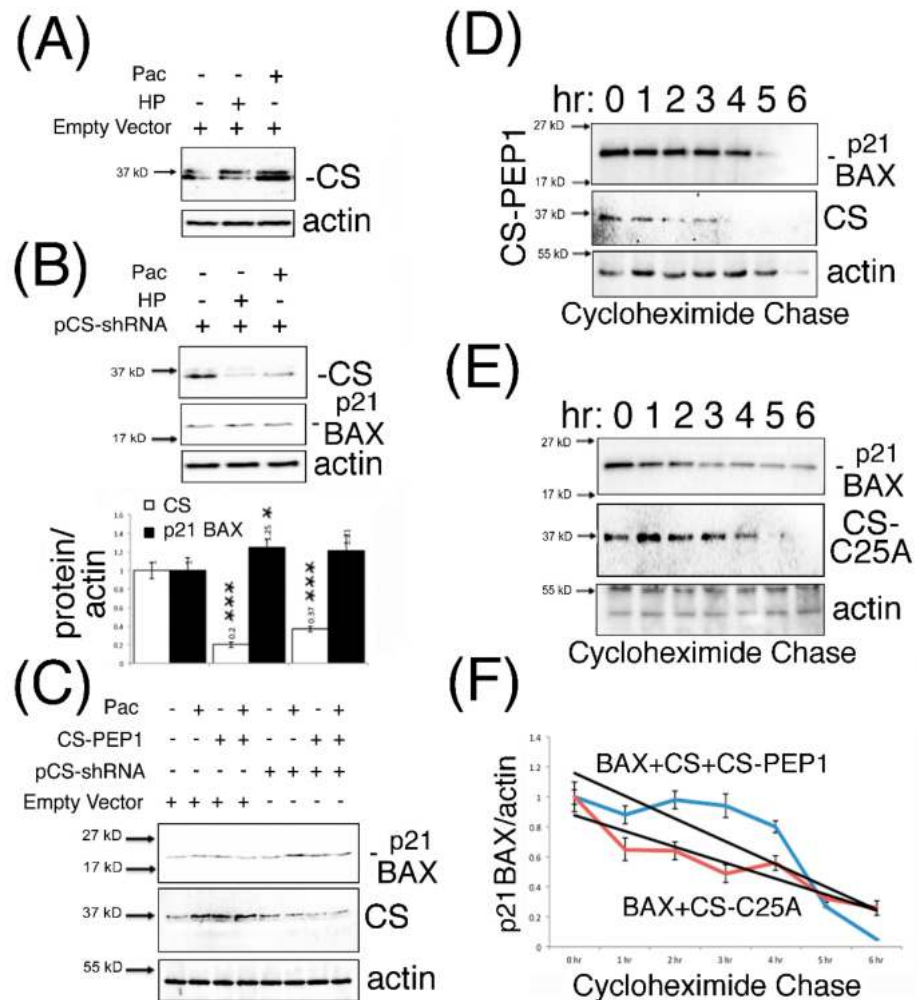
### 3.5. Knockdown Expression Cathepsin S and CS-PEP1-Mediated Cathepsin S Inhibition Rescues p21 BAX Destabilization

Previous findings have reported that CS expression is amenable to interference using shRNA approaches, as seen for CS-mediated regulation of the BRCA1 protein in breast cancer cells [30]. Consequently, we adopted a similar approach to ask whether the knockdown expression of CS could modulate steady-state endogenous p21 BAX protein levels, in the presence and absence of CS-PEP1 mediated inhibition of CS protease activity. As seen from Figure 5A, Pac- or HP-treatment of HEK293 cells could induce endogenous CS protein levels in HEK293 cells. Such an effect could also be abrogated in the presence of CS-shRNA expression, and from which enhanced p21 BAX protein levels were observed (Figure 5B). Furthermore, CS-PEP1 treatment appeared to show minimal synergistic effects on CS-knockdown-mediated steady-state p21 BAX protein levels in Pac treated HEK293 cells (Figure 5C). Lastly, the positive stabilizing effects of CS-PEP1 or CS-C25A on p21 BAX levels were supported further by cycloheximide pulse chase analyses, where p21 BAX when co-expressed with CS and CS-PEP1 treatment (Figure 5D) were seen to have similar protein stability levels to p21 BAX when co-expressed with CS-C25A (Figure 5E) over a 6 hr time course (Figure 5F).

### 3.6. Polyubiquitinated BAX (p120BAX) Is a Novel Substrate Targeted for Cleavage by Cathepsin S

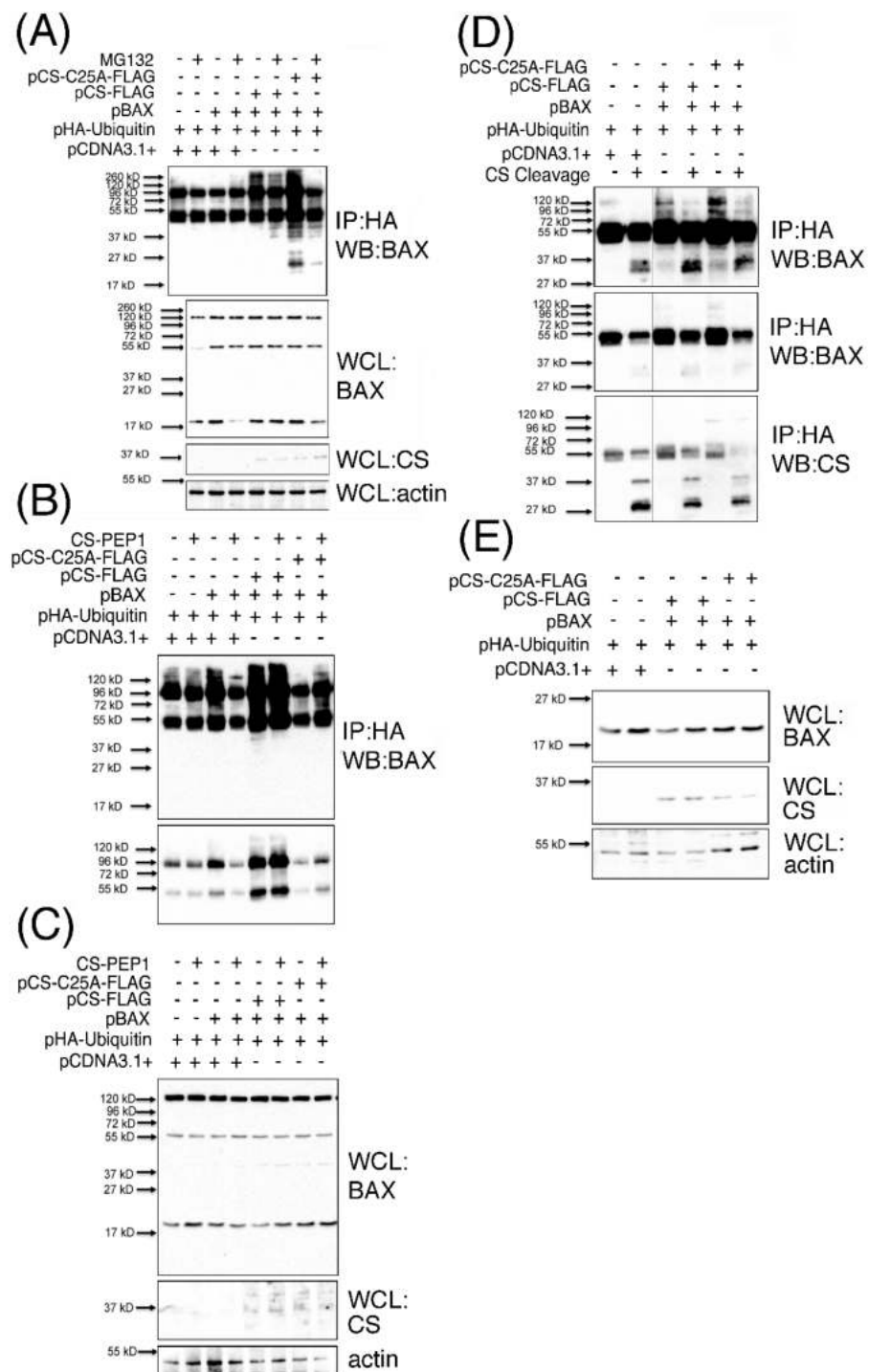
The accumulation of a number of BAX-derived protein species ranging in sizes 37–120-kD, which were readily detected from CS-PEP1 treated cells also captured our attention from Figure 4C, and which did not appear to correspond with the reported 80-, 96-, 160- or 260- kD homo-oligomerized sizes for the BAX protein [22]. Consequently, we hypothesized that the 120 kD BAX-derivative protein that was clearly visible from this data (Figure 4C) may represent a novel polyubiquitinated form of BAX arising in a CS-expression dependent manner. This was confirmed through identifying such a sized derivative amongst additional mono- and poly-ubiquitinated BAX derivatives, which were visible as a characteristic protein ‘ladder’ (or smear) in immunoprecipitates derived from cell extracts co-expressing p21 BAX, with CS or CS-C25A (Figure 6A), in the protein range from 27–260 kD. Briefly, polyubiquitinated BAX derivatives were detected upon BAX and CS co-expression (Figure 6A, lane 5) in comparison to BAX expression alone (Figure 6A, lane 3), implying that BAX polyubiquitination is CS expression-dependent. Under these expression conditions, and in the presence of MG132-mediated proteasomal inhibition, polyubiquitinated BAX derivative levels (Figure 6A, lane 4) were also enhanced in the presence of CS co-expression (Figure 6A, lane 6). Such findings suggest that BAX ubiquitination is CS expression-dependent and that the arising ubiquitinated BAX derivatives can also accumulate in the presence of proteasomal inhibition. Moreover, polyubiquitinated BAX derivatives were seen to accumulate upon BAX co-expression with CS-C25A (Figure 5A, lane 7) and less so in the presence of proteasomal inhibition (Figure 6A, lane 8), which would seem to suggest that the disposal of CS catalytic activity also permits the accumulation of polyubiquitinated BAX protein derivatives. For simplicity, we focused on the effects of CS-mediated accumulation of BAX ubiquitinated derivatives in the absence of proteasomal inhibition and observed the accumulation of 45–150 kD polyubiquitinated BAX species, upon basal CS inhibition in the presence of CS-PEP1 stimulation (Figure 6B, lane 4), or upon CS-C25A co-expression (Figure 6B, lane 8). Here, ubiquitinated BAX derivatives were readily observed in the presence of CS expression (Figure 6B, lane 5) and the levels of which could be marginally enhanced upon CS-PEP1 co-treatment of cells (Figure 6B, lane 6). These observations confirmed our previous findings (from Figure 6A) that positive CS protein expression (as seen from Figure 6C) permits the accumulation of ubiquitinated BAX derivatives and that the inhibition of CS activity also mediates the accumulation of such protein species, as seen with the presence of 120 kD polyubiquitinated BAX derivative (p120BAX). Based on these collective findings, we next asked whether the p120BAX polyubiquitinated derivative might be a substrate for active CS, *in vitro* (Figure 6D). Here, p120BAX was present in greater abundance upon CS-C25A and

p21 BAX co-expression (Figure 6D, lane 5), in comparison to CS and p21 BAX co-expression (Figure 6D, lane 3) and that p120BAX could be cleaved by activated CS into three distinct polypeptides of approximate sizes 37, 38 and 45 kD, *in vitro* (Figure 6D). Moreover, these findings were supported by the positive expression of BAX and CS proteins in whole cell lysates (Figure 6E).



**Figure 5.** p21 BAX protein is stabilized in the presence of CS-shRNA expression, with or without CS-PEP1 co-treatment in HEK293 cells. HEK293 cells were transfected with 3 μg of empty vector (pTER, Panel A) or pCS-shRNA (Panel B) for 24 h, stimulated with Pac (5 μg/mL) or HP (1 μM) for a further 24 h and equal volumes of WCLs analyzed for endogenous CS (white bars) and p21 BAX (black bars) expression using Western blotting. Endogenous p21 BAX, CS and actin levels were detected from equal volumes of HEK293 soluble cell lysates by Western blotting, following 24 h of pCS-shRNA transfection (3 μg) and Pac (5 μg/mL) with CS-PEP1 (10 μM) co-stimulation (Panel C) for a further 24 hr. HEK293 cells co-transfected with pBAX-HA and pCS-FLAG or pBAX-HA and pCS-C25A-FLAG for 6 hr were stimulated with carrier or 10 μM CS-PEP1 for 18 h and treated with 20 μM cycloheximide. After 1 h, at the time points indicated, cells were lysed and equal volumes of soluble WCLs analyzed for p21 BAX, CS and actin expression using Western blotting (Panels D, E). Expression levels for p21 BAX were quantified, standardized for actin and expressed in relation to levels seen at T = 0 h. BAX and CS co-expression in the presence of CS-PEP1 stimulation (blue curve) and p21 BAX with CS-C25A co-expression (red curve) are indicated as trend lines (black curves, Panel 5F). Quantified data are presented as the mean ± SEM and its significance (where  $p < 0.05$ ) determined, using a two-way Student's *t*-test (\*  $p < 0.05$  and \*\*\*  $p < 0.001$ ).





**Figure 6.** Ubiquitinated BAX protein species accumulate in the presence of pCS-C25A expression or CS-PEP1 stimulation of cells, and are cleaved by active CS in vitro. HEK293 cells expressing p21 BAX with CS-FLAG (or CS-C25A-FLAG) and HA-Ubiquitin for 24 h were treated with 10  $\mu$ M MG132 or carrier for 5 h. Equal volumes of cleared whole cell lysates (WCLs) were immunoprecipitated (IP) using *anti*-HA antibodies and the immune complexes analyzed for BAX content using an *anti*-BAX antibody (Abcam) by Western blotting (WB). WCLs were also analyzed for BAX, CS (Invitrogen) and actin (Panel A). HEK293 cells co-expressing CS-FLAG or pCS-C25A-FLAG with BAX and HA-ubiquitin for 6 hr were treated further for 24 h with 10  $\mu$ M CS-PEP1 and equal volumes of cleared WCLs immunoprecipitated using *anti*-HA antibodies. Immune complexes were analyzed for BAX protein using Western blotting at long- (Panel B, top panel) and short- exposures (Panel B, lower panel). Equal volumes of WCLs were also subjected to Western blotting to detect BAX, CS and actin

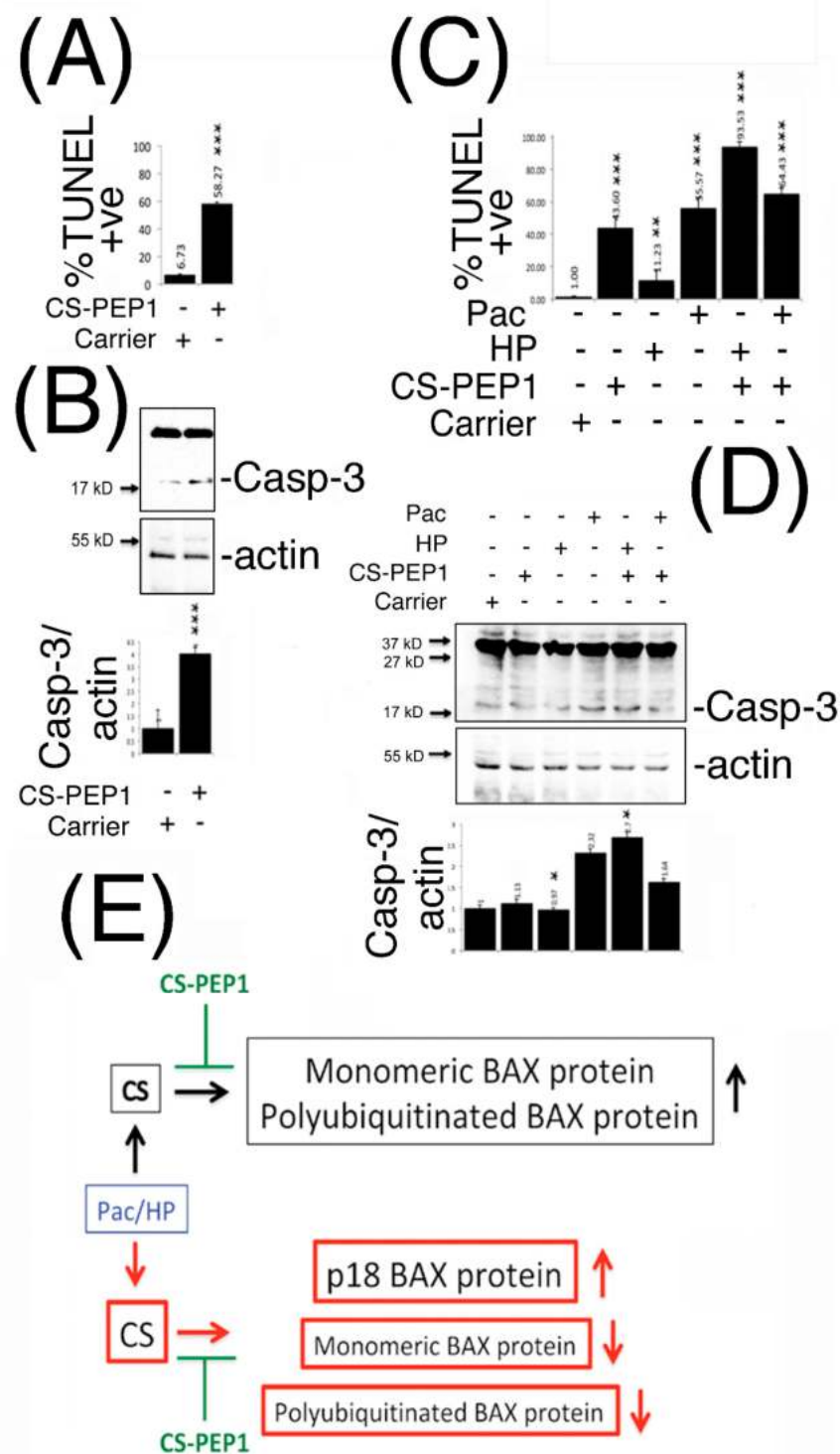
expression levels (Panel C). HEK293 cells co-expressing BAX with CS-FLAG or CS-C25A-FLAG and HA-ubiquitin were lysed and equal volumes of cleared WCLs immunoprecipitated with *anti*-HA antibody. Immune complexes were washed and incubated in the presence of active CS at pH 7 and subjected to Western blotting to detect BAX-Ubiquitin-HA protein species (Panel D) after long- (top panel) or short-exposure times (middle panel). Here, CS expression was also detected by Western blotting (Panel D, lower panel). Equal volumes of WCLs were also subjected to Western blotting to detect BAX (Abcam), CS (Invitrogen) and actin (Abcam) expression (Panel E).

Collectively, such findings suggest that CS co-expression with BAX mediates BAX polyubiquitination and that in the presence of CS inhibition (in intact cells), BAX ubiquitinated protein levels are enhanced, and that one of these derivatives (p120BAX) can be cleaved by CS. These observations point to a scenario where the formation of BAX-ubiquitinated derivatives may require CS-mediated cleavage of p21 BAX as a prerequisite for the formation of polyubiquitinated BAX protein species (such as p120BAX), and which can be further cleaved by CS as a possible mechanism for CS-mediated depletion of cellular BAX protein levels.

### 3.7. Peptide CS-PEP1 Induces Apoptosis of HEK293 and 769P Kidney Cells

In furthering our understanding of what input CS-PEP1 may have on modulating conventional chemotherapy treatment regimes, we next sought to determine the biological effects of CS-PEP1 (and CS-inhibition) on apoptosis of mammalian cells. Stimulation of HEK293 cells with CS-PEP1 increased apoptotic cell numbers approximately 10-fold, from 6 to 58% in a caspase-3 activation-dependent manner (Figure 7A,B and Supplementary Figure S4).

Similarly, treatment of 769P cells with CS-PEP1 alone enhanced apoptotic cell numbers from 1% to around 43%, while it also synergized the apoptotic-inducing effects of hydrogen peroxide from 11 to 93% (Figure 7C and Supplementary Figure S5). Paclitaxel-induced apoptosis was observed at around 55%, and for which CS-PEP1 treatment had the effect of increasing to 64% (Figure 7C), probably through the activation of caspase-3 (Figure 7D).



**Figure 7.** CS-PEP1 enhances apoptosis of HEK293 and 769P cells through enhanced caspase-3 activation, and interferes with a novel CS-mediated regulatory paradigm for the BAX protein. HEK293 (Panel A) or 769P cells (Panel C) were respectively co-stimulated with CS-PEP1 (10  $\mu$ M), HP (5  $\mu$ M) or Pac (5  $\mu$ g/mL) for 24 h and apoptotic cells quantified after TUNEL staining. Equal volumes of soluble whole cell lysates (WCLs) prepared from cells treated identically as in Panels A and C were analyzed for active caspase-3 (Casp-3) and actin expression (Panels B and D). Expression levels of active caspase-3 were quantified and standardized for actin expression in relation to cell stimulated with carrier alone (Panels B and D, lower panels). (Panel E), At basal cathepsin S protein expression levels, BAX protein predominantly exists as a monomeric p21 form and which can undergo polyubiquitination-mediated destabilization (black boxes). Under Pac- and HP-stimulatory

conditions (blue box), which induce *CTSS* gene expression, steady state levels of p21 monomeric BAX can be abrogated through the formation of a p18 kD BAX cleavage product and a p120kD-polyubiquitinated derivative of BAX (red boxes). Both axes of regulation can be negatively modulated by peptide CS-PEP1 (green), which consequently enhances cellular apoptosis, using a two-way Student's *t*-test (\*  $p < 0.05$ , \*\*  $p < 0.01$  and \*\*\*  $p < 0.001$ ).

#### 4. Discussion

Herein, we report that the *CTSS* (and *BAX*) genes are induced in response to Paclitaxel (Pac) or hydrogen peroxide (HP) treatments of kidney cells and that monomeric- and polyubiquitinated-BAX are novel substrates for the cysteine protease cathepsin S. Through the treatment of cells with the novel therapeutic peptide CS-PEP1, we could target cathepsin S protease activity, which gave rise to enhanced levels of monomeric p21 BAX protein in mammalian cells and in vitro. Additionally, CS-PEP1 showed promising activity in inducing apoptosis of HEK293 or 769P cells, either alone or in conjunction with Pac treatment. Collectively, such findings highlight a novel mechanism that connects *CTSS* expression with the intrinsic arm of the apoptotic pathway and which can be targeted for therapeutic purposes.

To support this model, the -1048 to -564 bp genomic DNA fragment upstream of the *CTSS* gene, showed positive transcriptional responsiveness to the effects of Pac and HP and the regulatory regions for which (until now) have remained unexplored [43–48]. Here, one transcription factor of relevance may be p53 as the predicted consensus binding sites for which [49] are located upstream of *CTSS* between -351 to -376 and -610 to -635 [50]. While p53 has also been suggested to contribute to lysosomal destabilization and apoptosis activation through its direct interaction with the lysosome [1,51,52], it may also contribute to lysosomal destabilization through it up regulating expression of the cathepsin D and cathepsin L genes [53–55].

As a central (and key) regulator of the intrinsic apoptosis pathway, whether p21 BAX is a substrate for cathepsin-mediated proteolysis has remained an area of controversy, with very little reported about which cathepsin member may be directly responsible for this [27]. When taken with additional findings which propose that total mitochondrial activated BAX protein levels are not equivalent to total cytosolic BAX protein (in apoptotic cells), the emphasis placed on p21 BAX cleavage as a possible key regulatory step during apoptosis has held high importance [22,56]. As reported herein, our findings are in good agreement with this latter line of research, as *CTSS* and *BAX* genes were inducibly expressed in kidney cells and from which concomitant increases in their transcriptional products were not reflected at the protein level. From our observations, CS could cleave p21 BAX in vitro and in mammalian cells, to yield cleavage intermediate products of sizes 18 and 17 kD, and which support earlier reports where the cleavage of p21 BAX at Asp-33 can give rise to increased p18 BAX levels, which enhance apoptosis and possess a very short half-life [27]. In this latter context, published findings that BAX can be localized in a perinuclear compartment [57], particularly under conditions that favor proteasomal inhibition [58] are in strong agreement with our observations as possibly being a unique subcellular compartment where BAX (and CS) can co-exist. From our findings, this has particular relevance as seen through the pH-dependency with which CS-mediated cleavage of p21 BAX (or its polyubiquitinated derivatives) can occur and which might have regulatory significance if this perinuclear compartment is lysosomally-derived. This could be important, as CS appears to have varying degrees of specificity towards our Bcl-x1 substrate in a pH-dependent manner (Figure 3). Whereas CS-PEP1 inhibits CS-mediated p21 BAX and GST-Bcl-x1 cleavage at pH 7, at the lower pH of 5 it inhibits CS-mediated p21 BAX cleavage better than CS-mediated Bc-x1 cleavage, in vitro. This level of pH selectivity that CS-PEP1 inhibitory activity is associated with could therefore highlight a novel regulatory mechanism, and which may be exploited for better therapeutic design and substrate-specific inhibition.

Based on the above novel findings, targeting CS indeed takes on greater significance, as the inhibition of CS activity may permit p21 BAX stabilization so that it may fulfill its

role as key activator of the intrinsic arm of the apoptotic pathway. While, CS-PEP1 appears to be inhibitory to cell growth at concentrations ranging from millimolar- to nanomolar-quantities, from our findings it appears to mechanistically have the effect of stabilizing p21 BAX protein levels in proportion to Bcl-xl protein levels in intact cells. Consequently, the rates at which cells undergo apoptosis based upon how sensitized they may have become upon exposure to CS-PEP1, does take on greater relevance and warrants further mechanistic clarification. Moreover, such factors do highlight important considerations for potentially permitting CS-PEP1 efficacy (or selectivity) to be modulated with greater effect in the context of characterizing it for further therapeutic development.

While the Parkin [59] and Ku70 [60] proteins are respective E3-ligase and DUB proteins for BAX, how CS interplays with their activity dynamics is a good question that has arisen from our findings. Whereas p47-, p55-species of ubiquitinated BAX have been reported in the past, their presence was positively correlated with a greater number of apoptotic cells [58] through the localization of ubiquitinated BAX to mitochondria. Whether these ubiquitinated BAX derivatives arise in a CS-dependent manner, either through partial ubiquitination and enhanced DUB activity, or a combination of these factors remains currently unknown. Nevertheless, our findings do support an emerging role for cathepsin S in the regulation of pathologically relevant proteins through the ubiquitination pathway, as an association that has been suggested previously in the instance of CS facilitating the ubiquitin dependent degradation of BRCA1 [30].

In summary, we propose that p21 BAX and polyubiquitinated BAX are novel substrates for the cysteine protease, CS. Additionally, CS activity can be targeted by CS-PEP1, which may enhance drug-mediated apoptosis of kidney cells through interfering with CS and the p21 BAX-Bcl-xl regulatory axis of the intrinsic pathway for apoptosis (Figure 7E).

## 5. Conclusions

In conclusion, Cathepsin S or BAX gene expression is induced upon the treatment of human kidney cell lines with Paclitaxel or Hydrogen Peroxide stimulation. p21 BAX and ubiquitinated BAX derivatives are novel substrates for activated cathepsin S *in vitro* or within intact mammalian cells, and is a reaction that can be therapeutically targeted by the novel therapeutic, CS-PEP1. Finally, CS-PEP1 can mechanistically induce apoptosis of kidney cells through BAX stabilization, Bcl-xl destabilization, cathepsin S inhibition, or a combination of these effects.

## 6. Patents

There is a patent resulting from this work.

**Supplementary Materials:** The following are available online at <https://www.mdpi.com/1999-4923/13/3/339/s1>. Figure S1: Quantification of CS and p21 BAX expression in HEK293 or 769P cells under Pac or HP stimulatory conditions; Figure S2: Quantification of p21 BAX expression in HEK293 or 769P cells under increasing levels of CS co-expression; Figure S3: Quantification of p21 BAX protein in the presence of CS-C25A expression or upon stimulation of HEK293 and 769P cells; Figure S4: CS-PEP1 stimulation induces apoptosis of HEK293 cells; Figure S5: CS-PEP1 stimulation induces apoptosis of 769P cells.

**Author Contributions:** Conceptualization, S.M.S.; Formal analysis, S.M.S.; Funding acquisition, A.A.Z.J.; Methodology, S.M.S., L.V.S., V.A.M. and N.V.G.; Visualization, S.M.S.; Writing—original draft, S.M.S.; Writing—review & editing, S.M.S., L.V.S., V.A.M., N.V.G., P.A.T. and A.A.Z.J. All authors have read and agreed to the published version of the manuscript.

**Funding:** This research was funded by the Russian Science Foundation, grant number 16-15-10410.

**Institutional Review Board Statement:** Not applicable.

**Informed Consent Statement:** Not applicable.

**Data Availability Statement:** The data presented in this study are available on request from the corresponding author. The data is not publicly available due to patent protection being sought for some of this work.

**Acknowledgments:** We acknowledge SeoYoung Kim (Ewha Womans University, Seoul 120-750, Korea) for plasmids pCS-FLAG and pCS-C25A-FLAG.

**Conflicts of Interest:** The authors declare no conflict of interest.

## References

- Soond, S.M.; Kozhevnikova, M.V.; Zamyatnin, A.A., Jr. ‘Patchiness’ and basic cancer research: Unravelling the proteases. *Cell Cycle* **2019**, *18*, 1687–1701. [CrossRef]
- Ohkuma, S.; Poole, B. Fluorescence probe measurement of the intralysosomal pH in living cells and the perturbation of pH by various agents. *Proc. Natl. Acad. Sci. USA* **1978**, *75*, 3327–3331. [CrossRef]
- Soond, S.M.; Kozhevnikova, M.V.; Townsend, P.A.; Zamyatnin, J.A.A. Cysteine Cathepsin Protease Inhibition: An update on its Diagnostic, Prognostic and Therapeutic Potential in Cancer. *Pharmaceutics* **2019**, *12*, 87. [CrossRef]
- Soond, S.M.; Kozhevnikova, M.V.; Frolova, A.S.; Savvateeva, L.V.; Plotnikov, E.Y.; Townsend, P.A.; Han, Y.-P.; Zamyatnin, A.A. Lost or Forgotten: The nuclear cathepsin protein isoforms in cancer. *Cancer Lett.* **2019**, *462*, 43–50. [CrossRef] [PubMed]
- Pranjol, Z.I.; Gutowski, N.J.; Hannemann, M.M.; Whatmore, J.L. The Potential Role of the Proteases Cathepsin D and Cathepsin L in the Progression and Metastasis of Epithelial Ovarian Cancer. *Biomolecules* **2015**, *5*, 3260–3279. [CrossRef] [PubMed]
- Pranjol, Z.I.; Zinovkin, D.A.; Maskell, A.R.T.; Stephens, L.J.; Achinovich, S.L.; Los’, D.M.; Nadyrov, E.A.; Hannemann, M.; Gutowski, N.J.; Whatmore, J.L. Cathepsin L-induced galectin-1 may act as a proangiogenic factor in the metastasis of high-grade serous carcinoma. *J. Transl. Med.* **2019**, *17*, 1–15. [CrossRef]
- Winiarski, B.K.; Cope, N.; Alexander, M.; Pilling, L.C.; Warren, S.; Acheson, N.; Gutowski, N.J.; Whatmore, J.L. Clinical Relevance of Increased Endothelial and Mesothelial Expression of Proangiogenic Proteases and VEGFA in the Omentum of Patients with Metastatic Ovarian High-Grade Serous Carcinoma. *Transl. Oncol.* **2014**, *7*, 267–276.e4. [CrossRef] [PubMed]
- Tabish, T.A.; Pranjol, Z.I.; Horsell, D.W.; Rahat, A.A.M.; Whatmore, J.L.; Winyard, P.G.; Zhang, S. Graphene Oxide-Based Targeting of Extracellular Cathepsin D and Cathepsin L As A Novel Anti-Metastatic Enzyme Cancer Therapy. *Cancers* **2019**, *11*, 319. [CrossRef] [PubMed]
- Wilkinson, R.D.A.; Williams, R.; Scott, C.J.; Burden, R.E. Cathepsin S: Therapeutic, diagnostic, and prognostic potential. *Biol. Chem.* **2015**, *396*, 867–882. [CrossRef] [PubMed]
- Cirman, T.; Orešić, K.; Mazovec, G.D.; Turk, V.; Reed, J.C.; Myers, R.M.; Salvesen, G.S.; Turk, B. Selective Disruption of Lysosomes in HeLa Cells Triggers Apoptosis Mediated by Cleavage of Bid by Multiple Papain-like Lysosomal Cathepsins. *J. Biol. Chem.* **2004**, *279*, 3578–3587. [CrossRef]
- Conus, S.; Pop, C.; Snipas, S.J.; Salvesen, G.S.; Simon, H.-U. Cathepsin D Primes Caspase-8 Activation by Multiple Intra-chain Proteolysis. *J. Biol. Chem.* **2012**, *287*, 21142–21151. [CrossRef]
- Siddiqui, W.A.; Ahad, A.; Ahsan, H. The mystery of BCL2 family: Bcl-2 proteins and apoptosis: An update. *Arch. Toxicol.* **2015**, *89*, 289–317. [CrossRef] [PubMed]
- Peña-Blanco, A.; Garcia-Saez, A.J. Bax, Bak and beyond—Mitochondrial performance in apoptosis. *FEBS J.* **2018**, *285*, 416–431. [CrossRef] [PubMed]
- Suzuki, M.; Youle, R.J.; Tjandra, N. Structure of Bax. *Cell* **2000**, *103*, 645–654. [CrossRef]
- Gahl, R.F.; He, Y.; Yu, S.; Tjandra, N. Conformational Rearrangements in the Pro-apoptotic Protein, Bax, as It Inserts into Mitochondria. *J. Biol. Chem.* **2014**, *289*, 32871–32882. [CrossRef] [PubMed]
- Hsu, Y.-T.; Wolter, K.G.; Youle, R.J. Cytosol-to-membrane redistribution of Bax and Bcl-XL during apoptosis. *Proc. Natl. Acad. Sci. USA* **1997**, *94*, 3668–3672. [CrossRef]
- Lovell, J.F.; Billen, L.P.; Bindner, S.; Shamas-Din, A.; Fradin, C.; Leber, B.; Andrews, D.W. Membrane Binding by tBid Initiates an Ordered Series of Events Culminating in Membrane Permeabilization by Bax. *Cell* **2008**, *135*, 1074–1084. [CrossRef]
- Kim, H.; Tu, H.-C.; Ren, D.; Takeuchi, O.; Jeffers, J.R.; Zambetti, G.P.; Hsieh, J.J.-D.; Cheng, E.H.-Y. Stepwise Activation of BAX and BAK by tBID, BIM, and PUMA Initiates Mitochondrial Apoptosis. *Mol. Cell* **2009**, *36*, 487–499. [CrossRef]
- Czabotar, P.E.; Westphal, D.; Dewson, G.; Ma, S.; Hockings, C.; Fairlie, W.D.; Lee, E.F.; Yao, S.; Robin, A.Y.; Smith, B.J.; et al. Bax Crystal Structures Reveal How BH3 Domains Activate Bax and Nucleate Its Oligomerization to Induce Apoptosis. *Cell* **2013**, *152*, 519–531. [CrossRef]
- Wei, M.C.; Lindsten, T.; Mootha, V.K.; Weiler, S.; Gross, A.; Ashiya, M.; Thompson, C.B.; Korsmeyer, S.J. tBID, a membrane-targeted death ligand, oligomerizes BAK to release cytochrome c. *Genome Res.* **2000**, *14*, 2060–2071.
- Hinds, M.G.; Lackmann, M.; Skea, G.L.; Harrison, P.J.; Huang, D.C.S.; Day, C.L. The structure of Bcl-w reveals a role for the C-terminal residues in modulating biological activity. *EMBO J.* **2003**, *22*, 1497–1507. [CrossRef] [PubMed]
- Antonsson, B.; Montessuit, S.; Sanchez, B.; Martinou, J.-C. Bax Is Present as a High Molecular Weight Oligomer/Complex in the Mitochondrial Membrane of Apoptotic Cells. *J. Biol. Chem.* **2001**, *276*, 11615–11623. [CrossRef]
- Oltvai, Z.N. Checkpoints of dueling dimers foil death wishes. *Cell* **1994**, *79*, 189–192. [CrossRef]
- Walensky, L.D. Targeting BAX to drug death directly. *Nat. Chem. Biol.* **2019**, *15*, 657–665. [CrossRef]

25. Souers, A.J.; Levenson, J.D.; Boghaert, E.R.; Ackler, S.L.; Catron, N.D.; Chen, J.; Dayton, B.D.; Ding, H.; Enschede, S.H.; Fairbrother, W.J.; et al. ABT-199, a potent and selective BCL-2 inhibitor, achieves antitumor activity while sparing platelets. *Nat. Med.* **2013**, *19*, 202–208. [CrossRef] [PubMed]
26. Baranski, Z.; De Jong, Y.; Ilkova, T.; Peterse, E.F.; Cleton-Jansen, A.-M.; Van De Water, B.; Hogendoorn, P.C.; Bovee, J.V.; Danen, E.H. Pharmacological inhibition of Bcl-xL sensitizes osteosarcoma to doxorubicin. *Oncotarget* **2015**, *6*, 36113–36125. [CrossRef] [PubMed]
27. Cao, X.; Deng, X.; May, W.S. Cleavage of Bax to p18 Bax accelerates stress-induced apoptosis, and a cathepsin-like protease may rapidly degrade p18 Bax. *Blood* **2003**, *102*, 2605–2614. [CrossRef]
28. Droga-Mazovec, G.; Bojič, L.; Petelin, A.; Ivanova, S.; Romih, R.; Repnik, U.; Salvesen, G.S.; Stoka, V.; Turk, V.; Turk, B. Cysteine Cathepsins Trigger Caspase-dependent Cell Death through Cleavage of Bid and Antiapoptotic Bcl-2 Homologues. *J. Biol. Chem.* **2008**, *283*, 19140–19150. [CrossRef]
29. Einzig, A.I.; Gorowski, E.; Sasloff, J.; Wiernik, P.H. Phase II Trial of Taxol in Patients with Metastatic Renal Cell Carcinoma. *Cancer Investig.* **1991**, *9*, 133–136. [CrossRef]
30. Kim, S.; Jin, H.; Seo, H.-R.; Lee, H.J.; Lee, Y.-S. Regulating BRCA1 protein stability by cathepsin S-mediated ubiquitin degradation. *Cell Death Differ.* **2019**, *26*, 812–825. [CrossRef]
31. Soond, S.M.; Chantry, A. Selective targeting of activating and inhibitory Smads by distinct WWP2 ubiquitin ligase isoforms differentially modulates TGF $\beta$  signalling and EMT. *Oncogene* **2011**, *30*, 2451–2462. [CrossRef] [PubMed]
32. Soond, S.M.; Everson, B.; Riches, D.W.H.; Murphy, G. ERK-mediated phosphorylation of Thr735 in TNF-converting enzyme and its potential role in TACE protein trafficking. *J. Cell Sci.* **2005**, *118*, 2371–2380. [CrossRef]
33. Soond, S.M.; Terry, J.L.; Colbert, J.D.; Riches, D.W.H. TRUSS, a Novel Tumor Necrosis Factor Receptor 1 Scaffolding Protein That Mediates Activation of the Transcription Factor NF- $\kappa$ B. *Mol. Cell. Biol.* **2003**, *23*, 8334–8344. [CrossRef] [PubMed]
34. Song, J.; Tan, H.; Perry, A.J.; Akutsu, T.; Webb, G.I.; Whisstock, J.C.; Pike, R.N. PROSPER: An Integrated Feature-Based Tool for Predicting Protease Substrate Cleavage Sites. *PLoS ONE* **2012**, *7*, e50300. [CrossRef]
35. Arnoult, D. Mitochondrial fragmentation in apoptosis. *Trends Cell Biol.* **2007**, *17*, 6–12. [CrossRef]
36. Vogler, M.; Walter, H.S.; Dyer, M.J.S. Targeting anti-apoptotic BCL2 family proteins in haematological malignancies—From pathogenesis to treatment. *Br. J. Haematol.* **2017**, *178*, 364–379. [CrossRef]
37. Villamil, J.C.M.; Mueller, A.N.; Demir, F.; Meyer, U.; Ökmen, B.; Hüynck, J.S.; Breuer, M.; Dauben, H.; Win, J.; Huesgen, P.F.; et al. A fungal substrate mimicking molecule suppresses plant immunity via an inter-kingdom conserved motif. *Nat. Commun.* **2019**, *10*, 1–15. [CrossRef]
38. Thuduppathy, G.R.; Hill, R.B. Acid destabilization of the solution conformation of Bcl-XL does not drive its pH-dependent insertion into membranes. *Protein Sci.* **2006**, *15*, 248–257. [CrossRef]
39. Yu-Wei, D.; Li, Z.; Xiong, S.; Huang, G.; Luo, Y.; Huo, T.; Zhou, M.; Zheng, Y. Paclitaxel induces apoptosis through the TAK1–JNK activation pathway. *FEBS Open Bio* **2020**, *10*, 1655–1667. [CrossRef]
40. Singh, S.K.; Lillard, J.W.; Singh, R. Reversal of drug resistance by planetary ball milled (PBM) nanoparticle loaded with resveratrol and docetaxel in prostate cancer. *Cancer Lett.* **2018**, *427*, 49–62. [CrossRef]
41. Pienta, K.J. Preclinical mechanisms of action of docetaxel and docetaxel combinations in prostate cancer. *Semin. Oncol.* **2001**, *28*, 3–7. [CrossRef]
42. Tian, H.; Zhang, B.; Di, J.; Jiang, G.; Chen, F.; Li, H.; Li, L.; Pei, D.; Zheng, J. Keap1: One stone kills three birds Nrf2, IKK $\beta$  and Bcl-2/Bcl-xL. *Cancer Lett.* **2012**, *325*, 26–34. [CrossRef]
43. Tsai, J.-Y.; Lee, M.-J.; Chang, M.D.-T.; Huang, H. The effect of catalase on migration and invasion of lung cancer cells by regulating the activities of cathepsin S, L, and K. *Exp. Cell Res.* **2014**, *323*, 28–40. [CrossRef] [PubMed]
44. Cano, D.M.; Calviño, E.; Rubio, V.; Herráez, A.; Sancho, P.; Tejedor, M.C.; Diez, J.C. Apoptosis induced by paclitaxel via Bcl-2, Bax and caspases 3 and 9 activation in NB4 human leukaemia cells is not modulated by ERK inhibition. *Exp. Toxicol. Pathol.* **2013**, *65*, 1101–1108. [CrossRef]
45. Miyashita, T.; Krajewski, S.; Krajewska, M.; Wang, H.G.; Lin, H.K.; Liebermann, D.A.; Hoffman, B.; Reed, J.C. Tumor suppressor p53 is a regulator of bcl-2 and bax gene expression in vitro and in vivo. *Oncogene* **1994**, *9*, 1799–1805. [PubMed]
46. Toshiyuki, M.; Reed, J.C. Tumor suppressor p53 is a direct transcriptional activator of the human bax gene. *Cell* **1995**, *80*, 293–299. [CrossRef]
47. Croteau, D.L.; Ap Rhys, C.M.J.; Hudson, E.K.; Dianov, G.L.; Hansford, R.G.; Bohr, V.A. An Oxidative Damage-specific Endonuclease from Rat Liver Mitochondria. *J. Biol. Chem.* **1997**, *272*, 27338–27344. [CrossRef]
48. Ströbel, T.; Swanson, L.; Korsmeyer, S.; Cannistra, S.A. BAX enhances paclitaxel-induced apoptosis through a p53-independent pathway. *Proc. Natl. Acad. Sci. USA* **1996**, *93*, 14094–14099. [CrossRef]
49. Brázda, V.; Fojta, M. The Rich World of p53 DNA Binding Targets: The Role of DNA Structure. *Int. J. Mol. Sci.* **2019**, *20*, 5605. [CrossRef]
50. Soond, S.M.; Savvateeva, L.V.; Makarov, V.A.; Gorokhovets, N.V.; Townsend, P.A.; Zamyatnin, J.A.A. Making Connections: p53 and the Cathepsin Proteases as Co-Regulators of Cancer and Apoptosis. *Cancers* **2020**, *12*, 3476. [CrossRef]
51. Yuan, X.-M.; Li, W.; Dalen, H.; Lotem, J.; Kama, R.; Sachs, L.; Brunk, U.T. Lysosomal destabilization in p53-induced apoptosis. *Proc. Natl. Acad. Sci. USA* **2002**, *99*, 6286–6291. [CrossRef]

52. Li, N.; Zheng, Y.; Chen, W.; Wang, C.; Liu, X.; He, W.; Xu, H.; Cao, X. Adaptor Protein LAPF Recruits Phosphorylated p53 to Lysosomes and Triggers Lysosomal Destabilization in Apoptosis. *Cancer Res.* **2007**, *67*, 11176–11185. [CrossRef]
53. Wu, G.S.; Saftig, P.; Peters, C.; El-Deiry, W.S. Potential role for Cathepsin D in p53-dependent tumor suppression and chemosensitivity. *Oncogene* **1998**, *16*, 2177–2183. [CrossRef] [PubMed]
54. Katara, R.; Mir, R.A.; Shukla, A.A.; Tiwari, A.; Singh, N.; Chauhan, S.S. Wild type p53-dependent transcriptional upregulation of cathepsin L expression is mediated by C/EBP $\alpha$  in human glioblastoma cells. *Biol. Chem.* **2010**, *391*, 1031–1040. [CrossRef]
55. Zhang, Q.-Q.; Wang, W.-J.; Li, J.; Yang, N.; Chen, G.; Wang, Z.; Liang, Z.-Q. Cathepsin L suppression increases the radiosensitivity of human glioma U251 cells via G2/M cell cycle arrest and DNA damage. *Acta Pharmacol. Sin.* **2015**, *36*, 1113–1125. [CrossRef] [PubMed]
56. Wood, D.E.; Thomas, A.; Devi, L.A.; Berman, Y.; Beavis, R.C.; Reed, J.C.; Newcomb, E.W. Bax cleavage is mediated by calpain during drug-induced apoptosis. *Oncogene* **1998**, *17*, 1069–1078. [CrossRef] [PubMed]
57. Nie, C.; Tian, C.; Zhao, L.; Petit, P.X.; Mehrpour, M.; Chen, Q. Cysteine 62 of Bax Is Critical for Its Conformational Activation and Its Proapoptotic Activity in Response to H<sub>2</sub>O<sub>2</sub>-induced Apoptosis. *J. Biol. Chem.* **2008**, *283*, 15359–15369. [CrossRef] [PubMed]
58. Li, B.; Dou, Q.P. Bax degradation by the ubiquitin/proteasome-dependent pathway: Involvement in tumor survival and progression. *Proc. Natl. Acad. Sci. USA* **2000**, *97*, 3850–3855. [CrossRef]
59. Johnson, B.N.; Berger, A.K.; Cortese, G.P.; Lavoie, M.J. The ubiquitin E3 ligase parkin regulates the proapoptotic function of Bax. *Proc. Natl. Acad. Sci. USA* **2012**, *109*, 6283–6288. [CrossRef] [PubMed]
60. Amsel, A.D.; Rathaus, M.; Kronman, N.; Cohen, H.Y. Regulation of the proapoptotic factor Bax by Ku70-dependent deubiquitylation. *Proc. Natl. Acad. Sci. USA* **2008**, *105*, 5117–5122. [CrossRef] [PubMed]







## Article

# Effects of Lapatinib on HER2-Positive and HER2-Negative Canine Mammary Carcinoma Cells Cultured In Vitro

Antonio Fernando Leis-Filho <sup>1</sup>, Patrícia de Faria Lainetti <sup>2</sup>, Priscila Emiko Kobayashi <sup>1</sup> , Carlos Eduardo Fonseca-Alves <sup>2,3,†</sup> and Renée Laufer-Amorim <sup>1,\*</sup>

<sup>1</sup> Department of Veterinary Clinic, Sao Paulo State University-UNESP, Botucatu 18618-681, Brazil; a.leis@unesp.br (A.F.L.-F.); priscila.e.kobayashi@unesp.br (P.E.K.)

<sup>2</sup> Department of Veterinary Surgery and Animal Reproduction, São Paulo State University-UNESP, Botucatu 18618-681, Brazil; patricia.lainetti@unesp.br (P.d.F.L.); carlos.e.alves@unesp.br (C.E.F.-A.)

<sup>3</sup> Institute of Health Sciences, Paulista University-UNIP, Bauru 17048-290, Brazil

\* Correspondence: renee.laufer-amorim@unesp.br; Tel.: +55-14-38802066

† These authors contributed equally to this work.

**Abstract:** HER2 is a prognostic and predictive marker widely used in breast cancer. Lapatinib is a tyrosine kinase inhibitor that works by blocking the phosphorylation of the receptor HER2. Its use is related to relatively good results in the treatment of women with HER2+ breast cancer. Thus, this study aimed to verify the effects of lapatinib on four canine primary mammary gland carcinoma cell cultures and two paired metastatic cell cultures. Cultures were treated with lapatinib at concentrations of 100, 500, 1000 and 3000 nM for 24 h and the 50% inhibitory concentration (IC<sub>50</sub>) for each cell culture was determined. In addition, a transwell assay was performed to assess the ability of lapatinib to inhibit cell migration. Furthermore, we verified *HER2* expression by RT-qPCR analysis of cell cultures and formalin-fixed paraffin-embedded tissues from samples corresponding to those used in cell culture. Lapatinib was able to inhibit cell proliferation in all cell cultures, but it was not able to inhibit migration in all cell cultures. The higher the expression of *HER2* in a culture, the more sensitive the culture was to treatment. This relationship may be an indication that the expression of *HER2* may be a predictive factor and opens a new perspective for the treatment of primary and metastatic mammary gland cancer.

**Keywords:** dog; cancer; comparative oncology; molecular targets

**Citation:** Leis-Filho, A.F.; de Faria Lainetti, P.; Emiko Kobayashi, P.; Fonseca-Alves, C.E.; Laufer-Amorim, R. Effects of Lapatinib on HER2-Positive and HER2-Negative Canine Mammary Carcinoma Cells Cultured In Vitro. *Pharmaceutics* **2021**, *13*, 897. <https://doi.org/10.3390/pharmaceutics13060897>

Academic Editor: Hassan Bousbaa

Received: 14 May 2021

Accepted: 11 June 2021

Published: 17 June 2021

**Publisher's Note:** MDPI stays neutral with regard to jurisdictional claims in published maps and institutional affiliations.



**Copyright:** © 2021 by the authors. Licensee MDPI, Basel, Switzerland. This article is an open access article distributed under the terms and conditions of the Creative Commons Attribution (CC BY) license (<https://creativecommons.org/licenses/by/4.0/>).

## 1. Introduction

Mammary gland neoplasms exhibit several similarities between women and dogs, such as their high incidence, spontaneous appearance, common environmental risk factors, hormone receptor expression and neoplastic growth markers. Therefore, research related to one species may have aspects that can be studied in a comparative manner [1,2].

Estrogen receptor (ER), progesterone receptor (PR) and epidermal growth factor 2 (HER2) are among the most commonly used markers in human medicine with validated predictive value. Breast cancer in women can be classified according to the expression of the receptors ER, PR and HER2. Breast tumors can be divided into the molecular subtypes luminal A, luminal B, HER2 overexpressing and triple negative. Luminal A tumors are ER+, PR+ and HER2−, while luminal B tumors are divided into two groups and can be ER+, PR+ or − and HER2+ or ER+, PR+ or − and HER2−; HER2 tumors are ER−, PR− and HER2+, and triple-negative tumors are ER−, PR− and HER2− [3–6].

HER2 is a tyrosine kinase receptor member of the epidermal growth factor receptor (EGFR) family, which is composed of EGFR (also known as HER1), HER2, HER3 and HER4 [7]. The receptors in this family are located in the cell membrane, and when they bind to an external ligand, with the exception of HER2, which does not contain this binding site, they form dimers with other members of the family so that the internal phosphate

domain is phosphorylated, triggering an intracellular response [8]. In addition, there is evidence that HER2 is the receptor that most often forms dimers with other members of the EGFR family [9]. Activation of these receptors is associated with increased survival, proliferation, and cell cycle progression [10].

HER2+ tumors have a prevalence of 13–15% among molecular subtypes, have a high Ki67 index and are generally high-grade tumors with a histology indicative of invasive carcinoma of no special type with aggressive disease characteristics; however, it is possible to use targeted therapies as treatment [5]. HER2 overexpression is related to shorter disease-free survival; reduced survival time; decreased ER and PR expression; increased cell proliferation, migration, tumor invasiveness, frequency of metastases, and angiogenesis; and decreased apoptosis [6]. Without targeted therapy, HER2+ cancers have a recurrence rate of up to 15% [4]. The survival rate of women diagnosed with tumors that overexpress HER2 is 92% over 20 months, 88% over 30 months, and decreases to almost 80% over 50 months [11]. In addition, brain metastasis of HER2+ breast tumors is common, affecting 50% of patients with metastatic disease [12].

Treatment of HER2-overexpressing tumors with targeted therapy produces a positive response when compared to treatments without the addition of targeted therapy [13]. Trastuzumab has been widely used, adding approximately 1 year to the disease-free interval of patients with this disease subtype [12], but even with this positive effect, some patients will still develop metastases or tumor recurrence after completion of the treatment [14,15]; therefore, new anti-HER2 drugs are being studied.

Lapatinib is an inhibitor of HER2 tyrosine kinase activity; it is considered a therapeutic alternative in the treatment of HER2+ neoplasms and acts as a reversible blocker of receptor phosphorylation. Lapatinib use is related to reduced disease progression and decreased axillary lymph node metastasis rates in women. Furthermore, because lapatinib is a small molecule, it can permeate the blood-brain barrier, making it an alternative therapy in cases of brain metastasis [16,17]. Lapatinib is an inhibitor of HER1/HER2 heterodimerization, and its action is independent of the HER1 status of tumors; it is also effective against HER2+ tumors resistant to treatment with trastuzumab [18,19] and is still an option in countries without access to other HER2 inhibitors and in cases of cardiac toxicity [19]. It should be used in combination, showing good results with capecitabine, and can be used as a second-line treatment for recurrent or metastatic HER2+ tumors [12,15,20]. In cell cultures of feline mammary cancer, lapatinib showed promising results, being able to inhibit cell viability when used as a single therapy and increase the action of anti-HER2 monoclonal antibodies such as trastuzumab and pertuzumab when used in combination. These results were observed both in cell cultures with high and low *HER2* expression [21,22].

According to Nguyen et al. [23], the overall survival rate of dogs with mammary gland tumors is 41.5% at one year and 54.1% at two years after surgery. The average survival times of animals after surgery for grade II and III tumors are 32.68 and 7.78 months, respectively [24]. In addition, the rate of metastasis of mammary gland tumors in dogs in general is 53% [25], and the recurrence rate of grade III tumors is 71.42% [24]. HER2+ mammary gland neoplasms in dogs represent approximately 8% of all the diagnosed molecular subtypes and are generally associated with a worse prognosis; larger tumors; higher histological grades, invasion, and proliferative indexes; and the presence of necrosis [25].

Canine mammary gland tumors are treated by surgical removal, and in some cases, the use of adjuvant chemotherapy is indicated, such as tumors with a more aggressive histological type, which have a higher rate of metastasis development. According to Cassali et al. [26], dogs that present with micropapillary carcinoma, solid carcinoma, carcinosarcoma, or pleomorphic lobular carcinoma, regardless of the degree, clinical stage and molecular subtype, are always indicated for chemotherapy. In addition, patients with tumors of a less aggressive subtype should undergo chemotherapy if the disease is grade III or above, and in any case when metastasis is present [26].

In veterinary medicine, there are no indications for selection of different chemotherapy protocols for different types of tumors, so carboplatin is widely applied in cases of female

mammary tumors, regardless of the stage, histopathological type, molecular classification of the tumor and metastasis status [26]. The use of adjuvant carboplatin, when compared to surgical treatment alone, increased the survival time of animals with breast cancer [27], and the administration of carboplatin with mitoxantrone seems to promote a longer survival period, even if a study was carried out with a limited number of animals [28]. Clinical studies to evaluate the effectiveness of chemotherapy in animals are scarce, and therefore, information varies considerably.

To the best of our knowledge, the effect of lapatinib on canine mammary gland tumors has not been published. Since canine mammary gland tumors are very common, with most tumors being potentially malignant, and the standard therapy is radical mastectomy with no effective chemotherapy protocols for the treatment of animals with metastatic disease [26], this study aimed to evaluate the antitumor effect of lapatinib on HER2+ and HER2– primary and metastatic canine mammary gland carcinoma cells cultured *in vitro*.

## 2. Materials and Methods

### 2.1. Reagents

All reagents used were of high purity and purchased from GE Healthcare (Uppsala, Sweden), Sigma-Aldrich (São Paulo, Brazil), and Merck SA (São Paulo, Brazil); otherwise, the manufacturer is indicated. In addition, mammary epithelial cell growth medium (MEGM™; Lonza Inc., Allendale, NJ, USA), Dulbecco's modified Eagle's medium (DMEM; Lonza Inc.), fetal bovine serum (FBS; LGC Biotechnology, Cotia, SP, Brazil), Dulbecco's phosphate-buffered saline (DPBS; Sigma Aldrich, St. Louis, MO, USA) and antibiotic/antimycotic solution (Thermo Fisher Scientific, Waltham, MA, USA) were used.

### 2.2. Inclusion Criteria

Samples that met all of the following criteria were included in this research: cell cultures of primary tumors that had paired formalin-fixed paraffin-embedded (FFPE) material and were classified according to Goldschmidt et al. [29], cell cultures characterized by cell phenotype and tumorigenicity *in vitro*, cell cultures with sufficient aliquots for triplicate analysis in all experiments and free of bacterial, mycoplasma and/or fungal contamination. Cell lines were previously established and characterized [30]. A total of six cell lines met the criteria. Among the cell lines, four cell lines were primary mammary carcinoma cells (UNESP-CM1, UNESP-CM5, UNESP-CM9 and UNESP-CM60) and two were mammary carcinoma metastases (UNESP-MM1 and UNESP-MM4) (Supplementary Materials Table S1)

### 2.3. In Silico Analysis of HER2 Homology

To assess the three-dimensional protein structure homology between human and canine HER2, an *in silico* analysis was performed. The amino acid sequences of the human (UniProtKB/Swiss-Prot: P04626.1) and canine (NCBI Reference Sequence: NP\_001003217.2) proteins were obtained from NCBI GenBank (<https://www.ncbi.nlm.nih.gov/genbank/> (accessed on 14 May 2021)). Prediction analysis of the homology of the three-dimensional structure of the HER2 protein was performed using Swiss software (Swiss Institute of Bioinformatics, Basel, Switzerland) (<https://swissmodel.expasy.org/> (accessed on 14 May 2021)).

### 2.4. Experimental Groups

The determination of the sample number in the study was based on that described by Lazic et al. [31]. Four samples of primary mammary carcinoma and two samples of metastatic tumors were selected and divided into two groups with three samples each according to the HER2 expression in the tissue: one group contained the HER2+ samples (UNESP-CM1, UNESP-CM9 and UNESP-CM60), and the other contained the HER2– samples (UNESP-MM1, UNESP-MM4 and UNESP-CM5). Both groups (HER2+ and HER2– cells) were treated with lapatinib. The cell culture UNESP-CM1 was used on the 15th passage, UNESP-CM5 on the 16th, UNESP-CM9 on the 17th, UNESP-CM60 on the 35th,

UNESP-MM1 on the 19th, and UNESP-MM4 on the 22nd. The passages used were chosen according to cell stability and aliquot availability [30].

### 2.5. HER2 Immunoreactivity

FFPE samples, paired with the cell cultures, were cut on a microtome (5 µm), transferred to positively charged slides (StarFrost™, Braunschweig, Germany) and dewaxed. The slides were subjected to antigen retrieval with citrate buffer (pH 6.0) in a pressure cooker (Pascal, Dako, Agilent Technologies, Santa Clara, CA, USA). Endogenous peroxidase activity was blocked with 8% hydrogen peroxide in methanol for 20 min and blocking of nonspecific proteins was carried out with 8% skim milk for 60 min; both steps were performed at room temperature. Antibody detection was performed using a polymer system (EnVision™ Dako, Agilent Technologies, Santa Clara, CA, USA). The anti-HER2 antibody from the Herceptest™ Kit (Dako, Carpinteria, CA, USA) was used according to the manufacturer's instructions, and 3,3'-diaminobenzidine (EnVision™ FLEX, High pH, Dako, Agilent Technologies, Santa Clara, CA, USA) was used as the chromogen. Counterstaining was performed with Harris hematoxylin. Negative controls were generated by omission of the primary antibody. The positive control used was provided with the manufacturer's kit. To consider canine samples HER2+, the criteria described in the commercial kit approved by the US Food and Drug Administration, Herceptest™, were followed. In summary, a score of 0 was given when no staining was observed or membrane staining was observed in <10% of tumor cells; a score of 1+ was given when faint or barely perceptible membrane staining was detected in >10% of tumor cells and the cells exhibited incomplete membrane staining; a score of 2+ was given when weak to moderate complete membrane staining was observed in >10% of tumor cells; and a score of 3+ was given when strong complete membrane staining was observed in >10% of tumor cells.

Six samples were submitted for immunohistochemistry. Among these, three were classified as negative for HER2 (two with a score of 1+ and one with a score of 0), and three were considered HER2 positive (three with a score of 3+) (Table 1, Figure 1).

**Table 1.** Classification of samples used in the study according to the expression of HER2 determined by immunohistochemistry using Herceptest™. The samples received scores according to the recommendations of the kit used.

Cell Type	UNESP-MM1	UNESP-MM4	UNESP-CM1	UNESP-CM5	UNESP-CM9	UNESP-CM60
HER2 expression	0	1+	3+	1+	3+	3+

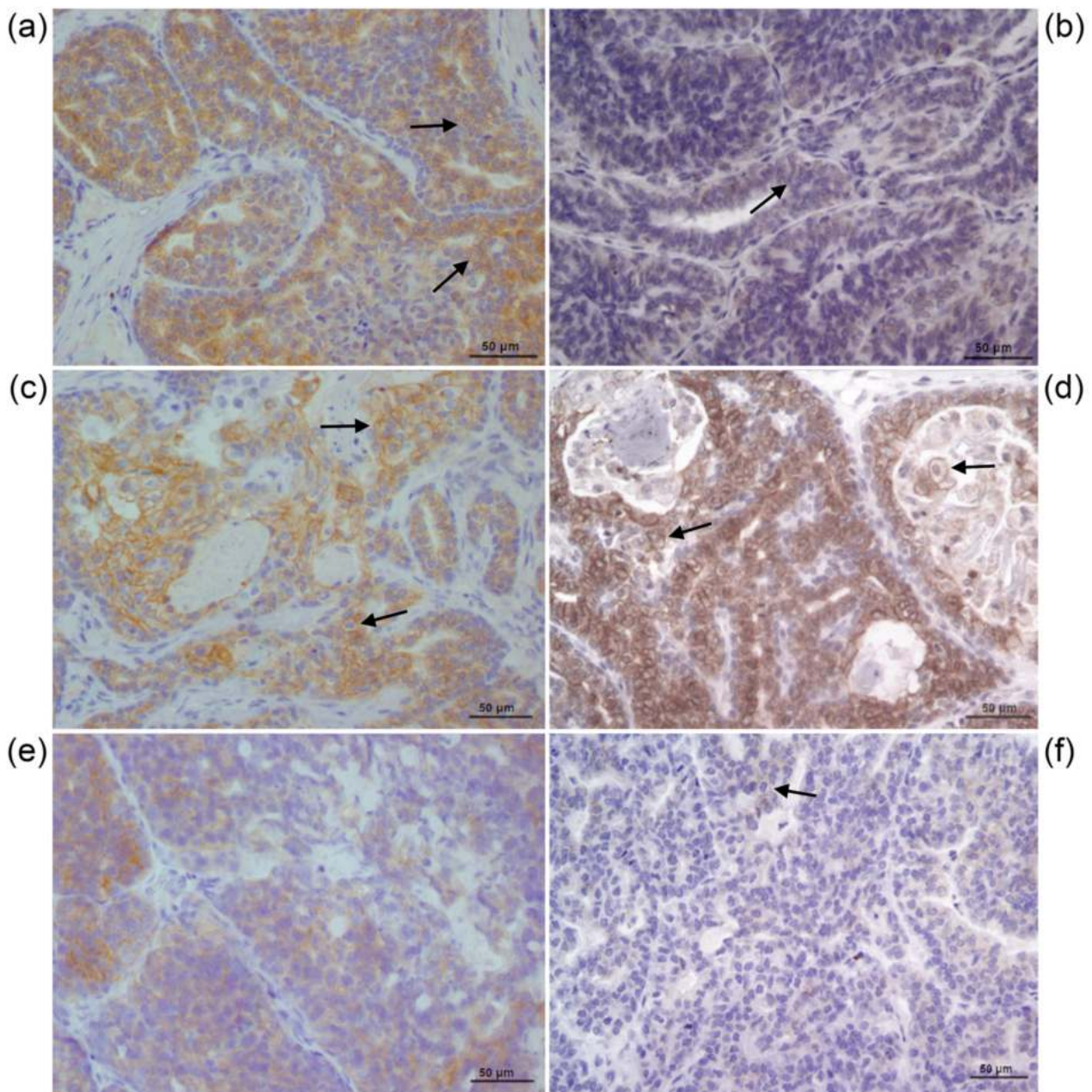
### 2.6. Lapatinib Treatment and Evaluation of Cellular Metabolic Activity

To evaluate the antitumor effect of lapatinib (50% inhibitory concentration, IC<sub>50</sub>), an in vitro MTT assay was performed. The drug was diluted in DMSO to a concentration of 2 mg/mL, and the highest dilution was used as the parameter for the control containing DMSO (at the same concentration as the highest concentration of lapatinib). Cells were cultured according to Lainetti et al. [30].

The concentrations of lapatinib tested were 100, 500, 1000, and 3000 nM [32], and cells were treated for 24 h to determine the IC<sub>50</sub>. Tumor cells were seeded in 96-well plates at a concentration of 10,000 cells/well and incubated for 24 h at 37 °C in DMEM containing 5% FBS. Subsequently, lapatinib was added to fresh medium without FBS, and the culture was incubated for an additional 24 h in a humidified atmosphere with 5% CO<sub>2</sub>.

After 24 h of cultivation, 10 µL of MTT solution (Sigma Aldrich, St. Louis, MO, USA) at a concentration of 0.5 mg/mL diluted in DPBS was added to each well, and the plate was incubated at 37 °C for 4 h. After the incubation, the formazan resulting from MTT cleavage was solubilized with DMSO. After 10 min of homogenization, the absorbance at 550 nm was determined with a microplate reader (Biochrom Asys Expert Plus Microplate Reader, Biochrom Ltd., Harvard Bioscience, Holliston, MA, USA). Based on the test results, the IC<sub>50</sub> [33] was determined using the formula: % of antioxidant activity = 100 – (absorbance

of the treated sample – absorbance of the blank)  $\times$  100/absorbance of the control cells, where the blank was DPBS and the cells in the control group were not treated with lapatinib.



**Figure 1.** Immunohistochemical analysis of HER2 in samples of canine mammary carcinoma. Cell membrane staining indicates a positive cell for HER2 expression (arrows). (a) UNESP-CM1; (b) UNESP-CM5; (c) UNESP-CM9; (d) UNESP-CM60; (e) UNESP-MM1; (f) UNESP-MM4.

### 2.7. RNA Extraction from Paraffin-Embedded Tissue and Cell Culture Samples and RT-qPCR Analysis

mRNA was extracted from FFPE samples and the corresponding cell cultures for *HER2* gene expression analysis. For mRNA extraction from the paraffin-embedded tissues, samples were cut on a microtome, and three sections of 10 micrometers were macrodissected and placed in 1.5 mL tubes. The extraction protocol of the RecoverAll™ Total Nucleic Acid Isolation Kit for FFPE (Invitrogen, Carlsbad, CA, USA) was followed. At the end of the protocol, the samples were treated with DNase to purify the RNA, and

the RNA concentration and purity were measured by determining the A280 absorbance and A260/A280 ratio on a spectrophotometer (NanoDrop™, ND-8000, Thermo Scientific, Waltham, MA, USA).

mRNA extraction from the six cell cultures was carried out in triplicate, and for this purpose, cryopreserved cells were thawed in a water bath at 37 °C, centrifuged (450 g, 5 min) and resuspended in DMEM supplemented with 1% antibiotic/antimycotic solution and 10% FBS. The cells were transferred to 6-well plates and cultured until they reached a minimum confluence of 70%. Then, they were washed 3 times with DPBS in an ice bath.

mRNA extraction followed the protocol recommended by the manufacturer (RNeasy Mini Kit, Qiagen, Hilden, Germany). The concentration and purity of the extracted mRNA were evaluated by determining the A280 absorbance and A260/A280 ratio on a spectrophotometer (NanoDrop™, ND-8000, Thermo Scientific, Waltham, MA, USA). To eliminate any contamination with genomic DNA, the total extracted RNA was treated with 1 U of DNase I amplification grade (Life Technologies, Carlsbad, CA, USA) in 10× DNase I reaction buffer and 25 mM EDTA, pH 8.0.

For both mRNA extracted from paraffin embedded tissue and that extracted from cells in culture, RNA was reverse transcribed into cDNA with 1 µg of total RNA and the Super-script III™ Reverse Transcriptase enzyme (Invitrogen). For this protocol, 1 µL of OligodT (500 µg/mL), 1 µL of random primers (100 µg/mL), 1 µL of dNTPs and RNase-free water were used. The mixture was heated to 65 °C for 5 min, 4 µL of 5× First-Strand Buffer transcription buffer (250 mM Tris-HCl, pH 8.3; 375 mM KCl; and 15 mM MgCl<sub>2</sub>) and 1 µL of 0.1 M DTT were added, and then 1 µL of the Super-script III enzyme (200 U/µL) was added, with the final volume of the mixture being 19 µL. The mixtures were incubated at 25 °C for 5 min and then at 50 °C for 1.5 h, followed by incubation at 70 °C for 15 min. Reactions were carried out on a PTC-100 thermocycler (Peltier-EffectCycling-MJ Research). At the end of transcription, cDNA was stored at −20 °C.

RT-qPCR amplifications were evaluated on an automatic thermocycler (QuantStudio™ 12K Flex Real-Time PCR System, 4471087, Applied Biosystems™, ThermoFisher Scientific, Carlsbad, CA, USA) and processed by the detection system after a variable number of cycles in the exponential phase.

The values obtained for expression in all samples were normalized as the ratio between the gene of interest (*HER2*) and reference genes *hypoxanthine phosphoribosyltransferase 1* (*HPRT*), *ribosomal protein S5* (*RPS5*) and *ribosomal protein S19* (*RPS19*) (selected in previous studies by the group). The primers used in this reaction are listed in Table 2.

Transcript expression was analyzed as the relative quantification (RQ) of the RNA expression in a sample using the formula  $2^{-\Delta\Delta C_t}$  [34]. The RQ of each sample was determined by comparison with normal FFPE mammary tissue samples.

### 2.8. Cell Migration Assay

For evaluation of the effect of lapatinib on cell migration, a transwell assay was used. All cell cultures evaluated in this assay went through a 24 h period “starvation” period in medium containing 0.2% FBS. After they were treated with trypsin and incubated in a humidified atmosphere containing 5% CO<sub>2</sub> at 37 °C for 5 min, the cells were loosened from the bottom of the bottle. Then, the trypsin was inactivated with MEGM™ supplemented with 5% FBS. Samples were centrifuged (450 g, 5 min) to remove the medium with a high concentration of FBS and then resuspended in MEGM™ supplemented with 0.2% FBS. Two hundred microliters of each cell culture suspension was placed in inserts (Greiner Bio-One, Kremsmünster, Austria) with a porous membrane of 8 µm at a concentration of  $1 \times 10^6$  cells/mL, and each insert was placed in a well of a 24-well plate containing MEGM™ supplemented with 10% FBS.

**Table 2.** Oligonucleotide sequences of the primers used for RT-qPCR.

Access Gene Symbol <sup>1</sup>	Oligonucleotide Sequence (5' > 3')
<i>HPRT</i>	Forward primer (5'-3') AGCTTGCTGGTGAAAAGGAC
	Reverse primer (3'-5') TTATAGTCAAGGGCATATCC
<i>RPS19</i>	Forward primer (5'-3') CCTTCCTCAAAAAGTCTGGG
	Reverse primer (3'-5') GAACGAGGGATGCTACTCTTG
<i>RPS5</i>	Forward primer (5'-3') TCACTGGTGAGAACCCCT
	Reverse primer (3'-5') TCACTGGTGAGAACCCCT
<i>HER2</i>	Forward primer (5'-3') GCTCTGGAGGGAGTCACAGGTTA
	Reverse primer (3'-5') ACTGAGGTTAGGCAGGCTGTCT

<sup>1</sup> GenBank (www.ncbi.nlm.nih.gov (accessed on 12 January 2021)).

Each cell culture was placed in six different inserts, three were used as control wells and three were used as treatment wells. For treatment wells, lapatinib was added to the insert at the IC<sub>50</sub> of each culture. After 24 h, the inserts were removed from the plate and placed in a new 24-well plate containing preheated trypsin. The samples were incubated in trypsin for 10 min in a humidified atmosphere containing 5% CO<sub>2</sub> at 37 °C. After that period, the trypsin-treated cells that released from the bottom of the inserts were placed in a Neubauer chamber, and the cells were counted.

### 2.9. Statistical Analysis

RQs were evaluated to determine the correlation of HER2 expression in paraffin-embedded tissue and that in culture samples by Spearman's correlation analysis. In addition, the Mann–Whitney test was used to assess the difference in HER2 expression between paraffin-embedded tissue and cell culture samples. Data obtained from the migration assay were statistically analyzed using the Mann–Whitney test. MTT results were analyzed using the Mann–Whitney test. The results of MTT and RT-qPCR assay were evaluated for correlations using the Spearman test. Statistical differences were considered significant when  $p < 0.05$ .

## 3. Results

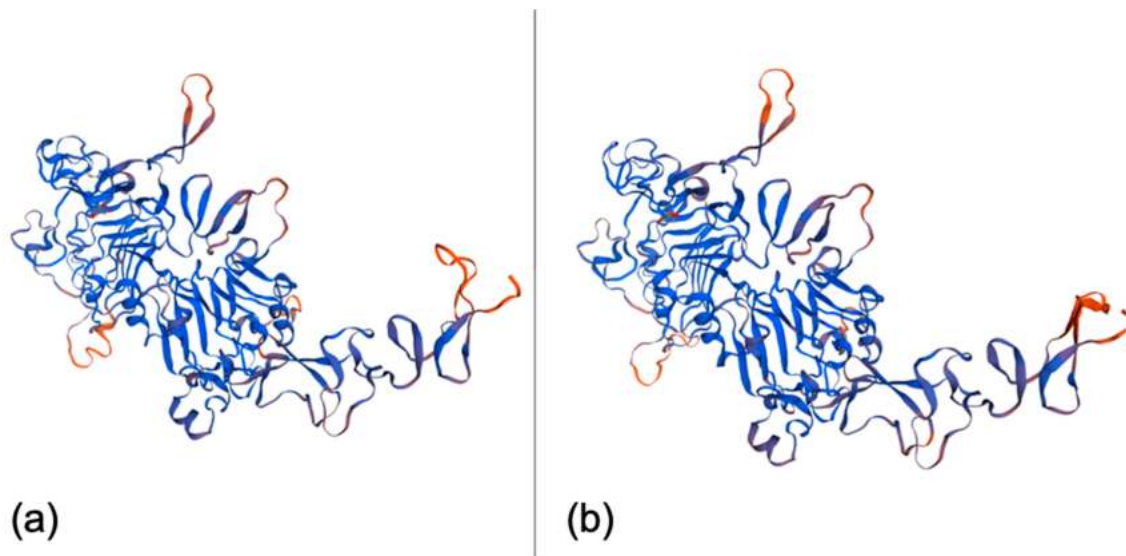
### 3.1. HER2 Homology

When compared on the Swiss model platform (Swiss Institute of Bioinformatics, Basel, Switzerland) (<https://swissmodel.expasy.org/> (accessed on 14 May 2021)), the three-dimensional structures of canine and human HER2 showed 95% homology (Figure 2), demonstrating high homology between the human and canine HER2 proteins.

### 3.2. Gene Expression

There was no statistical correlation between the expression of *HER2* in paraffin-embedded samples and the immunohistochemical score ( $p = 0.13$ ).





**Figure 2.** (a) 3D model of human HER2 generated from the UniProtKB/Swiss-Prot sequence P04626.1. (b) Canine HER2 3D model generated from the NCBI reference sequence NP\_001003217.2. Both images were generated using the online tool Swiss model (Swiss Institute of Bioinformatics, Basel, Switzerland) (<https://swissmodel.expasy.org/> (accessed on 14 May 2021)).

### 3.3. Cell Viability

All primary cultures showed decreased cellular metabolic activity at all tested drug concentrations in an MTT assay. The  $IC_{50}$  values of the six cell cultures were between 14.06 nM and 584.80 nM (Figure 3).

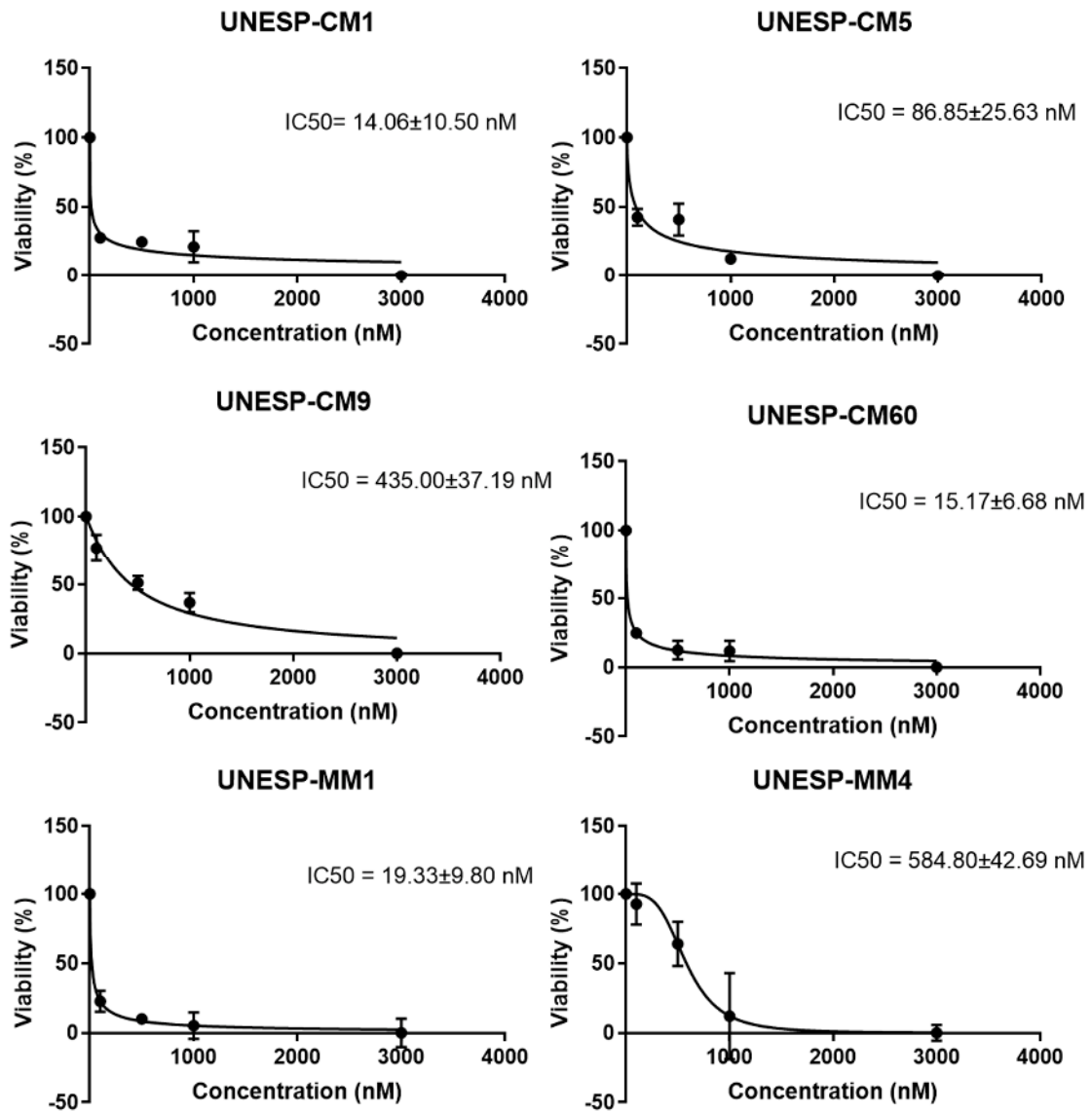
There was no significant difference between the  $IC_{50}$  of the HER2+ group and that of the HER2− group ( $p = 4$ ) (Figure 4), and there was no significant difference in the  $IC_{50}$  among the primary and metastatic cell lines ( $p = 0.53$ ).

### 3.4. Correlation between HER2 Expression and the $IC_{50}$

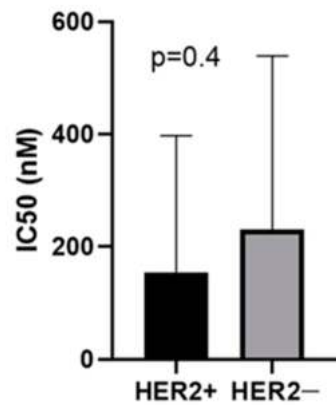
Spearman's correlation analysis revealed a negative correlation ( $p = 0.04$ ) between the RQ of cell culture samples and the  $IC_{50}$ ; that is, the higher the HER2 expression of a sample was, the lower the  $IC_{50}$  of lapatinib for that culture.

### 3.5. Cell Migration

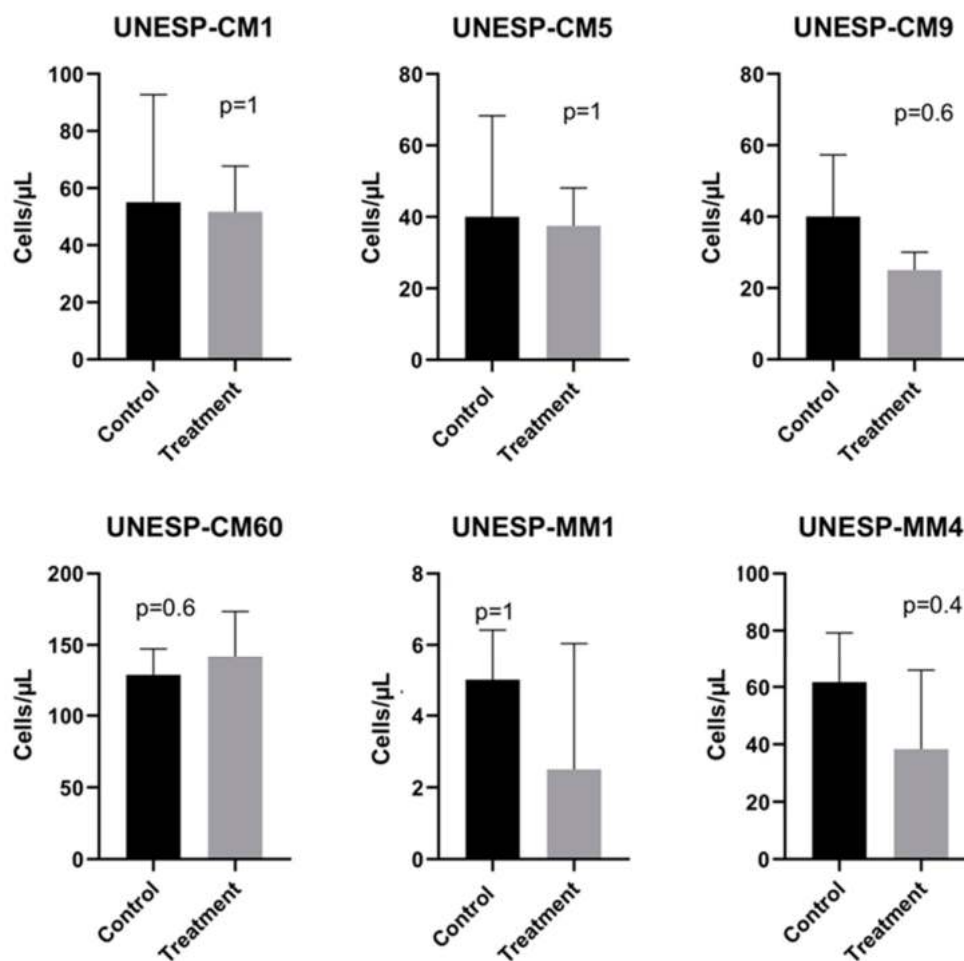
In a migration assay, there was no significant difference between the group treated with lapatinib and the control group in any cell culture (Figure 5). Additionally, there was no difference when grouping the cells by HER2 expression and their origin (non-metastatic primaries, metastatic primaries and metastases) as seen on the Supplementary Materials Figures S1 and S2.



**Figure 3.** Percentage of viable cells in an MTT assay of primary cultures of canine breast carcinoma (UNESP-CM1, UNESP-CM5, UNESP-CM9 UNESP-CM60) and metastases (UNESP-MM1 and UNESP-MM4) treated with lapatinib at 100, 500, 1000 or 3000 nM for 24 h.



**Figure 4.** Comparison by Mann–Whitney test of the IC<sub>50</sub> values of the HER2+ and HER2– groups ( $p = 0.4$ ).



**Figure 5.** Concentration (cells/ $\mu\text{L}$ ) of cells in the wells of each cell culture after the migration assay protocol. The Mann–Whitney test was used to compare the migration of the control and treatment groups.

#### 4. Discussion

In clinical practice, trastuzumab is considered the first-line choice for treatment of human breast cancer overexpressing HER2 [35]. However, advanced tumors can become resistant to trastuzumab, and in these cases, the use of lapatinib alone or in combination leads to a better antitumor response [36–38]. Female dogs can be considered a model of human breast cancer, but only for some specific subtypes, such as the micropapillary, solid, and anaplastic subtypes [39] and inflammatory breast cancer [40].

Singer et al. [41] studied the homology between canine and human HER2 and predicted the binding of anti-HER2 drugs with canine HER2. The HER2 proteins of humans and dogs showed high homology of 92.31% in the amino acid sequence. In addition, important sequences, such as the binding region for trastuzumab and cetuximab, were conserved in canine HER2. Moreover, there was predicted binding between these monoclonal antibodies and canine HER2.

In our assessment of the three-dimensional homology of the structures of human and canine HER2, the homology was even greater, with 95% similarity, so it is very likely that polyclonal antibodies developed to recognize human HER2 can recognize canine HER2. Thus, this similarity in proteins is also important, as it indicates that targeted therapies developed for human use should be applicable in dogs.

Lapatinib efficiently inhibited the proliferation of HER2+ and HER2– canine mammary carcinoma cell cultures in vitro. Interestingly, the cell lines exhibited dose-dependent cell viability. Thus, higher concentrations produced lower cell viability. This result agrees with the findings in humans, which showed that lapatinib was able to reduce the viability

and proliferation of breast cancer cells and induce breast cancer cell death [41–44]. Similar results were also reported in feline mammary cancer cell cultures, where lapatinib both alone and in association with other drugs such as rapamycin, trastuzumab and pertuzumab, was able to inhibit cell proliferation [21,22].

In assessing the ability of lapatinib to inhibit the migration of canine mammary cancer cells, we confirmed that just as in human breast cancer cells, lapatinib alone is not able to satisfactorily inhibit migration regardless of the cell sensitivity to the drug [45]. However, when associated with isothiocyanates, compounds present in abundance in cruciferous vegetables, lapatinib was shown to inhibit the migration of breast cancer cells in women [45,46]. Lapatinib in combination with foretinib, an inhibitor of hepatocyte growth factor receptor, was also found to inhibit migration in triple-negative human breast cancer cell lines due to its action on EGFR [47]. These findings create interesting possibilities for future studies in canine mammary gland tumors assessing the combination of other pharmaceutical compounds with lapatinib.

In our study, lapatinib inhibited cell viability in samples of primary and metastatic neoplasms even with low or negative HER2 expression. This action is also observed in humans and makes lapatinib an excellent therapeutic option in the treatment of metastatic breast neoplasms [48,49]. Therefore, lapatinib is a possible alternative that should be studied for the treatment of dogs with metastatic disease. Another important factor to be considered in the use of lapatinib to treat metastases is its good ability to penetrate different body tissues due to the small size of the molecule [8].

Although our study focused on HER2+ neoplasms, lapatinib has also been studied as a possible therapeutic alternative for triple-negative breast neoplasms, which generally show increased EGFR expression [47,48,50]. Studies on this subtype have demonstrated the ability of lapatinib, when combined with other drugs, to inhibit the migration of triple-negative human breast cancer cells [47]. In addition, in a study of human patients with metastatic triple-negative breast cancer treated with lapatinib and veliparib, 35% (6/17) of the patients responded to the therapy, with less than 10% of the patients having adverse effects, all of which were moderate [48].

Therefore, although lapatinib inhibited cell proliferation in all cell cultures, even in three of them considered negative for HER2, we emphasize that five of the six tumors had HER2 expression, even if at a low level. Thus, the drug may have acted on the few HER2 molecules present, and in the case of the cell line UNESP-MM1, the action could be related to binding to EGFR [16,51], this ability of lapatinib to inhibit EGFR phosphorylation has already been described in feline mammary cancer cells [22]. In addition, similar to the activity of any tyrosine kinase inhibitor, nonspecific binding with other tyrosine kinase receptors can occur [16,51].

The negative correlation between the expression of HER2 in cells and the  $IC_{50}$ , that is, the higher the expression of HER2 in a cell culture was, the lower the  $IC_{50}$  of lapatinib of that sample, is an indication that, as in humans, lapatinib acts mainly on HER2 in canine cells, reducing the viability of neoplastic cells [32,52]. In addition, the correlation between HER2 expression in cultured cells and cell sensitivity to lapatinib is a strong indication that the level of expression of this receptor may be a predictive factor for therapies using lapatinib, which opens the door for further *in vivo* studies in dogs.

## 5. Conclusions

Lapatinib was able to reduce the viability of primary and metastatic canine mammary carcinoma cells cultured *in vitro*, and its effectiveness was directly linked to the expression of HER2, which opens a perspective for the treatment of animals with both primary mammary neoplasms and metastasis, especially those that overexpress HER2.

**Supplementary Materials:** The following are available online at <https://www.mdpi.com/article/10.3390/pharmaceutics13060897/s1>, Figure S1: Mann-Whitney analysis of cell migration. There was no statistical difference in any analysis (a): All cell cultures. (b): HER2+ cell cultures. (c): HER2– cell cultures, Figure S2: ANOVA evaluation of cell culture migration when grouped into non-metastatic

primaries, metastatic primaries and metastases. Non-metastatic primaries versus metastatic primaries  $p = 0.2873$ ; Non-metastatic primaries versus metastases  $p = 1$ ; Metastatic primaries versus metastases  $p = 0.1822$ . Table S1. Clinical data from animals with mammary carcinoma used for primary cell culture.

**Author Contributions:** Conceptualization, A.F.L.-F., C.E.F.-A. and R.L.-A.; Data Curation, A.F.L.-F., P.d.F.L. and P.E.K.; Formal Analysis, A.F.L.-F., P.d.F.L. and P.E.K.; Methodology, A.F.L.-F., P.d.F.L. and P.E.K.; Resources, C.E.F.-A. and R.L.-A.; Supervision, C.E.F.-A. and R.L.-A.; Writing—Original Draft, A.F.L.-F.; Writing—Review and Editing, P.d.F.L., P.E.K., C.E.F.-A. and R.L.-A. All authors have read and agreed to the published version of the manuscript.

**Funding:** This research was funded by Coordenação de Aperfeiçoamento de Pessoal de Nível Superior-Brasil (CAPES) (grant number: 001) and the São Paulo Research Foundation—FAPESP (grant number: 2018/14041-4).

**Institutional Review Board Statement:** The study was conducted according to the guidelines of the Declaration of Helsinki and approved by the Ethics Committee on Animal Use (CEUA) of the Veterinary Teaching Hospital of São Paulo State University (protocol code 0260/2018, approved on 16/01/2019).

**Acknowledgments:** The authors thank Márcio de Carvalho for his help with RT-qPCR.

**Conflicts of Interest:** The authors declare no conflict of interest.

## References

1. Yu, R.M.C.; Cheah, Y.K. The roles of miRNAs in human breast cancer and canine mammary tumor. *Appl. Cancer Res.* **2017**, *37*, 37. [CrossRef]
2. Sahabi, K.; Selvarajah, G.T.; Abdullah, R.; Cheah, Y.K.; Tan, G.C. Comparative aspects of microRNA expression in canine and human cancers. *J. Veter. Sci.* **2018**, *19*, 162–171. [CrossRef]
3. Sorlie, T.; Perou, C.M.; Tibshirani, R.; Aas, T.; Geisler, S.; Johnsen, H.; Hastie, T.; Eisen, M.B.; van de Rijn, M.; Jeffrey, S.S.; et al. Gene expression patterns of breast carcinomas distinguish tumor subclasses with clinical implications. *Proc. Natl. Acad. Sci. USA* **2001**, *98*, 10869–10874. [CrossRef]
4. Fragomeni, S.M.; Sciallis, A.; Jeruss, J.S. Molecular Subtypes and Local-Regional Control of Breast Cancer. *Surg. Oncol. Clin. N. Am.* **2018**, *27*, 95–120. [CrossRef]
5. Harbeck, N.; Penault-Llorca, F.; Cortes, J.; Gnant, M.; Houssami, N.; Poortmans, P.; Ruddy, K.; Tsang, J.; Cardoso, F. Breast cancer. *Nat. Rev. Dis. Prim.* **2019**, *5*, 1–31. [CrossRef]
6. Ross, J.S.; Slodkowska, E.A.; Symmans, W.F.; Pusztai, L.; Ravdin, P.M.; Hortobagyi, G.N. The HER-2 Receptor and Breast Cancer: Ten Years of Targeted Anti-HER-2 Therapy and Personalized Medicine. *Oncology* **2009**, *14*, 320–368. [CrossRef]
7. Anderson, N.G.; Ahmad, T. ErbB receptor tyrosine kinase inhibitors as therapeutic agents. *Front. Biosci.* **2002**, *7*, 1926. [CrossRef]
8. Roskoski, R. The ErbB/HER receptor protein-tyrosine kinases and cancer. *Biochem. Biophys. Res. Commun.* **2004**, *319*, 1–11. [CrossRef]
9. Arkhipov, A.; Shan, Y.; Kim, E.T.; O Dror, R.; E Shaw, D. Her2 activation mechanism reflects evolutionary preservation of asymmetric ectodomain dimers in the human EGFR family. *eLife* **2013**, *2*, e00708. [CrossRef]
10. Holbro, T. The ErbB receptors and their role in cancer progression. *Exp. Cell Res.* **2003**, *284*, 99–110. [CrossRef]
11. Arciero, C.A.; Guo, Y.; Jiang, R.; Behera, M.; O'Regan, R.; Peng, L.; Li, X. ER+/HER2+ Breast Cancer Has Different Metastatic Patterns and Better Survival Than ER−/HER2+ Breast Cancer. *Clin. Breast Cancer* **2019**, *19*, 236–245. [CrossRef]
12. Waks, A.G.; Winer, E.P. Breast Cancer Treatment: A Review. *JAMA* **2019**, *321*, 288–300. [CrossRef]
13. Howlader, N.; Cronin, K.A.; Kurian, A.W.; Andridge, R. Differences in Breast Cancer Survival by Molecular Subtypes in the United States. *Cancer Epidemiol. Biomark. Prev.* **2018**, *27*, 619–626. [CrossRef]
14. Escrivá-De-Romaní, S.; Arumí, M.; Bellet, M.; Saura, C. HER2-positive breast cancer: Current and new therapeutic strategies. *Breast* **2018**, *39*, 80–88. [CrossRef]
15. Kreutzfeldt, J.; Rozeboom, B.; Dey, N.; De, P. The trastuzumab era: Current and upcoming targeted HER2+ breast cancer therapies. *Am. J. Cancer Res.* **2020**, *10*, 1045–1067. [PubMed]
16. Arteaga, C.L.; Sliwkowski, M.X.; Osborne, C.K.; Perez, E.A.; Puglisi, F.; Gianni, L. Treatment of HER2-positive breast cancer: Current status and future perspectives. *Nat. Rev. Clin. Oncol.* **2011**, *9*, 16–32. [CrossRef]
17. Patel, T.A.; Ensor, J.E.; Creamer, S.L.; Boone, T.; Rodriguez, A.A.; Niravath, P.A.; Darcourt, J.G.; Meisel, J.L.; Li, X.; Zhao, J.; et al. A randomized, controlled phase II trial of neoadjuvant ado-trastuzumab emtansine, lapatinib, and nab-paclitaxel versus trastuzumab, pertuzumab, and paclitaxel in HER2-positive breast cancer (TEAL study). *Breast Cancer Res.* **2019**, *21*, 1–9. [CrossRef] [PubMed]

18. Vernieri, C.; Milano, M.; Brambilla, M.; Mennitto, A.; Maggi, C.; Cona, M.S.; Prisciandaro, M.; Fabbroni, C.; Celio, L.; Mariani, G.; et al. The trastuzumab era: Current and upcoming targeted HER2+ breast cancer therapies. *Am. J. Cancer Res.* **2020**, *10*, 1045–1067, PMID:PMC7191090. [PubMed]
19. Bredin, P.; Walshe, J.M.; Denduluri, N. Systemic therapy for metastatic HER2-positive breast cancer. *Semin. Oncol.* **2020**, *47*, 259–269. [CrossRef]
20. Kunte, S.; Abraham, J.; Montero, A.J. Novel HER2-targeted therapies for HER2-positive metastatic breast cancer. *Cancer* **2020**, *126*, 4278–4288. [CrossRef]
21. Gameiro, A.; Nascimento, C.; Correia, J.; Ferreira, F. HER2-Targeted Immunotherapy and Combined Protocols Showed Promising Antiproliferative Effects in Feline Mammary Carcinoma Cell-Based Models. *Cancers* **2021**, *13*, 2007. [CrossRef] [PubMed]
22. Gameiro, A.; Almeida, F.; Nascimento, C.; Correia, J.; Ferreira, F. Tyrosine Kinase Inhibitors Are Promising Therapeutic Tools for Cats with HER2-Positive Mammary Carcinoma. *Pharmaceutics* **2021**, *13*, 346. [CrossRef] [PubMed]
23. Nguyen, F.; Peña, L.; Ibsch, C.; Loussouarn, D.; Gama, A.; Rieder, N.; Belousov, A.; Campone, M.; Abadie, J. Canine invasive mammary carcinomas as models of human breast cancer. Part 1: Natural history and prognostic factors. *Breast Cancer Res. Treat.* **2018**, *167*, 635–648. [CrossRef]
24. Peña, L.; De Andrés, P.J.; Clemente, M.; Cuesta, P.; Pérez-Alenza, M.D. Prognostic Value of Histological Grading in Noninflammatory Canine Mammary Carcinomas in a Prospective Study with Two-Year Follow-Up. *Veter Pathol.* **2012**, *50*, 94–105. [CrossRef] [PubMed]
25. Gama, A.; Alves, A.; Schmitt, F. Identification of molecular phenotypes in canine mammary carcinomas with clinical implications: Application of the human classification. *Virchows Archiv.* **2008**, *453*, 123–132. [CrossRef]
26. Cassali, G.; Damasceno, K.; Bertagnolli, A.; Estrela-Lima, A.; Lavalle, G.; Santis, G.; Nardi, A.; Fernandes, C.; Cogliati, B.; Sobral, R.; et al. Consensus regarding the diagnosis, prognosis and treatment of canine mammary tumors: Benign mixed tumors, carcinomas in mixed tumors and carcinosarcomas. *Braz. J. Veter Pathol.* **2017**, *10*, 555–574. [CrossRef]
27. Lavalle, G.E.; Campos, C.B.; Bertagnolli, A.C.; Cassali, G.D. Canine malignant mammary gland neoplasias with advanced clinical staging treated with carboplatin and cyclooxygenase inhibitors. *In Vivo* **2012**, *2693*, 375–379. [PubMed]
28. Tran, C.M.; Moore, A.S.; Frimberger, A. Surgical treatment of mammary carcinomas in dogs with or without postoperative chemotherapy. *Veter Comp. Oncol.* **2016**, *14*, 252–262. [CrossRef] [PubMed]
29. Goldschmidt, M.; Peña, L.; Rasotto, R.; Zappulli, V. Classification and Grading of Canine Mammary Tumors. *Veter Pathol.* **2011**, *48*, 117–131. [CrossRef]
30. Lainetti, P.D.F.; Brandi, A.; Filho, A.F.L.; Prado, M.C.M.; Kobayashi, P.E.; Laufer-Amorim, R.; Fonseca-Alves, C.E. Establishment and Characterization of Canine Mammary Gland Carcinoma Cell Lines with Vasculogenic Mimicry Ability in vitro and in vivo. *Front. Veter Sci.* **2020**, *7*, 583874. [CrossRef]
31. Lazic, S.E.; Clarke-Williams, C.J.; Munafò, M.R. What exactly is ‘N’ in cell culture and animal experiments? *PLoS Biol.* **2018**, *16*, e2005282. [CrossRef]
32. Nahta, R.; Yuan, L.X.; Du, Y.; Esteva, F.J. Lapatinib induces apoptosis in trastuzumab-resistant breast cancer cells: Effects on insulin-like growth factor I signaling. *Mol. Cancer Ther.* **2007**, *6*, 667–674. [CrossRef] [PubMed]
33. Negri, J.M.; McMillin, D.W.; Delmore, J.; Mitsiades, N.; Hayden, P.; Klippel, S.; Hideshima, T.; Chauhan, D.; Munshi, N.C.; Buser, C.A.; et al. In vitro anti-myeloma activity of the Aurora kinase inhibitor VE-465. *Br. J. Haematol.* **2009**, *147*, 672–676. [CrossRef] [PubMed]
34. Livak, K.J.; Schmittgen, T.D. Analysis of relative gene expression data using real-time quantitative PCR and the  $2^{-\Delta\Delta CT}$  Method. *Methods* **2001**, *25*, 402–408. [CrossRef]
35. Maximiano, S.; Magalhães, P.; Guerreiro, M.P.; Morgado, M. Trastuzumab in the Treatment of Breast Cancer. *BioDrugs* **2016**, *30*, 75–86. [CrossRef] [PubMed]
36. Riera, R.; De Soárez, P.C.; Puga, M.E.D.S.; Ferraz, M.B. Lapatinib for treatment of advanced or metastasized breast cancer: Systematic review. *Sao Paulo Med. J.* **2009**, *127*, 295–301. [CrossRef] [PubMed]
37. Opdam, F.L.; Guchelaar, H.-J.; Beijnen, J.H.; Schellens, J.H. Lapatinib for Advanced or Metastatic Breast Cancer. *Oncology* **2012**, *17*, 536–542. [CrossRef]
38. Yang, F.; Huang, X.; Sun, C.; Li, J.; Wang, B.; Yan, M.; Jin, F.; Wang, H.; Zhang, J.; Fu, P.; et al. Lapatinib in combination with capecitabine versus continued use of trastuzumab in breast cancer patients with trastuzumab-resistance: A retrospective study of a Chinese population. *BMC Cancer* **2020**, *20*, 1–10. [CrossRef]
39. Al-Mansour, M.A.; Kubba, M.A.; Al-Azreg, S.A.; Dribika, S.A. Comparative histopathology and immunohistochemistry of human and canine mammary tumors. *Open Veter J.* **2018**, *8*, 243–249. [CrossRef]
40. De Andrés, P.J.; Illera, J.C.; Cáceres, S.; Díez, L.; Pérez-Alenza, M.D.; Peña, L. Increased levels of interleukins 8 and 10 as findings of canine inflammatory mammary cancer. *Veter Immunol. Immunopathol.* **2013**, *152*, 245–251. [CrossRef]
41. Singer, J.; Weichselbaumer, M.; Stockner, T.; Mechtcheriakova, D.; Sobanov, Y.; Bajna, E.; Wrba, F.; Horvat, R.; Thalhammer, J.G.; Willmann, M.; et al. Comparative oncology: ErbB-1 and ErbB-2 homologues in canine cancer are susceptible to cetuximab and trastuzumab targeting. *Mol. Immunol.* **2012**, *50*, 200–209. [CrossRef]
42. Guan, M.; Tong, Y.; Guan, M.; Liu, X.; Wang, M.; Niu, R.; Zhang, F.; Dong, N.; Shao, J.; Zhou, Y. Lapatinib Inhibits Breast Cancer Cell Proliferation by Influencing PKM2 Expression. *Technol. Cancer Res. Treat.* **2018**, *17*. [CrossRef]

43. Showalter, L.E.; Oechsle, C.; Ghimirey, N.; Steele, C.; Czerniecki, B.J.; Koski, G.K. Th1 cytokines sensitize HER-expressing breast cancer cells to lapatinib. *PLoS ONE* **2019**, *14*, e0210209. [CrossRef] [PubMed]
44. Ma, S.; Dielschneider, R.F.; Henson, E.S.; Xiao, W.; Choquette, T.R.; Blankstein, A.R.; Chen, Y.; Gibson, S.B. Ferroptosis and autophagy induced cell death occur independently after siramesine and lapatinib treatment in breast cancer cells. *PLoS ONE* **2017**, *12*, e0182921. [CrossRef]
45. Kaczyńska, A.; Herman-Antosiewicz, A. Combination of lapatinib with isothiocyanates overcomes drug resistance and inhibits migration of HER2 positive breast cancer cells. *Breast Cancer* **2016**, *24*, 271–280. [CrossRef] [PubMed]
46. Wu, X.; Zhou, Q.-H.; Xu, K. Are isothiocyanates potential anti-cancer drugs? *Acta Pharmacol. Sin.* **2009**, *30*, 501–512. [CrossRef]
47. Simiczjew, A.; Dratkiewicz, E.; Van Troys, M.; Ampe, C.; Styczeń, I.; Nowak, D. Combination of EGFR Inhibitor Lapatinib and MET Inhibitor Foretinib Inhibits Migration of Triple Negative Breast Cancer Cell Lines. *Cancers* **2018**, *10*, 335. [CrossRef]
48. Stringer-Reasor, E.M.; May, J.E.; Olariu, E.; Caterinicchia, V.; Li, Y.; Chen, D.; Della Manna, D.L.; Rocque, G.B.; Vaklavas, C.; Falkson, C.I.; et al. An open-label, pilot study of veliparib and lapatinib in patients with metastatic, triple-negative breast cancer. *Breast Cancer Res.* **2021**, *23*, 1–12. [CrossRef]
49. Ma, F.; Ouyang, Q.; Li, W.; Jiang, Z.; Tong, Z.; Liu, Y.; Li, H.; Yu, S.; Feng, J.; Wang, S.; et al. Pyrotinib or Lapatinib Combined With Capecitabine in HER2-Positive Metastatic Breast Cancer with Prior Taxanes, Anthracyclines, and/or Trastuzumab: A Randomized, Phase II Study. *J. Clin. Oncol.* **2019**, *37*, 2610–2619. [CrossRef] [PubMed]
50. Abo-Zeid, M.A.; Abo-Elfadl, M.T.; Gamal-Eldeen, A.M. Evaluation of lapatinib cytotoxicity and genotoxicity on MDA-MB-231 breast cancer cell line. *Environ. Toxicol. Pharmacol.* **2019**, *71*, 103207. [CrossRef] [PubMed]
51. Broekman, F. Tyrosine kinase inhibitors: Multi-targeted or single-targeted? *World J. Clin. Oncol.* **2011**, *2*, 80–93. [CrossRef] [PubMed]
52. Konecny, G.E.; Pegram, M.D.; Venkatesan, N.; Finn, R.; Yang, G.; Rahmeh, M.; Untch, M.; Rusnak, D.W.; Spehar, G.; Mullin, R.J.; et al. Activity of the Dual Kinase Inhibitor Lapatinib (GW572016) against HER-2-Overexpressing and Trastuzumab-Treated Breast Cancer Cells. *Cancer Res.* **2006**, *66*, 1630–1639. [CrossRef] [PubMed]



Review

# Behind the Adaptive and Resistance Mechanisms of Cancer Stem Cells to TRAIL

Adriana G. Quiroz-Reyes<sup>1</sup>, Paulina Delgado-Gonzalez<sup>1</sup>, Jose Francisco Islas<sup>1</sup> , Juan Luis Delgado Gallegos<sup>1</sup> , Javier Humberto Martínez Garza<sup>2</sup> and Elsa N. Garza-Treviño<sup>1,\*</sup>

- <sup>1</sup> Department of Biochemistry and Molecular Medicine, Faculty of Medicine, Autonomous University of Nuevo Leon, San Nicolás de los Garza 64460, Mexico; adri.quirroz.ry@gmail.com (A.G.Q.-R.); paulina.delgadogn@uanl.edu.mx (P.D.-G.); jose.islasc@uanl.mx (J.F.I.); jdelgado.me0174@uanl.edu.mx (J.L.D.G.)
- <sup>2</sup> Department of Human Anatomy, Faculty of Medicine, Autonomous University of Nuevo Leon, San Nicolás de los Garza 64460, Mexico; javier.martinezgr@uanl.edu.mx
- \* Correspondence: elsa.garzatr@uanl.edu.mx

**Abstract:** Tumor necrosis factor (TNF)-related apoptosis-inducing ligand (TRAIL), also known as Apo-2 ligand (Apo2L), is a member of the TNF cytokine superfamily. TRAIL has been widely studied as a novel strategy for tumor elimination, as cancer cells overexpress TRAIL death receptors, inducing apoptosis and inhibiting blood vessel formation. However, cancer stem cells (CSCs), which are the main culprits responsible for therapy resistance and cancer remission, can easily develop evasion mechanisms for TRAIL apoptosis. By further modifying their properties, they take advantage of this molecule to improve survival and angiogenesis. The molecular mechanisms that CSCs use for TRAIL resistance and angiogenesis development are not well elucidated. Recent research has shown that proteins and transcription factors from the cell cycle, survival, and invasion pathways are involved. This review summarizes the main mechanism of cell adaption by TRAIL to promote response angiogenic or pro-angiogenic intermediates that facilitate TRAIL resistance regulation and cancer progression by CSCs and novel strategies to induce apoptosis.

**Keywords:** TRAIL; cancer stem cells; TRAIL resistance; angiogenesis

**Citation:** Quiroz-Reyes, A.G.; Delgado-Gonzalez, P.; Islas, J.F.; Gallegos, J.L.D.; Martínez Garza, J.H.; Garza-Treviño, E.N. Behind the Adaptive and Resistance Mechanisms of Cancer Stem Cells to TRAIL. *Pharmaceutics* **2021**, *13*, 1062. <https://doi.org/10.3390/pharmaceutics13071062>

Academic Editor: Hassan Bousbaa

Received: 2 June 2021  
Accepted: 30 June 2021  
Published: 10 July 2021

**Publisher's Note:** MDPI stays neutral with regard to jurisdictional claims in published maps and institutional affiliations.



**Copyright:** © 2021 by the authors. Licensee MDPI, Basel, Switzerland. This article is an open access article distributed under the terms and conditions of the Creative Commons Attribution (CC BY) license (<https://creativecommons.org/licenses/by/4.0/>).

## 1. Introduction

Apoptosis, or programmed cell death, is a naturally occurring mechanism that eliminates damaged cells. Intracellular signals from mitochondria or by ligands that bind to receptors on the cell membrane, such as Fas, tumor necrosis factor (TNF)- $\alpha$ /TNF receptor 1, Apo-3 ligand/death receptor (DR) 3, and TNF-related apoptosis-inducing ligand (TRAIL), can initiate apoptosis [1,2]. Intrinsic and extrinsic pathways can activate apoptosis. The extrinsic pathway is induced by signals that activate cell surface death receptors, such as the binding of TNF- $\alpha$  to TNF-R1. Meanwhile, an example of an intrinsic pathway can be seen as induced by the B cell lymphoma 2 (Bcl-2)-regulated mitochondrial pathway, leading to a release of cytochrome c, which associates with apoptotic protease activating factor 1 (APAF-1) and pro-caspase-9, forming the apoptosome, leading to the activation of caspase-9 [3]. Thus, apoptosis plays an important role in physiological processes, including the development of cardiovascular and neurological diseases and malignancies [4].

TRAIL was discovered in the last decade of the 20th century [5]. It is a TNF-related type 2 transmembrane protein encoded by the NFSF10 gene located on human chromosome 3 at 3q26. In the organism, TRAIL is part of the mechanism by which the immune system reacts against malignant cells, inducing apoptosis with minimal cytotoxicity toward normal cells [6]. The TRAIL protein consists of 281 amino acids of 33 KDa and, in its fully glycosylated form, 41 KDa. However, TRAIL is cleaved at the 114 amino acid position by cysteine proteases to produce soluble TRAIL, a protein of 24 KDa called sTRAIL. For



TRAIL to fully activate, an insertion of 12–16 amino acids in the receptor-binding site is required [7]. Physiologically, TRAIL is secreted by different tissue cells in the spleen, lung, prostate, placenta, kidney, cytotoxic T cells, and natural killer cells. Monocytes and dendritic cells can express TRAIL on their surface after stimulation with interferon- $\beta$  (IFN- $\beta$ ), which boosts antitumoral activity. In addition, there is a trace of sTRAIL in blood plasma (approximately 100 pg/mL) [8].

TRAIL can bind to five different receptors. DR4 and DR5 are death receptors (TRAIL-R1 and TRAIL-R2). Decoy receptors (DcR1 or DcR2, also TRAIL-R3 and TRAIL-R4) are anti-apoptosis receptors. The first receptors are overexpressed in tumors, and the latter are expressed mainly in normal cells [9]. The difference between both receptor types is the lack of cytoplasmic domains required for apoptosis activation. Another receptor discovered to bind TRAIL is osteoprotegerin (OPG). OPG is a soluble receptor that inhibits TRAIL apoptosis [10]. DR5 has been reported to be more efficient in apoptosis induction. However, DR5 nuclear localization in tumor cells is a signal of resistance to TRAIL [11].

DR4 and DR5 are transmembrane proteins with several cysteine-rich domains (CRDs) in their extracellular region, a single transmembrane domain, and a death domain (DD) in their intracellular region. DDs are homotypic protein modules organized in six  $\alpha$ -helices that act as binding sites for other proteins and communicate the apoptotic signal to the cell interior [7]. After TRAIL binding to DR4 and DR5 occurs, their trimerization initiates by the interaction of the DD and the Fas-associated death domain (FADD), inducing TRAIL receptors that expose the death effector domain (DED) and the formation of the death-inducing signaling complex (DISC) [3]. Next, the DISC recruits pro-caspase-8 and cleaves it. Cleaved caspase-8 decreases the membrane potential and converts Bid to truncated Bid (tBid). Then, tBid, p53, Noxa, Puma, and Bax form the pore-forming complex in the mitochondria outer membrane [12]. After pore formation, cytochrome C is released into the cytoplasm, interacting with dATP. Pro-caspase-9 is then recruited to Apaf-1 to form the Apaf-1/caspase-9 apoptosome [13]. Active caspases are proteolytic proteins that bench to cytosolic and nuclear targets; caspases cause cleavage of actin filaments of the cytoskeleton, the inhibitor of caspase-activated DNase (ICAD) that avoids activation of caspase-activated DNase (CAD) that destroys DNA [12].

This mechanism of cell death, which has been widely studied in the context of cancer and other diseases, is efficient. Many basic and clinical studies have demonstrated a relevant role in selectively inducing apoptosis, and in tumor cells, this has been demonstrated. Therefore, apoptosis continues to be a therapeutic target that needs to be studied.

## 2. Recombinant TRAIL

Recombinant versions of human APO2L/TRAIL have been developed and used in clinical trials due to their potential as antitumoral therapy. However, there has been some limitation in their use as an anticancer drug because of their short half-life in blood, fast elimination, and resistance by cancer cells [10]. Dulanermin is a recombinant non-tagged TRAIL used in clinical trials. However, this protein has not shown important therapeutical benefits due to poor efficiency binding to TRAIL receptors [14]; another form of Dulanermin, Apo2L.XL, presents higher pro-apoptotic activity by artificial cross-linking [7].

Tumoral cells can generate TRAIL resistance by downregulation of DR4 and DR5 and inhibition of the CD95/Fas domain [6]. Moreover, the signal received in TRAIL receptors can be switched to activate non-canonical signaling, inducing pro-inflammatory, pro-survival, and proliferation characteristics. This signal involves a complex integrated by receptor-interacting serine/threonine protein kinase 1 (RIPK1), tumor necrosis factor (TNF) receptor-associated factor 2 (TRAF2), and TNF receptor-associated death domain (TRADD), activating pro-tumor pathways, such as I $\kappa$ B/NF- $\kappa$ B, MAPK/ERK, STAT3, PI3K, Akt, JAK2, and Src [10].

The development of different recombinant TRAIL therapies has gained importance as a new strategy for reducing cancer progress. As mentioned before, TRAIL receptors have

been discovered mainly in cancer cells; however, their overexpression has been reported in a particular population of cancer cells in tumors called cancer stem cells (CSCs).

### 3. Cancer Stem Cells and TRAIL

CSCs are a subpopulation of cells that represent a low percentage within the tumor niche. These cells have pluripotency, self-renewal, and tumorigenic properties, such as invasiveness, plasticity, and maintenance, and are the main cause of chemoresistance and cancer relapse. Several CSC markers have been identified, such as homing cell adhesion molecule (CD44) [15], aldehyde dehydrogenase (ALDH) [15], CD326 [16], and CD133 [17]. Although some of these markers are useful for identification and therapeutic targets, they are further found in normal stem cells and are not specific [16].

Epithelial–mesenchymal transition (EMT) is a process associated with the stemness of cancer cells, which is critical during cancer progression. This process of EMT implicates the conversion of epithelial cells into a mesenchymal phenotype with loss of cell–cell junctions, altering cell–ECM interactions and cytoskeletal organization [18]. EMT mediators can stimulate the increased malignancy associated with the CSC phenotype, such as migration and invasion by protein expression and activation of transcription factors. These factors include SNAI1 and SNAI2 (Snail and Slug), ZEB1 (dEF1/TCF8), and ZEB2 and Twist. Others are Prrx1, Sox4, Sox9, Klf4, and members of the AP-1 (Jun/Fos) family [19]. Pathways involved in EMT include transforming growth factor-beta (TGF- $\beta$ ), bone morphogenetic protein (BPM), receptor tyrosine kinase (RTK), Wnt/ $\beta$ -catenin, Notch, Hedgehog, signal transducer and activator of transcription 3 (STAT3), extracellular matrix (ECM), and hypoxia [20].

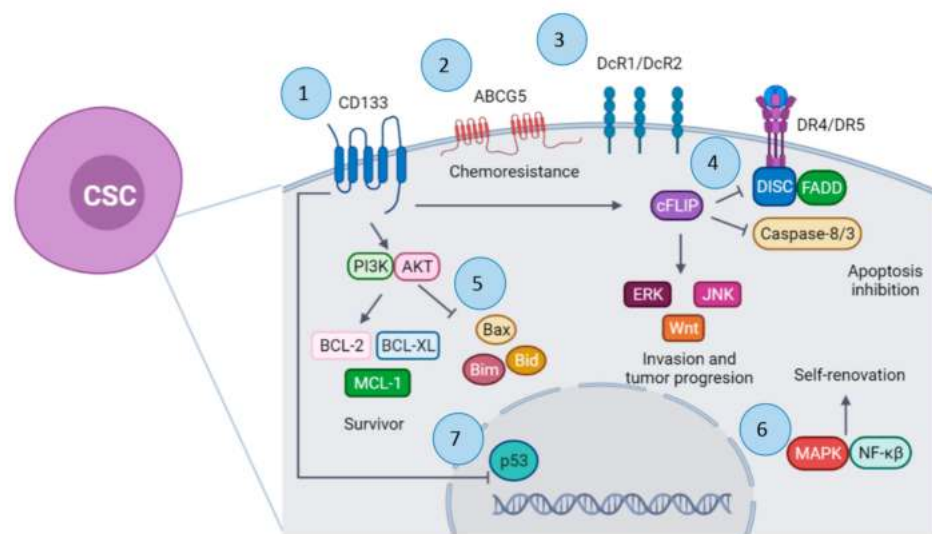
Genes of stem lineage Oct-4 and Nanog upregulate the process of EMT by binding to the promoters of Zeb1, Zeb2, Twist1, Prrx1, and miR-21. In addition, Sox2 increases slug expression, activating the STAT3/ hypoxia-inducible 1alpha (HIF-1 $\alpha$ ) signaling pathway, inducing EMT and promoting metastasis [20–22]. Altogether, these factors improve the protection of senescence and apoptosis and regulate cell progression and resistance to chemotherapy and radiotherapy, reducing E-cadherin expression, which drives to a mesenchymal state. In the tumor microenvironment, cancer cells secrete factors, such as TGF- $\beta$ , hepatocyte growth factor (HGF), and platelet-derived growth factor (PDGF), activating changes in EMT [23]. Moreover, TGF- $\beta$  is a major inducer of EMT since it can interact with other growth factors, such as epidermal growth factor (EGF), to influence the malignant transformation of CSCs and tumor-associated stromal fibrosis [23]. Once activated, EMT increases the expression of genes involved in stemness and stem cell markers. Additionally, in breast cancer, EMT increases stem cell phenotypes, such as CD44+/CD24- markers. EMT markers, such as E-cadherin,  $\beta$ -catenin, Snail, and Vimentin, correlate with CD133 expression, invasion, and metastasis of CSCs [20].

### 4. TRAIL Resistance Mechanism

EMT promotes TRAIL resistance and silencing of E-cadherin, which inhibits apoptosis due to the lack of efficient DISC assembly by ligated TRAIL receptors [10]. CD133 is a cell marker commonly expressed in CSCs, such as in colorectal cancer (CRC) and glioma [13]. Other CSC markers include CD44, nestin, and sox-2, usually co-expressing with CD133 [9,23]. CD133-positive cells present high ATP-binding cassette transporter (ABCG5) expression related to chemoresistance [12]. For this reason, these cells are novel targets for cancer therapy [12]. Embryonic pathways, such as Notch, Wnt, Hedgehog, and Hippo, are overactivated in CSCs to maintain their stem cell characteristics [24]. The Wnt signaling pathway participates in the chemoresistance of CD133-positive cells in CRC; thus, it is also considered a potential target [25]. Moreover, CD133 activates the PI3K pathway, and this, Akt, whose activation leads to upregulation of anti-apoptosis factors, such as BCL-2, BCL-XL, and MCL-1, decreases the pro-apoptotic factors Bid, Bax, and Bim [12].

Although TRAIL is a promising anticancer therapy, which can induce apoptosis in tumoral cells instead of normal cells, some CSC tumoral cells develop resistance to TRAIL (Figure 1) [26]. However, TRAIL treatment resistance has been developed by a variety of

cancers [27]. Another TRAIL resistance mechanism associated with downregulation of the death receptors DR4 and DR5 is overexpression of the decoy receptors DcR1 and DcR2 and overexpression of apoptosis inhibitors, such as cFLIP. It is suggested that activation of NF- $\kappa$ B could upregulate DR5 expression [9]. In turn, activation of the NF- $\kappa$ B pathway by TRAIL is associated with improvement of tumor growth, clonal expansion, and CSC signaling [6]. TRAIL-R2 or DR5 promotes invasion and metastasis of KRAS-mutated cancers by activating Rac1/phosphatidylinositol-3-kinase (PI3K) signaling. This metastasis process is cell-autonomous and mediated by the membrane-proximal domain (MDP) of the receptor [28]. In addition, it is reported that TRAIL-R downregulation and apoptosis resistance are mediated by signals, such as Src, Talin, PI3K, and MAPK. Phosphatase and tensin homolog (PTEN) protein negatively regulates the PI3K/AKT/mTOR pathway, working as a tumor suppressor gene, and EMT [29].



**Figure 1.** Mechanism of apoptosis resistance by cancer stem cells (CSCs). 1. CD133 activates the PI3K/AKT pathway. 2. Overexpression of ATP-binding cassette transporter (ABCG5). 3. Overexpression of decoy receptors (DcR1/DcR2) and down-regulation of DR4/DR5 receptors. 4. Overexpression of cFLIP protein. 5. Downregulation of pro-apoptotic factors. 6. Upregulation of MAPK and NF- $\kappa$ B pathways. 7. Downregulation of p53. Created with BioRender.com (accessed on 25 May 2021).

Moreover, the molecule ONC201/TIC10 can induce apoptosis by the TRAIL pathway, showing great results *in vitro* and *in vivo*. It is currently being used in phase I/II clinical trials for advanced-stage cancer, such as breast cancer, colon cancer, and glioblastoma. The mechanism of ONC201/TIC10 is the inactivation in CSCs of Akt and ERK signaling, inducing Foxo3 nuclear translocation and transcription of TRAIL, independent of the p53 status. In addition, this leads to the expression of the TRAIL receptor DR5. This molecule improves the half-life, distribution, route of administration, and activity of recombinant TRAIL and TRAIL-agonist antibodies, the main problems in its clinical application [30].

CD133-positive cells can also develop TRAIL resistance by overexpression of FLICE-like inhibitory protein (FLIP), inhibiting the DISC ensemble and TRAIL apoptosis. Moreover, p53 protein expression has an inverse relationship with CD133 expression [12]. cFLIP overexpression is also associated with TRAIL resistance in cancer cells. cFLIP inhibits caspase-8 and caspase-3 activation [9]. The expression of FLIP, a caspase-8 inhibitor, is higher in CD133-positive cells than in CD133-negative cells. CD133 upregulates FLIP expression, and this protein inhibits autophagy and activates ERK, JNK, ERK, and Wnt pathways. FLIP also inhibits FADD [12,26]. According to some studies, suppression of cytoplasmic cFLIP and elevated nuclear cFLIP levels are associated with regulating the Wnt pathway, which impacts the maintenance of CSCs. Inhibition of cFLIP further reduces

beta-catenin levels and inhibits Wnt target gene expression, whereas overexpression of nuclear cFLIP promotes Wnt target gene expression [31]. In addition, downregulating Wnt/ $\beta$ -catenin signaling impacts TRAIL sensitivity and reduces EMT [32,33]. TRAIL resistance is also associated with activation of self-renewing pathways by mitogen-activated protein kinases (MAPKs) and NF- $\kappa$ B, both negatively regulated by PTEN. The high expression of PTEN correlates with a better TRAIL response in tumors and with the reverse process of EMT (mesenchymal–epithelial transition (MET)) [34].

Although there are CSCs resistant to TRAIL, some research groups have reported that CSCs are susceptible to TRAIL activity after stimulation with small-molecule compounds, such as CDDP, etoposide, PS-341 (bortezomib), tunicamycin, rottlerin, brandisianins, sodium butyrate, and inostamycin [35]. Other natural compounds, such as kurarinone, icaritin, and withanolide E, are reported to downregulate cFLIP expression and TRAIL-resistant cancer cell sensitization to TRAIL-induced apoptosis. Natural compounds, such as silibinin, gingerol, and indomethacin, are reported to possess both mechanisms of sensitizing TRAIL-resistant cancer cells. The most relevant results are summarized in Table 1. A TRAIL-sensitive phenotype can be observed in different types of cancers and under different conditions. TRAIL can induce contrasting effects in tumoral cells, mainly controlled by the TME. The combination of TRAIL with some compounds prevents CSC TRAIL resistance and induces its elimination as sulforaphane [6]. Additional treatment with cisplatin combined with recombinant TRAIL could restore the expression of death receptors and Fas domain activity [6]. Dickkopf-1 (DKK-1) diminishes the expression of CD133, and consequently, proliferation, migration, and invasion of cancer cells diminish [25]. Agonists of TRAIL receptors have not presented enough efficacy due to the complexity of TRAIL signaling [10].

**Table 1.** Treatments that increase TRAIL sensitivity.

Treatment	Cancer	Effect	Reference
Goniothalamine plus TRAIL	Colorectal cancer	Enhance cytotoxicity and apoptosis	[35]
Icaritin plus TRAIL	Glioblastoma	Enhance apoptosis by c-FLIP downregulation and inhibition of NF- $\kappa$ B activity	[36]
Micelle-in-liposomes with piperlongumine plus TRAIL	Prostate cancer	Increase sensitization to TRAIL apoptosis in cancer cells	[37]
Silibinin plus TRAIL	Glioma	Enhance apoptosis by upregulation of DR5 and downregulation of cFLIP and survival	[38]
SH122 plus TRAIL	Prostate cancer	Enhanced TRAIL-induced apoptosis via D5R and the mitochondrial pathway	[39]
MSC/dTRAIL-TK gene therapy	Renal cell carcinoma	Enhance sensitization to TRAIL and increase apoptosis	[40]
Duloxetine plus TRAIL	Lung cancer	Enhance apoptosis of tumor cells through inhibition of autophagy	[41]
3-Methyladenine and chloroquine plus TRAIL	Malignant melanoma and osteosarcoma	Enhance pro-apoptotic mitochondrial pathway of tumor cells through inhibition of autophagy	[42]
Adenovirus-p53 plus TRAIL	Ovarian and nasopharyngeal squamous cancer	Overexpression of DR5 receptor in cancer cells to increase apoptosis by TRAIL	[43]
Adenovirus E1A plus adenovirus-hTRAIL	Hepatic cancer	Enhance apoptosis by upregulation of TRAIL receptors	[44]
MiR-760 plus TRAIL	Non-small-cell lung cancer	Enhance apoptosis by targeting FOXA1	[45]

## 5. Microenvironment and TRAIL Activity

The interaction of cells in the TME and CSCs can change the signaling mechanism of TRAIL in a tumor, leading to cell death or disease progression [46]. An antitumor TME is made by normal fibroblasts, dendritic cells (DC), natural killer (NK) cells, cytotoxic T cells, and M1 tumor-associated macrophages (TAMs) with the release of pro-inflammatory cytokines [10]. In contrast, a protumor TME includes M2 TAMs producing anti-inflammatory cytokines; myeloid-derived suppressor cells (MDSCs); regulatory T cells (Tregs) and B cells; cancer-associated fibroblasts (CAFs); and TIE2-expressing monocytes, mast cells, pericytes, and endothelial cells. In addition, neutrophils and T helper cells present both roles, pro- and anti-tumorigenic activity [47]. Different factors can regulate the production and secretion of TRAIL by several immune cells from the innate and adaptive immune systems. On the other hand, these similar factors can regulate the expression of membrane bound TRAIL and its receptors in the cellular microenvironment from components in TME, such as cells, cytokines, pH, oxygen levels, and matrix components [7]. For example, cytokines as IFNs can activate TRAIL transcription by the IRF1/STAT complex. TRAIL and TRAIL-R transcription is also mediated by stress-induced factors, such as nuclear factor of activated T cells (NFAT), Forkhead Box (FOX) proteins, NF- $\kappa$ B, C/EBP homologous protein, activator protein 1 (AP1), and p53 [10].

Physiologically, the TRAIL/TRAIL-R system regulates the homeostasis of adaptive immune cells by inducing apoptosis of aberrantly activated T cells. NK cells eliminate aberrant tumor cells by granule release (perforin/granzyme) in the innate immune system. This release is dependent on membrane receptor interactions involving FasL, TNF $\alpha$ , and TRAIL. TNF $\alpha$  increases TRAIL expression in mesenchymal stem cells (MSCs), inhibiting tumor growth by apoptosis induction of cancer cells [7]. In addition, DNA released from MSCs could act as damage-associated molecular patterns (DAMPs) that via TLR3-dependent NF- $\kappa$ B feed-forward loop further increase TRAIL expression on MSCs. Furthermore, TNF $\alpha$ -activated MSCs also produce IFN $\beta$  due to DNA/RNA released from apoptotic cells, thus enhancing TRAIL expression [10]. The activation of NK cells by IL12 generates IFN $\gamma$ , which enhances TRAIL expression [48].

Monocytes can also express TRAIL and target TRAIL-R in tumoral cells. It is seen that IFN $\alpha$  increases the release of soluble TRAIL by monocytes and promotes apoptosis of tumoral cells [27,49]. Moreover, macrophages secrete matrix metalloproteinase 12 (MMP12), which can mimic TRAIL and induce apoptosis in tumor cells [50]. TRAIL also induces CD14 and CD11b expression in monocytes, promoting its M1 differentiation and its phagocytic capacity and antitumor activity [51]. In addition, by TRAIL stimulation, macrophages produce pro-inflammatory cytokines IL1 $\beta$ , IL6, and TNF $\alpha$  in an NF- $\kappa$ B-dependent way [10].

As a component of the ECM, elastin microfibril interface-located protein 2 (EMILIN2) can bind to TRAIL receptors DR4 and DR5, inducing clustering and co-localization on lipid rafts from cell membrane, and then induce activation of apoptosis [10]. Hypoxia factors, such as HIF-1 $\alpha$ , are associated with PKC $\epsilon$  down-modulation, which acts as a key molecular event that promotes apoptosis by TRAIL in hypoxic tumor cells. In addition, the expression of vascular cell adhesion molecule-1 (VCAM-1) by tumors has been proposed as an immune escape mechanism and improves metastasis. VCAM-1 and  $\alpha$ 4 integrin interaction promotes T cell migration away from the tumor, reducing CD8+ T cell infiltration [52]. Cytotoxic T cells (CTLs) are the main effectors of the adaptive immune system against tumor cells, expressing TRAIL and TRAIL-R. This TRAIL expression is stimulated by interaction with TRAIL receptors on tumoral cells [10]. In addition, IFN $\alpha$  stimulates CTLs to increase TRAIL expression. Dendritic cells (DCs) participate in innate and adaptive immunity, acting as a bridge between both responses [53]. DCs present antigens to T cells; however, cytotoxic DCs activated by IFN $\alpha$  or IFN $\gamma$  present antitumor activity by the TRAIL system [54]. TRAIL reduces T regulatory cells (Tregs), while increasing the CD8+ CTLs population [10].

TRAIL shares homology with FasL, another member of the TNF family that can induce T cell apoptosis. In a pro-tumoral TME, TRAIL, soluble or membrane bound, can induce apoptosis in IL2-secreting T cells but not inactivated T cells [55]. Fas ligand (FasL/CD95L)

expressed by tumors allows them to inhibit T cell recognition and elimination. FasL is associated with immune escape because it binds to Fas in the T cell membrane and induces apoptotic signals. In addition, galectin-1 participates in the immunosuppressive tumor microenvironment, improving FasL activity [52]. It seems that cancer cells can release microvesicles with FAS and TRAIL, which, instead, induce apoptosis of cancer cells and target and eliminate CTLs as an immune escape mechanism. In multiple myeloma cancer cells, TRAIL bound to membranes can eliminate osteoclasts and bone formation, consequently improving the distribution of cancer cells to other tissues and allow metastasis development [10]. In metastatic tumors, cells can evade immune surveillance by inducing cell death of tumor-infiltrating lymphocytes (TILs). CRC cells expressing TRAIL can induce apoptosis of CD8+ cells by this mechanism [56]. In lymphomas, cancer cells can develop TRAIL resistance by the expression of CD40, a co-stimulatory receptor for interaction with CD4+ T cells that protects apoptosis by TRAIL. CD40 upregulates NF- $\kappa$ B, cFLIP, and Bcl-XL [10,31].

In this microenvironment of resistant tumor cells, TRAIL can potentiate immune suppressive effects of Tregs. Tumor-infiltrating Tregs reduce antitumor immune responses by secretion of TGF $\beta$ , IL10, and IL35, inhibiting CTL, NK cell, and DC activity. IL35 can stimulate macrophages and neutrophil polarization to an M2 anti-inflammatory state that promotes tumor development. Another cytokine that suppresses TRAIL activity in cancer cells is IL8, by upregulation of cFLIP in a CXCR2- and NF- $\kappa$ B-dependent way [57]. In addition, cancer cells from primary tumors release IL4, increasing the expression of anti-apoptotic proteins, such as cFLIP, Bcl-XL, and Bcl-2 [58]. It is important to note that even when cancer cells are resistant to TRAIL, exposure activates the secretion of the immune-suppressive cytokines, IL8, CXCL1, CXCL5, and CCL2 in a FADD-dependent way [59].

CCL2 is important because it seems to modulate the immune environment to a pro-tumoral state when interacting with cells with CCR2 receptors. As mentioned before, the interaction of cancer cells with endogenous TRAIL induces FADD-dependent secretion of CCL2, which polarizes monocytes to the M2 macrophage phenotype [59]. In addition, TRAIL receptors and FADD can promote NF- $\kappa$ B activation and proliferation of tumor cells. Moreover, CCL2 supports tumor growth by acting as a chemoattractant for MDSCs and monocytes, promoting its M2 differentiation by their CD206 expression [28]. The reduction in TRAIL expression is stimulated by IL6, IL1 $\beta$ , IL17, and G-CSF through STAT3-dependent downregulation and upregulation of MMP9. The result is immune suppression and a pro-angiogenic state [10].

## 6. TRAIL Activity in Angiogenesis

Angiogenesis allows the support of tissue growth and organ function under physiological and pathological conditions. During the pathological process, such as cancer, this mechanism helps the tumor feed, supply oxygen, and eliminate waste from the body [49]. The process of generating new blood vessels occurs through several different mechanisms: (1) from pre-existing vasculature; (2) inducing new blood vessel formation through a process involving formation and outgrowth of sprouts (tip cells), which eventually fuse with an existing vessel or newly formed sprout; (3) vasculogenesis (neo-vascularization from endothelial progenitor cells); (4) vascular mimicry, in which aggressively growing tumor cells can form vessel-like structures, which are formed without the contribution of endothelial cells, and that represents an alternate channel for tumor cells to source sufficient blood supply and nutrients; and (5) trans-differentiation of CSCs (neo-vascularization in tumors through differentiation of CSCs to endothelial cells) [60].

Normal stem cells and CSCs grow primarily in vascular niches due to a perivascular microenvironment [61]. Tumors can be vascularized through the cooperation of endothelial cells [62]. The involvement of CSC is key to promote angiogenesis in cancer and disease progression. Studies suggest that Notch signaling plays an essential role in angiogenesis through interactions with Notch ligands to cross-talk with other pathways, such as vascular

endothelial growth factor (VEGF) signaling [63]. However, the vascular niche of cancer is rich in abnormal blood vessels. These abnormalities are induced by hypoxia, low pH, and high pressure of a hostile interstitial fluid. Hypoxia also activates NF- $\kappa$ B and promotes EMT [64].

Furthermore, hypoxia increases hypoxia-inducible 1 $\alpha$  (HIF1 $\alpha$ ) in cancer cells [65]. Moreover, hypoxia increases nitric oxide (NO), which activates the Wnt/b-catenin signaling pathway, VEGF-A, and, ultimately, angiogenesis [66]. Angiogenesis is orchestrated within the tumor mass that harbors various host-derived cells, regulated by secreted regulators, such as VEGFR2, the expression of Tie-2 monocytes, fibroblasts, endothelial cells, and innate and adaptive immune cells that are central regulators of pro-angiogenic VEGF and angiopoietin signaling [67]. The role of CD133 in angiogenesis was recently reported since it is observed that it regulates the expression of the angiogenic protein vascular endothelial growth factor (VEGF) by activating the Wnt/b-catenin signaling pathway and promoting greater recruitment of endothelial progenitor cells (CPEs) in CSC-enriched tumors. This mechanism increases VEGF-A and interleukin 8 (IL8) expression. Both factors cause neovascularization and tumor growth [60].

TRAIL can modulate angiogenesis as endothelial cells from tumor vasculature also express TRAIL receptors; this indicates that endothelial cells are sensitive to TRAIL apoptosis [68]. However, TRAIL modulates multiple cellular functions in endothelial cells involving the ECM necessary for vascular remodeling. TRAIL regulates FGF-2 angiogenic function in human endothelial cells (HMEC-1); FGF2 is a growth factor that activates endothelial cell proliferation, migration, and tubule formation [69]. Mice lacking TRAIL have increased vascular leakage. In vitro, TRAIL at low concentrations (10 ng/mL) reduces angiotensin II-induced oxidative stress, leukocyte adhesion, and permeability as it prevents redistribution of VE-cadherin from the cell membrane [70]. The effects induced by TRAIL involve NOX4, which participates in the generation of oxygen species and catalyzing the transfer of electrons from NADPH to O<sub>2</sub>. Via NOX4, TRAIL promotes angiogenesis by modulation of H<sub>2</sub>O<sub>2</sub> production, eNOS phosphorylation, and NO production [71]. Low production of H<sub>2</sub>O<sub>2</sub> from NOX4 activates MAPK family members, the TGF- $\beta$ 1/SMAD2/3 pathway of PI3K/AKT signaling, and cell proliferation, migration, and angiogenesis [26]. Moreover, angiogenesis induced by TRAIL can improve perfusion in ischemic disease, as TRAIL receptors are expressed by vascular smooth muscle cells and cardiomyocytes from the cardiovascular system, contributing to the pathophysiology of cardiovascular diseases. In addition, TRAIL can induce apoptosis of vascular smooth muscle cells [72].

Conversely, TRAIL administration has anti-angiogenic action, inducing tumor starvation and downregulation of OPG receptors [10,64]. sTRAIL confirmed its anti-angiogenetic potential, even higher compared to recombinant human TRAIL (rhTRAIL). Therefore, sTRAIL seems to have a double effect in this model generating PDAC cell death and reducing angiogenesis. Thus, TRAIL could induce apoptosis in tumoral and endothelial cells, even when TRAIL resistance develops. In cancer, anti-angiogenic therapy has been used to sensitize cells to TRAIL. However, there exist different resistance mechanisms to anti-angiogenic agents that could inhibit TRAIL activity [73].

## 7. Regulation Mechanism

MicroRNAs (miRNAs or miRs) are a set of 18–24-nucleotide-long strands that can silence or downregulate the expression of their targets by base-pairing with the respective miRNA response elements found in the 3'UTR of the mRNA. In this way, there is a destabilization of the target mRNA; therefore, the efficiency of processing is reduced, which leads to an overall protein decrease [74]. What is even more remarkable is that a single miR is known to have hundreds if not thousands of targets that may be involved in many cell regulatory processes, including differentiation and apoptosis [75,76]. Not surprisingly, miRs have been shown to have different expression patterns when comparing cancerous with normal tissue, and even within cancer, malignant states often vary in expression [77].

TRAIL is a member of the TNF family, which, when activated, can induce apoptosis in tumor cells with no cytotoxicity to normal cells [78]. Unfortunately, many human cancer cells are resistant to TRAIL-induced apoptosis; hence, pharmacological studies have had significant drawbacks. Nonetheless, there is a silver lining as researchers are currently unraveling the different miRs involved in TRAIL regulation and TRAIL-induced apoptosis, which could, in turn, become either targets of TRAIL resistance or direct targets that induce TRAIL-induced apoptosis [78,79]. Interestingly, TRAIL resistance seems to be enhanced by PTEN and TIMP3 downregulation. To achieve this, the cluster of miR-221/222 promotes the phosphorylation of Akt, enriching the population of CD44<sup>+</sup> cells, which are known to enhance invasion and tumorigenicity [27,80,81]. In addition, miR-221 can also downregulate proapoptotic, Bcl-2-modifying factor (Bmf), and p53 upregulated modulator of apoptosis (PUMA) [82]. Moreover, miR-221 has been detected in several cancer pathologies and has been identified in high levels in peripheral blood, making it an excellent biomarker for early detection [83]. We should note that although the mechanisms are not yet fully determined, it has been shown that BMF and certain energy enzymes are involved in TRAIL-induced necrosis, most likely through the TNF-R1 via activation of RIPKs, which promote mitochondrial fragmentation through MLKL and PGAM5 [69,76]. Opposing this activity, the activation of miR-125b, miR-224, and miR-122 can target Mcl-1 and Bcl-w, both anti-apoptotic factors [27,84,85].

Another interesting regulator in TRAIL apoptosis is miR-25, as it has been implicated to block TRAIL death receptor (DR) 4, thereby blocking induced apoptosis. Additionally, predictive analysis has also confirmed Bim and Mcl-1 as targets for miR-25 [86,87]. In the case of DR4, bioinformatic analysis has determined direct targeting of the 3' UTR of DR4 by miR-25 [86]. Moreover, DR4 can also be repressed by Hedgehog signaling G13, thereby serving as an antagonist to TRAIL-induced apoptosis [88]. miR-25 is associated with the sensitivity of liver cancer stem cells to TRAIL-induced apoptosis. Studies have reported that the knockdown of miR-25 promotes TRAIL-induced apoptosis by inhibiting the PI3K/Akt/Bad signaling pathway through the miR-25/PTEN axis. The combination of anti-miR-25 and TRAIL may represent a novel strategy for treating LCSCs [89].

PTEN has a key function in the regulation of cell survival pathways, such as the aforementioned PI3K/AKT/mTOR and MAPK pathways; its inhibition by different mi-RNAs (miR-21, miR-221, miR-23b, miR-214) has been associated with resistance to chemotherapeutic agents, as well as proapoptotic mechanisms, such as those induced by TRAIL [90]. In addition, it inhibits metastasis development, invasion, and angiogenesis [29,91,92]. Meanwhile, miR-25-3p (part of the miR-25 cluster) has been shown to promote malignant phenotypes by also regulating the PTEN/Akt pathway and the promotion of the epithelial–mesenchymal transition similarly, as does miR-92a in non-small-cell lung cancer cells (NSCLC) and miR-129-5p in retinoblastomas by targeting PAX6 [93–95]. In addition, Wan et al. showed that miR-25-3p can induce Vimentin and Snail and suppress E-cadherin, which enhances invasiveness [86,96].

MiR-148a has an interesting effect on cancer, as it has been demonstrated to both reduce tumorigenesis and induce TRAIL apoptosis. Particularly, MMP15 and ROCK1, crucial players in invasion, have been shown as direct targets of miR-148a [97]. In addition, the NF- $\kappa$ B/p65 pathway, which leads to TRAIL resistance, has been previously shown to be under the control of miR-30c, miR-100, and miR-21 [97,98]. Partial elucidation of the mechanism of resistance by miR-21 involves downregulation of caspase-8, which blocks receptor-interacting protein-1 cleavage; meanwhile, miR-30 involves direct binding to the 3' UTR of metastasis-associated protein-1, promoting invasion [99]. Finally, miR-100 has been shown to target mTOR, a key regulator of motility by the PI3K/Akt pathway, which leads to the regulation of 4E-BP1 and p70S6K pathways. Interestingly, p70S6K is a cell cycle effector that directly regulates mRNA in cell cycle progression [100].

TRAIL-mediated apoptosis in prostate cancer seems to correlate directly with the expression of miR-135a-3p. Shin et al. investigated the role of Tanshinone I. Their research concluded that co-treatment directly with TRAIL upregulates DR5 and miR-135a-3p. Moreover, when using miR-135a-3p mimics, PARP cleavage further increases, leading to



an increase in apoptotic key regulator Bcl2-associated X protein (Bax) [101]. Still under investigation, there are several miRs of the miR-519 and miR-520 families that have been predicted to also indirectly activate proapoptotic factors Bax and Bak or enhance caspase 8 and 3 activity by FADD activity; in addition, KEGG analysis also shows that most of the targets of these families are associated with the PI3K/Akt pathway, similarly to miR-100, and although many of the hypothesized genes continue to require validation, both the NF- $\kappa$ B-inducing kinase and RELA have been confirmed [102,103].

### 8. Mechanism against TRAIL Resistance

TRAIL presents a limitation in its use as antitumoral therapy, as many primary tumors develop resistance to monotherapy with recombinant TRAIL and TRAIL receptor agonists [104]. Thus, the need to combine strategies to increase TRAIL sensitization and prevent resistance is clear. Table 2 shows different approaches being carried out using TRAIL as a therapeutic target in clinical trials that combine drugs or other strategies.

**Table 2.** Recombinant TRAIL use in clinical trials.

Recombinant TRAIL	Disease	Phase	Clinical Trial
Recombinant human Apo-2 ligand for injection	Non-small-cell lung cancer (NSCLC) stage IV	3	NCT03083743
Recombinant human TRAIL–trimer fusion protein (SCB-313)	Malignant pleural effusions	1	NCT038669697
	Peritoneal malignancies	1	NCT03443674
	Peritoneal carcinomatosis	1	NCT04047771
rhApo2L/TRAIL (AMG 951) with chemotherapy bevacizumab	Non-small-cell lung cancer (NSCLC)	2	NCT00508625
Dulanermin plus rituximab	Non-Hodgkin’s lymphoma	1, 2	NCT00400764
Dulanermin plus Camptosar <sup>®</sup> /Eribitux <sup>®</sup> or FOLFIRI	Metastatic colorectal cancer	1	NCT00671372
Dulanermin with FOLFOX and bevacizumab	Metastatic colorectal cancer	1	NCT00873756

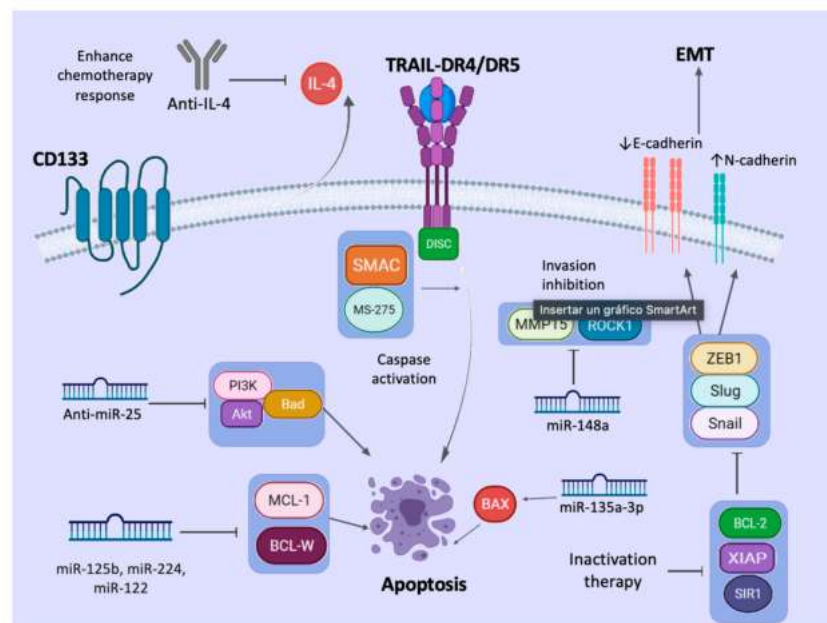
Targeting CSCs by TRAIL can be difficult as fast resistance development is reported. Todaro et al. presented that CD133+ CSCs from colon carcinomas can release IL4 to prevent apoptosis. However, they can be sensitized, as Loebinger et al. showed that MSC-expressing TRAIL can migrate to tumors and reduce tumor growth and metastasis of primary cancer. The combination of TRAIL plus chemotherapy with mitoxantrone increases the synergistic effect, improving apoptosis of putative CSCs. In CSCs that produce IL4, the administration of the IL4R $\alpha$  antagonist of anti-IL4 neutralizing antibodies enhances the sensitivity of CD133+ cells to chemotherapy with oxaliplatin and 5-FU [105]. As another example, MSCs expressing TRAIL inhibit metastasis of the non-small-cell lung cancer (NSCLC)-derived H460 cell line combined with Claudin-7. This small molecule regulates mitogen-activated protein kinase/extracellular signal-regulated kinase (MEK/ERK) signaling pathways. Other studies have shown that targeting of the XIAP molecule increases CSC sensitivity to TRAIL in pancreatic cancer, reducing metastasis. CD133+ CSCs from brain overexpress BCL-2 after TRAIL induction, and its knockdown enhances CSC sensitivity to TRAIL. In nasopharyngeal carcinoma, the use of a second mitochondria-derived activator of caspases (SMAC) mimics the induced inhibitor of apoptosis (IAP) degradation and enhances TRAIL apoptosis. Moreover, the knockdown of Sirtuin 1 (SIR1) sensitizes CSCs from colon cancer to TRAIL cytotoxicity [106].

Some studies have shown that TRAIL-induced apoptosis is regulated by post-translational modifications of death receptors [45]. O-glycosylation of DR4 and DR5 is proven to control the sensitivity of many cancer cells to TRAIL [36]. Subsequently, Dufour et al. reported that N-glycosylated DR4 promotes TRAIL signaling [46]. We previously found that DR5 is activated by fucosylation for TRAIL-induced apoptosis using our TRAIL variants [47]. A relationship between HDAC inhibition and glycosylation patterns has been reported.

This finding can be an explanation for the increased sensitivity of TRAIL receptors in the presence of HDAC inhibitors.

Epigenetic factors, such as drug resistance and immune evasion mechanisms, allow tumor progression. Histone deacetylases (HDACs) are important promoters of TRAIL resistance via TRAIL receptors. Since HDACs are associated with changes in glycosylation patterns, O-glycosylation, N-glycosylation, and fucosylation in DR4 and DR5 receptors are necessary to improve TRAIL signaling. Thus, HDAC inhibitors have been proposed as another strategy against cancer since they maintain glycosylation in TRAIL receptors [107]. In addition, HDAC inhibitors act in synergy with TRAIL by upregulating the mitochondrial pathway; downregulating NF- $\kappa$ B and its gene products, such as cyclin D1, Bcl-2, Bcl-XL, VEGF, HIF-1a, IL6, IL8, MMP-2, and MMP-9; and upregulating the pro-apoptotic proteins Bax, Bak, and p21/CIP1 and TRAIL receptors DR4 and DR5 in cancer cells [108].

It has been reported that the HDAC inhibitor MS-275 can sensitize TRAIL-resistant breast cancer xenografts in nude mice through upregulation of DR4 and DR5 TRAIL receptors, inducing apoptosis, tumor cell growth inhibition, angiogenesis, and metastasis. All these mechanisms generate a reversion of EMT, upregulate E-cadherin, and downregulate N-cadherin and transcription factors, such as Snail, Slug, and ZEB1 [108]. Moreover, the compound suberoylanilide hydroxamic acid (SAHA), another HDAC inhibitor, significantly increases the expression of Caspase-3 and the expression in MDA-MB-231 but not in MCF-7 breast cancer cells [109]. Recently, hypersensitization of CSCs to TRAIL required TRAIL-R2 and increased microenvironmental stress by the endoplasmic reticulum stress inducer celecoxib [110]. Therefore, microenvironmental modification could be a strategy to improve TRAIL sensitivity of CSCs. In addition, more research on agents that can act on CSC spheroids and thus avoid tumor progression, metastasis, and angiogenesis is needed [111]. Figure 2 summarizes the different approaches that could be used against TRAIL resistance in CSCs.



**Figure 2.** Mechanisms against TRAIL resistance. Therapeutic agents against TRAIL resistance by CSCs have been discovered. The use of anti-IL4 antibodies enhances the chemotherapy response. HDAC inhibitors, such as MS-275 and second mitochondria-derived activator of caspases (SMAC), sensitize CSCs resistant to TRAIL and potentiate apoptosis. Inactivation of BCL-2, SIR1, and XIAP inhibits EMT. Some miRNAs and anti-miRNAs could be used as additional strategies against cancer. Anti-miR-25 inhibits PI3K/Akt activation; miR-125b, miR-224, and miR-122 inhibit anti-apoptotic proteins MCL-1 and BCL-W; miR-135a-3p activates pro-apoptotic proteins, such as BAX; and miR-148a inhibits proteins related to invasion of CSCs, such as MMP15 and ROCK1. Created with BioRender.com (accessed on 25 May 2021).

## 9. Conclusions

Cancer treatments have evolved; however, cancer cells have developed several resistance mechanisms. TRAIL research demonstrates that this protein can induce tumor cell apoptosis of a wide variety of cancers when used as a recombinant TRAIL or TRAIL receptor agonist. CSC populations inside tumors have developed ways to evade this mechanism and activate survival pathways, proliferation, and angiogenesis that allow tumor progression. Likewise, CSCs can modulate the microenvironment to improve immune cell and cytokine recruitment, hypoxia, and the action of microRNAs generated by those cells. Thus, a reaction strategy has been developed that uses the combination of drugs and chemotherapeutic agents to increase CSC sensitivity to TRAIL and thereby facilitate its elimination, which reduces metastasis.

**Author Contributions:** A.G.Q.-R. designed the images and wrote, analyzed, and corrected the manuscript. P.D.-G. made the literature analysis and wrote and discussed the revised manuscript of this review. J.F.I. and J.L.D.G. made the literature analysis, wrote part of the text. J.H.M.G. corrected and revised the manuscript. E.N.G.-T. supervised, directed, and edited the manuscript. All authors have read and agreed to the published version of the manuscript.

**Funding:** This research received no external funding.

**Institutional Review Board Statement:** Not applicable.

**Informed Consent Statement:** Not applicable.

**Acknowledgments:** Special thanks to personal of Support Publication Scientific, Facultad de Medicina, UANL your time and expertise in reviewing this manuscript.

**Conflicts of Interest:** All authors indicated no potential conflicts of interest in publishing this manuscript.

## Abbreviations

ABCG5	ATP-binding cassette transporter
APAF-1	Apoptotic protease activating factor 1
AP1	Activator protein 1
Apo2L	Apo-2 ligand
Bcl-2	B-cell lymphoma 2
BPM	Bone morphogenetic protein
CAD	Caspase-activated DNase
CAF	Cancer-associated fibroblasts
CRC	Colorectal cancer
CRD	Cysteine-rich domain
CSCs	Cancer stem cells
CTLs	Cytotoxic T cells
DAMPs	Damage-associated molecular patterns
DCs	Dendritic cells
DED	Death-inducing signaling complex
DCRs	Decoy receptors
DD	Death domain
DISC	Death-inducing signaling complex
DKK-1	Dickkopf-1
DR	Death receptor
EGF	Epidermal growth factor
ECM	Extracellular matrix
EMT	Epithelial–mesenchymal transition
EMILIN2	Elastin microfibril interface-located protein 2
FADD	Fas-associated death domain
FLIP	FLICE-like inhibitory protein
FOX	Forkhead Box

HGF	Hepatocyte growth factor
HIF-1 $\alpha$	Hypoxia-inducible 1alpha
ICAD	Inhibitor of caspase-activated DNase
IFN- $\beta$	Interferon- $\beta$
IL8	Interleukin 8
MAPK	mitogen-activated protein kinase
MDP	membrane-proximal domain
MDSC	myeloid-derived suppressor cells
MET	mesenchymal–epithelial transition
miRNAs or miRs	microRNAs
MMP12	matrix metalloproteinase 12
MSCs	Mesenchymal stem cells
NFAT	Nuclear factor of activated T cells
NK	Natural killer
NO	Nitric oxide
NSCLC	Non-small-cell lung cancer
OPG	Osteoprotegerin
PDGF	Platelet-derived growth factor
PI3K	Phosphatidylinositol-3-kinase
PTEN	Phosphatase and tensin homolog
rhTRAIL	Recombinant human TRAIL
sTRAIL	Soluble TRAIL
TAMs	Tumor-associated macrophages
TGF- $\beta$	Transforming growth factor-beta
Tregs	Regulatory T cells
TILs	Tumor-infiltrating lymphocytes
VEGF	Vascular endothelial growth factor
TNF	Tumor necrosis factor
TRAF2	Tumor receptor-associated factor 2
TRAIL	Tumor necrosis factor (TNF)-related apoptosis-inducing ligand
TNF- $\alpha$	Tumor necrosis factor-alpha
VCAM-1	Vascular cell adhesion molecule-1
VEGF	Vascular endothelial growth factor

## References

- Johnstone, R.W.; Ruefli, A.A.; Lowe, S.W. Apoptosis: A link between cancer genetics and chemotherapy. *Cell* **2002**, *108*, 153–164. [CrossRef]
- Elmore, S. Apoptosis: A review of programmed cell death. *Toxicol. Pathol.* **2007**, *35*, 495–516. [CrossRef] [PubMed]
- Wong, S.H.M.; Kong, W.Y.; Fang, C.-M.; Loh, H.-S.; Chuah, L.-H.; Abdullah, S.; Ngai, S.C. The TRAIL to cancer therapy: Hindrances and potential solutions. *Crit. Rev. Oncol.* **2019**, *143*, 81–94. [CrossRef]
- Teringova, E.; Tousek, P. Apoptosis in ischemic heart disease. *J. Transl. Med.* **2017**, *15*, 87. [CrossRef]
- Holoch, P.A.; Griffith, T.S. TNF-related apoptosis-inducing ligand (TRAIL): A new path to anti-cancer therapies. *Eur. J. Pharmacol.* **2009**, *625*, 63–72. [CrossRef] [PubMed]
- Labsch, S.; Liu, L.; Bauer, N.; Zhang, Y.; Aleksandrowicz, E.; Gladkich, J.; Schönsiegel, F.; Herr, I. Sulforaphane and TRAIL induce a synergistic elimination of advanced prostate cancer stem-like cells. *Int. J. Oncol.* **2014**, *44*, 1470–1480. [CrossRef] [PubMed]
- Naval, J.; de Miguel, D.; Gallego-Lleyda, A.; Anel, A.; Martinez-Lostao, L. Importance of TRAIL molecular anatomy in receptor oligomerization and signaling. Implications for cancer therapy. *Cancers* **2019**, *11*, 444. [CrossRef] [PubMed]
- Merino, D.; Lalaoui, N.; Morizot, A.; Solary, E.; Micheau, O. TRAIL in cancer therapy: Present and future challenges. *Expert Opin. Ther. Targets* **2007**, *11*, 1299–1314. [CrossRef] [PubMed]
- Liu, J.; Gao, Q.; Xie, T.; Liu, Y.; Luo, L.; Xu, C.; Shen, L.; Wan, F.; Lei, T.; Ye, F. Synergistic effect of TRAIL and irradiation in elimination of glioblastoma stem-like cells. *Clin. Exp. Med.* **2018**, *18*, 399–411. [CrossRef]
- De Looff, M.; de Jong, S.; Kruyt, F.A.E. Multiple interactions between cancer cells and the tumor microenvironment modulate trail signaling: Implications for TRAIL receptor targeted therapy. *Front. Immunol.* **2019**, *10*, 1530. [CrossRef]
- Yuan, X.; Gajan, A.; Chu, Q.; Xiong, H.; Wu, K.; Wu, G.S. Developing TRAIL/TRAIL death receptor-based cancer therapies. *Cancer Metastasis Rev.* **2018**, *37*, 733–748. [CrossRef] [PubMed]
- Behrooz, A.B.; Syahir, A.; Ahmad, S. CD133: Beyond a cancer stem cell biomarker. *J. Drug Target.* **2019**, *27*, 257–269. [CrossRef] [PubMed]
- Zhang, R.; Xu, J.; Zhao, J.; Bai, J. Knockdown of miR-27a sensitizes colorectal cancer stem cells to TRAIL by promoting the formation of Apaf-1-caspase-9 complex. *Oncotarget* **2017**, *8*, 45213–45223. [CrossRef] [PubMed]

14. de Miguel, D.; Lemke, J.; Anel, A.; Walczak, H.; Martinez-Lostao, L. Onto better TRAILs for cancer treatment. *Cell Death Differ.* **2016**, *23*, 733–747. [CrossRef]
15. Sahlberg, S.H.; Spiegelberg, D.; Glimelius, B.; Stenerlöv, B.; Nestor, M. Evaluation of cancer stem cell markers CD133, CD44, CD24: Association with AKT isoforms and radiation resistance in colon cancer cells. *PLoS ONE* **2014**, *9*, e94621. [CrossRef]
16. Kim, W.-T.; Ryu, A.C.J. Cancer stem cell surface markers on normal stem cells. *BMB Rep.* **2017**, *50*, 285–298. [CrossRef]
17. Singh, M.; Yelle, N.; Venugopal, C.; Singh, S.K. EMT: Mechanisms and therapeutic implications. *Pharmacol. Ther.* **2018**, *182*, 80–94. [CrossRef]
18. Kim, T.; Veronese, A.; Pichiorri, F.; Lee, T.J.; Jeon, Y.-J.; Volinia, S.; Pineau, P.; Marchio, A.; Palatini, J.; Suh, S.-S.; et al. p53 regulates epithelial–mesenchymal transition through microRNAs targeting ZEB1 and ZEB. *J. Exp. Med.* **2011**, *208*, 875–883. [CrossRef]
19. Babaei, G.; Aziz, S.G.-G.; Jaghi, N.Z.Z. EMT, cancer stem cells and autophagy; The three main axes of metastasis. *Biomed. Pharmacother.* **2021**, *133*, 110909. [CrossRef]
20. Zhao, X.; Sun, B.; Sun, D.; Liu, T.; Che, N.; Gu, Q.; Dong, X.; Li, R.; Liu, Y.; Li, J. Slug promotes hepatocellular cancer cell progression by increasing sox2 and nanog expression. *Oncol. Rep.* **2014**, *33*, 149–156. [CrossRef]
21. Javaeed, A.; Ghauri, S.K. Metastatic potential and prognostic significance of SOX2: A meta-analysis. *World J. Clin. Oncol.* **2019**, *10*, 234–246. [CrossRef]
22. Zhou, P.; Li, B.; Liu, F.; Zhang, M.; Wang, Q.; Liu, Y.; Yao, Y.; Li, D. The epithelial to mesenchymal transition (EMT) and cancer stem cells: Implication for treatment resistance in pancreatic cancer. *Mol. Cancer* **2017**, *16*, 1–11. [CrossRef]
23. Stantic, M.; Zobalova, R.; Prokopova, K.; Neuzil, J.; Dong, L.-F. Cancer cells with high expression of CD133 exert FLIP upregulation and resistance to TRAIL-induced apoptosis. *BioFactors* **2008**, *34*, 231–235. [CrossRef]
24. Clara, J.A.; Monge, C.; Yang, Y.; Takebe, N. Targeting signalling pathways and the immune microenvironment of cancer stem cells—a clinical update. *Nat. Rev. Clin. Oncol.* **2020**, *17*, 204–232. [CrossRef] [PubMed]
25. Akbari, M.; Shanebandi, D.; Asadi, M.; Shomali, N.; Faraji, A.; Khaze, V.; Pakdel, A.; Mokhtarzadeh, A.; Ebrahimi, A.A.; Shabani, A.; et al. Effects of CD133 silencing on survival and migration of HT-29 colorectal cancer cells. *Iran. J. Immunol.* **2019**, *16*, 246–257.
26. Garofalo, M.; di Leva, G.; Romano, G.; Nuovo, G.; Suh, S.-S.; Nganheu, A.; Taccioli, C.; Pichiorri, F.; Alder, H.; Secchiero, P.; et al. miR-221&222 Regulate TRAIL resistance and enhance tumorigenicity through PTEN and TIMP3 downregulation. *Cancer Cell* **2009**, *16*, 498–509. [CrossRef]
27. Hartwig, T.; Montinaro, A.; von Karstedt, S.; Sevko, A.; Surinova, S.; Chakravarthy, A.; Taraborrelli, L.; Draber, P.; Lafont, E.; Vargas, F.A.; et al. The TRAIL-induced cancer secretome promotes a tumor-supportive immune microenvironment via CCR. *Mol. Cell* **2017**, *65*, 730–742.e5. [CrossRef]
28. Zhang, J.; Chen, D.; Liang, S.; Wang, J.; Liu, C.; Nie, C.; Shan, Z.; Wang, L.; Fan, Q.; Wang, F. miR-106b promotes cell invasion and metastasis via PTEN mediated EMT in ESCC. *Oncol. Lett.* **2018**, *15*, 4619–4626. [CrossRef] [PubMed]
29. Prabhu, V.V.; Allen, J.E.; Dicker, D.T.; El-Deiry, W.S. Small molecule ONC201/TIC10 targets chemotherapy-resistant colorectal cancer stem-like cells in an Akt/Foxo3a/TRAILdependent manner. *Cancer Res.* **2015**, *75*, 1423–1432. [CrossRef]
30. French, R.; Hayward, O.; Jones, S.; Yang, W.; Clarkson, R. Cytoplasmic levels of cFLIP determine a broad susceptibility of breast cancer stem/progenitor-like cells to TRAIL. *Mol. Cancer* **2015**, *14*, 1–13. [CrossRef] [PubMed]
31. Jalving, M.; Heijink, D.M.; Koornstra, J.J.; Ek, W.B.-V.; Zwart, N.; Wesseling, J.; Sluiter, W.J.; de Vries, E.G.E.; Kleibeuker, J.H.; de Jong, S. Regulation of TRAIL receptor expression by -catenin in colorectal tumours. *Carcinogenesis* **2013**, *35*, 1092–1099. [CrossRef]
32. Coelho, B.P.; Fernandes, C.F.D.L.; Boccacino, J.M.; Souza, M.C.D.S.; Melo-Escobar, M.I.; Alves, R.N.; Prado, M.B.; Iglesia, R.P.; Cangiano, G.; Mazzaro, G.L.R.; et al. Multifaceted WNT signaling at the crossroads between epithelial-mesenchymal transition and autophagy in glioblastoma. *Front. Oncol.* **2020**, *10*, 597743. [CrossRef]
33. Xu, J.; Zhou, J.-Y.; Wei, W.-Z.; Wu, G.S. Activation of the akt survival pathway contributes to TRAIL resistance in cancer cells. *PLoS ONE* **2010**, *5*, e10226. [CrossRef]
34. Sophonmithiprasert, T.; Nilwarangkoon, S.; Nakamura, Y.; Watanapokasin, R. Goniotalamin enhances TRAIL-induced apoptosis in colorectal cancer cells through DR5 upregulation and cFLIP downregulation. *Int. J. Oncol.* **2015**, *47*, 2188–2196. [CrossRef] [PubMed]
35. Pretzsch, E.; Bösch, F.; Neumann, J.; Ganschow, P.; Bazhin, A.; Guba, M.; Werner, J.; Angele, M. Mechanisms of metastasis in colorectal cancer and metastatic organotropism: Hematogenous versus peritoneal spread. *J. Oncol.* **2019**, *2019*, 7407190. [CrossRef] [PubMed]
36. Hui, L.; Chen, Y. Tumor microenvironment: Sanctuary of the devil. *Cancer Lett.* **2015**, *368*, 7–13. [CrossRef]
37. Zwirner, N.W.; Ziblat, A. Regulation of NK cell activation and effector functions by the IL-12 family of cytokines: The case of IL-27. *Front. Immunol.* **2017**, *8*, 25. [CrossRef]
38. Griffith, B.T.S.; Wiley, S.R.; Kubin, M.Z.; Sedger, L.M.; Maliszewski, C.R.; Fanger, N.A. Monocyte-mediated tumoricidal activity via the tumor necrosis factor-related cytokine, TRAIL. *Cell* **1999**, *189*, 1343–1353. [CrossRef]
39. Tecchio, C.; Huber, V.; Scapini, P.; Calzetti, F.; Margotto, D.; Todeschini, G.; Pilla, L.; Martinelli, G.; Pizzolo, G.; Rivoltini, L.; et al. IFN $\alpha$ -stimulated neutrophils and monocytes release a soluble form of TNF-related apoptosis-inducing ligand (TRAIL/Apo-2 ligand) displaying apoptotic activity on leukemic cells. *Blood* **2004**, *103*, 3837–3844. [CrossRef]
40. Kessenbrock, K.; Plaks, V.; Werb, Z. Matrix metalloproteinases: Regulators of the tumor. *Cell* **2010**, *141*, 52–67. [CrossRef]

41. Secchiero, P.; Gonelli, A.; Mirandola, P.; Melloni, E.; Zamai, L.; Celeghini, C.; Milani, D.; Zauli, G. Tumor necrosis factor-related apoptosis-inducing ligand induces monocytic maturation of leukemic and normal myeloid precursors through a caspase-dependent pathway. *Blood* **2002**, *100*, 2421–2429. [CrossRef]
42. Wu, A.A.; Drake, V.; Huang, A.; Chiu, S.; Zheng, L. Reprogramming the tumor microenvironment: Tumor-induced immunosuppressive factors paralyze T cells. *Oncol Immunology* **2015**, *4*, e1016700. [CrossRef]
43. de Winde, C.M.; Munday, C.; Acton, S.E. Molecular mechanisms of dendritic cell migration in immunity and cancer. *Med. Microbiol. Immunol.* **2020**, *209*, 515–529. [CrossRef]
44. Fanger, N.A.; Maliszewski, C.R.; Schooley, K.; Griffith, T.S. Human dendritic cells mediate cellular apoptosis via tumor necrosis factor-related apoptosis-inducing ligand (trail). *J. Exp. Med.* **1999**, *190*, 1155–1164. [CrossRef]
45. Rossin, A.; Miloro, G.; Hueber, A.-O. TRAIL and FasL functions in cancer and autoimmune diseases: Towards an increasing complexity. *Cancers* **2019**, *11*, 639. [CrossRef]
46. Vinay, D.S.; Ryan, E.P.; Pawelec, G.; Talib, W.H.; Stagg, J.; Elkord, E.; Lichtor, T.; Decker, W.K.; Whelan, R.L.; Kumara, H.M.C.S.; et al. Immune evasion in cancer: Mechanistic basis and therapeutic strategies. *Semin. Cancer Biol.* **2015**, *35*, S185–S198. [CrossRef]
47. Facciabene, A.; Motz, G.T.; Coukos, G. T-Regulatory Cells: Key players in tumor immune escape and angiogenesis: Figure. *Cancer Res.* **2012**, *72*, 2162–2171. [CrossRef]
48. Hallett, M.A.; Venmar, K.T.; Fingleton, B. Cytokine stimulation of epithelial cancer cells: The similar and divergent functions of IL-4 and IL-13. *Cancer Res.* **2012**, *72*, 6338–6343. [CrossRef]
49. Jeong, J.-H.; Ojha, U.; Lee, Y.M. Pathological angiogenesis and inflammation in tissues. *Arch. Pharmacol. Res.* **2021**, *44*, 1–15. [CrossRef]
50. Lugano, R.; Ramachandran, M.; Dimberg, A. Tumor angiogenesis: Causes, consequences, challenges and opportunities. *Cell. Mol. Life Sci.* **2019**, *77*, 1745–1770. [CrossRef]
51. Plaks, V.; Kong, N.; Werb, Z. The cancer stem cell niche: How essential is the niche in regulating stemness of tumor cells? *Cell Stem Cell* **2015**, *16*, 225–238. [CrossRef]
52. Annan, D.A.-M.; Kikuchi, H.; Maishi, N.; Hida, Y.; Hida, K. Tumor endothelial cell—A biological tool for translational cancer research. *Int. J. Mol. Sci.* **2020**, *21*, 3238. [CrossRef] [PubMed]
53. Zhao, Y.; Bao, Q.; Renner, A.; Camaj, P.; Eichhorn, M.; Ischenko, I.; Angele, M.; Kleespies, A.; Jauch, K.-W.; Bruns, C. Cancer stem cells and angiogenesis. *Int. J. Dev. Biol.* **2011**, *55*, 477–482. [CrossRef]
54. Ping, Y.-F.; Zhang, X.; Bian, X.-W. Cancer stem cells and their vascular niche: Do they benefit from each other? *Cancer Lett.* **2016**, *380*, 561–567. [CrossRef]
55. Jun, J.C.; Rathore, A.; Younas, H.; Gilkes, D.; Polotsky, V.Y. Hypoxia-inducible factors and cancer. *Curr. Sleep Med. Rep.* **2017**, *3*, 1–10. [CrossRef]
56. Vallée, A.; Guillevin, R.; Vallée, J.-N. Vasculogenesis and angiogenesis initiation under normoxic conditions through Wnt/ $\beta$ -catenin pathway in gliomas. *Rev. Neurosci.* **2017**, *29*, 71–91. [CrossRef]
57. Rivera, L.B.; Bergers, G. Myeloid cell-driven angiogenesis and immune regulation in tumors. *Trends Immunol.* **2015**, *36*, 240–249. [CrossRef]
58. Chen, P.-L.; Easton, A.S. Evidence that tumor necrosis factor-related apoptosis inducing ligand (TRAIL) inhibits angiogenesis by inducing vascular endothelial cell apoptosis. *Biochem. Biophys. Res. Commun.* **2010**, *391*, 936–941. [CrossRef] [PubMed]
59. Cartland, S.P.; Genner, S.W.; Zahoor, A.; Kavurma, M.M. Comparative Evaluation of TRAIL, FGF-2 and VEGF-A-induced angiogenesis in vitro and in vivo. *Int. J. Mol. Sci.* **2016**, *17*, 2025. [CrossRef]
60. Patil, M.S.; Cartland, S.P.; Kavurma, M.M. TRAIL signals, extracellular matrix and vessel remodelling. *Vasc. Biol.* **2020**, *2*, R73–R84. [CrossRef]
61. di Bartolo, B.; Cartland, S.; Prado-Lourenco, L.; Griffith, T.S.; Gentile, C.; Ravindran, J.; Azahri, N.S.M.; Thai, T.; Yeung, A.W.S.; Thomas, S.R.; et al. Tumor necrosis factor-related apoptosis-inducing ligand (TRAIL) promotes angiogenesis and ischemia-induced neovascularization via NADPH oxidase 4 (NOX4) and nitric oxide-dependent mechanisms. *J. Am. Hear. Assoc.* **2015**, *4*, e002527. [CrossRef] [PubMed]
62. Goncalves, I.; Singh, P.; Tengryd, C.; Cavalera, M.; Mattisson, I.Y.; Nitulescu, M.; Persson, A.F.; Volkov, P.; Engström, G.; Orholm-Melander, M.; et al. sTRAIL-R2 (soluble TNF [tumor necrosis factor]-related apoptosis-inducing ligand receptor 2) a marker of plaque cell apoptosis and cardiovascular events. *Stroke* **2019**, *50*, 1989–1996. [CrossRef] [PubMed]
63. Chen, C.; Li, L.; Zhou, H.J.; Min, W. The role of NOX4 and TRX2 in angiogenesis and their potential cross-talk. *Antioxidants* **2017**, *6*, 42. [CrossRef]
64. Islas, J.F.; Moreno-Cuevas, J.E. A microRNA perspective on cardiovascular development and diseases: An update. *Int. J. Mol. Sci.* **2018**, *19*, 2075. [CrossRef]
65. Xu, L.; Leng, H.; Shi, X.; Ji, J.; Fu, J. MiR-155 promotes cell proliferation and inhibits apoptosis by PTEN signaling pathway in the psoriasis. *Biomed. Pharmacother.* **2017**, *90*, 524–530. [CrossRef]
66. Hamada, S.; Masamune, A.; Miura, S.; Satoh, K.; Shimosegawa, T. MiR-365 induces gemcitabine resistance in pancreatic cancer cells by targeting the adaptor protein SHC1 and pro-apoptotic regulator BAX. *Cell. Signal.* **2014**, *26*, 179–185. [CrossRef] [PubMed]
67. Lujambio, A.; Lowe, S.W. The microcosmos of cancer. *Nat. Cell Biol.* **2012**, *482*, 347–355. [CrossRef]
68. Lu, T.; Shao, N.; Ji, C. Targeting microRNAs to modulate TRAIL-induced apoptosis of cancer cells. *Cancer Gene Ther.* **2012**, *20*, 33–37. [CrossRef]

69. Xiao, F.; Chen, J.; Lian, C.; Han, P.; Zhang, C. Tumor necrosis factor-related apoptosis-inducing ligand induces cytotoxicity specific to osteosarcoma by microRNA response elements. *Mol. Med. Rep.* **2014**, *11*, 739–745. [CrossRef]
70. Zhou, R.; Yuan, P.; Wang, Y.; Hunsberger, J.G.; Elkahlon, A.; Wei, Y.; Damschroder-Williams, P.; Du, J.; Chen, G.; Manji, H.K. Evidence for selective microRNAs and their effectors as common long-term targets for the actions of mood stabilizers. *Neuropsychopharmacology* **2008**, *34*, 1395–1405. [CrossRef]
71. Li, D.; Ji, L.; Liu, L.; Liu, Y.; Hou, H.; Yu, K.; Sun, Q.; Zhao, Z. Characterization of circulating microRNA expression in patients with a ventricular septal defect. *PLoS ONE* **2014**, *9*, e106318. [CrossRef]
72. Villanova, L.; Carecchia, S.; De Maria, R.; Fiori, M.E. Micro-economics of apoptosis in cancer: ncRNAs modulation of BCL-2 family members. *Int. J. Mol. Sci.* **2018**, *19*, 958. [CrossRef]
73. Xie, X.; Huang, Y.; Chen, L.; Wang, J. miR-221 regulates proliferation and apoptosis of ovarian cancer cells by targeting BMF. *Oncol. Lett.* **2018**, *16*, 6697–6704. [CrossRef]
74. Voigt, S.; Philipp, S.; Davarnia, P.; Winoto-Morbach, S.; Röder, C.; Arenz, C.; Trauzold, A.; Kabelitz, D.; Schütze, S.; Kalthoff, H.; et al. TRAIL-induced programmed necrosis as a novel approach to eliminate tumor cells. *BMC Cancer* **2014**, *14*, 74. [CrossRef]
75. Sun, J.; Lu, H.; Wang, X.; Jin, H. MicroRNAs in hepatocellular carcinoma: Regulation, function, and clinical implications. *Sci. World J.* **2013**, *2013*, 1–14. [CrossRef]
76. Razumilava, N.; Bronk, S.F.; Smoot, R.L.; Fingas, C.D.; Werneburg, N.W.; Roberts, L.; Mott, J.L. miR-25 targets TNF-related apoptosis inducing ligand (TRAIL) death receptor-4 and promotes apoptosis resistance in cholangiocarcinoma. *Hepatology* **2012**, *55*, 465–475. [CrossRef]
77. Zeng, Z.; Li, Y.; Pan, Y.; Lan, X.; Song, F.; Sun, J.; Zhou, K.; Liu, X.; Ren, X.; Wang, F.; et al. Cancer-derived exosomal miR-25-3p promotes pre-metastatic niche formation by inducing vascular permeability and angiogenesis. *Nat. Commun.* **2018**, *9*, 1–14. [CrossRef] [PubMed]
78. Kurita, S.; Mott, J.L.; Almada, L.L.; Bronk, S.F.; Werneburg, N.W.; Sun, S.-Y.; Roberts, L.R.; Fernandez-Zapico, M.E.; Gores, G.J. GLI3-dependent repression of DR4 mediates hedgehog antagonism of TRAIL-induced apoptosis. *Oncogene* **2010**, *29*, 4848–4858. [CrossRef] [PubMed]
79. Feng, X.; Jiang, J.; Shi, S.; Xie, H.; Zhou, L.; Zheng, S. Knockdown of miR-25 increases the sensitivity of liver cancer stem cells to TRAIL-induced apoptosis via PTEN/PI3K/Akt/Bad signaling pathway. *Int. J. Oncol.* **2016**, *49*, 2600–2610. [CrossRef] [PubMed]
80. Panner, A.; Crane, C.A.; Weng, C.; Feletti, A.; Parsa, A.T.; Pieper, R.O. A novel PTEN-dependent link to ubiquitination controls FLIPs stability and TRAIL sensitivity in glioblastoma multiforme. *Cancer Res.* **2009**, *69*, 7911–7916. [CrossRef] [PubMed]
81. El Sharkawi, F.Z.; Ewais, S.M.; Fahmy, R.H.; Rashed, L.A. PTEN and TRAIL genes loaded zein nanoparticles as potential therapy for hepatocellular carcinoma. *J. Drug Target.* **2017**, *25*, 513–522. [CrossRef]
82. Wang, H.; Xu, C.; Kong, X.; Li, X.; Kong, X.; Wang, Y.; Ding, X.; Yang, Q. Trail resistance induces epithelial-mesenchymal transition and enhances invasiveness by suppressing PTEN via miR-221 in breast cancer. *PLoS ONE* **2014**, *9*, e99067. [CrossRef]
83. Lu, C.; Shan, Z.; Hong, J.; Yang, L. MicroRNA-92a promotes epithelial-mesenchymal transition through activation of PTEN/PI3K/AKT signaling pathway in non-small cell lung cancer metastasis. *Int. J. Oncol.* **2017**, *51*, 235–244. [CrossRef] [PubMed]
84. Fu, F.; Jiang, W.; Zhou, L.; Chen, Z. Circulating exosomal miR-17-5p and miR-92a-3p predict pathologic stage and grade of colorectal cancer. *Transl. Oncol.* **2018**, *11*, 221–232. [CrossRef] [PubMed]
85. Liu, Y.; Liang, G.; Wang, H.; Liu, Z. MicroRNA-129-5p suppresses proliferation, migration and invasion of retinoblastoma cells through PI3K/AKT signaling pathway by targeting PAX6. *Pathol. Res. Pr.* **2019**, *215*, 152641. [CrossRef]
86. Zi, Y.; Zhang, Y.; Wu, Y.; Zhang, L.; Yang, R.; Huang, Y. Downregulation of microRNA-25-3p inhibits the proliferation and promotes the apoptosis of multiple myeloma cells via targeting the PTEN/PI3K/AKT signaling pathway. *Int. J. Mol. Med.* **2020**, *47*, 1. [CrossRef] [PubMed]
87. Joshi, P.; Jeon, Y.-J.; Laganà, A.; Middleton, J.; Secchiero, P.; Garofalo, M.; Croce, C.M. MicroRNA-148a reduces tumorigenesis and increases TRAIL-induced apoptosis in NSCLC. *Proc. Natl. Acad. Sci. USA* **2015**, *112*, 8650–8655. [CrossRef]
88. Farooqi, A.A.; Gadaleta, C.D.; Ranieri, G.; Fayyaz, S.; Marech, I. New frontiers in promoting TRAIL-mediated cell death: Focus on natural sensitizers, miRNAs, and nanotechnological advancements. *Cell Biophys.* **2015**, *74*, 3–10. [CrossRef] [PubMed]
89. Xia, Y.; Chen, Q.; Zhong, Z.; Xu, C.; Wu, C.; Liu, B.; Chen, Y. Down-regulation of MiR-30c promotes the invasion of non-small cell lung cancer by targeting MTA1. *Cell. Physiol. Biochem.* **2013**, *32*, 476–485. [CrossRef]
90. Xu, C.; Zeng, Q.; Xu, W.; Jiao, L.; Chen, Y.; Zhang, Z.; Wu, C.; Jin, T.; Pan, A.; Wei, R.; et al. miRNA-100 inhibits human bladder urothelial carcinogenesis by directly targeting mTOR. *Mol. Cancer Ther.* **2013**, *12*, 207–219. [CrossRef]
91. Shin, E.A.; Sohn, E.J.; Won, G.; Choi, J.-U.; Jeong, M.; Kim, B.; Kim, M.-J.; Kim, S.-H. Upregulation of microRNA135a-3p and death receptor 5 plays a critical role in Tanshinone I sensitized prostate cancer cells to TRAIL induced apoptosis. *Oncotarget* **2014**, *5*, 5624–5636. [CrossRef] [PubMed]
92. Kim, Y.; Schwabe, R.; Qian, T.; Lemasters., J.; Brenner, D. TRAIL-mediated apoptosis requires NF-kappaB inhibition and the mitochondrial permeability transition in human hepatoma cells. *Hepatology* **2002**, *36*, 1498–1508.
93. Nguyen, P.N.N.; Huang, C.-J.; Sugii, S.; Cheong, S.K.; Choo, K.B. Selective activation of miRNAs of the primate-specific chromosome 19 miRNA cluster (C19MC) in cancer and stem cells and possible contribution to regulation of apoptosis. *J. Biomed. Sci.* **2017**, *24*, 1–14. [CrossRef]





94. Ralff, M.D.; El-Deiry, W.S. TRAIL pathway targeting therapeutics. *Expert Rev. Precis. Med. Drug Dev.* **2018**, *3*, 197–204. [CrossRef] [PubMed]
95. Han, L.; Shi, S.; Gong, T.; Zhang, Z.; Sun, X. Cancer stem cells: Therapeutic implications and perspectives in cancer therapy. *Acta Pharm. Sin. B* **2013**, *3*, 65–75. [CrossRef]
96. Fakiruddin, K.S.; Ghazalli, N.; Lim, M.N.; Zakaria, Z.; Abdullah, S. Mesenchymal stem cell expressing TRAIL as targeted therapy against sensitised tumour. *Int. J. Mol. Sci.* **2018**, *19*, 2188. [CrossRef]
97. Zhang, B.; Liu, B.; Chen, D.; Setroikromo, R.; Haisma, H.J.; Quax, W.J. Histone deacetylase inhibitors sensitize TRAIL-induced apoptosis in colon cancer cells. *Cancers* **2019**, *11*, 645. [CrossRef] [PubMed]
98. Srivastava, R.K.; Kurzrock, R.; Shankar, S. MS-275 Sensitizes TRAIL-resistant breast cancer cells, inhibits angiogenesis and metastasis, and reverses epithelial-mesenchymal transition in vivo. *Mol. Cancer Ther.* **2010**, *9*, 3254–3266. [CrossRef] [PubMed]
99. Zhou, W.; Feng, X.; Han, H.; Guo, S.; Wang, G. Synergistic effects of combined treatment with histone deacetylase inhibitor suberoylanilide hydroxamic acid and TRAIL on human breast cancer cells. *Sci. Rep.* **2016**, *6*, 28004. [CrossRef]
100. Stöhr, D.; Schmid, J.O.; Beigl, T.B.; Mack, A.; Maichl, D.S.; Cao, K.; Budai, B.; Fullstone, G.; Kontermann, R.E.; Mürdter, T.E.; et al. Stress-induced TRAILR2 expression overcomes TRAIL resistance in cancer cell spheroids. *Cell Death Differ.* **2020**, *27*, 3037–3052. [CrossRef]
101. Vinogradov, S.; Wei, X. Cancer stem cells and drug resistance: The potential of nanomedicine. *Nanomedicine* **2012**, *7*, 597–615. [CrossRef]
102. Han, H.; YunXu, Z.; Hou, P.; Jiang, C.; Liu, L.; Tang, M.; Yang, X.; Zhang, Y.; Liu, Y. Icaritin sensitizes human glioblastoma cells to TRAIL-induced apoptosis. *Cell Biophys.* **2015**, *72*, 533–542. [CrossRef]
103. Zhang, Z.; Patel, S.B.; King, M.R. Micelle-in-liposomes for sustained delivery of anticancer agents that promote potent TRAIL-induced cancer cell apoptosis. *Molecules* **2020**, *26*, 157. [CrossRef] [PubMed]
104. Son, Y.-G.; Kim, E.H.; Kim, J.Y.; Kim, S.U.; Kwon, T.K.; Yoon, A.-R.; Yun, C.-O.; Choi, K.S. Silibinin sensitizes human glioma cells to TRAIL-mediated apoptosis via DR5 up-regulation and down-regulation of c-FLIP and survivin. *Cancer Res.* **2007**, *67*, 8274–8284. [CrossRef]
105. Dai, Y.; Liu, M.; Tang, W.; Li, Y.; Lian, J.; Lawrence, T.S.; Xu, L. A Smac-mimetic sensitizes prostate cancer cells to TRAIL-induced apoptosis via modulating both IAPs and NF-kappaB. *BMC Cancer* **2009**, *9*, 392. [CrossRef] [PubMed]
106. Kim, S.W.; Kim, S.J.; Park, S.H.; Yang, H.G.; Kang, M.C.; Choi, Y.W.; Kim, S.M.; Jeun, S.-S.; Sung, Y.C. Complete regression of metastatic renal cell carcinoma by multiple injections of engineered mesenchymal stem cells expressing dodecameric TRAIL and HSV-TK. *Clin. Cancer Res.* **2013**, *19*, 415–427. [CrossRef] [PubMed]
107. Zinnah, K.; Park, S.-Y. Duloxetine enhances TRAIL-mediated apoptosis via AMPK-mediated inhibition of autophagy flux in lung cancer cells. *Anticancer Res.* **2019**, *39*, 6621–6633. [CrossRef]
108. Onoe-Takahashi, A.; Suzuki-Karasaki, M.; Suzuki-Karasaki, M.; Ochiai, T.; Suzuki-Karasaki, Y. Autophagy inhibitors regulate TRAIL sensitivity in human malignant cells by targeting the mitochondrial network and calcium dynamics. *Int. J. Oncol.* **2019**, *54*, 1734–1746. [CrossRef]
109. Kim, K.; Takimoto, R.; Dicker, D.; Chen, Y.; Gazitt, Y.; El-Deiry, W. Enhanced TRAIL sensitivity by p53 overexpression in human cancer but not normal cell lines. *Int. J. Oncol.* **2001**, *18*, 241–247. [CrossRef]
110. Hu, B.; Zhu, H.; Qiu, S.; Su, Y.; Ling, W.; Xiao, W.; Qi, Y. Enhanced TRAIL sensitivity by E1A expression in human cancer and normal cell lines: Inhibition by adenovirus E1B19K and E3 proteins. *Biochem. Biophys. Res. Commun.* **2004**, *325*, 1153–1162. [CrossRef]
111. Zhang, X.; Wang, L.; Liu, Y.; Huang, W.; Cheng, D. MiR-760 enhances TRAIL sensitivity in non-small cell lung cancer via targeting the protein FOXA1. *Biomed. Pharmacother.* **2018**, *99*, 523–529. [CrossRef] [PubMed]





## Article

# Persistent Properties of a Subpopulation of Cancer Cells Overexpressing the Hedgehog Receptor Patched

Álvaro Javier Feliz Morel <sup>1,†</sup>, Anida Hasanovic <sup>1,†</sup>, Aurélie Morin <sup>2</sup>, Chloé Prunier <sup>3</sup>, Virginie Magnone <sup>1</sup>, Kevin Lebrigand <sup>1</sup>, Amaury Aouad <sup>1</sup>, Sarah Cogoluegnes <sup>1</sup>, Judith Favier <sup>2</sup>, Claude Pasquier <sup>4</sup>  
and Isabelle Mus-Veteau <sup>1,\*</sup>

<sup>1</sup> Université Côte d'Azur, CNRS, Institut de Pharmacologie Moléculaire et Cellulaire (IPMC), 06560 Valbonne, France; javitto28@gmail.com (Á.J.F.M.); anida160@hotmail.com (A.H.); magnone@ipmc.cnrs.fr (V.M.); lebrigand@ipmc.cnrs.fr (K.L.); amaury.aouad@univ-cotedazur.fr (A.A.); cogoluegnes@ipmc.cnrs.fr (S.C.)

<sup>2</sup> Université de Paris, PARCC, INSERM, Equipe Labellisée par la Ligue Contre le Cancer, CEDEX 15, 75737 Paris, France; aurelie.morin@gmail.com (A.M.); judith.favier@inserm.fr (J.F.)

<sup>3</sup> INOVOTION, Biopolis-5 Av. du Grand Sablon, 38700 La Tronche, France; chloe.prunier@inovotion.com

<sup>4</sup> Université Côte d'Azur, CNRS-UMR7271, Laboratoire d'Informatique, Signaux et Systèmes de Sophia Antipolis (I3S), 06560 Valbonne, France; claude.pasquier@univ-cotedazur.fr

\* Correspondence: mus-veteau@ipmc.cnrs.fr

† These authors equally contributed to this work.

**Citation:** Feliz Morel, Á.J.; Hasanovic, A.; Morin, A.; Prunier, C.; Magnone, V.; Lebrigand, K.; Aouad, A.; Cogoluegnes, S.; Favier, J.; Pasquier, C.; et al. Persistent Properties of a Subpopulation of Cancer Cells Overexpressing the Hedgehog Receptor Patched. *Pharmaceutics* **2022**, *14*, 988. <https://doi.org/10.3390/pharmaceutics14050988>

Academic Editor: Hassan Bousbaa

Received: 19 January 2022

Accepted: 29 April 2022

Published: 5 May 2022

**Publisher's Note:** MDPI stays neutral with regard to jurisdictional claims in published maps and institutional affiliations.



**Copyright:** © 2022 by the authors. Licensee MDPI, Basel, Switzerland. This article is an open access article distributed under the terms and conditions of the Creative Commons Attribution (CC BY) license (<https://creativecommons.org/licenses/by/4.0/>).

**Abstract:** Despite the development of new therapeutic strategies, cancer remains one of the leading causes of mortality worldwide. One of the current major challenges is the resistance of cancers to chemotherapy treatments inducing metastases and relapse of the tumor. The Hedgehog receptor Patched (Ptch1) is overexpressed in many types of cancers. We showed that Ptch1 contributes to the efflux of doxorubicin and plays an important role in the resistance to chemotherapy in adrenocortical carcinoma (ACC), a rare cancer which presents strong resistance to the standard of care chemotherapy treatment. In the present study, we isolated and characterized a subpopulation of the ACC cell line H295R in which Ptch1 is overexpressed and more present at the cell surface. This cell subpopulation is more resistant to doxorubicin, grows as spheroids, and has a greater capability of clonogenicity, migration, and invasion than the parental cells. Xenograft experiments performed in mice and in ovo showed that this cell subpopulation is more tumorigenic and metastatic than the parental cells. These results suggest that this cell subpopulation has cancer stem-like or persistent cell properties which were strengthened by RNA-seq. If present in tumors from ACC patients, these cells could be responsible for therapy resistance, relapse, and metastases.

**Keywords:** Patched; chemotherapy resistance; metastases; cancer stem cells; persistent cells; adrenocortical carcinoma

## 1. Introduction

Cancer development is a complex process combining mutational accumulation and dynamic changes. Tumors usually involve heterogeneous cell populations (stem cells, progenitors or differentiated tumor cells) with functionally divergent phenotypes (mitotic or not, migratory or static, pro-angiogenic or not) [1,2]. Such heterogeneity underlies the lethal outcome of cancer, therapeutic failure, and drug resistance [3,4]. Cancer stem cells (CSCs) are of particular interest in this context. They are a subpopulation of tumor cells with unlimited self-renewal potential, capable of giving rise to all tumor cell types within a tumor, and resistant to many conventional anticancer treatments that affect more differentiated tumor cells. In 2018, 18.1 million cancers were diagnosed worldwide and 9.6 million people died. These deaths were often the result of recurrences or metastases due to the resistance of cancer cells to the chemotherapy treatments used and the lack of response to immunotherapy.

The resistance of cancer cells to chemotherapy is therefore one of the major challenges in the clinical management of cancer. This phenomenon called multidrug resistance (MDR) induces less sensitivity of cancer cells to classical and targeted chemotherapies, and has been intensively studied. Many mechanisms such as increased DNA damage repair, modification or alteration of drug or target proteins, drug efflux, reduced apoptosis, hypoxia or transformation of epithelial cells to mesenchymal cells can induce MDR [5,6].

Drug efflux induced by the overexpression of the ATP-binding cassette (ABC) transporters has been considered the most prominent underlying mechanism for MDR [7]. Since the discovery of the P-glycoprotein (Pgp or MDR1) over 35 years ago, some studies have linked ABC transporter expression to poor outcome in several cancer types, leading to the development of Pgp inhibitors tested in clinical trials to overcome MDR [8]. At least three generations of Pgp inhibitors have been tested. All these compounds failed in clinical trials due to lack of potency, off-target effects or toxicity issues. Members of the ABC superfamily transport toxins, sugars, amino acids, nucleotides and metabolites out of cells, and protects cells against toxic molecules, including drugs with very different chemical structures [9]. Thus, ABC transporters are particularly important for the functioning of healthy cells, and that is why, to date, no inhibitors of ABC transporters have obtained approval from FDA [10,11]. Therefore, a treatment able to overcome chemotherapy resistance and then eliminate the resistant cancer cells responsible for the relapse and metastases (also called persister cells) is still an unmet, urgent medical need.

The Hedgehog (Hh) signaling pathway has a crucial role during early embryonic development, controlling cell differentiation and proliferation. In adults, this pathway regulates stem cell homeostasis and tissue regeneration. The Hh signaling pathway activation has been correlated with an increase in cancer development, progression and metastasis. Indeed, many aggressive cancers present an aberrant activation of the Hh signaling pathway [12], particularly in cells that present a chemotherapy resistance, i.e., cancer stem cells (tumor-initiating cells/persistent cells) [13]. The expression of the Hh receptor, Patched (Ptch1), is expressed upon activation of the Hh pathway. This receptor is overexpressed in many primary cancers (i.e., brain, breast, colon, melanoma, prostate and ovary) (see [14] for a review), and some studies proposed Ptch1 as an early marker of thyroid and gastric cancers [15,16].

We have discovered that Ptch1 is a multidrug transporter that contributes to the efflux of chemotherapeutic agents and plays an important role in the resistance to chemotherapy in adrenocortical carcinoma and melanoma cells [17–19]. Adrenocortical carcinoma (ACC) is a rare cancer which presents strong resistance to the most efficient available treatment composed of a mixture of chemotherapeutic agents (etoposide, doxorubicin and cisplatin) combined with the adrenolytic substance mitotane (EDP-M) [20,21]. Our analyses showed that Ptch1 was present in primary tumor samples from the 70 ACC patients of the cohort studied [18]. Decreasing endogenous Ptch1 expression using siRNA strongly inhibited the efflux of doxorubicin (dxr) from ACC cells indicating that Ptch1 is involved in dxr efflux in ACC cells. Accordingly, we showed that ACC cells rendered resistant to dxr express more Ptch1 than parental cells.

In adults, Ptch1 is poorly expressed in healthy cells and functions as a drug efflux pump only in cancer cells. Indeed, Ptch1 activity uses the proton gradient as an energy source and transports chemotherapeutic agents out of the cells against a proton entry. This requires the extracellular medium to be more acidic than the intracellular medium, which is a characteristic of cancer cells known as the Warburg effect [22]. Indeed, the high glucose consumption of cancer cells causes the extracellular medium to become more acidic and allows Ptch1 to drive the chemotherapeutic agents out of the cells. This makes Ptch1 an innovative and highly promising therapeutic target to improve the effectiveness of anticancer chemotherapeutic treatments without toxicity for healthy cells.

We have developed screening tests to identify molecules that inhibit the resistance to dxr conferred by human Ptch1 to yeast, and the efflux of dxr by Ptch1 [23]. This led to the discovery of three inhibitors of Ptch1 drug efflux. Methiothepin, a drug-like compound

antagonist of the serotonin receptor, increases the efficacy of dxr against ACC cells in vitro and in vivo [18], and of dxr and vemurafenib against melanoma cells [24]; Astemizole, a non-sedating antihistaminergic drug increases the efficacy of dxr and cisplatin against ACC cells in vitro [25]; and Panicein A hydroquinone (PAH) produced by marine sponges increases the efficacy of dxr and cisplatin against melanoma cells in vitro [26], and of vemurafenib against BRAF<sup>V600E</sup> melanoma cells in vitro and in vivo [19].

In the present study, we isolated and characterized a subpopulation of the ACC cell line H295R in which Ptch1 is overexpressed and more present at the cell plasma membrane. The in vitro, in vivo and RNA-seq studies performed reveal that these cells are more resistant to chemotherapy than the parental cell line and have cancer stem-like or persistent cell properties.

## 2. Materials and Methods

### 2.1. Chemical and Biological Material

Doxorubicin hydrochloride (dxr) was purchased from Sigma-Aldrich, Burlington, MA, USA, Methiothepin maleate (P375) was purchased from Santa Cruz, CA, USA: CAS number: 20229-30-5; MW: 472.62; molecular formula: C<sub>20</sub>H<sub>24</sub>N<sub>2</sub>S<sub>2</sub>.C<sub>4</sub>H<sub>4</sub>O<sub>4</sub>.

The human adrenocortical carcinoma cell line H295R and H295R-PM-Ptc+ were cultured in DMEM/F12 medium supplemented with 2% of NuSerum (BD), 1% ITS (1.0 mg/mL recombinant human insulin, 0.55 mg/mL human transferrin (substantially iron-free), and 0.5 g/mL sodium selenite, 100×, BD), 1% GlutaMAX (Gibco), Penicillin/Streptomycin 1% 100x (Gibco). H295RdxrR was obtained by adding increasing concentrations of doxorubicin up to 0.2 μM in the culture medium over 6 months. Cells were cultured in Falcon flasks or plates (Corning, Inc., Corning, NY, USA) at 37 °C and 5% CO<sub>2</sub>/95% air water-saturated atmosphere.

### 2.2. Flow Cytometry

Cells were collected using Accutase (StemCell), centrifuged and incubated with monoclonal rat anti-Ptch1 antibody (MAB41051 R&D Systems; 10 μg/mL) and then with anti-rat antibody coupled to Alexa 594 in ice in FACS buffer (PBS buffer with FBS 5% and EDTA 2 μM). FACS analyses were performed using DB LSRFortessa (BioSciences). Sorting of H295R-PM-Ptc+ was performed using BD FACSAria III.

### 2.3. Immunofluorescence

Cells were seeded on coverslips in 24-well plates and allowed to grow to 80% confluence. Cells were fixed with 1% paraformaldehyde (PFA), incubated for 2 h on ice with rat anti-Ptch1 antibody (MAB41051 R&D Systems; 10 μg/mL) and then with anti-rat antibody coupled to Alexa 594 in PBS buffer with 0.1% BSA. Images were acquired with a Zeiss Axioplan 2 fluorescence microscope coupled to a digital charge-coupled device camera using a 40×/1.3 Plan NeoFluar objective and filter for Alexa 594.

### 2.4. Western-Blot

Western-blots were performed using standard techniques. Cells were lysed using RIPA (radioimmunoprecipitation assay) buffer. Total protein amount from cell lysates was determined using DC Protein Assay (500–0116; BioRad, Hercules, CA, USA). 80 μg of total extract was loaded per sample and separated on an 8% SDS-PAGE gel, then transferred to nitrocellulose membrane (Amersham). Unspecific binding was reduced by incubating the membranes in blocking buffer (20 mM Tris-HCl pH 7.5, 45 mM NaCl, Tween 20 0.1% and non-fat milk 5%) for 1 h at room temperature. Nitrocellulose membranes were then incubated overnight at 4 °C with rat anti-Ptch1 antibody (MAB41051 R&D Systems; 1 μg/mL), rabbit anti-ADCY2 (Abnova) (1/1000), rabbit anti-Gli2 (Abcam) (1/1000), rabbit anti-ABCG2 (Genetex) (1/500), rabbit anti-GRK5 (Genetex) (1/1000), rabbit anti-SLUG (SNAI2) (Genetex) (1/2500), rabbit anti-SOX5 (Genetex) (1/1000), rabbit anti-Nanog (Cell Signaling Technology) (1/1000), and mouse anti-tubulin (Sigma) (1/1000) or rabbit anti-

GAPDH (Abcam ab37168) (1/10,000). After 3 washes, membranes were incubated with the corresponding horseradish peroxidase (HRP)-coupled secondary antibody for 45 min (goat anti-rat IgG HRP conjugate (Life Technologies; 1/2000), goat anti-rabbit IgG HRP conjugate (Invitrogen, 1/5000) or goat anti-mouse IgG HRP conjugate (Dako, 1/5000)). HRP signal was revealed using an ECL Prime Western blotting detection reagent (RPN2232; Amersham) and detected using a Fusion FX Imager (Vilber Lourmat).

### 2.5. Cytotoxicity Assay

Cytotoxicity assays were performed as described in [18]. Cells were grown in 96-well plates until 70–80% of confluence before replacing medium with 100  $\mu$ L of complete medium containing methiothepin or DMSO as control (methiothepin solvent). Following an incubation of 2 h at 37 °C and 5% CO<sub>2</sub>, 100  $\mu$ L of medium containing increasing concentrations of doxorubicin (dxr) were added to the cells. After 48 h incubation at 37 °C and 5% CO<sub>2</sub>, the cytotoxic effect of dxr was addressed using neutral red assay (NR). NR was diluted in complete medium (50  $\mu$ g/mL), and cells were incubated for 3 h in 100  $\mu$ L of NR solution at 37 °C 5% CO<sub>2</sub>. NR incorporated into living cells by lysosomes was measured using a Multiskan Go Microplate Spectrophotometer (Thermo Scientific, Waltham, MA, USA). IC<sub>50</sub> was calculated using GraphPad Prism 6 software.

### 2.6. Doxorubicin Accumulation in Cells

Cells were seeded on coverslips placed in 24-well plates. Once cells reached 80% of confluence, the cells' medium was replaced with a physiological buffer (140 mM NaCl, 5 mM KCl, 1 mM CaCl<sub>2</sub>, 1 mM MgSO<sub>4</sub>, 5 mM glucose, 20 mM HEPES, pH 7.4) containing 2  $\mu$ M of doxorubicin (dxr). After different incubation time points (15, 30, 60, 180 and 240 min), coverslips were fixed with PFA 4% in PBS, washed with PBS and mounted using a SlowFade Gold antifade reagent containing DAPI (Invitrogen). Images of the coverslips were taken using a Zeiss Axioplan 2 fluorescence microscope coupled to a charge-coupled device camera using a 40 $\times$ /1.3 Plan NeoFluar objective and filters for Alexa 594. Dxr fluorescence was measured using ImageJ software 2015. Around 100 cells (selection of cells was performed randomly) from three different coverslips were measured for each time point and condition of the experiment.

### 2.7. Clonogenic Assay

Five thousand cells were seeded in 24 well plates. After 14 days, cells were fixed using PFA 4% and then colored using crystal violet 0.4%. Pictures of the colored colonies were taken, and crystal violet was solubilized in PBS buffer containing SDS 2%. The absorbance at 620 nm of the solubilized crystal violet was measured using Multiskan Go Microplate Spectrophotometer (Thermo Fisher Scientific, Waltham, MA, USA).

### 2.8. Transwell Invasion Assay

Invasion was measured using a CytoSelect 24-well cell invasion assay according to the manufacturer's instructions (Cell Biolabs). Briefly,  $3 \times 10^5$  cells were seeded in the upper chamber of the transwell in complete culture medium, and complete culture medium was added in the lower chamber. The plate was incubated at 37 °C in 5% CO<sub>2</sub> for 6 days to induce invasion towards the lower chamber. Noninvasive cells were removed from the upper side of the chamber, and invasive cells were stained and quantified by optical density at 560 nm using a Multiskan Go Microplate Spectrophotometer (Thermo Scientific, Waltham, MA, USA). Obtained values were normalized to the number of cells (from triplicate wells).

### 2.9. Wound-Healing Assay

Cells were seeded in 24 well plates in complete culture medium. When cells formed a confluent carpet, a wound was performed with a p200 tip. Two pictures were taken at two different points of the wound for each well. The images were taken every 15 min during 24 h using a Cytation 5 Cell Imaging Multi-Mode Reader (Biotek, Agilent, Santa Clara, CA,

USA). Images were analyzed using a macro for ImageJ developed by MICA (Microscopie Imagerie Côte d'Azur) and the reclosing slope was calculated. Migration was measured as the wound area decrease for 24 h ( $\text{pixel}^2/\text{time}$ ). Since cells could not completely reclose the wound within 24 h, cells were kept in culture, and images were taken 12 and 20 days after the wound, using Leica DM IRB (5 $\times$ ).

#### 2.10. *In ovo Experiment*

*In ovo* experiments were performed by INOVOTION SAS (Biopolis, 5 avenue du grand sablon, La Tronche, 38700, France–STU20210623).

Fertilized White Leghorn eggs were incubated at 37 °C with 50% relative humidity for 9 days. On day 9, the chorioallantoic membrane (CAM) was dropped down by drilling a small hole through the eggshell into the air sac, and a 1 cm<sup>2</sup> window was cut in the eggshell above the CAM. Then,  $3 \times 10^6$  H295R or H295R-PM-Ptc+ cells were inoculated onto the CAM of each egg and the eggs were randomized into groups. On day E18, the upper portion of the CAM (with tumor) was removed, washed with PBS buffer and then fixed in PFA for 48 h. After that, tumors were carefully cut away from normal CAM tissue and weighed. Chicken embryos livers were collected (10 livers per group). Genomic DNA was extracted using a commercial kit and analyzed by real time qPCR with specific primer for Human Alu sequences [27]. Calculation of C<sub>q</sub> for each sample, mean C<sub>q</sub> and relative amounts of metastases for each group were directly managed by the Bio-Rad CFX Maestro software 2.0.

#### 2.11. *Experiments in Mice*

Seven-week-old immunodeficient NMRI Nude mice were injected in renal subcapsular with  $3 \times 10^6$  H295R or H295R-PM-Ptc+ cells in 40  $\mu\text{L}$  of PBS/matrigel 1:1 v:v. Ten mice received H295R parental cells and 10 mice received H295R-PM-Ptc+ cells. Mice were sacrificed 45 days after cell injection, and the tumors were collected, weighed, fixed and included in paraffin. Project CEEA 17-108 accepted by the ethic committee under number MESR 15476.

#### 2.12. *Immunofluorescence on Mouse Tumor Slides*

Paraffin embedded tumors were sliced at 4  $\mu\text{m}$  thickness using HM 340E Electronic Rotary Microtome (ThermoFisher Scientific). Tumor slices were rehydrated in xylene and using decreasing concentrations of ethanol. Slices were deparaffinized at low pressure at 100–106 °C for 20 min in citrate buffer at pH 6. PBS buffer with Triton 0.1% was used to permeabilize cells. Unspecific binding was blocked using a PBS buffer with FBS 1%. Slices were incubated for 1 h with anti-human KI67 mouse antibody 556003 (BD Biosciences, Franklin Lakes, NJ, USA) and then with anti-mouse antibody coupled to Alexa 488. DAPI was used to stain nuclei. Images were taken with a Zeiss Axioplan 2 fluorescence microscope coupled to a digital charge-coupled device camera using a 40 $\times$ /1.3 Plan NeoFluar objective and filter for Alexa 488. The diameters of 20 nuclei of SRC (sample randomly chosen) were measured in two slices of each tumor using imageJ software.

#### 2.13. *Statistical Analysis*

Comparison between H295R and H295R-PM-Ptc+ cells analysis was done using a two tailed student test, \* for  $p$ -value < 0.05, \*\* for  $p$ -value < 0.001 and \*\*\* for  $p$ -value < 0.0001.

#### 2.14. *RNA-Seq*

Libraries were generated from 500 ng of total RNA from parental H295R and H295R-PM-Ptc+ cells using Truseq Stranded mRNA kit (Illumina). Libraries were then quantified with Qubit dsDNA High Sensitivity Assay Kit (Invitrogen) and pooled. A measure of 4 nM of this pool was sequenced on a NextSeq 500 platform (Illumina) with 2  $\times$  75 bp paired-end

chemistry. All sequencing results were submitted in the GEO database under the super series accession number GSE189424 [28].

Reads were mapped with STAR 2.4.0a on human genome (build hg38). Counting was performed with featureCounts (subread-1.4.6-p1-Linux-x86\_64, “-primary-g gene\_name -p-s 1-M “ options) using Ensembl GRCh38.76 release. Statistical analysis was performed using R version 3.3.1. The reproducibility of the replicates for each condition was assessed by performing principal component analysis using the R package “htSeqTools” (R package version 1.14.0; data not shown). Functions from the Bioconductor package DESeq2 were used to normalize data for differences in their sequencing depth and assess differential expression. The Benjamini–Hochberg method was used to control the false discovery rate. Results of DESeq2 differential expression analysis are presented in Supplementary Materials Table S1. Genes considered as differentially expressed with a  $p$ -value  $< 0.05$  and an absolute log<sub>2</sub> fold change  $> 1$  are listed in Supplementary Materials Table S2. Genes associated with a  $p$ -value  $< 0.05$  are listed in Supplementary Materials Table S3.

Functional enrichments for Gene Ontology terms, KEGG, WikiPathways and Reactome Pathways were retrieved using Cytoscape [29] and the StringApp plugin [30]. The enrichments of differentially expressed genes reported in Supplementary Materials Table S2 are listed in the “enrichments underexpressed”, “enrichments overexpressed” and “enrichments all” worksheets in Supplementary Materials Table S2.

AMINE (Active Module Identification through Network Embedding) [31] was used to identify modules of genes whose expression was triggered in the biological experiments. The interaction of different genes in the experimental conditions were then compared to a background database, indicating an involvement of these genes in the studied process. String database [32] was used to retrieve gene interaction data with a combined evidence score greater than 0.7. Measurements of the activity of genes are represented by the  $p$ -values computed by DESeq2.

Internally, the method merges the interaction data with the genes’ associated  $p$ -values to generate an attributed gene network in which vertices represent genes, edges represent interactions between genes and each vertex is annotated with a numeric attribute reflecting its associated  $p$ -value. The method relies on Node2vec [33] to learn a vector representation of the interaction network. As a result, each gene is represented by a vector in an embedded space in which the cosine distance between the vectors representing the nodes accurately reflects their proximity in the original network. The algorithm then uses a greedy approach to build increasingly large clusters of genes based on the similarity of their encoding vectors and evaluates them according to a metric considering the activity of the contained genes. The details of the method are described in [31].

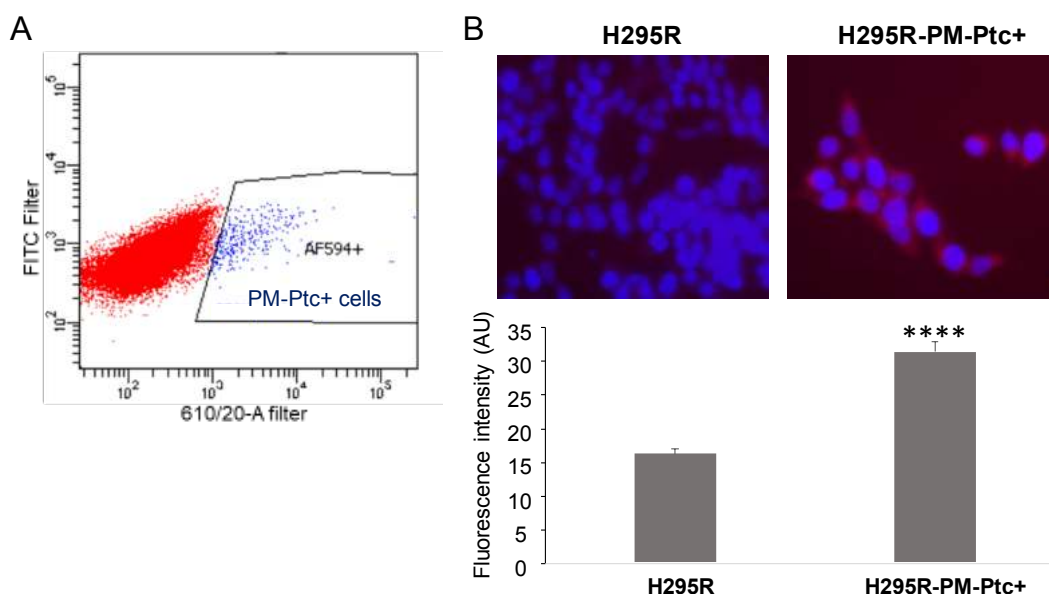
However, this whole internal workflow is transparent to users who can simply apply the method on their differential expression data from the web site [34]. On this site, it is possible to perform the identification of the active modules by simply uploading the file generated by DESeq2 and specifying the index of the column containing the gene names, the index of the  $p$ -value column and the index of the log<sub>2</sub> fold change. The output generated by AMINE consists of an Excel file listing the identified modules.

### 3. Results:

#### 3.1. A Small Subpopulation of the ACC Cell Line H295R Presents an Increased Amount of Ptch1 at the Plasma Membrane

We previously showed that Ptch1 is well expressed in the ACC cell line H295R [18]. Here, the expression of Ptch1 at the cell surface of H295R cells was addressed by FACS using an antibody directed against an extracellular loop of Ptch1. Surprisingly, only a small percentage ( $1.26\% \pm 0.11$ ;  $n = 9$ ) of H295R cells presented Ptch1 at the plasma membrane (PM) (Figure 1A). This subpopulation of H295R cells was sorted and amplified and named H295R-PM-Ptc+. The immunofluorescence study performed with the same anti-Ptch1 antibody on non-permeabilized cells confirmed the presence of higher levels of Ptch1 at

the plasma membrane from H295R-PM-Ptc+ cells as compared to parental H295R cells (Figure 1B).

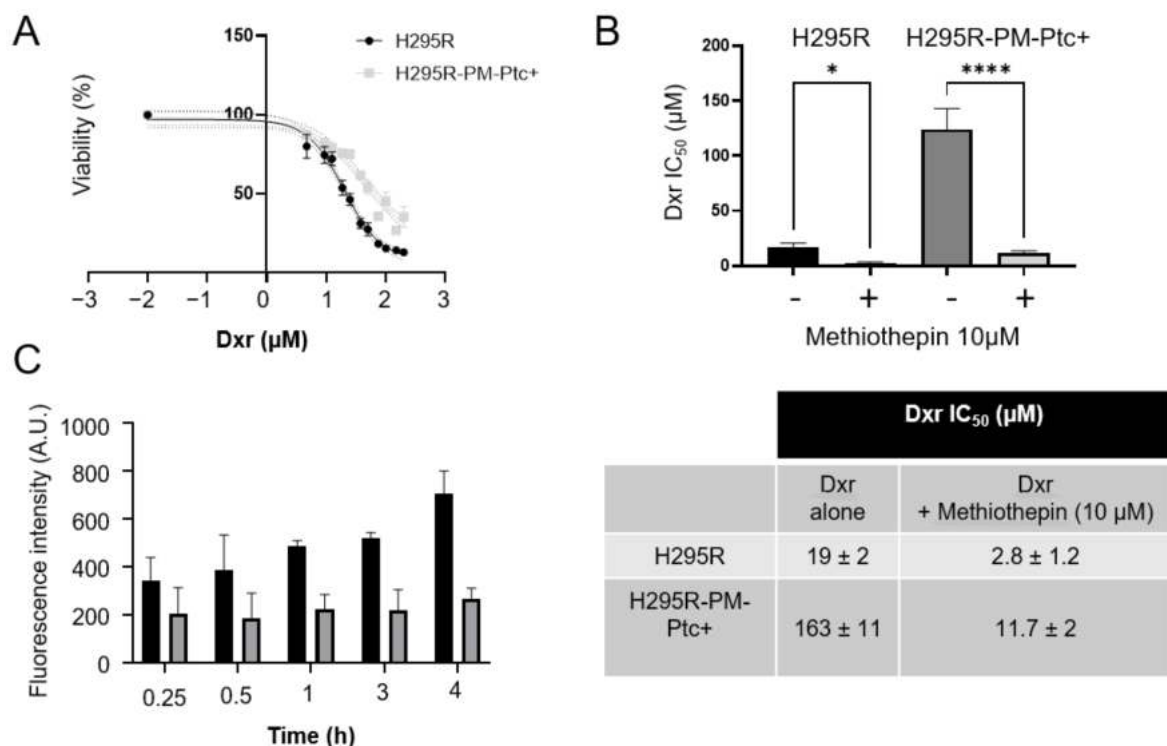


**Figure 1. A small population of ACC cells H295R overexpresses Ptch1 at the plasma membrane.** (A) H295R were labeled with an anti-Ptch1 antibody directed against the extracellular loop and cells presenting Ptch1 at their plasma membrane (H295R-PM-Ptc+ AF594+ cells) were sorted. AF594+ in blue represents the percentage of cells with Ptch1 at the cell surface (H295R-PM-Ptc+ cells). (B) Surface labeling of Ptch1 using anti-Ptch1 antibody directed against the extracellular loop of Ptch1 (Alexa 594 in red) on nonpermeabilized parental H295R and H295R-PM-Ptc+ cells. Nuclei were stained with DAPI (in blue). The histogram represents the mean  $\pm$  SEM of Alexa 594 fluorescence intensity per cell (\*\*\*\*:  $p$ -value  $< 0.00005$  ( $p$ -value =  $2 \times 10^{-36}$ )).

### 3.2. H295R-PM-Ptc+ Cells Are More Resistant to Chemotherapy Than Parental Cells

When H295R-PM-Ptc+ cells were treated for 48 h with increasing concentrations of doxorubicin (dxd), they showed an increased dxd IC<sub>50</sub> compared to parental H295R cells indicating that these cells are more resistant to dxd (Figure 2A,B). This is in good agreement with our previous study showing that H295R cells rendered resistant to dxd express more Ptch1 proteins than control cells [18]. Using the natural fluorescence of dxd, we measured the accumulation of dxd in cells after various incubation times with dxd. As shown in Figure 2C, dxd accumulates less in H295R-PM-Ptc+ cells than in H295R cells. The difference in accumulation increases with the time of incubation with dxd indicating that these cells efflux more dxd than the parental cells. This result is coherent with those obtained in our previous study showing that the depletion by 60% of Ptch1 protein in H295R cells using specific siRNAs equally reduced dxd efflux by 60%, confirming that Ptch1 is a major dxd efflux pump in these cells [18]. To confirm that the increase of resistance to doxorubicin of H295R-PM-Ptc+ cells was related to the increase in the level of expression of Ptch1 at the cell membrane, we treated the cells with methiothepin, an inhibitor of Ptch1 drug efflux activity, in the presence of increasing concentrations of dxd. As shown in Figure 2B, methiothepin increased the cytotoxicity of dxd on H295R-PM-Ptc+ cells even better than on parental H295R cells. Indeed, the presence of 10  $\mu$ M of methiothepin decreased 14 times and 7 times the IC<sub>50</sub> of dxd on H295R-PM-Ptc+ cells and on parental H295R cells, respectively (Figure 2C). This result confirms that the stronger resistance of H295R-PM-Ptc+ cells is correlated to the increased level of Ptch1 at the plasma membrane of these cells.





**Figure 2.** H295R-PM-Ptc+ cells are more resistant to chemotherapy than parental cells. (A) Doxorubicin (dxr) cytotoxicity. H295R and H295R-PM-Ptc+ cells were treated for 48 h with increasing concentrations of dxr before cell viability measure. (B) Doxorubicin IC<sub>50</sub> of H295R-PM-Ptc+ and H295R parental cells in the absence or the presence of 10 μM of the Ptc1 efflux inhibitor methiothepin. (C) H295R-PM-Ptc+ cells accumulate less doxorubicin than parental H295R cells. Cells on coverslips were incubated with 2 μM dxr for 15, 30, 60, 180 and 240 min and immediately fixed with PFA. Dxr fluorescence was acquired using a filter for Alexa 594 and quantified using ImageJ software. About 100 cells (from three wells) were scored per condition per experiment. All data presented are the mean ± SEM of at least 3 independent experiments. Significance is attained at *p*-value < 0.05 (\*), (\*\*\*\* *p* < 0.00005).

### 3.3. H295R-PM-Ptc+ Cells Show Superior In Vitro Clonogenic, Migratory and Invasive Capabilities Than Parental H295R Cells

We observed that H295R-PM-Ptc+ cells presented a different growth pattern. They formed cell clusters which look like spheroids instead of the single cell monolayer attachment pattern of the parental H295R cells (Figure 3A), and they grew slightly but not significantly slower than parental H295R cells (Figure 3B).

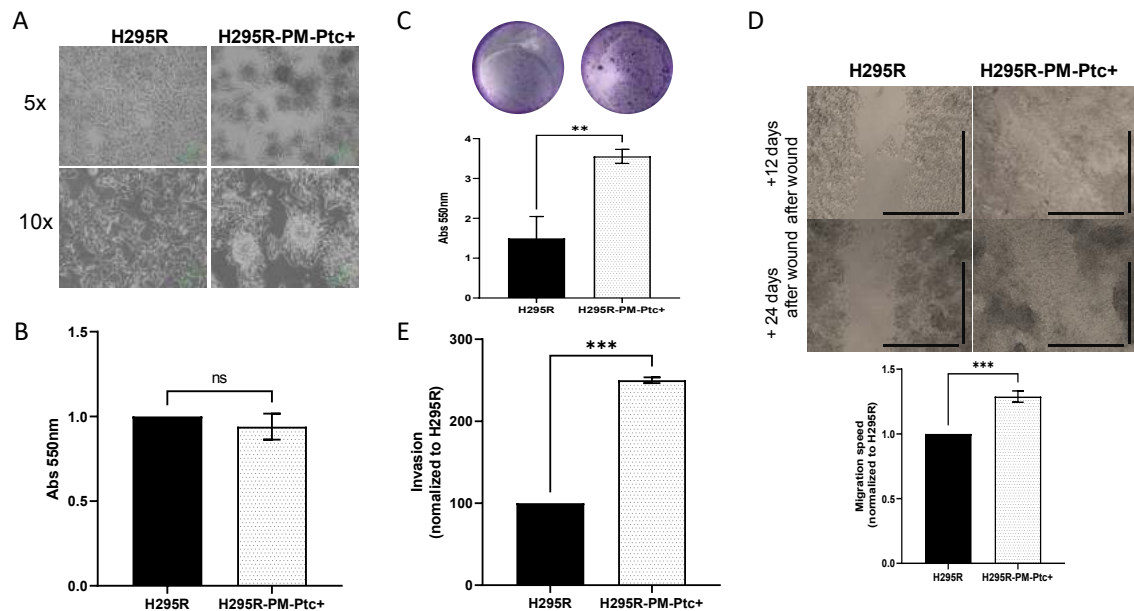
We then compared the ability of each cell group to form clones. For this, H295R-PM-Ptc+ and H295R cells were seeded at 5000 cells/well in 24 well plates for 14 days, and then fixed and colored using violet crystal. The quantification showed that H295R-PM-Ptc+ formed significantly more clones than the parental cell line (Figure 3C).

To compare the migration ability of these cells, we performed a wound healing assay in which, after a scratch in a confluent monolayer of cells, the closing of the wound was monitored by taking a picture of the wound every 15 min for 24 h. To measure the speed of closing, the wound area was measured for each time point. H295R-PM-Ptc+ cells showed a migration speed 1.3 times greater than the parental H295R cell line over the first 24 h (Figure 3D). Accordingly, H295R-PM-Ptc+ cells were able to close the wound completely after 20 days, whereas H295R cells did not.

The invasiveness properties of these cells were addressed using a transwell invasion assay. After correction to take into account the proliferation differences in each experiment, the data showed that the number of cells able to pass through the Matrigel-coated filters

was significantly higher with H295R-PM-Ptc+ cells compared to the parental H295R cells (Figure 3E).

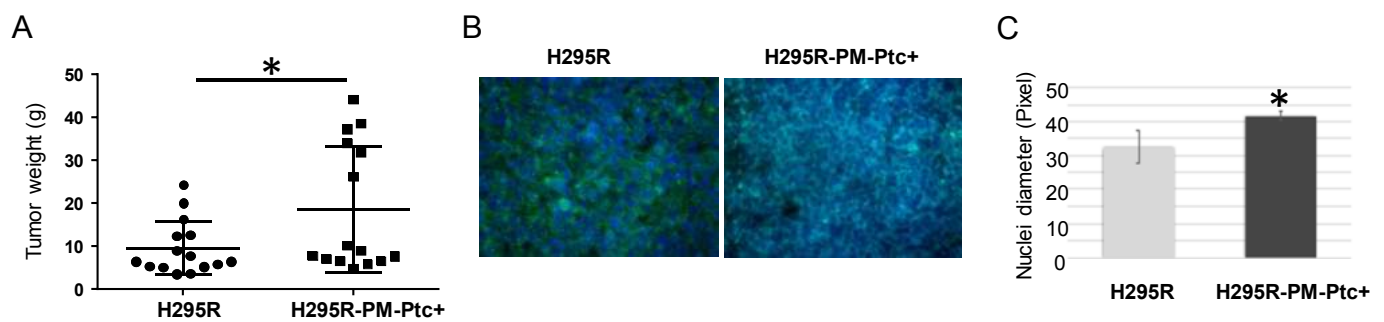
Taken together, our results strongly suggest that H295R-PM-Ptc+ cells possess an increased ability to form clones, to migrate and are more invasive than the parental cells.



**Figure 3.** H295R PM-Ptc+ cells are more aggressive than parental H295R cells. (A) H295R-PM-Ptc+ cells present a different growth pattern. (B) H295R-PM-Ptc+ show non-significant lower proliferative properties as H295R cells over 72 h ( $n = 3$ ; no significant difference (ns)). (C) H295R-PM-Ptc+ cells form more clones than ACC cells 14 days after seeding 5000 cells/well. Histogram represents the quantification of clones formed using crystal violet for 3 independent experiments ( $p = 0.003$ ). A representative image of clones stained with crystal violet is provided for each cell group. (D) H295R-PM-Ptc+ cells migrate faster than H295R cells. Migration ability of the two cell groups was evaluated using wound healing experiment. Slope of migration for 24 h, normalized to H295R,  $n = 5$ , ( $p = 0.005$ ). H295R-PM-Ptc+ cells completely reclose the wound compared to H295R cells, images taken 12 and 20 days after producing the wound ( $5\times$  objective, scale =  $100\ \mu\text{m}$ ). (E) H295R-PM-Ptc+ cells are more invasive than parental cells. More H295R-PM-Ptc+ cells were able to pass through Matrigel-coated filters compared to H295R. Invasion was normalized to H295R and proliferation differences, cells passed through the filter were counted and reported to the total cell number ( $n = 2$ ). All data presented are the mean  $\pm$  SEM of independent experiments. \*\*:  $p$ -value  $< 0.005$ , \*\*\*:  $p$ -value  $< 0.0005$ .

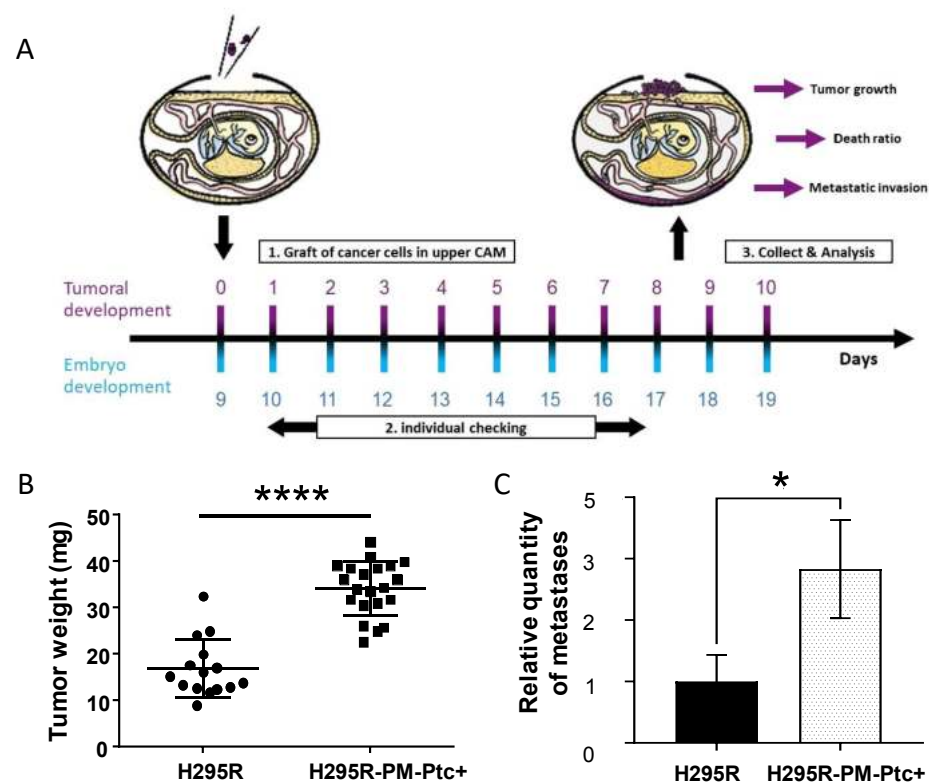
### 3.4. H295R-PM-Ptc+ Cells Are More Tumorigenic and Metastatic In Vivo Than Parental Cells

Tumorigenicity of H295R-PM-Ptc+ cells was addressed in mice. NMRI nude mice underwent a renal subcapsular injection with H295R and H295R-PM-Ptc+ cells. Forty-five days after the injection, mice were sacrificed, and tumors were collected, weighed, fixed and included in paraffin for immunohistochemistry and immunofluorescence analyses. The results show that H295R-PM-Ptc+ cells formed tumors significantly bigger compared to the parental H295R cells (Figure 4A). The labelling of tumor slices with an antibody against Ki67, a marker of proliferative cells, showed no difference in the amount of Ki67-positive cells between both tumor groups (Figure 4B). Interestingly, the nuclei in H295R-PM-Ptc+ cells were significantly bigger when compared to those of the parental cells (Figure 4C).



**Figure 4.** H295R-PM-Ptc+ cells are more tumorigenic than parental cells in mice. Each mouse received a renal subcapsular injection of H295R PM-Ptc+ or parental H295R cells ( $3 \times 10^6$  cells; 10 mice for each cell group). After 45 days, mice were sacrificed, tumors were collected, weighed and fixed. (A) The mean weight of H295R-PM-Ptc+ tumors is significantly higher than H295R tumors ( $n = 9$ ; \*:  $p$ -value  $< 0.05$  ( $p = 0.018$ )). (B) KI67 immunostaining on tumor slices. KI67 is marked with anti-human KI67 antibody recognized with a secondary antibody coupled to Alexa 488 (green staining) and DAPI (blue staining). Images were taken with an epifluorescence microscope (40 $\times$ ). (C) Tumors derived from H295R-PM-Ptc+ cells present bigger nuclei compared to tumors from parental cells. For each tumor, 20 nuclei diameters were measured (SRC-sample randomly chosen) from slides using imageJ software. Six H295R tumors and seven H295R PM-PTC+ tumors (\*:  $p$ -value  $< 0.005$ ).

Tumorigenesis and metastases were then addressed in ovo. This system consists of the injection of H295R-PM-Ptc+ cells or parental H295R cells at the chorioallantoic membrane (CAM) of two groups of fertilized white leghorn eggs at day 9 of embryonic development (E9). At day 18 of embryonic development (E18), tumors and embryos were collected and analyzed (Figure 5A). The tumors originated from H295R-PM-Ptc+ were significantly bigger than H295R tumors, confirming the results obtained in mice (Figure 5B). Metastasis quantification was addressed using real time qPCR with human ALU sequences allowing the detection of the presence of human cells in the chicken embryos' organs. As ACC cells have a hepatic tropism, genomic DNA was extracted from the livers of the embryos. Real time qPCR revealed that there were more metastases in the livers of embryos from eggs injected with H295R-PM-Ptc+ compared to those from eggs injected with parental H295R cells (Figure 5C).



**Figure 5.** H295R-PM-Ptc+ cells are more tumorigenic and metastatic than parental ACC cells in ovo. (A) Schematic representation of the study. On day 9 of egg development (E9)  $3 \times 10^6$  H295R-PM-Ptc+ and H295R cells were injected in the chorioallantoic membrane (CAM) from two groups of 20 eggs. At E18 tumors from CAM and embryos were collected. (B) H295R-PM-Ptc tumors collected on E18 were bigger than H295R tumors ( $n = 15$  for H295R graft and  $n = 21$  for H295R-PM-Ptc+; \*\*\*\*:  $p$ -value  $< 0.00005$ ). (C) Metastasis in liver was addressed using human Alu sequences by real time qPCR. H295R-PM-Ptc+ xenografted cells form more metastases in the embryo liver compared to H295R xenografted cells (mean  $\pm$  SEM  $n = 9$ ; \*:  $p$ -value  $< 0.05$  ( $p = 0.03$ )).

### 3.5. H295R-PM-Ptc+ Cells Differentially Express Genes Associated with EMC, Invasion, Metastasis and Cancer Stem Cell Properties

Differential gene expression analysis with DESeq2 was used to estimate the changes between the experimental conditions. Standard filtering with a  $p$ -value  $< 0.05$  and an absolute  $\log_2$  fold change  $> 1$  holds 57 underexpressed genes and 15 overexpressed genes (Supplementary Materials Table S2). Functional enrichments for Gene Ontology terms, KEGG, WikiPathways and Reactome Pathways identified with a false discovery rate (FDR)  $< 0.05$  are listed in the “enrichments underexpressed”, “enrichments overexpressed” and “enrichments all” worksheets in Supplementary Materials Table S2. No enrichments could be attributed to overexpressed genes. Underexpressed genes, as well as the set of all differentially expressed genes (DEG) were enriched with fairly broad annotations related to development, morphogenesis, cell adhesion, response to stimulus or extracellular matrix organization. Being more stringent, or looser in the selection of genes that are considered over- or underexpressed does not help to obtain more precise insight into the biological processes that are at work.

By selecting genes with a  $p$ -value  $< 0.05$  and setting no constraints on their minimum variation, we obtained 2374 differentially expressed genes with 1076 overexpressed genes and 1298 underexpressed genes (Supplementary Materials Table S3). The functional enrichments performed on this extended list result in annotations that were similar and as broad as those obtained with the more stringent list presented in Supplementary Materials Table S2. From the 2374 DEGs, we selected 41 DEGs of interest regarding the characteristics of H295R-PM-Ptc+ cells with 26 overexpressed (in red) and 15 underexpressed (in blue)

(Table 1, Figure 6). As expected, Ptch1 gene was one of the most overexpressed genes. All these DEGs are related to tumorigenicity, playing a role in the Hedgehog signaling activation, tumor progression, cancer stem cell (CSC) maintenance, chemotherapy resistance, epithelial to mesenchymal transition (EMT), metastasis and cancer cell survival or endocytosis.

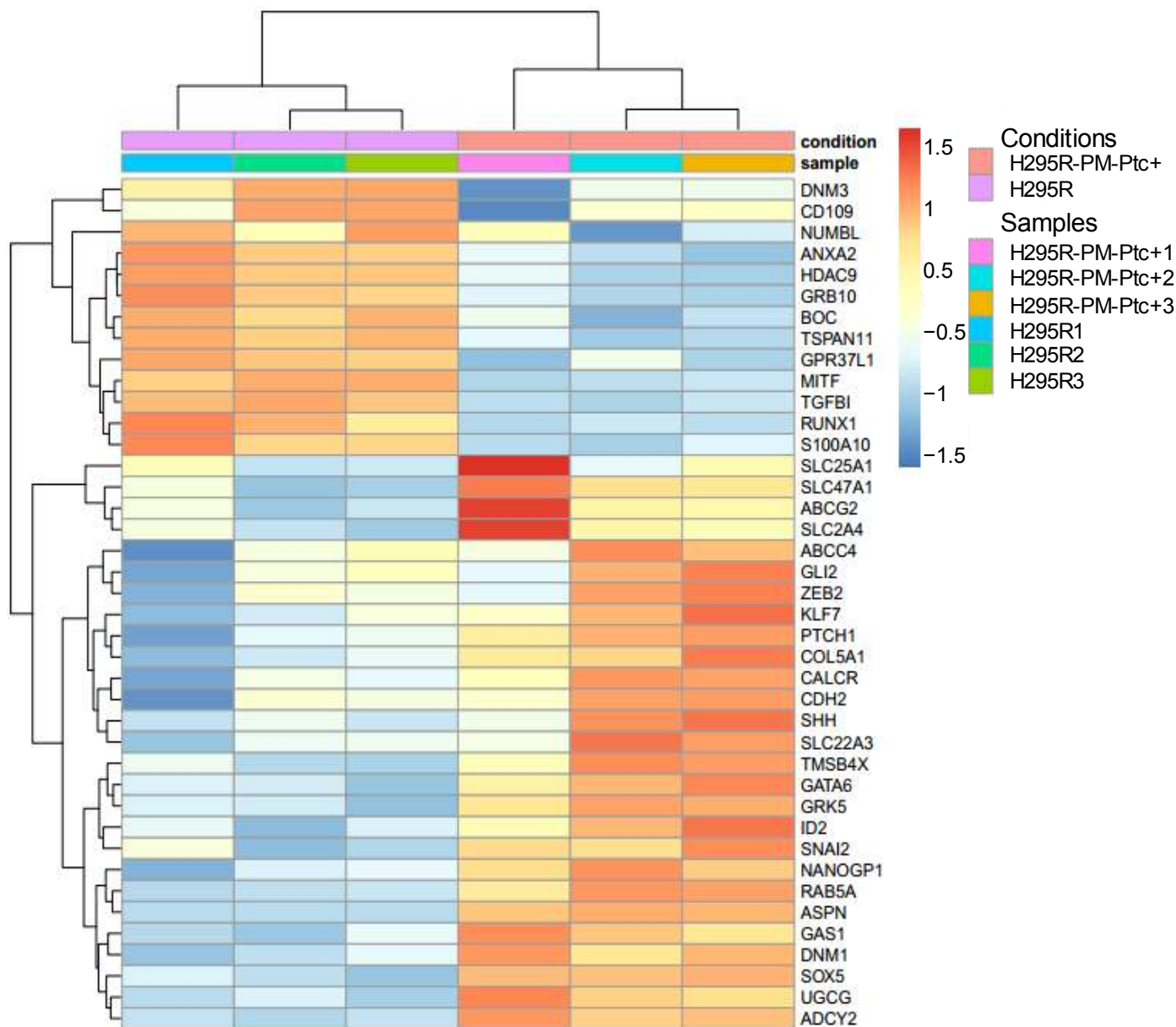


Figure 6. Heat map of differentially expressed genes (DEG) between H295R-PM-Ptc+ and parental H295R cells of interest for their role in cancer.

**Table 1.** Differentially expressed genes (DEG) between H295R-PM-Ptc+ and parental H295R cells selected for their role in cancer. Genes overexpressed are indicated in red and genes underexpressed are in blue.

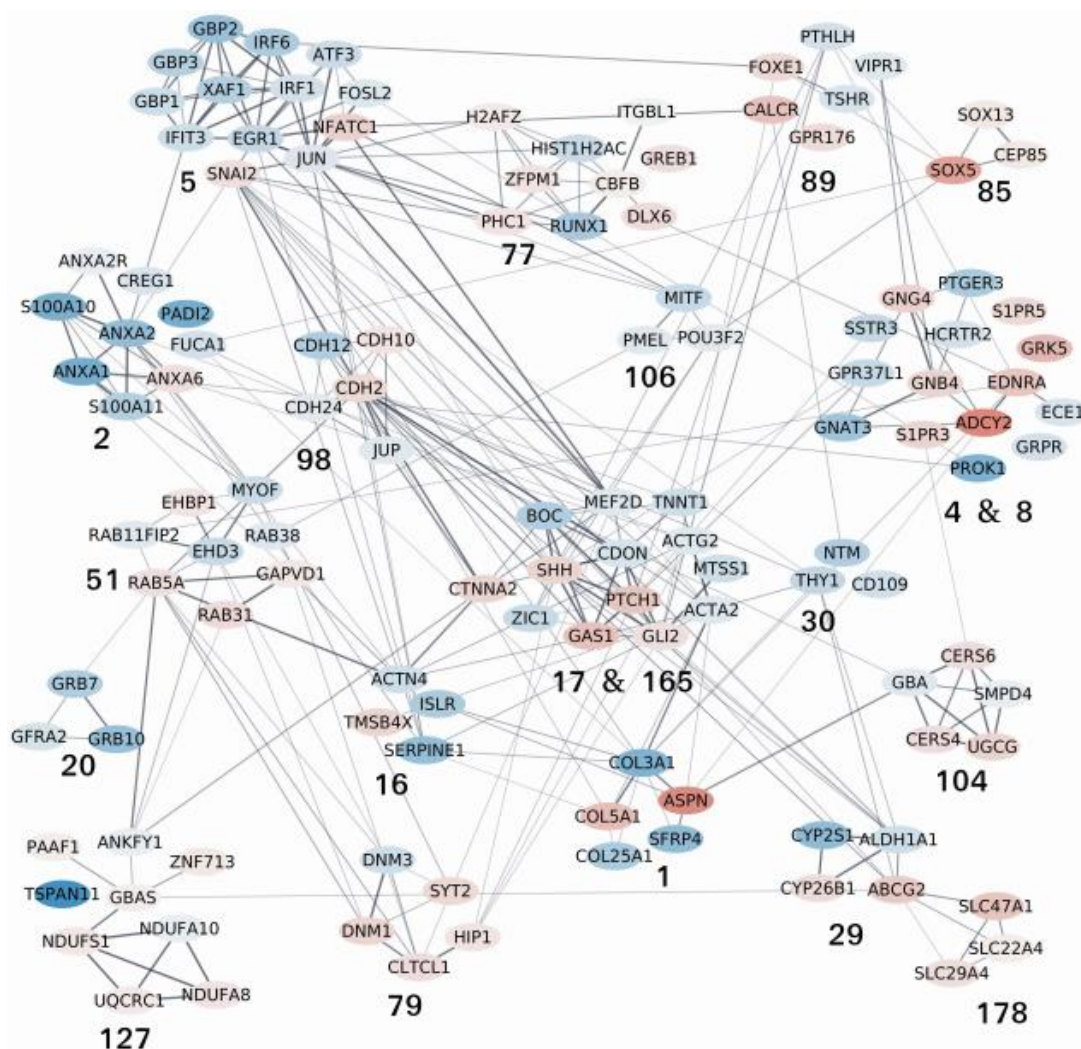
GDE	H295R-PM-Ptc+/ H295R Log2	p-Value	Role in Cancer
<b>Hedgehog (Hh) Signaling Pathway</b>			
PTCH1	+0.629	$1.08 \times 10^{-6}$	Hh target gene. drug efflux. chemotherapy resistance
GAS1	+0.724	$4.52 \times 10^{-8}$	Hh pathway activation
SHH	+0.421	$2.82 \times 10^{-3}$	
BOC	−0.794	$3.25 \times 10^{-7}$	BOC endocytosis via NUMB is required for Ptc1 internalization and Shh signaling
HDAC9	−0.925	$6.59 \times 10^{-17}$	Negative regulator of Hh signaling
GPR37L1	−0.548	$1.27 \times 10^{-4}$	Interacts with Ptc1 for Hh signaling modulation
NUMBL	−0.286	$1.47 \times 10^{-2}$	Negative regulator of canonical Shh signaling. Required for BOC and Ptc1 internalization
<b>Tumor Suppressor</b>			
DNM3	−0.427	$1.21 \times 10^{-4}$	Decreased expression is associated with worse prognosis
RUNX1	−0.898	$9.00 \times 10^{-11}$	Represses breast CSC phenotype through direct inhibition of Zeb1/2. Low RunX1 expression is associated with poor patient survival
<b>CSC Maintenance</b>			
UGCG	+0.418	$2.70 \times 10^{-7}$	CSC maintenance and chemotherapy resistance. increase antiapoptotic gene expression
SOX5	+1.149	$7.70 \times 10^{-17}$	Overexpressed in CSC in lung cancer, promotes migration, invasion and metastasis. Predicts poor prognosis
NANOGP1	+0.424	$6.42 \times 10^{-4}$	Self-renewal transcription factor, maintenance of CSC, EMT and metastasis.
GATA6	+0.444	$1.18 \times 10^{-4}$	Maintenance of stem cell phenotype, regulated by Nanog
KLF7	+0.456	$9.06 \times 10^{-4}$	Upregulated in quiescent cells Restores hematopoietic stem cells niche
COL5A1	+0.754	$4.58 \times 10^{-9}$	Quiescence and self-renewal of stem cells
CALCR	+0.696	$1.90 \times 10^{-6}$	Maintains cells in a quiescent state
MITF	−0.564	$1.58 \times 10^{-10}$	Low MITF is associated to slow cycling and senescence phenotype, dedifferentiation and treatment resistance
GRB10	−1.104	$5.20 \times 10^{-16}$	Deletion promotes hematopoietic stem cell self-renewal and regeneration
<b>CSC and Chemotherapy Resistance</b>			
ABCG2	+0.592	$1.39 \times 10^{-4}$	Drug efflux. Resistance to chemotherapy
ABCC4	+0.352	$1.94 \times 10^{-2}$	Chemotherapy resistance. CSC marker
SLC47A1	+0.667	$6.46 \times 10^{-8}$	SLC transporters in chemotherapy resistance
SLC2A4	+0.429	$9.32 \times 10^{-4}$	Energy production of cancer cells, migration, metastasis
SLC22A3	+0.339	$4.10 \times 10^{-3}$	Cell invasion and filopodia formation, metastasis
ID2	+0.294	$1.08 \times 10^{-3}$	Inhibition of differentiation and maintenance of self-renewal and multipotency in stem cells

Table 1. Cont.

GDE	H295R-PMPTc+/H295R Log2	p-Value	Role in Cancer
<b>EMT</b>			
TMSB4X	+0.434	$6.13 \times 10^{-5}$	Suppresses E-cadherin expression, promotes cancer cell growth and migration
SNAI2	+0.295	$1.36 \times 10^{-3}$	Triggers EMT, blocks cell cycle and confers resistance to cell death
RAB5A	+0.256	$8.33 \times 10^{-4}$	Migration and metastasis
ASPN	+1.476	$2.51 \times 10^{-22}$	Promotes cell migration and invasion
CDH2	+0.390	$2.63 \times 10^{-3}$	Mesenchymal marker
CD109	−0.425	$6.50 \times 10^{-3}$	Co-receptor of TGFB1 Inversely correlates with EMT, migration and invasion
TGFB1	−1.75	$2.83 \times 10^{-29}$	TGFB1 deficiency predisposes mice to tumor development
<b>Metastasis, Cancer Cell Survival</b>			
ADCY2	+1.56	$5.63 \times 10^{-24}$	Involved in metastasis. High expression related to worse survival.
DNM1	+0.452	$1.05 \times 10^{-4}$	Invasion and metastasis
GRK5	+0.831	$3.84 \times 10^{-9}$	Tumor progression
<b>Endocytosis</b>			
S100A10	−1.473	$3.86 \times 10^{-21}$	Undifferentiated phenotype and poor prognostic-low level in metastatic melanoma
ANXA2	−1.144	$8.08 \times 10^{-16}$	ANXA2 and S100A10 heterotetramer is involved in regulation of endocytosis.
ST6GAL1	+0.668	$1.54 \times 10^{-10}$	Inhibition of endocytosis GL-Lect dependent. High tumor grade, metastasis and reduced patient prognosis
CERS6	+0.314	$5.55 \times 10^{-3}$	
<b>Adrenocortical Carcinoma Markers</b>			
STAR	−0.289	$4.21 \times 10^{-2}$	Lower expression this steroidogenic enzymes is associated with a less differentiated phenotype.
ZNRF3	−0.315	$3.21 \times 10^{-3}$	Low expression: negative prognostic marker of ACC
SYP	−0.453	$3.11 \times 10^{-6}$	Differentiation marker in tumor diagnosis

From the raw output of DESeq2, we performed a search for active modules using AMINE [31] which is a method designed to identify the modules of genes that are triggered in a biological experiment (the output of AMINE is presented in Supplementary Materials Table S4). Among the 188 active modules identified by AMINE, we selected those that contain one or more of the identified genes of interest listed in Table 1. This enables the identification of 21 modules, whose composition is detailed in Supplementary Materials Table S5. A graphical representation of the interactions between the proteins encoded by the genes within the outlined modules is proposed in Figure 7. In the figure, each module is identified by its number (specified in Supplementary Materials Table S5). The details of all the enrichments of the modules with a FDR < 0.05 are presented in Supplementary Materials Table S6. Some modules that exhibit many interactions between their members have been grouped together; this is the case for modules 4 and 8 as well as 17 and 165. Unlike the enrichments obtained by selecting only the most deregulated genes, the identification of active modules makes it possible to identify more specific molecular pathways or processes. Modules 17 and 165 are in the center of the graph and interact with many of the other modules. These modules contain components of the Hedgehog signaling pathway, and their differential expression reveals an activation of the pathway. Indeed, Shh and Gli2 which are well-known activators of the pathway and Ptch1, which is an Hh target gene, are

overexpressed. CDON and BOC are essential cell surface modulators of the Hh pathway. In their absence, Gas1, an Hh-binding protein, mediates Hh signaling [35]. The number and composition of the 21 active modules, their representative enrichment and the role of differentially expressed genes (DEGs) in cancers are summarized in Table 2.



**Figure 7.** Network of protein–protein interactions between the members of the active modules containing one or more of the identified genes of interest listed in Table 1. The nodes on the network correspond to genes. Node colors represent the log<sub>2</sub> fold change values of the corresponding gene on a scale varying from blue (for the most underexpressed genes) to red (for the most overexpressed genes). Edges correspond to interactions reported in the String database with a combined evidence score  $\geq 0.4$ . Each module is identified by its number (specified in Supplementary Materials Tables S2 and S3). The complete lists of the enrichments of all the modules are shown in Supplementary Materials Table S4.

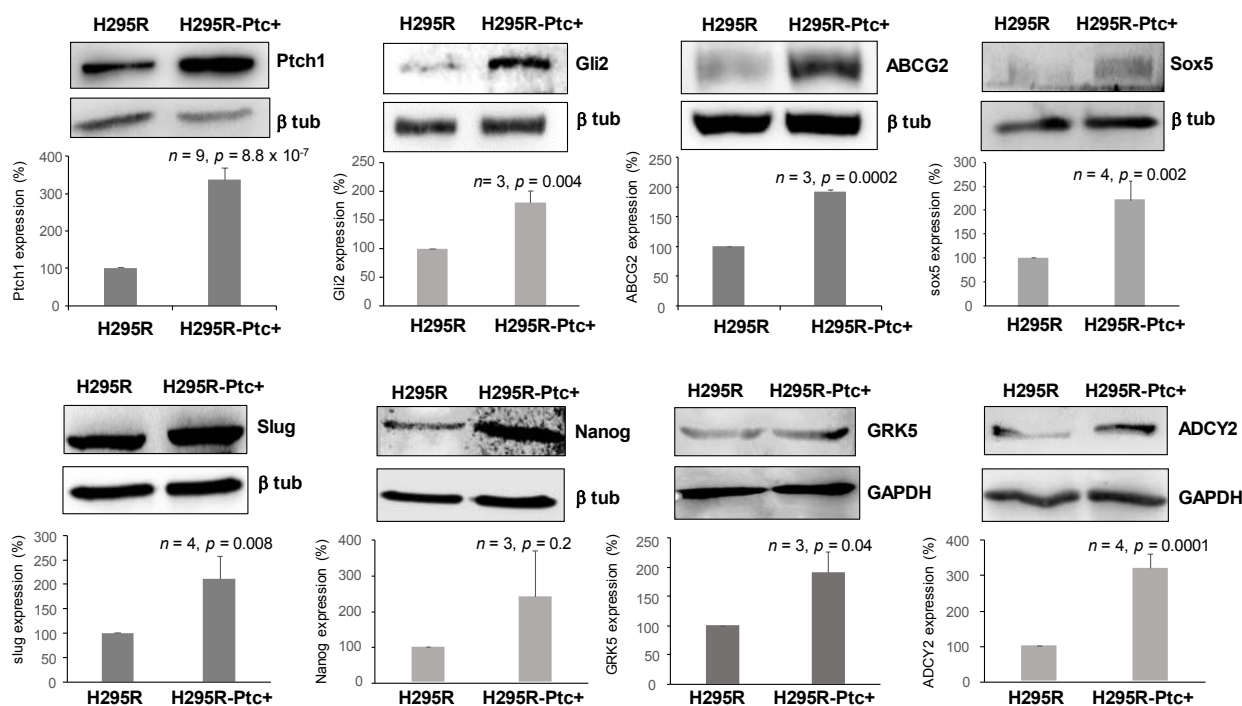


**Table 2.** Composition of active modules containing one or more of the identified genes of interest listed in Table 1 (in bold) with genes upregulated in red and genes downregulated in blue, representative enrichment and role of differentially expressed genes (DEGs) in cancers.

Module Number and Composition	Representative Enrichment	Role of the DEGs in Cancer
<b>1</b> <b>ASPN</b> , <b>COL5A1</b> , COL25A1, COL3A1, SFRP4	Extracellular matrix organization	CSC maintenance, EMT
<b>2</b> <b>ANXA6</b> , <b>ANXA1</b> , <b>ANXA2</b> , <b>ANXA2R</b> , GREG1, FUCA1, PADI2, <b>S100A10</b> , S100A11	Vesicle transport, cell adhesion	Cancer development and progression, poorer prognosis
<b>4 and 8</b> <b>ADCY2</b> , <b>S1PR3</b> , <b>S1PR5</b> , <b>EDNRA</b> , <b>GNB4</b> , <b>GNG4</b> , <b>GRK5</b> , GNAT3, GPR37L1, PTGER3, SSTR3, ECE1, GRPR, HCRTR2, PROK1	Signaling by GPCR	Regulation of CSC, cancer cell survival, metastasis, poor prognosis
<b>5</b> <b>NFATC1</b> , <b>SNAI2</b> , ATF3, EGR1, FOSL2, GBP1, GBP2, GBP3, IFIT3, IRF1, IRF6, JUN, XAF1	Regulation of cell population proliferation	Maintenance of mesenchymal phenotype, invasive migration, metastasis, poor prognosis, chemotherapy resistance
<b>16</b> <b>TMSB4X</b> , ACTN4, ISLR, SERPINE1	Platelet degranulation	EMT induction and metastasis
<b>17 and 165</b> <b>PTCH1</b> , <b>SHH</b> , <b>GLI2</b> , <b>CTNNA2</b> , <b>GAS1</b> , <b>BOC</b> , <b>CDON</b> , MEF2D, TNNT1, ZIC1, ACTA2, ACTG2, MTSS1	Hedgehog signaling, cell differentiation, cell fate specification, development	Hedgehog pathway activation, CSC maintenance, tumor cell survival
<b>20</b> GFRA2, <b>GRB10</b> , GRB7	RET signaling	Stem cell self-renewal
<b>29</b> <b>ABCG2</b> , <b>CYP26B1</b> ALDH1A1, CYP2S1	Retinoic acid metabolic process	Chemotherapy resistance, CSC, poor prognosis
<b>51</b> <b>EHBP1</b> , <b>GAPVD1</b> , <b>RAB5A</b> , <b>RAB31</b> , EHD3, MYOF, RAB11, FIP2, RAB38	Endosome membrane, endocytosis	Membrane trafficking, endocytosis, cancer cell motility and invasiveness, cancer development and progression, metastasis
<b>77</b> <b>DLX6</b> , <b>GREB1</b> , <b>HIST1</b> , <b>H2AC</b> , <b>CBFB</b> , <b>H2AFZ</b> , ITGBL1, PHC1, <b>RUNX1</b> , ZFPM1	Negative regulation of differentiation	Poor patient survival, malignant phenotype and metastasis, tumor progression and development, cell proliferation, migration and EMT
<b>79</b> <b>CLTCL1</b> , <b>DNM1</b> , HIP1, SYT2, <b>DNM3</b>	Endocytosis, membrane trafficking	Proliferation, migration and invasion, cancer progression and metastasis, poor prognosis
<b>85</b> <b>CEP85</b> <b>SOX13</b> <b>SOX5</b>	Transcription factors, cell-cycle progression	CSC maintenance, EMT, invasion, metastasis
<b>89</b> <b>CALCR</b> , <b>FOXE1</b> , <b>GPR176</b> , <b>PTHLH</b> , <b>TSHR</b> , VIPR1	G protein-coupled receptor activity	Stem cell maintenance
<b>98</b> <b>CDH10</b> , <b>CDH2</b> , <b>CDH12</b> , <b>CDH24</b> , JUP	Cell–cell adhesion	EMT, cell migration and invasion, poor prognosis
<b>104</b> <b>CERS4</b> , <b>CERS6</b> , <b>UGCG</b> , GBA, SMPD4	Sphingolipid metabolism	Multidrug resistance, proliferation of cancer cells, cell migration and metastasis
<b>106</b> <b>MITE</b> , PMEL, POU3F2	Melanoma phenotype switching	Enrichment of stem cells, de-differentiated state and invasiveness
<b>127</b> <b>GBAS</b> , <b>NDUFA8</b> <b>NDUFS1</b> <b>PAAF1</b> <b>UQCRC1</b> <b>ZNF713</b> , <b>ANKFY1</b> , <b>NDUFA10</b> <b>TSPAN11</b>	Mitochondrial respiratory chain complex	Malignant behavior of cancer cells, cell cycle progression
<b>178</b> <b>SLC22A4</b> <b>SLC29A4</b> <b>SLC47A1</b>	SLC-mediated transmembrane transport	Cell proliferation, epithelial-to-mesenchymal transition

We then performed Western-blot on H295R and H295R-PM-Ptc+ cell extracts to find out if the differences observed at the RNA level were reflected at the protein level for some DEGs. Figure 8 shows that the protein level of several DEGs such as Ptc1, Gli2, ABCG2, SOX5, GRK5, ADCY2, Nanog and SNAI2 (Slug) was significantly increased in H295R-PM-Ptc+ cell extracts. This result is in good agreement with RNAseq data and

shows that some proteins involved in cancer stem cell maintenance are overexpressed in H295R-PM-Ptc+ cells.



**Figure 8.** Protein expression of some differentially expressed genes between H295R cells parental and H295R PM-Ptc+ cells FACS sorted and amplified. Western blots were performed using anti-DEG antibodies, and  $\beta$ -tubulin or GAPDH antibodies for the loading control. Signals on Western blots were quantified using ImageJ software. Data presented are the mean  $\pm$  SEM of at least 3 independent experiments. *p*-values were calculated using Student's *t*-test.

#### 4. Discussion

In this study, we isolated and characterized a small subpopulation of the adrenocortical carcinoma (ACC) cell line H295R that overexpresses Ptch1 and presents more Ptch1 at their plasma membrane, called H295R-PM-Ptc+ (Figure 1). This cell subpopulation was found to be more resistant to the chemotherapeutic drug doxorubicin (Figure 2). This is in good agreement with our previous study showing that H295R cells rendered resistant to doxorubicin express more Ptch1 than control cells [18]. These results also strengthen our previous data suggesting that the Hedgehog receptor Ptch1 strongly contributes to chemotherapy resistance of H295R cells by exporting drugs such as doxorubicin out of these cells [18]. We were more surprised by the results showing that this subpopulation of cells grew as spheroids, and had a greater capability of clonogenicity, migration and invasion in vitro than the parental cells (Figure 3). Moreover, xenograft experiments performed in mice and in ovo demonstrated that cells amplified from the subpopulation of H295R-PM-Ptc+ were more tumorigenic and more metastatic than the parental cells in vivo (Figures 4 and 5). This is in good agreement with in vitro observations, and strongly suggests that H295R-PM-Ptc+ have properties similar to those of cancer stem cells or tumor-initiating cells or persistent cells. Cancer stem cells (CSCs) or persistent cells are a subpopulation of cells identified in most types of liquid and solid cancers by cell surface markers more or less specific of the tumor-type that have the driving force of carcinogenesis [36,37]. CSCs present a different behavior when compared to the other cells within the same tumor, in particular, they have distinctive self-renewal, proliferation and differentiation faculties. CSCs play a critical role in cancer initiation, progression and recurrence, metastases formation, and resistance to therapy. The acquisition of this aggressive and MDR phenotype is due to different cellular mechanisms, i.e., drug-efflux pump activation, enhanced capacity of

DNA damage repair, dysregulation of signaling pathways involved in cell growth and development, altered cell metabolism and diminished apoptosis response.

To better characterize H295R-PM-Ptc+ cells and confirm the hypothesis that these cells are cancer stem-like cells, we performed an RNA-seq analysis which revealed that 2374 genes were significantly differentially expressed in H295R-PM-Ptc+ derived cells in comparison with H295R parental cells. The overexpression of some of these genes was confirmed at the protein level by comparing H295R-PM-Ptc+ cell extracts to parental H295R cell extracts (Figure 8). These RNA-seq and the Western-blot analyses confirmed the strong overexpression of Ptch1 in H295R-PM-Ptc+. Indeed, a variety of primary tumors and cancer cell lines (i.e., lung, ovary, prostate, colon, brain and myeloid leukemia) overexpress Ptch1 (see the Human Protein Atlas website (<http://www.proteinatlas.org/ENSG00000185920-PTCH1/cancer>, [14] for a review, accessed on 10 January 2022). Im and colleagues showed that in 190 over 334 tissue microarrays from breast cancer patient samples the overexpression of Ptch1 was significantly correlated with a more aggressive tumor growth, advanced cancer stages and lymph node metastasis [38]. Papadopoulos and co-workers reported an overexpression of Ptch1 in colorectal cancers, and their analysis of esophageal biopsy specimens from patients treated with chemotherapy revealed elevated levels of Ptch1 expression in 76% of the cases [39]. Interestingly, decreased response to chemotherapy, large tumor size and locoregional progression of esophageal squamous cell carcinoma seem associated to a high expression of Ptch1 [40]. Furthermore, Ptch1 expression has been proposed to be an early marker for gastric and thyroid cancers [15,16], and more recently a prognosis marker for relapse in high-risk prostate cancer patients [41]. Moreover, our recent studies showed that Ptch1 is present in primary tumor samples from all adrenocortical carcinoma patients of the cohort studied [18], and that Ptch1 is present in the metastases of all 365 melanoma patients of a TCGA cohort and correlates with a poorer the prognosis [19].

The differentially expressed genes (DEGs) from the RNAseq analysis have been grouped into 188 active modules. Twenty-one of these modules and their interactions are presented in the Figure 7 and the Table 2. The differential expression of genes from modules 17 and 165 revealed an activation of the Hedgehog (Hh) signaling pathway in good agreement with the overexpression of **Ptch1** which is an Hh target gene. Moreover, the overexpression of the transcription factor **Gli2** involved in the Hh signaling activation was also shown at the protein level (Figure 8). The Hh signaling is a determinant pathway for tumor progression and cancer stem cell maintenance. For example, decreased **CDON** expression was also observed in a large fraction of human colorectal cancer and was associated with intestinal tumor progression in mice [42]. **BOC** inactivation resulted in reduced proliferation and progression of early medulloblastomas to advanced cancer [43]. Interestingly, CDON and BOC have been suggested to regulate Hh signaling through the modulation of Ptch1 distribution at the cell surface. Their down-expression in H295R-PM-Ptc+ cells could explain the presence of more Ptch1 at the plasma membrane of these cells [44]. Remarkably, modules 17 and 165 are in the center of the graph and interact with many of the other modules. The differential expression of the genes contained in modules 1, 4 and 8, 5, 16, 17 and 165, 51, 77, 79, 98 and 178 is associated with epithelial to mesenchymal transition (EMT) which can be triggered by tumor cells, cancer development and progression, metastasis, and correlated with poor prognosis, while the differential expression of the genes contained in modules 1, 5, 17 and 165, 20, 29, 85, 89 and 106 is more involved in CSC maintenance, and that of the genes contained in modules 5, 17 and 165, 29 and 104 is associated with chemotherapy resistance. Some illustrations are given below:

Proteins from **module 98**, and more particularly the N-cadherin **CDH2**, present strong interactions with proteins from modules 17 and 165. Cadherins are transmembrane glycoproteins involved in cell–cell adhesion during embryogenesis, tissue morphogenesis, differentiation and carcinogenesis. The loss of epithelial cadherin (E-cadherin), by affecting cell–cell adhesion, induces EMT and tumor progression. Many signaling pathways activated during tumorigenesis affect cadherin cell–cell adhesion which contributes to tumor progression and metastasis [45]. N-cadherin promotes thyroid tumorigenesis through

modulating major signaling pathways [46]. CDH2 has been reported to be highly expressed in metastatic liver cancer. By analyzing gastric cancer (GC) patients in two independent cohorts, Luo and co-workers showed that cadherins CDH2, CDH6, CDH7 and CDH10 were significantly associated with a poor GC prognosis [47]. Moreover, the knockdown of **JUP**, a cell–cell junction protein homologue of  $\beta$ -catenin involved in adhesion junction and desmosome composition, causes EMT, promotes GC-cell migration and invasion, and was closely correlated with GC malignancy and poor prognostics [48].

Proteins from **module 5**, and more specifically **Snai2** (Slug), are strongly interacting with proteins from modules 17 and 165 and 98. H295R-PM-Ptc+ cells present an overexpression of Snai2 at the RNA and protein level. This C2H2-type zinc finger transcription factor also called Slug has antiapoptotic activity, and participates in EMT, tumor progression, stem and or/progenitor maintenance, tumor metastasis, cellular differentiation, vascular remodeling, and DNA damage repair. Snai2 plays a role in breast carcinoma as well as leukemia by downregulation of E-cadherin, which supports the mesenchymal phenotype and enables metastasis of tumor cells [49]. Snai2 is also associated with a poor prognosis of luminal B HER2<sup>+</sup>/ERBB2<sup>+</sup> breast cancers [50] and directly contributes to cisplatin resistance in ovarian cancer [51]. **NFATC1**, a nuclear factor of activated T-cells c1, is also upregulated in H295R-PM-Ptc+ cells and is associated with malignancy in several cancer models. Different NFAT isoforms are overexpressed in diverse hematologic malignancies and solid tumors. The overexpression of this gene seems to be involved in single cell fate, increasing the ability of the cancer cells to migrate/invade and differentiate but also to survive in both the tumor and the associated microenvironment. NFATC1 overexpression in high-grade serous ovarian carcinomas was associated with poor overall survival and of early relapse [52]. **GBP1, 2, 3** and **ATF3** genes are downregulated in H295R-PM-Ptc+ cells. Guanylate-binding proteins belongs to the dynamin superfamily. These GTPases are important effectors of cell dynamics acting on membrane, cytoskeleton and cell cycle progression. GBP1, considered a tumor-repressor gene, was found to be downregulated in colorectal cancer [53]. It was reported that transfection of GBP2 in colorectal cancer (CRC) cells inhibited their growth and increased their sensitivity to paclitaxel in a paclitaxel-resistant CRC, impairing Wnt signaling [54]. Dysregulation of ATF3, a cyclic AMP-dependent transcription factor, has been observed in diverse cancers, especially in various step of tumorigenesis. Low ATF3 expression was correlated to shorter survival and poorer prognosis in gastric cancer patients [55]. Moreover, the expression of ATF3 in SW620 CRC cells inhibits cell growth and stem cell-like characteristics [56]. Overall, differential expression of genes from module 5 are involved in the maintenance of the mesenchymal phenotype, invasive migration, metastasis, poor prognosis, and chemotherapy resistance.

**Module 1** is in interaction with modules 17 and 165 and 16. It contains five DEGs with two being highly overexpressed in H295R-PM-Ptc+ cells: **ASPN** and **COL5A1**. The collagen family gene **COL5A1** has been identified as a possible predictor of recurrence after radiation therapy for vestibular schwannoma (VS) [57] and related to brain metastasis in breast cancer patients [58]. The extracellular matrix protein asporin (**ASPN**) has been shown to promote cell migration and invasion [59] and may be a key molecule in facilitating tumor spreading [60]. Sasaki and co-workers recently suggested that asporin expression could reprogram cancer cells to acquire resistance to oxidative stress [61].

Proteins from **module 16** are in interaction with those from modules 17 and 165, 98 and 1. **TMSB4X** (Thymosin beta 4 X-linked), which is upregulated in H295R-PM-Ptc+ cells, has been proposed to suppress E-cadherin expression, and to promote cancer cell growth and migration. The overexpression of TMSB4X was found significantly associated with poor prognosis of overall survival and recurrence-free survival in head and neck squamous cell carcinoma (HNSCC) patients. The global proteomics analysis identified TMSB4X as a new biomarker of HNSCC whose functions resulted in enhanced proliferation and metastasis in vitro and in vivo [62].

**Modules 4 and 8** contain the most overexpressed gene, **ADCY2**. **ADCY2** overexpression was confirmed at the protein level. The adenylate cyclase ADCY2 is overexpressed

in prostate and colon cancer metastases, and in pancreatic neuroendocrine tumors [63]. It is considered as a strong metastatic marker. The sphingosine-1-phosphate receptor 3 (**S1PR3**) and 5 (**S1PR5**) are closely related G-Protein-coupled receptors involved in the lipid-mediated regulation of CSC via Notch signaling and cancer cell survival [64,65]. The binding of the lipid S1P (Sphingosine-1-phosphate) to the Sphingosine-1-phosphate receptors (S1PR1, S1PR2, S1PR3, S1PR4 and S1PR5) triggers different pathways involved in cell differentiation, proliferation, angiogenesis and migration [66]. Upregulation of the guanine nucleotide binding-protein gamma subunit 4 protein (**GNB4**) was significantly associated with primary tumor, nodal metastasis, histological grade, vascular invasion and mitotic rate [67,68]. High expression of **EDNRA** is associated with metastasis and poor outcome in patients with advanced bladder cancer [69]. **PROK1** gene which is involved in cell-to-cell contact, epithelial tissue differentiation, Ca<sup>2+</sup> release, lipid synthesis, and chemotaxis is downregulated in H295R-PM-Ptc+ cells. Prostaglandin receptor EP3 (**PTGER3**) downregulation was shown to contribute to prostate carcinogenesis and to progression from androgen-dependent prostate cancer to castration-resistant prostate cancer [70].

In **Module 79**, dynamin 3 (**DNM3**) which functions as a tumor suppressor in various malignancies is downregulated in H295R-PM-Ptc+ cells. The low expression of **DNM3** was significantly associated with high pathological grading of cervical cancer [71]. In contrast, **DNM1** is overexpressed in H295R-PM-Ptc+ cells, as in colon cancer where high **DNM1** expression was significantly correlated with perineural and lymphatic invasion and predicted poor prognosis [72]. Moreover, the overexpression of Huntingtin-interacting protein 1 (**HIP1**) has also been observed in prostate and colon tumor cells where **HIP1** expression was significantly associated with prostate cancer progression and metastasis. Studies suggest that **HIP1** is a cellular survival factor which may play a role in tumorigenesis by allowing the survival of precancerous or cancerous cells [73].

The overexpression of genes from **module 104** is associated with sphingolipid pathway, migration, metastasis and chemotherapy resistance. Sphingolipids are lipids associated to the membrane implicated in signaling pathways which regulate cell migration, growth and death. In cancers, sphingolipids regulate pathways involved in tumor progression, metastasis, invasion and lethal mitophagy [74]. The activity of **UGCG** (UDP-glucose ceramide glucosyltransferase) is related to multidrug resistance and cell proliferation in different cancer types. In breast cancer cells, the overexpression of **UGCG** was shown to increase glycolysis and oxidative phosphorylation [75]. The ceramide synthase encoded by the gene **CERS6** was shown to be required for cell migration and metastasis in lung cancer [76].

**Module 29** contains four DEGs in strong interaction with modules 17 and 165. The RNAseq showed that **ABCG2** is overexpressed in H295R-PM-Ptc+ cells, and this was confirmed at the protein level by Western-blot. This ABC transporter is a direct transcriptional target of Hh signaling and has been shown to be involved in drug tolerance [77]. **ABCG2** is a well-known marker of cancer stem-like cells and contributes to the resistance of these cells to chemotherapy [36].

**Module 2** contains the two most underexpressed genes **S100A10** and **ANXA2**. A decreased expression of the S100 calcium-binding protein (**S100A10**) has been shown to reduce the intracellular calcium concentration and the rate of phagocytosis. It may be associated with an undifferentiated phenotype and poor prognosis in gastric cancer [78]. Annexin 2 (**ANXA2**) is an important regulator of cell–cell adhesion. This protein is negatively correlated with the differentiation status of ESCC tumors with less differentiated malignant tumors, having the lowest **ANXA2** levels. **ANXA2** depletion has been shown to cause the depletion of **S100A10** protein [79]. Indeed, **S100A10** associates with **ANXA2** and **ANXA1** in heterotetramers involved in the regulation of endocytosis, exocytosis, focal adhesion dynamics, cell proliferation, oxidative stress and apoptosis [80,81]. Silencing **ANXA2** was shown to downregulate **S100A10** and to inhibit breast cancer proliferation and invasion [82]. Moreover, a tissue microarray analysis described that decreased expression of **ANXA1** is correlated with breast cancer development and progression [83].

Genes from **module 51** are also involved in membrane trafficking, endocytosis, cancer cell motility and invasiveness, cancer development and progression and metastases. Two genes coding for RAB proteins are overexpressed in H295R-PM-Ptc+ cells, **RAB5a** and **RAB31**. The RAB protein family belongs to the subgroup of the GTPase superfamily. RAB proteins participate in cellular trafficking by regulating the dynamics of the membrane compartments, the Golgi complex organization and the sorting and delivery of secretory and membrane proteins. There is now a special focus on members of the RAB family due to the possible implication in cancer progression [84]. RAB5a overexpression has been identified to be involved in cancer cell motility and invasiveness. It has been associated with lung, stomach, and hepatocellular carcinomas [85], and with axillary lymph node metastasis in breast cancer patients [86]. Increased RAB31 expression in cancer-associated fibroblasts was suggested to promote colon cancer progression [87].

**Module 77** contains genes whose differential expression is associated with negative regulation of differentiation. **RUNX1** (runt-related transcription factor 1) is known as a tumor suppressor in hematopoietic malignancies. Low RUNX1 expression is associated with poor patient survival [88]. In renal cell carcinoma, **DLX6-AS1** (long non-coding RNA (LncRNA) distal-less homeobox 6 antisense 1) was shown as an oncogene, and its expression was positively correlated with the development and progression of the tumor [89]. DLX6-AS1 promotes cell proliferation, migration and EMT of gastric cancer [90], and enhanced secondary cisplatin resistance of lung squamous cell carcinoma [91]. **GREB1** (an estrogen receptor-regulated tumor promoter) overexpression in ovarian cancer cell lines increased cell proliferation and migration and promoted a mesenchymal morphology [92].

The overexpression of genes from **modules 85 and 89** is associated with CSC maintenance, EMT, invasion and metastasis. The transcription factors SOX, belonging to the sex-determining region Y (SRY)-related HMG-box family, are important for cell fate determination, embryonic and cancer development. RNAseq and Western-blot data indicate that **SOX5** is overexpressed in H295R-PM-Ptc+ cells compared to parental H295R cells. SOX5 is known to participate in EMT in different cancer types (i.e., breast, prostate, hepatocellular, lung adenocarcinoma and osteosarcoma) [93–95]. **SOX13** promotes colorectal cancer metastasis by transactivating SNAI2 and c-MET [96] and regulates cancer stem-like properties and tumorigenicity in hepatocellular carcinoma cells [97]. Calcitonin receptor **CALCR** is a G protein-coupled receptor that binds the peptide hormone calcitonin and is involved in the maintenance of calcium homeostasis. Its overexpression has been shown to keep muscle stem cells in a quiescent state [98]. The forkhead box (Fox) family of transcription factors consists of more than 50 proteins that are Hh signaling targets and involved in tissue-specific transcription and cell fate determination during embryogenesis and cell survival. **FOXP1** was shown to control mesenchymal stem cell commitment and senescence during skeletal aging [99].

Interestingly, the downregulation of two genes from **module 106** are associated with cancer cell phenotype switching: the microphthalmia-associated transcription factor (**MITF**) and the POU domain transcription factor **POU3F2** (better known as BRN2) [100]. Cells with low MITF have been assigned a quiescent invasive phenotype and display invasive properties [101]. Moreover, a low transcriptional activity of MITF would predict poor outcomes for melanoma patients. A zebrafish model that mimics human resistant-melanoma subtypes exhibiting low MITF showed an upregulation of genes involved in stemness and invasiveness [102]. Goding and co-workers reported that the level of MITF induces different states of melanocytes: maintenance of differentiation (MITF-high), proliferation (MITF-intermediate) or slow-proliferative and invasive cells with tumor-initiating properties (MITF-low). Melanoma cells could therefore change reversibly from a proliferative status to an invasive state according to the so-called rheostat model [103].

Therefore, the results from our RNA-seq study are in good agreement with the features of H295R-PM-Ptc+ cells observed in experiments reported in the Figures 1–5, and reveal several aspects that help us to better understand and define H295R-PM-Ptc+ cells:

1. The differential expression of genes from several modules suggests an inhibition of membrane trafficking and endocytosis. Moreover, gene coding for **ST6GAL1** and **CERS6** known to inhibit the clathrin-independent endocytosis mediated by glycosphingolipid and lectins (GL-Lect) [104] are overexpressed in H295R-PM-Ptc+ cells. The differential expression of these genes could inhibit the endocytosis of Ptch1 normally induced by its ligand Sonic hedgehog and explain the presence of Ptch1 at the plasma membrane of H295R-PM-Ptc+ cells.

2. The overexpression of Ptch1 and its presence at the plasma membrane of H295R-PM-Ptc+ cells explains that these cells are more resistant to chemotherapy. Several other genes known to induce chemotherapy resistance are also overexpressed, supporting the chemoresistance feature of these cells.

3. The differential expressions of genes from almost all the modules are involved in cancer progression, cell migration or invasion, and are often associated with poor prognosis.

All these characteristics suggest that these cells are cancer stem-like or persistent cells. Indeed, several differentially expressed genes are known to be involved in stem cell and/or quiescence maintenance. The differential expression of other genes has been associated to de-differentiation in different tumors. Several genes specific to adrenocortical carcinoma are downregulated. One of these genes is **STAR** that encodes for a steroidogenic acute regulatory protein responsible for cholesterol transport to the mitochondria which is the rate-limiting step in steroid hormone production [105]. This transport protein is present in steroid-producing cells such as ovary theca and luteal cells, testis Leydig cells and some adrenocortical cells. A lower expression of steroidogenic enzymes such as STAR is consistent with a less differentiated phenotype. Synaptophysin (**SYP**) is an integral membrane glycoprotein that occurs in presynaptic vesicles of neurons and in similar vesicles of the adrenal medulla. A study from Wiedenmann and co-authors [106] concluded that synaptophysin was expressed independently of other neuronal differentiation markers and proposed that it be used as a differentiation marker in tumor diagnosis. **ZNRF3** was the most frequently altered gene, corresponding to 21% of ACC cases [107]. This gene encodes a cell surface transmembrane E3 ubiquitin ligase that acts as a negative feedback regulator of the canonical Wnt/ $\beta$ -catenin signaling. The study performed on a cohort of 82 adults with ACC suggested that the low expression of ZNRF3 was associated with a decrease in overall survival, while high ZNRF3 expression was associated with optimistic recurrence-free survival and concluded that low expression of ZNRF3 is a negative prognostic marker of ACC [108]. Accumulating evidence indicates that H295R-PM-Ptc+ cells have a de-differentiated state.

Two melanoma cell subpopulations were described as contributing to targeted therapy and immunotherapy resistance [109]. These two subpopulations exhibited a slow cell cycle activity, a de-differentiated state and invasiveness, and were described by two different models, namely, the cancer stem cell (CSC) model and the microphthalmia-associated transcription factor (MITF)-rheostat phenotype switching model. In the CSC model, melanoma cells are organized hierarchically. Cells can differentiate from CSCs to progenitor cells and then to fully differentiated melanoma cells but cannot de-differentiate in the opposite direction. CSCs contribute to cell survival and multidrug resistance. They can give rise to melanoma cell populations more resistant to treatments. In the MITF-rheostat model, melanoma cells are organized horizontally. Their proliferative (high levels of MITF expression (MITF-high) or invasive (low levels of MITF (MITF-low) phenotypes are interchangeable. In this model, therapeutic resistance is induced by senescent subclones exhibiting extremely high or low MITF expression levels. Bai and co-workers [109] proposed a new model explaining the development of therapeutic resistance by the dynamic fluctuation of cell states providing a reservoir of cells for tumor reorganization. This model combines cell state dynamic oscillation at the single-cell level with the cell ensemble continuous reshaping at the population level. This could also be the case of the ACC H295R cell line and explain the presence of a small population of H295R cells with stemness, invasive and chemoresistance properties.

Altogether, our study strongly supports the hypothesis that H295R-PM-Ptc+ sub-population has cancer stem-like or persistent cell properties. If present in ACC patients, these cells could be responsible for therapy resistance, relapse and metastases, and may be eliminated by using a Ptch1 drug efflux inhibitor in combination with chemotherapy. Moreover, the presence of Ptch1 at the cell surface could be a marker of the presence of these persistent cell populations in ACC patient biopsies.

**Supplementary Materials:** The following supporting information can be downloaded at: <https://www.mdpi.com/article/10.3390/pharmaceutics14050988/s1>, Supplementary Materials Table S1: Differential gene expression analysis with DESeq2 was used to estimate the changes between the experimental conditions. Supplementary Materials Table S2: Differentially expressed genes identified by DESeq2 with an adjusted p-value less than 0.05. Supplementary Materials Table S3: Differentially expressed genes identified by DESeq2 with an adjusted p-value less than 0.05 and a log2 fold change greater than 1 or less than −1. Supplementary Materials Table S4: Active gene modules identified by AMINE. Supplementary Materials Table S5: Active gene modules containing one or more genes of interest from Table 1. Supplementary Materials Table S6: Detailed list of enrichments found for each active module from Supplementary Materials Table S3.

**Author Contributions:** Conceptualization and design I.M.-V.; development of methodology I.M.-V., A.M., C.P. (Chloé Prunier), K.L. and C.P. (Claude Pasquier); acquisition of data, Á.J.F.M., A.H., A.M., V.M., A.A. and S.C., analysis and interpretation of data, Á.J.F.M., A.H., A.M., C.P. (Chloé Prunier), K.L., C.P. (Claude Pasquier) and I.M.-V.; writing—original draft, Á.J.F.M. and I.M.-V.; writing—review and editing, Á.J.F.M., A.H., A.M., C.P. (Chloé Prunier), K.L., J.F., C.P. (Claude Pasquier) and I.M.-V.; funding acquisition I.M.-V.; resources, K.L., J.F., C.P. (Chloé Prunier), C.P. (Claude Pasquier) and I.M.-V.; supervision I.M.-V. All authors have read and agreed to the published version of this manuscript.

**Funding:** This work was supported by grants from Centre National de la Recherche Scientifique (CNRS) through the “Soutien au transfert” program, Association France Cancer, Region Provence Alpes Côte d’Azur through the APRF program (2013–17362), Canceropôle PACA, French National Research Agency (ANR) through the Investments for the Future UCA<sup>JEDI</sup> (ANR-15-IDEX-01) and LABEX SIGNALIFE program (ANR-11-LABX-0028-01).

**Institutional Review Board Statement:** The animal study protocol was approved by the Institutional Ethics Committee CEEA (Project CEEA 17-108, number MESR 15476).

**Informed Consent Statement:** Not applicable.

**Acknowledgments:** We are indebted to Carmen Rugiero for the transwell invasion assay. We acknowledge the UCAGenomiX platform, partner of the National Infrastructure France Génomique, supported by the Commissariat Aux Grands Investissements (ANR-10-INBS-09-03, ANR-10-INBS-09-02).

**Conflicts of Interest:** The authors declare no conflict of interest.

## References

1. Andervont, H.B. *Biological Aspects of Cancer*. Julian Huxley. Harcourt, Brace, New York, 1958. 156 pp. \$3.75. *Science* **1958**, *127*, 1440–1441. [CrossRef]
2. Johnson, B.E.; Mazon, T.; Hong, C.; Barnes, M.; Aihara, K.; McLean, C.Y.; Fouse, S.D.; Yamamoto, S.; Ueda, H.; Tatsuno, K.; et al. Mutational Analysis Reveals the Origin and Therapy-Driven Evolution of Recurrent Glioma. *Science* **2014**, *343*, 189–193. [CrossRef] [PubMed]
3. Prieto-Vila, M.; Takahashi, R.-U.; Usuba, W.; Kohama, I.; Ochiya, T. Drug Resistance Driven by Cancer Stem Cells and Their Niche. *Int. J. Mol. Sci.* **2017**, *18*, 2574. [CrossRef] [PubMed]
4. Mikubo, M.; Inoue, Y.; Liu, G.; Tsao, M.-S. Mechanism of Drug Tolerant Persister Cancer Cells: The Landscape and Clinical Implication for Therapy. *J. Thorac. Oncol.* **2021**, *16*, 1798–1809. [CrossRef] [PubMed]
5. Balzerano, A.; Paccosi, E.; Proietti-De-Santis, L. Evolutionary Mechanisms of Cancer Suggest Rational Therapeutic Approaches. *Cytogenet. Genome Res.* **2021**, *161*, 362–371. [CrossRef] [PubMed]
6. Bukowski, K.; Kciuk, M.; Kontek, R. Mechanisms of Multidrug Resistance in Cancer Chemotherapy. *Int. J. Mol. Sci.* **2020**, *21*, 3233. [CrossRef]
7. Ozben, T. Mechanisms and strategies to overcome multiple drug resistance in cancer. *FEBS Lett.* **2006**, *580*, 2903–2909. [CrossRef]
8. Wang, J.-Q.; Yang, Y.; Cai, C.-Y.; Teng, Q.-X.; Cui, Q.; Lin, J.; Assaraf, Y.G.; Chen, Z.-S. Multidrug resistance proteins (MRPs): Structure, function and the overcoming of cancer multidrug resistance. *Drug Resist. Updat.* **2021**, *54*, 100743. [CrossRef]



9. Cree, I.A.; Charlton, P. Molecular chess? Hallmarks of anti-cancer drug resistance. *BMC Cancer* **2017**, *17*, 1–8. [CrossRef]
10. Kathawala, R.J.; Gupta, P.; Ashby, C.R., Jr.; Chen, Z.-S. The modulation of ABC transporter-mediated multidrug resistance in cancer: A review of the past decade. *Drug Resist. Updat.* **2015**, *18*, 1–17. [CrossRef]
11. Robey, R.W.; Pluchino, K.M.; Hall, M.D.; Fojo, A.T.; Bates, S.E.; Gottesman, M.M. Revisiting the role of ABC transporters in multidrug-resistant cancer. *Nat. Rev. Cancer* **2018**, *18*, 452–464. [CrossRef] [PubMed]
12. Scales, S.J.; de Sauvage, F.J. Mechanisms of Hedgehog pathway activation in cancer and implications for therapy. *Trends Pharmacol. Sci.* **2009**, *30*, 303–312. [CrossRef] [PubMed]
13. Cochrane, C.; Szczepny, A.; Watkins, D.N.; Cain, J.E. Hedgehog Signaling in the Maintenance of Cancer Stem Cells. *Cancers* **2015**, *7*, 1554–1585. [CrossRef] [PubMed]
14. Hasanovic, A.; Mus-Veteau, I. Targeting the Multidrug Transporter Ptk1 Potentiates Chemotherapy Efficiency. *Cells* **2018**, *7*, 107. [CrossRef] [PubMed]
15. Saze, Z.; Terashima, M.; Kogure, M.; Ohsuka, F.; Suzuki, H.; Gotoh, M. Activation of the Sonic Hedgehog Pathway and Its Prognostic Impact in Patients with Gastric Cancer. *Dig. Surg.* **2012**, *29*, 115–123. [CrossRef]
16. Xu, X.; Ding, H.; Rao, G.; Arora, S.; Saclarides, C.P.; Esparaz, J.; Gattuso, P.; Solorzano, C.C.; A Prinz, R. Activation of the Sonic Hedgehog pathway in thyroid neoplasms and its potential role in tumor cell proliferation. *Endocr. -Relat. Cancer* **2012**, *19*, 167–179. [CrossRef]
17. Bidet, M.; Tomico, A.; Martin, P.; Guizouarn, H.; Mollat, P.; Mus-Veteau, I. The Hedgehog Receptor Patched Functions in Multidrug Transport and Chemotherapy Resistance. *Mol. Cancer Res.* **2012**, *10*, 1496–1508. [CrossRef]
18. Hasanovic, A.; Ruggiero, C.; Jung, S.; Rapa, I.; Signetti, L.; Ben Hadj, M.; Terzolo, M.; Beuschlein, F.; Volante, M.; Hantel, C.; et al. Targeting the multidrug transporter Patched potentiates chemotherapy efficiency on adrenocortical carcinoma in vitro and in vivo. *Int. J. Cancer* **2018**, *143*, 199–211. [CrossRef]
19. Signetti, L.; Elizarov, N.; Simsir, M.; Paquet, A.; Douguet, D.; Labbal, F.; Debayle, D.; Di Giorgio, A.; Biou, V.; Girard, C.; et al. Inhibition of Patched Drug Efflux Increases Vemurafenib Effectiveness against Resistant BrafV600E Melanoma. *Cancers* **2020**, *12*, 1500. [CrossRef]
20. Lalli, E.; Luconi, M. The next step: Mechanisms driving adrenocortical carcinoma metastasis. *Endocr. Relat. Cancer* **2018**, *25*, R31–R48. [CrossRef]
21. Uchihara, M.; Tanioka, M.; Kojima, Y.; Nishikawa, T.; Sudo, K.; Shimoi, T.; Noguchi, E.; Maeshima, A.M.; Yonemori, K. Clinical management and outcomes associated with etoposide, doxorubicin, and cisplatin plus mitotane treatment in metastatic adrenocortical carcinoma: A single institute experience. *Int. J. Clin. Oncol.* **2021**, *26*, 2275–2281. [CrossRef] [PubMed]
22. Edamaghi, M.; Wojtkowiak, J.W.; Gillies, R.J. pH sensing and regulation in cancer. *Front. Physiol.* **2013**, *4*, 370. [CrossRef]
23. Fiorini, L.; Mus-Veteau, I. Method to Screen Multidrug Transport Inhibitors Using Yeast Overexpressing a Human MDR Transporter. In *Heterologous Expression of Membrane Proteins*; Humana Press: New York, NY, USA, 2016; Volume 1432, pp. 303–318. [CrossRef]
24. Durand, N.; Simsir, M.; Signetti, L.; Labbal, F.; Ballotti, R.; Mus-Veteau, I. Methiothepin Increases Chemotherapy Efficacy against Resistant Melanoma Cells. *Molecules* **2021**, *26*, 1867. [CrossRef] [PubMed]
25. Hasanovic, A.; Simsir, M.; Choveau, F.S.; Lalli, E.; Mus-Veteau, I. Astemizole Sensitizes Adrenocortical Carcinoma Cells to Doxorubicin by Inhibiting Patched Drug Efflux Activity. *Biomedicines* **2020**, *8*, 251. [CrossRef] [PubMed]
26. Fiorini, L.; Tribalat, M.-A.; Sauvard, L.; Cazareth, J.; Lalli, E.; Broutin, I.; Thomas, O.P.; Mus-Veteau, I. Natural paniceins from mediterranean sponge inhibit the multidrug resistance activity of Patched and increase chemotherapy efficiency on melanoma cells. *Oncotarget* **2015**, *6*, 22282–22297. [CrossRef] [PubMed]
27. Funakoshi, K.; Bagheri, M.; Zhou, M.; Suzuki, R.; Abe, H.; Akashi, H. Highly sensitive and specific Alu-based quantification of human cells among rodent cells. *Sci. Rep.* **2017**, *7*, 1–12. [CrossRef]
28. Mus-Veteau, I. Comparison of Gene Expression between Parental Adrenocortical Carcinoma Cells and a Subpopulation Overexpressing Ptk1. Available online: <https://www.ncbi.nlm.nih.gov/geo/query/acc.cgi?acc=GSE189424> (accessed on 19 January 2022).
29. Shannon, P.; Markiel, A.; Ozier, O.; Baliga, N.S.; Wang, J.T.; Ramage, D.; Amin, N.; Schwikowski, B.; Ideker, T. Cytoscape: A software environment for integrated models of Biomolecular Interaction Networks. *Genome Res.* **2003**, *13*, 2498–2504. [CrossRef]
30. Doncheva, N.T.; Morris, J.H.; Gorodkin, J.; Jensen, L.J. Cytoscape StringApp: Network Analysis and Visualization of Proteomics Data. *J. Proteome Res.* **2018**, *18*, 623–632. [CrossRef]
31. Pasquier, C.; Guerlais, V.; Pallez, D.; Rapetti-Mauss, R.; Soriani, O. Identification of active modules in interaction networks using node2vec network embedding. *bioRxiv* **2021**, 2021.09.22.461345. [CrossRef]
32. Szklarczyk, D.; Morris, J.H.; Cook, H.; Kuhn, M.; Wyder, S.; Simonovic, M.; Santos, A.; Doncheva, N.T.; Roth, A.; Bork, P.; et al. The STRING database in 2017: Quality-controlled protein–protein association networks, made broadly accessible. *Nucleic Acids Res.* **2017**, *45*, D362–D368. [CrossRef]
33. Grover, A.; Leskovec, J. node2vec. *KDD* **2016**, 2016, 855–864. [CrossRef] [PubMed]
34. Pasquier, C. Active Module Deletion with AMINE Algorithm. Available online: <http://amine.i3s.unice.fr/> (accessed on 10 January 2022).

35. Izzi, L.; Lévesque, M.; Morin, S.; Laniel, D.; Wilkes, B.C.; Mille, F.; Krauss, R.S.; McMahon, A.P.; Allen, B.L.; Charron, F. Boc and Gas1 Each Form Distinct Shh Receptor Complexes with Ptch1 and Are Required for Shh-Mediated Cell Proliferation. *Dev. Cell* **2011**, *20*, 788–801. [CrossRef] [PubMed]
36. Zhou, H.-M.; Zhang, J.-G.; Zhang, X.; Li, Q. Targeting cancer stem cells for reversing therapy resistance: Mechanism, signaling, and prospective agents. *Signal Transduct. Target. Ther.* **2021**, *6*, 62. [CrossRef] [PubMed]
37. Najafi, M.; Farhood, B.; Mortezaee, K. Cancer stem cells (CSCs) in cancer progression and therapy. *J. Cell. Physiol.* **2019**, *234*, 8381–8395. [CrossRef] [PubMed]
38. Im, S.; Choi, H.J.; Yoo, C.; Jung, J.-H.; Jeon, Y.-W.; Suh, Y.J.; Kang, C.S. Hedgehog Related Protein Expression in Breast Cancer: Gli-2 Is Associated with Poor Overall Survival. *Korean J. Pathol.* **2013**, *47*, 116–123. [CrossRef]
39. Papadopoulos, V.; Tsapakidis, K.; Galdo, N.R.-D.; Papandreou, C.N.; Del Galdo, F.; Anthoney, A.; Sakellaridis, N.; Dimas, K.; Kamposioras, K. The Prognostic Significance of the Hedgehog Signaling Pathway in Colorectal Cancer. *Clin. Color. Cancer* **2016**, *15*, 116–127. [CrossRef]
40. Zhu, W.; You, Z.; Li, T.; Yu, C.; Tao, G.; Hu, M.; Chen, X. Correlation of Hedgehog Signal Activation with Chemoradio-therapy Sensitivity and Survival in Esophageal Squamous Cell Carcinomas. *Jpn. J. Clin. Oncol.* **2010**, *41*, 386–393. [CrossRef]
41. Gonnissen, A.; Isebaert, S.; Perneel, C.; McKee, C.M.; Van Utterbeeck, F.; Lerut, E.; Verrill, C.; Bryant, R.J.; Joniau, S.; Muschel, R.J.; et al. Patched 1 Expression Correlates with Biochemical Relapse in High-Risk Prostate Cancer Patients. *Am. J. Pathol.* **2018**, *188*, 795–804. [CrossRef]
42. Delloye-Bourgeois, C.; Gibert, B.; Rama, N.; Delcros, J.-G.; Gadot, N.; Scoazec, J.-Y.; Krauss, R.; Bernet, A.; Mehlen, P. Sonic Hedgehog Promotes Tumor Cell Survival by Inhibiting CDON Pro-Apoptotic Activity. *PLOS Biol.* **2013**, *11*, e1001623. [CrossRef]
43. Mille, F.; Tamayo-Orrego, L.; Lévesque, M.; Remke, M.; Korshunov, A.; Cardin, J.; Bouchard, N.; Izzi, L.; Kool, M.; Northcott, P.A.; et al. The Shh Receptor Boc Promotes Progression of Early Medulloblastoma to Advanced Tumors. *Dev. Cell* **2014**, *31*, 34–47. [CrossRef]
44. Song, J.Y.; Holtz, A.M.; Pinskey, J.M.; Allen, B.L. Distinct structural requirements for CDON and BOC in the promotion of Hedgehog signaling. *Dev. Biol.* **2015**, *402*, 239–252. [CrossRef] [PubMed]
45. Kaszak, I.; Witkowska-Piłaszewicz, O.; Niewiadomska, Z.; Dworecka-Kaszak, B.; Toka, F.N.; Jurka, P. Role of Cadherins in Cancer—A Review. *Int. J. Mol. Sci.* **2020**, *21*, 7624. [CrossRef] [PubMed]
46. Da, C.; Wu, K.; Yue, C.; Bai, P.; Wang, R.; Wang, G.; Zhao, M.; Lv, Y.; Hou, P. N-cadherin promotes thyroid tumorigenesis through modulating major signaling pathways. *Oncotarget* **2016**, *8*, 8131–8142. [CrossRef] [PubMed]
47. Luo, S.; Lin, R.; Liao, X.; Li, D.; Qin, Y. Identification and verification of the molecular mechanisms and prognostic values of the cadherin gene family in gastric cancer. *Sci. Rep.* **2021**, *11*, 23674. [CrossRef] [PubMed]
48. Chen, T.-J.; Dehghanian, S.Z.; Chan, T.-C.; He, H.-L.; Li, W.-S.; Abdollahi, S.; Chen, N.-Y.; Li, C.-F.; Shiue, Y.-L. High G protein subunit beta 4 protein level is correlated to poor prognosis of urothelial carcinoma. *Med Mol. Morphol.* **2021**, *54*, 356–367. [CrossRef]
49. Zhou, W.; Gross, K.M.; Kuperwasser, C. Molecular regulation of Snai2 in development and disease. *J. Cell Sci.* **2019**, *132*, jcs235127. [CrossRef]
50. You, S.; Knudsen, B.S.; Erho, N.; Alshalalfa, M.; Takhar, M.; Al-Deen Ashab, H.; Davicioni, E.; Karnes, R.J.; Klein, E.A.; Den, R.B.; et al. Integrated Classification of Prostate Cancer Reveals a Novel Luminal Subtype with Poor Outcome. *Cancer Res.* **2016**, *76*, 4948–4958. [CrossRef]
51. Haslehurst, A.M.; Koti, M.; Dharsee, M.; Nuin, P.; Evans, K.; Geraci, J.; Childs, T.; Chen, J.; Li, J.; Weberpals, J.; et al. EMT transcription factors snail and slug directly contribute to cisplatin resistance in ovarian cancer. *BMC Cancer* **2012**, *12*, 91. [CrossRef]
52. Li, L.; Duan, Z.; Yu, J.; Dang, H.-X. NFATc1 regulates cell proliferation, migration, and invasion of ovarian cancer SKOV3 cells in vitro and in vivo. *Oncol. Rep.* **2016**, *36*, 918–928. [CrossRef]
53. Britzen-Laurent, N.; Lipnik, K.; Ocker, M.; Naschberger, E.; Schellerer, V.S.; Croner, R.S.; Vieth, M.; Waldner, M.; Steinberg, P.; Hohenadl, C.; et al. GBP-1 acts as a tumor suppressor in colorectal cancer cells. *Carcinogenesis* **2012**, *34*, 153–162. [CrossRef]
54. Wang, J.; Min, H.; Hu, B.; Xue, X.; Liu, Y. Guanylate-binding protein-2 inhibits colorectal cancer cell growth and increases the sensitivity to paclitaxel of paclitaxel-resistant colorectal cancer cells by interfering Wnt signaling. *J. Cell. Biochem.* **2019**, *121*, 1250–1259. [CrossRef] [PubMed]
55. Xie, G.; Dong, P.; Chen, H.; Xu, L.; Liu, Y.; Ma, Y.; Zheng, Y.; Yang, J.; Zhou, Y.; Chen, L.; et al. Decreased expression of ATF3, orchestrated by  $\beta$ -catenin/TCF3, miR-17-5p and HOXA11-AS, promoted gastric cancer progression via increased  $\beta$ -catenin and CEMIP. *Exp. Mol. Med.* **2021**, *53*, 1706–1722. [CrossRef] [PubMed]
56. Huang, C.; Chen, C.; Zheng, F.; Ni, X.; Lin, J.; Wu, W.; Lai, X. ATF3 inhibits the growth and stem cells-like features of SW620 colorectal cancer cells in vitro. *J. Mens. Health* **2021**, *17*, 287–294. [CrossRef]
57. Shi, Q.; Yan, X.; Wang, J.; Zhang, X. Collagen Family Genes Associated with Risk of Recurrence after Radiation Therapy for Vestibular Schwannoma and Pan-Cancer Analysis. *Dis. Markers* **2021**, *2021*, 1–15. [CrossRef] [PubMed]
58. Zhang, L.; Wang, L.; Yang, H.; Li, C.; Fang, C. Identification of potential genes related to breast cancer brain metastasis in breast cancer patients. *Biosci. Rep.* **2021**, *41*, BSR20211615. [CrossRef] [PubMed]
59. Wang, L.; Wu, H.; Wang, L.; Zhang, H.; Lu, J.; Liang, Z.; Liu, T. Asporin promotes pancreatic cancer cell invasion and migration by regulating the epithelial-to-mesenchymal transition (EMT) through both autocrine and paracrine mechanisms. *Cancer Lett.* **2017**, *398*, 24–36. [CrossRef] [PubMed]


60. Itoh, G.; Takagane, K.; Fukushi, Y.; Kuriyama, S.; Umakoshi, M.; Goto, A.; Yanagihara, K.; Yashiro, M.; Tanaka, M. Cancer-associated fibroblasts educate normal fibroblasts to facilitate cancer cell spreading and T-cell suppression. *Mol. Oncol.* **2021**, *16*, 166–187. [CrossRef]
61. Sasaki, Y.; Takagane, K.; Konno, T.; Itoh, G.; Kuriyama, S.; Yanagihara, K.; Yashiro, M.; Yamada, S.; Murakami, S.; Tanaka, M. Expression of asporin reprograms cancer cells to acquire resistance to oxidative stress. *Cancer Sci.* **2021**, *112*, 1251–1261. [CrossRef]
62. Chi, L.-H.; Chang, W.-M.; Chang, Y.-C.; Chan, Y.-C.; Tai, C.-C.; Leung, K.-W.; Chen, C.-L.; Wu, A.T.; Lai, T.-C.; Li, Y.-C.; et al. Global Proteomics-based Identification and Validation of Thymosin Beta-4 X-Linked as a Prognostic Marker for Head and Neck Squamous Cell Carcinoma. *Sci. Rep.* **2017**, *7*, 1–13. [CrossRef]
63. Duerr, E.-M.; Mizukami, Y.; Ng, A.; Xavier, R.J.; Kikuchi, H.; Deshpande, V.; Warshaw, A.L.; Glickman, J.; Kulke, M.H.; Chung, D.C. Defining molecular classifications and targets in gastroenteropancreatic neuroendocrine tumors through DNA microarray analysis. *Endocr. Relat. Cancer* **2008**, *15*, 243–256. [CrossRef]
64. Hirata, N.; Yamada, S.; Shoda, T.; Kurihara, M.; Sekino, Y.; Kanda, Y. Sphingosine-1-phosphate promotes expansion of cancer stem cells via S1PR3 by a ligand-independent Notch activation. *Nat. Commun.* **2014**, *5*, 4806. [CrossRef] [PubMed]
65. Yang, C.; Yamashita, M.; Suda, T. A Novel Function of Sphingolipid Signaling via S1PR3 in Hematopoietic and Leukemic Stem Cells. *Blood Cancer Discov.* **2020**, *2*, 3–5. [CrossRef] [PubMed]
66. Watters, R.J.; Wang, H.-G.; Sung, S.-S.; Loughran, T.P.; Liu, X. Targeting sphingosine-1-phosphate receptors in cancer. *Anti-Cancer Agents Med. Chem.* **2011**, *11*, 810–817. [CrossRef] [PubMed]
67. Chen, X.; Fu, Y.; Xu, H.; Teng, P.; Xie, Q.; Zhang, Y.; Yan, C.; Xu, Y.; Li, C.; Zhou, J.; et al. SOX5 predicts poor prognosis in lung adenocarcinoma and promotes tumor metastasis through epithelial-mesenchymal transition. *Oncotarget* **2017**, *9*, 10891–10904. [CrossRef] [PubMed]
68. Tanaka, H.; Kanda, M.; Miwa, T.; Umeda, S.; Sawaki, K.; Tanaka, C.; Kobayashi, D.; Hayashi, M.; Yamada, S.; Nakayama, G.; et al. G-protein subunit gamma-4 expression has potential for detection, prediction and therapeutic targeting in liver metastasis of gastric cancer. *Br. J. Cancer* **2021**, *125*, 220–228. [CrossRef] [PubMed]
69. Laurberg, J.R.; Jensen, J.B.; Schepeler, T.; Borre, M.; Ørntoft, T.F.; Dyrskjøt, L. High expression of GEM and EDNRA is associated with metastasis and poor outcome in patients with advanced bladder cancer. *BMC Cancer* **2014**, *14*, 1–10. [CrossRef]
70. Kashiwagi, E.; Shiota, M.; Yokomizo, A.; Itsumi, M.; Inokuchi, J.; Uchiumi, T.; Naito, S. Prostaglandin receptor EP3 mediates growth inhibitory effect of aspirin through androgen receptor and contributes to castration resistance in prostate cancer cells. *Endocr. Relat. Cancer* **2013**, *20*, 431–441. [CrossRef]
71. Fa, J. Dynamin 3 overexpression suppresses the proliferation, migration and invasion of cervical cancer cells. *Oncol. Lett.* **2021**, *22*, 1–8. [CrossRef]
72. Hu, M.; Gu, J.; Su, W.; Zhang, Z.; Zhu, B.; Wang, Q.; Xing, C. DNMI1: A Prognostic Biomarker Associated with Immune Infiltration in Colon Cancer—A Study Based on TCGA Database. *BioMed Res. Int.* **2021**, *2021*, 1–9. [CrossRef]
73. Rao, D.; Hyun, T.S.; Kumar, P.D.; Mizukami, I.F.; Rubin, M.A.; Lucas, P.; Sanda, M.G.; Ross, T.S. Huntingtin-interacting protein 1 is overexpressed in prostate and colon cancer and is critical for cellular survival. *J. Clin. Investig.* **2002**, *110*, 351–360. [CrossRef]
74. Sheridan, M.; Ogrtmen, B. The Role of Ceramide Metabolism and Signaling in the Regulation of Mitophagy and Cancer Therapy. *Cancers* **2021**, *13*, 2475. [CrossRef] [PubMed]
75. Schömel, N.; Gruber, L.; Alexopoulos, S.J.; Trautmann, S.; Olzomer, E.M.; Byrne, F.L.; Hoehn, K.L.; Gurke, R.; Thomas, D.; Ferreirós, N.; et al. UGCG overexpression leads to increased glycolysis and increased oxidative phosphorylation of breast cancer cells. *Sci. Rep.* **2020**, *10*, 8182. [CrossRef] [PubMed]
76. Suzuki, M.; Cao, K.; Kato, S.; Mizutani, N.; Tanaka, K.; Arima, C.; Tai, M.C.; Nakatani, N.; Yanagisawa, K.; Takeuchi, T.; et al. CERS6 required for cell migration and metastasis in lung cancer. *J. Cell. Mol. Med.* **2020**, *24*, 11949–11959. [CrossRef] [PubMed]
77. Singh, R.R.; Kunkalla, K.; Qu, C.; Schlette, E.; Neelapu, S.S.; Samaniego, F.; Vega, F. ABCG2 is a direct transcriptional target of hedgehog signaling and involved in stroma-induced drug tolerance in diffuse large B-cell lymphoma. *Oncogene* **2011**, *30*, 4874–4886. [CrossRef] [PubMed]
78. Zhang, Q.; Zhu, M.; Cheng, W.; Xing, R.; Li, W.; Zhao, M.; Xu, L.; Li, E.; Luo, G.; Lu, Y. Downregulation of 425G>A variant of calcium-binding protein S100A14 associated with poor differentiation and prognosis in gastric cancer. *J. Cancer Res. Clin. Oncol.* **2014**, *141*, 691–703. [CrossRef] [PubMed]
79. Bharadwaj, A.; Bydoun, M.; Holloway, R.; Waisman, D. Annexin A2 Heterotetramer: Structure and Function. *Int. J. Mol. Sci.* **2013**, *14*, 6259–6305. [CrossRef]
80. Hitchcock, J.K.; Katz, A.A.; Schäfer, G. Dynamic reciprocity: The role of annexin A2 in tissue integrity. *J. Cell Commun. Signal.* **2014**, *8*, 125–133. [CrossRef]
81. Taylor, J.R.; Fernandez, D.J.; Thornton, S.M.; Skeate, J.; Lühen, K.P.; Da Silva, D.M.; Langen, R.; Kast, W.M. Heterotetrameric annexin A2/S100A10 (A2t) is essential for oncogenic human papillomavirus trafficking and capsid disassembly, and protects virions from lysosomal degradation. *Sci. Rep.* **2018**, *8*, 1–15. [CrossRef]
82. Zhang, J.; Guo, B.; Zhang, Y.; Cao, J.; Chen, T. Silencing of the annexin II gene down-regulates the levels of S100A10, c-Myc, and plasmin and inhibits breast cancer cell proliferation and invasion. *Saudi Med. J.* **2010**, *31*, 374–381.
83. Shen, D.; Nooraie, F.; Elshimali, Y.; Lonsberry, V.; He, J.; Bose, S.; Chia, D.; Seligson, D.; Chang, H.R.; Goodglick, L. Decreased expression of annexin A1 is correlated with breast cancer development and progression as determined by a tissue microarray analysis. *Hum. Pathol.* **2006**, *37*, 1583–1591. [CrossRef]

84. Chua, C.E.L.; Tang, B.L. The role of the smallGTPase Rab31 in cancer. *J. Cell. Mol. Med.* **2014**, *19*, 1–10. [CrossRef] [PubMed]
85. Zhao, Z.; Liu, X.-F.; Wu, H.-C.; Zou, S.-B.; Wang, J.-Y.; Ni, P.-H.; Chen, X.-H.; Fan, Q.-S. Rab5a overexpression promoting ovarian cancer cell proliferation may be associated with APPL1-related epidermal growth factor signaling pathway. *Cancer Sci.* **2010**, *101*, 1454–1462. [CrossRef] [PubMed]
86. Yang, P.-S.; Yin, P.-H.; Tseng, L.-M.; Yang, C.-H.; Hsu, C.-Y.; Lee, M.-Y.; Horng, C.-F.; Chi, C.-W. Rab5A is associated with axillary lymph node metastasis in breast cancer patients. *Cancer Sci.* **2011**, *102*, 2172–2178. [CrossRef] [PubMed]
87. Yang, T.; Zhiheng, H.; Zhanhuai, W.; Qian, X.; Yue, L.; Xiaoxu, G.; Jingsun, W.; Shu, Z.; Kefeng, D. Increased RAB31 Expression in Cancer-Associated Fibroblasts Promotes Colon Cancer Progression Through HGF-MET Signaling. *Front. Oncol.* **2020**, *10*, 1747. [CrossRef]
88. Hong, D.; Fritz, A.J.; Finstad, K.H.; Fitzgerald, M.P.; Weinheimer, A.; Viens, A.L.; Ramsey, J.; Stein, J.L.; Lian, J.B.; Stein, G.S. Suppression of Breast Cancer Stem Cells and Tumor Growth by the RUNX1 Transcription Factor. *Mol. Cancer Res.* **2018**, *16*, 1952–1964. [CrossRef]
89. Zhao, Z.; Liang, S.; Sun, F. LncRNA DLX6-AS1 Promotes Malignant Phenotype and Lymph Node Metastasis in Prostate Cancer by Inducing LARGE Methylation. *Front. Oncol.* **2020**, *10*, 1172. [CrossRef]
90. Wu, Q.; Ma, J.; Meng, W.; Hui, P. DLX6-AS1 promotes cell proliferation, migration and EMT of gastric cancer through FUS-regulated MAP4K1. *Cancer Biol. Ther.* **2019**, *21*, 17–25. [CrossRef]
91. Zhao, X.; Wang, J.; Zhu, R.; Zhang, J.; Zhang, Y. DLX6-AS1 activated by H3K4me1 enhanced secondary cisplatin resistance of lung squamous cell carcinoma through modulating miR-181a-5p/miR-382-5p/CELF1 axis. *Sci. Rep.* **2021**, *11*, 1–13. [CrossRef]
92. Hodgkinson, K.; Forrest, L.A.; Vuong, N.; Garson, K.; Djordjevic, B.; Vanderhyden, B.C. GREB1 is an estrogen receptor-regulated tumour promoter that is frequently expressed in ovarian cancer. *Oncogene* **2018**, *37*, 5873–5886. [CrossRef]
93. Hu, J.; Tian, J.; Zhu, S.; Sun, L.; Yu, J.; Tian, H.; Dong, Q.; Luo, Q.; Jiang, N.; Niu, Y.; et al. Sox5 contributes to prostate cancer metastasis and is a master regulator of TGF- $\beta$ -induced epithelial mesenchymal transition through controlling Twist1 expression. *Br. J. Cancer* **2017**, *118*, 88–97. [CrossRef]
94. Chen, Y.; Yang, L.; Qin, Y.; Liu, S.; Qiao, Y.; Wan, X.; Zeng, H.; Tang, X.; Liu, M.; Hou, Y. Effects of differential distributed-JUP on the malignancy of gastric cancer. *J. Adv. Res.* **2020**, *28*, 195–208. [CrossRef] [PubMed]
95. Sun, C.; Ban, Y.; Wang, K.; Sun, Y.; Zhao, Z. SOX5 promotes breast cancer proliferation and invasion by transactivation of EZH2. *Oncol. Lett.* **2019**, *17*, 2754–2762. [CrossRef] [PubMed]
96. Du, F.; Li, X.; Feng, W.; Qiao, C.; Chen, J.; Jiang, M.; Qiu, Z.; Qian, M.; Tian, D.; Nie, Y.; et al. SOX13 promotes colorectal cancer metastasis by transactivating SNAI2 and c-MET. *Oncogene* **2020**, *39*, 3522–3540. [CrossRef] [PubMed]
97. Jiao, H.; Fang, F.; Fang, T.; You, Y.; Feng, M.; Wang, X.; Yin, Z.; Zhao, W. SOX13 regulates cancer stem-like properties and tumorigenicity in hepatocellular carcinoma cells. *Am. J. Cancer Res.* **2021**, *11*, 760–772. [PubMed]
98. Yamaguchi, M.; Watanabe, Y.; Ohtani, T.; Uezumi, A.; Mikami, N.; Nakamura, M.; Sato, T.; Ikawa, M.; Hoshino, M.; Tsuchida, K.; et al. Calcitonin Receptor Signaling Inhibits Muscle Stem Cells from Escaping the Quiescent State and the Niche. *Cell Rep.* **2015**, *13*, 302–314. [CrossRef]
99. Li, H.; Liu, P.; Xu, S.; Li, Y.; Dekker, J.D.; Li, B.; Fan, Y.; Zhang, Z.; Hong, Y.; Yang, G.; et al. FOXP1 controls mesenchymal stem cell commitment and senescence during skeletal aging. *J. Clin. Investig.* **2017**, *127*, 1241–1253. [CrossRef]
100. Simmons, J.; Pierce, C.J.; Al-Ejeh, F.; Boyle, G.M. MITF and BRN2 contribute to metastatic growth after dissemination of melanoma. *Sci. Rep.* **2017**, *7*, 1–12. [CrossRef]
101. Carreira, S.; Goodall, J.; Denat, L.; Rodriguez, M.; Nuciforo, P.; Hoek, K.S.; Testori, A.; LaRue, L.; Goding, C.R. Mitf regulation of Dia1 controls melanoma proliferation and invasiveness. *Genes Dev.* **2006**, *20*, 3426–3439. [CrossRef]
102. Travnickova, J.; Wojciechowska, S.; Khamseh, A.; Gautier, P.; Brown, D.V.; Lefevre, T.; Brombin, A.; Ewing, A.; Capper, A.; Spitzer, M.; et al. Zebrafish MITF-Low Melanoma Subtype Models Reveal Transcriptional Subclusters and MITF-Independent Residual Disease. *Cancer Res.* **2019**, *79*, 5769–5784. [CrossRef]
103. Hoek, K.S.; Goding, C.R. Cancer stem cells versus phenotype-switching in melanoma. *Pigment. Cell Melanoma Res.* **2010**, *23*, 746–759. [CrossRef]
104. Johannes, L. The Cellular and Chemical Biology of Endocytic Trafficking and Intracellular Delivery—The GL-Lect Hypothesis. *Molecules* **2021**, *26*, 3299. [CrossRef] [PubMed]
105. Christenson, L. Steroidogenic acute regulatory protein (StAR) and the intramitochondrial translocation of cholesterol. *Biochim. Biophys. Acta Mol. Cell Biol. Lipids* **2000**, *1529*, 175–187.
106. Wiedenmann, B.; Franke, W.W.; Kuhn, C.; Moll, R.; E Gould, V. Synaptophysin: A marker protein for neuroendocrine cells and neoplasms. *Proc. Natl. Acad. Sci. USA* **1986**, *83*, 3500–3504. [CrossRef] [PubMed]
107. Faillot, S.; Assie, G. ENDOCRINE TUMOURS: The genomics of adrenocortical tumors. *Eur. J. Endocrinol.* **2016**, *174*, R249–R265. [CrossRef]
108. Brondani, V.; Lacombe, A.; Mariani, B.; Montenegro, L.; Soares, I.; Bezerra-Neto, J.; Tanno, F.; Srougi, V.; Chambo, J.; Mendonca, B.; et al. Low Protein Expression of both ATRX and ZNRF3 as Novel Negative Prognostic Markers of Adult Adrenocortical Carcinoma. *Int. J. Mol. Sci.* **2021**, *22*, 1238. [CrossRef]
109. Bai, X.; Fisher, D.E.; Flaherty, K.T. Cell-state dynamics and therapeutic resistance in melanoma from the perspective of MITF and IFN $\gamma$  pathways. *Nat. Rev. Clin. Oncol.* **2019**, *16*, 549–562. [CrossRef]



Article

# CHRNA5 Contributes to Hepatocellular Carcinoma Progression by Regulating YAP Activity

Yan Fu <sup>1,†</sup> , Hongfei Ci <sup>1,†</sup> , Wei Du <sup>1</sup>, Qiongzhu Dong <sup>1,2,\*</sup>  and Huliang Jia <sup>1,\*</sup>

<sup>1</sup> Department of General Surgery, Huashan Hospital, Fudan University, Shanghai 200040, China; 19111220072@fudan.edu.cn (Y.F.); 20211220051@fudan.edu.cn (H.C.); 21211220043@fudan.edu.cn (W.D.)

<sup>2</sup> Key Laboratory of Whole-Period Monitoring and Precise Intervention of Digestive Cancer, Shanghai Municipal Health Commission (SMHC), Institute of Fudan-Minhang Academic Health System, Minhang Hospital, Fudan University, Shanghai 200437, China

\* Correspondence: qzhdong@fudan.edu.cn (Q.D.); huliangjia@fudan.edu.cn (H.J.); Tel./Fax: +86-21-5423-7960 (Q.D.); +86-21-5288-7175 (H.J.)

† These authors contributed equally to this work.

**Abstract:** Hepatocellular carcinoma (HCC) is a major health concern worldwide. A better understanding of the mechanisms underlying the malignant phenotype is necessary for developing novel therapeutic strategies for HCC. Signaling pathways initiated by neurotransmitter receptors, such as  $\alpha 5$ -nicotinic acetylcholine receptor (CHRNA5), have been reported to be implicated in tumor progression. However, the functional mechanism of CHRNA5 in HCC remains unclear. In this study, we explored the role of CHRNA5 in HCC and found that CHRNA5 expression was increased in human HCC tissues and positively correlated with the T stage ( $p < 0.05$ ) and AJCC phase ( $p < 0.05$ ). The KM plotter database showed that the high expression level of CHRNA5 was strongly associated with worse survival in HCC patients. Both in vitro and in vivo assays showed that CHRNA5 regulates the proliferation ability of HCC by regulating YAP activity. In addition, CHRNA5 promotes the stemness of HCC by regulating stemness-associated genes, such as Nanog, Sox2 and OCT4. Cell migration and invasion assays demonstrated that CHRNA5 significantly enhanced the metastasis of HCC by regulating epithelial–mesenchymal transition (EMT)-associated genes. Furthermore, we found that CHRNA5 regulates the sensitivity of sorafenib in HCC. Our findings suggest that CHRNA5 plays a key role in the progression and drug resistance of HCC, and targeting CHRNA5 may be a strategy for the treatment of HCC.

**Keywords:** HCC; CHRNA5; metastasis; stemness property; sorafenib sensitivity

**Citation:** Fu, Y.; Ci, H.; Du, W.; Dong, Q.; Jia, H. CHRNA5 Contributes to Hepatocellular Carcinoma Progression by Regulating YAP Activity. *Pharmaceutics* **2022**, *14*, 275. <https://doi.org/10.3390/pharmaceutics14020275>

Academic Editors: Hassan Bousbaa and Patrick J. Sinko

Received: 7 December 2021

Accepted: 20 January 2022

Published: 25 January 2022

**Publisher's Note:** MDPI stays neutral with regard to jurisdictional claims in published maps and institutional affiliations.



**Copyright:** © 2022 by the authors. Licensee MDPI, Basel, Switzerland. This article is an open access article distributed under the terms and conditions of the Creative Commons Attribution (CC BY) license (<https://creativecommons.org/licenses/by/4.0/>).

## 1. Introduction

HCC, one of the most common fatal tumors with an increasing incidence rate, is the fourth most common cause of cancer-related death worldwide [1]. Various factors, including chronic hepatitis B virus (HBV) infection, alcohol consumption, and type 2 diabetes, are regarded as triggers for HCC development [2,3]. Although great efforts have been made in developing innovative therapeutic strategies for HCC, the five-year survival rate remains low, mainly due to the high rates of drug resistance, tumor metastasis, and recurrence [4]. Sorafenib is a well-known treatment agent for HCC. By targeting several tyrosine kinases, such as VEGFR, PDGFR, and RAF, sorafenib can suppress the proliferation and angiogenesis of tumors [5]. However, limited benefits were observed in HCC patients receiving sorafenib treatment, mainly due to the development of drug resistance [6]. HCC cells that survived long-term treatment with sorafenib exhibited enhanced stemness properties and an EMT phenotype, which were closely associated with the resistance of various anticancer therapies and cancer remission [7]. Thus, deciphering the mechanisms underlying stemness properties and sorafenib resistance is essential for HCC treatment.

The Hippo signaling pathway plays a crucial role in regulating organ development, tissue homeostasis, and regeneration [8]. Dysregulation of the Hippo signaling pathway has already been observed in multiple tumors, including HCC [9]. Yes-associated protein (YAP) and tafazzin (TAZ), two core transcriptional coactivators in the Hippo signaling pathway, are regulated by a series of kinase cascades consisting of the serine/threonine kinases mammalian sterile 20-like kinase 1 and 2 (MST1 and MST2) and large tumor suppressor 1 and 2 (LATS1 and LATS2) [10]. YAP and TAZ were retained in the cytoplasm and deprived of transcriptional activity after being phosphorylated by LATS1/2. Inactivation of the Hippo signaling pathway leads to increased YAP activity, contributing to the enhanced malignant phenotype of tumor cells. In HCC, Hippo signaling can inhibit HCC formation, and activation of YAP transcription activity is critical for HCC proliferation [11]. The contribution of YAP to drug resistance in HCC was also reported, and manipulating YAP activity may be a plausible therapeutic strategy for HCC.

Nicotinic acetylcholine receptors (nAChRs), ligand-gated ion channels that are mainly expressed in the plasma membranes of certain neurons on the postsynaptic side of the neuromuscular junction, are also expressed in some non-neuronal cells [12]. nAChRs can be activated to mediate fast signal transmission at synapses by the endogenous neurotransmitter acetylcholine (ACh) or by the exogenous tertiary alkaloids nicotine and tobacco alkaloid [13–15]. nAChR-based targeted therapies for nervous system disorders, including Alzheimer's disease, depression, Parkinson's disease, Tourette's syndrome, and nicotine addiction, have been investigated [15,16]. Recently, numerous studies revealed that nAChRs also play significant roles in cancer progression [17]. For example,  $\alpha 7$ -nAChR was found to be associated with cancer cell proliferation and migration, exhibiting the potential to serve as a therapeutic target for tumors [18].  $\alpha 5$ -Nicotinic acetylcholine receptor (CHRNA5) is a member of the nicotinic acetylcholine receptor superfamily. CHRNA5 was initially recognized as an important regulator in nicotine addiction and nicotine-dependent lung cancer development [19,20]. CHRNA5-mediated  $\text{Ca}^{2+}$  influx was found to activate MAPK and VEGF signaling pathways, thereby contributing to tumor progression in lung cancer [21]. Recently, several studies identified the critical role of CHRNA5 in several other cancers. CHRNA5, upregulated in breast cancer, was identified as the secondary estrogen signaling network and exhibited prognostic value in breast cancer [22]. In melanoma, CHRNA5 was reported to modulate cancer growth by regulating the Notch1 signaling pathway [23]. Another study found that CHRNA5 could promote radioresistance via regulating E2F transcription factor activity in oral squamous cell carcinoma [24]. However, the role of CHRNA5 in HCC remains largely unknown. Here, our study focused on revealing the role of CHRNA5 in HCC progression. We found that CHRNA5 contributes to HCC progression through the YAP-dependent modulation of proliferation ability, the EMT phenotype, and stemness properties. Our study demonstrates the clinical and biological significance of CHRNA5 in HCC, and CHRNA5 might serve as a promising prognostic biomarker and therapeutic target for HCC.

## 2. Materials and Methods

### 2.1. Cell Culture

Human HCC cell lines Huh7 and PLC/PRF/5 (PLC) were obtained from Shanghai Cell Bank, Chinese Academy of Sciences. All cell lines were cultured in Dulbecco's modified Eagle's medium (DMEM, HyClone, Logan, UT, USA) supplemented with 10% fetal bovine serum (FBS; Gibco, Carlsbad, CA, USA) and penicillin/streptomycin (1%; Gibco, Carlsbad, CA, USA). Cells were maintained in a humidified incubator with 5%  $\text{CO}_2$  at 37 °C.

### 2.2. Patient Samples

In total, 70 paired HCC samples and adjacent normal counterparts were obtained from Huashan Hospital from November 2015 to December 2016. Diagnoses were made by two pathologists independently. All specimens were fixed with formalin and embedded in paraffin. Written informed consent was provided by all patients. The methods and

experimental protocols performed in this study were approved by the Human Research Ethics Committee of Huashan Hospital.

### 2.3. RNA Interference and Plasmid Transfection

When the cells reached 70% confluence, transfection was carried out according to the lipofectamine 3000 (Invitrogen, Waltham, MA, USA) instructions. Lentiviral short hairpin RNA (shRNA) targeting CHRNA5 (CCGGGCTCGATTCTATTCGCTACATCTCGAGATGTAGCGAATAGAATCG AGCTTTTTG for sh1, and CCGGCCTGATGACTATGGTGGAACTCTCGAGTATTCCACCATAGTCATCA GGTTTTT for sh2) and control vectors (sh-NC) obtained from Sigma-Aldrich were loaded into the PLKO plasmid. The CHRNA5 CDS sequence was loaded into the PCDH plasmid for CHRNA5 overexpression in HCC cells.

### 2.4. Cell Viability Assay

CCK8 test kits were employed to test cell viability following the manufacturer's instructions. After being seeded in 96-well plates, cancer cells were incubated with DMEM containing 10% CCK8 for 2 h, and the absorbance was measured at 450 nm.

### 2.5. TdT-Mediated dUTP Nick-End Labeling (TUNEL) Assay

To detect sorafenib-induced apoptosis, we conducted a TUNEL assay according to the manufacturer's instructions (Beyotime Biotechnology, Shanghai, China). DAPI was used to stain the nucleus. Cells were imaged with a fluorescent microscope.

### 2.6. cDNA Synthesis and qRT-PCR Assay

Trizol reagent (Invitrogen, Waltham, MA, USA) was used to extract total RNA, and NanoDrop2000 was used for RNA quantification. The total RNA was reverse-transcribed into cDNA for qRT-PCR analysis following the manufacturer's instructions for Prime-Script RT Reagent Kit (TaKaRa, Otsu City, Shiga Prefecture, Japan). Then, quantitative real-time PCR assays were conducted using the ABI7500 system according to the protocol. The primer sequences for qRT-PCR were as follows: CHRNA5-Forward: 5'-GCCAGAGTGCCAGTGAGAAG-3', CHRNA5-Reverse: 5'-CGAGGCCAGCTGAGCAA-3'; GAPDH-Forward: 5'-TCGGAGTCAACGGATTGGT-3', GAPDH-Reverse: 5'-TTCCCGTTCTCAGCCTTGAC-3'.

### 2.7. Western Blot

The protein concentration was determined using a BCA kit after cells were lysed in radioimmunoprecipitation assay (RIPA) buffer. Then, the proteins were boiled with loading buffer at 100 °C for 15 min. Polyacrylamide gel electrophoresis and membrane transfer were carried out as previously described [25]. The membrane was incubated with primary antibodies against CHRNA5 (Thermo Fisher Scientific, Waltham, MA, USA), E-cadherin (CST, Danvers, MA, USA), N-cadherin (CST, Danvers, MA, USA), vimentin (CST, Danvers, MA, USA), YAP (CST, Danvers, MA, USA), OCT4 (Abclonal, Wuhan, Hubei, China), Nanog (Abclonal, Wuhan, Hubei, China), Sox2 (Abclonal, Wuhan, Hubei, China), histone H3 (CST, Danvers, MA, USA), and GAPDH (CST, Danvers, MA, USA) at 4 °C overnight. Then, the membrane was further incubated with secondary antibody for one hour at room temperature, and enhanced chemiluminescence (ECL) reagent was used to visualize the protein bands using a Gel Doc EZ Imager. GAPDH was used as an internal reference.

### 2.8. Colony Formation Assay

Transfected Huh7 and PLC cells (1000 cells/well) were seeded into 6-well plates and cultured for 2 weeks. Finally, colonies were counted after being fixed with 4% paraformaldehyde and stained with 0.1% crystal violet.



### 2.9. Cell Migration and Invasion Assay

Cells at the logarithmic growth phase were harvested and resuspended in serum-free medium to be seeded in transwell chambers for detecting their migration ability. For the invasion assay, cells were seeded in transwell chambers containing Matrigel. After 24 h or 48 h, the transwell chambers were collected. Cells were fixed with 4% paraformaldehyde and stained with crystal violet. The numbers of invading and migrating cells were counted under a light microscope.

### 2.10. CHRNA5 Expression and Clinical Information from the Cancer Genome Atlas (TCGA)

The RNA-sequencing-based gene expression data of 374 HCC tumor samples and 50 normal samples were downloaded using the “TCGAbiolinks” package (TCGAbiolinks: an R/Bioconductor package for integrative analysis of TCGA data). The clinical data of the corresponding 374 HCC patients were downloaded from The Cancer Genome Atlas (TCGA, <https://portal.gdc.cancer.gov/>, last date for accession: 15 August 2021). We used “R” to normalize the original RNA-sequencing data to transcripts per million reads (TPM) [26]. After excluding the samples lacking mRNA expression or clinical information, we included 370 HCC patients for the clinical and prognosis analysis.

### 2.11. Gene Ontology (GO) and Kyoto Encyclopedia of Genes and Genomes (KEGG) Enrichment Analysis

The genes correlated with CHRNA5 were confirmed using “corr” packages in R. To assess the biological function of CHRNA5-correlated genes, Gene Ontology (GO) and Kyoto Encyclopedia of Genes and Genomes (KEGG) pathway analyses were performed using the R package “clusterProfiler”, and values with  $p < 0.05$  were considered to be statistically significant [27]. All statistical data analyses in this study were performed using R software (version 4.1.1).

### 2.12. Animal Study

PLC-NC, PLC-sh CHRNA5, Huh7-CMV, and Huh7-CHRNA5 OE cells ( $2 \times 10^6$ ) were injected subcutaneously into the left flank of 3–4-week-old male nude mice kept in the SPF animal laboratory. Tumor weight was measured after sacrificing the mice by anesthesia at the end of the experiment. Every nude mouse received humane care in accordance with the National Institutes of Health guidelines (NIH Publications No. 8023). The animal study was performed following the protocols approved by the Institutional Animal Care and Use Committee of Fudan University.

### 2.13. Statistical Analysis

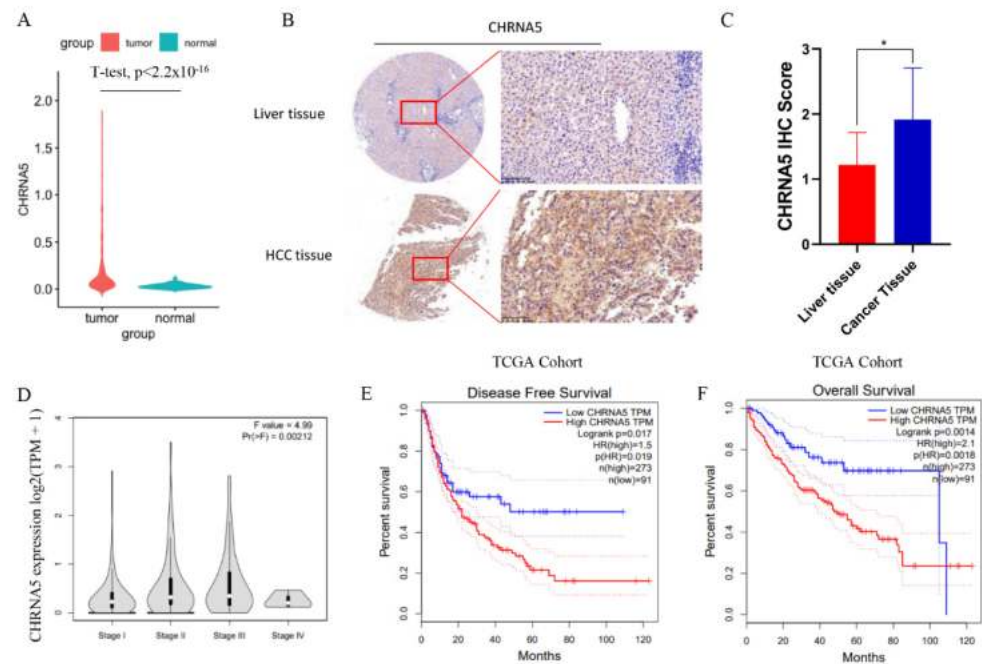
For statistical analysis, experiments were repeated three times. All data were analyzed by SPSS 21.0 (Chicago, IL, USA) and GraphPad Prism 8.0.1 (La Jolla, CA, USA).  $\chi^2$ -Tests, two-tailed Student’s *t*-test, Spearman’s rank correlation, and Kaplan-Meier analysis were used according to the data type. Values with  $p < 0.05$  were regarded as statistically significant.

## 3. Results

### 3.1. CHRNA5 Is Significantly Overexpressed in Hepatocellular Carcinoma and Correlated with Poor Prognosis of HCC Patients

To investigate the expression pattern of CHRNA5 in HCC tissues, we analyzed data from the TCGA database and found that the mRNA expression level of CHRNA5 was significantly higher in HCC tissues compared with that in adjacent normal liver tissues ( $p < 0.05$ ) (Figure 1A). We further detected the CHRNA5 protein level and also found increased CHRNA5 expression in HCC tissues (Figure 1B,C). The correlation between CHRNA5 expression and the corresponding clinicopathological parameters was analyzed using data from the TCGA database. The results suggested that there was a close association between the CHRNA5 mRNA expression level and tumor stage (Figure 1D), suggesting that CHRNA5 plays a role in tumor progression. We further explored the relationship

between the CHRNA5 expression level and the clinical characteristics of HCC patients, including gender, age, T stage, distant metastasis, AJCC phase, and vascular invasion. The results revealed significant correlations between the CHRNA5 expression level and T stage ( $p < 0.05$ ) and AJCC phase ( $p < 0.05$ ) (Table 1). Using the GEPIA database to analyze the prognostic value of CHRNA5 in HCC, we found that HCC patients with a higher mRNA expression level of CHRNA5 exhibited poorer disease-free survival and overall survival after surgery (Figure 1E,F). These results indicate that CHRNA5 contributes to cancer progression and poor prognosis in HCC patients.



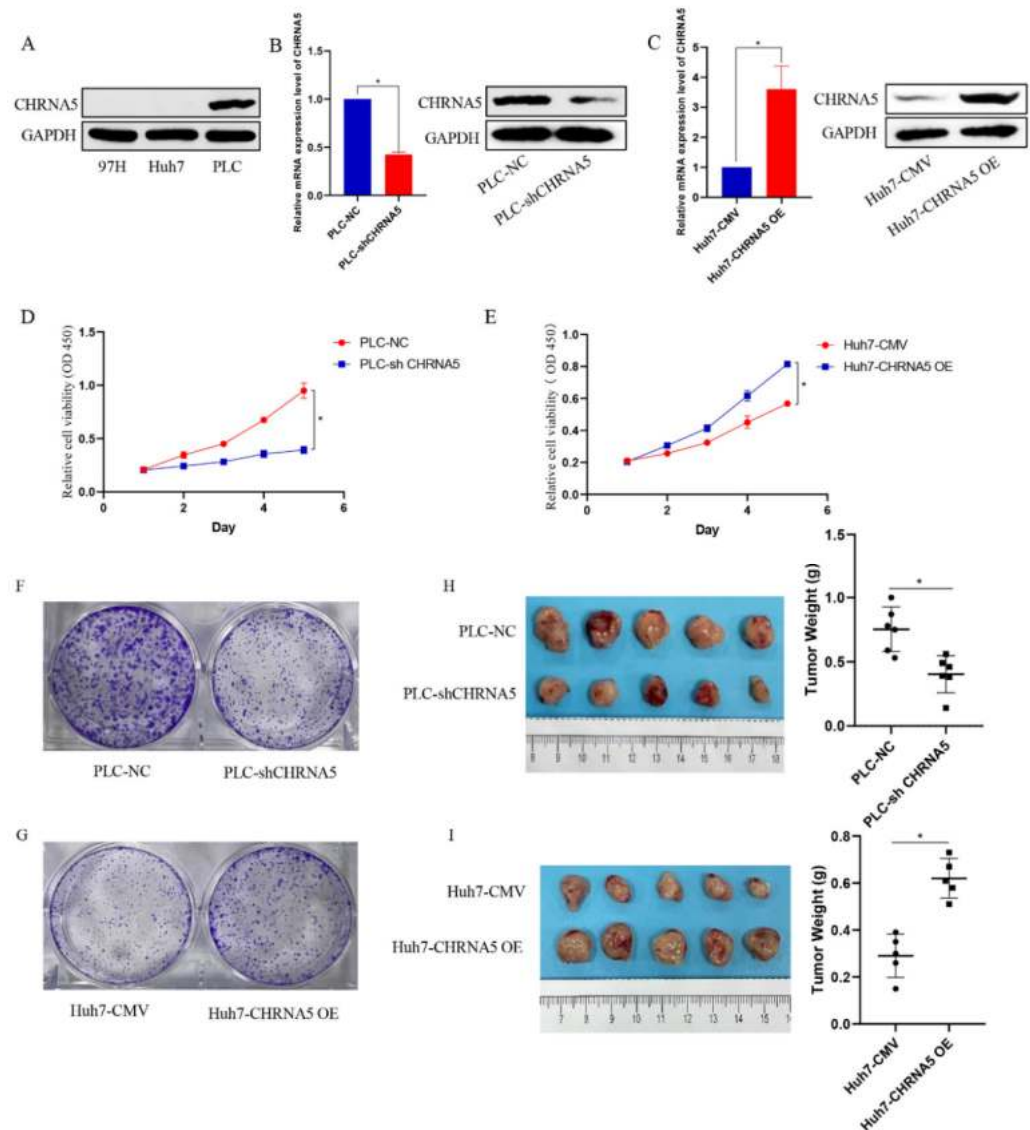
**Figure 1.** Increased expression of CHRNA5 in HCC. (A) Increased mRNA expression of CHRNA5 in HCC compared with that in normal liver tissue; (B,C) increased protein expression of CHRNA5 in HCC compared with that in normal liver tissue; (D) CHRNA5 mRNA expression level in HCC at different stages; (E,F) relationship between CHRNA5 expression and the prognosis of HCC patients. \*  $p < 0.05$ .

**Table 1.** The association between CHRNA5 mRNA expression and clinicopathological characteristics in HCC.

Characteristics	CHRNA5 Expression		p Value
	High	Low	
Age			
≤65	66	65	0.7963
>65	34	38	
Gender			
Male	57	78	0.0072
Female	43	25	
T stage			
T1	46	68	0.0074
T2-4	54	35	
Metastasis			
M0	97	102	0.3639
M1	3	1	
AJCC phase			
I	46	66	0.0112
II-IV	54	37	
Vascular Invasion			
No	63	73	0.296
Yes	37	30	

### 3.2. CHRNA5 Promotes Proliferation of HCC Cells

To explore the cellular functions of CHRNA5 in HCC, we generated a CHRNA5-overexpressing Huh7 cell line and a CHRNA5-silencing PLC cell line based on the basal expression level of CHRNA5 in Huh7, PLC, and 97H (Figure 2A–C). The CCK8 assay revealed that silencing CHRNA5 markedly inhibited the proliferation ability of PLC cells, and CHRNA5 overexpression improved the proliferation ability of Huh7 cells (Figure 2D,E), suggesting that CHRNA5 plays a critical role in promoting HCC cell proliferation. We carried out a colony formation assay to further observe the long-term effect of silencing or overexpressing CHRNA5 on the proliferation of HCC cells. As expected, the number of colonies was significantly reduced after silencing CHRNA5 in the PLC cell line and was markedly increased after CHRNA5 overexpression in the Huh7 cell line (Figure 2F,G). To investigate the growth-promoting effect in vivo, we developed subcutaneous xenograft models of PLC-NC, PLC-shCHRNA5, Huh7-CMV, and Huh-CHRNA5 OE cells in nude mice. The results revealed that CHRNA5 silencing significantly inhibited tumor growth, and CHRNA5 overexpression markedly promoted tumor growth in vivo (Figure 1H,I), further suggesting that CHRNA5 plays a critical role in promoting the proliferation ability of HCC cells.

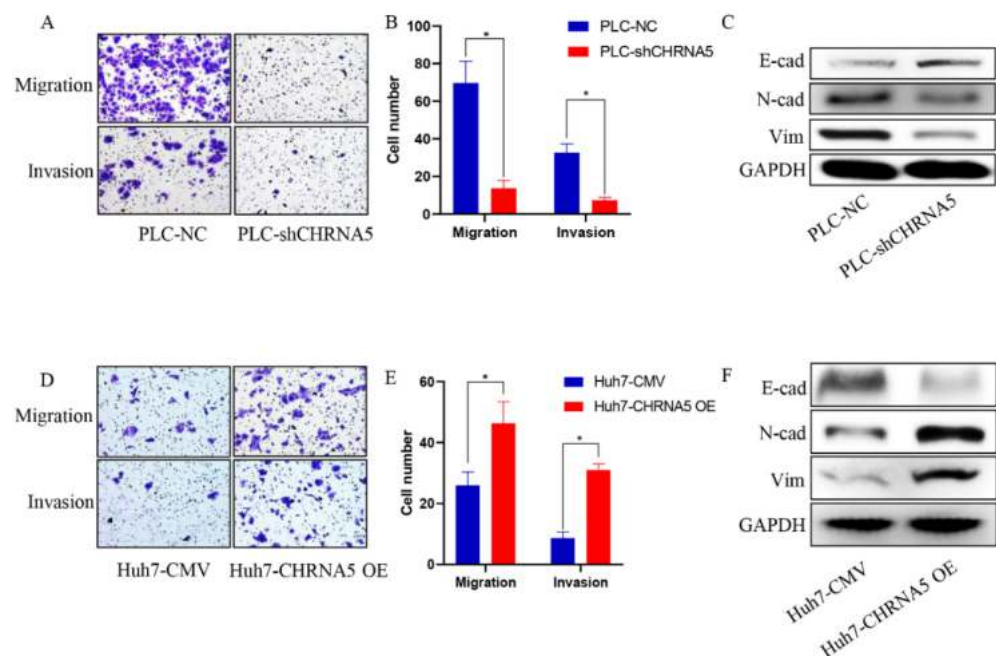


**Figure 2.** CHRNA5 regulates the proliferation ability of HCC cells. (A) The protein expression level of CHRNA5 in HCC cell lines, including MHCC-97H, Huh7, and PLC cells; (B) real-time qPCR and

Western blot analysis of the knockdown efficiency of CHRNA5 in PLC cell lines; (C) real-time qPCR and Western blot analysis of the overexpression efficiency of CHRNA5 in Huh7 cell lines; (D) CCK8 assay of PLC-NC and PLC-sh CHRNA5 cell lines; (E) CCK8 assay of Huh7-CMV and Huh7-CHRNA5 OE cell lines; (F) colony formation assay of PLC-NC and PLC-sh CHRNA5 cell lines; (G) colony formation assay of Huh7-CMV and Huh7-CHRNA5 OE cell lines; (H) image of tumors from PLC-NC and PLC-sh CHRNA5 cell lines subcutaneously injected into mice and tumor weight; (I) image of tumors from Huh7-CMV and Huh7-CHRNA5 OE cell lines subcutaneously injected into mice and tumor weight. \*  $p < 0.05$ .

### 3.3. CHRNA5 Promotes Invasion and Migration of HCC

Furthermore, silencing CHRNA5 markedly inhibited the migration and invasion ability of PLC cells (Figure 3A,B) and downregulated the expression of EMT-associated markers, such as N-cad and vimentin (Figure 3C). Accordingly, CHRNA5 overexpression significantly increased the migration and invasion ability of Huh7 cells by upregulating EMT-associated genes (Figure 3D–F). These results revealed that CHRNA5 was also involved in the migration and invasion of HCC cells by regulating the EMT phenotype.

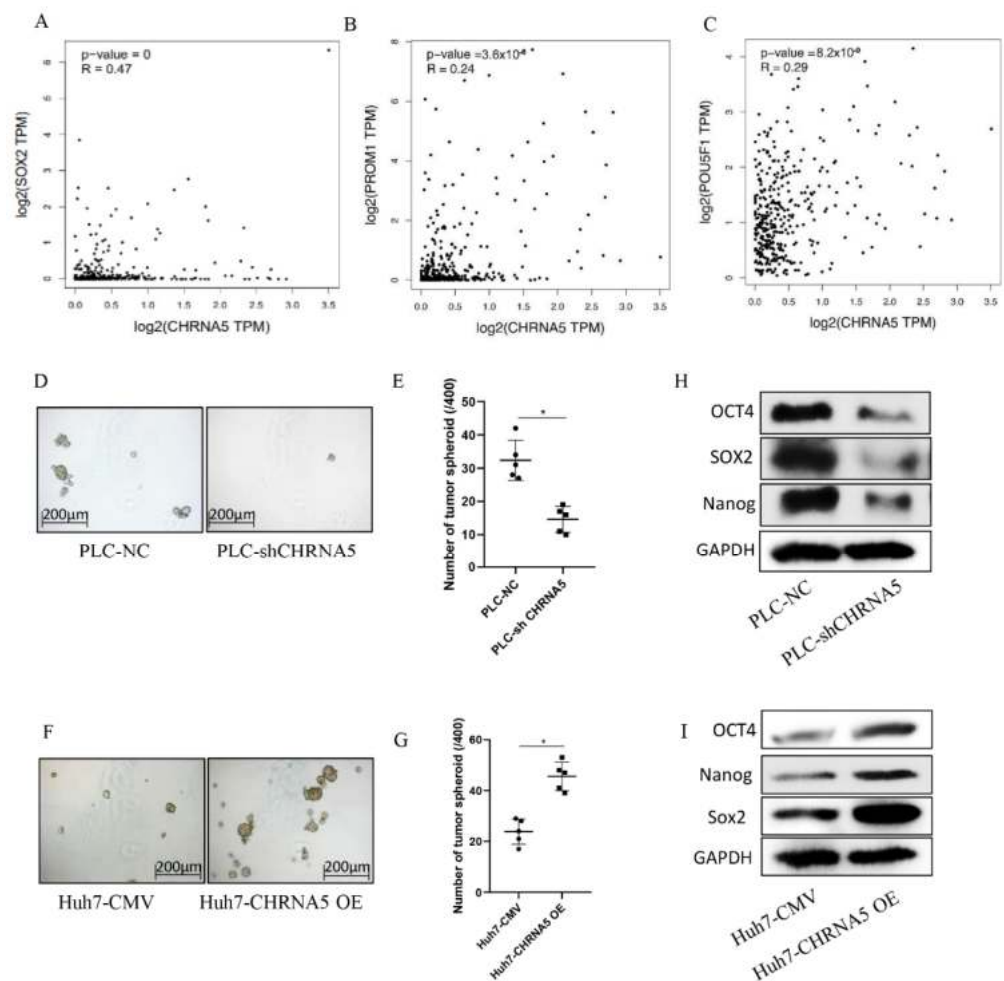


**Figure 3.** CHRNA5 promotes HCC migration and invasion via regulating EMT phenotype. (A,B) Effects of silencing CHRNA5 on HCC migration and invasion were determined by transwell assays; (C) effects of silencing CHRNA5 on expression of EMT-associated markers in HCC; (D,E) effects of CHRNA5 overexpression on HCC migration and invasion were determined by transwell assays; (F) effects of CHRNA5 overexpression on expression of EMT-associated markers in HCC. \*  $p < 0.05$ .

### 3.4. CHRNA5 Promotes Stemness Properties of HCC

From the TCGA database, we observed that CHRNA5 was positively correlated with stemness-associated genes, such as Sox2, CD133, and OCT4 (Figure 4A–C). The tumor spheroid formation assay is a commonly used method to detect the stemness properties of cancer cells [25]. To further determine whether CHRNA5 plays a regulatory role in maintaining the stemness properties of HCC, we carried out a spheroid formation assay. The results showed that silencing CHRNA5 inhibited the tumor spheroid formation ability of PLC cells (Figure 4D,E), and CHRNA5 overexpression increased the tumor sphere formation ability of Huh7 cells (Figure 4F,G), indicating that CHRNA5 has a regulatory role in maintaining the stemness properties of HCC cells. In addition, Western blot analysis revealed that CHRNA5 participated in regulating stemness-associated genes, such as OCT4,

Nanog, and Sox2 (Figure 4H,I). These results indicate that CHRNA5 maintains stemness properties by regulating stemness-associated genes in HCC.

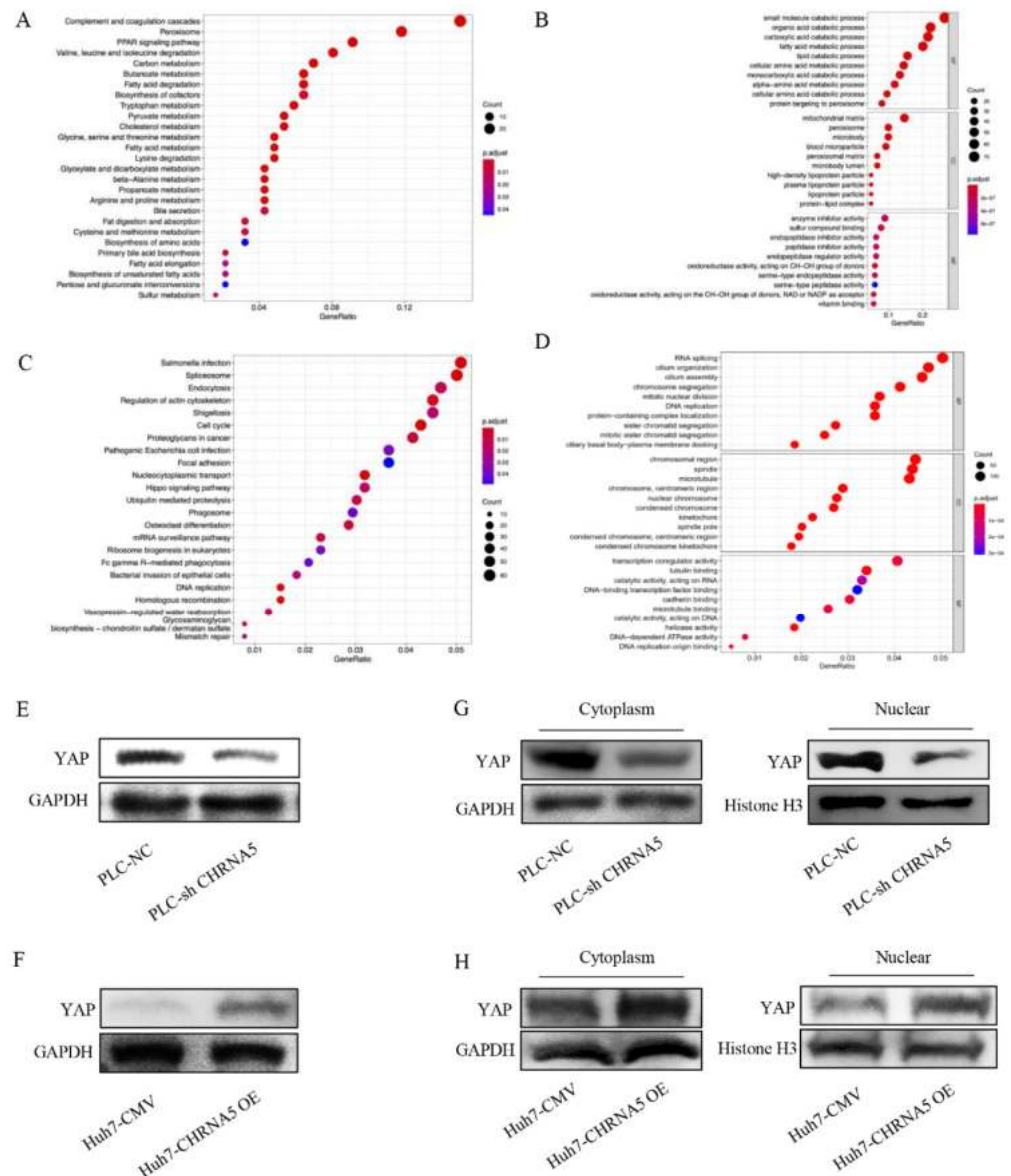


**Figure 4.** CHRNA5 promotes HCC spheroid formation ability via regulating stemness-associated genes. (A–C) Correlation between CHRNA5 mRNA expression level and stemness-associated genes in TCGA database; (D,E) effects of CHRNA5 silencing on HCC spheroid formation ability; (F,G) effects of CHRNA5 overexpression on HCC spheroid formation ability; (H) effects of CHRNA5 silencing on the expression of stemness-associated genes; (I) effects of CHRNA5 overexpression on the expression of stemness-associated genes. \*  $p < 0.05$ .

### 3.5. CHRNA5 Regulates YAP Activity in HCC

We used the online analysis tool LinkedOmics to identify genes that were significantly correlated with CHRNA5 in HCC. Genes negatively correlated with CHRNA5 (Figure 5A,B) and positively correlated with CHRNA5 (Figure 5C,D) were incorporated into KEGG and GO analyses. The results reveal that CHRNA5 is associated with many important cancer-related signaling pathways, such as cell cycle regulation, DNA replication, mismatch repair, and the Hippo signaling pathway in HCC. YAP is an important component of the Hippo signaling pathway and plays a critical role in pro-proliferation and anti-apoptosis [28]. To further check whether CHRNA5 can regulate the Hippo signaling pathway in HCC, we detected the YAP expression level after silencing or overexpressing CHRNA5. The results revealed that YAP expression was significantly downregulated after silencing CHRNA5 and markedly upregulated after overexpressing CHRNA5 in HCC cells (Figure 5E,F). The transcriptional activity of YAP was closely associated with its subcellular localization. Therefore, we further detected the YAP expression level in the cytoplasm and nucleus after CHRNA5 knockdown or overexpression. The results revealed that silencing CHRNA5

significantly inhibited the nuclear accumulation of YAP in the PLC cell line, and CHRNA5 overexpression markedly augmented YAP nuclear accumulation in the Huh7 cell line (Figure 5G,H), further suggesting that CHRNA5 has a critical role in regulating YAP activity.

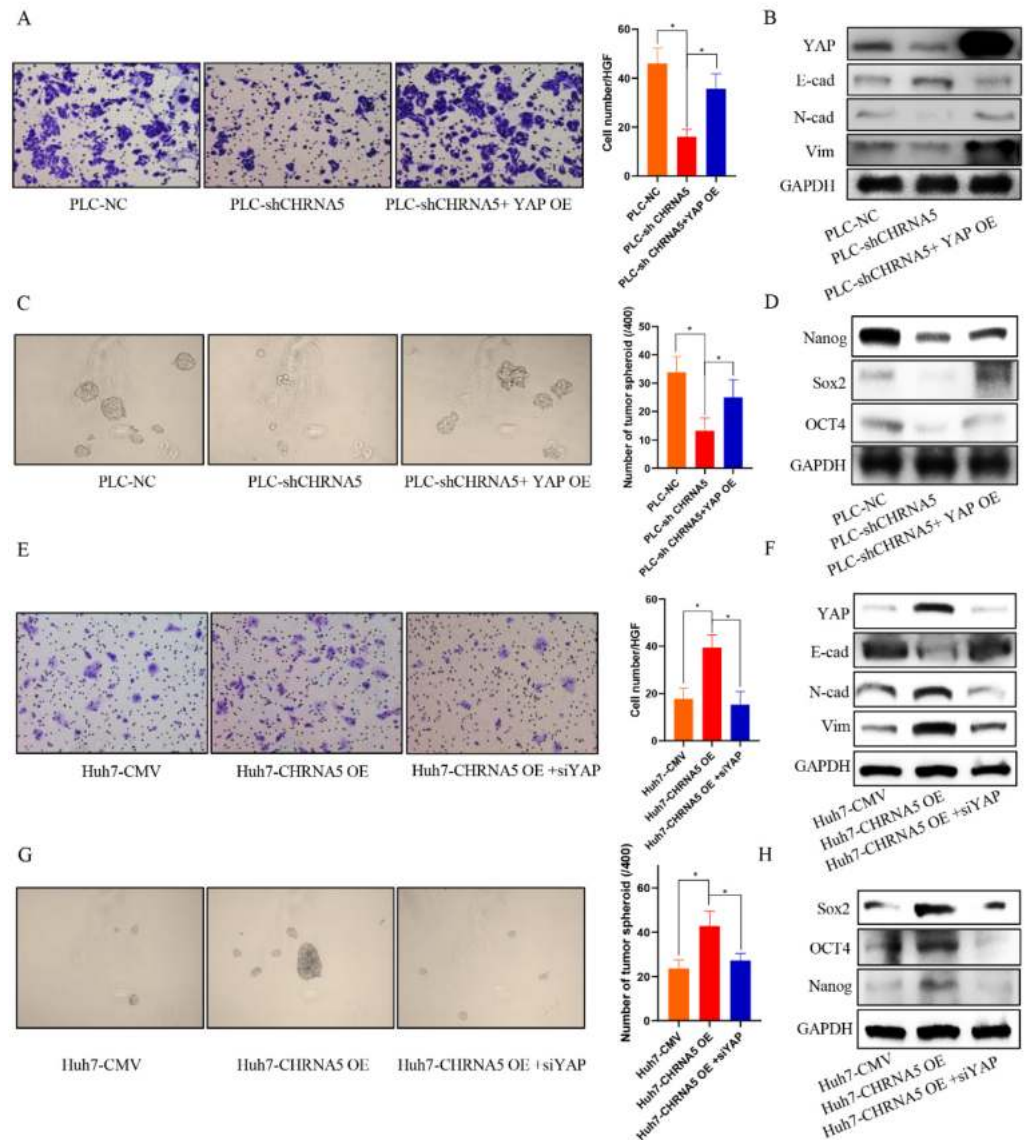


**Figure 5.** CHRNA5 regulates YAP activity in HCC. (A) KEGG analysis of genes negatively correlated with CHRNA5 in HCC; (B) GO analysis of genes negatively correlated with CHRNA5 in HCC; (C) KEGG analysis of genes positively correlated with CHRNA5 in HCC; (D) GO analysis of genes positively correlated with CHRNA5 in HCC; (E) Western blot analysis of YAP in PLC-NC and PLC-sh CHRNA5 cell lines; (F) Western blot analysis of YAP in Huh7-CMV and Huh7-CHRNA5 OE cell lines; (G) Western blot analysis of YAP expression in cytoplasm and nucleus from PLC-NC and PLC-sh CHRNA5 cell lines; (H) Western blot analysis of YAP expression in cytoplasm and nucleus from Huh7-CMV and Huh7-CHRNA5 OE cell lines.

### 3.6. YAP Plays an Essential Role in the Contribution of CHRNA5 to Malignant Phenotype of HCC

To uncover whether YAP plays an essential role in the contribution of CHRNA5 to the HCC malignant phenotype, we overexpressed YAP in CHRNA5-silencing PLC cell lines and silenced YAP expression in CHRNA5-overexpressing Huh7 cell lines. The results revealed that YAP overexpression partially reversed the inhibitory effect of silencing CHRNA5 on the migration ability and expression of EMT-associated markers (Figure 6A,B).

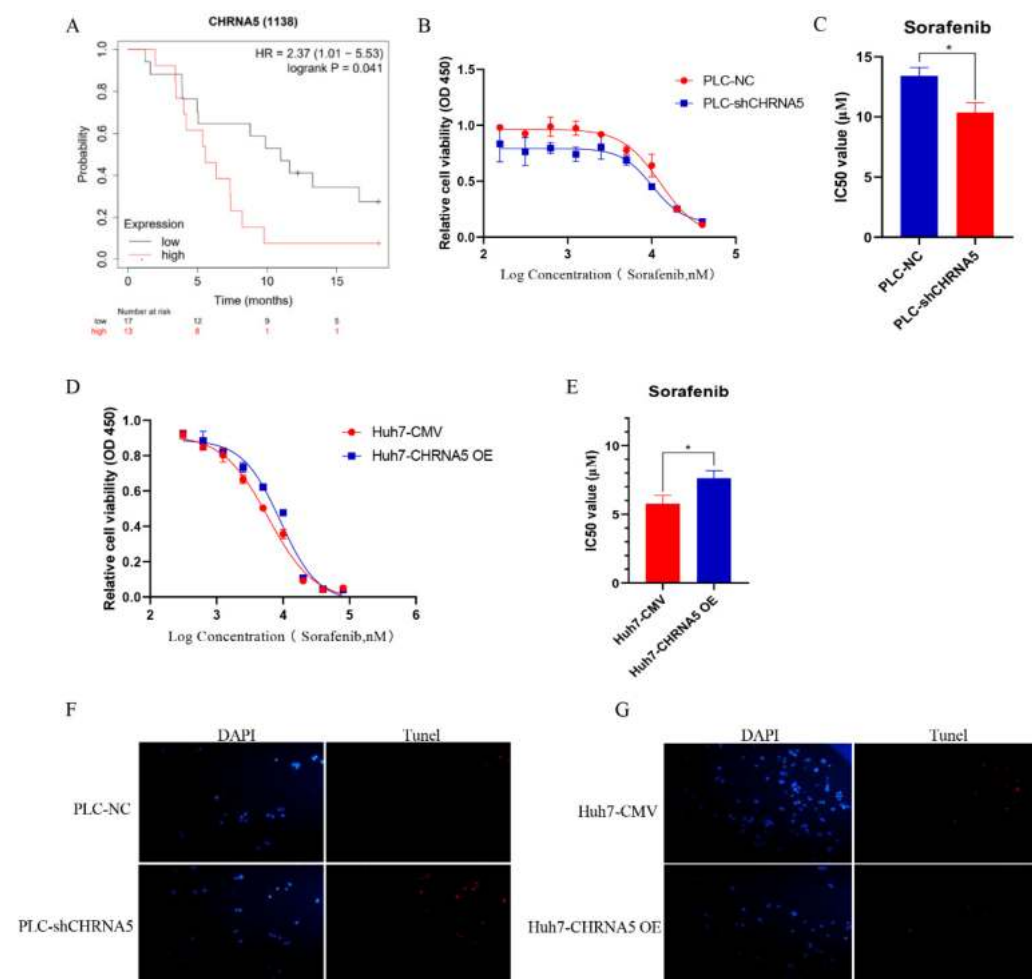
Furthermore, the inhibitory effects of silencing CHRNA5 on the tumor spheroid formation ability of PLC cell lines and the expression of stemness-associated genes were also attenuated after overexpressing YAP (Figure 6C,D). Accordingly, the opposite effect was observed after silencing YAP in CHRNA5-overexpressing Huh7 cell lines (Figure 6E–H). These results suggest that CHRNA5 can regulate the malignant phenotype of HCC cell lines by modulating YAP activity.



**Figure 6.** YAP plays an essential role in the contribution of CHRNA5 to malignant phenotype of HCC. (A) YAP overexpression partially rescued the inhibitory effect of silencing CHRNA5 on the migration ability of HCC cells; (B) YAP overexpression partially rescued the inhibitory effect of silencing CHRNA5 on the expression of EMT-associated markers; (C) YAP overexpression partially rescued the inhibitory effect of silencing CHRNA5 on the spheroid formation ability of HCC cells; (D) YAP overexpression partially rescued the inhibitory effect of silencing CHRNA5 on the expression of stemness-associated genes; (E) the inhibitory effect of silencing CHRNA5 on the migration ability of HCC cells was attenuated after overexpressing YAP; (F) the inhibitory effect of silencing CHRNA5 on the expression of EMT-associated markers in HCC cells was attenuated after overexpressing YAP; (G) the inhibitory effect of silencing CHRNA5 on the spheroid formation ability of HCC cells was attenuated after overexpressing YAP; (H) the inhibitory effect of silencing CHRNA5 on the expression of stemness-associated genes in HCC cells was attenuated after overexpressing YAP. \*  $p < 0.05$ .

### 3.7. CHRNA5 Regulates Sorafenib Sensitivity in HCC

Several studies have already uncovered that YAP activity is closely associated with sorafenib resistance in HCC [29,30]. In addition, stemness properties were also reported to share a close association with sorafenib sensitivity in HCC [31]. Therefore, we further evaluated the effect of CHRNA5 on HCC sensitivity to sorafenib. From the TCGA database, we observed that a higher expression level of CHRNA5 was correlated with a worse OS in HCC patients receiving sorafenib treatment (Figure 7A), suggesting that CHRNA5 might be associated with sorafenib sensitivity in HCC. An in vitro assay also revealed that silencing CHRNA5 significantly decreased the IC<sub>50</sub> of HCC cells (Figure 7B,C), which was markedly increased when CHRNA5 was overexpressed (Figure 7D,E). The TUNEL assay also revealed that CHRNA5 silencing augmented the apoptosis of HCC cells induced by sorafenib, whereas CHRNA5 overexpression attenuated the apoptosis of HCC cells induced by sorafenib (Figure 7F,G). These results suggest that CHRNA5 contributes to sorafenib resistance in HCC and has the potential to serve as an indicator for predicting sorafenib sensitivity in HCC patients.



**Figure 7.** CHRNA5 regulates sorafenib sensitivity in HCC. (A) The effect of CHRNA5 on the OS of HCC patients receiving sorafenib treatment; (B,C) IC<sub>50</sub> of sorafenib in PLC-NC and PLC-sh-CHRNA5 cell lines; (D,E) IC<sub>50</sub> of sorafenib in Huh7-CMV and Huh7-CHRNA5 OE cell lines; (F) TUNEL detection of PLC-NC and PLC-shCHRNA5 cell lines treated with sorafenib; (G) TUNEL detection of Huh7-CMV and Huh7-CHRNA5 OE cell lines treated with sorafenib. \*  $p < 0.05$ , + Censored Data.

## 4. Discussion

CHRNA5, a member of the superfamily of ligand-gated ion channels, is a vital receptor for nicotine [32]. Thus, previous studies regarding CHRNA5 have largely focused on its



role in nicotine dependence and lung cancer progression [33]. In this study, for the first time, we investigated the role of CHRNA5 in HCC. The results reveal that CHRNA5 expression level is upregulated in HCC tissues and is closely associated with tumor T stage, AJCC phase, and patient prognosis. These results suggest the involvement of CHRNA5 in HCC progression. The role of CHRNA5 in tumor proliferation was previously reported. In oral squamous cell carcinoma, CHRNA5 was reported to regulate the activity of the E2F signaling pathway, a critical regulator of cell cycle and stemness properties (33986804), contributing to tumor growth and treatment resistance [24,25]. Ozlen Konu et al. also reported that CHRNA5 silencing in breast cancer significantly inhibited tumor growth, which might be attributed to the significant inhibition of cell-cycle-associated genes after CHRNA5 silencing [34]. Their study suggested that CHRNA5 might regulate cell cycle arrest during the G1 phase by modulating the activity of retinoblastoma family proteins (RB), which regulate E2F1 activity by binding with E2F1 [35]. To further validate the functional role of CHRNA5 in HCC, we induced lentivirus-mediated overexpression or silencing of CHRNA5. We found that CHRNA5 is crucial for the proliferation of HCC cells both in vitro and in vivo, consistent with the conclusion of previous studies in other types of cancers. Tumor invasion and metastasis are challenges in the clinical treatment of HCC. EMT is regarded as a critical step in tumor invasion and metastasis [36]. A previous study suggested that CHRNA5 could regulate the migration and invasion ability of melanoma cells [23]. Similarly, our study indicated that CHRNA5 could enhance the invasion and metastasis ability of HCC by regulating EMT-associated genes. All of these data suggest that CHRNA5 plays a critical role in the malignant phenotype of HCC.

Sorafenib is a multitarget molecular drug and is one of the main treatment strategies for advanced HCC. By suppressing the activity of various receptor tyrosine kinase and VEGF/Raf/MER/ERK-mediated multiple signaling pathways, sorafenib can inhibit tumor cell proliferation and angiogenesis in vivo [37]. Despite the fact that sorafenib can extend the patient's overall survival, limited benefits were observed in more than 70% of patients with advanced HCC as a result of drug resistance. Therefore, it is clinically meaningful to explore the mechanisms of sorafenib resistance in HCC patients. Our results revealed that CHRNA5 silencing could augment sorafenib sensitivity, and CHRNA5 overexpression could attenuate sorafenib sensitivity, indicating the regulatory role of CHRNA5 in sorafenib sensitivity in HCC. Accordingly, among patients receiving sorafenib treatment, those with a higher expression level of CHRNA5 exhibited a worse OS compared with those with a lower expression level of CHRNA5. These results indicate that CHRNA5 has a pivotal role in sorafenib resistance in HCC. There is a growing amount of evidence indicating that stemness properties, closely associated with cancer initiation and progression, also play a significant role in treatment resistance [38]. The maintenance of stemness properties relies on the activation of stemness-associated genes, such as Sox2, OCT4, and Nanog [38]. Moreover, several stemness-associated signaling pathways, such as Wnt/ $\beta$ -catenin signaling, Notch signaling, and JAK/STAT signaling, also greatly contribute to stemness properties in HCC [39]. In HCC, stemness properties are closely associated with drug resistance, tumor metastasis, and recurrence [39]. Stemness properties are closely associated with the EMT phenotype, which was previously reported to contribute to sorafenib resistance in HCC [40,41]. Several other studies also reported that stemness properties are closely associated with sorafenib resistance in HCC [42]. Ozlen Konu et al. observed a close association between CHRNA5 and Wnt/ $\beta$ -catenin signaling, from which we can propose that CHRNA5 might also regulate the stemness properties of breast cancer cells [34]. Consistent with their study, our study also indicated that CHRNA5 could maintain the stemness properties of HCC cells by regulating stemness-associated genes, to which the regulatory role of CHRNA5 in sorafenib sensitivity could be partially attributed. Stemness properties are also closely associated with chemotherapy resistance and radiotherapy resistance [43]. Thus, it is possible that CHRNA5 might also contribute to resistance to chemotherapy and radiotherapy in HCC, but further experiments are needed to test this hypothesis. In fact, previous studies have already identified the role of CHRNA5 in the resistance to

chemotherapy in breast cancer and the resistance to radiotherapy in oral squamous cell carcinoma [24].

YAP, playing an essential role in cancer progression, was reported to be implicated in modulating various malignant phenotypes of cancer cells, such as cell proliferation, migration, invasion, apoptosis resistance, EMT phenotype, and stemness properties [44–46]. In this study, data from the TCGA database exhibited a close association between CHRNA5 and the Hippo signaling pathway in HCC. Further *in vitro* assays revealed that CHRNA5 could regulate YAP activity, and YAP silencing was sufficient to reverse the CHRNA5-mediated tumor-promoting effect. Thus, these results suggest that CHRNA5 promotes HCC progression by modulating YAP activity. Recent studies also suggested the contribution of YAP to drug sensitivity in HCC through various mechanisms. Yuan Zhou et al. reported that YAP contributes to chemotherapy resistance via regulating the Rac family small guanosine triphosphatase 1 (RAC1)—reactive oxygen species (ROS)—mTOR signaling pathway [47]. Darko Castven et al. reported that YAP induced stem-like properties and accounted for the acquired resistance to sorafenib in HCC cells [48]. Ruize Gao et al. also reported that YAP could transcriptionally initiate the expression of SLC7A11, a key transporter maintaining intracellular glutathione homeostasis, causing resistance to sorafenib-induced ferroptosis in HCC [29]. Consistent with previous studies, our study reveals that downregulation of YAP activity caused by CHRNA5 silencing leads to enhanced sensitivity to sorafenib. Thus, YAP plays a critical role in the contribution of CHRNA5 to stemness properties, EMT phenotype, and sorafenib resistance in HCC.

## 5. Conclusions

In conclusion, our study demonstrates that CHRNA5 plays a significant role in promoting the malignant phenotype of HCC by regulating YAP activity. Its role in sorafenib resistance suggests the potential of CHRNA5 to serve as an indicator for sorafenib sensitivity, and targeting CHRNA5 might be a strategy for HCC treatment.

**Author Contributions:** Study design, Q.D., H.J. and Y.F.; acquisition and analysis of data, Y.F., H.C., W.D., H.J. and Q.D.; drafting of the manuscript, Y.F., H.C. and W.D.; revision of the manuscript H.J. and Q.D.; Y.F. and H.C. are co-first authors. All authors have read and agreed to the published version of the manuscript.

**Funding:** This work was supported by the National Natural Science Foundation of China (81872356), the Program of Shanghai Academic Research Leader (20XD1400900) and the Project of Medical Engineering, Fudan University (yg2021-017).

**Institutional Review Board Statement:** The animal study was performed in accordance with the National Institutes of Health guidelines (NIH Publications No. 8023). Patient samples used in this study were approved by the Human Research Ethics Committee of Huashan Hospital (No. 2017-041, approved 21 February 2017).

**Informed Consent Statement:** Each of the enrolled patients provided written informed consent.

**Data Availability Statement:** No additional data are available.

**Acknowledgments:** We are grateful to Yirui Li (School of Nursing, Fudan University) for her assistance in the correction of grammatical mistakes in this article.

**Conflicts of Interest:** The authors have no conflict of interests related to this publication.

## References

1. Yang, J.D.; Hainaut, P.; Gores, G.J.; Amadou, A.; Plymoth, A.; Roberts, L.R. A global view of hepatocellular carcinoma: Trends, risk, prevention and management. *Nat. Rev. Gastroenterol. Hepatol.* **2019**, *16*, 589–604. [CrossRef] [PubMed]
2. Welzel, T.M.; Graubard, B.I.; Quraishi, S.; Zeuzem, S.; Davila, J.A.; El-Serag, H.B.; McGlynn, K.A. Population-attributable fractions of risk factors for hepatocellular carcinoma in the United States. *Am. J. Gastroenterol.* **2013**, *108*, 1314–1321. [CrossRef] [PubMed]
3. Dietrich, P.; Hellerbrand, C. Non-alcoholic fatty liver disease, obesity and the metabolic syndrome. *Best Pract. Res. Clin. Gastroenterol.* **2014**, *28*, 637–653. [CrossRef] [PubMed]

4. Malek, N.P.; Schmidt, S.; Huber, P.; Manns, M.P.; Greten, T.F. The diagnosis and treatment of hepatocellular carcinoma. *Dtsch. Arztebl. Int.* **2014**, *111*, 101–106. [CrossRef]
5. Ikeda, M.; Morizane, C.; Ueno, M.; Okusaka, T.; Ishii, H.; Furuse, J. Chemotherapy for hepatocellular carcinoma: Current status and future perspectives. *Jpn. J. Clin. Oncol.* **2018**, *48*, 103–114. [CrossRef]
6. Llovet, J.M.; Ricci, S.; Mazzaferro, V.; Hilgard, P.; Gane, E.; Blanc, J.F.; de Oliveira, A.C.; Santoro, A.; Raoul, J.L.; Forner, A.; et al. Sorafenib in advanced hepatocellular carcinoma. *N. Engl. J. Med.* **2008**, *359*, 378–390. [CrossRef]
7. Li, Y.; Chen, G.; Han, Z.; Cheng, H.; Qiao, L.; Li, Y. IL-6/STAT3 Signaling Contributes to Sorafenib Resistance in Hepatocellular Carcinoma Through Targeting Cancer Stem Cells. *Onco. Targets Ther.* **2020**, *13*, 9721–9730. [CrossRef]
8. Halder, G.; Johnson, R.L. Hippo signaling: Growth control and beyond. *Development* **2011**, *138*, 9–22. [CrossRef]
9. Plouffe, S.W.; Hong, A.W.; Guan, K.L. Disease implications of the Hippo/YAP pathway. *Trends Mol. Med.* **2015**, *21*, 212–222. [CrossRef]
10. Calses, P.C.; Crawford, J.J.; Lill, J.R.; Dey, A. Hippo Pathway in Cancer: Aberrant Regulation and Therapeutic Opportunities. *Trends Cancer* **2019**, *5*, 297–307. [CrossRef]
11. Liu, Y.; Wang, X.; Yang, Y. Hepatic Hippo signaling inhibits development of hepatocellular carcinoma. *Clin. Mol. Hepatol.* **2020**, *26*, 742–750. [CrossRef] [PubMed]
12. Lam, D.C.; Girard, L.; Ramirez, R.; Chau, W.S.; Suen, W.S.; Sheridan, S.; Tin, V.P.; Chung, L.P.; Wong, M.P.; Shay, J.W.; et al. Expression of nicotinic acetylcholine receptor subunit genes in non-small-cell lung cancer reveals differences between smokers and nonsmokers. *Cancer Res.* **2007**, *67*, 4638–4647. [CrossRef] [PubMed]
13. Albuquerque, E.X.; Pereira, E.F.; Alkondon, M.; Rogers, S.W. Mammalian nicotinic acetylcholine receptors: From structure to function. *Physiol. Rev.* **2009**, *89*, 73–120. [CrossRef] [PubMed]
14. Improgo, M.R.; Scofield, M.D.; Tapper, A.R.; Gardner, P.D. From smoking to lung cancer: The CHRNA5/A3/B4 connection. *Oncogene* **2010**, *29*, 4874–4884. [CrossRef]
15. Arneric, S.P.; Holladay, M.; Williams, M. Neuronal nicotinic receptors: A perspective on two decades of drug discovery research. *Biochem. Pharmacol.* **2007**, *74*, 1092–1101. [CrossRef]
16. Romanelli, M.N.; Gratteri, P.; Guandalini, L.; Martini, E.; Bonaccini, C.; Gualtieri, F. Central nicotinic receptors: Structure, function, ligands, and therapeutic potential. *ChemMedChem* **2007**, *2*, 746–767. [CrossRef]
17. Chen, J.; Cheuk, I.W.Y.; Shin, V.Y.; Kwong, A. Acetylcholine receptors: Key players in cancer development. *Surg. Oncol.* **2019**, *31*, 46–53. [CrossRef]
18. Bouzat, C.; Lasala, M.; Nielsen, B.E.; Corradi, J.; Esandi, M.D.C. Molecular function of alpha7 nicotinic receptors as drug targets. *J. Physiol.* **2018**, *596*, 1847–1861. [CrossRef]
19. Benowitz, N.L. Nicotine addiction. *N. Engl. J. Med.* **2010**, *362*, 2295–2303. [CrossRef]
20. Chen, L.S.; Baker, T.; Hung, R.J.; Horton, A.; Culverhouse, R.; Hartz, S.; Saccone, N.; Cheng, I.; Deng, B.; Han, Y.; et al. Genetic Risk Can Be Decreased: Quitting Smoking Decreases and Delays Lung Cancer for Smokers with High and Low CHRNA5 Risk Genotypes—A Meta-Analysis. *EBioMedicine* **2016**, *11*, 219–226. [CrossRef]
21. Niu, X.M.; Lu, S. Acetylcholine receptor pathway in lung cancer: New twists to an old story. *World J. Clin. Oncol.* **2014**, *5*, 667–676. [CrossRef] [PubMed]
22. Shehwana, H.; Keskus, A.G.; Ozdemir, S.E.; Acikgoz, A.A.; Biyik-Sit, R.; Cagnan, I.; Gunes, D.; Jahja, E.; Cingir-Koker, S.; Olmezer, G.; et al. CHRNA5 belongs to the secondary estrogen signaling network exhibiting prognostic significance in breast cancer. *Cell. Oncol.* **2021**, *44*, 453–472. [CrossRef] [PubMed]
23. Dang, N.; Meng, X.; Qin, G.; An, Y.; Zhang, Q.; Cheng, X.; Huang, S. alpha5-nAChR modulates melanoma growth through the Notch1 signaling pathway. *J. Cell. Physiol.* **2020**, *235*, 7816–7826. [CrossRef] [PubMed]
24. Lin, C.H.; Lee, H.H.; Kuei, C.H.; Lin, H.Y.; Lu, L.S.; Lee, F.P.; Chang, J.; Wang, J.Y.; Hsu, K.C.; Lin, Y.F. Nicotinic Acetylcholine Receptor Subunit Alpha-5 Promotes Radioresistance via Recruiting E2F Activity in Oral Squamous Cell Carcinoma. *J. Clin. Med.* **2019**, *8*, 1454. [CrossRef] [PubMed]
25. Fu, Y.; Hu, C.; Du, P.; Huang, G. E2F1 Maintains Gastric Cancer Stemness Properties by Regulating Stemness-Associated Genes. *J. Oncol.* **2021**, *2021*, 6611327. [CrossRef] [PubMed]
26. Wagner, G.P.; Kin, K.; Lynch, V.J. Measurement of mRNA abundance using RNA-seq data: RPKM measure is inconsistent among samples. *Theory Biosci.* **2012**, *131*, 281–285. [CrossRef]
27. Yu, G.; Wang, L.G.; Han, Y.; He, Q.Y. clusterProfiler: An R package for comparing biological themes among gene clusters. *OMICS* **2012**, *16*, 284–287. [CrossRef]
28. Chen, Q.; Zhou, X.W.; Zhang, A.J.; He, K. ACTN1 supports tumor growth by inhibiting Hippo signaling in hepatocellular carcinoma. *J. Exp. Clin. Cancer Res.* **2021**, *40*, 23. [CrossRef]
29. Gao, R.; Kalathur, R.K.R.; Coto-Llerena, M.; Ercan, C.; Buechel, D.; Shuang, S.; Piscuoglio, S.; Dill, M.T.; Camargo, F.D.; Christofori, G.; et al. YAP/TAZ and ATF4 drive resistance to Sorafenib in hepatocellular carcinoma by preventing ferroptosis. *EMBO Mol. Med.* **2021**, *13*, e14351. [CrossRef]
30. Sun, T.; Mao, W.; Peng, H.; Wang, Q.; Jiao, L. YAP promotes sorafenib resistance in hepatocellular carcinoma by upregulating survivin. *Cell. Oncol.* **2021**, *44*, 689–699. [CrossRef]
31. Loh, J.J.; Li, T.W.; Zhou, L.; Wong, T.L.; Liu, X.; Ma, V.W.S.; Lo, C.M.; Man, K.; Lee, T.K.; Ning, W.; et al. FSTL1 Secreted by Activated Fibroblasts Promotes Hepatocellular Carcinoma Metastasis and Stemness. *Cancer Res.* **2021**, *81*, 5692–5705. [CrossRef]

32. Grozio, A.; Catassi, A.; Cavaliere, Z.; Paleari, L.; Cesario, A.; Russo, P. Nicotine, lung and cancer. *Anticancer Agents Med. Chem.* **2007**, *7*, 461–466. [CrossRef]
33. Russo, P.; Del Bufalo, A.; Milic, M.; Salinaro, G.; Fini, M.; Cesario, A. Cholinergic receptors as target for cancer therapy in a systems medicine perspective. *Curr. Mol. Med.* **2014**, *14*, 1126–1138. [CrossRef]
34. Cingir Koker, S.; Jahja, E.; Shehwana, H.; Keskus, A.G.; Konu, O. Cholinergic Receptor Nicotinic Alpha 5 (CHRNA5) RNAi is associated with cell cycle inhibition, apoptosis, DNA damage response and drug sensitivity in breast cancer. *PLoS ONE* **2018**, *13*, e0208982. [CrossRef]
35. Dyson, N. The regulation of E2F by pRB-family proteins. *Genes Dev.* **1998**, *12*, 2245–2262. [CrossRef]
36. Liu, M.; Yang, J.; Xu, B.; Zhang, X. Tumor metastasis: Mechanistic insights and therapeutic interventions. *MedComm* **2021**, *2*, 587–617. [CrossRef]
37. Reiss, K.A.; Yu, S.; Mamtani, R.; Mehta, R.; D’Addeo, K.; Wileyto, E.P.; Taddei, T.H.; Kaplan, D.E. Starting Dose of Sorafenib for the Treatment of Hepatocellular Carcinoma: A Retrospective, Multi-Institutional Study. *J. Clin. Oncol.* **2017**, *35*, 3575–3581. [CrossRef]
38. Fu, Y.; Du, P.; Zhao, J.; Hu, C.; Qin, Y.; Huang, G. Gastric Cancer Stem Cells: Mechanisms and Therapeutic Approaches. *Yonsei Med. J.* **2018**, *59*, 1150–1158. [CrossRef]
39. Lv, D.; Chen, L.; Du, L.; Zhou, L.; Tang, H. Emerging Regulatory Mechanisms Involved in Liver Cancer Stem Cell Properties in Hepatocellular Carcinoma. *Front. Cell Dev. Biol.* **2021**, *9*, 691410. [CrossRef]
40. van Zijl, F.; Zulehner, G.; Petz, M.; Schneller, D.; Kornauth, C.; Hau, M.; Machat, G.; Grubinger, M.; Huber, H.; Mikulits, W. Epithelial-mesenchymal transition in hepatocellular carcinoma. *Future Oncol.* **2009**, *5*, 1169–1179. [CrossRef]
41. Hirao, A.; Sato, Y.; Tanaka, H.; Nishida, K.; Tomonari, T.; Hirata, M.; Bando, M.; Kida, Y.; Tanaka, T.; Kawaguchi, T.; et al. MiR-125b-5p Is Involved in Sorafenib Resistance through Ataxin-1-Mediated Epithelial-Mesenchymal Transition in Hepatocellular Carcinoma. *Cancers* **2021**, *13*, 4917. [CrossRef] [PubMed]
42. Xia, S.; Pan, Y.; Liang, Y.; Xu, J.; Cai, X. The microenvironmental and metabolic aspects of sorafenib resistance in hepatocellular carcinoma. *EBioMedicine* **2020**, *51*, 102610. [CrossRef] [PubMed]
43. Liu, Y.P.; Zheng, C.C.; Huang, Y.N.; He, M.L.; Xu, W.W.; Li, B. Molecular mechanisms of chemo- and radiotherapy resistance and the potential implications for cancer treatment. *MedComm* **2021**, *2*, 315–340. [CrossRef] [PubMed]
44. Mohajan, S.; Jaiswal, P.K.; Vatanmakarian, M.; Yousefi, H.; Sankaralingam, S.; Alahari, S.K.; Koul, S.; Koul, H.K. Hippo pathway: Regulation, deregulation and potential therapeutic targets in cancer. *Cancer Lett.* **2021**, *507*, 112–123. [CrossRef] [PubMed]
45. Su, D.; Lin, Z. Dichloroacetate attenuates the stemness of hepatocellular carcinoma cells via promoting nucleus-cytoplasm translocation of YAP. *Environ. Toxicol.* **2021**, *36*, 975–983. [CrossRef]
46. Wang, S.; Li, H.; Wang, G.; Zhang, T.; Fu, B.; Ma, M.; Quan, Z.; Chen, G. Yes-associated protein (YAP) expression is involved in epithelial-mesenchymal transition in hepatocellular carcinoma. *Clin. Transl. Oncol.* **2016**, *18*, 172–177. [CrossRef]
47. Zhou, Y.; Wang, Y.; Zhou, W.; Chen, T.; Wu, Q.; Chutturghoon, V.K.; Lin, B.; Geng, L.; Yang, Z.; Zhou, L.; et al. YAP promotes multi-drug resistance and inhibits autophagy-related cell death in hepatocellular carcinoma via the RAC1-ROS-mTOR pathway. *Cancer Cell Int.* **2019**, *19*, 179. [CrossRef]
48. Castven, D.; Czauderna, C.; Becker, D.; Pereira, S.; Schmitt, J.; Weinmann, A.; Shah, V.; Hajduk, J.; Keggenhoff, F.; Binder, H.; et al. Acquired Resistance to Antiangiogenic Therapies in Hepatocellular Carcinoma Is Mediated by Yes-Associated Protein 1 Activation and Transient Expansion of Stem-Like Cancer Cells. *Hepatol. Commun.* **2021**. [CrossRef]



Review

# Recent Progress in Lipid Nanoparticles for Cancer Theranostics: Opportunity and Challenges

Sarah I. Bukhari <sup>1</sup>, Syed Sarim Imam <sup>1</sup>, Mohammad Zaki Ahmad <sup>2</sup>, Parameswara Rao Vuddanda <sup>3</sup>, Sultan Alshehri <sup>1,4</sup>, Wael A. Mahdi <sup>1</sup> and Javed Ahmad <sup>2,\*</sup>

<sup>1</sup> Department of Pharmaceutics, College of Pharmacy, King Saud University, Riyadh 11451, Saudi Arabia; sbukhari@ksu.edu.sa (S.I.B.); simam@ksu.edu.sa (S.S.I.); salshehri1@ksu.edu.sa (S.A.); wmahdi@ksu.edu.sa (W.A.M.)

<sup>2</sup> Department of Pharmaceutics, College of Pharmacy, Najran University, Najran 11001, Saudi Arabia; mzahmad@nu.edu.sa

<sup>3</sup> Research Centre for Topical Drug Delivery and Toxicology (TDDT), University of Hertfordshire, Hertfordshire AL10 9AB, UK; p.r.vuddanda@herts.ac.uk

<sup>4</sup> Department of Pharmaceutical Sciences, College of Pharmacy, Almaarefa University, Riyadh 11597, Saudi Arabia

\* Correspondence: jahmad18@gmail.com or jahmed@nu.edu.sa

**Citation:** Bukhari, S.I.; Imam, S.S.; Ahmad, M.Z.; Vuddanda, P.R.; Alshehri, S.; Mahdi, W.A.; Ahmad, J. Recent Progress in Lipid Nanoparticles for Cancer Theranostics: Opportunity and Challenges. *Pharmaceutics* **2021**, *13*, 840. <https://doi.org/10.3390/pharmaceutics13060840>

Academic Editor: Hassan Bousbaa

Received: 3 May 2021

Accepted: 2 June 2021

Published: 7 June 2021

**Publisher's Note:** MDPI stays neutral with regard to jurisdictional claims in published maps and institutional affiliations.

**Abstract:** Cancer is one of the major leading causes of mortality in the world. The implication of nanotherapeutics in cancer has garnered splendid attention owing to their capability to efficiently address various difficulties associated with conventional drug delivery systems such as non-specific biodistribution, poor efficacy, and the possibility of occurrence of multi-drug resistance. Amongst a plethora of nanocarriers for drugs, this review emphasized lipidic nanocarrier systems for delivering anticancer therapeutics because of their biocompatibility, safety, high drug loading and capability to simultaneously carrying imaging agent and ligands as well. Furthermore, to date, the lack of interaction between diagnosis and treatment has hampered the efforts of the nanotherapeutic approach alone to deal with cancer effectively. Therefore, a novel paradigm with concomitant imaging (with contrasting agents), targeting (with biomarkers), and anticancer agent being delivered in one lipidic nanocarrier system (as cancer theranostics) seems to be very promising in overcoming various hurdles in effective cancer treatment. The major obstacles that are supposed to be addressed by employing lipidic theranostic nanomedicine include nanomedicine reach to tumor cells, drug internalization in cancer cells for therapeutic intervention, off-site drug distribution, and uptake via the host immune system. A comprehensive account of recent research updates in the field of lipidic nanocarrier loaded with therapeutic and diagnostic agents is covered in the present article. Nevertheless, there are notable hurdles in the clinical translation of the lipidic theranostic nanomedicines, which are also highlighted in the present review along with plausible countermeasures.

**Keywords:** cancer; multi-drug resistance; enhanced permeation and retention effect; nanotherapeutics; cancer theranostic; clinical translation



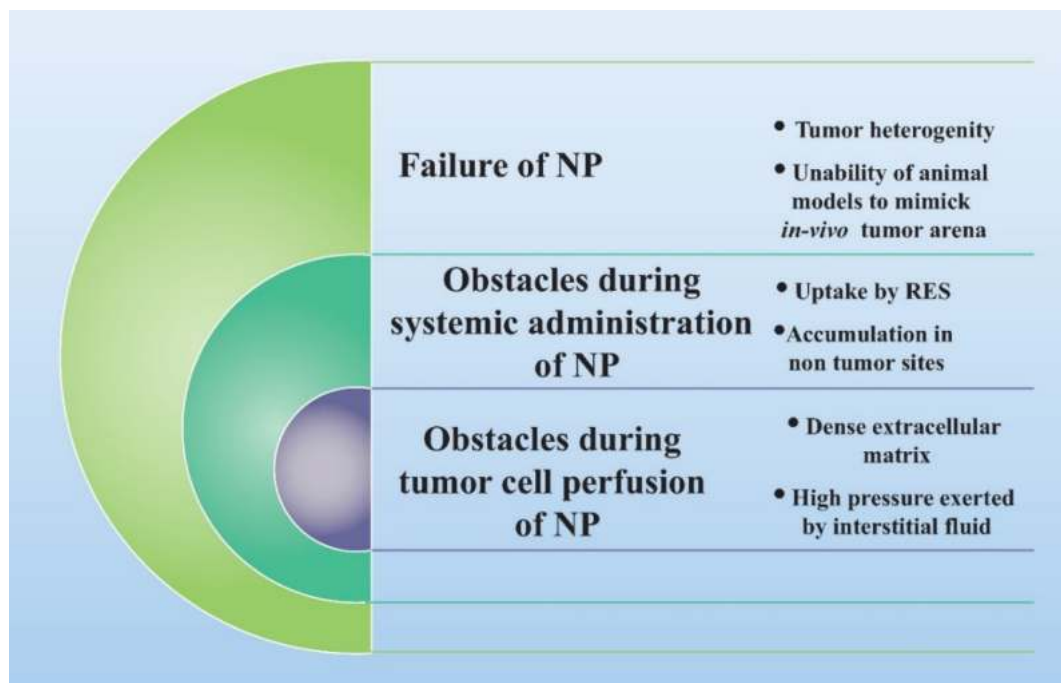
**Copyright:** © 2021 by the authors. Licensee MDPI, Basel, Switzerland. This article is an open access article distributed under the terms and conditions of the Creative Commons Attribution (CC BY) license (<https://creativecommons.org/licenses/by/4.0/>).

## 1. Introduction

At present, cancer is one of the leading causes of mortality worldwide. As per the demographic provided by the world health organization (WHO), cancer is accountable for approximately 10 million deaths in 2020 [1–4]. The emerging area of nanotechnology has proved very promising in cancer therapeutics [5]. Despite tremendous efforts in the research area of carcinomas alleviation through nanomedicines, there are a very few approved nanomedicines such as Doxil<sup>®</sup>, Myocet<sup>®</sup>, Abraxane<sup>®</sup>, Depocyt<sup>®</sup>, Genexol<sup>®</sup> [5,6]. The FDA-approved Doxil was thought to be a revolutionary lipidic nanomedicine when it was successfully developed. However, it was demonstrated in a clinical study that it exhibited poor therapeutic efficacy [7,8]. Harrington and colleagues conducted a study in

which they monitored tumor uptake of  $^{111}\text{In}$ -labelled poly(ethylene glycol) coated (PEGylated) liposomes in 17 patients with locally advanced cancers [9]. In this study, they were able to successfully demonstrate the major reason for the therapeutic failure of Doxil [9]. The study outcome revealed a very important and highly ignored aspect of in vivo fate of nanomedicines, targeting different forms of carcinomas. The study has confirmed that the accumulation of  $^{111}\text{In}$ -liposomes did take place in tumor restricted areas, but the concentration of nanoformulation that was retained in the tumor cells varied largely across different patients and tumor types [9,10]. In cancer patients, it has been established that enhanced permeation and retention effect (EPR) in which tumor vasculature becomes impaired and lymphatic drainage becomes deficient, facilitates drug accumulation in tumor cells, but that concept cannot be generalized after such findings [9,10]. Several factors affect nanomedicine accumulation and retention in tumor cells that need substantial consideration, such as tumor heterogeneity that causes diversified uptake of nanomedicines [11,12]. Tumor heterogeneity could be attributed to the distinctive cellular morphology, expression of efflux or influx transporters such as P-glycoprotein, presence of receptors, gene expression, metabolism, proliferation, and metastatic potential.

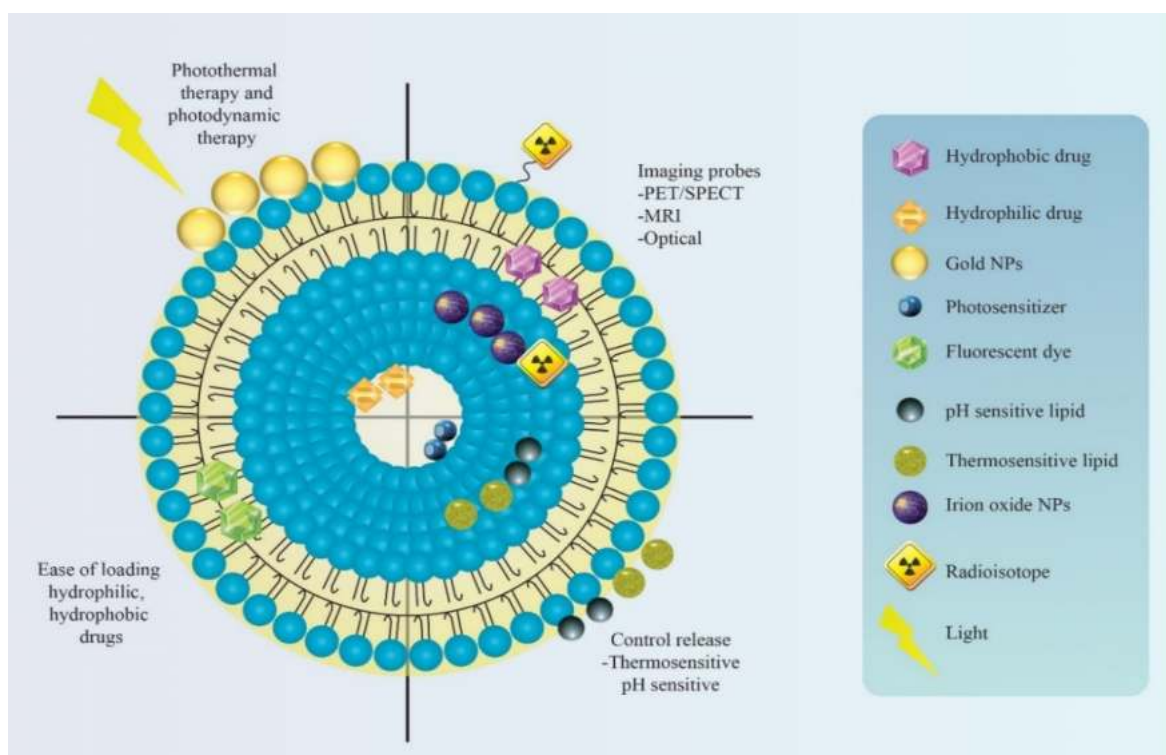
Besides, there is considerable constraint at different levels of nanomedicine administration (as shown in Figure 1) journey in vivo that governs the overall therapeutic efficacy of nanomedicines. When nanomedicine is administered systemically, then it encounters different physical, chemical, and physiological barriers that hinder its reach to tumor cells. After getting across these barriers, there are significant hindrances at the tumor microenvironment level that severely affect drug accumulation [11–13]. These hindrances include abnormal structure and highly variable density of tumor vasculature that greatly interfere with the optimal diffusion of nanomedicines. In addition, the pressure exerted by interstitial fluid and tightly packed tumor cells is very high, which avert the diffusion of nanomedicines across the tumor milieu. Moreover, a highly dense extracellular matrix greatly restricts nanoparticle extravasation and interstitial diffusion (Figure 1) [11–13].



**Figure 1.** Barriers to efficacious in vivo performance of nanomedicines.

Therefore it was realized that there is a major lacuna in our knowledge of the pathophysiological complexities and heterogeneity of tumor sites that affect the therapeutic efficacy of nanomedicines. Those patients are not even identified who are likely to benefit most from given nanomedicine-based chemotherapy [14].

Then next, the *in vivo* nanomedicine behavior knowledge is restricted to animal data and the animal models used do not mimic the actual *in vivo* conditions [15–20]. Usually, the NPs targeted for solid tumors after systemic administration are accumulated in the tumor through the EPR effect. Nevertheless, several crucial aspects related to EPR interpretation have been greatly overlooked, such as the influence of nanomedicine–protein interaction, blood circulation, tumor tissue penetration, and tumor cell internalization. Furthermore, all these biological processes are greatly affected by nanomedicine properties (for example, size, geometry, surface features) thus there are so many factors governing EPR effects driven *in vivo* nanomedicine behavior that cannot be predicted from animal data for humans. To date, there is not a single model that can completely replicate the entire facets of human malignancy [15–17]. This issue can be addressed if diagnosis and therapy can be combined as one approach in developing lipidic nanomedicines targeting cancers (Figure 2).



**Figure 2.** Brief depiction of how lipidic theranostic can help in cancer alleviation via multi-functionalized aspects such as coupling of the imaging probe, surface with gold nanoparticles for photothermal therapy.

A cancer diagnosis has a very significant role in the context of precision of chemotherapeutic medication. Diagnosis specifically implicates recognizing the presence of a tumor in the body and evaluating its extent to identify if it is at its early developmental stage or re-occurrence case [1,2]. Importantly, identification of precancerous lesions could result in a successful intervention of cancer and its complete alleviation. Early diagnosis is certainly life-saving in cancer treatment. Once the existence of cancer is confirmed, diagnostic tools are implicated in identifying specific molecular abnormalities in tumors that govern the medications to be provided accordingly. Nowadays, with advances in biomedical technologies, novel diagnostic approaches are being investigated that will enable the identification of cancerous and precancerous cells at the molecular level and provide information about their pathophysiology. The combination of diagnostics with therapeutics makes it easy to know the progress of treatment and the real-time state of cancer while receiving therapy. Moreover, imaging agents/drug trackers can help greatly to know the *in vivo* fate or traveling of a drug in systemic circulation or at the tumor and can also determine the kinetics aspect of anticancer drug/drug loaded formulation [20,21]. That is why the use of imaging



biomarkers such as radioactive substances taken up by tumors and visualized through diagnostic modalities such as Computed Tomography (CT), Magnetic resonance imaging (MRI), positron emission tomography (PET), and single-photon emission computed tomography (SPECT) is attaining a lot of attention in oncology these days. Taking into consideration the phenomenon of tumor metastases on the way to cancer mortality, the combinatorial approach of diagnosis and treatment that is theranostic will be of substantial importance for the assessment of EPR and nanomedicine penetration. The clinical translation of anticancer nanomedicines could see a breakthrough outcome via the introduction of a theranostic approach that can intently trace the *in vivo* fate of drugs and assess the progression of alleviation of human tumors via encapsulated nanomedicines [18–21].

Therefore, the diagnosis in combination with therapy is quintessential for embarking on a level of cancer treatment that could offer highly efficacious clinical outcomes. In this review, an insight of a combination of therapy and diagnosis, which is called theranostic, is provided, covering the brighter prospects and the challenges accompanied with it. The lipidic nanomedicine-based theranostic is also the highlight of this present review. A comprehensive account of different research updates in the field of lipidic nanocarrier loaded with diagnostic agents is envisaged. Nevertheless, there are notable hurdles in the clinical translation of the lipidic theranostic nanomedicines, which are also discussed in the upcoming section of the present review.

## 2. Significance of Lipid-Based Theranostic Nanoparticles in Cancer Therapy

Early detection of carcinomas is of great pertinence for their successful alleviation. Firstly the diagnosis of the type of tumor, its metastatic state, and the patient history need to be identified to initiate the appropriate therapy. Here theranostic plays a crucial role. Once correctly and profoundly diagnosed, then the nanomedicine-based therapy could be started relevantly. However, the monitoring of the *in vivo* fate of nanomedicine is a vital aspect of assessing the progression and efficacy of cancer therapy. That is why co-encapsulation of imaging agents and drugs in a single nanocarrier system could contribute significantly in assessing the progression of treatment and exact and precise state of the response of cancer towards provided therapy [21–23].

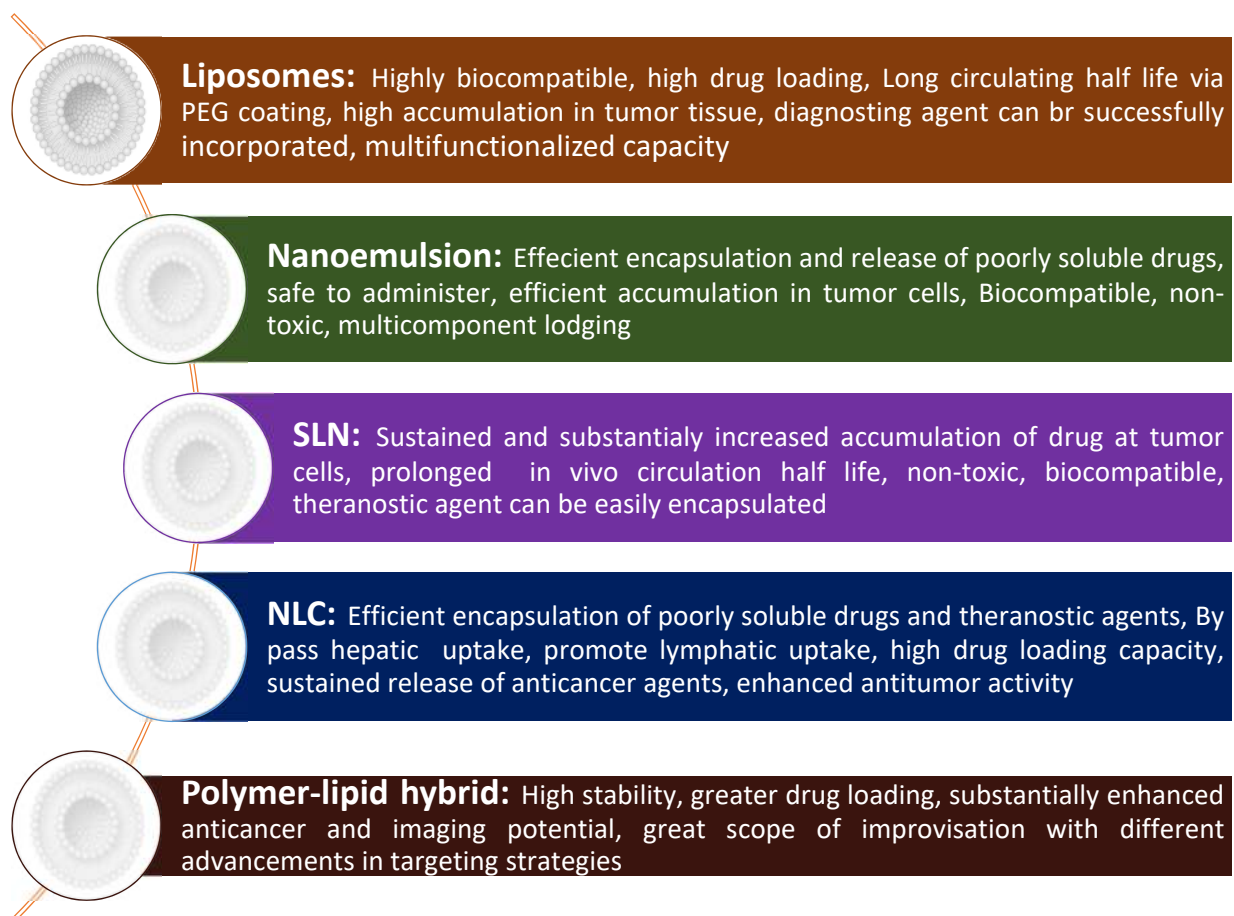
Theranostic nanomedicine could be prepared in multiple manners. The lipid nanocarriers have been proven superiority over polymeric and inorganic nanoparticles in terms of biocompatibility, safety, and biodegradability besides other beneficial considerations from a cancer theranostic perspective (as summarized in Figure 3) [7–9]. Therefore, in this review, we are concerned with lipidic theranostic for cancer, and we will be focusing on the vesicular or micellar lipidic structures. Different shapes and structures can be formulated depending on the type of lipidic nanocarrier chosen (as shown in Figure 4). In nanoemulsions, the theranostic agent and drug are entrapped in oil globules targeted for specific tumor sites. In liposomes, imaging agents can be encapsulated with drugs either in an aqueous core or bilayer lipidic shell. In solid lipid nanostructure (SLN), the imaging agent is intercalated in the solidified lipid matrix. Whereas, in nanostructure lipid carrier (NLC), the drug and the imaging agent are dispersed in the imperfections of oil and solid lipid hybrid matrix. However, optimizing lipid theranostic nanomedicines with balanced size, shape, polydispersity index, surface charge, and stability, is a challenging task in itself that we will discuss in detail in later sections.

The imaging agent that is incorporated with the drug in lipidic vesicles must possess great compatibility with conventional diagnostic techniques such as X-ray, ultrasound (US), CT, MRI, PET, or SPECT [24]. The contrasting agents used in theranostic usually include metals or inorganic agents (such as iron oxide) as they exhibit free electrons whose excitatory phase can be used as imaging modalities (MRI). Different semiconductor-based nanoparticulate systems (such as quantum dots) of colloidal dimension are also being extensively employed in *in vivo* diagnostics [25]. Fluorescent silicon nanoparticles are also employed as an imaging agent for foreseeing *in vivo* prospects [26].

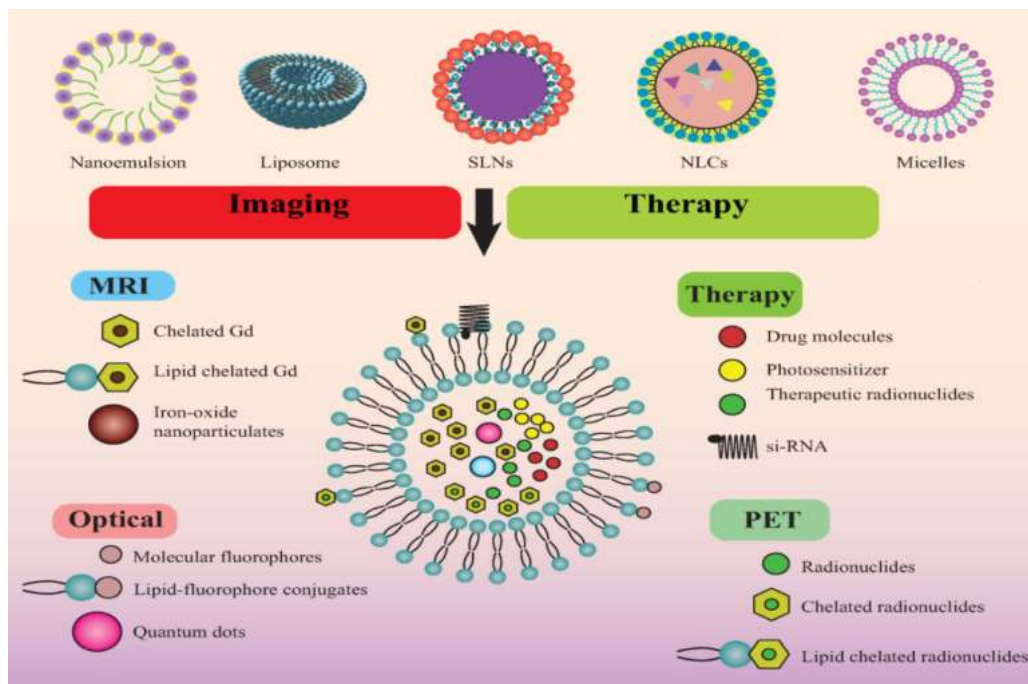
MRI is one of the most commonly used diagnostic modalities, which depends upon mobile protons of water molecules for detecting signals. The MRI images can be perceived via proton concentration in body tissues or else via their longitudinal and transversal relaxation times, T1 and T2, respectively. A plethora of contrast agents are being used for MRI. Amongst them, fluorine-containing contrast agents have garnered splendid attention. Owing to its excellent magnetic property, 100% natural abundance, one-half spin, sensitivity, and gyromagnetic ratio comparable to a proton, fluorine has become the contrast agent of choice for MRI. Furthermore, with  $^{19}\text{F}$  in vivo tracing and imaging can be accomplished without any background signals created by endogenous fluorine. Nonetheless, there has been a limitation with fluorine as its large concentration (10–50 millimolar) is needed for adequate signal intensity in comparison to other contrast agents [27].

The promising combination of imaging along with nanomedicine-based therapy has the extremely worthy potential of overcoming the pathophysiological hurdles that undermine the efficiency of cancer therapy. The simultaneous examination of nanomedicine reach to tumor cells, amount of drug release, off-site tumor drug distribution, and uptake via host immune system are those aspects, which can tremendously affect the therapeutic outcome.

Until recently, the lack of interaction between diagnosis and treatment has hampered efforts to deal with cancer effectively. This new paradigm with simultaneous multifunctionality of imaging (with contrasting agents), targeting (with biomarkers), and delivering chemotherapeutic agents in one lipidic nanocarrier system seems to be very promising in overcoming various hurdles in effective cancer treatment.



**Figure 3.** Potential advantages of different types of lipidic formulations in cancer theranostic.



**Figure 4.** Different types of lipid nanoparticles *viz.* nanoemulsion, liposome, solid lipid nanoparticle (SLN), nanostructured lipid carrier (NLC), and micelles with significant utility in cancer imaging and therapy.

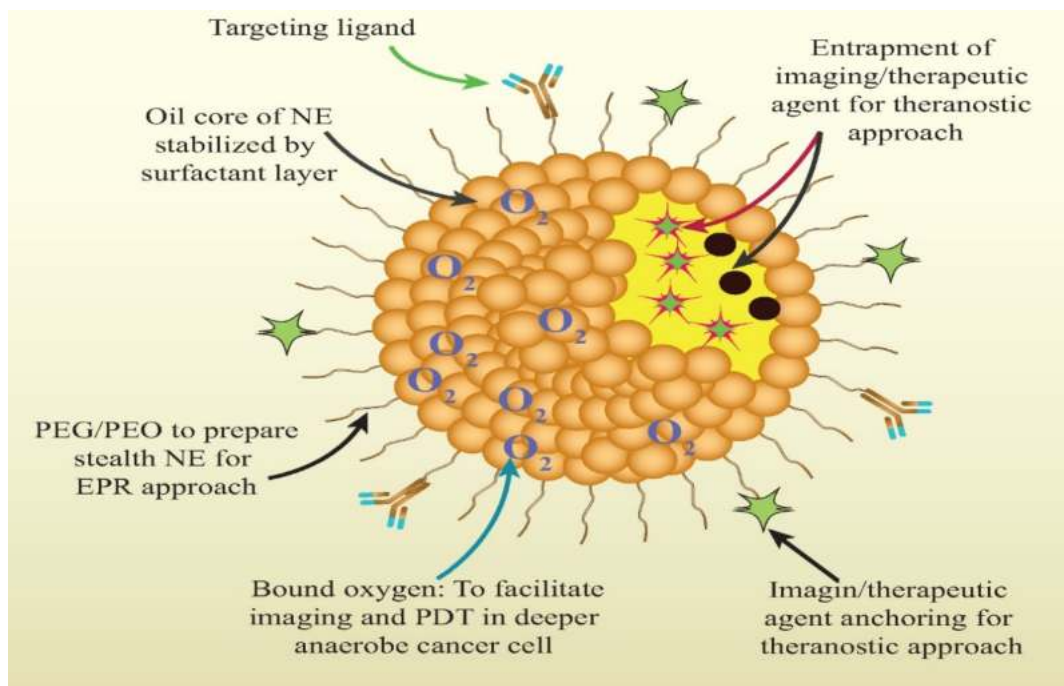
### 3. Different Types of Lipid Nanoparticles for Cancer Theranostics: An Update of Recent Studies

Biocompatibility and safety are the major reasons for choosing a lipidic nanocarrier system as cancer theranostic in this review. Certainly, prolonged *in vivo* circulation half-life, high encapsulation capacities for drug and imaging agents, substantial accumulation at tumor sites, and improvisation susceptibility for multiple functioning are the other significant advantages with lipidic nanocarrier system [28–30]. Lipidic nanocarriers have their own sets of advantages, which give them an edge over other nanoformulations. Recent research studies demonstrated lipidic theranostic nanomedicines to be a promising and potential approach for raising the efficacy of cancer treatment to a hallmark level, as discussed hereunder. The different lipidic nanocarriers include liposomes, nanoemulsions, SLN, NLC, and lipid nanocapsules. However, advanced lipidic nanocarriers such as SLN and NLC are still unexplored for cancer theranostic as there are very few studies conducted thus far.

#### 3.1. Nanoemulsion

Nanoemulsions have gained huge attention for the efficient delivery of lipophilic anticancer drugs. The nanometric size, large surface area, thermodynamic stability, high drug loading capacity, easy scalability, biocompatibility, favorable drug release profile are the characteristic attributes of nanoemulsion that make it worthy of profound exploration in chemotherapeutics [31,32]. The nanoemulsions, mostly oil-in-water types, are optically transparent colloidal dispersion constituted of oil and water, wherein surfactants and co-surfactants create a stable coating over the dispersed droplets to form a physicochemically stable nanoformulation [32]. The excipients of nanoemulsion are generally recognized as safe (GRAS) grade making the formulation highly safe to administer with improved bioavailability and therapeutic efficacy. Different strategies have been reported of late, wherein contrast and chemotherapeutic agents are entrapped in nanoemulsion for selectively targeting tumor microenvironment (TME) for both diagnostic and therapeutic drive [33–37]. Nonetheless, there are many obstacles in their journey from animal models to afflicted cancer patients, including firstly physicochemical stability of theranostic na-

noemulsion, subsequently, its *in vivo* fate, then degradation, and clearance from the system, along with long-term stability and toxicities concerns. Various attempts have been made thus far to surmount these hurdles and to entrap chemotherapeutic agents and diagnostic agents in nanoemulsion, particularly from the perspective of developing an efficient cancer theranostic agent that is highly capable of clinical translation (Figure 5).



**Figure 5.** Brief depiction of how lipidic theranostic can help in cancer alleviation via multi-functionalized aspects such as coupling of the surface with targeting ligand; entrapped theranostic agent, PEG coating on the surface for evading systemic clearance, bound oxygen for enhancing photothermal therapy, surface anchored contrasting agent.

The major challenge associated with developing lipid theranostic nanomedicine, which is also the major limitation in their clinical translation, is that the incorporation of several components in one nanocarrier [38]. This integration of numerous constituents in nanodispersion causes polydispersity, heterogeneity, and also difficulty in scalability issues [38]. In an attempt to address these issues, Zhang and coworkers 2020, developed fluorinated nanoemulsions with remarkably improved fluorescence imaging signals for selective and sensitive tumor detection [38]. Their theranostic approach was highly capable of selectively recognizing the specific type of tumor (integrin  $\alpha\beta 3$  overexpressed cancer cells), potential tracing of *in vivo* fate of nanoemulsion, and offering highly efficient photodynamic therapy. The meticulous approach averted many ingrained concerns with conventional nanomedicine, including polydisperse polymers, heterogeneous constituents, and complex formulation. Importantly, this approach imparted multiple functional aspects to the nanoparticles with tumor-targeting accompanied with quantitative and sensitive multimodal imaging (FL,  $^{19}\text{F}$  MRI,  $^{129}\text{Xe}$  hyper-CEST MRI), and PDT with a high therapeutic index [38]. Huang and associates 2019, designed an integrated system of multimodal imaging signals and PDT function into a poly(ethylene glycol)-boron dipyrromethene amphiphile (PEG-F54-BODIPY) with 54 fluorine-19 ( $^{19}\text{F}$ ), as an “all-in-one” nanocarrier [39]. This novel amphiphile acquired various unique and desirable attributes that make it potential cancer theranostic agents. The developed nanoemulsion was having distinctive structure-based fluorescent, photoacoustic, and magnetic resonance properties and prolonged tumor retention time for repeated PDT treatment, and great biocompatibility. The study outcomes revealed in the melanoma cancer xenograft model, developed nanoemulsion can be efficiently used as an activatable nanoprobe with improved sensitivity of multimodal imaging

for tumor recognition [39]. One more very interesting attempt was made by Fernandes and Kolios 2019, to increase the selectivity and targeting of nanomedicine for substantially afflicting cancer cells without causing any harm to nearby cells and off-tumor areas [40]. The fabricated perfluorohexane nanoemulsions possess the ability to selectively target cancer cells as these nanoparticles carry therapeutic agents, which have slow release rates and become vaporized into perfluorohexane bubbles without any rise in temperatures that could affect normal cellular function. Their ability to use higher concentrations of theranostic agents could be of significant advantage in improving therapeutic efficacy and imaging ability in clinical applications. In this study, the ability of nanoemulsions to carry therapeutic agents, doxorubicin, and paclitaxel, specifically for the treatment of breast cancer, was investigated. The study outcome revealed that perfluorohexane nanoemulsion could be efficiently internalized in cancer cells and could cause significant cell death. The developed nanoemulsion with concurrent laser excitation capability exhibited tremendous potential for destroying all tumor cells and emerging as a competent theranostic agent for averting the growth of cancer cells [40]. Furthermore, Zheng and associates, 2019 fabricated a novel nanoemulsion with a porphyrin shell (NewPS), and it was the simplest yet multifunctional nanoemulsion system developed thus far [41]. The porphyrin salt shell permitted the encapsulation and stabilization of the oil core, yielding a monodisperse, spherical nanostructure with excellent colloidal stability. The inherent multimodality of porphyrins enabled the multifunctionality of NewPS for imaging and phototherapy. Moreover, the oily core facilitates the efficient loading of hydrophobic anticancer molecules. The study established formable and intelligible, surfactant-free nanoplatforms for theranostic cancer applications. This novel two-component NewPS served as an innovative avenue for multimodal cancer imaging, phototherapy, and image-guided drug delivery [41].

In light of such studies, it is anticipated that nanoemulsions-based theranostic could offer promising opportunities in cancer treatment.

### 3.2. Liposomes

Liposomes stand tall in the crowd of conventional lipidic nanocarrier systems owing to their inimitable characteristic attributes. Their unique structure comprised of unilamellar lipid bilayers that nest an aqueous core offers great flexibility of easy incorporation of multicomponent. It also provides an option for both hydrophilic and lipophilic chemotherapeutic drugs and contrast agents. Besides biocompatibility, safety, biodegradability aspects, liposomes also offer an enormous scope of surface improvisation for selectively targeting tumor cells [42]. Recent literature highlights that liposomes have been amongst the topmost area of active research of cancer theranostics. At present, they are being largely investigated for incorporating and targeting cancer via contrast agent such as  $^{64}\text{Cu}$  [43] and  $^{14}\text{C}$  isotopes [44], QDs [45], gadolinium (Gd)-based contrast agents [46], super paramagnetic iron oxide particles (SPIONs) [47], and fluorescent probes [46,48].

The upcoming section will throw light upon the latest research studies that have confirmed the substantial potential of liposomes as cancer theranostic that could be successfully taken to clinics.

Prasad and associates 2021; fabricated liposomal nanotheranostics in which gold nanoparticles (AuNPs) and emissive graphene quantum dots (GQDs) were encapsulated along with a chemotherapeutic agent [49]. The surface of the liposome was functionalized with folic acid for targeted delivery. The prepared targeted liposomal theranostic demonstrated site-specific tumor diagnosis and photo-triggered tumor extirpation. The study outcome confirmed specific and enhanced cellular uptake, prolonged internalization in tumors, and substantial contrasting and therapeutic efficacy of nanotheranostic liposomes with dual imaging probes. The synergistic effect of anticancer drugs and photothermal effect exhibited superior tumor impedance, in contrast, to stand-alone therapy. Moreover, these multicomponent loaded liposomes have good colloidal stability, biocompatibility, and biodegradability as demonstrated in *in vivo* imaging. Therefore the developed nano

hybrid liposome nanotheranostic served as a safe and tremendously potential platform for multifunctional tumor diagnosis and targeted therapy [49].

Furthermore, Karpuz and associates 2020, investigated the *in vivo* therapeutic prospect and contrasting efficacy of paclitaxel and vinorelbine loaded, Tc-99m radiolabeled, folate targeted nanosized liposomes [50]. The study outcomes demonstrated targeted delivery of chemotherapeutic agents, which got efficiently lodged in tumor vasculature and resided there for a prolonged time, causing substantial reduction of tumor growth. The *in vivo* images confirmed mitigated off-site accumulation and toxic effect of liposome theranostic nanomedicines [50].

In another interesting research study, a very serious issue of brain metastasis (BM) and tyrosine kinase inhibitor (TKI) resistance that are the two major challenges in non-small cell lung cancer (NSCLC) treatment were addressed [51]. Yin and associates designed a dual-targeting liposomal system for co-delivery of gefitinib and simvastatin to treat BM of NSCLC. The study confirmed via fluorescence imaging that dual-targeted liposome could efficiently cross the blood–brain barrier and is highly capable of reversing drug resistance. Therefore, the developed liposomal formulation represents a potential strategy for treating advanced NSCLC patients with BM [51].

Bush and coworkers 2020 also came up with an interesting concept of acoustic cluster therapy (ACT) that constitutes of co-administration of a formulation containing microbubble constellations, along with regular anticancer drug and local US insonation of the targeted tumor tissue. The microbubble cluster efficiently resided in the tumor's microvasculature [52]. The therapeutic efficacy of ACT with liposomal doxorubicin for the treatment of triple-negative breast cancer using orthotopic human tumor xenografts in athymic mice was assessed. The study outcome established substantial increase in the therapeutic efficacy of Doxil<sup>®</sup> when combined with ACT [52]. Another crucial study that encourages the concept of application of liposome in cancer theranostic was conducted by Prabhakar and Banerjee 2019 [53]. They formulated submicron-sized ( $528.7 \pm 31.7$  nm) nanobubble-paclitaxel liposome (NB-PTXLp) complexes for ultrasound imaging and ultrasound responsive drug delivery in cancer cells. The concept resulted in more than 300-fold higher anticancer activity of NB-PTXLps in the presence of ultrasound in MiaPaCa-2, Panc-1, MDA-MB-231, and AW-8507 cell lines, in contrast to commercial formulation Abraxane<sup>®</sup>. Therefore, the novel NB-PTXLps served to be a promising and triflingly invasive theranostic scaffold for cancer therapy in the forthcoming scenario [53].

The research studies discussed in this section undoubtedly unveiled enormous opportunities to facilitate the targeted chemotherapeutic delivery with concomitant *in vivo* imaging utilizing liposomes. Further research is envisaged to take these studies to clinical trials.

### 3.3. Solid Lipid Nanoparticles (SLN)

The second-generation lipid nanocarrier includes SLN, which are spherical colloidal nanoparticles with a solid lipid core comprised of waxes, triglycerides, fatty acids, and are stabilized by surfactants. Their size usually falls within the 50–100 nm range and is exclusively known for their biocompatibility, higher susceptibility of lymphatic uptake, and sustained drug release [54,55]. In cancer, alleviation chemotherapeutics loaded SLN is very promising [54–56]. Nonetheless, they are capable of efficiently carrying contrast agents along with anticancer drugs and provide simultaneous treatment and diagnosis, as evident in outcomes of recent research studies. Kuang and coworkers have demonstrated in their study that solid lipid nanoparticles (SLNs) conjugated with c(RGDyK) were designed as efficient carriers to improve the targeted delivery of IR-780 to the tumors [57]. The multifunctional cRGD-IR-780 SLN significantly improved the tumor-specific targeting, efficacy of photothermal therapy along with spontaneous imaging of *in vivo* journey of SLN incorporated IR-780 iodide nanomedicine [57].

SLNs have been investigated for integrating many contrasting agents, particularly superparamagnetic iron oxide [58], technetium-99 (<sup>99m</sup>Tc), <sup>64</sup>Cu [59], and quantum dots [60,61]. Very recently, a research study came up with SLN cancer theranostic wherein SLN was

encapsulated with QD as a contrast agent [54,62]. The chemotherapeutic agent was the combination of Paclitaxel and siRNA. The solid lipid matrix was interspersed with paclitaxel and QD whereas siRNA, which was anionic, was electrostatically linked on the outer cationic surface. The combination of dual therapeutic agent paclitaxel and siRNA loaded in SLN got efficiently accumulated in lung carcinoma and exhibited synergistic anticancer activity. Importantly QD fluorescence in SLN made it possible to track higher in vivo cellular uptake of SLN on-site and mitigated uptake at off-site cancer cells. This study confirmed the potential theranostic applicability of SLN as a nanocarrier [54,62].

In another interesting research study, Morel and associates have revealed the successful integration of gadolinium (Gd) (III) complexes in SLN that would be contributing as an efficient and favorable oral contrast agent for MRI [63]. The percentage of Gd (III) complex entrapped in SLN was substantially higher as confirmed by average longitudinal relaxivity for Gd (III) complex in SLN system and pure water (25 °C, pH 7, 20 MHz) [63].

Another research study conducted by Andreozzi and associates is clear evidence of the multifunctional theranostic ability of SLN [59]. They radiolabelled SLN with  $^{64}\text{Cu}$  and assessed its bio-distribution by in vivo quantitative assessment, PET imaging, and ex vivo gamma counting. The study outcomes validated the simultaneous in vivo imaging and tumor ablation potential SLN theranostic, which is also safe, biocompatible, and biodegradable [59].

The research studies conducted thus far are very limited in numbers, and several other important aspects of SLN also need profound exploration from a cancer theranostic perspective, such as stimulation of lymphatic absorption by SLN. Whatever literature we have discussed can corroborate the efficient in vivo imaging and drug delivery utilizing SLNs along with the safe theranostic application, biocompatibility, and biodegradability, of developed nanomedicine. The results established that the SLN theranostic nanoformulation developed is optimistic for hallmark contribution in the field of cancer treatment with simultaneous diagnosis.

### 3.4. Nanostructured Lipid Carriers (NLC)

NLC is a smart next-generation nanocarrier with a unique hybrid matrix of solid and liquid lipids stabilized by surfactants. The imperfect crystalline or amorphous structure possesses an enormous potential of high drug loading and improvised drug release. Latest research studies indicate the promising role of NLC in cancer theranostic. Of late, Li and coworkers successfully developed a multifunctional nanocarrier of Coumarin 6 fluorescent dye and IR 780 encapsulated CXCR4-targeted NLCs for breast cancer alleviation also employing photodynamic therapy [64]. The developed system proved to be highly efficient in debilitating tumor progression and metastasis and concurrently allowing imaging [64].

Olerile and coworkers prepared a NLC loaded with QD and paclitaxel that was highly capable of monitoring and tracking tumor growth and simultaneously impeding tumor cells in the murine tumor model of hepatocellular carcinoma [65]. Researchers confirmed the great cancer theranostic potential of NLC as it was efficiently enabling targeted delivery with concomitant in vivo imaging [65].

Another very promising approach in the area of cancer theranostic utilizing NLC was reported. Camptothecin encapsulated-NLC was formulated conjoined with QD and fluorescent imaging probes that were capable of detecting the lodging, internalization, cytotoxicity, and biodistribution of NLC nanomedicine [66]. The study outcome established that NLC coordinated with QDs and an anticancer drug offered efficient tumor imaging and drug delivery and such accomplishment with a novel nanocarrier system was remarkable and worth mentioning here [66].

An interesting attempt was made to deliver paclitaxel-loaded NLC with folic acid dispersed hybrid lipid matrix [67]. The paclitaxel-loaded NLC was radiolabeled with  $^{99\text{m}}\text{Tc}(\text{CO})^{3+}$ . Due to the imperfection in a matrix structure, too many components were efficiently loaded in NLC as reflected by in vitro stability of developed formulation, which was up to the mark (>90%). Results indicated that  $^{99\text{m}}\text{Tc}(\text{CO})^{3+}$ -radiolabelled paclitaxel NLC

was capable of identifying folate receptors overexpressed in tumor cells. The developed formulation was successfully localized at the specific targeted tumor areas without any off-site distribution and the uptake by RES on intravenous administration. The concurrent imaging efficiently depicted the *in vivo* fate of paclitaxel-loaded NLC that is very much desirable for an optimal therapeutic implication [67].

As the data concerning NLC theranostic for cancer is very restricted, there is a great need for a lot more investigation to be envisaged to explicitly explore multiple beneficial aspects of advanced lipid nanocarrier and pave the way for their successful clinical translation.

### 3.5. Lipid Nanocapsules (LNCs)

LNCs are also amongst the next-generation lipid nanocarrier systems with lipoprotein-like structures whose size falls within 1–100 nm. The structure of LNCs is a blend amidst polymeric nanoparticles and liposomes as they have an oily core with an exterior built of a tensioactive rigid membrane. LNCs are a novel lipid nanocarrier system and can be prepared via phase inversion of emulsions and organic solvent-free-based procedures [68].

Nevertheless, researchers consider LNCs as an optimistic platform for cancer theranostic as well. A very recent study further confirmed the promising outlook of LNCs in cancer theranostic. To selectively target tumor cells, QDs-based lipid nanocapsules (LNCs) encapsulated with celecoxib, and honokiol were designed and investigated. The study outcome revealed efficient accumulation and intracellular uptake of LNCs in tumor cells, and their internalization was progressively traceable via fluorescence restoration. The LNCs established highly improved and superior anticancer efficacy of LNCs against breast cancer cells. The developed system could be applied as a potential multifunctional nanotheranostic for imaging and targeted therapy of breast cancer [69].

### 3.6. Lipid-Based Micelles

Lipid-based micelles are the spherical structure of lipid molecules, in which they aligned themselves in aqueous solutions. This class of lipid nanocarrier system is unexplored to date, but it could also serve as a potential and promising therapeutic cum diagnostic nanomedicine for cancer treatment. In a study, Ma and coworkers developed a lipid-based micelle encapsulated with docetaxel (M-DOC) that possessed marked anticancer efficacy and mitigated toxicity in the xenograft breast cancer model [70]. The lipid-based micelles need to be duly explored for their cancer theranostic potential in the near future.

Table 1 enlists the different lipidic nanomedicine investigated for the theranostic applications in cancer and summarizes their theranostic outcomes in different experimental models.

**Table 1.** Theranostic application of lipidic nanomedicines for cancer therapy.

Lipidic Nanocarrier	Chemotherapeutic Agent	Diagnostic Agent/Modality	Experimental Model	Theranostic Outcome	Ref.
Nanoemulsion	PDT	fluorinated cryptophane-A and porphyrin self-assembled onto the surface of fluorinated nanoemulsions- <sup>19</sup> F MRI and fluorescence imaging	Xenograft A549 tumor mice.	A high therapeutic efficacy; low toxicity; high tumor accumulation of nanoemulsion	[38]
	PDT	Fluorescence probe/photoacoustic/ <sup>19</sup> F magnetic resonance multimodal	A375 melanoma xenograft model	The remarkable efficiency of PDT on hypoxic solid tumors via a single injection of the drug; outstanding diagnostic ability	[39]
	Doxorubicin and Paclitaxel	Perfluorohexane (PFH) vaporized bubbles as an Ultrasound contrast agent	MCF-7 cells	Markedly enhanced PFH-NEs targeting and lodging in tumor region with simultaneous treatment monitoring.	[40]
	Paclitaxel and PDT	Porphyrin NE shell-based photoacoustic imaging and fluorescence imaging; CT contrast	Mice bearing tumors	multimodal cancer imaging, highly efficient phototherapy and image-guided drug delivery	[41]



Table 1. Cont.

Lipidic Nanocarrier	Chemotherapeutic Agent	Diagnostic Agent/Modality	Experimental Model	Theranostic Outcome	Ref.
Liposomes	Doxorubicin HCl	gold nanoparticles (AuNPs) and emissive graphene quantum dots (GQDs)	Breast tumor-bearing mice models	specific and enhanced cellular uptake, prolonged internalization in tumor and substantial contrasting and therapeutic efficacy	[49]
	Paclitaxel and vinorelbine	Tc-99m radiolabeled	NSCLC tumor-bearing C57BL/6 mice	Effectively inhibited tumor growth completely restricted lung metastasis	[50]
	Gefitinib and simvastatin	Fluorescence imaging	Brain Metastasis (BM) mouse model developed by intracranial transplant of the H1975 NSCLC cells	Efficient permeation across the blood-brain barrier and high capability of reversing drug resistance.	[51]
	Doxorubicin	Acoustic cluster therapy (ACT); Ultrasound insonation	orthotopic human tumor xenografts in athymic mice	Substantial increase therapeutic efficacy of Doxil <sup>®</sup> when combined with ACT	[52]
	Paclitaxel and ultrasound responsive drug delivery	Ultrasound imaging	MiaPaCa-2, Panc-1, MDA-MB-231, and AW-8507 cell lines	300-fold higher anticancer activity in contrast to ABRAXANE.	[53]
SLN	Paclitaxel and siRNA	Quantum dots	A549 cancer cells	Efficient in situ visualization of intracellular translocation of SLNs into cancer cells.	[54, 62]
		<sup>64</sup> Cu, PET imaging, and ex vivo gamma counting	Mice	<sup>64</sup> Cu-radiolabelled SLN and their biodistribution was efficiently quantitatively evaluated	[59]
NLC	Paclitaxel	Quantum dots	HepG2 cells/Female Kunming mice	Imaging established splendid capability of the co-loaded NLC to specifically target and detect the H22 tumor.	[65]
	IR 780 and Photothermal therapy	fluorescent probe coumarin 6	4T1-luc cell line in BALB/c female mice	Notably enhanced photothermal anti-tumor effect as well as anti-metastatic efficacy in vivo	[64]
	Camptothecin	Quantum dots	Melanoma cells	camptothecin accumulation in melanomas increased by 6.4-fold	[66]
	Paclitaxel	<sup>99m</sup> Tc(CO) <sub>3</sub> <sup>+</sup>	Wistar Albino rats.	Substantially high cellular uptake and concurrent imaging	[67]
Lipid nanocapsule	Celecoxib and honokiol	fluorescent mercaptopropionic acid-capped cadmium telluride was coupled with quantum dots as an imaging probe	human breast cancer cells: MCF-7 and MDA-MB-231; EAT model	Highly improved and superior anticancer efficacy; Efficiently traceable LNC internalization	[69]
Lipid-Polymer Hybrid	Platinum (IV) (Pt(IV)) prodrug	(glutathione (GSH)-sensitive platinum (IV) for Ultrasound imaging	$\alpha$ v $\beta$ 3- and $\alpha$ v $\beta$ 5-positive SKOV3 human ovarian tumor cells and $\alpha$ v $\beta$ 3- and $\alpha$ v $\beta$ 5-negative A2780 human ovarian tumor cells	Significant therapeutic efficacy and limited side effect	[71]

## 4. Advancement in Lipid-Based Nanoparticles for Cancer Theranostics

### 4.1. Polymer-Lipid Hybrid System

Lipid polymer hybrid is next-generation lipid nanocarriers and has obtained its foundation from the amalgamation of liposomes and polymeric nanoparticles. They have a polymeric core enclosed by a lipid bilayer shell kind of structure. Many researchers claim it to be a very promising nanocarrier for anticancer drug delivery, however, its potential is not duly tapped and remains unexplored to date. In recent research, Huang and associates developed multifunctional tumor-targeted polymer-lipid hybrid nanoformulation, which was loaded with ultrasound contrast agents (glutathione (GSH)) and prodrug (Pt(IV)) for targeted delivery of theranostic nanomedicine against ovarian cancer. The nanosized formulation was composed of a perfluorohexane (PFH) liquid core, a hybrid lipid-polymer shell, and an active targeting ligand, which demonstrated improved cellular uptake. The study findings established Pt(IV) encapsulated lipid-polymer as a novel multimodality

platform exhibiting excellent anticancer activity and substantially reduced toxicity and signifying a powerful theranostic nanomedicine for combating ovarian cancer [71]. The research outcome encourages further exploration of this class of lipidic nanocarriers to be envisaged for beneficial prospects in the field of cancer theranostic.

#### 4.2. Endogenous High-Density Lipoprotein Derived Nanoparticles

Nanocarrier systems comprising endogenous high-density lipoprotein (HDL) could emerge as potential lipidic nanocarrier-centered cancer theranostic options owing to their non-immunogenicity, complete biodegradation, and infrequent reticuloendothelial system (RES) uptake [72–74]. HDL-like peptide- phospholipid nanovesicles (HPPS) imitate the structural and functional attributes of plasma-derived HDL [74–77]. He and coworkers recognized a TfR mAb (monoclonal antibody) tailored nanomedicines for improved tumor targeting. They demonstrated that drug entrapped HPPS based nanomedicines adapted with explicit ligands could muddle to receptors on the surface of tumor cells, resulting in the accretion of nanomedicines on the exterior surface of targeted cells [75–90]. It was concluded that developed HPPS based nanomedicine holds the potential to strengthen targeting to tumor cells and attains favored recognition by specific antibodies in a complex biological setting [91]. Such intricately woven novel research concept needs to be brought forth and encouraged thus that these kinds of potential research perceptions can be multiplied. Huge benefits can be extracted from such studies for accomplishing successful targeting of lipidic cancer theranostic nanomedicine.

Fayad and coworkers presented very interesting work on HDL-based multimodal nanotheranostic for targeting and imaging tumors [92]. The developed HDL nanoparticles got non-selectively accumulated and selectively binding to angiogenic active blood vessels. For targeting such angiogenic endothelial cells, HDL was reconstituted with gadolinium chelates and fluorescent dyes, and their surface was functionalized with  $\alpha v \beta 3$ -integrin-specific RGD peptides. The incorporation of such peptides felicitated uptake of HDL-based nanoparticles by angiogenic endothelial cells as visualized in MRI after administration of developed nanoparticles in tumor-bearing mice. The study findings demonstrated the substantial possibility of redirecting HDL from their natural route towards tumor-ridden blood vessels along with successful imaging and tracing of an entire pathological process [92].

#### 4.3. Hybrid Lipid-Inorganic Nanomaterials

Most recently, there has been a paramount focus shifted towards an exploration of hybrid lipid-inorganic nanomaterials, which combine and multiply the desirable attributes of both classes of nanocarriers, including lipidic nanocarriers and inorganic nanoparticles. The lipid nanocarrier system employed for such application includes liposomes, nanoemulsion, solid lipid nanoparticles, and lipoproteins. In contrast to singly functionalized counterparts, this hybrid multifunctional system offers many beneficial outcomes in cancer theranostic such as stimuli-triggered anticancer drug release, photothermal therapy, and bioimaging. The internalization of inorganic material inside the lipid nanocarrier governs their functional aspects as there are different spatial lodging based on the structure of lipidic assemblies. The inorganic material can reside in the surface coating of lipid nanocarriers as surface-bound nanomaterial, or it can be lodged in bilayer lipids lamellae in liposomes, and certainly, the inorganic material can also be internalized in the core structure of lipidic nanocarrier [93]. A plethora of investigational studies are reported in which gold (Au) was used as an inorganic nanomaterial for preparing hybrid lipid-inorganic nanoparticles for cancer theranostic. The considerably low toxicity, ease of improvising surface chemistry, tunable size and shape, and substantial electronic property make Au a metal of choice for preparing inorganic nanoparticles and their hybrid lipid nanoformulations that have great potential for bioimaging site-specific drug release, and photothermal cancer therapy [93]. Other potential inorganic materials that have been explored for preparing hybrid lipid-inorganic nanomaterial include silver and palladium nanoparticles. In addition, one of

the most commonly used approaches include SPIONs, which are ideal contrast agent for MRI owing to their biocompatibility and distinctive magnetic properties [94]. Moreover, the potential of semiconducting nanoparticles (QDs) is becoming widely accredited in bioimaging as optical probes over conventional organic dyes [95].

The recent study findings focusing on hybrid lipid-inorganic nanomaterials are clear evidence of their potential in cancer theranostic. In a study, Kang and Ko have developed a hybrid lipid inorganic nanomaterial by efficiently incorporating docetaxel in Au nanoparticles and then encapsulating this Au nanoparticle in thermosensitive phospholipid lipid bilayer coating [96]. The outcome of the study established enhanced cellular uptake, internalization, and cytotoxicity of hybrid lipid inorganic nanoformulation in comparison to uncoated drug-loaded Au nanoparticles. The study findings strongly encourage the implication of drug-encapsulated lipid-coated anisotropic nanoparticles for amplifying therapeutic prospects of chemotherapy [96]. The recent research concluded the feasibility of breast cancer cell detection via conformance of the inorganic metal-nanoemulsion hybrid [97]. An improvisation was made in perfluorocarbon or QD nanoemulsions by incorporating N-hydroxysuccinimide modified phospholipids in the surfactant formulation, as this would enable conjugation of prepared hybrid QD nanoemulsion with the amine groups in antibodies. Such antibodies targeting growth factors are overexpressed in human breast cancer cells, which would be easily able to bind with nanoemulsions. The research study demonstrated the selective linking of hybrid nanoemulsion with its target breast cancer cell line [97]. Interestingly, low-density lipoprotein (LDL) encapsulating Au nanoparticles were explored for their biolabeling capability [98]. Administration of dodecanethiolcapped Au nanoparticles loaded LDL in mice with B16-F10 tumor resulted in selective uptake by tumor-associated macrophages that play a vital role in metastasis of tumor cells. The study findings confirmed the substantial potential of hybrid Au-LDL nanoformulation in *in vivo* tracking and treating of tumors without causing off-site damage [98]. In another study by Bao and coworkers, hybrid liposome nanoformulation wherein paclitaxel Au nanoparticles were embedded in its bilayer lipid lamellae demonstrated remarkably prolonged release rate and extended circulation time. The hybrid exhibited notable potential for enhancing the therapeutic efficacy of incorporated anticancer agents [99]. Mounting evidence has elucidated the potential of palladium nanoparticles as contrast agents for photothermal and anticancer therapy. Nevertheless, research works focused on hybrid lipid assemblies incorporating such palladium nanoparticles established excellent anticancer activity as well as site-specific uptake and internalization of a therapeutic agent through these hybrids [100,101]

Certainly, there are serious toxicity concerns with the use of inorganic nanomaterial. For example, oxidation of silver (Ag) to toxic  $\text{Ag}^+$  ion in biological milieu can cause toxic effects that must be controlled. Here hybrid lipid encapsulation could come to the rescue of such lethal transformation. By tuning the lipidic membrane composition, the release of  $\text{Ag}^+$  ions can be prevented. Moreover, studies have established that the physicochemical features, size, shape, surface, coating, surface area contribute significantly in dictating the hybrid lipid inorganic nanomaterial toxicity and its biological interactions [102]. Therefore, skillfully designed hybrid lipid inorganic nanomaterial exhibits the potential of overcoming the toxicity issue of incorporated metals.

#### 4.4. Cancer Tumor Cell Targeting Theranostic Vector

At present, the active area of targeting circulating tumor cells (CTC) via theranostic vectors before the homing and progression of carcinomas is largely explored for improving cancer therapeutic intervention. The CTCs are those cells that are detached from primary solid tumors and traverse through blood and lymph to form secondary tumors [103]. Therefore, detection and targeting of CTC may result in early diagnosis and prevention of cancer and its metastasis. Determination of CTC concentration in blood could provide valuable information about the diseased state [103]. Therefore, estimating CTC concentration would contribute significantly in monitoring remission and relapse and assessing response to

chemotherapy [103]. In a study by Bhattacharyya and associates, antibody-targeted Au nanoparticles were employed for CTC detection in breast cancer cell line T47D [103]. The study outcomes established Au nanoparticles as a promising approach for detecting and capturing CTC in a photoacoustic flowmeter. The study findings established an abundant scope of diagnosis of disease at an early stage in various solid tumors and its successful treatment. Such encouraging findings mark a new paradigm for cell-specific molecular analysis for individualized cancer therapy via capturing of CTC [103].

### **5. Impact of Physicochemical Attributes of Lipid Nanoparticles in Improving In Vivo Performance of Cancer Theranostics**

A recent study conducted by Tahmasbi and associates established that physicochemical facade, predominantly shape and size, greatly influences the efficiency of the lipidic theranostic nanomedicines [104]. Mounting literature confirmed that spherical nanomedicines having a diameter within 20–100 nm lead to optimal tumor accretion owing to the EPR effect. However, dissimilar EPR attributes have been testified owing to nonspherical nanostructures (i.e., nanorods) [104,105].

The EPR effect refers to the selective buildup of lipidic theranostic nanomedicine at the tumor locations through extravasation via endothelial cells from the dripping vasculature. Accounting to the recent evidence, the physicochemical attributes of the lipidic theranostic nanomedicine comprising size, shape, charge, etc., possess greater potential in dictating tumor accumulation in contrast to active targeting on the exterior of nanomedicines [105]. Consequently, lipidic theranostic nanomedicine can be formulated for targeted tissues as well as for non-specific cell absorption by optimizing their physicochemical properties in the absence of targeted ligands [105]. Lately, it has been verified that shape greatly impacts cellular uptake [106,107]. Myriads of studies confirmed the diversified morphology-dependent anticancer efficacies for the same chemical compositions [108,109]. For the discoidal shape of lipidic nanomedicine having sizes <50 nm, tumor accumulation efficiency is not explored until recently [110–113]. For lipidic theranostic nanomedicine greater than 100 nm, needle-like rods have shown the maximum cellular uptake, trailed by shapes such as spheres, cylinders, and cubes, as evident in supporting studies [104,105]. For sub-100 nm lipidic theranostic nanomedicine, spheres demonstrated enhanced uptake by tumor cells over rods [104,105].

Nonetheless, the fluidity of lipid membranes can fluctuate with charge (negative or positive) and may persuade local gelation [104]. Neutral and slightly negative lipidic theranostic nanomedicine are found to maintain the longest half-life in blood [104,112,113]. Lipidic theranostic nanomedicine that has a positive charge could ensue the issues of platelet aggregation and hemolysis [104,112,113]. The competence of such a platform to fine-tune surface charge is another benefit in addition to size and shape adjustment that plays a crucial role in improvising biological behavior and clinical outcomes of lipid theranostic nanomedicines [104].

The absence of specificity with inactive targeting determined by the nanosize of lipidic theranostic nanomedicine has restricted efficiency. Mounting literature revealed that active targeting to the tumors might augment the intracellular uptake and lessen the lipidic theranostic nanomedicine's spread in healthy tissues. A rational approach to attain this objective is to exploit specific interactions between the targeting molecules on the lipidic theranostic nanomedicine's surface and overexpressed receptors of the cancer cells. Few ligands, namely transferrin, and folate can considerably enhance site-specific targeting [104]. Predominantly, folate has emerged as one of the targeting ligands for selective delivery of involved diagnostic and therapeutic agents owing to the overexpressed folate receptor (FR) in a myriad of tumor tissues, including kidney, lung, ovarian, cervical, breast, epithelial, brain and colon tumors, whereas limited in healthy organs and tissues. Folic acid being nonimmunogenic, unchanging over wide ranges of temperatures and pH values, can bind to the folate receptor after pairing with drugs or imaging markers. Consequently, folic acid has been extensively used as targeted therapy in cancers on account of its high binding

affinity to FR, simplicity of conjugation to different lipidic theranostic nanomedicine, and the widespread distribution of FR in a substantial portion of human cancers [104]

## 6. Limitation of Lipid Nanoparticles-Based Cancer Theranostics

The major limitation with lipidic nanoparticles is their tendency to fuse, especially if the size of prepared nanoformulation is below 100 nm [114]. The fusion, in turn, results in increased non-uniformity and dispersity in size and escape of encapsulated contents from the lipid vesicles [114]. However, this issue can be addressed by covering the surface of lipid nanoparticles with polyethylene glycol coating. Another issue of great concern with lipidic nanoparticles is their stability over a longer duration of periods. It is certain that after storage for long periods, apparently intact lipid nanomaterials show a different biodistribution due to changes in physicochemical characteristics and alterations of the surface coating attributes [114].

Nonetheless, Carregal-Romero and associates have raised forth this very significant aspect of the influence of long-term stability of polyethylene glycol coating on contrast agent encapsulated nanoparticles and its *in vivo* fate [114]. They investigated the biodistribution of iron oxide nanoparticles, which were employed as dual contrast agents for MRI and SPECT imaging [114,115]. They developed these theranostic nanoparticles by coprecipitation of  $^{111}\text{In}$ -doped magnetic nanoparticles, followed by coating with polyethylene glycol [115]. Then they examined the physicochemical characteristics of freshly prepared nanoparticle solution and an aged nanoprobe solution that was stored for 9 months. The characteristic evaluation demonstrated comparable results of size distributions, zeta potentials, and morphology. However, after systemic administration of these two nanoparticle preparation in mice, completely distinct biodistribution pattern were observed [115]. The freshly prepared nanoprobe solution was mostly internalized in the kidney, whereas the aged nanoparticles were heavily concentrated in the liver. Therefore, the study outcomes concluded that there might occur some small level structural changes in polyethylene glycol coating that cannot be detected by dynamic light scattering and transmission electron microscopy, which have led to a remarkable alteration in *in vivo* behavior. Therefore this report established a substantial role of long-term stability polyethylene coating in dictating the biological behavior of theranostic nanoparticles [115].

The size of theranostic nanomedicine is also very crucial in determining its *in vivo* fate and clinical outcomes. It has been established in different studies that if the diameter of nanoparticles is larger than 100 nm then the particles get accumulated in the liver and spleen, whereas nanoparticles having a diameter smaller than 10–15 nm are usually eliminated by renal clearance [114]. Therefore nanomedicines with desirable particle diameters between 10 and 100 nm are supposed to have longer blood circulation times and accessibility to tumoral tissues and organs [114]. Furthermore, low polydispersity index (PDI) and size stability are very significant as they avert aggregation of nanoparticles, which could occur because of an inappropriate surface coating. The aggregated nanoparticle can be easily engulfed by the RES [114,115]. Nonetheless, polyethylene glycol coating is very effective in ensuring stability to the nanoparticles and thereby mitigating their opsonization, macrophage uptake, and RES clearance and increasing the blood circulation time [114].

Importantly, with every approved lipid nanomedicine, a possibility of intratumoral heterogeneity and variability of response to chemotherapy is evident. Unquestionably, the tumor microenvironment contributes largely in dictating how chemotherapeutic agents interact with cancer cells in that particular microenvironment, which in turn can impact proliferation, differentiation, morphology, and a range of cellular functions [116]. To envisage the clinical outcome of lipid-based theranostic nanomedicine, substantial emphasis should be given to universal heterogeneity issues with extraordinary conformity in terms of cancer cells, tumor microenvironment, and pathophysiological architecture [116]. However, with current theranostic and imaging modalities, complete biological approximation of the

interaction of native tumor and a chemotherapeutic agent is not possible, which greatly hampers the accurate mapping and clinical findings.

### 7. Challenges in Clinical Translation of Lipid Nanoparticles for Cancer Theranostics

An extensive scope has been conveyed by lipidic theranostic nanomedicine in enhancing the health of humans through providing an understanding of diagnosis, prevention, and treatment of diseases. Even after substantial technological advancement in this area (as presented in Table 2), there is still a long way ahead for lipidic cancer nanotheranostic in becoming a new criterion for the diagnosis and treatment of diseases. Nano-bio interaction is a prime opposition for the transferal of lipidic theranostic nanomedicine to clinics. Disorders like inflammation, immunoreactions, or related illness can come up when a contrasting agent in lipidic theranostic nanomedicine interacts with biological material because of its incompatibility or potential toxicity. The extent of toxicity is immensely based on some parameters, which include the solubility of the nanoformulation, size, and zeta-potential [117]. Once entered into a biological system, nanovesicles tend to interact with proteins, and that results in the development of 'corona' on its surface. Such adsorption, in turn, results in the alteration of their stability, biodistribution, dispersibility, toxicity profile, pharmacokinetics, and size [118,119]. This has also been shown in many studies that adverse immunogenic reactions and allergies are happening by nanoparticles [120,121]. Hence, it becomes vital to study the physicochemical characteristics of nanomedicines for heterogeneity and pathophysiology of human diseases. More importantly, a generalized size outlook of lipidic theranostic nanomedicine is not possible as chemotherapy is distinct for every patient, and this may pose a hurdle in clinical translation [122]. Nanomedicines with good therapeutic efficacy might not be a good diagnostic tool necessarily, as suggested by the evidence. In a recent study, it was found that tumor uptake and tumor visualization performed with anti-EGFR coated gold nanoparticles with 20 nm size showed increased tumor uptake, whereas the same gold nanoparticles of 50 nm size illustrated excellent CT contrast [123]. This study suggested that the size-dependent distribution of theranostic nanomedicines in tumors limits its use as a theranostic agent [123]. Hence, the safety profile of nanotheranostic in humans continues to be a major concern for which long-term monitoring of patients in both early and advanced phases of clinical trials is required. One more important obstruction for the clinical translation of lipidic theranostic nanomedicines is the complexity in formulating a reproducible and controllable synthesis process. Nanomedicines synthesis on a large scale faces challenges like varied physical and chemical characteristics, low yield, and insufficient batch-to-batch reproducibility. The complex and laborious manufacturing process of nanomedicines makes it difficult to focus on physic-chemical attributes as the emphasis is more on quality and cost [122,124]. It becomes a task to produce lipidic theranostic nanomedicines on a large scale as they constitute more precise chemistry and multifunctional unit. Moreover, control along with good manufacturing practices are required to boost lipid theranostic medicine's reach to clinics from a laboratory.

**Table 2.** Lipidic nanocarrier based cancer theranostic in clinical stage of progress.

Lipidic Nanocarrier	Attributes	Cancer Type	Sponsors	Clinical Trial ID/Phase
Liposomes	Evaluating Immunogenic Chemotherapy Combined With Ipilimumab and Nivolumab in Patients With Metastatic Luminal B Breast Cancer	Breast Cancer	Oslo University Hospital	NCT03409198, Phase 2B
Liposomes	To study the distribution profile and radiation dosimetry of 188Re-BMEDALiposomes.	Tumors	Nuclear Energy Research Institute of Taiwan.	NCT02271516 Phase 1
Liposomes	To study the MTD of EphA2 siRNA –encapsulated liposomes, evaluate efficacy in the tumor cell, which we cannot be cured by treatment.	Solid Tumors	M.D. Anderson Cancer Center National Cancer Institute (NCI)	NCT02191878 Phase 3
Lipid-based Nanoparticles	To study proposes targeted delivery cytotoxic drugs, via formulated LTSL activated by using focused ultrasound (FUS).	Liver Tumor	University of Oxford	NCT02181075 Phase 1

Another important issue that is required to be addressed is the extensive gap between regulatory authorities and the scientific community. Many government agencies are monitoring the commercialization of nanomedicine based on regulatory issues related to the safety profile, quality control, patent protection, and manufacturing practices. Lack of clear regulatory and safety guidelines affects the timely and effective translation of lipidic theranostic to market [125,126]. Even though the general regulatory standards have been cleared by the nanomedicines presently available in the market, further revision is required to be sure of the safety, efficacy, and quality of other nano theranostic for human use since the present standards might not be sufficient.

#### *Approach to Overcome the Challenges*

A lot of research efforts are required to overcome the biological barriers associated with lipidic cancer nanotheranostic. It is important to have a profound understanding of the correlation of disease heterogeneity and patient biology with nanomedicine, which is also the prime reason for the failures of promising nanoformulation in clinical trials. One of the strategies for mitigating clinical translation failures is the arduous assessment of nanoformulation in various animal models before starting the clinical trials. Expedient information regarding the suitability of lipidic theranostic nanomedicine can be obtained through preclinical studies before treatment and imaging of human subjects [127]. Nanotoxicology profiles consisting of standardized assay protocols for immunotoxicity, genotoxicity, and cytotoxicity should be to be implemented and followed to evaluate the potential risk in patients [128].

Academic laboratories are coming up with nanomedicine-based drug-delivery systems with great emphasis on new technological and scientific developments that succeed at a small scale. These laboratories normally know the technical issues, which occur in the industry for the commercializing processes. A strong collaboration among pharmaceutical companies and academic laboratory groups is required to be established to bridge this gap. There is a need to develop modified rules, which will be listed under good manufacturing practices that are suitable for large-scale synthesis of lipidic theranostic nanomedicines. To identify the key process and formulation variables for nanomedicine optimization and address batch-to-batch variation, optimization software such as Aspen (AspenTech,

Bedford, MA, USA) can be implemented in an industrial setting. For tightly controlled and robust manufacturing, this might be instrumental [129]. In conclusion, a positive outcome in manufacturing depends highly on how well the personnel is trained regarding the challenges, hurdles, and specificities related to the products. There is no doubt regarding the influence of lipidic theranostic nanomedicines on the health of humans in the clinic still. If the aforementioned lessons are applied in the early stages of development, it can help the producers prepare to develop efficient products.

## 8. Conclusions

The present manuscript brings forth the latest research updates in the field of lipid-based nanocarriers on cancer theranostic. The study findings are very motivating and strongly encourage a splendid exploration of lipidic nanocarrier in the area of cancer theranostic and make the outcomes clinically swappable. Moreover, this review provides a sound discussion over the impact of physicochemical attributes of lipid nanoparticles in improving in vivo performance of cancer theranostics. The review also discusses the limitations and suggests relevant solutions for the successful development of lipid-based cancer theranostic nanomedicines of improved attributes to pave their way to the clinics. Additionally, this review will provide a convenient guide for the researcher to know the significant findings of the recent studies carried out in the field of lipid nano carrier-based cancer theranostic in the last few years.

**Author Contributions:** Conceptualization and methodology, S.I.B., S.S.I.; software, J.A., M.Z.A.; formal analysis, S.A., J.A.; resources, M.Z.A., J.A.; writing—original draft preparation, S.S.I., S.I.B.; writing—review and editing, J.A., S.A., M.Z.A., P.R.V., visualization, J.A., M.Z.A., P.R.V.; project administration, S.S.I., J.A., W.A.M.; funding acquisition, W.A.M. All authors have read and agreed to the published version of the manuscript.

**Funding:** Deanship of Scientific Research at King Saud University, Saudi Arabia: RG-1441-443.

**Institutional Review Board Statement:** Not applicable.

**Informed Consent Statement:** Not applicable.

**Data Availability Statement:** Not applicable.

**Acknowledgments:** The authors extend their appreciation to the Deanship of Scientific Research at King Saud University for funding this work through research group No. (RG-1441-443).

**Conflicts of Interest:** The authors declare no conflict of interest.

## References

1. Ferlay, J.; Laversanne, M.; Ervik, M.; Lam, F.; Colombet, M.; Mery, L.; Piñeros, M.; Znaor, A.; Soerjomataram, I.; Bray, F. *Global Cancer Observatory: Cancer Today*; International Agency for Research on Cancer: Lyon, France, 2020. Available online: <https://gco.iarc.fr/today> (accessed on 15 February 2021).
2. Available online: <https://www.who.int/news-room/fact-sheets/detail/cancer> (accessed on 15 April 2021).
3. *GBD Results Tool*; Institute for Health Metrics, University of Washington: Seattle, WA, USA, 2020. Available online: <http://ghdx.healthdata.org/gbd-results-tool> (accessed on 22 February 2021).
4. de Martel, C.; Georges, D.; Bray, F.; Ferlay, J.; Clifford, G.M. Global burden of cancer attributable to infections in 2018: A worldwide incidence analysis. *Lancet Glob. Health* **2020**, *8*, e180–e190. [CrossRef]
5. Iyer, A.K.; Khaled, G.; Fang, J.; Maeda, H. Exploiting the enhanced permeability and retention effect for tumor targeting. *Drug Discov. Today* **2006**, *11*, 812e818. [CrossRef] [PubMed]
6. Gabizon, A.A. Selective tumor localization and improved therapeutic index of anthracyclines encapsulated in long-circulating liposomes. *Cancer Res.* **1992**, *52*, 891–896. [PubMed]
7. Northfelt, D.W.; Dezube, B.J.; Thommes, J.A.; Miller, B.J.; Fischl, M.A.; Friedman-Kien, A.; Kaplan, L.D.; Du Mond, C.; Mamelok, R.D.; Henry, D.H. Pegylated-liposomal doxorubicin versus doxorubicin, bleomycin, and vincristine in the treatment of AIDS-related Kaposi's sarcoma: Results of a randomized phase III clinical trial. *J. Clin. Oncol.* **1998**, *16*, 2445–2451. [CrossRef] [PubMed]



8. O'Brien, M.E.; Wigler, N.; Inbar, M.; Rosso, R.; Grischke, E.; Santoro, A.; Catane, R.; Kieback, D.G.; Tomczak, P.; Ackland, S.P.; et al. Reduced cardiotoxicity and comparable efficacy in a phase III trial of pegylated liposomal doxorubicin HCl (CAELYX®/Doxil®) versus conventional doxorubicin for first-line treatment of metastatic breast cancer. *Ann. Oncol.* **2004**, *15*, 440–449. [CrossRef] [PubMed]
9. Harrington, K.J.; Mohammadtaghi, S.; Uster, P.S.; Glass, D.; Peters, A.M.; Vile, R.G.; Stewart, J.S. Effective targeting of solid tumors in patients with locally advanced cancers by radiolabeled pegylated liposomes effective targeting of solid tumors in patients with locally advanced cancers by radiolabeled pegylated liposomes. *Clin. Cancer Res.* **2001**, *7*, 243–254. [PubMed]
10. Hansen, A.E.; Petersen, A.L.; Henriksen, J.R.; Boerresen, B.; Rasmussen, P.; Elema, D.R.; af Rosenschöld, P.M.; Kristensen, A.T.; Kjær, A.; Andresen, T.L. Positron emission tomography based elucidation of the enhanced permeability and retention effect in dogs with cancer using Copper-64 liposomes. *ACS Nano* **2015**, *9*, 6985–6995. [CrossRef]
11. Nichols, J.W.; Bae, Y.H. Odyssey of a cancer nanoparticle: From injection site to site of action. *Nano Today* **2012**, *7*, 606–618. [CrossRef]
12. Wilhelm, S.; Tavares, A.J.; Dai, Q.; Ohta, S.; Audet, J.; Dvorak, H.F.; Chan, W.C.W. Analysis of nanoparticle delivery to tumours. *Nat. Rev. Mater* **2016**, *1*, 16014. [CrossRef]
13. Minchinton, A.I.; Tannock, I.F. Drug penetration in solid tumours. *Nat. Rev. Cancer* **2006**, *6*, 583–592. [CrossRef]
14. Ferrari, M. Cancer nanotechnology: Opportunities and challenges. *Nat. Rev. Cancer* **2005**, *5*, 161–171. [CrossRef] [PubMed]
15. Maeda, H. Toward a full understanding of the EPR effect in primary and metastatic tumors as well as issues related to its heterogeneity. *Adv. Drug Deliv. Rev.* **2015**, *91*, 3–6. [CrossRef] [PubMed]
16. Hrkach, J.; Von Hoff, D.; Ali, M.M.; Andrianova, E.; Auer, J.; Campbell, T.; De Witt, D.; Figa, M.; Figueiredo, M.; Horhota, A.; et al. Preclinical development and clinical translation of a PSMA-targeted docetaxel nanoparticle with a differentiated pharmacological profile. *Sci. Transl. Med.* **2012**, *4*, 128–139. [CrossRef]
17. Eliasof, S.; Lazarus, D.; Peters, C.G.; Case, R.I.; Cole, R.O.; Hwang, J.; Schluep, T.; Chao, J.; Lin, J.; Yen, Y.; et al. Correlating preclinical animal studies and human clinical trials of a multifunctional, polymeric nanoparticle. *Proc. Natl. Acad. Sci. USA* **2013**, *110*, 15127–15132. [CrossRef] [PubMed]
18. Zuckerman, J.E.; Gritli, I.; Tolcher, A.; Heidel, J.D.; Lim, D.; Morgan, R.; Chmielowski, B.; Ribas, A.; Davis, M.E.; Yen, Y. Correlating animal and human phase Ia/Ib clinical data with CALAA-01, a targeted, polymer-based nanoparticle containing siRNA. *Proc. Natl. Acad. Sci. USA* **2014**, *111*, 11449–11454. [CrossRef] [PubMed]
19. Meads, M.B.; Gatenby, R.A.; Dalton, W.S. Environment-mediated drug resistance: A major contributor to minimal residual disease. *Nat. Rev. Cancer* **2009**, *9*, 665–674. [CrossRef]
20. Karnik, R.; Gu, F.; Basto, P.; Cannizzaro, C.; Dean, L.; Kyei-Manu, W.; Langer, R.; Farokhzad, O.C. Microfluidic platform for controlled synthesis of polymeric nanoparticles. *Nano Lett.* **2008**, *8*, 2906–2912. [CrossRef]
21. Haider, N.; Fatima, S.; Taha, M.; Rizwanullah, M.; Firdous, J.; Ahmad, R.; Mazhar, F.; Khan, M.A. Nanomedicines in Diagnosis and Treatment of Cancer: An Update. *Curr. Pharm. Des.* **2020**, *26*, 1216–1231. [CrossRef]
22. Sakr, T.M.; El-Hashash, M.A.; El-Mohty, A.A.; Essa, B.M. 99mTc-gallic-gold nanoparticles as a new imaging platform for tumor targeting. *Appl. Radiat. Isot.* **2020**, *164*, 109269. [CrossRef]
23. El-Ghareb, W.I.; Swidan, M.M.; Ibrahim, I.T.; Abd El-Bary, A.; Tadros, M.I.; Sakr, T.M. 99mTc-Doxorubicin-loaded gallic acid-gold nanoparticles (99mTc-DOX-loaded GA-Au NPs) as a multifunctional theranostic agent. *Int. J. Pharm.* **2020**, *586*, 119514. [CrossRef] [PubMed]
24. Kim, M.; Jang, J.; Cha, C. Carbon nanomaterials as versatile platforms for theranostic applications. *Drug Discov. Today* **2017**, *22*, 1430–1437. [CrossRef]
25. Ding, K.; Jing, L.; Liu, C.; Hou, Y.; Gao, M. Magnetically engineered Cd-free quantum dots as dual-modality probes for fluorescence/magnetic resonance imaging of tumors. *Biomaterials* **2014**, *35*, 1608–1617. [CrossRef] [PubMed]
26. Park, S.M.; Aalipour, A.; Vermesh, O.; Yu, J.H.; Gambhir, S.S. Towards clinically translatable in vivo nanodiagnostics. *Nat. Rev. Mater.* **2017**, *2*, 17014. [CrossRef] [PubMed]
27. Hequet, E.; Henoumont, C.; Djouana Kenfack, V.; Lemaure, V.; Lazzaroni, R.; Boutry, S.; Vander Elst, L.; Muller, R.N.; Laurent, S. Design, Characterization and Molecular Modeling of New Fluorinated Paramagnetic Contrast Agents for Dual 1H/19F MRI. *Magnetochemistry* **2020**, *6*, 8. [CrossRef]
28. Ngandeu Neubi, G.M.; Opoku-Damoah, Y.; Gu, X.; Han, Y.; Zhou, J.; Ding, Y. Bio-inspired drug delivery systems: An emerging platform for targeted cancer therapy. *Biomater. Sci.* **2018**, *6*, 958–973. [CrossRef]
29. Ovais, M.; Khalil, A.T.; Ayaz, M.; Ahmad, I.; Nethi, S.K.; Mukherjee, S. Biosynthesis of Metal Nanoparticles via Microbial Enzymes: A Mechanistic Approach. *Int. J. Mol. Sci.* **2018**, *19*, 4100. [CrossRef]
30. Zhang, L.; Sheng, D.; Wang, D.; Yao, Y.; Yang, K.; Wang, Z.; Deng, L.; Chen, Y. Bioinspired multifunctional melanin-based nanoliposome for photoacoustic/magnetic resonance imaging-guided efficient photothermal ablation of cancer. *Theranostics* **2018**, *8*, 1591–1606. [CrossRef] [PubMed]
31. Sahu, P.; Das, D.; Mishra, V.K.; Kashaw, V.; Kashaw, S.K. Nanoemulsion: A novel eon in cancer chemotherapy. *Mini Rev. Med. Chem.* **2017**, *17*, 1778–1792. [CrossRef]
32. Choudhury, H.; Gorain, B.; Chatterjee, B.; Mandal, U.; Sengupta, P.; Tekade, R.K. Pharmacokinetic and pharmacodynamic features of nanoemulsion following oral, intravenous, topical and nasal route. *Curr. Pharm. Des.* **2017**, *23*, 2504–2531. [CrossRef]

33. Choudhury, H.; Gorain, B.; Tekade, R.K.; Pandey, M.; Karmakar, S.; Pal, T.K. Safety against nephrotoxicity in paclitaxel treatment: Oral nanocarrier as an effective tool in preclinical evaluation with marked in vivo antitumor activity. *Regul. Toxicol. Pharmacol.* **2017**, *91*, 179–189. [CrossRef] [PubMed]
34. Md, S.; Gan, S.Y.; Haw, Y.H.; Ho, C.L.; Wong, S.; Choudhury, H. In vitro neuroprotective effects of naringenin nanoemulsion against b-amyloid toxicity through the regulation of amyloidogenesis and tau phosphorylation. *Int. J. Biol. Macromol.* **2018**, *118*, 1211–1219. [CrossRef] [PubMed]
35. Choudhury, H.; Gorain, B.; Karmakar, S.; Biswas, E.; Dey, G.; Barik, R.; Mandal, M.; Pal, T.K. Improvement of cellular uptake, in vitro antitumor activity and sustained release profile with increased bioavailability from a nanoemulsion platform. *Int. J. Pharm.* **2014**, *460*, 131–143. [CrossRef]
36. Gadhava, D.; Gorain, B.; Tagalpallewara, A.; Kokarea, C. Intranasal teriflunomide microemulsion: An improved chemotherapeutic approach in glioblastoma. *J. Drug Deliv. Sci. Technol.* **2019**, *51*, 276–289. [CrossRef]
37. Sánchez-López, E.; Guerra, M.; Dias-Ferreira, J.; Lopez-Machado, A.; Ettcheto, M.; Cano, A.; Espina, M.; Camins, A.; Garcia, M.L.; Souto, E.B. Current applications of nanoemulsions in cancer therapeutics. *Nanomaterials* **2019**, *9*, E821. [CrossRef]
38. Zhang, H.; Yu, Q.; Li, Y.; Yang, Z.; Zhou, X.; Chen, S.; Jiang, Z.X. Fluorinated cryptophane-A and porphyrin-based theranostics for multimodal imaging-guided photodynamic therapy. *Chem. Commun.* **2020**, *56*, 3617–3620. [CrossRef]
39. Zhang, Y.; Bo, S.; Feng, T.; Qin, X.; Wan, Y.; Jiang, S.; Li, C.; Lin, J.; Wang, T.; Zhou, X.; et al. Versatile Theranostic Nanoemulsion for Architecture-Dependent Multimodal Imaging and Dually Augmented Photodynamic Therapy. *Adv Mater.* **2019**, *31*, e1806444. [CrossRef]
40. Fernandes, D.A.; Kolios, M.C. Near-infrared absorbing nanoemulsions as nonlinear ultrasound contrast agents for cancer theranostics. *J. Mol. Liq.* **2019**, *287*, 110848. [CrossRef]
41. Patel, N.R.; Piroyan, A.; Ganta, S.; Morse, A.B.; Candiloro, K.M.; Solon, A.L.; Nack, A.H.; Galati, C.A.; Bora, C.; Maglaty, M.A.; et al. In Vitro and In Vivo evaluation of a novel folate-targeted theranostic nanoemulsion of docetaxel for imaging and improved anticancer activity against ovarian cancers. *Cancer Biol. Ther.* **2018**, *19*, 1555–8576. [CrossRef] [PubMed]
42. Silva, C.O.; Pinho, J.O.; Lopes, J.M.; Almeida, A.J.; Gaspar, M.M.; Reis, C. Current trends in cancer nanotheranostics: Metallic, polymeric, and lipid-based systems. *Pharmaceutics* **2019**, *11*, 22. [CrossRef]
43. Petersen, A.L.; Hansen, A.E.; Gabizon, A.; Andresen, T.L. Liposome imaging agents in personalized medicine. *Adv. Drug Deliv. Rev.* **2012**, *64*, 1417–1435. [CrossRef]
44. Al-Jamal, W.T.; Al-Jamal, K.T.; Tian, B.; Cakebread, A.; Halket, J.M.; Kostarelos, K. Tumor Targeting of Functionalized Quantum Dot–Liposome Hybrids by Intravenous Administration. *Mol. Pharmaceut.* **2009**, *6*, 520–530. [CrossRef]
45. Wang, Q.; Chao, Y.M. Multifunctional quantum dots and liposome complexes in drug delivery. *J. Biomed. Res.* **2018**, *32*, 91–106.
46. Lamichhane, N.; Udayakumar, T.S.; D’souza, W.D.; Simone Ii, C.B.; Raghavan, S.R.; Polf, J.; Mahmood, J. Liposomes: Clinical Applications and Potential for Image-Guided Drug Delivery. *Molecules* **2018**, *23*, 288. [CrossRef]
47. Martínez-González, R.; Estelrich, J.; Busquets, M.A. Liposomes Loaded with Hydrophobic Iron Oxide Nanoparticles: Suitable T<sub>2</sub> Contrast Agents for MRI. *Int. J. Mol. Sci.* **2016**, *17*, 1209. [CrossRef] [PubMed]
48. Xing, J.; Liu, D.; Zhou, G.; Li, Y.; Wang, P.; Hu, K.; Gu, N.; Ji, M. Liposomally formulated phospholipid-conjugated novel near-infrared fluorescence probe for particle size effect on cellular uptake and biodistribution in vivo. *Colloids Surf. B Biointerfaces* **2018**, *161*, 588–596. [CrossRef]
49. Prasad, R.; Jain, N.K.; Yadav, A.S.; Chauhan, D.S.; Devrukhkar, J.; Kumawat, M.K.; Shinde, S.; Gorain, M.; Thakor, A.S.; Kundu, G.C.; et al. Liposomal nanotheranostics for multimodal targeted in vivo bioimaging and near-infrared light mediated cancer therapy. *Commun. Biol.* **2020**, *3*, 284. [CrossRef] [PubMed]
50. Karpuz, M.; Silindir-Gunay, M.; Ozer, A.Y.; Ozturk, S.C.; Yanik, H.; Tuncel, M.; Aydin, C.; Esendagli, G. Diagnostic and therapeutic evaluation of folate-targeted paclitaxel and vinorelbine encapsulating theranostic liposomes for non-small cell lung cancer. *Eur. J. Pharm. Sci.* **2021**, *156*, 105576. [CrossRef] [PubMed]
51. Yin, W.; Zhao, Y.; Kang, X.; Zhao, P.; Fu, X.; Mo, X.; Wang, Y.; Huang, Y. BBB-penetrating codelivery liposomes treat brain metastasis of non-small cell lung cancer with EGFR790M mutation. *Theranostics* **2020**, *10*, 6122–6135. [CrossRef] [PubMed]
52. Bush, N.; Healey, A.; Shah, A.; Box, G.; Kirkin, V.; Eccles, S.; Sontum, P.C.; Kotopoulos, S.; Kvåle, S.; van Wamel, A.; et al. Theranostic Attributes of Acoustic Cluster Therapy and Its Use for Enhancing the Effectiveness of Liposomal Doxorubicin Treatment of Human Triple Negative Breast Cancer in Mice. *Front. Pharmacol.* **2020**, *11*, 75. [CrossRef]
53. Prabhakar, A.; Banerjee, R. Nanobubble Liposome Complexes for Diagnostic Imaging and Ultrasound-Triggered Drug Delivery in Cancers: A Theranostic Approach. *ACS Omega* **2019**, *4*, 15567–15580. [CrossRef]
54. Mssi, S.V.; Torchilin, V.P. Recent trends in the use of lipidic nanoparticles as pharmaceutical carriers for cancer therapy and diagnostics. *J. Mater. Chem. B* **2013**, *1*, 5201–5209. [CrossRef]
55. Lopes, R.M.; Gaspar, M.M.; Pereira, J.; Eleutério, C.V.; Carvalheiro, M.; Almeida, A.J.; Cruz, M.E.M. Liposomes versus lipid nanoparticles: Comparative study of lipid-based systems as oryzalin carriers for the treatment of leishmaniasis. *J. Biomed. Nanotechnol.* **2014**, *10*, 3647–3657. [CrossRef] [PubMed]
56. Mehnert, W.; Mader, K. Solid lipid nanoparticles: Production, characterization and applications. *Adv. Drug Deliv. Rev.* **2001**, *47*, 165–196. [CrossRef]





57. Kuang, Y.; Zhang, K.; Cao, Y.; Chen, X.; Wang, K.; Liu, M.; Pei, R. Hydrophobic IR-780 Dye Encapsulated in cRGD-Conjugated Solid Lipid Nanoparticles for NIR Imaging-Guided Photothermal Therapy. *ACS Appl. Mater. Interfaces* **2017**, *9*, 12217–12226. [CrossRef] [PubMed]
58. Peira, E.; Marzola, P.; Podio, V.; Aime, S.; Sbarbati, A.; Gasco, M.R. In vitro and in vivo study of solid lipid nanoparticles loaded with superparamagnetic iron oxide. *J. Drug Target.* **2003**, *11*, 19–24. [CrossRef] [PubMed]
59. Andreozzi, E.; Seo, J.W.; Ferrara, K.; Louie, A. Novel method to label solid lipid nanoparticles with <sup>64</sup>Cu for positron emission tomography imaging. *Bioconjug. Chem.* **2011**, *22*, 808–818. [CrossRef] [PubMed]
60. Shuhendler, A.J.; Prasad, P.; Leung, M.; Rauth, A.M.; DaCosta, R.S.; Wu, X.Y. A novel solid lipid nanoparticle formulation for active targeting to tumor  $\alpha\beta 3$  integrin receptors reveals cyclic RGD as a double-edged sword. *Adv. Healthc. Mater.* **2012**, *1*, 600–608. [CrossRef]
61. Bae, K.H.; Lee, J.Y.; Lee, S.H.; Park, T.G.; Nam, Y.S. Optically traceable solid lipid nanoparticles loaded with siRNA and paclitaxel for synergistic chemotherapy with in situ imaging. *Adv. Healthc. Mater.* **2013**, *2*, 576–584. [CrossRef] [PubMed]
62. Bentolila, L.A.; Ebenstein, Y.; Weiss, S. Quantum dots for in vivo small-animal imaging. *J. Nucl. Med.* **2009**, *50*, 493–496. [CrossRef]
63. Morel, S.; Terreno, E.; Ugazio, E.; Aime, S.; Gasco, M.R. NMR relaxometric investigations of solid lipid nanoparticles (SLN) containing gadolinium (III) complexes. *Eur. J. Pharm. Biopharm.* **1998**, *45*, 157–163. [CrossRef]
64. Li, H.; Wang, K.; Yang, X.; Zhou, Y.; Ping, Q.; Oupicky, D.; Sun, M. Dualfunction nanostructured lipid carriers to deliver IR780 for breast cancer treatment: Anti-metastatic and photothermal anti-tumor therapy. *Acta Biomater.* **2017**, *53*, 399–413. [CrossRef]
65. Olerile, L.D.; Liu, Y.; Zhang, B.; Wang, T.; Mu, S.; Zhang, J.; Selotlegeng, L.; Zhang, N. Nearinfrared mediated quantum dots and paclitaxel co-loaded nanostructured lipid carriers for cancer theragnostic. *Colloids Surf. B Biointerfaces* **2017**, *150*, 121–130. [CrossRef] [PubMed]
66. Hsu, S.-H.; Wen, C.-J.; Al-Suwayeh, S.A.; Huang, Y.-J.; Fang, J.-Y. Formulation design and evaluation of quantum dot-loaded nanostructured lipid carriers for integrating bioimaging and anticancer therapy. *Nanomedicine* **2013**, *8*, 1253–1269. [CrossRef] [PubMed]
67. Ucar, E.; Teksoz, S.; Ichedef, C.; Kilcar, A.Y.; Medine, E.I.; Ari, K.; Parlak, Y.; Sayit Bilgin, B.E.; Unak, P. Synthesis, characterization and radiolabeling of folic acid modified nanostructured lipid carriers as a contrast agent and drug delivery system. *Appl. Radiat. Isot.* **2017**, *119*, 72–79. [CrossRef]
68. Huynh, N.T.; Passirani, C.; Saulnier, P.; Benoit, J.P. Lipid nanocapsules: A new platform for nanomedicine. *Int. J. Pharm.* **2009**, *379*, 201–209. [CrossRef] [PubMed]
69. AbdElhamid, A.S.; Zayed, D.G.; Helmy, M.W.; Ebrahim, S.M.; Bahey-El-Din, M.; Zein-El-Dein, E.A.; El-Gizawy, S.A.; Elzoghby, A.O. Lactoferrin-tagged quantum dots-based theranostic nanocapsules for combined COX-2 inhibitor/herbal therapy of breast cancer. *Nanomedicine* **2018**, *13*, 2637–2656. [CrossRef]
70. Ma, M.; Hao, Y.; Liu, N.; Yin, Z.; Wang, L.; Liang, X.; Zhang, X. A novel lipid-based nanomicelle of docetaxel: Evaluation of antitumor activity and biodistribution. *Int. J. Nanomed.* **2012**, *7*, 3389–3398. [CrossRef]
71. Huang, H.; Dong, Y.; Zhang, Y.; Ru, D.; Wu, Z.; Zhang, J.; Shen, M.; Duan, Y.; Sun, Y. GSH-sensitive Pt(IV) prodrug-loaded phase-transitional nanoparticles with a hybrid lipid-polymer shell for precise theranostics against ovarian cancer. *Theranostics* **2019**, *9*, 1047–1065. [CrossRef]
72. Zhang, X.; Huang, G. Synthetic lipoprotein as nano-material vehicle in the targeted drug delivery. *Drug Deliv.* **2017**, *24*, 16–21. [CrossRef]
73. Zhang, Z.; Cao, W.; Jin, H.; Lovell, J.F.; Yang, M.; Ding, L.; Chen, J.; Corbin, I.; Luo, Q.; Zheng, G. Biomimetic nanocarrier for direct cytosolic drug delivery. *Angew. Chem. Int. Ed. Engl.* **2009**, *48*, 9171–9175. [CrossRef]
74. Yang, M.; Chen, J.; Cao, W.; Ding, L.; Ng, K.K.; Jin, H.; Zhang, Z.; Zheng, G. Attenuation of nontargeted cell-kill using a high-density lipoprotein-mimicking peptide-phospholipid nanoscaffold. *Nanomedicine* **2011**, *6*, 631–641. [CrossRef] [PubMed]
75. Lin, Q.; Jin, C.S.; Huang, H.; Ding, L.; Zhang, Z.; Chen, J.; Zheng, J. Nanoparticle-enabled, image-guided treatment planning of target specific RNAi therapeutics in an orthotopic prostate cancer model. *Small* **2014**, *10*, 3072–3082. [CrossRef] [PubMed]
76. Rosenblum, D.; Joshi, N.; Tao, W.; Karp, J.M.; Peer, D. Progress and challenges towards targeted delivery of cancer therapeutics. *Nat. Commun.* **2018**, *9*, 1410. [CrossRef] [PubMed]
77. Daniels, T.R.; Delgado, T.; Rodriguez, J.A.; Helguera, G.; Penichet, M.L. The transferrin receptor part I: Biology and targeting with cytotoxic antibodies for the treatment of cancer. *Clin. Immunol.* **2006**, *121*, 144–1458. [CrossRef] [PubMed]
78. Das Gupta, A.; Shah, V.I. Correlation of transferrin receptor expression with histologic grade and immunophenotype in chronic lymphocytic leukemia and non-Hodgkin's lymphoma. *Hematol. Pathol.* **1990**, *4*, 37–41.
79. Prior, R.; Reifenberger, G.; Wechsler, W. Transferrin receptor expression in tumours of the human nervous system: Relation to tumour type, grading and tumour growth fraction. *Virchows Arch. A Pathol. Anat. Histopathol.* **1990**, *416*, 491–496. [CrossRef]
80. Singh, M.; Mugler, K.; Hailoo, D.W.; Burke, S.; Nemesure, B.; Torkko, K.; Shroyer, K.R. Differential expression of transferrin receptor (TfR) in a spectrum of normal to malignant breast tissues: Implications for in situ and invasive carcinoma. *Appl. Immunohistochem. Mol. Morphol.* **2011**, *19*, 417–423. [CrossRef]
81. Callens, C.; Moura, I.C.; Lepelletier, Y.; Coulon, S.; Renand, A.; Dussiot, M.; Ghez, D.; Benhamou, M.; Monteiro, R.C.; Bazarbachi, A.; et al. Recent advances in adult T-cell leukemia therapy: Focus on a new anti-transferrin receptor monoclonal antibody. *Leukemia* **2008**, *22*, 42–48. [CrossRef]

82. He, Q.; Sun, X.; Chu, C.; Jiang, Q.; Zhu, H.; He, Y.; Yue, T.; Wang, R.; Lei, P.; Shen, G. Endocytosis of a functionally enhanced GFP-tagged transferrin receptor in CHO cells. *PLoS ONE* **2015**, *10*, e0122452. [CrossRef]
83. Luck, A.N.; Mason, A.B. Structure and dynamics of drug carriers and their interaction with cellular receptors: Focus on serum transferrin. *Adv. Drug Deliv. Rev.* **2013**, *65*, 1012–1019. [CrossRef]
84. Tortorella, S.; Karagiannis, T.C. Transferrin receptor-mediated endocytosis: A useful target for cancer therapy. *J. Membr. Biol.* **2014**, *247*, 291–307. [CrossRef] [PubMed]
85. Tros de Iarduya, C.; Duzgunes, N. Delivery of therapeutic nucleic acids via transferrin and transferrin receptors: Lipoplexes and other carriers. *Expert Opin. Drug Deliv.* **2013**, *10*, 1583–1591. [CrossRef] [PubMed]
86. Lei, P.; He, Y.; Ye, Q.; Zhu, H.F.; Yuan, X.M.; Liu, J.; Xing, W.; Wu, S.; Dai, W.; Shen, X.; et al. Antigen-binding characteristics of AbCD71 and its inhibitory effect on PHA-induced lymphoproliferation. *Acta Pharmacol. Sin.* **2007**, *28*, 1659–1664. [CrossRef]
87. Qing, Y.; Shuo, W.; Zhihua, W.; Huifen, Z.; Ping, L.; Lijiang, L.; Xiaorong, Z.; Liming, C.; Daiwen, X.; Yu, H.; et al. The in vitro antitumor effect and in vivo tumor-specificity distribution of human-mouse chimeric antibody against transferrin receptor. *Cancer Immunol. Immunother.* **2006**, *55*, 1111–1121. [CrossRef]
88. Li, J.; Weng, X.; Liang, Z.; Zhong, M.; Chen, X.; Lu, S.; Sun, W.; Song, Y.; Wu, X.; Shen, G. Viral specific cytotoxic T cells inhibit the growth of TfR-expressing tumor cells with antibody targeted viral peptide/HLA-A2 complex. *Cell Immunol.* **2010**, *263*, 154–160. [CrossRef]
89. Liu, Y.; Tao, J.; Li, Y.; Yang, J.; Yu, Y.; Wang, M.; Xu, X.; Huang, C.; Huang, W.; Dong, J.; et al. Targeting hypoxia-inducible factor-1alpha with Tf-PEI-shRNA complex via transferrin receptor-mediated endocytosis inhibits melanoma growth. *Mol. Ther.* **2009**, *17*, 269–277. [CrossRef] [PubMed]
90. Ye, Q.; Hu, H.; Wang, Z.; Lu, T.; Hu, Z.; Zeng, X.; Zhang, S.; Liu, J.; Lei, P.; Wang, C.Y.; et al. Generation and functional characterization of the anti-transferrin receptor single-chain antibody-GAL4 (TfRscFv-GAL4) fusion protein. *BMC Biotechnol.* **2012**, *12*, 91. [CrossRef] [PubMed]
91. He, Q.; Guo, Z.; Fu, M.; Tang, H.; Zhu, H.; Shen, G.; He, Y.; Lei, P. Establishment of a hTfR mAb-functionalized HPPS theranostic nanoplatform. *Nanotheranostics* **2020**, *4*, 119–128. [CrossRef]
92. Chen, W.; Jarzyna, P.A.; van Tilborg, G.A.F.; Nguyen, V.A.; Cormode, D.P.; Klink, A.; Griffioen, A.W.; Randolph, G.J.; Fisher, E.A.; Mulder, W.J.M.; et al. RGD peptide functionalized and reconstituted high-density lipoprotein nanoparticles as a versatile and multimodal tumor targeting molecular imaging probe. *FASEB J.* **2010**, *24*, 1689–1699. [CrossRef]
93. Yang, X.; Yang, M.; Pang, B.; Vara, M.; Xia, Y. Gold Nanomaterials at Work in Biomedicine. *Chem. Rev.* **2015**, *115*, 10410–10488. [CrossRef] [PubMed]
94. Alarcon, E.I.; Vulesevic, B.; Argawal, A.; Ross, A.; Bejjani, P.; Podrebara, J.; Ravichandran, R.; Phopase, J.; Suuronen, E.J.; Griffith, M. Coloured cornea replacements with anti-infective properties: Expanding the safe use of silver nanoparticles in regenerative medicine. *Nanoscale* **2016**, *8*, 6484–6489. [CrossRef]
95. Chandra, S.; Barick, K.C.; Bahadur, D. Oxide and hybrid nanostructures for therapeutic applications. *Adv. Drug Deliv. Rev.* **2011**, *63*, 1267–1281. [CrossRef] [PubMed]
96. Kang, J.H.; Ko, Y.T. Lipid-coated gold nanocomposites for enhanced cancer therapy. *Int. J. Nanomed.* **2015**, *10*, 33–45.
97. Bae, P.K.; Chung, B.H. Multiplexed detection of various breast cancer cells by perfluorocarbon/quantum dot nanoemulsions conjugated with antibodies. *Nano Converg.* **2014**, *1*, 23. [CrossRef]
98. Allijn, I.E.; Leong, W.; Tang, J.; Gianella, A.; Mieszawska, A.J.; Fay, F.; Ma, G.; Russell, S.; Callo, C.B.; Gordon, R.E.; et al. Gold Nanocrystal Labeling Allows Low-Density Lipoprotein Imaging from the Subcellular to Macroscopic Level. *ACS Nano* **2013**, *7*, 9761–9770. [CrossRef] [PubMed]
99. Zhang, N.; Chen, H.; Liu, A.Y.; Shen, J.J.; Shah, V.; Zhang, C.; Hong, J.; Ding, Y. Gold conjugate-based liposomes with hybrid cluster bomb structure for liver cancer therapy. *Biomaterials* **2016**, *74*, 280–291. [CrossRef]
100. Huang, X.; Tang, S.; Mu, X.; Dai, Y.; Chen, G.; Zhou, Z.; Ruan, F.; Yang, Z.; Zheng, N. Freestanding palladium nanosheets with plasmonic and catalytic properties. *Nat. Nanotechnol.* **2011**, *6*, 28–32. [CrossRef]
101. Adams, C.P.; Walker, K.A.; Obare, S.O.; Docherty, K.M. Size-Dependent Antimicrobial Effects of Novel Palladium Nanoparticles. *PLoS ONE* **2014**, *9*, e85981. [CrossRef] [PubMed]
102. Miesen, T.J.; Engstrom, A.M.; Miesen, T.J.; Miesen, T.J.; Frost, D.C.; Ajjarapu, R.; Lira, C.N.; Mackiewicz, M.R. A hybrid lipid membrane coating “shape-locks” silver nanoparticles to prevent surface oxidation and silver ion dissolution. *RCS Adv.* **2020**, *10*, 15677–15693.
103. Bhattacharyya, K.; Goldschmidt, B.S.; Hannink, M.; Alexander, S.; Jurkevic, A.; Viator, J.A. Gold nanoparticle-mediated detection of circulating cancer cells. *Clin. Lab. Med.* **2012**, *32*, 89–101. [CrossRef]
104. Tahmasbi Rad, A.; Chen, C.W.; Aresh, W.; Xia, Y.; Lai, P.S.; Nieh, M.P. Combinational Effects of Active Targeting, Shape, and Enhanced Permeability and Retention for Cancer Theranostic Nanocarriers. *ACS Appl. Mater Interfaces* **2019**, *11*, 10505–10519. [CrossRef] [PubMed]
105. Danhier, F. To Exploit the Tumor Microenvironment: Since the EPR Effect Fails in the Clinic, What Is the Future of Nanomedicine? *J. Control. Release* **2016**, *244*, 108–121. [CrossRef] [PubMed]
106. Blanco, E.; Shen, H.; Ferrari, M. Principles of Nanoparticle Design for Overcoming Biological Barriers to Drug Delivery. *Nat. Biotechnol.* **2015**, *33*, 941–951. [CrossRef] [PubMed]

107. Agarwal, R.; Singh, V.; Journey, P.; Shi, L.; Sreenivasan, S.; Roy, K. Mammalian Cells Preferentially Internalize Hydrogel Nanodiscs over Nanorods and Use Shape-Specific Uptake Mechanisms. *Proc. Natl. Acad. Sci. USA*. **2013**, *110*, 17247–17252. [CrossRef] [PubMed]
108. Truong, N.P.; Whittaker, M.R.; Mak, C.W.; Davis, T.P. The Importance of Nanoparticle Shape in Cancer Drug Delivery. *Expert Opin. Drug Deliv.* **2015**, *12*, 129–142. [CrossRef]
109. Nagahama, K.; Kawano, D.; Oyama, N.; Takemoto, A.; Kumano, T.; Kawakami, J. Self-Assembling Polymer Micelle/Clay Nanodisk/ Doxorubicin Hybrid Injectable Gels for Safe and Efficient Focal Treatment of Cancer. *Biomacromolecules* **2015**, *16*, 880–889. [CrossRef]
110. Sun, W.; Parowatkin, M.; Steffen, W.; Butt, H.J.; Mailänder, V.; Wu, S. Ruthenium-Containing Block Copolymer Assemblies: Red-Light-Responsive Metallopolymers with Tunable Nanostructures for Enhanced Cellular Uptake and Anticancer Phototherapy. *Adv. Healthc. Mater.* **2016**, *5*, 467–473. [CrossRef]
111. Sun, W.; Wen, Y.; Thiramanas, R.; Chen, M.; Han, J.; Gong, N.; Wagner, M.; Jiang, S.; Meijer, M.S.; Bonnet, S.; et al. Red-Light-Controlled Release of Drug–Ru Complex Conjugates from Metallopolymer Micelles for Phototherapy in Hypoxic Tumor Environments. *Adv. Funct. Mater.* **2018**, *28*, 1804227. [CrossRef]
112. Ernsting, M.J.; Murakami, M.; Roy, A.; Li, S.D. Factors Controlling the Pharmacokinetics, Biodistribution and Intratumoral Penetration of Nanoparticles. *J. Control. Release* **2013**, *172*, 782–794. [CrossRef]
113. Tan, J.; Shah, S.; Thomas, A.; Ou-Yang, H.D.; Liu, Y. The Influence of Size, Shape and Vessel Geometry on Nanoparticle Distribution. *Microfluid. Nanofluid.* **2013**, *14*, 77–87. [CrossRef]
114. Carregal-Romero, S.; Plaza-García, S.; Piñol, R.; Murillo, J.L.; Ruiz-Cabello, J.; Padro, D.; Millán, A.; Ramos-Cabrer, P. MRI Study of the Influence of Surface Coating Aging on the In Vivo Biodistribution of Iron Oxide Nanoparticles. *Biosensors* **2018**, *8*, 127. [CrossRef]
115. Gómez-Vallejo, V.; Puigivila, M.; Plaza-García, S.; Szczupak, B.; Piñol, R.; Murillo, J.L.; Sorribas, V.; Lou, G.; Veintemillas, S.; Ramos-Cabrer, P.; et al. PEG-copolymer-coated iron oxide nanoparticles that avoid the reticuloendothelial system and act as kidney MRI contrast agents. *Nanoscale* **2018**, *10*, 14153–14164. [CrossRef]
116. Majumder, B.; Baraneedharan, U.; Thiyagarajan, S.; Radhakrishnan, P.; Narasimhan, H.; Dhandapani, M.; Brijwani, N.; Pinto, D.D.; Prasath, A.; Shanthappa, B.U.; et al. Predicting clinical response to anticancer drugs using an ex vivo platform that captures tumour heterogeneity. *Nat. Commun.* **2015**, *6*, 6169. [CrossRef]
117. Dilnawaz, F.; Acharya, S.; Sahoo, S.K. Recent trends of nanomedicinal approaches in clinics. *Int. J. Pharm.* **2018**, *538*, 263–278. [CrossRef] [PubMed]
118. Riehemann, K.; Schneider, S.W.; Luger, T.A.; Godin, B.; Ferrari, M.; Fuchs, H. Nanomedicine—Challenge and perspectives. *Angew. Chem. Int. Ed. Engl.* **2009**, *48*, 872–897. [CrossRef] [PubMed]
119. Shi, J.; Kantoff, P.W.; Wooster, R.; Farokhzad, O.C. Cancer nanomedicine: Progress, challenges and opportunities. *Nat. Rev. Cancer* **2017**, *17*, 20–37. [CrossRef]
120. Jackman, J.A.; Meszaros, T.; Fulop, T.; Urbanics, R.; Szebeni, J.; Cho, N.J. Comparison of complement activation-related pseudoallergy in miniature and domestic pigs: Foundation of a validatable immune toxicity model. *Nanomedicine* **2016**, *12*, 933–943. [CrossRef]
121. Szebeni, J.; Storm, G. Complement activation as a bioequivalence issue relevant to the development of generic liposomes and other nanoparticulate drugs. *Biochem. Biophys. Res. Commun.* **2015**, *468*, 490–497. [CrossRef] [PubMed]
122. Hua, S.; de Matos, M.B.C.; Metselaar, J.M.; Storm, G. Current trends and challenges in the clinical translation of nanoparticulate nanomedicines: Pathways for translational development and commercialization. *Front. Pharmacol.* **2018**, *9*, 790. [CrossRef]
123. Dreifuss, T.; Betzer, O.; Shilo, M.; Popovtzer, A.; Motiei, M.; Popovtzer, R. A challenge for theranostics: Is the optimal particle for therapy also optimal for diagnostics? *Nanoscale* **2015**, *7*, 15175–15184. [CrossRef]
124. Sainz, V.; Connot, J.; Matos, A.I.; Peres, C.; Zupancic, E.; Moura, L.; Silva, L.C.; Florindo, H.F.; Gaspar, R.S. Regulatory aspects on nanomedicines. *Biochem. Biophys. Res. Commun.* **2015**, *468*, 504–510. [CrossRef] [PubMed]
125. Gaspar, R. Regulatory issues surrounding nanomedicines: Setting the scene for the next generation of nanopharmaceuticals. *Nanomedicine* **2007**, *2*, 143–147. [CrossRef] [PubMed]
126. Tinkle, S.; McNeil, S.E.; Muhlebach, S.; Bawa, R.; Borchard, G.; Barenholz, Y.; Tamarkin, L.; Desai, N. Nanomedicines: Addressing the scientific and regulatory gap. *Ann. N. Y. Acad. Sci.* **2014**, *1313*, 35–56. [CrossRef] [PubMed]
127. Hare, J.I.; Lammers, T.; Ashford, M.B.; Puri, S.; Storm, G.; Barry, S.T. Challenges and strategies in anti-cancer nanomedicine development: An industry perspective. *Adv. Drug Deliv. Rev.* **2017**, *108*, 25–38. [CrossRef] [PubMed]
128. Accomasso, L.; Cristallini, C.; Giachino, C. Risk assessment and risk minimization in nanomedicine: A need for predictive, alternative, and 3Rs strategies. *Front. Pharmacol.* **2018**, *9*, 228. [CrossRef] [PubMed]
129. Ragelle, H.; Danhier, F.; Preat, V.; Langer, R.; Anderson, D.G. Nanoparticle-based drug delivery systems: A commercial and regulatory outlook as the field matures. *Expert Opin. Drug Deliv.* **2017**, *14*, 851–864. [CrossRef]

Review

# Chronicles of Nanoerythroosomes: An Erythrocyte-Based Biomimetic Smart Drug Delivery System as a Therapeutic and Diagnostic Tool in Cancer Therapy

Shamama Javed <sup>1</sup>, Sultan Alshehri <sup>2,3</sup> , Ambreen Shoaib <sup>4</sup>, Waquar Ahsan <sup>5</sup> , Muhammad Hadi Sultan <sup>1</sup>, Saad Saeed Alqahtani <sup>4</sup>, Mohsin Kazi <sup>2</sup>  and Faiyaz Shakeel <sup>2,\*</sup> 

<sup>1</sup> Department of Pharmaceutics, College of Pharmacy, Jazan University, P.O. Box 114, Jazan 45142, Saudi Arabia; sjahmad@jazanu.edu.sa (S.J.); mhsultan@jazanu.edu.sa (M.H.S.)

<sup>2</sup> Department of Pharmaceutics, College of Pharmacy, King Saud University, P.O. Box 2457, Riyadh 11451, Saudi Arabia; salshehri1@ksu.edu.sa (S.A.); mkazi@ksu.edu.sa (M.K.)

<sup>3</sup> Department of Pharmaceutical Sciences, College of Pharmacy, Almaarefa University, Riyadh 11597, Saudi Arabia

<sup>4</sup> Department of Clinical Pharmacy, College of Pharmacy, Jazan University, P.O. Box 114, Jazan 45142, Saudi Arabia; asahmad@jazanu.edu.sa (A.S.); ssalqahtani@jazanu.edu.sa (S.S.A.)

<sup>5</sup> Department of Pharmaceutical Chemistry, College of Pharmacy, Jazan University, P.O. Box 114, Jazan 45142, Saudi Arabia; wmohammad@jazanu.edu.sa

\* Correspondence: fsahmad@ksu.edu.sa; Tel.: +966-1467-3139

**Citation:** Javed, S.; Alshehri, S.; Shoaib, A.; Ahsan, W.; Sultan, M.H.; Alqahtani, S.S.; Kazi, M.; Shakeel, F. Chronicles of Nanoerythroosomes: An Erythrocyte-Based Biomimetic Smart Drug Delivery System as a Therapeutic and Diagnostic Tool in Cancer Therapy. *Pharmaceutics* **2021**, *13*, 368. <https://doi.org/10.3390/pharmaceutics13030368>

Academic Editor: Hassan Bousbaa

Received: 21 February 2021

Accepted: 8 March 2021

Published: 10 March 2021

**Publisher's Note:** MDPI stays neutral with regard to jurisdictional claims in published maps and institutional affiliations.

**Abstract:** Recently, drug delivery using natural biological carriers has emerged as one of the most widely investigated topics of research. Erythrocytes, or red blood cells, can act as potential carriers for a wide variety of drugs, including anticancer, antibacterial, antiviral, and anti-inflammatory, along with various proteins, peptides, enzymes, and other macromolecules. The red blood cell-based nanocarrier systems, also called nanoerythroosomes, are nanovesicles poised with extraordinary features such as long blood circulation times, the ability to escape immune system, the ability to release the drug gradually, the protection of drugs from various endogenous factors, targeted and specified delivery of drugs, as well as possessing both therapeutic and diagnostic applications in various fields of biomedical sciences. Their journey over the last two decades is escalating with fast pace, ranging from in vivo to preclinical and clinical studies by encapsulating a number of drugs into these carriers. Being biomimetic nanoparticles, they have enhanced the stability profile of drugs and their excellent site-specific targeting ability makes them potential carrier systems in the diagnosis and therapy of wide variety of tumors including gliomas, lung cancers, breast cancers, colon cancers, gastric cancers, and other solid tumors. This review focuses on the most recent advancements in the field of nanoerythroosomes, as an excellent and promising nanoplatform for the novel drug delivery of various drugs particularly antineoplastic drugs along with their potential as a promising diagnostic tool for the identification of different tumors.

**Keywords:** nanoerythroosome; nanoerythrocyte; nanovesicles; biomimetic; cancer therapy; diagnostics; imaging agents



**Copyright:** © 2021 by the authors. Licensee MDPI, Basel, Switzerland. This article is an open access article distributed under the terms and conditions of the Creative Commons Attribution (CC BY) license (<https://creativecommons.org/licenses/by/4.0/>).

## 1. Introduction

Erythrocytes (ER) or the red blood cells (RBC) are the most abundant blood cells responsible for the transport of gases from lungs to the tissues [1]. Over the past two decades, they have been exploited to develop various biomimetic cell-based carrier systems, including resealed erythrocytes (RE), genetically engineered RBCs, as well as RBC-membrane coated nanoparticles (NP) (RBC-m-NP) for various biomedical applications. Their transition from preclinical studies to clinical stage is a proof of being smart and effective enough to be used as novel drug delivery vehicles. Other than erythrocytes, other blood cells such as platelets and leukocytes can also be used as carrier system for a variety of drugs [2].

All these cell-based drug carrier systems are superior and have various advantages over other drug-delivery systems such as micro- and nano-particles in terms of properties such as prolonged circulation time, biocompatibility, biodegradability, non-immunogenicity, ease of preparation, and flexibility in use [3], apart from improved patient compliance by extending the time of release of drugs from these systems. Escaping the rapid clearance from body and specificity for the target are other major advantages associated with such carriers [4]. These extraordinary features helped the carrier erythrocytes (C-ER) to emerge as potential drug-carrier systems for the therapy of cellular infections, cardiovascular disorders, cancer therapy, gene therapy, and other ailments [5]. Recently, several other cell-based drug delivery strategies such as bacterial ghosts, dendritic cells (DC) and genetically engineered stem cells have also emerged owing to the successful application of C-ERs [6].

Nanoerythrocytes (NER) are the C-ERs which are recognized as modern day, novel, and smart drug delivery systems associated with increased bioavailability, improved pharmacokinetics, and low toxicity [7]. As a physiological carrier, NERs can release the drug in circulation for weeks, have high loading capacity, are easy to be processed and have good ability to accommodate biologics, antigens, contrasting agents, peptides, proteins, enzymes, and macromolecules using different chemical and physical based methods [8,9]. Innumerable examples are available in the literature discussing the drug delivery by C-ERs for applications in drug targeting to the reticuloendothelial system (RES), enzyme therapy and improvement in the delivery of oxygen to the tissues [10,11]. One of such example is the delivery of bovine serum albumin (BSA) as a model antigen, which can be loaded on the human erythrocytes and delivered to the RES [12]. C-ERs are the unique drug delivery system that is also known to be capable of modulating the immune responses [13]. Amongst different antineoplastic drugs, methotrexate, etoposide, doxorubicin, and carboplatin have been successfully encapsulated in these carriers previously [14]. C-ERs are shown to protect the carried therapeutics such as antibiotics, antineoplastics, corticosteroids, peptides, and enzymes from being inactivated by different endogenous factors. The three main mechanisms, by which these C-ERs work are prolongation of circulation half-life, slow drug release, and organ-specific targeting [15]. Regulatory aspects of carrier erythrocytes and industrial developments are evolving day by day. However, their production scalability, process validation and quality control is still challenging enough for successful industrialization [16].

This review focuses on the NERs which have emerged as a promising and versatile platform for the successful delivery of a number of drugs in particular the antineoplastic drugs. Recent advancements in the field of NERs along with the nanoformulations developed and used in the cancer and non-cancer therapy are covered. The diagnostic and imaging applications of NERs, as well as the recent patents and clinical trials associated with these carriers have also been discussed.

## 2. Fabrication of NERs

Various methods have been successfully utilized for the fabrication of NERs in order to enhance membrane permeability and cellular targeting of therapeutic agents. These methods are described below [17–20].

### 2.1. Dilutional Hemolysis and Resealing Method

Hemolysis and resealing method is commonly used method for drug loading into erythrocytes. In this technique, the erythrocytes are exposed to hypotonic solution (0.4% *w/v* sodium chloride) until it reaches a critical value of volume or pressure in order to rupture the cells. Then, resealing is carried out in order to restore osmotic properties [19]. Dilutional hemolysis utilizing hypotonic solution (0.4% *w/v* sodium hydroxide) at 0 °C and resealing at 37 °C has been utilized as cellular carriers for the successful delivery of low molecular weight drugs like  $\beta$ -glucosidase and  $\beta$ -galactosidase [20]. This technique is the simplest and fastest technique for the preparation of NERs. The main disadvantages of this

technique are low drug loading efficiency (1–8%) and considerable loss of hemoglobin and other cellular components [19,20].

### 2.2. *Preswell Dilutional Hemolysis Method*

The preswell dilutional hemolysis technique has been developed for the improvement of drug loading efficiencies. In this technique, an initial swelling of erythrocytes is achieved using slightly hypotonic solution, followed by low-speed centrifugation. The drug loading efficiencies of some drugs such as ibuprofen and thyroxin have been significantly increased using preswell dilutional hemolysis technique compared to dilutional hemolysis technique [17].

### 2.3. *Hypotonic Dialysis Method*

The main problems of dilution techniques is the low drug-loading efficiencies. This problem of such dilutional techniques can be overcome using hypotonic dialysis technique. In hypotonic dialysis technique, the lysis and resealing are carried out within dialysis tube. This technique offers high drug entrapment efficiency, high drug-loading efficiency, and high cells recovery compared to dilutional techniques. However, long processing time and special instruments are required for this technique. This method has been successfully utilized for the loading of various enzymes (asparaginase, galactosidase, and glucoserebrosidase, etc.) and drugs (gentamicin, adriamycin, and furamycin, etc.) [17,21].

### 2.4. *Use of Red Cell Loader*

The instrument like red cell loader is used for the loading of non-diffusible drugs into erythrocytes. Using this technique, the drugs are loaded into small volume of blood within 2 h at room temperature under blood banking conditions. The drug loading up to 30% and cell recovery of 30–50% can be achieved using this technique [18].

### 2.5. *Isotonic Osmotic Lysis*

It is also known as osmotic pulse technique which can be achieved by chemical or physical means. The chemical which are used to achieve isotonic hemolysis are urea, polyethylene glycols, and ammonium chloride. This technique is not immune to the changes in the composition of membrane structures [17,18].

### 2.6. *Membrane Perturbation Technique*

This technique is based on the enhancement in the membrane permeability of erythrocytes when the cells are exposed under certain chemicals or drugs. The membrane permeability of erythrocytes was enhanced under exposure to an antibiotic amphotericin B. This technique has been applied to load an antitumor drug daunomycin into erythrocytes of rat and human. However, this technique is irreversible and hence not very popular [17,18].

### 2.7. *Lipid Fusion Technique*

This technique is used for the loading of drug-loaded lipid vesicles into erythrocytes. Drug-loaded lipid vesicles can be directly fused into human erythrocytes, which could result into exchange with a lipid-entrapped drug. This technique has been successfully applied for the loading of inositol monophosphate into human erythrocytes for the improvement of oxygen carrying capacity of the cells. However, the drug-loading capacity of this technique is too low (1%) [18,19].

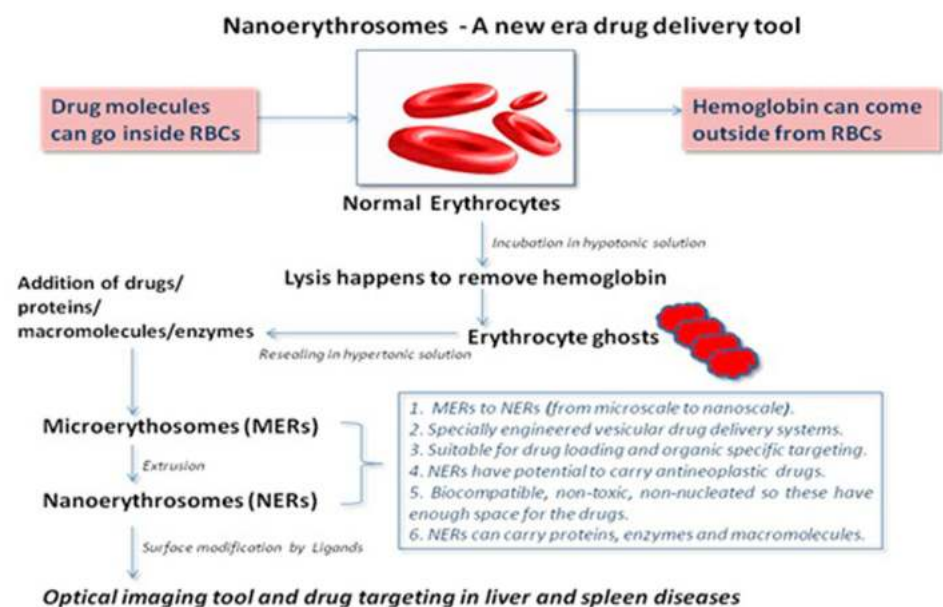
Some other techniques such as extrusion, sonication, and electrical breakdown techniques have also been utilized for the loading of drugs into human erythrocytes [18].

## 3. **NERs as an Efficient Drug Delivery Tool**

The compendium of knowledge and several research studies available on the RBC-based carrier systems led to the development of more advanced RBC-membrane derived liposomes also called as NERs. It has opened a new vista of its futuristic application in



the field of nanomedicine with greater potentials. These are NPs often designated with other names such as functionalized-NPs, hybrid-NPs, biomimetic-NPs, and targeted-NPs in the literature [22–24]. The NERs, being nanosized derivatives of erythrocytes, exhibit important properties such as biodegradability, biocompatibility, excellent release profiles, and organ and site-specific targetability. The prolonged circulation time in blood for NERs is owing to the higher surface area-to-volume ratio than the parent erythrocytes (approximately 80 times higher). Extra care is necessary while handling parent erythrocytes for maximum drug loading. The hemoglobin and cytoplasmic contents of the erythrocytes are removed using a controlled hypertonic solution mediated hemolysis followed by the loading of therapeutic agents. This process of removal of cellular contents should be in such a controlled manner that the plasma membrane should not be disrupted and the cells are allowed to form seamless nanosized capsule. One erythrocyte can be fragmented into thousands of NERs depending upon the recovered cell percentage post removal of its organelles. The NERs are prepared from the hemoglobin (Hb)-free erythrocyte ghosts using sonication, extrusion, and electrical impulses techniques. Uniform nanosized NERs are obtained using extrusion technique which is the most efficient technique amongst all. The nanosizing technique, lysis media, and processing temperature have considerable impact on the development of stable and viable NERs-based formulations. Owing to the biomimetic properties of NERs, these can be utilized for the efficient encapsulation of peptides, enzymes, genetic materials, toxins, and contrasting agents which can be applied for the treatment of liver, lymph nodes, and spleen disorders, as well as various types of carcinomas [23–25]. Similar to liposomes, NERs are the nanovesicles prepared by the extrusion of RBC ghosts, are membrane-covered nanoscale containers, discrete spherical in shape, with unilamellar membrane of 4.5  $\mu\text{m}$  thickness and having diameter up to 100 nm (Figure 1). However, the disadvantages associated with liposomes and monoclonal antibodies are not present in NERs and these show excellent colloidal stability in both buffer and serum at room temperature [25].



**Figure 1.** Preparation of nanoerythrocytes (NER) from normal erythrocytes (ER).

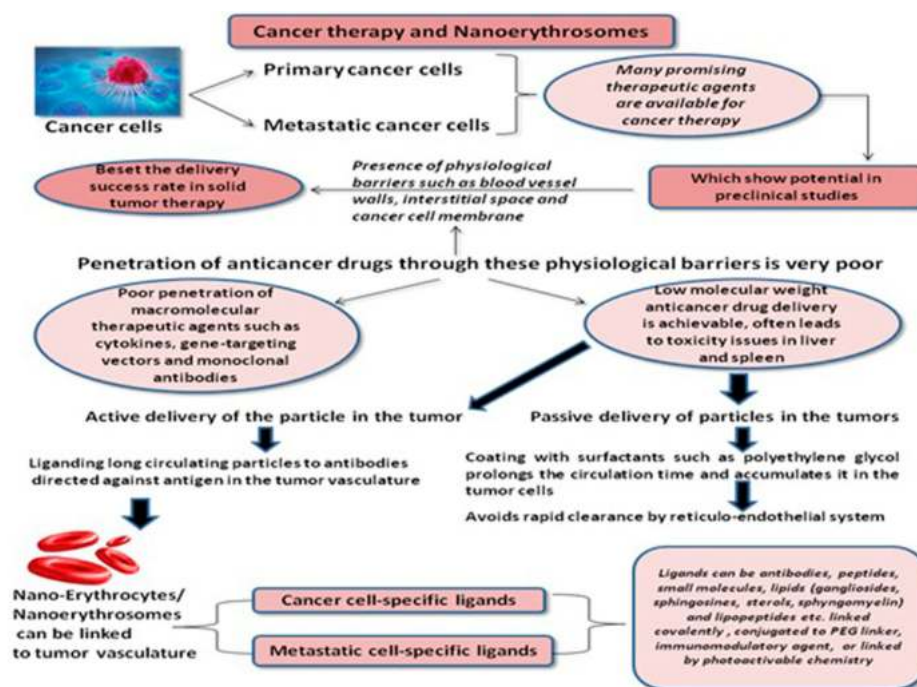
## 4. Applications of NERs in Cancer Therapy and Diagnosis

### 4.1. NERs in Cancer Therapy

The important studies on NERs and their formulations for the application in cancer therapy are summarized in Table 1. NERs are artificial, synthetic, biomimetic, and presently the most investigated and sought after RBC cell-based carrier systems under this category. These RBC cell-based carrier systems have covered a path of progress from conven-

tional REs (microscale) to the most advanced NERs (nanoscale). These RBC-nanovesicles (RBC-NV) are fused onto the core NPs through extrusion, sonication, and electroporation techniques. Being biomimetic NPs, NERs attain specific functions including ligand recognition, tumor-targeting, longer blood circulation time, and ability to escape the immune system. These activities lead to the core-shell interactions, mimicking the source cells, and improving the therapeutic efficacy of drugs through specific delivery and enhanced drug-accumulation inside the tumor [26]. NERs marked the beginning of an unparalleled approach towards the therapy of a number of diseases including cancer owing to multiple advantages such as small size, ability to encapsulate antineoplastic drugs, and organ-specific targeting which further gave them added advantages over their other carrier counterparts in cancer nanomedicine. The surface of NERs can be modified using tumor-targeting ligands, which further improve the drug efficacy and optimize drug pharmacokinetics.

The loading and delivery of antineoplastic drugs using various pharmaceutical and nanotechnological engineering techniques is one of the most important applications of NERs. The unique techniques of surface modification and functionalization provide additional attractive feature to this delivery system and further increase its potential in cancer therapy (Figure 2).



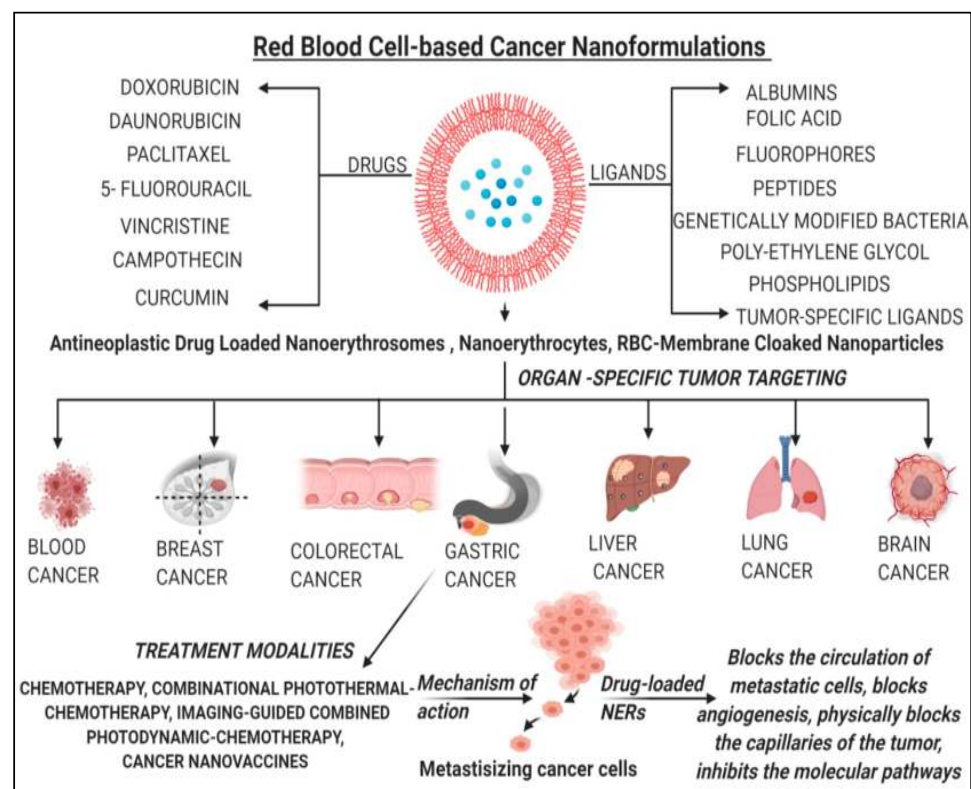
**Figure 2.** Role of NERs in cancer therapy.

Numerous studies have been performed in the field of cancer therapy using NERs over the last two decades and multitude of its medical applications in other ailments diversify their applications in the arena of drug delivery as therapeutic, diagnostic, theragnostics, and imaging tool [27]. The nanomedicines have the ability to deliver the drugs directly to the individual organs to avoid the adverse or side effects; however, the drug delivery by conventional nanocarriers is limited by difficulty in delivering to most target organs and dire need of the affinity moieties [28].

The poor drug loading, low anti-tumor efficacy, and rapid clearance from the blood circulation are the major challenges faced by the conventional anti-cancer nanocarriers. The most challenging part is the high uptake of nanocarriers by the liver and spleen because of RES. The majority of nanocarriers injected intravascularly end up in the liver causing hepatotoxicity [29]. The NERs, as an innovative drug delivery system, provides with high drug loading capacity, specificity in targeting tumor cells, and synergistic anti-

cancer sensitization using human erythrocyte membrane as delivery platform. This novel technology can be used in treating and preventing cancer metastasis such as breast cancer metastasis, mainly by blocking the circulation of metastatic cancer cells by inhibiting angiogenesis and capturing circulating endothelial progenitors that are recruited to the tumor. They also physically block (infarction) the capillaries of the tumor or the metastasis. The inhibition of molecular pathways of the metastatic invasion and cancer growth is the latest therapeutic approach for cancer metastasis. The physical blocking of metastasis and angiogenesis by incorporating tumor- and angiogenesis-specific ligands such as antibodies, small molecules and peptides into the plasma membrane of erythrocytes is very novel [30].

Polymeric-NPs as intravascular drug delivery vehicles have been studied extensively in past but their applications are beset by rapid clearance from the circulation by RES. This led to the development of NERs as novel cancer drug delivery systems for the optimal delivery of various anticancer pharmaceutical agents. These anticancer drugs, when administered intravenously, cannot reach the tumor site efficiently owing to their weak specificity which results into lower therapeutic potential and serious side effects. One of the major reasons of multidrug resistance (MDR) and thereby chemotherapy failure is the efflux of anticancer drugs mediated by P-glycoprotein (P-gp). This problem is overcome to an extent when these anticancer agents are delivered to the tumors in combination with P-gp inhibitors and this has proven to be an effective strategy [31]. An organ-specific or site-specific nano-drug delivery system based on human RBCs is a newer and effective strategy of the present decade (Figure 3).



**Figure 3.** Summary of red blood cell (RBC)-based anticancer nanoformulations (anti-cancer-loaded-NERs) along with their mechanisms.

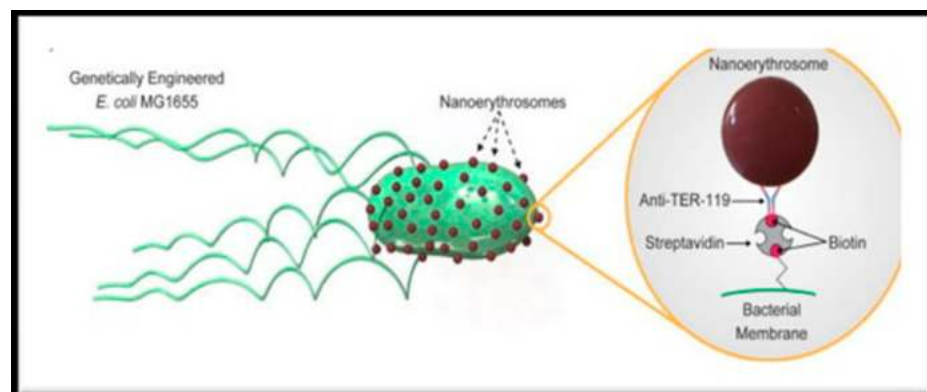
The anticancer drug delivery using NERs was first carried out by a team of researchers two decades ago in 1994, when they explored the anticancer drug daunorubicin (DAU) and prepared the DAU-NERs for enhanced antineoplastic potential. DAU was linked covalently to the NERs using glutaraldehyde as homobifunctional linking arm, and it was observed that the cytotoxicity of conjugated drug was higher as compared to the free drug when assessed on P388D1 cancer cell line [32]. Results indicated that these

DAU-NER conjugates could potentially be utilized as drug carriers in CDF1 leukemia tumors. The mechanism behind the cellular uptake was neither the diffusion through cell membrane nor endocytosis but free DAU was found to slowly release by hydrolysis of glutaraldehyde linking arm, producing a high concentration of free DAU in the cells vicinity for a long period of time [33], and phagocytosis of DAU-NER complex was not involved [34]. The biodistribution of <sup>125</sup>I-NERs purified by dialysis followed by intravenous (IV) and intraperitoneal (IP) injections in CD1 mice was investigated in another study. NERs were rapidly (less than 30 min) removed from the systemic circulation after IV administration, however, the IP administration showed a higher uptake by liver and spleen, accumulation in lungs and marked activity was observed in the inguinal lymph nodes after 2 h of the administration [35].

Earlier, the surface modification of NPs could be achieved using polymers such as poloxamines, poloxamers and polyethylene glycols, to avoid opsonization, but now, these NPs could be anchored to the surface of RBCs to escape the clearance by RES as the RBCs are able to do so. This leads to a novel approach in the intravascular drug delivery system as RBC-anchored NPs. The RBC-anchored polymeric NPs were prepared using polystyrene NPs modified with carboxyl groups (110, 220, 450, and 1100 nm in diameter). An improved in vivo circulation lifetime was achieved using RBC-anchored NPs [36]. In another study by the same research group, RBC-anchored NPs were eventually get detached from RBCs owing to the shear forces and subsequently get cleared up in the liver and spleen [37]. The surface modifications of NERs is possible with glutaraldehyde, antibodies, and carbohydrates (sialic acid), which improve their target specificity and prolong their in vivo circulation time, helps escape the RES and protects the drug from the inactivation by endogenous chemicals and enzymes [38,39]. Based on this approach, a top-down biomimetic approach was reported utilizing particle functionalization. The fluorophore-loaded biomimetic NPs were prepared using poly (*d,l*-lactide-co-glycolide) (PLGA) polymer and fused with RBC-derived vesicles. The prepared RBC-fused biomimetic NPs were injected in mice. Results revealed superior circulation half-life in cases of biomimetic-NPs as compared to control group-NPs which were coated with conventional synthetic stealth materials. An increased particle retention time of 72 h in the blood was observed which proved the approach as very unique and effective in the NPs functionalization [40]. In another study, RBC-membrane-cloaked polymeric NPs were prepared by lipid-insertion technique utilizing fluorescein isothiocyanate (FITC)-polyethylene glycol (PEG)-lipid. The FITC-PEG-lipid NPs were functionalized with folate and nucleolin-targeting aptamer AS1411 showed a receptor-specific targeted delivery when tested against the cancer cell lines models [41]. Another promising integration of cell-based drug delivery and nanotechnology was seen when RBCs were linked to iron oxide-NPs pre-coated with chlorine-e<sup>6</sup> and a well-known chemotherapeutic drug, doxorubicin (DOX) was loaded for an imaging-guided combined chemotherapy-photodynamic therapy of carcinomas. Interestingly, the marked synergism and excellent therapeutic results were observed in animal tumor model [42]. In another report, the oxygen self-enriched biomimetic RBCs were prepared by cloaking the albumin-NPs containing indocyanine green (ICG) and perfluorocarbon (PFC) with RBC membranes. The rapid clearance of conventional nanocarriers by RES and low singlet oxygen quantum (0.08) of ICG often resulted into limited phytotherapeutic efficacy. The prepared oxygen self-enriched RBCs had long circulation time, high oxygen carrying capacity, and biomimetic properties ideal for clinical cancer phototherapy treatment [43]. Another novel NERs-ghost delivery system was developed to transport sodium transhinone-IIA sulphonate (STS-Nano-RBC) for IV use in rats. These nanosystems had narrow particle size distribution, good stability for 21 days, and better loading efficiency as compared to conventional STS injections in vivo [44].

BackgroundIt is now evident that the adverse effects associated with the conventional cancer therapy (chemotherapy, surgery, and radiotherapy) can effectively be addressed by applying the nanomedicine approach. Nano-engineering makes targets achievable and with diverse surface functionalization methods, nowadays RBCs are not only targeting

drug carriers but therapeutic and imaging diagnostic tools as well, what we commonly term as theranostics [45]. Recently, RBC membrane-loaded with hydrophobic drug camptothecin were prepared which were non-covalently labeled with amphiphilic fluorophore nanovesicles (NVs). These NVs were overall stable, nonphagocytic and exhibited minor stimulation of macrophages for cytokine release. Intravenously injected NVs in balb/c mice exhibited better retention over 48 h and minimal accumulation in vital organs such as heart, liver, and kidneys [46]. NE-membrane-chaperoned 5-fluorouracil (5-FU) liposomes were also prepared as biomimetic delivery system to target hepatocellular carcinoma cell lines. Liposomes of 5-FU were prepared by thin film hydration method using dipalmitoyl phosphatidylcholine (DPPC) and cholesterol. NE-membrane-chaperoned 5-FU liposomes were prepared by extrusion technique. The drug-targeting capability of NE-membrane-chaperoned liposomes was higher than conventional 5-FU solution [47]. The most recent advances in this field include antigen delivery systems using NERs in which the tumor antigens are loaded onto the NERs using fusion tumor cell membranes. This nanosystem was shown to markedly inhibit the tumor growth in B16F10 and 4T1 tumor models in vivo [48]. A new NER-tailoring technique evolved recently, wherein, the NERs in the size range of 200 to 300 nm were produced by addition of phospholipids DPPC to ghost RBCs [49]. In yet other significant research, bio-hybrid microswimmers were developed which had the integration of motile-microorganisms with artificial cargo carriers to revolutionize targeted-cargo delivery. In this study, genetically-engineered flagellated *Escherichia coli* species were integrated with RBC-derived NERs through conjugation of streptavidin-modified microorganisms with biotin-modified NERs using non-covalent streptavidin-biotin interactions. The high fabrication efficiency and good motility performance was achieved with these personalized biohybrid microswimmers, as shown in Figure 4 [50].



**Figure 4.** Biohybrid microswimmers using genetically modified *E. coli* bacterium and NERs for targeted cargo-delivery (Image adopted from reference [50], APL Bioeng, 2020, which was published under a creative commons attribution (CC BY) license).

#### 4.2. NERs in Immunotherapy

The main focus of cancer immunotherapy is to manipulate the patient's own immune system to recognize and destroy the cancer cells. The NPs-based drug delivery systems show their therapeutic potential by evading the immune system of hosts and delivering the drug efficiently and safely to the site of action. In lieu of this, an erythrocyte membrane-enveloped PLGA NPs (PLGA-NP) based nanovaccine was developed for hgp 10025-33, an antigenic peptide and monophosphoryl lipid (MPLA), a toll-like receptor-4 agonist. To target the antigen presenting cells (APC), a mannose-inserted membrane structure was constructed in the lymphatic organ and the prepared nanovaccine showed increased retention of protein content in the erythrocytes, improved in vitro cellular uptake, inhibition of tumor growth, prolonged tumor-occurring time, and reduced tumor metastasis, resulting in a potential nanoplatform for the delivery of antigens in the immunotherapy of cancer [51]. After the conventional mono-chemotherapy, research was carried out on combination

chemotherapy approach for cancer treatment by these carrier systems. A programmed co-delivery of paclitaxel (PAX) and DOX as the hydrophilic-lipophilic chemotherapeutic drug pair into the magnetic *O*-carboxymethyl-chitosan NPs further masked using Arg-Gly-Asp anchored erythrocyte membrane was achieved and compared with the conventionally prepared PEG coated NPs. Superior circulation time, improved tumor accumulation, and better tumor uptake was demonstrated using biomimetic-NPs with much lower side effects as compared to their counterpart [52].

In an attempt to counter the insufficient targeting ability of NERs which beset their clinical applications [53], several PAX-loaded polymeric NPs were linked to the biomimetic 4T1-breast cancer cell membranes. Polymeric NPs were prepared using poly(caprolactone) and pluronic copolymer F68. The novel nanoformulation demonstrated superior interactions with the source tumor cells, prolonged circulation time, and higher cell-specific targeting of the homotypic primary tumors and metastasis [54]. The in-combination advantages of erythrocytes and NPs have so far offered three types of RBC-based nanomedicines: (i) whole erythrocytes, (ii) cell membrane-coated NPs, and (iii) NERs and together they offer optimal blend of important features as a multifunctional platform in the cancer immunotherapy [55]. Similarly, curcumin-loaded NERs (CUR-NER) were prepared by sonication method showing nearly uniform spheres with diameter ( $245.7 \pm 1.3$  nm), encapsulation efficiency ( $50.65\% \pm 1.36\%$ ) and loading efficiency ( $6.27\% \pm 0.29\%$ ). These CUR-NERs were efficiently taken up by the cancer cells which displayed good anti-tumor efficacy [56].

The molecular targeting of the RBC membrane glycoprotein-A (GPA) receptor can mediate the membrane attachment of protein based-therapeutics which can open diverse applications of NERs for preclinical and clinical biocompatibility [57]. A cell membrane-coated NP platform for the new antitumor drug gambogic acid (GA) was developed in order to improve its limited clinical applications owing to its poor aqueous solubility. The biomimetic nanocarrier system was prepared using PLGA polymer. The prepared PLGA nanocarrier system was found to show improved stability and biocompatibility. In addition, the GA-loaded RBC-m- PLGA-NPs showed better antitumor efficacy and lesser toxicity as compared with the free GA in the treatment of colorectal cancer [58]. In another study, a novel RBC-based artificial APC (aAPC) system was developed which can mimic the antigen presenting dendritic cells (DC) and activate T-cells. This system had promising applications in the transfer of adoptive T-cells and even in the activation of circulating T-cells directly for the immunotherapy of cancer [59].

#### 4.3. NERs in Cancer Imaging and Diagnostics

For the in vivo cancer imaging, RBC-up-conversion NPs (RBC-UCNP) were developed for cancer targeting and imaging recently. UCNPs were functionalized using 1,2-distearoyl-sn-glycero-3-phosphoethanolamine-*N*-[methoxy(polyethylene glycol)-2000] (ammonium salt) (DSPE-PEG). RBC-UCNPs were obtained using extrusion method and showed superior chemical and optical features. These RBC-UCNPs were utilized successfully for in vivo tumor imaging [60]. The biomimetic RBC membrane-coated ferric oxide ( $\text{Fe}_3\text{O}_4$ ) magnetic NPs (RBC-MNP) prepared using microfluidic electroporation strategy also exhibited better treatment effect in imaging-guided cancer therapy [61]. Therefore, biomimetic-NPs derived from erythrocytes, white blood cells, cancer cells, stem cells, platelets, or bacterial ghost cells are engineered therapeutic carrier system presently garnering lot of attention for their applications in diagnostics, imaging, drug delivery, vaccines, and immune-modulation, etc. [62]. The limitations of fluorescence image-guided tumor surgery and photodynamic therapy including lesser penetration depth, lower signal-to-noise ratio of traditional first near infra-red (NIR) window (NIR-I) fluorescence, as well as the hypoxic tumor environment can be overcome by RBCs-based multimodal probe. This probe was able to show improved tumor targeting and fluorescent probes retention post IV injection, therefore, the second NIR window (NIR-II) fluorescence bioimaging-guided absolute tumor resection and highly efficient photodynamic therapy could be achieved [63].

#### 4.4. NERs in Cancer Combination Therapy

In continuation to explore the cancer combination therapy using NERs, a hybrid biomimetic RBCs-melanoma cells (B16-F10) coating (RBC-B16 hybrid membrane) along with the loading of camouflaged DOX on the hollow copper sulfide (CuS)-NPs were developed for the melanoma therapy and compared with the bare CuS-NPs. Interestingly, the DOX-loaded RBC-B16-coated CuS-NPs exhibited excellent synergistic effects as the photothermal-chemotherapeutic agent and were 100% effective in inhibiting the melanoma tumor growth [64]. Small molecular drug co-assemblies of 10-hydroxycamptothecin (10-HCPT) and ICG were fabricated in RBC membranes as a biomimetic and combinational therapeutic tool for prolonged circulation time, controlled drug release, and synergistic chemo-photothermal therapy. The prepared NPs had a diameter of ~150 nm, core-shell structure, high drug load (~92 wt%), and decreased uptake by RES. Compared to individual treatment, the NPs under dual stimuli showed high increased apoptosis in tumor cells [65]. PAX-loaded biocompatible nanosystems derived from human ER membranes were constructed to enhance the targeting of the drug for the treatment of gastric cancer. With a lipid insertion method, a phospholipid derivative, 1,2-distearoyl-*sn*-glycero-3-phosphoethanolamine-*N*-(maleimide[polyethyleneglycol]-3400) (DSPE-PEG-MAL) was inserted into the ER membrane-derived tumor-targeting molecular vesicles. The spherical and uniformly sized ( $171.7 \pm 4.7$  nm) nanosystems were obtained which exhibited biphasic release pattern of the drug. When subjected to in vivo testing in Balb/c nude mice, the nanosystems showed accumulation of the drug into the tumor site within 2 h of the administration reducing the tumor volume to 61% [66]. In a similar study, folic acid (FA) as a tumor-targeting molecule and magnetic nanoparticles (MNP) were coated on the RBC-surface using lipophilic interaction and chemical conjugation techniques, respectively. MNPs were functionalized using DSPE-PEG-FA. Functionalized MNPs were conjugated with RBC ter 119 antigen. These engineered RBCs quickly adhered to the circulating tumor cells (CTC) and conjugated to form RBC-CTC conjugates which released the CTCs upon treatment with RBC-lysis buffer followed by centrifugation [67]. The targeted delivery of DOX in the treatment of liver cancer was also studied in another report. The surface modified NERs loaded with DOX were prepared and their surfaces were modified with FA and PEG for their tumor targeting ability. Compared to the conventional DOX injection, FA-PEG-DOX-Nano-RBCs were reported to prolong the drug circulation time in vivo and augmented the concentration and accumulation of drug in liver tumor cells [68].

A novel, targeted, biomimetic nanoplatform for combined cancer chemotherapy and phototherapy was achieved by embedding the BSA encapsulated with 1,2-diaminocyclohexane-platinum (II) and ICG for targeting peptide-modified erythrocyte membrane in order to improve the tumor internalization. The nano-therapeutic system had tumor-specific targeting ability with efficient removal of tumors, as well as suppression of metastasis in vivo by combined photothermal therapy and chemotherapy under phototriggering [69]. A nanoworm, biomimetic NER for siRNA delivery has also been reported in literature wherein, the RBC membrane cloaking protected siRNA from degradation by RNase A. The siRNA vector stayed longer in the blood circulation than that of both negatively charged BSA spheres, as well as positively charged BSA and showed the ability to escape from late lysosomes and endosomes in order to achieve efficient transfection for knockdown of genes. These biomimetic worm-like NERs charge reversible gene vector is a novel method for much effective in vivo siRNA therapy [70].

The magnitude of research carried out on the delivery of drugs bound to erythrocytes emphasized more on controlled release, improved pharmacokinetics and pharmacodynamics profiles of drugs such as anti-neoplastics, anti-inflammatory, anti-thrombotics, and anti-microbials, etc. [71]. Poised with unique advantages in drug transportation, RBC-based systems were further developed and in yet another study, an albumin bound NIR dye and DOX as a chemotherapeutic agent were co-encapsulated inside the RBCs and their surfaces were modified using target protein to achieve tumor targeting. The RBC membranes were destroyed using an external NIR laser and light-induced photothermal

heating which resulted into the release of drugs effectively. This work was novel, smart, and highly promising in the field of targeted combination therapy of cancer (photothermal and chemotherapy) [72]. Similarly, the immunocompatible nanocarriers cloaked in RBC membrane were utilized for drug targeting. DOX-loaded PLGA NPs were prepared using double emulsification method and RBC membrane vesicles were prepared using a sonication method. Biomimetic RBC-NPs were prepared by fusing DOX-loaded PLGA NPs into RBC membrane vesicles. The prepared biomimetic-NPs of DOX shrouded inside the RBC membranes showing good inhibition of tumor growth as compared to the treatment with free drug [73]. Recently, dual-functional exosome-based super-paramagnetic NP-clusters were developed for the cancer therapy and the *in vivo* studies on murine hepatoma-22 subcutaneous cancer cells demonstrated the suppression of tumor growth by these novel drug carriers under an external magnetic field [53].

The photothermal therapy (PTT) is a highly efficient method for the induction of tumor neoantigen release *in situ* and it has great potential to be used in the cancer immunotherapy. Nanovesicles of biomimetic black phosphorous quantum dots (BPQD) coated with ER membranes (RM) nanovesicles [BPQD-RMNV] exhibited longer circulation time and better tumor accumulation *in vivo* in breast cancer cells. The BPQD-RMNV mediated PTT combined with anti-program death-1 (aPD-1) treatment markedly deferred residual and metastatic cancer growth *in vivo*. Therefore, the combination of BPQD-RMNV-mediated PTT with immune checkpoint-blockade antibodies were found to improve the permeation and efficacy of CD8<sup>+</sup> T cells inside the tumor restraining the growth of basal-like breast cancer cells *in vitro* [74]. In another study, graphene oxide NPs were prepared by incorporating ICG as photosensitizer along with DOX as the chemotherapeutic agent and the shell was made of RBC-membrane inserted with FA as targeting molecule. These NPs showed excellent biocompatibility and remarkable ability to evade the RES clearance [75]. Hybrid membranes of various kinds of cells could efficiently be coated onto the surface of NPs in order to achieve the desired functions [76]. The coating using cell membranes has emerged as an upcoming strategy for improving the properties of nanomaterials. In lieu of this, RBC membrane was fused with MCF-7 breast cancer cell membrane and hybrid membrane-camouflaged melanin NPs were prepared for improving the therapeutic potential of PTT. Melanin-RBCs showed both prolonged blood circulation time and homotypic targeting to the MCF-7 breast cancer cells [76].

#### 4.5. NERs in Glioma Therapy

Amongst all cancers, glioma is the most fatal with limited options of treatment and a very low survival rate. It is extremely challenging for NPs to cross blood brain barrier (BBB) and blood brain tumor barrier (BBTB). Researchers recently designed RBC-membrane-coated solid-lipid-NPs-based nanocarrier system with T-7 and NGR peptide to counter these challenges, to evade the BBB and to reach the glioma. The NPs of peptides T-7 and NGR were prepared using DSPE-PEG and fused with RBC membrane. These biomimetic nanocarriers showed enough potential to deliver the model drug vincristine to the brain [77]. Similarly, RBC-membrane-coated-nanocrystals modified with the tumor-targeting peptide c(RGDyK) were developed for their potential to treat glioma. Docetaxel-loaded nanocrystals were prepared using streptavidin-PEG-DSPE and biotin-DSPE-c(RGDyK) and fused with RBC membrane. These nanocarriers showed improved tumor accumulation and enhanced therapeutic efficacy *in vivo* in mice with subcutaneous tumor and orthotropic glioma. These nanosystems displayed higher drug loading, excellent biocompatibility, long-term stability, and were found to be suitable for brain delivery [78]. RBC-hitchhiking is another valuable technological tool and a new formulation development strategy of complexing NPs with the RBCs for the treatment of aggressive and small cancers, including lung cancer [79].



#### 4.6. NERs in Overcoming Drug Resistance

RBC-membrane-derived vesicles (RDV) coated poly (acrylic acid) cystamine hydrochloride-*D*- $\alpha$ -tocopherol succinate (PAAssVES) NPs were developed using emulsification method followed by solvent-volatilization method and finally was loaded with anticancer drug sorafenib (SFN). The obtained RDV-coated NPs (RDV-NP) showed excellent stability and particle size of 113.5 nm with  $-10.7$  mV zeta potential. In comparison to the free SFN treatment, RDV-NPs demonstrated longer circulating time [80]. To overcome MDR in breast cancer treatment, NERs could be an ideal approach for the co-delivery of anticancer drugs with a p-gp inhibitor. In lieu of this, FA-modified NER system was developed to simultaneously transport tariquidar and paclitaxel and evaluated for its *in vitro* and *in vivo* properties. The nanocarrier was observed to be of size  $159.8 \pm 1.4$  nm and zeta potential  $-10.98$  mV, respectively. It showed a sustained release of paclitaxel within 120 h in both pH 6.5 and 7.4 media. Cytotoxicity studies on MCF-7 cells showed that both paclitaxel and tariquidar were able to inhibit the proliferation of MCF-7 cells and pharmacokinetic studies revealed prolonged drug release for all nanoformulations [81]. For the development of nanomedicine to target gliomas, it is important for them to have the capability to cross the BBB, as well as the BBTB. In this light, a preparation based on PLGA-NPs coated with ER-membrane with dual-modified peptide ligands was developed. Euphorbia factor-L1 was used as model drug, and these NPs were taken up by the cells and showed the ability to cross both BBB and BBTB, thereby producing cytotoxic effects *in vitro*. Furthermore, *in vivo* studies supported these results and the prepared NPs could enter the brain, targeting tumor tissues and significantly extending the life span [82]. Subsequently, NERs of 5-FU for liver cancer treatment were prepared for improved pharmacokinetic and biodistribution of 5-FU. The 5-FU-loaded chitosan coated-poly (lactide-co-glycolic acid)-NPs-NEs chitosomes had narrow particle size distribution, desirable encapsulation efficiency and sustained release profile of up to 72 h, which suggested that these nanosystems were able to deliver 5-FU with enhanced targetability to the liver cells [83]. In another recent study, the surface of NERs was decorated with two different fluorophores: 7-amino-4-methylcumarin and dibenzocyclooctinecyanine with glutaraldehyde. The NER-derivatives exhibited higher stability in physiological conditions [84].

**Table 1.** Anticancer nanoformulations of nanoerythrocytes (NER), their surface modification and specific tumor targeting ability.

Name of The Anticancer Drug/Agents	Type of RBC-Based Nanoformulation	Modification/Functionalization/Ligands	Type of Surface	Reported Applications	Ref.
DAU	NERs	DAU was covalently linked by glutaraldehyde to the NERs		CDFI leukemia tumor	[32]
DOX	RBC-Iron oxide NPs	Pre-coated with chlorime <sup>6</sup>		For imaging-guided combined photodynamic and chemotherapy of cancers	[42]
ICG and Perfluorocarbon (PFC)	RBC membrane cloaked albumin NPs			Ideal for clinical cancer phototherapy treatment	[43]
Sodium Translithione II A sulphonate	Drug loaded nano-RBCs			Nanosystem was better than conventional injection in-vivo	[44]
Camptothecin	RBC-membrane loaded nanovesicles	Labelled non-covalently with amphiphilic fluorophore		–	[46]
5-FU	Biomimetic nanoerythrocyte-membrane-chaperoned liposomes			Hepatocellular carcinoma	[47]
Engineered <i>E. coli</i> sp.	Biohybrid microswimmers (RBC-NERs)	Conjugation of streptavidin-modified bacteria with biotin-modified-NERs using non-covalent streptavidin interaction		Targeted cargo delivery system	[50]
Antigenic peptide Hgp 10025-33	Erythrocyte membrane enveloped PLGA-NPs	Mannose-inserted membrane structure was constructed to actively target antigen presenting cells in lymphatic organs		Cancer nanovaccine in cancer immunotherapy	[51]
Co-delivery of PAX and DOX	Magnetic O-Carboxy methyl chitosan NPs	Camouflaged with an Arg-Gly-Asp anchored ER-membrane		Better tumor uptake	[52]
PAX	Biomimetic polymeric NPs	–		4T1-breast cancer cell membrane	[54]
Curcumin (CUR)	Biomimetic RBC-membrane coated PLGA NPs	–		Enhanced antitumor activity	[56]
Gambogic acid	Upconversion NP coated with RBC-membranes	–		Colorectal cancer	[58]
FA	Drug loaded RBC-membrane coated copper sulphide NPs	Surface-modified with ligands for active targeting of cancer cells		For in-vivo cancer imaging	[60]
DOX	Biomimetic RBC membrane nanovesicles			100% melanoma tumor growth inhibition rate	[64]
10-Hydroxy Camptothecin and ICG	Encapsulated in human erythrocyte membrane	A phospholipid derivative was used for tumor targeting into ER-membrane derived nanovesicles		Synergistic chemo-photothermal therapy	[65]
PAX	Magnetic NPs coated on the surface of RBCs	Chemical conjugation and hydrophobic interactions between RBC-circulating tumor cells		Gastric cancer	[66]
FA	Nanoworms, biomimetic NERs	Surface modified by FA and PEG		Enhanced tumor targeting ability	[67]
DOX	Coencapsulated inside RBCs	Albumin bound NIR dye		Enhanced tumor targeting ability in vivo in liver cancer	[68]
siRNA	RBC-coated membrane	–		Efficient siRNA therapy in vivo	[70]
DOX	NPs of graphene oxide-DOX-RBC-membrane-ICG as photosensitizer	–		Combinational photothermal and chemotherapy of cancer	[72]
DOX	RBC-membrane coated solid lipid NPs	–		For the treatment of solid tumors	[73]
DOX	Nano-erythrocytes (NEs)	FA		Had excellent ability to evade RES	[75]
Vincristine	PLGA-NPs coated with ER-membrane	T7 and NGR peptide		Brain delivery for treatment of gliomas	[78]
Codeelivery of PAX and Tariquidar	FU-loaded chitosan-coated-PLGA-NPs-NE-chitosomes	Dual-modified peptide ligands		Breast cancer management	[81]
Euphorbia factor L1		–		Brain delivery for gliomas	[82]
5-FU		–		Liver targeting	[83]

In vitro uptake by macrophages, in vivo biodistribution and pharmacokinetic studies demonstrated that the RBC-membrane is a better alternative to PEG, which is currently the gold standard for nanoparticles “stealth”. The combination of natural cell membranes with synthetic NPs poses a novel and biomimetic strategy for the designing of nanomaterials which additionally displays a wide range of biomedical applications, owing to the properties of functional materials used [85]. The biomimetic-NPs have attracted increasing attention in pharmaceutical and biomedical applications by imitating the structures and the functions of biological systems including longer blood circulation time. Nevertheless, the circulation time of these NPs is still far lesser than that of the native cells, which limits their applications greatly [86,87]. Accordingly, a camouflage comprising ER-membranes renders NPs as a platform that has combined advantages of native ER-membrane as well as of nanomaterials. When, they are injected into the animal models in vivo, the ER-membrane-coated NPs imitate and behave like RBCs and interact with the surrounding macromolecules to achieve longer circulation time [88].

### 5. Applications of NERs in Non-Cancer Therapies

NERs have been extensively investigated for the therapy and diagnosis of various forms of cancers and that has further encouraged the researchers to test their applications for non-cancer diseases. The findings are interestingly very promising which has opened a new vista for the applications of NERs. In one such study, the NERs of antimalarial drug pyrimethamine (PRY) were developed by sonication method which showed good stability and controlled in vivo release. Developed NERs improved the treatment of malaria when combined with artemisinin drug [89]. In another interesting research, artesunate (ART) conjugated NERs were prepared to increase the stability, decrease the toxicity, cost, and drug leakage for the treatment of malaria. The optimized ART-NER nanoformulations were non-aggregated, uniformly sized, with drug loading of  $25.20 \pm 1.3 \mu\text{g}/\text{mL}$  and when administered IV, showed higher plasma drug concentration as compared to free drug in vivo [90]. For the treatment of atherosclerosis, the nanomaterials can be explored and it is believed that they can serve as a powerful tool in its treatment. In an attempt to achieve this, biomimetic, well defined core-shell-nanocomplexes of rapamycin (RAP)-loaded PLGA-NPs cloaked with RBC were created with negative surface charge. The prepared nanosystems were shown to be safe and effective in the management of atherosclerosis as the biomimetic behavior of RBCs resulted in decreased macrophage-mediated phagocytosis and increased aggregation of NPs in the atherosclerotic plaques using targeted delivery [91]. Most of the applications of NERs were limited to the IV, IP, and sub-cutaneous (SC) routes of administration. To explore other possible routes of administration, they were also investigated as inhalational drug carriers in few studies successfully. In one such study, NERs were conjugated with CARSKNKDC (CAR), a cell permeable peptide and fasudil, a rho-kinase (ROCK) inhibitor using hypnotic-lysis and extrusion method for prolonged pulmonary vasodilation. The NPs obtained were of spherical shape with average size  $161.3 \pm 1.37 \text{ nm}$  and % entrapment efficiency (EE)  $48.81 \pm 1.96\%$ , which showed stability of around 3 weeks at  $4^\circ\text{C}$ , and the drug fasudil was shown to be released in a controlled release pattern for more than 48 h. The reduction in the pulmonary arterial pressure upon intratracheal administration of CAR-fasudil-NERs was approximately 2-fold more specific to the lungs in comparison to fasudil alone [92]. Few other studies in the literature also suggest that the NERs can effectively be utilized for inhalational delivery of fasudil drug as cell-derived carriers [93,94].

### 6. Biosensing Applications of RBC-Mediated Carriers Systems

The cutting-edge RBC-mediated anti-cancer drug delivery by NERs is well established along with their applications in some of the non-cancer diseases. Additionally, the in vivo nanobiosensor-based theragnostic application of RBCs has emerged as a topic of interest in present days for advanced medical diagnostics, analytical chemistry, and environmental monitoring [95–97]. Their extraordinary profusion, mobility, and loading capacity makes

them an attractive tool for sensing the analytes present in the blood. The sensor-loaded ERs or the dubbed erythrosensors can be re-infused in the blood and can be used for the measurement of analyte levels in the blood stream [96]. Previously, 3-D focusing of RBCs in microchannel flows for bio-sensing applications has also been reported [98]. Additionally, the fluorescent sensors were incorporated inside ERs followed by non-invasive monitoring to follow changes in plasma analyte concentrations [99]. For the management of diseases such as diabetes, there exists a need for long-term, minimal-invasive system to monitor blood glucose as analyte. Currently employed methods suffer from disadvantages of low patient compliance for the finger stick test and require regular calibrations for continuous glucose monitoring. The RBCs can act as a biocompatible carrier of sensing assays for such long-term monitoring procedures. They can serve as long-term (>1 to 2 months), continuously circulating biosensors in the diagnosis and management of such long term diseases [100]. Similarly, the fusion of quantum dots (QD) with living cell membranes for bio-sensing capability in imaging technique is a flexible approach for controlled, hydrophobic QDs-based fluorescence analysis of living cellular membranes [101].

### **7. Recent Patents on NERs for Cancer Therapy**

In this section, the important and recent patents related to the use of NERs as bioactive carriers in cancer therapy are summarized. The description of the invention and its pharmaceutical advantages are mentioned in Table 2 for the quick understanding of the readers. The recent patents enlisted here show the viability of this approach for delivering the antineoplastic drugs to their required targeted site of action. The enhanced potential of the antineoplastic drugs loaded in NERs carrier system points towards the growth of this novel drug delivery system in cancer therapy [102–111].

Table 2. Recent patents available on NERs as carrier system for cancer therapy.

Patent Number	Invention Title	Description of The Invention	Pharmaceutical Advantages	Ref.
US5653999	NERs as bioactive carrier	A complex comprising of a bioactive agent coupled to vesicles derived from ERs. Prepared ERs had size less than 1 µm and substantially free of hemoglobin.	DAU-NERs conjugate had a higher antineoplastic activity than the free bioactive agent.	[102]
WO1998011919A3	Polyethylene glycol conjugated NERs, method of making same and use thereof.	Long circulating NERs avoid rapid clearance by RES.	Prolonged circulation time.	[103]
US20040180094A1	Activation agents on the surface of encapsulation vesicles	Target ligands can be synthetic, semi-synthetic and naturally occurring such as antibiotics, hormones, lectins, glycoproteins, peptides, amino acids, polypeptides, sugars, saccharides, carbohydrates, cofactors, bioactive agents, and genetic materials such as nucleotides and nucleosides, etc.	The present invention addressed drug resistance problems in vivo by attaching optimal target ligand to encapsulation vesicles.	[104]
US8211656	Biological targeting composition and methods of using the same.	Targeted delivery of imaging agents, drugs, peptides, proteins, and pharmaceuticals using modified RBCs is described here.	Modified RBCs can carry a variety of therapeutic moieties for the treatment of various ailments including cancer.	[105]
US20130202625	Use of human erythrocytes for prevention and treatment of cancer dissemination and growth.	Cancer metastasis specially breast cancer metastasis can be prevented by blocking the circulation of metastatic cells and by blocking angiogenesis such as capturing endothelial progenitors that are recruited to the tumor, or by physically blocking of the capillaries of the tumor or the metastasis.	RBCs have potential for use as therapeutics as they are easily retrieved from a patient, non-immunogenic, and are biologically designed to navigate the microcirculation including tortuous tumor vasculature.	[106]
US20200138987	Composition for material delivery including exosome mimetics derived from RBCs, and use thereof.	Exosome mimetics derived from RBCs are used for material delivery such as drug, radioactive material and fluorescent materials, etc.	Exosomes (small vesicles, 30nm-100nm) have drawn attention as new drug delivery carrier system for targeted delivery to a specific organ and can be used as imaging tools.	[107]
US20200289666	Biomimetic anisotropic polymeric particles with naturally derived cell membranes for enhanced drug delivery.	Biomimetic particles can be used in the treatment of excessive bleeding, thalassemia, thrombopenia, cancer, infectious diseases, etc.	Particles comprised of polymeric core of defined shape, size, surface from naturally derived cell membranes such as RBCs, have application in drug delivery and cell engineering.	[108]
US20170367990	Use of NPs coated with RBC membranes to enable blood transfusion.	An inner core of nanoparticle comprised of non-cellular compound and an outer surface comprise of cellular membrane derived from RBCs.	Suitable in blood transfusion for giving a blood-source with a mismatched type of blood, or potentially a mismatched blood type to a recipient.	[109]
US10596197	Red blood cell membrane derived microparticles and their use for the treatment of lung diseases.	Treatment with RBCs-MPs to the lung through inhalational route promoted the expression of immune regulatory cytokines including IL-10 and reduced inflammatory responses and injury to the lungs.	Have remarkable potential as immuno-modulating agent for a number of lung disorders such as chronic-obstructive pulmonary disorder (COPD), bronchitis, acute lung injury, pulmonary fibrosis, etc.	[110]
US20170095510	Use of NPs coated with red blood cell membranes to treat hemolytic diseases and disorders.	Hemolytic diseases are auto-immune disorders caused by an attack of said mammal RBCs by said mammal's own body or in between pregnant mammal and fetus RBCs.	Invention will be employed in nano-engineering, molecular biology etc.	[111]

## 8. Recent Clinical Trials on Anticancer Drug-Loaded NERs

The comprehensive and detailed investigations on the RBC-mediated drug delivery strategy have grown rapidly and, currently, the research and development on these strategies have transformed and advanced to the pre-clinical and clinical phases. None of the anticancer drug loaded-RBC-technology has reached the market till now, however, few clinical trials on RBC-based technology have been conducted for dexamethasone-21-phosphate in ataxia telangiectasia, asparaginase in pancreatic cancer, lymphoblastic leukemia, thymidine phosphorylase in mitochondrial neuro-gastrointestinal encephalomyopathy and RTX-134 in phenylketonuria, etc., as reported [112]. A phase IIb open-label study on ER-encapsulated asparaginase (Eryaspase) in combination with chemotherapy in second-line advanced pancreatic adenocarcinoma [NCT02195180] is being carried out [113]. Eryaspase in combination with chemotherapy (gemcitabine) was associated with improvements in overall survival (OS) and progression-free survival (PFS), irrespective of asparagine synthetase (ASNS) expression in second-line advanced pancreatic adenocarcinoma. A Phase III trial is underway [114]. An open-label, randomized, multicentered, phase-III trial on Eryaspase in patients with pancreatic ductal adenocarcinoma and those who failed only one prior-line of systemic anticancer therapy for advanced stage of pancreatic cancer were also reported [NCT03665441] [115]. Another clinical trial on Eryaspase was a randomized phase II/III investigation by combining carboplatin and gemcitabine chemotherapy versus chemotherapy-alone as first-line treatment in metastatic or locally recurrent triple-negative breast cancer [NCT03674242] patients [116]. A clinical trial study on PEGylated-asparaginase-encapsulated in erythrocytes for patients with acute lymphoblastic leukemia (ALL) is also underway [NCT03267030] [117] as shown in Table 3.

**Table 3.** List of clinical trials available for asparaginase encapsulated in erythrocytes (Eryaspase).

Clinicaltrial.gov Identifier	NCT03674242	NCT03665441	NCT02195180	NCT03267030
Drug encapsulated in erythrocyte		Asparaginase encapsulated in erythrocytes (Eryaspase)		
Eryaspase combined with other anti-cancer drugs	Eryaspase combined with gemcitabine or carboplatin	Eryaspase combined with either gemcitabine plus abraxane, or irinotecan-based therapy	Eryaspase combined with gemcitabine or 5-fluorouracil/oxaliplatin/leucovorin (FOLFOX)	Eryaspase combined with GRASPA
Purpose	Treatment	Treatment	Treatment	Treatment
Cancer type	Triple negative breast cancer	Pancreatic adenocarcinoma	Progressive metastatic pancreatic carcinoma	Acute lymphoblastic leukemia
Recruitment status	Recruiting	Active, not recruiting	Completed	Completed
Sponsor	ERYtech Pharma	ERYtech Pharma	ERYtech Pharma	Birgitte Klug Albertsen
Study-type	Interventional	Interventional	Interventional	Interventional
No of participants	64	500	141	55
Allocation	Randomized	Randomized	Randomized	N/A
Intervention model	Parallel assignment	Parallel assignment	Parallel assignment	Single group assignment
Masking	Open label	Open label	Open label	Open label
Phase	Phase 2/3	Phase 3	Phase 2	Phase 2
Start of the study	June 2019	September 2018	July 2014	August 2017
Completion of the study	October 2020	October 2021	November 2017	October 2020

## 9. Conclusions

The NERs are the RBC-derived nanocarrier systems having extraordinary features among which the long blood circulation time, controlled release of drug over a long period of time, ability of escaping the immune system and targeted delivery of drugs to the site of action are the main features. These properties led to an extensive investigation on NERs and the results have shown promising potential for NERs to be developed as a novel, biomimetic and efficient drug delivery system for the effective and targeted delivery of drugs including anticancer drugs and others. In addition, NERs have also been studied as a powerful diagnostic tool for the diagnosis of various tumors. The encouraging findings of the in vitro and in vivo studies conducted on NERs further lead to the advancement to clinical trials stage and the efficacy and safety is being tested on human beings. However, the NERs still suffer from the disadvantages related to scalability and validation which is one of the limiting factors for its industrialization. Nevertheless, many studies are underway to utilize the NERs as a multifaceted drug delivery tool and it has shown substantial capabilities of being developed and applied for human use.

**Author Contributions:** Conceptualization, F.S. and S.J.; methodology, S.A.; A.S.; W.A.; M.H.S.; S.S.A. and M.K.; software, S.J. and A.S.; validation, F.S., S.A. and M.H.S.; formal analysis, W.A.;

investigation, A.S.; S.J.; F.S. and S.A.; resources, S.J.; data curation, S.J.; F.S. and A.S.; writing—original draft preparation, A.S.; writing—review and editing, F.S.; S.A.; A.S.; M.H.S.; M.K. and S.S.A.; visualization, S.A.; supervision, F.S.; project administration, F.S.; funding acquisition, S.A. All authors have read and agreed to the published version of the manuscript.

**Funding:** This work was funded by the Deanship of Scientific Research (DSR) at King Saud University, Riyadh, Saudi Arabia through research group project number RGP-1438-013. The APC was funded by DSR.

**Institutional Review Board Statement:** Not applicable.

**Informed Consent Statement:** Not applicable.

**Data Availability Statement:** This study did not report any data.

**Acknowledgments:** The authors are thankful to the Deanship of Scientific Research at King Saud University, Riyadh, Saudi Arabia for funding this work through research group project number RGP-1438-013.

**Conflicts of Interest:** The authors declare no conflict of interest.

## References

- Lutz, H.; Hu, S.; Dinh, P.-U.; Cheng, K. Cells and cell derivatives as drug carriers for targeted delivery. *Med. Drug Discov.* **2019**, *3*, 100014. [CrossRef]
- Han, X.; Wang, C.; Liu, Z. Red Blood Cells as Smart Delivery Systems. *Bioconjugate Chem.* **2018**, *29*, 852–860. [CrossRef] [PubMed]
- Sun, Y.; Su, J.; Liu, G.; Chen, J.; Zhang, X.; Zhang, R.; Jiang, M.; Qiu, M. Advances of blood cell-based drug delivery systems. *Eur. J. Pharm. Sci.* **2017**, *96*, 115–128. [CrossRef] [PubMed]
- Kharazi, A.Z.; Zargar, S.M.; Hafshejani, D.K.; Eskandarinia, A.; Rafienia, M. A review of controlled drug delivery systems based on cells and cell membranes. *J. Med. Signals Sensors* **2019**, *9*, 181–189. [CrossRef]
- Millán, C.G.; Gandarillas, C.I.C.; Marinero, M.L.S.; Lanao, J.M. Cell-based drug-delivery platforms. *Ther. Deliv.* **2012**, *3*, 25–41. [CrossRef]
- Pierige, F.; Serafini, S.; Rossi, L.; Magnani, M. Cell-based drug delivery. *Adv. Drug Deliv. Rev.* **2008**, *60*, 286–295. [CrossRef] [PubMed]
- Hamidi, M.; Tajerzadeh, H. Carrier Erythrocytes: An Overview. *Drug Deliv.* **2003**, *10*, 9–20. [CrossRef]
- Hamidi, M.; Zarrin, A.; Foroozesh, M.; Mohammadi-Samani, S. Applications of carrier erythrocytes in delivery of biopharmaceuticals. *J. Control Rel.* **2007**, *118*, 145–160. [CrossRef] [PubMed]
- Rossi, L.; Serafini, S.; Pierigé, F.; Antonelli, A.; Cerasi, A.; Fraternali, A.; Chiarantini, L.; Magnani, M. Erythrocyte-based drug delivery. *Expert Opin. Drug Deliv.* **2005**, *2*, 311–322. [CrossRef]
- Magnani, M.; Pierigé, F.; Rossi, L. Erythrocytes as a novel delivery vehicle for biologics: From enzymes to nucleic acid-based therapeutics. *Ther. Deliv.* **2012**, *3*, 405–414. [CrossRef]
- Zarrin, A.; Foroozesh, M.; Hamidi, M. Carrier erythrocytes: Recent advances, present status, current trends and future horizons. *Expert Opin. Drug Deliv.* **2014**, *11*, 433–447. [CrossRef] [PubMed]
- Hamidi, M.; Zarei, N.; Zarrin, A.; Mohammadi-Samani, S. Preparation and in vitro characterization of carrier erythrocytes for vaccine delivery. *Int. J. Pharm.* **2007**, *338*, 70–78. [CrossRef]
- Villa, C.H.; Anselmo, A.C.; Mitragotri, S.; Muzykantov, V. Red blood cells: Supercarriers for drugs, biologicals, and nanoparticles and inspiration for advanced delivery systems. *Adv. Drug Deliv. Rev.* **2016**, *106*, 88–103. [CrossRef]
- Millán, C.G.; Marinero, M.L.S.; Castañeda, A.Z.; Lanao, J.M. Drug, enzyme and peptide delivery using erythrocytes as carriers. *J. Control. Release* **2004**, *95*, 27–49. [CrossRef] [PubMed]
- Dmitrieva, L.A.; Pivovarov, Y.I.; Kurilskaya, T.E.; Sergeeva, A.S. Modern state of problem of delivery of medicines with use of erythrocytes as cell-carriers. *Patol. Fiziol. Eksperimental'naiia Ter.* **2016**, *60*, 88–94.
- Bourgeaux, V.; Lanao, J.M.; Bax, B.E.; Godfrin, Y. Drug-loaded erythrocytes: On the road toward marketing approval. *Drug Des. Dev. Ther.* **2016**, *10*, 665–676. [CrossRef] [PubMed]
- Kumar, A.; Verma, M.; Jha, K.K. Resealed erythrocytes as a carrier for drug targeting: A review. *Pharm. Innov.* **2012**, *1*, 8–16.
- Nangare, K.A.; Powar, S.D.; Payghan, S.A. Nanoerythrocytes: Engineered erythrocytes as a novel carrier for the targeted drug delivery. *Asian J. Pharm.* **2016**, *10*, S223–S233.
- Wadhwa, R.; Aggarwal, T.; Thapliyal, N.; Kumar, A.; Priya; Yadav, P.; Kumari, V.; Reddy, B.S.C.; Chandra, P.; Maurya, P.K. Red blood cells as an efficient in vitro model for evaluating the efficacy of metallic nanoparticles. *3 Biotech.* **2019**, *9*, E279. [CrossRef]
- Zhou, Y.; Wu, H.-H.; Ping, Y.; Gao, J.-Q. Fabrication of Cell-Derived Biomimetic Drug Delivery System. *Nanofabrication* **2019**, *5*, 1–18. [CrossRef]
- Dale, G.; Villacorte, D.; Beutler, E. High-yield entrapment of proteins into erythrocytes. *Biochem. Med.* **1977**, *18*, 220–225. [CrossRef]

22. Li, R.; He, Y.; Zhang, S.; Qin, J.; Wang, J. Cell membrane-based nanoparticles: A new biomimetic platform for tumor diagnosis and treatment. *Acta Pharm. Sin. B* **2018**, *8*, 14–22. [CrossRef] [PubMed]
23. Sushnitha, M.; Evangelopoulos, M.; Tasciotti, E.; Taraballi, F. Cell Membrane-Based Biomimetic Nanoparticles and the Immune System: Immunomodulatory Interactions to Therapeutic Applications. *Front. Bioeng. Biotechnol.* **2020**, *8*, 627. [CrossRef] [PubMed]
24. Gong, C.; Yu, X.; You, B.; Wu, Y.; Wang, R.; Han, L.; Wang, Y.; Gao, S.; Yuan, Y. Macrophage-cancer hybrid membrane-coated nanoparticles for targeting lung metastasis in breast cancer therapy. *J. Nanobiotechnology* **2020**, *18*, 1–17. [CrossRef] [PubMed]
25. Kuo, Y.C.; Wu, H.C.; Hoang, D.; Bentley, W.E.; D'Souza, W.D.; Raghavan, S.R. Colloidal properties of nanoerythrocytes derived from bovine red blood cells. *Langmuir* **2016**, *32*, 171–179. [CrossRef]
26. Vijayan, V.; Uthaman, S.; Park, I.-K. Cell Membrane Coated Nanoparticles: An Emerging Biomimetic Nanoplatform for Targeted Bioimaging and Therapy. *Adv. Exp. Med. Biol.* **2018**, *1064*, 45–59. [CrossRef]
27. Bhateria, M.; Rachumallu, R.; Singh, R.; Bhatta, R.S. Erythrocytes-based synthetic delivery systems: Transition from conventional to novel engineering strategies. *Expert Opin. Drug Deliv.* **2014**, *11*, 1219–1236. [CrossRef] [PubMed]
28. Poonia, N.; Kharb, R.; Lather, V.; Pandita, D. Nanostructured lipid carriers: Versatile oral delivery vehicle. *Futur. Sci. OA* **2016**, *2*, FSO135. [CrossRef]
29. Yao, Y.; Zang, Y.; Qu, J.; Tang, M.; Zhang, T. The toxicity of metallic nanoparticles on liver: The subcellular damages, mechanisms, and outcomes. *Int. J. Nanomed.* **2019**, *14*, 8787–8804. [CrossRef] [PubMed]
30. Esenaliev, R.O. Radiation and Nanoparticles for Enhancement of Drug Delivery in Solid Tumors. U.S. Patent 6165440, 26 December 2000.
31. Xue, X.; Liang, X.-J. Overcoming drug efflux-based multidrug resistance in cancer with nanotechnology. *Chin. J. Cancer* **2012**, *31*, 100–109. [CrossRef]
32. Lejeune, A.; Moorjani, M.; Gicquaud, C.; Lacroix, J.; Poyet, P.; Gaudreault, R. Nanoerythrocyte, a new derivative of erythrocyte ghost: Preparation and antineoplastic potential as drug carrier for daunorubicin. *Anticancer Res.* **1994**, *14*, 915–919. [PubMed]
33. Moorjani, M.; Lejeune, A.; Gicquaud, C.; Lacroix, J.; Poyet, P.; Gaudreault, R.C. Nanoerythrocytes, a new derivative of erythrocyte ghost II: Identification of the mechanism of action. *Anticancer Res.* **1996**, *16*, 2831–2836. [PubMed]
34. Lejeune, A.; Poyet, P.; Gaudreault, R.C.; Gicquaud, C. Nanoerythrocytes, a new derivative of erythrocyte ghost: III. Is phagocytosis involved in the mechanism of action? *Anticancer Res.* **1997**, *17*, 3599–3603. [PubMed]
35. Désilets, J.; Lejeune, A.; Mercer, J.; Gicquaud, C. Nanoerythrocytes, a new derivative of erythrocyte ghost: IV. Fate of reinjected nanoerythrocytes. *Anticancer Res.* **2001**, *21*, 1741–1747.
36. Chambers, E.; Mitragotri, S. Prolonged circulation of large polymeric nanoparticles by non-covalent adsorption on erythrocytes. *J. Control. Release* **2004**, *100*, 111–119. [CrossRef]
37. Chambers, E.; Mitragotri, S. Long circulating nanoparticles via adhesion on red blood cells: Mechanism and extended circulation. *Exp. Biol. Med.* **2007**, *232*, 958–966.
38. Hirlekar, R.S.; Patel, P.D.; Dand, N.; Kadam, V.J. Drug Loaded Erythrocytes: As Novel Drug Delivery System. *Curr. Pharm. Des.* **2008**, *14*, 63–70. [CrossRef]
39. Muzykantov, V.R. Drug delivery by red blood cells: Vascular carriers designed by mother nature. *Expert Opin. Drug Deliv.* **2010**, *7*, 403–427. [CrossRef]
40. Hu, C.M.J.; Zhang, L.; Aryal, S.; Cheung, C.; Fang, R.H.; Zhang, L. Erythrocyte membrane-camouflaged polymeric nanoparticles as a biomimetic delivery platform. *Proc. Nat. Acad. Sci. USA* **2011**, *108*, 10980–10985. [CrossRef] [PubMed]
41. Fang, R.H.; Hu, C.M.J.; Chen, K.N.H.; Luk, B.T.; Carpenter, C.W.; Gao, W.; Li, S.; Zhang, D.E.; Lu, W.; Zhang, L. Lipid-insertion enables targeting functionalization of erythrocyte membrane-cloaked nanoparticles. *Nanoscale* **2013**, *5*, 8884–8888. [CrossRef]
42. Wang, C.; Sun, X.; Cheng, L.; Yin, S.; Yang, G.; Li, Y.; Liu, Z. Multifunctional theranostic red blood cells for magnetic-field-enhanced in vivo combination therapy of cancer. *Adv. Mater.* **2014**, *26*, 4794–4802. [CrossRef] [PubMed]
43. Ren, H.; Liu, J.; Li, Y.; Wang, H.; Ge, S.; Yuan, A.; Hu, Y.; Wu, J. Oxygen self-enriched nanoparticles functionalized with erythrocyte membranes for long circulation and enhanced phototherapy. *Acta Biomater.* **2017**, *59*, 269–282. [CrossRef] [PubMed]
44. Dong, X.; Niu, Y.; Ding, Y.; Wang, Y.; Zhao, J.; Leng, W.; Qin, L. Formulation and Drug Loading Features of Nano-Erythrocytes. *Nanoscale Res. Lett.* **2017**, *12*, 202. [CrossRef]
45. Sun, D.; Chen, J.; Wang, Y.; Ji, H.; Peng, R.; Jin, L.; Wu, W. Advances in refunctionalization of erythrocyte-based nanomedicine for enhancing cancer-targeted drug delivery. *Theranostics* **2019**, *9*, 6885–6900. [CrossRef]
46. Malhotra, S.; Dumoga, S.; Sirohi, P.; Singh, N. Red Blood Cells-Derived Vesicles for Delivery of Lipophilic Drug Camptothecin. *ACS Appl. Mater. Interfaces* **2019**, *11*, 22141–22151. [CrossRef]
47. Alqahtani, S.A.; Harisa, G.I.; Badran, M.M.; Alghamdi, K.M.; Kumar, A.; Salem-Bekhit, M.M.; Ahmad, S.F.; Alanazi, F.K. Nanoerythrocyte membrane-chaperoned 5-fluorouracil liposomes as biomimetic delivery platforms to target hepatocellular carcinoma cell lines. *Artif. Cells, Nanomed. Biotechnol.* **2019**, *47*, 989–996. [CrossRef]
48. Han, X.; Shen, S.; Fan, Q.; Chen, G.; Archibong, E.; Dotti, G.; Liu, Z.; Gu, Z.; Wang, C. Red blood cell-derived nanoerythrocyte for antigen delivery with enhanced cancer immunotherapy. *Sci. Adv.* **2019**, *5*, eaaw6870. [CrossRef] [PubMed]
49. Deák, R.; Mihály, J.; Szigyártó, I.C.; Beke-Somfai, T.; Turiák, L.; Drahos, L.; Wacha, A.; Bóta, A.; Varga, Z. Nanoerythrocytes tailoring: Lipid induced protein scaffolding in ghost membrane derived vesicles. *Mater. Sci. Eng. C* **2020**, *109*, 110428. [CrossRef]
50. Buss, N.; Yasa, O.; Alapan, Y.; Akolpoglu, M.B.; Sitti, M. Nanoerythrocyte-functionalized biohybrid microswimmers. *APL Bioeng.* **2020**, *4*, 026103. [CrossRef] [PubMed]



51. Guo, Y.; Wang, D.; Song, Q.; Wu, T.; Zhuang, X.; Bao, Y.; Kong, M.; Qi, Y.; Tan, S.; Zhang, Z. Erythrocyte Membrane-Enveloped Polymeric Nanoparticles as Nanovaccine for Induction of Antitumor Immunity against Melanoma. *ACS Nano* **2015**, *9*, 6918–6933. [CrossRef] [PubMed]
52. Fu, Q.; Lv, P.; Chen, Z.; Ni, D.; Zhang, L.; Yue, H.; Yue, Z.; Wei, W.; Ma, G. Programmed co-delivery of paclitaxel and dox-orubicin boosted by camouflaging with erythrocyte membrane. *Nanoscale* **2015**, *7*, 4020–4030. [CrossRef]
53. Qi, H.; Liu, C.; Long, L.; Ren, Y.; Zhang, S.; Chang, X.; Qian, X.; Jia, H.; Zhao, J.; Sun, J.; et al. Blood Exosomes Endowed with Magnetic and Targeting Properties for Cancer Therapy. *ACS Nano* **2016**, *10*, 3323–3333. [CrossRef]
54. Sun, H.; Su, J.; Meng, Q.; Yin, Q.; Chen, L.; Gu, W.; Zhang, P.; Zhang, Z.; Yu, H.; Wang, S.; et al. Cancer-Cell-Biomimetic Nanoparticles for Targeted Therapy of Homotypic Tumors. *Adv. Mater.* **2016**, *28*, 9581–9588. [CrossRef]
55. Zhang, H. Erythrocytes in nanomedicine: An optimal blend of natural and synthetic materials. *Biomater. Sci.* **2016**, *4*, 1024–1031. [CrossRef] [PubMed]
56. Cheng, Q.F.; Qian, H.Q.; Zhang, D.H.; Huang, Y.; Sha, H.Z.; Liu, B.R. Evaluation for preparation and anticancer efficacy in vitro of drug-loaded nanoerythrocytes. *Zhongguo Zhong Yao Za Zhi* **2016**, *41*, 2093–2097.
57. Sahoo, K.; Karumuri, S.; Koralege, R.S.H.; Flynn, N.H.; Hartson, S.; Liu, J.; Ramsey, J.D.; Kalkan, A.K.; Pope, C.; Ranjan, A. Molecular and Biocompatibility Characterization of Red Blood Cell Membrane Targeted and Cell-Penetrating-Peptide-Modified Polymeric Nanoparticles. *Mol. Pharm.* **2017**, *14*, 2224–2235. [CrossRef] [PubMed]
58. Zhang, Z.; Qian, H.; Yang, M.; Li, R.; Hu, J.; Li, L.; Yu, L.; Liu, B.; Qian, X. Gambogic acid-loaded biomimetic nanoparticles in colorectal cancer treatment. *Int. J. Nanomed.* **2017**, *12*, 1593–1605. [CrossRef]
59. Sun, X.; Han, X.; Xu, L.; Gao, M.; Xu, J.; Yang, R.; Liu, Z. Surface-Engineering of Red Blood Cells as Artificial Antigen Presenting Cells Promising for Cancer Immunotherapy. *Small* **2017**, *13*, 1701864. [CrossRef]
60. Rao, L.; Meng, Q.F.; Bu, L.; Cai, B.; Huang, Q.; Sun, Z.J.; Zhang, W.F.; Li, A.; Shi-Guo, S.S.; Liu, W.; et al. Erythrocyte membrane-coated upconversion nanoparticles with minimal protein adsorption for enhanced tumor imaging. *ACS Appl. Mater. Interf.* **2017**, *9*, 2159–2168. [CrossRef]
61. Rao, L.; Cai, B.; Bu, L.-L.; Liao, Q.-Q.; Guo, S.-S.; Zhao, X.-Z.; Dong, W.-F.; Liu, W. Microfluidic Electroporation-Facilitated Synthesis of Erythrocyte Membrane-Coated Magnetic Nanoparticles for Enhanced Imaging-Guided Cancer Therapy. *ACS Nano* **2017**, *11*, 3496–3505. [CrossRef] [PubMed]
62. Narain, A.; Asawa, S.; Chhabria, V.; Patil-Sen, Y. Cell membrane coated nanoparticles: Next-generation therapeutics. *Nanomedicine* **2017**, *12*, 2677–2692. [CrossRef]
63. Wang, P.; Wang, X.; Luo, Q.; Li, Y.; Lin, X.; Fan, L.; Zhang, Y.; Liu, J.; Liu, X. Fabrication of Red Blood Cell-Based Multimodal Theranostic Probes for Second Near-Infrared Window Fluorescence Imaging-Guided Tumor Surgery and Photodynamic Therapy. *Theranostics* **2019**, *9*, 369–380. [CrossRef] [PubMed]
64. Wang, D.; Dong, H.; Li, M.; Cao, Y.; Yang, F.; Zhang, K.; Dai, W.; Wang, C.; Zhang, X. Erythrocyte-cancer hybrid membrane camouflaged hollow copper sulfide nanoparticles for prolonged circulation life and homotypic-targeting photothermal/chemotherapy of melanoma. *ACS Nano* **2018**, *12*, 5241–5252. [CrossRef] [PubMed]
65. Ye, S.; Wang, F.; Fan, Z.; Zhu, Q.; Tian, H.; Zhang, Y.; Jiang, B.; Hou, Z.; Li, Y.; Su, G. Light/pH-Triggered biomimetic red blood cell membranes camouflaged small molecular drug assemblies for imaging-guided combinational chemo-photothermal therapy. *ACS Appl. Mater. Interf.* **2019**, *11*, 15262–15275. [CrossRef]
66. Chen, H.; Sha, H.; Zhang, L.; Qian, H.; Chen, F.; Ding, N.; Ji, L.; Zhu, A.; Xu, Q.; Meng, F.; et al. Lipid insertion enables targeted functionalization of paclitaxel-loaded erythrocyte membrane nanosystem by tumor-penetrating bispecific recombinant protein. *Int. J. Nanomed.* **2018**, *13*, 5347–5359. [CrossRef]
67. Zhu, D.-M.; Wu, L.; Suo, M.; Gao, S.; Xie, W.; Zan, M.-H.; Liu, A.; Chen, B.; Wu, W.-T.; Ji, L.-W.; et al. Engineered red blood cells for capturing circulating tumor cells with high performance. *Nanoscale* **2018**, *10*, 6014–6023. [CrossRef] [PubMed]
68. Wang, Y.; Chen, X.; He, D.; Zhou, Y.; Qin, L. Surface-modified nanoerythrocyte loading DOX for targeted liver cancer chemotherapy. *Mol. Pharm.* **2018**, *15*, 5728–5740. [CrossRef]
69. Liu, W.; Ruan, M.; Wang, Y.; Song, R.; Ji, X.; Xu, J.; Dai, J.; Xue, W. Light-triggered biomimetic nanoerythrocyte for tumor-targeted lung metastatic combination therapy of malignant melanoma. *Small* **2018**, *14*, E1801754. [CrossRef] [PubMed]
70. Wang, Y.; Ji, X.; Ruan, M.; Liu, W.; Song, R.; Dai, J.; Xue, W. Worm-Like Biomimetic Nanoerythrocyte Carrying siRNA for Melanoma Gene Therapy. *Small* **2018**, *14*, e1803002. [CrossRef]
71. Villa, C.H.; Pan, D.C.; Zaitsev, S.; Cines, D.B.; Siegel, D.L.; Muzykantov, V.R. Delivery of drugs bound to erythrocytes: New avenues for an old intravascular carrier. *Ther. Deliv.* **2015**, *6*, 795–826. [CrossRef] [PubMed]
72. Sun, X.; Wang, C.; Gao, M.; Hu, A.; Liu, Z. Remotely Controlled Red Blood Cell Carriers for Cancer Targeting and Near-Infrared Light-Triggered Drug Release in Combined Photothermal-Chemotherapy. *Adv. Funct. Mater.* **2015**, *25*, 2386–2394. [CrossRef]
73. Luk, B.T.; Fang, R.H.; Hu, C.-M.J.; Copp, J.A.; Thamphiwatana, S.; Dehaini, D.; Gao, W.; Zhang, K.; Li, S.; Zhang, L. Safe and Immunocompatible Nanocarriers Cloaked in RBC Membranes for Drug Delivery to Treat Solid Tumors. *Theranostics* **2016**, *6*, 1004–1011. [CrossRef]
74. Liang, X.; Ye, X.; Wang, C.; Xing, C.; Miao, Q.; Xie, Z.; Chen, X.; Zhang, X.; Zhang, H.; Mei, L. Photothermal cancer immunotherapy by erythrocyte membrane-coated black phosphorus formulation. *J. Control Rel.* **2019**, *296*, 150–161. [CrossRef] [PubMed]

75. Li, J.; Huang, X.; Huang, R.; Jiang, J.; Wang, Y.; Zhang, J.; Jiang, H.; Xiang, X.; Chen, W.; Nie, X.; et al. Erythrocyte membrane camouflaged graphene oxide for tumor-targeted photothermal-chemotherapy. *Carbon* **2019**, *146*, 660–670. [CrossRef]
76. Jiang, Q.; Liu, Y.; Guo, R.; Yao, X.; Sung, S.; Pang, Z.; Yang, W. Erythrocyte-cancer hybrid membrane-camouflaged melanin nanoparticles for enhancing photothermal therapy efficacy in tumors. *Biomaterials* **2019**, *192*, 292–308. [CrossRef] [PubMed]
77. Fu, S.; Liang, M.; Wang, Y.; Cui, L.; Gao, C.; Chu, X.; Liu, Q.; Feng, Y.; Gong, W.; Yang, M.; et al. Dual-Modified Novel Biomimetic Nanocarriers Improve Targeting and Therapeutic Efficacy in Glioma. *ACS Appl. Mater. Interfaces* **2018**, *11*, 1841–1854. [CrossRef] [PubMed]
78. Chai, Z.; Ran, D.; Lu, L.; Zhan, C.; Ruan, H.; Hu, X.; Xie, C.; Jiang, K.; Li, J.; Zhou, J.; et al. Ligand-Modified Cell Membrane Enables the Targeted Delivery of Drug Nanocrystals to Glioma. *ACS Nano* **2019**, *13*, 5591–5601. [CrossRef]
79. Zelepukin, I.V.; Yaremenko, A.V.; Shipunova, V.O.; Babenyshev, A.V.; Balalaeva, I.V.; Nikitin, P.I.; Deyev, S.M.; Nikitin, M.P. Nanoparticle-based drug delivery via RBC-hitchhiking for the inhibition of lung metastases growth. *Nanoscale* **2019**, *11*, 1636–1646. [CrossRef]
80. Chu, Y.; Zhang, J.; Pan, H.; Shi, J.; Wang, J.; Chen, L. Preparation and evaluation of long circulating erythrocyte membrane-cloaked anti-cancer drug delivery system. *Drug Deliv. Transl. Res.* **2020**, *10*, 1278–1287. [CrossRef]
81. Zhong, P.; Chen, X.; Guo, R.; Chen, X.; Chen, Z.; Wei, C.; Li, Y.; Wang, W.; Zhou, Y.; Qin, L. Folic acid-modified nanoerythrocyte for codelivery of paclitaxel and tariquidar to overcome breast cancer multidrug resistance. *Mol. Pharm.* **2020**, *17*, 1114–1126. [CrossRef] [PubMed]
82. Cui, Y.; Sun, J.; Hao, W.; Chen, M.; Wang, Y.; Xu, F.; Gao, C. Dual-Target Peptide-Modified Erythrocyte Membrane-Enveloped PLGA Nanoparticles for the Treatment of Glioma. *Front. Oncol.* **2020**, *10*, 563938. [CrossRef]
83. Alqahtani, S.A.; Harisa, G.I.; Alomrani, A.H.; Alanazi, F.K.; Badran, M.M. Improved pharmacokinetic and biodistribution of 5-fluorouracil loaded biomimetic nanoerythrocytes decorated nanocarriers for liver cancer treatment. *Colloids Surf. B: Biointerfaces* **2021**, *197*, 111380. [CrossRef]
84. Fornasier, M.; Porcheddu, A.; Casu, A.; Raghavan, S.R.; Jönsson, P.; Schillén, K.; Murgia, S. Surface-modified nanoerythrocytes for potential optical imaging diagnostics. *J. Coll. Interf. Sci.* **2021**, *582*, 246–253. [CrossRef] [PubMed]
85. Rao, L.; Xu, J.-H.; Cai, B.; Liu, H.; Li, M.; Jia, Y.; Xiao, L.; Guo, S.-S.; Liu, W.; Zhao, X.-Z. Synthetic nanoparticles camouflaged with biomimetic erythrocyte membranes for reduced reticuloendothelial system uptake. *Nanotechnology* **2016**, *27*, 085106. [CrossRef] [PubMed]
86. Li, B.; Wang, F.; Gui, L.; He, Q.; Yao, Y.; Chen, H. The potential of biomimetic nanoparticles for tumor-targeted drug delivery. *Nanomedicine* **2018**, *13*, 2099–2118. [CrossRef]
87. Li, H.; Jin, K.; Luo, M.; Wang, X.; Zhu, X.; Liu, X.; Jiang, T.; Zhang, Q.; Wang, S.; Pang, Z. Size Dependency of Circulation and Biodistribution of Biomimetic Nanoparticles: Red Blood Cell Membrane-Coated Nanoparticles. *Cells* **2019**, *8*, 881. [CrossRef]
88. Xia, Q.; Zhang, Y.; Li, Z.; Hou, X.; Feng, N. Red blood cell membrane-camouflaged nanoparticles: A novel drug delivery system for antitumor application. *Acta Pharm. Sin. B* **2019**, *9*, 675–689. [CrossRef] [PubMed]
89. Agnihotri, J.; Jain, N.K. Biodegradable long circulating cellular carrier for antimalarial drug pyrimethamine. *Artif. Cells Nanomed. Biotechnol.* **2013**, *41*, 309–314. [CrossRef]
90. Agnihotri, J.; Saraf, S.; Singh, S.; Bigoniya, P. Development and evaluation of anti-malarial bio-conjugates: Artesunate-loaded nanoerythrocytes. *Drug Deliv. Transl. Res.* **2015**, *5*, 489–497. [CrossRef] [PubMed]
91. Wang, Y.; Zhang, K.; Qin, X.; Li, T.; Qiu, J.; Yin, T.; Huang, J.; McGinty, S.; Pontrelli, G.; Ren, J.; et al. Biomimetic Nanotherapies: Red Blood Cell Based Core-Shell Structured Nanocomplexes for Atherosclerosis Management. *Adv. Sci.* **2019**, *6*, 1900172. [CrossRef] [PubMed]
92. Gupta, N.; Patel, B.; Nahar, K.; Ahsan, F. Cell permeable peptide conjugated nanoerythrocytes of fasudil prolong pulmonary arterial vasodilation in PAH rats. *Eur. J. Pharm. Biopharm.* **2014**, *88*, 1046–1055. [CrossRef]
93. Gupta, N.; Patel, B.; Ahsan, F. Nano-Engineered Erythrocyte Ghosts as Inhalational Carriers for Delivery of Fasudil: Preparation and Characterization. *Pharm. Res.* **2014**, *31*, 1553–1565. [CrossRef] [PubMed]
94. Rahid, J.; Nahar, K.; Raut, S.; Keshavarz, A.; Ahsan, F. Fasudil and DETA NANOate, loaded in peptide-modified liposomal carrier, slow PAH progression upon pulmonary delivery. *Mol. Pharm.* **2018**, *15*, 1755–1765. [CrossRef] [PubMed]
95. Koleva, L.; Bovt, E.; Ataullakhanov, F.; Sinauridze, E. Erythrocytes as Carriers: From Drug Delivery to Biosensors. *Pharmaceutics* **2020**, *12*, 276. [CrossRef] [PubMed]
96. Zhu, R.; Avsiech, T.; Popov, A.; Bykov, A.; Meglinski, I. In vivo nano-biosensing element of red blood cell-mediated delivery. *Biosens. Bioelectron.* **2021**, *175*, 112845. [CrossRef]
97. López, S.C.B.; Meissner, K.E. Characterization of carrier erythrocytes for biosensing applications. *J. Biomed. Opt.* **2017**, *22*, 91510. [CrossRef] [PubMed]
98. Kim, Y.W.; Yoo, J.Y. Three-dimensional focusing of red blood cells in microchannel flows for bio-sensing applications. *Biosens. Bioelectron.* **2009**, *24*, 3677–3682. [CrossRef]
99. Milanick, M.A.; Ritter, S.; Meissner, K. Engineering erythrocytes to be erythrocytes: First steps. *Blood Cells Mol. Dis.* **2011**, *47*, 100–106. [CrossRef] [PubMed]
100. Ritter, S.C.; Milanick, M.A.; Meissner, K.E. Encapsulation of FITC to monitor extracellular pH: A step towards the development of red blood cells as circulating blood analyte biosensors. *Biomed. Opt. Express* **2011**, *2*, 2012–2021. [CrossRef] [PubMed]

101. Guo, X.; Zhang, Y.; Liu, J.; Yang, X.; Huang, J.; Li, L.; Wan, L.; Wang, K. Red blood cell membrane-mediated fusion of hydrophobic quantum dots with living cell membranes for cell imaging. *J. Mater. Chem. B* **2016**, *4*, 4191–4197. [CrossRef] [PubMed]
102. Gaudreault, R.C.; Claude, G.; Patrick, P. Nanoerythrocytes Bioactive Agent Carrier. U.S. Patent 5653999, 5 August 1997.
103. Joyce, T. Polyethyleneglycol Conjugated Nanoerythrocytes, Method of Making Same and Use Thereof. Patent No. WO1998011919A3, 4 June 1998.
104. Muzykantov, V.; Brener, J.; Myerson, J. Methods and Compositions for Drug Delivery. U.S. Patent 20180243440, 30 August 2018.
105. Hyde, R.A.; Ishikawa, M.Y.; Jung, E.K.Y.; William, G.; Langer, A.A.L.; Levien, E.C.; Tegreene, R.A.; Weaver, C.T.; Whitmer, T.A.; Wood, C., Jr.; et al. Biological Targeting Compositions and Methods of Using the Same. U.S. Patent 8211656, 7 March 2012.
106. Dmitri, S.; Guixin, S. Use of Human Erythrocytes for Prevention and Treatment of Cancer Dissemination and Growth. U.S. Patent 20130202625, 8 August 2013.
107. Ahn, B.C.; Son, S.H.; Prakash, G. Composition for Material Delivery, Including Exosome Mimetics Derived from red Blood Cells, and Use Thereof. U.S. Patent 20200138987, 7 May 2020.
108. Green, J.J.; Meyer, R.A.; Ben-Akiva, E. Biomimetic Anisotropic Polymeric Particles with Naturally Derived Cell Membranes for enhanced DRUG Delivery. U.S. Patent 20200289666, 17 September 2020.
109. Lee, T. Use of Nanoparticles Coated with red Blood Cell Membranes to Enable Blood Transfusion. U.S. Patent 20170367990, 8 October 2017.
110. Lee, J.S.; Corcoran, T.E.; Kagan, V. Red Blood Cell Membrane-Derived Microparticles and Their Use for the Treatment of Lung Disease. U.S. Patent 10004764, 27 September 2018.
111. Lee, T. Use of Nanoparticles Coated with Red Blood Cell Membranes to Treat Hemolytic Diseases and Disorders. U.S. Patent 20170095510, 6 April 2017.
112. Rossi, L.; Pierigè, F.; Aliano, M.P.; Magnani, M. Ongoing Developments and Clinical Progress in Drug-Loaded Red Blood Cell Technologies. *BioDrugs* **2020**, *34*, 265–272. [CrossRef] [PubMed]
113. Efficacy and Safety of L-Asparaginase Encapsulated in RBC Combined with Gemcitabine or FOLFOX in 2nd Line for Progressive Metastatic Pancreatic Carcinoma. NCT02195180. Available online: <https://clinicaltrials.gov/ct2/show/NCT02195180> (accessed on 20 January 2021).
114. Hammel, P.; Fabienne, P.; Mineur, L.; Metges, J.-P.; Andre, T.; De La Fouchardiere, C.; Louvet, C.; El Hajbi, F.; Faroux, R.; Guimbaud, R.; et al. Erythrocyte-encapsulated asparaginase (eryaspase) combined with chemotherapy in second-line treatment of advanced pancreatic cancer: An open-label, randomized Phase IIb trial. *Eur. J. Cancer* **2020**, *124*, 91–101. [CrossRef] [PubMed]
115. Study of Eryaspase in Combination with Chemotherapy Versus Chemotherapy Alone as 2nd-line Treatment in PAC (Trybeca-1). NCT03665441. Available online: <https://clinicaltrials.gov/ct2/show/NCT03665441> (accessed on 20 January 2021).
116. Study of Eryaspase in Combination with Chemotherapy Versus Chemotherapy Alone as 1st Line Treatment of TNBC (TRYbeCA-2). NCT03674242. Available online: <https://clinicaltrials.gov/ct2/show/NCT03674242> (accessed on 20 January 2021).
117. Asparaginase Encapsulated in Erythrocytes for Patients with All and Hypersensitivity to PEG-Asparaginase. NCT03267030. Available online: <https://clinicaltrials.gov/ct2/show/NCT03267030> (accessed on 20 January 2021).

Review

# Inorganic Nanoparticles Applied for Active Targeted Photodynamic Therapy of Breast Cancer

Hanieh Montaseri , Cherie Ann Kruger \*  and Heidi Abrahamse 

Laser Research Centre, Faculty of Health Sciences, University of Johannesburg, P.O. Box 17011, Doornfontein 2028, South Africa; montaseri.hanieh@gmail.com (H.M.); habrahamse@uj.ac.za (H.A.)  
\* Correspondence: cherier@uj.ac.za; Tel.: +27-11-559-6860

**Abstract:** Photodynamic therapy (PDT) is an alternative modality to conventional cancer treatment, whereby a specific wavelength of light is applied to a targeted tumor, which has either a photosensitizer or photochemotherapeutic agent localized within it. This light activates the photosensitizer in the presence of molecular oxygen to produce phototoxic species, which in turn obliterate cancer cells. The incidence rate of breast cancer (BC) is regularly growing among women, which are currently being treated with methods, such as chemotherapy, radiotherapy, and surgery. These conventional treatment methods are invasive and often produce unwanted side effects, whereas PDT is more specific and localized method of cancer treatment. The utilization of nanoparticles in PDT has shown great advantages compared to free photosensitizers in terms of solubility, early degradation, and biodistribution, as well as far more effective intercellular penetration and uptake in targeted cancer cells. This review gives an overview of the use of inorganic nanoparticles (NPs), including: gold, magnetic, carbon-based, ceramic, and up-conversion NPs, as well as quantum dots in PDT over the last 10 years (2009 to 2019), with a particular focus on the active targeting strategies for the PDT treatment of BC.

**Citation:** Montaseri, H.; Kruger, C.A.; Abrahamse, H. Inorganic Nanoparticles Applied for Active Targeted Photodynamic Therapy of Breast Cancer. *Pharmaceutics* **2021**, *13*, 296. <https://doi.org/10.3390/pharmaceutics13030296>

Academic Editor: Anna Angela Barba

Received: 26 January 2021

Accepted: 15 February 2021

Published: 24 February 2021

**Publisher's Note:** MDPI stays neutral with regard to jurisdictional claims in published maps and institutional affiliations.



**Copyright:** © 2021 by the authors. Licensee MDPI, Basel, Switzerland. This article is an open access article distributed under the terms and conditions of the Creative Commons Attribution (CC BY) license (<https://creativecommons.org/licenses/by/4.0/>).

**Keywords:** Breast cancer treatment; Photodynamic therapy; Inorganic nanoparticles; Active targeting

## 1. Introduction

Breast cancer (BC) is the most prevalent malignancy among women worldwide [1]. Cisplatin (cis-diammine-dichloroplatinum (II)) is currently an approved drug that can be utilized for the treatment of various cancers, since it inhibits DNA replication and chain elongation [1]. Although numerous anticancer drugs have been developed over the years for BC treatment, it still remains a therapeutic challenge; since BC can metastasize, become resistant to certain drugs, as well as exhibit lesions of recurrence after surgery [2]. More importantly, conventional anticancer drugs, when administered, spread throughout the body, and thus affect healthy cells and tissues, instead of just the localized tumor area, which requires treatment [3].

The effectiveness of photodynamic therapy (PDT) in ablating localized BC tumors, with limited side-effects is a significant breakthrough in unconventional treatments [4]. PDT can be performed as an adjuvant to other therapies, since it enables selective, as well as localized damage to tumors and their surrounding vasculature [4]. PDT is based on the activation of a nontoxic photosensitizer (PS) with an appropriate light to produce reactive oxygen species (ROS), which in turn eradicates cancer cells [4]. However, due to the hydrophobic nature of most PSs, they have high tendency to aggregate in aqueous solution, reducing the efficacy of PDT treatment [5]. In addition, PSs do not tend to bind to tumor cells selectively, resulting in poor specificity uptake in cancer cells and so localized normal tissues can become affected during treatment [6]. In this context, the combination of nanotechnology and PDT in the form of nanoplatforms is of great importance, whereby PSs are covalently or non-covalently bound to the nanoparticles (NPs) [6]. The selectivity of

the nano delivery agents can be also enhanced using active targeting, whereby antibodies and small ligands can be bound to NPs, and so allow for PSs to be specifically (as well as directly) delivered into targeted tumor cells [6]. Therefore, the aim of this review is to collate and discuss the types of inorganic NPs that have been used for the active (as well as targeted) delivery of PSs within PDT BC treatment.

## 2. Conventional Treatments of Breast Cancer

Chemotherapy, surgery, and radiotherapy are the main therapies utilized for small sized BC tumors [7]. Some other less invasive treatments, such as cryotherapy, laser ablation, and radiofrequency ablation (RFA), have also been developed for early stage BC [8,9]. In spite of promising developments in the treatment of early BC, surgery is generally the first option. Often, positive BC tumor margins can remain unresected, and so the possibility of reoccurrence is eminent. Thus, most often, patients require additional surgeries and chemotherapy treatments [10,11]. In this context, new (and far more effective) treatment modalities are sought after in order to mitigate the collateral damage, as well as improve the treatment outcomes of BC.

## 3. Photodynamic Therapy (PDT) and Photosensitizers (PSs)

PDT is an alternative non-invasive therapeutic technique for the treatment of various types of cancers and non-oncological diseases [4]. PDT is painless and its selectivity to cancer cells is well tolerated by patients [12]. It involves three main aspects: (1) a photo active compound or PS that accumulates in neoplastic cells; (2) local light to excite and activate the PS; as well as (3) surrounding tumor molecular oxygen [13]. When a PS becomes activated through illumination at an appropriate wavelength and it reacts with surrounding molecular oxygen, it produces reactive oxygen species (ROS) and singlet oxygen, which destroys localized tumor cells [13].

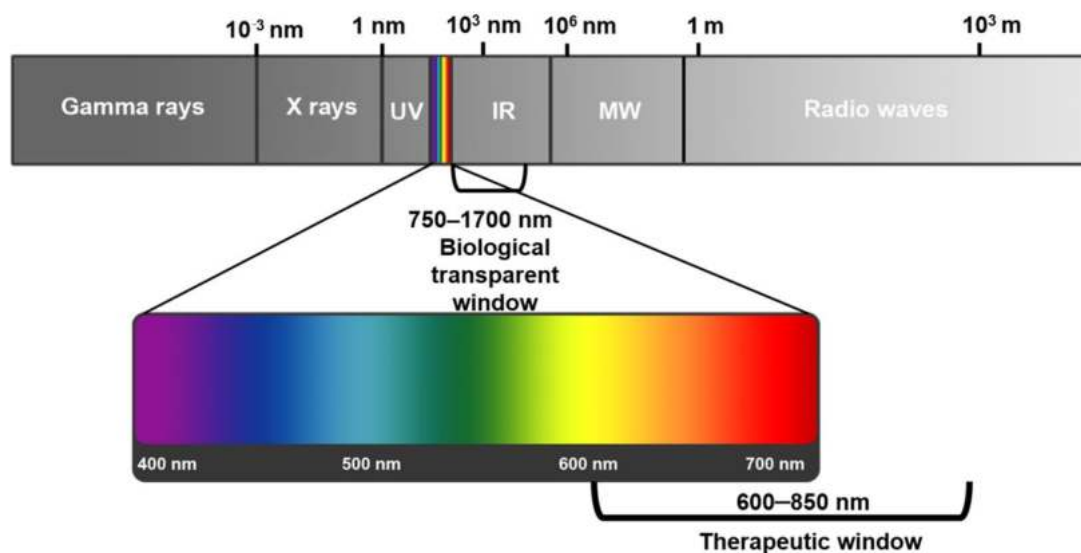
Among the broad spectrum of light, ultraviolet (UV) light (200–400 nm) may damage biological components, and so its biomedical applications are restrained, while visible light in the range of 400–650 nm can be utilized for activation of various PSs [13]. In addition, “biological transparent windows” in near infrared (NIR)-I (750–1000 nm) and NIR-II window (1000–1700 nm) enjoy low absorption and scattering, with deep tissue penetration and low auto-fluorescence from biological tissues, and so can be utilized for biophotonic imaging [14,15].

Tissue penetration depth of light can be sometimes limiting, which can affect the amount of PS activated, which in turn affects the amount of ROS and singlet oxygen produced to kill tumor cells [16]. Short wavelengths (<650 nm) generally have a lower penetration depth in tissues, while longer wavelength (above 850 nm) ranges are not sufficient enough to excited or activate PSs [16]. Thus, the most appropriate wavelength for PDT is between the range of 600 and 850 nm, which is known as the “phototherapeutic window” (Figure 1) [16].

The most effective PSs in PDT cancer applications are chemically pure and stable, as well as have minimal dark toxicity and side effects, with ideal hydrophilic properties [17]. Additionally, PSs should have strong absorption within the range of 600–850 nm, as to ensure, limited scattering, high tissue depth penetration, with maximum extinction coefficients [17].

Hematoporphyrin derivative (HpD) and photofrin are the first-generation commercial PSs, known for harsh PDT unwanted side effects [18]. While aminolevulinic acid (ALA), esterified derivatives of ALA and phthalocyanine compounds, which are considered second generation PSs, are known to produce minimal PDT side effects, with improved ROS generation, due to their longer absorption wavelengths, with improved tissue depth penetration [18]. Moreover, conjugation of second generation PSs to various biological carriers (such as nanoparticles) are referred to as third generation PSs, since these “carrier” conjugations generally allow PSs to selectively accumulate in cancer cells [19].

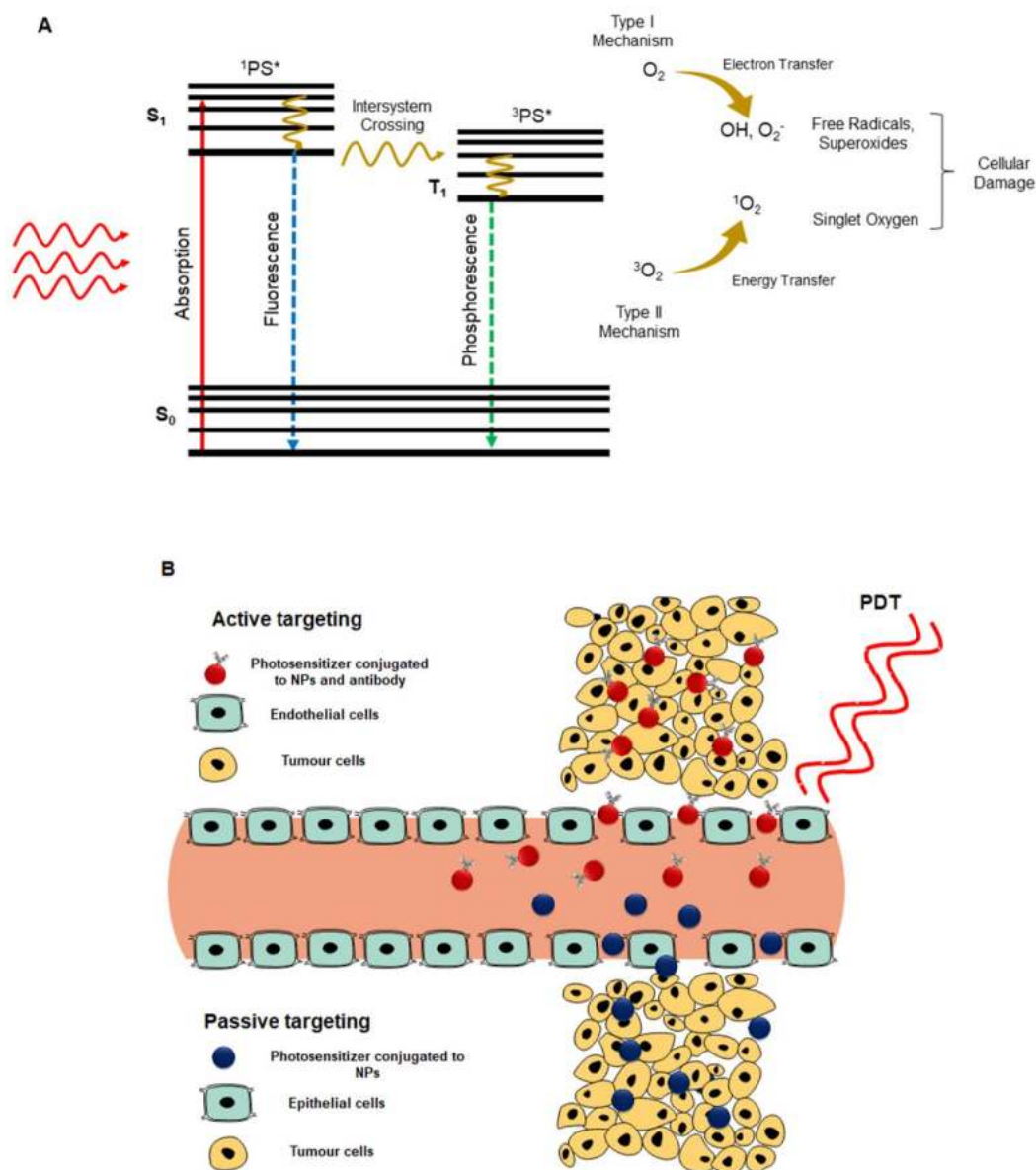
Thus, the activation wavelength, solubility, octanol/water partition coefficient, and molar extinction coefficient are of great importance for determining the potency of a PS in PDT. The main parameters of some PSs are compared in Table S1.



**Figure 1.** Electromagnetic spectrum showing the ideal phototherapeutic window for photodynamic therapy (PDT) treatment of cancer.

#### 4. Mechanisms of Photodynamic Therapy

There are two main PDT mechanisms, which occur in tumor cells, in the presence of molecular oxygen (Figure 2). Upon irradiation of a PS with a wavelength of light coinciding its absorption spectrum, the PS molecule becomes converted from a ground state to a singlet excited state [20]. The PS drug loses a part of its energy through fluorescence and the remainder is transferred and so the singlet state PS becomes excited to a triplet state. In a type I mechanism, the triplet excited state PS interacts with biomolecules from tumors surroundings to form radicals, which react with molecular oxygen to produce ROS, such as hydrogen peroxides, superoxide anion radicals, and hydroxyl radicals [20]. In the type II mechanism, the energy from an excited triple state PS is directly transferred to triplet state oxygen ( $^3\text{O}_2$ ) to form singlet oxygen ( $^1\text{O}_2$ ) (Figure 2A) [20]. Both ROS and  $^1\text{O}_2$  induce cancer tumor cell death via either apoptotic, necrotic, or autophagy cell death pathways, depending on the intracellular localization of a PS [21]. Apoptotic cell death is usually due to mitochondrial PS localization and damage, whereas necrotic cell death is mostly due to cell membrane damage and loss of integrity. Within autophagy cell death, usually the PS induces endoplasmic reticulum or lysosomes damage; however, this form of PDT induced tumor cell death is not favored since cells can recover [21].



**Figure 2.** (A) PDT mechanism of action, as well as (B) passive and active tumor photosensitizer (PS) targeting approaches to generate reactive oxygen species (ROS) and singlet oxygen for tumor destruction (PS\* indicates an excited state photosensitizer).

### 5. Passive and Active Targeting PS Uptake Strategies

PS subcellular localization uptake can be classified into either passive or specifically active targeting (Figure 2B). Passive PS uptake is encouraged via the permeability and retention (EPR) effect, which causes tumor tissues to present a leaky vasculature [22]. It is a natural occurring process, which utilizes the difference in anatomical and pathophysiological abnormalities of cancer tissue versus normal cells to improve PS passivation in tumor cells [22]. When nanoparticle carriers are bound to PS, they tend to promote the passive uptake of PSs via the EPR effect [22]. Active targeting requires the binding of specific targeting ligands, such as antibodies, peptides, aptamers, folic acid (FA), small ligands, or carbohydrates, onto the surface of PS-loaded nanocarrier systems, which are explicitly overexpressed only on cancer cell receptors; thus, PS uptake in these cells is specifically enhanced and actively internalized [22].

In comparison to passive targeting, nanoparticle active targeting most definitely does provide a more selective absorption of PS in tumor cells with improved PS concentration

accumulation; thus, higher accumulation of the nanocarrier and cellular concentration of the drug into the cells will take place [22,23].

## 6. Nanoparticle Delivery Systems for PDT

Drug delivery systems based on nanoparticles (NPs) are a promising approach in PDT to enhance PS absorption in cancer cells. A large surface to volume ratio of the NPs can promote the loading capacity of PSs and so improves concentration delivery and either passive or active uptake in cancer cells [24]. In addition, anchoring of PSs to NPs can improve either the stability and solubility, as well as reduce dark toxicity and enhance localized delivery, to improve PDT treatment outcomes and minimize unwanted side effects [24]. Moreover, the small size of NPs, not only assists PSs to accumulate in cancer cells via passive or active targeting, but also allows these nanocarrier to mimic biological molecules and, thus, easily pass through immune system barriers [25]. In relation to active targeting, PS nanocarriers are usually further functionalized with specific ligands, which are compatible to overexpressed tumor sites, to improve their biocompatibility and specific targeted absorption [26].

Various organic and inorganic NP carrier platforms have been developed over the years for improved PS uptake and enhanced PDT treatment of BC. In this current review, the utilization of actively targeted inorganic NPs for PDT of BC has been discussed over 10 years.

## 7. Types of Inorganic NPs Utilized for Active Breast Cancer Targeting PDT Treatments

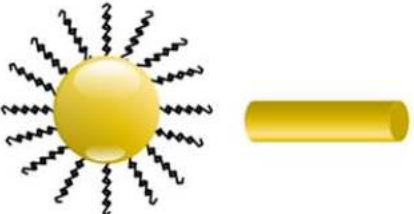

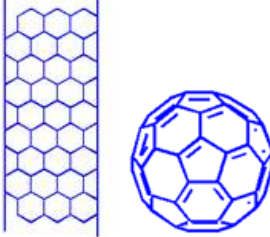


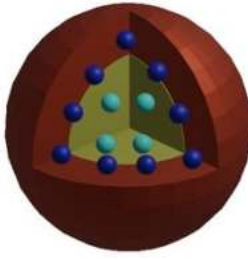
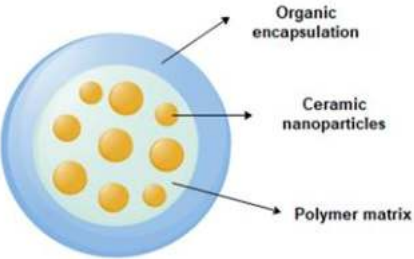
Inorganic NPs have great advantages over organic nanomaterials through their high stability, tunable size, and optical properties, as well as ease of surface functionalization to make them more biocompatible within biological applications [27,28]. Additionally, metallic and inorganic NPs have a lower degradation rate when compared to organic NPs [29]. The main characteristics of inorganic NPs have been summarized in Table 1.

### 7.1. Noble Metal Nanoparticles

Among various types of metallic NPs, gold NPs are ideal candidates for PS delivery into the body, due to their inertness, low toxicity, and limited side effects, as well as ease of synthesis and surface functionalization [30]. Furthermore, gold NPs are able to enhance the passive uptake of a PS-carrier system in tumor cells via the EPR effect [30,31]. Moreover, gold NPs possess a large surface area, which can be functionalized with a variety of ligands for active targeting [32]. Considering the high binding affinity of gold to thiol and amine groups, these NPs can be easily functionalized with antibodies, proteins, nucleic acids, and carbohydrates, which enable selective targeting and enhanced PS delivery in cancer tissues [33].



**Table 1.** Main properties and structures of inorganic nanoparticles (NPs).

Inorganic NPs	Properties	Structure	Reference
Gold NPs	High surface to volume ratio, easy functionalization with antibodies, suitable for passive and active targeting, near infrared absorption, localized surface plasmon resonance (LSPR) characteristics		[34]
Magnetic NPs	Selective destruction of cancer cells due to heat release, superparamagnetism, and high field irreversibility		[35]
Carbon-based NPs	High strength, electron affinity, water solubility, and biocompatibility		[36,37]
Quantum dots	Broad excitation and narrow emission spectra, with high quantum yields and photostability		[38]
Silica NPs	High biocompatibility and stability, with easy surface functionalization		[28]
Upconversion NPs	Used for the treatment of deep-seated tumors and exhibit lower phototoxicity		[28,39]
Ceramic NPs	Controlled release of drugs, easy incorporation of hydrophilic and hydrophobic drugs, with high loading capacity		[40]

Gold NPs can be employed for imaging contrast agents and radiosensitizers thanks to the high atomic number of gold [30]. Furthermore, since gold NPs have a high atomic number and optical properties of light absorbance within near infrared (NIR) wavelengths [14], they generate heat when exposed to NIR laser irradiation, through surface plasmon resonance effects, allowing them to induce hyperthermia in tumor cells and so assist in improving PDT treatment outcomes [30]. In addition, since gold NPs peak absorbance wavelength is within the visible range of 400–600 nm, NIR light is transmitted through normal cells with low absorption [41], resulting in hyperthermia induction in cancer cells, with very little damage to surrounding healthy cells [42]. Lastly, the surface plasmon resonance effect of gold NPs within the NIR region enhances singlet oxygen and ROS generation [28], and so they tend to improve the overall treatment effect of PDT [31].

Studies by Li et al. (2009) noted that the passive tumor uptake of gold PS nanoconjugates in BC cells could be enhanced by binding them to active targeting biomarkers [43]. With respect to active targeting, a novel 4-component anti HER-2 antibody–zinc–phthalocyanine derivative–polyethylene glycol–gold NP conjugates were prepared for the *in vitro* PDT treatment of SK-BR-3 (BC cells with HER-2 receptors), MDA-MB-231 (BC cells without the receptor overexpression), and normal breast cells (MCF-10A) [44]. The study noted that the binding of the antibody to the gold PS nanoconjugate did not have an effect on the rate of singlet oxygen production and fluorescence microscopy demonstrated higher BC cellular uptake in SK-BR-3 cells, due to active HER-2 receptor targeting [44]. Within PDT treatments using 633 nm laser irradiation, the gold PS antibody nanoconjugate induced 40% cell death in SK-BR-3 cells, whereas MDA-MB-231 only noted 25%, and normal MCF-10A reported 7% cell death [44]. These findings suggested that active antibody receptor targeting enhanced the delivery of the PS in BC, which has over expressed HER-2 receptors, and so significantly improved the overall treatment outcomes of PDT [44].

In a similar study, gold NPs were stabilized with hydrophobic zinc phthalocyanine PS (C11Pc) and hydrophilic polyethylene glycol (PEG) for the PDT treatment of SK-BR-3 BC [45]. The C11Pc-PEG gold NPs were then further functionalized with jacalin (a lectin specific for cancer-associated Thomsen–Friedenreich (T) carbohydrate antigen) or with monoclonal antibodies specific for the human epidermal growth factor receptor-2 (HER-2) [45]. The study revealed that the NP conjugates were more specifically internalized within the acidic organelles SK-BR-3 BC cells [45]. Within PDT treatments under 633 nm irradiation, both jacalin and antibody conjugates at C11Pc equivalent concentrations of 1  $\mu$ M and 1.15  $\mu$ M, showed 99% cell death [45]. However, antibody-conjugates note the main advantages of limited PS dark toxicity, when compared to the jacalin-conjugates in SK-BR-3 BC cells, since prior to irradiation, antibody-conjugates reported a 58.9–70.2% viability, whereas jacalin-conjugates noted 85.5–98.5% [45].

Relating to the PDT effect of zinc phthalocyanine PSs on BC cells, gold NPs were functionalized with two substituted zinc (II) phthalocyanine PSs, with differing carbon chain lengths (C3Pc or C11Pc), a lactose derivative for stabilization, and a BC galectin-1 targeting agent [32]. These functionalized NPs–PSs were utilized to evaluate *in vitro* PDT efficiency of two breast adenocarcinoma cell lines namely, SK-BR-3 and MDA-MB-231 [32]. The conducted studies showed that the galectin-1 receptors overexpressed on the surface of MDA-MB-231 cells could only be targeted via the lactose-C3Pc-AuNPs, whereas the lactose-C11Pc-AuNPs in SK-BR-3 cells reported no active galectin-1 targeting. Furthermore, post-PDT (at 633 nm) no internalization and cell death was observed in MDA-MB-231 cells treated with lactose-C11Pc-AuNPs. Whereas, the lactose-C3Pc-AuNPs reported significant galectin-1 receptor targeting in both BC cell lines and noted far higher cytotoxicity in comparison to the C11Pc PS [32].

The PDT effect of gold NPs prepared via biphasic and monophasic approaches on SK-BR-3 *in vitro* cultured human BC cells was further elaborated by Penon et al. (2017) [46]. The gold NPs were further functionalized with a porphyrin derivative and PEG (PR-AuNP-PEG) synthesized using two different protocols [46]. The monophasic method reported more porphyrin derivative attached ligands per NP and higher singlet oxygen

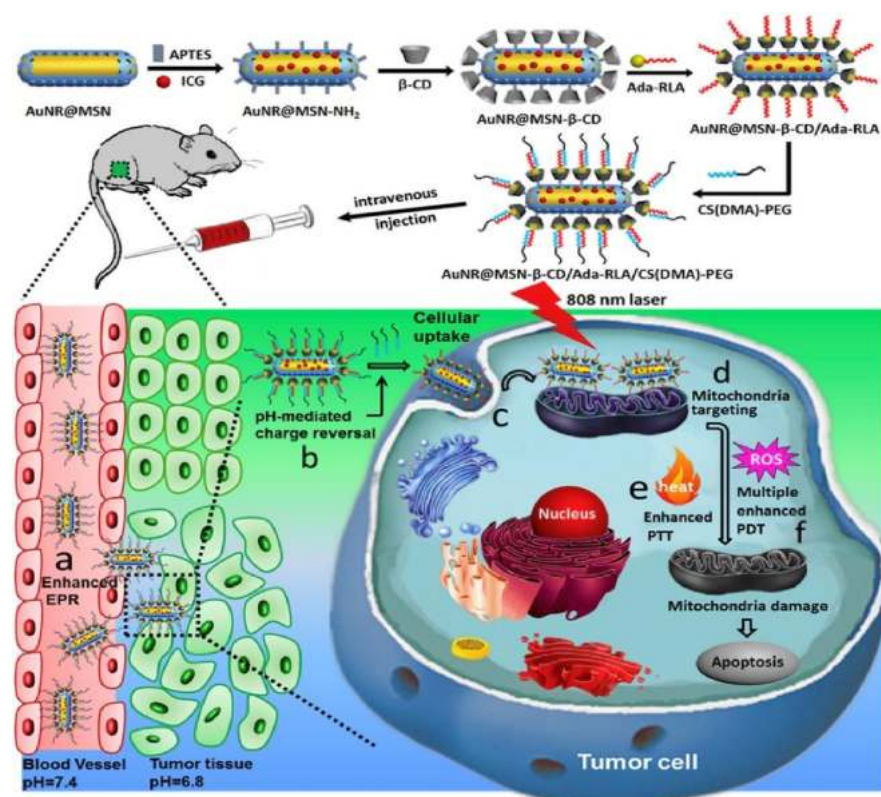
species yields than when compared to the biphasic nanoconjugates [46]. The researchers then covalently linked an anti-erbB2 antibody (PR-AuNP-PEG-Ab) to the monophasic PR-AuNP-PEG nanoconjugates, to target the overexpressed erbB2 receptors on the surface of SK-BR-3 BC cells [46]. Overall, the study noted higher cellular PR PS targeted uptake in BC cells when compared to normal cells, suggesting it had solubilized the PS, with significant cellular damage after 495 nm laser irradiation PDT treatment [46].

In other studies, gold nanostars have showed promising characteristics for Raman diagnostics. Since gold nanostars have tunable plasmon bands in the NIR tissue optical window, as well as multiple sharp branches, these act as “hot-spots” and so are capable of the surface-enhanced Raman scattering (SERS) effect [47]. Inspired by the unique SERS properties of gold nanostars, Fales et al. (2013) proposed the utilization of these nanostars for the Raman imaging and PDT treatment of BT-549 BC cells [48]. The nanotheranostic system comprised of a Raman-labelled gold nanostar, protoporphyrin IX (PpIX) PS, and a cell-penetrating peptide (CPP) known as transactivator of transcription (TAT) to enhance PS intercellular accumulation of the nanoplatform [48]. The gold nanostars were also coated with PEG and silica shells to enhance particle stability and PS-loading capacity [48]. Raman imaging results noted that the nanoplatform actively accumulated in the BC cells, due to the overexpression presence of TAT peptides [47]. The PDT treatment of BT-549 BC cells with 0.1 nM nanoconjugate and 633 nm irradiation revealed a higher photocytotoxicity and cell death, when compared to the 0.1 nM PpIX-loaded NP platforms without TAT [48].

The application of gold nanomaterials has been further developed to gold nanorod applications for successful BC active targeting PDT treatments. The enhanced active uptake of gold nanorods within in vitro cultured MCF-7 BC cells was found when gold nanorods were conjugated with anti-HER-2 antibodies [49]. Dube et al. (2018) reported that the conjugation of a complex of glycosylated zinc phthalocyanine to gold nanorods (AuNRs) could improve triplet, singlet, and fluorescence quantum yields, more than gold nanospheres (AuNSs), in PDT applications [50]. PDT results at 680 nm noted that less than 50% viable MCF-7 cells were found at a concentration of  $\geq 40$   $\mu\text{g}/\text{mL}$  complex-AuNRs, while this same result was only achievable at a concentration of  $\geq 80$   $\mu\text{g}/\text{mL}$  complex-AuNSs, suggesting that AuNRs improve PS uptake and PDT outcomes at far lower concentrations [50].

A nanoplatform of AuNR@MSN-RLA/CS(DMA)-PEG was also proposed for the combinational PDT/photothermal therapy (PTT) of MCF-7 breast cancer [51]. Gold nanorods were coated with mesoporous silica (AuNR@MSN) and  $\beta$ -cyclodextrin ( $\beta$ -CD), as well as loaded with Indocyanine green (ICG) [51]. The nanoplatform was then grafted with an Ada modified RLA peptide ([RLARLAR]<sub>2</sub>), to enhance plasma membrane permeability and mitochondria-targeting capacity to form AuNR@MSN-ICG-  $\beta$ -CD/Ada-RLA [51]. Then 2,3-dimethylmaleic anhydride (DMA)-modified chitosan oligosaccharide-block-poly (ethylene glycol) polymer (CS(DMA)-PEG) was coated onto the surface of AuNR@MSN-ICG-  $\beta$ -CD/Ada-RLA to serve as a charge-switchable and anti-fouling layer (Figure 3) [51]. Within in vitro MCF-7 BC cytotoxicity assays, the nanoconjugate showed no obvious toxicity prior to laser irradiation [51]. MCF-7 cells treated with AuNR@MSN-ICG-  $\beta$ -CD/Ada-RLA/CS(DMA)-PEG at pH 6.8 displayed a higher inhibition and cellular uptake when compared to AuNR@MSN-ICG, suggesting that CS(DMA)-PEG coating protected the nanoplatform from hydrolysis, and so promoted cancer cell uptake [51]. Moreover, the weak acidity microenvironment of cancer cells could reverse the charge of the AuNR@MSN-ICG-  $\beta$ -CD/Ada-RLA/CS(DMA)-PEG nanoplatform, promoting mitochondrial targeting and overall improved ROS generation [51]. When MCF-7 BC cells were treated with the nanoconjugate and 808 nm NIR laser irradiation, the AuNR@MSN-ICG-  $\beta$ -CD/Ada-RLA/CS(DMA)-PEG complex noted the highest PDT and PTT inhibition relative to control groups, due to its overall stability and superior ROS, which was mediated by the plasmonic photothermal effects and local electric field of the DMA AuNR [51]. In vivo investigations within xenograft nude mouse models noted a higher tumor temperature in mice treated with AuNR@MSN-ICG-  $\beta$ -CD/Ada-RLA/CS(DMA)-PEG than when compared to those

treated with AuNR@MSN-ICG, suggesting the DMA coated nanoconjugates were far more superior at treating BS in combination with PDT and PTT therapy [51].



**Figure 3.** Schematic representation of multifunctional nanoplatform AuNR@MSN and its in vivo process. Reprinted with permission from reference [51] Copyright 2018 Elsevier.

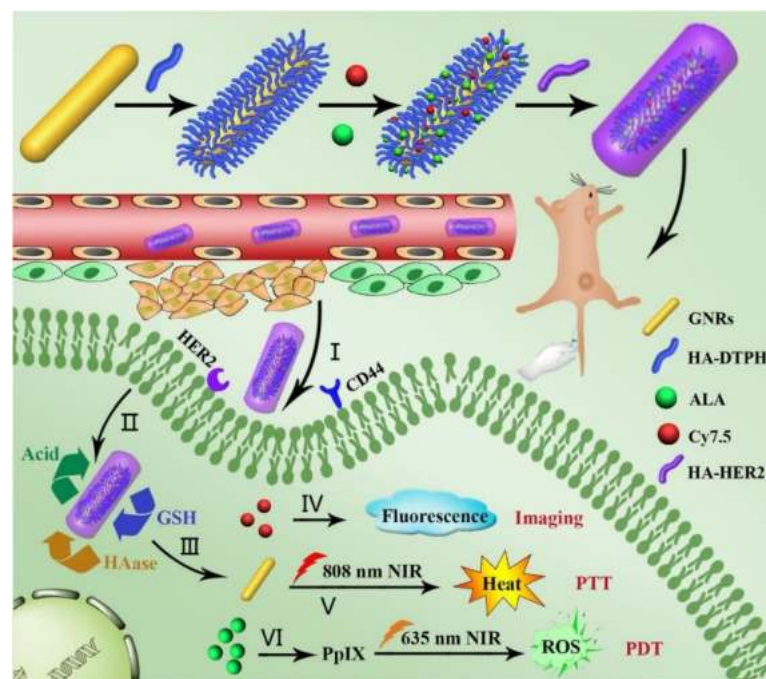
A chlorine e6 PS based (Ce6)-AuNR@SiO<sub>2</sub>-d-CPP nanoconjugate template was developed by synthesizing gold nanorods and passivating PEGylated mesoporous SiO<sub>2</sub> onto the gold NPs surface core to entrap the Ce6 PS [52]. Then, a D-type cell penetrating peptide (d-CPP) was linked to the gold nano shell to direct active PS targeting of the nanocarrier towards human BC MCF-7 cells [52]. Free Ce6, AuNR@SiO<sub>2</sub>-mPEG, and Ce6-AuNR@SiO<sub>2</sub>-d-CPP showed no dark cytotoxicity within in vitro cultured BC cells. The combinative PDT (650 nm)/PTT (808 nm) therapy results on BC cultured cells noted that Ce6-AuNR@SiO<sub>2</sub>-d-CPP provided the highest treatment outcomes and caused almost complete cell death [52]. The injection of Ce6-AuNR@SiO<sub>2</sub>-d-CPP into a nude mouse BC xenografts and exposure to PTT/PDT combinational therapy noted a significant decrease in tumor weight sizes [52].

Dendrimer-encapsulated NPs (DENs) were first reported in 1998, whereby metal ions were encapsulated within dendrimers, and to reduce them to produce zerovalent DENs [37]. DENs are synthetic polar macromolecules consisting of branches that emanate from a core that has functional groups of neutral, positive, or negative charges [53]. They are monodisperse NPs, which have lower toxicity in cells, a high surface reactivity, as well as allow for slow release and, thus, report a great accumulation in tumor cells, making them suitable for various drug delivery enhancement applications [54]. Poly(propyleneimine) (PPI) and poly(amidoamine) (PAMAM) dendrimers are some examples of DENs [55].

In this regard, one study evaluated the applicability of multiple particles delivery complexes (MPDC) for the PDT treatment of MCF-7 BC cell, using 680 nm laser irradiation [56]. The MPDC was comprised of gold NP encapsulated dendrimers (AuDENPs) and a sulfonated zinc-phthalocyanine mix (ZnPc<sub>mix</sub>) [56]. The morphology of the PDT AuDENPs-ZnPc<sub>mix</sub> treated BC cells noted an altered appearance from epithelial-like to irregular and a 59% of apoptotic cell death was found, in comparison to control groups [56].

In addition, a decrease in the polarized mitochondrial membranes of the BC cells and an increase in the depolarized cell membranes were observed after PDT treatment, with an increase in caspase 3/7 activity and cytotoxicity being found [56].

Recently, a multi-stimuli-responsive theranostic nanoplatform for the fluorescence imaging-guided PDT/PTT dual-therapy of MCF-7 BC cells was proposed [57]. The nanoplatform was based on functionalizing AuNRs with hyaluronic acid (HA), and subsequently conjugating anti-HER-2 antibody, 5-aminolevulinic acid (ALA) and Cy7.5 onto the HA, to enhance active PDT targeting and fluorescence imaging respectively (Figure 4) [57]. Cellular uptake efficiency of AuNR-HA<sup>-ALA/Cy7.5</sup>-HER-2 noted a significantly improved uptake of 75.5% in MCF-7 cells when compared to control groups, which received AuNR-HA<sup>-ALA/Cy7.5</sup> of 36%, suggesting the nanoplatform improved PS uptake via the specific HER-2 receptor mediated dual-targeting strategy [57]. Furthermore, AuNR-HA<sup>-ALA/Cy7.5</sup>-HER-2 single treated PDT MCF-7 cells at 635 nm reported a 75.6% decrease in cell viability, and cells treated with singular PTT at 808 nm noted a 58.4% decrease in cell viability [57]. Overall, a combinative PDT/PTT modality at a 5.5 µg/mL ALA concentration with the AuNR-HA<sup>-ALA/Cy7.5</sup>-HER-2 nanoplatform noted a significant 61.2% cell death [57]. Within in vivo studies on BC-induced mice, this dual treatment modality showed a rapid decrease in tumor sizes 20-days post treatment [57].



**Figure 4.** Schematic illustration for preparing GNR-HA<sup>-ALA/Cy7.5</sup>-HER2 with triple-responsive drug release and its application for HER2/CD44 dual-targeted and fluorescence imaging-guided combined PDT/ photothermal therapy (PTT) treatment of breast cancer. Reprinted with permission from reference [57]. Copyright 2019 Elsevier.

NP drug carriers are sometimes easily recognized and cleared from the body via the mononuclear-phagocyte system (MPS); thus, the surface of NPs drug carriers are generally coated with PEG to act as a shield, and so reduce this biological clearance [58]. However, some studies have noted that upon second administration of PEGylated NP drug carriers the human body can sometimes become stimulated to produce anti-PEG antibodies, resulting in the unwanted rapid clearance of the PEGylated NP, decreasing overall drug uptake in tumor cells [58–60]. In order to alleviate the rapid clearance of NPs via MPS, researchers have focused on red blood cells (RBCs), since they are a natural long-circulation delivery vehicle, which do not interfere or impact on the functionality of NPs [61–63].

In a study, cationized gold nanoclusters (CAuNCs) with various initial sizes of 150, 200, and 300 nm were constructed and coated with HA (CAuNCs@HA) [58]. In order to increase the circulation of the CAuNCs@HA nanoclusters, an RBC membrane was attached to its surface forming mCAuNCs@HA [58]. The mCAuNCs@HA nanoclusters were then loaded with a pheophorbide A (PheoA) PS, which is a ROS-responsive prodrug paclitaxel dimer (PXTK) and an anti-PD-L1 peptide dPPA forming pPP-mCAuNCs@HA [58]. This combinative PDT, chemotherapy and immunotherapy treatment approach was investigated within in vitro cultured 4T1 BC cells [58]. The study confirmed that the RBC membrane improved the overall PS in vitro cellular uptake in 4T1 cells, which was found to be a 2.02-, 1.55-, and 1.95-fold higher uptake for NP-300, NP-200, and NP-150 nm pPP-mCAuNCs@HA, respectively, when compared to uncoated groups [58]. The study also demonstrated that the 650 nm laser irradiation PDT induced late apoptosis with pPP-mCAuNCs@HA was a 2.41-fold higher than when compared to pPP-mCAuNCs@HA without irradiation [58]. The anti-tumor therapeutic effects within in vivo 4T1 tumor bearing female mice treated with pPP-mCAuNCs@HA and irradiation was 2.47-fold higher than when compared to groups injected with pPP-mCAuNCs@HA without irradiation [58].

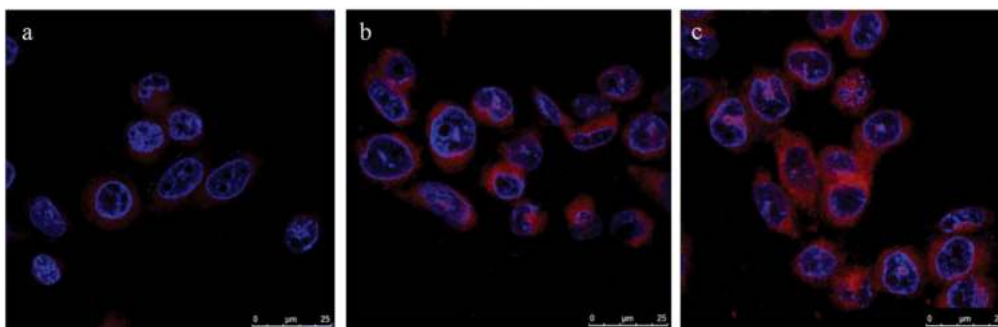
The successful applications of gold NPs in BC PDT active targeting treatments within in vitro and in vivo studies have led to more clinical applications [64]. In spite of the fact that gold NPs are inert for bio-tissues and are an alternative platform for PS delivery in PDT BC treatment studies, particular care must be exercised within clinical studies to noted their long-term toxicity and biodistribution, as some tend to have a limited clearance in the spleen and liver; however, this phenomenon is highly dependent on the different shape, size, and surface charge of AuNP [64].

## 7.2. Magnetic Nanoparticles

Magnetic NPs (MNPs) have drawn tremendous attention within in vivo and in vitro biomedical uses, because of their high field irreversibility, small size, and surface functionality [35,65]. Within in vitro studies, MNPs have been employed in magnetorelaxometry, diagnostic separation, and selection applications, whilst within therapeutic studies they have been utilized to induce hyperthermia and promote active drug-targeting, as well as assist in diagnostic applications, such as nuclear magnetic resonance imaging (NMR) [66].

Narsireddy et al. (2014) fabricated chitosan coated Fe<sub>3</sub>O<sub>4</sub> NPs, which were deposited with gold NPs followed by lipoic acid conjugation [67]. A 5,10,15,20-tetrakis(4-hydroxyphenyl)-21H,23H-porphyrin PS was also attached onto the surface of gold NPs to form Fe<sub>3</sub>O<sub>4</sub>-Au-LA-PS (MGPS) [67]. In order to improve targeting of this nanoconjugate, human epidermal growth factor receptor specific peptide (Affibody HER-2) was anchored onto its chitosan coat forming Aff-MGPS [67]. The PDT effects of Aff-MGPS were then investigate within in vitro cultured SK-OV-3 BC cells, which are HER-2 positive [67]. The cellular uptake efficiency of the targeted Aff-MGPS was far more superior than when compared to free PS or NPs controls alone (Figure 5) [67]. In addition, no dark toxicity was observed for MGPS or Aff-MGPS nanoplatforms, while free PS noted high dark toxicity [67]. Furthermore, the Aff-MGPS nanoplatforms noted improved targeted peptide uptake in BC cells when compared to group controls [67]. The targeted PDT specific delivery of Aff-MGPS was further assessed in nude SK-OV-3 BC induced tumor mice, in comparison to MGPS treatment alone at 120 J/cm<sup>2</sup>, and tumor volumes in mice grew slower in Aff-MGPS PDT treated mice than when compared to MGPS irradiation treatment alone, suggesting Affibody HER-2 enhanced BC PDT targeted treatment outcomes [67].

The photodynamic anticancer activities of magnetic Fe<sub>3</sub>O<sub>4</sub> NPs on BC was further investigated through the conjugation of Ce6 and FA onto its surface to form Fe<sub>3</sub>O<sub>4</sub>-Ce6-FA [68]. The synthesized nanoconjugate could effectively produce <sup>1</sup>O<sub>2</sub> and ROS, with no dark toxicity being found [68]. Within PDT Fe<sub>3</sub>O<sub>4</sub>-Ce6-FA 660 nm experiments, MCF-7 in vitro BC cells reported a concentration-dependent manner decrease in viability, and increased apoptotic cell death pathway activation via caspase 3/7, with notable nuclear fragmentation and plasma membrane translocation [68].



**Figure 5.** Cellular uptake of (a) free PS, (b)  $\text{Fe}_3\text{O}_4$ -Au-LA-PS (MGPS) and (c) Affibody-MGPS by SK-OV-3 cells. Reprinted with permission from reference [67]. Copyright 2014 Elsevier.

Within a study conducted by Matlou et al. (2018) the aim was to assess the PDT activity of two zinc phthalocyanine (Pc) derivatives: Zn mono cinnamic acid phthalocyanine and zinc mono carboxyphenoxy phthalocyanine complexes, which were covalently linked to a FA targeting agent and an amino functionalized  $\text{Fe}_2\text{O}_3$  MNP (AMNPs) [69]. The dark toxicity of this MNP PS carrier noted a significant decrease after attachment of the FA complex [69]. The *in vitro* MCF-7 PDT effect of Pc-AMNPs noted a significant 60% cell death under 670 nm irradiation, when compared to Pc-FA, which only reported a 40% cell death [69].

$\text{Fe}_3\text{O}_4$  and  $\text{Fe}_2\text{O}_3$  NPs are supermagnetic [70], and so release a significant amount of heat upon external exposure to laser irradiation and, thus, these NPs are highly effective in combinative PTT and PDT applications to destroy cancer cells [71]. Furthermore, when these magnetic NPs are PEGylating or bound to other polymers, their rapid clearance from the MPS can be alleviated [72]. However, PDT applications with MNPs cannot be taken lightly, as free  $\text{Fe}^{2+}$  may react with oxygen or hydrogen peroxide to form  $\text{Fe}^{3+}$  and hydroxyl radicals, which are toxic and can damage DNA; thus, the confirmation of the stability of these NP as PS carriers is crucial [70].

Even though only a few studies have been performed using MNPs for the active PDT treatment of BC, their superparamagnetic PTT hyperthermia properties have been demonstrated as a powerful and efficient approach in clinical trials of unresectable tumors or cancers representing terminal illness [73]. Furthermore, MNPs can be utilized in multiple therapeutic and diagnostic strategies [73], as well as eradicating apoptosis resistant cancer cells, since they generate heat intracellularly within the lysosomes and the tumor stroma, and so can obliterate tumor cells completely via necrotic cell death [74,75]. Thus, further studies and investigations utilizing MNPs for the effective treatment of BC is an ongoing need.

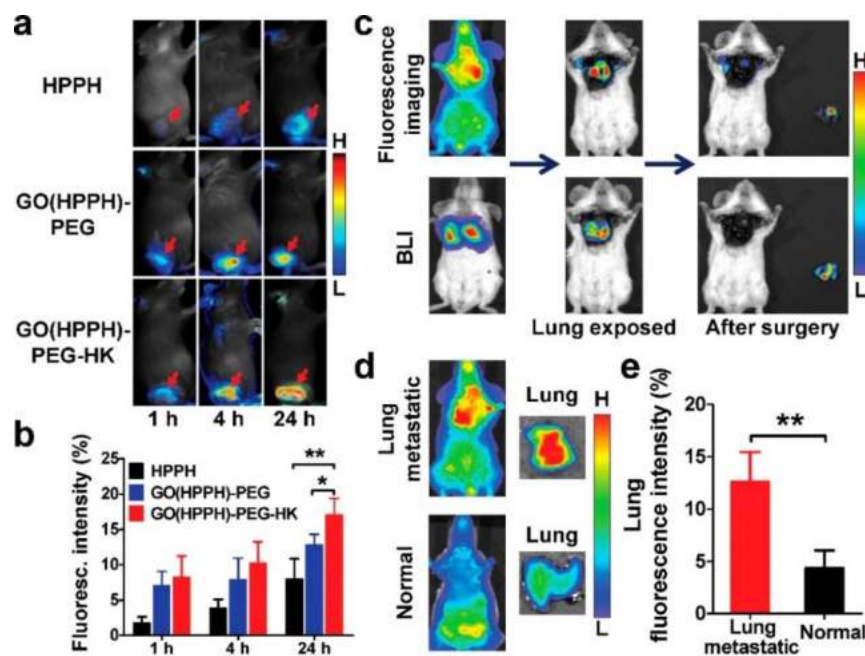
### 7.3. Carbon-Based Nanoparticles

Fullerene, carbon nanotubes, and graphene are carbon nanomaterials, which are commonly utilized as PS nanocarriers in PDT applications [76–78]. When PSs are attached via covalent or non-covalent bonding to functionalized carbon-based nanomaterials, they often provide improved solubility and biocompatibility in PDT treatments [36]. Fullerenes are carbon-based nanomaterials, which present in the forms of tubes, ellipsoids, or spheres, and successfully produce ROS upon irradiation exposure at an appropriate wavelength [28]. Single walled or multi-walled carbon nanotubes are other types of PS nanocarriers used in PDT cancer treatments [28]. Since carbon nanotubes present advantageous characteristics, such as fast elimination, low cytotoxicity, ease of functionalization, and reliable internalization through endocytosis, it makes them ideal PS nanocarriers in PDT [28]. Regarding graphene nanomaterials, due to their large surface areas they offer high therapeutic loading capacities for enhanced PS uptake in tumor cells [79].

In studies performed by Shi et al. (2014), fullerene-iron oxide NPs (IONP) were synthesized and functionalized with PEG, Ce6, and FA (C60-IONP-PEG-FA) for the active

tumor targeting [80]. The performance of these multifunctional NPs was studied for their PDT effect, radiofrequency thermal therapy (RTT), and magnetic targeting, within *in vitro* MCF-7 BC cells and *in vivo* BC mice models [80]. Individual *in vitro* PDT assays at concentration of 16  $\mu\text{g}/\text{mL}$  C60-IONP-PEG-FA and 532 nm laser irradiation, 31.3% viability was reported, and individual RTT therapy at the same concentration with 13.56 MHz radiofrequency noted a 36.9% of viable cells [80]. In combinational C60-IONP-PEG-FA RTT, followed by PDT, *in vitro* assays reported a significant 18.8% of cells only being found to be viable [80]. Within *in vivo* studies on S180 BC tumor-bearing mice, individual PDT and PTT applications induced 62% and 37% of apoptosis, respectively, and the integration both treatments could enhance apoptotic cell death to 96% [80].

By taking advantage of the ultra-high loading capacity of graphene oxide (GO) through  $\pi$ - $\pi$  stacking and hydrophobic interactions [81], GO(HPPH)-PEG-HK was prepared by functionalizing it with PEG-GO, so that a HK peptide (which binds specifically to integrin  $\alpha\text{v}\beta\text{6}$  on BC tumors) could be linked to it [82]. This actively functionalized nanoconjugate was then coated with a Photochlor (2-[1-hexyloxyethyl]-2-devinyl pyropheophorbide- $\alpha$ , HPPH) PS [83]. The large surface area of GO enabled conjugation of multiple HK peptides and high concentrations of HPPH, allowing for improved *in vivo* PDT treatment outcomes of BC [83]. Within *in vivo* 4T1 BC tumor mouse models, results reported that GO(HPPH)-PEG-HK under 671 nm laser irradiation that tumor growths remarkably decreased in comparison to control groups [83]. Furthermore, studies went on to note that remarkable increases in the CD40<sup>+</sup> and CD70<sup>+</sup> fractions in treated mice after PDT treatment with GO(HPPH)-PEG-HK induced dendritic cell maturation and so promoted anti-tumor immunity in the 4T1 tumor model (Figure 6) [83]. Thus, this actively functionalized nanoconjugate via PDT application could reduce *in vivo* BC tumor sizes, as well as trigger host anti-tumor immunity, to cause the inhibition of metastasis and further tumor growth [83].



**Figure 6.** (a) Optical images of 4T1 tumor-bearing BALB/c mice, (b) quantitative analysis uptake by 4T1 tumors after injection of HPPH, GO(HPPH)-PEG, or GO(HPPH)-PEG-HK, (c) *In vivo* optical imaging and BLI of 4T1-fLuc tumor-bearing BALB/c mice after injection of GO(HPPH)-PEG-HK. (d,e) Optical images and quantitative analysis of lung uptake of GO(HPPH)-PEG-HK by 4T1-fLuc tumor-bearing and normal BALB/c mice at 24 h post-injection. Reprinted with permission from reference [83]. Copyright 2017 American Chemical Society. \*  $p < 0.05$ , \*\*  $p < 0.01$ .



Overall, very few studies have been conducted using carbon-based nanomaterials for the active PDT targeting of BC. However, from the above studies, it can be seen that the combination of the synergistic effects of carbon-based NPs with PSs can improve the efficacy of BC PDT treatment [76]. It is worth mentioning that fullerene cages, such as C60 [84] and carbon nanotubes [85], can act alone as PSs in PDT applications and so self-generate ROS from photons owing to their  $\pi$  bond electrons [86]. Thus, fullerene derivatives alone are competitive PSs for in vivo PDT or preclinical treatment [87], since no additional PS is required to generate ROS and, thus, should be researched further for BC treatment [76]. Despite all of the idealistic properties carbon nanotubes have, they sometimes can induce asbestos-like inflammation [73], which is a carcinogenic, and so their individual toxicity needs to be fully investigated and understood [88].

#### 7.4. Semiconductor Quantum Dots (QDs)

Quantum dots are a subclass of fluorescent nanomaterials, which have unique chemical and physical properties compared to organic dyes [89]. They have been utilized as multifunctional nanocarriers for PDT thanks to their high quantum yields, simple surface modification, and tunable optical properties [90]. They are also excellent donors in fluorescence resonance energy transfer (FRET) applications [91]. To date, no studies have been investigated relating to the application of active targeted QDs for the PDT treatment of BC.

Studies by Monroe et al. (2019) only performed a spectrophotometric assay in order to assess the cellular uptake, cytotoxicity, and ROS generation of graphene QDs (GQDs) associated with methylene blue (MB) PS against in vitro cultured MCF-7 BC cells [92]. This study reported that MB improved cytotoxicity and ROS generation when compared to a 1:1 GQD:MB ratio [92].

In another study, Zn(II) phthalocyanines (ZnPcs) with different substitutes were fabricated and conjugated to GQDs to investigate the in vitro PDT activity of Pc-GQDs conjugates in a human BC in vitro MCF-7 cell line [93]. The conjugate and Pcs alone did not report dark toxicity and in vitro PDT studies noted that Pc-GQDs conjugates enhanced treatment outcomes when compared to Pcs administration alone [93].

The above QD-based BC PDT studies have paved a new avenue for researchers to synthesize various targeted-QDs against breast cancer. It has been reported that QDs have potential cytotoxicity under UV irradiation to act as efficient PSs [90]. Furthermore, NIR fluorescent QDs provide improved PS water solubility, chemical stability, and low optical interference with biological tissues in PDT cancer treatments, when compared to small molecule-based PSs administered alone [94]. Additionally, the large surface area of QDs also enables the conjugation of multiple PSs and ligands for targeted photodynamic imaging [90]. Nevertheless, one of the most controversial problems with QD-based PDT is the high toxicity they possess, since most consist of toxic heavy metals, such as cadmium ions, and so they tend to be under investigated [90,95]. In order to alleviate some of these issues cadmium free QDs, such as zinc and indium based QDs [96], substituted with other elements, such as silicon or carbon [97], or their incorporation into polymeric NPs [98] have been proposed to enhance their application in diagnostic applications and PDT cancer clinical trials [99]. Overall, it is envisaged that QDs, particularly GQDs, will open the door to a multitude of new opportunities for PDT treatment of BC, and through continued research, they could subsequently be able to provide high biocompatibility and improved PS solubility in biological media, with less unwanted toxic effects.

#### 7.5. Ceramic Nanoparticles

Ceramics NPs are inorganic solids made up oxides, carbides, carbonates, and phosphates, and have properties that range between metals and non-metals [40]. Silica (SiO<sub>2</sub>), titanium oxide (TiO<sub>2</sub>), alumina (Al<sub>2</sub>O<sub>3</sub>), zirconia (ZrO<sub>2</sub>), calcium carbonate (CaCO<sub>3</sub>), and hydroxyapatite (HA) are some examples of ceramic NPs with porous characteristics that can be fabricated to control the release of drugs [40]. The main features of ceramic NPs are high loading capacity, stability, and chemical inertness, as well as heat resistance and

ease of conjugation to either hydrophilic or hydrophobic drugs [29], making them highly advantageous for drug delivery, imaging, photodegradation of dyes, and photocatalysis applications [37,40,100].

#### 7.5.1. Silica Nanoparticles

Silica is an oxide of silicon and one of the most efficient materials for controlled drug delivery, since it can store and be controlled to gradually release therapeutic drugs [40]. Mesoporous silica nanoparticles (MSNs) are formed by polymerizing silica, and so have distinctive properties, such as tunable pore size (allowing for a high therapeutic drug loading capacity capacities) [101], large surface area to volumes, automatic release of drugs, as well as ease of functionalization with various functional groups or ligands, offering actively targeted drug delivery capabilities [40]. Thus, within PDT applications, PSs can be easily covalently linked or encapsulated onto the surface of silica NPs for favorable cancer treatment outcomes [28].

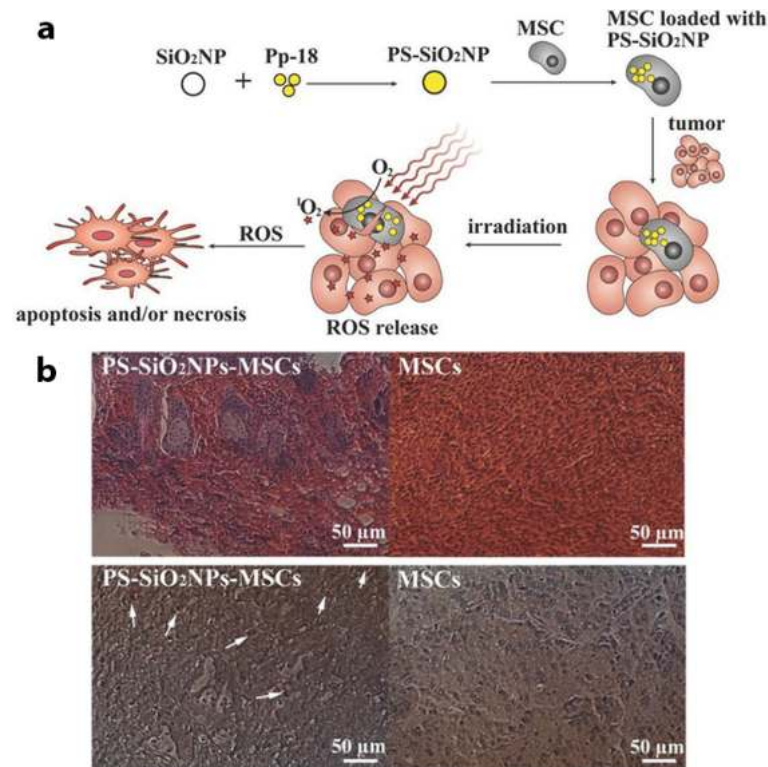
A nanosystem comprised of mesoporous silica NPs (MSN) with covalent anchoring of a synthesized anionic porphyrin PS and BC targeting mannose was presented by Brevet et al. (2009) [102]. The study confirmed that PS mannose-functionalized NPs within in vitro cultured MDA-MB-231 BC cells improved the efficiency of PDT relative to the non-functionalized NPs, since it induced 99% cell death when irradiated at 630–680 nm with 6 mW/cm<sup>2</sup>, while non irradiated control groups only noted 19% cell death [102].

Another promising nanoconjugate PS depended on a two-photon absorption, which integrated a two-photon excitation (TPE) with silica nanotechnology [103,104]. Conventional PSs require the absorption of a single photon equal to the band-gap energy of a PSs [105]. However, when a PS absorbs two lower energy photons of infrared light, TPE can occur and the sum of the photon energies are equal to the band-gap of energy, leading to a deeper light penetration and lower photo-bleaching of the actual PS [105–109]. Furthermore, in a TPE, the nonlinearity of photon absorption allows a PS activation to occur at the focal point of a laser beam, and so allows for greater spatial control of PS activation in three-dimensional (3D) tumor models, decreasing off-target phototoxicity in surrounding healthy tissues [110,111].

With respect to the TPE–PDT, a porphyrin functionalized porous silica NP (pSiNP) was coupled to a mannose targeting moiety to investigate the imaging and PDT potentials within in vitro cultured MCF-7 BC cells [112]. When compared to other two-photon absorbing nanoparticles such as, CdSe quantum dots, gold nanorods, or carbon dots, pSiNPs appear to be biodegradable in vivo [113], since their silicon components degrade to silicic acid, which can quickly be eliminated by kidneys [112,113]. The authors of this showed that the pSiNP with mannose moieties were able to actively accumulate in MCF-7 BC cells, with far higher PDT efficacy, since phototoxicity results noted a 2.3-fold better outcome for two photon PDT at 800 nm than when compared to one-photon excitation at 650 nm [112].

Within studies performed by Cao et al. (2014), in order to enhance PS accumulation in BC cells, it was proposed to use mesenchymal stem cells (MSCs) to directly deliver a PS to in vitro cultured MCF-7 cells [114]. The application of MSCs in PDT cancer treatments seems promising, as various studies have demonstrated that they have a naturally high tumor affinity within in vivo tumors, they can be easily isolated from bone marrow and modified to carry desired drugs, as well as be efficiently implanted into patients to avoid immune system clearance [115–118]. In this study, porous hollow silica NPs were conjugated to a purpurin-18 PS (PS-SiO<sub>2</sub>NPs) and then they were loaded into the MSCs cells (PS-SiO<sub>2</sub>NPs-MSCs) for in vivo PDT studies in MCF-7 modified mouse models (Figure 7a) [114]. Results noted that the BC tumor affinity of the MSCs was not inhibited by loading PS-SiO<sub>2</sub>NPs into the MSCs, and that intercellular ROS generation proportionally increased with PS-SiO<sub>2</sub>NPs-MSCs conjugation upon laser irradiation, suggesting the in vivo BC tumors retained the PS [114]. In addition, within PDT studies, the in vivo groups that received PS-SiO<sub>2</sub> NPs-MSCs reported far greater tumor growth inhibition than

when compared to control groups, which received unmodified MSCs without loading PS-SiO<sub>2</sub>NPs, suggesting that the MSCs cells were capable of high PS BC tumor affinity targeting (Figure 7b) [114].



**Figure 7.** (a) PDT treatment of cancer cell using PS-loaded SiO<sub>2</sub>NPs into MSCs, (b) In vivo PDT treatment on tumors one day after co-injection of MCF-7 cancer cells and MSCs with (group 1: PS-SiO<sub>2</sub>NPs-MSCs group) or without (group 2: control MSCs group) PS-SiO<sub>2</sub>NPs loaded. Reprinted with permission from reference [114]. Copyright 2014 Wiley Online Library.

Studies by Bharathiraja et al. (2017) reported that silica NPs decorated with Ce6 and FA (silica-Ce6-FA) could accumulate far higher within in vitro cultured MDA-MB-231 BC cells, when compared to free Ce6 [119]. Even though the level of ROS generated by silica-Ce6-FA nanoconjugate was moderately lower than when compared to free Ce6, at 680 nm PDT, the study showed that due to the folate receptor targeting in the nanoconjugate, the PS uptake in BC cells was improved, and so higher cell death was observed than when compared to free Ce6 administration alone [119].

Although, NIR light within the range of 630–800 nm is employed as an excitation PDT source to treat deep-seated cancer tissues [120], most clinically approved PSs have a low absorption in NIR region, and so their overall penetration depth is less than 1 cm [121]. Thus, researchers have also begun to investigate X-ray sources for use in X-ray-mediated PDT (X-PDT), since they are able to penetrate far deeper into tissues, which perhaps better outcomes [112]. Within these applications PSs need a system to convert X-rays into UV-visible photons, since they cannot absorb X-ray photons directly [112]. Scintillating nanoparticles or nanoscintillators, such as lanthanide doped rare-earth nanoparticles [122], have emerged as energy transducer for this conversion and deep seated X-PDT treatment [123–125].

Studies by Sengar et al. (2018) investigated X-PDT for the deep penetration of BC tumors [126]. They synthesized Y<sub>2.99</sub>Pr<sub>0.01</sub>Al<sub>5</sub>O<sub>12</sub>-based (YP) mesoporous silica (MS) coated NPs and functionalized them with PpIX and FA (YPMS@PpIX@FA) for the X-PDT treatment of BC cells with overexpressed folate receptors (*Folr 1*) [126]. The utilized BC in vitro cell lines were PyMT-R221A mouse BC cells (which have high levels of folate receptors), as well as 4T1 BC cells (which have low folate expression) [126]. PyMT-R221A mouse BC

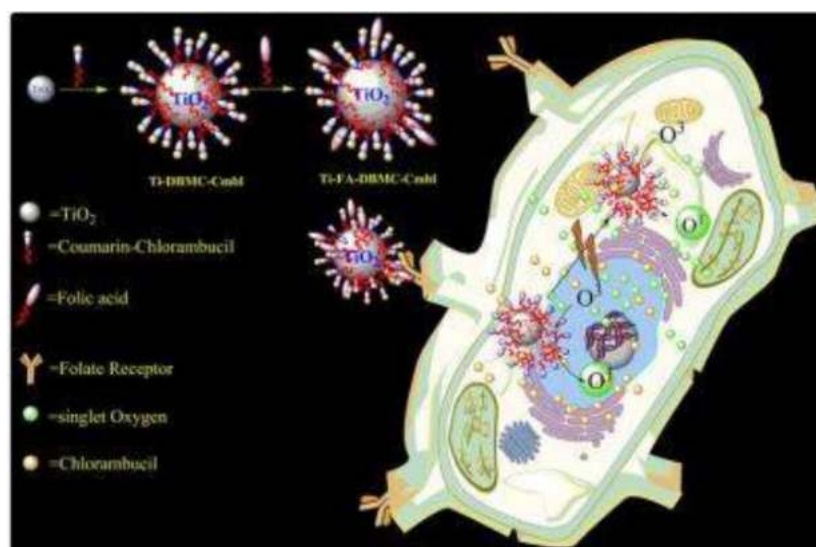
cells reported higher cellular uptake of YPMS@PpIX@FA when compared to 4T1 BC cells, revealing that FA targeting of this nanoconjugate was functional [126]. Additionally, non-activated YPMS@PpIX@FA reported a low cytotoxicity when used at concentrations below 25 µg/ml, while upon light activation at 365 nm, a remarkable decrease in PyMT-R221A mouse BC cells was observed [126]. Lastly, administration of YPMS@PpIX@FA suspension at a single dose of up to 125 mg/kg did not cause the death or any detectable behavior in inoculated CD1 mice [126].

Overall, it can be observed from the above in vitro and in vivo studies that silica NPs seem very promising for the PDT treatment of BC, and due to their non-toxicity and rapid renal clearance, the move forward of these studies into clinical applications is pertinent.

### 7.5.2. Titanium Oxide Nanoparticles

Titanium dioxide (TiO<sub>2</sub>), also called titania, is another type of ceramic NP, which possesses chemical and biological inertness, photostability, photoactivity, and high stability within biomedical applications [127]. More importantly, the strong oxidizing and reducing ability TiO<sub>2</sub> has when photoexcited with irradiation at <390 nm can produce ROS, which consequently induces apoptotic cell death in BC cells [128].

Studies by Gangopadhyay et al. (2015), constructed TiO<sub>2</sub> NPs and decorated them with a 7,8-dihydroxy coumarin PS chromophore and chlorambucil (Ti-DBMC-CmbI NPs) and FA (Ti-FA-DBMC-CmbI NPs) to serve as a chemotherapeutic drug and phototrigger, respectfully in PDT/chemotherapy treatments of in vitro cultured MDA-MB BC cells (Figure 8) [129]. After 60 min of PDT laser irradiation at ≥410 nm, cells treated with Ti-DBMC-CmbI NPs noted a 35% cell viability, whereas cell treated with Ti-FA-DBMC-CmbI NPs reported a mere 19% cell viability and more significant apoptotic cell death [129]. Overall, results revealed that the synergic effect of both targeted PDT and well known chemotherapeutic drug chlorambucil was successful for the eradication of MDA-MB BC cells [129].



**Figure 8.** PDT and chemotherapeutic effects of Ti-FA-DBMC-CmbI NPs on MDA-MB BC cells. Reprinted with permission from reference [129]. Copyright 2015 Royal Chemical Society.

In general, ceramic NPs show great potential in carrying PSs in PDT application to targeted BC tumors, due to their excellent chemical inertness and high heat resistance. However, since limited studies have been performed using ceramic NPs in BC, it is constructive to highlight that a suitable method in relation to their synthesis to control size, porosity, surface area to volume ratio, should be fine-tuned in order to allow for a high PS pay loading capacity and reduce any possible unwanted biological clearance issues [129].

### 7.6. Other Inorganic Nanoparticles

Cerium oxide NPs (or nanoceria/ceria NPs) are considered from a lanthanide metal oxide that can be used as an ultraviolet absorber [130]. They have antioxidant properties at a physiological pH, while their oxidases activity in tumors idealistically functions in an acidic microenvironment [131,132]. Nanoceria NPs alone tend to have a poor water solubility so they are generally coated with polymers to enhance biocompatibility, stability, and their overall solubility [133].

A multifunctional drug delivery system of PPCNPs-Ce6/FA was introduced by Li et al. (2016) and it comprised of Ce6/FA-loaded branched polyethylenimine-PEGylation ceria NPs (PPCNPs) for the possible PDT targeting of drug resistant in vitro BC MCF-7/ADR cells in combination with chemotherapeutic agent DOX [134]. The results revealed that internalization efficiency and diffusion of the synthesized nanoplateform with positive surface charges via endocytosis in BC cells was far higher than free Ce6 [134]. PDT efficiency under 660 nm irradiation in BC cells treated with the PPCNPs-Ce6/FA reported a 35% apoptotic and necrotic cell death, while BC cells treated with PPCNPs-Ce6 only noted an overall 25% cell death [134]. Moreover, results reported that low-dose PPCNPs-Ce6/FA PDT remarkably improved the chemotoxicity of DOX in in vitro MCF-7/ADR BC cells in a dose-dependent manner [134]. In vivo PDT studies within MCF-7/ADR athymic nude mouse xenograft models showed a significant 96% reduction in the tumor volume when injected with PPCNPs-Ce6/FA, in comparison to a 25% reduction when PPCNPs-Ce6 was applied [134].

In relation to metastatic triple-negative BC (mTNBC), numerous studies have noted that treatments, such as radiation, cytotoxic chemotherapy, and surgical interventions are ineffective and so this has driven researchers to consider immunotherapy for the possible treatment of mTNBC [135,136]. Tumor immunotherapy relies on the fact that BC cells can be eradicated by host cytotoxic CD8<sup>+</sup> T cells [137,138].

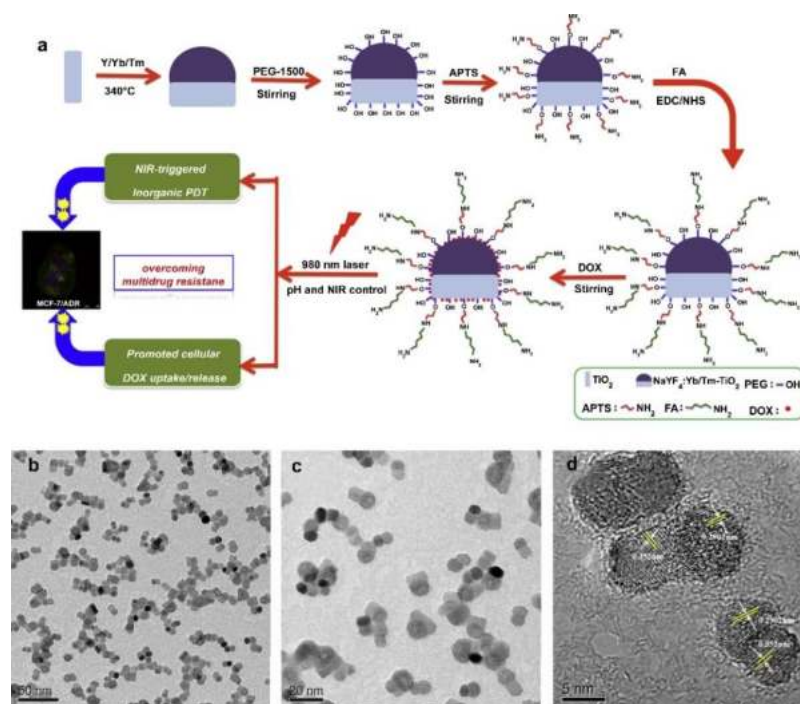
In this regard, Duan et al. (2016) introduced a promising strategy using a checkpoint blockade-based immunotherapy for the treatment of primary in vitro 4T1 BC tumors [139]. A non-toxic core-shell comprising of ZnP@pyro NPs was fabricated using Zn and pyrophosphate (ZnP) and a pyrolipid PS was incorporated into its core, for PDT applications, while a PD-L1 antibody was added for checkpoint blockade immunotherapy [139]. Results reported that the immunogenic ZnP@pyro NPs were non-toxic prior to light activation [139]. Within PDT studies, they successfully eliminated in vitro BC cells upon 670 nm irradiation, through apoptotic and necrotic cell death [139]. PDT in vivo investigations of the ZnP@pyro NPs on orthotopic 4T1 tumor-bearing mice demonstrated that this immunogenic PS nanocarrier enhanced PS uptake via the EPR effect for high tumor accumulation, as well as disrupted tumor vasculature and increased tumor immunogenicity [139]. The authors also claimed that the ZnP@pyro NPs not only prohibited the further metastasis, but also inhibited pre-existing metastatic tumors growth by generating systemic anti-tumor immunity [139].

### 7.7. Upconversion Nanoparticles

The unique “photon upconversion” process of upconversion NPs(UCNPs) has been applied in low tissue penetration depth PDT applications [140,141]. Upconversion is an anti-Stokes shift, which is defined as the conversion of NIR light to a shorter wavelength of light in the visible region [140]. Thus, UCNPs are able to absorb two or more low energy photons and, thus, show a unique anti-Stokes shift of fluorescence emission in UV-Vis wavelengths (300–700 nm) under NIR light excitation (750–1400 nm) [142]. UCNPs can be utilized in biomedical applications as they have shown improved reduced fluorescence background, with lowered phototoxicity [39]. Therefore, in order to treat deep-seated tumors, PSs in NPs are excited with longer wavelength [28] and emitted fluorescence by UCNPs, so can excite PS electrons effectively to produce efficient amounts of singlet oxygen in PDT applications [143].

In 1991, Cai et al., utilized novel TiO<sub>2</sub> or ZnO semiconductors, which had photo-effects, such as inorganic PSs for the PDT treatment of cancer [144]. These semiconductors promoted electrons from valance bands to conduction bands upon PDT UV irradiation, leaving electron hole pairs [28] and so resulted in oxidation or reduction of chemical species, such as water and oxygen around the TiO<sub>2</sub> or ZnO semiconductors, to generate ROS [145,146].

In this regard, Janus nanostructures comprised of NaYF<sub>4</sub>:Yb/Tm UCNP with TiO<sub>2</sub> inorganic PSs were synthesized by Zeng et al. (2015) and loaded with FA and DOX (FA-NPs-DOX) (Figure 9) for NIR-triggered inorganic targeted PDT and chemotherapy treatment of drug-sensitive MCF-7 and drug resistant MCF-7/ADR BC cells within in vitro and in vivo applications [147]. The chemotherapeutic results alone revealed that the FA-targeted nanocomposite promoted the cellular uptake of DOX, as well as caused a viability decline of 44.4% in MCF-7 and 28.9% in MCF-7/ADR BC cells [147]. However, combinational chemotherapy and PDT results under 980 nm NIR irradiation, noted a far higher significant decrease in cellular viability, whereby only 5.8% MCF-7 cells were found viable and 17.6% of MCF-7/ADR BC drug resistant cells were found to alive [147]. Within PDT in vivo assessments on female BALB/c (nu/nu) nude mice, MCF-7 tumor growths reported a 99.34% inhibition of growth, while MCF-7/ADR tumor growths noted a 96.74% decline, when treated with FA-NPs-DOX + NIR [147].



**Figure 9.** (a) Synthesis of DOX-loaded, FA-targeted NaYF<sub>4</sub>:Yb/TmTiO<sub>2</sub> nanocomposites for NIR-triggered PDT and chemotherapy in resistant breast cancer, (b–d) TEM and HRTEM images of NaYF<sub>4</sub>:Yb/TmTiO<sub>2</sub> nanocomposites. Reprinted with permission from reference [147]. Copyright 2015 Elsevier.

In studies by Zeng et al. (2015), HER-2-targeted multifunctional nanoprobe based on 808 nm-excitation bound to NaGdF<sub>4</sub>:Yb,Er@NaGdF<sub>4</sub>:Yb@NaGdF<sub>4</sub>:Yb,Nd UCNP, with Ce6 PS and SiO<sub>2</sub> (T-UCNPs@Ce6@mSiO<sub>2</sub>) were fabricated for 808 nm irradiation PDT and magnetic resonance imaging (MRI) within in vitro MDA-MB-435 BC cells [143]. Regarding the cellular uptake, the accumulation amount of T-UCNPs@Ce6@mSiO<sub>2</sub> in in vitro BC cells was 1–2 times higher than those treated with UCNP@Ce6@mSiO<sub>2</sub>, due to HER-2 active targeting [143]. Furthermore, the PDT treatment of in vitro BC cells using non-targeted UCNP@Ce6@mSiO<sub>2</sub> reported a 16.4% cell viability, whereas cells treated with

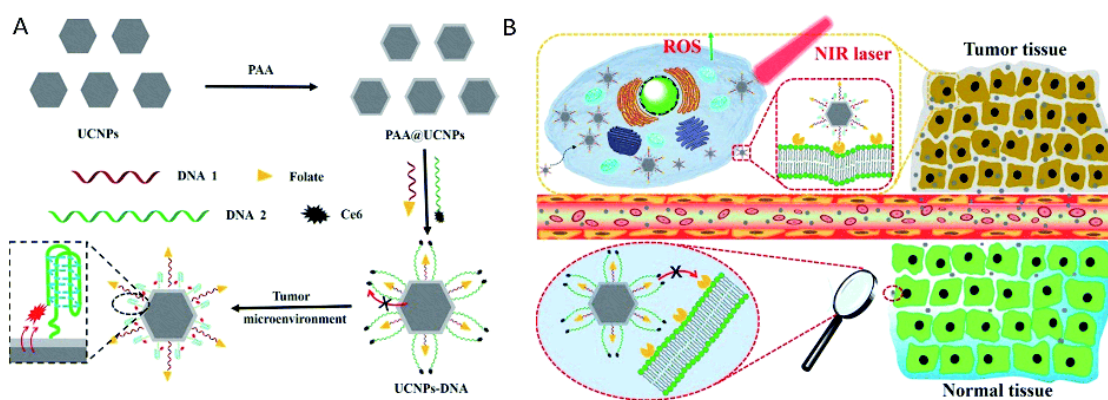
T-UCNPs@Ce6@mSiO<sub>2</sub> noted a 6.8% cell viability, suggesting that the PDT efficiency improvement was due to active targeting [143]. Additionally, *in vitro* T-UCNPs@Ce6@mSiO<sub>2</sub> PDT, reported a significant 16.5% for early apoptosis and 10.2% for late apoptosis cell death [143]. The *in vivo* PDT investigation of nanocomposite in MDA-MB-435 tumor-bearing nude mice indicated that the targeted T-UCNPs@Ce6@mSiO<sub>2</sub> significantly enhanced tumor accumulation of up to 12%, whereas the non-targeted UCNPs@Ce6@mSiO<sub>2</sub> only noted a 2% accumulation potential [143]. Furthermore, the MR signal was far higher and stronger in T-UCNPs@Ce6@mSiO<sub>2</sub> treated mice than when compared to those treated with UCNPs@Ce6@mSiO<sub>2</sub> [143].

Within studies by Wang et al. (2017) Lanthanide-doped UCNPs were encapsulated in fourth-generation poly amido amine (PAMAM) dendrimers, bearing 64 peripheral amines (G4) and Ce6 to assess NIR-triggered PDT in 2D and 3D *in vitro* MCF-7 BC [142]. The internal cavities within the dendrimers enabled the trapping of small molecules through host-guest affinity and so enhance the cellular uptake of the UCNPs [142]. More importantly, when Ce6 was loaded onto the dendrimer-modified UCNPs, and 660 nm PDT laser irradiation applied in 2D models 50% cell death was noted, whereas approximately 70% cell death was found in those treated with 980 nm PDT laser irradiation [142]. These findings confirmed that the NIR could pass through the 2D BC tumor cell model membranes and organelles to reach and effectively activate the UCNPs, and so enhance PDT efficacy with deeper tissue penetration [142]. With reference to the 3D model, 980 nm NIR light noted a deep tumor penetration and produced cell death that was consistent with the 2D model results [142]. Moreover, *in vivo* PDT assessments using 980 nm irradiation in 4T1 BC tumor-bearing mouse models treated with high doses of the UCNPs, demonstrated significant tumor growth inhibition, through induction of the  $\gamma$ H2AXser139 protein marker for DNA double strand breaks; thus, substantial DNA damage was observed [142].

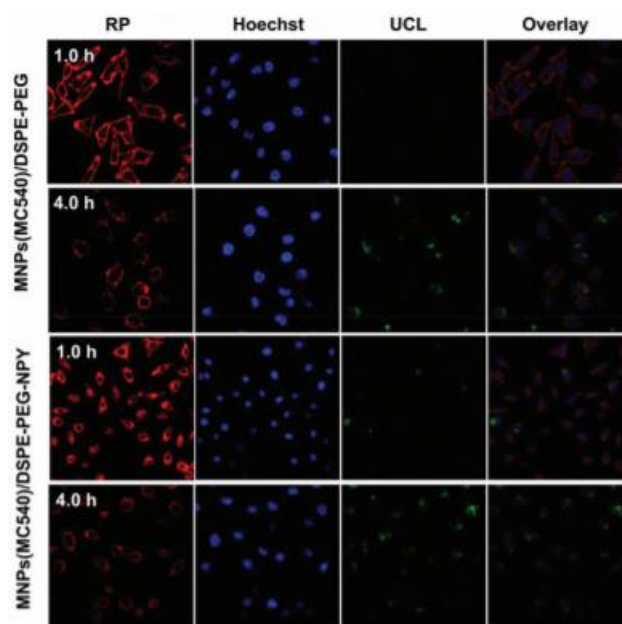
A precise tumor-specific UCNP targeting strategy was assessed by Yu et al. (2018) for the enhanced PDT treatment of *in vitro* MCF-7 BC cells [148]. NaYF<sub>4</sub>:Yb<sup>3+</sup>, Er<sup>3+</sup> UCNPs capped with polyacrylic acid (UCNPs@PAA) were fabricated and modified with FA and Ce6 PS, as well as were functionalized with DNA sequences of varying lengths (Figure 10A) [148]. The *in vitro* cellular uptake results showed that the fabricated UCNPs@PAA-DNA located efficiently within BC lysosomes via effective folate receptor targeting (Figure 10B) [148]. Significant reduction within *in vitro* 980 nm PDT treated BC cells with UCNPs@PAA-DNA was reported [148]. The study stated that the Ce6 PS on the longer DNA nanocomposite moved to the vicinity of the UCNPs and generated singlet oxygen upon NIR irradiation, through Förster resonance energy transfer (FRET). The study proposed that when the fabricated UCNP reached the BC tumor cells, the C base-rich long DNA within the nanocomposite could form a C-quadruplex and the FA groups overexpressed on the folate receptors of BC cells could be attracted, and so efficiently active BC tumor targeting was achieved [148]. Furthermore, the pre-protective strategy using UCNPs@PAA-DNA with longer DNA alleviated any other possible side effects on the normal cells, as the FA groups of the shorter DNA was protected by this longer DNA to preclude any possible binding with normal cell folate receptors [148]. *In vivo* PDT experiments within BALB/c mice with BC xenograft tumors not only demonstrated the successful accumulation of the nanocomposites, but also eliminated tumor volume tenfold in comparison to control groups [148].

Generally, NP particle size can affect their overall uptake and retention in the liver, kidney, and spleen [149], furthermore large sized NPs can induce high toxicity, with unwanted side effects and heightened cellular phagocytosis [150]. Thus, within clinical applications, they tend to be more inclined towards the use of small NPs, which report less retention and unwanted toxicity [151]. Within a study performed by Yu et al. (2018) a core-multishell nanocomposite (MNPs(MC540)/DSPE-PEG-NPY) was constructed that was an ultrasmall size for the *in vitro* and *in vivo* PDT evaluation within MCF-7 BC cells [151]. This UCNP nanostructure was based on a multifunctional Y<sub>1</sub>R<sub>s</sub>-targeting ligand [Pro30, Nle31, Bpa32, Leu34]NPY(28–36), abbreviated to NPY and loaded

with merocyanine 540 (MC540) PS to form  $\text{LiLuF}_4:\text{Yb,Er}@n\text{LiGdF}_4@m\text{SiO}_2$  (MNPs) [151]. Then 1,2-distearoyl-sn-glycero-3-phosphoethanolamine-N-carboxy (polyethylene glycol)—2000] (DSPE-PEG) was coated onto the surface of MNPs to improve water solubility and biocompatibility of the final nanocomposite [151]. Within 980 nm *in vitro* PDT assays BC MCF-7 cells treated with MNPs(MC540) noted a 84.8% cell death, whereas those treated with MNPs(MC540)/DSPE-PEG reported a 86.7% cell death and those treated with MNPs(MC540)/DSPE-PEG-NPY noted a 93.5% cell death, suggestive that active targeting and uptake was present (Figure 11) [151]. Within 980 nm *in vivo* PDT assays on MCF-7 BC induced female BALB/c nude mice tumor volumes of the groups treated with MNPs(MC540), MNPs(MC540)/DSPE-PEG, and MNPs(MC540)/DSPE-PEG-NPY increased over the first 4 days and then decreased on the sixth day after a double PDT application was performed [151]. After 28 days of a double PDT application, mice injected with MNPs(MC540)/DSPE-PEG-NPY showed no tumor growth [151].



**Figure 10.** (A) Schematic preparation of UCNPs@PAA–DNA and (B) specific tumor targeting for PDT treatment of MCF-7 cells [148]. Published by The Royal Society of Chemistry (RSC).



**Figure 11.** Confocal laser scanning microscopy of MCF-7 incubated with MNPs(MC540)/DSPE-PEG-NPY or MNPs(MC540)/DSPE-PEG. Reprinted with permission from reference [151]. Copyright 2018 Royal Chemical Society.

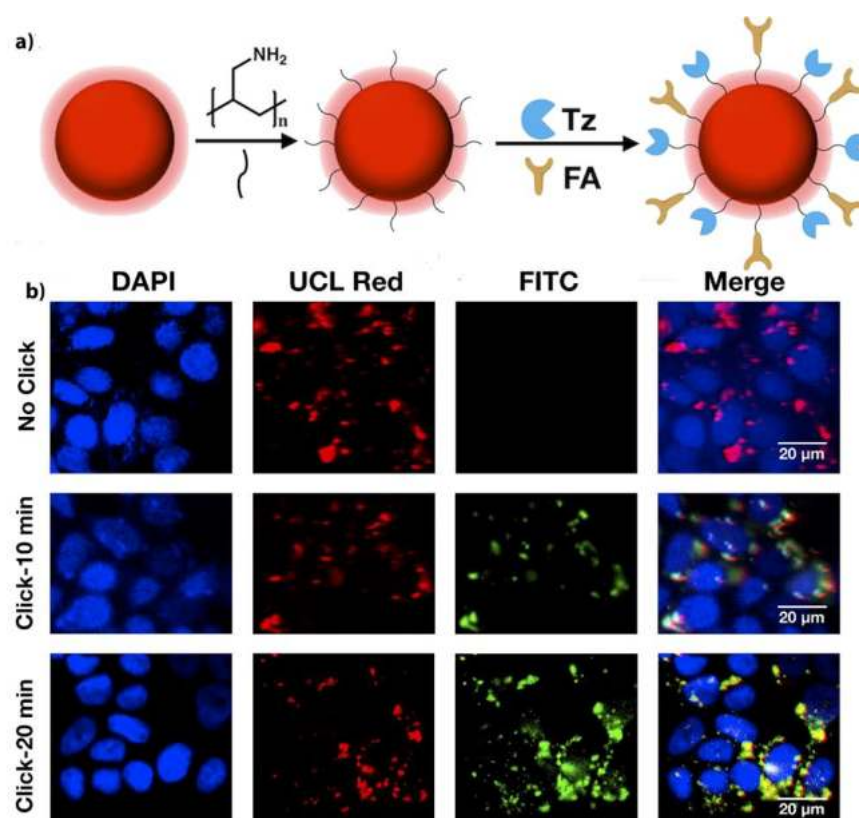
In a study performed by Ramírez-García et al. (2018), a UCNP nanoconjugate was constructed for the targeted PDT and imaging against HER-2-positive BC cells, as well as to try



and overcome the limited tumor cell depth penetration visible light has [152]. NaYF<sub>4</sub>:Yb,Er UCNPs were fabricated and attached to a zinc tetracarboxyphenoxy phthalocyanine (ZnPc) PS and a trastuzumab (Tras) HER-2 specific monoclonal antibody to form a UCNPs-ZnPc-Tras nanocomposite [152]. The covalent bonds between UCNPs and ZnPc resulted in resonance energy transfer from the NPs to the PS, which in turn produced cytotoxic singlet oxygen and higher <sup>1</sup>O<sub>2</sub> quantum yields when compared to control groups [152]. The PDT efficacy of this nanocomposite was evaluated in vitro within HER-2 positive SK-BR-3 and HER-2 negative MCF-7 human BC cells [152]. Cytotoxicity assays post-PDT at 975 nm noted higher values in HER-2 positive SK-BR-3 BC cells than when compared to HER-2 negative MCF-7 human BC cells, suggestive that enhanced PS targeting uptake was present due to specific HER-2 targeting [152]. Moreover, post-PDT HER-2 positive SK-BR-3 BC cells noted a 93.5% cell death, when compared to HER-2 negative MCF-7 human BC cells which reported a mere 21.8% cell death, suggestive that this nanocomposite was capable of specific and far more enhanced HER-2 positive BC receptor mediated targeted PDT [152].

As previously mentioned, photocatalysis TiO<sub>2</sub> NPs are nontoxic and have a high photochemical stability to yield improved levels of ROS upon irradiation [153]. When TiO<sub>2</sub> NPs are utilized within PDT applications as PS, a far higher and controlled loading with improved uptake has been reported [154]. Furthermore, other studies noted that when doping metal atoms, such as ZrO<sub>2</sub>, are attached to TiO<sub>2</sub> heterostructures, they can temporarily constrain the high recombination rate of photogenerated electron-hole pairs in TiO<sub>2</sub> NPs when electron-hole pairs migrate from the inside of the photocatalyst to the surface, improving PDT treatment outcomes [154,155]. In a more recent study performed by Ramírez-García et al. (2019), a NaYF<sub>4</sub>:Yb,Tm UCNP core was fabricated and coated with photo-effecting material TiO<sub>2</sub>-ZrO<sub>2</sub> as a shell to improve NIR-triggered PDT (NaYF<sub>4</sub>:Yb,Tm@TiO<sub>2</sub>/ZrO<sub>2</sub> core@shell NPs) [153]. The monoclonal antibody known as Tras was also added to the UCNPs surface, to improve its overall NP PS active targeting within HER-2 positive in vitro cultured SK-BR-3 human BC cells [153]. Within PDT assays at 975 nm irradiation at 400 µg/mL the NaYF<sub>4</sub>:Yb,Tm@TiO<sub>2</sub>/ZrO<sub>2</sub>-tras nanocomposite reported 76% cell death, whereas control groups treated with single TiO<sub>2</sub> UCNP that lacked ZrO<sub>2</sub> attachment, only 40% cell death was found [153]. Overall, these results revealed that the combinative photocatalytic activity of TiO<sub>2</sub>-ZrO<sub>2</sub> within the final nanocomposite, improved the PDT treatment outcomes in BC cells due to higher levels of ROS being produced [153].

Studies by Feng et al. (2019) employed a promising strategy called a “all-in-one”, whereby imaging and therapeutic PDT functions were integrated into one nanoplatform, by anchoring a PSs to UCNPs to allow for dual imaging-guided PDT within in vitro MCF-7 BC cells [156]. A bioorthogonal chemical reaction was utilized in this study to allow for a “off/on” state of PDT, in order to circumvent any issues associated with photoactivity of preloaded norbornene-rose bengal (RB-NB) PS, since it can produce skin photosensitivity and so damage normal cells [156]. Thus, a NaYF<sub>4</sub>: Er, Yb@NaYF<sub>4</sub> UCNP was synthesized and covalently bound to a pre-targeting tetrazine (Tz) and FA molecule to form a UCNPs-Tz/FA-PEG (Figure 12a), which was utilized as the one handle of the bioorthogonal reaction in tracking and imaging of deep-seated tumors, since it lacked PS [156]. Then when the RB-NB PS were attached on the surface of the nanoplatform via a bioorthogonal chemical reaction (as the other handle of the UCNP), it demonstrated efficient PS targeting, UCNP energy transfer to the PS, with high yields of ROS and so enhanced treatment within in vitro BC tumors under 980 nm irradiation (Figure 12b) [156]. Upconversion luminescence (UCL) imaging of the nude mice injected with MCF-7 BC cells showed high accumulation of the nanoplatform in tumor sites, due to FA active targeting and EPR effect [156]. Furthermore, in vivo PDT assays on these tumor bearing mice when treated with NPs-Tz/FA-PEG + RB-NB under 980 nm irradiation provided 75.5% decrease in tumor size when compared to control groups [156].



**Figure 12.** (a) Schematic synthesis of UCNPs-Tz/FA-PEG, (b) MCF-7 cells treated with UCNPs-Tz/FA-PEG or UCNPs-FA-PEG for UCL imaging with 980 nm light excitation (red channel), and click reaction with FITC-NB (green channel), and stained with DAPI (blue channel). Top: control (no click), middle: click for 10 min and bottom: click for 20 min. Reprinted with permission from reference [156]. Copyright 2019 Elsevier.

A lot of research has been carried within the utilization of UCNPs for the enhanced PS delivery and PDT treatment of BC, due to their ability to be allow for PS activation within the higher NIR wavelength ranges, and consequently be able to provide deeper penetration of tumor tissues, when compared to visible light applications, since the upconversion visible emission from UCNPs can excite PS to produce more ROS [140,157]. It is envisaged that the integration of UCNPs with more NIR penetrable light and idealistic PSs will potentiate near-future targeted PDT BC clinical trials.

## 8. Conclusions and Perspectives

BC is invasive form of cancer, which can metastasize, and frequently recurs after treatment [2]. Many conventional therapies utilized for BC often present themselves with some form of resistance and unwanted side-effects, and surgery is invasive [3]. In this sense, actively targeted PDT is gaining a prominent position as a non-invasive, limited side effect approach for the treatment of BC.

The combination of NPs with PSs, to passively, as well as actively enhance their accumulation in tumor tissues more selectively in order to enhance PDT treatment outcomes, as well as lessen the unwanted side effects on localized tissues is fast becoming a popular approach [22,23].

Inorganic NPs have unique properties, which assist in reducing PS leaching, allow for a high loading capacity of PSs, improve PS passive uptake via the EPR effect, and allow for ease of functionalization with various ligands to promote active PS absorption and, thus, allow for the overall enhancement of PDT BC treatment [27,158]. Furthermore, inorganic and metallic PS nanocarriers are less susceptible to degradation and do not release attached

PSs, but rather allow activated ROS after irradiation to diffuse out of them, when compared to organic NPs, and so are more prominently utilized within the field of PDT [29,158].

Gold NPs for example have shown surface plasmon resonance effects that can intensify singlet oxygen quantum yield, as well as induce hyperthermia promoting the overall effect of PDT [28]. Furthermore, inorganic NPs, such as UCNPs can provide a deeper penetration of light in tumors [140] or porous silica NPs allow for the entrapment of oxygen to improve overall PDT treatment outcomes [28].

Anchoring of active targeting moieties to PS-loaded inorganic NPs, allow nanosystems to be specifically directed towards BC cells only, allowing enhanced PS accumulation, which is localized in tumor target cells, only limiting unwanted side effects on normal cells [22,23]. It is also noteworthy to emphasize that the number of receptors per tumor cell is  $10^5$ , while the number of the PS molecules that can be attached to an inorganic NP to obviate cancer cells is  $10^7$ , allowing each tumor receptor to be able to at least receive a  $10^2$  PS concentration [159]. Thus, the binding of targeting ligand to PS-loaded NPs is imperative to ensure the highest uptake possible of PSs in tumor cells, in order to promote PDT treatment outcomes [159].

It is postulated that, in the near future, the applications of nanotechnology to potentiate PDT should allow for the widespread of breast cancer amongst women to be overcome [159]. However, additional comprehensive studies are still required to scrutinize the physiochemical, pharmacokinetic properties, and safety profiles of nanocarriers, so that maximum accumulation and PS uptake can be attained in the target tissues. In addition, although anchoring of the PSs on the surface of NPs can enhance their biocompatibility, the potential toxic effects and unwanted liver and renal accumulation, must be taken into consideration. Thus, it is imperative that the above discussed and reviewed inorganic NP studies for the actively applied targeted PDT treatment of BC in vitro and in vivo be investigated further within clinical trials, so that the possible future targeted PDT treatment of BC can become a reality.

**Supplementary Materials:** The following are available online at <https://www.mdpi.com/1999-4923/13/3/296/s1>, Table S1: spectroscopic and physicochemical properties of some photosensitizers utilized for PDT of cancer.

**Author Contributions:** H.M.: conceptualization, acquisition, analysis of data, writing original draft, final approval. C.A.K.: conceptualization, co-supervision, writing revision and editing, final approval of version to be published. H.A.: conceptualization, supervision, writing revision and editing, funding acquisition, final approval. All authors have read and agreed to the published version of the manuscript.

**Funding:** This research was funded by the South African Research Chairs Initiative of the Department of Science and Technology and National Research Foundation of South Africa, grant number 98337.

**Institutional Review Board Statement:** Not applicable.

**Informed Consent Statement:** Not applicable.

**Conflicts of Interest:** The authors declare no conflict of interest. This manuscript is based on our original research and has neither been published, nor is being considered elsewhere for publication. Additionally, all of the authors note that they do not have any relationships that they believe could be construed as a conflict of interest with regards to the manuscript review process. The funders had no role in the design of the study; in the collection, analyses, or interpretation of data; in the writing of the manuscript, or in the decision to publish the results

## References

1. Crescenzi, E.; Varriale, L.; Iovino, M.; Chiaviello, A.; Veneziani, B.M.; Palumbo, G. Photodynamic therapy with indocyanine green complements and enhances low-dose cisplatin cytotoxicity in MCF-7 breast cancer cells. *Mol. Cancer Ther.* **2004**, *3*, 537–544.
2. Karrison, T.G.; Ferguson, D.J.; Meier, P. Dormancy of Mammary Carcinoma After Mastectomy. *J. Natl. Cancer Inst.* **1999**, *91*, 80–85. [CrossRef] [PubMed]
3. Maham, A.; Tang, Z.; Wu, H.; Wang, J.; Lin, Y. Protein-Based Nanomedicine Platforms for Drug Delivery. *Small* **2009**, *5*, 1706–1721. [CrossRef] [PubMed]

4. Agostinis, P.; Berg, K.; Cengel, K.A.; Foster, T.H.; Girotti, A.W.; Gollnick, S.O.; Hahn, S.M.; Hamblin, M.R.; Juzeniene, A.; Kessel, D.; et al. Photodynamic therapy of cancer: An update. *CA Cancer J. Clin.* **2011**, *61*, 250–281. [CrossRef]
5. Keene, J.P.; Kessel, D.; Land, E.J.; Redmond, R.W.; Truscott, T.G. DIRECT DETECTION OF SINGLET OXYGEN SENSITIZED BY HAEMATOPORPHYRIN AND RELATED COMPOUNDS. *Photochem. Photobiol.* **1986**, *43*, 117–120. [CrossRef] [PubMed]
6. Derycke, A.S.; de Witte, P.A. Liposomes for photodynamic therapy. *Adv. Drug Deliv. Rev.* **2004**, *56*, 17–30. [CrossRef] [PubMed]
7. Banerjee, S.; MacRobert, A.; Mosse, C.; Periera, B.; Bown, S.; Keshtgar, M. Photodynamic therapy: Inception to application in breast cancer. *Breast* **2017**, *31*, 105–113. [CrossRef] [PubMed]
8. Vlastos, G.; Verkooijen, H.M. Minimally Invasive Approaches for Diagnosis and Treatment of Early-Stage Breast Cancer. *Oncologist* **2007**, *12*, 1–10. [CrossRef]
9. Mastrangelopoulou, M.; Grigalavicius, M.; Berg, K.; Ménard, M.; Theodossiou, T.A. Cytotoxic and Photocytotoxic Effects of Cercosporin on Human Tumor Cell Lines. *Photochem. Photobiol.* **2018**, *95*, 387–396. [CrossRef] [PubMed]
10. Lee, J.; Park, H.Y.; Kim, W.W.; Jeong, J.Y.; Lee, Y.-D.; Choi, M.-H.; Kim, S.; Park, J.-Y.; Jung, J.H. Combination Treatment with Photodynamic Therapy and Laser Ablation in Breast Cancer: An Animal Model Study. *Photomed. Laser Surg.* **2017**, *35*, 505–512. [CrossRef] [PubMed]
11. Gray, R.J.; Pockaj, B.A.; Garvey, E.; Blair, S. Intraoperative Margin Management in Breast-Conserving Surgery: A Systematic Review of the Literature. *Ann. Surg. Oncol.* **2017**, *25*, 18–27. [CrossRef] [PubMed]
12. Kwiatkowski, S.; Knap, B.; Przystupski, D.; Saczko, J.; Kędzierska, E.; Knap-Czop, K.; Kotlińska, J.; Michel, O.; Kotowski, K.; Kulbacka, J. Photodynamic therapy – mechanisms, photosensitizers and combinations. *Biomed. Pharmacother.* **2018**, *106*, 1098–1107. [CrossRef] [PubMed]
13. Son, J.; Yi, G.; Yoo, J.; Park, C.; Koo, H.; Choi, H.S. Light-responsive nanomedicine for biophotonic imaging and targeted therapy. *Adv. Drug Deliv. Rev.* **2019**, *138*, 133–147. [CrossRef] [PubMed]
14. Weissleder, R. A clearer vision for in vivo imaging. *Nat. Biotechnol.* **2001**, *19*, 316–317. [CrossRef] [PubMed]
15. Smith, A.M.; Mancini, M.C.; Nie, S. Bioimaging: Second window for in vivo imaging. *Nat Nanotechnol.* **2009**, *4*(11), 710. [CrossRef] [PubMed]
16. Mazzone, G.; Russo, N.; Sicilia, E. Theoretical investigation of the absorption spectra and singlet-triplet energy gap of positively charged tetraphenylporphyrins as potential photodynamic therapy photosensitizers. *Can. J. Chem.* **2013**, *91*, 902–906. [CrossRef]
17. Yoon, I.; Li, J.Z.; Shim, Y.K. Advance in Photosensitizers and Light Delivery for Photodynamic Therapy. *Clin. Endosc.* **2013**, *46*, 7–23. [CrossRef]
18. Dobson, J.; De Queiroz, G.F.; Golding, J.P. Photodynamic therapy and diagnosis: Principles and comparative aspects. *Vet. J.* **2018**, *233*, 8–18. [CrossRef]
19. Allison, R.R.; Sibata, C.H. Oncologic photodynamic therapy photosensitizers: A clinical review. *Photodiagn. Photodyn. Ther.* **2010**, *7*, 61–75. [CrossRef]
20. Zhang, J.; Jiang, C.; Longo, J.P.F.; Azevedo, R.B.; Zhang, H.; Muehlmann, L.A. An updated overview on the development of new photosensitizers for anticancer photodynamic therapy. *Acta Pharm. Sin. B* **2018**, *8*, 137–146. [CrossRef]
21. Kessel, D.; Oleinick, N.L. Photodynamic Therapy and Cell Death Pathways. In *Methods in Molecular Biology*; Springer International Publishing: Cham, Switzerland, 2010; Volume 635, pp. 35–46.
22. Danhier, F.; Feron, O.; Pr at, V. To exploit the tumor microenvironment: Passive and active tumor targeting of nanocarriers for anti-cancer drug delivery. *J. Control. Release* **2010**, *148*, 135–146. [CrossRef] [PubMed]
23. Pawar, P.V.; Domb, A.J.; Kumar, N. Systemic Targeting Systems-EPR Effect, Ligand Targeting Systems. In *Advances in Delivery Science and Technology*; Springer International Publishing: Cham, Switzerland, 2013; pp. 61–91.
24. Calixto, G.M.F.; Bernegossi, J.; De Freitas, L.M.; Fontana, C.R.; Chorilli, M. Nanotechnology-Based Drug Delivery Systems for Photodynamic Therapy of Cancer: A Review. *Mol.* **2016**, *21*, 342. [CrossRef]
25. Yoon, H.-J.; Jang, W.-D. Nanotechnology-based photodynamic therapy. *J. Porphyrins Phthalocyanines* **2013**, *17*, 16–26. [CrossRef]
26. Du, B.; Jia, S.; Wang, Q.; Ding, X.; Liu, Y.; Yao, H.; Zhou, J. A self-targeting, dual ros/ph-responsive apoferritin nanocage for spatiotemporally controlled drug delivery to breast cancer. *Biomacromolecules* **2018**, *19*, 1026–1036. [CrossRef] [PubMed]
27. Cheng, S.-H.; Lo, L.-W. Inorganic nanoparticles for enhanced photodynamic cancer therapy. *Curr. Drug Discov. Technol.* **2011**, *8*, 269–276. [CrossRef] [PubMed]
28. Colombeau, L.; Acherar, S.; Baros, F.; Arnoux, P.; Gazzali, A.M.; Zaghdoudi, K.; Toussaint, M.; Vanderesse, R.; Frochot, C. Inorganic Nanoparticles for Photodynamic Therapy. *Topics in Current Chemistry* **2016**, *370*, 113–134. [CrossRef] [PubMed]
29. Moreno-Vega, A.-I.; Gomez-Quintero, T.; Nunez-Anita, R.-E.; Acosta-Torres, L.-S.; Casta o, V. Polymeric and ceramic nanoparticles in biomedical applications. *J. Nanotechnol.* **2012**, *2012*, 1–10. [CrossRef]
30. Lee, J.; Chatterjee, D.K.; Lee, M.H.; Krishnan, S. Gold nanoparticles in breast cancer treatment: Promise and potential pitfalls. *Cancer Lett.* **2014**, *347*, 46–53. [CrossRef]
31. Penon, O.; Pati o, T.; Barrios, L.; Nogu es, C.; Amabilino, D.B.; Wurst, K.; P rez-Garc a, L. A New Porphyrin for the Preparation of Functionalized Water-Soluble Gold Nanoparticles with Low Intrinsic Toxicity. *ChemistryOpen* **2014**, *4*, 127–136. [CrossRef]
32. Calavia, P.G.; Chambrier, I.; Cook, M.J.; Haines, A.H.; Field, R.A.; Russell, D.A. Targeted photodynamic therapy of breast cancer cells using lactose-phthalocyanine functionalized gold nanoparticles. *J. Colloid Interface Sci.* **2018**, *512*, 249–259. [CrossRef]
33. Wang, S.; Lu, G. Applications of Gold Nanoparticles in Cancer Imaging and Treatment. In *Noble and Precious Metals - Properties, Nanoscale Effects and Applications*; IntechOpen: London, UK, 2018.

34. Calavia, P.G.; Bruce, G.; Pérez-García, L.; Russell, D.A. Photosensitizer-gold nanoparticle conjugates for photodynamic therapy of cancer. *Photochem. Photobiol. Sci.* **2018**, *17*, 1534–1552. [CrossRef] [PubMed]
35. Akbarzadeh, A.; Samiei, M.; Davaran, S. Magnetic nanoparticles: Preparation, physical properties, and applications in biomedicine. *Nanoscale Res. Lett.* **2012**, *7*, 144. [CrossRef]
36. Hong, E.J.; Choi, D.G.; Shim, M.S. Targeted and effective photodynamic therapy for cancer using functionalized nanomaterials. *Acta Pharm. Sin. B* **2016**, *6*, 297–307. [CrossRef] [PubMed]
37. Khan, I.; Saeed, K.; Khan, I. Nanoparticles: Properties, applications and toxicities. *Arab. J. Chem.* **2019**, *12*, 908–931. [CrossRef]
38. Valizadeh, A.; Mikaeili, H.; Samiei, M.; Farkhani, S.M.; Zarghami, N.; Kouhi, M.; Akbarzadeh, A.; Davaran, S. Quantum dots: Synthesis, bioapplications, and toxicity. *Nanoscale Res. Lett.* **2012**, *7*, 480. [CrossRef] [PubMed]
39. Punjabi, A.; Wu, X.; Tokatli-Apollon, A.; El-Rifai, M.; Lee, H.; Zhang, Y.; Wang, C.; Liu, Z.; Chan, E.M.; Duan, C.; et al. Amplifying the Red-Emission of Upconverting Nanoparticles for Biocompatible Clinically Used Prodrug-Induced Photodynamic Therapy. *ACS Nano* **2014**, *8*, 10621–10630. [CrossRef]
40. Thomas, S.C.; Harshita; Mishra, P.K.; Talegaonkar, S. Ceramic Nanoparticles: Fabrication Methods and Applications in Drug Delivery. *Curr. Pharm. Des.* **2015**, *21*, 6165–6188. [CrossRef] [PubMed]
41. Day, E.S.; Morton, J.G.; West, J.L. Nanoparticles for Thermal Cancer Therapy. *J. Biomech. Eng.* **2009**, *131*, 074001. [CrossRef] [PubMed]
42. Huang, X.; Jain, P.K.; El-Sayed, I.H.; El-Sayed, M.A. Plasmonic photothermal therapy (PPTT) using gold nanoparticles. *Lasers Med. Sci.* **2007**, *23*, 217–228. [CrossRef]
43. Li, J.-L.; Wang, L.; Liu, X.-Y.; Zhang, Z.-P.; Guo, H.-C.; Liu, W.-M.; Tang, S.-H. In vitro cancer cell imaging and therapy using transferrin-conjugated gold nanoparticles. *Cancer Lett.* **2009**, *274*, 319–326. [CrossRef] [PubMed]
44. Stuchinskaya, T.; Moreno, M.; Cook, M.J.; Edwards, D.R.; Russell, D.A. Targeted photodynamic therapy of breast cancer cells using antibody–phthalocyanine–gold nanoparticle conjugates. *Photochem. Photobiol. Sci.* **2011**, *10*, 822–831. [CrossRef]
45. Obaid, G.; Chambrier, I.; Cook, M.J.; Russell, D.A. Cancer targeting with biomolecules: A comparative study of photodynamic therapy efficacy using antibody or lectin conjugated phthalocyanine-PEG gold nanoparticles. *Photochem. Photobiol. Sci.* **2015**, *14*, 737–747. [CrossRef] [PubMed]
46. Penon, O.; Marín, M.J.; Russell, D.A.; Pérez-García, L. Water soluble, multifunctional antibody-porphyrin gold nanoparticles for targeted photodynamic therapy. *J. Colloid Interface Sci.* **2017**, *496*, 100–110. [CrossRef]
47. Yuan, H.; Fales, A.M.; Khoury, C.G.; Liu, J.; Vo-Dinh, T. Spectral characterization and intracellular detection of Surface-Enhanced Raman Scattering (SERS)-encoded plasmonic gold nanostars. *J. Raman Spectrosc.* **2012**, *44*, 234–239. [CrossRef] [PubMed]
48. Fales, A.M.; Yuan, H.; Vo-Dinh, T. Cell-penetrating peptide enhanced intracellular Raman imaging and photodynamic therapy. *Mol. Pharm.* **2013**, *10*, 2291–2298. [CrossRef] [PubMed]
49. Etchegoin, P.G. Quo vadis surface-enhanced Raman scattering? *Phys. Chem. Chem. Phys.* **2009**, *11*, 7348–7349. [CrossRef]
50. Dube, E.; Oluwole, D.O.; Nwaji, N.; Nyokong, T. Glycosylated zinc phthalocyanine-gold nanoparticle conjugates for photodynamic therapy: Effect of nanoparticle shape. *Spectrochim. Acta Part A: Mol. Biomol. Spectrosc.* **2018**, *203*, 85–95. [CrossRef] [PubMed]
51. Liu, J.; Liang, H.; Li, M.; Luo, Z.; Zhang, J.; Guo, X.; Cai, K. Tumor acidity activating multifunctional nanopatform for NIR-mediated multiple enhanced photodynamic and photothermal tumor therapy. *Biomaterials* **2018**, *157*, 107–124. [CrossRef]
52. Liu, L.; Xie, H.-J.; Mu, L.-M.; Liu, R.; Su, Z.-B.; Cui, Y.-N.; Xie, Y.; Lu, W.-L. Functional chlorin gold nanorods enable to treat breast cancer by photothermal/photodynamic therapy. *Int. J. Nanomed.* **2018**, *13*, 8119–8135. [CrossRef] [PubMed]
53. Guo, R.; Shi, X. Dendrimers in Cancer Therapeutics and Diagnosis. *Curr. Drug Metab.* **2012**, *13*, 1097–1109. [CrossRef]
54. Kim, Y.; Park, E.J.; Na, D.H. Recent progress in dendrimer-based nanomedicine development. *Arch. Pharmacol. Res.* **2018**, *41*, 571–582. [CrossRef] [PubMed]
55. Scott, R.W.J.; Wilson, A.O.M.; Crooks, R.M. Synthesis, Characterization, and Applications of Dendrimer-Encapsulated Nanoparticles. *J. Phys. Chem. B* **2005**, *109*, 692–704. [CrossRef]
56. Mfouo-Tynga, I.; Houreld, N.N.; Abrahamse, H. Evaluation of cell damage induced by irradiated Zinc-Phthalocyanine-gold dendrimeric nanoparticles in a breast cancer cell line. *Biomed. J.* **2018**, *41*, 254–264. [CrossRef]
57. Xu, W.; Qian, J.; Hou, G.; Wang, Y.; Wang, J.; Sun, T.; Ji, L.; Suo, A.; Yao, Y. A dual-targeted hyaluronic acid-gold nanorod platform with triple-stimuli responsiveness for photodynamic/photothermal therapy of breast cancer. *Acta Biomater.* **2019**, *83*, 400–413. [CrossRef] [PubMed]
58. Yu, W.; He, X.; Yang, Z.; Yang, X.; Xiao, W.; Liu, R.; Xie, R.; Qin, L.; Gao, H. Sequentially responsive biomimetic nanoparticles with optimal size in combination with checkpoint blockade for cascade synergetic treatment of breast cancer and lung metastasis. *Biomaterials* **2019**, *217*, 119309. [CrossRef]
59. Zheng, X.; Zhou, F.; Wu, B.; Chen, W.R.; Xing, D. Enhanced Tumor Treatment Using Biofunctional Indocyanine Green-Containing Nanostructure by Intratumoral or Intravenous Injection. *Mol. Pharm.* **2012**, *9*, 514–522. [CrossRef] [PubMed]
60. Schellekens, H.; Hennink, W.E.; Brinks, V. The Immunogenicity of Polyethylene Glycol: Facts and Fiction. *Pharm. Res.* **2013**, *30*, 1729–1734. [CrossRef] [PubMed]
61. Gao, W.; Hu, C.-M.J.; Fang, R.H.; Luk, B.T.; Su, J.; Zhang, L. Surface Functionalization of Gold Nanoparticles with Red Blood Cell Membranes. *Adv. Mater.* **2013**, *25*, 3549–3553. [CrossRef] [PubMed]

62. Fang, R.H.; Hu, C.-M.J.; Zhang, L. Nanoparticles disguised as red blood cells to evade the immune system. *Expert Opin. Biol. Ther.* **2012**, *12*, 385–389. [CrossRef]
63. Jiang, Q.; Luo, Z.; Men, Y.; Yang, P.; Peng, H.; Guo, R.; Tian, Y.; Pang, Z.; Yang, W. Red blood cell membrane-camouflaged melanin nanoparticles for enhanced photothermal therapy. *Biomaterials* **2017**, *143*, 29–45. [CrossRef] [PubMed]
64. Jiang, X.-M.; Wang, L.-M.; Wang, J.; Chen, C.-Y. Gold nanomaterials: Preparation, chemical modification, biomedical applications and potential risk assessment. *Appl. Biochem. Biotechnol.* **2012**, *166*, 1533–1551. [CrossRef] [PubMed]
65. Grancharov, S.G.; Zeng, H.; Sun, S.; Wang, S.X.; O'Brien, S.; Murray, C.; Kirtley, J.; Held, G. Bio-functionalization of mono-disperse magnetic nanoparticles and their use as biomolecular labels in a magnetic tunnel junction based sensor. *J. Phys. Chem. B* **2005**, *109*, 13030–13035. [CrossRef]
66. Piao, Y.; Kim, J.; Na, H.B.; Kim, D.; Baek, J.S.; Ko, M.K.; Lee, J.H.; Shokouhimehr, M.; Hyeon, T. Wrap-bake-peel process for nanostructural transformation from  $\beta$ -FeOOH nanorods to biocompatible iron oxide nanocapsules. *Nat. Mater.* **2008**, *7*, 242. [CrossRef]
67. Narsireddy, A.; Vijayashree, K.; Irudayaraj, J.; Manorama, S.V.; Rao, N.M. Targeted in vivo photodynamic therapy with epidermal growth factor receptor-specific peptide linked nanoparticles. *Int. J. Pharm.* **2014**, *471*, 421–429. [CrossRef]
68. Choi, K.-H.; Nam, K.C.; Cho, G.; Jung, J.-S.; Park, B.J. Enhanced photodynamic anticancer activities of multifunctional magnetic nanoparticles ( $\text{Fe}_3\text{O}_4$ ) conjugated with chlorin e6 and folic acid in prostate and breast cancer cells. *Nanomaterials* **2018**, *8*, 722. [CrossRef] [PubMed]
69. Matlou, G.G.; Oluwole, D.O.; Prinsloo, E.; Nyokong, T. Photodynamic therapy activity of zinc phthalocyanine linked to folic acid and magnetic nanoparticles. *J. Photochem. Photobiol. B: Biol.* **2018**, *186*, 216–224. [CrossRef] [PubMed]
70. Dulińska-Litewka, J.; Łazarczyk, A.; Hałubiec, P.; Szafranski, O.; Karnas, K.; Karewicz, A. Superparamagnetic Iron Oxide Nanoparticles—Current and Prospective Medical Applications. *Materials* **2019**, *12*, 617. [CrossRef]
71. Khot, V.; Pawar, S. Magnetic Hyperthermia with Magnetic Nanoparticles: A Status Review. *Curr. Top. Med. Chem.* **2014**, *14*, 572–594. [CrossRef]
72. Duguet, E.; Vasseur, S.; Mornet, S.; Devoisselle, J.-M. Magnetic nanoparticles and their applications in medicine. *Nanomedicine* **2006**, *1*, 157–168. [CrossRef] [PubMed]
73. Zottel, A.; Paska, A.V.; Jovčevska, I. Nanotechnology Meets Oncology: Nanomaterials in Brain Cancer Research, Diagnosis and Therapy. *Materials* **2019**, *12*, 1588. [CrossRef]
74. Kolosnjaj-Tabi, J.; Wilhelm, C. Magnetic nanoparticles in cancer therapy: How can thermal approaches help? *Nanomedicine* **2017**, *12*, 573–575. [CrossRef] [PubMed]
75. Kolosnjaj-Tabi, J.; Di Corato, R.; Lartigue, L.; Marangon, I.; Guardia, P.; Silva, A.K.A.; Luciani, N.; Clément, O.; Flaud, P.; Singh, J.V.; et al. Heat-Generating Iron Oxide Nanocubes: Subtle “Destructurators” of the Tumoral Microenvironment. *ACS Nano* **2014**, *8*, 4268–4283. [CrossRef]
76. Hong, G.; Diao, S.; Antaris, A.L.; Dai, H. Carbon Nanomaterials for Biological Imaging and Nanomedicinal Therapy. *Chem. Rev.* **2015**, *115*, 10816–10906. [CrossRef]
77. Huang, P.; Wang, S.; Wang, X.; Shen, G.; Lin, J.; Wang, Z.; Guo, S.; Cui, D.; Yang, M.; Chen, X. Surface Functionalization of Chemically Reduced Graphene Oxide for Targeted Photodynamic Therapy. *J. Biomed. Nanotechnol.* **2015**, *11*, 117–125. [CrossRef] [PubMed]
78. Liu, Q.; Xu, L.; Zhang, X.; Li, N.; Zheng, J.; Guan, M.; Fang, X.; Wang, C.; Shu, C. Enhanced Photodynamic Efficiency of an Aptamer-Guided Fullerene Photosensitizer toward Tumor Cells. *Chem. Asian J.* **2013**, *8*, 2370–2376. [CrossRef] [PubMed]
79. Mosinger, J.; Lang, K.; Kubát, P. Photoactivatable Nanostructured Surfaces for Biomedical Applications. In *Topics in Current Chemistry*; Springer International Publishing: Cham, Switzerland, 2016; Volume 370, pp. 135–168.
80. Shi, J.; Wang, L.; Gao, J.; Liu, Y.; Zhang, J.; Ma, R.; Liu, R.; Zhang, Z. A fullerene-based multi-functional nanoplatfor for cancer theranostic applications. *Biomaterials* **2014**, *35*, 5771–5784. [CrossRef]
81. Tian, B.; Wang, C.; Zhang, S.; Feng, L.; Liu, Z. Photothermally Enhanced Photodynamic Therapy Delivered by Nano-Graphene Oxide. *ACS Nano* **2011**, *5*, 7000–7009. [CrossRef]
82. Gao, L.; Zhang, C.; Gao, D.; Liu, H.; Yu, X.; Lai, J.; Wang, F.; Lin, J.; Liu, Z. Enhanced Anti-Tumor Efficacy through a Combination of Integrin  $\alpha\beta 6$ -Targeted Photodynamic Therapy and Immune Checkpoint Inhibition. *Theranostics* **2016**, *6*, 627–637. [CrossRef] [PubMed]
83. Yu, X.; Gao, D.; Gao, L.; Lai, J.; Zhang, C.; Zhao, Y.; Zhong, L.; Jia, B.; Wang, F.; Chen, X.; et al. Inhibiting Metastasis and Preventing Tumor Relapse by Triggering Host Immunity with Tumor-Targeted Photodynamic Therapy Using Photosensitizer-Loaded Functional Nanographenes. *ACS Nano* **2017**, *11*, 10147–10158. [CrossRef] [PubMed]
84. Yamakoshi, Y.; Umezawa, N.; Ryu, A.; Arakane, K.; Miyata, N.; Goda, Y.; Masumizu, T.; Nagano, T. Active Oxygen Species Generated from Photoexcited Fullerene ( $\text{C}_{60}$ ) as Potential Medicines:  $\text{O}_2^{\bullet -}$  versus  $^1\text{O}_2$ . *J. Am. Chem. Soc.* **2003**, *125*, 12803–12809. [CrossRef]
85. Murakami, T.; Nakatsuji, H.; Inada, M.; Matoba, Y.; Umeyama, T.; Tsujimoto, M.; Isoda, S.; Hashida, M.; Imahori, H. Photodynamic and photothermal effects of semiconducting and metallic-enriched single-walled carbon nanotubes. *J. Am. Chem. Soc.* **2012**, *134*, 17862–17865. [CrossRef] [PubMed]

86. Zakharian, T.Y.; Seryshev, A.; Sitharaman, B.; Gilbert, B.E.; Knight, V.; Wilson, L.J. A Fullerene–Paclitaxel Chemotherapeutic: Synthesis, Characterization, and Study of Biological Activity in Tissue Culture. *J. Am. Chem. Soc.* **2005**, *127*, 12508–12509. [CrossRef] [PubMed]
87. Sharma, S.K.; Chiang, L.Y.; Hamblin, M.R. Photodynamic therapy with fullerenes in vivo: Reality or a dream? *Nanomedicine* **2011**, *6*, 1813–1825. [CrossRef] [PubMed]
88. Wolfram, J.; Zhu, M.; Yang, Y.; Shen, J.; Gentile, E.; Paolino, D.; Fresta, M.; Nie, G.; Chen, C.; Shen, H.; et al. Safety of Nanoparticles in Medicine. *Curr. Drug Targets* **2015**, *16*, 1671–1681. [CrossRef] [PubMed]
89. Kamila, S.; McEwan, C.; Costley, D.; Atchison, J.; Sheng, Y.; Hamilton, G.R.C.; Fowley, C.; Callan, J.F. Diagnostic and Therapeutic Applications of Quantum Dots in Nanomedicine. In *Topics in Current Chemistry*; Springer International Publishing: Cham, Switzerland, 2016; Volume 370, pp. 203–224.
90. Tripathi, S.K.; Kaur, G.; Khurana, R.K.; Kapoor, S.; Singh, B. Quantum Dots and their Potential Role in Cancer Theranostics. *Crit. Rev. Ther. Drug Carr. Syst.* **2015**, *32*, 461–502. [CrossRef] [PubMed]
91. Samia, A.C.S.; Dayal, S.; Burda, C. Quantum Dot-based Energy Transfer: Perspectives and Potential for Applications in Photodynamic Therapy. *Photochem. Photobiol.* **2006**, *82*, 617–625. [CrossRef]
92. Monroe, J.D.; Belekov, E.; Er, A.O.; Smith, M.E. Anticancer Photodynamic Therapy Properties of Sulfur-Doped Graphene Quantum Dot and Methylene Blue Preparations in MCF-7 Breast Cancer Cell Culture. *Photochem. Photobiol.* **2019**, *95*, 1473–1481. [CrossRef]
93. Nene, L.C.; Managa, M.E.; Oluwole, D.O.; Mafukidze, D.M.; Sindelo, A.; Nyokong, T. The photo-physicochemical properties and in vitro photodynamic therapy activity of differently substituted-zinc (II)-phthalocyanines and graphene quantum dots conjugates on MCF7 breast cancer cell line. *Inorganica Chim. Acta* **2019**, *488*, 304–311. [CrossRef]
94. Anas, A.; Akita, H.; Harashima, H.; Itoh, T.; Ishikawa, M.; Biju, V. Photosensitized breakage and damage of DNA by CdSe–ZnS quantum dots. *J. Phys. Chem. B* **2008**, *112*, 10005–10011. [CrossRef]
95. Kievit, F.M.; Zhang, M. Cancer nanotheranostics: Improving imaging and therapy by targeted delivery across biological barriers. *Adv. Mater.* **2011**, *23*, H217–H247. [CrossRef]
96. Yong, K.-T.; Ding, H.; Roy, I.; Law, W.-C.; Bergey, E.J.; Maitra, A.; Prasad, P.N. Imaging Pancreatic Cancer Using Bioconjugated InP Quantum Dots. *ACS Nano* **2009**, *3*, 502–510. [CrossRef] [PubMed]
97. Bilan, R.; Nabiev, I.; Sukhanova, A. Quantum Dot-Based Nanotools for Bioimaging, Diagnostics, and Drug Delivery. *ChemBioChem* **2016**, *17*, 2103–2114. [CrossRef]
98. Weng, K.C.; Noble, C.O.; Papahadjopoulos-Sternberg, B.; Chen, F.F.; Drummond, D.C.; Kirpotin, D.B.; Wang, D.; Hom, Y.K.; Hann, B.; Park, J.W. Targeted tumor cell internalization and imaging of multifunctional quantum dot-conjugated immunoliposomes in vitro and in vivo. *Nano Lett.* **2008**, *8*, 2851–2857. [CrossRef]
99. Zrazhevskiy, P.; Sena, M.; Gao, X. Designing multifunctional quantum dots for bioimaging, detection, and drug delivery. *Chem. Soc. Rev.* **2010**, *39*, 4326–4354. [CrossRef] [PubMed]
100. Mai, W.X.; Meng, H. Mesoporous silica nanoparticles: A multifunctional nano therapeutic system. *Integr. Biol.* **2013**, *5*, 19–28. [CrossRef] [PubMed]
101. Chen, Y.-C.; Huang, X.-C.; Luo, Y.-L.; Chang, Y.-C.; Hsieh, Y.-Z.; Hsu, H.-Y. Non-metallic nanomaterials in cancer theranostics: A review of silica- and carbon-based drug delivery systems. *Sci. Technol. Adv. Mater.* **2013**, *14*, 044407. [CrossRef] [PubMed]
102. Brevet, D.; Gary-Bobo, M.; Raehm, L.; Richeter, S.; Hocine, O.; Amro, K.; Loock, B.; Couleaud, P.; Frochot, C.; Morère, A.; et al. Mannose-targeted mesoporous silica nanoparticles for photodynamic therapy. *Chem. Commun.* **2009**, 1475–1477. [CrossRef] [PubMed]
103. Zou, Q.; Zhao, H.; Zhao, Y.; Fang, Y.; Chen, D.; Ren, J.; Wang, X.; Wang, Y.; Gu, Y.; Wu, F. Effective Two-Photon Excited Photodynamic Therapy of Xenograft Tumors Sensitized by Water-Soluble Bis(arylidene)cycloalkanone Photosensitizers. *J. Med. Chem.* **2015**, *58*, 7949–7958. [CrossRef] [PubMed]
104. Pawlicki, M.; Collins, H.A.; Denning, R.G.; Anderson, H.L. Two-Photon Absorption and the Design of Two-Photon Dyes. *Angew. Chem. Int. Ed.* **2009**, *48*, 3244–3266. [CrossRef] [PubMed]
105. Shanmugam, V.; Selvakumar, S.; Yeh, C.-S. Near-infrared light-responsive nanomaterials in cancer therapeutics. *Chem. Soc. Rev.* **2014**, *43*, 6254–6287. [CrossRef]
106. Starkey, J.R.; Rebane, A.K.; Drobizhev, M.A.; Meng, F.; Gong, A.; Elliott, A.; McInnerney, K.; Spangler, C.W. New Two-Photon Activated Photodynamic Therapy Sensitizers Induce Xenograft Tumor Regressions after Near-IR Laser Treatment through the Body of the Host Mouse. *Clin. Cancer Res.* **2008**, *14*, 6564–6573. [CrossRef] [PubMed]
107. Shen, X.; Li, S.; Li, L.; Yao, S.Q.; Xu, Q.H. Highly Efficient, Conjugated-Polymer-Based Nano-Photosensitizers for Selectively Targeted Two-Photon Photodynamic Therapy and Imaging of Cancer Cells. *Chem. Eur. J.* **2015**, *21*, 2214–2221. [CrossRef] [PubMed]
108. Qian, J.; Wang, D.; Cai, F.; Zhan, Q.; Wang, Y.; He, S. Photosensitizer encapsulated organically modified silica nanoparticles for direct two-photon photodynamic therapy and In Vivo functional imaging. *Biomaterials* **2012**, *33*, 4851–4860. [CrossRef] [PubMed]
109. Park, Y.I.; Lee, K.T.; Suh, Y.D.; Hyeon, T. Upconverting nanoparticles: A versatile platform for wide-field two-photon microscopy and multi-modal in vivo imaging. *Chem. Soc. Rev.* **2015**, *44*, 1302–1317. [CrossRef] [PubMed]
110. Shen, Y.; Shuhendler, A.J.; Ye, D.; Xu, J.-J.; Chen, H.-Y. Two-photon excitation nanoparticles for photodynamic therapy. *Chem. Soc. Rev.* **2016**, *45*, 6725–6741. [CrossRef] [PubMed]

111. Denk, W.; Strickler, J.H.; Webb, W.W. Two-photon laser scanning fluorescence microscopy. *Science* **1990**, *248*, 73–76. [CrossRef]
112. Secret, E.; Maynadier, M.; Gallud, A.; Chaix, A.; Bouffard, E.; Gary-Bobo, M.; Marcotte, N.; Mongin, O.; El Cheikh, K.; Hugues, V.; et al. Two-Photon Excitation of Porphyrin-Functionalized Porous Silicon Nanoparticles for Photodynamic Therapy. *Adv. Mater.* **2014**, *26*, 7643–7648. [CrossRef]
113. Park, J.-H.; Gu, L.; Von Maltzahn, G.; Ruoslahti, E.; Bhatia, S.N.; Sailor, M.J. Biodegradable luminescent porous silicon nanoparticles for in vivo applications. *Nat. Mater.* **2009**, *8*, 331–336. [CrossRef] [PubMed]
114. Cao, B.; Yang, M.; Zhu, Y.; Qu, X.; Mao, C. Stem Cells Loaded with Nanoparticles as a Drug Carrier for In Vivo Breast Cancer Therapy. *Adv. Mater.* **2014**, *26*, 4627–4631. [CrossRef]
115. Kidd, S.; Spaeth, E.; Dembinski, J.L.; Dietrich, M.; Watson, K.; Klopp, A.; Battula, V.L.; Weil, M.; Andreeff, M.; Marini, F.C. Direct Evidence of Mesenchymal Stem Cell Tropism for Tumor and Wounding Microenvironments Using In Vivo Bioluminescent Imaging. *Stem Cells* **2009**, *27*, 2614–2623. [CrossRef]
116. Ren, Y.-J.; Zhang, H.; Huang, H.; Wang, X.-M.; Zhou, Z.-Y.; Cui, F.-Z.; An, Y.-H. In vitro behavior of neural stem cells in response to different chemical functional groups. *Biomater.* **2009**, *30*, 1036–1044. [CrossRef]
117. Zhu, H.; Cao, B.; Zhen, Z.; Laxmi, A.A.; Li, D.; Liu, S.; Mao, C. Controlled growth and differentiation of MSCs on grooved films assembled from monodisperse biological nanofibers with genetically tunable surface chemistries. *Biomater.* **2011**, *32*, 4744–4752. [CrossRef] [PubMed]
118. Sonabend, A.M.; Ulasov, I.V.; Tyler, M.A.; Rivera, A.A.; Mathis, J.M.; Lesniak, M.S. Mesenchymal Stem Cells Effectively Deliver an Oncolytic Adenovirus to Intracranial Glioma. *STEM CELLS* **2008**, *26*, 831–841. [CrossRef] [PubMed]
119. Bharathiraja, S.; Moorthy, M.S.; Manivasagan, P.; Seo, H.; Lee, K.D.; Oh, J. Chlorin e6 conjugated silica nanoparticles for targeted and effective photodynamic therapy. *Photodiagn. Photodyn. Ther.* **2017**, *19*, 212–220. [CrossRef]
120. Yuan, A.; Wu, J.; Tang, X.; Zhao, L.; Xu, F.; Hu, Y. Application of Near-Infrared Dyes for Tumor Imaging, Photothermal, and Photodynamic Therapies. *J. Pharm. Sci.* **2013**, *102*, 6–28. [CrossRef] [PubMed]
121. Ntziachristos, V.; Bremer, C.; Weissleder, R. Fluorescence imaging with near-infrared light: New technological advances that enable in vivo molecular imaging. *Eur. Radiol.* **2003**, *13*, 195–208. [CrossRef] [PubMed]
122. Hu, J.; Tang, Y.; Elmenoufy, A.H.; Xu, H.; Cheng, Z.; Yang, X. Nanocomposite-Based Photodynamic Therapy Strategies for Deep Tumor Treatment. *Small* **2015**, *11*, 5860–5887. [CrossRef] [PubMed]
123. Bulin, A.-L.; Truillet, C.; Chouikrat, R.; Lux, F.; Frochot, C.; Amans, D.; LeDoux, G.; Tillement, O.; Perriat, P.; Barberi-Heyob, M.; et al. X-ray-Induced Singlet Oxygen Activation with Nanoscintillator-Coupled Porphyrins. *J. Phys. Chem. C* **2013**, *117*, 21583–21589. [CrossRef]
124. Chen, H.; Wang, G.D.; Chuang, Y.-J.; Zhen, Z.; Chen, X.; Biddinger, P.; Hao, Z.; Liu, F.; Shen, B.; Pan, Z. Nanoscintilla-tor-mediated X-ray inducible photodynamic therapy for in vivo cancer treatment. *Nano Lett.* **2015**, *15*, 2249–2256. [CrossRef]
125. Kaščáková, S.; Giuliani, A.; Lacerda, S.; Pallier, A.; Mercère, P.; Tóth, É.; Réfrégiers, M. X-ray-induced radiophotodynamic therapy (RPDT) using lanthanide micelles: Beyond depth limitations. *Nano Res.* **2015**, *8*, 2373–2379. [CrossRef]
126. Sengar, P.; Juárez, P.; Verdugo-Meza, A.; Arellano, D.L.; Jain, A.; Chauhan, K.; Hirata, G.A.; Fournier, P.G.J. Development of a functionalized UV-emitting nanocomposite for the treatment of cancer using indirect photodynamic therapy. *J. Nanobiotechnol.* **2018**, *16*, 1–19. [CrossRef] [PubMed]
127. Ramimoghadam, D.; Bagheri, S.; Abd Hamid, S.B. Biotemplated synthesis of anatase titanium dioxide nanoparticles via lignocellulosic waste material. *BioMed Res. Int.* **2014**, *2014*, 1–7. [CrossRef]
128. Kitsiou, P.; Lagopati, N.; Tsilibary, E.-P.; Falaras, P.; Papazafiri, P.; Pavlatou, E.P.; Kotsopoulou, E. Effect of nanostructured TiO<sub>2</sub> crystal phase on photoinduced apoptosis of breast cancer epithelial cells. *Int. J. Nanomed.* **2014**, *9*, 3219–3230. [CrossRef] [PubMed]
129. Gangopadhyay, M.; Mukhopadhyay, S.K.; Karthik, S.; Barman, S.; Singh, N.D.P. Targeted photoresponsive TiO<sub>2</sub>-coumarin nanoconjugate for efficient combination therapy in MDA-MB-231 breast cancer cells: Synergic effect of photodynamic therapy (PDT) and anticancer drug chlorambucil. *MedChemComm* **2015**, *6*, 769–777. [CrossRef]
130. Zholobak, N.; Ivanov, V.; Shcherbakov, A.; Shaporev, A.; Polezhaeva, O.; Baranchikov, A.; Spivak, N.; Tretyakov, Y. UV-shielding property, photocatalytic activity and photocytotoxicity of ceria colloid solutions. *J. Photochem. Photobiol. B: Biol.* **2011**, *102*, 32–38. [CrossRef] [PubMed]
131. Asati, A.; Santra, S.; Kaittanis, C.; Nath, S.; Perez, J.M. Oxidase-Like Activity of Polymer-Coated Cerium Oxide Nanoparticles. *Angew. Chem. Int. Ed.* **2009**, *48*, 2308–2312. [CrossRef] [PubMed]
132. Culcasi, M.; Benameur, L.; Mercier, A.; Lucchesi, C.; Rahmouni, H.; Asteian, A.; Casano, G.; Botta, A.; Kovacic, H.; Pietri, S. EPR spin trapping evaluation of ROS production in human fibroblasts exposed to cerium oxide nanoparticles: Evidence for NADPH oxidase and mitochondrial stimulation. *Chem.-Biol. Interact.* **2012**, *199*, 161–176. [CrossRef] [PubMed]
133. RajeshKumar, S.; Naik, P. Synthesis and biomedical applications of Cerium oxide nanoparticles—A Review. *Biotechnol. Rep.* **2018**, *17*, 1–5. [CrossRef] [PubMed]
134. Li, H.; Liu, C.; Zeng, Y.-P.; Hao, Y.-H.; Huang, J.-W.; Yang, Z.-Y.; Li, R. Nanoceria-mediated drug delivery for targeted photodynamic therapy on drug-resistant breast cancer. *ACS Appl. Mater. Interfaces* **2016**, *8*, 31510–31523. [CrossRef]
135. Vanneman, M.; Dranoff, G. Combining immunotherapy and targeted therapies in cancer treatment. *Nat. Rev. Cancer* **2012**, *12*, 237–251. [CrossRef] [PubMed]
136. Couzin-Frankel, J. Cancer Immunotherapy. *Science* **2013**, *342*, 1432–1433. [CrossRef]



137. Rooney, M.S.; Shukla, S.A.; Wu, C.J.; Getz, G.; Hacohen, N. Molecular and Genetic Properties of Tumors Associated with Local Immune Cytolytic Activity. *Cell* **2015**, *160*, 48–61. [CrossRef] [PubMed]
138. Schumacher, T.N.; Schreiber, R.D. Neoantigens in cancer immunotherapy. *Science* **2015**, *348*, 69–74. [CrossRef]
139. Duan, X.; Chan, C.; Guo, N.; Han, W.; Weichselbaum, R.R.; Lin, W. Photodynamic Therapy Mediated by Nontoxic Core–Shell Nanoparticles Synergizes with Immune Checkpoint Blockade To Elicit Antitumor Immunity and Antimetastatic Effect on Breast Cancer. *J. Am. Chem. Soc.* **2016**, *138*, 16686–16695. [CrossRef] [PubMed]
140. Wang, F.; Banerjee, D.; Liu, Y.; Chen, X.; Liu, X. Upconversion nanoparticles in biological labeling, imaging, and therapy. *Analyst* **2010**, *135*, 1839–1854. [CrossRef] [PubMed]
141. Mader, H.S.; Kele, P.; Saleh, S.M.; Wolfbeis, O.S. Upconverting luminescent nanoparticles for use in bioconjugation and bioimaging. *Curr. Opin. Chem. Biol.* **2010**, *14*, 582–596. [CrossRef]
142. Wang, B.-Y.; Liao, M.-L.; Hong, G.-C.; Chang, W.-W.; Chu, C.-C. Near-Infrared-Triggered Photodynamic Therapy toward Breast Cancer Cells Using Dendrimer-Functionalized Upconversion Nanoparticles. *Nanomaterials* **2017**, *7*, 269. [CrossRef] [PubMed]
143. Zeng, L.; Pan, Y.; Zou, R.; Zhang, J.; Tian, Y.; Teng, Z.; Wang, S.; Ren, W.; Xiao, X.; Zhang, L.; et al. 808 nm-excited upconversion nanoprobe with low heating effect for targeted magnetic resonance imaging and high-efficacy photodynamic therapy in HER2-overexpressed breast cancer. *Biomaterials* **2016**, *103*, 116–127. [CrossRef] [PubMed]
144. Cai, R.; Hashimoto, K.; Itoh, K.; Kubota, Y.; Fujishima, A. Photokilling of Malignant Cells with Ultrafine TiO<sub>2</sub> Powder. *Bull. Chem. Soc. Jpn.* **1991**, *64*, 1268–1273. [CrossRef]
145. Wang, K.; Qin Cheng, W.; Wang, F.; Bai, S.; Li, S.; Li, Z. Coating a N-doped TiO<sub>2</sub> shell on dually sensitized upconversion nanocrystals to provide NIR-enhanced photocatalysts for efficient utilization of upconverted emissions. *Inorg. Chem. Front.* **2016**, *3*, 1190–1197. [CrossRef]
146. Fujishima, A.; Honda, K. Electrochemical Photolysis of Water at a Semiconductor Electrode. *Nat. Cell Biol.* **1972**, *238*, 37–38. [CrossRef] [PubMed]
147. Zeng, L.; Pan, Y.; Tian, Y.; Wang, X.; Ren, W.; Wang, S.; Lu, G.; Wu, A. Doxorubicin-loaded NaYF<sub>4</sub>:Yb/Tm–TiO<sub>2</sub> inorganic photosensitizers for NIR-triggered photodynamic therapy and enhanced chemotherapy in drug-resistant breast cancers. *Biomaterials* **2015**, *57*, 93–106. [CrossRef]
148. Yu, Z.; Ge, Y.; Sun, Q.; Pan, W.; Wan, X.; Li, N.; Tang, B. A pre-protective strategy for precise tumor targeting and efficient photodynamic therapy with a switchable DNA/upconversion nanocomposite. *Chem. Sci.* **2018**, *9*, 3563–3569. [CrossRef]
149. Blanco, E.; Shen, H.; Ferrari, M. Principles of nanoparticle design for overcoming biological barriers to drug delivery. *Nat. Biotechnol.* **2015**, *33*, 941–951. [CrossRef]
150. Kettiger, H.; Schipanski, A.; Wick, P.; Huwyler, J. Engineered nanomaterial uptake and tissue distribution: From cell to organism. *Int. J. Nanomed.* **2013**, *8*, 3255.
151. Yu, Z.; Xia, Y.; Xing, J.; Li, Z.; Zhen, J.; Jin, Y.; Tian, Y.; Liu, C.; Jiang, Z.; Li, J. Y 1-receptor–ligand-functionalized ultrasmall up-conversion nanoparticles for tumor-targeted trimodality imaging and photodynamic therapy with low toxicity. *Nanoscale* **2018**, *10*, 17038–17052. [CrossRef] [PubMed]
152. Ramírez-García, G.; Panikar, S.S.; López-Luke, T.; Piazza, V.; Honorato-Colin, M.A.; Camacho-Villegas, T.; Hernández-Gutiérrez, R.; De La Rosa-Cruz, E. An immunconjugated up-conversion nanocomplex for selective imaging and photodynamic therapy against HER2-positive breast cancer. *Nanoscale* **2018**, *10*, 10154–10165. [CrossRef]
153. Ramírez-García, G.; De la Rosa, E.; López-Luke, T.; Panikar, S.S.; Salas, P. Controlling trapping states on selective theranostic core@ shell (NaYF<sub>4</sub>:Yb,Tm@TiO<sub>2</sub>-ZrO<sub>2</sub>) nanocomplexes for enhanced NIR-activated photodynamic therapy against breast cancer cells. *Dalton Trans.* **2019**, *48*, 9962–9973. [CrossRef]
154. Pirzada, B.M.; Mir, N.A.; Qutub, N.; Mehraj, O.; Sabir, S.; Muneer, M. Synthesis, characterization and optimization of photocatalytic activity of TiO<sub>2</sub>/ZrO<sub>2</sub> nanocomposite heterostructures. *Mater. Sci. Eng. B* **2015**, *193*, 137–145. [CrossRef]
155. Xu, A.-W.; Gao, Y.; Liu, H.-Q. The Preparation, Characterization, and their Photocatalytic Activities of Rare-Earth-Doped TiO<sub>2</sub> Nanoparticles. *J. Catal.* **2002**, *207*, 151–157. [CrossRef]
156. Feng, Y.; Wu, Y.; Zuo, J.; Tu, L.; Que, I.; Chang, Y.; Cruz, L.J.; Chan, A.; Zhang, H. Assembly of upconversion nanophoto-sensitizer in vivo to achieve scatheless real-time imaging and selective photodynamic therapy. *Biomaterials* **2019**, *201*, 33–41. [CrossRef] [PubMed]
157. Guo, Y.; Kumar, M.; Zhang, P. Nanoparticle-Based Photosensitizers under CW Infrared Excitation. *Chem. Mater.* **2007**, *19*, 6071–6072. [CrossRef] [PubMed]
158. Lucky, S.S.; Soo, K.C.; Zhang, Y. Nanoparticles in Photodynamic Therapy. *Chem. Rev.* **2015**, *115*, 1990–2042. [CrossRef] [PubMed]
159. Huang, Y.-Y.; Sharma, S.K.; Dai, T.; Chung, H.; Yaroslavsky, A.; Garcia-Diaz, M.; Chang, J.; Chiang, L.Y.; Hamblin, M.R. Can nanotechnology potentiate photodynamic therapy? *Nanotechnol. Rev.* **2012**, *1*, 111–146. [CrossRef] [PubMed]



Review

# Cell-Penetrating Peptides: Applications in Tumor Diagnosis and Therapeutics

Jeffrey Stiltner, Kayla McCandless and Maliha Zahid \*

Rangos Research Center, Department of Developmental Biology, University of Pittsburgh School of Medicine, 530 45th Street, Pittsburgh, PA 15201, USA; JES362@pitt.edu (J.S.); KAM514@pitt.edu (K.M.)

\* Correspondence: maz7@pitt.edu; Tel.: +1-412-692-8893; Fax: 412-692-6184

**Abstract:** Since their identification over twenty-five years ago, the plethora of cell-penetrating peptides (CPP) and their applications has skyrocketed. These 5 to 30 amino acid in length peptides have the unique property of breaching the cell membrane barrier while carrying cargoes larger than themselves into cells in an intact, functional form. CPPs can be conjugated to fluorophores, activatable probes, radioisotopes or contrast agents for imaging tissues, such as tumors. There is no singular mechanism for translocation of CPPs into a cell, and therefore, many CPPs are taken up by a multitude of cell types, creating the challenge of tumor-specific translocation and hindering clinical effectiveness. Varying strategies have been developed to combat this issue and enhance their diagnostic potential by derivatizing CPPs for better targeting by constructing specific cell-activated forms. These methods are currently being used to image integrin-expressing tumors, breast cancer cells, human histiocytic lymphoma and protease-secreting fibrosarcoma cells, to name a few. Additionally, identifying safe, effective therapeutics for malignant tumors has long been an active area of research. CPPs can circumvent many of the complications found in treating cancer with conventional therapeutics by targeted delivery of drugs into tumors, thereby decreasing off-target side effects, a feat not achievable by currently employed conventional chemotherapeutics. Myriad types of chemotherapeutics such as tyrosine kinase inhibitors, antitumor antibodies and nanoparticles can be functionally attached to these peptides, leading to the possibility of delivering established and novel cancer therapeutics directly to tumor tissue. While much research is needed to overcome potential issues with these peptides, they offer a significant advancement over current mechanisms to treat cancer. In this review, we present a brief overview of the research, leading to identification of CPPs with a comprehensive state-of-the-art review on the role of these novel peptides in both cancer diagnostics as well as therapeutics.

**Citation:** Stiltner, J.; McCandless, K.; Zahid, M. Cell-Penetrating Peptides: Applications in Tumor Diagnosis and Therapeutics. *Pharmaceutics* **2021**, *13*, 890. <https://doi.org/10.3390/pharmaceutics13060890>

Academic Editor: Hassan Bousbaa

Received: 19 May 2021

Accepted: 9 June 2021

Published: 15 June 2021

**Keywords:** cell-penetrating peptides; protein transduction domains; tumor imaging; targeted therapies

**Publisher's Note:** MDPI stays neutral with regard to jurisdictional claims in published maps and institutional affiliations.



**Copyright:** © 2021 by the authors. Licensee MDPI, Basel, Switzerland. This article is an open access article distributed under the terms and conditions of the Creative Commons Attribution (CC BY) license (<https://creativecommons.org/licenses/by/4.0/>).

## 1. Introduction

As so often happens in science, the discovery of cell-penetrating peptides (CPP) was a serendipitous one. Two independent groups of researchers working on the human immunodeficiency virus (HIV) viral coat Trans-activator of Transcription (Tat) protein observed the protein's ability to cross cell membrane barriers without any transfection reagents [1,2]. Similarly, the homeobox Antennapedia (Antp) transcription factor of *Drosophila melanogaster* was demonstrated to enter nerve cells in a receptor-independent manner, where it could then regulate neural morphogenesis [3]. Further mapping studies of the domains within Tat and Antp responsible for the observed transduction led to the identification of the first two CPPs: the 11 amino acid cationic, arginine- and lysine-rich domain of Tat protein (YGRKKR-RQRRR) [4] and the 16 amino acid sequence from the third helix of the Antennapedia domain (RQIKIWFQNRRMKWKK) termed Antp, also known as penetratin [5]. The next big development in the field of CPPs came with the demonstration of Tat peptide's ability

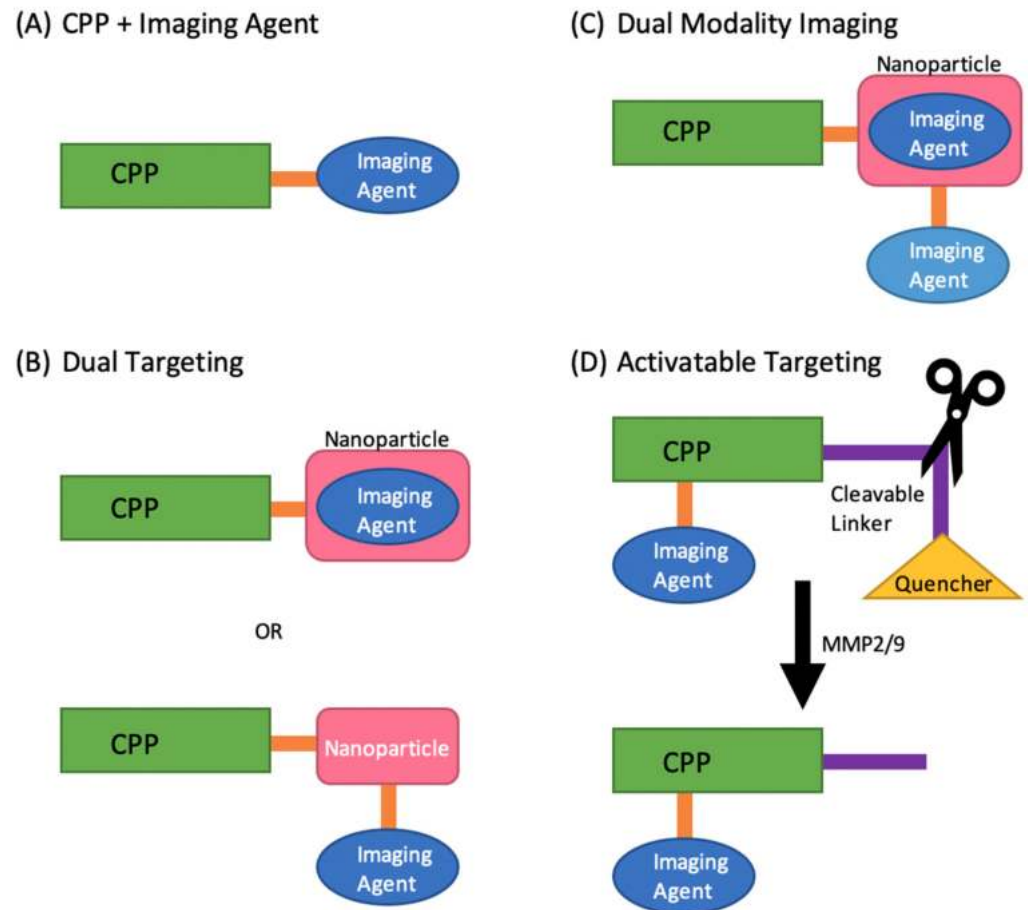
to cross cell membrane barriers while carrying cargo many times its size in a functional form [6]. Since this initial description, the plethora of CPPs has expanded exponentially. Although the first two CPPs identified were non-cell specific, researchers have utilized phage-display methodologies to identify multiple tissue-specific peptides. Phage display was a technique developed by Smith in 1985 [7], and for which he subsequently received the Nobel prize for chemistry in 2018 [8]. The technique of phage display was initially utilized to identify NRG and RGD motifs targeting tumor cells, and the utility of these peptides in delivering chemotherapeutic agents specifically to tumor vasculature was demonstrated [9]. Phage display has also been used to identify peptides targeting vascular endothelium [10], synovial tissue [11], dendritic cells [12], pancreatic islet cells [13] and cardiac myocytes [14]. Additionally, this list continues to grow every year. Hence, no one review article can do full justice to the entire breadth of CPPs, tissue and non-tissue selective, their myriad cargoes, and the number of disease conditions being tackled using them. Therefore, out of necessity, this review will be limited to tumor-homing CPPs, and utility of these in tumor imaging and tumor-specific therapeutics. Interested readers are referred to several recent comprehensive reviews on other uses of CPPs [15,16].

## 2. Cell-Penetrating Peptides as Tumor Imaging Agents

CPPs are a promising tool for tumor imaging due to their high binding affinity, small size, specific uptake, high stability, rapid clearance from non-specific targets, and retention in specific targets [17–21]. They can be conjugated to radioisotopes, fluorophore-labeled or activatable probes, nanoparticles (NPs), polymers, quantum dots, metal chelates, and other contrast agents in order to image tumors [22–27]. CPPs are able to carry, transport, and deliver these imaging agents, providing the imaging cargo with intracellular access and functionality. Since every CPP is different and has varying chemical properties due to differences in their amino acid sequence, each faces its own challenges. An additional layer of complexity comes from the cargo it carries as that too can affect the chemical properties. Therefore, it is always important to assess the shortcomings of each CPP individually and when loaded with its cargo [28,29]. Some challenges to using CPPs for tumor imaging include serum stability, immunogenicity, cytotoxicity, and endosomal entrapment [30,31]. There is also no singular mechanism for translocation of CPPs into a cell, and therefore many CPPs are taken up by a multitude of cell types, creating the challenge of tumor-specific translocation and hindering clinical effectiveness [32]. Various strategies are currently being developed to combat these issues and enhance tumor diagnostic imaging. Some examples include selecting CPPs for their targeting abilities or labeling CPPs with specific cell-activated constructs [33,34]. One of the strategies is to select CPPs to image cancer tissues by taking advantage of overexpression of integrins by tumors, as seen in breast cancer, human histiocytic lymphoma U937, HT-1080 human fibrosarcoma cells, and SCC-7 tumors, to name a few [35–37].

Non-tumor-targeting CPPs have nevertheless been used for imaging tumors. Although Tat cannot specifically target tumors, its stability in vivo and rapid translocation across cell membranes show promising abilities as peptide chelates and fluorophore conjugates to serve as imaging agents (Figure 1). One study labeled the Tat peptide with technetium-<sup>99m</sup> (<sup>99m</sup>Tc), one of the most common radioisotopes for medical imaging. The peptide was synthesized using two functional domains, the first being the non-cell-specific, membrane permeant portion of the Tat protein (Tat peptide), and the second domain using a peptide-based chelator for <sup>99m</sup>Tc ( $\epsilon$ -KGC). The [<sup>99m</sup>Tc]-Tat-peptide combination was imaged in mice using a gamma scintillation camera and, as expected, showed whole-body distribution [38]. Another study also used non-specific CPPs labeled with fluorophores instead of isotopes. The CPPs studied consisted of Tat, penetratin (Pen), or octa-arginine L-enantiomer (R8). Each CPP was synthesized with a cysteine or glycyl cysteine amide and labeled with Alexa660 at the C-terminus, injected into HeLa xenografted into nude mice and imaged using an IVIS Spectrum System. The accumulation of R8 in tumors was significantly higher than all other CPPs. Since the number of arginine residues affects

internalization efficiency, and D-enantiomers decrease degradation by proteases, the L- and D-forms of the oligoarginines (2, 8, 12, and 16 mers) were repeated. The results showed the D-isomer of R8 as having the highest accumulation in tumors. This study not only highlights CPPs as promising agents for tumor imaging, but also demonstrates how changes in peptide amino acid sequence and configuration can affect their physicochemical properties, leading to a CPP better suited to the task of imaging [39].



**Figure 1.** (A) CPP + imaging agent directly combines a specific or non-specific CPP with an imaging agent via a linker and/or conjugation. (B) Dual targeting combines a CPP with another target-specific component, such as a nanoparticle, via a linker and/or conjugation. An imaging agent can then be linked to the combination or embedded within a nanoparticle. (C) Dual-modality imaging combines a CPP with two imaging agents, allowing for different imaging methods. In this case, the imaging agents are attached via a linker and embedded within a nanoparticle. (D) Activatable targeting combines CPP and an imaging agent with a MMP2/9-cleavable linker and quencher for the imaging agent. The CPP can only be imaged when MMP2/9 are present to cleave off the quencher.

A separate strategy to enhance tumor targeting is by dual targeting. In this method, the CPP is conjugated with another agent to increase its targeting ability (Figure 1). Huang et al. synthesized linear RGERPPR (RGE) and cyclic-peptide CRGDRGPDC (cRGD) due to their demonstrated higher affinity for multiple tumor cell lines. The linear RGE and cRGD were conjugated to a lipid carrier in order to enhance cell uptake and tumor targeting. The lipid carrier was embedded with the fluorescent dye DiR for tumor imaging. MDA-MB-231 breast tumor xenograft mouse models were injected with the conjugate and imaged using a near-infrared fluorescence imaging system. The linear RGE conjugate showed the highest uptake and retention in tumors, making RGE and the CPP-NP combination promising tools for tumor imaging [40]. Another study used the CPP and NP dual targeting combination to target tumor cells, but with the addition of another imaging agent for dual-modality

imaging (Figure 1) (photoacoustic (PA) and MRI imaging). In this study, the CPP, F3 peptide, and NP, poly(lactic-co-glycolic acid) (PLGA), were used for their cell targeting and penetrating abilities, respectively. The sonosensitizer, methylene blue, was embedded in Gd-DTPA-BMA-linked-PLGA to combine the new imaging modality, PA, with the current clinical imaging modality MRI. MDA-MB-231 tumor-bearing mice were injected with the synthesized F3-PLGA@MB/Gd NP and evaluated using dual-imaging. The results showed that F3-PLGA@MB/Gd NP had the highest concentration in tumors compared to the non-targeted groups in both PA and MRI, most notably at 6 h post-injection. Again, this study highlights a promising CPP (F3) and CPP-NP combination for tumor imaging, demonstrating that there are multiple variations of CPPs and combinations that can be used to advance tumor imaging [41].

Another strategy to enhance tumor imaging is via use of activatable CPPs (ACPPs). In this method, the CPP contains a region which can penetrate cells and carry cargo (polycation), a region which can target metalloproteases-2 (MMP-2) and MMP-9 (protease-cleavable linker), and a region which quenches the function of the cell-penetrating region (polyanion). When activated by MMP-2 and MMP-9, the neutralizing region is cleaved and the CPP can enter the cell (Figure 1). Since MMP-2 and MMP-9 are over expressed in many cancer lines, the hypothesis was that ACPPs will preferentially target tumors over non-tumor tissues. A recent study used an ACPP labeled with Cy5 to target and image colorectal cancer. In vivo and ex vivo fluorescent imaging was performed using an IVIS imaging system in HCT-116 xenograft nude mice. The results showed that ACPP-Cy5 accumulated in tumors, and liver metastases, making it a promising imaging agent for detecting tumors as well as metastases [42]. Specific cargo can also be attached to ACPPs to enhance tumor targeting and imaging abilities. Macromolecules can increase circulation time and tumor uptake, decrease background noise through less glomerular and synovial filtration, amplify the amount of imaging agent on a single peptide, decrease toxicity, and allow for multimodality imaging. Olson et al. conjugated polyamidoamine dendrimer to the polycationic domain of an ACPP. Using Cy5 and Gd chelates allowed for dual labeling of the ACPP dendrimer combination for fluorescent and MRI imaging in tumor-bearing mice. The results showed better uptake and tumor specificity than previously reported results, once again illustrating the myriad ways in which CPPs can be altered and combined to improve tumor imaging [43].

### 3. Cell-Penetrating Peptides as Vectors for Targeted Drug Delivery to Tumors

Cancer is a leading cause of mortality globally, second only to cardiovascular diseases [44]. In 2017, cancer claimed the lives of nearly 10 million people worldwide [44]. As the average life expectancy, standard of living and access to healthcare increase, people are living longer lives, with consequently a shift in mortality rates from infectious diseases [45] to a rise in cancer-related mortality that is predicted to increase globally over the coming decades. Despite advancements in oncological research and medicine, conventional chemotherapeutics still have many limitations and deficiencies. One example is doxorubicin, a common chemotherapeutic agent, which suffers from poor tumor penetrance [46]. This poor penetration translates into deeper areas of the tumor not receiving adequate drug concentrations allowing cancer cells to remain viable and continue to mutate and proliferate [46]. A second issue is the high interstitial pressure present in tumors which blocks efficient delivery of drugs through transcapillary transport [47,48]. This elevated interstitial pressure causes a radially outward pressure away from the tumor, making access by chemotherapeutics through simple diffusion challenging [48]. Another issue is development of tumor resistance to chemotherapy over time [49], the mechanism of which is not well understood, but is thought to involve cancer stem cells playing a role, leading to tumor relapses [50]. Another issue with modern cancer drugs are the large doses needed due to lack of targeting specificity [51,52], which contributes substantially to toxicity and side effects, making chemotherapy poorly tolerated by patients [53].

Cell-penetrating peptides have shown great preclinical and clinical evidence overcoming many of the shortfalls of conventional chemotherapeutics. Multiple drugs have been attached to cell-penetrating peptides in preclinical research in an attempt to target tumors. Five classes in particular have shown great promise: conventional chemotherapeutics, pro-apoptotic peptides/proteins, NP formulated peptides, antitumor antibodies and siRNA. Co-administration of a cell-penetrating peptide with a tumor-targeting drug allowed the drug to penetrate into tumor's extravascular space in a tumor-specific and neuropilin-1-dependent manner [54]. Interestingly enough, peptide coadministration with a wide variety of tumor-targeting drugs, such as small molecule chemotherapeutics, NPs, and monoclonal antibodies, have all had their therapeutic indices increased as a result of this coadministration [54–56]. Thus, the increased tissue permeability seen with these tumor-targeting drugs co-administered with cell-penetrating peptides is a viable strategy for overcoming the poor penetration of currently available chemotherapeutics.

Another promising area of development in cell-penetrating peptides is their apparent ability to overcome drug resistance issues previously seen with modern anticancer drugs. iRGD is a cyclic 9 amino acid residue peptide that was identified using in vivo screening of phage display libraries in mice with tumors [54]. This peptide has unique tumor-homing abilities that has led it to be a candidate for antitumor drug delivery [54]. In one study, the peptide iRGD was administered with nab-paclitaxel, an albumin-bound form of paclitaxel, leading to effective treatment of a previously resistant breast cancer xenograft [54]. While an exact mechanism by which CPP co-administration reduces drug resistance is unknown, it is hypothesized that co-administration could result in drugs entering via endocytosis rather than by classical mechanisms through the cell membrane, resulting in a greater amount of cellular uptake of the chemotherapeutic [49,57]. Furthermore, due to the excellent targeting and transduction of drugs attached to CPPs, a lower systemic drug dose can be used so that the body's natural mechanisms that induce resistance are less of a factor [58]. Modern anticancer chemotherapeutics lack targeting specificity, which often results in side effects such as nausea, insomnia, bone marrow depression, fatigue, weakness, and many other adverse effects [59]. All malignant tumor masses contain certain molecular markers that are not expressed in normal cells or are expressed at significantly lower rates [60]. Receptors such as IL-11R $\alpha$ , GRP78, EphA5 have been found to be differentially overexpressed in tumor cells and thus make attractive candidates for targeting [61,62]. By coupling an anticancer drug to a targeting ligand for these receptors, the drug can effectively accumulate in the tumor, leading to greater therapeutic effect and fewer side effects [60,62].

Remarkably, recent research suggests that drug delivery with cell-penetrating peptides may also occur via a second general mechanism known as the bystander effect [63]. This pathway allows for co-administration of a drug payload without the drug actually being covalently attached to the cell-penetrating peptide [63]. The pathway involved in this bystander effect is known as the C-end Rule (CendR) pathway, which is an endocytic transport pathway related to but distinct from micropinocytosis [63]. iRGD has been shown to be the peptide that activates this pathway [63]. This peptide binds to a tumor-specific receptor, after which it is proteolytically cleaved and then binds to a second receptor, neuropilin-1, resulting in activation of the CendR pathway [63]. The endocytic vesicles that are formed in the CendR pathway are large and can contain and hence transport a large amount of extracellular fluid [63], including chemotherapeutic drugs present in the interstitium. This phenomenon of the CendR pathway explains why certain peptides can transport drug payloads that are simply co-administered with the peptide and not necessarily covalently attached to the peptide. Many preclinical trials have utilized iRGD and the CendR pathways to deliver anticancer drugs. In one study, a wide variety of anticancer drugs were co-administered with iRGD and all saw an increase in their therapeutic indices [54]. In another study, the anticancer effects of gemcitabine were enhanced in a murine pancreatic cancer model that overexpressed neuropilin-1 when co-administered with Irgd [64]. Similar results have been seen in studies examining gastric

cancers and hepatocellular carcinoma [65,66]. These successful preclinical trials that co-administered anticancer drugs with iRGD validate the CendR pathway and provide a basis for future clinical research.

Conventional chemotherapeutics have shown promise when attached to cell-penetrating peptides. Paclitaxel is a widely used chemotherapeutic. Paclitaxel can stop mitosis and cause cell death by binding to microtubules [67]. As mentioned earlier, many conventional chemotherapeutics, such as paclitaxel, have issues such as poor solubility, toxicity and acquired resistance. Conjugating paclitaxel to various cell-penetrating peptides has proven to be advantageous in minimizing these negative aspects and maximizing therapeutic effects [68–71]. Of particular interest is the recent work in attaching octa-arginine to the C2' position of paclitaxel via a disulfide linker [70,71]. When attached to octa-arginine, paclitaxel was able to overcome drug resistance, and increase solubility [70,71]. In mice with ovarian cancer the octa-arginine-paclitaxel conjugate had a 4.8-fold higher therapeutic response compared with paclitaxel alone [71]. Another commonly used chemotherapeutic, doxorubicin, has also shown promising results when attached to a CPP. Doxorubicin is a topoisomerase II inhibitor that has been used clinically to treat many types of cancer [72], but faces many of the same issues as paclitaxel. Doxorubicin has an intrinsic P-glycoprotein overexpression, which makes it particularly difficult to obtain effective therapeutic tumoral concentrations and can cause resistance [73,74]. In one study, a Tat–doxorubicin conjugate was designed and administered to resistant KB-V1 tumor cells. The results showed 86% of tumor cell cytotoxicity with the Tat–doxorubicin conjugate versus only 14% with doxorubicin alone [75].

Pro-apoptotic proteins have also shown preclinical promise when attached to CPPs particularly p53 [76–78]. 11 poly-arginine peptides (11R) have also been shown to suppress the proliferation of oral cancer [76]. The conjugate 11R–p53 suppressed activity of the p21/WAF promoter thus stopping the proliferation of cancer cells [76]. Further studies have shown that linking the polyarginine-p53 fusion protein to the NH<sub>2</sub>-terminal of a modified influenza virus subunit was able to inhibit the proliferation of bladder cancer [77,78]. Thus, p53 as a pro-apoptotic protein has shown great promise when attached to CPPs, leading to halting proliferation of many different types of cancer cells.

Monoclonal antibodies have long been used in medicine particularly in immunotherapy. However, one of the main concerns with using monoclonal antibodies in oncology has been the issues with cell penetration due to their large size (150 kDa) [79]. By attaching these antitumor antibodies to CPPs, studies have shown promise in overcoming this cell membrane barrier. The cell-penetrating antibody 3E10 recognizes and physically binds to the N-terminus of RAD51 subsequently sequestering it in the cytoplasm and preventing it from binding to DNA and causing damage leading to cancer [79]. Another cell-penetrating antibody, RT11, has been shown to be internalized and selectively bind to activated GTP-bound form of oncogenic Ras mutants which blocks downstream signaling of these mutants and prevents the proliferation of tumor cells [80]. Other research has shown great promise in designing cell-penetrating antibodies with high cell-specificity and high endosomal escape efficacy such as epCT65 which has great potential for medical applications such as cystolic delivery of drug payloads to tumors [80]. There are currently 12 FDA-approved antibodies used for treating cancer and despite their promise in preclinical research when attached to CPP, there are still issues with them such as solubility and intracellular stability [78].

Antibodies formulated with CPPs into NPs are another promising strategy since they have increased solubility and intracellular stability compared to antibodies alone [79,81]. CapG is part of the actin filament, often overexpressed in breast cancer, and is believed to play a role in tumor cell metastasis [82]. Attaching a nanoparticle that works against CapG to various CPPs has been shown to be an effective strategy in reducing breast cancer metastasis [81,82]. More recent research suggests that just the presence of NPs in addition to a CPP and antitumor drug enhances the effect of the latter [83]. One study showed that the delivery of a pro-apoptotic drug as part of a NP-CPP system increased antitumor

activity by a factor of 100–300 [83]. This system has shown incredible promise in treating glioblastoma in preclinical research [83]. Interestingly enough, attaching the CPP iRGD to NPs increased its antimetastatic activity as compared to when it is just used as a soluble peptide [78,84].

Small interfering RNA (siRNA) are non-coding RNAs that stop the expression of certain genes by degrading mRNA created during translation. This ultimately prevents ribosomes from translating the mRNAs into functional proteins [85–89]. SiRNAs have shown great potential at treating cancer, but their adaption in clinical settings has been slow due to a lack of safe and effective vehicle for delivery [85]. SiRNAs are intrinsically susceptible to degradation by enzymes, endosomal entrapment and poor cellular uptake [85–89]. Various types of delivery vehicles have been tested to deliver siRNA such as lipids, cationic polymers, inorganic materials and many others; however, synthetic polypeptides were shown to be the most effective [85]. CPPs have shown promise in preclinical research as safe and effective vehicles for siRNA to target tumors. Many peptides, such as CPP33, gh625, PD-L1, and PEG-SS-PEI, have been used in combination with siRNA to target various forms of cancer to great success in animal models [85–89]. Not only did these peptides coupled to siRNA increase the ability to enter tumor cells, but they helped aid in endosomal escape of the siRNAs once they were internalized into cells [85–89]. CPP33 loaded with siPLK1 (an siRNA to target A549 lung cancer cells) exhibited additional endosomal escape but also prolonged blood circulation, enhanced tumor accumulation and effective suppression of tumor growth [85]. Additionally, coupling siRNA to cell-penetrating peptides reduced the concentration of siRNA required to achieve reduction in tumor size [88]. These CPPs with their siRNA payloads have shown enhanced antitumor effects in multiple types of cancer in mice including lung, breast and liver cancers [85–89]. Thus, conjugating siRNAs to CPPs offers another promising avenue in clinical research for the overall treatment of cancer.

#### 4. Clinical Trials Using CPPs as Cancer Therapeutics

The authors currently know of ten clinical trials involving CPPs to treat cancer. This number is expected to increase as additional advancements are made in the arena of targeted cancer therapeutics. Of the ten clinical trials discussed in the table below (Table 1), six have completed at least Phase 1a and are continuing onto Phase 1b and Phase 2; the other four are in the process of recruiting and completing Phase 1. Aileron therapeutics appear to be a leader in innovation with their ALRN-6924 peptide that is being successfully employed in half of the clinical studies discussed below. ALRN-6924 is a CPP that disrupts interaction between p53 tumor suppressor protein and its inhibitors MDMX and MDM2 [90–94]. This peptide has been tested alone for safety and efficacy as well as combined to many anticancer drugs such as cytarabine, paclitaxel and topotecan [90–94]. Phase 1 clinical trials have shown that ALRN-6924 alone and in combination is safe and increases the therapeutic index of the covalently attached drugs [90–94]. ALRN-6924 is currently being employed in two clinical trials that are in Phase 2 and have shown promising results in cancer treatment including pediatric cases [93,94]. Another peptide currently in clinical trial is BT1718, designed to target and inhibit the function of MT1-MMP by recognizing and attaching itself to the MT1-MMP protein [95]. Once it is attached it is internalized into cancer cells [95]. P28 is another CPP being evaluated currently in two cancer clinical trials. It is derived from azurin and targets solid tumors that resist standard methods of treatment [96,97]. Both of these trials have completed Phase 1 and look promising at treating solid tumors resistant to conventional chemotherapeutics. PEP-010 is another peptide about to begin enrollment into a Phase I trial to assess its safety profile [98].



**Table 1.** Summary of various clinical trials utilizing CPPs in anticancer therapies.

Sponsor	ClinicalTrials.gov Identifier	Study Stage	CPP Employed	Cancer Targeted	Drug Employed with CPP	Study Size
Aileron Therapeutics [90]	NCT02264613	Phase 1—Completed Phase 2a—Completed	ALRN-6924	Solid tumor, lymphoma, and peripheral T-cell lymphoma	ALRN-6924—alone and in combination with palbociclib	149
Aileron Therapeutics [91]	NCT02909972	Phase 1—Completed	ALRN-6924	Acute myeloid leukemia, and advanced myelodysplastic syndrome	ALRN-6924—alone and in combination with cytarabine	55
Aileron Therapeutics [92]	NCT03725436	Phase 1	ALRN-6924	Advanced, metastatic or unresectable solid tumors	ALRN-6924—in combination with paclitaxel	45
Aileron Therapeutics [93]	NCT03654716	Phase 1	ALRN-6924	Pediatric leukemia, pediatric brain tumor, pediatric solid tumor, pediatric lymphoma	ALRN-6924—alone or in combination with cytarabine for patients with leukemia	69
Aileron Therapeutics [94]	NCT04022876	Phase 1a—Completed Phase 1b Phase 2	ALRN-6924	Small cell lung cancer	Phase 1b—ALRN-6924 with topotecan Phase 2—topotecan alone and in combination with ALRN-6924	120
Cancer Research UK [95]	NCT03486730	Phase 1 Phase 2	BT1718	Advanced solid tumors, non-small cell lung cancer, non-small cell lung sarcoma, and esophageal cancer	BT1718—alone	130
CDG Therapeutics and Dr. Tapas K. Das Gupta [96]	NCT00914914	Phase 1—Completed	P28	Refractory solid tumors	P28—alone	15
Pediatric Brain Tumor Consortium/National Cancer Institute (NCI) [97]	NCT01975116	Phase 1—Completed	P28	Recurrent or progressive central nervous system tumors	P28—alone	18
Institut Curie [98]	NCT04733027	Phase 1	PEP-010	Metastatic solid tumor cancer	PEP-010—alone PEP-010—in combination with paclitaxel	56
Amal Therapeutics [99]	NCT04046445	Phase 1a—Completed Phase 1b	ATP128	Stage IV colorectal cancer	ATP128—alone and in combination with BI 754091	32

## 5. Summary

Since their identification nearly twenty-five years ago, the number and applications of CPPs, both in the arena of tumor diagnostics and therapeutics, continue to grow at a brisk pace. Combining them as novel vectors for targeted delivery of both established and

emerging therapeutics has the potential to reduce drug doses, decrease tumor resistance and reduce off-target adverse effects that so often limit dosage of chemotherapeutics, as well as adversely affect patient quality of life. While the future of CPPs in medicine is promising, there are still many issues and challenges that need to be addressed to make their future in medicine feasible. One such challenge will be endosomal entrapment of the peptides; this could potentially be overcome by conjugating drugs or peptides to a peptide that causes endosomal lysis. Another issue to overcome is the human body's natural immune response and the body's generation of antibodies that target antitumor drugs. This could be overcome by delivering immunosuppressants with the peptide–drug combination, or finding ways to locally administer the conjugate. Finding a way to deliver peptides successfully to specific organelles within specific types of cells is another challenge. While CPPs have shown promise at delivering cargo to specific cell types, there needs to be more work on targeting specific organelles. One possible solution to this is to add organelle localization sequences to peptides as well as adding endosome-lytic peptides. Finally, proteases are also a concern as they could break down the peptide. This could be overcome by using the D-enantiomers of the amino acid forming the peptide or protecting the CPPs in liposomal or nanoparticle formulations. All of this goes to show that CPPs have immense potential in both cancer diagnostic and therapeutic applications; however, further research is needed for them to become truly efficacious in the field of oncology.

**Funding:** All authors are supported by an R01 grant HL153407 from the NHLBI awarded to M.Z.

**Institutional Review Board Statement:** Not applicable.

**Informed Consent Statement:** Not applicable.

**Conflicts of Interest:** The authors declare no conflict of interest.

**Disclosures:** The authors list no disclosures, nor relationships with industry in relationship to the presented work.

## References

1. Frankel, A.D.; Pabo, C.O. Cellular uptake of the tat protein from human immunodeficiency virus. *Cell* **1988**, *55*, 1189–1193. [CrossRef]
2. Green, M.; Loewenstein, P.M. Autonomous functional domains of chemically synthesized human immunodeficiency virus tat trans-activator protein. *Cell* **1988**, *55*, 1179–1188. [CrossRef]
3. Joliot, A.; Pernelle, C.; Deagostini-Bazin, H.; Prochiantz, A. Antennapedia homeobox peptide regulates neural morphogenesis. *Proc. Natl. Acad. Sci. USA* **1991**, *88*, 1864–1868. [CrossRef] [PubMed]
4. Green, M.; Ishino, M.; Loewenstein, P.M. Mutational analysis of HIV-1 Tat minimal domain peptides: Identification of trans-dominant mutants that suppress HIV-LTR-driven gene expression. *Cell* **1989**, *58*, 215–223. [CrossRef]
5. DeRossi, D.; Joliot, A.H.; Chassaing, G.; Prochiantz, A. The third helix of the Antennapedia homeodomain translocates through biological membranes. *J. Biol. Chem.* **1994**, *269*, 10444–10450. [CrossRef]
6. Schwarze, S.R.; Ho, A.; Vocero-Akbani, A.; Dowdy, S.F. In vivo protein transduction: Delivery of a biologically active protein into the mouse. *Science* **1999**, *285*, 1569–1572. [CrossRef] [PubMed]
7. Smith, G.P. Filamentous fusion phage: Novel expression vectors that display cloned antigens on the virion surface. *Science* **1985**, *228*, 1315–1317. [CrossRef]
8. Smith, G.P. Phage Display: Simple Evolution in a Petri Dish (Nobel Lecture). *Angew. Chem. Int. Ed. Engl.* **2019**, *58*, 14428–14437. [CrossRef]
9. Arap, W.; Pasqualini, R.; Ruoslahti, E. Cancer treatment by targeted drug delivery to tumor vasculature in a mouse model. *Science* **1998**, *279*, 377–380. [CrossRef]
10. Nicklin, S.; White, S.J.; Watkins, S.J.; Hawkins, R.E.; Baker, A.H. Selective Targeting of Gene Transfer to Vascular Endothelial Cells by Use of Peptides Isolated by Phage Display. *Circulation* **2000**, *102*, 231–237. [CrossRef]
11. Mi, Z.; Lu, X.; Mai, J.C.; Ng, B.G.; Wang, G.; Lechman, E.R.; Watkins, S.C.; Rabinowich, H.; Robbins, P.D. Identification of a synovial fibroblast-specific protein transduction domain for delivery of apoptotic agents to hyperplastic synovium. *Mol. Ther.* **2003**, *8*, 295–305. [CrossRef]
12. Chamarthy, S.P.; Jia, L.; Kovacs, J.R.; Anderson, K.R.; Shen, H.; Firestone, S.M.; Meng, W.S. Gene delivery to dendritic cells facilitated by a tumor necrosis factor alpha-competing peptide. *Mol. Immunol.* **2004**, *41*, 741–749. [CrossRef] [PubMed]

13. Rehman, K.K.; Bertera, S.; Bottino, R.; Balamurugan, A.N.; Mai, J.C.; Mi, Z.; Trucco, M.; Robbins, P.D. Protection of islets by in situ peptide-mediated transduction of the Ikappa B kinase inhibitor Nemo-binding domain peptide. *J. Biol. Chem.* **2003**, *278*, 9862–9868. [CrossRef] [PubMed]
14. Zahid, M.; Phillips, B.E.; Albers, S.M.; Giannoukakis, N.; Watkins, S.C.; Robbins, P.D. Identification of a Cardiac Specific Protein Transduction Domain by In Vivo Biopanning Using a M13 Phage Peptide Display Library in Mice. *PLoS ONE* **2010**, *5*, e12252. [CrossRef] [PubMed]
15. Taylor, R.E.; Zahid, M. Cell Penetrating Peptides, Novel Vectors for Gene Therapy. *Pharmaceutics* **2020**, *12*, 225. [CrossRef] [PubMed]
16. Zahid, M.; Robbins, P.D. Cell-type specific penetrating peptides: Therapeutic promises and challenges. *Molecules* **2015**, *20*, 13055–13070. [CrossRef] [PubMed]
17. Alves, I.D.; Bechara, C.; Walrant, A.; Zaltsman, Y.; Jiao, C.-Y.; Sagan, S. Relationships between Membrane Binding, Affinity and Cell Internalization Efficacy of a Cell-Penetrating Peptide: Penetratin as a Case Study. *PLoS ONE* **2011**, *6*, e24096. [CrossRef] [PubMed]
18. Ward, B.; Seal, B.L.; Brophy, C.M.; Panitch, A. Design of a bioactive cell-penetrating peptide: When a transduction domain does more than transduce. *J. Pept. Sci.* **2009**, *15*, 668–674. [CrossRef]
19. Rennert, R.; Wespe, C.; Beck-Sickinger, A.G.; Neundorff, I. Developing novel hCT derived cell-penetrating peptides with improved metabolic stability. *Biochim. Biophys. Acta Biomembr.* **2006**, *1758*, 347–354. [CrossRef]
20. Neundorff, I.; Rennert, R.; Franke, J.; Kozle, I.; Bergmann, R. Detailed Analysis Concerning the Biodistribution and Metabolism of Human Calcitonin-Derived Cell-Penetrating Peptides. *Bioconjugate Chem.* **2008**, *19*, 1596–1603. [CrossRef]
21. Lindgren, M.E.; Hällbrink, M.M.; Elmquist, A.M.; Langel, Ü. Passage of cell-penetrating peptides across a human epithelial cell layer in vitro. *Biochem. J.* **2004**, *377*, 69–76. [CrossRef]
22. Santra, S.; Yang, H.; Stanley, J.T.; Holloway, P.H.; Moudgil, B.M.; Walter, G.; Mericle, R.A. Rapid and effective labeling of brain tissue using TAT-conjugated CdS:Mn/ZnS quantum dots. *Chem. Commun.* **2005**, 3144–3146. [CrossRef]
23. Medintz, I.L.; Pons, T.; Delehanty, J.B.; Susumu, K.; Brunel, F.M.; Dawson, P.E.; Mattoussi, H. Intracellular Delivery of Quantum Dot–Protein Cargos Mediated by Cell Penetrating Peptides. *Bioconjugate Chem.* **2008**, *19*, 1785–1795. [CrossRef]
24. Zhang, K.; Fang, H.; Chen, Z.; Taylor, J.-S.A.; Wooley, K.L. Shape Effects of Nanoparticles Conjugated with Cell-Penetrating Peptides (HIV Tat PTD) on CHO Cell Uptake. *Bioconjugate Chem.* **2008**, *19*, 1880–1887. [CrossRef]
25. Böhmová, E.; Pola, R.; Pechar, M.; Parnica, J.; Machová, D.; Janoušková, O.; Etrych, T. Polymer Cancerostatics Containing Cell-Penetrating Peptides: Internalization Efficacy Depends on Peptide Type and Spacer Length. *Pharmaceutics* **2020**, *12*, 59. [CrossRef] [PubMed]
26. Boonyarattanakalin, S.; Athavankar, S.; Sun, Q.; Peterson, B.R. Synthesis of an artificial cell surface receptor that enables oligohistidine affinity tags to function as metal-dependent cell-penetrating peptides. *J. Am. Chem. Soc.* **2006**, *128*, 386–387. [CrossRef] [PubMed]
27. Jiao, C.-Y.; Delaroché, D.; Burlina, F.; Alves, I.; Chassaing, G.; Sagan, S. Translocation and Endocytosis for Cell-penetrating Peptide Internalization. *J. Biol. Chem.* **2009**, *284*, 33957–33965. [CrossRef] [PubMed]
28. Hällbrink, M.; Florén, A.; Elmquist, A.; Pooga, M.; Bartfai, T.; Langel, Ü. Cargo delivery kinetics of cell-penetrating peptides. *Biochim. Biophys. Acta Biomembr.* **2001**, *1515*, 101–109. [CrossRef]
29. Youngblood, D.S.; Hatlevig, S.A.; Hassinger, J.N.; Iversen, P.L.; Moulton, H.M. Stability of cell-penetrating peptide-morpholino oligomer conjugates in human serum and in cells. *Bioconjugate Chem.* **2007**, *18*, 50–60. [CrossRef] [PubMed]
30. Mäger, I.; Eiríksdóttir, E.; Langel, K.; El Andaloussi, S.; Langel, Ü. Assessing the uptake kinetics and internalization mechanisms of cell-penetrating peptides using a quenched fluorescence assay. *Biochim. Biophys. Acta Biomembr.* **2010**, *1798*, 338–343. [CrossRef]
31. Suhorutnsenko, J.; Oskolkov, N.; Arukuusk, P.; Kurrikoff, K.; Eriste, E.; Copolovici, D.-M.; Lange, U. Cell-penetrating peptides, Peptides, show no evidence of toxicity and immunogenicity in vitro and in vivo. *Bioconjugate Chem.* **2011**, *22*, 2255–2262. [CrossRef]
32. Richard, J.-P.; Melikov, K.; Vives, E.; Ramos, C.; Verbeure, B.; Gait, M.J.; Chernomordik, L.V.; Lebleu, B. Cell-penetrating Peptides: A reevaluation of the mechanism of cellular uptake. *J. Biol. Chem.* **2003**, *278*, 585–590. [CrossRef]
33. Sauter, M.; Strieker, M.; Kleist, C.; Wischnjow, A.; Daniel, V.; Altmann, A.; Haberkorn, U.; Mier, W. Improving antibody-based therapies by chemical engineering of antibodies with multimeric cell-penetrating peptides for elevated intracellular delivery. *J. Control Release* **2020**, *322*, 200–208. [CrossRef]
34. Jiang, T.; Olson, E.S.; Nguyen, Q.T.; Roy, M.; Jennings, P.A.; Tsien, R.Y. Tumor imaging by means of proteolytic activation of cell-penetrating peptides. *Proc. Natl. Acad. Sci. USA* **2004**, *101*, 17867–17872. [CrossRef] [PubMed]
35. Qi, X.-R.; Shi, N.-Q.; Gao, W.; Xiang, B. Enhancing cellular uptake of activable cell-penetrating peptide–doxorubicin conjugate by enzymatic cleavage. *Int. J. Nanomed.* **2012**, *7*, 1613–1621. [CrossRef]
36. Kolesinska, B.; Eyer, K.; Robinson, T. Interaction of beta(3) /beta(2) -peptides, consisting of Val-Ala-Leu segments, with POPC giant unilamellar vesicles (GUVs) and white blood cancer cells (U937)—A new type of cell-penetrating peptides, and a surprising chain-length dependence of their vesicle- and cell-lysing activity. *Chem. Biodivers.* **2015**, *12*, 697–732.
37. Qiu, W.-X.; Liu, L.-H.; Li, S.-Y.; Lei, Q.; Luo, G.-F.; Zhang, X.-Z. ACPI Conjugated Gold Nanorods as NanoplatforM for Dual Image Guided Activatable Photodynamic and Photothermal Combined Therapy In Vivo. *Small* **2017**, *13*. [CrossRef]
38. Polyakov, V.; Sharma, V.; Dahlheimer, J.L.; Pica, C.M.; Luker, G.D.; Piwnicka-Worms, D. Novel Tat-peptide chelates for direct transduction of technetium-99m and rhenium into human cells for imaging and radiotherapy. *Bioconjugate Chem.* **2000**, *11*, 762–771. [CrossRef] [PubMed]

39. Nakase, I.; Konishi, Y.; Ueda, M.; Saji, H.; Futaki, S. Accumulation of arginine-rich cell-penetrating peptides in tumors and the potential for anticancer drug delivery in vivo. *J. Control Release* **2012**, *159*, 181–188. [CrossRef] [PubMed]
40. Huang, R.; Li, J.; Kebebe, D.; Wu, Y.; Zhang, B.; Liu, Z. Cell penetrating peptides functionalized gambogic acid-nanostructured lipid carrier for cancer treatment. *Drug Deliv.* **2018**, *25*, 757–765. [CrossRef]
41. Li, Y.; Hao, L.; Liu, F.; Yin, L.; Yan, S.; Zhao, H.; Ding, X.; Guo, Y.; Cao, Y.; Li, P.; et al. Cell penetrating peptide-modified nanoparticles for tumor targeted imaging and synergistic effect of sonodynamic/HIFU therapy. *Int. J. Nanomed.* **2019**, *14*, 5875–5894. [CrossRef] [PubMed]
42. Zeng, Z.; Chen, J.; Luo, S.; Dong, J.; Hu, H.; Yang, Z.; Feng, X.; Liu, Y.; Liu, B.; Pan, G.; et al. Targeting and imaging colorectal cancer by activatable cell-penetrating peptides. *Am. J. Transl. Res.* **2020**, *12*, 1754–1766. [PubMed]
43. Olson, E.S.; Jiang, T.; Aguilera, T.A.; Nguyen, Q.T.; Ellies, L.G.; Scadeng, M.; Tsien, R.Y. Activatable cell penetrating peptides linked to nanoparticles as dual probes for in vivo fluorescence and MR imaging of proteases. *Proc. Natl. Acad. Sci. USA* **2010**, *107*, 4311–4316. [CrossRef]
44. Collaborators GBDCoD. Global, regional, and national age-sex specific mortality for 264 causes of death, 1980-2016: A systematic analysis for the Global Burden of Disease Study 2016. *Lancet* **2017**, *390*, 1151–1210. [CrossRef]
45. Ryerson, A.B.; Ehemann, C.R.; Altekruse, S.F.; Ward, J.W.; Jemal, A.; Sherman, R.L.; Henley, S.J.; Holtzman, D.; Lake, A.; Noone, A.-M.; et al. Annual Report to the Nation on the Status of Cancer, 1975-2012, featuring the increasing incidence of liver cancer. *Cancer* **2016**, *122*, 1312–1337. [CrossRef] [PubMed]
46. Primeau, A.J.; Rendon, A.; Hedley, D.; Lilge, L.; Tannock, I.F.; Koido, S.; Hara, E.; Homma, S.; Torii, A.; Toyama, Y.; et al. The Distribution of the Anticancer Drug Doxorubicin in Relation to Blood Vessels in Solid Tumors. *Clin. Cancer Res.* **2005**, *11*, 8782–8788. [CrossRef] [PubMed]
47. Jain, R.K.; Baxter, L.T. Mechanisms of heterogeneous distribution of monoclonal antibodies and other macromolecules in tumors: Significance of elevated interstitial pressure. *Cancer Res.* **1988**, *48*, 7022–7032. [PubMed]
48. Heldin, C.-H.; Rubin, K.; Pietras, K.; Östman, A. High interstitial fluid pressure—an obstacle in cancer therapy. *Nat. Rev. Cancer* **2004**, *4*, 806–813. [CrossRef] [PubMed]
49. Hu, C.M.; Zhang, L. Therapeutic nanoparticles to combat cancer drug resistance. *Curr. Drug Metab.* **2009**, *10*, 836–841. [CrossRef]
50. Zhao, J. Cancer stem cells and chemoresistance: The smartest survives the raid. *Pharmacol. Ther.* **2016**, *160*, 145–158. [CrossRef]
51. Parveen, S.; Sahoo, S.K. Polymeric nanoparticles for cancer therapy. *J. Drug Target.* **2008**, *16*, 108–123. [CrossRef]
52. Cho, K.; Wang, X.; Nie, S.; Chen, Z.; Shin, D.M. Therapeutic Nanoparticles for Drug Delivery in Cancer. *Clin. Cancer Res.* **2008**, *14*, 1310–1316. [CrossRef]
53. Szakács, G.; Paterson, J.K.; Ludwig, J.A.; Booth-Genthe, C.; Gottesman, M.M. Targeting multidrug resistance in cancer. *Nat. Rev. Drug Discov.* **2006**, *5*, 219–234. [CrossRef]
54. Sugahara, K.N.; Teesalu, T.; Karmali, P.P.; Kotamraju, V.R.; Agemy, L.; Greenwald, D.R.; Ruoslahti, E. Coadministration of a Tumor-Penetrating Peptide Enhances the Efficacy of Cancer Drugs. *Science* **2010**, *328*, 1031–1035. [CrossRef]
55. Khawli, L.A.; Hu, P.; Epstein, A.L. NHS76/PEP2, a Fully Human Vasopermeability-Enhancing Agent to Increase the Uptake and Efficacy of Cancer Chemotherapy. *Clin. Cancer Res.* **2005**, *11*, 3084–3093. [CrossRef]
56. Kinoshita, R.; Ishima, Y.; Chuang, V.T.G.; Nakamura, H.; Fang, J.; Watanabe, H.; Shimizu, T.; Okuhira, K.; Ishida, T.; Maeda, H.; et al. Improved anticancer effects of albumin-bound paclitaxel nanoparticle via augmentation of EPR effect and albumin-protein interactions using S-nitrosated human serum albumin dimer. *Biomaterials* **2017**, *140*, 162–169. [CrossRef]
57. Huwyler, J.; Cerletti, A.; Fricker, G.; Eberle, A.N.; Drewe, J. By-passing of P-glycoprotein Using Immunoliposomes. *J. Drug Target.* **2002**, *10*, 73–79. [CrossRef]
58. Greish, K. Enhanced permeability and retention of macromolecular drugs in solid tumors: A royal gate for targeted anticancer nanomedicines. *J. Drug Target.* **2007**, *15*, 457–464. [CrossRef] [PubMed]
59. Colagiuri, B.; Dhillon, H.; Butow, P.N.; Jansen, J.; Cox, K.; Jacquet, J. Does Assessing Patients’ Expectancies About Chemotherapy Side Effects Influence Their Occurrence? *J. Pain Symptom Manag.* **2013**, *46*, 275–281. [CrossRef] [PubMed]
60. Ruoslahti, E.; Bhatia, S.N.; Sailor, M.J. Targeting of drugs and nanoparticles to tumors. *J. Cell Biol.* **2010**, *188*, 759–768. [CrossRef] [PubMed]
61. Yao, V.J.; D’Angelo, S.; Butler, K.S.; Theron, C.; Smith, T.L.; Marchiò, S.; Gelovani, J.G.; Sidman, R.L.; Dobroff, A.S.; Brinker, C.J.; et al. Ligand-targeted theranostic nanomedicines against cancer. *J. Control Release* **2016**, *240*, 267–286. [CrossRef] [PubMed]
62. Ruoslahti, E. Peptides as Targeting Elements and Tissue Penetration Devices for Nanoparticles. *Adv. Mater.* **2012**, *24*, 3747–3756. [CrossRef] [PubMed]
63. Ruoslahti, E. Tumor penetrating peptides for improved drug delivery. *Adv. Drug Deliv. Rev.* **2017**, *110–111*, 3–12. [CrossRef]
64. Akashi, Y.; Oda, T.; Ohara, Y.; Miyamoto, R.; Kurokawa, T.; Hashimoto, S.; Enomoto, T.; Yamada, K.M.; Satake, M.; Ohkohchi, N. Anticancer effects of gemcitabine are enhanced by co-administered iRGD peptide in murine pancreatic cancer models that overexpressed neuropilin-1. *Br. J. Cancer* **2014**, *110*, 1481–1487. [CrossRef]
65. Sha, H.; Zou, Z.; Xin, K.; Bian, X.; Cai, X.; Lu, W.; Chen, J.; Chen, G.; Huang, L.; Blair, A.M.; et al. Tumor-penetrating peptide fused EGFR single-domain antibody enhances cancer drug penetration into 3D multicellular spheroids and facilitates effective gastric cancer therapy. *J. Control Release* **2015**, *200*, 188–200. [CrossRef]

66. Schmithals, C.; Köberle, V.; Korkusuz, H.; Pleli, T.; Kakoschky, B.; Augusto, E.A.; Ibrahim, A.A.; Arencibia, J.M.; Vafaizadeh, V.; Groner, B.; et al. Improving Drug Penetrability with iRGD Leverages the Therapeutic Response to Sorafenib and Doxorubicin in Hepatocellular Carcinoma. *Cancer Res.* **2015**, *75*, 3147–3154. [CrossRef] [PubMed]
67. Chipman, S.D.; Oldham, F.B.; Pezzoni, G.; Singer, J.W. Biological and clinical characterization of paclitaxel poliglumex (PPX, CT-2103), a macromolecular polymer–drug conjugate. *Int. J. Nanomed.* **2006**, *1*, 375–383. [CrossRef]
68. Gao, Y.; Kuang, Y.; Guo, Z.F.; Guo, Z.; Krauss, I.J.; Xu, B. Enzyme-instructed molecular self-assembly confers nanofibers and a supramolecular hydrogel of taxol derivative. *J. Am. Chem. Soc.* **2009**, *131*, 13576–13577. [CrossRef] [PubMed]
69. Tong, R.; Cheng, J. Drug-Initiated, Controlled Ring-Opening Polymerization for the Synthesis of Polymer-Drug Conjugates. *Macromolecules* **2012**, *45*, 2225–2232. [CrossRef]
70. Yin, Y.; Wu, X.; Yang, Z.; Zhao, J.; Wang, X.; Zhang, Q.; Yuan, M.; Xie, L.; Liu, H.; He, Q. The potential efficacy of R8-modified paclitaxel-loaded liposomes on pulmonary arterial hypertension. *Pharm. Res.* **2013**, *30*, 2050–2062. [CrossRef] [PubMed]
71. Dubikovskaya, E.A.; Thorne, S.H.; Pillow, T.H.; Contag, C.H.; Wender, P.A. Overcoming multidrug resistance of small-molecule therapeutics through conjugation with releasable octaarginine transporters. *Proc. Natl. Acad. Sci. USA* **2008**, *105*, 12128–12133. [CrossRef]
72. Hong, K.; Khwaja, A.; Liapi, E.; Torbenson, M.S.; Georgiades, C.S.; Geschwind, J.-F.H. New Intra-arterial Drug Delivery System for the Treatment of Liver Cancer: Preclinical Assessment in a Rabbit Model of Liver Cancer. *Clin. Cancer Res.* **2006**, *12*, 2563–2567. [CrossRef] [PubMed]
73. Gottesman, M.M.; Fojo, T.; Bates, S.E. Multidrug resistance in cancer: Role of ATP-dependent transporters. *Nat. Rev. Cancer* **2002**, *2*, 48–58. [CrossRef] [PubMed]
74. Goldstein, L.J.; Galski, H.; Fojo, A.; Willingham, M.; Lai, S.L.; Gazdar, A.; Pirker, R.; Green, A.; Crist, W.; Brodeur, G.M.; et al. Expression of a multidrug resistance gene in human cancers. *J. Natl. Cancer Inst.* **1989**, *81*, 116–124. [CrossRef] [PubMed]
75. Zhang, P.; Cheetham, A.G.; Lock, L.L.; Cui, H. Cellular Uptake and Cytotoxicity of Drug–Peptide Conjugates Regulated by Conjugation Site. *Bioconjugate Chem.* **2013**, *24*, 604–613. [CrossRef]
76. Takenobu, T.; Tomizawa, K.; Matsushita, M.; Li, S.-T.; Moriwaki, A.; Lu, Y.-F.; Matsui, H. Development of p53 protein transduction therapy using membrane-permeable peptides and the application to oral cancer cells. *Mol. Cancer Ther.* **2002**, *1*, 1043–1049. [PubMed]
77. Michiue, H.; Tomizawa, K.; Wei, F.-Y.; Matsushita, M.; Lu, Y.-F.; Ichikawa, T.; Tamiya, T.; Date, I.; Matsui, H. The NH<sub>2</sub> Terminus of Influenza Virus Hemagglutinin-2 Subunit Peptides Enhances the Antitumor Potency of Polyarginine-mediated p53 Protein Transduction. *J. Biol. Chem.* **2005**, *280*, 8285–8289. [CrossRef]
78. Jauset, T.; Beaulieu, M.E. Bioactive cell penetrating peptides and proteins in cancer: A bright future ahead. *Curr. Opin. Pharmacol.* **2019**, *47*, 133–140. [CrossRef] [PubMed]
79. Turchick, A.; Hegan, D.C.; Jensen, R.B.; Glazer, P.M. A cell-penetrating antibody inhibits human RAD51 via direct binding. *Nucleic Acids Res.* **2017**, *45*, 11782–11799. [CrossRef]
80. Shin, S.-M.; Choi, D.-K.; Jung, K.; Bae, J.; Kim, J.-S.; Park, S.-W.; Song, K.-H.; Kim, Y.-S. Antibody targeting intracellular oncogenic ras mutants exerts anti-tumour effects after systemic administration. *Nat. Commun.* **2017**, *8*, 15090. [CrossRef]
81. Van Impe, K.; Bethuyne, J.; Cool, S.; Impens, F.; Ruano-Gallego, D.; De Wever, O.; Vanloo, B.; Van Troys, W.; Lambein, K.; Boucherie, C.; et al. A nanobody targeting the F-actin capping protein CapG restrains breast cancer metastasis. *Breast Cancer Res.* **2013**, *15*, R116. [CrossRef] [PubMed]
82. Agemy, L.; Friedmann-Morvinski, D.; Kotamraju, V.R.; Roth, L.; Sugahara, K.N.; Girard, O.; Mattrey, R.F.; Verma, I.M.; Ruoslahti, E. Targeted nanoparticle enhanced proapoptotic peptide as potential therapy for glioblastoma. *Proc. Natl. Acad. Sci. USA* **2011**, *108*, 17450–17455. [CrossRef] [PubMed]
83. Hamilton, A.M.; Aidoudi-Ahmed, S.; Sharma, S.; Kotamraju, V.R.; Foster, P.J.; Sugahara, K.N.; Ruoslahti, E.; Rutt, B.K. Nanoparticles coated with the tumor-penetrating peptide iRGD reduce experimental breast cancer metastasis in the brain. *J. Mol. Med.* **2015**, *93*, 991–1001. [CrossRef] [PubMed]
84. Sugahara, K.N.; Braun, G.B.; De Mendoza, T.H.; Kotamraju, V.R.; French, R.P.; Lowy, A.M.; Teesalu, T.; Ruoslahti, E. Tumor-Penetrating iRGD Peptide Inhibits Metastasis. *Mol. Cancer Ther.* **2015**, *14*, 120–128. [CrossRef] [PubMed]
85. Qiu, M.; Ouyang, J.; Wei, Y.; Zhang, J.; Lan, Q.; Deng, C.; Zhong, Z. Selective Cell Penetrating Peptide-Functionalized Envelope-Type Chimeric Lipopepsomes Boost Systemic RNAi Therapy for Lung Tumors. *Adv. Heal. Mater.* **2019**, *8*, e1900500. [CrossRef]
86. Ben Djemaa, S.; Herve-Aubert, K.; Lajoie, L.; Falanga, A.; Galdiero, S.; Nedellec, S.; Souce, M.; Munnier, E.; Chourpa, I.; David, S.; et al. gH625 Cell-Penetrating Peptide Promotes the Endosomal Escape of Nanovectorized siRNA in a Triple-Negative Breast Cancer Cell Line. *Biomacromolecules* **2019**, *20*, 3076–3086. [CrossRef] [PubMed]
87. Li, G.; Gao, Y.; Gong, C.; Han, Z.; Qiang, L.; Tai, Z.; Tian, J.; Gao, S. Dual-Blockade Immune Checkpoint for Breast Cancer Treatment Based on a Tumor-Penetrating Peptide Assembling Nanoparticle. *ACS Appl. Mater. Interfaces* **2019**, *11*, 39513–39524. [CrossRef]
88. Furukawa, K.; Tanaka, M.; Oba, M. siRNA delivery using amphipathic cell-penetrating peptides into human hepatoma cells. *Bioorganic Med. Chem.* **2020**, *28*, 115402. [CrossRef]
89. Zhang, C.; Yuan, W.; Wu, Y.; Wan, X.; Gong, Y. Co-delivery of EGFR and BRD4 siRNA by cell-penetrating peptides-modified redox-responsive complex in triple negative breast cancer cells. *Life Sci.* **2021**, *266*, 118886. [CrossRef]
90. Aileron Therapeutics. ALRN-6924 in Patients with Advanced Solid Tumors or Lymphomas; National Library of Medicine: Bethesda, MD, USA, 2014; NCT02264613 (ClinicalTrials.gov Identifier).

91. Aileron Therapeutics. *Safety Study of ALRN-6924 in Patients with Acute Myeloid Leukemia or Advanced Myelodysplastic Syndrome*; National Library of Medicine: Bethesda, MD, USA, 2016; NCT02909972 (ClinicalTrials.gov Identifier).
92. Aileron Therapeutics. *ALRN-6924 and Paclitaxel in Treating Patients with Advanced, Metastatic, or Unresectable Solid Tumors*; National Library of Medicine: Bethesda, MD, USA, 2018; NCT03725436 (ClinicalTrials.gov Identifier).
93. Aileron Therapeutics. *Phase 1 Study of the Dual MDM2/MDMX Inhibitor ALRN-6924 in Pediatric Cancer*; National Library of Medicine: Bethesda, MD, USA, 2018; NCT03654716 (ClinicalTrials.gov Identifier).
94. Aileron Therapeutics. *A Study of ALRN-6924 for the Prevention of Topotecan-induced Myelosuppression During Treatment for Small Cell Lung Cancer*; National Library of Medicine: Bethesda, MD, USA, 2019; NCT04022876 (ClinicalTrials.gov Identifier).
95. Cancer Research, UK. *BT1718 in Patients with Advanced Solid Tumours*; National Library of Medicine: Bethesda, MD, USA, 2018; NCT03486730 (ClinicalTrials.gov Identifier).
96. Das Gupta, T.K. *Safety Study of a Cell Penetrating Peptide (p28) to Treat Solid Tumors That Resist Standard Methods of Treatment*; National Library of Medicine: Bethesda, MD, USA, 2009; NCT00914914 (ClinicalTrials.gov Identifier).
97. Pediatric Brain Tumor Consortium. *p28 in Treating Younger Patients with Recurrent or Progressive Central Nervous System Tumors*; National Library of Medicine: Bethesda, MD, USA, 2013; NCT01975116 (ClinicalTrials.gov Identifier).
98. Institut Curie. *First-in-human Phase I to Evaluate PEP-010 as Single Agent and in Combination with Paclitaxel (CleverPeptide)*; National Library of Medicine: Bethesda, MD, USA, 2021; NCT04733027 (ClinicalTrials.gov Identifier).
99. Amal Therapeutics. *Phase 1b Study to Evaluate ATP128, With or Without BI 754091, in Patients with Stage IV Colorectal Cancer (KISIMA-01)*; National Library of Medicine: Bethesda, MD, USA, 2019; NCT04046445 (ClinicalTrials.gov Identifier).





Review

# Signaling Pathway Inhibitors, miRNA, and Nanocarrier-Based Pharmacotherapeutics for the Treatment of Lung Cancer: A Review

Shadab Md <sup>1,2,3,\*</sup> , Nabil A. Alhakamy <sup>1,2,3</sup> , Shahid Karim <sup>4</sup>, Gamal A Gabr <sup>5</sup>, Mohammad Kashif Iqbal <sup>6,7</sup> and Samar S. A. Murshid <sup>8</sup>

- <sup>1</sup> Department of Pharmaceutics, Faculty of Pharmacy, King Abdulaziz University, Jeddah 21589, Saudi Arabia; nalhakamy@kau.edu.sa
  - <sup>2</sup> Center of Excellence for Drug Research & Pharmaceutical Industries, King Abdulaziz University, Jeddah 21589, Saudi Arabia
  - <sup>3</sup> Mohamed Saeed Tamer Chair for Pharmaceutical Industries, King Abdulaziz University, Jeddah 21589, Saudi Arabia
  - <sup>4</sup> Department of Pharmacology, Faculty of Medicine, King Abdulaziz University, Jeddah 21589, Saudi Arabia; skaled@kau.edu.sa
  - <sup>5</sup> Department of Pharmacology and Toxicology, College of Pharmacy, Prince Satam Bin Abdulaziz University, Al-Kharj 16278, Saudi Arabia; g.gabr@psau.edu.sa
  - <sup>6</sup> Department of Pharmaceutics, School of Pharmaceutical Education and Research, Jamia Hamdard, New Delhi 110062, India; mkashifiqbal@ymail.com
  - <sup>7</sup> Sentiss Research Centre, Product Development Department, Sentiss Pharma Pvt Ltd., Gurugram 122001, India
  - <sup>8</sup> Department of Natural Products and Alternative Medicine, Faculty of Pharmacy, King Abdulaziz University, Jeddah 21589, Saudi Arabia; samurshid@kau.edu.sa
- \* Correspondence: shaque@kau.edu.sa

**Citation:** Md, S.; Alhakamy, N.A.; Karim, S.; Gabr, G.A.; Iqbal, M.K.; Murshid, S.S.A. Signaling Pathway Inhibitors, miRNA, and Nanocarrier-Based Pharmacotherapeutics for the Treatment of Lung Cancer: A Review. *Pharmaceutics* **2021**, *13*, 2120. <https://doi.org/10.3390/pharmaceutics13122120>

Academic Editor: Hassan Bousbaa

Received: 2 November 2021

Accepted: 7 December 2021

Published: 8 December 2021

**Publisher's Note:** MDPI stays neutral with regard to jurisdictional claims in published maps and institutional affiliations.



**Copyright:** © 2021 by the authors. Licensee MDPI, Basel, Switzerland. This article is an open access article distributed under the terms and conditions of the Creative Commons Attribution (CC BY) license (<https://creativecommons.org/licenses/by/4.0/>).

**Abstract:** Lung cancer is one of the most commonly diagnosed cancers and is responsible for a large number of deaths worldwide. The pathogenic mechanism of lung cancer is complex and multifactorial in origin. Thus, various signaling pathways as targets for therapy are being examined, and many new drugs are in the pipeline. However, both conventional and target-based drugs have been reported to present significant adverse effects, and both types of drugs can affect the clinical outcome in addition to patient quality of life. Recently, miRNA has been identified as a promising target for lung cancer treatment. Therefore, miRNA mimics, oncomiRs, or miRNA suppressors have been developed and studied for possible anticancer effects. However, these miRNAs also suffer from the limitations of low stability, biodegradation, thermal instability, and other issues. Thus, nanocarrier-based drug delivery for the chemotherapeutic drug delivery in addition to miRNA-based systems have been developed so that existing limitations can be resolved, and enhanced therapeutic outcomes can be achieved. Thus, this review discusses lung cancer's molecular mechanism, currently approved drugs, and their adverse effects. We also discuss miRNA biosynthesis and pathogenetic role, highlight pre-clinical and clinical evidence for use of miRNA in cancer therapy, and discussed limitations of this therapy. Furthermore, nanocarrier-based drug delivery systems to deliver chemotherapeutic drugs and miRNAs are described in detail. In brief, the present review describes the mechanism and up-to-date possible therapeutic approaches for lung cancer treatment and emphasizes future prospects to bring these novel approaches from bench to bedside.

**Keywords:** lung cancer; angiogenesis; apoptosis; miRNA; oncomiRs

## 1. Introduction

According to World Health Organization (WHO), lung cancer (LC) is a major cause of death and is the second most commonly diagnosed cancer worldwide. According to the published report in 2020, 2.2 million (11.44%) new lung cancer cases were diagnosed, and 1.8 million (18%) deaths were reported worldwide. It is further predicted that by the end



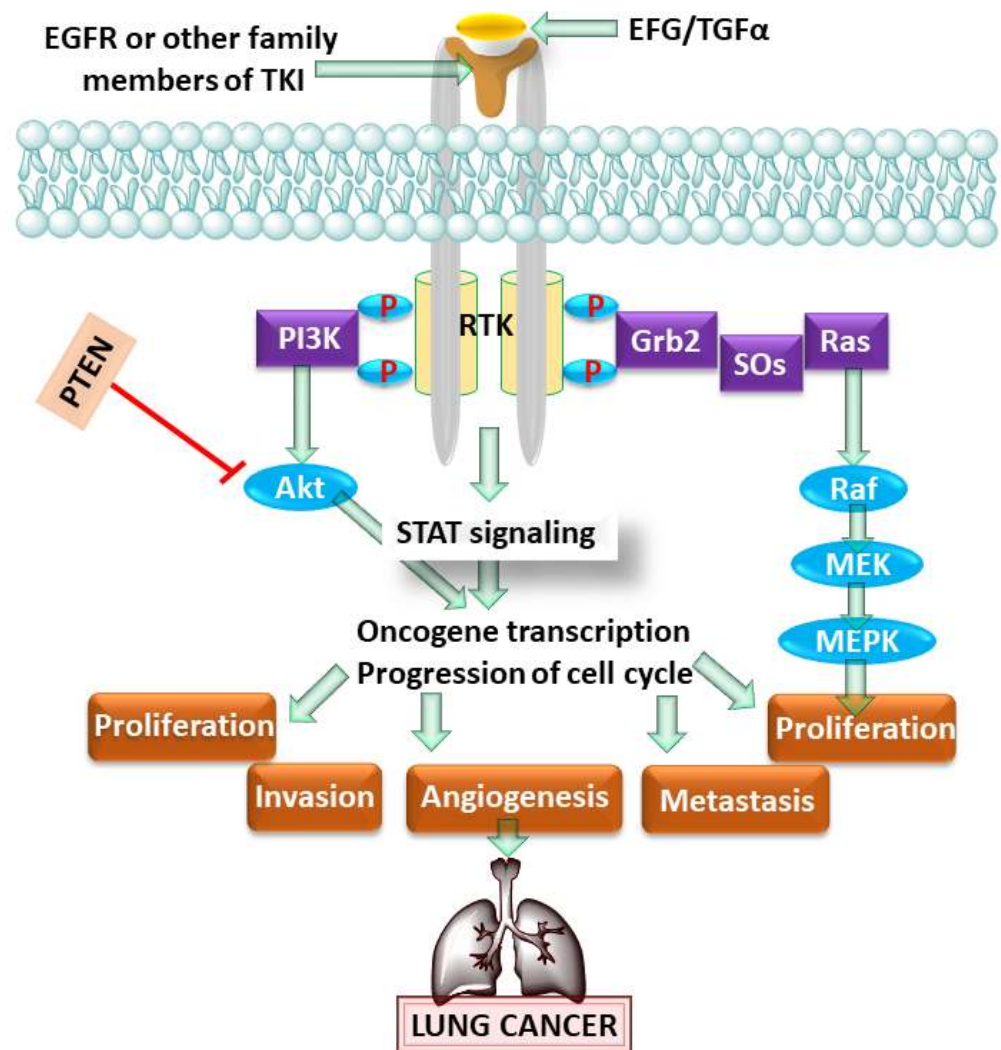
of 2035, the mortality rate due to LC may exceed 3 million [1,2]. LC is the leading cause of death in men, whereas it is the third leading cause of death in women following breast and colon cancer [2]. As per published report in 2021, in 112 countries, prostate cancer has been commonly diagnosed as the leading cause of death, followed by LC in 93 countries and colorectal cancer in 11 countries [2]. Another challenge for LC is its survival rate. The average survival rate of patients was reported to be 10–20% with the highest survival rates found in Japan, Israel, and Korea (33%, 27%, and 25%, respectively) [2]. Among various risk factors, smoking is one of the factors that is responsible for the pathogenesis of LC. More than 80% of deaths among confirmed cases of LC are caused by smoking, while 4.7–14% are caused by inhaling particles less than 2.5  $\mu\text{M}$  ( $\text{PM}_{2.5}$ ) [3]. It has also been demonstrated that passive smoking contributes to one-third of the total cases. Among various airborne particulates and gases, asbestos (a carcinogen) is primarily responsible for LC, and when smokers are exposed to it, the chance of developing LC increases significantly [4–8]. Radon is a gas produced by radium 226 that becomes trapped in buildings with poor ventilation. Radon emits an alpha particle, and hence, exposure to this gas initiates an LC cascade. Aside from the factors mentioned above, previous exposure to heavy metals, such as nickel, chromium, aromatic hydrocarbons, ether, and  $\alpha$ 1-antitrypsin deficiency have been identified as major causes of LC [9–11]. However, with the understanding of the cellular and molecular etiology, it was found that miRNA deregulation significantly contributes in the etiology of LC. Based on the histological findings, LC is subdivided into small cell and non-small cell LC (SCLC and NSCLC). NSCLC represents approximately 85–90% of cases, and SCLC represents 10–15% of cases [12]. At present, chemotherapy, radiotherapy, and surgery either alone or in combination are the available therapeutic regimens. Among the three available options, chemotherapy is extensively used. However, the use of chemotherapy or targeted anticancer drugs is associated with multiple challenges, such as unintended side effects, multi-organ toxicities, and drug resistance [13]. Chemotherapeutic drugs are non-selective in nature, which means, when administered, they damage healthy or normal cells in addition to cancerous cells, resulting in homeostatic alterations. To overcome these challenges, nanocarrier-based targeted drug delivery and miRNA-based pharmacotherapeutic regimens with site-specific mechanisms of action have been developed. Thus, in this review, we discuss the mechanistic pathogenesis of lung cancer, available pharmacotherapeutic regimens, their challenges and limitations, promising roles of various nano-encapsulated natural/synthetic drugs, and the emerging role of miRNA in the management and treatment of LC.

## 2. Signaling Pathways and Targeted Therapy in LC

The pathogenesis of LC is complex and multifactorial in origin. Its pathogenesis is mediated by several cellular and molecular signaling pathways, and selective targeting of these pathways is now being considered as a novel and targeted therapeutic approach for treating LC [13]. Signaling pathways are either stimulated by the pro-oncogenes or inhibited by anti-oncogenes, resulting in tumor proliferation, migration, angiogenesis, and apoptotic escape [14]. Thus, inhibition of pro-oncogenes and stimulation of anti-oncogene-related signaling pathways are emerging targets for various pharmacotherapeutics.

### 2.1. Epidermal Growth Factor (EGFR) Receptor Deregulation and EGFR Inhibitors in LC

Altered cellular proliferation is considered as one of the primary causes of LC initiation and progression, in which normal or healthy cells are transformed into malignant cells [15]. Numerous published reports have shown the pathogenetic role of the epidermal growth factor receptor (EGFR) in tumor initiation and progression. EGFR is a member of the tyrosine kinase receptor (RTK) family, as shown in Figure 1 [16]. In clinical studies, 43–89% of cases of NSCLC were found to be related to EGFR mutations [17].



**Figure 1.** Showing the role of the epidermal growth factor receptor (EGFR) pathway in lung cancer. epidermal growth factor (EGF), transforming growth factor (TGF $\alpha$ ), Growth factor receptor-bound protein 2 (Grb2), son of sevenless (SOs), Mitogen-activated protein kinase (MAPK) and signal transducer and activator of transcription (STAT).

Currently, erlotinib and gefitinib are the two drugs that cause functional inactivation of the EGFR intracellular domain and are used to treat lung cancer [14]. Cetuximab and bevacizumab are two potent monoclonal antibodies (mAb) and act as EGFR blockers [14]. When cetuximab was used in combination with radiotherapy, a synergistic anticancer effect was observed. When cisplatin and vinorelbine were used in combination with cetuximab, a significant improvement in patient survival rate was found [18]. Additionally, erlotinib and gefitinib were shown to penetrate the lung's tumor cells more potentially than cetuximab [19]. A Phase III clinical trial (OPTIMAL) was conducted to compare the efficacy and tolerability of erlotinib against standard chemotherapy. Among patients with EGFR mutation, specifically with EGFR 19 deletion or an EGFR L858R point mutation, the results revealed significant clinical outcomes with minimal side effects [20]. TORCH, another Phase III trial, was conducted to determine the efficacy of erlotinib and cisplatin–gemcitabine among the patient with advanced NSCLC, and the outcome showed superior efficacy of erlotinib [21]. Similarly, the Phase III TITAN trial was conducted to check the efficacy of erlotinib against docetaxel among the patients of recurrent NSCLC. The result showed no significant difference in terms of clinical outcome, effectiveness, and safety of erlotinib versus chemotherapy in second-line treatment of patients with advanced, non-small-cell

lung cancer with poor prognosis [22]. The outcome of the Phase III trial (INFORM), in which gefitinib was studied as maintenance therapy among patients with advanced NSCLC, showed significantly beneficial clinical outcomes [23]. Likewise, cetuximab (an anti-EGFR mAb) was also tested in a Phase III clinical trial (FLEX), and the outcome of this trial showed significant clinical benefit and reduced EGFR expression [24].

2.2. Vascular Endothelial Growth Factor (VEGF) Receptor Deregulation and VEGF Inhibitors in LC

Angiogenesis is the process of development of vasculature from coexisting blood vessels in response to normal physiological processes such as growth, reproduction, and development of various organs. Angiogenesis is strictly controlled under normal physiological conditions and occurs only for a limited period [25]. However, during carcinogenesis, the physiological balance becomes disrupted, and uncontrolled angiogenesis occurs as shown in Figure 2. During angiogenesis, endothelial and cancerous cells release pro-angiogenic factors, such as vascular endothelial growth factor, fibroblast growth factor, and transforming growth factor-beta (VEGF, FGF, and TGF- $\beta$ , respectively) that regulate angiogenesis in association with other signaling molecules [25].

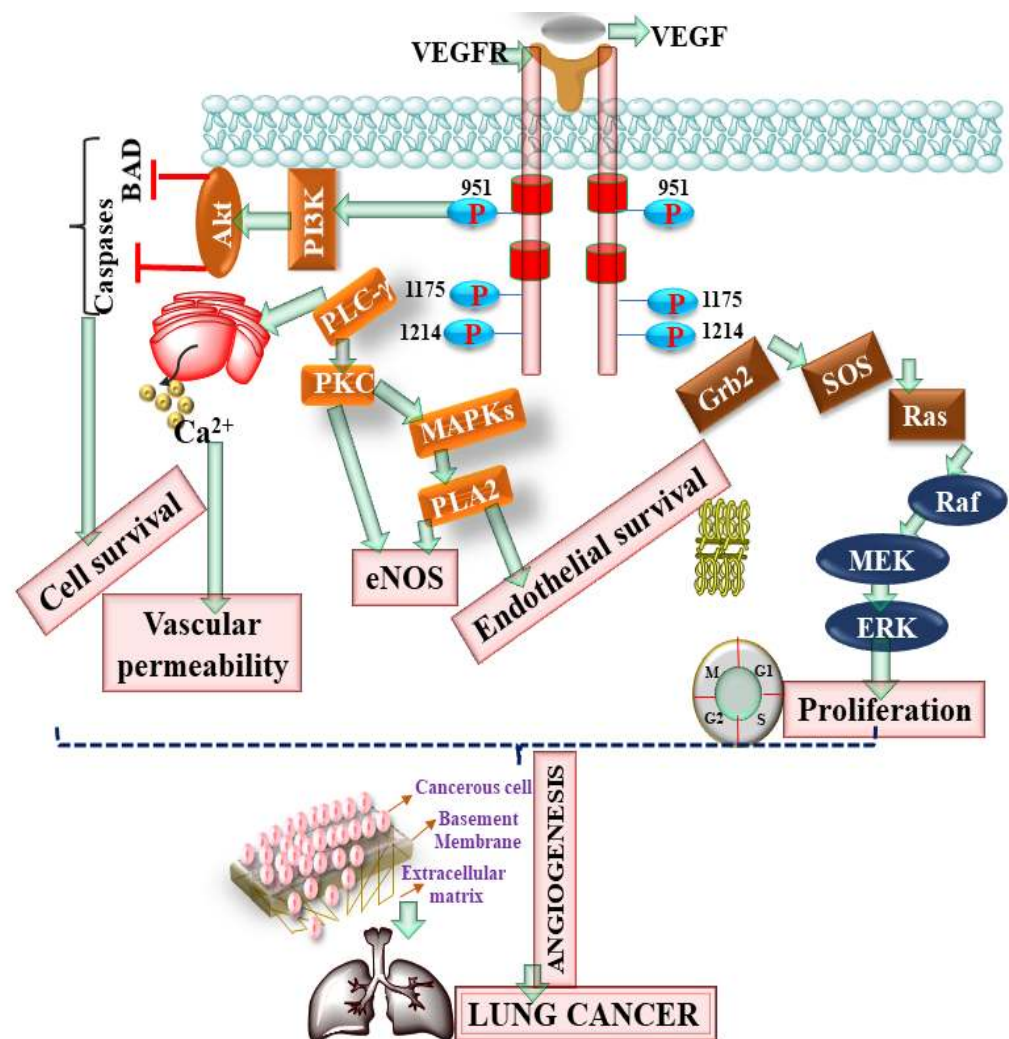


Figure 2. Showing the role of the vascular endothelial growth factor receptor (VEGFR) pathway in lung cancer. Protein kinase B (Akt), phosphoinositide 3-kinases (PI3K), (PLC), phospholipase C (PLC), protein kinase C (PKC), Phospholipase A2 (PLA2), extracellular-signal-regulated kinase (ERK), and endothelial nitric oxide synthase (eNOS).

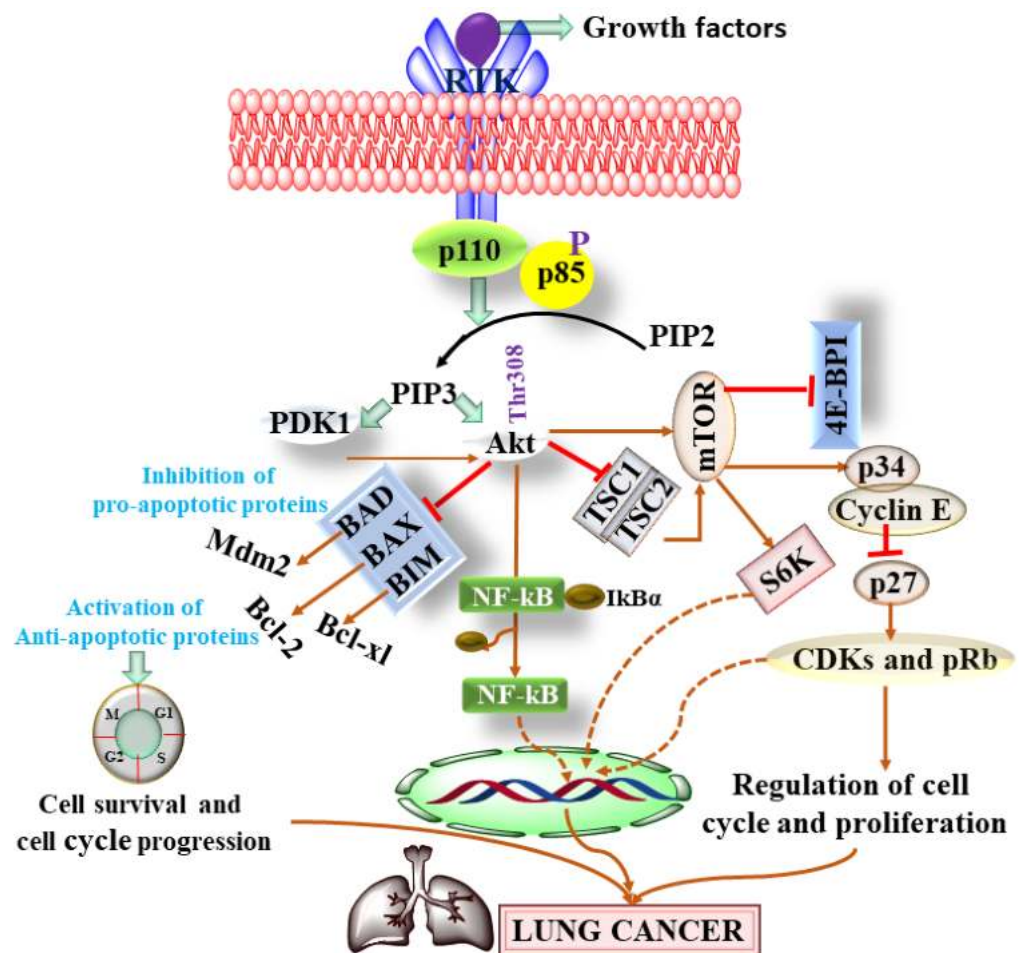
Pazopanib is a tyrosine kinase inhibitor (TKI) that inhibits the growth of tumor cells and the process of angiogenesis [26]. A Phase II clinical trial was conducted to determine the efficacy of pazopanib among patients with NSCLC. The study's outcome showed excellent tolerability and reduction in the tumor volume [26]. Vandetanib is also a TKI and inhibits EGFR and VEGF. A Phase III clinical trial (ZEPHYR) was conducted to determine the efficacy and tolerability among the patients with NSCLC. However, unfortunately, the outcome of this trial showed non-significant clinical outcomes and some serious side effects [27]. Bevacizumab is a mAb and is the first approved drug to inhibit angiogenesis via selectively targeting VEGF among NSCLC patients [28]. In a Phase III clinical trial (ECOG 4599), the combined use of bevacizumab with carboplatin and paclitaxel showed a significant clinical outcome along with prominent hypertension [29]. In another Phase III clinical trial (BeTa), the combination of bevacizumab and erlotinib was studied among NSCLC patients [30]. However, in another Phase III clinical trial, bevacizumab used in combination with cisplatin and gemcitabine demonstrated a significant improvement in survival time [31]. Apart from these three drugs, motesanib, axitinib and BIBF1120 are currently being evaluated in different clinical trial phases [32].

### 2.3. PI3K/AKT/mTOR Signaling Pathway and PI3K/AKT/mTOR Inhibitors in LC

Phosphoinositide 3-kinase (PI3K) is one of the important members of the lipid kinase family. HER2 and IGF receptors are considered upstream regulators of PI3K [33]. Under stressed conditions or after ligand binding, p11 regulates phosphorylation of PIP2 to PIP3 and results in the activation of protein kinase B (AKT) [33]. Once AKT is activated, it becomes separated from the surface of the cell membrane and modulates various downstream signaling pathways as shown in Figure 3. Mammalian target of rapamycin (mTOR) is one of the important and extensively studied serine/threonine kinases and is present in the form of mTOR1 and mTOR2, as shown in Figure 3 [33].

Considering the role of the PI3K/AKT/mTOR signaling pathway in LC, it was found that this pathway is significantly activated (50–73%) in NSCLC [34,35]. Apart from PI3K/AKT's proven role in LC, the study also showed the involvement of the mTOR pathway and reported 30% mutated mTOR among 188 patients [36].

The pan-PI3K inhibitors are a class of drugs that bind to p110 and abrogate PI3K activation. The PI3K inhibitors, GDC 0941, 0032, and 0973, PX-866, BKM 120, XL-147, and BAY 80-6946 are some of the recently developed pan-PI3K inhibitors for LC patients in various clinical studies [36]. Apart from the pan-PI3K inhibitors, AKT inhibitors have also been developed to eventually stop LC tumor survival and mitogenic properties. GDC 0068, NVP-BKM120, GSK 2141795, MK2206, perifosine A-443654, and GSK690693 are AKT inhibitors that have shown significant antitumor effects in LC patients [36]. Additionally, when the AKT inhibitor, MK-2206, was used with other chemotherapeutic drugs, such as docetaxel, doxorubicin, and erlotinib, the combinations showed significant synergistic anticancer effects [36]. Everolimus, ridaforolimus, deforolimus, and temsirolimus are mTOR1 inhibitors and are approved for treating various types of cancer, including LC. The mTOR1 inhibitors, such as everolimus, were tested in combination with gefitinib, docetaxel, and sorafenib, and the outcome of these studies showed synergistic antitumor effects [37]. Apart from mTOR1 inhibitors, dual mTOR1/2 inhibitors have also been developed and tested in various clinical studies. OSI-027 and INK128 are two mTOR1/2 inhibitors that additionally show inhibitory actions toward VEGF and heat inducible factor (HIF-1 $\alpha$ ) [38]. Interestingly, not only dual mTOR1/2 inhibitors, but also PI3K/mTOR inhibitors, act as inhibitors of both PI3K and mTOR [36]. XL765, BEZ235, PF-04691502, NVP-BEZ235, BGT226, PI-103, and GDC-0980 are some of the tested dual-acting PI3K/mTOR inhibitors among patients with LC [36].



**Figure 3.** Showing the role of PI3K/Akt pathway in lung cancer. Pyruvate dehydrogenase kinases (PDKs), Phosphatidylinositol 4,5-bisphosphate (PIP), mammalian target of rapamycin (mTOR), eukaryotic translation initiation factor 4E-binding protein 1 (4E-BP1), TSC Complex Subunit 1 (TSC1), cyclin-dependent kinase (CDK), pRB (retinoblastoma protein), mouse double minute 2 (Mdm2), nuclear factor kappa-light-chain-enhancer of activated B cells (NF- $\kappa$ B) and nuclear factor of kappa light polypeptide gene enhancer in B-cells inhibitor, alpha (IKB $\alpha$ ).

#### 2.4. p53, Bax/Bcl-2, Fas, and p16INK4/Cyclin D1/Rb Pathway Dysfunction and Their Inhibitors in LC

p53 is one of the most extensively explored tumor suppressor genes; it acts as a gatekeeper and maintains genetic stability. p53 senses stress, mutagenic action, damage to DNA, hypoxia, and activation of pro-oncogenes [39]. In LC, the p53 mutation has been extensively studied [39]. Exposure to PM<sub>2.5</sub>, cigarette smoke, and other carcinogens cause transverse mutation, for example, change of TA to GT and GC to TA (G–A) transitions, which are responsible for LC [40]. Various downstream signaling molecules, such as B-cell lymphoma 2 (Bcl-2), which is anti-apoptotic and downregulated, Bcl-2-associated X protein (Bax), which is pro-apoptotic and upregulated, Fas, tumor necrosis factor receptor-like apoptosis-inducing ligand (TRAIL), and death receptor 5 (TRAIL-DR5; upregulated) are under the control of p53 and act to modulate apoptosis in LC [41].

One of the important features of cancer cells is evasion of apoptosis. Apoptotic evasion is an important phenomenon that promotes both tumor growth and proliferation [42]. Bcl-2 and Bax are two apoptotic proteins involved in mitochondrial-mediated apoptosis [42]. In LC, overexpression of Bax and deficiency of Bcl-2 proteins have been reported [43]. Death receptor-mediated apoptosis is another mechanism involved in the antitumor effect [44]. When FasL binds to its receptor, the subsequent signaling pathway is activated and causes

apoptosis via caspase-8. In LC, the Fas receptor was found to be downregulated, suggesting apoptotic evasion [44].

ABT-737 and Bcl-2 antisense oligonucleotides were developed to trigger apoptosis in the case of NSCLC [45]. Considering the role of TRAIL in LC, rhTRAIL (AMG 951), Mapatumumab (anti-TRAIL-R1 mAb), and AMG 655 have been developed to target the death receptor in the lungs [32]. These drugs are currently under different phases of clinical trials and are in the pipeline for approval. Apart from these pipeline drugs, several small molecules, such as sorafenib (RAF/MEK/ERK inhibitor), AZD6244 (mitogen-activated extracellular signal-regulated kinase (MEK) inhibitor), and enzastaurin (serine/threonine inhibitor) are being tested either alone or in combination with other anticancer drugs among the patient with LC [32].

### 3. Limitations of the Approved and Pipeline Drugs of Lungs Cancer

Currently, various anticancer drugs have been approved for the treatment and management of LC. However, most of the conventional and signaling pathway-specific drugs exhibit significant long- and short-term adverse effects, such as cardiotoxicity, hepatotoxicity, nephrotoxicity, rashes, and others [46]. Apart from these significant adverse effects, these approved drugs also cause drug resistance, leading to a poor rate of patient survival and low quality of life. In one of the clinical studies, cisplatin and etoposide were used for the treatment of LC, and thrombocytopenia, leukopenia, and neutropenia were observed [47]. Additionally, most chemotherapeutics are administered via the oral route. These drugs possess poor solubility, low bioavailability, and permeability, and cause GI irritation. To overcome this problem, inhalation-based drug delivery was used, but unfortunately, the direct exposure of the drug to the lungs caused significant pulmonary toxicity. Details of the mechanism of action, year of approval, and adverse effects are shown in Table 1.

**Table 1.** Showing the details of FDA approved drugs and their adverse effects.

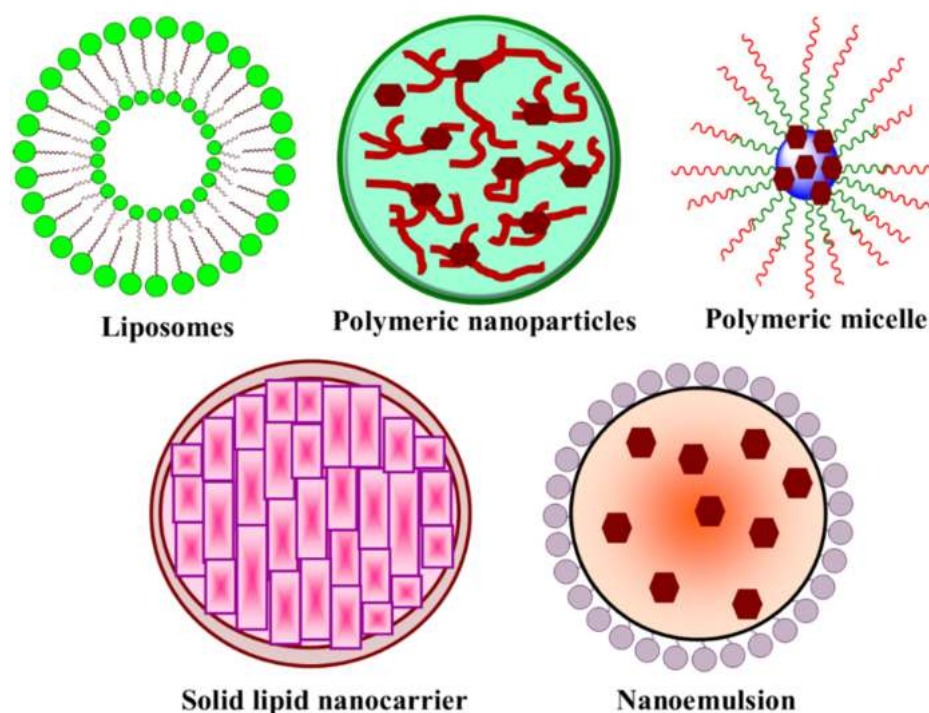
Drugs	Year of Approval	Mechanism of Action	Adverse Effect	References
Afatinib	2013	EGFR tyrosine kinase inhibitor	Diarrhea, rash, mucositis, swelling of the lips, nail infection, and nose bleeds.	[48]
Alectinib	2017	EGFR tyrosine kinase inhibitor	Bloody urine, joint pain or swelling, increased blood pressure, immobility, and nephrotoxicity.	[48]
Amivantamab-vmjw	2021	EGFR tyrosine kinase inhibitor	Shortness of breath, muscle and joint pain, swelling of hands.	[48]
Atezolizumab	2020	PD-1 receptor inhibitor	Bladder pain, bloating, ear congestion and dyspnea.	[47]
Bevacizumab	2006	VEGF inhibitor	Cardiotoxicity, alopecia, xeroderma, hemorrhage, proteinuria, and necrotizing fasciitis.	[49]
Brigatinib	2020	Inhibitor of AKT, ERK, and STAT3	Headache, skin rashes, nausea, constipation and numbness.	[47]
Capmatinib	2020	MET kinase inhibitor	Loss of appetite, chest pain and bloating.	[47]
Cemiplimab-rwlc	2021	PD-1 receptor inhibitor	Blisters, immobility, gland and joint swelling and mouth ulcers.	[47]
Ceritinib	2017	ALK phosphorylation inhibitor	Reduced hemoglobin, hepatotoxicity, and nephrotoxicity.	[47]
Crizotinib	2016	RTK inhibitor	Oedema, reduced appetite, loss of taste and hepatotoxicity.	[47]
Dabrafenib	2017	BRAF and RAF kinase inhibitor	Joint pain, papilloma, alopecia, and hepatotoxicity.	[47]

Table 1. Cont.

Drugs	Year of Approval	Mechanism of Action	Adverse Effect	References
Dacomitinib	2018	EGFR tyrosine kinase inhibitor	Dermatitis, acne, stomatitis, dry skin, and paronychia.	[48]
Docetaxel	2005	Microtubule depolymerization inhibition	Neutropenia, dysgeusia hypersensitivity, anemia, thrombocytopenia, anorexia, nail disorders and fluid retention.	[47]
Doxorubicin	1970	Topoisomerase II inhibitor	Cardiotoxicity, hepatotoxicity and nephrotoxicity.	[47]
Durvalumab	2020	PD-1 receptor inhibitor	Musculoskeletal pain, loss of appetite, and UTI.	[47]
Entrectinib	2019	RTK inhibitor	Peripheral edema, hepato-reno toxicity, myelotoxicity.	[47]
Erlotinib	2010	EGFR tyrosine kinase inhibitor	Fatigue, rashes, hepatotoxicity, cough, mouth ulceration, and dry skin.	[48]
Everolimus	2016	mTORC1 inhibitor	Insomnia, weight loss, and dry mouth.	[48]
Gefitinib	2015	EGFR tyrosine kinase inhibitor	Rash, diarrhea, hepatotoxicity, acne, and anorexia.	[48]
Gemcitabine	2005	DNA synthesis inhibitor	Hair loss, nausea, mouth ulcer.	[47]
Ipilimumab	2020	Inhibition of T-cell inactivation	Diarrhea, fatigue, skin rash, and pruritus.	[49]
Methotrexate	1970	Dihydrofolate reductase inhibitor	Alopecia, hepatotoxicity, and tender gums.	[47]
Necitumumab	2015	EGFR tyrosine kinase inhibitor	Weight loss, hypokalemia, mouth ulcer, acne, and chest infection.	[47]
Nivolumab	2018	PD-1 receptor inhibitor	Lymphopenia, fatigue, diarrhea, pruritus, and vitiligo.	[49]
Osimertinib	2020	EGFR tyrosine kinase inhibitor	Diarrhea, nausea, reduced appetite, dry skin, paronychia.	[48]
Paclitaxel protein-bound nanoparticle	2012	Causes cell cycle arrest	Low blood counts, alopecia, mouth ulcer, peripheral neuropathy, arthralgias, and myalgias.	[47]
Pembrolizumab	2016	PD-1 receptor inhibitor	Anemia, hypertension, hyponatremia, hypoalbuminemia, and cough.	[49]
Pemetrexed	2017	Purine and pyrimidine synthesis inhibitor	Weight loss, vomiting, fatigue, loss of appetite, and insomnia.	[49]
Pralsetinib	2020	RET kinase inhibitor	Shortness of breath, cough, bleeding gums, nosebleeds, and mental confusion.	[49]
Ramucirumab	2020	VEGF inhibitor	Cardiotoxicity, wound healing problem and skin rashes.	[49]
Selpercatinib	2020	RTK inhibitor	Dry mouth, hypertension, peripheral edema, diabetes, and hepatotoxicity.	[47]
Sotorasib	2021	KRAS G12C inhibitor	Bone/joint pain, constipation, and stomach pain.	[47]
Tepotinib	2021	Kinase inhibitor	Anxiety, tachycardia, loss of appetite, sore throat, and stomach pain.	[47]
Trametinib	2015	MEK $\frac{1}{2}$ inhibitor	Losing of fingernails, eye dryness, damaged taste buds, dry skin, and canker sores.	[47]
Vinorelbine	1994	Cycle arrest via binding with microtubular spindle	Muscle or joint pain, constipation, and loss of appetite	[47]

#### 4. Nanocarrier-Based Targeted Drug Delivery in LC

As far as conventional chemotherapeutic drugs are concerned, no doubt these agents are potent and effective therapeutic moieties. Still, non-specificity, adverse effects, and poor pharmacokinetic profiles are limiting factors for their use [50]. Thus, in recent years, various nanocarriers, such as liposomes, nanoemulsions, polymeric nanoparticles, and polymeric micelles have been fabricated, as shown in Figure 4 [51]. This development is in response to problems caused by conventional drugs can be overcome and targeted drug delivery, enhanced pharmacological effect, and mitigation of adverse effects can be achieved [51]. These nanocarrier systems vary greatly in shapes, sizes, and surface charges. One of the advantages of these nanocarriers is the delivery of various drugs without using any toxic excipients [52]. Concerning targeted drug delivery in the lung, nanocarriers easily cross the various barriers and prolong the drug residence time in the tumor environment via escape from mucociliary clearance and phagocytosis in lung cells [53]. Currently, various nanocarriers are being studied in the clinical and preclinical setups, and some of them have entered clinical trials.



**Figure 4.** Showing various nanocarriers used for drug delivery in lung cancer.

##### 4.1. Polymeric Nanoparticles

Polymeric nanoparticles (PNPs) are mainly prepared from either natural or synthetic polymers. Based on the surface charge, polymeric PNPs are classified as cationic or anionic. Cationic PNPs are positively charged because of the presence of primary, secondary or tertiary amines, and subdivided as natural or synthetic PNPs. Cationic polymers are less toxic, possess improved encapsulation efficacy and offers controlled release. Additionally, cationic polymers can encapsulate hydrophobic drugs which are otherwise impermeable to the cell membrane and DNA. Some of the commonly studied polymers used in the fabrication of PNPs consist of chitosan, cyanoacrylates, poly (lactic-co-glycolic) acid (PLGA), gelatin, poly alkyl-, poly (lactic acid) (PLA), albumin, and polycaprolactone. These polymers are biodegradable and offer a controlled release pattern. Currently used intravenous anticancer drugs for lung cancer treatment are not feasible for patients as their use has been reported to cause systemic toxicities, pain, and discomfort. Orally-used anticancer drugs suffer from the lack of significant clinical efficacy and adverse effects. Thus, due



to the distinctive properties of PNPs in terms of sizes and zeta potentials, they have been regarded as a revolutionary anticancer drug administration approach to treat LC [54,55].

A significant anticancer effect with minimal toxicities was observed when taxanes were loaded with polyethylene–polylactide (PEG–PLA) and studied in *in vitro* and *in vivo* studies [54]. Similarly, when paclitaxel and cisplatin were loaded into PEG–PLA copolymers, an excellent anticancer effect was offered. Based on the outcome, the Phase I clinical trial was successfully completed, and the Phase II clinical trial (Genexol-PM) was initiated among NSCLC patients [56]. In another study, the PEG–PLA copolymer was used to load gemcitabine for oral drug delivery, and the developed nanoformulation is currently undergoing a Phase II clinical trial [57]. Recently, polycaprolactone (PCL)- and chitosan-loaded mucoadhesive nanoformulations were developed for lung-targeted drug delivery [12]. When the docetaxel nanoparticle was compared with Taxotere (injectable docetaxel), a superior anticancer potential of the docetaxel nanoparticle was found [58]. Cisplatin and doxorubicin are extensively used in the treatment for LC, but these drugs' side effects are limiting factors for their use. To overcome this problem, cisplatin and doxorubicin were loaded into gelatin and poly (isobutyl cyanoacrylate) polymers, and the developed nanofabrication showed a potent antitumor effect with minimal toxicity [59]. In one study, hyaluronic acid in conjugation with cisplatin NP was explored in an *in vivo* study. Even when administered intravenously, the outcome showed a more significant antitumor effect than the conventional formulation [60]. Additionally, the outcome of the study showed minimal neurotoxicity and nephrotoxicity [60].

#### 4.2. Liposome

Liposomes are bi-layered phospholipid nanocarriers and are classified as either unilamellar or multilamellar vesicles [61]. Unilamellar vesicles consist of a single bilayer, whereas multilamellar vesicles are composed of multilamellar vesicles. The size of the liposome varies from 1 to 100 nm and possesses the property of incorporating both lipophilic and hydrophilic drugs; hence, the therapeutic efficacy of the formulation is enhanced [61]. The stability, drug loading capacity, and release pattern of liposomes depend on the size and the number of the lipidic bilayer. Considering liposome-mediated pulmonary drug delivery, the use of phospholipid and cholesterol are considered as most effective and biocompatible [61].

Additionally, liposome-mediated drug delivery has been studied to overcome the problem of drug resistance and reduce side effects [62]. One of the advantages of liposomes is that the surface of the liposome can be modified, and hence, desirable targeted drug delivery can be achieved. Thus, among the various NPs, liposomes are considered as the most successful carrier system for the lungs [62]. Many of the United Food and Drug Administration (USFDA)-approved liposomal drugs are commercially available on the market. As an amphiphilic carrier system, hydrophilic drugs, such as doxorubicin and paclitaxel, can be easily loaded into a liposome [63]. When etoposide and docetaxel were incorporated into liposomes and tested for the anticancer potential in lung cancer, a significant synergistic pro-apoptotic activity via enhanced p53 activity was found [64]. A paclitaxel liposome was developed, and when pharmacokinetic profiling was done after nebulization, the area under the curve (AUC) of the nanoformulation was found to be twenty-fold higher than the paclitaxel administered via the intravenous route [65]. A significant reduction in tumor mass was found when this paclitaxel liposomal formulation was studied for its antitumor potential. As we have previously discussed, cisplatin is an extensively used drug for LC, but nephrotoxicity and hematological toxicity often restrict its use [65]. Thus, sustained-release liposomal cisplatin was fabricated to overcome this problem, and a Phase I study is ongoing. In one interesting study, an interleukin 2 (IL-2) liposome inhalation formulation was designed, fabricated, and tested, and the outcome of the study showed no evidence of toxicity, and it was found to be safe for LC patients [66].

### 4.3. Nanoemulsion

Nanoemulsions (NEs) are one of the most extensively studied nanocarriers for various disease conditions. NEs can be formulated as water in oil or oil in water, having a particle diameter in the range of 20 to 200 nm [67]. NEs are transparent and stable and consist of hydrophilic and hydrophobic phases, surfactant, and cosurfactant. Thus, most of the hydrophilic or hydrophobic drugs can be incorporated into the NE for effective targeted delivery [67]. Additionally, NE is considered an ideal carrier system for the delivery of anticancer drugs as far as bioavailability, stability, release pattern, and targeted delivery is concerned [68]. Moreover, NE protects the drug against ultraviolet (UV)-induced degradation; microbe-induced degradation offers long-term storage and can be administered intravenously, topically, or orally [69]. Considering NE in lung cancer, various synthetic, semisynthetic, and natural drugs have been incorporated into NEs and have been studied for possible anticancer effects [50,68]. Doxorubicin is another extensively used anticancer drug, but cardiotoxicity, nephrotoxicity, and hepatotoxicity are limiting factors for its use. Thus, pH-sensitive NE was explored for the possible efficacy and toxicity mitigation. The outcome of the study showed improved effectiveness and reduced mortality among the patients [70]. Paclitaxel is another extensively used anticancer drug used to treat LC, but dose-related toxicity and pharmacokinetics limit its use. Thus, to overcome this problem, NE containing paclitaxel in conjugation with hyaluronic acid was fabricated and tested in NSCLC [71]. Docetaxel was also fabricated in oil–water emulsion in which medium-chain triglycerides were used as the oil phase. When this formulation was tested for its anticancer potential, the study's outcome showed improved AUC, slow clearance, improved volume of distribution, and tumor necrosis (as analyzed by the histopathological study) [72]. Curcuminoids are isolated from *Curcuma longa* and have been explored for multiple pharmacological activities. To enhance the pharmacological activity of lung cancer, NEs of curcuminoids were fabricated and studied in lung cancer cell lines (H460 and A549 cells). The study's outcome showed significant antitumor activity via reduced expression of cyclin-dependent kinase 1 (CDK1), cyclin B, increased expression of p21, p53, and cell cycle arrest at the G/M phase [6]. Curcumin is among the most explored natural bioactive compounds for use in treating different types of cancer. However, curcumin suffers from the limitation of low solubility, low bioavailability, and rapid hepatic metabolism [73]. Thus, NEs of curcumin were fabricated and explored for their possible antitumor efficacy [73]. The fabricated formulation showed enhanced entrapment efficiency and improved release pattern. Furthermore, a 7.4-fold increase in bioavailability was found as compared to conventional formulation upon oral administration [73]. The molecular mechanism involved in the anticancer potential of curcumin NE in lung adenocarcinoma was found to be a modulation of extracellular receptor kinase, cyclooxygenase-2, protein kinase C, matrix metalloproteinases, and activating transcription factor 2 (ERK 1/2, COX-2, PKC, MMPs, and ATF-2, respectively) signaling pathways [74,75]. Similarly, diferuloylmethane isolated from the turmeric, 9-bromo noscapine (a tubulin-binding alkaloid), and quercetin are natural products and possess potent antitumor activities. Despite being potent and effective molecules, these two drugs suffer from pharmacokinetic limitations. Hence, their NEs were fabricated and explored for possible anticancer effects in LC [76–78]. The study outcome showed an improved pharmacokinetic profile and enhanced antitumor activity via apoptosis initiation and angiogenesis inhibition [78]. Lycobetaine (LBT) is a well-known alkaloid and showed significant anticancer potential via topoisomerases I and II inhibition. However, lycobetaine has a short half-life and poor bioavailability and hence, its NE was fabricated and tested in LC [79]. Danshen, tanshinones, and *Brucea javanica* oil are well-known Chinese herbs and possess potent anticancer potential. However, to enhance their pharmacological and pharmaceutical potentials, their NEs were formulated and studied in in vitro and in vivo setups [80–83].

#### 4.4. Polymeric Micelle

Polymeric micelles (PMs) are biodegradable and biocompatible nanocarriers that have shown great potential for targeted drug delivery of chemotherapeutic drugs in LC [84]. They are self-assembled amphiphilic NPs that become aggregated in the presence of copolymers and solvents [84]. A wide variety of polymers are available for PM fabrication, and the choice of these polymers depends upon compatibility with the selected drugs to allow incorporation, desired loading capacity, and stability. The cores of the PMs are hydrophobic, and poorly soluble drugs are generally incorporated into these micelles [85]. PMs offer the advantages of prolonging circulation time, bypassing hepatic metabolism, and offering an improved volume of distribution. PM sizes vary from 20 to 200 nm; hence, they can easily travel through the tumor microenvironment and escape from the reticuloendothelial system (RES), usually found in the liver, spleen, kidney, lymph nodes, and bone marrow cells [85]. A large number of polymers, such as poly(styrene-co-maleic anhydride [SMA]), poly(ethylene glycol)-block-poly(D,L-lactic acid [PEG-b-PLA]), poly(ethylene glycol)-block-poly(D,L-lactic-co-glycolic-acid [PEGb-PLGA]), poly(ethylene-glycol)-block-poly( $\epsilon$ -caprolactone [PEGePCL]), poly(*N*-vinylpyrrolidone)-block-poly( $\epsilon$ -caprolactone [PVP-b-PCL]), pluronic, D- $\alpha$ -tocopheryl polyethylene glycol and PEG-poly(amino acid [PEGePAA]) have been studied for targeted delivery of chemotherapeutic drugs into the LC tumor [84]. SMA is a synthetic copolymer composed of maleic acid and albumin. SMA is advantageous as it is stable in the body fluid and is non-toxic [86]. SMA conjugated to neocarzinostatin was explored for the anticancer effect in lung cancer, while SMA conjugated to paclitaxel was studied for the anticancer potential against adenocarcinoma [87]. PEG-b-PLA is an FDA-approved excipient and is used for the encapsulation of various anticancer drugs [88]. PEG-b-PLA is a copolymer consisting of PLA and PEG and offers excellent properties for the encapsulation of anticancer drugs. The ratio of PLA and PEG determines the release rate and pattern of encapsulated drugs, in which low molecular weight structures showed rapid release pattern whereas high molecular weight showed a delayed release pattern [88–90]. Recently, paclitaxel, curcumin, and rapamycin encapsulated polymeric are being investigated for their possible effect against lung cancer. The FDA also approves PEG-b-PLGA, and it is a biodegradable polymer [91]. Similar to PEG-b-PLA, the release pattern of the drug from PEG-b-PLGA can be modulated via a change in the ratio of PEG, glycolide, and lactide [91]. PEG-b-PLGA loaded with paclitaxel and doxorubicin was studied in NSCLC. The outcome of the study showed improved and synergistic antitumor potential of these two drugs along with minimal side effects [92]. Similarly, paclitaxel and cisplatin were also encapsulated and studied for the synergistic anticancer effect in combination with radiotherapy [93].

#### 5. The Limitations of Nanocarrier Drug Delivery Systems and miRNA as Emerging Tools against Lung Cancer

Currently, a lot of research is going into the development and delivery of safe and effective nano carrier-based systems targeting LC, but most of these drugs failed in clinical trials [94]. Some of the investigated reasons for the failure appear to be a lack of precise mechanism of action, toxicity due to excipient or particle size, and higher retention times in the circulatory system [53]. Thus, looking into the potential of nanocarriers against lung cancer and negative outcome in the clinical trials, researchers are now using FDA-approved excipients. Additionally, the nanocarriers have to cross numerous barriers and obstacles, such as dense matrix, protein-corona effect, phagocytosis, and drug efflux proteins before reaching the site of action [1]. Moreover, different types of tumor microenvironments respond differently to the same nanocarriers, which is one of the major issues [1]. Recently, Doxil has been reported to accumulate in Kaposi sarcoma, related to acquired immunodeficiency syndrome (AIDS), and this issue is a major area of concern for clinicians [95]. Additionally, a deep understanding of nanomedicine in the tumor microenvironment is lacking because of the unavailability of reliable preclinical models. Although xenograft models are currently being used, the findings from these models differ significantly from

the human tumor microenvironment [95]. Thus, to overcome these challenges, microRNA (miRNA)-based therapeutics are being explored as possible therapeutic tools in LC [96].

## 6. miRNAs and Lung Cancer

Currently, many chemotherapeutics are being explored for their possible anticancer effects, but most of them suffer from pharmacokinetic limitations and exhibit significant toxic effects [47]. Thus, a nano carrier-based drug delivery system was explored to address this limitation, but unfortunately, a lacuna in the desired therapeutic effect still exists. Thus, recently the role of miRNA is under investigation for its possible application in the management and treatment of LC [96]. RNA polymerase II was found to be responsible for the transcription of miRNA or pri-miRNA, upon which ribonuclease Drosha further acts, and pri-miRNA is converted into pre-miRNA [97]. This process occurs in the nucleus, and once pre-miRNA is formed, it moves out of the nucleus and into the cytoplasm, in which it is cleaved and mature miRNA is produced as shown in Figure 5 [97]. The mature mRNA gets incorporated or loaded into RNA-induced silencing complex (RISC) and argonaute. Finally, these miRNAs are involved in the silencing of mRNA. The miRNA usually binds with the complementary sequence of mRNA at three prime ends and inhibits the translation process [97]. It was further found that a single miRNA regulates the function of multiple mRNAs in humans. More than 50% of genes involved in LC are associated with miRNA [98]. Thus, miRNA is considered an emerging pathogenic factor in LC etiology and has emerged as a clinically relevant tool for managing and treating LC [99]. Based on the involvement of miRNA in carcinogenesis, miRNAs are classified as oncomiRs and tumor suppressor miRNA [99]. As the name suggests, oncomiRs are responsible for overexpression of pro-oncogenes or suppression of tumor suppressor genes, and are consistently found to be overexpressed in the tumor cells [96]. Tumor-suppressor miRNA suppresses the translatory activity of mRNA that is responsible for oncogene transcription. Thus, oncomiRs cause tumor initiation, progression, angiogenesis, invasion, and metastasis [96].

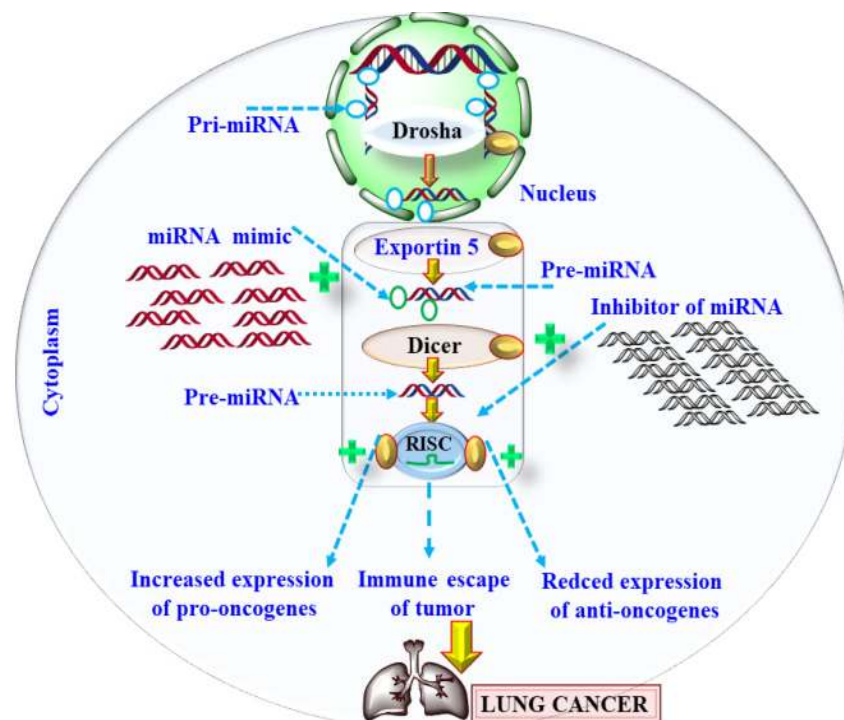


Figure 5. Showing the biosynthesis and the role of miRNA in lung cancer.

### 6.1. Mechanism of miRNA Deregulation in Lung Cancer

Involvement of miRNA in pathogenesis has been well established, and it was found that the factors that affect the biosynthesis of miRNA at the pri- or pre-miRNA level are primarily responsible for causing dysregulated miRNA and carcinogenesis [100]. Recently, p53, c-Myc, and E2F were identified as the transcription factors responsible for increased oncomiRs and reduced tumor suppressor miRNA expression [101,102]. Apart from the role of these transcription factors, epigenetic malfunction was also found to be an important factor in the increased level of dysregulated miRNA. Studies have suggested the role of hypo or hypermethylation and alterations in histone acetylation [103]. CpG methylation was studied for the increased expression of miR-223 that leads to acute myeloid leukemia [104]. Similarly, methylation of DNA and histone deacetylation were associated with dysregulated miRNA in bladder cancer [105]. Additionally, reduced expression of miRNA-148a and miR-34b and their associations with carcinogenesis were found to be associated with methylation of CpG [106].

miR-29b was found to be reduced in NSCLC, whereas miR-29b was found to increase the sensitivity of cisplatin in LC [107]. The epithelial–mesenchymal transition (EMT) is one of the critical steps in tumor metastasis, and recently, miR-101, miR-200, miR-27, miR15b, and miR-451 were found to be suppressed and involved in EMT in LC [108–110]. Similarly, miR-17-92, miR21, miR-16, miR-200c, miR-34, and miR-29b were found to be overexpressed in LC and act as oncomiRs [111]. In LC, miR-21, and phosphatase and tensin homolog deleted on chromosome 10 (PTEN) were found to be downregulated and positively correlated with chemoresistance against TKIs. However, selectively targeting miR-21 and PTEN can be used to chemo-sensitize cisplatin in NSCLC [112]. miR-34 (a-c) has been extensively explored for involvement in the cell cycle progression via modulation of c-Myc, Bcl-2, sirtuin-1, forkhead box P1 (FOXP1), and histone deacetylase (HDACs). Among these subtypes of miRNAs, miR-34c was found to be down-regulated in LC [113,114]. miR-212 and miR-350 have been reported as tumor suppressor miRNAs that exhibit antitumor effects in LC via TRAIL-mediated apoptosis [111]. Thus, looking into the therapeutic involvement of miRNA in LC, two therapeutic approaches are currently used: (1) inhibition or blockage of oncomiRs and (2) stimulation of tumor suppressor miRNA. Various carriers, such as small molecules, oligonucleotides, or viruses, are currently being used to target the various miRNA as shown in Figure 6.

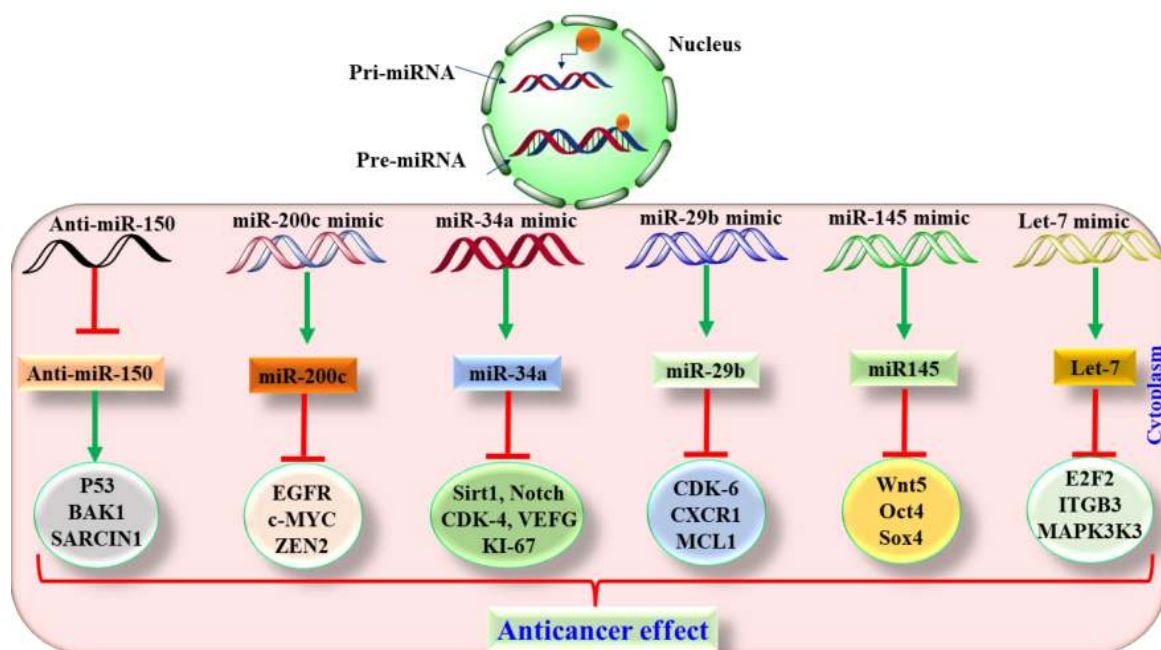


Figure 6. Role of various miRNA in lung cancer.

### 6.2. Preclinical Based Evidence of miRNA in Lung Cancer

Generally, for targeting oncomiRs, antisense anti-miR oligonucleotides (AMO) or locked nucleic acid (LNA), miRNA sponges, or miRNA antagonists are used. AMO is synthetic antisense complementary to the targeted miRNA [96]. AMO binds to the miRNA and inhibits its interaction with the mRNA so that the translation of oncogenic proteins is inhibited and the mRNA performs its normal functions [115]. AMO is thermally unstable and has poor aqueous solubility [116]. Hence, LNA with improved thermal stability and enhanced aqueous solubility was developed. The use of LNA has been reported to silence miR-21 and results in increased apoptosis and reduced tumor burden [117]. Similar to LNA, antagonists and miRNA sponges have been explored to silence the oncomiRs [118]. Apart from miRNA inhibition, restoration of miRNA is also an important therapeutic approach for treatment and management of LC. Generally, miRNA mimics or viral vectors (lentivirus, adenovirus, and retrovirus) are responsible for the miRNA expression (miR-15 and let-7) and are used to restore the normal activity of miRNA functionally [118]. Considering LC, miR-34, 29b, 20c, 145, and let-7 are tumor suppressor miRNAs, and their levels were found to be downregulated in LC [111]. To restore the normal functioning of tumor suppressor miRNA, H460/A549 cells for NSCLC were treated with the let-7 mimic, and the outcome of the study showed a significant antitumor effect [113,119]. Based on the outcome of this study, let-7 was dissolved in lipid base. It was further evaluated in a xenograft model, and a significant reduction in tumor volume was observed [119]. As we have already discussed, miR-34a is downregulated in cancer; hence, synthetic miR-34a was formulated in a lipid-based vehicle and administered to the NSCLC mice. Surprisingly, the use of this lipid-based miRNA-34s caused an effective reduction in cancer severity [113]. The observed mechanism involved in the anticancer effect was found to be reduced expression of ki-67, CDK4, and Bcl-2 [113]. Additionally, the use of this mimic was found to be safe as no sign of toxicity was observed in liver, kidney, and heart [113]. In one interesting studies, miR-145 was administered intratumorally in a lung adenocarcinoma model of mice by incorporating it into the biodegradable polyurethane-branched polyethyleneimine [120]. The study's outcome showed EMT inhibition, increased apoptosis, reduced tumor growth, and angiogenesis [120]. Similar to miR-34a, miR-29b is also a tumor suppressor gene, and in the absence of the normal functioning of miR-29b, CDK-6 is activated and regulates the cascade of tumorigenesis [111]. Thus, a cationic-carrier-based miRNA was developed to incorporate mir-29b and administered to the A549 xenograft mice model to yield a significant antitumor effect [111].

### 6.3. Translatory and Clinical-Based Evidence of miRNA in Lung Cancer

After looking into the potent role of miRNA in the pathogenesis of LC and various preclinical studies reported so far, pharmaceutical industries have come forward to initiate studies for therapeutic implications. Recently, LNA for targeting miR-122 (SPC3649) was developed by Santaris Pharma [121,122]. This anti-miRNA was the one that was entered into a clinical trial [123,124]. MRX34 is a miR-34a mimic, and its efficacy in NSCLC has been investigated in a Phase I clinical trial (NCT01829971) with the concept of miRNA replacement therapy [125,126]. Another clinical trial (NCT01829971) has shown absolute safety, efficacy, and tolerability of this compound. Based on the outcome of these trials, Phase I (NCT02862145) was continued, and a Phase II trial was designed [111]. However, in 2016, severe immunotherapeutic adverse effects (cytokine syndrome) were reported, and this study was terminated [111]. Similarly, another ongoing trial (NCT02862145) involving MRX34 in melanoma was stopped due to unwanted side effects. Apart from MRX34, MesomiR-1 has been entered into a Phase I clinical trial (NCT02369198) for treating NSCLC [111].

## 7. Challenges in Developing miRNA-Based Therapeutics

In recent years, miRNA-based therapy has gained significant attention for LC management and treatment. Indeed, miRNA-based therapy offers several advantages over con-

ventional and target-based therapy, however some hurdles still need to be overcome [127]. One of the major hurdles is successful penetration by the oncomiRs or tumor suppressor miRNA into the tumor cells [128]. Tumor cells consist of an extensive vascular network and a complex leaky surface that significantly alters miRNA penetration into the tumor [128]. Another major challenge for successful miRNA delivery is maintaining their stability and integrity in the systemic circulation. When an miRNA enters the systemic circulation, miRNA is degraded immediately by various RNAases and eventually cleared from the circulation [127].

Additionally, administered miRNA is also excreted via renal excretion [129]. Apart from renal clearance, fast hepatic metabolism, RE and splenic Kuffer's cell-mediated uptake and phagocytosis via the phagosome are other barriers limiting miRNA-based therapeutic outcomes [129]. Apart from these discussed limitations, miRNAs have also been reported to induce immunotoxicity. This limitation occurs because when miRNAs are administered, the innate immune system undergoes activation and causes immunotoxicity in which interferons or Toll-like receptors (INFs or TLRs) are activated [130]. Importantly, miRNA has been reported to cause off-target silencing of various genes and results in unwanted side effects [111,130].

#### *Nanocarrier-Based miRNA Delivery in Lung Cancer*

As we have already discussed, despite the therapeutic potential of miRNA, this system suffers from major pharmacokinetic limitations and exhibits immunotoxicity and off-target gene silencing. Thus, to overcome these limitations, nanocarrier-based miRNA (NC-miR) delivery has been used for the selective targeting of lung cancer cells [131]. When NC-miR delivery is used for lung cancer, several factors, such as tumor vasculature, interstitial fluid pressure, extracellular matrix composition, and lymphatic drainage are taken into consideration [131]. One of the most extensively used NC for the delivery of miRNA is polymeric nanoparticles [132].

Polymeric nanocarriers have also been studied for targeted delivery of miRNA in LC [133]. PEI, LGA, and poly(amidoamine [PAMAM]) are some of the well-studied cationic synthetic polymers [134]. These polymers are advantageous in terms of enhanced stability, cellular specificity, cellular uptake, a low toxicity profile, and being non-immunogenic [134]. PEI was recently used to successfully deliver miR-145 and miR-33a in a xenograft model of colon cancer. The outcome of this study showed an increase in apoptosis and a reduction in tumor growth [134]. miR-154 in combination with cisplatin encapsulated in polyurethane–polyethyleneimine was also studied in LC [135]. In one interesting study, polyarginine–disulfide in conjugation with PEI was studied for the targeted delivery of miR-145 in prostate cancer [136]. A disulphide linker was used to enhance biocompatibility and exhibit desired cytotoxic effects [136]. The study's outcome showed a significant reduction in the rate of tumor growth and increase in the duration of survival. Poly(L-lysine) and polyethyleneimine were used to successfully deliver anti-miR-21 in breast cancer, whereas miR-145 was delivered via polyurethane conjugated with PEI for the treatment of LC [135,137]. Apart from the aforementioned polymeric nanocarriers, *N*-(3-aminopropyl) methacrylamide (APM), ethylene glycol dimethacrylate (EGDMA), and acrylamide (AAM) have been used for the delivery of miRNA, such as anti-miR-21 [138,139]. Gemcitabine is one potent anti-cancer drug, but it suffers from the limitation of chemoresistance. Recent findings have demonstrated the chemosensitizing property of miR-205; hence, a PEG and polypropylene carbonate copolymer nanocarrier was used for delivery of miR-205 in pancreatic cancer [140]. The study's outcome showed a reduction in resistance, tumor size, growth, and weight, and caused an effective reversal of metastasis and tumor invasion [140]. Similarly, a poly( $\epsilon$ -caprolactone [PCL]) and PEG nanocarrier was used for the delivery of miR-200c and docetaxel, and the outcome was studied in both in vitro and in vivo studies [141]. PLGA is another FDA-approved polymer with an established safety profile for miRNA drug delivery [142]. PLGA offers the advantage of surface modification and multiple ligand targeting [142]. When miR-221 was encapsulated into PLGA, increased

apoptosis, reduced tumor growth, migration, angiogenesis and invasion was observed in lung and hepatic carcinoma [143]. Moreover, when PLGA in combination with PEF was studied for miR-10b in addition to anti-miR-21 delivery, a significant reduction in the rate of tumor growth was observed in breast cancer [144]. Additionally, PLGA in combination with PEI was used for co-delivery of doxorubicin and miR-542-3p. The outcome of the study showed enhanced loading capacity, increased drug uptake, cytotoxicity, and significant anti-tumor effects [145].

Dendrimers are branched polymers with the presence of an amine branch that acts as a proton sponge and helps in endosomal escape. Dendrimers have been extensively used for the targeted delivery of miRNA in various types of cancer. Poly-amidoamine (PAMAM) is a cationic polymer and one of the commonly used dendrimers used for the delivery of miRNA [146]. Recently, PAMAM was used as a nanocarrier for the targeted delivery of miR-21 in brain tumors, and the outcome of the study showed an increase in apoptosis and reduction in the rate of tumor growth [146]. Similarly, codelivery of miR-205 and anti-miR-221 using PAMAM showed a significant reduction in tumor size and an increase in survival [147].

It is also important to highlight that various natural polymers, such as chitosan and peptides, have also been studied to deliver miRNA [139]. Chitosan is extensively studied in natural polymers and reported to be biocompatible, safe, and biodegradable [139]. Chitosan and hyaluronic acid nano-complexes were used to incorporate miR-34a and doxorubicin and miR-145 in breast cancer, and the outcome of the study showed synergistic antitumor effects [148,149]. A self-assembly noncomplex was prepared by using protamine sulfate and hyaluronic acid and successfully incorporated miR-34a for the targeted delivery in breast cancer [150]. Similarly, aptamer-conjugated atelocollagen loaded miR-15a and miR16-1 (tumor suppressor miRNA) was used for targeted delivery in prostate cancer [151].

Apart from PNPs, lipid-based nanocarriers for the targeted delivery of miRNA in LC have been extensively studied. Currently, cationic, anionic, and neutral lipid-based nanocarriers (liposomes) have been studied. Liposomes easily cross the cell membrane and release the miRNA inside the cells. However, liposomes suffer from low selectivity and specificity; hence, surface modification techniques have been used to overcome these limitations [152]. Cationic liposomes are more often used for miRNA delivery because of their enhanced cell membrane affinity [107]. They are comparatively easy in terms of production and are considered safe, non-immunogenic, and non-pathogenic. In LC, reduced miR-29b was shown to be positively correlative with pathogenesis. Thus, when a cationic liposome-encapsulated with miR-29b was used, a significant reduction in tumor growth rate was observed [107]. Similarly, the administration of cationic liposomes encapsulated with miR-107 yielded a significant anti-tumor effect [153]. Based on successful preclinical and clinical reports of cationic liposomes, several products such as Lipofectamine<sup>®</sup>, TransIT<sup>®</sup> 2020, and Oligofectamine<sup>™</sup> are now commercially available [154]. Despite being a potent nanocarrier for miRNA delivery, liposome use is limited because of low stability and nonspecific binding affinity toward serum proteins. Hence, to overcome these limitations, polymers, such as PEG, have been conjugated to enhance their stability and half-life [155]. Moreover, liposomes offer the advantage of synergistic drug delivery of chemotherapeutic drugs and miRNA. Recently, cisplatin in combination with miR-375 has been successfully delivered using liposomes in lung cancer [89]. Liposome-based miR-34a and miR-200c have been studied for possible anticancer effects in LC, and the study outcome's shows promising anticancer effects [156]. Additionally, miR-135a-loaded cationic immunoliposomes was also explored in cancer therapy [154].

For a long time, inorganic components have been used to fabricate nanocarriers, keeping the size and morphology as the top priority. Inorganic materials are non-toxic, non-irritating, biocompatible, and easy to synthesize. Among various inorganic nanocarriers, gold nanoparticles (AuNP) have been extensively used for the targeted delivery of miRNA in various types of cancer [157]. AuNPs are advantageous in terms of shape, size, biocompatibility, physio-chemical properties, surface functionalization, and amphiphilic-



ity [139]. AuNP encapsulated with miR-205 was used to treat prostate cancer in PC-3 cell lines in which the administration of nanocarriers showed enhanced apoptosis in addition to reduced proliferation and rates of tumor growth [139]. It was found that the presence of miR-20a is associated with a pro-oncogenic role and protects the tumor cells against doxorubicin-induced cytotoxicity [139]. Thus, cysteamine-functionalized AuNP was used for the delivery of miR-31 that acted as a suppressor of miR-20a and exhibited a significant anti-tumour effect [158]. It was further found that AuNP showed a 10–20-fold increase in concentrations of miR-31 and miR-1323 as compared to the conventional delivery in neuroblastoma and ovarian cell lines [139]. Additionally, when thiolated AuNP was used to deliver miR-145, a significant anti-tumor effect was observed in prostate and breast cancer [159].

Silica is one of the extensively used inorganic materials and has also been successfully used to fabricate nanocarriers for the targeted delivery of miRNA in various types of cancer [160]. Mesoporous silica nanoparticles (MSN) are silica-based inorganic nanocarriers that offer the advantage of safe, biocompatible, stable, and greater surface loading of miRNA [160]. MSN was successfully used for the delivery of miRNA-34, which is a tumor suppressor for miRNA [161]. The use of MSN-loaded miR-34 showed an increase in apoptosis and reduction in tumor growth in tumor cells. Recently, an immunoliposome loaded with PD-L1 antibody and miR-10a was tested in a cancer model, and the outcome of the study showed the significant anticancer potential of this nanocarrier system [139]. MSN was also used for the delivery of temozolomide and anti-miR-221, which eventually resulted in inhibition of the cell cycle, proliferation, and stimulated apoptosis, and overcame the issue of drug resistance [162].

Recently, magnetic compounds were also used for the targeted drug delivery of miRNA in cancer. In one study, zinc–iron oxide loaded with lethal-7a miRNA was used to treat cancer [163]. Similarly, lanthanide Ce<sup>3/4+</sup> cations combined with oxidized PEI were used to deliver antisense miR-486, anti-miR-99a, and anti-miR-21 into human CMK leukemia and pancreatic cells [164]. Apart from MSN, carbonate apatite has been studied for the possible nanocarrier property for miRNAs. In one of the studies, miR-4689 was incorporated into carbonate apatite NP to target KRAS in addition to AKT in cancer cells [165]. Similarly, miR-29b-1-5p was also incorporated into carbonate apatite NP against Caco cell lines with confirmed KRAS mutation. The outcome of the study showed increased apoptosis, reduced proliferation, and a better safety profile [166].

## 8. Conclusions and Future Prospects

LC is one of the major causes of morbidity and mortality worldwide. The etiology of LC has been identified as multifactorial in origin [167,168]. Various signaling pathways and molecules are involved in the initiation, progression, angiogenesis, and invasion of LC [14]. Many conventional and signaling molecular-based targeted drugs have been approved by the FDA, and many more are in the pipeline. Undoubtedly, the clinical use of these approved drugs has contributed significantly to increasing progression-free survival and improved patients' quality of life [14]. However, most of these drugs suffer from pharmacokinetic limitations of low solubility, low bioavailability, and fast hepatic metabolism, which are not capable of reaching the target site, or penetration across the tumor cell [47]. Not only this, but most of the approved drugs also suffer from the pharmacodynamic limitation of severe adverse effects when used through oral and intravenous routes [47]. In order to overcome these limitations, inhalation and intratumoral routes were used, but unfortunately, these approaches were also not up to the expectation [169,170]. Thus, nanocarrier-based targeted drug delivery was used in which many of the approved drugs were encapsulated into the suitable nanocarrier to minimize pharmacokinetics and dose-related adverse effects [53]. Additionally, nanocarrier-based drug delivery increases stability, avoids fast hepatic metabolism, and ensures the maximum drug concentration at the site of action [53]. A large number of preclinical and clinical studies have confirmed the therapeutic utility of nanocarrier-based drug delivery in LC [53]. Currently, a few clinical

trials are being conducted so that more and more patients can benefit from this therapeutic approach [170].

It is of further importance to understand that the epithelial tissue of the lungs is the center of origin, and inhalation-based therapy has access to this area. However, NSCLC or SCLC can originate from any part of the lungs, such as bronchial epithelium, peripheral bronchioles, or alveolar epithelium [171]. Thus, a nanocarrier for the treatment of SCLC or NSCLC must reach a specific area for exerting a desired pharmacological effect. For example, NC with particles size of 5 to 10  $\mu\text{m}$  can reach the central epithelium [171]. However, a particle size in the range of 0.1 to 3  $\mu\text{m}$  is needed for crossing the deep pulmonary tissue. Moreover, an ideal nanocarrier must exhibit a sustained drug release profile, and for the treatment of stage IV lung cancer, systemic absorption is desirable. At this stage, tumor cells gain access to lymph nodes or vital organs [172]. Thus, with the same nanocarrier system, systemic in addition to localized absorption of the drug is challenging. Thus, extensive research concluded that a multilamellar liposome is the best option for localized absorption, whereas dendrimers are suitable for systemic absorption [173].

Another problem encountered in using nanocarriers in LC is the later stage of diagnosis. Presuming that it is diagnosed at the early stage, patients also have difficulty in breathing, breathlessness, lower tidal volume, and total lung capacity. In such cases, drug delivery and absorption from the peripheral tissue are difficult [172]. Hence, spacers and power sources were used to deliver drugs at the nano size so that they could be absorbed in the deep tissue. Despite being a novel and promising therapeutic approach, nanocarrier-based drug delivery has limitations, such as toxicity due to multiple components, phagocytosis, and drug efflux ineffectiveness due to complex vasculature and the inability to penetrate the tumor mass [174]. Hence, recently, miRNA has been identified as an emerging weapon against lung cancer. However, the use of necked miRNA was associated with fast degradation by RNase, problems in crossing biological membranes, rapid clearance, and thermal instability when administered [99]. Hence, techniques, such as chemical modification, encapsulating them in suitable nanocarriers, and using cationic polymers, have been used to overcome these limitations [175]. Currently, a few nanocarrier-based (lipid-based) miRNAs, such as MRX34, miR-34a, and let-7, are under clinical investigation for possible use in LC treatment [175].

Thus, based on the in-depth literature survey, available clinical evidence, and completed clinical trials, we suggest that a safe and effective nanocarrier system should be developed for the targeted delivery of chemotherapeutic drugs in addition to miRNA. Genomic expression of mRNA in addition to pathway enrichment analysis should be done to identify selective targets for miRNA. Furthermore, to avoid the toxicity and off-targeted side effects and also achieve cell/target-specific delivery of chemotherapeutic drugs and miRNA, low dose combinations of miRNA and anticancer drugs, radiotherapy, and immunotherapy can be used. Additionally, the antibody-coated combination of miRNA and existing anticancer agents should be used in a suitable nanocarrier system. This novel drug delivery system may pave the way for clinical treatment in the coming years.

**Author Contributions:** Conceptualization, S.M., N.A.A. and M.K.I.; methodology, S.M., N.A.A., M.K.I., G.A.G., S.K., S.S.A.M.; software, M.K.I., G.A.G., S.K., S.S.A.M.; investigation, S.M., N.A.A. and M.K.I. data curation, S.M., N.A.A., M.K.I., G.A.G., S.K., S.S.A.M.; writing—S.M., N.A.A., M.K.I., G.A.G., S.K., S.S.A.M.; writing—review and editing, S.M., N.A.A. and S.K.; project administration, S.M. and N.A.A.; funding acquisition, N.A.A. and M.K.I. All authors have read and agreed to the published version of the manuscript.

**Funding:** The Deanship of Scientific Research (DSR) at King Abdulaziz University, Jeddah, Saudi Arabia, has funded this project under grant no. (FP-020-43).

**Institutional Review Board Statement:** Not applicable.

**Informed Consent Statement:** Not applicable.

**Data Availability Statement:** The data presented in this study are available in article.

**Acknowledgments:** The authors acknowledge DSR for technical and financial support.

**Conflicts of Interest:** The authors declare no conflict of interest.

## References

1. Kumar, M.; Jha, A.; Dr, M.; Mishra, B. Targeted drug nanocrystals for pulmonary delivery: A potential strategy for lung cancer therapy. *Expert Opin. Drug Deliv.* **2020**, *17*, 1459–1472. [CrossRef] [PubMed]
2. Sung, H.; Ferlay, J.; Siegel, R.L.; Laversanne, M.; Soerjomataram, I.; Jemal, A.; Bray, F. Global cancer statistics 2020: GLOBOCAN estimates of incidence and mortality worldwide for 36 cancers in 185 countries. *CA Cancer J. Clin.* **2021**, *71*, 209–249. [CrossRef] [PubMed]
3. Turner, M.C.; Andersen, Z.J.; Baccarelli, A.; Diver, W.R.; Gapstur, S.M.; Pope, C.A., III; Prada, D.; Samet, J.; Thurston, G.; Cohen, A. Outdoor air pollution and cancer: An overview of the current evidence and public health recommendations. *CA Cancer J. Clin.* **2020**, *70*, 460–479. [CrossRef]
4. Merewether, E.R.A.; Price, C. *Report on Effects of Asbestos Dust on the Lungs and Dust Suppression in the Asbestos Industry. Part I. Occurrence of Pulmonary Pibrosis and Other Pulmonary Affections in Asbestos Workers*; H.M.S.O.: London, UK, 1930.
5. Cooke, W.E. Pulmonary asbestosis. *Br. Med. J.* **1927**, *2*, 1024. [CrossRef]
6. Wood, W.B.; Gloyne, S.R. Pulmonary Asbestosis. *Lancet* **1930**, 445–448. [CrossRef]
7. Suraya, A.; Nowak, D.; Sulistomo, A.W.; Ghanie Icksan, A.; Syahrudin, E.; Berger, U.; Bose-O'Reilly, S. Asbestos-related lung cancer: A hospital-based case-control study in Indonesia. *Int. J. Environ. Res. Public Health* **2020**, *17*, 591. [CrossRef]
8. Kwak, K.; Kang, D.; Paek, D. Environmental exposure to asbestos and the risk of lung cancer: A systematic review and meta-analysis. *Occup. Environ. Med.* **2021**. [CrossRef]
9. Cooper, W.A.; Lam, D.C.; O'Toole, S.A.; Minna, J.D. Molecular biology of lung cancer. *J. Thorac. Dis.* **2013**, *5*, S479.
10. Su, D.; Ma, S.; Liu, P.; Jiang, Z.; Lv, W.; Zhang, Y.; Deng, Q.; Smith, S.; Yu, H. Genetic polymorphisms and treatment response in advanced non-small cell lung cancer. *Lung Cancer* **2007**, *56*, 281–288. [CrossRef]
11. Swanton, C.; Govindan, R. Clinical implications of genomic discoveries in lung cancer. *N. Engl. J. Med.* **2016**, *374*, 1864–1873. [CrossRef] [PubMed]
12. Solomon, B.J.; Bauer, T.M.; Felip, E.; Besse, B.; James, L.P.; Clancy, J.S.; Klamerus, K.J.; Martini, J.-F.; Abbattista, A.; Shaw, A.T. Safety and efficacy of lorlatinib (PF-06463922) from the dose-escalation component of a study in patients with advanced ALK+ or ROS1+ non-small cell lung cancer (NSCLC). *J. Clin. Oncol.* **2016**, *34*, 9009. [CrossRef]
13. Rosell, R.; Karachaliou, N.; Arrieta, O. Novel molecular targets for the treatment of lung cancer. *Curr. Opin. Oncol.* **2020**, *32*, 37–43. [CrossRef] [PubMed]
14. Cheng, L.; Alexander, R.E.; MacLennan, G.T.; Cummings, O.W.; Montironi, R.; Lopez-Beltran, A.; Cramer, H.M.; Davidson, D.D.; Zhang, S. Molecular pathology of lung cancer: Key to personalized medicine. *Mod. Pathol.* **2012**, *25*, 347–369. [CrossRef] [PubMed]
15. Brambilla, E.; Gazdar, A. Pathogenesis of lung cancer signalling pathways: Roadmap for therapies. *Eur. Respir. J.* **2009**, *33*, 1485–1497. [CrossRef] [PubMed]
16. Tumbriak, H.L.; Heimsoeth, A.; Sos, M.L. The next tier of EGFR resistance mutations in lung cancer. *Oncogene* **2021**, *40*, 1–11. [CrossRef]
17. Gupta, R.; Dastane, A.M.; Forozan, F.; Riley-Portuguez, A.; Chung, F.; Lopategui, J.; Marchevsky, A.M. Evaluation of EGFR abnormalities in patients with pulmonary adenocarcinoma: The need to test neoplasms with more than one method. *Mod. Pathol.* **2009**, *22*, 128–133. [CrossRef] [PubMed]
18. Rosell, R.; Robinet, G.; Szczesna, A.; Ramlau, R.; Constenla, M.; Menecier, B.; Pfeifer, W.; O'Byrne, K.J.; Welte, T.; Kolb, R. Randomized phase II study of cetuximab plus cisplatin/vinorelbine compared with cisplatin/vinorelbine alone as first-line therapy in EGFR-expressing advanced non-small-cell lung cancer. *Ann. Oncol.* **2008**, *19*, 362–369. [CrossRef]
19. Langer, C.J. Emerging role of epidermal growth factor receptor inhibition in therapy for advanced malignancy: Focus on NSCLC. *Int. J. Radiat. Oncol. Biol. Phys.* **2004**, *58*, 991–1002. [CrossRef]
20. Zhou, C.; Wu, Y.-L.; Chen, G.; Feng, J.; Liu, X.-Q.; Wang, C.; Zhang, S.; Wang, J.; Zhou, S.; Ren, S. Erlotinib versus chemotherapy as first-line treatment for patients with advanced EGFR mutation-positive non-small-cell lung cancer (OPTIMAL, CTONG-0802): A multicentre, open-label, randomised, phase 3 study. *Lancet Oncol.* **2011**, *12*, 735–742. [CrossRef]
21. Gridelli, C.; Ciardiello, F.; Gallo, C.; Feld, R.; Butts, C.; Gebbia, V.; Maione, P.; Morgillo, F.; Genestreti, G.; Favaretto, A. First-line erlotinib followed by second-line cisplatin-gemcitabine chemotherapy in advanced non-small-cell lung cancer: The TORCH randomized trial. *J. Clin. Oncol.* **2012**, *30*, 3002–3011. [CrossRef]
22. Ciuleanu, T.; Stelmakh, L.; Cicenias, S.; Miliuskas, S.; Grigorescu, A.C.; Hillenbach, C.; Johannsdottir, H.K.; Klughammer, B.; Gonzalez, E.E. Efficacy and safety of erlotinib versus chemotherapy in second-line treatment of patients with advanced, non-small-cell lung cancer with poor prognosis (TITAN): A randomised multicentre, open-label, phase 3 study. *Lancet Oncol.* **2012**, *13*, 300–308. [CrossRef]
23. Zhang, L.; Ma, S.; Song, X.; Han, B.; Cheng, Y.; Huang, C.; Yang, S.; Liu, X.; Liu, Y.; Lu, S. Gefitinib versus placebo as maintenance therapy in patients with locally advanced or metastatic non-small-cell lung cancer (INFORM; C-TONG 0804): A multicentre, double-blind randomised phase 3 trial. *Lancet Oncol.* **2012**, *13*, 466–475. [CrossRef]

24. Pirker, R.; Pereira, J.R.; Von Pawel, J.; Krzakowski, M.; Ramlau, R.; Park, K.; De Marinis, F.; Eberhardt, W.E.; Paz-Ares, L.; Störkel, S. EGFR expression as a predictor of survival for first-line chemotherapy plus cetuximab in patients with advanced non-small-cell lung cancer: Analysis of data from the phase 3 FLEX study. *Lancet Oncol.* **2012**, *13*, 33–42. [CrossRef]
25. Teleanu, R.I.; Chircov, C.; Grumezescu, A.M.; Teleanu, D.M. Tumor angiogenesis and anti-angiogenic strategies for cancer treatment. *J. Clin. Med.* **2020**, *9*, 84. [CrossRef]
26. Altorki, N.; Lane, M.E.; Bauer, T.; Lee, P.C.; Guarino, M.J.; Pass, H.; Felip, E.; Peylan-Ramu, N.; Garpide, A.; Grannis, F.W. Phase II proof-of-concept study of pazopanib monotherapy in treatment-naïve patients with stage I/II resectable non-small-cell lung cancer. *J. Clin. Oncol.* **2010**, *28*, 3131–3137. [CrossRef]
27. Lee, J.S.; Hirsh, V.; Park, K.; Qin, S.; Blajman, C.R.; Perng, R.-P.; Chen, Y.-M.; Emerson, L.; Langmuir, P.; Manegold, C. Vandetanib versus placebo in patients with advanced non-small-cell lung cancer after prior therapy with an epidermal growth factor receptor tyrosine kinase inhibitor: A randomized, double-blind phase III trial (ZEPHYR). *J. Clin. Oncol.* **2012**, *30*, 1114–1121. [CrossRef]
28. Ferrara, N.; Hillan, K.J.; Gerber, H.-P.; Novotny, W. Discovery and development of bevacizumab, an anti-VEGF antibody for treating cancer. *Nat. Rev. Drug Discov.* **2004**, *3*, 391–400. [CrossRef]
29. Dahlberg, S.; Sandler, A.; Brahmer, J.; Schiller, J.; Johnson, D. Clinical course of advanced non-small cell lung cancer (NSCLC) patients (pts) experiencing hypertension (HTN) during treatment (TX) with bevacizumab (B) in combination with carboplatin (C) and paclitaxel (P) on E4599. *J. Clin. Oncol.* **2009**, *27*, 8042. [CrossRef]
30. Herbst, R.S.; Ansari, R.; Bustin, F.; Flynn, P.; Hart, L.; Otterson, G.A.; Vlahovic, G.; Soh, C.-H.; O'Connor, P.; Hainsworth, J. Efficacy of bevacizumab plus erlotinib versus erlotinib alone in advanced non-small-cell lung cancer after failure of standard first-line chemotherapy (BeTa): A double-blind, placebo-controlled, phase 3 trial. *Lancet* **2011**, *377*, 1846–1854. [CrossRef]
31. Reck, M.; von Pawel, J.; Zatloukal, P.; Ramlau, R.; Gorbounova, V.; Hirsh, V.; Leighl, N.; Mezger, J.; Archer, V.; Moore, N. Phase III trial of cisplatin plus gemcitabine with either placebo or bevacizumab as first-line therapy for nonsquamous non-small-cell lung cancer: AVAiL. *J. Clin. Oncol.* **2009**, *27*, 1227–1234. [CrossRef]
32. Ray, M.R.; Jablons, D.; He, B. Lung cancer therapeutics that target signaling pathways: An update. *Expert Rev. Respir. Med.* **2010**, *4*, 631–645. [CrossRef] [PubMed]
33. Tan, A.C. Targeting the PI3K/Akt/mTOR pathway in non-small cell lung cancer (NSCLC). *Thorac. Cancer* **2020**, *11*, 511–518. [CrossRef]
34. Papadimitrakopoulou, V. Development of PI3K/AKT/mTOR pathway inhibitors and their application in personalized therapy for non-small-cell lung cancer. *J. Thorac. Oncol.* **2012**, *7*, 1315–1326. [CrossRef]
35. Tsurutani, J.; Fukuoka, J.; Tsurutani, H.; Shih, J.H.; Hewitt, S.M.; Travis, W.D.; Jen, J.; Dennis, P.A. Evaluation of two phosphorylation sites improves the prognostic significance of Akt activation in non-small-cell lung cancer tumors. *J. Clin. Oncol.* **2006**, *24*, 306–314. [CrossRef] [PubMed]
36. Cheng, H.; Shcherba, M.; Pendurti, G.; Liang, Y.; Piperdi, B.; Perez-Soler, R. Targeting the PI3K/AKT/mTOR pathway: Potential for lung cancer treatment. *Lung Cancer Manag.* **2014**, *3*, 67–75. [CrossRef]
37. Kim, L.C.; Cook, R.S.; Chen, J. mTORC1 and mTORC2 in cancer and the tumor microenvironment. *Oncogene* **2017**, *36*, 2191–2201. [CrossRef]
38. Gadgeel, S.M.; Wozniak, A. Preclinical rationale for PI3K/Akt/mTOR pathway inhibitors as therapy for epidermal growth factor receptor inhibitor-resistant non-small-cell lung cancer. *Clin. Lung Cancer* **2013**, *14*, 322–332. [CrossRef] [PubMed]
39. Brambilla, E.; Brambilla, C. p53 and lung cancer. *Pathologie-Biologie* **1997**, *45*, 852–863.
40. Zhao, H.; Yang, B.; Xu, J.; Chen, D.-m.; Xiao, C.-l. PM2. 5-induced alterations of cell cycle associated gene expression in lung cancer cells and rat lung tissues. *Environ. Toxicol. Pharmacol.* **2017**, *52*, 77–82. [CrossRef]
41. Rasheduzzaman, M.; Jeong, J.-K.; Park, S.-Y. Resveratrol sensitizes lung cancer cell to TRAIL by p53 independent and suppression of Akt/NF-κB signaling. *Life Sci.* **2018**, *208*, 208–220. [CrossRef]
42. Giacomini, A.; Taranto, S.; Rezzola, S.; Matarazzo, S.; Grillo, E.; Bugatti, M.; Scotuzzi, A.; Guerra, J.; Di Trani, M.; Presta, M. Inhibition of the FGF/FGFR system induces apoptosis in lung cancer cells via c-Myc downregulation and oxidative stress. *Int. J. Mol. Sci.* **2020**, *21*, 9376. [CrossRef] [PubMed]
43. Shivapurkar, N.; Reddy, J.; Chaudhary, P.M.; Gazdar, A.F. Apoptosis and lung cancer: A review. *J. Cell. Biochem.* **2003**, *88*, 885–898. [CrossRef] [PubMed]
44. Yuan, X.; Gajan, A.; Chu, Q.; Xiong, H.; Wu, K.; Wu, G.S. Developing TRAIL/TRAIL death receptor-based cancer therapies. *Cancer Metastasis Rev.* **2018**, *37*, 733–748. [CrossRef] [PubMed]
45. Shahverdi, M.; Amini, R.; Amri, J.; Karami, H. Gene Therapy with MiRNA-Mediated Targeting of Mcl-1 Promotes the Sensitivity of Non-Small Cell Lung Cancer Cells to Treatment with ABT-737. *Asian Pac. J. Cancer Prev. APJCP* **2020**, *21*, 675. [CrossRef]
46. Cooper, S.; Spiro, S.G. Small cell lung cancer: Treatment review. *Respirology* **2006**, *11*, 241–248. [CrossRef]
47. Amararathna, M.; Goralski, K.; Hoskin, D.W.; Rupasinghe, H.V. Pulmonary nano-drug delivery systems for lung cancer: Current knowledge and prospects. *J. Lung Health Dis.* **2019**, *3*, 11–28. [CrossRef]
48. Biswas, B.; Ghadyalpatil, N.; Krishna, M.; Deshmukh, J. A review on adverse event profiles of epidermal growth factor receptor-tyrosine kinase inhibitors in non-small cell lung cancer patients. *Indian J. Cancer* **2017**, *54*, 55. [CrossRef]
49. Guan, M.; Zhou, Y.-P.; Sun, J.-L.; Chen, S.-C. Adverse events of monoclonal antibodies used for cancer therapy. *BioMed Res. Int.* **2015**, *2015*, 1–13. [CrossRef] [PubMed]

50. Choudhury, H.; Pandey, M.; Gorain, B.; Chatterjee, B.; Madheswaran, T.; Md, S.; Mak, K.-K.; Tambuwala, M.; Chourasia, M.K.; Kesharwani, P. Nanoemulsions as effective carriers for the treatment of lung cancer. In *Nanotechnology-Based Targeted Drug Delivery Systems for Lung Cancer*; Elsevier: Amsterdam, The Netherlands, 2019; pp. 217–247.
51. Sharma, P.; Mehta, M.; Dhanjal, D.S.; Kaur, S.; Gupta, G.; Singh, H.; Thangavelu, L.; Rajeshkumar, S.; Tambuwala, M.; Bakshi, H.A. Emerging trends in the novel drug delivery approaches for the treatment of lung cancer. *Chem.-Biol. Interact.* **2019**, *309*, 108720. [CrossRef]
52. Iqbal, A.; Syed, M.A.; Najmi, A.K.; Azam, F.; Barreto, G.E.; Iqbal, M.K.; Ali, J.; Haque, S.E. Nano-engineered nerolidol loaded lipid carrier delivery system attenuates cyclophosphamide neurotoxicity—Probable role of NLRP3 inflammasome and caspase-1. *Exp. Neurol.* **2020**, *334*, 113464. [CrossRef]
53. Abdelaziz, H.M.; Gaber, M.; Abd-Elwakil, M.M.; Mabrouk, M.T.; Elgohary, M.M.; Kamel, N.M.; Kabary, D.M.; Freag, M.S.; Samaha, M.W.; Mortada, S.M. Inhalable particulate drug delivery systems for lung cancer therapy: Nanoparticles, microparticles, nanocomposites and nanoaggregates. *J. Control. Release* **2018**, *269*, 374–392. [CrossRef] [PubMed]
54. Jung, J.; Park, S.-J.; Chung, H.K.; Kang, H.-W.; Lee, S.-W.; Seo, M.H.; Park, H.J.; Song, S.Y.; Jeong, S.-Y.; Choi, E.K. Polymeric nanoparticles containing taxanes enhance chemoradiotherapeutic efficacy in non-small cell lung cancer. *Int. J. Radiat. Oncol. Biol. Phys.* **2012**, *84*, e77–e83. [CrossRef] [PubMed]
55. Ray, L. Polymeric Nanoparticle-Based Drug/Gene Delivery for Lung Cancer. In *Nanotechnology-Based Targeted Drug Delivery Systems for Lung Cancer*; Elsevier: Amsterdam, The Netherlands, 2019; pp. 77–93.
56. Kim, D.-W.; Kim, S.-Y.; Kim, H.-K.; Kim, S.-W.; Shin, S.; Kim, J.; Park, K.; Lee, M.; Heo, D.S. Multicenter phase II trial of Genexol-PM, a novel Cremophor-free, polymeric micelle formulation of paclitaxel, with cisplatin in patients with advanced non-small-cell lung cancer. *Ann. Oncol.* **2007**, *18*, 2009–2014. [CrossRef] [PubMed]
57. Ahn, H.K.; Jung, M.; Sym, S.J.; Shin, D.B.; Kang, S.M.; Kyung, S.Y.; Park, J.-W.; Jeong, S.H.; Cho, E.K. A phase II trial of Cremophor EL-free paclitaxel (Genexol-PM) and gemcitabine in patients with advanced non-small cell lung cancer. *Cancer Chemother. Pharmacol.* **2014**, *74*, 277–282. [CrossRef] [PubMed]
58. Mehrotra, A.; Nagarwal, R.C.; Pandit, J.K. Lomustine loaded chitosan nanoparticles: Characterization and in-vitro cytotoxicity on human lung cancer cell line L132. *Chem. Pharm. Bull.* **2011**, *59*, 315–320. [CrossRef]
59. Nafee, N.; Schneider, M.; Friebel, K.; Dong, M.; Schaefer, U.; Mürdter, T.; Lehr, C.-M. Treatment of lung cancer via telomerase inhibition: Self-assembled nanoplexes versus polymeric nanoparticles as vectors for 2'-O-Methyl-RNA. *Eur. J. Pharm. Biopharm.* **2012**, *80*, 478–489. [CrossRef] [PubMed]
60. Al-Hallak, K.M.; Azarmi, S.; Anwar-Mohamed, A.; Roa, W.H.; Löbenberg, R. Secondary cytotoxicity mediated by alveolar macrophages: A contribution to the total efficacy of nanoparticles in lung cancer therapy? *Eur. J. Pharm. Biopharm.* **2010**, *76*, 112–119. [CrossRef]
61. Large, D.E.; Abdelmessih, R.G.; Fink, E.; Auguste, D.T. Liposome composition in drug delivery design, synthesis, characterization, and clinical application. *Adv. Drug Deliv. Rev.* **2021**, *176*, 113851. [CrossRef]
62. Jiménez-López, J.; Bravo-Caparrós, I.; Cabeza, L.; Nieto, F.R.; Ortiz, R.; Perazzoli, G.; Fernández-Segura, E.; Cañizares, F.J.; Baeyens, J.M.; Melguizo, C. Paclitaxel antitumor effect improvement in lung cancer and prevention of the painful neuropathy using large pegylated cationic liposomes. *Biomed. Pharmacother.* **2021**, *133*, 111059. [CrossRef]
63. Hussain, S. Nanomedicine for treatment of lung cancer. *Lung Cancer Pers. Med.: Novel Ther. Clin. Manag.* **2016**, *890*, 137–147.
64. Garbuzenko, O.B.; Saad, M.; Pozharov, V.P.; Reuhl, K.R.; Mainelis, G.; Minko, T. Inhibition of lung tumor growth by complex pulmonary delivery of drugs with oligonucleotides as suppressors of cellular resistance. *Proc. Natl. Acad. Sci. USA* **2010**, *107*, 10737–10742. [CrossRef] [PubMed]
65. Miao, Y.-Q.; Chen, M.-S.; Zhou, X.; Guo, L.-M.; Zhu, J.-J.; Wang, R.; Zhang, X.-X.; Gan, Y. Chitosan oligosaccharide modified liposomes enhance lung cancer delivery of paclitaxel. *Acta Pharmacol. Sin.* **2021**, *42*, 1714–1722. [CrossRef]
66. Miyoshi, T.; Misumi, N.; Hiraike, M.; Mihara, Y.; Nishino, T.; Tsuruta, M.; Kawamata, Y.; Hiraki, Y.; Kozono, A.; Ichiki, M. Risk factors associated with cisplatin-induced nephrotoxicity in patients with advanced lung cancer. *Biol. Pharm. Bull.* **2016**, *39*, 2009–2014. [CrossRef]
67. Choradiya, B.R.; Patil, S.B. A Comprehensive Review on Nanoemulsion as an Ophthalmic Drug Delivery System. *J. Mol. Liq.* **2021**, *339*, 116751. [CrossRef]
68. Gurpreet, K.; Singh, S. Review of nanoemulsion formulation and characterization techniques. *Indian J. Pharm. Sci.* **2018**, *80*, 781–789. [CrossRef]
69. Singh, Y.; Meher, J.G.; Raval, K.; Khan, F.A.; Chaurasia, M.; Jain, N.K.; Chourasia, M.K. Nanoemulsion: Concepts, development and applications in drug delivery. *J. Control. Release* **2017**, *252*, 28–49. [CrossRef] [PubMed]
70. dos Santos Câmara, A.L.; Nagel, G.; Tschiche, H.R.; Cardador, C.M.; Muehlmann, L.A.; de Oliveira, D.M.; Alvim, P.Q.; Azevedo, R.B.; Calderón, M.; Figueiro Longo, J.P. Acid-sensitive lipidated doxorubicin prodrug entrapped in nanoemulsion impairs lung tumor metastasis in a breast cancer model. *Nanomedicine* **2017**, *12*, 1751–1765. [CrossRef]
71. Kim, J.-E.; Park, Y.-J. Improved antitumor efficacy of hyaluronic acid-complexed paclitaxel nanoemulsions in treating non-small cell lung cancer. *Biomol. Ther.* **2017**, *25*, 411. [CrossRef]
72. Li, X.; Du, L.; Wang, C.; Liu, Y.; Mei, X.; Jin, Y. Highly efficient and lowly toxic docetaxel nanoemulsions for intravenous injection to animals. *Die Pharm.* **2011**, *66*, 479–483.

73. Wan, K.; Sun, L.; Hu, X.; Yan, Z.; Zhang, Y.; Zhang, X.; Zhang, J. Novel nanoemulsion based lipid nanosystems for favorable in vitro and in vivo characteristics of curcumin. *Int. J. Pharm.* **2016**, *504*, 80–88. [CrossRef] [PubMed]
74. Lev-Ari, S.; Starr, A.; Katzburg, S.; Berkovich, L.; Rimmon, A.; Ben-Yosef, R.; Vexler, A.; Ron, I.; Earon, G. Curcumin induces apoptosis and inhibits growth of orthotopic human non-small cell lung cancer xenografts. *J. Nutr. Biochem.* **2014**, *25*, 843–850. [CrossRef]
75. Fan, Z.; Duan, X.; Cai, H.; Wang, L.; Li, M.; Qu, J.; Li, W.; Wang, Y.; Wang, J. Curcumin inhibits the invasion of lung cancer cells by modulating the PKC $\alpha$ /Nox-2/ROS/ATF-2/MMP-9 signaling pathway. *Oncol. Rep.* **2015**, *34*, 691–698. [CrossRef] [PubMed]
76. Sun, L.; Wan, K.; Hu, X.; Zhang, Y.; Yan, Z.; Feng, J.; Zhang, J. Functional nanoemulsion-hybrid lipid nanocarriers enhance the bioavailability and anti-cancer activity of lipophilic diferuloylmethane. *Nanotechnology* **2016**, *27*, 085102. [CrossRef] [PubMed]
77. Jyoti, K.; Kaur, K.; Pandey, R.S.; Jain, U.K.; Chandra, R.; Madan, J. Inhalable nanostructured lipid particles of 9-bromo-noscapine, a tubulin-binding cytotoxic agent: In vitro and in vivo studies. *J. Colloid Interface Sci.* **2015**, *445*, 219–230. [CrossRef]
78. Arbain, N.A.N.; Basri, M.; Salim, N.; Wui, W.; Rahman, M.A. Aerosolized nanoemulsion system encapsulating quercetin for lung cancer treatment. *Mater. Today Proc.* **2018**, *5*, S137–S142. [CrossRef]
79. Zhao, H.; Lu, H.; Gong, T.; Zhang, Z. Nanoemulsion loaded with lycobetaine–oleic acid ionic complex: Physicochemical characteristics, in vitro, in vivo evaluation, and antitumor activity. *Int. J. Nanomed.* **2013**, *8*, 1959. [CrossRef] [PubMed]
80. Zhang, Y.; Jiang, P.; Ye, M.; Kim, S.-H.; Jiang, C.; Lü, J. Tanshinones: Sources, pharmacokinetics and anti-cancer activities. *Int. J. Mol. Sci.* **2012**, *13*, 13621–13666. [CrossRef]
81. Lee, W.Y.; Liu, K.W.; Yeung, J.H. Reactive oxygen species-mediated kinase activation by dihydrotanshinone in tanshinones-induced apoptosis in HepG2 cells. *Cancer Lett.* **2009**, *285*, 46–57. [CrossRef]
82. Lee, W.; Liang, Y.; Chen, B. Effects of tanshinone nanoemulsion and extract on inhibition of lung cancer cells A549. *Nanotechnology* **2016**, *27*, 495101. [CrossRef] [PubMed]
83. Liu, T.-t.; Mu, L.-Q.; Dai, W.; Wang, C.-b.; Liu, X.-Y.; Xiang, D.-X. Preparation, characterization, and evaluation of antitumor effect of Brucea javanica oil cationic nanoemulsions. *Int. J. Nanomed.* **2016**, *11*, 2515. [CrossRef]
84. Bahman, F.; Elkaissi, S.; Greish, K.; Taurin, S. Polymeric Micelles in Management of Lung Cancer. In *Nanotechnology-Based Targeted Drug Delivery Systems for Lung Cancer*; Elsevier: Amsterdam, The Netherlands, 2019; pp. 193–216.
85. Matsumura, Y.; Kataoka, K. Preclinical and clinical studies of anticancer agent-incorporating polymer micelles. *Cancer Sci.* **2009**, *100*, 572–579. [CrossRef]
86. Maeda, H.; Ueda, M.; Morinaga, T.; Matsumoto, T. Conjugation of poly (styrene-co-maleic acid) derivatives to the antitumor protein neocarzinostatin: Pronounced improvements in pharmacological properties. *J. Med. Chem.* **1985**, *28*, 455–461. [CrossRef]
87. Dalela, M.; Shrivastav, T.; Kharbanda, S.; Singh, H. pH-sensitive biocompatible nanoparticles of paclitaxel-conjugated poly (styrene-co-maleic acid) for anticancer drug delivery in solid tumors of syngeneic mice. *ACS Appl. Mater. Interfaces* **2015**, *7*, 26530–26548. [CrossRef]
88. Yang, Z.L.; Li, X.R.; Yang, K.W.; Liu, Y. Amphotericin B-loaded poly (ethylene glycol)–poly (lactide) micelles: Preparation, freeze-drying, and in vitro release. *J. Biomed. Mater. Res. Part A* **2008**, *85*, 539–546. [CrossRef]
89. Cho, H.; Gao, J.; Kwon, G.S. PEG-b-PLA micelles and PLGA-b-PEG-b-PLGA sol–gels for drug delivery. *J. Control. Release* **2016**, *240*, 191–201. [CrossRef]
90. Xiao, R.Z.; Zeng, Z.W.; Zhou, G.L.; Wang, J.J.; Li, F.Z.; Wang, A.M. Recent advances in PEG–PLA block copolymer nanoparticles. *Int. J. Nanomed.* **2010**, *5*, 1057.
91. Makadia, H.K.; Siegel, S.J. Poly lactic-co-glycolic acid (PLGA) as biodegradable controlled drug delivery carrier. *Polymers* **2011**, *3*, 1377–1397. [CrossRef] [PubMed]
92. Wang, H.; Zhao, Y.; Wu, Y.; Hu, Y.-L.; Nan, K.; Nie, G.; Chen, H. Enhanced anti-tumor efficacy by co-delivery of doxorubicin and paclitaxel with amphiphilic methoxy PEG-PLGA copolymer nanoparticles. *Biomaterials* **2011**, *32*, 8281–8290. [CrossRef] [PubMed]
93. Tian, J.; Min, Y.; Rodgers, Z.; Au, K.M.; Hagan, C.T.; Zhang, M.; Roche, K.; Yang, F.; Wagner, K.; Wang, A.Z. Co-delivery of paclitaxel and cisplatin with biocompatible PLGA–PEG nanoparticles enhances chemoradiotherapy in non-small cell lung cancer models. *J. Mater. Chem. B* **2017**, *5*, 6049–6057. [CrossRef] [PubMed]
94. Liao, Z.; Wong, S.W.; Yeo, H.L.; Zhao, Y. Nanocarriers for cancer treatment: Clinical impact and safety. *NanoImpact* **2020**, *20*, 100253. [CrossRef]
95. James, N.; Coker, R.; Tomlinson, D.; Harris, J.; Gompels, M.; Pinching, A.; Stewart, J. Liposomal doxorubicin (Doxil): An effective new treatment for Kaposi’s sarcoma in AIDS. *Clin. Oncol.* **1994**, *6*, 294–296. [CrossRef]
96. Uddin, A.; Chakraborty, S. Role of miRNAs in lung cancer. *J. Cell. Physiol.* **2018**. [CrossRef]
97. Xia, H.; Wu, J.; Li, M. MiRNA Identification, Characterization and Integrated Network Analysis for Flavonoid Biosynthesis in Brassicacorporaphanus. *Hortic. Plant J.* **2021**. [CrossRef]
98. Di Leva, G.; Garofalo, M.; Croce, C.M. MicroRNAs in cancer. *Ann. Rev. Pathol.: Mech. Dis.* **2014**, *9*, 287–314. [CrossRef]
99. Lin, P.; Yu, S.; Yang, P. MicroRNA in lung cancer. *Br. J. Cancer* **2010**, *103*, 1144–1148. [CrossRef] [PubMed]
100. Iqbal, M.A.; Arora, S.; Prakasam, G.; Calin, G.A.; Syed, M.A. MicroRNA in lung cancer: Role, mechanisms, pathways and therapeutic relevance. *Mol. Asp. Med.* **2019**, *70*, 3–20. [CrossRef] [PubMed]
101. Wang, B.; Hsu, S.h.; Wang, X.; Kutay, H.; Bid, H.K.; Yu, J.; Ganju, R.K.; Jacob, S.T.; Yuneva, M.; Ghoshal, K. Reciprocal regulation of microRNA-122 and c-Myc in hepatocellular cancer: Role of E2F1 and transcription factor dimerization partner 2. *Hepatology* **2014**, *59*, 555–566. [CrossRef] [PubMed]

102. Hermeking, H. The miR-34 family in cancer and apoptosis. *Cell Death Differ.* **2009**, *17*, 193–199. [CrossRef]
103. Suzuki, H.; Maruyama, R.; Yamamoto, E.; Kai, M. Epigenetic alteration and microRNA dysregulation in cancer. *Front. Genet.* **2013**, *4*, 258. [CrossRef]
104. Fazi, F.; Racanicchi, S.; Zardo, G.; Starnes, L.M.; Mancini, M.; Travaglini, L.; Diverio, D.; Ammatuna, E.; Cimino, G.; Lo-Coco, F. Epigenetic silencing of the myelopoiesis regulator microRNA-223 by the AML1/ETO oncoprotein. *Cancer Cell* **2007**, *12*, 457–466. [CrossRef]
105. Saito, Y.; Liang, G.; Egger, G.; Friedman, J.M.; Chuang, J.C.; Coetzee, G.A.; Jones, P.A. Specific activation of microRNA-127 with downregulation of the proto-oncogene BCL6 by chromatin-modifying drugs in human cancer cells. *Cancer Cell* **2006**, *9*, 435–443. [CrossRef]
106. Lujambio, A.; Calin, G.A.; Villanueva, A.; Ropero, S.; Sánchez-Céspedes, M.; Blanco, D.; Montuenga, L.M.; Rossi, S.; Nicoloso, M.S.; Faller, W.J. A microRNA DNA methylation signature for human cancer metastasis. *Proc. Natl. Acad. Sci. USA* **2008**, *105*, 13556–13561. [CrossRef]
107. Wu, Y.; Crawford, M.; Mao, Y.; Lee, R.J.; Davis, I.C.; Elton, T.S.; Lee, L.J.; Nana-Sinkam, S.P. Therapeutic delivery of microRNA-29b by cationic lipoplexes for lung cancer. *Mol. Ther.-Nucleic Acids* **2013**, *2*, e84. [CrossRef]
108. Ye, Z.; Yin, S.; Su, Z.; Bai, M.; Zhang, H.; Hei, Z.; Cai, S. Downregulation of miR-101 contributes to epithelial-mesenchymal transition in cisplatin resistance of NSCLC cells by targeting ROCK2. *Oncotarget* **2016**, *7*, 37524. [CrossRef]
109. Jin, Z.; Guan, L.; Song, Y.; Xiang, G.; Chen, S.; Gao, B. MicroRNA-138 regulates chemoresistance in human non-small cell lung cancer via epithelial mesenchymal transition. *Eur. Rev. Med. Pharmacol. Sci.* **2016**, *20*, 1080–1086. [PubMed]
110. Nishijima, N.; Seike, M.; Soeno, C.; Chiba, M.; Miyanaga, A.; Noro, R.; Sugano, T.; Matsumoto, M.; Kubota, K.; Gemma, A. miR-200/ZEB axis regulates sensitivity to nintedanib in non-small cell lung cancer cells. *Int. J. Oncol.* **2016**, *48*, 937–944. [CrossRef] [PubMed]
111. Xue, J.; Yang, J.; Luo, M.; Cho, W.C.; Liu, X. MicroRNA-targeted therapeutics for lung cancer treatment. *Expert Opin. Drug Deliv.* **2017**, *12*, 141–157. [CrossRef] [PubMed]
112. Wang, R.-T.; Xu, M.; Xu, C.-X.; Song, Z.-G.; Jin, H. Decreased expression of miR216a contributes to non-small-cell lung cancer progression. *Clin. Cancer Res.* **2014**, *20*, 4705–4716. [CrossRef]
113. Wiggins, J.F.; Ruffino, L.; Kelnar, K.; Omotola, M.; Patrawala, L.; Brown, D.; Bader, A.G. Development of a lung cancer therapeutic based on the tumor suppressor microRNA-34. *Cancer Res.* **2010**, *70*, 5923–5930. [CrossRef] [PubMed]
114. Craig, V.; Tzankov, A.; Flori, M.; Schmid, C.; Bader, A.; Müller, A. Systemic microRNA-34a delivery induces apoptosis and abrogates growth of diffuse large B-cell lymphoma in vivo. *Leukemia* **2012**, *26*, 2421–2424. [CrossRef]
115. Quemener, A.M.; Bachelot, L.; Forestier, A.; Donnou-Fournet, E.; Gilot, D.; Galibert, M.D. The powerful world of antisense oligonucleotides: From bench to bedside. *Wiley Interdiscip. Rev. RNA* **2020**, *11*, e1594. [CrossRef]
116. Shi, S.-J.; Zhong, Z.-R.; Liu, J.; Zhang, Z.-R.; Sun, X.; Gong, T. Solid lipid nanoparticles loaded with anti-microRNA oligonucleotides (AMOs) for suppression of microRNA-21 functions in human lung cancer cells. *Pharm. Res.* **2012**, *29*, 97–109. [CrossRef]
117. Vester, B.; Wengel, J. LNA (locked nucleic acid): High-affinity targeting of complementary RNA and DNA. *Biochemistry* **2004**, *43*, 13233–13241. [CrossRef] [PubMed]
118. Cho, W.C. MicroRNAs as therapeutic targets for lung cancer. *Expert Opin. Ther. Targets* **2010**, *14*, 1005–1008. [CrossRef] [PubMed]
119. Trang, P.; Medina, P.P.; Wiggins, J.F.; Ruffino, L.; Kelnar, K.; Omotola, M.; Homer, R.; Brown, D.; Bader, A.G.; Weidhaas, J.B. Regression of murine lung tumors by the let-7 microRNA. *Oncogene* **2010**, *29*, 1580–1587. [CrossRef] [PubMed]
120. Akao, Y.; Nakagawa, Y.; Naoe, T. let-7 microRNA functions as a potential growth suppressor in human colon cancer cells. *Biol. Pharm. Bull.* **2006**, *29*, 903–906. [CrossRef] [PubMed]
121. Monroig-Bosque, P.d.C.; Rivera, C.A.; Calin, G.A. MicroRNAs in cancer therapeutics: “from the bench to the bedside”. *Expert Opin. Biol. Ther.* **2015**, *15*, 1381–1385. [CrossRef]
122. Bansal, P.; Christopher, A.; Kaur, R.; Kaur, G.; Kaur, A.; Gupta, V. MicroRNA therapeutics: Discovering novel targets and developing specific therapy. *Perspect. Clin. Res.* **2016**, *7*, 68–74. [CrossRef]
123. Elmen, J.; Lindow, M.; Schütz, S.; Lawrence, M.; Petri, A.; Obad, S.; Lindholm, M.; Hedtjörn, M.; Hansen, H.F.; Berger, U.; et al. Kauppinen S2008 LNA-mediated microRNA silencing in non-human primates. *Nature* **2008**, *452*, 896–899. [CrossRef]
124. Lindow, M.; Kauppinen, S. Discovering the first microRNA-targeted drug. *J. Cell Biol.* **2012**, *199*, 407–412. [CrossRef]
125. Beg, M.S.; Brenner, A.; Sachdev, J.; Ejadi, S.; Borad, M.; Kang, Y.-K.; Lim, H.; Kim, T.; Bader, A.; Stoudemire, J. Abstract C43: Safety, tolerability, and clinical activity of MRX34, the first-in-class liposomal miR-34 mimic, in patients with advanced solid tumors. *Clin. Trials* **2015**, *14*, C43.
126. Hong, D.S.; Kang, Y.-K.; Brenner, A.J.; Sachdev, J.C.; Ejadi, S.; Borad, M.J.; Kim, T.-Y.; Lim, H.Y.; Park, K.; Becerra, C. MRX34, a liposomal miR-34 mimic, in patients with advanced solid tumors: Final dose-escalation results from a first-in-human phase I trial of microRNA therapy. *J. Clin. Oncol.* **2016**, *34*, 2508. [CrossRef]
127. Mollaei, H.; Safaralizadeh, R.; Rostami, Z. MicroRNA replacement therapy in cancer. *J. Cell. Physiol.* **2019**, *234*, 12369–12384. [CrossRef]
128. Segal, M.; Slack, F.J. *Challenges Identifying Efficacious miRNA Therapeutics for Cancer*; Taylor & Francis: Abingdon, UK, 2020.
129. Kumar, V.; Mundra, V.; Peng, Y.; Wang, Y.; Tan, C.; Mahato, R.I. Pharmacokinetics and biodistribution of polymeric micelles containing miRNA and small-molecule drug in orthotopic pancreatic tumor-bearing mice. *Theranostics* **2018**, *8*, 4033. [CrossRef]

130. Lu, L.F.; Liston, A. MicroRNA in the immune system, microRNA as an immune system. *Immunology* **2009**, *127*, 291–298. [CrossRef] [PubMed]
131. Ganju, A.; Khan, S.; Hafeez, B.B.; Behrman, S.W.; Yallapu, M.M.; Chauhan, S.C.; Jaggi, M. miRNA nanotherapeutics for cancer. *Drug Discov. Today* **2017**, *22*, 424–432. [CrossRef]
132. Wu, Y.; Crawford, M.; Yu, B.; Mao, Y.; Nana-Sinkam, S.P.; Lee, L.J. MicroRNA delivery by cationic lipoplexes for lung cancer therapy. *Mol. Pharm.* **2011**, *8*, 1381–1389. [CrossRef] [PubMed]
133. Miyazaki, T.; Uchida, S.; Nagatoishi, S.; Koji, K.; Hong, T.; Fukushima, S.; Tsumoto, K.; Ishihara, K.; Kataoka, K.; Cabral, H. Polymeric nanocarriers with controlled chain flexibility boost mRNA delivery in vivo through enhanced structural fastening. *Adv. Healthc. Mater.* **2020**, *9*, 2000538. [CrossRef]
134. Ibrahim, A.F.; Weirauch, U.; Thomas, M.; Grünweller, A.; Hartmann, R.K.; Aigner, A. MicroRNA replacement therapy for miR-145 and miR-33a is efficacious in a model of colon carcinoma. *Cancer Res.* **2011**, *71*, 5214–5224. [CrossRef]
135. Chiou, G.-Y.; Cherng, J.-Y.; Hsu, H.-S.; Wang, M.-L.; Tsai, C.-M.; Lu, K.-H.; Chien, Y.; Hung, S.-C.; Chen, Y.-W.; Wong, C.-I. Cationic polyurethanes-short branch PEI-mediated delivery of Mir145 inhibited epithelial–mesenchymal transdifferentiation and cancer stem-like properties and in lung adenocarcinoma. *J. Control. Release* **2012**, *159*, 240–250. [CrossRef]
136. Zhang, T.; Xue, X.; He, D.; Hsieh, J.-T. A prostate cancer-targeted polyarginine-disulfide linked PEI nanocarrier for delivery of microRNA. *Cancer Lett.* **2015**, *365*, 156–165. [CrossRef]
137. Gao, S.; Tian, H.; Guo, Y.; Li, Y.; Guo, Z.; Zhu, X.; Chen, X. miRNA oligonucleotide and sponge for miRNA-21 inhibition mediated by PEI-PLL in breast cancer therapy. *Acta Biomater.* **2015**, *25*, 184–193. [CrossRef] [PubMed]
138. Liu, C.; Wen, J.; Meng, Y.; Zhang, K.; Zhu, J.; Ren, Y.; Qian, X.; Yuan, X.; Lu, Y.; Kang, C. Efficient delivery of therapeutic miRNA nanocapsules for tumor suppression. *Adv. Mater.* **2015**, *27*, 292–297. [CrossRef] [PubMed]
139. Fernandez-Piñeiro, I.; Badiola, I.; Sanchez, A. Nanocarriers for microRNA delivery in cancer medicine. *Biotechnol. Adv.* **2017**, *35*, 350–360. [CrossRef]
140. Mittal, A.; Chitkara, D.; Behrman, S.W.; Mahato, R.I. Efficacy of gemcitabine conjugated and miRNA-205 complexed micelles for treatment of advanced pancreatic cancer. *Biomaterials* **2014**, *35*, 7077–7087. [CrossRef]
141. Liu, Q.; Li, R.-T.; Qian, H.-Q.; Wei, J.; Xie, L.; Shen, J.; Yang, M.; Qian, X.-P.; Yu, L.-X.; Jiang, X.-Q. Targeted delivery of miR-200c/DOC to inhibit cancer stem cells and cancer cells by the gelatinases-stimuli nanoparticles. *Biomaterials* **2013**, *34*, 7191–7203. [CrossRef]
142. Cheng, C.J.; Saltzman, W.M. Polymer nanoparticle-mediated delivery of microRNA inhibition and alternative splicing. *Mol. Pharm.* **2012**, *9*, 1481–1488. [CrossRef]
143. Li, F.; Wang, F.; Zhu, C.; Wei, Q.; Zhang, T.; Zhou, Y.L. miR-221 suppression through nanoparticle-based miRNA delivery system for hepatocellular carcinoma therapy and its diagnosis as a potential biomarker. *Int. J. Nanomed.* **2018**, *13*, 2295. [CrossRef]
144. Devulapally, R.; Sekar, N.M.; Sekar, T.V.; Foygel, K.; Massoud, T.F.; Willmann, J.R.K.; Paulmurugan, R. Polymer nanoparticles mediated codelivery of anti-miR-10b and anti-miR-21 for achieving triple negative breast cancer therapy. *ACS Nano* **2015**, *9*, 2290–2302. [CrossRef]
145. Wang, S.; Zhang, J.; Wang, Y.; Chen, M. Hyaluronic acid-coated PEI-PLGA nanoparticles mediated co-delivery of doxorubicin and miR-542-3p for triple negative breast cancer therapy. *Nanomed.: Nanotechnol. Biol. Med.* **2016**, *12*, 411–420. [CrossRef] [PubMed]
146. Ren, Y.; Zhou, X.; Mei, M.; Yuan, X.-B.; Han, L.; Wang, G.-X.; Jia, Z.-F.; Xu, P.; Pu, P.-Y.; Kang, C.-S. MicroRNA-21 inhibitor sensitizes human glioblastoma cells U251 (PTEN-mutant) and LN229 (PTEN-wild type) to taxol. *BMC Cancer* **2010**, *10*, 1–13. [CrossRef] [PubMed]
147. Conde, J.; Oliva, N.; Atilano, M.; Song, H.S.; Artzi, N. Self-assembled RNA-triple-helix hydrogel scaffold for microRNA modulation in the tumour microenvironment. *Nat. Mater.* **2016**, *15*, 353–363. [CrossRef]
148. Deng, X.; Cao, M.; Zhang, J.; Hu, K.; Yin, Z.; Zhou, Z.; Xiao, X.; Yang, Y.; Sheng, W.; Wu, Y. Hyaluronic acid-chitosan nanoparticles for co-delivery of MiR-34a and doxorubicin in therapy against triple negative breast cancer. *Biomaterials* **2014**, *35*, 4333–4344. [CrossRef]
149. Santos-Carballal, B.; Aaldering, L.; Ritzeveld, M.; Pereira, S.; Sewald, N.; Moerschbacher, B.; Götte, M.; Goycoolea, F.M. Physicochemical and biological characterization of chitosan-microRNA nanocomplexes for gene delivery to MCF-7 breast cancer cells. *Sci. Rep.* **2015**, *5*, 1–15. [CrossRef] [PubMed]
150. Wang, S.; Cao, M.; Deng, X.; Xiao, X.; Yin, Z.; Hu, Q.; Zhou, Z.; Zhang, F.; Zhang, R.; Wu, Y. Degradable Hyaluronic Acid/Protamine Sulfate Interpolyelectrolyte Complexes as miRNA-Delivery Nanocapsules for Triple-Negative Breast Cancer Therapy. *Adv. Healthc. Mater.* **2015**, *4*, 281–290. [CrossRef]
151. Hao, Z.; Fan, W.; Hao, J.; Wu, X.; Zeng, G.Q.; Zhang, L.J.; Nie, S.F.; Wang, X.D. Efficient delivery of micro RNA to bone-metastatic prostate tumors by using aptamer-conjugated atelocollagen in vitro and in vivo. *Drug Deliv.* **2016**, *23*, 864–871. [CrossRef]
152. Kurmi, B.D.; Kayat, J.; Gajbiye, V.; Tekade, R.K.; Jain, N.K. Micro-and nanocarrier-mediated lung targeting. *Expert Opin. Drug Deliv.* **2010**, *7*, 781–794. [CrossRef]
153. Piao, L.; Zhang, M.; Datta, J.; Xie, X.; Su, T.; Li, H.; Teknos, T.N.; Pan, Q. Lipid-based nanoparticle delivery of Pre-miR-107 inhibits the tumorigenicity of head and neck squamous cell carcinoma. *Mol. Ther.* **2012**, *20*, 1261–1269. [CrossRef] [PubMed]
154. Decastro, M.; Saijoh, Y.; Schoenwolf, G.C. Optimized cationic lipid-based gene delivery reagents for use in developing vertebrate embryos. *Dev. Dyn.* **2006**, *235*, 2210–2219. [CrossRef] [PubMed]



155. Bikram, M.; Lee, M.; Chang, C.-W.; Janát-Amsbury, M.-M.; Kern, S.E.; Kim, S.W. Long-circulating DNA-complexed biodegradable multiblock copolymers for gene delivery: Degradation profiles and evidence of dysopsonization. *J. Control. Release* **2005**, *103*, 221–233. [CrossRef] [PubMed]
156. Gao, Y.; Gao, F.; Ma, J.-l.; Sun, W.-z.; Song, L.-p. The potential clinical applications and prospects of microRNAs in lung cancer. *OncoTargets Ther.* **2014**, *7*, 901. [CrossRef] [PubMed]
157. Peng, J.; Wang, R.; Sun, W.; Huang, M.; Wang, R.; Li, Y.; Wang, P.; Sun, G.; Xie, S. Delivery of miR-320a-3p by gold nanoparticles combined with photothermal therapy for directly targeting Sp1 in lung cancer. *Biomater. Sci.* **2021**, *9*, 6528–6541. [CrossRef] [PubMed]
158. Ghosh, R.; Singh, L.C.; Shohet, J.M.; Gunaratne, P.H. A gold nanoparticle platform for the delivery of functional microRNAs into cancer cells. *Biomaterials* **2013**, *34*, 807–816. [CrossRef] [PubMed]
159. Ekin, A.; Karatas, O.F.; Culha, M.; Ozen, M. Designing a gold nanoparticle-based nanocarrier for microRNA transfection into the prostate and breast cancer cells. *J. Gene Med.* **2014**, *16*, 331–335. [CrossRef] [PubMed]
160. Zhu, Z.; Ni, D.; Teng, J.; Cheng, Y.; Zhuang, B.; Yang, Z. Folic Acid-Conjugated Mesoporous Silica Nanoparticles and MicroRNA-128-3p Combined with Adriamycin Alleviates the Progression of Non-Small Cell Lung Cancer. *J. Biomater. Tissue Eng.* **2021**, *11*, 1714–1721. [CrossRef]
161. Tivnan, A.; Orr, W.S.; Gubala, V.; Nooney, R.; Williams, D.E.; McDonagh, C.; Prenter, S.; Harvey, H.; Domingo-Fernández, R.; Bray, I.M. Inhibition of neuroblastoma tumor growth by targeted delivery of microRNA-34a using anti-disialoganglioside GD2 coated nanoparticles. *PLoS ONE* **2012**, *7*, e38129. [CrossRef]
162. Bertucci, A.; Prasetyanto, E.A.; Septiadi, D.; Manicardi, A.; Brognara, E.; Gambari, R.; Corradini, R.; De Cola, L. Combined delivery of temozolomide and anti-miR221 PNA using mesoporous silica nanoparticles induces apoptosis in resistant glioma cells. *Small* **2015**, *11*, 5687–5695. [CrossRef]
163. Yin, P.T.; Shah, B.P.; Lee, K.B. Combined magnetic nanoparticle-based microRNA and hyperthermia therapy to enhance apoptosis in brain cancer cells. *Small* **2014**, *10*, 4106–4112. [CrossRef]
164. Lellouche, E.; Israel, L.; Bechor, M.; Attal, S.; Kurlander, E.; Asher, V.; Dolitzky, A.; Shaham, L.; Izraeli, S.; Lellouche, J.-P. MagRET nanoparticles: An iron oxide nanocomposite platform for gene silencing from MicroRNAs to long noncoding RNAs. *Bioconjugate Chem.* **2015**, *26*, 1692–1701. [CrossRef]
165. Hossain, S.; Stanislaus, A.; Chua, M.J.; Tada, S.; Tagawa, Y.-i.; Chowdhury, E.H.; Akaike, T. Carbonate apatite-facilitated intracellularly delivered siRNA for efficient knockdown of functional genes. *J. Control. Release* **2010**, *147*, 101–108. [CrossRef]
166. Inoue, A.; Mizushima, T.; Wu, X.; Okuzaki, D.; Kambara, N.; Ishikawa, S.; Wang, J.; Qian, Y.; Hirose, H.; Yokoyama, Y. A miR-29b byproduct sequence exhibits potent tumor-suppressive activities via inhibition of NF- $\kappa$ B signaling in KRAS-mutant colon cancer cells. *Mol. Cancer Ther.* **2018**, *17*, 977–987. [CrossRef]
167. Li, J.; Li, X.; Zhang, C.; Zhang, C.; Wang, H. A signature of tumor immune microenvironment genes associated with the prognosis of non-small cell lung cancer. *Oncol. Rep.* **2020**, *43*, 795–806. [CrossRef] [PubMed]
168. Brennan, P.; Hainaut, P.; Boffetta, P. Genetics of lung-cancer susceptibility. *Lancet Oncol.* **2011**, *12*, 399–408. [CrossRef]
169. Zhao, W.; Zhu, B.; Hutchinson, A.; Pesatori, A.C.; Consonni, D.; Caporaso, N.E.; Zhang, T.; Wang, D.; Shi, J.; Landi, M.T. Clinical Implications of Inter-and Intratumor Heterogeneity of Immune Cell Markers in Lung Cancer. *J. Natl. Cancer Inst.* **2021**. [CrossRef] [PubMed]
170. Yadav, K.S.; Upadhyaya, A.; Misra, A. Targeted drug therapy in nonsmall cell lung cancer: Clinical significance and possible solutions-part II (role of nanocarriers). *Expert Opin. Drug Deliv.* **2021**, *18*, 103–118. [CrossRef] [PubMed]
171. Mayekar, M.K.; Bivona, T.G. Current landscape of targeted therapy in lung cancer. *Clin. Pharmacol. Ther.* **2017**, *102*, 757–764. [CrossRef]
172. Rosell, R.; Karachaliou, N. Optimizing lung cancer treatment approaches. *Nat. Rev. Clin. Oncol.* **2015**, *12*, 75–76. [CrossRef]
173. Liu, Y.; Fang, J.; Kim, Y.-J.; Wong, M.K.; Wang, P. Codelivery of doxorubicin and paclitaxel by cross-linked multilamellar liposome enables synergistic antitumor activity. *Mol. Pharm.* **2014**, *11*, 1651–1661. [CrossRef]
174. Babu, A.; Templeton, A.K.; Munshi, A.; Ramesh, R. Nanoparticle-based drug delivery for therapy of lung cancer: Progress and challenges. *J. Nanomater.* **2013**, *2013*, 1–11. [CrossRef]
175. Kumar, K.; Chawla, R. Nanocarriers-mediated therapeutics as a promising approach for treatment and diagnosis of lung cancer. *J. Drug Deliv. Sci. Technol.* **2021**, *65*, 102677. [CrossRef]



## Article

# Light- and Melanin Nanoparticle-Induced Cytotoxicity in Metastatic Cancer Cells

Victoria R. Gabriele <sup>1,†</sup>, Robabeh M. Mazhabi <sup>2,†</sup>, Natalie Alexander <sup>3</sup> , Purna Mukherjee <sup>3</sup>, Thomas N. Seyfried <sup>3</sup> , Njemuwa Nwaji <sup>2</sup> , Eser M. Akinoglu <sup>2</sup>, Andrzej Mackiewicz <sup>4</sup>, Guofu Zhou <sup>2,5</sup> , Michael Giersig <sup>2,6</sup> , Michael J. Naughton <sup>1</sup> and Krzysztof Kempa <sup>1,\*</sup>

<sup>1</sup> Department of Physics, Boston College, Chestnut Hill, MA 02467, USA; gabrievi@bc.edu (V.R.G.); naughton@bc.edu (M.J.N.)

<sup>2</sup> International Academy of Optoelectronics at Zhaoqing, South China Normal University, Zhaoqing 526238, China; r.motaghd@zq-scnu.org (R.M.M.); njemuwa.nwaji@zq-scnu.org (N.N.); e.a@fu-berlin.de (E.M.A.); guofu.zhou@m.scnu.edu.cn (G.Z.); giersig@physik.fu-berlin.de (M.G.)

<sup>3</sup> Department of Biology, Boston College, Chestnut Hill, MA 02467, USA; njalexander343@gmail.com (N.A.); purna.mukherjee@bc.edu (P.M.); thomas.seyfried@bc.edu (T.N.S.)

<sup>4</sup> Greater Poland Cancer Centre, Poznan University of Medical Sciences, 61-867 Poznan, Poland; mackiewicz.aa@gmail.com

<sup>5</sup> Guangdong Provincial Key Laboratory of Optical Information Materials and Technology & Institute of Electronic Paper Displays, South China Academy of Advanced Optoelectronics, South China Normal University, Guangzhou 510006, China

<sup>6</sup> Institute of Fundamental Technological Research of Polish Academy of Sciences, 02-106 Warsaw, Poland

\* Correspondence: kris.kempa@bc.edu

† These authors contributed equally to this paper.

**Citation:** Gabriele, V.R.;

Mazhabi, R.M.; Alexander, N.;

Mukherjee, P.; Seyfried, T.N.;

Nwaji, N.; Akinoglu, E.M.;

Mackiewicz, A.; Zhou, G.; Giersig, M.;

et al. Light- and Melanin

Nanoparticle-Induced Cytotoxicity in

Metastatic Cancer Cells.

*Pharmaceutics* **2021**, *13*, 965.

[https://doi.org/10.3390/](https://doi.org/10.3390/pharmaceutics13070965)

[pharmaceutics13070965](https://doi.org/10.3390/pharmaceutics13070965)

Academic Editor: Hassan Bousbaa

Received: 21 May 2021

Accepted: 23 June 2021

Published: 26 June 2021

**Publisher's Note:** MDPI stays neutral with regard to jurisdictional claims in published maps and institutional affiliations.

**Abstract:** Melanin nanoparticles are known to be biologically benign to human cells for a wide range of concentrations in a high glucose culture nutrition. Here, we show cytotoxic behavior at high nanoparticle and low glucose concentrations, as well as at low nanoparticle concentration under exposure to (nonionizing) visible radiation. To study these effects in detail, we developed highly monodispersed melanin nanoparticles (both uncoated and glucose-coated). In order to study the effect of significant cellular uptake of these nanoparticles, we employed three cancer cell lines: VM-M3, A375 (derived from melanoma), and HeLa, all known to exhibit strong macrophagic character, i.e., strong nanoparticle uptake through phagocytic ingestion. Our main observations are: (i) metastatic VM-M3 cancer cells massively ingest melanin nanoparticles (mNPs); (ii) the observed ingestion is enhanced by coating mNPs with glucose; (iii) after a certain level of mNP ingestion, the metastatic cancer cells studied here are observed to die—glucose coating appears to slow that process; (iv) cells that accumulate mNPs are much more susceptible to killing by laser illumination than cells that do not accumulate mNPs; and (v) non-metastatic VM-NM1 cancer cells also studied in this work do not ingest the mNPs, and remain unaffected after receiving identical optical energy levels and doses. Results of this study could lead to the development of a therapy for control of metastatic stages of cancer.

**Keywords:** melanoma; melanin nanoparticles; cytotoxicity; laser medical applications; hyperthermia



**Copyright:** © 2021 by the authors. Licensee MDPI, Basel, Switzerland. This article is an open access article distributed under the terms and conditions of the Creative Commons Attribution (CC BY) license (<https://creativecommons.org/licenses/by/4.0/>).

## 1. Introduction

The emergence of nanoparticle (NP) technology in biomedicine has led to many applications [1,2]. These include tumor imaging and targeting [3], tissue engineering [4], drug delivery [5], tumor destruction [6], pathogen detection [7], and protein detection [8], among others. Sufficiently small nonpolar NPs can cross biological barriers and translocate across cells, tissues, and organs [9]. In contrast, polar NPs can enter cells only by utilizing endocytotic pathways [10,11]. The internalization process of NPs by cells is a key factor in determining their biomedical function, toxicity, and biodistribution [11]. Adjusting chemo-physical properties of NPs, such as size, shape, and surface properties, is a major factor for

optimization of targeting and cellular uptake, as well as intracellular trafficking [12]. Zeta potential ( $\xi$ ) could be an important biophysical parameter for quantification of the cellular interactions [13–15].

Meanwhile, it has been also known for over a century that biomolecules can be irreversibly damaged by *ionizing radiation*, via photons with energy sufficient to break covalent bonds. For example, ultraviolet (UV) radiation is known to cause catastrophic damage to cells [16], and X-rays and even harder radiation have been long applied to treat cancer [17]. Such radiation damages of cells and tissue is largely indiscriminate, with minimal or no spectral control or biospecificity. Therefore, geometric targeting must be used to achieve some degree of macro-scale selectivity. *Non-ionizing radiation*, with photons of much lower energy can, at sufficient intensity, also cause irreversible damage to biomolecules via non-linear processes (under high local electric or thermal field). Geometric targeting can be improved with such radiation due to the availability of lensing, in particular in the visible frequency range. Irreversible damage of geometrically microtargeted yeast cells was recently demonstrated, using laser tweezers employing a low power (80 mW), near infrared (NIR) laser focused to a spot of about 1  $\mu\text{m}$  diameter ( $\sim 10^{10} \text{ W/m}^2$ ) [18]. Most importantly, however, nonlinear effects produced by non-ionizing radiation allow for spectral resolution of the excitation. Spectra in the NIR and far IR (FIR) ranges consist typically of characteristic groups of absorbance maxima, which form so called “fingerprint” spectra, and which can be used to identify a given molecule [19]. A recent theoretical paper [20] suggested that such fingerprint spectra can be used to selectively damage target molecules within a cell. Such purely spectral selectivity of molecular dissociation would be highly desirable in future therapies, but it is currently very hard (or impossible) to achieve/implement, mainly because the spectra of different biomolecules (ranging from viral to cellular, healthy or cancerous) are very similar, typically with only some amplitude variations, but at similar or the same peak spectral locations (wavelengths) [21]. An additional complication is the generally small radiation penetration depth, apart from a few high transparency spectral windows [21,22].

These technical difficulties can be overcome with the incorporation of strongly light-absorbing targets, such as NPs. For example, light absorption by melanin NPs is very strong (typically an order of magnitude more than typical cells) over a wide spectral range, a fact that has been exploited in the detection of metastatic melanoma circulating tumor cells (CTC) [23,24]. Several papers [23,25] have shown that, for wavelengths around 500 nm and between 700 nm and 900 nm, melanoma cells dominate absorption over that of blood, suggesting they may be able to be overheated with radiation at those wavelengths. In fact, melanin-filled NPs have been used recently to trigger cell death by overheating (over 42 °C) in tumors [26]. In such tumor therapy, radiation in the NIR high transparency window ( $\sim 800 \text{ nm}$  wavelength) is typically used.

We have developed highly monodispersed glucose-coated melanin nanoparticles (mNP@G), and have used these to reveal massive NP uptake by the three cancer cell lines, VM-M3, A375, and HeLa, which confirm these cell types’ macrophagic character. Zeta potential measurements suggest that this character is related to binding and cellular internalization effects. Importantly, we find that the viability of all studied cells dramatically decreases at a sufficiently high concentration of mNP@G and reduction of the glucose level in the culture nutrition. We also performed a series of radiation experiments on cancer cells moderately filled with mNP@G. We employed light in the visible transmission window of blood at 532 nm wavelength [22,23], and demonstrated that there exist power levels and doses of this radiation that violently destroy cancer cells sensitized with mNPs, but that are evidently safe for cells unsensitized with mNPs.

While melanin, the pigment present in abundance in melanoma cells, plays an important role in skin protection against ultraviolet radiation, it also affects melanoma behavior by adjusting epidermal homeostasis [27,28]. Melanoma is, of course, a serious skin cancer, originating from mutated melanocytes, melanin-producing cells [29]. Highly metastatic, it causes about 60,000 deaths per year globally [30]. Very limited progress

treating melanoma has been achieved with chemotherapy [31], immunotherapy [32], radiotherapy [33], surgery [34,35], or other therapies [36,37]. Melanin synthesis, a multistep and highly regulated route, determines the difference between the function of normal and cancerous cells [38]. Different from healthy melanocytes, in which melanin synthesis is controlled by various factors and plays an important biological role, melanin pigmentation in melanoma cells is dysregulated, which leads to heavy pigmentation of these cells [39,40]. Sarna et al. [41] have suggested that the elastic properties of melanoma cells are affected by the melanin presence, and play a key role in melanoma metastasis [38]. Other studies confirm that melanin pigmentation is an important factor in determining the fate of cancer cells [39,42]. Metabolic functions of normal cells are dramatically changed in the cancerous state, and this transformation makes cancer cells strongly dependent on high rates of glucose uptake [43,44].

To achieve rapid cancer cell proliferation *in vitro*, cell culturing methods commonly use high glucose of Dulbecco's modified Eagle's medium (DMEM, 25 mM or 4500  $\mu\text{g}\cdot\text{mL}^{-1}$ ). Normal serum glucose levels in the body are usually constant between 4 and 6 mM (720–1080  $\mu\text{g}\cdot\text{mL}^{-1}$ ). However, the body may experience a drop in glucose level to 2.5 mM (450  $\mu\text{g}\cdot\text{mL}^{-1}$ ), and even further in tissue, in the case of nutrient deficiencies. Accordingly, glucose level reduction has been applied for cancer treatment through different methods such as fasting or modifying (e.g., ketogenic) diet [45,46].

## 2. Materials and Methods

### 2.1. Reagents

Chemicals were purchased from commercial sources with high purity and used as received. Malignant melanoma A375 and HeLa cell lines were obtained from the Shanghai Institute of Cell Biology (Shanghai, China). The cells were cultured in DMEM (Solarbio, Beijing, China) with 10% fetal bovine serum (Solarbio) and 5% antibiotics (100 Unit  $\text{mL}^{-1}$  penicillin and 100  $\mu\text{g}\cdot\text{mL}^{-1}$  streptomycin) from Sigma-Aldrich (St. Louis, MO, USA). The cells were incubated in a cell incubator under 95% humidity and 5%  $\text{CO}_2$  at 37 °C. To seed and harvest the cells, Trypsin-EDTA (0.25%) from Sigma was utilized, and Trypan blue (0.4%) from Gibco was applied for cell counting purposes.

### 2.2. Synthesis of Melanin Nanoparticles, mNP

The synthesis of highly spherical monodispersed mNPs was accomplished using the oxidative polymerization of dopamine hydrochloride in the presence of ethanol and ammonia solution at room temperature. A mixture of aqueous ammonia solution ( $\text{NH}_4\text{OH}$ , 0.5 mL for 320 nm-diameter mNPs), ethanol (40 mL), and deionized water (90 mL) was stirred at room temperature for 30 min. This was followed by addition of 0.5 g of dopamine hydrochloride dissolved in water. A gradual change in color of the solution from light brown to dark brown was observed. The reaction was continued for 24 h, and the formed mNPs were extracted through centrifugation at 7000 rpm, and washed three times with deionized water. Different sizes of nominally spherical nanoparticles were obtained by varying the volume of ammonium hydroxide, while following the same protocol.

### 2.3. Preparation of Glucose-Coated Melanin Nanoparticles, mNP@G

As-prepared mNPs (20 mg) were dissolved in tris-buffer (0.01 M, pH 7.5) and stirred for 10 min followed by addition of 0.5 g acetylglucosamine sugar dissolved in 10 mL deionized water. The reaction mixture was stirred for 24 h and then collected through centrifugation. After repeated washing with deionized water, the obtained mNP@G product was redispersed in 1.5 mL of deionized water for further characterization.

### 2.4. Cell Viability Measurements

Using Cell Counting Kit-8 assay (CCK-8, Sigma-Aldrich, St. Louis, MO, USA), cell viability was determined according to the manufacturer's protocol with some modification, as explained in Supplementary Materials and Figure S1. The CCK-8 colorimetric assay

involves metabolic bioreduction of WST-8 [2-(2-methoxy-4-nitrophenyl)-3-(4-nitrophenyl)-5-(2,4-disulfophenyl)-2H-tetrazolium, mono-sodium salt] in the presence of 1-methoxy PMS as an electron mediator, producing a water-soluble orange colored formazan dye. The amount of produced formazan is directly proportional to the number of living cells and can be measured by spectrophotometric method via absorbance of 460 nm. For these measurements, VM-M3, A375, and HeLa cancer cells were seeded, and injected at controlled concentrations into 24 well plates. The cells were incubated overnight in 5% CO<sub>2</sub> atmosphere at 37 °C to allow adherence to the plate. For comparison, the cells were treated with different concentrations of mNPs and also mNP@G, and the plates were returned to the incubator for 15 h. Afterwards, 50 µL of CCK-8 was added to every well in culture medium, and after incubation for 3 h, the upper orange solution was removed, collected in centrifuge tubes, and centrifuged for 15 min at 10,000 rpm in order to remove the melanin nanoparticles from the formazan solution. Thereafter, the absorbance of the solution from every tube was measured separately by spectrophotometer (Lambda 950, PerkinElmer, Boston, MA, USA) in the wavelength range of 350–550 nm, and the viability was calculated at the maximum absorption wavelength (460 nm).

### 2.5. Biocompatibility and Cytotoxicity Measurements

Biocompatibility and cytotoxicity of various concentrations of mNPs and mNP@G from 140 to 2100 µg·mL<sup>-1</sup> were studied via cell viability and proliferation of the A375 and HeLa cell lines, with the latter also studied in high (4500 mg·L<sup>-1</sup>) and low glucose (1000 mg·L<sup>-1</sup>) growth media, using CCK-8 assays kits (Sigma-Aldrich, St. Louis, MO, USA). To complete this study, we used UV-Vis spectrophotometry to evaluate cell viability, cell membrane damage and cell toxicity.

### 2.6. Theoretical Estimate of the Thermal Effects

To estimate the photothermal response of the in-blood circulating tumor cells sensitized with mNPs, we modeled the cell as a water droplet with average radius  $r_c \approx 5 \times 10^{-6}$  m, immersed in blood serum, which for simplicity is also modeled as water, with thermal conductivity  $k_m = 0.6$  W·K<sup>-1</sup>·m<sup>-1</sup>, specific heat  $c_w = 4186$  J·kg<sup>-1</sup>·K<sup>-1</sup>, and density  $\rho_w = 1000$  kg·m<sup>-3</sup>. The initial temperature of the cell and the blood is  $T_0$ . The cell is filled with a number  $N$  of much smaller, but highly radiation-absorbing mNPs. Each mNP has radius of  $r_m \approx 10^{-7}$  m and thermal conductivity  $k_m = 0.1$  W·K<sup>-1</sup>·m<sup>-1</sup>. The time evolution of the average temperature change  $\Delta T_c = T_c - T_0$  of a single cell is approximately given by:

$$\alpha \frac{\partial \Delta T_c}{\partial t} \approx \varnothing - \beta \Delta T_c \quad (1)$$

where  $\alpha = \frac{4}{3} r_c \rho_w c_w$ ,  $\beta = 4k_w/r_c$ , and  $\varnothing$  is the radiation power density absorbed in all mNPs, given approximately by  $\varnothing \approx \varnothing_{inc} N \left(\frac{r_m}{r_c}\right)^2$ , under the assumptions that the mNPs absorb the radiation perfectly and the radius of the laser beam in our experiment is roughly  $r_c$ . The solution to Equation (1) is

$$\Delta T_c = (\varnothing/\beta) \left[ 1 - \exp\left(-\frac{\beta}{\alpha} t\right) \right] \quad (2)$$

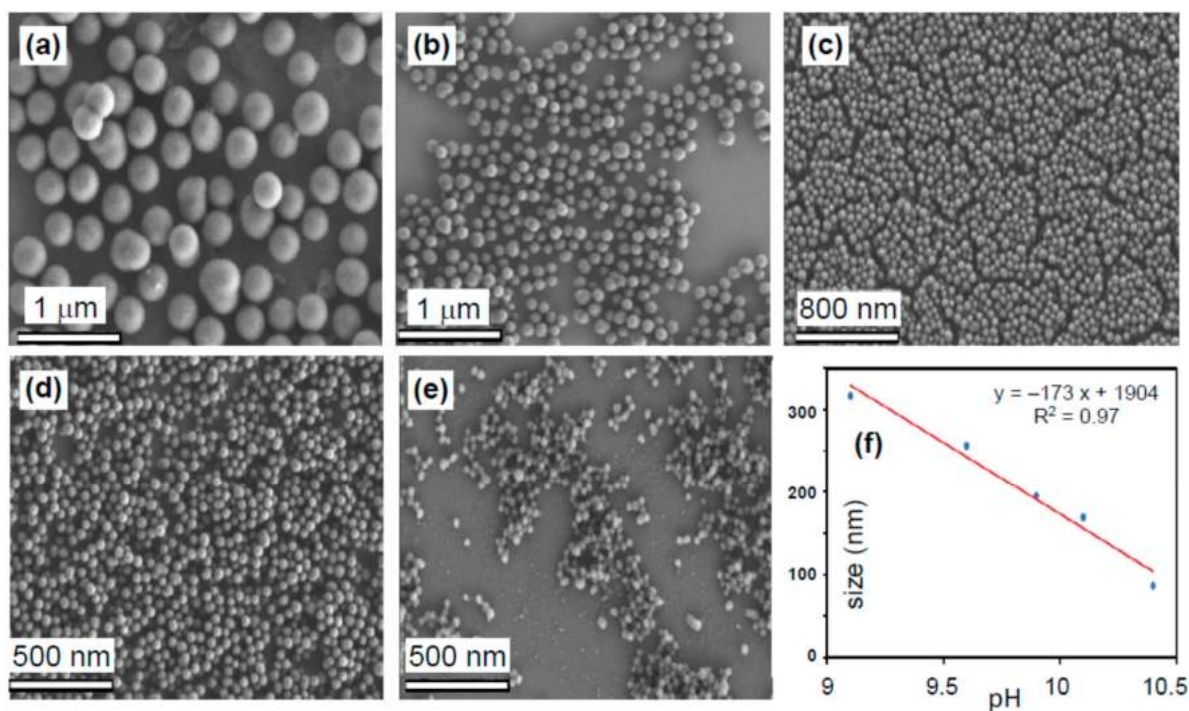
The maximum temperature increase is achieved for  $\frac{\beta}{\alpha} t \gg 1$ , or for  $t \gg \frac{\alpha}{\beta} = \frac{r_c^2 \rho_w c_w}{3k_w} = t_c$ , such that  $\Delta T_{cmax} = \varnothing/\beta = \varnothing r_c/4k_w$ . Choosing a value of  $N = 1000$ , which corresponds to a low mNP load, and a power density as applied in this work,  $\varnothing_{inc} \approx 10^9$  W·m<sup>-2</sup>, we estimate  $\varnothing \approx 4 \times 10^{10}$  W·m<sup>-2</sup>. With  $\beta = 0.5 \times 10^6$  W·Km<sup>-2</sup>, Equation (2) gives  $\Delta T_{cmax} \approx 1000$  K. This is the order of heating that causes rapid boiling of the cell interior, and can lead to the cell lysis observed in our experiment, as discussed later. The time to achieve such a level of heating is of the order of  $t_{max} \gg t_c \approx 10^{-4}$  s. It is important to note that this power density has no effect on the cells not having mNPs and immersed in water,

since the penetration length in water at this frequency is very large,  $\eta \approx 10$  m. Thus, a negligible fraction of the incoming radiation, of order  $\varnothing \approx \varnothing_{inc} \frac{2r_c}{\eta} \approx \varnothing_{inc} 10^{-6} = 10^3 \text{ W}\cdot\text{m}^{-2}$ , is absorbed in a cell, in general agreement with our experiments. It is also in good agreement with laser tweezer experiments [38] in which cells, free of any nanoparticles, were subjected to NIR radiation with power density  $\varnothing_{inc} = 3.8 \times 10^{10} \text{ W}\cdot\text{m}^{-2}$  for 15 min. It was shown in that experiment that this much larger power density and dose as compared with our experiment caused no delay in cell growth or increased mortality. Our simple estimate thus well explains the basic physics of our experiments with radiation.

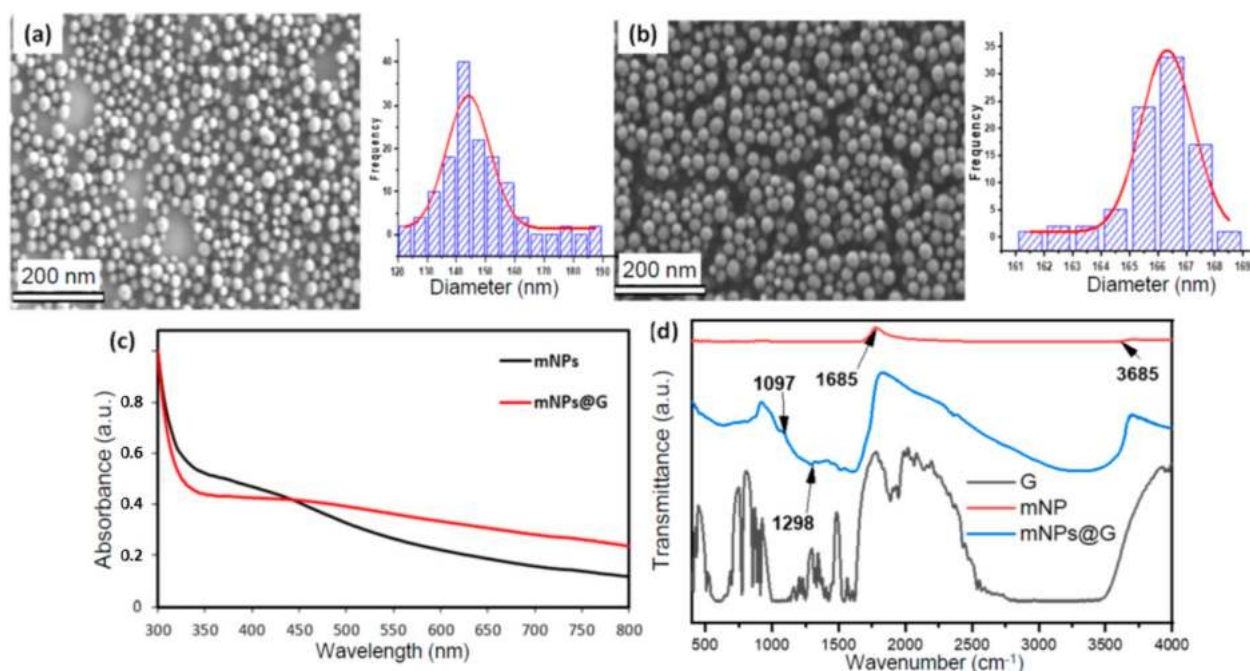
### 3. Results and Discussion

#### 3.1. Characterization of mNP@G

Figure 1 shows SEM images of as-prepared mNPs of different sizes (between 100 and 300 nm,  $\pm 17$  nm), obtained by variation of the  $\text{NH}_4\text{OH}$  solution volume. As seen in Figure 1f, the mNP diameter is a linear function of the solution pH. As shown in Figure 2, a slight increase in size, e.g., from 145 nm for mNPs to 166 nm for mNPs@G (i.e., with  $\sim 10$  nm average glucose coating thickness), was observed after surface functionalization with amino sugar, indicating surface coverage by the glucose. Figure 2c shows the optical absorption of aqueous solutions containing mNPs and mNP@G at the same concentration ( $0.1 \text{ g}\cdot\text{L}^{-1}$ ), recorded using UV-Vis-NIR spectroscopy. The spectra are similar, with the higher absorption of mNP@G in the visible range due to glucose coating. Surface functional groups of nanomaterials intended for biomedical application are crucial for their hydrophilicity and dispersibility in water and various biofluids. Thus, the chemical groups of melanin and the corresponding sugar-coated analog samples were determined using FTIR spectroscopy (Figure 2d). The intense C=O stretches from aromatic rings and/or carboxyl groups of the mNPs that almost suppressed other peaks can be observed at  $1685 \text{ cm}^{-1}$ . The broad OH stretch of glucosamine alone can be visibly seen between  $2700\text{--}3500 \text{ cm}^{-1}$ . The FTIR of the mNPs@G displayed an overlap of  $\text{NH}_2/\text{OH}$  stretching around  $3200\text{--}3500 \text{ cm}^{-1}$ . The C–O and C–C vibrational band arising from Schiff's base reaction can be seen at  $1097 \text{ cm}^{-1}$  and  $1298 \text{ cm}^{-1}$  in the mNPs@G (Figure 2d), indicating successful functionalization.



**Figure 1.** SEM images of mNPs in different volumes of  $\text{NH}_4\text{OH}$ : (a) 0.5 (b) 1.0, (c) 1.5, (d) 2.0, and (e) 2.5 mL. (f) Plot of mNP diameter vs. pH of  $\text{NH}_4\text{OH}$  solution.

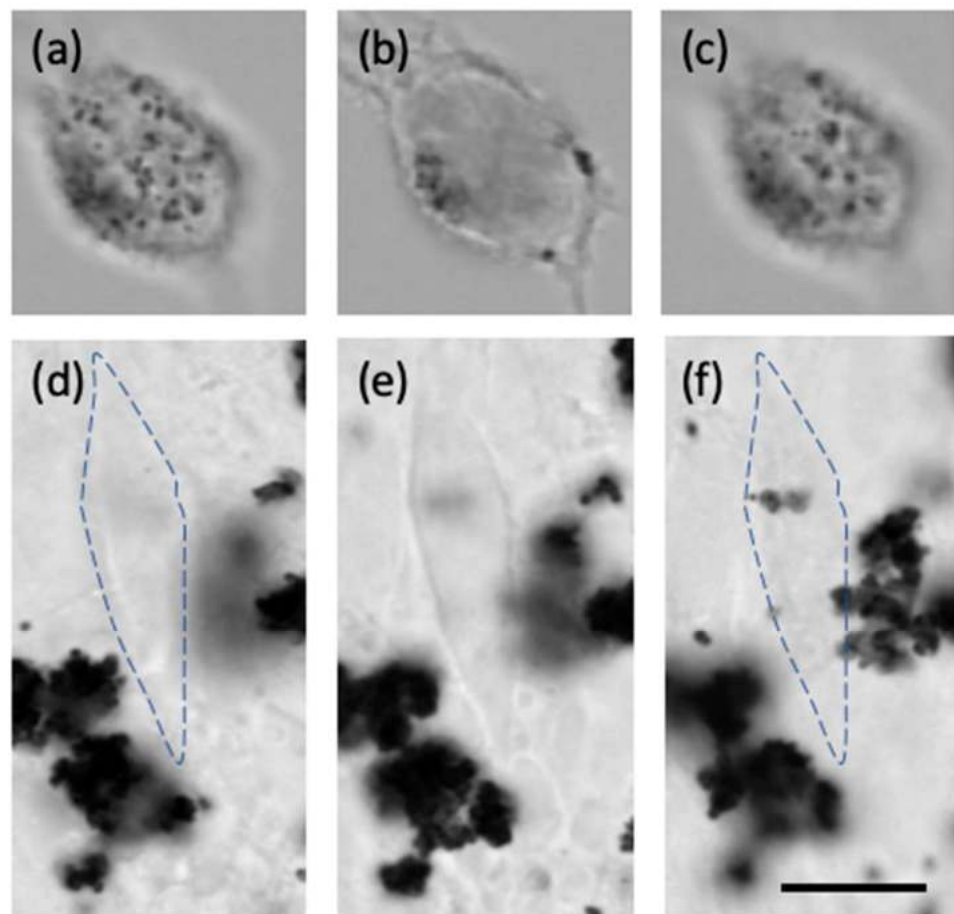


**Figure 2.** (a,b) SEM images and the corresponding size distribution histograms for mNP and mNP@G, respectively; (c) UV-Vis absorption of mNP (black) and mNP@G (red line). (d) FTIR spectra of terminal amino glucose (black line), mNP (red line), and mNPs@G (blue line).

### 3.2. Cell Viability after mNP and mNP@G Uptake

The main observations in this part of our study are: (1) non-cancerous or non-malignant cancer cells studied here do not ingest mNPs, (2) the studied malignant cancer cells massively absorb mNPs (macrophagic/phagocytic character), (3) this uptake is much stronger for the glucose-coated mNPs, (4) cell viability diminishes with increasing number of absorbed mNPs, and (5) lower glucose content in the cell nutrition dramatically reduces cell viability.

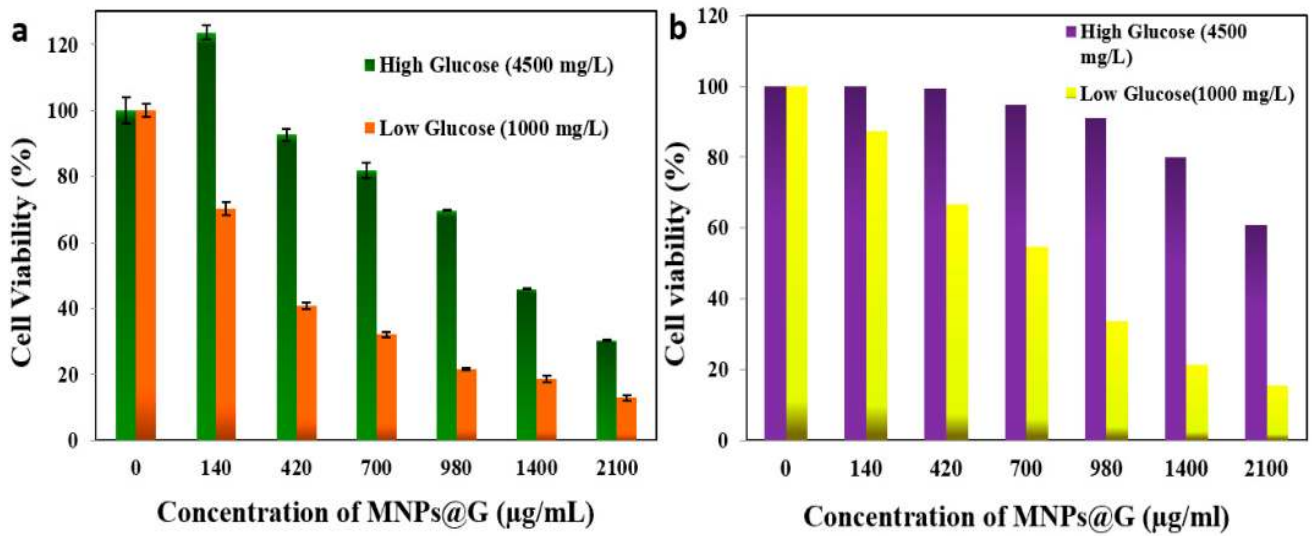
Figure 3 exemplifies the observations (1) and (2). It shows optical microscope images of a VM-M3 cell (top panels) and a VM-NM1 cell (bottom panels), both exposed to approximately the same amount of mNPs (26 h incubation time), and taken with focal planes at increasing depth into a cell (from left to right). This allows one to view cell interiors, and the nominal location of the absorbed nanoparticles. Clearly, the malignant VM-M3 cell contains mNPs throughout its interior. In contrast, the non-malignant VM-NM1 cell has no mNPs in its interior; these agglomerated in large clumps outside the cell. This confirms that only the malignant cells have phagocytic behavior. Similarly, in several similar tests (not shown here), we observed that healthy, non-cancerous cells also do not ingest mNPs.



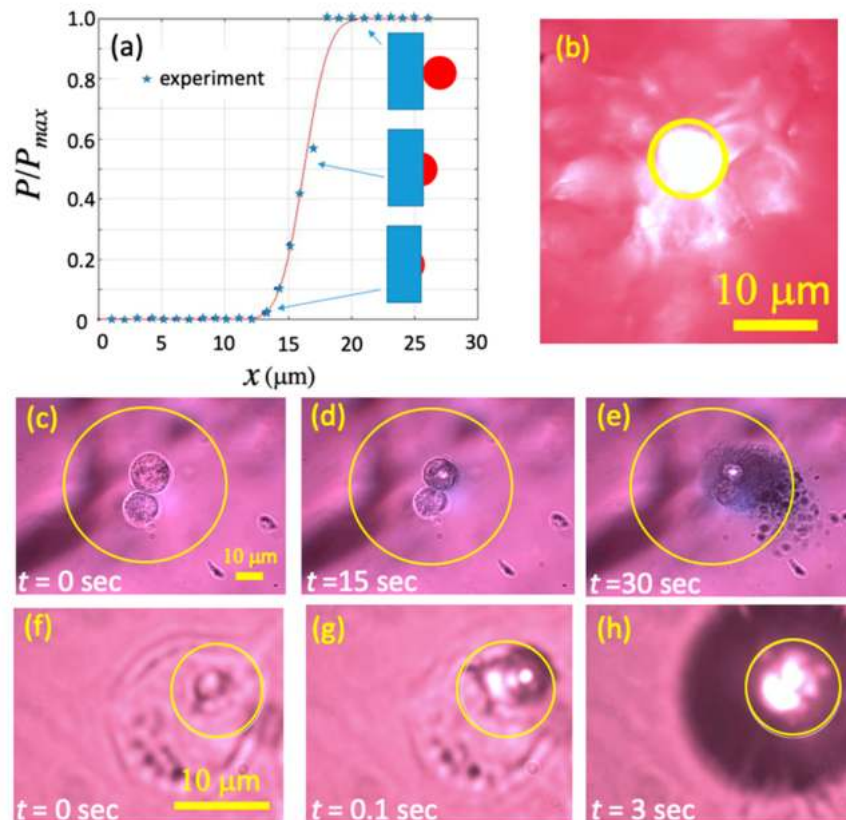
**Figure 3.** Optical microscope images of a VM-M3 cell (a–c) and a VM-NM1 cell (d–f), taken at changing focal plane depths: near the top cell surface (a,d), middle of the cell (b,e), and near the bottom cell surface (c,f). Both cells are shown after 26 h incubation with mNPs. The common scale bar is 10  $\mu$ m. The dashed line in (d,f) outlines the cell shape as in (e).

Figure 4 exemplifies observations (3), (4) and (5) listed above. Figure 5a shows A375 cell viability versus concentration of mNP@G for two different glucose concentrations in the growth medium, and Figure 3b shows similar effects for the HeLa cells that normally, in contrast to the melanoma cells, contain no melanin nanoparticles. For more details, see the Supplementary Materials. Note that a much longer incubation time (62 h) was used for higher concentrations of glucose in the growth medium compared to lower concentrations. This is simply because cells absorb the molecular glucose from the growth medium before they begin absorbing the much larger, glucose-coated nanoparticles. Thus, the incubation time approximately scales with the glucose concentration in the growth medium. The reason for higher cell viability at the same mNP concentration in high glucose concentration is not entirely clear. However, it is consistent with the Warburg effect according to which cancer cells benefit from increased amounts of glucose in the medium. One mechanism could be strengthening the cancer cell metabolism, which reduces the cytotoxic effects of mNPs. These suggest that a low glucose diet (e.g., ketogenic) for cancer therapies based on nanoparticles could be beneficial. Our results are in broad agreement with other reports on a variety of cancer cells [47–50].





**Figure 4.** (a) A375 melanoma and (b) HeLa cell viability according to CCK-8 assay as a function of mNP@G concentration after 62 h incubation in high glucose growth medium ( $4500 \text{ mg}\cdot\text{L}^{-1}$ ) and 15 h incubation in low glucose growth medium ( $1000 \text{ mg}\cdot\text{L}^{-1}$ ).



**Figure 5.** (a) Optical power (scaled to its maximum) versus position, measured using the blade edge shading effect. The insets sketch approximate blade-beam relative locations at selected points. (b) Optical image of the laser spot obtained by using the fluorescent card. (c–e) Images of two VM-M3 cells moderately filled with mNPs, at various exposure times to laser light, at 10× magnification (light power density  $\mathcal{O}_{inc} \approx 6 \times 10^7 \text{ W}\cdot\text{m}^{-2}$ ). (f–h) Images of a VM-M3 cell moderately filled with mNPs, at various exposure times to laser radiation, at 100× magnification (power density  $\mathcal{O}_{inc} \approx 1.4 \times 10^9 \text{ W}\cdot\text{m}^{-2}$ ). Yellow circles mark approximate beam diameter, which changes with magnification.

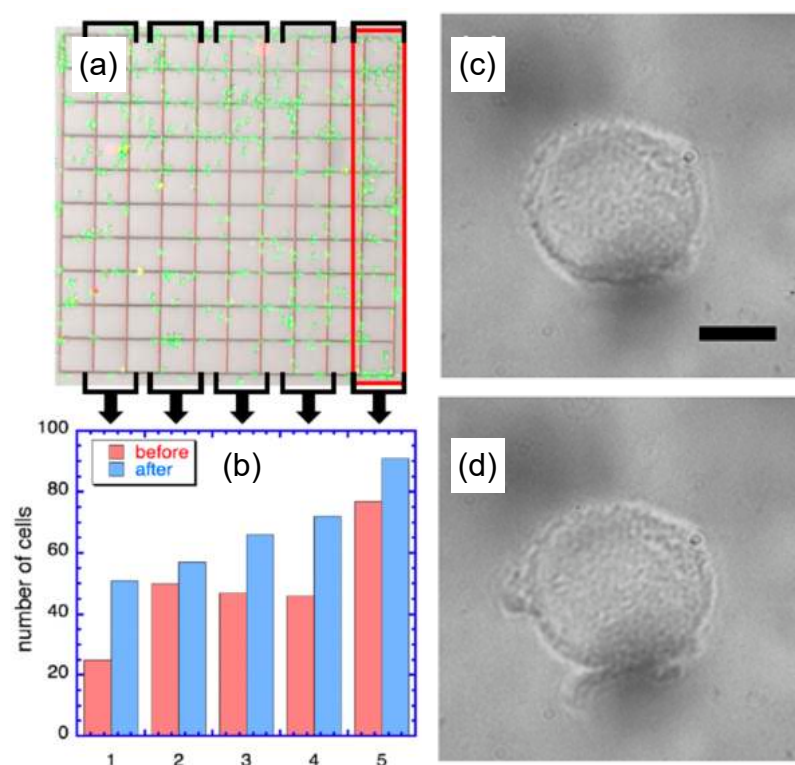
The mechanism of the mNPs cytotoxicity is unclear at this point. It might be due to the nanoscopic size of the mNPs, which dramatically increases surface area for molecular chemical reactions with the cell interior components. Note that the melanin produced by melanocytes occurs in the form of microcrystals (average diameter  $D$ ), much larger than mNPs in the current work (each with average diameter  $d$ ) and thus, for the same melanin volume, have much smaller surface area (approximately  $d/D$ ). If melanin had some finite surface-based cytotoxic effect, it would be expected to be enhanced with mNPs. Biologically active melanin has indeed been reported to be cytotoxic [51].

### 3.3. Cell Viability after Exposure to Radiation

Our custom-designed laser system employed a 532 nm wavelength diode pumped solid state laser, coupled to the input port of a fluorescent microscope. The beam was aligned and centered to the back aperture of an objective, and reflected light was filtered with a dichroic mirror. The sample was viewed and data recorded via Thorcam. The laser spot size on the sample was determined by the knife edge technique. As the blade moves across the laser spot, the measured laser light power  $P$  varies from zero to  $P_{max}$ , and the shortest distance between these corresponding edge locations is recorded. This measurement is averaged over different heights and the diameter of the spot is then extrapolated by fitting a hyperbolic equation. Figure 5a shows a scaled plot of  $P$  vs. position  $x$  (with arbitrary origin) and the insets sketch approximate blade-beam locations at selected points. Figure 5b shows an optical image of the laser spot (with diameter  $D \approx 7 \mu\text{m}$ , marked by a yellow circle) on a fluorescent card, for a chosen magnification setup on the microscope.

Figure 5c–e shows images of two VM-M3 cells moderately filled with mNPs, at various exposure times to laser radiation, and at an identical magnification setup. Due to filtering, the laser spot is invisible, so its outline is marked with a  $\sim 50 \mu\text{m}$  diameter yellow circle. The power density is moderate,  $\Phi_{inc} \approx 6 \times 10^7 \text{ W}\cdot\text{m}^{-2}$ , but enough to initiate visible cell damage after 15 s of exposure, and catastrophic cell damage (explosion) after 30 s. To better match the size of the laser spot to cell dimensions, we have changed the magnification setup and laser power. The effect of that scenario on a (different) VM-M3 cell, again moderately filled with mNPs, is shown in Figure 5f–h. This time, the laser spot (also marked with a yellow circle) has diameter  $\sim 7 \mu\text{m}$ , and the corresponding power density is much larger,  $\Phi_{inc} \approx 1.4 \times 10^9 \text{ W}\cdot\text{m}^{-2}$ . The figure shows that the damage is now very localized, clearly starting at the clusters of mNPs, with damage obvious already after 0.1 s exposure, and complete catastrophic cell damage after only 3 s. The white spots visible inside the high laser intensity regions are due to photoluminescence of highly excited mNPs. The results in this figure confirm a well-known fact that visible light can inflict damage to cells, including catastrophic damage. Such a process would be of little therapeutic use if it was not selective.

We found that the level of radiation capable of catastrophically destroying mNP-filled VM-M3 cells, like in Figure 5, is safe for VM-M3 cells not sensitized with mNPs. In this experiment, mNP-unfilled cells were grown on a microscopic slide, marked with a  $1 \text{ mm} \times 1 \text{ mm}$  grid to track cells throughout the experiment. The optical microscope image of the slide, shown Figure 6a, was taken 24 h after exposure to laser light of cells in the box numbered 5 (solid-red outline). The cells experienced the same power density (and approximately the same exposure time) as the cell shown in Figure 5h. The cells in the bracketed boxes 1–4 were not exposed to the laser. During the 24 h, the cells were incubated, and at the end, the Live/Dead Cell Staining Kit II (PromoKine) assay was applied, to visualize cell viability. Figure 6a shows that the cells take up the Calcein-AM dye, resulting in green fluorescence, and are not permeable to the EthD-II dye, which would result in red fluorescence. Thus, all cells remain alive.



**Figure 6.** Effect of laser light on VM-M3 cells unfilled with mNPs. (a) Live/dead cell staining test: all cells luminesce green and none red, indicating all are alive and growing. Only cells within the red-outlined, bracketed box have been exposed to the laser. (b) Bar diagram of cell counts in boxes 1–5, with red = before and blue = 24 h after laser exposure of cells in box 5, all in growth medium. (c) An mNP-free, single VM-M3 cell before and (d) after laser exposure as described in the text. Scale bar 10  $\mu\text{m}$ .

Figure 6b shows a population bar diagram in the corresponding 5 boxes, where each box is represented by two bars: red bars before and blue bars after laser illumination of box 5. The red bars show that the initial cell distribution was roughly uniform in boxes 2–4 (with an average cell number per box  $\sim 47$ ), box 1 had  $\sim 25$ , and box 5,  $\sim 75$  cells. After 24 h, the number of alive cells increased in all boxes (growing cells), including laser-exposed box 5. It is also clear that the overall distribution of cells on the grid changed, with the number of cells per box gradually increasing, e.g., to  $\sim 50$  in box 1 and to  $\sim 90$  in box 5. This effect likely results from a combination of natural cell population growth and temperature rise from laser heating of box 5, and the heat transfer away from this box. The resulting temperature profile during illumination would then be asymmetric, with a gradual temperature drop towards box 1, with cell growth reflecting this profile. Recorded movies of the details of these mNP-filled cells explosively damaged, as well as of the unfilled cells remaining unaffected, can be found in the Supplementary Materials. To demonstrate the lack of visible damage at the microscopic level, we show optical images of a single, mNP-unfilled MV-M3 cell before (panel c), and after (panel d) laser illumination, at the same level as applied in panel (a). As expected, the radiation produces no visible change in the cell.

The main results in this part of our study are: (a) compared with the cytotoxicity of nanoparticles alone, laser-induced cell death requires much lower density of absorbed nanoparticles, (b) all cells filled with absorbing nanoparticles (e.g., mNPs) are destroyed by radiation, at sufficient power level—this would include melanoma cells, naturally filled with melanin microcrystals, and (c) there is a laser power range at which the nanoparticle-filled cancer cells are violently destroyed, while the nanoparticle-free cells remain alive. This is a key finding of this work, since the nanoparticle-filled cells do not have to be

so violently destroyed to be killed, and so the applied laser power level can be strongly reduced. This lower power level obviously will not damage the nanoparticle-free cells.

Our nanoparticle-based strategy could be used as a basis for or part of a cancer therapy (e.g., optochemotherapy), for example to target circulating tumor cells which mediate metastasis. In such a therapy, an intravenous injection could accomplish the first stage of the mNPs feeding into CTCs. This step could be enhanced by additional bio-engineered CTC targeting schemes. Next, in one possible scenario, one could expose the blood of a cancer patient to light externally, in a dialysis-like scheme. This would lead to a dramatic reduction in the CTC population, thus significantly reducing the effects of metastasis.

#### 4. Conclusions

We have observed massive cellular uptake of melanin nanoparticles by the studied metastatic cancer cells (macrophagic/phagocytic character) which, at sufficiently high density, causes a cytotoxic effect. This effect is further enhanced by coating the nanoparticles with glucose, and simultaneous reduction of the glucose level in the growth medium. We also demonstrated that nonionizing visible light at moderate power levels kills these metastatic cancer cells, at much lower mNP uptake levels. Cell death occurs in this case via hyperthermia-induced lysis, and we found this process to be target-selective, as nonmalignant cancer cells studied here that could not ingest the melanin nanoparticles remain unaffected, despite receiving identical optical energy levels and doses. This technique could enhance a future cancer metastasis preventing therapy.

**Supplementary Materials:** The following are available online at <https://www.mdpi.com/article/10.3390/pharmaceutics13070965/s1>. Scheme S1: WST-8 based cytotoxicity assay mechanism, Table S1: Zeta potential  $\zeta$  of cancer cells and nanoparticles in buffer, Video S1: video corresponding to Figure 6, Video S2: recorded video of un-sensitized VM-M3 cells exposed to laser treatment (not being apparently damaged), Video S3: recorded video of sensitized (melanin-filled) VM-M3 cells exposed to laser treatment under identical conditions as Video S2 (being damaged).

**Author Contributions:** Conceptualization, K.K., M.G., M.J.N. and T.N.S.; methodology, K.K., M.G., M.J.N., T.N.S., A.M., V.R.G. and R.M.M.; validation, K.K., M.G. and M.J.N.; formal analysis, V.R.G., R.M.M., N.A., P.M. and N.N.; resources, K.K., M.G., M.J.N., T.N.S. and E.M.A.; data curation, V.R.G., R.M.M.; writing—original draft preparation, V.R.G., R.M.M., K.K. and N.N.; writing—review and editing, K.K., M.G., M.J.N. and T.N.S.; visualization, V.R.G., R.M.M., N.N. and E.M.A.; supervision, K.K., M.J.N., M.G. and G.Z.; project administration, K.K., M.J.N., M.G., G.Z. and E.M.A.; funding acquisition, K.K., M.G., M.J.N., G.Z. and E.M.A. All authors have read and agreed to the published version of the manuscript.

**Funding:** This research was funded by the US National Science Foundation, grant number PHY-1748906, the Guangdong Innovative and Entrepreneurial Team Program, grant number 2016ZT06C517, and the Science and Technology Program of Guangzhou, grant number 2019050001.

**Institutional Review Board Statement:** Not applicable.

**Informed Consent Statement:** Not applicable.

**Data Availability Statement:** The data presented in this study are available on request from the corresponding author.

**Conflicts of Interest:** The authors declare no conflict of interest.

#### References

1. Serpooshan, V.; Quinn, T.M.; Muja, N.; Nazhat, S.N. Hydraulic permeability of multilayered collagen gel scaffolds under plastic compression-induced unidirectional fluid flow. *Acta Biomater.* **2013**, *9*, 4673–4680. [CrossRef]
2. Shi, J.; Kantoff, P.W.; Wooster, R.; Farokhzad, O.C. Cancer nanomedicine: Progress, challenges and opportunities. *Nat. Rev. Cancer* **2017**, *17*, 20–37. [CrossRef]
3. Rogach, A.L.; Ogris, M. Near-infrared-emitting semiconductor quantum dots for tumor imaging and targeting. *Curr. Opin. Mol. Ther.* **2010**, *12*, 331–339.

4. De La Isla, A.; Brostow, W.; Bujard, B.; Estevez, M.; Rodriguez, J.R.; Vargas, S.; Castaño, V.M. Nanohybrid scratch resistant coatings for teeth and bone viscoelasticity manifested in tribology. *Mater. Res. Innov.* **2003**, *7*, 110–114. [CrossRef]
5. Versiani, A.F.; Astigarraga, R.G.; Rocha, E.S.O.; Barboza, A.P.M.; Kroon, E.G.; Rachid, M.A.; Souza, D.G.; Ladeira, L.O.; Barbosa-Stancioli, E.F.; Jorio, A.; et al. Multi-walled carbon nanotubes functionalized with recombinant Dengue virus 3 envelope proteins induce significant and specific immune responses in mice. *J. Nanobiotechnol.* **2017**, *15*, 26. [CrossRef]
6. Chatterjee, D.K.; Diagaradjane, P.; Krishnan, S. Nanoparticle-mediated hyperthermia in cancer therapy. *Ther. Deliv.* **2011**, *2*, 1001–1014. [CrossRef]
7. Edelstein, R.L.; Tamanaha, C.R.; Sheehan, P.E.; Miller, M.M.; Baselt, D.R.; Whitman, L.J.; Colton, R.J. The BARC biosensor applied to the detection of biological warfare agents. *Biosens. Bioelectron.* **2000**, *14*, 805–813. [CrossRef]
8. Cai, D.; Ren, L.; Zhao, H.; Xu, C.; Zhang, L.; Yu, Y.; Wang, H.; Lan, Y.; Roberts, M.F.; Chuang, J.H.; et al. A molecular-imprint nanosensor for ultrasensitive detection of proteins. *Nat. Nanotechnol.* **2010**, *5*, 597–601. [CrossRef]
9. Lai, S.K.; Hida, K.; Man, S.T.; Chen, C.; Machamer, C.; Schroer, T.A.; Hanes, J. Privileged delivery of polymer nanoparticles to the perinuclear region of live cells via a non-clathrin, non-degradative pathway. *Biomaterials* **2007**, *28*, 2876–2884. [CrossRef]
10. Mahmoudi, M.; Meng, J.; Xue, X.; Liang, X.J.; Rahman, M.; Pfeiffer, C.; Hartmann, R.; Gil, P.R.; Pelaz, B.; Parak, W.J.; et al. Interaction of stable colloidal nanoparticles with cellular membranes. *Biotechnol. Adv.* **2014**, *32*, 679–692. [CrossRef] [PubMed]
11. Chou, L.Y.T.; Ming, K.; Chan, W.C.W. Strategies for the intracellular delivery of nanoparticles. *Chem. Soc. Rev.* **2011**, *40*, 233–245. [CrossRef]
12. Nel, A.E.; Mädler, L.; Velegol, D.; Xia, T.; Hoek, E.M.V.; Somasundaran, P.; Klaessig, F.; Castranova, V.; Thompson, M. Understanding biophysicochemical interactions at the nano-bio interface. *Nat. Mater.* **2009**, *8*, 543–557. [CrossRef]
13. Hunter, R.J. *Zeta Potential in Colloid Science*, 1st ed.; Academic Press: San Diego, CA, USA, 1981; ISBN 9780123619617.
14. Zhang, Y.; Yang, M.; Portney, N.G.; Cui, D.; Budak, G.; Ozbay, E.; Ozkan, M.; Ozkan, C.S. Zeta potential: A surface electrical characteristic to probe the interaction of nanoparticles with normal and cancer human breast epithelial cells. *Biomed. Microdevices* **2008**, *10*, 321–328. [CrossRef] [PubMed]
15. Altankov, G.; Richau, K.; Groth, T. The role of surface zeta potential and substratum chemistry for regulation of dermal fibroblasts interaction. *Mater. Werkst.* **2003**, *34*, 1120–1128. [CrossRef]
16. Moan, J.; Peak, M.J. Effects of UV radiation on cells. *J. Photochem. Photobiol. B Biol.* **1989**, *4*, 21–34. [CrossRef]
17. Baskar, R.; Lee, K.A.; Yeo, R.; Yeoh, K.-W. Cancer and radiation therapy: Current advances and future directions. *Int. J. Med. Sci.* **2012**, *9*, 193–199. [CrossRef]
18. Pilát, Z.; Jonáš, A.; Ježek, J.; Zemánek, P. Effects of infrared optical trapping on *Saccharomyces cerevisiae* in a microfluidic system. *Sensors* **2017**, *17*, 2640. [CrossRef]
19. Rothman, L.S.; Gordon, I.E.; Babikov, Y.; Barbe, A.; Chris Berner, D.; Bernath, P.F.; Birk, M.; Bizzocchi, L.; Boudon, V.; Brown, L.R.; et al. The HITRAN2012 molecular spectroscopic database. *J. Quant. Spectrosc. Radiat. Transf.* **2013**, *130*, 4–50. [CrossRef]
20. Gabriele, V.R.; Shvonski, A.; Hoffman, C.S.; Giersig, M.; Herczynski, A.; Naughton, M.J.; Kempa, K. Towards spectrally selective catastrophic response. *Phys. Rev. E* **2020**, *101*, 62415. [CrossRef]
21. Gamage, S.; Howard, M.; Makita, H.; Cross, B.; Hastings, G.; Luo, M.; Abate, Y. Probing structural changes in single enveloped virus particles using nano-infrared spectroscopic imaging. *PLoS ONE* **2018**, *13*, e0199112. [CrossRef]
22. Lee, S.Y.; Yoon, K.A.; Jang, S.H.; Ganbold, E.O.; Uuriintuya, D.; Shin, S.M.; Ryu, P.D.; Joo, S.W. Infrared spectroscopy characterization of normal and lung cancer cells originated from epithelium. *J. Vet. Sci.* **2009**, *10*, 299–304. [CrossRef] [PubMed]
23. Galanzha, E.I.; Shashkov, E.V.; Spring, P.M.; Suen, J.Y.; Zharov, V.P. In vivo, noninvasive, label-free detection and eradication of circulating metastatic melanoma cells using two-color photoacoustic flow cytometry with a diode laser. *Cancer Res.* **2009**, *69*, 7926–7934. [CrossRef]
24. Luo, X.; Mitra, D.; Sullivan, R.J.; Wittner, B.S.; Kimura, A.M.; Pan, S.; Hoang, M.P.; Brannigan, B.W.; Lawrence, D.P.; Flaherty, K.T.; et al. Isolation and molecular characterization of circulating melanoma cells. *Cell Rep.* **2014**, *7*, 645–653. [CrossRef]
25. Vasefi, F.; MacKinnon, N.; Saager, R.; Kelly, K.M.; Maly, T.; Booth, N.; Durkin, A.J.; Farkas, D.L. Separating melanin from hemodynamics in nevi using multimode hyperspectral dermoscopy and spatial frequency domain spectroscopy. *J. Biomed. Opt.* **2016**, *21*, 114001. [CrossRef] [PubMed]
26. Jiang, Q.; Luo, Z.; Men, Y.; Yang, P.; Peng, H.; Guo, R.; Tian, Y.; Pang, Z.; Yang, W. Red blood cell membrane-camouflaged melanin nanoparticles for enhanced photothermal therapy. *Biomaterials* **2017**, *143*, 29–45. [CrossRef]
27. Slominski, A.; Kim, T.-K.; Brożyna, A.A.; Janjetovic, Z.; Brooks, D.L.P.; Schwab, L.P.; Skobowiat, C.; Józwicki, W.; Seagroves, T.N. The role of melanogenesis in regulation of melanoma behavior: Melanogenesis leads to stimulation of HIF-1 $\alpha$  expression and HIF-dependent attendant pathways. *Arch. Biochem. Biophys.* **2014**, *563*, 79–93. [CrossRef]
28. Slominski, A.; Tobin, D.J.; Shibahara, S.; Wortsman, J. Melanin pigmentation in mammalian skin and its hormonal regulation. *Physiol. Rev.* **2004**, *84*, 1155–1228. [CrossRef]
29. Zhang, W.; Tang, B.; Huang, Q.; Hua, Z. Galangin inhibits tumor growth and metastasis of B16F10 melanoma. *J. Cell. Biochem.* **2013**, *114*, 152–161. [CrossRef]
30. American Society of Clinical Oncology, cancer.net. 2020. Available online: <https://www.cancer.net/cancer-types/melanoma/statistics> (accessed on 10 March 2021).

31. Suzuki, H.; Sasaki, E.; Motai, R.; Goto, S.; Nishikawa, D.; Beppu, S.; Terada, H.; Sawabe, M.; Hanai, N. Safety and efficacy of salvage neck dissection following carbon-ion radiotherapy with chemotherapy for a Patient with mucosal malignant melanoma of head and neck. *Diagnostics* **2020**, *10*, 82. [CrossRef]
32. Cabrita, R.; Lauss, M.; Sanna, A.; Donia, M.; Skaarup Larsen, M.; Mitra, S.; Johansson, I.; Phung, B.; Harbst, K.; Vallon-Christersson, J.; et al. Tertiary lymphoid structures improve immunotherapy and survival in melanoma. *Nature* **2020**, *577*, 561–565. [CrossRef]
33. Filippi, A.R.; Fava, P.; Badellino, S.; Astrua, C.; Ricardi, U.; Quaglino, P. Radiotherapy and immune checkpoints inhibitors for advanced melanoma. *Radiother. Oncol.* **2016**, *120*, 1–12. [CrossRef]
34. Wang, J.-J.; Li, Z.-F.; Li, X.-J.; Han, Z.; Zhang, L.; Liu, Z.-J. Effects of microRNA-136 on melanoma cell proliferation, apoptosis, and epithelial-mesenchymal transition by targeting PMEL through the Wnt signaling pathway. *Biosci. Rep.* **2017**, *37*. [CrossRef]
35. Enomoto, L.M.; Levine, E.A.; Shen, P.; Votanopoulos, K.I. Role of surgery for metastatic melanoma. *Surg. Clin. N. Am.* **2020**, *100*, 127–139. [CrossRef]
36. Hocker, T.L.; Singh, M.K.; Tsao, H. Melanoma genetics and therapeutic approaches in the 21st century: Moving from the benchside to the bedside. *J. Investig. Dermatol.* **2008**, *128*, 2575–2595. [CrossRef]
37. Pisano, M.; Pagnan, G.; Loi, M.; Mura, M.E.; Tilocca, M.G.; Palmieri, G.; Fabbri, D.; Dettori, M.A.; Delogu, G.; Ponzoni, M.; et al. Antiproliferative and pro-apoptotic activity of eugenol-related biphenyls on malignant melanoma cells. *Mol. Cancer* **2007**, *6*, 8. [CrossRef]
38. Slominski, R.M.; Zmijewski, M.A.; Slominski, A.T. The role of melanin pigment in melanoma. *Exp. Dermatol.* **2015**, *24*, 258–259. [CrossRef]
39. Brożyna, A.A.; Jóźwicki, W.; Roszkowski, K.; Filipiak, J.; Slominski, A.T. Melanin content in melanoma metastases affects the outcome of radiotherapy. *Oncotarget* **2016**, *7*, 17844–17853. [CrossRef]
40. Lazova, R.; Pawelek, J.M. Why do melanomas get so dark? *Exp. Dermatol.* **2009**, *18*, 934–938. [CrossRef]
41. Sarna, M.; Zadło, A.; Hermanowicz, P.; Madeja, Z.; Burda, K.; Sarna, T. Cell elasticity is an important indicator of the metastatic phenotype of melanoma cells. *Exp. Dermatol.* **2014**, *23*, 813–818. [CrossRef]
42. Sarna, M.; Krzykawska-Serda, M.; Jakubowska, M.; Zadło, A.; Urbanska, K. Melanin presence inhibits melanoma cell spread in mice in a unique mechanical fashion. *Sci. Rep.* **2019**, *9*, 9280. [CrossRef]
43. Sandulache, V.C.; Ow, T.J.; Pickering, C.R.; Frederick, M.J.; Zhou, G.; Fokt, I.; Davis-Malesevich, M.; Priebe, W.; Myers, J.N. Glucose, not glutamine, is the dominant energy source required for proliferation and survival of head and neck squamous carcinoma cells. *Cancer* **2011**, *117*, 2926–2938. [CrossRef]
44. Han, L.; Ma, Q.; Li, J.; Liu, H.; Li, W.; Ma, G.; Xu, Q.; Zhou, S.; Wu, E. High glucose promotes pancreatic cancer cell proliferation via the induction of EGF expression and transactivation of EGFR. *PLoS ONE* **2011**, *6*, e27074. [CrossRef]
45. Lee, C.; Longo, V.D. Fasting vs dietary restriction in cellular protection and cancer treatment: From model organisms to patients. *Oncogene* **2011**, *30*, 3305–3316. [CrossRef]
46. De Lorenzo, M.S.; Baljinnyam, E.; Vatner, D.E.; Abarzúa, P.; Vatner, S.F.; Rabson, A.B. Caloric restriction reduces growth of mammary tumors and metastases. *Carcinogenesis* **2011**, *32*, 1381–1387. [CrossRef]
47. Da Silva, L.P.; Oliveira, S.; Pirraco, R.P.; Santos, T.C.; Reis, R.L.; Marques, A.P.; Correlo, V.M. Eumelanin-releasing spongy-like hydrogels for skin re-epithelialization purposes. *Biomed. Mater.* **2017**, *12*, 25010. [CrossRef]
48. Scognamiglio, F.; Travan, A.; Turco, G.; Borgogna, M.; Marsich, E.; Pasqua, M.; Paoletti, S.; Donati, I. Adhesive coatings based on melanin-like nanoparticles for surgical membranes. *Colloids Surf. B Biointerfaces* **2017**, *155*, 553–559. [CrossRef]
49. Perring, J.; Crawshay-Williams, F.; Huang, C.; Townley, H.E. Bio-inspired melanin nanoparticles induce cancer cell death by iron adsorption. *J. Mater. Sci. Mater. Med.* **2018**, *29*, 181. [CrossRef]
50. Liopo, A.; Su, R.; Oraevsky, A.A. Melanin nanoparticles as a novel contrast agent for optoacoustic tomography. *Photoacoustics* **2015**, *3*, 35–43. [CrossRef]
51. Madhusudhan, D.N.; Mazhari, B.B.Z.; Dastager, S.G.; Agsar, D. Production and cytotoxicity of extracellular insoluble and droplets of soluble melanin by *Streptomyces lusitanus* DMZ-3. *BioMed Res. Int.* **2014**, *2014*, 306895. [CrossRef] [PubMed]





## Article

# Stimuli-Responsive Nanofibers Containing Gold Nanorods for On-Demand Drug Delivery Platforms

Baljinder Singh <sup>1,†</sup>, Nutan Shukla <sup>1</sup>, Junkee Kim <sup>1</sup>, Kibeom Kim <sup>2,†</sup>  and Myoung-Hwan Park <sup>1,2,3,4,\*</sup> 

- <sup>1</sup> Department of Convergence Science, Sahmyook University, Seoul 01795, Korea; vishalmasih94@gmail.com (B.S.); nutanshukla14@gmail.com (N.S.); junkee0215@naver.com (J.K.)  
<sup>2</sup> Convergence Research Center, Nanobiomaterials Institute, Sahmyook University, Seoul 01795, Korea; kibumy@syu.ac.kr  
<sup>3</sup> Department of Chemistry and Life Science, Sahmyook University, Seoul 01795, Korea  
<sup>4</sup> N to B Co., Ltd., Business Incubator Center, Hwarang-ro, Nowon-gu, Seoul 01795, Korea  
\* Correspondence: mpark@syu.ac.kr  
† These authors contributed equally to this work.

**Abstract:** On-demand drug delivery systems using nanofibers have attracted significant attention owing to their controllable properties for drug release through external stimuli. Near-infrared (NIR)-responsive nanofibers provide a platform where the drug release profile can be achieved by the on-demand supply of drugs at a desired dose for cancer therapy. Nanomaterials such as gold nanorods (GNRs) exhibit absorbance in the NIR range, and in response to NIR irradiation, they generate heat as a result of a plasmon resonance effect. In this study, we designed poly (N-isopropylacrylamide) (PNIPAM) composite nanofibers containing GNRs. PNIPAM is a heat-reactive polymer that provides a swelling and deswelling property to the nanofibers. Electrospun nanofibers have a large surface-area-to-volume ratio, which is used to effectively deliver large quantities of drugs. In this platform, both hydrophilic and hydrophobic drugs can be introduced and manipulated. On-demand drug delivery systems were obtained through stimuli-responsive nanofibers containing GNRs and PNIPAM. Upon NIR irradiation, the heat generated by the GNRs ensures shrinking of the nanofibers owing to the thermal response of PNIPAM, thereby resulting in a controlled drug release. The versatility of the light-responsive nanofibers as a drug delivery platform was confirmed in cell studies, indicating the advantages of the swelling and deswelling property of the nanofibers and on-off drug release behavior with good biocompatibility. In addition, the system has potential for the combination of chemotherapy with multiple drugs to enhance the effectiveness of complex cancer treatments.

**Citation:** Singh, B.; Shukla, N.; Kim, J.; Kim, K.; Park, M.-H. Stimuli-Responsive Nanofibers Containing Gold Nanorods for On-Demand Drug Delivery Platforms. *Pharmaceutics* **2021**, *13*, 1319. <https://doi.org/10.3390/pharmaceutics13081319>

Academic Editor: Hassan Bousbaa

Received: 29 July 2021

Accepted: 18 August 2021

Published: 23 August 2021

**Keywords:** on-demand drug delivery systems; electrospun nanofibers; poly (N-isopropylacrylamide); gold nanorods

**Publisher's Note:** MDPI stays neutral with regard to jurisdictional claims in published maps and institutional affiliations.



**Copyright:** © 2021 by the authors. Licensee MDPI, Basel, Switzerland. This article is an open access article distributed under the terms and conditions of the Creative Commons Attribution (CC BY) license (<https://creativecommons.org/licenses/by/4.0/>).

## 1. Introduction

On-demand drug delivery systems (DDSs), which are programmable in a patient-friendly manner, can spatially and temporally control drug delivery at a particular site and the rate of drug release over a specific period of time [1–3]. Recently, the development of on-demand DDSs from stimuli-responsive nanomaterials, which provide a controlled and pulsatile release of drugs at certain concentrations in the body, has received significant interest [4–6]. Conventional DDSs pose some challenges such as difficulty in controlling the drug release rate, unsuitability of the drugs for other body organs, and the production process of the system [7,8]. Several drugs are not appropriate for oral drug delivery, owing to their limitation of drug degradation under the acidic and alkaline conditions of the stomach and intestine, respectively [9,10]. Intravenous injection for drug delivery can resolve some of the problems that occur in oral drug delivery; however, this system also has various issues such as the drug administration requiring professional skill, specific storage



issues, and sterility [11,12]. Furthermore, side-effects on nontargeted sites in the body are another major issue in DDSs [13,14]. Therefore, it is necessary to explore an innovative drug delivery platform that can maintain sustained and controlled drug release during the treatment cycle, achieve a targeted drug delivery, and circumvent the abovementioned challenges [15].

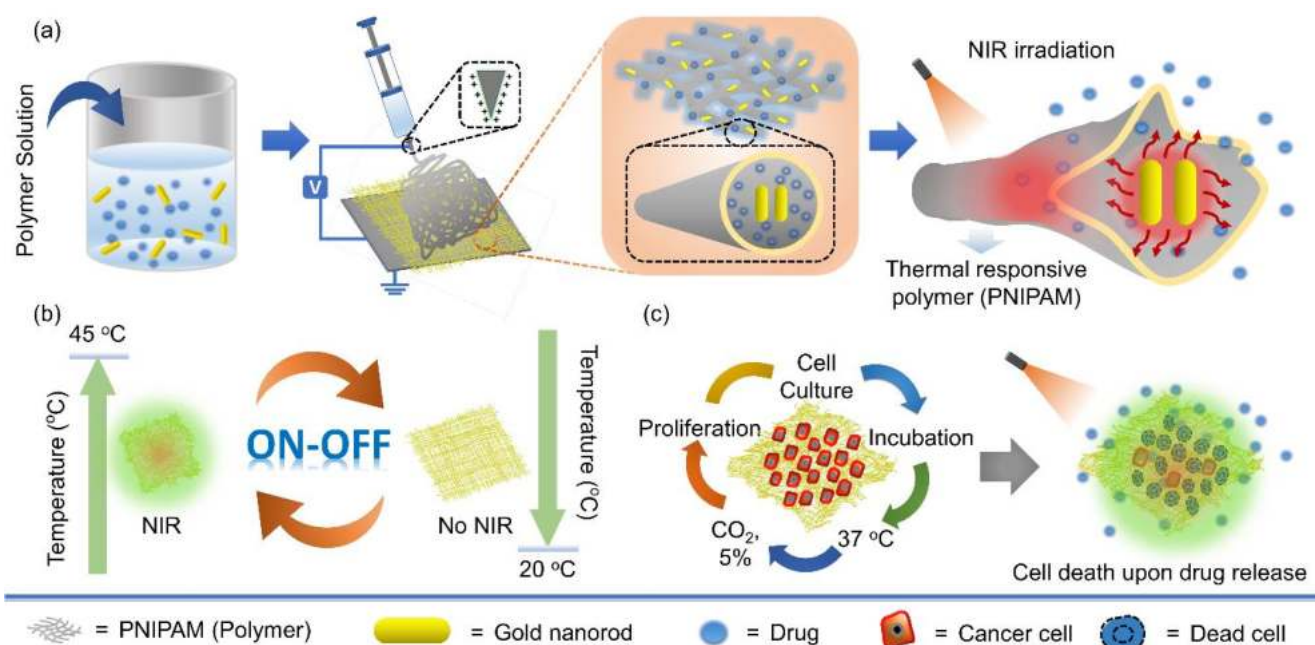
As a result, implantable drug delivery has emerged as an adequate platform for local drug delivery in cancer by aiming at the tumor site and effectively removing the damage by migrating from the bloodstream to the target tissue [16]. Hence, stimuli-responsive nanomaterials as nanocarriers enhance the therapeutic potential for the development of a platform for effective drug delivery in cancer therapy [17–19]. Smart polymeric nanofibers are promising materials for therapeutic platforms with advanced biomedical applications owing to their high biocompatibility, high drug encapsulation efficacy, ease of surface modification, and controllable characteristics [20–22]. The nanofibers with anticancer drugs can provide sustained drug release at the local targeted sites [23,24]. The main advantage of local drug delivery at the targeted site is to prevent undesirable side-effects at nontargeted sites, which also enhances the drug efficacy by delivering high concentrations of the drug at the desired sites [25,26]. Therefore, smart DDSs based on such nanofibers are required to enable on-demand release for effective treatment. Thus, the DDSs can attain an anticipated mode of drug delivery by sparing the healthy cells.

Nanofibers can play an essential role in wound dressing and can be a good drug carrier in skin cancer treatment with promising properties such as curing, controlling the chemical environment around the wound area that can maintain proper moisture, and protecting the wound from further damage [27]. In this case, nanofiber-based drug delivery with nontoxic behavior and skin compatibility can be an optimistic system by providing controlled drug release with an effective concentration to the wound site and skin cancer area [28]. On-demand drug release from nanofibers can be achieved based on the choice of responsive materials and encapsulation methods [29,30]. Smart nanomaterials have been widely developed because of their responsive behavior to external stimuli such as pH, temperature, light, and ultrasound [31–34]. Among all these external stimuli, light has received considerable attention because of its ease of use and better spatiotemporal control [35]. Ultraviolet (UV)-light-responsive systems have disadvantages such as poor tissue penetration and harmful effects on cells and tissues due to the accumulation of DNA damage, and if the body is unable to repair this damage, it can begin to divide and grow in an uncontrolled manner and lead to cancer [36,37]. In contrast, NIR light exhibits good and deep tissue penetration and is also safe for cells and tissues [38,39].

Several nanofibers with inorganic nanoparticles such as Au, Ag, Fe<sub>3</sub>O<sub>4</sub>, Si, and graphene oxide introduced inside or on the surface of the nanofibers have been prepared, which play important roles in DDSs [40–43]. Among them, gold nanorods (GNRs) have attracted significant attention due to their strong absorption in the NIR range (650–900 nm), which is harmless to the human body [44,45]. GNRs are attractive probes for cancer imaging because of their highly effective absorption in the NIR region, a spectral window that permits photons to penetrate biological tissues with relatively high transmittance. Apart from being attractive probes for cancer imaging, the GNRs are also heat-generating sources owing to their surface plasmon resonance (SPR) effect [46–48]. In this study, nanofibers were prepared using poly(*N*-isopropylacrylamide) (PNIPAM)—a temperature-responsive polymer—because it has potential applications in DDSs [49]. PNIPAM causes a reversible phase transition at a specific temperature defined as the lower critical solution temperature (LCST). At temperatures below the LCST, PNIPAM expands in water through intermolecular hydrogen bonding between the polymer chains of PNIPAM and water molecules. These intermolecular hydrogen bonds are replaced by intramolecular hydrogen bonds between CO and NH groups along the PNIPAM chain at temperatures above the LCST. This results in the aggregation of polymers in water. Most of the polymers are not crosslinked; hence, they are easily soluble in water [50]. Nanofibers from the PNIPAM homopolymer are unstable in water; therefore, cross-linking for copolymerization is required to enhance

the stability of the nanofibers in an aqueous solution [51–53]. The PNIPAM nanofibers containing GNRs exhibit optical sensitivity, and the heat generated by the GNRs can control the swelling and deswelling property due to the thermal sensitivity of PNIPAM [54]. This method can be used in various treatments that generate local heat through NIR irradiation, which can penetrate body tissues to up to 10 cm without serious damage to surrounding tissues [55]. The photothermal effect becomes strong by introducing the porous structures and GNRs inside the nanofiber, and the thermal/optical response speed can be increased by rapidly increasing the temperature above the LCST of PNIPAM. The crosslinked composite nanofibers can be used as an on–off drug release system by simply irradiating the surface with NIR [56].

PNIPAM nanofibers containing GNRs with fast thermal/optical response, high heating rate, and high structural stability were prepared through the electrospinning method [57]. Electrospun nanofibers provide easy surface functionalization in the space between small fibers and have high surface-area-to-volume and porosity mass ratios [58,59]. In electrospinning, when a high voltage is applied to a solution being discharged at a constant speed through a nozzle, it forms a Taylor cone by electrostatic force. Furthermore, the solvent evaporates instantaneously, forming nanofibers with a large surface area in the collector grounded with the polymer [60,61]. Through a simple electrospinning process, therapeutic drugs can be conveniently introduced into nanofibers [62,63]. Until now, studies have been conducted on nanofibers in which drugs are introduced using various substances such as antibiotic, chemotherapeutic, and vitamin substances [64]. However, a DDS using composite materials emerges as a promising platform because nanofibers have a long-time stability due to the presence of drugs and GNRs, which is convenient for the on–off cyclic profile of the drug release (Scheme 1). This method provides efficient loading of low-solubility drugs into the nanofibers and is suitable for the encapsulation and release of hydrophobic and hydrophilic drugs. This ideal system allows drugs to be safely introduced into DDSs and to control drug release to treat cancers or overcome other complex diseases [65–67]. The objective of this study was to achieve a platform that addresses problems with conventional release methods, such as insufficient drug release at targeted sites owing to drug waste at nontargeted sites and externally uncontrolled release due to the treatment period that leads to reopening and painful operations [68]. The embedding of GNRs into the matrix of nanofibers elevates them to a new category of biomaterials capable of reacting to stimulation [69]. Using this approach, we developed a method to treat glioblastoma (GBM), also known as a grade IV astrocytoma, a fast-growing and aggressive brain tumor through the externally controlled release of camptothecin (CPT), which can promote a senescence-like phenotype in brain cancer cells [70]. The direct delivery of chemotherapy agents to the brain is a clinically proven method for treating glioblastoma multiforme, but current technologies have significant limitations, including severe local tissue toxicity and a limited diffusional penetration of agents, which limit its application and effectiveness [71]. CPT-loaded nanofibers can be delivered to a stereotactically specified position in the brain, providing the simultaneous control of drug release location, diffusion, and duration in our new method [72]. This CPT analog can improve the efficacy and stability on the tumor site for more effective local anticancer therapies against brain cancers cells [73]. Therefore, we used the U-87 MG cell line in this study. Hence, this study emerges as a novel approach for externally controlled drug release for efficient therapeutic effects in cancer treatment.



**Scheme 1.** Schematic illustration of stimuli-responsive nanofibers containing GNRs for on-demand drug delivery platform. (a) Fabrication of nanofiber through electrospinning technique and drug release upon NIR irradiation. (b) On–off cyclic profile of the nanofibers. (c) Cell proliferation on the nanofibers and cell death upon drug release.

## 2. Materials and Methods

### 2.1. Materials

Poly(N-isopropylacrylamide) (MW 300,000 Da, Polysciences, Warrington, PA, USA), octaglycidyl polyhedral oligomeric silsesquioxane (OpePOSS) (Hybrid Plastics Inc., Hattiesburg, MS, USA), 2-ethyl-4-methylimidazole (EMI), gold(III) chloride trihydrate ( $\text{HAuCl}_4 \cdot 3\text{H}_2\text{O}$ ), cetyltrimethylammonium bromide (CTAB), sodium borohydride ( $\text{NaBH}_4$ ), silver nitrate ( $\text{AgNO}_3$ ), ascorbic acid, 11-bromo-1-undecanol (98%), triphenylmethanethiol (97%), methanesulfonyl chloride ( $\text{MsCl}$ , 98%), trifluoroacetic acid (TFA,  $\geq 99\%$ , liquid), triisopropylsilane (TIS, 98%), and triethylamine (TEA,  $\geq 99\%$ ) were purchased from Sigma-Aldrich (St. Louis, MO, USA) and used as received. Other organic solvents required for ligand synthesis were purchased from Sigma-Aldrich (St. Louis, MO, USA). Fluorescein was purchased from JUNSEI (Tokyo, Japan). CPT was purchased from TCI (Tokyo, Japan). The  $^1\text{H-NMR}$  graph was measured with a  $\text{CDCl}_3$  solvent using a JEOL ECX-400 400 MHz (JEOL, Tokyo, Japan) spectrometer. Cells were obtained from the Korean Cell Line Bank (Seoul, Korea). All cell reagents for in vitro studies such as phosphate-buffered saline solution (PBS), Dulbecco's modified Eagle's medium (DMEM), fetal bovine serum (FBS), penicillin–streptomycin, and trypsin-ethylenediaminetetraacetic acid (trypsin-EDTA) were all purchased from Sigma-Aldrich (St. Louis, MO, USA). The cell viability was quantified using 3-(4,5-dimethylthiazol-2-yl)-2,5-diphenyltetrazolium bromide (MTT), which was purchased from Sigma-Aldrich (St. Louis, MO, USA). Fluorescence spectra were collected using a Neosys-2000 UV-Vis spectrophotometer (Scinco, Twin Lakers, WI, USA) and a QM-400 spectrophotometer (Horiba Scientific, Piscataway, NJ, USA). A diode laser system with a wavelength of 808 nm and continuous-wave operation mode was used as photo-stimulation, and temperature traces were recorded using a Ti95 infrared camera (Fluke, Washington, WA, USA). The cell viability was measured using a microplate reader (Tecan Trading AG, ZH, Switzerland).

### 2.2. Preparation of Both Organic and Water-Soluble TMA-GNRs

The GNRs used in this study were prepared according to the well-known seed-mediated growth method using CTAB, and the stability of GNRs in organic solvents was

ensured through surface modification of the GNRs with HS-C<sub>11</sub>-trimethyl ammonium (TMA), as reported by Jeong et al. [74].

### 2.3. Characterization of GNRs

The morphology of GNRs was investigated by transmission electron microscopy (TEM) (Tokyo, Japan, JEOL JEM-2010). GNRs were dispersed in ionized water (IW). A single drop of GNR solution was applied on a carbon-coated copper grid (200 mesh) and allowed to dry at ambient temperature before imaging with a 50 nm scale bar. The SPR spectra of GNRs were examined using UV–Vis spectroscopy (Scinco, USA) in the wavelength range of 400–1100 nm by adding 2 mL of GNRs solution to a 4 mL quartz cuvette. Zeta potential analysis was determined by adding a maximum of 400 µL of the three different samples to a zeta potential cuvette with a positive and a negative electrode. The equilibration time for each was set at 120 s, with a total of 50 runs. Three separate tests were carried out under these conditions.

### 2.4. Fabrication of Light-Responsive Electrospun Nanofibers

To make 5 mL of polymeric solution for electrospinning, 0.5 g (10%) of PNIPAM, 0.15 g (3%) of OpePOSS, and 0.01 g (0.2%) of EMI were dissolved in 4 mL of DMF:THF 1:1. The mixture was stirred for 4 h at room temperature. Finally, 1 mL of TMA-GNRs DMF:THF 1:1 solution (200 nM) was added to the obtained solution, and the mixture was stirred for an additional hour to form a uniform solution. A certain polymer concentration that produces the nanofibers of the same diameter and suitable uniformity was chosen. If the concentration is low, the diameter of the resulting fibers becomes nonuniform and some bonds or even the fibers may not be formed. Conversely, at higher concentration, the diameter of the fibers is large; hence, the rate of penetration of water is slow, which affects the response speed of the composite film. The resulting homogeneous polymer solution was injected into a 10 mL plastic syringe. During electrospinning, a direct-current voltage of 13.5 kV was applied to the needle, and the polymer solution was supplied at a flow rate of 0.05 mL/min at room temperature. Furthermore, the distance between the needle and the collection plate was 12 cm. The electrospinning process was performed at 26.4 °C and 45–50% relative humidity (RH) measured by a thermo hygrometer. The prepared nanofibers were placed in a vacuum oven at 160 °C for 4 h to crosslink the PNIPAM nanofibers.

### 2.5. Characterization of Nanofibers

The morphologies of nanofiber scaffolds were analyzed using a scanning electron microscope (SEM) (Tokyo, Japan, JEOL JSM-6510) and confocal laser scanning microscopy (CLSM) (Solms, Germany, Leica TCS SP8). The nanofibers containing GNRs and fluorescein were prepared and cut into circles of 1 cm diameter using a biopsy punch. The nanofiber samples were coated with 250 Å of gold via a Denton Desk V Sputter Coater. The SEM images were obtained at an accelerated voltage of 20 kV and 20 µm scale bar. Fiber diameter distribution histograms were quantified using the SEM micrographs. For each sample, 10 random field images were taken, and 10 fibers were measured in each image. The samples from the same nanofibers with a diameter of 1 cm were taken for CLSM. In this analysis, two samples were prepared that were the original dry nanofiber and water-treated nanofiber. The CLSM images were obtained under 63× magnification. All these characterizations were observed at room temperature.

### 2.6. On-Demand Drug Release

To study the behavior of NIR-responsive drug release at different irradiation times, nanofibers containing GNRs and fluorescein (model drug) were prepared. The nanofibers were cut into circles of 1 cm diameter using a biopsy punch and added in 1.5 mL of IW. To check the fluorescence intensity of drug release, the sample tube, which was placed 10 cm from the center of a laser probe, was irradiated directly on the nanofiber sample by a diode

laser (808 nm) at a laser power of  $1.6 \text{ W/cm}^2$  up to 60 min at 10 min intervals. The drug release was confirmed by fluorescence spectroscopy after every 10 min of the same sample tube. The pulsatile drug release was performed in a cyclic on–off manner by 10 min of no NIR light irradiation and 2 min of NIR light irradiation at a laser power of  $1.6 \text{ W/cm}^2$  up to 60 min, and the solution was quantified via a QM-400 spectrophotometer after 10 min of no irradiation and 2 min of irradiation. Furthermore, the cumulative drug release with  $0.6 \text{ W/cm}^2$ ,  $1.1 \text{ W/cm}^2$ , and  $1.6 \text{ W/cm}^2$  laser powers was performed. In this experiment, four different samples were used, and the laser power irradiated up to 60 min at 5 min intervals. For all these drug release experiments, all the samples containing the same amount of drug ( $2 \mu\text{g}$ ) were used and the experiment was performed at room temperature.

### 2.7. Biocompatibility and Toxicity

Cell studies were performed to evaluate the biocompatibility and toxicity of the nanofibers containing GNRs and fluorescein using the U-87 MG (brain cancer cells) cell line. The nanofibers were cut into circles of 1 cm diameter using a biopsy punch and attached to the bottom of a 24-well plate. Prior to cell seeding, all wells containing nanofibers were preconditioned overnight in DMEM containing 10% FBS and 1% penicillin/streptomycin at  $37 \text{ }^\circ\text{C}$  in a 5%  $\text{CO}_2$  incubator. Thereafter, the media were refreshed and the cells with a density of  $3 \times 10^3$  cells/well were cultured on the nanofibers under the same conditions mentioned above. After 24 h, the supernatant was discarded, and the cells were incubated with trypsin-EDTA for 5 min to detach from the surface of the nanofibers for cell counting.

### 2.8. MTT Assay for Cell Viability

PNIPAM nanofibers containing GNRs and CPT were prepared. In addition, 1 cm-diameter circles of the nanofiber samples were used, each of which contained  $30 \mu\text{g}$  of payload. Further, 500 cells/well were incubated in a 96-well plate for 24 h in DMEM containing 10% FBS and 1% penicillin/streptomycin at  $37 \text{ }^\circ\text{C}$  in a 5%  $\text{CO}_2$  incubator before experiments. The samples were irradiated with NIR light at different laser powers for 2, 10, and 20 min to release the drug from the nanofibers to the cells in the 96-well plate. After 2–4 h of incubation, the MTT assay was conducted using a microplate reader at 570 nm absorption. In this analysis, three control groups such as only cells without nanofibers (cells w/o NFs), nanofibers containing GNRs without CPT (NFs+GNRs), and nanofibers containing GNRs with CPT (NFs+GNRs+CPT) were prepared. The test group analysis was performed based on different laser powers. The laser powers used in this experiment were 0.6, 1.1, and  $1.6 \text{ W/cm}^2$ .

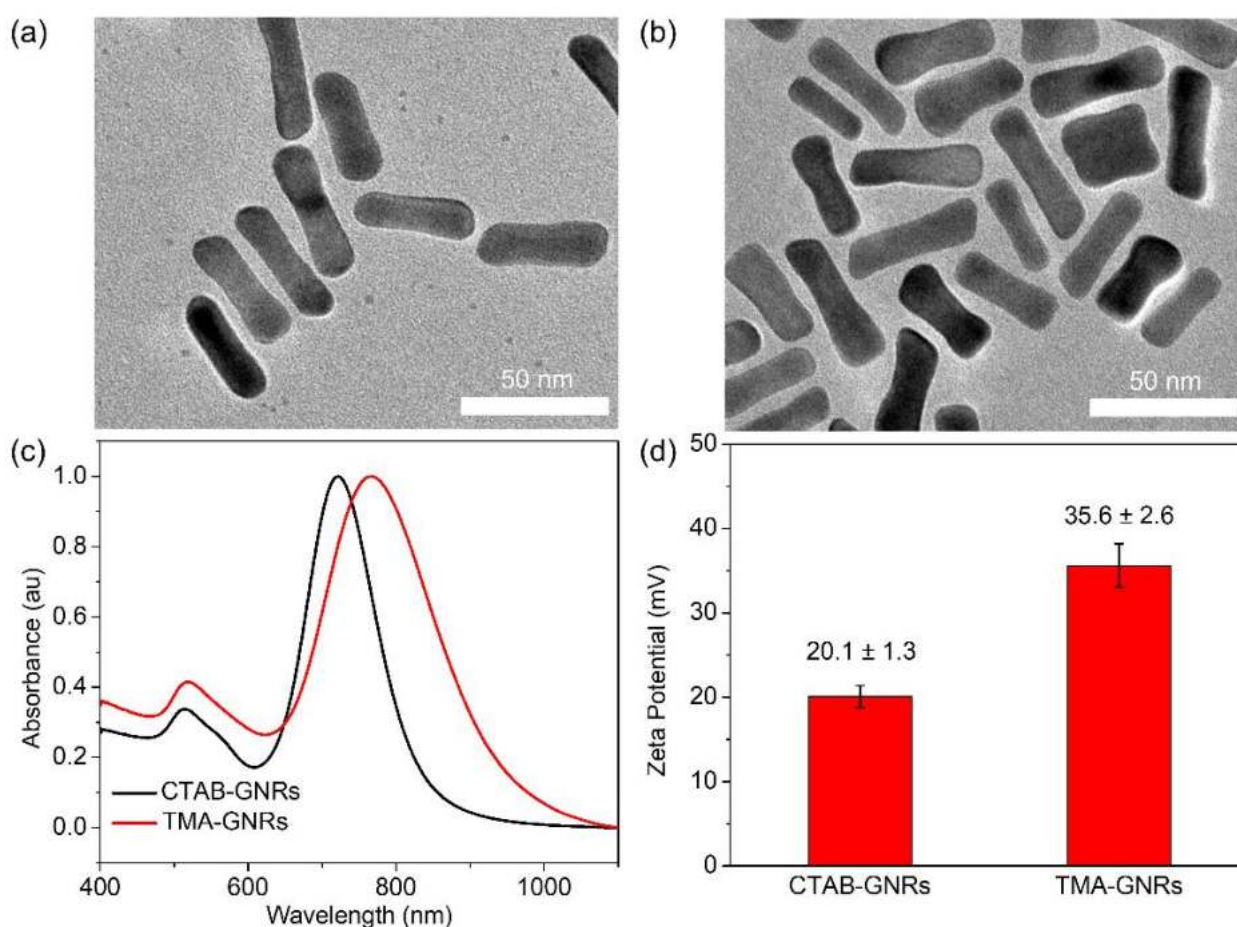
### 2.9. Data and Statistical Analysis

All statistical analyses were performed using ANOVA analysis with a test level set at  $p \leq 0.05$ , which was considered to be a statistically significant difference. The results of all numerical variables were examined by the statistical mean, standard deviation, and graphical analysis using GraphPad Prism 9.2.0 software (GraphPad Software, San Diego, Inc., CA, USA). All cell viability tests were performed with three independent samples from each group for all the different assays.

## 3. Results and Discussion

The plasmon-based photothermal effect of GNRs has become an excellent source of controlled drug release with potential applications and outstanding properties in DDSs. As mentioned earlier, GNRs have strong absorption in the NIR wavelength range; hence, in this study, we irradiated GNRs with NIR light to generate heat to shrink the nanofibers, which results in drug release. The GNRs used in this study were prepared using CTAB, which is a toxic surfactant and unstable in organic solvents. Hence, surface modification was performed on the GNRs to ensure good stability in organic solvents. For this purpose, CTAB attached on the surface of the GNRs was exchanged with TMA through the ligand exchange process. The obtained TMA-GNRs exhibited good stability in DMF:THF 1:1, which we used

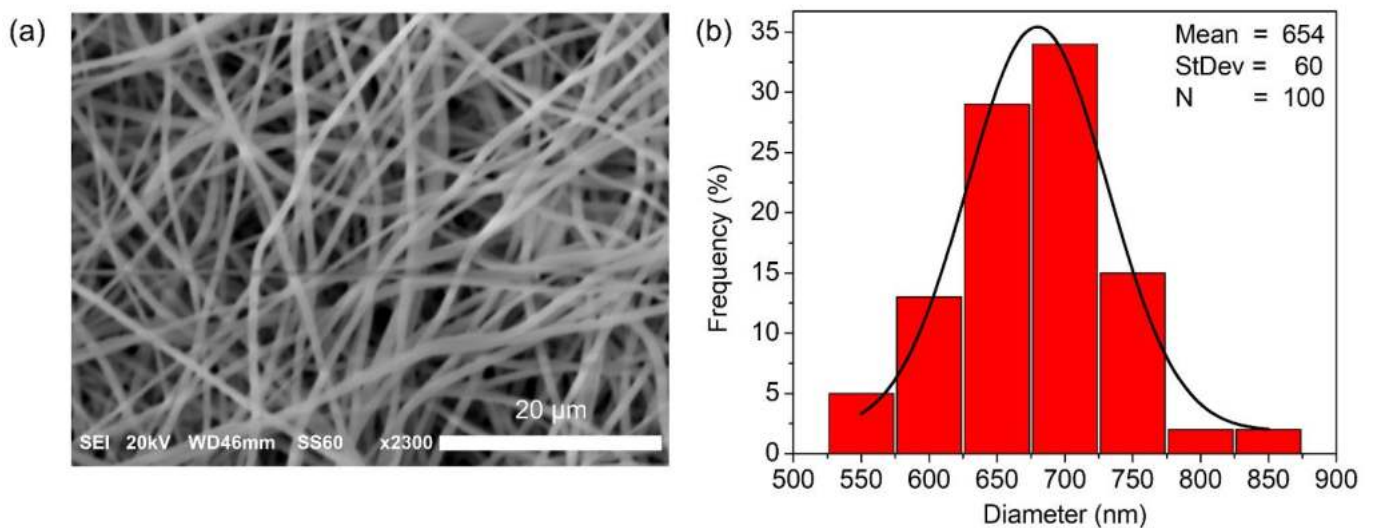
as the electrospinning solution. CTAB-GNRs and TMA-GNRs were characterized through TEM, UV-Vis spectroscopy, and the zeta potential (Figure 1). The TEM images (Figure 1a,b) show that the GNRs retained their rod shape even after exchanging the surface functionality from CTAB to TMA. The UV-Vis spectrum (Figure 1c) of the CTAB-GNRs solution was confirmed to have specific peaks at 513 nm and 722 nm. Furthermore, in the UV-vis spectrum of TMA-GNRs, the peaks corresponding to TMA-GNRs appeared at 519 nm and 765 nm. Due to the change in the dielectric constant of the environment of each GNR and the sensitivity to the different organic solvents used for the spectrum measurement, the absorption spectra of TMA-GNRs showed pronounced shifts in both the transverse and longitudinal surface plasmon resonance (LSPR) bands after ligand exchange. The zeta potential (Figure 1d) value of CTAB-GNRs was measured at  $20.1 \pm 1.3$  mV, whereas that of TMA-GNRs increased to  $35.6 \pm 2.6$  mV owing to the high charge density after surface modification, which indicates that TMA successfully replaced CTAB from the surface of the GNRs.



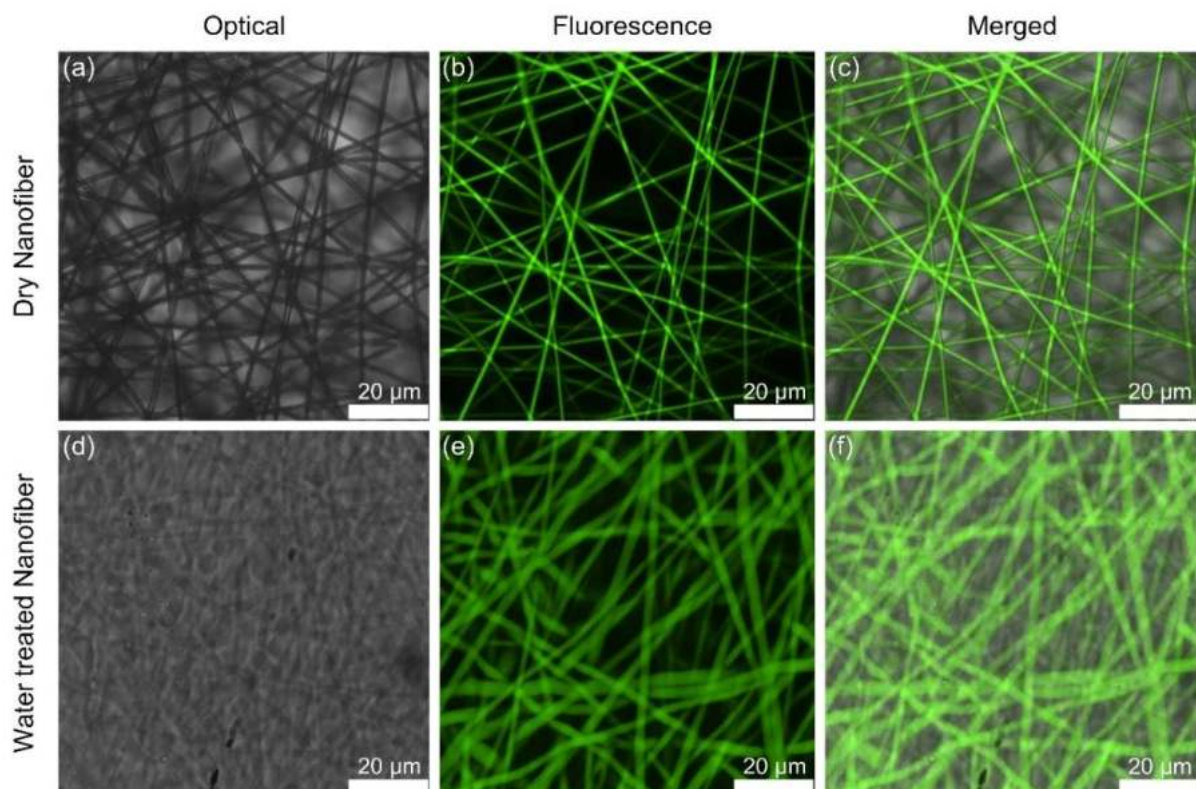
**Figure 1.** TEM images of (a) CTAB-GNRs and (b) TMA-GNRs; (c) UV-Vis spectra of CTAB-GNRs and TMA-GNRs; and (d) zeta potential of CTAB-GNRs and TMA-GNRs.

In general, the morphology of nanofibers does not depend only on the electrospinning solution, but also on the parameters of the electrospinning process such as flow rate, high voltage, and distance between the nozzle and the collector. All the parameters used in this method were selected based on the requirements of this study. As shown in Figure 2a, SEM images of the nanofibers obtained the morphology after electrospinning and had an average diameter of 600–700 nm [54]. The nanofibers had a 34% frequency of 700 nm and a 29% frequency of 650 nm, according to the diameter distribution histogram in Figure 2b. As shown in Figure 3, the fluorescein-loaded nanofibers were visualized using CLSM. The CLSM images in Figure 3a show optical images of the dry nanofibers, and a strong

green fluorescence matrix is observed in Figure 3b,c, thereby indicating that fluorescein was successfully loaded onto the matrix of the nanofibers. The CLSM of the fluorescein-loaded nanofibers was measured in two different states, that is, original dry nanofibers and water-treated nanofibers. In Figure 3a–c, the dry nanofibers exhibited uniform nanofibrous structures with an average diameter of 600–700 nm. In addition, Figure 3d–f show that the nanofibers were swollen, and their average diameter increased to 2  $\mu\text{m}$  after immersing in water.



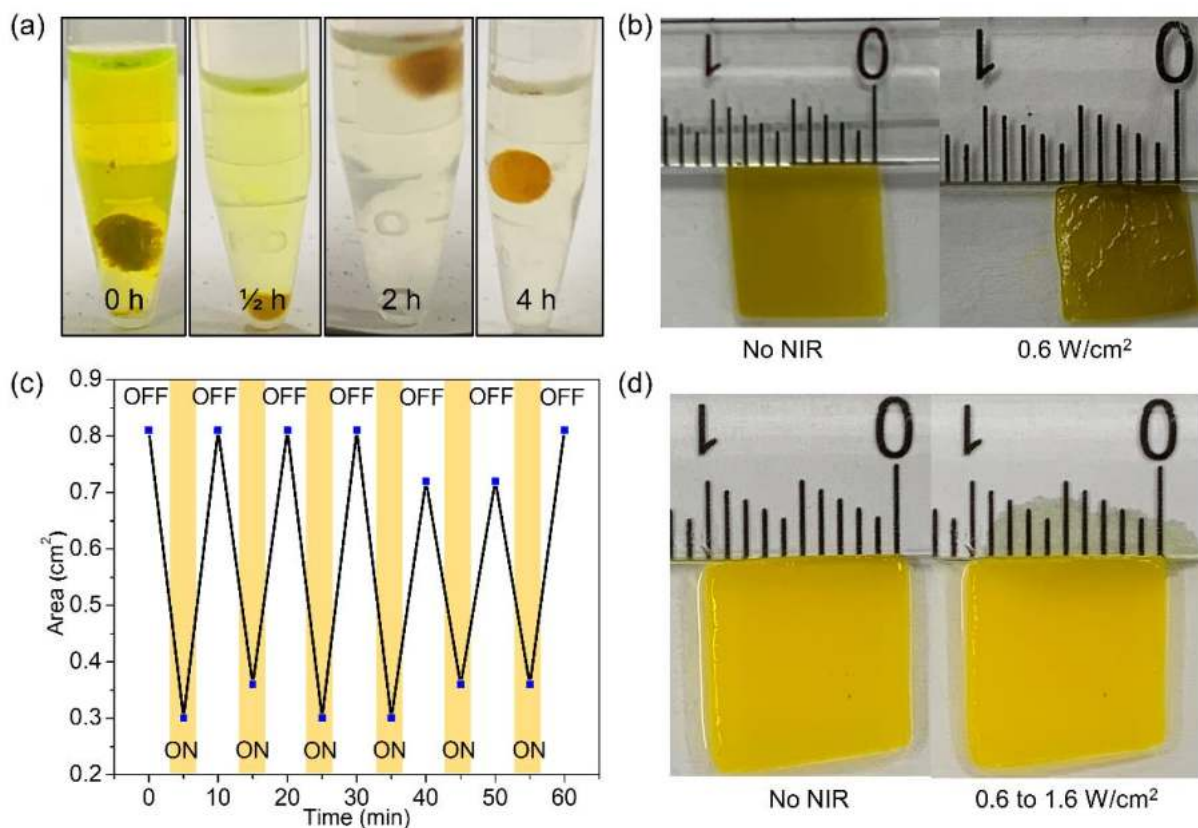
**Figure 2.** (a) SEM images and (b) diameter distribution histogram of the nanofibers.



**Figure 3.** CLSM images of the nanofiber containing fluorescein. (a–c) Original dry nanofibers. (d–f) Water-treated nanofibers.

The crosslinking of PNIPAM and OpePOSS through heat treatment at 160  $^{\circ}\text{C}$  is a promising method for the high and long-time stability of nanofibers in an aqueous solution.

Heat-treatment at 160 °C for 0.5, 2 h, 4 h, and 0 h with four different samples confirmed the cross-linking of prepared nanofibers containing GNRs and fluorescein for on-demand drug release in Figure 4a. The time of 0 h indicates that no heat treatment was provided. As shown in Figure 4a, the nanofibers with 0 h, 0.5 h, and 2 h of heat treatment had low stability with fluorescein leaking in water. However, after 4 h of heat treatment, the high stability of the nanofibers was observed without any fluorescein leakage. Meanwhile, the stimuli-responsive behavior of the nanofibers containing GNRs was investigated using NIR light (Figure 4b). The NIR laser power of 0.6 W/cm<sup>2</sup> was considered as a minimal power. As shown in Figure 4c, the original nanofibers had a surface area of 0.81 cm<sup>2</sup>; however, when the nanofibers were exposed to the NIR light, they immediately shrank, and their surface area decreased to 0.3 cm<sup>2</sup>. Moreover, Figure 4c demonstrates that when the NIR light was off, the nanofibers returned to the original surface area. These quick and reversible area changes upon the irradiation of the NIR light in a cyclic on–off manner were observed without any significant defects. On the other hand, the nanofibers without GNRs did not respond to the NIR light (Figure 4d), even after increasing the laser power from 0.6 W/cm<sup>2</sup> to 1.6 W/cm<sup>2</sup>, indicating that the system had a strong photothermal effect owing to the presence of the GNRs. These results also confirmed the presence of GNRs in the matrix of the nanofibers.

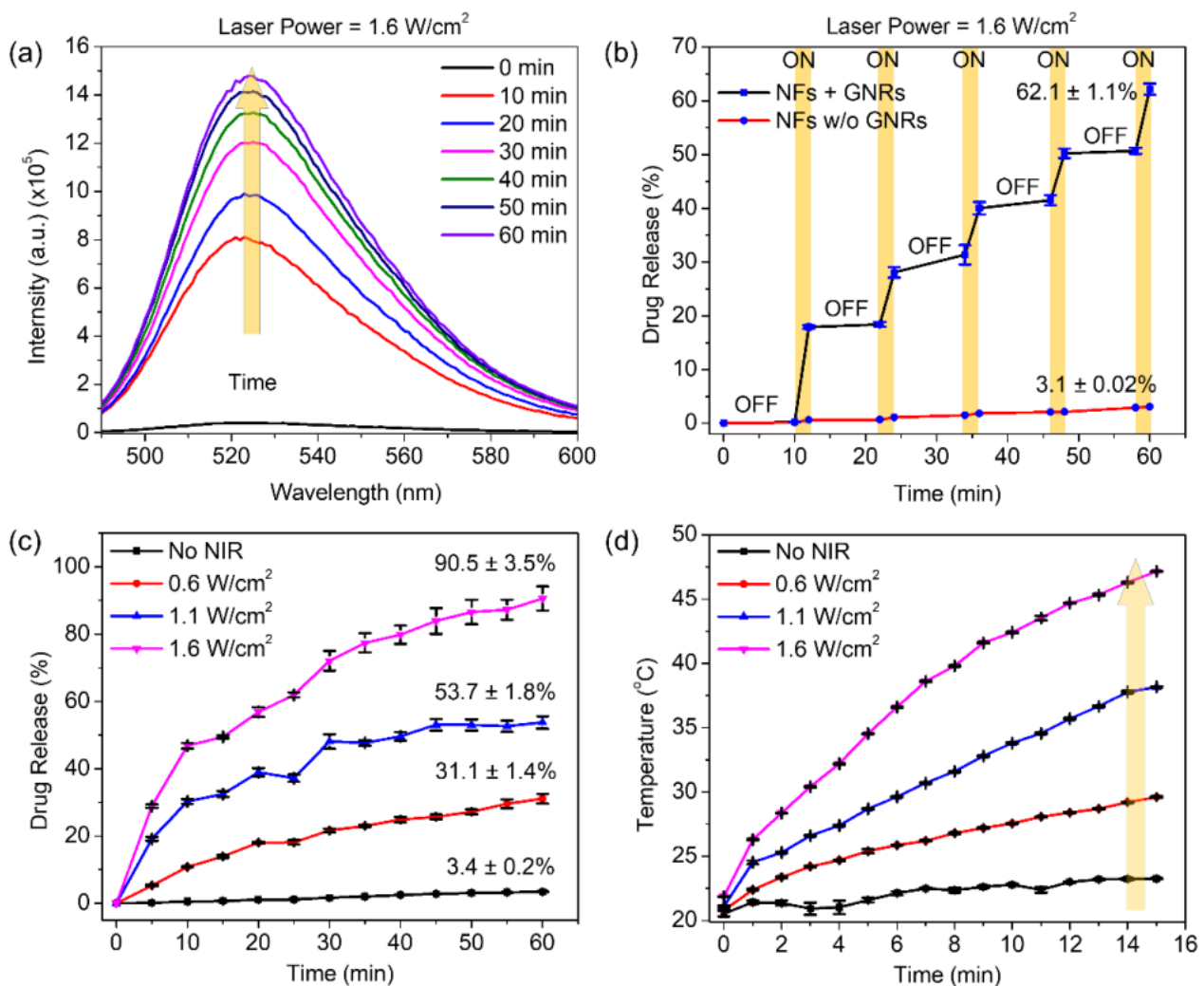


**Figure 4.** (a) Heat treatment of nanofiber under 160 °C. (b) Digital images of the area changes of the whole nanofiber containing GNRs upon irradiation of NIR light. (c) Change in area of the whole nanofiber containing GNRs as a function of cycles of temperature alternation upon the NIR irradiation. (d) Digital images of the area of the whole nanofiber without GNRs in the presence and absence of NIR light irradiation.

The characteristics of the controlled drug release, as a photothermal response to the irradiated NIR light, from the nanofibers containing GNRs and fluorescein were confirmed with a fluorescence spectrophotometer (Figure 5). The NIR-triggered drug release from the nanofibers was monitored (Figure 5a). The nanofiber samples of 1 cm diameter with 2 µg of fluorescein (a model drug) were immersed in 1.5 mL of water at room temperature, and the NIR laser with a power of 1.6 W/cm<sup>2</sup> directly irradiated the nanofibers. The drug release

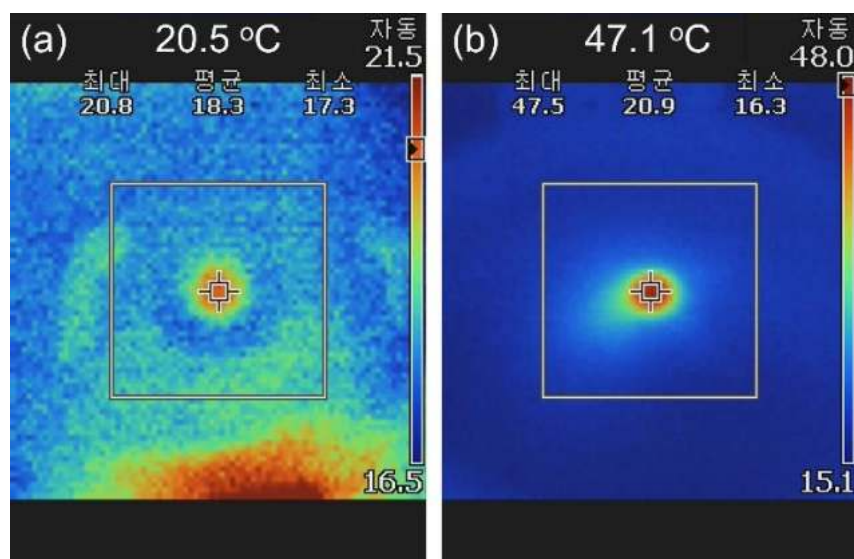


was observed every 10 min. The drug release intensity increased after every 10 min upon NIR irradiation. The thermal response to the NIR light by the GNRs was confirmed. When the nanofibers were not irradiated with the NIR light, there was a slight emission of the drug; hence, the slope of the fluorescence graph was low. However, when the nanofibers were irradiated with the NIR light, the drug was released, and the slope of the fluorescence graph increased rapidly. The on-off drug release profile was further confirmed (Figure 5b). The on-off mechanism was performed in the sequence of 10 min of no NIR light irradiation and 2 min of NIR light irradiation (of power  $1.6 \text{ W/cm}^2$ ). This cyclic process showed that  $62.1 \pm 1.1\%$  of drug was released until 60 min. In each step, the nanofibers shrunk owing to the increase in temperature upon NIR light irradiation and swelled when we turned off the NIR light. This process ensured the swelling and deswelling property of the nanofibers [75]. Different laser powers were used to investigate the drug release behavior from the matrix of the nanofibers. The different laser powers exhibited different release rates and amounts of drugs. The laser powers  $0.6$ ,  $1.1$ , and  $1.6 \text{ W/cm}^2$  resulted in drug releases of  $31.1 \pm 1.4\%$ ,  $53.7 \pm 1.8\%$ , and  $90.5 \pm 3.5\%$ , respectively, as shown in Figure 5c. In the absence of light, a small amount of drug release was observed from the nanofibers, indicating that the GNRs played an essential role as a heat-generating source. These findings appeared to be appropriate for biomedical practice with a drug release of more than 90% within 60 min [76].



**Figure 5.** (a) Fluorescence intensity of drug release. (b) Pulsatile drug release from the nanofibers through the cyclic on-off of NIR light irradiation at different time intervals. (c) Cumulative drug release from the matrix of the nanofibers with different laser powers. (d) Rate of change in temperature for different laser powers.

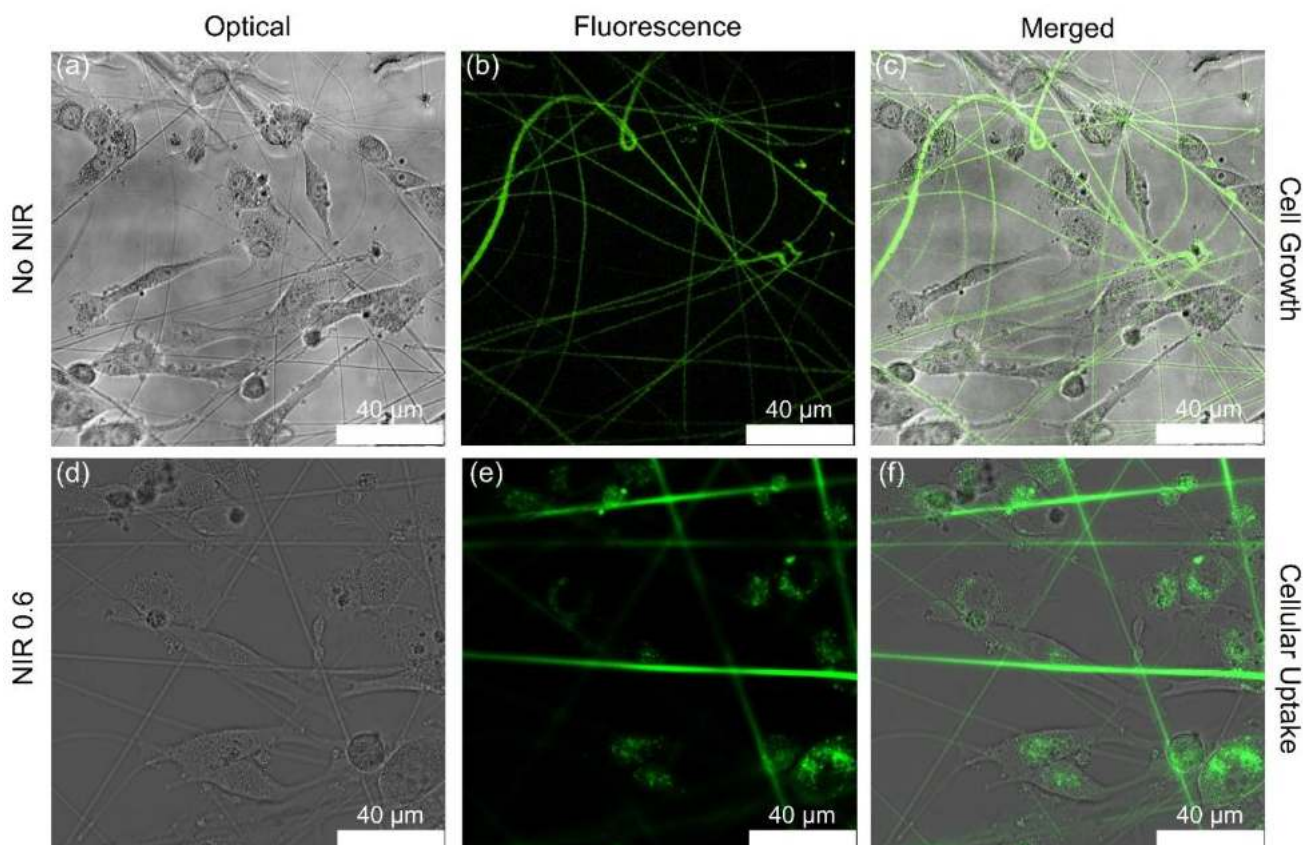
In addition, the NIR thermal response characteristics of the nanofibers were further confirmed. It was observed that the increase in water temperature depended on the power of the NIR laser light source, and the water temperature increased above 45 °C when irradiated with the NIR laser with a power of 1.6 W/cm<sup>2</sup>. As shown in Figure 5d, upon 15 min of NIR laser irradiation of powers 0.6, 1.1, and 1.6 W/cm<sup>2</sup>, the water temperature increased to the average values of 29.6 ± 0.05, 38.1 ± 0.03, and 47.1 ± 0.03 °C, respectively. These results confirm the capability of hyperthermia therapy for cancer treatment. When the nanofibers were placed in water at room temperature and the NIR laser irradiated the nanofibers, the increase in the water temperature was recorded using an infrared camera (Figure 6). Furthermore, the nanofibers did not increase the water temperature in the absence of GNRs or light.



**Figure 6.** Infrared camera images of the nanofibers (a) without GNRs and (b) with GNRs.

The biocompatibility and toxicity of the fluorescein-loaded nanofibers were evaluated through cell studies. The nanofiber samples were preconditioned before adding the cells. The U-87MG cells with a density of  $3 \times 10^3$  cells/well were cultured in a 24-well plate without the nanofibers as a control and on the surface of the nanofibers in a DMEM solution at 37 °C in a 5% CO<sub>2</sub> incubator. The cell growth and morphology were monitored for 24 and 48 h. The cells maintained a proper morphology even on the surface of the nanofibers, similar to that observed in the controls. After 48 h, the supernatant was discarded, and the cells were incubated with trypsin-EDTA for 5 min to detach the cells. The number of adhered cells increased by  $508 \times 10^3$  cells/well in the control and  $431 \times 10^3$  cells/well on the nanofibers, demonstrating the capability of easy cell growth on the surface of the nanofibers. Furthermore, according to the results, nanofibers were found noncytotoxic in the absence of NIR light owing to successful cell proliferation (Figure 7a–c).

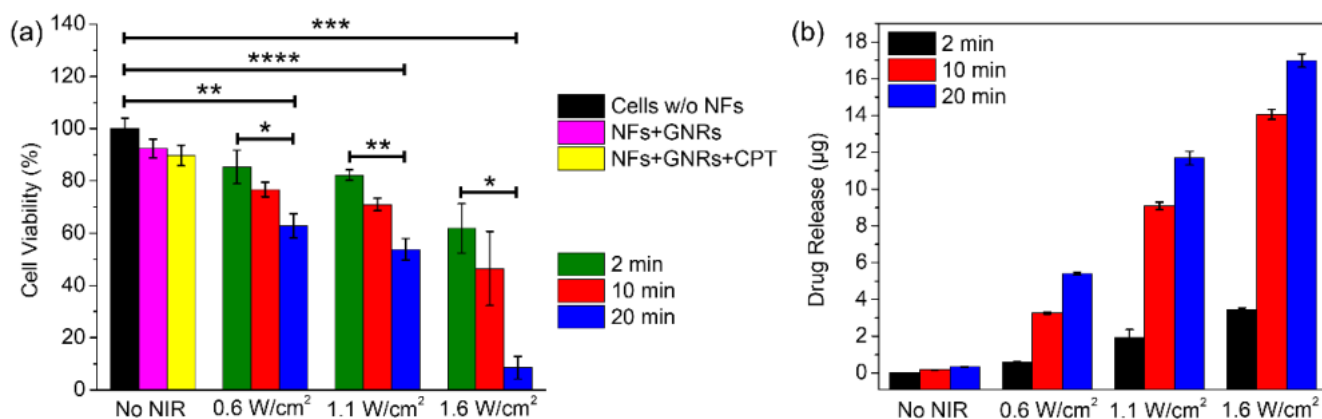
The cellular uptake was evaluated through cell culturing with a density of  $3 \times 10^3$  cells/well on the nanofibers, and the cells were incubated for 24 h under the same conditions mentioned above. The cellular uptake of released fluorescein was measured using CLSM in the absence and presence of NIR light. First, the nanofibers were not exposed to NIR light, which resulted in no release of fluorescein. As shown in Figure 7a–c, fluorescence intensity was not observed in the cells after 6 h of incubation. Then, the NIR light (0.6 W/cm<sup>2</sup>) irradiated the nanofibers for 5 min, which provided the fluorescence intensity inside the cells, indicating the release of fluorescein upon NIR light irradiation (Figure 7d–f) [77,78].



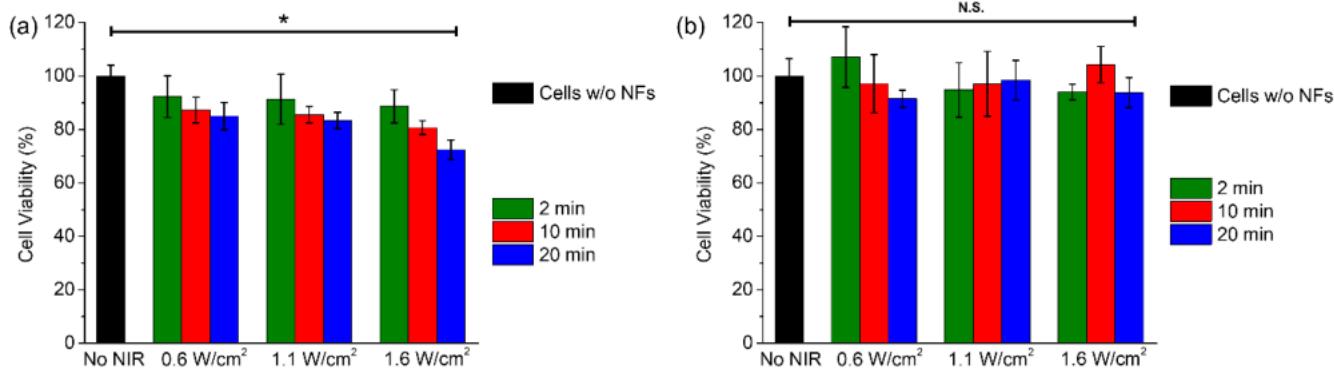
**Figure 7.** CLSM images of cell proliferation and cellular uptake on the surface of the nanofibers. (a–c) Cells on the surface of the nanofibers (no NIR irradiation). (d–f) Cellular uptake after 6 h of incubation and 5 min of NIR irradiation at  $0.6 \text{ W/cm}^2$ .

MTT assay was performed to evaluate the therapeutic potential of our platform through cell viability with U87 cells, and CPT was chosen as an anti-cancer drug. Cells were incubated for 24 h at  $37^\circ\text{C}$  in a 5%  $\text{CO}_2$  incubator before experiments. In this analysis, three control groups were prepared as: only cells without nanofibers (cells w/o NFs), nanofibers containing GNRs without CPT (NFs+GNRs), and nanofibers containing GNRs with CPT (NFs+GNRs+CPT). Figure 8a shows that there was no substantial decrease in cell viability (approximately  $7.6 \pm 3.6\%$ ) in the case of NFs+GNRs, whereas NFs+GNRs+CPT showed a  $10.2 \pm 3.9\%$  decrease in cell viability. The nanofibers containing both GNRs and CPT showed maximum cell death upon irradiation of different laser powers after drug release. According to the results, upon NIR light irradiation at  $0.6 \text{ W/cm}^2$  for 2, 10, and 20 min, the cell viabilities were  $85.3 \pm 6.4\%$ ,  $76.6 \pm 2.7\%$ , and  $62.8 \pm 4.7\%$ , respectively. Upon the NIR irradiation at  $1.1 \text{ W/cm}^2$  for 2, 10, and 20 min, the cell viabilities were  $82.2 \pm 2.03\%$ ,  $70.9 \pm 2.4\%$ , and  $53.7 \pm 4.1\%$ , respectively. Furthermore, upon the NIR light irradiation at  $1.6 \text{ W/cm}^2$  for 2, 10, and 20 min, the cell viabilities were  $61.8 \pm 9.5\%$ ,  $46.4 \pm 14.1\%$ , and  $8.5 \pm 4.3\%$ , respectively. The highest cell death was achieved upon increasing the irradiation time and laser power. In Figure 8b, the amount of released CPT has been reported. As shown in Figure 8b, without NIR light irradiation for 2, 10, and 20 min, no significant amount of drug was released. Upon NIR light irradiation at  $0.6 \text{ W/cm}^2$  for 2, 10, and 20 min,  $0.6 \pm 0.01$ ,  $3.2 \pm 0.04$ , and  $5.4 \pm 0.07 \mu\text{g}$  of drug were released, respectively. At irradiation with  $1.1 \text{ W/cm}^2$  of laser power for 2, 10, and 20 min, the released amounts were  $1.2 \pm 0.4$ ,  $9.0 \pm 0.2$ , and  $11.6 \pm 0.36 \mu\text{g}$ , respectively. Moreover, upon the NIR light irradiation at  $1.6 \text{ W/cm}^2$  for 2, 10, and 20 min, the drug release amounts were  $3.4 \pm 0.06$ ,  $14.0 \pm 0.2$ , and  $16.9 \pm 0.35 \mu\text{g}$ , respectively. The hyperthermia effect was obtained due to the presence of GNRs in nanofibers. Cell viability decreased as the NIR laser power increased, as seen in Figure 9a. As the GNRs were present in the matrix of the nanofibers,

the hyperthermia effect weakened owing to the poor exposure of the GNRs to the cancer cells. As a result of the hyperthermia treatment, the number of dead cells increased as the temperature increased above 40 °C. The most severe hyperthermia effects were observed in the case of NIR irradiation at 1.6 W/cm<sup>2</sup>, that is, as the temperature increased in the range from 41 °C to 45 °C, the cell viability decreased to 88.6 ± 6.2%, 80.7 ± 2.6%, and 72.3 ± 0.05% after 2, 10, and 20 min of NIR light exposure, respectively [79,80]. The toxicity of the NIR light was also investigated (Figure 9b). There was no significant reduction in the cell viability when the cells were exposed to the NIR light at 0.6, 1.1, and 1.6 W/cm<sup>2</sup>, thereby indicating that the NIR light was less toxic to the cells. Based on these findings, we conclude that our method appears to be promising for on-demand drug release and therapeutic efficacy in cancer treatment.



**Figure 8.** (a) Cell viability of U87 cells owing to CPT release from the nanofibers upon NIR irradiation at different time intervals. (b) Amount of drug release from the nanofibers upon NIR irradiation at different time intervals. \*  $p \leq 0.05$ , \*\*  $p \leq 0.01$ , \*\*\*  $p \leq 0.001$ , \*\*\*\*  $p \leq 0.0001$ .



**Figure 9.** (a) Hyperthermia evaluation using the nanofibers containing GNRs with U87 cells. (b) NIR light toxicity for the U87 cells in the absence of the nanofibers. \*  $p \leq 0.05$ . N.S. indicates that the difference was not significant.

#### 4. Conclusions

Herein, we developed PNIPAM nanofibers containing GNRs and drugs that can control the drug release through NIR light irradiation. As CTAB–GNRs are stable only in water and are not dispersed in organic solvents, TMA–GNRs were prepared through an exchange reaction with TMA ligands that are well-dispersed in organic solvents. To prevent the PNIPAM nanofibers from dissolving in water below the LCST, stable PNIPAM nanofibers were prepared through a crosslinking reaction with OpePOSS. The PNIPAM nanofibers containing GNRs and drugs obtained through electrospinning have high thermal/optical responsiveness. In this study, the on-demand drug release was achieved through our versatile nanofiber platform. The results showed that the fabricated nanofibers are structurally stable and have a very large surface-area-to-volume ratio for effective delivery of drugs. A

strong photothermal effect was observed by introducing the GNRs in the nanofibers. The heat generated by the GNRs upon NIR light irradiation could control the swelling and deswelling property of the nanofibers owing to the thermal sensitivity of PNIPAM, which results in drug release. This optimal method allows both hydrophilic and hydrophobic drugs to be safely introduced into DDSs and control the drug release to treat cancers and other complex diseases. Through cell studies, good biocompatibility of the nanofibers was confirmed. Furthermore, our method may contribute to the application of the sequential release of multiple drugs, which is the scope of our future studies.

**Author Contributions:** Conceptualization, B.S., K.K., and M.-H.P.; methodology, B.S.; formal analysis, B.S.; investigation, B.S., N.S., J.K., K.K., and M.-H.P.; writing—original draft preparation, B.S.; writing—review and editing, B.S., K.K., and M.-H.P.; supervision, K.K., and M.-H.P.; project administration, M.-H.P.; funding acquisition, M.-H.P. All authors have read and agreed to the published version of the manuscript.

**Funding:** This research was funded by the National Research Foundation of Korea (NRF-2019R1F1A1 061629) and by the Commercialization Promotion Agency for R&D Outcomes (2021sanhagyeon-007).

**Institutional Review Board Statement:** Not applicable.

**Informed Consent Statement:** Not applicable.

**Data Availability Statement:** The data presented in this study are available on request from the corresponding author. The data are not publicly available due to institutional policies.

**Conflicts of Interest:** The authors declare no conflict of interest. The company had no role in the design of the study; in the collection, analyses, or interpretation of data; in the writing of the manuscript, or in the decision to publish the results.

## References

1. Park, H.; Yang, S.; Kang, J.Y.; Park, M.-H. On-demand drug delivery system using micro-organogels with gold nanorods. *ACS Med. Chem. Lett.* **2016**, *7*, 1087–1091. [CrossRef]
2. Sun, M.; Duan, X. Recent advances in micro/nanoscale intracellular delivery. *Nanotechnol. Precis. Eng.* **2020**, *3*, 18–31. [CrossRef]
3. Kim, K.; Lee, S.; Jin, E.; Palanikumar, L.; Lee, J.H.; Kim, J.C.; Nam, J.S.; Jana, B.; Kwon, T.-H.; Kwak, S.K. MOF× biopolymer: Collaborative combination of metal-organic framework and biopolymer for advanced anticancer therapy. *ACS Appl. Mater. Inter.* **2019**, *11*, 27512–27520. [CrossRef] [PubMed]
4. Mura, S.; Nicolas, J.; Couvreur, P. Stimuli-responsive nanocarriers for drug delivery. *Nat. Mater.* **2013**, *12*, 991–1003. [CrossRef]
5. Park, H.; Yang, S.; Park, M.-H. Rapid and staggered release of small hydrophobic drugs using a micro-organogel embedded film. *Toxicol. Environ. Health Sci.* **2014**, *6*, 238–243. [CrossRef]
6. Kim, K.; Jo, M.-C.; Jeong, S.; Palanikumar, L.; Rotello, V.M.; Ryu, J.-H.; Park, M.-H. Externally controlled drug release using a gold nanorod contained composite membrane. *Nanoscale* **2016**, *8*, 11949–11955. [CrossRef]
7. Liu, H.; Fu, Y.; Li, Y.; Ren, Z.; Li, X.; Han, G.; Mao, C. A fibrous localized drug delivery platform with NIR-triggered and optically monitored drug release. *Langmuir* **2016**, *32*, 9083–9090. [CrossRef] [PubMed]
8. Fu, Y.; Chen, X.; Mou, X.; Ren, Z.; Li, X.; Han, G. A dual-color luminescent localized drug delivery system with ratiometric-monitored doxorubicin release functionalities. *ACS Biomater. Sci. Eng.* **2016**, *2*, 652–661. [CrossRef]
9. Gupta, H.; Bhandari, D.; Sharma, A. Recent trends in oral drug delivery: A review. *Recent Pat. Drug Deliv. Formul.* **2009**, *3*, 162–173. [CrossRef] [PubMed]
10. Liu, K.; Jiang, X.; Hunziker, P. Carbohydrate-based amphiphilic nano delivery systems for cancer therapy. *Nanoscale* **2016**, *8*, 16091–16156. [CrossRef]
11. Eek, D.; Krohe, M.; Mazar, I.; Horsfield, A.; Pompilus, F.; Friebe, R.; Shields, A.L. Patient-reported preferences for oral versus intravenous administration for the treatment of cancer: A review of the literature. *Patient Prefer. Adherence* **2016**, *10*, 1609.
12. Chen, H.; Jin, Y.; Wang, J.; Wang, Y.; Jiang, W.; Dai, H.; Pang, S.; Lei, L.; Ji, J.; Wang, B. Design of smart targeted and responsive drug delivery systems with enhanced antibacterial properties. *Nanoscale* **2018**, *10*, 20946–20962. [CrossRef]
13. Yetisgin, A.A.; Cetinel, S.; Zuvun, M.; Kosar, A.; Kutlu, O. Therapeutic nanoparticles and their targeted delivery applications. *Molecules* **2020**, *25*, 2193. [CrossRef]
14. Fan, L.; Yang, J.; Leung, K.C.-F.; Song, C.; Li, Q. Noninvasive real-time monitoring of local drug release using nano-Au-absorbed self-decomposable SiO<sub>2</sub> carriers. *Nanoscale* **2018**, *10*, 15332–15338. [CrossRef] [PubMed]
15. Fu, Y.; Li, X.; Sun, C.; Ren, Z.; Weng, W.; Mao, C.; Han, G. pH-triggered SrTiO<sub>3</sub>: Er nanofibers with optically monitored and controlled drug delivery functionality. *ACS Appl. Mater. Interfaces* **2015**, *7*, 25514–25521. [CrossRef] [PubMed]
16. Chen, Z.; Chen, Z.; Zhang, A.; Hu, J.; Wang, X.; Yang, Z. Electrospun nanofibers for cancer diagnosis and therapy. *Biomater. Sci.* **2016**, *4*, 922–932. [CrossRef] [PubMed]

17. Salehi, R.; Irani, M.; Rashidi, M.-R.; Aroujalian, A.; Raisi, A.; Eskandani, M.; Haririan, I.; Davaran, S. Stimuli-responsive nanofibers prepared from poly (N-isopropylacrylamide-acrylamide-vinylpyrrolidone) by electrospinning as an anticancer drug delivery. *Des. Monomers Polym.* **2013**, *16*, 515–527. [CrossRef]
18. Cui, H.; Ma, R.; Chen, L.; Zhang, H. Effect of particle-particle interaction on dielectrophoretic single particle trap in a sudden contraction flow. *Nanotechnol. Precis. Eng.* **2018**, *1*, 236–241. [CrossRef]
19. Dey, S.; Patel, A.; Raina, K.; Pradhan, N.; Biswas, O.; Thummer, R.P.; Manna, D. A stimuli-responsive anticancer drug delivery system with inherent antibacterial activities. *Chem. Commun.* **2020**, *56*, 1661–1664. [CrossRef] [PubMed]
20. Lin, X.; Tang, D.; Yu, Z.; Feng, Q. Stimuli-responsive electrospun nanofibers from poly (N-isopropylacrylamide)-co-poly (acrylic acid) copolymer and polyurethane. *J. Mater. Chem. B* **2014**, *2*, 651–658. [CrossRef]
21. Raza, A.; Rasheed, T.; Nabeel, F.; Hayat, U.; Bilal, M.; Iqbal, H. Endogenous and exogenous stimuli-responsive drug delivery systems for programmed site-specific release. *Molecules* **2019**, *24*, 1117. [CrossRef] [PubMed]
22. Jia, H.-R.; Zhu, Y.-X.; Liu, X.; Pan, G.-Y.; Gao, G.; Sun, W.; Zhang, X.; Jiang, Y.-W.; Wu, F.-G. Construction of dually responsive nanotransformers with nanosphere–nanofiber–nanosphere transition for overcoming the size paradox of anticancer nanodrugs. *ACS Nano* **2019**, *13*, 11781–11792. [CrossRef]
23. Balaji, A.; Vellayappan, M.; John, A.; Subramanian, A.; Jaganathan, S.; Supriyanto, E.; Razak, S. An insight on electrospun-nanofibers-inspired modern drug delivery system in the treatment of deadly cancers. *RSC Adv.* **2015**, *5*, 57984–58004. [CrossRef]
24. Zhao, S.; Zhang, S.; Ma, J.; Fan, L.; Yin, C.; Lin, G.; Li, Q. Double loaded self-decomposable SiO<sub>2</sub> nanoparticles for sustained drug release. *Nanoscale* **2015**, *7*, 16389–16398. [CrossRef] [PubMed]
25. Yang, G.; Wang, J.; Wang, Y.; Li, L.; Guo, X.; Zhou, S. An implantable active-targeting micelle-in-nanofiber device for efficient and safe cancer therapy. *ACS Nano* **2015**, *9*, 1161–1174. [CrossRef]
26. Kim, K.; Choi, H.; Choi, E.S.; Park, M.-H.; Ryu, J.-H. Hyaluronic acid-coated nanomedicine for targeted cancer therapy. *Pharmaceutics* **2019**, *11*, 301. [CrossRef] [PubMed]
27. Li, R.; Cheng, Z.; Wen, R.; Zhao, X.; Yu, X.; Sun, L.; Zhang, Y.; Han, Z.; Yuan, Y.; Kang, L. Novel SA@ Ca<sup>2+</sup>/RCSPs core-shell structure nanofibers by electrospinning for wound dressings. *RSC Adv.* **2018**, *8*, 15558–15566. [CrossRef]
28. Wang, W.; Lu, K.-J.; Yu, C.-H.; Huang, Q.-L.; Du, Y.-Z. Nano-drug delivery systems in wound treatment and skin regeneration. *J. Nanobiotechnol.* **2019**, *17*, 1–15. [CrossRef] [PubMed]
29. Lou, L.; Subbiah, S.; Smith, E.; Kendall, R.J.; Ramkumar, S.S. Functional PVA/VB2/TiO<sub>2</sub> Nanofiber Webs for Controlled Drug Delivery. *ACS Appl. Bio Mater.* **2019**, *2*, 5916–5929. [CrossRef]
30. Zhang, Z.; Tian, Z.; Chang, C.; Wang, X.; Zhang, X.; Ouyang, C.; Gu, J.; Han, J.; Zhang, W. Active-thermal-tunable terahertz absorber with temperature-sensitive material thin film. *Nanotechnol. Precis. Eng.* **2018**, *1*, 123–128.
31. Pham, S.H.; Choi, Y.; Choi, J. Stimuli-Responsive Nanomaterials for Application in Antitumor Therapy and Drug Delivery. *Pharmaceutics* **2020**, *12*, 630. [CrossRef] [PubMed]
32. Arai, Y.; Jee, S.Y.; Kim, S.M.; Kwon, Y.; Jang, W. Biomedical applications and safety issues of gold nanoparticles. *Toxicol. Environ. Health Sci.* **2012**, *4*, 1–8. [CrossRef]
33. Das, M.; Shim, K.H.; An, S.S.A.; Yi, D.K. Review on gold nanoparticles and their applications. *Toxicol. Environ. Health Sci.* **2011**, *3*, 193–205. [CrossRef]
34. Singh, B.; Shukla, N.; Cho, C.-H.; Kim, B.S.; Park, M.-H.; Kim, K. Effect and application of micro-and nanobubbles in water purification. *Toxicol. Environ. Health Sci.* **2021**, *13*, 1–8. [CrossRef]
35. Chen, H.; Zhao, Y. Applications of light-responsive systems for cancer theranostics. *ACS Appl. Mater. Interfaces* **2018**, *10*, 21021–21034. [CrossRef] [PubMed]
36. Wang, X.; Xuan, Z.; Zhu, X.; Sun, H.; Li, J.; Xie, Z. Near-infrared photoresponsive drug delivery nanosystems for cancer photo-chemotherapy. *J. Nanobiotechnol.* **2020**, *18*, 1–19. [CrossRef] [PubMed]
37. Yang, G.; Liu, J.; Wu, Y.; Feng, L.; Liu, Z. Near-infrared-light responsive nanoscale drug delivery systems for cancer treatment. *Coord. Chem. Rev.* **2016**, *320*, 100–117. [CrossRef]
38. Chen, Z.; Xiong, Y.; Etchenique, R.; Wu, S. Manipulating pH using near-infrared light assisted by upconverting nanoparticles. *Chem. Commun.* **2016**, *52*, 13959–13962. [CrossRef]
39. Liu, D.; García-López, V.; Gunasekera, R.S.; Greer Nilewski, L.; Alemany, L.B.; Aliyan, A.; Jin, T.; Wang, G.; Tour, J.M.; Pal, R. Near-infrared light activates molecular nanomachines to drill into and kill cells. *ACS Nano* **2019**, *13*, 6813–6823. [CrossRef]
40. Cong, H.P.; Qiu, J.H.; Yu, S.H. Thermoresponsive poly (N-isopropylacrylamide)/graphene/Au nanocomposite hydrogel for water treatment by a laser-assisted approach. *Small* **2015**, *11*, 1165–1170. [CrossRef]
41. Li, B.; Smilgies, D.-M.; Price, A.D.; Huber, D.L.; Clem, P.G.; Fan, H. Poly (N-isopropylacrylamide) surfactant-functionalized responsive silver nanoparticles and superlattices. *ACS Nano* **2014**, *8*, 4799–4804. [CrossRef]
42. Singh, B.; Lee, J.; Kim, H.-G.; Park, M.-H.; Kim, K. Colorimetric detection of copper ions using porphyrin-conjugated silica nanoparticles. *Toxicol. Environ. Health Sci.* **2020**, *12*, 381–389. [CrossRef]
43. Chahinez, T.; Rachid, R.; Salim, G.; Lamia, B.; Ghazala, Z.; Nadjiba, T.; Aya, S.; Sara, H.; Hajer, C.; Samira, B. Toxicity of Fe<sub>3</sub>O<sub>4</sub> nanoparticles on oxidative stress status, stromal enzymes and mitochondrial respiration and swelling of *Oryctolagus cuniculus* brain cortex. *Toxicol. Environ. Health Sci.* **2016**, *8*, 349–355. [CrossRef]
44. Jang, B.; Park, J.-Y.; Tung, C.-H.; Kim, I.-H.; Choi, Y. Gold nanorod–photosensitizer complex for near-infrared fluorescence imaging and photodynamic/photothermal therapy in vivo. *ACS Nano* **2011**, *5*, 1086–1094. [CrossRef] [PubMed]

45. Tabish, T.A.; Dey, P.; Mosca, S.; Salimi, M.; Palombo, F.; Matousek, P.; Stone, N. Smart gold nanostructures for light mediated cancer theranostics: Combining optical diagnostics with photothermal therapy. *Adv. Sci.* **2020**, *7*, 1903441. [CrossRef]
46. Zhang, Z.; Wang, L.; Wang, J.; Jiang, X.; Li, X.; Hu, Z.; Ji, Y.; Wu, X.; Chen, C. Mesoporous silica-coated gold nanorods as a light-mediated multifunctional theranostic platform for cancer treatment. *Adv. Mater.* **2012**, *24*, 1418–1423. [CrossRef] [PubMed]
47. Yang, S.; Palanikumar, L.; Jeong, S.; Kim, K.; Lee, J.; Jeoung, E.; Kim, C.; Ryu, J.H.; Park, M.H. Synergistic Effect of Photothermal Therapy and Chemotherapy Using Camptothecin-Conjugated Gold Nanorods. *Part. Part. Syst. Charact.* **2018**, *35*, 1700307. [CrossRef]
48. Shukla, N.; Singh, B.; Kim, H.J.; Park, M.H.; Kim, K. Combinational Chemotherapy and Photothermal Therapy Using a Gold Nanorod Platform for Cancer Treatment. *Part. Part. Syst. Charact.* **2020**, *37*, 2000099. [CrossRef]
49. Wei, Z.; Zhao, W.; Wang, Y.; Wang, X.; Long, S.; Yang, J. Novel PNIPAm-based electrospun nanofibres used directly as a drug carrier for “on-off” switchable drug release. *Colloids Surf. B* **2019**, *182*, 110347. [CrossRef]
50. Hribar, K.C.; Lee, M.H.; Lee, D.; Burdick, J.A. Enhanced release of small molecules from near-infrared light responsive polymer–nanorod composites. *ACS Nano* **2011**, *5*, 2948–2956. [CrossRef]
51. Kim, Y.-J.; Ebara, M.; Aoyagi, T. Temperature-responsive electrospun nanofibers for ‘on-off’ switchable release of dextran. *Sci. Technol. Adv. Mater.* **2012**, *13*, 064203. [CrossRef]
52. Deng, L.; Chen, J.; Zhang, Z.; Zeng, W. Thermo-responsive PNIPAm-based composite nanofibers prepared by electrospinning. *Int. J. Electrochem. Sci.* **2018**, *13*, 7347–7355. [CrossRef]
53. Durr, N.J.; Larson, T.; Smith, D.K.; Korgel, B.A.; Sokolov, K.; Ben-Yakar, A. Two-photon luminescence imaging of cancer cells using molecularly targeted gold nanorods. *Nano Lett.* **2007**, *7*, 941–945. [CrossRef] [PubMed]
54. Wang, J.; Sutti, A.; Wang, X.; Lin, T. Fast responsive and morphologically robust thermo-responsive hydrogel nanofibres from poly (N-isopropylacrylamide) and POSS crosslinker. *Soft Matter.* **2011**, *7*, 4364–4369. [CrossRef]
55. Fomina, N.; McFearin, C.L.; Sermsakdi, M.; Morachis, J.M.; Almutairi, A. Low power, biologically benign NIR light triggers polymer disassembly. *Macromolecules* **2011**, *44*, 8590–8597. [CrossRef] [PubMed]
56. Kawano, T.; Niidome, Y.; Mori, T.; Katayama, Y.; Niidome, T. PNIPAM gel-coated gold nanorods for targeted delivery responding to a near-infrared laser. *Bioconjugate Chem.* **2009**, *20*, 209–212. [CrossRef]
57. Reneker, D.H.; Yarin, A.L.; Fong, H.; Koombhongse, S. Bending instability of electrically charged liquid jets of polymer solutions in electrospinning. *J. Appl. Phys.* **2000**, *87*, 4531–4547. [CrossRef]
58. Shin, Y.; Hohman, M.; Brenner, M.P.; Rutledge, G. Electrospinning: A whipping fluid jet generates submicron polymer fibers. *Appl. Phys. Lett.* **2001**, *78*, 1149–1151. [CrossRef]
59. Saravanan, R.K.; Naqvi, T.K.; Patil, S.; Dwivedi, P.K.; Verma, S. Purine-blended nanofiber woven flexible nanomats for SERS-based analyte detection. *Chem. Commun.* **2020**, *56*, 5795–5798. [CrossRef]
60. Hohman, M.M.; Shin, M.; Rutledge, G.; Brenner, M.P. Electrospinning and electrically forced jets. I. Stability theory. *Phys. Fluids* **2001**, *13*, 2201–2220. [CrossRef]
61. Hohman, M.M.; Shin, M.; Rutledge, G.; Brenner, M.P. Electrospinning and electrically forced jets. II. Applications. *Phys. Fluids* **2001**, *13*, 2221–2236. [CrossRef]
62. Kenawy, E.-R.; Bowlin, G.L.; Mansfield, K.; Layman, J.; Simpson, D.G.; Sanders, E.H.; Wnek, G.E. Release of tetracycline hydrochloride from electrospun poly (ethylene-co-vinylacetate), poly (lactic acid), and a blend. *J. Control. Release* **2002**, *81*, 57–64. [CrossRef]
63. Ra, E.J.; Kim, T.H.; Yu, W.J.; An, K.H.; Lee, Y.H. Ultramicropore formation in PAN/camphor-based carbon nanofiber paper. *Chem. Commun.* **2010**, *46*, 1320–1322. [CrossRef] [PubMed]
64. Chew, S.; Wen, Y.; Dzenis, Y.; Leong, K.W. The role of electrospinning in the emerging field of nanomedicine. *Curr. Pharm. Design* **2006**, *12*, 4751–4770. [CrossRef] [PubMed]
65. Sekhon, S.S.; Ahn, G.; Park, G.-Y.; Park, D.-Y.; Lee, S.-H.; Ahn, J.-Y.; Kim, Y.-H. The Role of aptamer loaded exosome complexes in the neurodegenerative diseases. *Toxicol. Environ. Health Sci.* **2019**, *11*, 85–93. [CrossRef]
66. Pan, J.; Hu, P.; Guo, Y.; Hao, J.; Ni, D.; Xu, Y.; Bao, Q.; Yao, H.; Wei, C.; Wu, Q. Combined magnetic hyperthermia and immune therapy for primary and metastatic tumor treatments. *ACS Nano* **2020**, *14*, 1033–1044. [CrossRef]
67. Niiyama, E.; Uto, K.; Lee, C.M.; Sakura, K.; Ebara, M. Hyperthermia nanofiber platform synergized by sustained release of paclitaxel to improve antitumor efficiency. *Adv. Healthc. Mater.* **2019**, *8*, 1900102. [CrossRef]
68. Liu, D.; Yang, F.; Xiong, F.; Gu, N. The smart drug delivery system and its clinical potential. *Theranostics* **2016**, *6*, 1306. [CrossRef]
69. Nakielski, P.; Pawłowska, S.; Rinoldi, C.; Ziai, Y.; De Sio, L.; Urbanek, O.; Zembrzycki, K.; Pruchniewski, M.; Lanzi, M.; Salatelli, E. Multifunctional platform based on electrospun nanofibers and plasmonic hydrogel: A smart nanostructured pillow for near-infrared light-driven biomedical applications. *ACS Appl. Mater. Interfaces* **2020**, *12*, 54328–54342. [CrossRef]
70. Morandi, E.; Severini, C.; Quercioli, D.; D’Ario, G.; Perdichizzi, S.; Capri, M.; Farruggia, G.; Mascolo, M.G.; Horn, W.; Vaccari, M. Gene expression time-series analysis of camptothecin effects in U87-MG and DBTRG-05 glioblastoma cell lines. *Mol. Cancer* **2008**, *7*, 1–16. [CrossRef]
71. Cha, G.D.; Kang, T.; Baik, S.; Kim, D.; Choi, S.H.; Hyeon, T.; Kim, D.-H. Advances in drug delivery technology for the treatment of glioblastoma multiforme. *J. Control. Release* **2020**, *328*, 350–367. [CrossRef]
72. Han, D.; Serra, R.; Gorelick, N.; Fatima, U.; Eberhart, C.G.; Brem, H.; Tyler, B.; Steckl, A.J. Multi-layered core-sheath fiber membranes for controlled drug release in the local treatment of brain tumor. *Sci. Rep.* **2019**, *9*, 1–12. [CrossRef]









73. Ghanbari-Movahed, M.; Kaceli, T.; Mondal, A.; Farzaei, M.H.; Bishayee, A. Recent advances in improved anticancer efficacies of camptothecin nano-formulations: A systematic review. *Biomedicines* **2021**, *9*, 480. [CrossRef] [PubMed]
74. Jeong, S.; Park, H.; Seon, D.; Choi, J.; Hong, K.B.; Lee, J.; Kim, C.; Kim, J.K.; Park, M.H. Modulatory functionalization of gold nanorods using supramolecular assemblies. *Chem. Asian J.* **2017**, *12*, 2591–2596. [CrossRef]
75. Ko, S.W.; Lee, J.Y.; Lee, J.; Son, B.C.; Jang, S.R.; Aguilar, L.E.; Oh, Y.M.; Park, C.H.; Kim, C.S. Analysis of drug release behavior utilizing the swelling characteristics of cellulosic nanofibers. *Polymers* **2019**, *11*, 1376. [CrossRef] [PubMed]
76. Krause, J.; Thommes, M.; Breitzkreutz, J. Immediate release pellets with lipid binders obtained by solvent-free cold extrusion. *Eur. J. Pharm. Biopharm.* **2009**, *71*, 138–144. [CrossRef] [PubMed]
77. Inagaki, F.F.; Furusawa, A.; Choyke, P.L.; Kobayashi, H. Enhanced nanodrug delivery in tumors after near-infrared photodynamic therapy. *Nanophotonics* **2019**, *8*, 1673–1688. [CrossRef]
78. Bálint, S.; Rao, S.; Sánchez, M.M.; Huntošová, V.; Miškovský, P.; Petrov, D. Diffusion and cellular uptake of drugs in live cells studied with surface-enhanced Raman scattering probes. *J. Biomed. Opt.* **2010**, *15*, 027005.
79. Kalamida, D.; Karagounis, I.V.; Mitrakas, A.; Kalamida, S.; Giatromanolaki, A.; Koukourakis, M.I. Fever-range hyperthermia vs. hypothermia effect on cancer cell viability, proliferation and HSP90 expression. *PLoS ONE* **2015**, *10*, e0116021. [CrossRef] [PubMed]
80. Hanini, A.; Lartigue, L.; Gavard, J.; Schmitt, A.; Kacem, K.; Wilhelm, C.; Gazeau, F.; Chau, F.; Ammar, S. Thermosensitivity profile of malignant glioma U87-MG cells and human endothelial cells following  $\gamma$ -Fe<sub>2</sub>O<sub>3</sub> NPs internalization and magnetic field application. *RSC Adv.* **2016**, *6*, 15415–15423. [CrossRef]





## Article

# Anti-Cancer Nanopowders and MAPLE-Fabricated Thin Films Based on SPIONs Surface Modified with Paclitaxel Loaded $\beta$ -Cyclodextrin

Rebecca Alexandra Puiu <sup>1</sup>, Paul Cătălin Balaure <sup>2,\*</sup>, Ema Constantinescu <sup>1</sup>, Alexandru Mihai Grumezescu <sup>1,3,4</sup>, Ecaterina Andronescu <sup>1</sup>, Ovidiu-Cristian Oprea <sup>5</sup>, Bogdan Stefan Vasile <sup>1</sup>, Valentina Grumezescu <sup>6</sup>, Irina Negut <sup>6</sup>, Ionela Cristina Nica <sup>3,7</sup> and Miruna Silvia Stan <sup>3,7</sup>

- <sup>1</sup> Department of Science and Engineering of Oxide Materials and Nanomaterials, Faculty of Applied Chemistry and Materials Science, Politehnica University of Bucharest, 011061 Bucharest, Romania; rebecca\_alexandra92@yahoo.com (R.A.P.); constantinescu.ema94@gmail.com (E.C.); a.grumezescu@upb.ro (A.M.G.); ecaterina.andronescu@upb.ro (E.A.); bogdan.vasile@upb.ro (B.S.V.)
  - <sup>2</sup> “Costin Nenitzescu” Department of Organic Chemistry, Faculty of Applied Chemistry and Materials Science, Politehnica University of Bucharest, 011061 Bucharest, Romania
  - <sup>3</sup> Research Institute of the University of Bucharest—ICUB, University of Bucharest, 050657 Bucharest, Romania; cristina.nica@drcd.unibuc.ro (I.C.N.); miruna.stan@bio.unibuc.ro (M.S.S.)
  - <sup>4</sup> Academy of Romanian Scientists, Ilfov No. 3, 50044 Bucharest, Romania
  - <sup>5</sup> Department of Inorganic Chemistry, Physical Chemistry and Electrochemistry, Politehnica University of Bucharest, 011061 Bucharest, Romania; ovidiu.oprea@upb.ro
  - <sup>6</sup> Lasers Department, National Institute for Lasers, Plasma and Radiation Physics, 077125 Magurele, Romania; valentina.grumezescu@infpr.ro (V.G.); negut.irina@infpr.ro (I.N.)
  - <sup>7</sup> Department of Biochemistry and Molecular Biology, Faculty of Biology, University of Bucharest, 050095 Bucharest, Romania
- \* Correspondence: pbalaure@gmail.com; Tel.: +40-21-402-3997

**Citation:** Puiu, R.A.; Balaure, P.C.; Constantinescu, E.; Grumezescu, A.M.; Andronescu, E.; Oprea, O.-C.; Vasile, B.S.; Grumezescu, V.; Negut, I.; Nica, I.C.; et al. Anti-Cancer Nanopowders and MAPLE-Fabricated Thin Films Based on SPIONs Surface Modified with Paclitaxel Loaded  $\beta$ -Cyclodextrin. *Pharmaceutics* **2021**, *13*, 1356. <https://doi.org/10.3390/pharmaceutics13091356>

Academic Editor: Sanjay Garg

Received: 3 July 2021

Accepted: 26 August 2021

Published: 28 August 2021

**Publisher's Note:** MDPI stays neutral with regard to jurisdictional claims in published maps and institutional affiliations.



**Copyright:** © 2021 by the authors. Licensee MDPI, Basel, Switzerland. This article is an open access article distributed under the terms and conditions of the Creative Commons Attribution (CC BY) license (<https://creativecommons.org/licenses/by/4.0/>).

**Abstract:** Globally, cancer is the second most common cause of death, and Europe accounts for almost 25% of the global cancer burden, although its people make up only 10% of the world's population. Conventional systemically administered anti-cancer drugs come with important drawbacks such as inefficiency due to poor bioavailability and improper biodistribution, severe side effects associated with low therapeutic indices, and the development of multidrug resistance. Therefore, smart nano-engineered targeted drug-delivery systems with tailored pharmacokinetics and biodistribution which can selectively deliver anti-cancer agents directly to the tumor site are the solution to most difficulties encountered with conventional therapeutic tools. Here, we report on the synthesis, physicochemical characterization, and in vitro evaluation of biocompatibility and anti-tumor activity of novel magnetically targetable SPIONs based on magnetite ( $\text{Fe}_3\text{O}_4$ ) nanoparticles' surface modified with  $\beta$ -cyclodextrin (CD) and paclitaxel (PTX)-guest-host inclusion complexes ( $\text{Fe}_3\text{O}_4@ \beta\text{-CD}/\text{PTX}$ ). Both pristine  $\text{Fe}_3\text{O}_4@ \beta\text{-CD}$  nanopowders and PTX-loaded thin films fabricated by MAPLE technique were investigated. Pristine  $\text{Fe}_3\text{O}_4@ \beta\text{-CD}$  and  $\text{Fe}_3\text{O}_4@ \beta\text{-CD}/\text{PTX}$  thin films were physicochemically characterized by X-ray diffraction (XRD), Fourier-transform infrared spectroscopy (FT-IR), thermal analysis, scanning electron microscopy (SEM), and transmission electron microscopy (TEM). The biocompatibility of bare magnetic nanocomposite thin films was evaluated by MTT cell viability assay on a normal 3T3 osteoblast cell line culture and by measuring the level of NO in the culture medium. No significant modifications, neither in cell viability nor in NO level, could be observed, thereby demonstrating the excellent biocompatibility of the SPIONs thin films. Inverted phase-contrast microscopy showed no evident adverse effect on the morphology of normal osteoblasts. On the other hand,  $\text{Fe}_3\text{O}_4@ \beta\text{-CD}/\text{PTX}$  films decreased the cell viability of the MG-63 osteosarcoma cell line by 85%, demonstrating excellent anti-tumor activity. The obtained results recommend these magnetic hybrid films as promising candidates for future delivery, and hyperthermia applications in cancer treatment.

**Keywords:** paclitaxel;  $\beta$ -Cyclodextrin; SPIONs

## 1. Introduction

In a recent press release [1,2], the International Agency for Research on Cancer and the World Health Organization put cancer as the second leading cause of death globally, with an estimated 9.6 million deaths in 2018, while the global cancer burden has risen 18.1 million new cases. Most of the new cases (23.4%) and deaths (20.3%) by cancer were registered in Europe. There is a strong need for more efficient, innovative therapeutic tools to optimize clinical outcomes, increase patient compliance, and improve patient quality of life in the context of this crisis.

Most conventional medicines currently used in cancer treatment suffer some major drawbacks such as poor bioavailability associated with low water solubility, improper biodistribution, and lack of controlled, selective delivery to targeted disease areas resulting in a low therapeutic index, severe adverse effects, the development of multidrug resistance (MDR), and even treatment failure. Pharmaceutical nanotechnology provides powerful tools for circumventing these drawbacks by increasing drug bioavailability, prolonging drug circulation time, decreasing the clearance rate, and increasing drug stability in physiological media. Nanocarriers' surfaces can be modified with targeting ligands which are guided by specific ligand–receptor interactions, allowing precise spatial control of nanocarrier localization within the body [3]. Moreover, smart nano-transporters can be engineered to trigger drug release in response to small microenvironmental changes in local pH, temperature, redox potential, and enzyme activity, as well as to remote, externally applied stimuli such as electric fields, laser pulses, ultrasounds, and magnetic fields [3–5]. Furthermore, nanovehicles can overcome MDR mechanisms, including decreased uptake and increased efflux of tumor cell drugs [6].

Among the various types of nanocarriers (organic polymers, inorganic polymers, lipids, metals, metal oxides), superparamagnetic iron oxide nanoparticles (SPIONs) have attracted increasing attention in recent years due to the benefits of site-specific magnetic guidance and drug release [7]. SPIONs display a number of remarkable characteristics such as biocompatibility [8] and sensitivity to an applied magnetic field [9] which makes them ideal candidates for theragnostic applications, meaning that they can be simultaneously used for imaging, targeting, and drug delivery [10–13]. Appropriately functionalized SPIONs have received FDA approval for clinical application as contrast agents in magnetic resonance imaging [14]. SPIONs can be passively targeted to tumoral zones due to their enhanced permeability and retention effect. After local accumulation, magnetic hyperthermia consisting of sudden temperature increase in the targeted diseased area exposed to an alternating magnetic field can induce the death of tumoral cells [15]. However, simple magnetite ( $\text{Fe}_3\text{O}_4$ ) nanoparticles are unstable in polar (aqueous) physiological fluids since they tend to reduce surface energy. They are intrinsically prone to aggregation through van der Waal's and magnetic dipole–dipole interactions [16–18]. Therefore, SPIONs surfaces should be modified to prevent agglomeration by covering them with a stabilizing shell of appropriate, biocompatible materials.

$\beta$ -Cyclodextrin ( $\beta$ -CD) is a macrocyclic oligosaccharide formed of seven D-glucopyranose units linked to each other by  $\alpha$ -1,4 glycosidic bonds [19]. It has the shape of a hollow truncated cone with a hydrophilic outer surface and a hydrophobic inner cavity. The hydrophobic interior of the cavity is lined with C-H groups with glycosidic oxygen in between, while the hydrophilic exterior is made up of the hydroxyl groups of the glucopyranose rings. All secondary hydroxyl groups are situated on the wider rim of the hollow truncated cone, whereas all primary hydroxyl groups are situated on the narrower rim. Due to these peculiar structural and shape features,  $\beta$ -CD molecules have the unique ability to entrap hydrophobic compounds in their internal cavity and solubilize them in an aqueous environment.

The formation of host–guest inclusion complexes relies on the complementarity of the two partners involved in the steric match. That is, the inclusion guest molecule must have a size that fits, at least partially, into the host cavity and interactionally matches the developing intermolecular forces during the inclusion process. Moreover, the inclusion complex's binding energy, which crucially affects the loading and release performances,

can be predicted by molecular docking studies [20,21]. Furthermore, cyclodextrins possess excellent biocompatibility, being largely studied as water-dispersible nanocarriers for the delivery of hydrophobic compounds and drugs like curcumin [22], paclitaxel [23], irinotecan [24], and ibuprofen [25]. An interesting study [26] uses the molecular docking and release of the guest molecule to construct pH-responsive CD-capped mesoporous silica nanoparticles.

All the above properties of  $\beta$ -CD make it an excellent surface modifier for SPIONs. It allows magnetite nanoparticles to become water-dispersible magnetically targetable nanovehicles suitable for hydrophobic anti-cancer drug delivery, magnetic hyperthermia, and theragnostic applications [9,10,27–31]. Some studies report that guest molecular docking also induces the self-assembly of SPIONs [22,23,32].

Here, we report the synthesis, characterization, biocompatibility, and in vitro anti-cancer outcome of magnetic nanocomposite vehicles based on PTX/ $\beta$ -CD inclusion complexes physically adsorbed onto  $\text{Fe}_3\text{O}_4$  nanoparticles. We studied both nanopowder composites and thin films deposited by matrix-assisted pulsed laser evaporation (MAPLE) technique [33].

## 2. Materials and Methods

### 2.1. Materials

All chemicals used for the synthesis of the nanostructured materials were purchased from Sigma-Aldrich (Merck Group, Darmstadt, Germany), namely anhydrous ferric chloride ( $\text{FeCl}_3$ , >99.99% trace metal basis), ferrous sulfate heptahydrate ( $\text{FeSO}_4 \cdot 7\text{H}_2\text{O}$ , >98%), ammonium hydroxide solution (25%  $\text{NH}_3$  in  $\text{H}_2\text{O}$ ),  $\beta$ -cyclodextrin, paclitaxel, dimethyl sulfoxide (DMSO), chloroform ( $\text{CHCl}_3$ ), analytical graded acetone ( $\text{C}_6\text{H}_6\text{O}$ ), and ethanol ( $\text{C}_2\text{H}_6\text{O}$ ).

### 2.2. Chemical Synthesis of $\beta$ -Cyclodextrin-Covered $\text{Fe}_3\text{O}_4$ Nanoparticles

$\text{Fe}_3\text{O}_4$ - $\beta$ -cyclodextrin nanoparticles ( $\text{Fe}_3\text{O}_4@ \beta\text{-CD}$ ) were prepared by the co-precipitation method, which involves base-induced simultaneous precipitation of ferrous ( $\text{Fe}^{2+}$ ) and ferric ( $\text{Fe}^{3+}$ ) ions in an aqueous solution [34]. In brief, solution 1 (Sn1) was prepared by dissolving ferrous sulfate and ferric chloride (molar ratio 1:2) in 300 mL demineralized water. Solution 2 (Sn2) consisted of 1 g  $\beta$ -CD and 9 mL ammonium hydroxide in 300 mL demineralized water. Next, Sn 1 was added dropwise into Sn2 using a pressure-equalizing dropping funnel under magnetic stirring. The precipitated magnetite nanoparticles were magnetically collected. After decantation of the liquid phase, the resultant powder was thoroughly washed three times with demineralized water and left to air dry at room temperature. The nanopowders were fully characterized by X-ray powder diffraction (XRD), scanning electron microscopy (SEM), transmission electron microscopy (TEM), Fourier transform infrared spectroscopy (FT-IR), and thermal analysis (simultaneous thermogravimetric analysis (TGA) and dynamic scanning calorimetry (DSC)).

### 2.3. Preparation of Paclitaxel Inclusion Complex

PTX- $\beta$ -CD inclusion complexes were prepared by the solvent evaporation method. To this end, 100 mg  $\text{Fe}_3\text{O}_4@ \beta\text{-CD}$  nanoparticles were redispersed in a solution of PTX (10 mg, selected based on previous research results reported by [35]) in chloroform (1 mL) was added and mixed in a grinding mortar until complete evaporation of chloroform. This was subsequently stored at 5 °C for further use.

### 2.4. Target Preparation and Deposition of $\text{Fe}_3\text{O}_4@$ Paclitaxel-Loaded $\beta$ -CD

Compared to solvent-based methods used to prepare thin films such as spin-coating, dip-coating, and drop-casting, MAPLE technique has the advantage of homogeneity on the deposited area and the possibility of tailoring the final thickness, which is of crucial importance for the efficacy and mechanical resistance of bioactive coatings [36].

We deposited Fe<sub>3</sub>O<sub>4</sub>@PTX-loaded β-CD thin films on glass and Si substrates which previously have been successively cleaned with acetone, ethanol, and deionized water in an ultrasonic bath for 15 min. The substrates were dried under a high purity nitrogen stream. The MAPLE targets consisted of a 2% suspension of Fe<sub>3</sub>O<sub>4</sub>@β-CD/PTX inclusion complex nanocomposites in DMSO which was poured into a pre-cooled target holder at 173 K and subsequently immersed in liquid nitrogen for 30 min. The MAPLE depositions were performed using a KrF\* excimer ( $\lambda = 248$  nm and  $\tau_{FWHM} = 25$  ns) COMPexPro 205 model, Lambda Physics-Coherent (Göttingen, Germany), that was operated at a repetition rate of 15 Hz. Three different fluences of the laser beam, i.e., 300, 400, and 500 mJ/cm<sup>2</sup>, respectively, were investigated. A number of laser pulses ranging between 22,000 and 75,000 were applied to each target. During MAPLE processing, the laser spot area was 30 mm<sup>2</sup> and the target holder was rotated with a frequency of 0.4 Hz. During the deposition process, the experimental parameters (i.e., substrate temperature, background pressure, and target to substrate distance) were maintained constant (room temperature, 1 Pa, 4 cm, respectively).

### 2.5. Physicochemical Characterization

The crystallinity of Fe<sub>3</sub>O<sub>4</sub>@β-CD nanopowders was investigated by XRD analysis carried out on a Shimadzu XRD 6000 diffractometer. X-ray diffraction patterns were recorded at room temperature using CuK $\alpha$  radiation ( $\lambda = 1.54056\text{\AA}$  at 15 mA and 30 kV) with the Bragg diffraction angle  $2\theta$  ranging between 10 and 80°.

The inner structure and morphology of the nanocomposites were investigated by TEM. The nanopowder TEM specimens were prepared by dispersal in ethanol and ultrasonic cleansing for 15 min. Next, the sample was placed on a carbon-coated copper grid and left to dry at room temperature. TEM images were obtained using a TecnaiTM G2 F30 S-TWIN electron microscope equipped with selected area electron diffraction (SAED) purchased from the FEI (Hillsboro, OR, USA) company. The microscope was operated in transmission mode at 300 kV. The guaranteed TEM point resolution and TEM line resolution were 2 Å and 1.02 Å, respectively.

The shape and size nano-details of the surface of the Fe<sub>3</sub>O<sub>4</sub>@β-CD composites were evaluated by SEM analyses performed on an FEI electron microscope, using secondary electron beams with energies of 30 keV.

To confirm the structural integrity of the thin films of bare and PTX-loaded β-CD surface-modified Fe<sub>3</sub>O<sub>4</sub> nanoparticles deposited by MAPLE technique at various fluences, we monitored the surface distribution of the chemical functional groups for CD and PTX by FT-IR chemical maps. IR mapping (IRM) was performed on a Nicolet iN10 MX FT-IR microscope with an MCT liquid nitrogen cooled detector in the 4000–1000 cm<sup>-1</sup> range. The spectral collection was made in reflection mode at 4 cm<sup>-1</sup> resolution. A total of 32 scans were co-added and converted to absorbance for each spectrum using OmnicPicta software (Thermo Scientific, Waltham, MA, USA). About 250 spectra were analyzed for each sample. The absorption peaks of C-H and C-O-C functional groups in CD and C=O carbonyl groups in PTX were chosen as specific spectral markers.

The thermal analyses were assessed with a Shimadzu DTG-TA-50H equipment (Carlsbad, CA, USA) from room temperature to 800 °C at a heating rate of 10 K min<sup>-1</sup>, under a flow of 20 mL min<sup>-1</sup> dried synthetic air (80% N<sub>2</sub> and 20% O<sub>2</sub>).

### 2.6. Biological Evaluation

The biocompatibility of Fe<sub>3</sub>O<sub>4</sub>@β-CD nanoparticle thin films on glass slides was evaluated in the presence of MC3T3-E1 murine osteoblast cultures. The anti-tumor efficiency of Fe<sub>3</sub>O<sub>4</sub>@PTX-loaded β-CD thin films on glass substrates was tested on MG-63 osteosarcoma cells. Both types of cell lines were cultured in Dulbecco's Modified Eagle Medium (DMEM) supplemented with 10% fetal bovine serum and antibiotic mixture at 37 °C in a humidified atmosphere with 5% CO<sub>2</sub>. All specimens, including the uncoated substrates (control), were sterilized by UV exposure for one hour before cell seeding.

The percentage of viable cells was measured with an MTT test, which involves the enzymatic reduction of the tetrazolium salt to insoluble formazan inside the metabolically active cells. The cells were seeded on top of uncoated and coated substrates at a cellular density of  $4 \times 10^4 \times \text{cells}/\text{cm}^2$ . Images on an inverted phase-contrast microscope (Olympus IX71, Tokyo, Japan) were taken after 24 h of incubation. Subsequently, the culture medium was removed and replaced with MTT solution (1 mg/mL concentration), followed by 2 h of standard incubation in dark conditions. The water-insoluble formazan crystals were dissolved with isopropanol. The absorbance (directly related to the number of metabolically active cells) was measured at 595 nm using a FlexStation 3 multi-mode microplate reader from Molecular Devices (San Jose, CA, USA).

The concentration of nitric oxide (NO) in the collected culture medium after 24 h of incubation was performed with Griess reagent, which is a stoichiometric solution (*v/v*) of 0.1% naphthylethylenediamine dihydrochloride and 1% sulphanilamide in 5%  $\text{H}_3\text{PO}_4$ . Increased NO levels are related to cytotoxic effects as this molecule is connected with inflammation and apoptosis processes. The absorbance of the mix was measured at 550 nm using the FlexStation 3 multi-mode GENios microplate reader, and the NO concentration was calculated from the standard  $\text{NaNO}_2$  curve.

Biological test results were analyzed using Student's *t*-test on Excel (Microsoft Office 2018). Statistically significant data were considered as having *p*-value of less than 0.05.

### 2.7. Preparation of Simulated Body Fluid and Procedure of Apatite-Forming Abilities

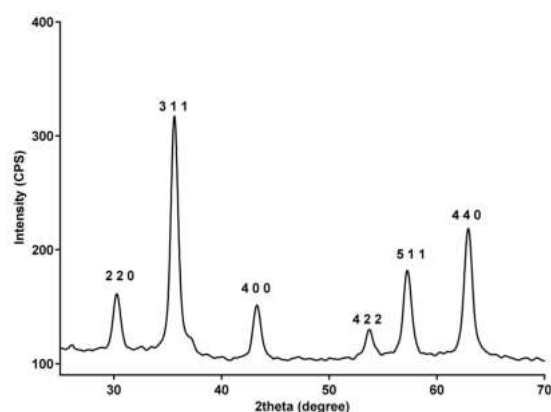
Simulated body fluid (SBF) was prepared according to the instructions presented by Kokubo et al. [37].

The thin films were immersed in SBF using 6-well plates. The 6-well plates were placed for 14 days in an unstirred thermostatic water bath at 37 °C. The experiment was done in triplicate. After 14 days, the samples were dried at room temperature and characterized using a Versa 3D DualBeam (FIB/SEM) scanning electron microscope.

## 3. Results

### 3.1. Physicochemical Characterization of $\text{Fe}_3\text{O}_4@ \beta\text{-CD}$ Nanopowders

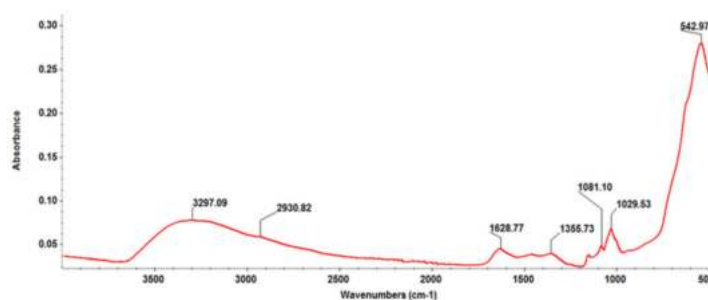
The XRD patterns of  $\text{Fe}_3\text{O}_4@ \beta\text{-CD}$  nanopowders are plotted in Figure 1. Sharp diffraction peaks appearing at  $2\theta = 30.31, 35.71, 43.31, 53.90, 57.61,$  and  $62.81$  were assigned to the (2 2 0), (3 1 1), (4 0 0), (4 2 2), (5 1 1), and (440) planes of the magnetite lattice, respectively, being in good agreement with the literature [38]. No other diffraction peaks corresponding to another iron oxide, such as  $\alpha\text{-Fe}_2\text{O}_3$  or  $\gamma\text{-Fe}_2\text{O}_3$ , could be observed.



**Figure 1.** XRD patterns of fabricated  $\text{Fe}_3\text{O}_4@ \beta\text{-CD}$  nanopowders.

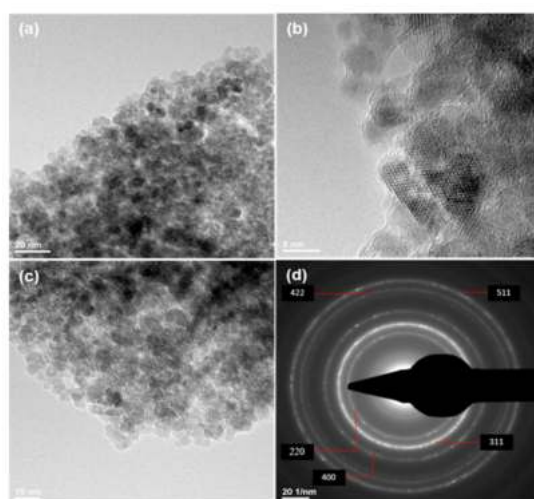
The main absorptions present in the FT-IR spectrum of  $\text{Fe}_3\text{O}_4@ \beta\text{-CD}$  nanocomposites (Figure 2) were as follows:  $3297 \text{ cm}^{-1}$  stretching vibrations of cyclodextrin OH groups,  $2930 \text{ cm}^{-1}$  anisomerous stretching vibrations of aliphatic C-H and  $\text{CH}_2$  bonds in  $\beta\text{-CD}$ ,  $1081 \text{ cm}^{-1}$  and  $1029 \text{ cm}^{-1}$  stretching vibrations of C-C, C-O-C bonds, and the wagging

vibration of the O-H bonds directly at the sugar ring, while the intense peak at  $543\text{ cm}^{-1}$  corresponds to the Fe-O stretching mode of the tetrahedral and octahedral sites [39–42].



**Figure 2.** FT-IR spectrum of  $\text{Fe}_3\text{O}_4@β\text{-CD}$  nanopowders.

The TEM images of the  $\text{Fe}_3\text{O}_4@β\text{-CD}$  nanopowders are plotted in Figure 3. At higher magnifications, one can distinguish a nanocrystalline magnetite phase without agglomeration and a low-ordered non-crystalline shell that can be attributed to the  $β\text{-CD}$  coating (Figure 3b). The recorded SAED ring pattern plotted in Figure 3d corresponds to the (220), (311), (400), (422), and (511) magnetite lattice planes being in perfect agreement with the high polycrystallinity of the magnetite phase and confirming once again the absence of any other crystalline phase.



**Figure 3.** TEM (a–c) micrographs and SAED pattern (d) of  $\text{Fe}_3\text{O}_4@β\text{-CD}$  nanopowders.

The simultaneous enthalpy and mass changes vs. temperature curves (DSC-TGA curves) for simple  $\text{Fe}_3\text{O}_4$  and  $β\text{-CD}$ -surface-modified magnetite are plotted in Figure 4. Figure 4 shows that the first mass loss of 1.74% occurs between room temperature and  $120^\circ\text{C}$ . It was attributed to the dehydration of  $\text{Fe}_3\text{O}_4$  and loss of the hydroxyl groups on the surface of  $\text{Fe}_3\text{O}_4$  nanoparticles in a slightly endothermic process. Next, two successive mass losses of 0.54% and 0.98% occur in the temperature ranges  $120\text{--}200^\circ\text{C}$  and  $200\text{--}300^\circ\text{C}$ , respectively, corresponding to the exothermic peaks at  $162.7^\circ\text{C}$  and  $246.8^\circ\text{C}$ . These peaks can be attributed to the thermal decomposition and oxidation of some organic matter impurities present on magnetite's surface. The strong exothermic peak observed at  $565.8^\circ\text{C}$  corresponds to a transformation of the  $\text{Fe}_3\text{O}_4$  into maghemite ( $\gamma\text{-Fe}_2\text{O}_3$ ). Unlike  $\text{Fe}_3\text{O}_4$ , the crystal lattice of  $\gamma\text{-Fe}_2\text{O}_3$  presents vacant cation sites, commonly in octahedral sites. The mass loss of the latter transformation is 1.28%. Thus, the total mass loss is 4.54%, corresponding to a residual mass of 95.45% wt. of the initial mass.  $\text{Fe}_3\text{O}_4@β\text{-CD}$  nanocomposite's DSC curve shows one endothermic peak at  $106^\circ\text{C}$  followed by three exothermic peaks at 188, 263.1, and  $520.7^\circ\text{C}$ , respectively. The sharp exothermic peak at  $188^\circ\text{C}$  is due

to the degradation of the  $\beta$ -CD organic phase deposited on the inorganic  $\text{Fe}_3\text{O}_4$  phase's surface. The conversion of magnetite to maghemite is marked by the exothermic peak at 520.7 °C. The residual mass is 84.04% wt. of the initial mass. The difference between the residual mass of pristine  $\text{Fe}_3\text{O}_4$  and the residual mass of  $\text{Fe}_3\text{O}_4@$  $\beta$ -CD nanocomposite is a rough estimate of the  $\beta$ -CD coating weight (11.51 g/100 g  $\text{Fe}_3\text{O}_4$ ).

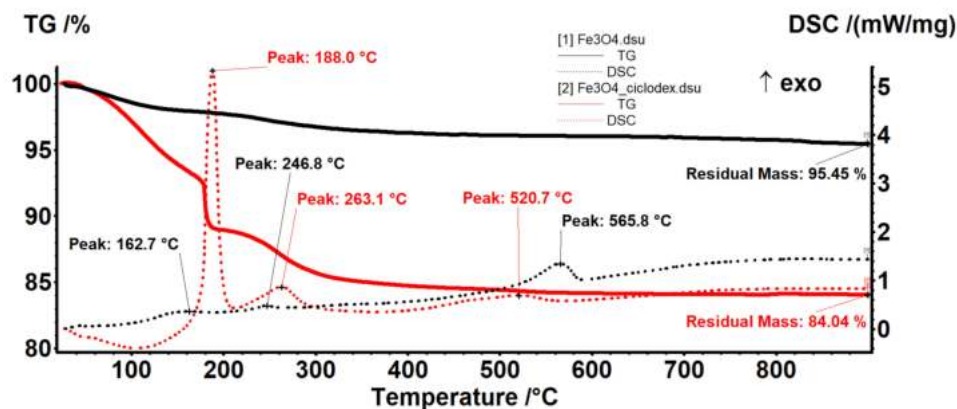


Figure 4. Thermal analysis for  $\text{Fe}_3\text{O}_4$  and  $\text{Fe}_3\text{O}_4@$  $\beta$ -CD nanopowder.

### 3.2. Physicochemical Characterization of $\text{Fe}_3\text{O}_4@$ $\beta$ -CD Thin Films

To evaluate the structural-functional groups' integrity after laser processing for the thin films deposited by the MAPLE technique, compared with drop-cast, we used the FT-IR imaging technique. Absorbance maps were created based on the minima of the second derivative of the spectral data. As specific spectral markers for  $\beta$ -CD, we used the absorptions' intensities at 2930 and 1029  $\text{cm}^{-1}$ , while for PTX, we choose as characteristic intensity the stretching ester/ketonic carbonyl vibration at 1739  $\text{cm}^{-1}$  [43,44].

Figure 5 depicts the second derivative infrared micrographs (IRM) of  $\text{Fe}_3\text{O}_4@$  $\beta$ -CD drop-cast, while Figures 6–8 plot the IRM of the same nanocomposite deposited by MAPLE technique at 300, 400, and 500  $\text{mJ}/\text{cm}^2$ , respectively. The lower intensities associated with significant chemical degradation of the monitored functional group are colored in blue, while higher intensities indicating a minimal chemical degradation are colored in red. Similar IR maps of PTX-loaded  $\text{Fe}_3\text{O}_4@$  $\beta$ -CD composites drop-cast and MAPLE-are plotted in Figures 9–12, respectively.

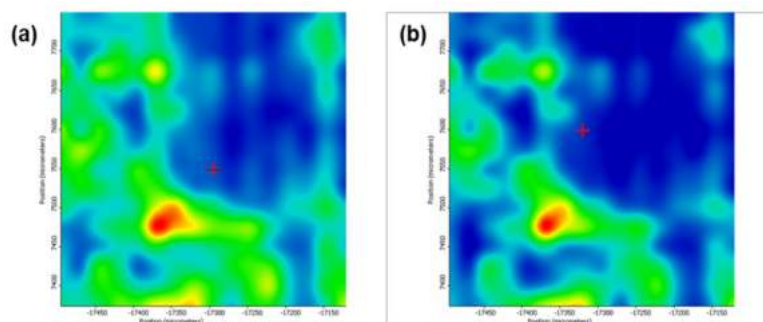
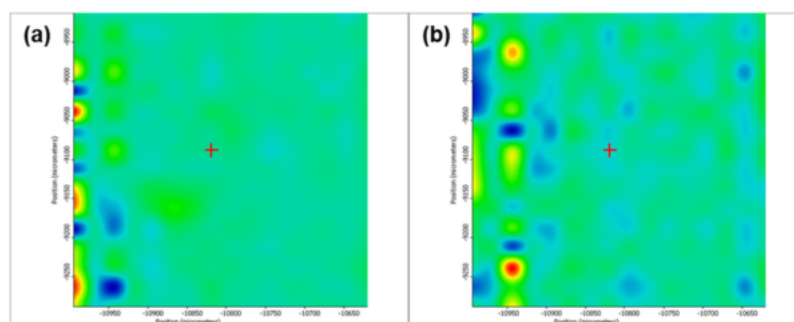
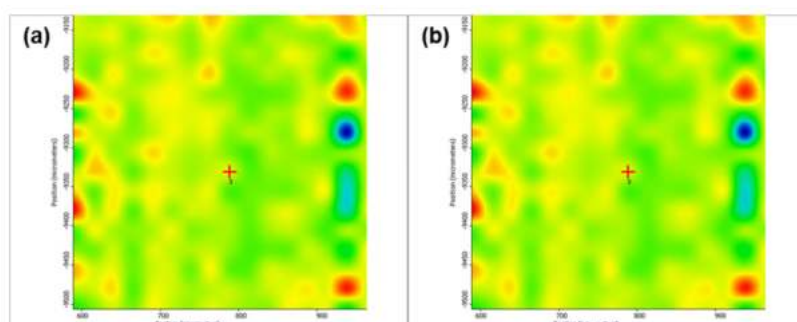


Figure 5. Second derivate IR mappings of  $\text{Fe}_3\text{O}_4@$  $\beta$ -CD drop-cast: surface intensity distribution of (a) C-H and  $\text{CH}_2$  stretching vibrations at 2930  $\text{cm}^{-1}$  and (b) C-O bond stretching vibrations at 1029  $\text{cm}^{-1}$ .

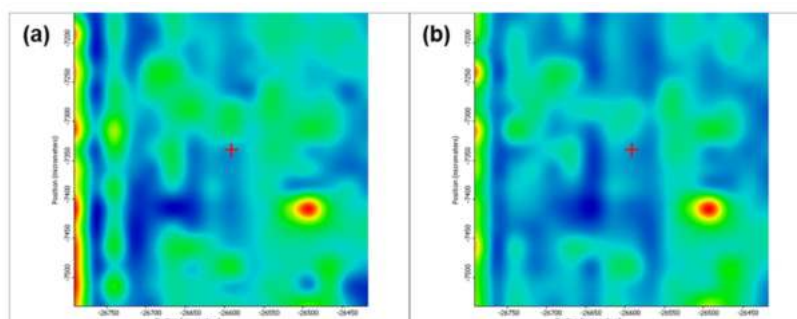




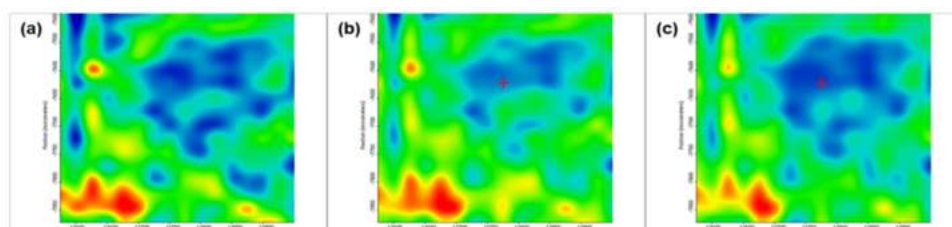
**Figure 6.** Second derivate IR mappings of  $\text{Fe}_3\text{O}_4@ \beta\text{-CD}$  thin films deposited at  $F = 300 \text{ mJ/cm}^2$ : surface intensity distribution of (a)  $2930 \text{ cm}^{-1}$  and (b)  $1029 \text{ cm}^{-1}$ .



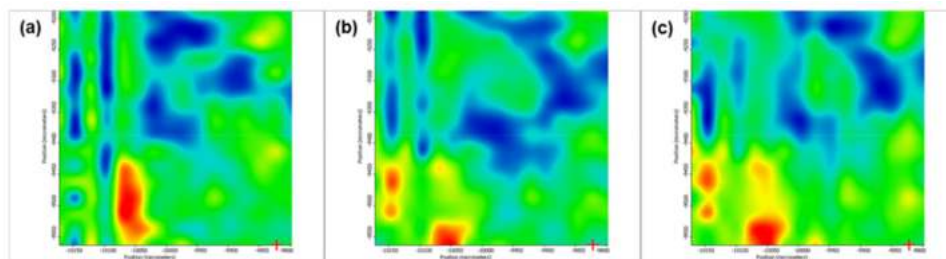
**Figure 7.** Second derivate IR mappings of  $\text{Fe}_3\text{O}_4@ \beta\text{-CD}$  thin films deposited at  $F = 400 \text{ mJ/cm}^2$ : surface intensity distribution of (a)  $2930 \text{ cm}^{-1}$  and (b)  $1029 \text{ cm}^{-1}$ .



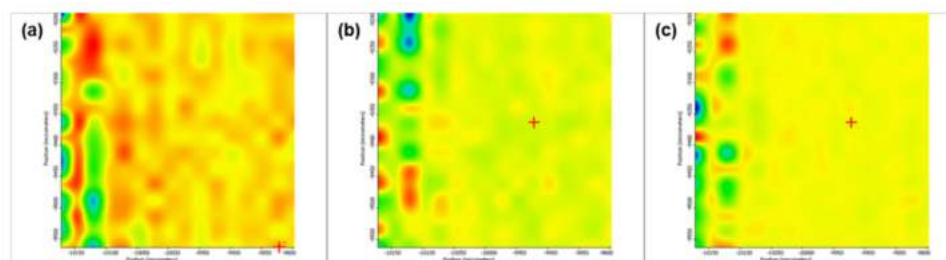
**Figure 8.** Second derivate IR mappings of  $\text{Fe}_3\text{O}_4@ \beta\text{-CD}$  thin films deposited at  $F = 500 \text{ mJ/cm}^2$ : surface intensity distribution of (a)  $2930 \text{ cm}^{-1}$  and (b)  $1029 \text{ cm}^{-1}$ .



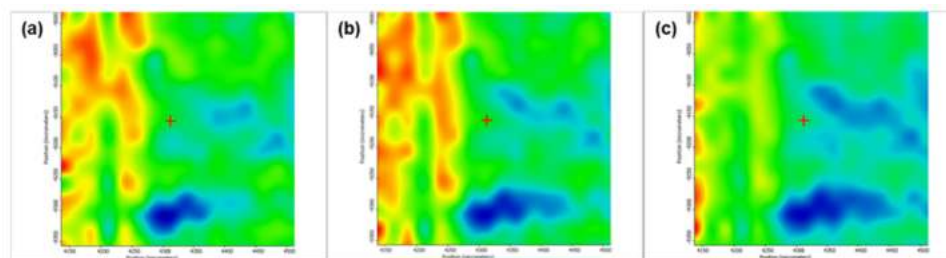
**Figure 9.** Second derivate IR mappings of  $\text{Fe}_3\text{O}_4@ \beta\text{-CD/PTX}$  drop-cast: surface intensity distribution of (a)  $2930 \text{ cm}^{-1}$ , (b)  $1029 \text{ cm}^{-1}$  and (c) ester/ketonic carbonyl vibration at  $1739 \text{ cm}^{-1}$ .



**Figure 10.** Second derivate IR mappings of Fe<sub>3</sub>O<sub>4</sub>@β-CD/PTX thin films deposited at F = 300 mJ/cm<sup>2</sup>: surface intensity distribution of (a) 2930 cm<sup>-1</sup>, (b) 1029 cm<sup>-1</sup> and (c) ester/ketonic carbonyl vibration at 1739 cm<sup>-1</sup>.

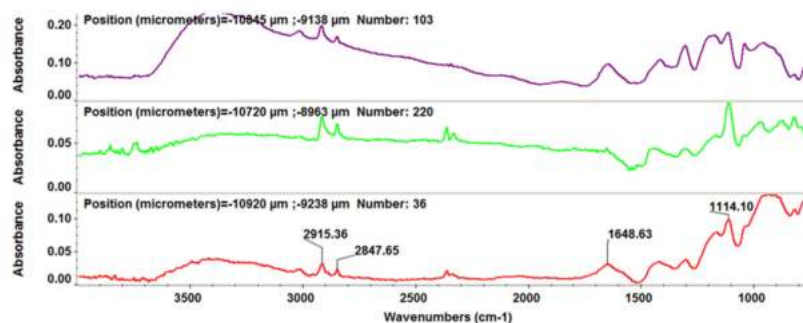


**Figure 11.** Second derivate IR mappings of Fe<sub>3</sub>O<sub>4</sub>@β-CD/PTX thin films deposited at F = 400 mJ/cm<sup>2</sup>: surface intensity distribution of (a) 2930 cm<sup>-1</sup>, (b) 1029 cm<sup>-1</sup> and (c) 1739 cm<sup>-1</sup>.

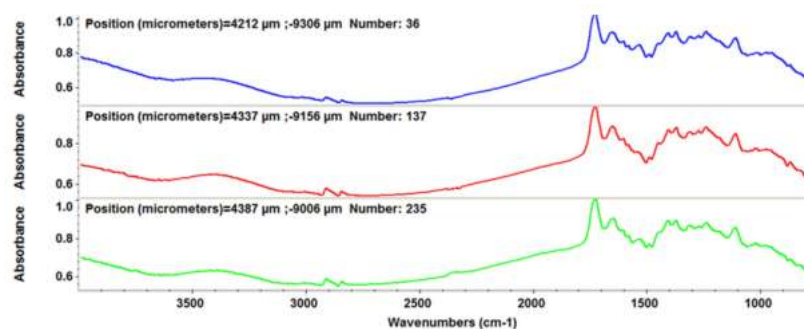


**Figure 12.** Second derivate IR mappings of Fe<sub>3</sub>O<sub>4</sub>@β-CD/PTX thin films deposited at F = 500 mJ/cm<sup>2</sup>: surface intensity distribution of (a) 2930 cm<sup>-1</sup>, (b) 1029 cm<sup>-1</sup> and (c) 1739 cm<sup>-1</sup>.

As can be seen from the comparative analysis of IRM micrographs (Figures 5–12), the best compromise between the deposition rate and the deposited material’s structural integrity was obtained for a laser beam fluence (F) of 400 mJ/cm<sup>2</sup>. IR spectra collected at different points in the surface distribution maps of spectral marker absorbance are shown for pristine (Figure 13) and Fe<sub>3</sub>O<sub>4</sub>@β-CD/PTX (Figure 14) thin films deposited at this optimal fluence value. Analysis of the FT-IR spectral data confirms the successful formation of the inclusion complex.



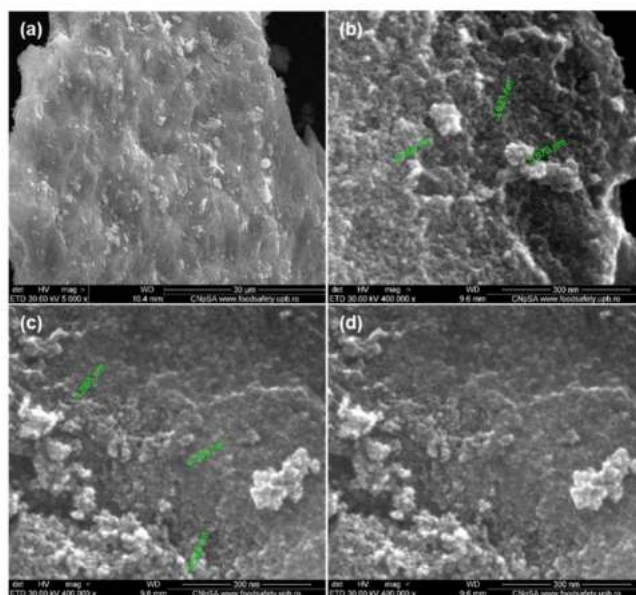
**Figure 13.** IR spectra recorded for bare Fe<sub>3</sub>O<sub>4</sub>@β-CD thin films deposited at F = 400 mJ/cm<sup>2</sup>.



**Figure 14.** IR spectra recorded for the thin films of  $\text{Fe}_3\text{O}_4@β\text{-CD}/\text{PTX}$  deposited at  $F = 400 \text{ mJ}/\text{cm}^2$ .

We analyzed these spectra comparatively, searching for differences due to PTX-specific absorptions. We focused our attention on two frequencies, namely the phenyl ring absorption band at  $1475 \text{ cm}^{-1}$  [45] and the carbonyl group absorption at  $1739 \text{ cm}^{-1}$ . The PTX band at  $1475 \text{ cm}^{-1}$  is almost completely masked in the  $\text{Fe}_3\text{O}_4@β\text{-CD}/\text{PTX}$  nanocomposites, indicating molecular docking of the phenyl ring structural moieties into the inner hydrophobic cavity of  $β\text{-CD}$ . On the other hand, as compared to bare  $β\text{-CD}$ -modified magnetite, in the IR spectrum of PTX-loaded  $\text{Fe}_3\text{O}_4@β\text{-CD}$ , there appears a sharp peak at  $\sim 1740 \text{ cm}^{-1}$  which clearly corresponds to the carbonyl moieties of PTX. Unlike the hydrophobic benzene rings, the polar carbonyl groups are most probably located outside of the inner cavity of  $β\text{-CD}$  and therefore remain unmasked. Hydrogen bonding with the outer surface OH groups slightly alters the aspect of the vibrational band of the latter. These significant spectral results were expected, being ascribed to host ( $β\text{-CD}$ )–guest (PTX) interactions in the inclusion complex.

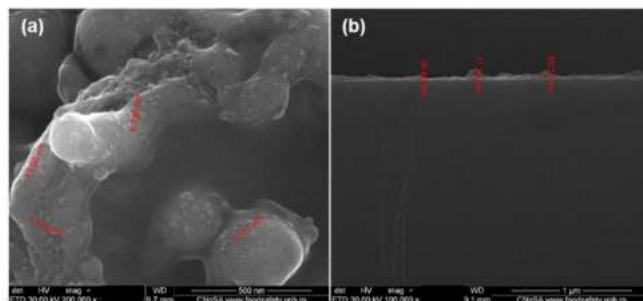
Surface morphological details (size and shape) of  $\text{Fe}_3\text{O}_4@β\text{-CD}$  nanocarrier powders were investigated by SEM. Agglomerated nanoparticles can be observed in the low-magnification ( $5000\times$ ) SEM micrograph (Figure 15a). High-magnification images ( $400,000\times$ ) revealed 3–5 nm-sized nanoparticles of well-defined spherical morphology (Figure 15b,c).



**Figure 15.** SEM micrographs of  $\text{Fe}_3\text{O}_4@β\text{-CD}$  nanopowders at (a) low-magnification ( $5000\times$ ) and (b–d) high-magnification ( $400,000\times$ ).

SEM analysis was also used to determine the shape, morphological and textural features of the thin films. Figure 16b show (at  $100,000\times$  magnification) the cross-section

of  $\text{Fe}_3\text{O}_4@ \beta\text{-CD}$  thin films deposited at  $400 \text{ mJ}/\text{cm}^2$  laser fluence. One can observe the uniform, compact, and agglomerated morphology of the film. The film's surface exhibits an irregular aspect with thicknesses varying from 18 nm up to 71 nm (Figure 16b).



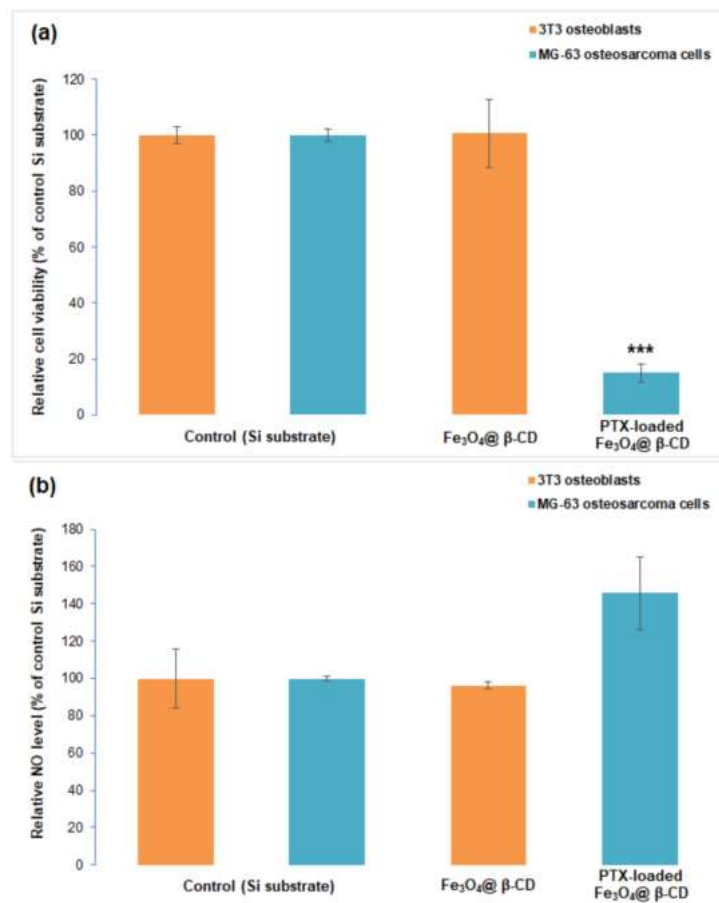
**Figure 16.** Plain view (a) and cross-section (b) SEM micrographs of  $\text{Fe}_3\text{O}_4@ \beta\text{-CD}/\text{PTX}$  deposited at  $400 \text{ mJ}/\text{cm}^2$ .

### 3.3. *In Vitro* Biocompatibility of $\text{Fe}_3\text{O}_4@ \beta\text{-CD}$ Nanocomposite Thin Films and Anti-Tumoral Activity of Paclitaxel-Loaded Films

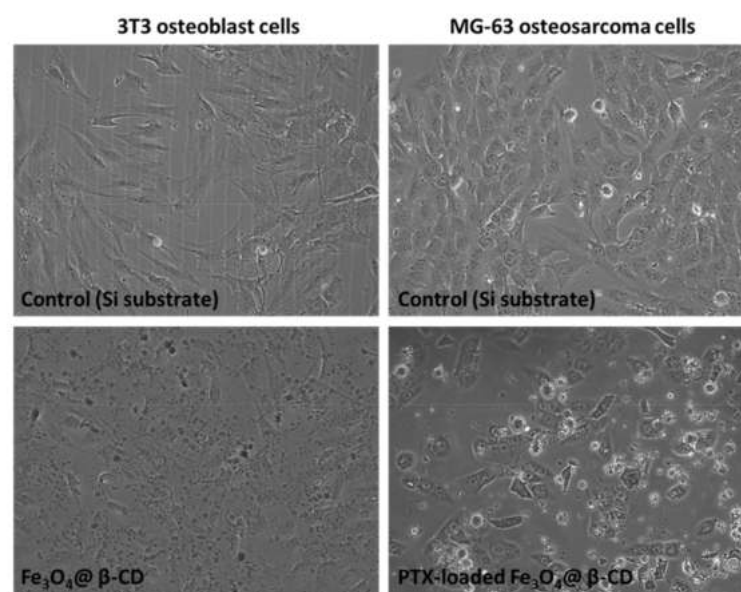
In order to evaluate the biocompatibility of our novel MAPLE-fabricated magnetic films represented by  $\text{Fe}_3\text{O}_4@ \beta\text{-CD}$  nanoparticles, we carried out simple cytotoxicity assays on a normal 3T3 osteoblast cell line culture. No change in cell viability was observed in the presence of the bare  $\beta\text{-CD}$  modified magnetite after performing MTT test (Figure 17a), and the level of NO in the culture medium was similar to the control (Figure 17b). The good biocompatibility of this  $\text{Fe}_3\text{O}_4@ \beta\text{-CD}$  nanocoating was also confirmed by phase-contrast microscopy, as no evident adverse effect on the morphology of normal osteoblasts was seen in Figure 18.

To evaluate the anti-tumor outcome of PTX-loaded  $\text{Fe}_3\text{O}_4@ \beta\text{-CD}$  nanocomposites, the MG-63 osteosarcoma cell line was used. A significant decrease to 85% of control (represented by a simple glass slide) proved the high efficiency of PTX-loaded  $\beta\text{-CD}$  surface-modified SPIONs deposited as thin films by MAPLE technique on glass substrates (Figure 17a). According to a previous report, PTX induced a decrease of MG-63 osteosarcoma cell viability of only 10% over control after 24 h of incubation [35]. Comparing the poor anti-tumoral activity of the free drug with the high efficiency of PTX-loaded  $\beta\text{-CD}$  surface-modified SPIONs deposited as thin films by MAPLE, we concluded that these modified surface have improved activity and great potential for anti-cancer applications. The NO level rose to 145% of the control (Figure 17b), suggesting the inflammatory effect induced by these PTX-loaded nanocomposites. Only a few tumor osteoblasts were noticed after 24 h of incubation with PTX-loaded  $\text{Fe}_3\text{O}_4@ \beta\text{-CD}$  nanocomposites in the phase-contrast microscopy images (Figure 18).

Regarding the design of new pharmacologically active composites for cancer therapy, it has previously been shown that PTX/hydroxypropyl- $\beta\text{-CD}$  complex-loaded liposomes have the potential as drug nanocarriers to treat lung adenocarcinoma [46]. The cyclodextrin- $\text{Fe}_3\text{O}_4$  formulation was also used to encapsulate camptothecin in order to improve its solubility and bioavailability for cancer cells. It has been confirmed that this could be used as a major nanocarrier for camptothecin to effectively treat colon cancer [47].



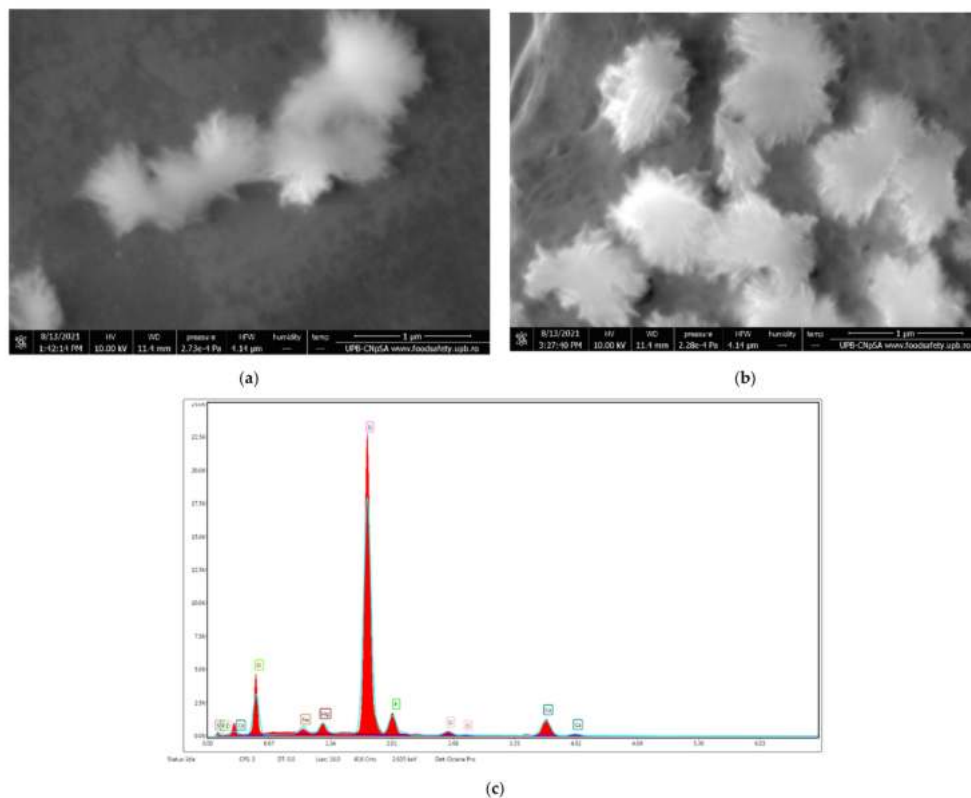
**Figure 17.** Biocompatibility of Fe<sub>3</sub>O<sub>4</sub>@β-CD nanoparticles on normal 3T3 osteoblasts (a) and anti-tumor efficiency of PTX-loaded Fe<sub>3</sub>O<sub>4</sub>@β-CD nanocomposites on MG-63 osteosarcoma cells (b) evidenced by the results of MTT (a) and Griess (b) assays. The results were calculated as mean values (*n* = 3) and expressed relative to control samples (\*\**p* < 0.001).



**Figure 18.** Images of phase-contrast microscopy of normal 3T3 osteoblasts and MG-63 osteosarcoma cells cultured on the surface of Fe<sub>3</sub>O<sub>4</sub>@β-CD and PTX-loaded Fe<sub>3</sub>O<sub>4</sub>@β-CD thin films, respectively. Objective used: 10×.

### 3.4. In Vitro Biocompatibility of $\text{Fe}_3\text{O}_4@ \beta\text{-CD}$ Nanocomposite Thin Films on SBF

A supplementary in vitro test was performed on the SBF. The samples were immersed in SBF for 14 days, and subsequently, the surface of the sample was evaluated using a VERSA 3D scanning electron microscope. The main results are plotted in Figure 19. The formation of biological apatite with needle-like structures on the surface of the  $\text{Fe}_3\text{O}_4@ \beta\text{-CD}$  thin coating can be seen in Figure 19a,b, and was also confirmed by EDS (Figure 19c).



**Figure 19.** SEM images (a,b) and EDS analysis (c) of  $\text{Fe}_3\text{O}_4@ \beta\text{-CD}$  after 14 days of incubation in SBF at 37 °C.

## 4. Conclusions

We succeeded in the preparation of both pristine and PTX-loaded  $\beta\text{-CD}$  surface-modified SPIONs, not only in the form of nanopowders but also as thin films deposited by MAPLE technique. The physicochemical characterization of nanopowders was carried out using XRD, SEM, TEM, SAED, FT-IR, TGA, and DSC. The structural integrity of the thin films, deposited at the optimal laser beam fluence of  $400 \text{ mJ}/\text{cm}^2$ , was proved by mapping the surface distribution of the FT-IR absorbances of characteristic spectral markers. Biocompatibility and cytotoxicity of the prepared magnetic hybrid nanocomposites were assessed in vitro by performing an MTT test on normal 3T3 cell line osteoblasts and osteosarcoma MG-63 cell lines. The pristine  $\beta\text{-CD}$  surface-modified nanopowders and thin films showed excellent biocompatibility and nocyctotoxic effect. On the other hand, magnetic thin films loaded with the anti-cancer drug PTX exhibited significantly increased affinity for tumoral cells. The above properties recommend our novel magnetic nanopowders and thin films as valuable candidates for future magnetically targeted drug delivery, theragnostic, and hyperthermia applications in cancer treatment.

**Author Contributions:** Conceptualization—R.A.P., P.C.B., A.M.G., E.A.; Methodology—A.M.G., E.A. and P.C.B.; Validation—O.-C.O., B.S.V., V.G. and M.S.S.; Investigation—R.A.P., E.C., B.S.V. and O.-C.O.; Resources—A.M.G., E.A., M.S.S. and V.G.; Writing—Original draft preparation—R.A.P., P.C.B., E.C., A.M.G., V.G., I.N., I.C.N., M.S.S. and O.-C.O.; Writing—Review and editing—R.A.P.,

A.M.G., E.C., V.G., M.S.S.; visualization—P.C.B., A.M.G. and E.A.; Supervision—E.A., A.M.G., P.C.B. All authors have read and agreed to the published version of the manuscript.

**Funding:** This research received no external funding.

**Institutional Review Board Statement:** Not applicable.

**Informed Consent Statement:** Not applicable.

**Data Availability Statement:** Available from the corresponding author upon request.

**Conflicts of Interest:** The authors declare no conflict of interest.

## References

- Alifu, N.; Sun, Z.; Zebibula, A.; Zhu, Z.; Zhao, X.; Wu, C.; Wang, Y.; Qian, J. Deep-red polymer dots with bright two-photon fluorescence and high biocompatibility for in vivo mouse brain imaging. *Opt. Commun.* **2017**, *399*, 120–126. [CrossRef]
- Ferlay, J.; Colombet, M.; Soerjomataram, I.; Dyba, T.; Randi, G.; Bettio, M.; Gavin, A.; Visser, O.; Bray, F. Cancer incidence and mortality patterns in Europe: Estimates for 40 countries and 25 major cancers in 2018. *Eur. J. Cancer* **2018**, *103*, 356–387. [CrossRef]
- Paul Catalin, B.; Alexandru Mihai, G. Smart Synthetic Polymer Nanocarriers for Controlled and Site-Specific Drug Delivery. *Curr. Top. Med. Chem.* **2015**, *15*, 1424–1490. [CrossRef]
- Paul Catalin, B.; Dragos, G.; Iulia Alexandra, G. Smart Triggered Release in Controlled Drug Delivery. *Curr. Drug Targets* **2018**, *19*, 318–327. [CrossRef]
- Arzani, H.; Adabi, M.; Mosafer, J.; Dorkoosh, F.; Khosravani, M.; Maleki, H.; Nekounam, H.; Kamali, M. Preparation of curcumin-loaded PLGA nanoparticles and investigation of its cytotoxicity effects on human glioblastoma U87MG cells. *Biointerface Res. Appl. Chem.* **2019**, *9*, 4225–4231. [CrossRef]
- Balaure, P.; Gudovan, D.; Gudovan, I. Organic polymeric nanomaterials as advanced tools in the fight against antibiotic-resistant infections. In *Functionalized Nanomaterials for the Management of Microbial Infection: A Strategy to Address Microbial Drug Resistance*; Boukherroub, R., Szunerits, S., Drider, D., Eds.; Elsevier: Amsterdam, The Netherlands, 2017; pp. 153–265.
- Dragoș, G.; Paul Cătălin, B.; Dan Eduard, M.; Adrian, F.; Bogdan, P.; Mihai, R. Functionalized magnetic nanoparticles for biomedical applications. *Curr. Pharm. Des.* **2015**, *21*, 6038–6054. [CrossRef]
- Al Faraj, A.; Shaik, A.P.; Shaik, A.S. Effect of surface coating on the biocompatibility and in vivo MRI detection of iron oxide nanoparticles after intrapulmonary administration. *Nanotoxicology* **2015**, *9*, 825–834. [CrossRef] [PubMed]
- Dulińska-Litewka, J.; Łazarczyk, A.; Hałubiec, P.; Szafranski, O.; Karnas, K.; Karewicz, A. Superparamagnetic Iron Oxide Nanoparticles—Current and Prospective Medical Applications. *Materials* **2019**, *12*, 617. [CrossRef] [PubMed]
- Liong, M.; Lu, J.; Kovochich, M.; Xia, T.; Ruehm, S.G.; Nel, A.E.; Tamanoi, F.; Zink, J.I. Multifunctional Inorganic Nanoparticles for Imaging, Targeting, and Drug Delivery. *ACS Nano* **2008**, *2*, 889–896. [CrossRef]
- Jain, T.K.; Richey, J.; Strand, M.; Leslie-Pelecky, D.L.; Flask, C.A.; Labhasetwar, V. Magnetic nanoparticles with dual functional properties: Drug delivery and magnetic resonance imaging. *Biomaterials* **2008**, *29*, 4012–4021. [CrossRef]
- Alghuthaymi, M. Magnetic-silica nanoshell for extraction of fungal genomic DNA from *Rhizopus oryzae*. *Biointerface Res. Appl. Chem.* **2020**, *10*, 4972–4976. [CrossRef]
- Mohamad, A.; Rizwan, M.; Keasberry, N.A.; Ahmed, M.U. Fabrication of label-free electrochemical food biosensor for the sensitive detection of ovalbumin on nanocomposite-modified graphene electrode. *Biointerface Res. Appl. Chem.* **2019**, *9*, 4655–4662. [CrossRef]
- Wang, Y.X. Superparamagnetic iron oxide based MRI contrast agents: Current status of clinical application. *Quant. Imaging Med. Surg.* **2011**, *1*, 35–40. [CrossRef]
- Silva, A.C.; Oliveira, T.R.; Mamani, J.B.; Malheiros, S.M.F.; Malavolta, L.; Pavon, L.F.; Sibov, T.T.; Amaro Junior, E.; Tannus, A.; Vidoto, E.L.G.; et al. Application of hyperthermia induced by superparamagnetic iron oxide nanoparticles in glioma treatment. *Int. J. Nanomed.* **2011**, *6*, 591–603. [CrossRef]
- Laurent, S.; Forge, D.; Port, M.; Roch, A.; Robic, C.; Vander Elst, L.; Muller, R.N. Magnetic iron oxide nanoparticles: Synthesis, stabilization, vectorization, physicochemical characterizations, and biological applications. *Chem. Rev.* **2008**, *108*, 2064–2110. [CrossRef]
- Elazab, H.A.; Gadalla, M.A.; Sadek, M.A.; El-Idreesy, T.T. Hydrothermal synthesis of graphene supported Pd/Fe<sub>3</sub>O<sub>4</sub> nanoparticles as efficient magnetic catalysts for Suzuki Cross-Coupling. *Biointerface Res. Appl. Chem.* **2019**, *9*, 3906–3911. [CrossRef]
- Rajendrachari, S.; Ceylan, K.B. The activation energy and antibacterial investigation of spherical Fe<sub>3</sub>O<sub>4</sub> nanoparticles prepared by *Crocus sativus* (Saffron) flowers. *Biointerface Res. Appl. Chem.* **2020**, *10*, 5951–5959. [CrossRef]
- Haroun, A.A.; Ahmed, E.F.; Hakeim, O.A. Multifunctional hyperbranched polyester grafted beta-cyclodextrin metal complexes for textile coating. *Biointerface Res. Appl. Chem.* **2020**, *10*, 6000–6006. [CrossRef]
- Haihem, S.; Abdelaziz, B.; Leila, N.; Imene, D.; Madi, F.; Eddine, K. Molecular docking study on  $\beta$ -cyclodextrin Interactions of metobromuron and [3-(p-bromophenyl)-1-methoxy-1-methylurea]. *J. Incl. Phenom. Macrocycl. Chem.* **2012**, *74*, 191–200. [CrossRef]
- Chen, P.; Yao, S.; Chen, X.; Huang, Y.; Song, H. A new strategy for the construction of  $\beta$ -cyclodextrin-based magnetic nanocarriers: A molecular docking technique. *New J. Chem.* **2019**, *43*, 4282–4290. [CrossRef]



22. Jayaprabha, K.N.; Joy, P.A. Citrate modified  $\beta$ -cyclodextrin functionalized magnetite nanoparticles: A biocompatible platform for hydrophobic drug delivery. *RSC Adv.* **2015**, *5*, 22117–22125. [CrossRef]
23. Jeon, H.; Kim, J.; Lee, Y.M.; Kim, J.; Choi, H.W.; Lee, J.; Park, H.; Kang, Y.; Kim, I.S.; Lee, B.H.; et al. Poly-paclitaxel/cyclodextrin-SPION nano-assembly for magnetically guided drug delivery system. *J. Control. Release Off. J. Control. Release Soc.* **2016**, *231*, 68–76. [CrossRef] [PubMed]
24. Monteiro, A.P.F.; Caminhas, L.D.; Ardisson, J.D.; Paniago, R.; Cortés, M.E.; Sinisterra, R.D. Magnetic nanoparticles coated with cyclodextrins and citrate for irinotecan delivery. *Carbohydr. Polym.* **2017**, *163*, 1–9. [CrossRef]
25. Chen, P.; Song, H.; Yao, S.; Tu, X.; Su, M.; Zhou, L. Magnetic targeted nanoparticles based on  $\beta$ -cyclodextrin and chitosan for hydrophobic drug delivery and a study of their mechanism. *RSC Adv.* **2017**, *7*, 29025–29034. [CrossRef]
26. Bai, L.; Zhao, Q.; Wang, J.; Gao, Y.; Sha, Z.; Di, D.; Han, N.; Wang, Y.; Zhang, J.; Wang, S. Mechanism study on pH-responsive cyclodextrin capped mesoporous silica: Effect of different stalk densities and the type of cyclodextrin. *Nanotechnology* **2015**, *26*, 165704. [CrossRef] [PubMed]
27. Mrówczyński, R.; Jędrzak, A.; Szutkowski, K.; Grześkowiak, B.F.; Coy, E. Cyclodextrin-Based Magnetic Nanoparticles for Cancer Therapy. *Nanomaterials* **2018**, *8*, 170. [CrossRef] [PubMed]
28. Shen, L.; Li, B.; Qiao, Y. Fe<sub>3</sub>O<sub>4</sub> Nanoparticles in Targeted Drug/Gene Delivery Systems. *Materials* **2018**, *11*, 324. [CrossRef] [PubMed]
29. Piehler, S.; Dähring, H.; Grandke, J.; Göring, J.; Couleaud, P.; Aires, A.; Cortajarena, A.L.; Courty, J.; Latorre, A.; Somoza, Á.; et al. Iron Oxide Nanoparticles as Carriers for DOX and Magnetic Hyperthermia after Intratumoral Application into Breast Cancer in Mice: Impact and Future Perspectives. *Nanomaterials* **2020**, *10*, 1016. [CrossRef]
30. Vangijzegem, T.; Stanicki, D.; Laurent, S. Magnetic iron oxide nanoparticles for drug delivery: Applications and characteristics. *Expert Opin. Drug Deliv.* **2019**, *16*, 69–78. [CrossRef]
31. Badruddoza, A.Z.M.; Rahman, M.T.; Ghosh, S.; Hossain, M.Z.; Shi, J.; Hidajat, K.; Uddin, M.S.  $\beta$ -Cyclodextrin conjugated magnetic, fluorescent silica core-shell nanoparticles for biomedical applications. *Carbohydr. Polym.* **2013**, *95*, 449–457. [CrossRef]
32. Hu, Q.-D.; Tang, G.-P.; Chu, P.K. Cyclodextrin-Based Host–Guest Supramolecular Nanoparticles for Delivery: From Design to Applications. *Acc. Chem. Res.* **2014**, *47*, 2017–2025. [CrossRef]
33. Grumezescu, V.; Socol, G.; Grumezescu, A.M.; Holban, A.M.; Ficai, A.; Trusca, R.; Bleotu, C.; Balaure, P.C.; Cristescu, R.; Chifiriuc, M.C. Functionalized antibiofilm thin coatings based on PLA-PVA microspheres loaded with usnic acid natural compounds fabricated by MAPLE. *Appl. Surf. Sci.* **2014**, *302*, 262–267. [CrossRef]
34. Pereira, C.; Pereira, A.M.; Fernandes, C.; Rocha, M.; Mendes, R.; Fernández-García, M.P.; Guedes, A.; Tavares, P.B.; Grenèche, J.-M.; Araújo, J.P.; et al. Superparamagnetic MFe<sub>2</sub>O<sub>4</sub> (M = Fe, Co, Mn) Nanoparticles: Tuning the Particle Size and Magnetic Properties through a Novel One-Step Coprecipitation Route. *Chem. Mater.* **2012**, *24*, 1496–1504. [CrossRef]
35. Liu, S.Y.; Song, S.X.; Lin, L.; Liu, X. Molecular Mechanism of Cell Apoptosis by Paclitaxel and Pirarubicin in a Human Osteosarcoma Cell Line. *Chemotherapy* **2010**, *56*, 101–107. [CrossRef]
36. Piqué, A.; McGill, R.A.; Chrisey, D.; Leonhardt, D.; Mslina, T.E.; Spargo, B.; Callahan, J.; Vachet, R.W.; Chung, R.; Bucaro, M. Growth of organic thin films by the matrix assisted pulsed laser evaporation (MAPLE) technique. *Thin Solid Film.* **1999**, *355*, 536–541. [CrossRef]
37. Kokubo, T.; Takadama, H. How useful is SBF in predicting in vivo bone bioactivity? *Biomaterials* **2006**, *27*, 2907–2915. [CrossRef] [PubMed]
38. Zhai, Y.; Liu, F.; Zhang, Q.; Gao, G. Synthesis of magnetite nanoparticle aqueous dispersions in an ionic liquid containing acrylic acid anion. *Colloids Surf. A Physicochem. Eng. Asp.* **2009**, *332*, 98–102. [CrossRef]
39. Kemelbekov, U.; Luo, Y.; Orynbeikova, Z.; Rustembekov, Z.; Haag, R.; Saenger, W.; Praliyev, K. IR, UV and NMR studies of  $\beta$ -cyclodextrin inclusion complexes of kazcaine and prosidol bases. *J. Incl. Phenom. Macrocycl. Chem.* **2011**, *69*, 181–190. [CrossRef]
40. Chen, J.; Qin, X.; Zhong, S.; Chen, S.; Su, W.; Liu, Y. Characterization of Curcumin/Cyclodextrin Polymer Inclusion Complex and Investigation on Its Antioxidant and Antiproliferative Activities. *Molecules* **2018**, *23*, 1179. [CrossRef] [PubMed]
41. Paczkowska, M.; Mizera, M.; Piotrowska, H.; Szymanowska-Powalowska, D.; Lewandowska, K.; Goscianska, J.; Pietrzak, R.; Bednarski, W.; Majka, Z.; Cielecka-Piontek, J. Complex of Rutin with  $\beta$ -Cyclodextrin as Potential Delivery System. *PLoS ONE* **2015**, *10*, e0120858. [CrossRef]
42. Stoia, M.; Istrate, R.; Păcurariu, C. Investigation of magnetite nanoparticles stability in air by thermal analysis and FTIR spectroscopy. *J. Therm. Anal. Calorim.* **2016**, *125*, 1185–1198. [CrossRef]
43. Velázquez, N.S.; Ferreyra, M.G.; Mengatto, L.N.; Santagapita, P.R.; Buera, M.P.; Luna, J.A. Paclitaxel/ $\beta$ -Cyclodextrin interactions, a perspective from pulsed NMR spectroscopy experiments. *Carbohydr. Res.* **2019**, *486*, 107828. [CrossRef] [PubMed]
44. Loh, G.O.K.; Tan, Y.T.F.; Peh, K.-K. Enhancement of norfloxacin solubility via inclusion complexation with  $\beta$ -cyclodextrin and its derivative hydroxypropyl- $\beta$ -cyclodextrin. *Asian J. Pharm. Sci.* **2016**, *11*, 536–546. [CrossRef]
45. Ye, Y.J.; Wang, Y.; Lou, K.Y.; Chen, Y.Z.; Chen, R.; Gao, F. The preparation, characterization, and pharmacokinetic studies of chitosan nanoparticles loaded with paclitaxel/dimethyl- $\beta$ -cyclodextrin inclusion complexes. *Int. J. Nanomed.* **2015**, *10*, 4309–4319. [CrossRef]



46. Shen, Q.; Shen, Y.; Jin, F.; Du, Y.Z.; Ying, X.Y. Paclitaxel/hydroxypropyl- $\beta$ -cyclodextrin complex-loaded liposomes for overcoming multidrug resistance in cancer chemotherapy. *J. Liposome Res.* **2020**, *30*, 12–20. [CrossRef] [PubMed]
47. Krishnan, P.; Rajan, M.; Kumari, S.; Sakinah, S.; Priya, S.P.; Amira, F.; Danjuma, L.; Pooi Ling, M.; Fakurazi, S.; Arulselvan, P.; et al. Efficiency of newly formulated camptothecin with  $\beta$ -cyclodextrin-EDTA-Fe<sub>3</sub>O<sub>4</sub> nanoparticle-conjugated nanocarriers as an anti-colon cancer (HT29) drug. *Sci. Rep.* **2017**, *7*, 10962. [CrossRef]

## Article

# Low Blue Dose Photodynamic Therapy with Porphyrin-Iron Oxide Nanoparticles Complexes: In Vitro Study on Human Melanoma Cells

Simona Nistorescu <sup>1,2</sup>, Ana-Maria Udrea <sup>1,3</sup>, Madalina Andreea Badea <sup>2</sup>, Iulia Lungu <sup>1,4</sup>, Mihai Boni <sup>1</sup>, Tatiana Tozar <sup>1</sup>, Florian Dumitrache <sup>1</sup>, Valentin-Adrian Maraloiu <sup>5</sup>, Roua Gabriela Popescu <sup>2</sup>, Claudiu Fleaca <sup>1</sup>, Ecaterina Andronescu <sup>4</sup>, Anca Dinischiotu <sup>2</sup>, Angela Staicu <sup>1,\*</sup> and Mihaela Balas <sup>2,\*</sup>

<sup>1</sup> National Institute of Laser, Plasma and Radiation Physics, 409 Atomistilor Str., 077125 Magurele, Romania; simona.stroescu@inflpr.ro (S.N.); ana.udrea@inflpr.ro (A.-M.U.); iulia.lungu@inflpr.ro (I.L.); mihai.boni@inflpr.ro (M.B.); tatiana.alexandru@inflpr.ro (T.T.); florian.dumitrache@inflpr.ro (F.D.); claudiu.fleaca@inflpr.ro (C.F.)

<sup>2</sup> Department of Biochemistry and Molecular Biology, Faculty of Biology, University of Bucharest, 91-95 Splaiul Independentei, 050095 Bucharest, Romania; badea\_andreea08@yahoo.com (M.A.B.); roua.popescu@drd.unibuc.ro (R.G.P.); ancadinischiotu@yahoo.com (A.D.)

<sup>3</sup> Research Institute of the University of Bucharest, Earth, Environmental and Life Sciences, Section-ICUB, 050663 Bucharest, Romania

<sup>4</sup> Faculty of Applied Chemistry and Materials Science, University Politehnica of Bucharest, 1-7 Gh. Polizu Str., 011061 Bucharest, Romania; ecaterina.andronescu@upb.ro

<sup>5</sup> National Institute of Materials Physics, 405 A Atomistilor Str., 077125 Magurele, Romania; maraloiu@infim.ro

\* Correspondence: angela.staicu@inflpr.ro (A.S.); mihaela.balas@bio.unibuc.ro (M.B.)

**Citation:** Nistorescu, S.; Udrea, A.-M.; Badea, M.A.; Lungu, I.; Boni, M.; Tozar, T.; Dumitrache, F.; Maraloiu, V.-A.; Popescu, R.G.; Fleaca, C.; et al. Low Blue Dose Photodynamic Therapy with Porphyrin-Iron Oxide Nanoparticles Complexes: In Vitro Study on Human Melanoma Cells. *Pharmaceutics* **2021**, *13*, 2130. <https://doi.org/10.3390/pharmaceutics13122130>

Academic Editor: Maria Nowakowska

Received: 2 November 2021

Accepted: 3 December 2021

Published: 10 December 2021

**Publisher's Note:** MDPI stays neutral with regard to jurisdictional claims in published maps and institutional affiliations.



**Copyright:** © 2021 by the authors. Licensee MDPI, Basel, Switzerland. This article is an open access article distributed under the terms and conditions of the Creative Commons Attribution (CC BY) license (<https://creativecommons.org/licenses/by/4.0/>).

**Abstract:** The purpose of this study was to investigate the effectiveness in photodynamic therapy of iron oxide nanoparticles ( $\gamma$ -Fe<sub>2</sub>O<sub>3</sub> NPs), synthesized by laser pyrolysis technique, functionalized with 5,10,15,20-(Tetra-4-sulfonatophenyl) porphyrin tetraammonium (TPPS) on human cutaneous melanoma cells, after only 1 min blue light exposure. The efficiency of porphyrin loading on the iron oxide nanocarriers was estimated by using absorption and FTIR spectroscopy. The singlet oxygen yield was determined via transient characteristics of singlet oxygen phosphorescence at 1270 nm both for porphyrin functionalized nanoparticles and rose bengal used as standard. The irradiation was performed with a LED (405 nm, 1 mW/cm<sup>2</sup>) for 1 min after melanoma cells were treated with TPPS functionalized iron oxide nanoparticles ( $\gamma$ -Fe<sub>2</sub>O<sub>3</sub> NPs\_TPPS) and incubated for 24 h. Biological tests revealed a high anticancer effect of  $\gamma$ -Fe<sub>2</sub>O<sub>3</sub> NPs\_TPPS complexes indicated by the inhibition of tumor cell proliferation, reduction of cell adhesion, and induction of cell death through ROS generated by TPPS under light exposure. The biological assays were combined with the pharmacokinetic prediction of the porphyrin.

**Keywords:** photodynamic therapy PDT; porphyrin; iron oxide nanoparticles; melanoma

## 1. Introduction

Melanoma is the most lethal type of skin cancer and the third form of malignancy encountered between the ages of 15 to 39 years, with an incidence constantly increasing. Among the risk factors involved in the evolution of aggressive skin the malignant tumor are found: family history, ultraviolet (UV) radiation exposure, or simply variations in pigmentation genes [1–3]. The pathogenic mechanism of melanoma involves two cell subpopulations in the epidermis, called melanocytes and keratinocytes. As a result of UV exposure, skin keratinocytes increase melanin generation by producing the melanocyte-stimulating hormone (MSH) that binds the melanocortin receptor 1 (MC1R) found on melanocytes surface. Briefly, the melanocytes transfer melanin to surrounding keratinocytes and protect the living cells. The melanoma risk appears as a cause of long exposure of the nuclei to UV damage and accumulation of the mutations in sensitive regions [3–7].

For the treatment of melanoma, a lot of therapies were developed: chemotherapy, immunotherapy, surgical resection, biochemotherapy, photodynamic therapy, and targeted therapy [8]. Among these, photodynamic therapy (PDT) is based on the generation of reactive oxygen species (ROS), especially singlet oxygen, by light exposure of unhealthy tissue, at a specific wavelength. The most important aspect of the procedure is the use of a photosensitizer (PS), a non-toxic agent that accumulates in the tumor and generates ROS by light irradiation [9–11]. Briefly, the PS molecule is first excited to the singlet state and through intersystem crossing forms the triplet state that then transfers the energy to ground state oxygen, generating excited singlet state oxygen ( $^1\text{O}_2$ ), the chief reactive species, which interacts with surrounding molecules and destroys them [9,12]. A PS agent must be: targeted to the tumor (able to accumulate in the tumor), a non-toxic compound, painless, easy to eliminate, stable in time, active only on illumination, and efficient in singlet oxygen generation [12,13].

Porphyrins, a group of organic compounds, are considered great PS agents that may be used to accept the energy of light and produce singlet oxygen in the presence of a triplet-state electron [9]. They are macrocyclic compounds with four pyrrole subunits interconnected at their  $\alpha$  carbon atoms, are found in hemoglobin and cytochromes structure, and have the function of a cofactor for redox-active enzymes. Moreover, their applications in the biomedical field as PS in PDT are associated with their optical and redox properties [14,15]. A large range of porphyrin derivatives can be used in PDT. The sulfonation of tetraphenyl porphyrin generates the tetra sulfonate porphyrin, an excellent producer of singlet oxygen, with high solubility in water, and a promising PS for PDT. Also, tetra sulfonate porphyrin is permeable through the cell membrane and has specific accumulation and activity on tumor cells both *in vitro* and *in vivo* [14,15].

Generally, the PDT begins 24 h before the light exposure, when PS, such as porphyrin [10], is administrated for its deposition and accumulation in the tumor. Interestingly, it was described that PS effectiveness in blood at the irradiation time determines tumor vasculature damage and, finally, affects the nutrient supply of the tumor. Thus, the PS action is not concentrated only in the tumor, the effect of irradiation being not only the induction of tumor cell death [16–22]. Moreover, PDT presents the limitation of a long *in vivo* half-life of the PS and the difficulty of its transport in deep tumor regions of the body [23].

Nevertheless, the porphyrin activity as PS in the specific cell target can be improved by many carriers (nanoparticles, micelles), being avoided the photosensitivity on healthy tissue. Delivery systems protect the PS and release it only under specific conditions, where ROS generation is required [24,25].

The use of nanoparticles as drug delivery systems proved to have multiple advantages, such as: high biocompatibility, ease of fabrication and functionalization, and the control of material size, and shape. Iron oxide nanoparticles are considered important tools in the modulation of PS action due to their ability to carry and transport therapeutic amounts of PS in the deep tumor regions of the body and to enhance the solubility of hydrophobic PS [23]. Besides, the iron oxide nanoparticles present magnetic properties that can be manipulated for medical application (cell labeling, gene delivery) or hyper/photo-thermal therapy application. The iron oxide nanoparticles have been already used as vehicles for the delivery of PS in PDT [26,27].

In this context, the purpose of this study was to investigate the anti-tumor effectiveness of iron oxide nanoparticles ( $\gamma\text{-Fe}_2\text{O}_3$  NPs) functionalized with 5,10,15,20-(Tetra-4-sulfonatophenyl) porphyrin tetraammonium (TPPS) on human cutaneous melanoma cells, after only 1 min light exposure. The water-soluble porphyrin, TPPS was chosen due to its potential application in cancer therapy, and infectious diseases [28].

The efficiency of porphyrin loading on the iron oxide nanocarriers, synthesized by laser pyrolysis technique, was estimated by using absorption and FTIR spectroscopy. Also, the singlet oxygen yield was determined via transient characteristics of singlet oxygen phosphorescence at 1270 nm for both, TPPS functionalized iron oxide nanoparticles ( $\gamma\text{-Fe}_2\text{O}_3$  NPs\_TPPS) and rose bengal used as standard. The irradiation was performed with

a LED (405 nm, 1 mW) for 1 min after melanoma cells were treated with  $\gamma$ -Fe<sub>2</sub>O<sub>3</sub> NPs\_TPPS complexes and incubated for 24 hours. It was proved that the light exposure increased the production of ROS generated in melanoma cells by porphyrin loaded nanoparticles, reduced the proliferation and cellular adhesion capacity, and induced cell death.

## 2. Materials and Methods

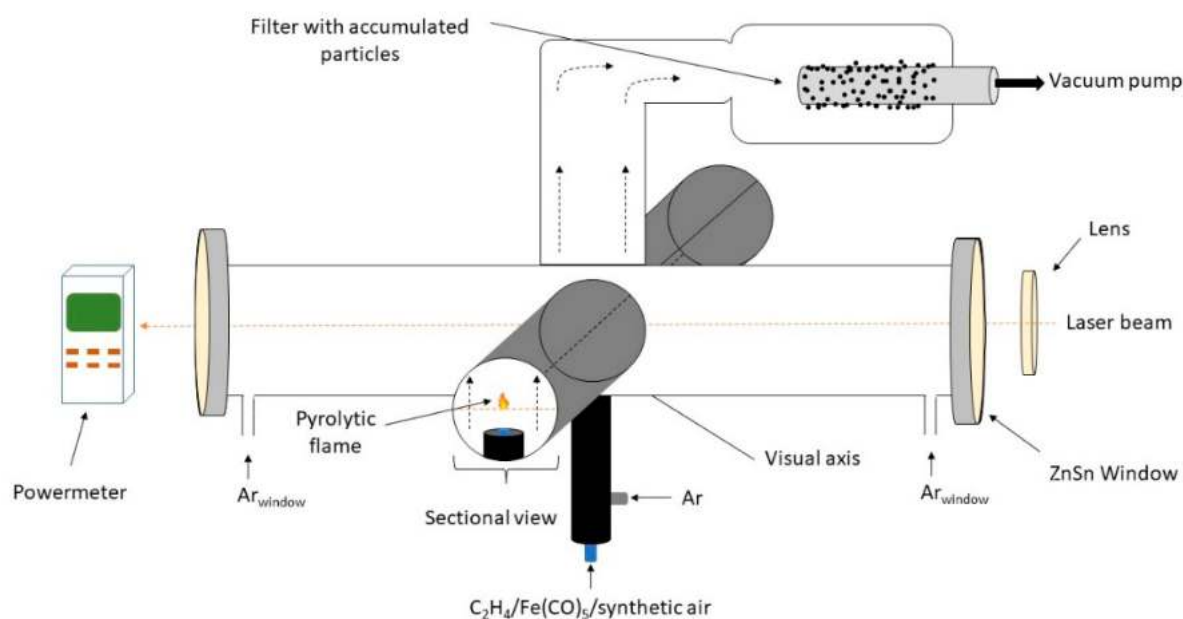
### 2.1. Chemical Compounds

The photosensitizer, 5,10,15,20-(Tetra-4-sulfonatophenyl) porphyrin tetraammonium (TPPS) (purity > 95%), was purchased from PorphyChem SAS, Dijon, France. Rose Bengal (95% purity), used as PS standard, was bought from Sigma Aldrich (Darmstadt, Germany).

For iron oxide nanoparticles (NPs) synthesis by laser pyrolysis technique, the reactive gas-es/vapors used were iron pentacarbonyl (Fe(CO)<sub>5</sub>) (99.999%, Merck, Darmstadt, Germany) as an iron precursor, synthetic air (Linde, Dublin, Ireland) as an oxidizing agent, and ethylene (C<sub>2</sub>H<sub>4</sub>, 99.99%, Linde, Dublin, Ireland) as laser energy transfer agent (i.e., sensitizer).

### 2.2. Iron Oxide Nanoparticle Synthesis

The experimental set-up for laser pyrolysis technique is presented in Figure 1. Due to the resonance between the emission line of the CO<sub>2</sub> infrared laser and the absorption line of the sensitizer gas, the ethylene molecules became vibrationally excited upon the interaction with IR photons, and the reactive mixture is heated very fast via collisions [29]. Also, the mixture is supplementary heated by the oxidation of iron-based species and ethylene molecules. Thus, the sudden formation of iron-based oxidized fragments/clusters is followed by their condensation into small iron oxide nanoparticles which emerge from the reaction zone.



**Figure 1.** Laser pyrolysis of iron oxide nanoparticles.

As presented in Figure 1, the reactant flow orthogonally intersects the focused continuous beam emitted by the CO<sub>2</sub> laser (70W maximum output power,  $\lambda = 10.6 \mu\text{m}$ ). This reactant flow is comprised of a mix of synthetic air (33 sccm) and iron pentacarbonyl vapors (6.6 sccm) transported by a bubbled ethylene flow (33 sccm). Coaxial argon (Ar) flow is used to both confine the gas precursors to the flow axis, as well as to 'guide' the freshly nucleated nanoparticles towards the collection chamber. The reaction zone can be clearly identified through a flame that emits in the visible spectrum. The temperature of the flame needs to be constant throughout the experiment and it can be easily measured using an

optical pyrometer. The process was described in detail elsewhere [29]. The experimental parameters used are presented in Table 1.

**Table 1.** Experimental data.

Sample	D-C <sub>2</sub> H <sub>4</sub> /Fe(CO) <sub>5</sub>	D-synth. Air	D-Ar Conf	D-Ar <sub>windows</sub>	T <sub>flame</sub>	P	P <sub>laser</sub>
unit	sccm	sccm	sccm	sccm	°C	mbar	W
FeO1	33/6.6	33	750	250	670	300	157/150

A water-soluble porphyrin, TPPS, was used as both a stabilizer and as an active component. Initially, the TPPS powder was added to a glass vessel with 20 mL distilled water (dH<sub>2</sub>O) having a pH = 5.5 and left 6 h in the ultrasound bath in order to ensure its solvation. Then the iron NPs were introduced in the TPPS solution, ensuring the equal concentration of 0.5 g/L of nanoparticles and TPPS. The 20 mL water-based suspension was homogenized in an ultrasound bath provided with a cooling system at 59 kHz and 20 °C for 12 h. The resulting suspension was then centrifuged at 10K rpm for 5 min and washed with dH<sub>2</sub>O several times, each time the solid deposit was redispersed while maintaining the initial water volume, with the ultrasonic bath (30 min).

### 2.3. Physicochemical Characterization

#### 2.3.1. Nanoparticle Characterization

In order to characterize the hydrodynamic size and stability of the nanoparticles suspensions, as well as the TPPS functionalized iron NPs suspensions, we utilized dynamic light scattering (DLS) measurements (Nanoparticle Analyzer SZ-100V2, Horiba, Kyoto, Japan) which employs a Diode-pumped solid-state (DPSS) laser emitting at 532 nm, with a power of 100–240 V AC ± 10%, 50 Hz/60 Hz; at a scattering angle of 173°. 1 mL volume of aqueous suspension was added in a quartz cuvette cell for hydrodynamic size measurements which were taken in triplicate for the following suspensions: γ-Fe<sub>2</sub>O<sub>3</sub> (0.5 g/L) in dH<sub>2</sub>O, and γ-Fe<sub>2</sub>O<sub>3</sub> (0.5 g/L) + TPPS (0.5 g/L) in dH<sub>2</sub>O. The same process was used for zeta potential measurements where a cell with electrodes (carbon, 6 mm) was used with a lower volume of solution.

XRD measurements on synthesized nanoparticles were carried out using a Panalytical X'Pert system (Malvern Panalytical Ltd., Malvern, United Kingdom) with Bragg-Bretano geometry: 0.02° step size, 30 s-time/step, 2θ: 15–80° with Cu Kα radiation tube and a graphite monochromator for the diffracted X-ray beam. The NPs from a diluted water suspension and also the final (stabilized and purified) water suspension containing NPs coated with TPPS was characterized with a transmission electron microscope (TEM) apparatus type Jeol ARM 200F also having an EDS facility. Two drops of water dispersions were deposited on a carbon-coated grid and allowed to dry at room temperature. The elemental composition of the as synthesized powder sample was evaluated by EDS-SEM using an FEI Quanta Inspect apparatus.

#### 2.3.2. Spectroscopic Methods

The efficiency of TPPS loading on iron oxide nanoparticles was determined by measuring the absorbance spectra using a Lambda 950 UV-Vis-NIR spectrophotometer (PerkinElmer, Inc., Waltham, MA, USA) and 10 mm thickness optical quartz cuvettes (PerkinElmer, Inc., Waltham, MA, USA). The absorption spectra were measured from 200 to 800 nm at room temperature (22–24 °C).

The experimental detection system used to measure the time-resolved phosphorescence signal of the photosensitized singlet oxygen at wavelength 1270 nm was described in detail elsewhere [30,31].

The laser beam used for excitation of TPPS molecules was emitted by the SHG (532 nm) of a Nd:YAG laser (6 ns pulse time width at half maximum, 10 Hz repetition rate, maximum energy per pulse 25 mJ) (Minilite II, Continuum, Excel Technology, Milpitas, CA, USA).

The TPPS molecule is first excited to the singlet state and through intersystem crossing forms the triplet state and then transfers the energy to ground state oxygen, generating excited singlet state oxygen ( $^1\text{O}_2$ ).

The laser spectroscopic technique for  $^1\text{O}_2$  species measurements is based on the radiative deexcitation of the singlet state through the phosphorescence emission at 1270 nm.

The phosphorescence is detected by a near-infrared (NIR) photomultiplier (PMT Module H10330, Hamamatsu, Japan) and measured with a digital scope (DPO-7254, Tektronix Inc, Beaverton, OR, USA). The phosphorescence transient signal is fitted with a mono-exponential function and the  $^1\text{O}_2$  lifetime is obtained is given by the decay constant.

The quantum yield of the singlet oxygen generation ( $\Phi_\Delta$ ) is determined using also a relative method to a reference standard. Rose Bengal (RB) which has 0.7 the quantum yield of singlet oxygen generation in water was used as a reference. The RB solutions and investigated solutions or suspensions were measured in the same experimental conditions and the quantum yield was determined using the equation [31]:

$$\Phi_\Delta = \Phi_\Delta^{ref} \frac{I}{I_{ref}} \frac{A_{ref}}{A} \frac{n^2}{n_{ref}^2} \frac{\tau}{\tau_{ref}} \quad (1)$$

where  $\Phi_\Delta$  is the quantum yield of singlet oxygen generation,  $I$  is the singlet oxygen phosphorescence intensity at the starting time of the laser pulse for the measured sample,  $A$  is the optical absorption of the sample at the laser excitation wavelength (532 nm),  $\tau$  is the lifetime of singlet oxygen in the measured sample and  $n$  is the solvent refractive index. The script *ref* indicates the measured values for the standard RB solutions. The intensity of phosphorescence at  $t = 0$  was obtained by the extrapolation to zero of the mono-exponential fitting functions for the experimental decay curves.

IR spectra were recorded with a FTIR spectrometer, model Nicolet iS50, under transmission mode over the wavenumber range of 4000–400  $\text{cm}^{-1}$ , at a resolution of 4  $\text{cm}^{-1}$ . The TPPS solutions, the  $\gamma\text{-Fe}_2\text{O}_3$  NPs, and complex  $\gamma\text{-Fe}_2\text{O}_3$  NPs\_TPPS suspensions were dried on optical grade KRS-5 plates.

The theoretical IR spectrum of TPPS was calculated using Gaussian09 software [32]. The molecular structure was subjected to geometry optimization followed by the calculation of vibrational wavenumbers using the density functional theory (DFT). The hybrid functional B3LYP method with 6-311G(2d) basis set was used.

## 2.4. Computational Approach

### 2.4.1. Molecular Modeling

TPPS structure was drawn and optimized using the Clean Geometry function of Discovery Studio Visualizer Software. The  $\text{NH}_4$  groups were removed from the structure for the molecular docking simulations, and we note the resulted structure TPPS.

The structures of our target proteins pro-caspase 3 (PDB code: 4JR0) [33] and caspase 3 (PDB code: 3DEI) [34] were imported from RCSB Protein Data Bank [35].

### 2.4.2. ADME-Tox Predictions

ADME-Tox prediction were made using 3 web services pkCSM [36], admetSAR [37], and ProTox-II [38].

### 2.4.3. Molecular Docking

We have predicted the interaction between TPPS and our target proteins: pro-caspase 3 and caspase 3 with AutoDock4.2.6 software [39] using our usual protocol [40,41]. We have performed blind docking simulations with the grid box grid points  $x y z$  (100, 110, 90) for human pro-caspase 3 respectively (126, 96, 82) for caspase 3. The spacing of the grid box is 0.375 Angstroms, and the Central Grid Point of Maps ( $x y z$ ) is (6.46 1.11 23.11) for pro-caspase 3 and (−33.06 10.36 −9.75) for caspase 3.

## 2.5. In Vitro Bioassay

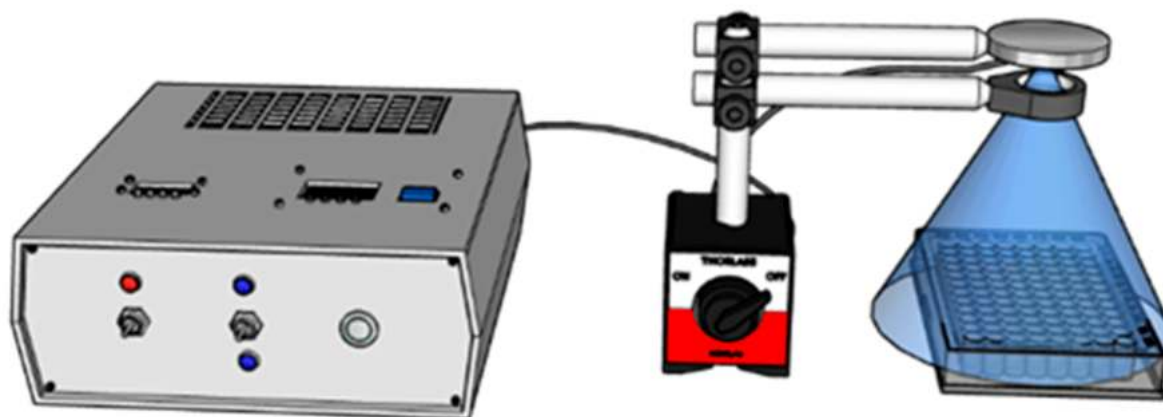
### 2.5.1. Cell Culture

Human cutaneous melanoma cell line, Mel-Juso, (ACC-74, ATCC, Manassas, VA, USA) derived from vertical growth phase amelanotic melanoma was maintained in 75 cm<sup>2</sup> culture flasks and RPMI (Roswell Park Memorial Institute, Buffalo, NY, USA) medium (1640, Gibco, Dublin, Ireland) supplemented with 1% antibiotics-antimycotics solution (Sigma-Aldrich, St. Louis, MO, USA) and fetal bovine serum (FBS, Gibco, by Life Technologies, Carlsbad, CA, USA) at a final concentration of 10%. At confluency of 80–90%, the cells were enzymatically detached from the culture flasks surface using a 0.25% trypsin–0.53 mM EDTA solution. Cell cultures were incubated in standard conditions (37 °C in an atmosphere with 5% CO<sub>2</sub>) and culture media was completely refreshed once every two days.

### 2.5.2. Cell Treatment and LED Irradiation Protocol

To perform the in vitro experiments, Mel-Juso cells were seeded at a density of  $5 \times 10^4$  cells/mL in 96 and 6-well plates and incubated at 37 °C, 5% CO<sub>2</sub>. After adhesion, the cells were treated with,  $\gamma$ -Fe<sub>2</sub>O<sub>3</sub> NPs\_TPPS, free  $\gamma$ -Fe<sub>2</sub>O<sub>3</sub> NPs and free porphyrin, diluted in complete culture medium until a final concentration of 0.05, 0.5, 2.75, 4.16, 5.5 and 11  $\mu$ g/mL for NPs, 0.01, 0.1, 0.5, 0.75, 1 and 2  $\mu$ g/mL for porphyrin and 0.05 + 0.01, 0.5 + 0.1, 2.75 + 0.5, 4.16 + 0.75, 5.5 + 1 and 11 + 2  $\mu$ g/mL for NPs + TPPS in  $\gamma$ -Fe<sub>2</sub>O<sub>3</sub> NPs\_TPPS, respectively. Untreated cells were used as control. To allow the internalization of porphyrin and NPs, cell cultures were incubated for 24 h at 37 °C, 5% CO<sub>2</sub>. Afterwards, the culture medium was replaced with a fresh one and the cells were irradiated or not for 0.5, 1, 2.5, and 5 min, and incubated at 37 °C. All experiments were performed at the interval of 24 h from the irradiation procedure. Before incubation with cells, the NPs and TPPS suspensions were sterilized using UVC radiation for 1 h. Verifications by absorption spectroscopy regarding possible photobleaching after UVC exposure were performed to be sure that the sterilization has no effect on suspensions. No changes of the spectra were noticed.

For cell exposure to UV light, a custom system of irradiation was developed (Figure 2). A 405 nm LED (Nikia, Japan, NVSU 233B) was used as a light source, with a radiant flux of 1400 mW. To control the intensity of LED and the time of irradiation, a Pulse Frequency Generator (PWM) and a Timer Relay Module were added to the power supply circuit.



**Figure 2.** LED Irradiation experimental setup.

A Plano-Convex Lens, with the focal length of  $f = 100$  mm, was placed between the LED and the plates, at a distance of 25 mm with respect to the light source to collect the entire radiation emitted by the diode (Figure 2), and 30 mm to the probe, to irradiate a large interest zone. The power density was measured at different duty cycles for the PWM, a calibration curve was drawn and used further in irradiation parameters selection.

### 2.5.3. Cell Morphology Examination

After 24 h of LED irradiation, cell morphological changes were examined by phase-contrast microscopy using an Olympus IX73 microscope (Olympus, Tokyo, Japan) equipped with a Hamamatsu ORCA-03G camera (A3472-06, Hamamatsu, Japan). Representative images were acquired with the CellSens Dimension software (v1.11, Olympus, Tokyo, Japan).

### 2.5.4. MTT Cell Viability Test

Melanoma cells were seeded at a density of 104 cells/well in 200  $\mu$ L culture media and treated with porphyrin (0.01–2  $\mu$ g/mL), NPs (0.05–11  $\mu$ g/mL) and  $\gamma$ -Fe<sub>2</sub>O<sub>3</sub> NPs\_TPPS (0.05 + 0.01–11 + 2  $\mu$ g/mL) for 24 h. After irradiation, Mel-Juso cells were incubated at 37 °C and the next day the culture media from each well was removed and replaced with 80  $\mu$ L of 1 mg/mL MTT solution. Further, the culture plates were incubated for 2 h at 37 °C. In the final step, the purple formazan crystals formed during the incubation were solubilized with 150  $\mu$ L isopropanol, and the absorbance of the samples was measured at 595 nm using a Flex Station 3 microplate reader (Molecular Devices, San Jose, CA, USA). Non-irradiated cells were treated in the same conditions.

### 2.5.5. Detection of Intracellular Reactive Oxygen Species (ROS) Production

Intracellular ROS production was measured using 2',7'-dichlorodihydrofluorescein diacetate compound (H<sub>2</sub>DCFDA, D6883, Sigma-Aldrich, St. Louis, MO, USA). Mel-Juso cells were seeded in 96-well culture plates (5 × 10<sup>4</sup> cells/mL) and treated with free TPPS (0.1–1  $\mu$ g/mL), free NPs (0.5–5.5  $\mu$ g/mL) and  $\gamma$ -Fe<sub>2</sub>O<sub>3</sub> NPs\_TPPS (0.5 + 0.1–5.5 + 1  $\mu$ g/mL). After 24 h, the culture medium was removed and the cells were incubated for 30 min, at 37 °C with 50  $\mu$ M H<sub>2</sub>DCFDA solution prepared in HBSS (Hanks' Balanced Salt Solution). Further, H<sub>2</sub>DCFDA solution was removed, and the cells were irradiated or not for 1 min at a power density of 1 mW/cm<sup>2</sup>. The fluorescence was read at Flex Station 3 microplate reader (ex. 485 nm/em. 520 nm) after 24 h of incubation. The cells from each well were counted using the Trypan Blue method. The values of relative fluorescence units (RFU) were divided by cell number.

### 2.5.6. Preparation of Cell Lysates

Mel-Juso cells were seeded in 6-well plates and treated with two different doses of TPPS (0.5 and 0.75  $\mu$ g/mL) and the corresponding concentrations of NPs (2.75 and 4.16  $\mu$ g/mL). After irradiation protocol and 24 h incubation, the cells were trypsinized. Further, the cell suspensions were centrifuged for 5 min, at 1500 rpm, 20 °C, and the cellular pellets were washed and resuspended in phosphate-buffered saline solution (PBS). The cell lysates were obtained by sonication of cell suspensions on ice, three times, using a Hielscher UP50H sonicator (80% amplitude, 1 cycle) and their centrifugation for 10 min, at 3000 rpm, 4 °C. The supernatants that resulted from centrifugation were collected and stored at –80 °C until biochemical determinations. The protein concentration of cellular lysates was estimated using Bradford reagent (B6916, Sigma-Aldrich, St. Louis, MO, USA) and a standard curve of 0–1.5 mg/mL bovine serum albumin (BSA).

### 2.5.7. Measurement of Reduced Glutathione (GSH) Intracellular Content

The GSH amount of treated and untreated cells was determined using the method based on the reaction between GSH and Ellman's reagent. Firstly, the cell lysates were deproteinized with an equal volume of 5% 5-sulfosalicylic acid and centrifuged for 10 min, at 10,000 rpm, 4 °C. Secondly, 10  $\mu$ L of supernatant were mixed with 150  $\mu$ L reaction mixture consisting of 1.5 mg/mL 5,5-dithio-bis-(2-nitrobenzoic acid) diluted in potassium phosphate buffer (K<sub>2</sub>HPO<sub>4</sub>/KH<sub>2</sub>PO<sub>4</sub>) 0.1 M, pH = 7, with 1 mM EDTA. Lastly, the samples were incubated at room temperature for 10 min and the absorbance was measured at 405 nm using a microplate reader. The GSH level of the samples was calculated using a 3.125–200  $\mu$ M GSH standard curve.



### 2.5.8. Western Blot Analysis

The expressions of some cell adhesion ( $\beta$ -catenin), proliferation (MCM-2), and apoptotic (caspase 3, Bax, NF- $\kappa$ B) markers were analyzed using the Western blot technique. The cell lysates were chemical (by mixing with a loading buffer containing SDS and  $\beta$ -mercaptoethanol) and thermic denatured (by heating at 95 °C for 5 min). Then, 40  $\mu$ g of protein from each extract were loaded and migrated on denaturing 8%, 10%, and 15% SDS-polyacrylamide gels in TRIS-glycine-SDS buffer, for 2 h. Further, the proteins were electrotransferred from polyacrylamide gels on a PVDF membrane (cat. no. IPVH00010, Merck, Darmstadt, Germany) using a BioRad system and TRIS-glycine-methanol buffer. The proteins detection was performed using Western Breeze Chromogenic Anti-Mouse and Anti-Rabbit kits (WB7103, WB7105, Invitrogen, Carlsbad, CA, USA). The membranes were incubated with blocking solution for 30 min, at room temperature, and let overnight with monoclonal anti-MCM-2 (sc-373702, Santa Cruz, Biotechnology, Dallas, TX, USA), anti- $\beta$ -catenin (sc-59737, Santa Cruz), and polyclonal anti-caspase 3 (sc-7148, Santa Cruz), anti-Bax (sc-493, Santa Cruz) and anti-NF- $\kappa$ B (sc-109, Santa Cruz) specific primary antibodies. The next day, the membranes were washed and then incubated for 30 min with conjugated-alkaline phosphatase secondary antibodies. The protein bands were revealed with BCIP/NBT chromogenic substrate, visualized with a ChemiDoc Imaging System (BioRad, Hercules, CA, USA) and quantified using ImageLab software. The results were normalized to a reference protein ( $\beta$ -actin).

### 2.5.9. Statistical Analysis

The results were calculated as an average of three replicates ( $n = 3$ ) and represented as percentages relative to control (untreated cells)  $\pm$  standard deviation. The statistical significance between treated cells and control was estimated using two-way ANOVA method performed with GraphPad Prism (Version 8, GraphPad Software, La Jolla, CA, USA) and Tukey's multiple comparisons test and the results were considered significant when the  $p$ -value was less than 0.05 (\*), 0.01 (\*\*), 0.001 (\*\*\*)

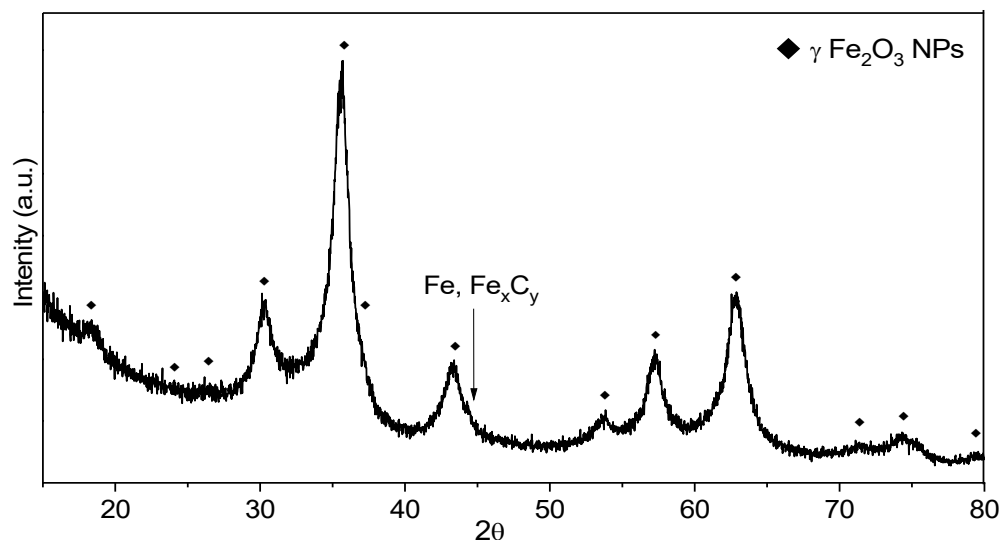
## 3. Results

### 3.1. Physicochemical Analysis

#### 3.1.1. Nanoparticle Characterization

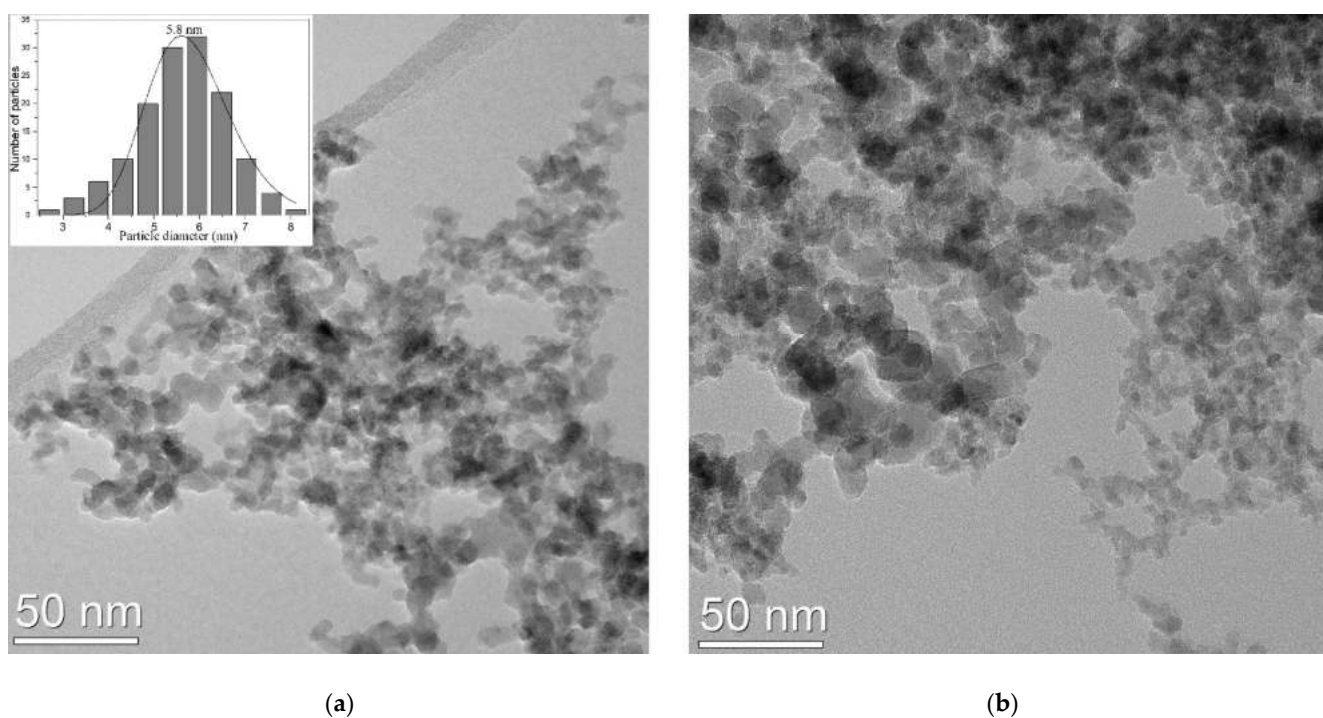
The X-ray diffractogram (Figure 3) of the synthesized powder sample indicated its nanophase feature and the crystalline structure can be assigned to  $\gamma$ -Fe<sub>2</sub>O<sub>3</sub>/Fe<sub>3</sub>O<sub>4</sub> phases: the position of theoretical diffraction peaks is illustrated with diamonds. The positions ( $2\theta$ ), and the full width at half maximum (B) of most relevant 5 peaks: (220), (311), (400), (511) and (440) were evaluated using pseudo-Voigt functions and OriginPro 2015 software. The mean value for the constant lattice was 8360 Å. The closest reference structure with that found for our sample is the  $\gamma$ -Fe<sub>2</sub>O<sub>3</sub> phase having PDF file: 00-039-1346 and a constant lattice of 8352 Å, whereas the magnetite (Fe<sub>3</sub>O<sub>4</sub>) phases have larger values (between 8.39 and 8.40 Å).

Based on the most intense peak at  $2\theta = 35.6^\circ$  associated with (311) plane and on the second one as the intensity at  $2\theta = 63.0^\circ$  associated with (440) plane, the mean crystal size of as synthesized NPs was found to be 5.7 nm and 6.1 nm according to the Debye-Scherrer equation:  $D_{hkl} = k \lambda / B \cos\theta$ . Here,  $D_{hkl}$  is crystallite size,  $k$  is the shape constant of typical 0.9 in most evaluations for quasi-spherical particles and  $\lambda$  is the wavelength of the X-ray. The presence of other iron-based crystalline phases (ex.  $\alpha$ Fe or Fe carbides) is not certain, their eventually minor contribution being masked by the background noise.



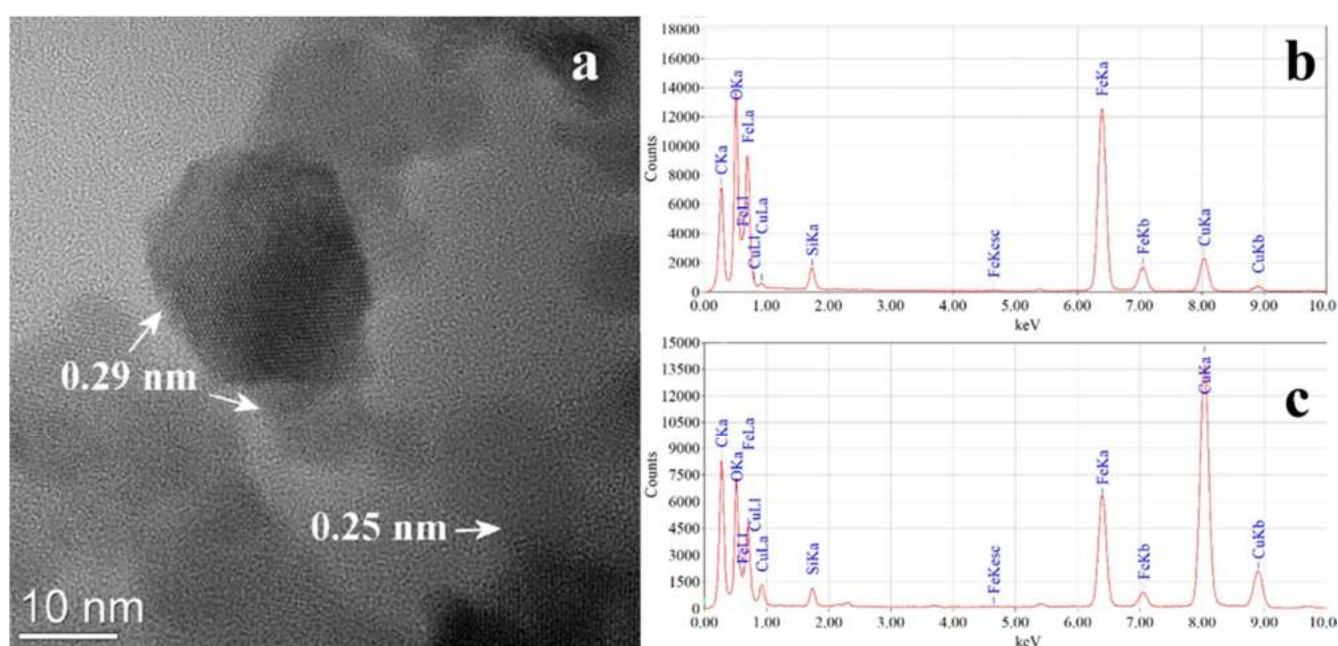
**Figure 3.** XRD patterns for as synthesized FeO1 nanoparticles (NPs).

The TEM image at medium resolution from the as synthesized NPs (Figure 4a) showed in majority quasi-spherical structures which appear to have a diameter between 3–9 nm with a particles distribution well fitted with log-normal function and a mean value of 5.8 nm (left inset). The NPs, probably due to their magnetic properties, were self-organized in loose agglomerates/aggregates containing hundreds of entities. In the case of porphyrin functionalized NPs on copper grid, visualized by TEM in Figure 4b, the NPs agglomerates contained particles with almost the same dimensions, with a mean diameter of 6.2 nm, having more compact zones, yet with no evidence of solid segregation of porphyrin-based bridges between NPs or separate clusters. The most probable spreading of adsorbed porphyrins at the NPs surface almost as single molecular layer can be the explanation of this very weak mean diameter NPs increase.



**Figure 4.** TEM images of the NPs (a) as synthesized nanoparticles (b) aggregates of NPs functionalised with TPPS.

As it can be seen from the presented HR-TEM image, (Figure 5a) the functionalized particles are spherical or polyhedral, the size of those identified here varying from 12 to 5 nm. The particles are mostly crystalline as monodomain and the observed interplanar distances can be ascribed to the (220) and (311) planes of  $\gamma\text{Fe}_2\text{O}_3/\text{Fe}_3\text{O}_4$  at 0.29 nm (2.96 Å) and 0.25 nm (2.52 Å) respectively. From both microscopes, NPs covered grids EDS analyzes were performed in different places where the NPs agglomerates are not attached to the original amorphous carbon layer of the TEM grids. Qualitatively the presence of O, Fe, and a minor contribution C was detected, all derived from NPs. The presence of S and the major contribution of C comes from the adsorbed pseudo-porphyrin whose molecules contain  $-\text{SO}_3^-$  groups. The other elements appear as an artefact from the grids (Cu) or sample manipulation (Si). The constant presence of sulphur peak in EDS spectra from different places of the grid and also an intensity ratio between Fe-K $\alpha$  and S-K $\alpha$  peaks between 25 to 35 was used by us as an instrument to optimize the preparation process for NPs functionalized suspension.



**Figure 5.** HR (high resolution) TEM Image of NPs functionalized with TPPS (a) and EDS spectra for synthesized NPs (b), and NPs functionalized with TPPS (c).

A thin (less than 0.1 mm thick) pellet prepared by cold pressing from the as synthesized sample was analyzed by EDS as SEM facility in order to evaluate the elemental composition. Mediating the values from three different positions the following elemental composition was determined: C-0.63 at. %, O-58.60 at. %, and Fe-40.77 at.%. The Fe/O ratio from these values matches  $\text{Fe}_2\text{O}_{3-0.13}$  stoichiometry.

Regarding the mean hydrodynamic size (Table 2), DLS measurements of the 0.5 g/L suspensions showed values of 138.0 nm for iron oxide nanoparticles and this value is consistent with the aggregate sizes measured at TEM investigation at low resolution. The higher value for the  $\gamma\text{-Fe}_2\text{O}_3$  NPs\_TPPS suspension (453 nm) could be explained by coalescence and compactization phenomena of the initial NPs aggregates due to the strong centrifugated forces acting during the purification process; an effect that cannot be fully reversed by using the ultrasound redispersion.

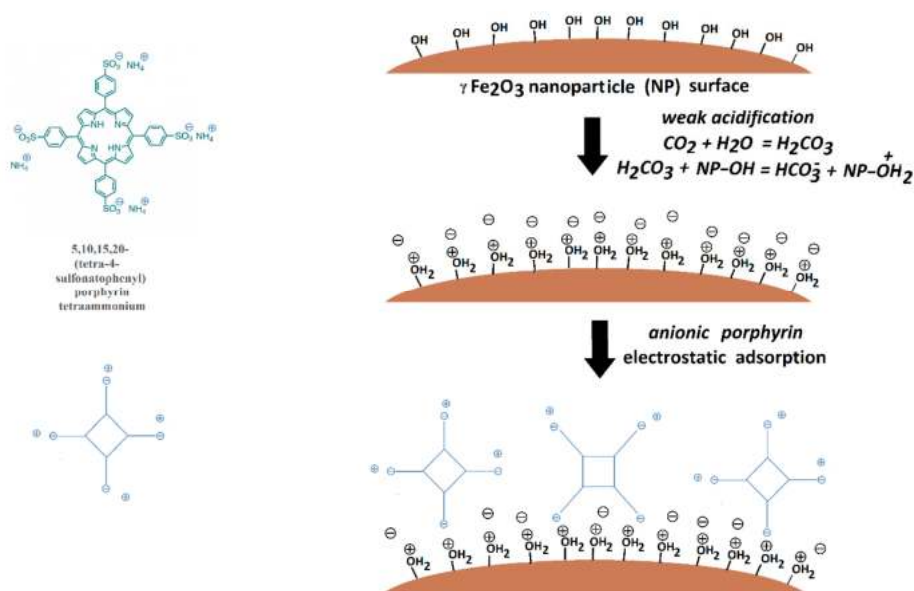
**Table 2.** The mean hydrodynamic size of the samples.

Sample	PI	Z-Average	Distribution Form
$\gamma$ -Fe <sub>2</sub> O <sub>3</sub> NPs	0.340	138.0 nm	Broad polydisperse
$\gamma$ -Fe <sub>2</sub> O <sub>3</sub> NPs_TPPS	0.414	453.1 nm	

Zeta potential values (Table 3) indicated good stability for  $\gamma$ -Fe<sub>2</sub>O<sub>3</sub> NPs (50.9 mV) and an excellent one for  $\gamma$ -Fe<sub>2</sub>O<sub>3</sub> NPs\_TPPS suspension (−90.9 mV) in slightly acidic dis-tilled water (due to dissolved CO<sub>2</sub> from the atmosphere). This result can be explained by the electrostatic adsorption of the negatively charged surface porphyrin onto the iron oxide nanoparticles surface. A schematic diagram explaining the process was pro-posed in Figure 6.

**Table 3.** Zeta potential values for the  $\gamma$ -Fe<sub>2</sub>O<sub>3</sub> NPs and  $\gamma$ -Fe<sub>2</sub>O<sub>3</sub> NPs\_TPPS samples

Sample	$\gamma$ -Fe <sub>2</sub> O <sub>3</sub> NPs	$\gamma$ -Fe <sub>2</sub> O <sub>3</sub> NPs_TPPS
Zeta Potential (Mean)	50.9 mV	−90.9 mV
Electrophoretic Mobility Mean	0.000394 cm <sup>2</sup> /Vs	−0.000704 cm <sup>2</sup> /Vs

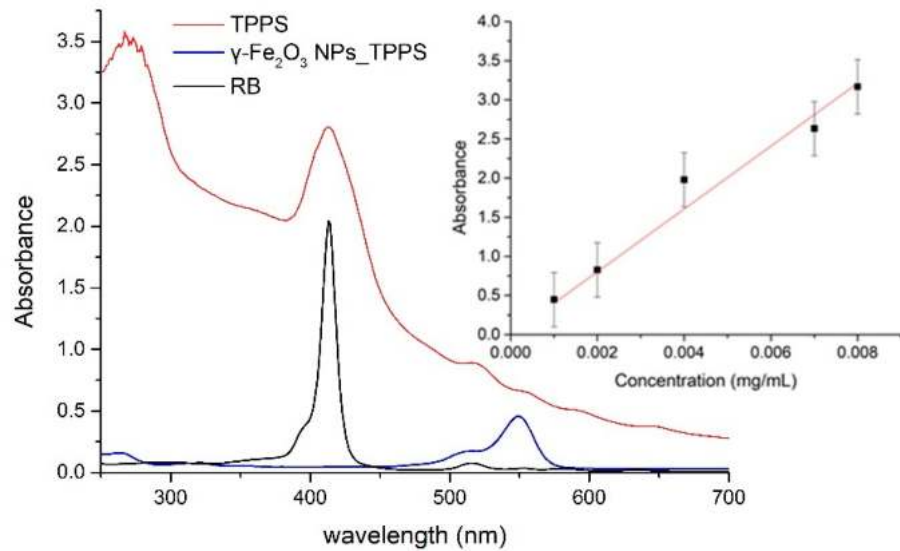


**Figure 6.** Schematic diagram of the adsorption process of the TPPS of the  $\gamma$ -Fe<sub>2</sub>O<sub>3</sub> surface.

### 3.1.2. Spectroscopic Analysis

#### Absorption Spectroscopy

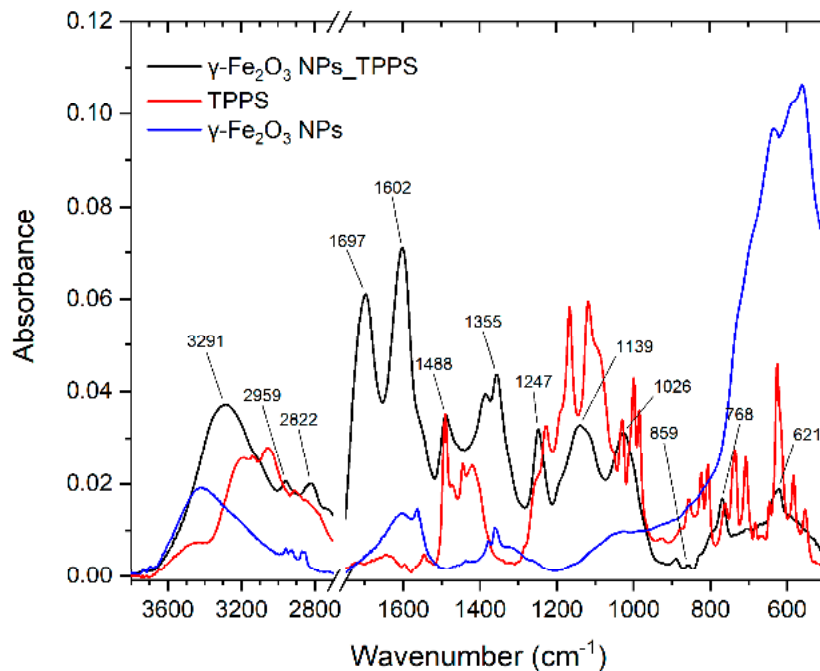
In Figure 7, the absorption spectrum for a TPPS solution in distilled water at concentration 0.004mg/mL is shown in comparison with the absorption spectrum for the water suspension of  $\gamma$ -Fe<sub>2</sub>O<sub>3</sub> nanoparticles functionalized with TPPS (0.0138 mg/mL concentration of iron nanoparticles). The absorption features of porphyrin with maxima at 413 nm, 518 nm, 555 nm, and 649 nm are clearly present in the spectrum of nanoparticles suspension and proves the  $\gamma$ -Fe<sub>2</sub>O<sub>3</sub> NPs and TPPS functionalization. In the inset of Figure 7, the standard curve for TPPS determined by the absorbance values for the peak at 413 nm at several concentrations is shown. Taking into account the absorbance of 1.04 for the  $\gamma$ -Fe<sub>2</sub>O<sub>3</sub> NPs\_TPPS suspension at 413 nm (background given by NPs diffusion subtracted), we can extrapolate from the standard curve a TPPS concentration of 0.0025 mg/mL in the  $\gamma$ -Fe<sub>2</sub>O<sub>3</sub> NPs\_TPPS complexes.



**Figure 7.** The absorption spectra for investigated samples: TPPS solution in distilled water at 0.004 mg/mL,  $\gamma$ - $\text{Fe}_2\text{O}_3$  NPs\_TPPS water suspension, RB solution at 0.004 mg/mL in distilled water. In the inset, the standard curve of TPPS absorbance versus concentration is shown.

The samples were investigated by FTIR spectroscopy to highlight the functionalization of the nanoparticles with the TPPS.

Figure 8 displays the FT-IR spectra of TPPS,  $\gamma$ - $\text{Fe}_2\text{O}_3$  NPs, and complex  $\gamma$ - $\text{Fe}_2\text{O}_3$  NPs\_TPPS.



**Figure 8.** FT-IR spectra of TPPS,  $\gamma$ - $\text{Fe}_2\text{O}_3$  NPs, and  $\gamma$ - $\text{Fe}_2\text{O}_3$  NPs\_TPPS.

The characteristics IR vibration of TPPS molecule were identified based on the existing literature [42–45] and the calculation molecular structure using Gaussian09 software. Table 4 presents the vibrational extracted from the experimental and theoretical spectra and their corresponding mode of vibration.

The IR spectra of TPPS presents the characteristic vibrations of the TPPS ring and the four  $\text{SO}_3^-$  groups connected to the molecule phenyl moiety [42–45]. The N–H stretching vibration is identified at  $3196\text{ cm}^{-1}$  and  $3133\text{ cm}^{-1}$  and C–H stretching vibration is observed

at 3056  $\text{cm}^{-1}$  and 2907  $\text{cm}^{-1}$ . The bands at 1490  $\text{cm}^{-1}$  and 1643  $\text{cm}^{-1}$  are attributed to the stretching vibration of C–C and C=C bonds in the benzene ring corresponding to sulfonatophenyl radical and TPPS ring. The in-plane deformation vibration of C=C and C=N from the TPPS ring is observed at 1398  $\text{cm}^{-1}$ . The band at 1250  $\text{cm}^{-1}$  represents the C–C stretching vibration between the aryl groups and the TPPS ring. The asymmetrical  $\text{SO}_3$  stretching vibrations are identified in the 1200–1100  $\text{cm}^{-1}$  spectral range, with two intense bands at 1165  $\text{cm}^{-1}$  and 1117  $\text{cm}^{-1}$  [42]. The 1003  $\text{cm}^{-1}$  and 738  $\text{cm}^{-1}$  are assigned to N–H wagging vibration, whereas the band with peak at 624  $\text{cm}^{-1}$  is attributed to the C–H wagging vibration of the benzene rings and deformation vibration of the TPPS ring.

**Table 4.** Experimental and theoretical vibration frequencies for TPPS with their corresponding modes of vibrations.

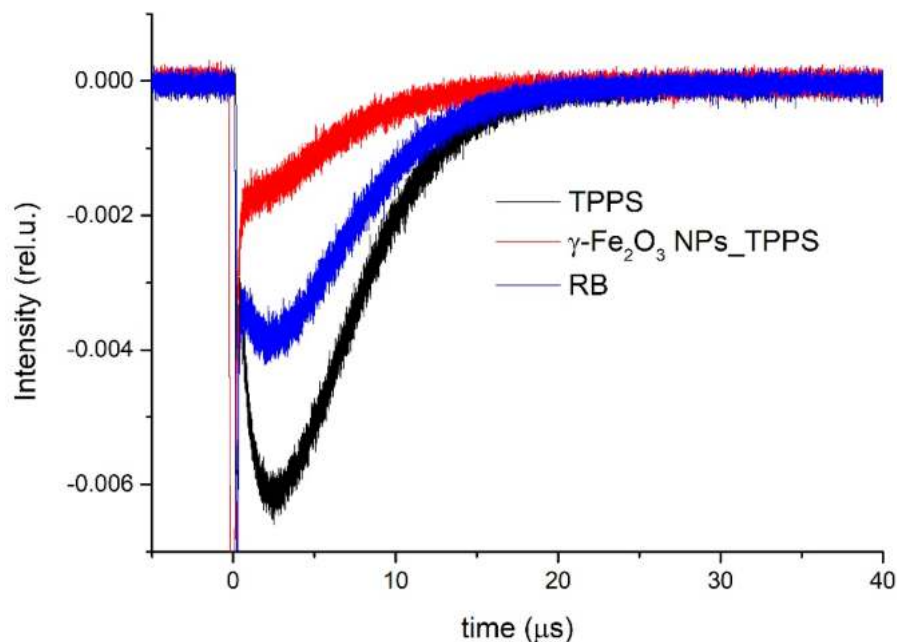
Wavenumber ( $\text{cm}^{-1}$ )		Mode of Vibration
Experimental	Theoretical	
1643	1620	stretching vibration of C–C and C=C bond (sulfonatophenyl radical)
1544	1559	stretching vibration of C–C and C=C bond (porphyrin ring/sulfonatophenyl radical)
1490	1477	stretching vibration of C–C and C=C bond (porphyrin ring/sulfonatophenyl radical)
1443	1436	stretching vibration of C–C and C=C bond (sulfonatophenyl radical)
1418	1416	stretching vibration of C–C and C=C bond (porphyrin ring)
1398	1346	in-plane deformation vibration of C=C and C=N (porphyrin ring)
1250	1252	C–C stretching vibration
1226	1213	C–H deformation vibration
1165	1154	symmetrical stretching vibrations S–O
1117	1124	asymmetrical stretching vibrations S–O
1025	1036	N–H and C–H deformation vibrations
998	1003	N–H wagging vibration
984	985	N–H and C–H deformation vibrations (porphyrin ring)/deformation vibrations of 4 neighbouring H-atoms (sulfonatophenyl radical)
855	839	deformation vibrations of 4 neighbouring H-atoms (sulfonatophenyl radical)
805	804	deformation vibrations of 4 neighbouring H-atoms (sulfonatophenyl radical) C–C skeletal vibration (porphyrin ring)
760	767	deformation vibrations of 4 neighbouring H-atoms (sulfonatophenyl radical)
734	740	deformation vibrations of 4 neighbouring H-atoms (sulfonatophenyl radical)
681	683	N–H wagging vibration
645	647	C–C skeletal vibration (sulfonatophenyl radical)
624	618	N–H wagging vibration
581	576	S–O wagging vibration

The IR spectrum of NP shows a broad peak at 3417  $\text{cm}^{-1}$  attributed to intermolecular hydrogen bond stretching vibration as the nanoparticle surface adsorbed the water. Further, this is supported by the appearance of the band with a peak at 1608  $\text{cm}^{-1}$  representing the O–H bending vibration of water molecules adsorbed on iron nanoparticles [46–48]. The bands with peaks at 2957  $\text{cm}^{-1}$ , 2925  $\text{cm}^{-1}$ , and 2870  $\text{cm}^{-1}$  correspond to the C–H stretching vibration, whereas the peaks at 1377  $\text{cm}^{-1}$  and 1360  $\text{cm}^{-1}$  are attributed to the C–H deformation vibration. In the range 770–450  $\text{cm}^{-1}$  is observed the stretching mode characteristic to Fe–O bond vibrations, with a peak at 560  $\text{cm}^{-1}$ .

In the  $\gamma\text{-Fe}_2\text{O}_3$  NPs\_TPPS complex IR spectrum are identified the characteristic bands of TPPS at 1488  $\text{cm}^{-1}$ , 859  $\text{cm}^{-1}$ , 768  $\text{cm}^{-1}$ , 620  $\text{cm}^{-1}$  and of  $\gamma\text{-Fe}_2\text{O}_3$  are identified at 1601  $\text{cm}^{-1}$ , 1374  $\text{cm}^{-1}$ , and 1355  $\text{cm}^{-1}$ . The biggest changes are observed for the C–H and N–H vibrations of the TPPS ring. The bands at 1643  $\text{cm}^{-1}$  and 734  $\text{cm}^{-1}$  from the TPPS spectrum, related to stretching vibration of C–C/C=C and to N–H wagging vibration bonds from the TPPS ring, are shifted to 1697  $\text{cm}^{-1}$  and 768  $\text{cm}^{-1}$  in the  $\gamma\text{-Fe}_2\text{O}_3$  NPs\_TPPS complex IR spectrum. This indicates the interactions of TPPS with the surface of  $\gamma\text{-Fe}_2\text{O}_3$  NPs that results in the stiffening of the TPPS ring [42,49] due to functionalization. More, a new band at 1247  $\text{cm}^{-1}$  appears that indicates the functionalization of TPPS to  $\gamma\text{-Fe}_2\text{O}_3$  due to the interaction of –OH of  $\gamma\text{-Fe}_2\text{O}_3$  with –NH from the TPPS ring.

### Singlet Oxygen Generation

Figure 9 shows the transient phosphorescence decay curves measured at 1270 nm for the singlet oxygen generated by the TPPS solution in distilled water,  $\gamma$ -Fe<sub>2</sub>O<sub>3</sub> NPs\_TPPS water suspension, and RB solution at 0.004 mg/mL in distilled water used as reference. The last has a known value of oxygen singlet quantum yield in water of 0.75 [50].



**Figure 9.** Time-resolved phosphorescence signals of singlet oxygen generated by the investigated samples.

The phosphorescence signals were registered in the same experimental configuration and conditions for all investigated samples and averaged over 1000 laser shots. To avoid saturation effects, low energy of the laser excitation radiation of 3 mJ per pulse was used.

Using  $\Phi_{\Delta}^{ref}$  value for RB in water of 0.75 [50] and Equation (1), we determined the quantum yield for singlet oxygen generation by  $\gamma$ -Fe<sub>2</sub>O<sub>3</sub> NPs\_TPPS complexes in water suspensions of 0.6. Also, the quantum yield of singlet oxygen generation by TPPS in water was found to be 0.8.

### 3.2. ADME-Tox Predictions

Since the compound is carried using the NP (so the Absorption and Distribution of the molecule may change), we focused on his toxicity. AdmeSAR and pkCSM predict that TPPS is soluble in water. TPPS has a 0.43 probability to be subcellular localized in the lysosome. Predictions show that this compound has a RatLD50 of 2.47 mol/kg according to admeSAR and 3066 mg/kg according to ProTox-II. This compound has a low toxicity class and probably is inactive as a carcinogen, immunotoxic, cytotoxic or mutagenic compound.

TPPS is inactive on the AhR receptor, the activation of this receptor being linked to immunosuppression, thymic involution, and immunotoxicity via transcriptional alterations [51]. The decrease of the mitochondrial membrane potential is associated with apoptosis [52], the prediction of inactivity of the TPPS derivative on mitochondrial membrane potential could suggest that this compound may not produce apoptosis.

TPPS is also inactive on p53 and ATAD5. Regarding hepatotoxicity, pkCSM and ProTox-II web services reported that this compound is not hepatotoxic. Overall, according to predictions made, TPPS is a non-toxic compound. We present the predicted results in Table 5.

**Table 5.** Toxicity predictions for TPPS4, using admeSAR pkCSM and ProTox-II webservices.

pkCSM			
Model	Predicted Values	Unit	
Water solubility	−2.892	log mol/L	
Hepatotoxicity	No	Yes/No	
admeSAR			
Model	Results	Probability	
Subcellular localization	Lysosome	0.4395	
Model	Predicted values	Unit	
Aqueous solubility	−3.3743	LogS	
Rat Acute Toxicity	2.4748	LD50, mol/kg	
ProTox-II			
Model	Predicted values	Unit	
Predicted LD50	3066	mg/kg	
Predicted Toxicity Class	5	1-bad 6-good	
Model	Results	Probability	
Hepatotoxicity	Inactive	0.65	
Carcinogenicity	Inactive	0.68	
Immunotoxicity	Inactive	0.96	
Mutagenicity	Inactive	0.62	
Cytotoxicity	Inactive	0.75	
Aryl hydrocarbon Receptor (AhR)	Inactive	0.78	
Mitochondrial Membrane Potential	Inactive	0.85	
Phosphoprotein p53	Inactive	0.86	
ATPase family AAA domain-containing protein 5 (ATAD5)	Inactive	0.94	

### 3.3. Molecular Docking Simulations

Molecules with estimated binding energy greater than  $-6$  kcal/mol have no biological action on that target [53,54]. When TPPS interacts with Pro-caspase3, our results show that it has the lowest predicted binding energy  $-9.31$  kcal/mol (Table 6).

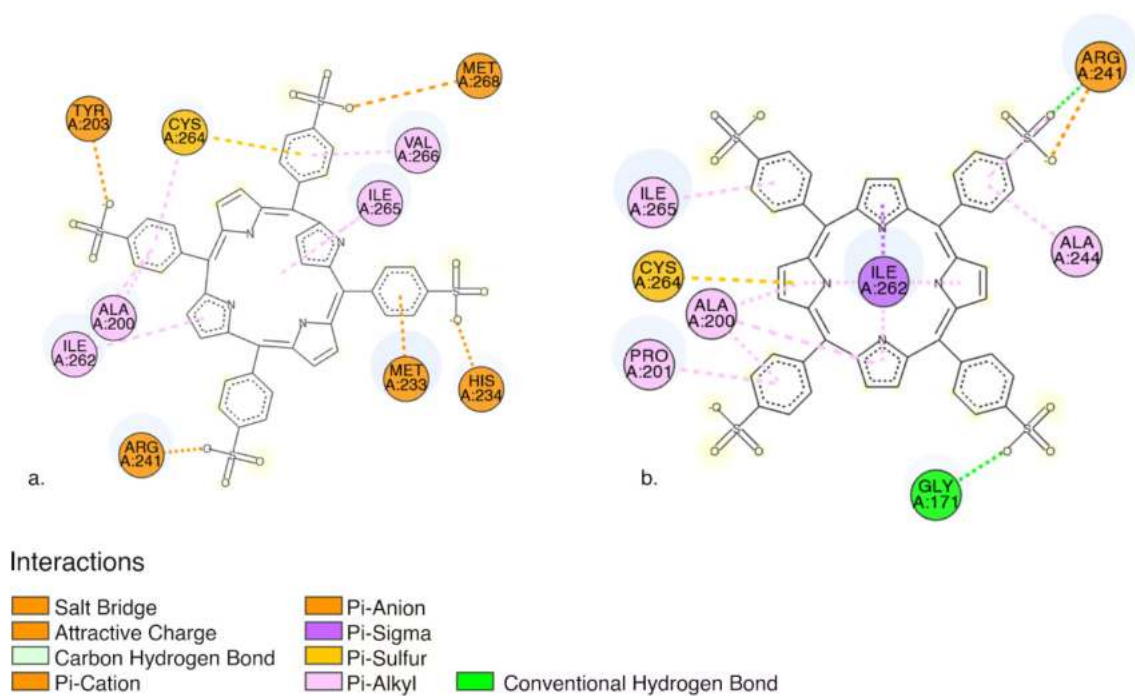
**Table 6.** Predicted lowest free energy of binding expressed in kcal/mol and inhibition constant ( $K_I$ ) expressed in nanomolar (nM) for pro-caspase 3 and caspase 3.

Target	Estimated Lowest Free Energy of Binding (kcal/mol)	$K_I$ (nM)
Pro-caspase 3	−9.31	150.72
Caspase 3	−7.74	2120

Pro-caspase 3 has the lowest predicted binding energy compared to caspase 3, implying that TPPS will most likely bind to pro-caspase (Table 6). In both cases, between TPPS and caspases, we obtained favorable interactions as follows: (i) non-classical carbon-hydrogen bond, (ii) electrostatic interactions, (iii) charge interactions: salt bridge, and attractive charge; (iv) Pi-charge: Pi-cation and Pi anion; (v) hydrophobic: Pi- Alkyl, Pi-Sigma interactions; and (iv) miscellaneous Pi-sulphur interactions (Figure 10).

The interaction situs in both cases is quite similar both pro-caspase 3 and caspase 3 form favourable interactions with amino acid residues: Ala200, Arg241, Ile 262, Cys264, Ile 265 (Figure 10).



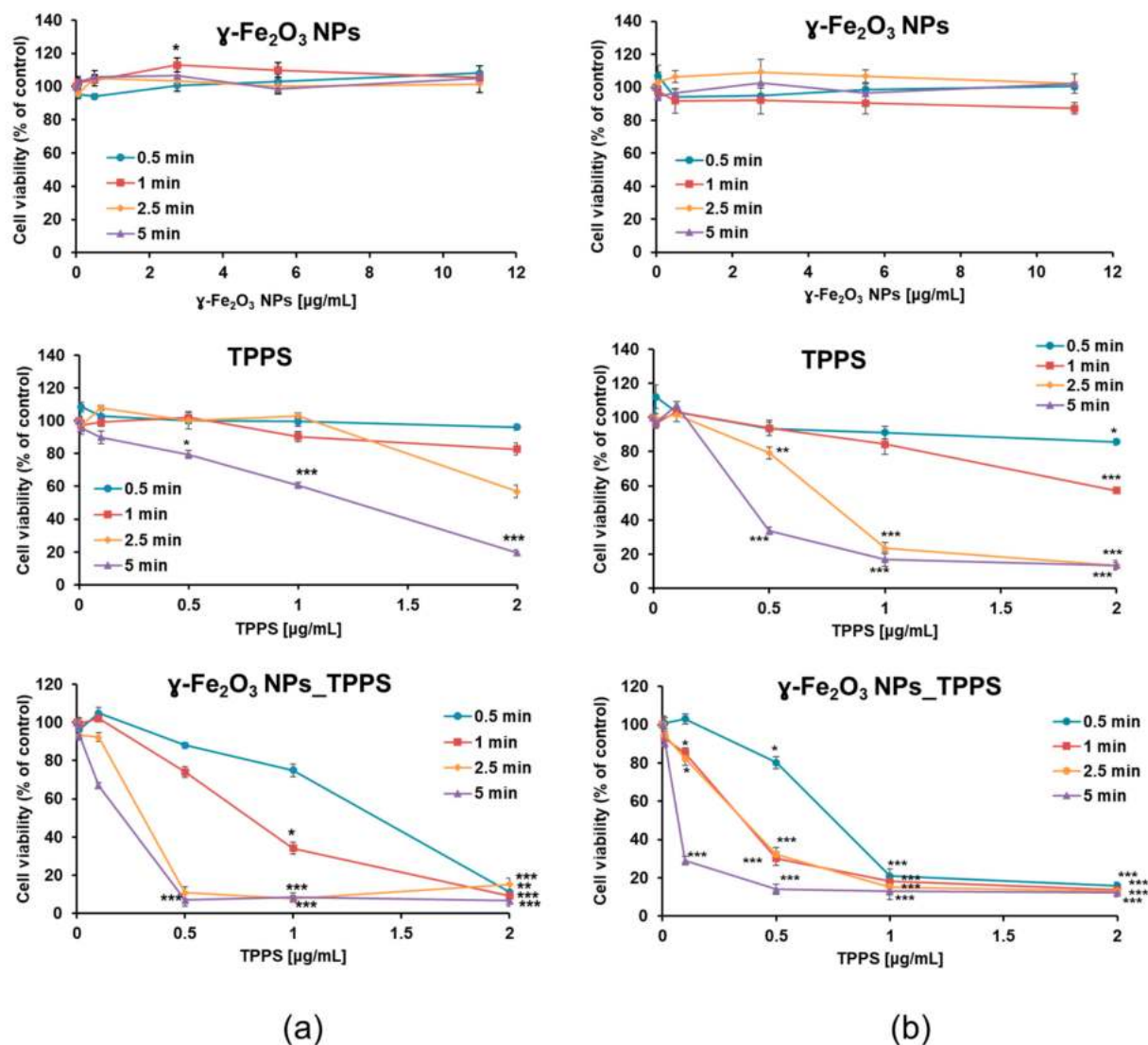


**Figure 10.** 2D visualization of (a) interactions between TPPS and pro-caspase3 amino acid residues (b) interactions between TPPS and caspase3 amino acid residues. The image was obtained using Discovery studio visualizer. (Dassault Systèmes (V20.1.0.19295), San Diego, CA, USA).

### 3.4. In Vitro Biological Studies

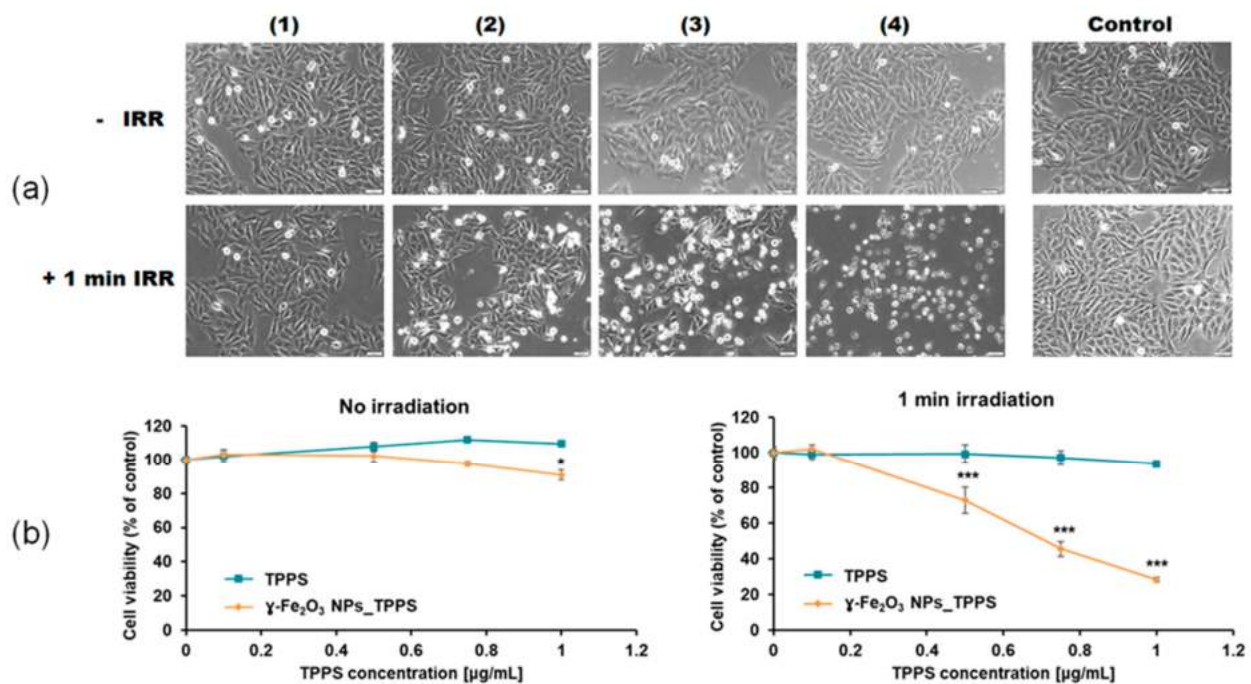
#### 3.4.1. Phototoxicity and Cell Morphologic Alterations

The photodynamic activity of  $\gamma\text{-Fe}_2\text{O}_3$  NPs\_TPPS complexes was evaluated in comparison with that of the individual components of the system and performed by MTT assay. After 24 h after treatment, the Mel-Juso cells were washed and then irradiated at 405 nm at 2 different power densities of 1 mW/cm<sup>2</sup> (Figure 11) and respectively, 2 mW/cm<sup>2</sup> (Figure 11b) for different time intervals (0.5, 1, 2.5 and 5 min). After irradiation, cells were incubated for another 24 h. As demonstrated in Figure 11, the phototoxicity of TPPS and  $\gamma\text{-Fe}_2\text{O}_3$  NPs\_TPPS on melanoma cells increased with the elevation of led power density and irradiation time. Moreover, the suppression of cell viability was dependent on the TPPS concentration. For example, the viability of cells exposed to 1  $\mu\text{g}/\text{mL}$  TPPS decreased by 40% compared to control after 5 min irradiation with 1 mW/cm<sup>2</sup> power density and by 80% when exposed to 2  $\mu\text{g}/\text{mL}$  in the same conditions. The results revealed that none of the applied conditions had a significant effect on cells treated with free  $\gamma\text{-Fe}_2\text{O}_3$  NPs, except for a slight increase corresponding to the dose of 2.75  $\mu\text{g}/\text{mL}$ , thus demonstrating their biocompatibility. However, the phototoxicity of TPPS was significantly enhanced in the presence of NPs. A pronounced reduction of cell viability was observed starting with a dose of 0.5  $\mu\text{g}/\text{mL}$  TPPS in cells incubated with  $\gamma\text{-Fe}_2\text{O}_3$  NPs\_TPPS compared with the one with free TPPS. As shown in Figure 11b, at 2 mW/cm<sup>2</sup> power density, regardless the irradiation time, cells that were treated with a concentration higher than 1  $\mu\text{g}/\text{mL}$  TPPS presented a very significant decrease of cellular viability. In comparison, at 1 mW/cm<sup>2</sup> power density, a higher percentage of cells survived only when irradiated for 0.5 and 1 min. Based on these results, irradiation of cells at 1 mW/cm<sup>2</sup> power density for 1 min was considered the most suitable setup for the next determinations.



**Figure 11.** Variation of Mell-Juso cell viability depending on irradiation time (min), led power density ( $\text{mW}/\text{cm}^2$ ) and treatment dose. Cells were incubated for 24 h with  $\gamma\text{-Fe}_2\text{O}_3$  NPs, TPPS and their complex at different concentrations and then irradiated for 0.5, 1, 2.5 and 5 min at (a) 1 and respectively (b) 2  $\text{mW}/\text{cm}^2$  power densities. After 24 h from irradiation cell viability was evaluated by MTT assay. Data ( $n = 3$ ) were expressed as percentages related to control (100%)  $\pm$  standard deviation (SD). The results were considered statistically significant when \*  $p < 0.05$ ; \*\*  $p < 0.01$ ; \*\*\*  $p < 0.001$  (sample vs. control).

Using these selected parameters, we evaluated the morphologic aspect of Mel-Juso cells and their viability after incubation with  $\gamma\text{-Fe}_2\text{O}_3$  NPs\_TPPS complexes and LED irradiation (Figure 12a,b). The morphologic aspect of non-irradiated cells was similar to that of the control, which is characteristic for epithelial cells presenting smooth, unruffled borders. When cells were irradiated for 1 min, the cells changed their aspect dependent by TPPS concentration. A significant decrease of cell density was noticed after incubation of cells with  $\gamma\text{-Fe}_2\text{O}_3$  NPs\_TPPS complexes starting from a dose of 0.5  $\mu\text{g}/\text{mL}$  TPPS. As observed in Figure 12a, plenty of cells detached from the substrate acquiring a round shape with irregular borders. Non-specific cell extensions and apoptotic vesicles were also detected at a dose higher than 0.75  $\mu\text{g}/\text{mL}$  TPPS.



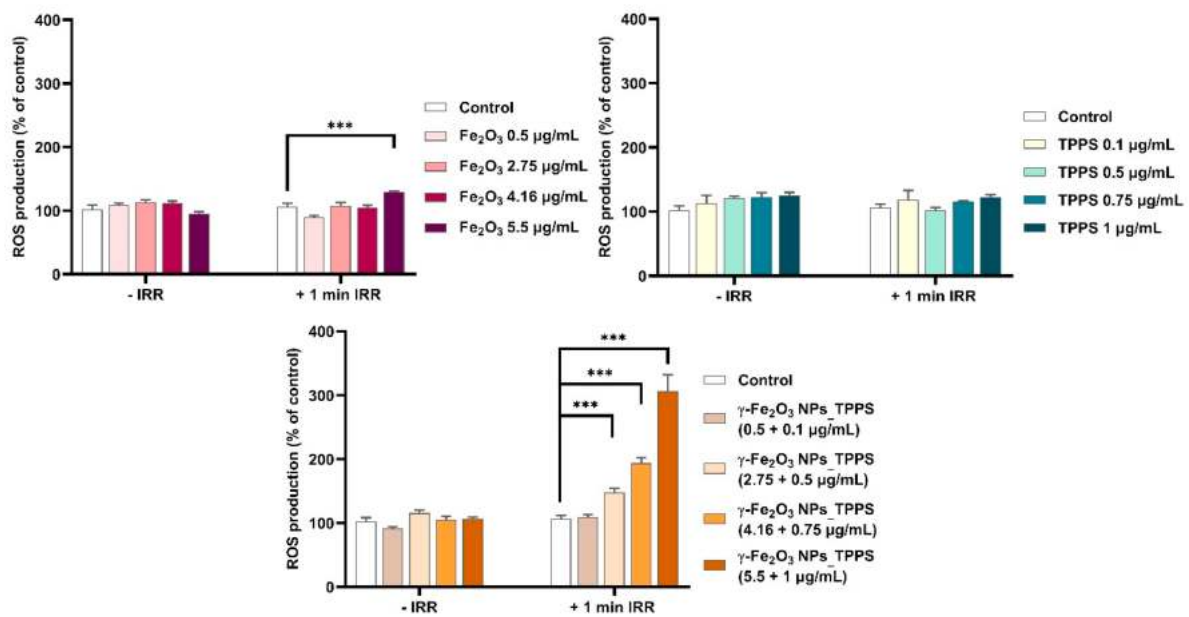
**Figure 12.** The effect of no irradiation vs. irradiation ( $\lambda \sim 405$  nm,  $1$  mW/cm<sup>2</sup>,  $1$  min) conditions on morphology and viability of treated Mel-Juso cells. (a) Bright-field images of Mel-Juso cells after 24 h exposure to different concentration of  $\gamma\text{-Fe}_2\text{O}_3$  NPs\_TPPS complex: (1)  $0.5$   $\mu\text{g/mL}$  NPs and  $0.1$   $\mu\text{g/mL}$  TPPS; (2)  $2.75$   $\mu\text{g/mL}$  NPs and  $0.5$   $\mu\text{g/mL}$  TPPS; (3)  $4.16$   $\mu\text{g/mL}$  NPs and  $0.75$   $\mu\text{g/mL}$  TPPS; (4)  $5.5$   $\mu\text{g/mL}$  NPs and  $1$   $\mu\text{g/mL}$  TPPS and subjected or not to led irradiation. Magnification 10X. Scale bar is  $50$   $\mu\text{m}$ . (b) Cell viability of Mel-Juso cells after 24 h incubation with TPPS and  $\gamma\text{-Fe}_2\text{O}_3$  NPs\_TPPS complex at different concentrations. Data ( $n = 3$ ) were expressed as percentages related to control  $\pm$  standard deviation (SD). The results were considered statistically significant when \*  $p < 0.05$ ; \*\*\*  $p < 0.001$  (sample vs. control).

The alterations noticed in the microscopic images were confirmed by MTT assay (Figure 12b). Without irradiation, exposure of Mel-Juso cells to  $\gamma\text{-Fe}_2\text{O}_3$  NPs\_TPPS complexes or free TPPS generated no significant toxicity except for the dose of  $1$   $\mu\text{g/mL}$   $\gamma\text{-Fe}_2\text{O}_3$  NPs\_TPPS complexes where viability slightly decrease by 10%. When irradiated, melanoma cells incubated with  $\gamma\text{-Fe}_2\text{O}_3$  NPs\_TPPS complexes presented a 45% viability compared to control at a dose of  $0.75$   $\mu\text{g/mL}$  TPPS. However, no significant changes were observed for cells incubated with free TPPS.

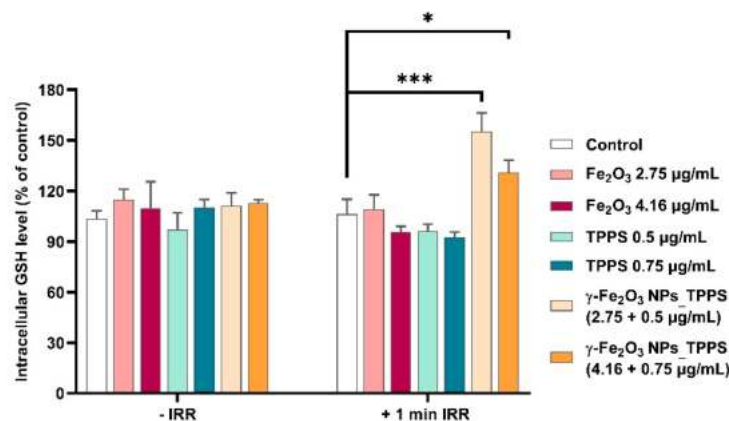
### 3.4.2. ROS Production and Antioxidant Protection

PDT-induced cell death generally occurs through the generation of intracellular ROS. Therefore, we measured intracellular ROS levels in melanoma cells to evaluate the photodynamic activity of synthesized complexes. As shown in Figure 13, under irradiation, the ROS production increased significantly in a dose-dependent manner in cells treated with  $\gamma\text{-Fe}_2\text{O}_3$  NPs\_TPPS complexes starting with a dose of  $2.75$   $\mu\text{g/mL}$  NPs and  $0.5$   $\mu\text{g/mL}$  TPPS respectively. Interestingly, no change of ROS level was detected in cells treated with free TPPS or  $\gamma\text{-Fe}_2\text{O}_3$  NPs excepting the highest dose of NPs where a slight elevation of ROS production was found. In non-irradiated conditions, the level of ROS in treated cells was similar to that of control.

In order to evaluate the antioxidant defense response of treated cells exposed or not to irradiation, the intracellular GSH level was measured (Figure 14). When irradiation was applied for  $1$  min, the GSH level increased significantly by 55% and 31% respectively compared to control in cells treated with the two selected doses of  $\gamma\text{-Fe}_2\text{O}_3$  NPs\_TPPS. In cells that were not exposed to LED light, we found that the GSH content of treated cells was almost similar to the one measured in control cells.



**Figure 13.** Intracellular ROS production after incubation for 24 h with different concentrations of  $\gamma$ -Fe<sub>2</sub>O<sub>3</sub> NPs, TPPS and their complex and exposure to no irradiation vs. 1 min irradiation ( $\lambda \sim 405$  nm, 1 mW/cm<sup>2</sup>) conditions. Data ( $n = 3$ ) were expressed as percentages related to control  $\pm$  standard deviation (SD). The results were considered statistically significant when  $*** p < 0.001$  (sample vs. control).

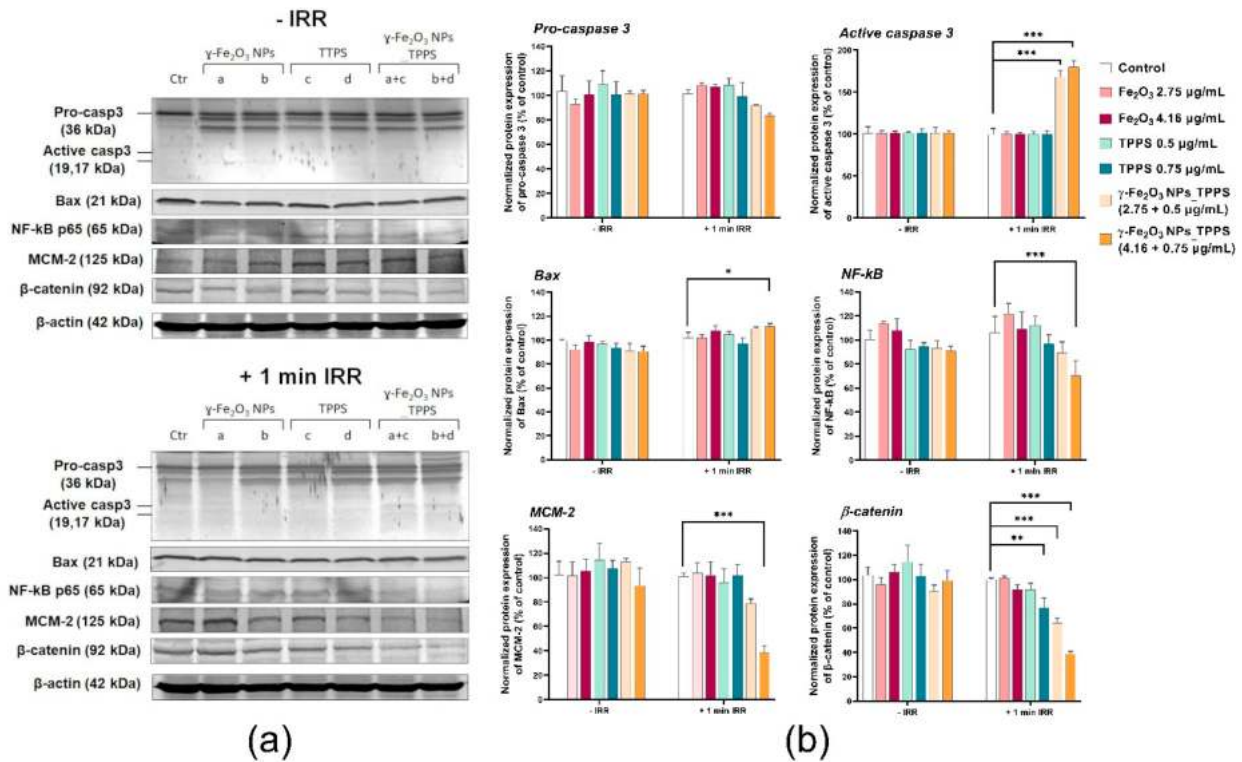


**Figure 14.** Variation of reduced glutathione (GSH) content in Mel-Juso cells incubated for 24 h with 2 different doses of  $\gamma$ -Fe<sub>2</sub>O<sub>3</sub> NPs, TPPS and their complex and submitted or not to 1 min led irradiation ( $\lambda \sim 405$  nm, 1 mW/cm<sup>2</sup>). Data ( $n = 3$ ) were expressed as percentages related to control  $\pm$  standard deviation (SD). The results were considered statistically significant when  $* p < 0.05$ ;  $*** p < 0.001$  (sample vs. control).

### 3.4.3. Protein Expression of Proliferation, Cell Adhesion and Apoptosis-Related Markers

To demonstrate the anti-tumor potential of  $\gamma$ -Fe<sub>2</sub>O<sub>3</sub> NPs\_TPPS in combination with LED irradiation, Western blotting analysis was performed on three apoptosis-related proteins, caspase 3, Bax and NF- $\kappa$ B, a proliferation marker MCM-2 and a component of adherens junctions, that promotes cell adhesion,  $\beta$ -catenin (Figure 15). The results showed a significant decrease of MCM-2 and  $\beta$ -catenin protein levels dependent on TPPS concentration in the Mel-Juso cells treated with  $\gamma$ -Fe<sub>2</sub>O<sub>3</sub> NPs\_TPPS and irradiated for 1 min at 1 mW/cm<sup>2</sup> power density. A slight decrease was also noticed in cells treated with free TPPS in a dose of 0.75  $\mu$ g/mL. No significant changes in the expression of these two proteins were observed in any of the other conditions. The protein level of pro-caspase 3 decreased concomitantly with the increase of caspase 3 expression, resulting in apoptosis activation in Mel-Juso cells treated with  $\gamma$ -Fe<sub>2</sub>O<sub>3</sub> NPs\_TPPS complexes and exposed to

irradiation. Elevation of Bax expression, a pro-apoptotic protein, was observed only in cells treated with the higher dose of  $\gamma\text{-Fe}_2\text{O}_3$  NPs\_TPPS (0.75  $\mu\text{g}/\text{mL}$  TPPS). For the same condition, we observed an inhibition of NF- $\kappa\text{B}$  protein expression compared to control cells, which confirm induction of apoptosis and suppression of proliferation. For non-irradiated cells, using the same doses and exposure intervals, no significant changes in the expression of the analyzed proteins were found.



**Figure 15.** The protein expression of Pro-caspase 3, caspase 3, Bax, NF- $\kappa\text{B}$ , MCM-2 and  $\beta$ -catenin in Mel-Juso cells after 24 h incubation with 2 different concentrations of  $\gamma\text{-Fe}_2\text{O}_3$  NPs, TPPS and their mixture and exposure to no irradiation vs. 1 min irradiation ( $\lambda \sim 405$  nm, 1 mW/cm<sup>2</sup>) conditions. (a) Blot bands corresponding to control (Ctr),  $\gamma\text{-Fe}_2\text{O}_3$  NPs (a. 2.75; b. 4.16  $\mu\text{g}/\text{mL}$ ), TPPS (c. 0.5; d. 0.75  $\mu\text{g}/\text{mL}$ ) and  $\gamma\text{-Fe}_2\text{O}_3$  NPs\_TPPS complex (a+c, b+d); (b) Quantification of blot images. Data ( $n = 3$ ) were normalized to  $\beta$ -actin and expressed as percentages related to control (100%)  $\pm$  standard deviation (SD). The results were considered statistically significant when \*  $p < 0.05$ ; \*\*  $p < 0.01$ ; \*\*\*  $p < 0.001$  (sample vs. control).

#### 4. Discussion

To evaluate the potential of the newly synthesized  $\gamma\text{-Fe}_2\text{O}_3$  NPs\_TPPS complexes in melanoma PDT, their anti-tumoral activity was investigated on amelanotic Mel-Juso cells exposed to 405 nm LED irradiation. The blue light treatment at 450 nm wavelength and 10 J/cm<sup>2</sup> had better results than red light in an in vitro melanoma study [55]. The efficiency and the safety of red (635 nm) and blue (400 nm) light in PDT of basal cell carcinoma seems to be equally safe and effective [56], but porphyrins expect to deliver better results at 410 nm than in red light [57]. In melanoma PDT treatment, flavin mononucleotide shows good results after blue light irradiation (450 nm), resulting in an 85–90% inhibition of tumour growth [58]. Although the low depth penetration of blue light (at 400 nm of 1 mm [59]), the low expression of melanin pigment present in Mel-Juso cells [60,61] can suggest that the 405 nm LED light only induces the activation of porphyrin derivate, without its absorption by melanin. Our results indicated the efficiency of the PDT procedure at 405 nm in vitro on Mel-Juso melanoma cells. Although, the low skin penetration depth that characterizes blue light limits the PDT impact in vivo, it can be applied to superficial tumors. The blue light was already used in clinical trials to treat actinic keratoses [62,63] and it was suggested that blue light improved skin texture and smoothness and that can be used for treating

photodamaged skin. The blue light is potentially safe and effective and could be employed for treatment of acne, acne rosacea, and sun-damaged skin [62]. Also, in [58] has been reported a melanoma xenograft regression in mice (85–90%) after blue light photoactivation. Taking into account all of these, future research is worth to be carried out for increasing the outcome of blue light PDT by controlling the PS activation and the reactions in the tegument tissue layers.

Previous studies showed that synthetic anionic porphyrins present high photoactivity and, accumulate rapidly and preferentially in tumor cells [64,65]. However, their use has been associated also with several disadvantages including aggregation, dark toxicity (in the absence of light) and side effects (e.g., neurotoxicity) which has impeded its development as a PS [65]. Using iron oxide nanoparticles as a vehicle can solve these disadvantages. Apart from being a PS agent, TPPS also improved the stability of the  $\gamma$ -Fe<sub>2</sub>O<sub>3</sub> NPs\_TPPS suspension and its aggregation significantly decreased. Moreover, using  $\gamma$ -Fe<sub>2</sub>O<sub>3</sub> in combination with PS can significantly enhance the PDT efficiency, apart from eliminating the side effects of simple PS. Also, due to the magnetic properties of these vehicles they can be used as a targeted method, thus increasing the selectivity of the PDT [11]. The strategy to combine porphyrin with NPs may lead to an increase of the delivery of this compound within the target cells, thus leading to the enhancement of the porphyrin photoactivity in PDT at smaller doses and to the reduction of systemic toxicity.

Our results showed that  $\gamma$ -Fe<sub>2</sub>O<sub>3</sub> NPs\_TPPS has an increased phototoxicity compared with free TPPS. The preliminary cytotoxicity studies revealed that the phototoxicity of  $\gamma$ -Fe<sub>2</sub>O<sub>3</sub> NPs\_TPPS is highly dependent on irradiation time, LED power density, and TPPS concentration. The Mel-Juso cell viability decreased dramatically with over 80% from control upon irradiation with 1 and 2 mW/cm<sup>2</sup> power densities for 5 min in the presence of  $\gamma$ -Fe<sub>2</sub>O<sub>3</sub> NPs\_TPPS corresponding to a TPPS concentration  $\geq 0.5$   $\mu$ g/mL. A different response was obtained in cells treated with free TPPS, in the same conditions. Here, the phototoxicity was significantly lower compared to the one of functionalized TPPS. No significant alteration of cell viability was noticed in cells incubated with free NPs which attests their high biocompatibility but also might suggest their capability of no interference in PDT. Considering these results, optimal experimental conditions for further analysis were established at 1 min irradiation and 1 mW/cm<sup>2</sup> power density.

Furthermore, we found that in the absence of irradiation, the melanoma cell viability has not been altered by incubation with TPPS or  $\gamma$ -Fe<sub>2</sub>O<sub>3</sub> NPs\_TPPS up to a concentration of 1  $\mu$ g/mL TPPS. Also, we showed that unfunctionalized TPPS did not exert toxicity under irradiation up to a concentration of 1  $\mu$ g/mL. These results might indicate a threshold of TPPS cytotoxicity in the melanoma cells subjected or not to irradiation at 1  $\mu$ g/mL. A dose of 0.75  $\mu$ g/mL of functionalized TPPS was necessary to reduce approximately half of the melanoma cell population (IC<sub>50</sub> dose) after 1 min irradiation followed by 24 h of incubation. A similar study showed that a 50% lethal concentration for TPPS applied on human skin melanoma G361 cells was  $4.24 \pm 0.12$   $\mu$ M, after 50 s of irradiation with a dose of 1 J/cm<sup>2</sup> and 24 h incubation of cells [66]. After a microscopic examination, we noticed significant morphologic alterations of melanoma cells incubated with  $\gamma$ -Fe<sub>2</sub>O<sub>3</sub> NPs\_TPPS which correspond to dead cells including unspecific cell extensions, ruffle borders shrinkage, blebbing or apoptotic vesicles. Many detached cells floating in the culture media were also present.

Despite the fact that TPPS is a good photosensitizer with a quantum yield of singlet oxygen generation of about 80% (determined via phosphorescence detection at 1270 nm), at concentrations up to 1  $\mu$ g/mL and at a very low dose of light irradiation (1 mW/cm<sup>2</sup> and 1 min exposure), it did not show a PDT effect, in contrast with the iron oxide nanoparticles having the same TPPS loading. Our studies showed that  $\gamma$ -Fe<sub>2</sub>O<sub>3</sub> NPs has led to a significant increase of TPPS photodynamic activity.

The photophysical studies showed for  $\gamma$ -Fe<sub>2</sub>O<sub>3</sub> NPs\_TPPS, a quantum yield of singlet oxygen generation of 60%, slightly lower than the porphyrin alone. These suggest

that the significant ROS increase is due to the ability of synthesized NPs to deliver the photosensitizer intracellularly.

The photooxidation efficiency of TPPS in melanoma cells increased in a concentration dependent manner when it was added in combination with NPs. These results are in correlation with the above cytotoxicity results and might suggest the contribution of NPs in the TPPS cell internalization and its accumulation in the cytosol. Our assumption is based on previous studies regarding the internalization of iron oxide NPs. It was shown that endocytosis is the most frequent mechanism of cellular uptake for this kind of nanoparticles [67]. More intracellular uptake pathways of iron oxide NPs were proposed including passive diffusion, micropinocytosis, receptor-mediated endocytosis, clathrin-mediated endocytosis, caveolin-mediated internalization, and other clathrin and caveolin-independent endocytosis [68]. Furthermore, several research studies indicated that the incubation with a higher concentration of NPs results in a higher internalization that could reach a maximum after 24 h of exposure [69]. In melanoma cells, it was shown that internalization of superparamagnetic iron oxide nanoparticles coated with polyvinyl alcohol and functionalized with amino groups is visible after 24 h of continuous exposure [70]. In another study, on human melanoma cells, it was shown that exposure to ultrasmall superparamagnetic iron oxide nanoparticles induced a clathrin-mediated uptake with the involvement of the endosomal-lysosomal pathway [71].

Iron oxide NPs are internalized into cells usually by endocytosis and digested to iron ions inside lysosomes where also NP-functionalized compounds are released in cytosol. This localization might contribute to the increase of efficiency of  $\gamma$ -Fe<sub>2</sub>O<sub>3</sub> NPs\_TPPS on cancer cells. The PDT efficacy might be also partly due to a release of lysosomal constituents such as cathepsins to the cytosol along with TPPS [72]. The released iron ions could also enhance PDT efficacy by contributing to the increase of ROS production. Iron ions are involved in catalyzation of the Fenton reaction, which produces highly reactive hydroxyl radical (OH•) from peroxide (H<sub>2</sub>O<sub>2</sub>) and superoxide anions (O<sub>2</sub><sup>-</sup>).

In cells, ROS production is balanced by enzymatic and non-enzymatic antioxidant defense systems. An excess of ROS induces the loss of antioxidant capacity and macromolecular damage thus triggering oxidative stress. In this direction, we further evaluated the intracellular GSH level in melanoma cells. This most abundant endogenous thiol compound, is a non-enzymatic antioxidant with important roles in maintaining redox homeostasis through direct scavenging or enzymatic catalysis of electrophilic and oxidant species [73,74]. The elevated GSH level found in tumor cells confers them therapeutic resistance by preserving the levels of cysteine and detoxification of xenobiotics [75]. Previous studies suggest that overexpression of GSH might be also correlated with resistance to PDT [76,77]. In the current study, we found that the treatment with  $\gamma$ -Fe<sub>2</sub>O<sub>3</sub> NPs\_TPPS under 1 min irradiation induced a slight elevation of GSH synthesis compared to control as a response to high ROS production. Moreover, we noticed that the increase of GSH content was inversely proportional with the increase of ROS level. These data indicate that the cells were not able to efficiently counteract the oxidative stress. Once installed, the oxidative stress can lead to significant oxidative modifications, including protein oxidation, lipid peroxidation, DNA damage, inflammation, perturbation of signaling pathways and activation of cell death mechanisms [78].

To further investigate the anti-tumor mechanisms triggered in melanoma cells following photodynamic activation of functionalized TPPS, we analyzed some specific protein markers involved in different cellular processes such as apoptosis, proliferation and cell adhesion. We obtained a decrease of pro-caspase 3 protein level in parallel with the activation of caspase 3 in cells incubated with  $\gamma$ -Fe<sub>2</sub>O<sub>3</sub> NPs\_TPPS at 0.5  $\mu$ g/mL and 0.75  $\mu$ g/mL TPPS and irradiated for 1 min. These results indicate activation of apoptosis in melanoma cells as cell death mechanisms. Additionally, in the same cells, we found a slight upregulation of Bax protein, a major member of the pro-apoptotic group of the Bcl-2 family, which can activate caspase-3 through the intrinsic apoptotic pathway. Because of the small increase of Bax protein expression, we assume that activation of caspase 3 in Mel-Juso cells was

achieved possibly by multiple pathways. Inhibition of NF- $\kappa$ B (nuclear factor kappa-light-chain-enhancer of activated B cells) in these cells also confirmed the induction of apoptosis but also the suppression of proliferation [79]. NF- $\kappa$ B plays a critical role in the cellular response to different stimuli including stress, free radicals and ultraviolet irradiation and controls signaling pathways involved in cell survival. The TPPS-mediated apoptosis was reported also in human gastric cancer HGC27 and SNU-1 cells treated with a dose of 6.25  $\mu$ M TPPS derivate and irradiation by a laser at 650 nm with 12 J/cm<sup>2</sup> [80].

In cells, DNA replication process is assisted by minichromosome maintenance proteins (MCMs), considered also proliferation markers and key tools in the diagnosis and prognosis of cancer [81]. Very recently, it was found that melanoma is characterized by elevated expressions of MCM-2–6 and MCM-10 proteins [82]. Moreover, MCM-2-index is correlated with lower survival rates and this protein in association with COX-2 and p-Akt1 contribute to cell-cycle dysregulation in melanoma [83]. Considering this, we have analyzed the expression of MCM-2 protein to evaluate the status of the proliferative capacity of tumor cells under tested conditions. The bands revealed on blot membranes showed a decreased expression of MCM-2 protein in Mel-Juso cells exposed to  $\gamma$ -Fe<sub>2</sub>O<sub>3</sub> NPs\_TPPS followed by irradiation, which confirmed the inhibition of melanoma cells proliferation. These results were also in correlation with the cytotoxicity evaluation and morphologic examination data. We assume that the decrease of MCM-2 protein expression may be a consequence of ROS overproduction induced in melanoma cells through TPPS activation after 1 min irradiation in the presence of  $\gamma$ -Fe<sub>2</sub>O<sub>3</sub> NPs\_TPPS. It is well known that overproduction of ROS is positively correlated with cell cycle arrest and apoptosis. ROS are highly active oxygen-containing molecules that play an essential role in cell cycle progression by regulating the ubiquitination process via intermediate phosphorylation of cyclins-dependent kinases (CDKs) and cell cycle regulatory molecules. MCM-2 is one of the molecules that regulate cell proliferation and the cell cycle via G1/S phase arrest. The regulatory mechanisms that modulate and control its activity are diverse and complex, particularly, phosphorylation by multiple kinases [84]. Compelling evidence showed that the decrease of MCM-2 expression may be a consequence of downregulation of CK2 $\alpha$  the catalytic subunits of protein kinase CK2 [85], or a result of Notch-mediated cell cycle arrest and its dependent kinases [86].

Furthermore, the protein expression of  $\beta$ -catenin, a structural component of cell–cell adhesions was also investigated. The role of  $\beta$ -catenin in melanoma is not completely understood. It's up-regulation has been linked to the suppression of melanoma cell invasion [87], but also was reported that blockade of  $\beta$ -catenin in metastatic melanoma cell lines induces apoptosis and inhibits proliferation, migration and invasion but not in primary melanoma cell lines [88]. In the current study, we found that protein expression of  $\beta$ -catenin was pronouncedly down-regulated in our primary melanoma cells when incubated with  $\gamma$ -Fe<sub>2</sub>O<sub>3</sub> NPs\_TPPS and then irradiated. A slight decrease in its expression was also registered in the irradiated cells treated with free TPPS at the highest concentration. The reduction of  $\beta$ -catenin protein expression may result following ROS generation. Previously, it was shown that the degradation of  $\beta$ -catenin in epidermal cells is caused by ROS accumulation through caspases activation. Simultaneously, damage of cell adhesion may induce ROS production and caspase activation, indicating a loop mechanism involved in cell death [89].

Taking all results into consideration, we tend to believe that in this case, suppression of  $\beta$ -catenin contributes to the induction of apoptosis, suppression of proliferation and reduction of cell adhesion.

## 5. Conclusions

This study proved the anti-tumoral effect of the newly synthesized  $\gamma$ -Fe<sub>2</sub>O<sub>3</sub> NPs functionalized with 5,10,15,20-(Tetra-4-sulfonatophenyl) porphyrin on human melanoma cells subjected to PDT by 405 nm LED irradiation. The NPs were synthesized by laser pyrolysis and their nanometric size and crystallinity were confirmed by DLS, XRD and TEM analyses. The loading efficiency of NPs with TPPS was estimated by using absorption spectroscopy.



The  $\gamma$ -Fe<sub>2</sub>O<sub>3</sub> NPs\_TPPS complexes showed a good efficiency for singlet oxygen generation, a quantum yield of 60% being determined by measurements of <sup>1</sup>O<sub>2</sub> phosphorescence at 1270 nm.

Predicted toxicity results suggested that this compound is probably safe to use, but future tests are needed. The low binding energy between TPPS and pro-caspase 3 suggests a possible affinity of TPPS to the inactive form of caspase.

The biological investigations showed that  $\gamma$ -Fe<sub>2</sub>O<sub>3</sub> NPs has led to a significant increase of TPPS photodynamic activity for a very low irradiation dose (1 mW/cm<sup>2</sup> irradiation intensity and 1 minute of exposure). Despite the fact that TPPS is a good photosensitizer with a high quantum yield of singlet oxygen generation, it did not show a PDT effect at our low light dose, in contrast to iron nanoparticles loaded with the same concentration of TPPS. This could possibly indicate a good cell internalization rate of newly synthesized  $\gamma$ -Fe<sub>2</sub>O<sub>3</sub> NPs functionalized with TPPS.

A threshold of TPPS cytotoxicity in melanoma cells exposed or not to blue light radiation was found at 1  $\mu$ g/mL. Moreover, we showed that photoactivated  $\gamma$ -Fe<sub>2</sub>O<sub>3</sub> NPs\_TPPS could trigger apoptosis in melanoma cells and might suppress tumor proliferation and cell adhesion by modulating the MCM-2 and  $\beta$ -catenin pathways.

**Author Contributions:** S.N. methodology and writing—original draft preparation; A.-M.U. software and writing—original draft preparation, M.A.B. formal analysis; I.L. methodology; formal analysis and writing—original draft preparation, M.B. (Mihai Boni) conceptualization and writing—original draft preparation; T.T. formal analysis, software and writing—original draft preparation, F.D. writing—review and editing; V.-A.M. formal analysis; R.G.P. formal analysis, writing—review and editing; C.F. methodology; E.A. writing—review and editing; A.D. writing—review and editing; A.S. methodology, project administration, supervision; writing—review and editing; M.B. (Mihaela Balas) formal analysis, methodology, writing—original draft preparation, review and editing. All authors have read and agreed to the published version of the manuscript.

**Funding:** This research was funded by grants of the Ministry of Research, Innovation and Digitization and CCCDI-UEFISCDI, project numbers PN-III-P2-2.1-PED-2019-4771, PN-III-P1-1.2-PCCDI-2017-072, within PNCDI III, and Nucleu Programme, ctr. No. 16N/08.02.2019.

**Conflicts of Interest:** The authors declare no conflict of interest.

## References

- O'Neill, C.H.; Scoggins, C.R. Melanoma. *J. Surg. Oncol.* **2019**, *120*, 873–881. [CrossRef] [PubMed]
- Tripp, M.K.; Watson, M.; Balk, S.J.; Swetter, S.M.; Gershenwald, J.E. State of the Science on Prevention and Screening to Reduce Melanoma Incidence and Mortality: The Time Is Now. *CA Cancer J. Clin.* **2016**, *66*, 460–480. [CrossRef]
- Davis, L.E.; Shalin, S.C.; Tackett, A.J. Current State of Melanoma Diagnosis and Treatment. *Cancer Biol. Ther.* **2019**, *20*, 1366–1379. [CrossRef] [PubMed]
- Williams, P.F.; Olsen, C.M.; Hayward, N.K.; Whiteman, D.C. Melanocortin 1 Receptor and Risk of Cutaneous Melanoma: A Meta-Analysis and Estimates of Population Burden. *Int. J. Cancer* **2011**, *129*, 1730–1740. [CrossRef]
- Seiberg, M. Keratinocyte–Melanocyte Interactions during Melanosome Transfer. *Pigment Cell Res.* **2001**, *14*, 236–242. [CrossRef]
- Leonardi, G.C.; Falzone, L.; Salemi, R.; Zanghì, A.; Spandidos, D.A.; McCubrey, J.A.; Candido, S.; Libra, M. Cutaneous Melanoma: From Pathogenesis to Therapy (Review). *Int. J. Oncol.* **2018**, *52*, 1071–1080. [CrossRef]
- Lugović-Mihčić, L.; Česić, D.; Vuković, P.; Novak-Bilić, G.; Šitum, M.; Špoljar, S. Melanoma Development: Current Knowledge on Melanoma Pathogenesis. *Acta Derm. Croat.* **2019**, *27*, 163–168.
- Domingues, B.; Lopes, J.M.; Soares, P.; Pópulo, H. Melanoma treatment in review. *Immunotargets Ther.* **2018**, *7*, 35–49. [CrossRef] [PubMed]
- Allison, R.R. Photodynamic Therapy: Oncologic Horizons. *Future Oncol.* **2014**, *10*, 123–124. [CrossRef]
- Luo, D.; Carter, K.A.; Miranda, D.; Lovell, J.F. Chemophototherapy: An Emerging Treatment Option for Solid Tumors. *Adv. Sci.* **2017**, *4*, 1600106. [CrossRef]
- Kwiatkowski, S.; Knap, B.; Przystupski, D.; Saczko, J.; Kędzierska, E.; Knap-Czop, K.; Kotlińska, J.; Michel, O.; Kotowski, K.; Kulbacka, J. Photodynamic Therapy—Mechanisms, Photosensitizers and Combinations. *Biomed. Pharmacother.* **2018**, *106*, 1098–1107. [CrossRef] [PubMed]
- Allison, R.R.; Downie, G.H.; Cuenca, R.; Hu, X.-H.; Childs, C.J.; Sibata, C.H. Photosensitizers in Clinical PDT. *Photodiagn. Photodyn. Ther.* **2004**, *1*, 27–42. [CrossRef]

13. Allison, R.R.; Sibata, C.H. Oncologic Photodynamic Therapy Photosensitizers: A Clinical Review. *Photodiagn. Photodyn. Ther.* **2010**, *7*, 61–75. [CrossRef]
14. Detty, M.R.; Gibson, S.L.; Wagner, S.J. Current Clinical and Preclinical Photosensitizers for Use in Photodynamic Therapy. *J. Med. Chem.* **2004**, *47*, 3897–3915. [CrossRef]
15. Ptaszek, M. Rational Design of Fluorophores for In Vivo Applications. In *Progress in Molecular Biology and Translational Science*; Elsevier: Amsterdam, The Netherlands, 2013; Volume 113, pp. 59–108. ISBN 978-0-12-386932-6.
16. Triesscheijn, M.; Ruevekamp, M.; Aalders, M.; Baas, P.; Stewart, F.A. Outcome of MTHPC Mediated Photodynamic Therapy Is Primarily Determined by the Vascular Response. *Photochem. Photobiol.* **2005**, *81*, 1161–1167. [CrossRef]
17. Veenhuizen, R.; Oppelaar, H.; Ruevekamp, M.; Schellens, J.; Dalesio, O.; Stewart, F. Does Tumour Uptake of Foscan Determine PDT Efficacy? *Int. J. Cancer* **1997**, *73*, 236–239. [CrossRef]
18. Chen, B.; de Witte, P.A. Photodynamic Therapy Efficacy and Tissue Distribution of Hypericin in a Mouse P388 Lymphoma Tumor Model. *Cancer Lett.* **2000**, *150*, 111–117. [CrossRef]
19. Cramers, P.; Ruevekamp, M.; Oppelaar, H.; Dalesio, O.; Baas, P.; Stewart, F.A. Foscan Uptake and Tissue Distribution in Relation to Photodynamic Efficacy. *Br. J. Cancer* **2003**, *88*, 283–290. [CrossRef]
20. Gomer, C.J.; Ferrario, A. Tissue Distribution and Photosensitizing Properties of Mono-L-Aspartyl Chlorin E6 in a Mouse Tumor Model. *Cancer Res.* **1990**, *50*, 3985–3990.
21. Koudinova, N.V.; Pinthus, J.H.; Brandis, A.; Brenner, O.; Bendel, P.; Ramon, J.; Eshhar, Z.; Scherz, A.; Salomon, Y. Photodynamic Therapy with Pd-Bacteriopheophorbide (TOOKAD): Successful in Vivo Treatment of Human Prostatic Small Cell Carcinoma Xenografts. *Int. J. Cancer* **2003**, *104*, 782–789. [CrossRef] [PubMed]
22. Schreiber, S.; Gross, S.; Brandis, A.; Harmelin, A.; Rosenbach-Belkin, V.; Scherz, A.; Salomon, Y. Local Photodynamic Therapy (PDT) of Rat C6 Glioma Xenografts with Pd-Bacteriopheophorbide Leads to Decreased Metastases and Increase of Animal Cure Compared with Surgery. *Int. J. Cancer* **2002**, *99*, 279–285. [CrossRef] [PubMed]
23. Seabra, A.B. Iron Oxide Magnetic Nanoparticles in Photodynamic Therapy: A Promising Approach Against Tumor Cells. In *Metal Nanoparticles in Pharma*; Springer: Cham, Switzerland, 2017; pp. 3–20. [CrossRef]
24. Walker, M.G.; Jarman, P.J.; Gill, M.R.; Tian, X.; Ahmad, H.; Reddy, P.A.N.; McKenzie, L.; Weinstein, J.A.; Meijer, A.J.H.M.; Battaglia, G.; et al. A Self-Assembled Metallomacrocyclic Singlet Oxygen Sensitizer for Photodynamic Therapy. *Chemistry* **2016**, *22*, 5996–6000. [CrossRef] [PubMed]
25. Lanzilotto, A.; Kyropoulou, M.; Constable, E.C.; Housecroft, C.E.; Meier, W.P.; Palivan, C.G. Porphyrin-Polymer Nanocompartments: Singlet Oxygen Generation and Antimicrobial Activity. *J. Biol. Inorg. Chem.* **2018**, *23*, 109–122. [CrossRef]
26. Penon, O.; Marín, M.J.; Amabilino, D.B.; Russell, D.A.; Pérez-García, L. Iron Oxide Nanoparticles Functionalized with Novel Hydrophobic and Hydrophilic Porphyrins as Potential Agents for Photodynamic Therapy. *J. Colloid Interface Sci.* **2016**, *462*, 154–165. [CrossRef] [PubMed]
27. Bechet, D.; Couleaud, P.; Frochot, C.; Viriot, M.-L.; Guillemin, F.; Barberi-Heyob, M. Nanoparticles as Vehicles for Delivery of Photodynamic Therapy Agents. *Trends Biotechnol.* **2008**, *26*, 612–621. [CrossRef]
28. Zhao, C.; Ur Rehman, F.; Yang, Y.; Li, X.; Zhang, D.; Jiang, H.; Selke, M.; Wang, X.; Liu, C. Bio-Imaging and Photodynamic Therapy with Tetra Sulphonatophenyl Porphyrin (TSPP)-TiO<sub>2</sub> Nanowhiskers: New Approaches in Rheumatoid Arthritis Theranostics. *Sci. Rep.* **2015**, *5*, 11518. [CrossRef] [PubMed]
29. Morjan, I.; Alexandrescu, R.; Dumitrache, F.; Birjega, R.; Fleaca, C.; Soare, I.; Luculescu, C.R.; Filoti, G.; Kuncer, V.; Vekas, L.; et al. Iron Oxide-Based Nanoparticles with Different Mean Sizes Obtained by the Laser Pyrolysis: Structural and Magnetic Properties. *J. Nanosci. Nanotechnol.* **2010**, *10*, 1223–1234. [CrossRef] [PubMed]
30. Nastasa, V.; Pascu, A.; Boni, M.; Smarandache, A.; Staicu, A.; Pascu, M.L. Insights into the Photophysics of Zinc Phthalocyanine and Photogenerated Singlet Oxygen in DMSO-Water Mixture. *Colloids Surf. A Physicochem. Eng. Asp.* **2016**, *505*, 197–203. [CrossRef]
31. Staicu, A.; Pascu, A.; Boni, M.; Pascu, M.L.; Enescu, M. Photophysical Study of Zn Phthalocyanine in Binary Solvent Mixtures. *J. Mol. Struct.* **2013**, *1044*, 188–193. [CrossRef]
32. Rawson, J.; Angiolillo, P.J.; Therien, M.J. Extreme Electron Polaron Spatial Delocalization in  $\pi$ -Conjugated Materials. *Proc. Natl. Acad. Sci. USA* **2015**, *112*, 13779–13783. [CrossRef]
33. Thomsen, N.D.; Koerber, J.T.; Wells, J.A. Structural Snapshots Reveal Distinct Mechanisms of Procaspase-3 and -7 Activation. *Proc. Natl. Acad. Sci. USA* **2013**, *110*, 8477–8482. [CrossRef]
34. Du, J.-Q.; Wu, J.; Zhang, H.-J.; Zhang, Y.-H.; Qiu, B.-Y.; Wu, F.; Chen, Y.-H.; Li, J.-Y.; Nan, F.-J.; Ding, J.-P.; et al. Isoquinoline-1,3,4-Trione Derivatives Inactivate Caspase-3 by Generation of Reactive Oxygen Species. *J. Biol. Chem.* **2008**, *283*, 30205–30215. [CrossRef] [PubMed]
35. Berman, H.M. The Protein Data Bank. *Nucleic Acids Res.* **2000**, *28*, 235–242. [CrossRef] [PubMed]
36. Pires, D.E.V.; Blundell, T.L.; Ascher, D.B. PKCSM: Predicting Small-Molecule Pharmacokinetic and Toxicity Properties Using Graph-Based Signatures. *J. Med. Chem.* **2015**, *58*, 4066–4072. [CrossRef] [PubMed]
37. Cheng, F.; Li, W.; Zhou, Y.; Shen, J.; Wu, Z.; Liu, G.; Lee, P.W.; Tang, Y. AdmetSAR: A Comprehensive Source and Free Tool for Assessment of Chemical ADMET Properties. *J. Chem. Inf. Model.* **2012**, *52*, 3099–3105. [CrossRef] [PubMed]
38. Banerjee, P.; Eckert, A.O.; Schrey, A.K.; Preissner, R. ProTox-II: A Webserver for the Prediction of Toxicity of Chemicals. *Nucleic Acids Res.* **2018**, *46*, W257–W263. [CrossRef]

39. Morris, G.M.; Huey, R.; Lindstrom, W.; Sanner, M.F.; Belew, R.K.; Goodsell, D.S.; Olson, A.J. AutoDock4 and AutoDockTools4: Automated Docking with Selective Receptor Flexibility. *J. Comput. Chem.* **2009**, *30*, 2785–2791. [CrossRef] [PubMed]
40. Nistorescu, S.; Gradisteanu Pircalabioru, G.; Udrea, A.-M.; Simon, A.; Pascu, M.L.; Chifiriuc, M.-C. Laser-Irradiated Chlorpromazine as a Potent Anti-Biofilm Agent for Coating of Biomedical Devices. *Coatings* **2020**, *10*, 1230. [CrossRef]
41. Tozar, T.; Santos Costa, S.; Udrea, A.-M.; Nastasa, V.; Couto, I.; Viveiros, M.; Pascu, M.L.; Romanitan, M.O. Anti-Staphylococcal Activity and Mode of Action of Thioridazine Photoproducts. *Sci. Rep.* **2020**, *10*, 18043. [CrossRef]
42. Bera, K.; Maiti, S.; Maity, M.; Mandal, C.; Maiti, N.C. Porphyrin–Gold Nanomaterial for Efficient Drug Delivery to Cancerous Cells. *ACS Omega* **2018**, *3*, 4602–4619. [CrossRef]
43. Zhang, Y.-H.; Chen, D.-M.; He, T.; Liu, F.-C. Raman and Infrared Spectral Study of Meso-Sulfonatophenyl Substituted Porphyrins (TPPSn, N = 1, 2A, 2O, 3, 4). *Spectrochim. Acta A Mol. Biomol. Spectrosc.* **2003**, *59*, 87–101. [CrossRef]
44. Aydin, M. Comparative Study of the Structural and Vibroelectronic Properties of Porphyrin and Its Derivatives. *Molecules* **2014**, *19*, 20988–21021. [CrossRef]
45. Lewandowska, K.; Rosiak, N.; Bogucki, A.; CieleckaPiontek, J. *Tuning Electronic and Magnetic Properties in Graphene Oxide—Porphyrins Complexes*; Open Science Framework: Charlottesville, VA, USA, 2019.
46. Durães, L.; Costa, B.F.O.; Vasques, J.; Campos, J.; Portugal, A. Phase Investigation of As-Prepared Iron Oxide/Hydroxide Produced by Sol–Gel Synthesis. *Mater. Lett.* **2005**, *59*, 859–863. [CrossRef]
47. Glisenti, A. Interaction of Formic Acid with Fe<sub>2</sub>O<sub>3</sub> Powders under Different Atmospheres: An XPS and FTIR Study. *Faraday Trans.* **1998**, *94*, 3671–3676. [CrossRef]
48. Coessens, V.; Schacht, E.; Domurado, D. Synthesis of Polyglutamine and Dextran Conjugates of Streptomycin with an Acid-Sensitive Drug-Carrier Linkage. *J. Control. Release* **1996**, *38*, 141–150. [CrossRef]
49. Lewandowska, K.; Rosiak, N.; Bogucki, A.; Cielecka-Piontek, J.; Mizera, M.; Bednarski, W.; Suchecki, M.; Szaciłowski, K. Supramolecular Complexes of Graphene Oxide with Porphyrins: An Interplay between Electronic and Magnetic Properties. *Molecules* **2019**, *24*, 688. [CrossRef]
50. DeRosa, M.C.; Crutchley, R.J. Photosensitized Singlet Oxygen and Its Applications. *Coord. Chem. Rev.* **2002**, *233–234*, 351–371. [CrossRef]
51. Stevens, E.A.; Mezrich, J.D.; Bradfield, C.A. The Aryl Hydrocarbon Receptor: A Perspective on Potential Roles in the Immune System. *Immunology* **2009**, *127*, 299–311. [CrossRef]
52. Gottlieb, E.; Armour, S.M.; Harris, M.H.; Thompson, C.B. Mitochondrial Membrane Potential Regulates Matrix Configuration and Cytochrome c Release during Apoptosis. *Cell Death Differ.* **2003**, *10*, 709–717. [CrossRef]
53. Udrea, A.-M.; Dinache, A.; Pagès, J.-M.; Pirvulescu, R.A. Quinazoline Derivatives Designed as Efflux Pump Inhibitors: Molecular Modeling and Spectroscopic Studies. *Molecules* **2021**, *26*, 2374. [CrossRef]
54. Udrea, A.-M.; Avram, S.; Nistorescu, S.; Pascu, M.-L.; Romanitan, M.O. Laser Irradiated Phenothiazines: New Potential Treatment for COVID-19 Explored by Molecular Docking. *J. Photochem. Photobiol. B Biol.* **2020**, *211*, 111997. [CrossRef]
55. Sparsa, A.; Faucher, K.; Sol, V.; Durox, H.; Boulinguez, S.; Doffoel-Hantz, V.; Calliste, C.-A.; Cook-Moreau, J.; Krausz, P.; Sturtz, F.G.; et al. Blue Light Is Phototoxic for B16F10 Murine Melanoma and Bovine Endothelial Cell Lines by Direct Cytocidal Effect. *Anticancer Res.* **2010**, *30*, 143–147.
56. Maytin, E.V.; Kaw, U.; Ilyas, M.; Mack, J.A.; Hu, B. Blue Light versus Red Light for Photodynamic Therapy of Basal Cell Carcinoma in Patients with Gorlin Syndrome: A Bilaterally Controlled Comparison Study. *Photodiagn. Photodyn. Ther.* **2018**, *22*, 7–13. [CrossRef]
57. Dougherty, T.J.; Gomer, C.J.; Henderson, B.W.; Jori, G.; Kessel, D.; Korbek, M.; Moan, J.; Peng, Q. Photodynamic Therapy. *JNCI J. Natl. Cancer Inst.* **1998**, *90*, 889–905. [CrossRef]
58. Akasov, R.A.; Sholina, N.V.; Khochenkov, D.A.; Alova, A.V.; Gorelkin, P.V.; Erofeev, A.S.; Generalova, A.N.; Khaydukov, E.V. Photodynamic Therapy of Melanoma by Blue-Light Photoactivation of Flavin Mononucleotide. *Sci. Rep.* **2019**, *9*, 9679. [CrossRef] [PubMed]
59. Ash, C.; Dubec, M.; Donne, K.; Bashford, T. Effect of Wavelength and Beam Width on Penetration in Light-Tissue Interaction Using Computational Methods. *Lasers Med. Sci.* **2017**, *32*, 1909–1918. [CrossRef] [PubMed]
60. Popa, I.L.; Milac, A.L.; Sima, L.E.; Alexandru, P.R.; Pastrama, F.; Munteanu, C.V.A.; Negroiu, G. Cross-Talk between Dopachrome Tautomerase and Caveolin-1 Is Melanoma Cell Phenotype-Specific and Potentially Involved in Tumor Progression. *J. Biol. Chem.* **2016**, *291*, 12481–12500. [CrossRef] [PubMed]
61. Martínez-Lorenzo, M.J.; Anel, A.; Alava, M.A.; Piñeiro, A.; Naval, J.; Lasierra, P.; Larrad, L. The Human Melanoma Cell Line MelJuSo Secretes Bioactive FasL and APO2L/TRAIL on the Surface of Microvesicles. Possible Contribution to Tumor Counterattack. *Exp. Cell Res.* **2004**, *295*, 315–329. [CrossRef] [PubMed]
62. Zelickson, B.; Counters, J.; Coles, C.; Selim, M. Light Patch: Preliminary Report of a Novel Form of Blue Light Delivery for the Treatment of Actinic Keratosis. *Dermatol. Surg.* **2006**, *31*, 375–378. [CrossRef]
63. Ericson, M.B.; Wennberg, A.-M.; Larkö, O. Review of Photodynamic Therapy in Actinic Keratosis and Basal Cell Carcinoma. *Ther. Clin. Risk Manag.* **2008**, *4*, 1–9.
64. Tita, S.P.S.; Perussi, J.R. The Effect of Porphyrins on Normal and Transformed Mouse Cell Lines in the Presence of Visible Light. *Braz. J. Med. Biol. Res.* **2001**, *34*, 1331–1336. [CrossRef] [PubMed]

65. Lin, Y.; Zhou, T.; Bai, R.; Xie, Y. Chemical Approaches for the Enhancement of Porphyrin Skeleton-Based Photodynamic Therapy. *J. Enzyme Inhib. Med. Chem.* **2020**, *35*, 1080–1099. [CrossRef]
66. Malina, L.; Tomankova, K.B.; Malohlava, J.; Jiravova, J.; Manisova, B.; Zapletalova, J.; Kolarova, H. The in Vitro Cytotoxicity of Metal-Complexes of Porphyrin Sensitizer Intended for Photodynamic Therapy. *Toxicol. Vitro.* **2016**, *34*, 246–256. [CrossRef] [PubMed]
67. Rybka, J.D. Radiosensitizing Properties of Magnetic Hyperthermia Mediated by Superparamagnetic Iron Oxide Nanoparticles (SPIONs) on Human Cutaneous Melanoma Cell Lines. *Rep. Pract. Oncol. Radiother.* **2019**, *24*, 152–157. [CrossRef]
68. Rueda-Gensini, L.; Cifuentes, J.; Castellanos, M.C.; Puentes, P.R.; Serna, J.A.; Muñoz-Camargo, C.; Cruz, J.C. Tailoring Iron Oxide Nanoparticles for Efficient Cellular Internalization and Endosomal Escape. *Nanomaterials* **2020**, *10*, 1816. [CrossRef] [PubMed]
69. Lee, S.H.; Park, D.J.; Yun, W.S.; Park, J.-E.; Choi, J.S.; Key, J.; Seo, Y.J. Endocytic Trafficking of Polymeric Clustered Superparamagnetic Iron Oxide Nanoparticles in Mesenchymal Stem Cells. *J. Control. Release* **2020**, *326*, 408–418. [CrossRef]
70. Petri-Fink, A.; Chastellain, M.; Juillerat-Jeanneret, L.; Ferrari, A.; Hofmann, H. Development of Functionalized Superparamagnetic Iron Oxide Nanoparticles for Interaction with Human Cancer Cells. *Biomaterials* **2005**, *26*, 2685–2694. [CrossRef]
71. Cengelli, F.; Voinesco, F.; Juillerat-Jeanneret, L. Interaction of Cationic Ultrasmall Superparamagnetic Iron Oxide Nanoparticles with Human Melanoma Cells. *Nanomedicine* **2010**, *5*, 1075–1087. [CrossRef] [PubMed]
72. Hung, H.-I.; Schwartz, J.M.; Maldonado, E.N.; Lemasters, J.J.; Nieminen, A.-L. Mitoferrin-2-Dependent Mitochondrial Iron Uptake Sensitizes Human Head and Neck Squamous Carcinoma Cells to Photodynamic Therapy. *J. Biol. Chem.* **2013**, *288*, 677–686. [CrossRef]
73. Forman, H.J.; Zhang, H.; Rinna, A. Glutathione: Overview of Its Protective Roles, Measurement, and Biosynthesis. *Mol. Asp. Med.* **2009**, *30*, 1–12. [CrossRef]
74. Gaucher, C.; Boudier, A.; Bonetti, J.; Clarot, I.; Leroy, P.; Parent, M. Glutathione: Antioxidant Properties Dedicated to Nanotechnologies. *Antioxidants* **2018**, *7*, 62. [CrossRef] [PubMed]
75. Kennedy, L.; Sandhu, J.K.; Harper, M.-E.; Cuperlovic-Culf, M. Role of Glutathione in Cancer: From Mechanisms to Therapies. *Biomolecules* **2020**, *10*, 1429. [CrossRef]
76. Bi, H.; Dai, Y.; Yang, P.; Xu, J.; Yang, D.; Gai, S.; He, F.; An, G.; Zhong, C.; Lin, J. Glutathione and H<sub>2</sub>O<sub>2</sub> Consumption Promoted Photodynamic and Chemotherapy Based on Biodegradable MnO<sub>2</sub>-Pt@Au<sub>25</sub> Nanosheets. *Chem. Eng. J.* **2019**, *356*, 543–553. [CrossRef]
77. Shen, Z.; Ma, Q.; Zhou, X.; Zhang, G.; Hao, G.; Sun, Y.; Cao, J. Strategies to Improve Photodynamic Therapy Efficacy by Relieving the Tumor Hypoxia Environment. *NPG Asia Mater.* **2021**, *13*, 1–19. [CrossRef]
78. Redza-Dutordoir, M.; Averill-Bates, D.A. Activation of Apoptosis Signalling Pathways by Reactive Oxygen Species. *Biochim Biophys. Acta* **2016**, *1863*, 2977–2992. [CrossRef] [PubMed]
79. Inhibition of NF- $\kappa$ B Signaling Pathway Induces Apoptosis and Suppresses Proliferation and Angiogenesis of Human Fibroblast-like Synovial Cells in Rheumatoid Arthritis.—Abstract—Europe PMC. Available online: <https://europepmc.org/article/pmc/5999456> (accessed on 25 October 2021).
80. Chen, J.-J.; Gao, L.-J.; Liu, T.-J. Photodynamic Therapy with a Novel Porphyrin-Based Photosensitizer against Human Gastric Cancer. *Oncol. Lett.* **2016**, *11*, 775–781. [CrossRef]
81. Yu, S.; Wang, G.; Shi, Y.; Xu, H.; Zheng, Y.; Chen, Y. MCMs in Cancer: Prognostic Potential and Mechanisms. *Anal. Cell. Pathol.* **2020**, *2020*, 3750294. [CrossRef]
82. Han, W.; Wu, Y.-Z.; Zhao, X.-Y.; Gong, Z.-H.; Shen, G.-L. Integrative Analysis of Minichromosome Maintenance Proteins and Their Prognostic Significance in Melanoma. *Front. Oncol.* **2021**, *11*, 3203. [CrossRef]
83. Soares, C.D.; Borges, C.F.; Sena-Filho, M.; Almeida, O.P.; de Stelini, R.F.; Cintra, M.L.; Graner, E.; Zecchin, K.G.; Jorge, J. Prognostic Significance of Cyclooxygenase 2 and Phosphorylated Akt1 Overexpression in Primary Nonmetastatic and Metastatic Cutaneous Melanomas. *Melanoma Res.* **2017**, *27*, 448–456. [CrossRef]
84. Fei, L.; Xu, H. Role of MCM2–7 Protein Phosphorylation in Human Cancer Cells. *Cell Biosci.* **2018**, *8*, 43. [CrossRef] [PubMed]
85. Schaefer, S.; Doktor, T.K.; Frederiksen, S.B.; Chea, K.; Hlavacova, M.; Bruun, G.H.; Rabjerg, M.; Andresen, B.S.; Dominguez, I.; Guerra, B. Down-regulation of CK2 $\alpha$  correlates with decreased expression levels of DNA replication minichromosome maintenance protein complex (MCM) genes. *Sci. Rep.* **2019**, *9*, 14581. [CrossRef] [PubMed]
86. Nosedá, M.; Niessen, K.; McLean, G.; Chang, L.; Karsan, A. Notch-Dependent Cell Cycle Arrest Is Associated with Downregulation of Minichromosome Maintenance Proteins. *Circ. Res.* **2005**, *97*, 102–104. [CrossRef] [PubMed]
87. Arozarena, I.; Bischof, H.; Gilby, D.; Belloni, B.; Dummer, R.; Wellbrock, C. In Melanoma, Beta-Catenin Is a Suppressor of Invasion. *Oncogene* **2011**, *30*, 4531–4543. [CrossRef] [PubMed]
88. Sinnberg, T.; Menzel, M.; Ewerth, D.; Sauer, B.; Schwarz, M.; Schaller, M.; Garbe, C.; Schitteck, B.  $\beta$ -Catenin Signaling Increases during Melanoma Progression and Promotes Tumor Cell Survival and Chemoresistance. *PLoS ONE* **2011**, *6*, e23429. [CrossRef] [PubMed]
89. Omori, E.; Matsumoto, K.; Ninomiya-Tsuji, J. Non-Canonical  $\beta$ -Catenin Degradation Mediates Reactive Oxygen Species-Induced Epidermal Cell Death. *Oncogene* **2011**, *30*, 3336–3344. [CrossRef] [PubMed]



## Article

# Versatile and Robust Method for Antibody Conjugation to Nanoparticles with High Targeting Efficiency

Indra Van Zundert <sup>1</sup>, Maria Bravo <sup>1</sup>, Olivier Deschaume <sup>2</sup>, Pierre Cybulski <sup>1</sup>, Carmen Bartic <sup>2</sup>, Johan Hofkens <sup>1</sup>, Hiroshi Uji-i <sup>1,3</sup>, Beatrice Fortuni <sup>1,\*</sup> and Susana Rocha <sup>1,\*</sup>

- <sup>1</sup> Molecular Imaging and Photonics, Department of Chemistry, KU Leuven, Celestijnenlaan 200F, 3001 Heverlee, Belgium; indra.vanzundert@kuleuven.be (I.V.Z.); maria.bravo@kuleuven.be (M.B.); pierre.cybulski@kuleuven.be (P.C.); johan.hofkens@kuleuven.be (J.H.); hiroshi.ujii@kuleuven.be (H.U.-i.)
- <sup>2</sup> Soft-Matter Physics and Biophysics, Department of Physics and Astronomy, KU Leuven, Celestijnenlaan 200D, Box 2416, 3001 Heverlee, Belgium; olivier.deschaume@kuleuven.be (O.D.); carmen.bartic@kuleuven.be (C.B.)
- <sup>3</sup> Research Institute for Electronic Science (RIES), Hokkaido University, N20W10, Kita Ward, Sapporo 001-0020, Japan
- \* Correspondence: beatrice.fortuni@kuleuven.be (B.F.); susana.rocha@kuleuven.be (S.R.)

**Abstract:** The application of antibodies in nanomedicine is now standard practice in research since it represents an innovative approach to deliver chemotherapy agents selectively to tumors. The variety of targets or markers that are overexpressed in different types of cancers results in a high demand for antibody conjugated-nanoparticles, which are versatile and easily customizable. Considering up-scaling, the synthesis of antibody-conjugated nanoparticles should be simple and highly reproducible. Here, we developed a facile coating strategy to produce antibody-conjugated nanoparticles using ‘click chemistry’ and further evaluated their selectivity towards cancer cells expressing different markers. Our approach was consistently repeated for the conjugation of antibodies against CD44 and EGFR, which are prominent cancer cell markers. The functionalized particles presented excellent cell specificity towards CD44 and EGFR overexpressing cells, respectively. Our results indicated that the developed coating method is reproducible, versatile, and non-toxic, and can be used for particle functionalization with different antibodies. This grafting strategy can be applied to a wide range of nanoparticles and will contribute to the development of future targeted drug delivery systems.

**Keywords:** mesoporous silica nanoparticles; antibody functionalization; targeted drug delivery systems

**Citation:** Van Zundert, I.; Bravo, M.; Deschaume, O.; Cybulski, P.; Bartic, C.; Hofkens, J.; Uji-i, H.; Fortuni, B.; Rocha, S. Versatile and Robust Method for Antibody Conjugation to Nanoparticles with High Targeting Efficiency. *Pharmaceutics* **2021**, *13*, 2153. <https://doi.org/10.3390/pharmaceutics13122153>

Academic Editor: Hassan Bousbaa

Received: 28 September 2021

Accepted: 8 December 2021

Published: 14 December 2021

**Publisher’s Note:** MDPI stays neutral with regard to jurisdictional claims in published maps and institutional affiliations.



**Copyright:** © 2021 by the authors. Licensee MDPI, Basel, Switzerland. This article is an open access article distributed under the terms and conditions of the Creative Commons Attribution (CC BY) license (<https://creativecommons.org/licenses/by/4.0/>).

## 1. Introduction

Despite the numerous advances in treatment options, cancer remains a leading cause of mortality worldwide. Existing methods bear limitations and complications, such as incomplete removal of the tumor and severe side effects. Therefore, a combination of treatments is often required to reach the desired results [1–3]. The urge to develop more effective therapies gave rise to intensive research in delivery of chemotherapeutics using nanoparticles. Engineered nanoparticles have been shown to serve as excellent drug nano-carriers. Among the advantages of using nanoparticles are their higher drug-loading capacity, the protection of the drugs against degradation during blood circulation, and the possibility to easily add other functionalities. As the size of particles can be tailored, nanoparticles between 20 and 200 nm can take advantage of the enhanced permeability and retention (EPR) effect, to passively accumulate near the tumor because of abnormal blood vessel architecture [4,5]. However, over the last years, increasing debate on the EPR effect has emerged, raising doubts about its reliability and applicability [6–8]. Moreover, it has been repeatedly reported that only a small percentage of nanoparticles intravenously injected in mouse models actually reaches the tumor cells [9–11]. This is caused by the obstacles or biological barriers encountered by nanoparticles, which limit their delivery

to the tumor. These include the bloodstream, the innate immune system, the endothelial wall, and the dense extracellular matrix (ECM) of the tumor [12,13]. The ECM consists of fibers (such as collagen and fibronectin), which are known to hamper the diffusion of nanoparticles significantly [14]. This, together with an increased interstitial fluid pressure at the tumor site, poses a substantial barrier for nanoparticle transport to the tumor. To this end, strategies that can enhance the delivery of nanoparticles are widely being explored today. Active targeting of nanoparticles to cancer cells is one of those strategies [15,16].

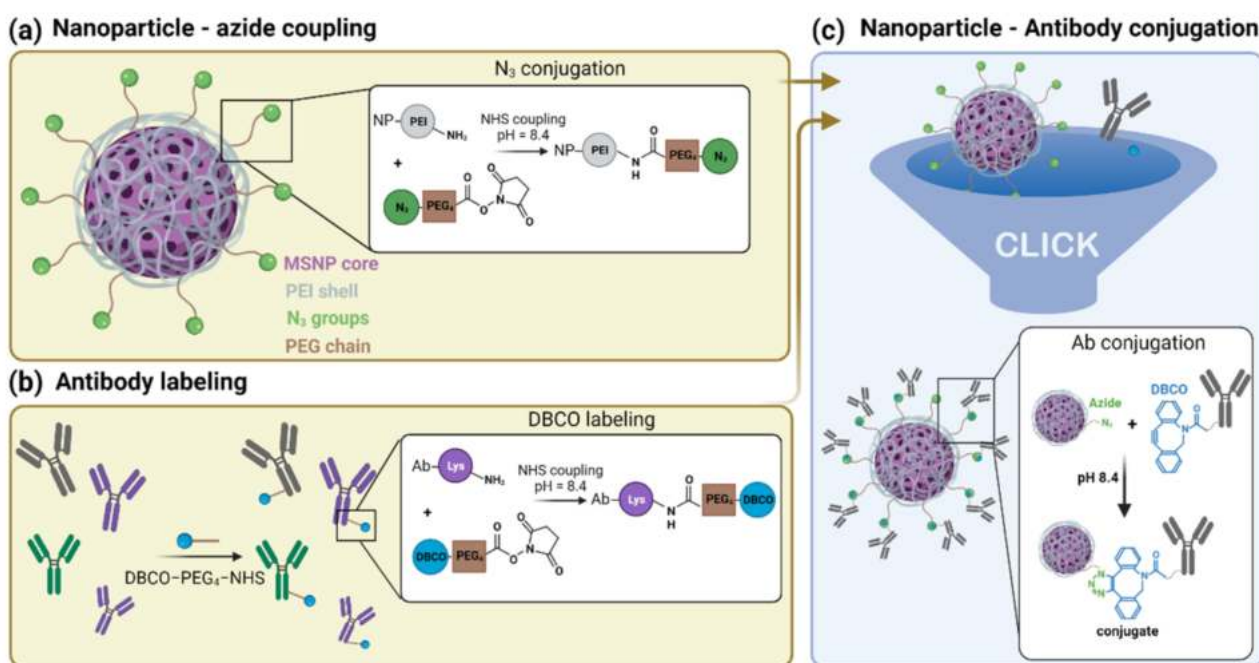
Over the years, a wide range of nanoparticles have been engineered and several approaches have been developed to promote nanoparticle internalization into specific cells. Often, nanoparticles are functionalized with ligands that recognize overexpressed receptors or markers present on the cancer cell membrane [5,17,18]. In doing so, they facilitate specific accumulation of the drug in cancer cells [19]. Folic acid or transferrin-conjugated nanoparticles are popular examples of such drug delivery systems (DDSs), as they bind to folate and transferrin receptors, respectively, overexpressed in certain cancers [18,20,21]. Typically, one nanoparticle is designed against a particular receptor or marker, hence targeting a specific cancer. However, patients with the same type of cancer can overexpress different markers. For instance, overexpression of the estrogen receptor (ER) is linked to a hormone-sensitive form of breast cancer (ER+), while HER2 is overexpressed in an aggressive and fast-growing type of breast cancer (HER2+) [22–24]. Given the variety in potential targets, there is a continuous search for simple methods to customize nanoparticles, turning them into versatile nano-carriers. To this end, antibodies have proven to be a promising strategy as they can be developed against most of the existing markers. The success of antibodies in targeting tumor cells has already been proven with the development of antibody–drug conjugates, which have emerged as powerful therapeutic agents in cancer therapies. To date, nine ADCs have been approved by the FDA for clinical use [25–29]. After the advances in antibody-drug conjugates, conjugation of antibodies to nanoparticles yields great therapeutic potential [30,31].

Conjugation of antibodies to nanoparticles can be achieved via different strategies, i.e., ionic adsorption (non-covalent attachment) [32], covalent binding (including carbodiimide chemistry [33], maleimide chemistry [34] and click-chemistry [35]) or using adapter molecules such as biotin [36]. In ionic adsorption, antibodies are linked to the nanoparticles via electrostatic interactions [37], leading to poor reproducibility and low stability [38]. Alternatively, adapter molecules, such as the avidin-biotin couple, can be implemented, but this interaction is influenced by the pH, affecting nanoparticle stability in more acidic conditions as found in the tumor microenvironment [39].

Covalent attachment is achieved by functionalizing the nanoparticle surface with functional groups (e.g., amine, carboxylic, maleimide etc.), which can react with the amino acid side chain of the antibody by standard conjugation methods. Covalent attachment of antibodies is generally preferred, provided that an appropriate approach is used. For instance, while EDC/NHS coupling is a common method for covalent attachment [40], it can result in oligomerization of antibody molecules [41]. Furthermore, some conjugation methods require the use of catalysts, often metals, that can lead to increased toxicity of the nanoparticles if not fully removed from the solution [42,43]. Therefore, when using covalent conjugation, a catalyst-free approach and vast optimization are important. Despite the progress in nanoparticle functionalization, there is still an urge for simple and reproducible strategies to conjugate antibodies to nanoparticles, enabling the development of versatile DDSs, which can easily be customized for selectivity towards different cancer markers.

In this work, we propose a simple and reproducible coating strategy for antibody conjugation to nanoparticles. To avoid the use of catalysts, we developed an approach based on copper-free click chemistry (Figure 1). Briefly, antibodies were labelled with a dibenzocyclooctyne (DBCO) moiety, while an Azide ( $N_3$ ) group was attached to the nanoparticles. The independent activation of the antibody and nanoparticles reduces the possibility of oligomerization of the antibody or aggregation of the particles. We proved the versatile nature of our method by creating two different types of particles,

either conjugated to an anti-Cluster of Differentiation 44 (anti-CD44) or anti-Epidermal Growth Factor Receptor (anti-EGFR) antibody, targeting CD44 or EGFR overexpressing cells, respectively. CD44 and EGFR are surface receptors that manifest themselves as important bio-markers in cancer [44,45]. In this report, mesoporous silica nanoparticles (MSNPs) were used as a model application for our coating strategy. In recent years, MSNPs have been pointed out as extremely promising tools in cancer research given their high biocompatibility, chemical stability, high drug-loading and -releasing capacities, straightforward functionalization and low-cost, scalable fabrication [46–48]. For these reasons, MSNPs were chosen as a study model of DDSs for further surface modifications. Nevertheless, we foresee that the coating strategy here presented can be easily applied to a wide range of nano-carriers besides MSNPs, as it only requires the presence of amine groups on the surface of the nanoparticle. This simple conjugation strategy will contribute to the up-scaling of antibody-conjugated nanoparticles and to the future developments of targeted nanoparticles with multiple functionalizations.



**Figure 1.** Schematic representation of the antibody-conjugated nanoparticle preparation: (a) Mesoporous silica nanoparticles (MSNPs) loaded with the drug (Doxorubicin) and coated with a polyethyleneimine (PEI) layer (gray) are grafted with an Azide moiety (N<sub>3</sub>, green) using NHS ester coupling. (b) The lysine residues (purple) of different antibodies were labelled with a DBCO moiety (blue) via NHS ester coupling. (c) Click chemistry reaction of the Azide-functionalized nanoparticle with the DBCO-labelled antibodies resulting in the final antibody-conjugated nanoparticle.

## 2. Materials and Methods

### 2.1. Materials

Mouse anti-human EGFR ( $\alpha$ EGFR, monoclonal, cat. BE0278) and rat anti-human CD44 ( $\alpha$ CD44, monoclonal, hermes-1, cat. BE0039) were purchased from Bio X Cell (Lebanon, NH, USA). Goat anti-rabbit IgG (cat. ab6702) was purchased from Abcam (Cambridge, United Kingdom). Secondary antibodies, donkey anti-rat IgG Alexa Fluor 488 (cat. A-21208) goat anti-mouse IgG Alexa Fluor 488 (cat. A11001), Dulbecco's modified eagle medium (DMEM), LysoTracker™ Deep Red, DiR lipophilic dye, Gentamicin, Dulbecco's phosphate buffered saline (PBS, no calcium, no magnesium), Formaldehyde (4% in PBS), trypsin-EDTA (0.5%), Hank's balanced salt solution (HBSS, no phenol red), Ethanol (absolute, 99.9%), donkey-anti-rat IgG-Alexa Fluor 488 (cat. A-21208), and Zeba™ Spin Desalting Columns (40K MWCO, 0.5 mL) were purchased from ThermoFisher Scientific (Waltham, MA, USA).



Tetraethyl orthosilicate (TEOS, 98%), cetyltrimethylammonium chloride solution (CTAC, 25% in H<sub>2</sub>O), triethanolamine (TEA, 99%), hydrochloric acid (HCl, 1 N), Rhodamine B basic violet 10 (RhoB, 93%), Fluorescein isothiocyanate (FITC), (3-Aminopropyl)triethoxysilane (APTES), polyethyleneimine solution (PEI, 50% w/v in H<sub>2</sub>O), Triton X-100 (0.1%), *N*-(3-dimethylaminopropyl)-*N'*-ethyl-carbodiimide (EDC, 97%), Dimethyl sulfoxide (DMSO, >99.5%) and 3D Petri Dish<sup>®</sup>—Microtissues were purchased from Sigma Aldrich (Saint Louis, MO, USA). Atto488 and Atto565 NHS ester conjugate were purchased from Atto-TEC GmbH (Martinshardt, Siegen, Germany). DBCO-PEG<sub>4</sub>-NHS-ester and N<sub>3</sub>-PEG<sub>4</sub>-NHS-ester were purchased from Click Chemistry Tools (Scottsdale, AZ, USA). The A549 cell line was obtained from Sigma Aldrich (ECACC 86012804). The A431, Hek293T and NIH3T3 cell lines were a kind gift from Prof. Hideaki Mizuno (KU Leuven, Belgium) [49,50]. The HepG2 cell line was obtained from Prof. Hitoshi Kasai (Institute of Multidisciplinary Research for Advanced Materials (IMRAM, Chome-1-1 Katahira, Aoba Ward, Sendai, Miyagi 980-8577, Japan [51]). BJ1-hTERT cells were a kind gift of Dr. Barderas (Instituto Salud D. Carlos III, Spain). FuGENE<sup>®</sup> 6 and Alexa Fluor 488 HaloTag<sup>®</sup> ligand were both purchased from Promega (Madison, WI, USA). The pcDNA3-EGFR-HaloTag<sup>®</sup> plasmid was a kind gift from the laboratory of Prof. Dr. Hideaki Mizuno (KU Leuven, Belgium). All the chemicals were used without further purifications.

## 2.2. CD44, EGFR and IgG Antibody Labelling

The antibodies (rat anti-human CD44, mouse anti-human EGFR and goat anti-rabbit IgG) were functionalized with DBCO-PEG<sub>4</sub>-NHS ester for conjugation onto the nanoparticles via copper-free click chemistry. In addition, a fluorescent label, Atto565-NHS ester (for the EGFR antibody and the IgG) or Atto488-NHS ester (for the CD44 antibody), was sometimes grafted onto the antibody for further investigations via fluorescence microscopy. The labelling of 500 µg of antibody was carried out in 50 mM of borate buffer pH 8.5 (antibody concentration 1 mg/mL). Then, 10 molar equivalents of DBCO-PEG<sub>4</sub>-NHS ester and 2 molar equivalents of Atto565-NHS ester or Atto488-NHS ester (when needed) were added to the reaction, according to Eggermont and Hammink et al. [52]. After 6 h under magnetic stirring at room temperature, the dual labelled antibodies were purified over a 0.5-mL 40K Zeba desalting column to remove residual-free Atto565-NHS ester and DBCO-PEG<sub>4</sub>-NHS ester molecules. After purification, absorption measurements were carried out using a UV-VIS spectrophotometer (BioDrop µLite, BioChrom in Figure S2). The absorption at different wavelengths was used to determine the concentration of protein, DBCO and fluorescence dyes ( $A_{280}$  for the antibody,  $A_{309}$  for DBCO,  $A_{488}$  for Atto488 and  $A_{565}$  for Atto565). The values obtained corresponded to a labelling degree of an average of 10 molecules of DBCO and 2 dye molecules per antibody (absorption spectra shown in Figure S2). Previous reports have shown that this degree of labelling does not induce loss of antibody specificity [53].

## 2.3. Synthesis MSNPs

The MSNPs were synthesized by the biphasic stratification method reported by Shen et al. [54]. In short, 0.18 g of TEA was mixed with a solution of 24 mL of CTAC and 36 mL of milli-Q water. This mixture was heated to 60 °C under magnetic stirring for 1 h. Next, 20 mL of TEOS (20 v/v % in octadecene) was slowly added with a syringe and the reaction was kept proceeding overnight. When fluorescein (FITC) was linked to the MSNPs' matrix (FITC encapsulation), 16.6 mg of FITC was dissolved in 10 mL 99.8% ethanol and 400 µL of (3-Aminopropyl)triethoxysilane (APTES). This mixture was stirred for 2 h under inert atmosphere to couple FITC to the aminosilane. After 2 h, the solution was added together with the TEOS. Next, the reaction was cooled down to room temperature and the nanoparticles were washed with a solution of HCl 1.1 M in water/ethanol (v/v = 1.25:10) with centrifugation-dispersion-sonication cycles to remove CTAC from the pores.

Subsequently, the nanoparticles were washed two times with milli-Q water in order to neutralize the pH.

#### 2.4. MSNP Dye/Drug Loading

The pores of the MSNPs were loaded with doxorubicin (Dox) or rhodamine B (RhoB) for cytotoxicity experiments and fluorescence imaging, respectively. Loading of RhoB was performed in milli-Q water under magnetic stirring for 3 h. For Dox loading, MSNPs were first dispersed in phosphate buffer (pH 9) to maximize the loading efficiency. To avoid Dox aggregation, the solution containing Dox and MSNPs was sonicated for 10 min. Next, the solution was stirred for 24 h at 400 rpm. After loading (of Dox or RhoB), the solution was centrifuged and the supernatant was replaced with milli-Q water and the Dox- and RhoB-loaded nanoparticles were re-suspended (MSNPs\_Dox and MSNPs\_RhoB, respectively). The supernatants of all the centrifugation steps were collected and measured with a spectrometer in order to quantify the Dox loaded inside the MSNPs. We estimated a Dox concentration in the MSNPs of approximately 50  $\mu\text{M}$ .

#### 2.5. MSNP Functionalization

To coat the nanoparticles with a PEI layer, a 0.75% PEI solution (in milli-Q water), adjusted to pH 7 (with 37% HCl) was added to the dye or drug-loaded MSNPs (1:1 ratio) in a plastic vial. This mixture was magnetically stirred for 3 h, yielding PEI-coated MSNPs. To facilitate the Azide conjugation, PEI-coated particles were dispersed in borate buffer (pH 8.5). To conjugate the NHS ester-PEG<sub>4</sub>-N<sub>3</sub> linker to the PEI amine groups, an NHS ester reaction was used. In detail, 1.5 mg NHS ester-PEG<sub>4</sub>-N<sub>3</sub> (in DMSO) were added to 500  $\mu\text{L}$  of PEI-MSNPs (10 mg/mL) in a dropwise manner and magnetically stirred for 4 h. After the reaction, the nanoparticles were centrifuged and re-dispersed in borate buffer (N<sub>3</sub>-PEI-MSNPs). To conjugate the desired antibody via a copper-free click reaction, 100  $\mu\text{g}$  of labelled antibody (50  $\mu\text{L}$  of 1 mg/mL labelled antibody solution in borate buffer) were added to 450  $\mu\text{L}$  of N<sub>3</sub>-PEI-MSNPs (10 mg/mL). The reaction was stirred for 6 h at room temperature. After the reaction, nanoparticles (Ab-PEI-MSNPs) were centrifuged at low speed (700 RPM) and re-dispersed in milli-Q water.

#### 2.6. Ab-PEI-MSNPs' Characterization

The synthesized nanoparticles were characterized by confocal fluorescence microscopy, scanning electron microscopy (SEM), and atomic force microscopy (AFM). For the fluorescence microscopy experiments, 60  $\mu\text{L}$  Ab-PEI-MNSP solution was pipetted in a Coverwell™ perfusion chamber (ThermoFisher Scientific) placed onto a #1 coverglass. After 30 min, when some nanoparticles had sedimented, the sample was imaged with a Leica TCS SP8 mini microscope (Wetzlar, Germany). For SEM measurements, nanoparticles were drop-casted onto an Indium-Tin Oxide-coated glass and dried. Next, the glass was coated with Au/Pd for 20 s. Nanoparticles were visualized using a FEI Quanta 250 FEG Scanning Electron Microscope (ThermoFisher Scientific). Zeta potential measurements were carried out on a Malvern Zetasizer system (Malvern, UK). For AFM characterization, an Agilent 5500 AFM with MAC III controller was used for morphological imaging in intermittent contact mode in air. MSNL-F ( $f = 120 \text{ kHz}$ ,  $k = 0.6 \text{ N m}^{-1}$ , tip radius of curvature  $< 12 \text{ nm}$ ) probes were used. The AFM topography images were leveled, line-corrected, and measured (line profiles for diameter determination) using Gwyddion, a free and open-source SPM (scanning probe microscopy) data visualization and analysis program (version 2.48) [55]. AFM samples were prepared on silicon substrates freshly cleaned in piranha solution. For bare and functionalized MSNPs that carry a negative surface charge, the clean substrate was first incubated in PAH, followed by rinsing and drying. On the other hand, PEI-modified MSNPs were deposited on a bare silicon substrate. For each sample, the nanoparticle suspension was incubated for 1 min on the substrate, before rinsing with ultrapure water and drying with pure nitrogen gas. To check the colloidal stability of the Ab-PEI-MSNPs, turbidity measurements were performed. Accordingly, the sample turbidity (optical density) of the nanoparticles dissolved in different media (milli-Q water, FBS and DMEM+ 10% FBS) was determined before and after 24 h of incubation at 37 °C by measuring the absorbance at 600 nm.

### 2.7. Cell Culture

A549 cells, HepG2, BJ1-hTERT, NIH3T3, Hek293 and A431 cells were cultured in 25 cm<sup>2</sup> culture flasks at 37 °C under 5% CO<sub>2</sub> atmosphere. All cell lines were maintained in DMEM medium with 10% FBS, 1% L-glutamax and 0.1% gentamicin. For fluorescence microscopy experiments, the cells were seeded in 29-mm, glass-bottom dishes (Cellvis, Mountain View, CA, USA) and grown until ~60% confluency before adding the nanoparticles.

### 2.8. Immunofluorescence Labeling

A549 and HepG2 cells were stained with both the dual-labelled (with DBCO and Atto488) and non-labelled CD44 antibody (rat anti-human CD44). First, cells were seeded in two glass-bottom dishes and grown overnight. Next, the cells were fixed with paraformaldehyde (4%) and the membrane was permeabilized with Triton X-100 (0.1%), for 10 min. The sample was carefully washed with PBS (1×) between each step. After washing, blocking was performed for 1 h with a bovine serum albumin solution (3% in PBS). The dual-labelled and non-labelled CD44 antibodies were added to the cells at a final concentration of 2 µg/mL and incubated overnight at 4 °C. After antibody incubation, the dual-labelled antibody samples were washed three times with PBS. The samples containing non-labelled antibody were washed three times with PBS and incubated with the secondary antibody, donkey-anti-rat IgG-AF488, at a final concentration of 1 µg/mL for 2 h. After that, the samples were washed with PBS. The same protocol was used for the immunofluorescent staining of A431 and Hek293 cells with both the dual-labelled and non-labelled EGFR antibody (mouse anti-human EGFR). In this case, a goat-anti-mouse IgG AF488 secondary antibody was used after incubation with the non-labelled antibody.

### 2.9. Ab-PEI-MSNPs' Targeting Efficiency

A549 cells, HepG2, BJ1-hTERT, NIH3T3, Hek293 and A431 cells were seeded in a 29 mm, glass-bottom dish and grown until 60–80% confluency. FITC-encapsulated nanoparticles with different functionalization (bare MSNP, PEI-coated MSNPs, EGFR or CD44 antibody-conjugated MSNPs, and IgG-conjugated MSNPs) were added to the cells to a final concentration of 50 µg/mL. After 6 h of incubation with the NPs, the cells were washed three times with PBS and fresh medium was added to the samples. The samples were placed back in the incubator for an additional 24 h incubation. Prior to imaging, the plasma membrane was stained using DiR (1 µM) in HBSS for 13 min and the sample was washed three times with HBSS. The resulting images were analyzed to quantify the amount of nanoparticle internalization by calculating the mean fluorescence intensity of the nanoparticle signal inside at least 20 cells per condition using the Fiji open source software (version 1.51). [56]. Briefly, the cell area (region of interest, ROI) was manually selected based on the membrane staining. Next, the mean fluorescence intensity of the nanoparticles was calculated for each ROI.

### 2.10. Transfection of Hek293

Hek293 was reverse transfected with a pcDNA3-EGFR-HaloTag<sup>®</sup> [50]. Transfection was carried out according to the supplier's protocol (FuGENE<sup>®</sup> 6, Promega). Briefly, 1 µg of DNA was added to 100 µL of serum-free DMEM medium together with 3 µL of the transfection reagent. This mixture was vortexed shortly and incubated for 17 min. Meanwhile, the cells were passaged and plated in 29-mm, glass-bottom dishes (Cellvis). After 17 min of incubation, the transfection mixture was added to the plated cells in a dropwise manner. The next day, αEGFR-PEI-MSNPs were added to the transfected Hek293 cells. After 3 h, the medium was refreshed to avoid continued uptake of nanoparticles. The cells were incubated with the nanoparticles for a total of 24 h. After incubation, EGF receptor was visualized in the transfected Hek293 cells after incubation with the Alexa Fluor 488 HaloTag<sup>®</sup> ligand (Promega) for 30 min at 37 °C (final ligand concentration of 250 nM in cell medium).

### 2.11. Fluorescence Microscopy

Confocal fluorescence imaging was performed on a Leica TCS SP8 mini microscope implementing a HC PL APO 63× water immersion objective (NA 1.2). Distinct diode lasers were used depending on the dye. For LysoTracker™ DeepRed and DiR lipophilic dye, a red, 638-nm diode laser was used at a laser power between 10 and 60 μW. For RhoB or Atto565 detection, a green, 552-nm diode laser was used for excitation (laser power between 20 and 80 μW), while the blue, 488-nm diode laser was used to excite Doxorubicin, FITC and Atto488 (laser power between 10 and 50 μW). The laser powers were measured at the objective. Detection was performed with HyD SMD high-sensitivity detectors in standard mode, operating in a detection range of 400 to 800 nm. The detection range was adjusted depending on the dye, with 500–550 nm for Atto488 and FITC detection, 570–600 nm for Doxorubicin, RhoB, and Atto565 and 650–750 nm for LysoTracker™ DeepRed and DiR lipophilic dye detection. The images were acquired with a z-step of 1 μm and line averaging of 3.

### 2.12. The αCD44-PEI-MSNPs' Intracellular Localization

A549 cells were incubated with αCD44-PEI-MSNPs\_RhoB for 24 h (at a final concentration of 50 μg/mL). The sample was then washed three times with PBS to remove extracellular nanoparticles and kept in HBSS during image acquisition. One sample was imaged immediately after 24-h incubation, while two other replicates were placed back in the incubator for the 48- and 72-h time points (after replacing the PBS for cell culture medium). Prior to imaging, the samples were washed with HBSS and the lysosomes were stained with LysoTracker™ Deep Red (100 nM final concentration in HBSS) for 15 min. After washing three times with PBS, the samples were imaged in HBSS. The fluorescence images acquired (see Fluorescence microscopy section) were processed and analyzed using Fiji and the built-in, co-localization plugin JACoP [57]. Within this plugin, Manders co-localization was found as an appropriate analysis strategy as this method measures the fraction of co-occurrence of the signal in two channels rather than their correlation [58]. After manual selection of the cell area with the region of interest (ROI) manager, the Manders' coefficient (MC) was calculated for 28–40 biological replicates for each time point (using three technical replicates). More specifically, MC indicates the fraction of pixels of the αCD44-PEI-MSNPs' ROI that overlap with the pixels of the LysoTracker ROI, resulting in a value between 0 and 1. One means that 100% of the pixels of the αCD44-PEI-MSNPs' ROI overlap with the pixels of the LysoTracker channel, with 0 being a 0% pixel overlap.

### 2.13. Doxorubicin Release

The αCD44-PEI-MSNPs were loaded with doxorubicin to a final concentration of 40 μM (αCD44-PEI-MSNPs\_Dox). A549 cells were incubated with αCD44-PEI-MSNPs\_Dox for 24 h. After 24 h of incubation, the sample was washed with PBS three times to remove extracellular nanoparticles and kept in HBSS during image acquisition. One sample was immediately measured (with confocal fluorescence microscopy), while two other replicates were placed back in the incubator for the 48- and 72-h time points (after replacing the PBS by cell culture medium). An additional sample was checked after 8 h of nanoparticle incubation, in order to monitor nanoparticle endocytosis. Prior to imaging, the samples were washed three times with PBS and the acidic vesicles were visualized by adding a solution containing LysoTracker™ Deep Red (100-nM final concentration in HBSS) for 15 min. After a final washing step with PBS, the samples were imaged in HBSS using a confocal microscope.

### 2.14. Cytotoxicity Studies

A549 and HepG2 cells were seeded in a 96-well plate at a density of  $2 \times 10^4$  cells/well. The next day, 25, 50, 100 and 200 nM of Dox and 25, 50, 100 and 200 μg/mL of empty and Dox-loaded αCD44-PEI-MSNPs were added to the A549 cells. Four biological replicates were prepared for each condition. Cells incubated with nanoparticles were washed with

PBS after 24 h of nanoparticle incubation to remove the excess of nanoparticles. The PBS was then replaced by fresh medium and the sample was placed in the cell incubator. Then, 72 h after the addition of free Dox or nanoparticles, the cells were washed 3× with PBS and fixed with 4% PFA (in PBS). Cells were incubated with Hoechst 33342 (1 µg/mL) for 1 h. After washing with PBS, the viable cells were imaged using a Lionheart FX automated microscope (BioTek, Santa Clara, CA, USA) implementing a 10× air objective (NA: 0.3) and a high-power LED of 365 nm, combined with a DAPI filter cube. Images were analyzed using the Gen5™ software (version 3.11.19).

### 2.15. Statistical Analysis

The data are displayed as means ± standard deviations and error bars indicate ± standard deviation. A randomization test was used to compare any two groups of values and performed in the online software tool “Plots of Difference” [59]. Statistical significance was reported as \*  $p < 0.05$ , \*\*  $p < 0.01$ , and \*\*\*  $p < 0.001$ .

## 3. Results and Discussion

### 3.1. The $\alpha$ CD44-Conjugated Nanoparticles

CD44 is a transmembrane glycoprotein receptor overexpressed in different cancers (e.g., breast, lung, colon, head and neck, and pancreatic cancer [60–63]) and cancer stem cells [64,65]. Its presence is often associated with high malignancy and chemo-resistance, making it an important cancer biomarker and target for cancer therapy. Hyaluronic acid (HA) is a ligand for the CD44 receptor and has, therefore, been widely exploited as a poly-mer coating in targeted DDSs [2,66,67]. The ligand, HA, is naturally present in the extracellular matrix (ECM), leading to possible competition between HA from the ECM and the HA on the nanoparticles. As an alternative, antibodies with a high affinity for CD44 can be implemented in the DDS to target the receptor [68–70].

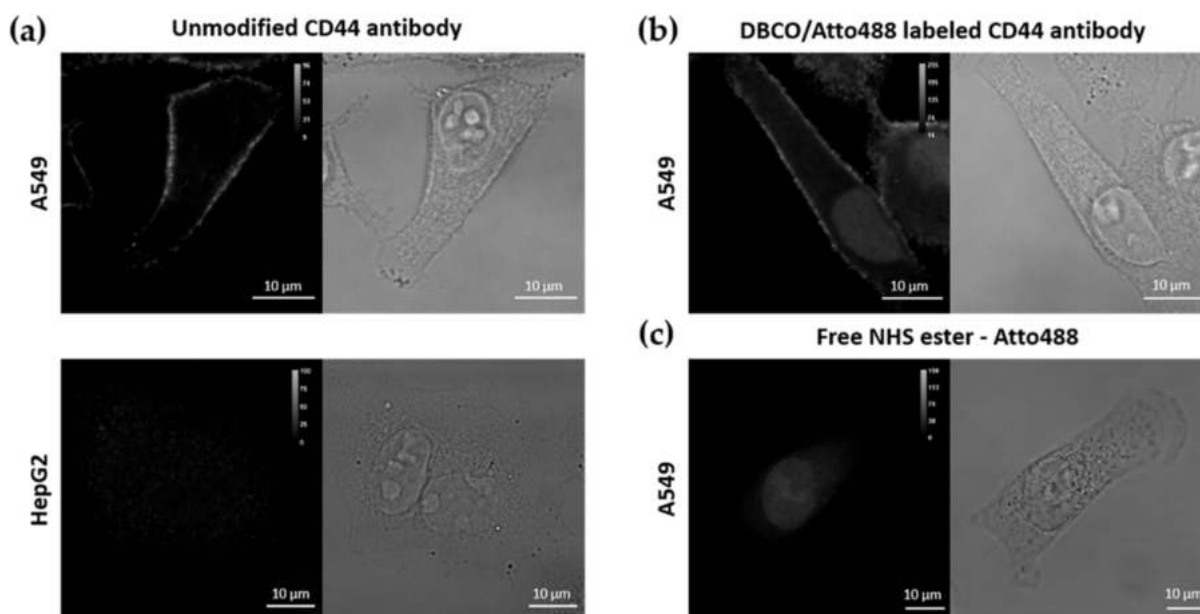
#### 3.1.1. Synthesis of Azide-Functionalized MSNPs

Our approach to conjugate antibodies to nanoparticles comprised the grafting of different groups on both the antibody and the nanoparticle, separately (Figure 1). As a model for nano-carriers, we used MSNPs. PEI-coated MSNPs were prepared as previously described [49]. Briefly, MSNPs were synthesized using the biphasic stratification method and loaded with either Dox or RhoB, for cytotoxicity studies or imaging assays, respectively. The fluorescence spectra of the dye/drug-loaded MSNPs are shown in Figure S1 (Supplementary Materials). A PEI layer (Mw = 1.3 kDa) was deposited on the MSNPs (PEI-MSNPs), through electrostatic interactions. In our approach, the PEI layer served two purposes: to provide the nanoparticles with the capability of endosomal escape (as reported by Fortuni et al. [49]) and to functionalize the surface of the NPs with amine groups. These amine groups were used as an anchor for further covalent functionalization. An Azide moiety was covalently linked to the PEI-MSNPs, making use of an NHS ester-PEG<sub>4</sub>-N<sub>3</sub> linker via NHS ester coupling (N<sub>3</sub>-PEI-MSNPs, Figure 1a). The central poly(ethylene)glycol (PEG) chain provided extra stealth to the DDS, increasing its biocompatibility. The resulting surface Azide groups served as docking sites for the antibodies.

#### 3.1.2. Labelling of CD44 Antibodies

To attach the antibody molecules to the Azide-grafted nanoparticles, the antibodies were functionalized with a DBCO moiety (Figure 1b). Additionally, for visualization purposes, a fluorescent dye (Atto488 or Atto565) was also added, yielding dual-labelled antibodies. As described in the Methods section, labelling of the lysine residues of the antibody was achieved via an NHS ester coupling reaction. The presence of the DBCO moiety was verified via UV-VIS absorption measurements (absorption peak at 309 nm, see Figure S2 in Supplementary Materials). To confirm that the addition of DBCO and/or fluorescent dye did not affect the specificity of the antibody, we performed immunostainings of two cell lines, A549 and HepG2 cells, with high and low expression level of CD44,

respectively [60]. Before testing the specificity of the DBCO/Atto488-labelled antibodies, the CD44 expression level in both cell lines was evaluated using immunofluorescence. For this, we stained the cells with an unmodified CD44 antibody, followed by a second staining step with a fluorescently labelled secondary antibody. As shown in Figure 2a, CD44 receptor molecules were detected in A549 cells (localized to the cell membrane), while no CD44 immunostaining was visible on the fluorescence images acquired for HepG2 cells. A549 cells stained with the DBCO/Atto488 dual-labelled CD44 antibodies displayed a fluorescence signal on the plasma membrane, indicating that the specificity of the antibody was retained after labelling (Figure 2b). The fluorescence signal present in the nucleus was attributed to the free dye molecules still present in solution after the labelling procedure (Figure 2c).



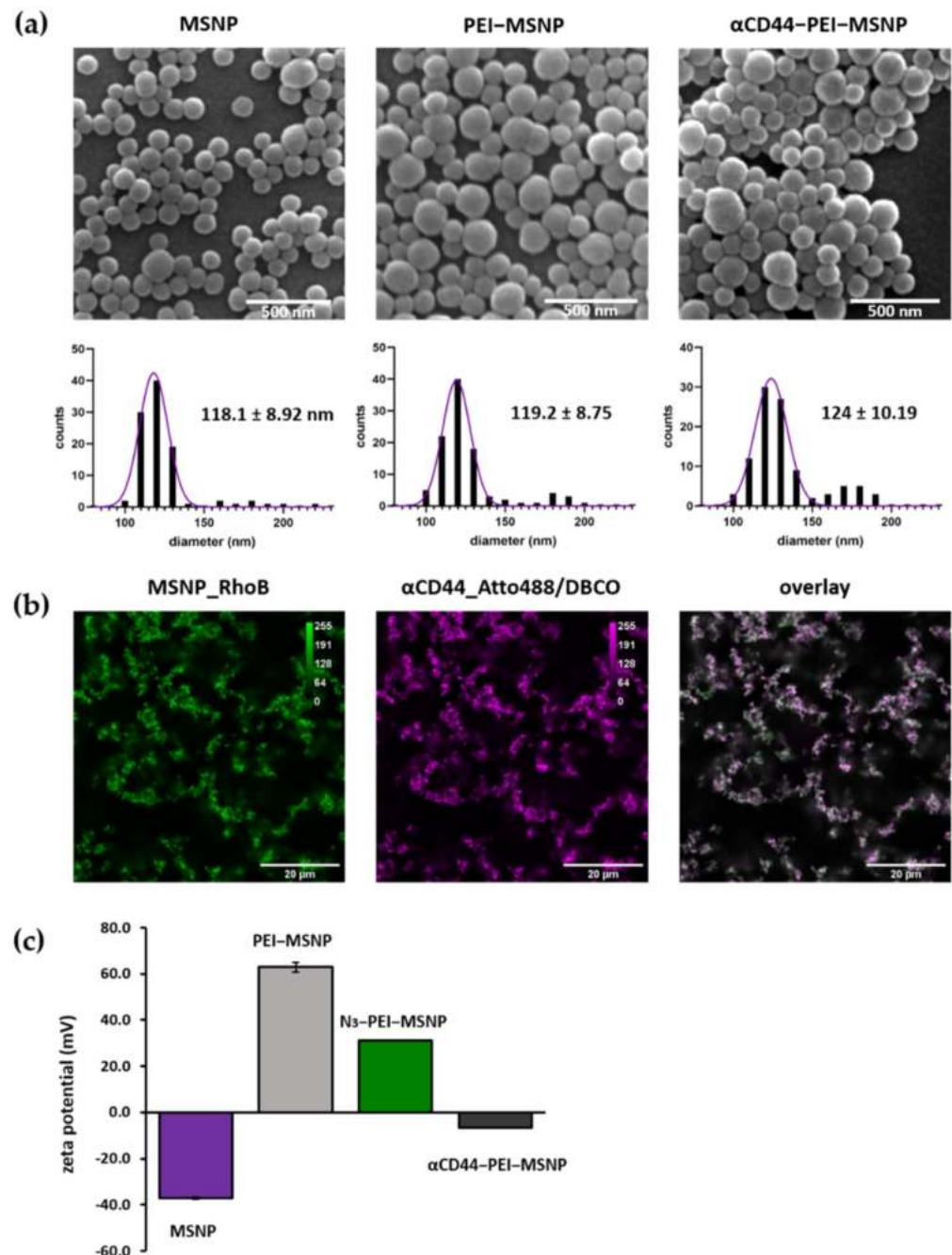
**Figure 2.** Immunofluorescence (IF) using (a) the unmodified primary rat anti-human CD44 antibody and a secondary donkey anti-rat IgG Alexa Fluor 488 antibody on A549 and HepG2 cells, (b) dual DBCO/Atto488-labelled CD44 antibodies in A549 cells and (c) free NHS ester-Atto488 molecules. Scale bar is 10 µm.

### 3.1.3. Synthesis and Characterization of $\alpha$ CD44-Conjugated MSNPs

The antibody was covalently linked on the nanoparticle via copper-free click chemistry between the Azide moiety and the DBCO-labelled antibody (generating  $\alpha$ CD44-PEI-MSNPs, Figure 1c). The developed nanoparticles were characterized using scanning electron microscopy (SEM), atomic force microscopy (AFM), zeta potential measurements, and fluorescence microscopy.

SEM images displayed a uniform size and shape homogeneity of the bare MSNPs, PEI-MSNPs and  $\alpha$ CD44-PEI-MSNPs (conjugation with  $\alpha$ CD44), with a mean diameter of 118, 119 and 124 nm, respectively (Figure 3a). The average size of the bare and PEI-coated MSNPs was in agreement with previous reports [49]. Further, a low degree of aggregation was observed in all the samples. Although there was no significant difference in diameter between the bare MSNPs and the PEI-MSNPs, a significant increase could be observed upon antibody functionalization ( $p < 0.05$ ). These results were confirmed with AFM measurements, where an average nanoparticle height of 121, 123 and 128 nm was detected for the MSNPs, PEI-MSNPs and  $\alpha$ CD44-PEI-MSNPs, respectively. The corresponding AFM images and plots are displayed in supporting information (Figure S3 in Supplementary Materials). The increase in MSNP height upon antibody functionalization indicated a

successful attachment to the surface. The small difference can be attributed to the average size of an antibody (in the range of 5 to 15 nm, depending on its orientation).



**Figure 3.** Characterization of bare (MSNPs), PEI-coated (PEI-MSNPs), Azide-functionalized (N<sub>3</sub>-PEI-MSNPs), and CD44-conjugated ( $\alpha$ CD44-PEI-MSNPs) mesoporous silica nanoparticles. (a) Representative SEM images and size distribution of the imaged particles. Values shown as mean  $\pm$  SD. Scale bar is 500 nm. (b) Confocal fluorescence images of  $\alpha$ CD44-PEI-MSNPs in which MSNPs were loaded with RhoB (first panel, green), while an Atto488 (and DBCO) label was conjugated to the CD44 antibody (second panel, magenta). An overlay is displayed in the third panel. Scale bar is 20  $\mu$ m. (c) Zeta-potential measurements given as mean  $\pm$  SD.

Zeta potential measurements were used to follow each step of the functionalization process. Bare MSNPs had a negative charge ( $-37.5$  mV) due to the partially deprotonated hydroxyl groups on the MSNP surface. Upon PEI coating, the zeta potential increased

to +63 mV as a result of the presence of amine groups in PEI. Subsequent coupling of the Azide moiety was reflected in a decrease in the zeta potential (+31 mV) (Figure 3c). This decrease can be associated with the formation of an amide upon NHS coupling to the amine. Since the amine was positively charged and the resulting amide was neutral, the reaction promoted a decrease in the overall charge. Finally, a further decrease in zeta potential (−6.7 mV) upon antibody grafting could be observed (Figure 3c). The charge of the nanoparticle after antibody conjugation can be related to the isoelectric point (IEP) of the antibody. Since the IEP of IgG antibodies lies between 6.6 and 7.2 [71], antibodies were expected to be negatively charged at neutral pH, which agreed with our zeta potential results and previously reported results [41,72]. To evaluate the uniformity of antibody conjugation, MSNPs were loaded with a dye (RhoB) before functionalization. Since the antibodies were fluorescently labelled (Atto488), the colocalization between the RhoB-loaded MSNPs and the antibody was evaluated with confocal fluorescence microscopy. Figure 3b shows a clear overlap between the Atto488-labelled antibody and the RhoB-loaded MSNPs. This fluorescence data supported the findings obtained from AFM and the zeta potential measurements, indicating the proper conjugation of the antibody.

The colloidal stability of the antibody-conjugated nanoparticles in the presence of serum was investigated using turbidity measurements. Turbidity measurements are a standard technique to detect particle aggregation, and are well described in literature [73]. This technique is based on the scattering of light by a solution of particles, which corresponds to the turbidity of the suspension. The scattered light is detected via the absorbance at 600 nm ( $OD_{600}$ ). This results in a value for the optical density of the samples, which is higher for more turbid samples. CD44 antibody-conjugated nanoparticles, dissolved in milli-Q water, FBS, and DMEM medium with 10% FBS (used for cell culture experiments), were incubated for 24 h at 37 °C. The  $OD_{600}$  was determined at time 0 and after 24 h of incubation. The absorbance values are presented in Table S1 (Supplementary Materials) and showed no significant increase in sample turbidity after 24 h of incubation in all the tested solutions, indicating that the particles were not prone to aggregation in the presence of serum proteins.

### 3.2. Selectivity and Efficiency of $\alpha$ CD44-Functionalized Particles

#### 3.2.1. Targeting Capability of $\alpha$ CD44-PEI-MSNPs

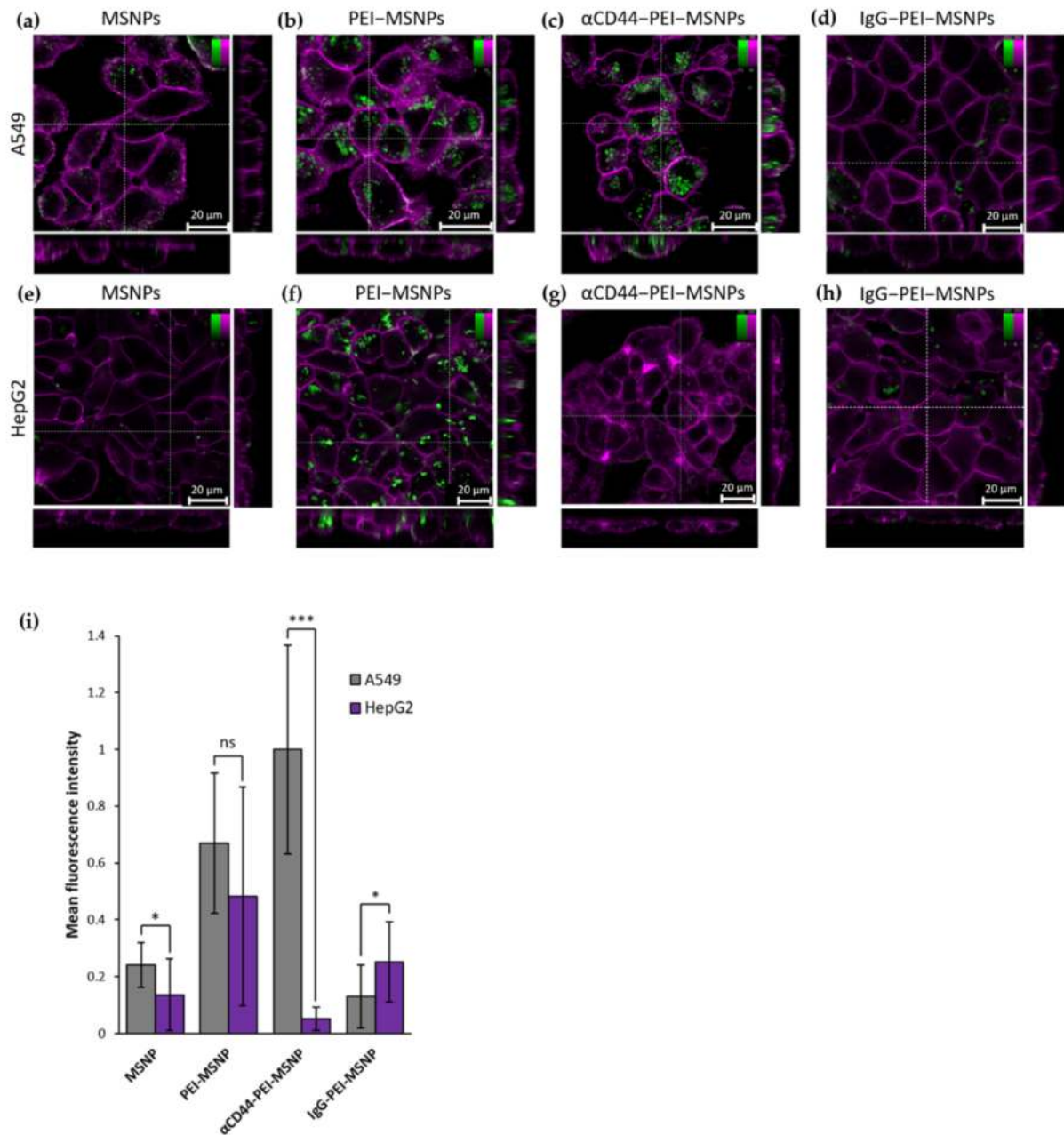
To assess the targeting capability of the antibody-conjugated MSNPs towards CD44-overexpressing cells, FITC-encapsulated MSNPs were used to monitor the cellular uptake via fluorescence microscopy. In this case, targeting capability refers to the selective uptake of the CD44 antibody-conjugated nanoparticles to CD44 receptor-overexpressing cells. The targeting efficiency was tested by comparing the number of nanoparticles internalized in A549 cells (human lung carcinoma cells, with CD44 receptor overexpression [74]) and HepG2 cells (liver carcinoma, with low CD44 receptor expression [75]). Both cell lines were incubated for 6 h with MSNPs presenting different functionalization: no coating (MSNPs), only a PEI coating (PEI-MSNPs) and both the PEI and antibody functionalization ( $\alpha$ CD44-PEI-MSNPs). As a control, the cells were also incubated with a nanoparticle conjugated to a non-specific IgG antibody (IgG-PEI-MSNPs). Afterwards, the medium was refreshed to avoid further nanoparticle internalization and the cells were incubated overnight (24 h incubation in total). The internalization was quantified by confocal fluorescence imaging after staining the plasma membrane with a lipid intercalating dye (DiR). The fluorescence images are shown in Figure 4. The uptake of bare MSNPs was minimal in both cell lines (Figure 4a,e), while a coating with PEI resulted in an increase in internalization in both A549 and HepG2 (Figure 4b,f). The increase in cellular uptake of nanoparticles upon PEI functionalization was in agreement with previous reports and can be attributed to the positive charge of PEI-MSNPs, leading to a higher interaction with the negatively charged plasma membrane, which facilitates nanoparticle internalization [49,51,76,77]. It is important to note that this enhanced uptake of PEI-coated MSNPs was cell line unspecific. Thanks to the charge drop (from +63 mV to −6.7 mV), this unspecific internalization was minimized



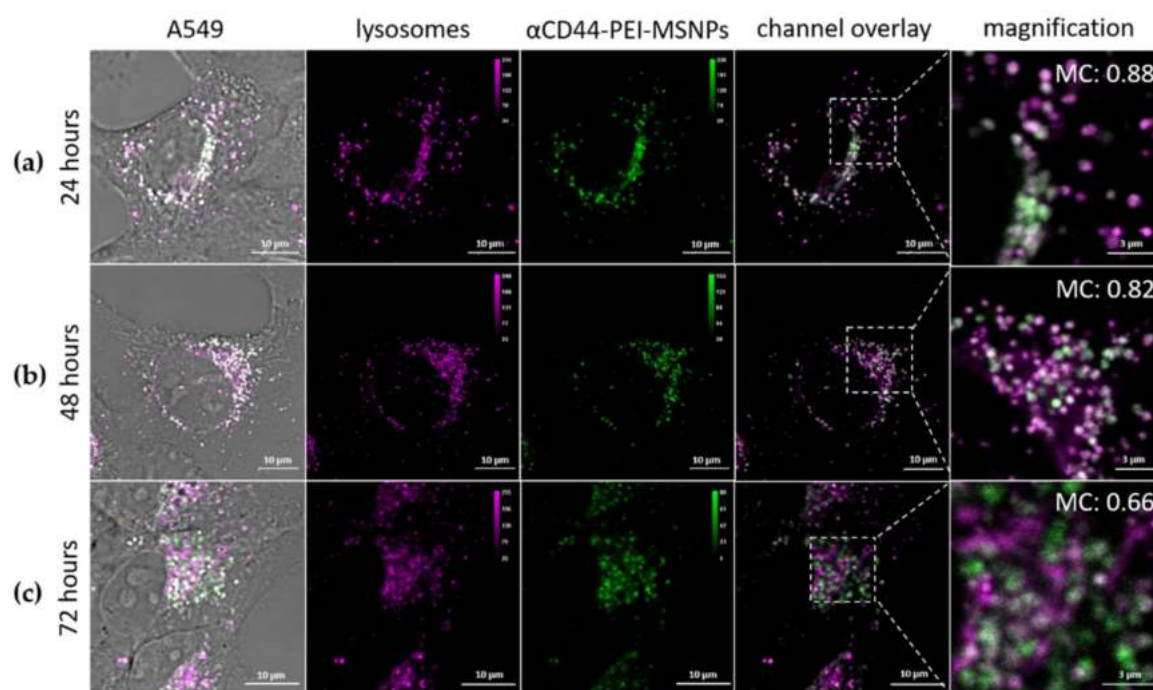
upon antibody conjugation to MSNPs. As such, uptake of  $\alpha$ CD44-PEI-MSNPs in HepG2 was lower, similar to the internalization of bare MSNP (Figure 4g). On the other hand, A549 cells incubated with  $\alpha$ CD44-PEI-MSNPs displayed a high number of internalized particles, especially when compared to bare MSNP (Figure 4e). A quantitative mean fluorescence intensity of the internalized nanoparticles revealed that there were 20 times more particles inside A549 cells when compared to HepG2 cells (Figure 4i). Incubation with the non-specific IgG-conjugated nanoparticles resulted in an uptake comparable to bare MSNPs in both A549 and HepG2 cells. This low internalization could be explained by the non-specificity of this antibody to membrane proteins in these cell lines and the negative zeta potential ( $-11.8$  mV) of the resulting IgG-conjugated nanoparticles (which minimized their non-specific uptake). To assure that the observed increase in cellular uptake in CD44-overexpressing cells was not linked to the specific cell lines used, we checked the uptake of  $\alpha$ CD44-PEI-MSNPs in two fibroblast cell lines, NIH3T3 (mouse embryonic fibroblasts with a low CD44 expression [78,79]) and BJ1-hTERT (human fibroblasts with high CD44 expression [80,81]), using the same experimental approach (Figure S4). The respective CD44 expression in the two cell lines was validated with a standard immunofluorescence staining of CD44 (Figure S5, Supplementary Materials). The discrepancy between the uptake of  $\alpha$ CD44-PEI-MSNPs in fibroblasts with different expression levels of CD44 confirmed the targeting efficiency of our nanoparticles after conjugation with the CD44 antibody.

### 3.2.2. Intracellular Trafficking

One of the main bottlenecks faced by DDSs is their entrapment in acidic vesicles and subsequent degradation, significantly limiting the overall efficiency of the DDS [82–84]. To this end, strategies have been developed to facilitate an endosomal escape, releasing the nanoparticles (or their cargo) into the cytoplasm. We previously showed that the addition of a PEI shell leads to the release of the nanoparticles in the cytoplasm [49]. To verify that conjugation to an antibody does not affect the endosomal escape capability of the PEI layer, the co-localization of  $\alpha$ CD44-PEI-MSNPs with lysosomes was monitored using fluorescence microscopy. Briefly, A549 cells were incubated with RhoB-loaded  $\alpha$ CD44-PEI-MSNPs for 24 h, after which the medium of the samples was refreshed, in order to avoid further nanoparticle internalization (i.e., only nanoparticles that were endocytosed within the first 24 h of incubation were followed). At each time point (24, 48 and 72 h after particle addition), the acidic vesicles were stained with LysoTracker Deep Red and the samples were imaged. Figure 5 shows representative fluorescence images at the different time points. To quantify the co-localization between the acidic vesicles and the  $\alpha$ CD44-PEI-MSNPs through time, the Manders' co-localization coefficient was calculated (Figure S6, Supplementary Materials). Briefly, an intensity-based threshold was used to calculate the areas of the image corresponding to nanoparticles and to lysosomes. The Manders' coefficient (MC) calculates the degree of overlap between objects in different channels (with 0 being no overlap and 1 indicating a complete overlap). Fluorescence images showed that, within 24 h, almost all nanoparticles were located inside the acidic vesicles (Figure 5a). While at 24 and 48 h, no relevant escape was observed with MC of 0.88 and 0.82 (Figure S6), a significant decrease in the co-localization of nanoparticles and lysosomes was found after 72 h (MC of 0.66), indicating that after 72 h a considerable number of  $\alpha$ CD44-PEI-MSNPs were localized outside the lysosomes (Figure 5c). Overall, these results suggest that the presence of  $\alpha$ CD44 on the surface of the nanoparticles does not affect the endosomolytic activity of the PEI coating as most of nanoparticles were able to dissociate from the lysosomes within 72 h. This was validated by the significant difference in MC found between 48 and 72 h (Figure S6). The endosomal escape rate was, however, slower than MSNPs coated with only PEI, where the majority of the particles escaped the lysosomes within 48 h (previously reported by our group [49]). Since the proton sponge effect is linked to the amine groups of the PEI, this delay might be associated with the reduced number of amine groups available, as part of these are used for N3 functionalization and further coupling to the antibodies.



**Figure 4.** Confocal fluorescence microscopy images showing the influence of different MSNP coatings on the uptake of nanoparticles in A549 and HepG2 cells. Internalization of bare MSNP (a,e), PEI-coated MSNPs (PEI-MSNPs, panels (b,f)), CD44-functionalized MSNPs ( $\alpha$ CD44-PEI-MSNPs, panels (c,g)), and IgG-functionalized MSNPs (IgG-PEI-MSNPs, panels d,h) in A549 cells (a–d) and HepG2 cells (e–h). Nanoparticles were loaded with Fluorescein (FITC, green) and the plasma membrane was stained with DiR (magenta). The central square represents a single xy plane, while the bottom and left panels are the xz and yz cross-sections, indicated by the dashed lines. Scale bar is 20  $\mu$ M; color bars display the intensity values. (i) Normalized mean fluorescence intensity of MSNP, PEI-MSNPs,  $\alpha$ CD44-PEI-MSNPs, and IgG-PEI-MSNPs internalized in A549 and HepG2 (20 cells per condition). The data were analyzed using Fiji (see Methods section for details). With ns: not significant, \* ( $p < 0.05$ ), \*\*\* ( $p < 0.001$ ).

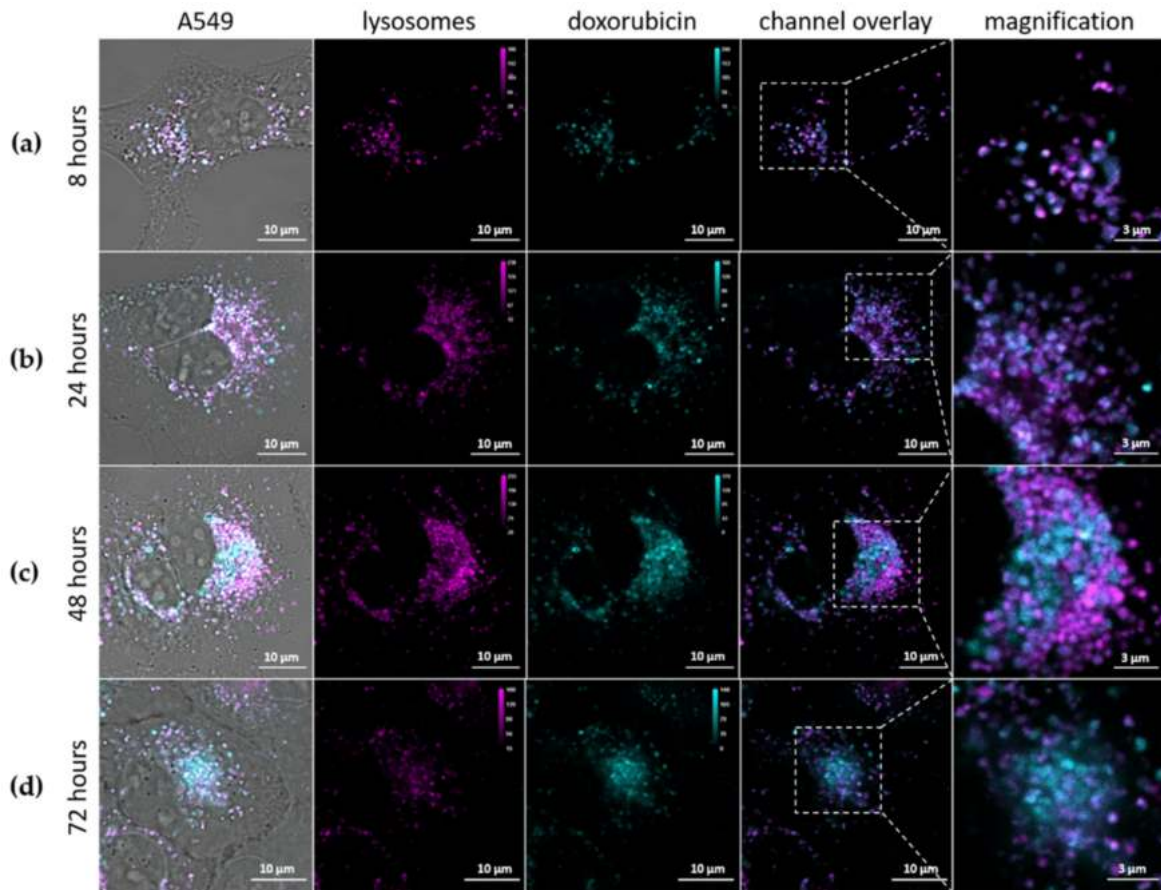


**Figure 5.** Intracellular localization of RhoB-loaded  $\alpha$ CD44-PEI-MSNPs (green) with respect to the lysosomes (Lysotracker Deep Red, magenta) over time. A549 cells were incubated with  $\alpha$ CD44-PEI-MSNPs (final concentration of 50  $\mu$ g/mL) for (a) 24 h (b) 48 h and (c) 72 h. The first column shows a complete merge including the transmission image, also displaying the cell areas. In the second and third columns, the lysosomes and nanoparticles are depicted, in purple and green, respectively. In the fourth and fifth columns, a channel overlay and respective magnification are shown. Scale bar is 10  $\mu$ m in the main images and 3  $\mu$ m in the magnified images.

### 3.2.3. Intracellular Release of Doxorubicin

As shown in the previous section, a considerable number of the internalized  $\alpha$ CD44-PEI-MSNPs were able to escape the acidic vesicles. Aside from the ability to escape the lysosomes, a higher efficiency requires that enough cargo can be released into the cytoplasm in a controlled fashion. To monitor the drug release after cellular uptake, doxorubicin was used as drug model and encapsulated in the pores of MSNPs prior to coating ( $\alpha$ CD44-PEI-MSNPs\_Dox). Dox is a cytostatic anticancer drug that is used to treat different types of cancer, for instance, leukemia, lymphoma, and breast cancer. Its mechanism of action is based on the intercalation with the DNA, resulting in cell death [85]. Due to the fluorescent nature of Dox, its intracellular localization could be monitored over time with confocal fluorescence microscopy. To show that  $\alpha$ CD44-PEI-MSNPs\_Dox carried Dox into the target cell and exhibited a controlled intracellular drug release, A549 cells were incubated with  $\alpha$ CD44-PEI-MSNPs\_Dox for 8, 24, 48 and 72 h. To avoid further nanoparticle internalization, the medium of the samples was refreshed 24 h after the addition of the nanoparticles. The acidic compartments were stained with LysoTracker Deep Red (magenta, Figure 6) to analyze the cargo (Dox, cyan) release/leakage from the lysosomes. While after 8 and 24 h, most of the Dox was still retained inside lysosomes (indicated by the high overlap between the Dox and the lysosomes, Figure 6a,b), increasing amounts of Dox discharged into the cytosol were observed after 48 and 72 h (Figure 6c,d). The overlap between the acidic vesicles and Dox molecules at 8 and 24 h indicated that, at this time point, Dox was presumably still inside the pores of the MSNPs or being slowly released inside the acidic vesicles. At an acidic pH, the silica hydroxyl groups are protonated, hindering the electrostatic interaction between the PEI and the silica surface. Therefore, we hypothesized that the decreased pH inside the lysosomes aids in the release of the shell and facilitates the consequent Dox release from the mesoporous silica pores. Accordingly, increasing

amounts of Dox were detected in the cytoplasm over 48 to 72 h (Figure 6c,d). Moreover, as shown in Figure 6d, the cells' morphology suggested cellular death, indicating that the cells were being killed by the successful release of the drug.

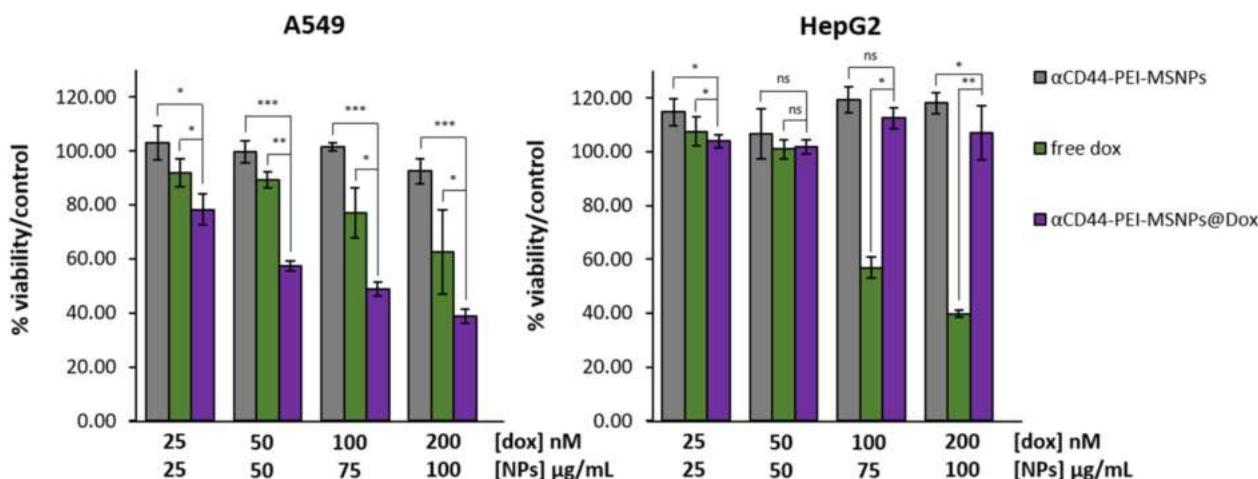


**Figure 6.** Intracellular release of Dox (cyan) from  $\alpha$ CD44-PEI-MSNPs\_Dox with respect to the lysosomes (magenta) over time. A549 cells were incubated with  $\alpha$ CD44-PEI-MSNPs\_Dox (final concentration of 50  $\mu$ g/mL) for (a) 8 h, (b) 24 h, (c) 48 h and (d) 72 h. The first column shows a complete merge including the transmission image, also displaying the cell contours. In the second and third columns, the lysosomes and Dox are depicted, in pink and cyan, respectively. In the fourth and fifth columns, a channel overlay and respective magnification are shown. Scale bar is 10  $\mu$ m in the main images and 3  $\mu$ m in the magnified images.

### 3.2.4. Cytotoxicity Studies

To evaluate the cytotoxicity of the antibody-coated MSNPs, the viability of A549 and HepG2 cells was investigated after 72 h of incubation with pure Dox, Dox-loaded nanoparticles ( $\alpha$ CD44-PEI-MSNPs@Dox), and empty nanoparticles ( $\alpha$ CD44-PEI-MSNPs). After 24 h of incubation with the nanoparticle/drug solution, the medium was refreshed to avoid the continued uptake of nanoparticles/drug in the medium and to better mimic the physiological scenario of nanoparticle clearing from the bloodstream. Different concentrations of Dox and nanoparticles were added, ranging from 25 nM to 200 nM for free Dox and 25 to 100  $\mu$ g/mL for the nanoparticles (Figure 7). For both cell lines, empty  $\alpha$ CD44-PEI-MSNPs could be considered non-toxic, reaching a minimum of 92% cell viability at the highest concentration (100  $\mu$ g/mL). For both cell lines, a dose-dependent response on the cell viability was observed for free Dox. We found an evident difference in the cell-killing effect between the free Dox and the Dox-loaded nanoparticles ( $p < 0.05$ ) for A549 cells. Dox-loaded  $\alpha$ CD44-PEI-MSNPs exhibited dose-dependent cytotoxic effects for A549 (reaching a minimum of 38% of viability at the highest concentration). This enhanced cytotoxicity of the Dox-loaded nanoparticles is linked to the high internalization rate of

the  $\alpha$ CD44-PEI-MSNPs followed by endosomal release and specific drug release in the cytoplasm. Importantly, the negligible internalization of  $\alpha$ CD44-PEI-MSNPs in HepG2 cells resulted in the absence of toxic effects when using Dox-loaded particles (viability similar to the control). The high cell viability also indicates that the drug did not leak from the nanoparticles into the extracellular environment.



**Figure 7.** Viability of A549 and HepG2 cells after 72-h incubation with different concentrations of free Dox, Dox-loaded  $\alpha$ CD44-PEI-MSNPs, and empty  $\alpha$ CD44-PEI-MSNPs. A549 and HepG2 cells that were not incubated with particles or drug were used as a control and represent 100% viability (data not shown). Dox concentrations are expressed in nM while nanoparticle concentrations are in  $\mu$ g/mL. Estimated Dox concentration loaded in the nanoparticles was 50  $\mu$ M. Error bars indicate  $\pm$  SD, with ns meaning not significant; \* ( $p < 0.05$ ), \*\* ( $p < 0.01$ ), and \*\*\* ( $p < 0.001$ ),  $n = 4$ .

From these results, it can be concluded that Dox-loaded  $\alpha$ CD44-PEI-MSNPs exhibited high toxicity to CD44-overexpressing cells only (higher than free Dox), while only limited to no toxicity was observed for the empty carrier. Consequently, a satisfying therapeutic efficiency can be concluded, through an efficient nanoparticle internalization and high drug payload delivery targeted to the cancer cell cytosol.

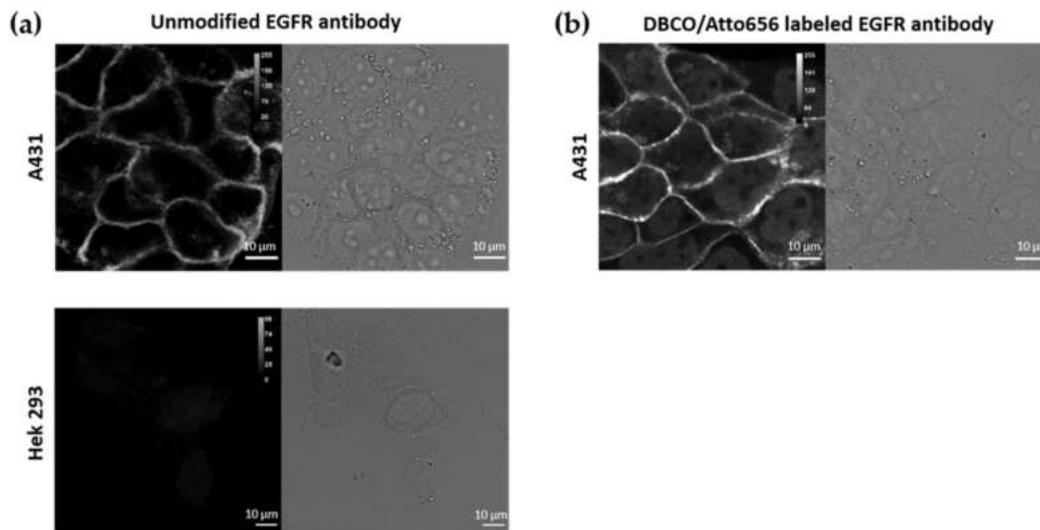
### 3.3. The $\alpha$ EGFR-Conjugated Nanoparticles

To prove the versatility of our antibody coating strategy, we targeted next a second cancer marker, EGFR. EGFR overexpression is related to different types of cancers and is often associated to a poor prognosis for the patient. Especially in glioblastoma, lung, and breast cancers, where EGFR stimulates tumor growth [44]. To this end, EGFR has emerged as a popular target for cancer cell-specific therapies. As a result, many nanoparticles targeting EGFR were developed, either via nanoparticle conjugation with its ligand, EGF, or by attaching EGFR antibodies [86–89].

#### 3.3.1. Labelling of the EGFR Antibodies

For labelling the EGFR antibodies, the same method was used as for the CD44 antibodies (Section 3.1.2). Similarly, labelling with DBCO was performed, enabling the conjugation of DBCO-EGFR antibodies to the Azide-coated nanoparticles. For fluorescence microscopy purposes, the EGFR antibodies were also conjugated to a dye (Atto565). The dual labelling of the EGFR antibodies with DBCO and Atto565 was carried out via an NHS ester coupling reaction with the antibodies' lysine residues (as described in Methods). We checked whether the specificity of the EGFR antibody was retained after dual labelling (with Atto565 and DBCO) by performing immunofluorescence on two cell lines, A431 and Hek293 cells, presenting high and low expression of EGFR, respectively [90,91]. First, the EGFR expression in the chosen cell lines, A431 and Hek293, was determined via immunofluorescence with the unmodified EGFR antibody (followed by staining with a fluorescently labelled secondary antibody, goat-anti-mouse IgG AF488). As shown in

Figure 8a, EGFR was visualized on the plasma membrane of A431 cells, while no EGFR could be detected in Hek293 cells. A431 cells stained with the DBCO/Atto565-labelled EGFR antibody also displayed the plasma membrane-localized signal, proving that the specificity of the EGFR antibody was not hindered by our labelling protocol (Figure 8b). A nuclear background could be observed, associated to free Atto565 molecules, similar to what was observed for the Atto488 molecules (see Section 3.1.2).

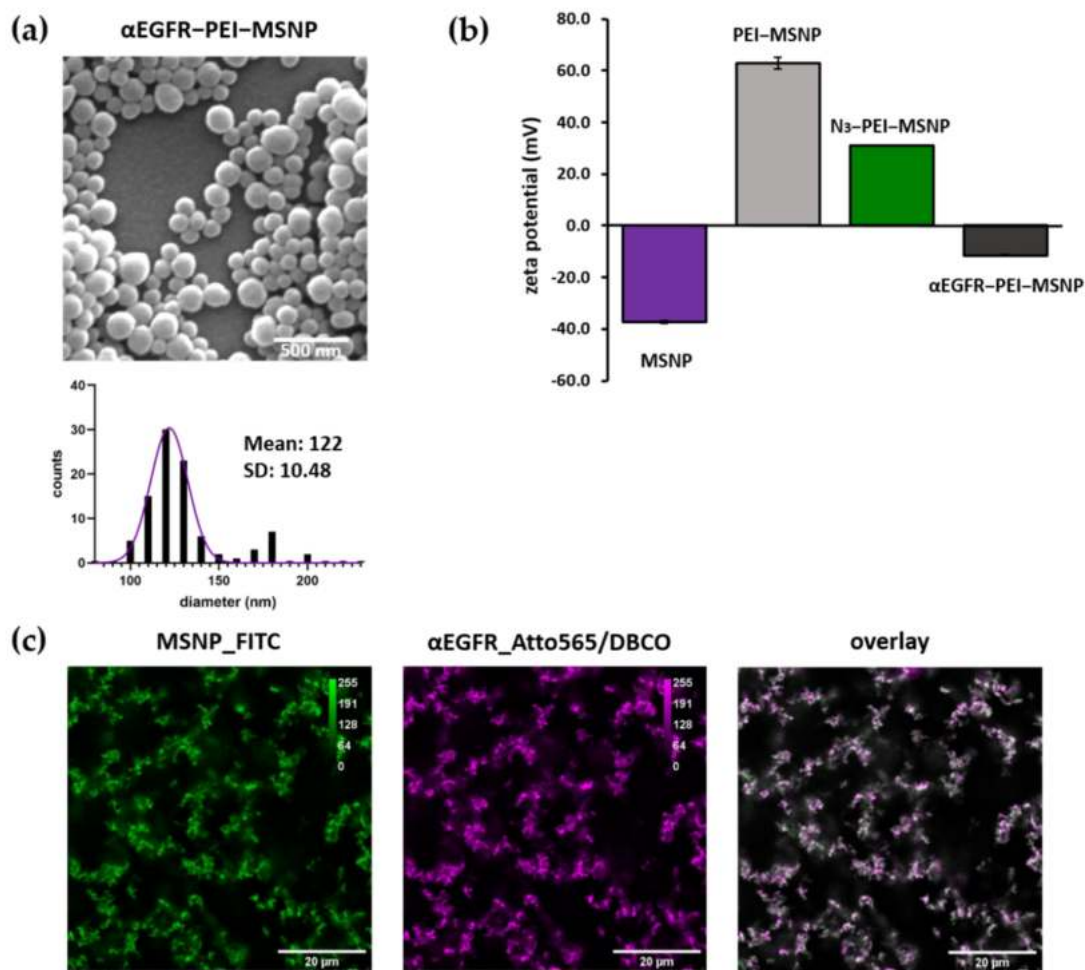


**Figure 8.** Immunofluorescence (IF) using (a) the unmodified primary mouse anti-human EGFR antibody followed by a labelled secondary antibody, goat anti-mouse IgG AF488, on A431 and Hek293 cells; (b) DBCO/Atto565-labelled EGFR antibodies in A431 cells. Scale bar is 10 µm.

### 3.3.2. Synthesis and Characterization of $\alpha$ EGFR-Conjugated MSNPs

The EGFR antibody was attached to the Azide-coated nanoparticles via the same approach ( $\alpha$ EGFR-PEI-MSNPs). Since the EGFR antibody was labelled with an Atto565 dye (as described in the previous section), to avoid spectral overlap during fluorescence microscopy studies, Azide-conjugated nanoparticles were labelled with Fluorescein (FITC). FITC was covalently attached to the silica matrix, as stated in the Methods section. The resulting  $\alpha$ EGFR-conjugated nanoparticles were characterized via SEM, AFM, zeta potential measurements, and fluorescence microscopy.

Similar to  $\alpha$ CD44-conjugated particles,  $\alpha$ EGFR-PEI-MSNPs displayed a uniform size and shape homogeneity (Figure 9a). With a mean diameter of 122 nm (as derived from the SEM data),  $\alpha$ EGFR-PEI-MSNPs were significantly bigger than the PEI-MSNPs (Figure 3a) ( $p < 0.05$ ) because of the EGFR layer. AFM measurements revealed an average nanoparticle diameter of 127 nm, which agreed with the SEM results (Figure S3). Zeta potential measurements were performed to check the different steps of nanoparticle functionalization. The zeta potential data of the bare MSNPs, PEI-grafted MSNPs (PEI-MSNPs), and Azide-conjugated MSNPs ( $N_3$ -PEI-MSNPs) were already discussed in Section 3.1.3. (Figure 3c). The  $\alpha$ EGFR-PEI-MSNPs displayed a negative zeta potential ( $-11.6$  mV), similar to the one of the MSNPs after conjugation with the CD44 antibody ( $\alpha$ CD44-PEI-MSNPs,  $-6.7$  mV) (Figure 9b). Additionally, in order to confirm uniform binding of the EGFR antibody, MSNPs were encapsulated with a fluorescent dye (FITC), while the EGFR antibody was labelled with another dye (Atto565). Accordingly, the co-localization between the EGFR antibody and the MSNPs could be determined via confocal fluorescence microscopy measurements. These data confirmed proper attachment of the EGFR antibody and uniform coverage of the nanoparticles with antibody molecules (Figure 9c).

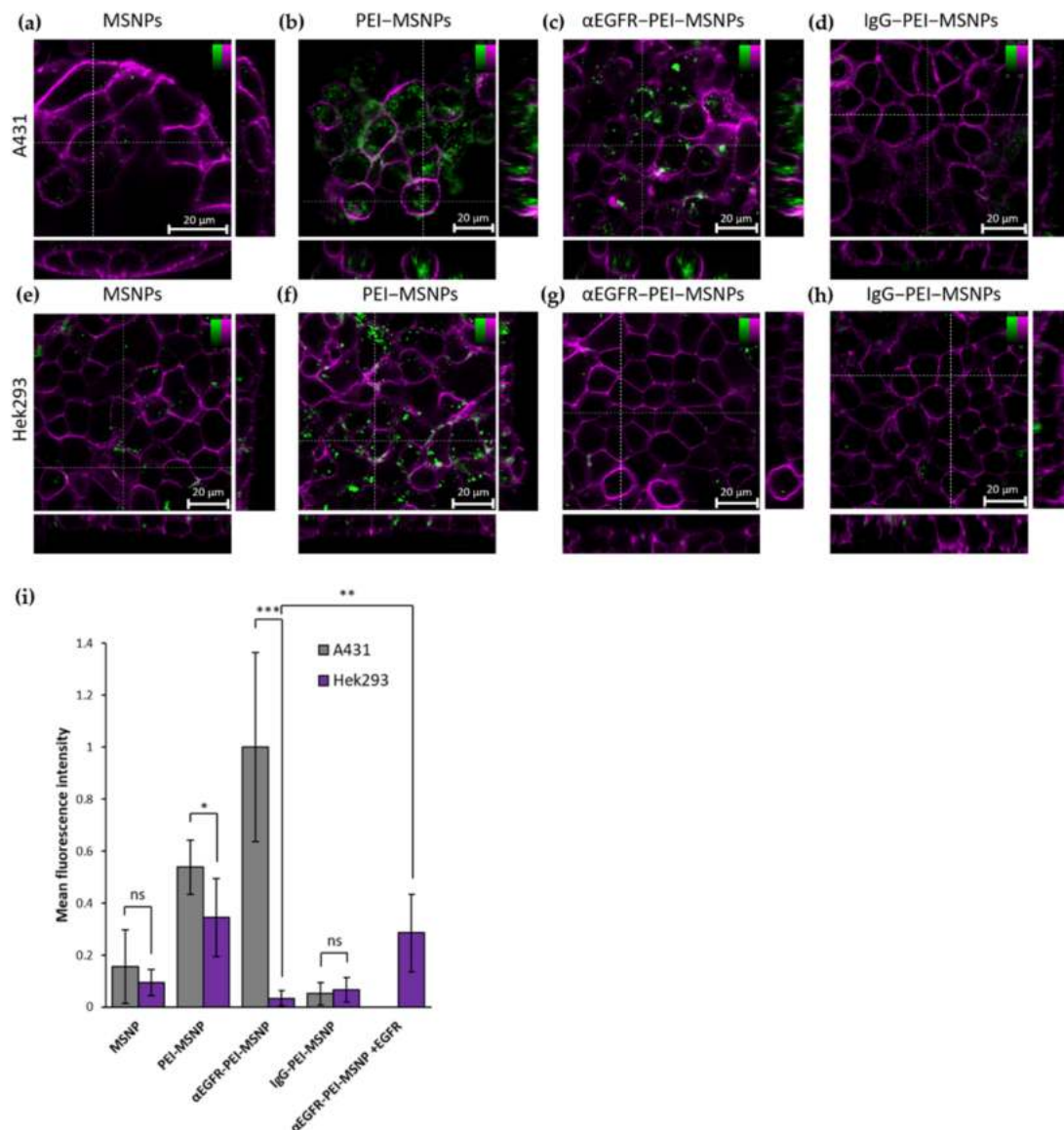


**Figure 9.** Characterization of EGFR-conjugated ( $\alpha$ EGFR-PEI-MSNPs) mesoporous silica nanoparticles. (a) Representative SEM image and size distribution of the imaged particles (values shown as mean  $\pm$  SD). Scale bar is 500 nm. (b) Zeta-potential measurements. (c) Confocal fluorescence images of sedimented nanoparticles on glass showing the overlay (third panel) of FITC-encapsulated MSNPs (first panel, green) and the Atto565/DBCO-labelled EGFR antibody (second panel, magenta).

### 3.3.3. Targeting Capability of $\alpha$ EGFR-PEI-MSNPs

The uptake of nanoparticles with different coatings (MSNPs, PEI-MSNPs,  $\alpha$ EGFR-PEI-MSNPs, and IgG-PEI-MSNPs) was compared between A431 (epidermoid carcinoma with high EGFR expression [86]) and Hek293 cells (human embryonic kidney cells with low EGFR expression [91]). In agreement with the results of the preceding experiment, bare MSNPs were internalized in A431 and Hek293 in a low amount (Figure 10a,e), and a similar increase in uptake could be detected for MSNPs with a PEI layer (Figure 10b,f). As predicted, conjugation of the EGFR antibody resulted in a significant discrepancy in particle uptake between A431 and Hek293 cells (Figure 10c,g,i). Hek293 displayed a similar uptake behavior for the  $\alpha$ EGFR-PEI-MSNPs and the bare MSNPs (Figure 10g) while, in A431 cells, there was an obvious increase in the number of  $\alpha$ EGFR-PEI-MSNPs internalized, especially when compared to bare MSNPs (Figure 10c). This increase can be attributed to the specific recognition of the EGFR receptor by the  $\alpha$ EGFR-PEI-MSNPs, proving cell specificity of these nanoparticles. Similar to A549 and HepG2, the incubation of A431 and Hek293 cells with the non-specific IgG-conjugated nanoparticles resulted in an internalization comparable to bare nanoparticles. As mentioned in Section 3.2.2, this is a consequence of the non-specificity of the IgG towards membrane proteins expressed in these cell lines and the negative zeta potential ( $-11.8$  mV) of the resulting IgG-conjugated nanoparticle (minimum non-specific uptake). To further evaluate the specificity of the

antibody-conjugated nanoparticles, expression of the EGFR receptor in Hek293 was induced by transiently transfecting Hek293 cells with a plasmid encoding an EGFR-HaloTag<sup>®</sup> fusion construct (see Methods section for details). A fluorescent ligand (Alexa Fluor 488 HaloTag<sup>®</sup> ligand) was used to identify the EGFR-expressing Hek293 cells via confocal fluorescence microscopy (Figure S7 in Supplementary Materials). Quantitative analysis of the fluorescence intensity revealed that Hek293 cells expressing EGFR molecules exhibited a higher uptake of  $\alpha$ EGFR-PEI-MSNPs (Figure 10i). This demonstrates that the internalization of  $\alpha$ EGFR-PEI-MSNPs is linked to the presence of the EGFR receptor on the cell membrane, further confirming the selectivity of the developed nanoparticles.



**Figure 10.** Confocal fluorescence microscopy stacks showing the influence of different MSNP coatings in A431 and Hek293 cells. (a–d) Internalization of MSNP, PEI-MSNP,  $\alpha$ EGFR-PEI-MSNP, and IgG-PEI-MSNP in A431 cells (from left to right). (e–h) Internalization of MSNP, PEI-MSNP,  $\alpha$ EGFR-PEI-MSNP, and IgG-PEI-MSNP in Hek293 cells (from left to right). Nanoparticles (encapsulated with fluorescein) are displayed in green and the plasma membrane is stained with DiI (magenta). Scale bar is 20  $\mu$ m; color bars display the intensity values. (i) Normalized mean fluorescence intensity of MSNP, PEI-MSNP,  $\alpha$ EGFR-PEI-MSNPs, and IgG-PEI-MSNPs internalized in A431 and Hek293 cells and  $\alpha$ EGFR-PEI-MSNPs in Hek293 cells transiently expressing EGFR (Hek293 + EGFR, 20 cells per condition). The data were analyzed using Fiji (see Methods section for details). With ns: not significant, \* ( $p < 0.05$ ), \*\* ( $p < 0.01$ ), and \*\*\* ( $p < 0.001$ ).



#### 4. Conclusions

In this work, we showed a facile method for the conjugation of different antibodies to nanoparticles using copper-free click chemistry. Here, mesoporous silica nanoparticles (MSNPs) were chosen as drug carriers and the base for further functionalization; however, other nanoparticles can be used. Similarly, the Doxorubicin loaded inside the MSNPs can be substituted by other drugs for different therapeutic applications.

The first step in our approach was to coat the nanoparticles with a PEI layer. The PEI amine groups provide the anchor for the covalent attachment of an Azide moiety, to which the DBCO-labelled antibodies were covalently linked via a simple click reaction. Importantly, click chemistry can be carried out under physiological conditions, without using any catalyst. Furthermore, the presence of the PEI layer reduced the effect of nanoparticle entrapment in the acidic vesicles (by taking advantage of the proton sponge effect) and supported the controlled drug release into the cancer cell.

All existing antibodies can be labeled with a DBCO group in the same controllable way (via an NHS-ester coupling with their amine groups) and their conjugation to the nanoparticles only requires the presence of an amine group on the nanoparticle surface. Therefore, this approach to produce antibody-conjugated nanoparticles is extremely versatile and has the potential to be widely applied. The antibody that is conjugated can be easily adapted (based on the expressed cancer markers) and the type of nanocarrier can be changed (as long as surface amine groups are present). Here, the versatility of our coating strategy was demonstrated with two different antibodies, a CD44 and an EGFR antibody, both showing excellent selectivity towards CD44- and EGFR-overexpressing cells, respectively. This simple method can significantly contribute to the field of personalized cancer therapy, where the treatment should be customized according to the cancer markers present in the tumor. In this regard, a variety of antibodies can be easily “clicked-on” for efficient targeting purposes.

**Supplementary Materials:** The following are available online at <https://www.mdpi.com/article/10.3390/pharmaceutics13122153/s1>: Figure S1. Emission and excitation spectra of drug and dye-loaded MSNPs. Figure S2. Absorbance for dual-labelled antibodies (IgG/DBCO/Atto565, EGFR/DBCO/Atto565 and CD44/DBCO/Atto565), non-labelled antibodies (IgG, EGFR and CD44) and DBCO only. Figure S3. (a) AFM images of MSNPs, PEI-MSNPs,  $\alpha$ CD44-PEI-MSNPs and  $\alpha$ CD44-PEI-MSNPs, (b) Graph of the average height measured with AFM (diameter). Figure S4. Confocal fluorescence microscopy images showing the influence of different MSNP coating in the uptake of nanoparticles in BJ1-tHERT and NIH 3T3 cells. Figure S5. Immunofluorescence (secondary goat-anti-rat IgG-AF488) staining showing the expression of absence of the CD44 receptor in Bj-hTERT and NIH 3T3, respectively. Figure S6. Manders' Coefficient (MC) representing the fraction of overlap between the  $\alpha$ CD44-PEI-MSNPs channel with the LysoTracker Deep Red channel. Figure S7. Internalization of  $\alpha$ EGFR-PEI-MSNPs in wild type Hek293 (left panel) and Hek293 cells transiently transfected with a pcDBA3-EGFR-HaloTag® (middle and right panel). Table S1.  $\alpha$ CD44-PEI-MSNPs aggregation in different solutions: average OD600 values for  $\alpha$ CD44-PEI-MSNPs dissolved in MilliQ water, FBS and DMEM with 10% FBS before and after 24 h of incubation at 37 °C.

**Author Contributions:** Conceptualization, I.V.Z., B.F. and S.R.; methodology, I.V.Z., M.B., P.C., O.D. and B.F.; formal analysis, I.V.Z. and O.D.; investigation, I.V.Z., M.B., P.C., O.D., B.F. and S.R.; writing—original draft preparation, I.V.Z., M.B. and S.R.; writing—review and editing, all authors; supervision, C.B., H.U.-i., J.H., B.F. and S.R.; funding acquisition, C.B., H.U.-i., J.H. and S.R. All authors have read and agreed to the published version of the manuscript.

**Funding:** This work was supported by the Research Foundation—Flanders (FWO, projects G0A5817N, G0D4519N, 1529418N, G081916N and G094717N), by KU Leuven (C14/16/053, C14/18/061, and KA/20/026). This collaborative work was also financially supported by the JSPS “Core-to-Core Program A. Advanced Research Networks”. I.V.Z. and B.F. acknowledge the support from FWO for their PhD and Postdoctoral fellowships, respectively (11F5419N and 12X1419N). P.C., J.H., H.U.-I., and S.R. acknowledge financial support from the SuperCol project that received funding from the European Union’s Horizon 2020 research and innovation program under the Marie Skłodowska-Curie grant agreement No. 860914. J.H. further acknowledges the Flemish government through long-term structural funding from Methusalem (CASAS2, Meth/15/04). Figure S5. immunofluorescence (secondary goat-anti-rat IgG-AF488) staining showing the expression of absence of the CD44 receptor in Bj-hTERT and NIH 3T3, respectively.

**Institutional Review Board Statement:** Not applicable.

**Informed Consent Statement:** Not applicable.

**Data Availability Statement:** The data presented in this study are available on request from the corresponding authors.

**Acknowledgments:** The authors acknowledge Roel Hammink (Radboud University, Nijmegen, NL) for the fruitful discussions concerning antibody functionalization and Hideaki Mizuno (KU Leuven) for providing us with the pcDNA3-EGFR-HaloTag<sup>®</sup> plasmid and cell lines. Figure 1 was created with Biorender.com (accessed date 1 May 2021).

**Conflicts of Interest:** There are no conflicts of interest regarding this research.

## References

1. Sriraman, S.K.; Aryasomayajula, B.; Torchilin, V.P. Barriers to Drug Delivery in Solid Tumors. *Tissue Barriers* **2014**, *2*, e29528. [CrossRef] [PubMed]
2. Cho, H.-J.; Yoon, I.-S.; Yoon, H.Y.; Koo, H.; Jin, Y.-J.; Ko, S.-H.; Shim, J.S.; Kim, K.; Kwon, I.C.; Kim, D.D. Polyethylene Glycol-Conjugated Hyaluronic Acid-Ceramide Self-Assembled Nanoparticles for Targeted Delivery of Doxorubicin. *Biomaterials* **2012**, *33*, 1190–1200. [CrossRef] [PubMed]
3. Yang, L.; Shi, P.; Zhao, G.; Xu, J.; Peng, W.; Zhang, J.; Zhang, G.; Wang, X.; Dong, Z.; Chen, F.; et al. Targeting Cancer Stem Cell Pathways for Cancer Therapy. *Signal Transduct. Target. Ther.* **2020**, *5*, 1–35. [CrossRef] [PubMed]
4. Greish, K. Enhanced Permeability and Retention (EPR) Effect for Anticancer Nanomedicine Drug Targeting. *Methods Mol. Biol.* **2010**, *624*, 25–37. [CrossRef]
5. Zwicke, G.L.; Mansoori, G.A.; Jeffery, C.J. Utilizing the Folate Receptor for Active Targeting of Cancer Nanotherapeutics. *Nano Rev.* **2012**, *3*, 18496. [CrossRef]
6. Akhter, M.H.; Beg, S.; Tarique, M.; Malik, A.; Afaq, S.; Choudhry, H.; Hosawi, S. Receptor-Based Targeting of Engineered Nanocarrier against Solid Tumors: Recent Progress and Challenges Ahead. *Biochim. Biophys. Acta Gen. Subj.* **2020**, *1865*, 129777. [CrossRef]
7. Wang, A.Z. EPR or no EPR? The Billion-Dollar Question. *Sci. Transl. Med.* **2015**, *7*, ec112–ec294. [CrossRef]
8. Nel, A.; Ruoslahti, E.; Meng, H. New Insights into “Permeability” as in the Enhanced Permeability and Retention Effect of Cancer Nanotherapeutics. *ACS Nano* **2017**, *11*, 9567–9569. [CrossRef] [PubMed]
9. Dai, Q.; Wilhelm, S.; Ding, D.; Syed, A.M.; Sindhvani, S.; Zhang, Y.; Chen, Y.Y.; MacMillan, P.; Chan, W.C. Quantifying the Ligand-Coated Nanoparticle Delivery to Cancer Cells in Solid Tumors. *ACS Nano* **2018**, *12*, 8423–8435. [CrossRef] [PubMed]
10. Zhang, H.; Lee, M.-Y.; Hogg, M.G.; Dordick, J.S.; Sharfstein, S.T. Gene Delivery in Three-Dimensional Cell Cultures by Superparamagnetic Nanoparticles. *ACS Nano* **2010**, *4*, 4733–4743. [CrossRef]
11. Wilhelm, S.; Tavares, A.J.; Dai, Q.; Ohta, S.; Audet, J.; Dvorak, H.F.; Chan, W.C. Analysis of Nanoparticle Delivery to Tumours. *Nat. Rev. Mater.* **2016**, *1*, 16014. [CrossRef]
12. Ukidve, A.; Cu, K.; Kumbhojkar, N.; Lahann, J.; Mitragotri, S. Overcoming Biological Barriers to Improve Solid Tumor Immunotherapy. *Drug Deliv. Transl. Res.* **2021**, *11*, 2276–2301. [CrossRef] [PubMed]
13. Zhou, Y.; Chen, X.; Cao, J.; Gao, H. Overcoming the Biological Barriers in the Tumor Microenvironment for Improving Drug Delivery and Efficacy. *J. Mater. Chem. B* **2020**, *8*, 6765–6781. [CrossRef] [PubMed]
14. Van Zundert, I.; Fortuni, B.; Rocha, S. From 2D to 3D Cancer Cell Models—The Enigmas of Drug Delivery Research. *Nanomaterials* **2020**, *10*, 2236. [CrossRef]
15. Sherman, M.H.; Yu, R.T.; Engle, D.D.; Ding, N.; Atkins, A.R.; Tiriack, H.; Collisson, E.A.; Connor, F.; Van Dyke, T.; Kozlov, S.; et al. Vitamin D Receptor-Mediated Stromal Reprogramming Suppresses Pancreatitis and Enhances Pancreatic Cancer Therapy. *Cell* **2014**, *159*, 80–93. [CrossRef]
16. Bertrand, N.; Wu, J.; Xu, X.; Kamaly, N.; Farokhzad, O.C. Cancer Nanotechnology: The Impact of Passive and Active Targeting in the Era of Modern Cancer Biology. *Adv. Drug Deliv. Rev.* **2014**, *66*, 2–25. [CrossRef] [PubMed]

17. Bhirde, A.A.; Patel, V.; Gavard, J.; Zhang, G.; Sousa, A.A.; Masedunskas, A.; Leapman, R.D.; Weigert, R.; Gutkind, J.S.; Rusling, J.F. Targeted Killing of Cancer Cells in vivo and in vitro with EGF-Directed Carbon Nanotube-based Drug Delivery. *ACS Nano* **2009**, *3*, 307–316. [CrossRef]
18. Gan, C.W.; Feng, S.-S. Transferrin-Conjugated Nanoparticles of Poly(Lactide)-D-Alpha-Tocopheryl Polyethylene Glycol Succinate Diblock Copolymer for Targeted Drug Delivery across the Blood-Brain Barrier. *Biomaterials* **2010**, *31*, 7748–7757. [CrossRef]
19. Gerber, D.E. Targeted Therapies: A New Generation of Cancer Treatments. *Am. Fam. Physician* **2008**, *77*, 311–319.
20. Gaspar, V.M.; Costa, E.C.; Queiroz, J.A.; Pichon, C.; Sousa, F.; Correia, I.J. Folate-Targeted Multifunctional Amino Acid-Chitosan Nanoparticles for Improved Cancer Therapy. *Pharm. Res.* **2015**, *32*, 562–577. [CrossRef]
21. Wang, X.; Li, J.; Wang, Y.; Koenig, L.; Gjyzezi, A.; Giannakakou, P.; Shin, E.H.; Tighiouart, M.; Chen, Z.; Nie, S.; et al. A Folate Receptor-Targeting Nanoparticle Minimizes Drug Resistance in a Human Cancer Model. *ACS Nano* **2011**, *5*, 6184–6194. [CrossRef]
22. Hsu, J.L.; Hung, M.-C. The Role of HER2, EGFR, and Other Receptor Tyrosine Kinases in Breast Cancer. *Cancer Metastasis Rev.* **2016**, *35*, 575–588. [CrossRef] [PubMed]
23. Lumachi, F.; Brunello, A.; Maruzzo, M.; Basso, U.; Basso, S.M.M. Treatment of Estrogen Receptor-Positive Breast Cancer. *Curr. Med. Chem.* **2013**, *20*, 596–604. [CrossRef] [PubMed]
24. Perou, C.M.; Sørlie, T.; Eisen, M.B.; van de Rijn, M.; Jeffrey, S.S.; Rees, C.A.; Pollack, J.R.; Ross, D.T.; Johnsen, H.; Aklen, L.A.; et al. Molecular Portraits of Human Breast Tumours. *Nature* **2000**, *406*, 747–752. [CrossRef]
25. Senter, P.D.; Sievers, E.L. The Discovery and Development of Brentuximab Vedotin for Use in Relapsed Hodgkin Lymphoma and Systemic Anaplastic Large Cell Lymphoma. *Nat. Biotechnol.* **2012**, *30*, 631–637. [CrossRef] [PubMed]
26. Amiri-Kordestani, L.; Blumenthal, G.M.; Xu, Q.C.; Zhang, L.; Tang, S.W.; Ha, L.; Weinberg, W.C.; Chi, B.; Candau-Chacon, R.; Hughes, P.; et al. FDA Approval: Ado-Trastuzumab Emtansine for the Treatment of Patients with HER2-Positive Metastatic Breast Cancer. *Clin. Cancer Res.* **2014**, *20*, 4436–4441. [CrossRef] [PubMed]
27. Wynne, J.; Wright, D.; Stock, W. Inotuzumab: From Preclinical Development to Success in B-cell Acute Lymphoblastic Leukemia. *Blood Adv.* **2019**, *3*, 96–104. [CrossRef]
28. Hafeez, U.; Parakh, S.; Gan, H.K.; Scott, A.M. Antibody–Drug Conjugates for Cancer Therapy. *Molecules* **2020**, *25*, 4764. [CrossRef] [PubMed]
29. Hammood, M.; Craig, A.W.; Leyton, J.V. Impact of Endocytosis Mechanisms for the Receptors Targeted by the Currently Approved Antibody-Drug Conjugates (ADCs)—A Necessity for Future ADC Research and Development. *Pharmaceutics* **2021**, *14*, 674. [CrossRef] [PubMed]
30. Johnston, M.C.; Scott, C.J. Antibody Conjugated Nanoparticles as a Novel Form of Antibody Drug Conjugate Chemotherapy. *Drug Discov. Today Technol.* **2018**, *30*, 63–69. [CrossRef]
31. Juan, A.; Cimas, F.J.; Bravo, I.; Pandiella, A.; Ocaña, A.; Alonso-Moreno, C. An Overview of Antibody Conjugated Polymeric Nanoparticles for Breast Cancer Therapy. *Pharmaceutics* **2020**, *12*, 802. [CrossRef] [PubMed]
32. Yu, K.; Zhao, J.; Zhang, Z.; Gao, Y.; Zhou, Y.; Teng, L.; Li, Y. Enhanced Delivery of Paclitaxel Using Electrostatically-Conjugated Herceptin-Bearing PEI/PLGA Nanoparticles against HER-Positive Breast Cancer Cells. *Int. J. Pharm.* **2016**, *497*, 78–87. [CrossRef]
33. Mi, Y.; Huang, Y.; Deng, J. The Enhanced Delivery of Salinomycin to CD133+ Ovarian Cancer Stem Cells through CD133 Antibody Conjugation with Poly(Lactic-Co-Glycolic Acid)-Poly(Ethylene Glycol) Nanoparticles. *Oncol. Lett.* **2018**, *15*, 6611–6621. [CrossRef] [PubMed]
34. Varshosaz, J.; Davoudi, M.A.; Rasoul-Amini, S. Docetaxel-Loaded Nanostructured Lipid Carriers Functionalized with Trastuzumab (Herceptin) for HER2-Positive Breast Cancer Cells. *J. Liposome Res.* **2018**, *28*, 285–295. [CrossRef]
35. Chen, S.; Florinas, S.; Teitgen, A.; Xu, Z.-Q.; Gao, C.; Wu, H.; Kataoka, K.; Cabral, H.; Christie, R.J. Controlled Fab Installation onto Polymeric Micelle Nanoparticles for Tuned Bioactivity. *Sci. Technol. Adv. Mater.* **2017**, *18*, 666–680. [CrossRef]
36. Wartlick, H.; Michaelis, K.; Balthasar, S.; Strebhardt, K.; Kreuter, J.; Langer, K. Highly Specific HER2-Mediated Cellular Uptake of Antibody-Modified Nanoparticles in Tumour Cells. *J. Drug Target.* **2004**, *12*, 461–471. [CrossRef]
37. Goossens, J.; Sein, H.; Lu, S.; Radwanska, M.; Muylldermans, S.; Sterckx, Y.G.-J.; Magez, S. Functionalization of Gold Nanoparticles with Nanobodies through Physical Adsorption. *Anal. Methods* **2017**, *9*, 3430–3440. [CrossRef]
38. Choi, J.-S.; Jang, W.S.; Park, J.-S. Comparison of Adsorption and Conjugation of Herceptin on Poly(Lactic-Co-Glycolic Acid) Nanoparticles—Effect on Cell Internalization in Breast Cancer Cells. *Mater. Sci. Eng. C Mater. Biol. Appl.* **2018**, *92*, 496–507. [CrossRef]
39. Jain, A.; Cheng, K. The Principles and Applications of Avidin-Based Nanoparticles in Drug Delivery and Diagnosis. *J. Control. Release* **2017**, *245*, 27–40. [CrossRef]
40. Sperling, R.A.; Parak, W.J. Surface Modification, Functionalization and Bioconjugation of Colloidal Inorganic Nanoparticles. *Philos. Trans. A Math. Phys. Eng. Sci.* **2010**, *368*, 1333–1383. [CrossRef]
41. Kim, C.; Galloway, J.F.; Lee, K.H.; Searson, P.C. Universal Antibody Conjugation to Nanoparticles Using the Fcγ Receptor I (FcγRI): Quantitative Profiling Of Membrane Biomarkers. *Bioconjug Chem.* **2014**, *25*, 1893–1901. [CrossRef]
42. Kim, E.; Koo, H. Biomedical Applications of Copper-Free Click Chemistry: In vitro, in vivo, and ex vivo. *Chem. Sci.* **2019**, *10*, 7835–7851. [CrossRef]
43. Egorova, K.S.; Ananikov, V.P. Toxicity of Metal Compounds: Knowledge and Myths. *Organometallics* **2017**, *36*, 4071–4090. [CrossRef]

44. Sigismund, S.; Avanzato, D.; Lanzetti, L. Emerging Functions of the EGFR in Cancer. *Mol. Oncol.* **2018**, *12*, 3–20. [CrossRef] [PubMed]
45. Naor, D.; Sionov, R.V.; Ish-Shalom, D. CD44: Structure, Function, and Association with the Malignant Process. *Adv. Cancer Res.* **1997**, *71*, 241–319. [CrossRef] [PubMed]
46. Slowing, I.I.; Trewyn, B.G.; Giri, S.; Lin, V.S.-Y. Mesoporous Silica Nanoparticles for Drug Delivery and Biosensing Applications. *Adv. Funct. Mater.* **2007**, *17*, 1225–1236. [CrossRef]
47. Wang, S. Ordered Mesoporous Materials for Drug Delivery. *Microporous Mesoporous Mater.* **2009**, *117*, 1–9. [CrossRef]
48. Garrido-Cano, I.; Candela-Noguera, V.; Herrera, G.; Cejalvo, J.M.; Lluch, A.; Marcos, M.D.; Sancenon, F.; Eroles, P.; Martínez-Mañez, R. Biocompatibility and Internalization Assessment of Bare and Functionalised Mesoporous Silica Nanoparticles. *Microporous Mesoporous Mater.* **2021**, *310*, 110593. [CrossRef]
49. Fortuni, B.; Inose, T.; Ricci, M.; Fujita, Y.; Van Zundert, I.; Masuhara, A.; Fron, E.; Mizuno, H.; Latterini, L.; Rocha, S.; et al. Polymeric Engineering of Nanoparticles for Highly Efficient Multifunctional Drug Delivery Systems. *Sci. Rep.* **2019**, *9*, 2666. [CrossRef]
50. Thirukkumaran, O.M.; Kluba, M.; Hofkens, J.; Mizuno, H. Autophosphorylation of EGFR at Y954 Facilitated Homodimerization and Enhanced Downstream Signals. *Biophys. J.* **2020**, *119*, 2127–2137. [CrossRef]
51. Taemaitree, F.; Fortuni, B.; Koseki, Y.; Fron, E.; Rocha, S.; Hofkens, J.; Uji-i, H.; Inose, T.; Kasai, H. FRET-Based Intracellular Investigation of Nanoprodugs toward Highly Efficient Anticancer Drug Delivery. *Nanoscale* **2020**, *12*, 16710–16715. [CrossRef]
52. Hammink, R.; Weiden, J.; Voerman, D.; Popelier, C.; Eggermont, L.J.; Schluck, M.; Figdor, C.G.; Verdoes, M. Semiflexible Immunobrushes Induce Enhanced T Cell Activation and Expansion. *ACS Appl. Mater. Interfaces* **2021**, *13*, 16007–16018. [CrossRef] [PubMed]
53. Wiener, J.; Kokotek, D.; Rosowski, S.; Lickert, H.; Meier, M. Preparation of Single- and Double-Oligonucleotide Antibody Conjugates and Their Application for Protein Analytics. *Sci. Rep.* **2020**, *10*, 1457. [CrossRef] [PubMed]
54. Shen, D.; Yang, J.; Li, X.; Zhou, L.; Zhang, R.; Li, W.; Chen, L.; Wang, R.; Zhang, F.; Zhao, D. Biphasic Stratification Approach to Three-Dimensional Dendritic Biodegradable Mesoporous Silica Nanospheres. *Nano Lett.* **2014**, *14*, 923–932. [CrossRef] [PubMed]
55. Nečas, D.; Klapetek, P. Gwyddion: An Open-Source Software for SPM Data Analysis. *Open Phys.* **2012**, *10*, 181–188. [CrossRef]
56. Schindelin, J.; Arganda-Carreras, I.; Frise, E.; Kaynig, V.; Longair, M.; Pietzsch, T.; Preibisch, S.; Rueden, C.; Saalfeld, S.; Schmid, B.; et al. Fiji: An Open-Source Platform for Biological-Image Analysis. *Nat. Methods* **2012**, *9*, 676–682. [CrossRef] [PubMed]
57. Bolte, S.; Cordelières, F.P. A Guided Tour into Subcellular Colocalization Analysis in Light Microscopy. *J. Microsc.* **2006**, *224*, 213–232. [CrossRef]
58. Manders, E.M.M.; Verbeek, F.J.; Aten, J.A. Measurement of Co-Localization of Objects in Dual-Colour Confocal Images. *J. Microsc.* **1993**, *169*, 375–382. [CrossRef]
59. Goedhart, J. Plots of Differences—A Web App for the Quantitative Comparison of Unpaired Data. *BioRxiv* **2019**, 578575. [CrossRef]
60. Penno, M.B.; August, J.T.; Baylin, S.B.; Mabry, M.; Linnoila, R.I.; Lee, V.S.; Croteau, D.; Yang, X.L.; Rosada, C. Expression of CD44 in Human Lung Tumors. *Cancer Res.* **1994**, *54*, 1381–1387.
61. Dalerba, P.; Dylla, S.J.; Park, I.-K.; Liu, R.; Wang, X.; Cho, R.W.; Hoey, T.; Gurney, A.; Huang, E.H.; Simeone, D.M.; et al. Phenotypic Characterization of Human Colorectal Cancer Stem Cells. *Proc. Natl. Acad. Sci. USA* **2007**, *104*, 10158–10163. [CrossRef]
62. Al-Hajj, M.; Wicha, M.S.; Benito-Hernandez, A.; Morrison, S.J.; Clarke, M.F. Prospective Identification of Tumorigenic Breast Cancer Cells. *Proc. Natl. Acad. Sci. USA* **2003**, *100*, 3983–3988. [CrossRef]
63. Arabi, L.; Badiie, A.; Mosaffa, F.; Jaafari, M.R. Targeting CD44 Expressing Cancer Cells with Anti-CD44 Monoclonal Antibody Improves Cellular Uptake and Antitumor Efficacy of Liposomal Doxorubicin. *J. Control. Release* **2015**, *220*, 275–286. [CrossRef]
64. Collins, A.T.; Berry, P.A.; Hyde, C.; Stower, M.J.; Maitland, N.J. Prospective Identification of Tumorigenic Prostate Cancer Stem Cells. *Cancer Res.* **2005**, *65*, 10946–10951. [CrossRef]
65. Ayob, A.Z.; Ramasamy, T.S. Cancer Stem Cells as Key Drivers of Tumour Progression. *J. Biomed. Sci.* **2018**, *25*, 20. [CrossRef] [PubMed]
66. Arpicco, S.; Lerda, C.; Dalla Pozza, E.; Costanzo, C.; Tsapis, N.; Stella, B.; Donadelli, M.; Dando, I.; Fattal, E.; Cattel, L.; et al. Hyaluronic Acid-Coated Liposomes for Active Targeting of Gemcitabine. *Eur. J. Pharm. Biopharm.* **2013**, *85*, 373–380. [CrossRef] [PubMed]
67. Chen, Z.; Li, Z.; Lin, Y.; Yin, M.; Ren, J.; Qu, X. Bioresponsive Hyaluronic Acid-Capped Mesoporous Silica Nanoparticles for Targeted Drug Delivery. *Chemistry* **2013**, *19*, 1778–1783. [CrossRef] [PubMed]
68. Wei, J.; Sun, J.; Liu, Y. Enhanced Targeting of Prostate Cancer-Initiating Cells by Salinomycin-Encapsulated Lipid-PLGA Nanoparticles Linked with CD44 Antibodies. *Oncol. Lett.* **2019**, *17*, 4024–4033. [CrossRef] [PubMed]
69. Wang, L.; Su, W.; Liu, Z.; Zhou, M.; Chen, S.; Chen, Y.; Lu, D.; Liu, Y.; Fan, Y.; Zheng, Y.; et al. CD44 Antibody-Targeted Liposomal Nanoparticles for Molecular Imaging and Therapy of Hepatocellular Carcinoma. *Biomaterials* **2012**, *33*, 5107–5114. [CrossRef]
70. Su, Z.; Liu, D.; Chen, L.; Zhang, J.; Ru, L.; Chen, Z.; Gao, Z.; Wang, X. CD44-Targeted Magnetic Nanoparticles Kill Head And Neck Squamous Cell Carcinoma Stem Cells In An Alternating Magnetic Field. *Int. J. Nanomed.* **2019**, *14*, 7549–7560. [CrossRef] [PubMed]

71. Danielsson, Å.; Ljunglöf, A.; Lindblom, H. One-Step Purification of Monoclonal IgG Antibodies from Mouse Ascites: An Evaluation of Different Adsorption Techniques Using High Performance Liquid Chromatography. *J. Immunol. Methods* **1988**, *115*, 79–88. [CrossRef]
72. Zhang, L.; Hu, D.; Salmain, M.; Liedberg, B.; Boujday, S. Direct Quantification of Surface Coverage of Antibody in IgG-Gold Nanoparticles Conjugates. *Talanta* **2019**, *204*, 875–881. [CrossRef] [PubMed]
73. Gregory, J. Monitoring Particle Aggregation Processes. *Adv. Colloid Interface Sci.* **2009**, *147–148*, 109–123. [CrossRef] [PubMed]
74. Foster, K.A.; Oster, C.G.; Mayer, M.M.; Avery, M.L.; Audus, K.L. Characterization of the A549 Cell Line as a Type II Pulmonary Epithelial Cell Model for Drug Metabolism. *Exp. Cell. Res.* **1998**, *243*, 359–366. [CrossRef] [PubMed]
75. Aden, D.P.; Fogel, A.; Plotkin, S.; Damjanov, I.; Knowles, B.B. Controlled Synthesis of HBsAg in a Differentiated Human Liver Carcinoma-Derived Cell Line. *Nature* **1979**, *282*, 615–616. [CrossRef]
76. Arvizo, R.R.; Miranda, O.R.; Thompson, M.A.; Pabelick, C.M.; Bhattacharya, R.; Robertson, J.D.; Rotello, V.M.; Prakash, Y.S.; Mukherjee, P. Effect of Nanoparticle Surface Charge at the Plasma Membrane and Beyond. *Nano Lett.* **2010**, *10*, 2543–2548. [CrossRef] [PubMed]
77. Xia, T.; Kovoichich, M.; Liong, M.; Meng, H.; Kabehie, S.; George, S.; Zink, J.I.; Nel, A.E. Polyethyleneimine Coating Enhances the Cellular Uptake of Mesoporous Silica Nanoparticles and Allows Safe Delivery of siRNA and DNA Constructs. *ACS Nano* **2009**, *3*, 3273–3286. [CrossRef]
78. Shao, J.; Liang, R.; Ding, D.; Zheng, X.; Zhu, X.; Hu, S.; Wei, H.; Wei, B. A Smart Multifunctional Nanoparticle for Enhanced Near-Infrared Image-Guided Photothermal Therapy Against Gastric Cancer. *IJN* **2021**, *16*, 2897–2915. [CrossRef]
79. Somasunderam, A.; Thivyanathan, V.; Tanaka, T.; Li, X.; Neerathilingam, M.; Lokesh, G.L.R.; Mann, A.; Peng, Y.; Ferrari, M.; Klostergaard, J.; et al. Combinatorial Selection of DNA Thioaptamers Targeted to the HA Binding Domain of Human CD44. *Biochemistry* **2010**, *49*, 9106–9112. [CrossRef] [PubMed]
80. Ouellette, M.M.; McDaniel, L.D.; Wright, W.E.; Shay, J.W.; Schultz, R.A. The Establishment of Telomerase-Immortalized Cell Lines Representing Human Chromosome Instability Syndromes. *Hum. Mol. Genet.* **2000**, *9*, 403–411. [CrossRef] [PubMed]
81. Okamoto, N.; Yasukawa, M.; Nguyen, C.; Kasim, V.; Maida, Y.; Possemato, R.; Shibata, T.; Ligon, K.L.; Fukami, K.; Hahn, W.C.; et al. Maintenance of Tumor Initiating Cells of Defined Genetic Composition by Nucleostemin. *Proc. Natl. Acad. Sci. USA* **2011**, *108*, 20388–20393. [CrossRef] [PubMed]
82. Andrian, T.; Riera, R.; Pujals, S.; Albertazzi, L. Nanoscopy for Endosomal Escape Quantification. *Nanoscale Adv.* **2021**, *3*, 10–23. [CrossRef]
83. Selby, L.I.; Cortez-Jugo, C.M.; Such, G.K.; Johnston, A.P.R. Nanoescapology: Progress toward Understanding the Endosomal Escape of Polymeric Nanoparticles. *Wiley Interdiscip. Rev. Nanomed. Nanobiotechnol.* **2017**, *9*, e1452. [CrossRef]
84. Degors, I.M.S.; Wang, C.; Rehman, Z.U.; Zuhorn, I.S. Carriers Break Barriers in Drug Delivery: Endocytosis and Endosomal Escape of Gene Delivery Vectors. *Acc. Chem. Res.* **2019**, *52*, 1750–1760. [CrossRef]
85. Tacar, O.; Sriamornsak, P.; Dass, C.R. Doxorubicin: An Update on Anticancer Molecular Action, Toxicity and Novel Drug Delivery Systems. *J. Pharm. Pharmacol.* **2013**, *65*, 157–170. [CrossRef]
86. Kralj, S.; Rojnik, M.; Kos, J.; Makovec, D. Targeting EGFR-Overexpressed A431 Cells with EGF-Labeled Silica-Coated Magnetic Nanoparticles. *J. Nanopart. Res.* **2013**, *15*, 1666. [CrossRef]
87. Patel, J.; Amrutiya, J.; Bhatt, P.; Javia, A.; Jain, M.; Misra, A. Targeted Delivery of Monoclonal Antibody Conjugated Docetaxel Loaded PLGA Nanoparticles into EGFR Overexpressed Lung Tumour Cells. *J. Microencapsul.* **2018**, *35*, 204–217. [CrossRef]
88. Kuroda, S.; Tam, J.; Roth, J.A.; Sokolov, K.; Ramesh, R. EGFR-Targeted Plasmonic Magnetic Nanoparticles Suppress Lung Tumor Growth by Abrogating G2/M Cell-Cycle Arrest and Inducing DNA Damage. *IJN* **2014**, *9*, 3825–3839. [CrossRef]
89. Acharya, S.; Dilnawaz, F.; Sahoo, S.K. Targeted Epidermal Growth Factor Receptor Nanoparticle Bioconjugates for Breast Cancer Therapy. *Biomaterials* **2009**, *30*, 5737–5750. [CrossRef]
90. Zhang, Y.; Li, X.; Xu, X.; Luo, W.-J. Construction of a High-EGFR Expression Cell Line and Its Biological Properties Comparing with A431 Cell. *Afr. J. Biotechnol.* **2010**, *9*, 4674–4680. [CrossRef]
91. Zhang, F.; Wang, S.; Yin, L.; Yang, Y.; Guan, Y.; Wang, W.; Xu, H.; Tao, N. Quantification of Epidermal Growth Factor Receptor Expression Level and Binding Kinetics on Cell Surfaces by Surface Plasmon Resonance Imaging. *Anal. Chem.* **2015**, *87*, 9960–9965. [CrossRef] [PubMed]

## Article

# HPMA Copolymer Mebendazole Conjugate Allows Systemic Administration and Possesses Antitumour Activity In Vivo

Martin Studenovský<sup>1,\*</sup>, Anna Rumlerová<sup>1</sup>, Jiřina Kovářová<sup>2</sup>, Barbora Dvořáková<sup>2</sup>, Ladislav Sivák<sup>2</sup>, Libor Kostka<sup>1</sup>, Daniel Berdár<sup>2</sup>, Tomáš Etrych<sup>1</sup> and Marek Kovář<sup>2,\*</sup>

<sup>1</sup> Institute of Macromolecular Chemistry, Czech Academy of Sciences, Heyrovského nám. 2, 16206 Prague, Czech Republic; annarumlerova@centrum.cz (A.R.); kostka@imc.cas.cz (L.K.); etrych@imc.cas.cz (T.E.)

<sup>2</sup> Institute of Microbiology, Czech Academy of Sciences, Vídeňská 1083, 14220 Prague, Czech Republic; jirina.kovarova@biomed.cas.cz (J.K.); dvorakova@bio-port.cz (B.D.); l.sivak@yahoo.com (L.S.); daniel.berdar@ibt.cas.cz (D.B.)

\* Correspondence: studenovsky@imc.cas.cz (M.S.); makovar@biomed.cas.cz (M.K.); Tel.: +420-296-809-230 (M.S.); +420-296-442-362 (M.K.)

**Abstract:** Mebendazole and other benzimidazole antihelmintics, such as albendazole, fenbendazole, or flubendazole, have been shown to possess antitumour activity, primarily due to their microtubule-disrupting activity. However, the extremely poor water-solubility of mebendazole and other benzimidazoles, resulting in very low bioavailability, is a serious drawback of this class of drugs. Thus, the investigation of their antitumour potential has been limited so far to administering repeated high doses given peroral (p.o.) or to using formulations, such as liposomes. Herein, we report a fully biocompatible, water-soluble, HPMA copolymer-based conjugate bearing mebendazole (P-MBZ;  $M_w$  28–33 kDa) covalently attached through a biodegradable bond, enabling systemic administration. Such an approach not only dramatically improves mebendazole solubility but also significantly prolongs the half-life and ensures tumour accumulation via an enhanced permeation and retention (EPR) effect in vivo. This P-MBZ has remarkable cytostatic and cytotoxic activities in EL-4 T-cell lymphoma, LL2 lung carcinoma, and CT-26 colon carcinoma mouse cell lines in vitro, with corresponding  $IC_{50}$  values of 1.07, 1.51, and 0.814  $\mu$ M, respectively. P-MBZ also demonstrated considerable antitumour activity in EL-4 tumour-bearing mice when administered intraperitoneal (i.p.), either as a single dose or using 3 intermittent doses. The combination of P-MBZ with immunotherapy based on complexes of IL-2 and anti-IL-2 mAb S4B6, potentially stimulating activated and memory  $CD8^+$  T cells, as well as NK cells, further improved the therapeutic effect.

**Keywords:** mebendazole; drug delivery; cancer therapy; polymer; HPMA; controlled drug release

**Citation:** Studenovský, M.; Rumlerová, A.; Kovářová, J.; Dvořáková, B.; Sivák, L.; Kostka, L.; Berdár, D.; Etrych, T.; Kovář, M. HPMA Copolymer Mebendazole Conjugate Allows Systemic Administration and Possesses Antitumour Activity In Vivo. *Pharmaceutics* **2022**, *14*, 1201. <https://doi.org/10.3390/pharmaceutics14061201>

Academic Editor: Hassan Bousbaa

Received: 17 May 2022

Accepted: 2 June 2022

Published: 4 June 2022

**Publisher's Note:** MDPI stays neutral with regard to jurisdictional claims in published maps and institutional affiliations.

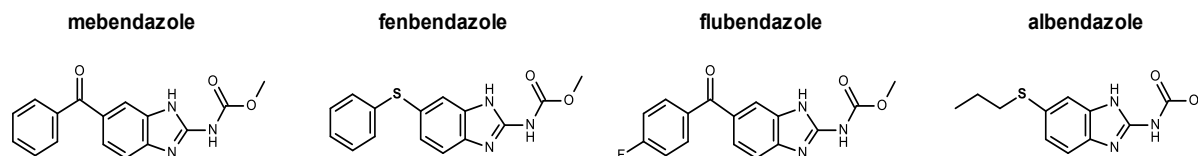


**Copyright:** © 2022 by the authors. Licensee MDPI, Basel, Switzerland. This article is an open access article distributed under the terms and conditions of the Creative Commons Attribution (CC BY) license (<https://creativecommons.org/licenses/by/4.0/>).

## 1. Introduction

Mebendazole (MBZ) belongs to the group of benzimidazole-based, broad-spectrum antihelmintics, and it has been used for this purpose since 1974, with its antitumour activity being described more than 30 years later [1–5]. MBZ, albendazole, flubendazole, and fenbendazole (Figure 1) are the most promising candidate antitumour agents and exert antitumour activity via the inhibition of tubulin assembly through binding to the colchicine-binding site of  $\beta$ -tubulin, thereby suppressing microtubule formation, followed by mitotic cell arrest and apoptosis [1,3]. The cytotoxic activity of MBZ leads to defective cellular structures, glucose metabolism, and intracellular trafficking [6], as well as Bcl-2 inactivation, causing the increased sensitivity of cancer cells to apoptosis [7]. Consequently, cell proliferation and formation of metastases were inhibited, and synergy with other anticancer drugs (e.g., docetaxel) has been described [1,8,9]. MBZ is also known to inhibit other factors involved in tumour progression, e.g., matrix metalloproteinase-2 activity and angiogenesis [7,10–12]. Furthermore, the benzimidazoles are not substrates for P-gp and

other ABC-transporters [11], thus avoiding the risk of inducing multidrug resistance in exposed cancer cells, and MBZ reduces P-gp expression.



**Figure 1.** Chemical structures of various benzimidazoles with anticancer activity.

Several studies have proved the antitumour activity of MBZ in a wide range of cancers, e.g., breast, ovary, lung and colorectal carcinoma, glioblastoma, and melanoma in vitro or in vivo [1,10,13,14]. MBZ demonstrates antitumour activity either as a single agent or in combination with other chemotherapeutics or radiotherapy, inhibiting tumour growth and metastatic spread. Moreover, MBZ also stimulates the antitumour immune response [15,16], but in vivo studies have not fully supported the in vitro data [17,18]. Nevertheless, the extremely poor water-solubility of most benzimidazoles is a serious disadvantage as MBZ is almost completely insoluble in physiologic buffers, thus preventing parenteral administration. Moreover, MBZ has poor bioavailability (~17–20%) upon p.o. administration, with considerable interindividual variability; thus, it is difficult to reach a serum level sufficient for antitumour activity [19,20].

A promising strategy for improving the pharmacologic features of low-molecular-weight drugs, particularly water-solubility and half-life in the circulation, is to employ an advanced drug-delivery system (DDS), such as polymer–drug conjugates, liposomes, or self-assembled micelles [21,22]. The water-soluble, biocompatible polymer carrier based on *N*-(2-hydroxypropyl)methacrylamide (HPMA) is one of the most successful DDSs described so far. Biologically active compounds, typically low-molecular-weight cancerostatic drugs, are covalently attached to this carrier via a defined spacer to achieve controlled release in the target tissue [23,24]. DDSs based on HPMA copolymers significantly reduce the toxicity of the attached drugs, ensuring their increased accumulation in solid tumours via the enhanced permeability and retention (EPR) effect [25,26]. HPMA copolymers bearing different cytostatic drugs have been extensively studied and have proved to possess excellent antitumour activity in numerous mouse and human tumours in vitro and in vivo [27].

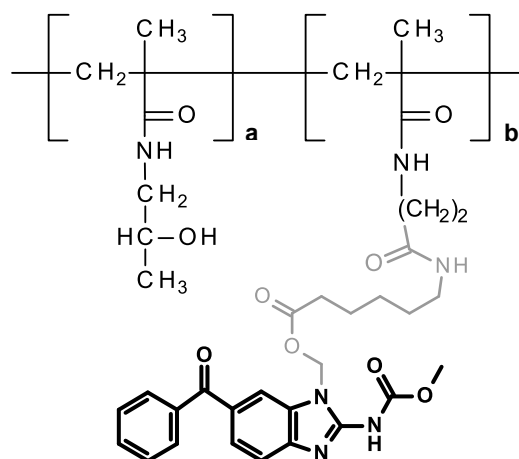
Herein, we report the antitumour activities of an HPMA copolymer conjugate bearing MBZ covalently linked to the carrier through a biodegradable bond. The conjugate showed very good water-solubility, enabling administration of MBZ into tumour-bearing mice via i.p. injection, and it showed promising antitumour activity.

## 2. Material and Methods

### 2.1. Synthesis of HPMA Copolymer Conjugate Bearing MBZ

The complete synthesis of the HPMA copolymer-bound MBZ has been described recently [28] and involves: (a) derivation of MBZ with a proper functional group enabling linkage to the polymer carrier; (b) preparation of side-chain functionalised HPMA copolymers; (c) and attachment of MBZ derivatives to the polymer precursors yielding the polymer conjugates of interest. In this study, two HPMA copolymer MBZ conjugates, referred to as conjugate **II** in the cited paper [28], were prepared and studied. The MBZ was bound to the polymer carrier via a 6-aminohexanoate-based ester linkage. The schematic structure of the conjugates is shown in Figure 2, and their characteristics are summarised in Table 1. All polymer molecular weights,  $M_n$  and  $M_w$ , were measured by gel permeation chromatography (GPC) using a Shimadzu HPLC system equipped with a GPC column (TSKgel G3000SWxl 300 × 7.8 mm; 5 μm), UV-Vis, refractive index (RI) Optilab<sup>®</sup>-rEX and multiangle light scattering (MALS) DAWN EOS (Wyatt Technology Co., Santa Barbara, CA, USA) detector using 80:20 methanol:sodium acetate buffer (pH 6.5; 0.3 M, flow rate

0.5 mL/min). The hydrodynamic diameter ( $D_h$ ) of the conjugates in PBS buffer (pH 7.4, 5 mg/mL, 25 °C) was measured by a Nano-ZS instrument (ZEN 3600, Malvern, UK). The intensity of scattered light was measured at angle  $\theta = 173^\circ$ , using a laser with a wavelength of 632.8 nm, and the data were analysed using the DTS (Nano) programme. All values were the mean of five or more independent measurements. The mebendazole content was determined by HPLC after treatment with 1% NaOH solution for 30 min. The analyses were performed via HPLC using a reverse-phase monolithic column (Chromolith Performance RP-18e 100 × 4.6 mm) with UV detection. A mixture of water and acetonitrile was used as an eluent at a gradient of 0–100% and a flow rate of 2.0 mL/min.



**Figure 2.** Structure of the HPMA copolymer conjugate bearing MBZ bound through a 6-aminohexanoate-based ester linkage.

**Table 1.** Characteristics of MBZ polymer conjugates and their precursors.

Conjugate	$M_w$ kDa	$\bar{D}$	Size ( $D_h$ ) nm	TT/MBZ Content $\text{mmol}\cdot\text{g}^{-1}$	Polymerisation Technique
poly(HPMA-co-Ma- $\beta$ -Ala-TT) (P-MBZ-A precursor)	28	1.4	8.2	0.33	free radical
poly(HPMA-co-Ma- $\beta$ -Ala-TT) (P-MBZ-B precursor)	35	1.1	8.6	0.35	RAFT
P-MBZ-A	32	1.6	10.1	0.28	free radical
P-MBZ-B	37	1.1	10.3	0.22	RAFT

## 2.2. Cell Lines

The following murine cancer cell lines from the American Type Culture Collection (ATCC, Manassas, VA, USA) were used: colon carcinoma CT-26, Lewis lung carcinoma LL2, and T-cell lymphoma EL-4. The EL-4 cell line was propagated in RPMI-1640 medium supplemented with 2 mM glutamine, 100 U/mL penicillin, 100  $\mu\text{g}/\text{mL}$  streptomycin, 1 mM Na pyruvate, 4.5 g/L of glucose, and 10% heat-inactivated FBS. Dulbecco's modified eagle medium (DMEM), supplemented with 4 mM glutamine, 100 U/mL penicillin, 100  $\mu\text{g}/\text{mL}$  streptomycin, 1.5 g/L Na bicarbonate, 4.5 g/L of glucose, 10 mM of HEPES solution, and 10% heat-inactivated FBS, was used to cultivate the LL2 cells. The CT-26 cell line was propagated in RPMI-1640 medium supplemented with 2 mM glutamine, 100 U/mL penicillin, 100  $\mu\text{g}/\text{mL}$  streptomycin, 1 mM Na pyruvate, 4.5 g/L of glucose, 10 mM of HEPES solution, 5 mL of nonessential amino acids, and 10% heat-inactivated FBS. Only cells with viability higher than 95% and within exponential growth were used for experiments. All employed cell lines were used for up to four passages upon thawing. All cell cultures were propagated under standard cultivation conditions (37 °C, 5%  $\text{CO}_2$  humidified atmosphere). Cells were cultivated until reaching ~80–90% confluence before



any use. All cell lines were routinely tested for mycoplasma (MycoAlert Mycoplasma Detection Kit, Lonza, Basel, Switzerland).

### 2.3. Mice

C57BL/6 (*H-2<sup>b</sup>*) mice were obtained from the animal facility at the Institute of Microbiology, Czech Academy of Sciences. Food and water were given ad libitum, and the mice were 9–15 weeks of age and weighed 19–22 g. The institutional guidelines for the care and use of laboratory animals were strictly followed in line with a protocol approved by the Institutional Animal Care and Use Committee of the Czech Academy of Sciences for all animal work (Prague, Czech Republic), and the experiments were conducted in compliance with local and European guidelines.

### 2.4. IL-2/S4B6 Complexes

Complexes were prepared by mixing recombinant mouse IL-2 (100 µg/mL; Peprotech, Cranbury, NJ, USA) with anti-IL-2 mAb S4B6 (BioXCell, Lebanon, NH, USA) at a molar ratio of 2:1. After 15 min incubation at room temperature, the complexes were diluted with PBS to the desired concentration before application.

### 2.5. In Vitro Proliferation Assay

To test the in vitro cytostatic activity of the MBZ and polymer conjugates bearing MBZ, inhibition of cell proliferation was determined using the [<sup>3</sup>H]-thymidine incorporation assay. EL-4, LL2, or CT-26 cells (5, 2, and  $0.75 \times 10^4$  /well for 24-, 48-, and 72-h incubation periods, respectively) were seeded in a 96-well, flat-bottom tissue culture plate (Nunc, Roskilde, Denmark). Titrated concentrations of the samples were added to the wells in quadruplicate, to reach a final volume of 250 µL. The plates were incubated in a 5% CO<sub>2</sub> at 37 °C for 24, 48, or 72 h, and then pulsed with 1 µCi (37 kBq) of [<sup>3</sup>H]-thymidine for the last 6 h of incubation. Next, we harvested the cells on glass fibre filters (PerkinElmer, Waltham, MA, USA) using a cell harvester (Tomtec, Orange, Hamden, CT, USA). A scintillation counter (1450 Microbeta TriLux, Wallac, Turku, Finland) was employed to measure the radioactivity of the samples by the use of plastic scintillator. Control cells were cultivated in a cultivation medium only. The activity of control cells was always higher than 20,000 cpm/well.

### 2.6. In Vitro Cytotoxicity Assay

A conventional MTT (3-(4,5-dimethylthiazol-2-yl)-2,5-diphenyltetrazolium bromide) assay was employed to determine the cytotoxicity of the MBZ and polymer conjugates bearing MBZ in EL-4, LL2, and CT-26 cells in vitro. Tested cells (5, 2, and  $0.75 \times 10^4$  /well for 24, 48, and 72 h incubation periods, respectively) were seeded into 96-well tissue culture plates with flat-bottoms (Nunc, Denmark), and they were cultivated with tested samples for 70 h as described above. Next, plates were centrifuged ( $200 \times g$ , 5 min, 4 °C), 200 µL of cultivation medium was aspirated from each well, and 120 µL of MTT (0.83 mg/mL) in culture medium was added to each well. Plates were cultivated for another 2 h at standard cultivation conditions. Finally, 200 µL of DMSO was added to each well, and the absorbance was determined after 15 min at 570 nm using a microplate reader (Infinite 200 PRO, TECAN, Männedorf, Switzerland).

### 2.7. Inhibition of Tumour Growth In Vivo

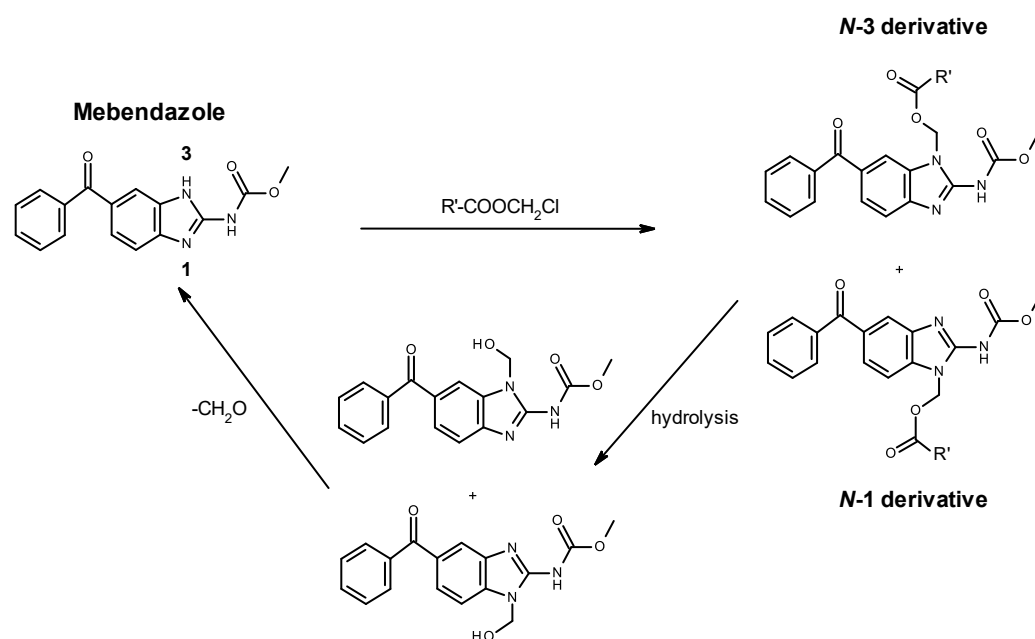
Female C57BL/6 mice were s.c. inoculated with  $1 \times 10^5$  EL-4 cells in 100 µL of sterile PBS on the shaved right anterior flank on day 0. Tumour-bearing mice were randomly distributed into experimental groups, and treatment was initiated on day 8 when the tumours reached about 5–7 mm in diameter. The doses were determined based on the mean body weight of each experimental group at the time of drug administration and given in 500 µL, injected i.p. The animals were observed three times a week for tumour progression, and the tumours were measured using callipers. The tumour size, body weight

and survival were recorded, with mice that survived until day 80 without any signs of a tumour considered as long-term survivors.

### 3. Results and Discussion

Two polymer conjugates bearing MBZ, namely P-MBZ-A and P-MBZ-B, differing in HPMA copolymer synthesis technique, were synthesised and used in the study. Free radical copolymerisation and reversible addition-fragmentation chain-transfer polymerisation (RAFT) polymerisation techniques were employed. While the free radical polymerisation gives rise to copolymers with rather broad dispersity, RAFT polymerisation enables the synthesis of copolymers with a dispersity close to 1. The conjugate properties are summarised in Table 1, with both polymers having a molecular weight under the threshold limit determined for similar HPMA-based copolymers [29]. Importantly, the hydrodynamic radius significantly increased when the mebendazole derivative was bound to the polymer precursors (from 8.2 to 10.1 nm in the free-radical variant and from 8.6 to 10.3 nm in the RAFT variant), attributed to the steric contribution of a bulky MBZ molecule in the conjugate. Moreover, this is advantageous for an enhanced EPR effect, thus increasing antitumour activity *in vivo*.

The linker between the MBZ and polymer carrier was designed to be cleaved by intracellular hydrolases [30], with the hydrolysis of the ester bond within the spacer followed by spontaneous rearrangement of the product releasing the free MBZ (Figure 3).

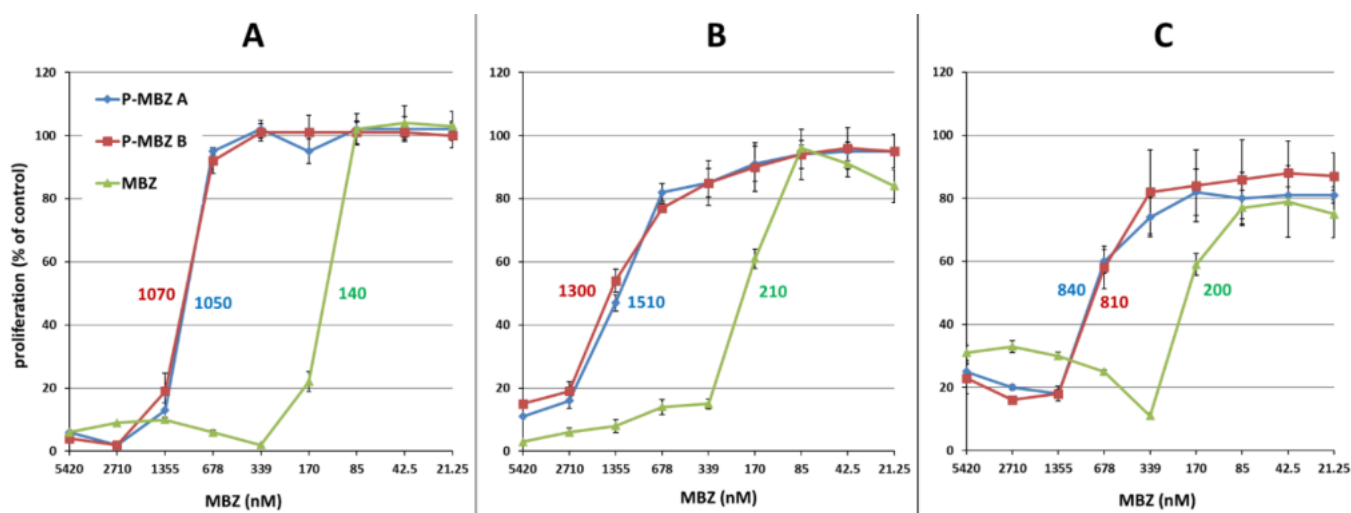


**Figure 3.** Generation and cleavage of the MBZ derivative. ( $R'$  represents the linker connected to the polymer.) A statistical mixture of *N*-1 and *N*-3 derivatives is formed due to the tautomerism of the MBZ molecule (1,3-H shift).

#### 3.1. Cytostatic Activity of P-MBZ Conjugates in Cancer Cell Lines of Various Origins *In Vitro*

The cytostatic activity of P-MBZ conjugates and free MBZ was first determined in T-cell lymphoma EL-4, lung carcinoma LL2, and colon carcinoma CT-26, with free MBZ showing very similar cytostatic activity in EL-4, LL2, and CT-26 cells, with an  $IC_{50}$  of 139, 210, and 200 nM, respectively, after 72 h incubation (Figure 4). Thus, the cytostatic activity of MBZ is comparable to doxorubicin since it has an  $IC_{50}$  typically  $\sim 75$ , 130, and 90 nM in these cell lines. This is in concordance with previously reported work showing similar, or even higher, cytostatic activity of MBZ in comparison to other clinically used cancerostatics, e.g., paclitaxel, 5-fluorouracil, oxaliplatin, and others, in different cancer cell lines [11]. **P-MBZ-A** and **P-MBZ-B** conjugates showed practically identical cytostatic activities (Figure 4), which

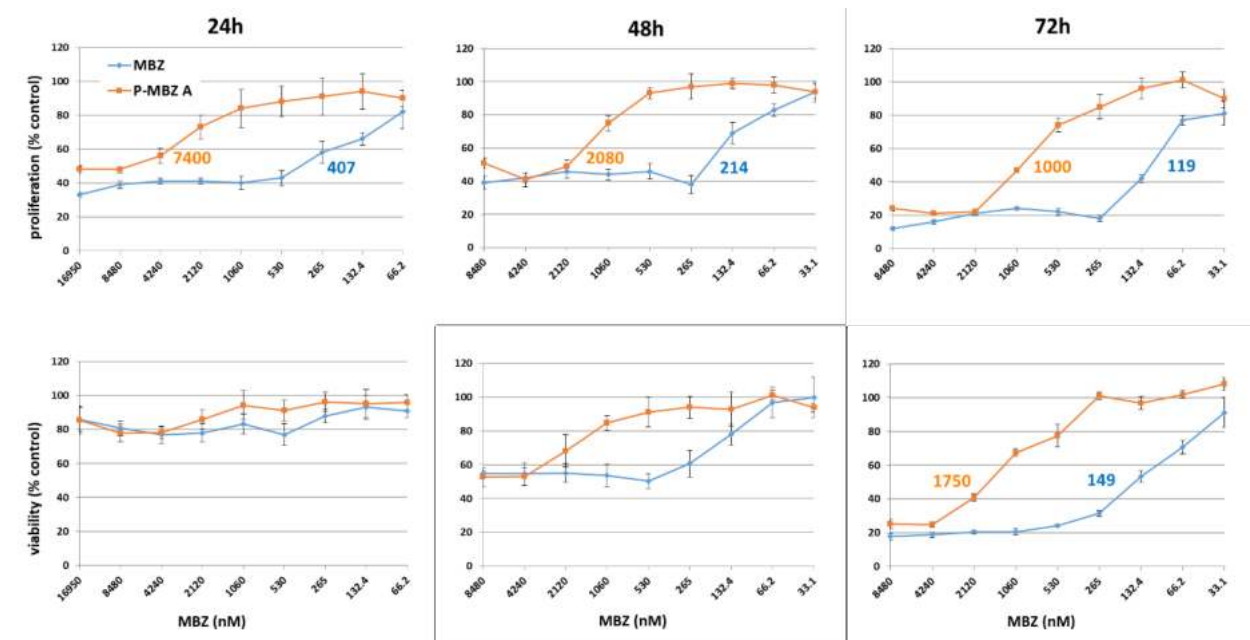
were about 4–8 times less potent than free MBZ ( $IC_{50} \sim 0.814\text{--}1.51 \mu\text{M}$ ). The difference in dispersity between **P-MBZ-A** and **P-MBZ-B** conjugates thus does not affect their in vitro cytostatic activity. The ratio between the cytostatic activities of free MBZ and polymer-MBZ conjugates was similar to that for doxorubicin and the HPMA copolymer conjugate bearing doxorubicin bound through a hydrazone bond [31], demonstrating that MBZ is effectively released from the polymer carrier to its pharmacologically active form. These results demonstrate that polymer-MBZ conjugates possess remarkable cytostatic activity in cancer cell lines of various origins in vitro.



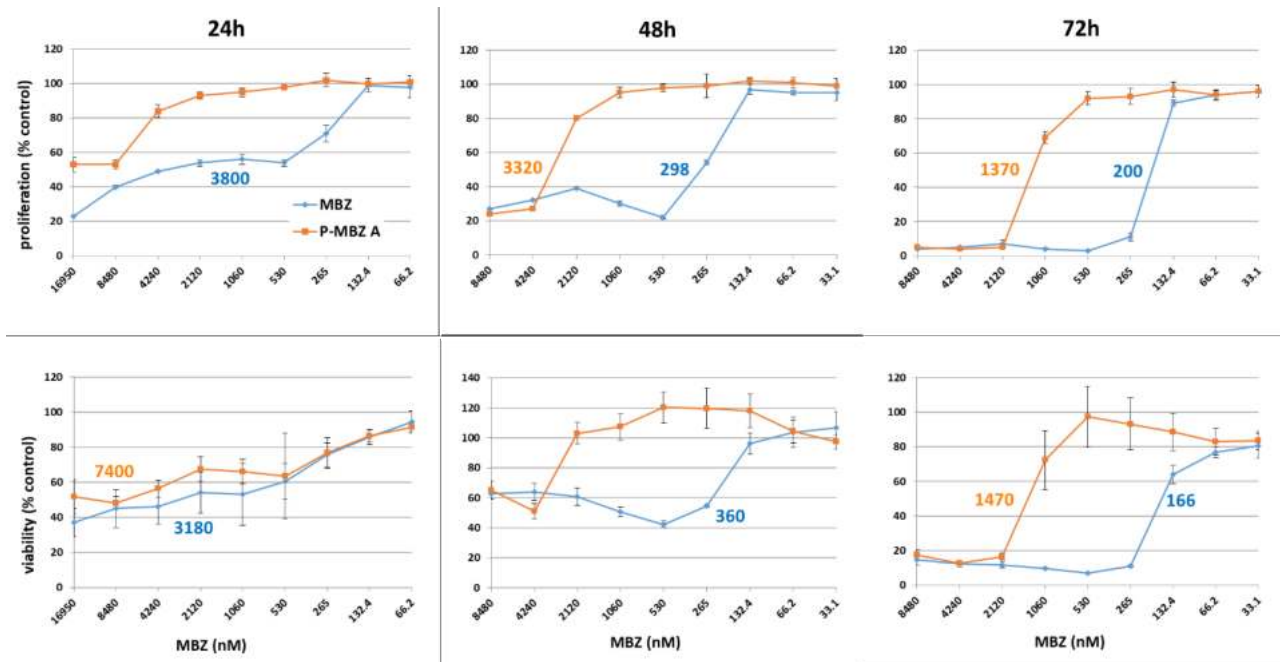
**Figure 4.** Cytostatic activity of polymer-bound mebendazole conjugates. Cytostatic activity of HPMA copolymer-bound mebendazole conjugates (**P-MBZ-A** and **P-MBZ-B**) and free mebendazole (MBZ) in EL-4 (A), LL2 (B) and CT-26 (C) murine cancer cell lines in vitro as determined by a [ $^3\text{H}$ ]-thymidine incorporation assay after 72 h of incubation. The calculated  $IC_{50}$  values (nM) are shown inside the graphs for all samples. Each experimental condition was performed in quadruplicate, and the results are shown as the proliferation of exposed cells relative to the controls (untreated cells)  $\pm$  SD. The experiment was repeated with similar results.

### 3.2. Kinetics of Cytostatic and Cytotoxic Activities of the P-MBZ-A Conjugate and MBZ In Vitro

The cytostatic and cytotoxic activities of **P-MBZ-A** conjugate and free MBZ were evaluated in LL2 and EL-4 cell lines after 24, 48, and 72 h of incubation (Figure 5), showing that the cytostatic effects of MBZ and **P-MBZ-A** are more rapid in the LL2 cell line than the cytotoxic one at very high concentrations ( $>5 \mu\text{M}$  MBZ). Both MBZ and **P-MBZ-A** inhibited proliferation of LL2 cells to less than 50% of controls after 24 h incubation, with little effect on cell viability. Almost-comparable cytostatic and cytotoxic effects were observed in both cell lines after 48 h of incubation, with **P-MBZ-A** conjugate showing slightly higher cytostatic activity than cytotoxic activity in LL2 cells ( $IC_{50}$  being 1 and  $1.75 \mu\text{M}$ , respectively) after 72 h, whereas the cytostatic and cytotoxic activities of **P-MBZ-A** conjugate were comparable in EL-4 cells. These results show that the cytostatic and cytotoxic effects of **P-MBZ-A** conjugate are expressed later in comparison to free MBZ, probably reflecting the release kinetics of the MBZ from the conjugate.



(A)

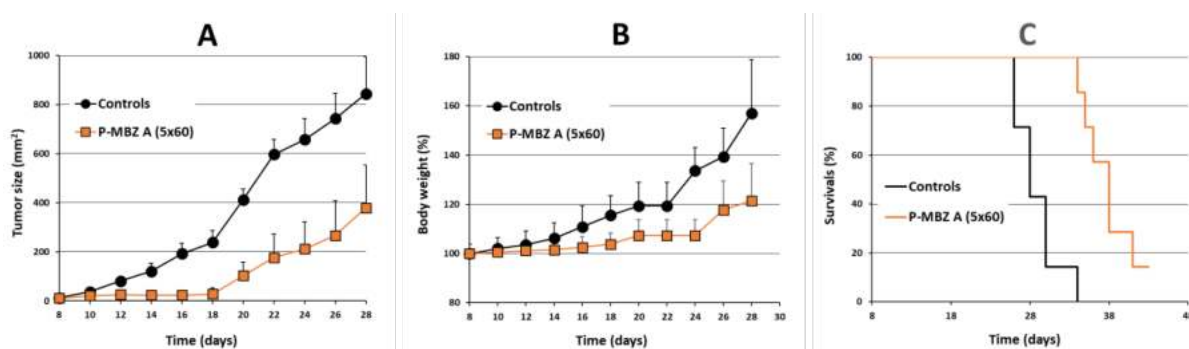


(B)

**Figure 5.** Kinetics of the cytostatic and cytotoxic activities of polymer-bound mebendazole conjugate. Cytostatic activity of HPMA copolymer-bound mebendazole conjugate (P-MBZ-A) and free mebendazole (MBZ) in LL2 (A) and EL-4 (B) murine cancer cell lines in vitro, as determined by [<sup>3</sup>H]-thymidine incorporation and MTT assays, respectively, after 24, 48, and 72 h of incubation. The calculated IC<sub>50</sub> values (nM) are shown inside the graphs for those samples where these values were reached. Each experiment was performed in quadruplicate, and the results are shown as the proliferation or viability of exposed cells relative to the controls (untreated cells) ± SD. The experiment was repeated with similar results.

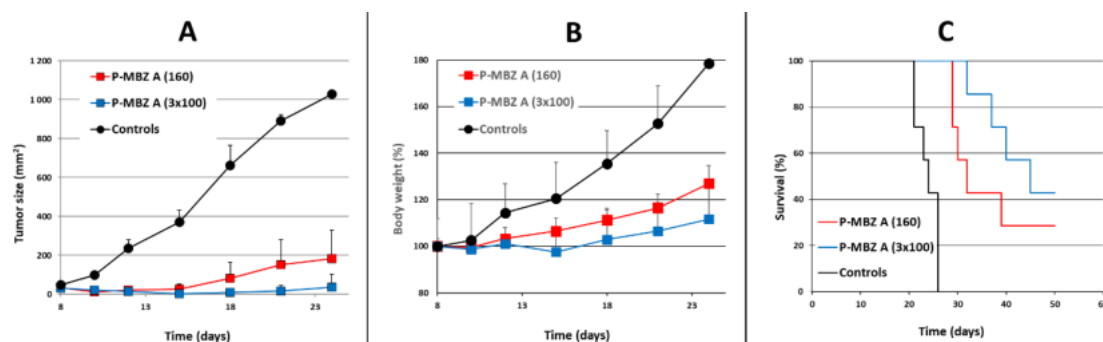
### 3.3. Antitumour Activity of P-MBZ-A Conjugate In Vivo

EL-4 tumours growing in syngeneic B6 mice were employed as a model to evaluate the antitumour activity of **P-MBZ-A** as the EL-4 tumour is a rapidly growing, resistant cancer model. First, we evaluated the antitumour activity of **P-MBZ-A** using a prolonged treatment schedule, where P-MBZ-A conjugate was administered i.p. in five doses given every second day. The dose of the conjugate in naïve B6 mice was titrated to determine the safe dose for the selected treatment schedule, which was approximately 60 mg MBZ/kg. B6 mice with progressively growing s.c. EL-4 tumours were treated with **P-MBZ-A** conjugate starting on day 8 post-tumour-cell inoculation (Figure 6), and the treatment was deemed safe as mice did not lose any weight (Figure 6B) or show any other signs of toxicity. **P-MBZ-A** conjugate effectively inhibited tumour growth up to day 18 (Figure 6A), after which the tumours exhibited growth kinetics similar to those of the controls, showing that **P-MBZ-A** was capable of the potent inhibition of tumour progression, but the treatment effect rapidly diminished thereafter. Survival of the mice treated with **P-MBZ-A** was 128% of the controls, with one mouse being completely cured (Figure 6C).



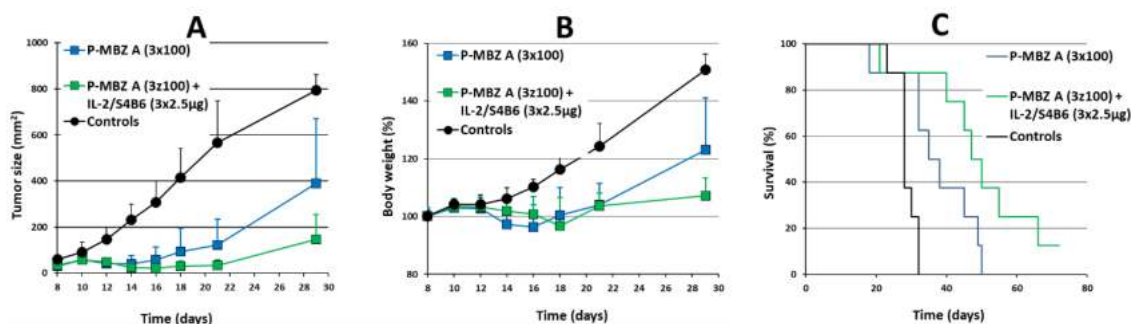
**Figure 6.** Antitumour activity of prolonged treatment with polymer-bound mebendazole conjugate in vivo. B6 mice ( $n = 7$ ) were s.c. inoculated with  $10^5$  EL-4 cells on day 0, then i.p. injected with 5 doses (60 mg mebendazole/kg per one dose) of HPMA copolymer-bound mebendazole conjugate (**P-MBZ-A** ( $5 \times 60$ )) on days 8, 10, 12, 14, and 16. Untreated mice were used as controls. Tumour growth (A), body weight (B), and survival (C) were monitored, and each experimental point (A,B) is the average of the experimental group  $\pm$  SD.

Next, the antitumour activity of **P-MBZ-A** conjugate, using a short-term treatment consisting of either a single dose or three doses given every second day, was evaluated. The safe dosage for these treatment schedules was approximately 160 and 100 mg MBZ/kg for a single dose and 3 doses, respectively. B6 mice bearing progressively growing s.c. EL-4 tumours were treated with P-MBZ-A conjugate starting on day 8 post-tumour-cell inoculation (Figure 7). Treated mice did not show any weight loss (Figure 7B) or any other sign of toxicity, with significant inhibition of tumour growth in both treatment groups (Figure 7A), which was considerably longer lasting compared to the previous treatment schedule. A total of 2 out of 7 mice treated with a single dose of P-MBZ-A were completely cured (Figure 7C), and the survival of the remaining mice was prolonged to 133% of the controls. The 3-dose schedule showed the highest efficacy since 3 out of 7 mice were completely cured, and the remaining mice survived an average of 161% longer than the controls.



**Figure 7.** Antitumour activity of short-term treatment with polymer-bound mebendazole conjugate in vivo. B6 mice ( $n = 7$ ) were s.c. inoculated with  $10^5$  EL-4 cells on day 0, then i.p. injected, either with 1 dose (160 mg mebendazole/kg) of HPMA copolymer-bound mebendazole conjugate (**P-MBZ-A** (160)) on day 8 or 3 doses (100 mg mebendazole/kg per one dose) of HPMA copolymer-bound mebendazole conjugate (**P-MBZ-A** ( $3 \times 100$ )) on days 8, 10, and 12. Untreated mice were used as controls. Tumour growth (A), body weight (B), and survival (C) were monitored, and each experimental point (A,B) is the average of the experimental group  $\pm$  SD.

Finally, we determined whether immunotherapy based on complexes of IL-2 and anti-IL-2 mAb S4B6 (IL-2co) can increase the therapeutic effect of **P-MBZ-A** conjugate. These complexes stimulate the expansion of activated and memory CD8<sup>+</sup> T-cells, as well as NK cells [32], and have been used previously in combination with HPMA copolymer conjugate bearing doxorubicin, demonstrating significant synergy in terms of antitumour activity in murine BCL1 leukaemia and B16-F10 melanoma. Thus, B6 mice bearing progressively growing s.c. EL-4 tumours were treated with either **P-MBZ-A** conjugate alone or in combination with IL-2co (Figure 8). The conjugate (100 mg MBZ/kg) was administered in 3 doses given on days 8, 10, and 12, while IL-2co was injected on days 14, 16, and 18. No treatment caused significant body weight loss (Figure 8B) or any other sign of toxicity. The treatment with **P-MBZ-A** alone was slightly less effective compared to the previous experiment regarding tumour growth inhibition as well as survival. No mice were completely cured, and survival was only prolonged to 131% of controls. However, **P-MBZ-A** conjugate in combination with IL-2co showed considerably higher antitumour efficacy, achieving stronger tumour growth inhibition and prolonged survival to 162% of controls. An experimental group treated with IL-2co alone was not included since such immunotherapy given as late as 14 days post-tumour-cell inoculation has no effect [33].



**Figure 8.** Potentiation of antitumour activity of polymer-bound mebendazole conjugate through IL-2 immunocomplexes in vivo. B6 mice ( $n = 8$ ) were s.c. inoculated with  $10^5$  EL-4 cells on day 0, then i.p. injected with 3 doses (100 mg mebendazole/kg per one dose) of HPMA copolymer-bound mebendazole conjugate (**P-MBZ-A** ( $3 \times 100$ )) on days 8, 10, and 12, or with the latter plus complexes of IL-2 and anti-IL-2 mAb S4B6 mAb (2.5 µg IL-2 per one dose) on days 14, 16, and 18 (**P-MBZ-A** ( $3 \times 100$ ) + IL-2co). Untreated mice were used as controls. Tumour growth (A), body weight (B), and survival (C) were monitored, and each experimental point (A,B) is the average of the experimental group  $\pm$  SD.

#### 4. Conclusions

The linear HPMA copolymer conjugate bearing MBZ covalently attached through a biodegradable bond possesses very good water-solubility, thus enabling parenteral administration, and it has cytostatic activity in the range of 240–450 ng MBZ/mL in several cancer cell lines of various tissue origins *in vitro*. Of note, the conjugate showed considerable *in vivo* antitumour activity without any signs of toxicity and could be potentiated through IL-2-based immunotherapy.

**Author Contributions:** Conceptualization, M.S. and M.K.; methodology, M.S. and M.K.; software, L.K.; validation, J.K.; formal analysis, A.R.; investigation, B.D.; resources, T.E.; data curation, L.S.; writing—original draft preparation, M.S. and M.K.; writing—review and editing, T.E.; visualization, D.B.; supervision, M.K.; project administration, M.S.; funding acquisition, T.E. and M.K. All authors have read and agreed to the published version of the manuscript.

**Funding:** This work was supported by the Czech Science Foundation (grant number 19-05649S) and the Institutional Research Concept RVO 61388971, by the Ministry of Education, Youth, and Sports of the Czech Republic within the Interexcellence program (project LTAUSA18083) and from the Academy of Sciences of Czech Republic (grant no. JSPS-22-01).

**Institutional Review Board Statement:** The animal study protocol was approved by the Institutional Review Board of the Institute of Microbiology, Academy of Sciences of the Czech Republic (protocol code 104/2016).

**Informed Consent Statement:** Not applicable.

**Data Availability Statement:** The data presented in this study are available on request from the corresponding author.

**Conflicts of Interest:** The authors declare no conflict of interest.

#### References

- Sasaki, J.; Ramesh, R.; Chada, S.; Gomyo, Y.; Roth, J.A.; Mukhopadhyay, T. The anthelmintic drug mebendazole induces mitotic arrest and apoptosis by depolymerizing tubulin in non-small cell lung cancer cells. *Mol. Cancer Ther.* **2002**, *1*, 1201–1209.
- Mukhopadhyay, T.; Sasaki, J.; Ramesh, R.; Roth, J.A. Mebendazole elicits a potent antitumor effect on human cancer cell lines both *in vitro* and *in vivo*. *Clin. Cancer Res.* **2002**, *8*, 2963–2969. [PubMed]
- Chu, S.W.; Badar, S.; Morris, D.L.; Pourgholami, M.H. Potent inhibition of tubulin polymerisation and proliferation of paclitaxel-resistant 1A9PTX22 human ovarian cancer cells by albendazole. *Anticancer Res.* **2009**, *29*, 3791–3796.
- Dogra, N.; Kumar, A.; Mukhopadhyay, T. Fenbendazole acts as a moderate microtubule destabilizing agent and causes cancer cell death by modulating multiple cellular pathways. *Sci. Rep.* **2018**, *8*, 11926. [CrossRef]
- Hou, Z.J.; Luo, X.; Zhang, W.; Peng, F.; Cui, B.; Wu, S.J.; Zheng, F.M.; Xu, J.; Xu, L.Z.; Long, Z.J.; et al. Flubendazole, FDA-approved anthelmintic, targets breast cancer stem-like cells. *Oncotarget* **2015**, *6*, 6326–6340. [CrossRef]
- Jornet, D.; Bosca, F.; Andreu, J.M.; Domingo, L.R.; Tormos, R.; Miranda, M.A. Analysis of mebendazole binding to its target biomolecule by laser flash photolysis. *J. Photochem. Photobiol. B* **2016**, *155*, 1–6. [CrossRef]
- Doudican, N.; Rodriguez, A.; Osman, I.; Orlow, S.J. Mebendazole induces apoptosis via Bcl-2 inactivation in chemoresistant melanoma cells. *Mol. Cancer Res.* **2008**, *6*, 1308–1315. [CrossRef]
- Rushworth, L.K.; Hewit, K.; Munnings-Tomes, S.; Somani, S.; James, D.; Shanks, E.; Dufes, C.; Straube, A.; Patel, R.; Leung, H.Y. Repurposing screen identifies mebendazole as a clinical candidate to synergise with docetaxel for prostate cancer treatment. *Br. J. Cancer* **2020**, *122*, 517–527. [CrossRef]
- Poruchynsky, M.S.; Komlodi-Pasztor, E.; Trostel, S.; Wilkerson, J.; Regairaz, M.; Pommier, Y.; Zhang, X.; Maity, T.K.; Robey, R.; Burotto, M.; et al. Microtubule-targeting agents augment the toxicity of DNA-damaging agents by disrupting intracellular trafficking of DNA repair proteins. *Proc. Natl. Acad. Sci. USA* **2015**, *112*, 1571–1576. [CrossRef]
- Pinto, L.C.; Moreira Soares, B.; Viana Pinheiro, J.J.; Riggins, G.J.; Pimentel Assumpcao, P.; Rodriguez Burbano, R.M.; Carvalho Montenegro, R. The anthelmintic drug mebendazole inhibits growth, migration and invasion in a gastric cancer cell model. *Toxicol. Vitro* **2015**, *29*, 2038–2044. [CrossRef] [PubMed]
- Pinto, L.C.; Moreira-Nunes, C.F.A.; Soares, B.M.; Burbano, R.M.R.; Lemos, J.A.R.; Montenegro, R.C. Mebendazole, an antiparasitic drug, inhibits drug transporters expression in a preclinical model of gastric peritoneal carcinomatosis. *Toxicol. Vitro* **2017**, *43*, 87–91. [CrossRef] [PubMed]
- Sung, S.J.; Kim, H.K.; Hong, Y.K.; Joe, Y.A. Autophagy is a potential target for enhancing the anti-angiogenic effect of mebendazole in endothelial cells. *Biomol. Ther.* **2019**, *27*, 117–125. [CrossRef] [PubMed]

13. Bai, R.Y.; Staedke, V.; Aprhys, C.M.; Gallia, G.L.; Riggins, G.J. Antiparasitic mebendazole shows survival benefit in 2 preclinical models of glioblastoma multiforme. *Neuro. Oncol.* **2011**, *13*, 974–982. [CrossRef] [PubMed]
14. Simbulan-Rosenthal, C.M.; Dakshanamurthy, S.; Gaur, A.; Chen, Y.S.; Fang, H.B.; Abdussamad, M.; Zhou, H.; Zapas, J.; Calvert, V.; Petricoin, E.F.; et al. The repurposed anthelmintic mebendazole in combination with trametinib suppresses refractory NRAS<sup>Q61K</sup> melanoma. *Oncotarget* **2017**, *8*, 12576–12595. [CrossRef]
15. Blom, K.; Senkowsky, W.; Jarvius, M.; Berglund, M.; Rubin, J.; Lenhammar, L.; Parrow, V.; Andersson, C.; Loskog, A.; Fryknas, M.; et al. The anticancer effect of mebendazole may be due to M1 monocyte/macrophage activation via ERK1/2 and TLR8-dependent inflammasome activation. *Immunopharmacol. Immunotoxicol.* **2017**, *39*, 199–210. [CrossRef]
16. Blom, K.; Rubin, J.; Berglund, M.; Jarvius, M.; Lenhammar, L.; Parrow, V.; Andersson, C.; Loskog, A.; Fryknas, M.; Nygren, P.; et al. Mebendazole-induced M1 polarisation of THP-1 macrophages may involve DYRK1B inhibition. *BMC Res. Notes* **2019**, *12*, 234. [CrossRef]
17. Williamson, T.; Bai, R.Y.; Staedtke, V.; Huso, D.; Riggins, G.J. Mebendazole and a non-steroidal anti-inflammatory combine to reduce tumour initiation in a colon cancer preclinical model. *Oncotarget* **2016**, *7*, 68571–68584. [CrossRef]
18. Zhang, F.; Li, Y.; Zhang, H.; Huang, E.; Gao, L.; Luo, W.; Wei, Q.; Fan, J.; Song, D.; Liao, J.; et al. Anthelmintic mebendazole enhances cisplatin's effect on suppressing cell proliferation and promotes differentiation of head and neck squamous cell carcinoma (HNSCC). *Oncotarget* **2017**, *8*, 12968–12982. [CrossRef]
19. Dawson, M.; Braithwaite, P.A.; Roberts, M.S.; Watson, T.R. The pharmacokinetics and bioavailability of a tracer dose of [3H]-mebendazole in man. *Br. J. Clin. Pharmacol.* **1985**, *19*, 79–86. [CrossRef]
20. Dawson, M.; Allan, R.J.; Watson, T.R. The pharmacokinetics and bioavailability of mebendazole in man: A pilot study using [3H]-mebendazole. *Br. J. Clin. Pharmacol.* **1982**, *14*, 453–455. [CrossRef]
21. Kopeček, J. Polymer-drug conjugates: Origins, progress to date and future directions. *Adv. Drug Deliv. Rev.* **2013**, *65*, 49–59. [CrossRef]
22. Nishiyama, N.; Kataoka, K. Current state, achievements, and future prospects of polymeric micelles as nanocarriers for drug and gene delivery. *Pharmacol. Ther.* **2006**, *112*, 630–648. [CrossRef]
23. Tavares, M.R.; Hrabankova, K.; Konefal, R.; Kana, M.; Rihova, B.; Etrych, T.; Sirova, M.; Chytil, P. HPMA-based copolymers carrying STAT3 inhibitor cucurbitacin-D as stimulus-sensitive nanomedicines for oncotherapy. *Pharmaceutics* **2021**, *13*, 179. [CrossRef] [PubMed]
24. Pola, R.; Pokorna, E.; Vockova, P.; Bohmova, E.; Pechar, M.; Karolova, J.; Pankrac, J.; Sefc, L.; Helman, K.; Trneny, M.; et al. Cytarabine nanotherapeutics with increased stability and enhanced lymphoma uptake for tailored highly effective therapy of mantle cell lymphoma. *Acta Biomater.* **2021**, *119*, 349–359. [CrossRef]
25. Maeda, H.; Wu, J.; Sawa, T.; Matsumura, Y.; Hori, K. Tumor vascular permeability and the EPR effect in macromolecular therapeutics: A review. *J. Control. Release* **2000**, *65*, 271–284. [CrossRef]
26. Maeda, H. Tumor-selective delivery of macromolecular drugs via the EPR effect: Background and future prospects. *Bioconjug. Chem.* **2010**, *21*, 797–802. [CrossRef] [PubMed]
27. Duncan, R. Development of HPMA copolymer-anticancer conjugates: Clinical experience and lessons learnt. *Adv. Drug Deliv. Rev.* **2009**, *61*, 1131–1148. [CrossRef]
28. Studenovský, M.; Rumlerova, A.; Kostka, L.; Etrych, T. HPMA-based polymer conjugates for repurposed drug mebendazole and other imidazole-based therapeutics. *Polymers* **2021**, *13*, 2530. [CrossRef] [PubMed]
29. Etrych, T.; Šubr, V.; Strohalm, J.; Šířová, M.; Říhová, B.; Ulbrich, K. HPMA copolymer-doxorubicin conjugates: The effects of molecular weight and architecture on biodistribution and in vivo activity. *J. Control. Release* **2012**, *164*, 346. [CrossRef]
30. Simplicio, A.L.; Clancy, J.M.; Gilmer, J.F. Prodrugs for amines. *Molecules* **2008**, *13*, 519–547. [CrossRef]
31. Ulbrich, K.; Etrych, T.; Chytil, P.; Jelínková, M.; Říhová, B. HPMA copolymers with pH-controlled release of doxorubicin: In vitro cytotoxicity and in vivo antitumor activity. *J. Control. Release* **2003**, *87*, 33–47. [CrossRef]
32. Tomala, J.; Chmelova, H.; Mrkvan, T.; Rihova, B.; Kovar, M. In vivo expansion of activated naive CD8+ T cells and NK cells driven by complexes of IL-2 and anti-IL-2 monoclonal antibody as a novel approach of cancer immunotherapy. *J. Immunol.* **2009**, *183*, 4904–4949. [CrossRef] [PubMed]
33. Sívák, L.; Šubr, V.; Kovářová, J.; Dvořáková, B.; Šířová, M.; Říhová, B.; Randárová, E.; Kraus, M.; Tomala, J.; Studenovský, M.; et al. Polymer-ritonavir derivate nanomedicine with pH-sensitive activation possesses potent anti-tumor activity in vivo via inhibition of proteasome and STAT3 signaling. *J. Control. Release* **2021**, *332*, 563–580. [CrossRef] [PubMed]





## Article

# Evaluation of 3-Borono-L-Phenylalanine as a Water-Soluble Boron Neutron Capture Therapy Agent

Naoya Kondo , Fuko Hirano and Takashi Temma \* 

Department of Biofunctional Analysis, Graduate School of Pharmaceutical Sciences, Osaka Medical and Pharmaceutical University, 4-20-1 Nasahara, Takatsuki 569-1094, Osaka, Japan; naoya.kondo@ompu.ac.jp (N.K.); ompu72121051@s.omp.ac.jp (F.H.)

\* Correspondence: takashi.temma@ompu.ac.jp; Tel.: +81-72-690-1040

**Abstract:** Although 4-borono-L-phenylalanine (4-BPA) is currently the only marketed agent available for boron neutron capture therapy (BNCT), its low water solubility raises concerns. In this study, we synthesized 3-borono-L-phenylalanine (3-BPA), a positional isomer of 4-BPA, with improved water solubility. We further evaluated its physicochemical properties, tumor accumulation, and biodistribution. The water solubility of 3-BPA was 125 g/L, which is more than 100 times higher than that of 4-BPA. Due to the high water solubility, we prepared the administration solution of 3-BPA without a solubilizer sugar, which is inevitably added to 4-BPA preparation and has adverse effects. In in vitro and in vivo experiments, boron accumulation in cancers after administration was statistically equivalent in both sugar-complexed 3-BPA and 4-BPA. Furthermore, the biodistribution of 3-BPA was comparable with that of sugar-complexed 3-BPA. Since 3-BPA has high water solubility and tumor targetability equivalent to 4-BPA, 3-BPA can replace 4-BPA in future BNCT.

**Keywords:** boron neutron capture therapy; 4-borono-L-phenylalanine; drug discovery; solubility

**Citation:** Kondo, N.; Hirano, F.; Temma, T. Evaluation of 3-Borono-L-Phenylalanine as a Water-Soluble Boron Neutron Capture Therapy Agent. *Pharmaceutics* **2022**, *14*, 1106. <https://doi.org/10.3390/pharmaceutics14051106>

Academic Editor: Hassan Bousbaa

Received: 2 May 2022

Accepted: 20 May 2022

Published: 22 May 2022

**Publisher's Note:** MDPI stays neutral with regard to jurisdictional claims in published maps and institutional affiliations.



**Copyright:** © 2022 by the authors. Licensee MDPI, Basel, Switzerland. This article is an open access article distributed under the terms and conditions of the Creative Commons Attribution (CC BY) license (<https://creativecommons.org/licenses/by/4.0/>).

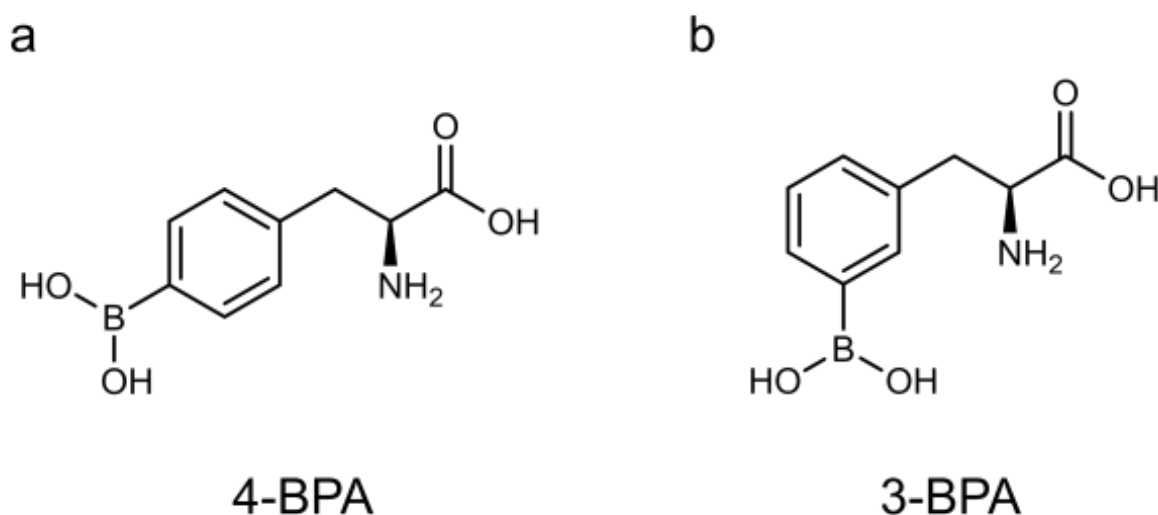
## 1. Introduction

Boron neutron capture therapy (BNCT) is a cancer treatment based on the nuclear reaction between boron ( $^{10}\text{B}$ ) atoms that are delivered into cancer cells and externally irradiated thermal neutrons. The alpha particles and Li nuclei produced in the nuclear reaction are high linear energy transfer radiation. They have a range of less than one cell's length, so boronoagents that can selectively deliver  $^{10}\text{B}$  atoms into tumor cells allow for cancer-selective treatment [1–3]. To date, two boronoagents, 4-borono-L-phenylalanine (4-BPA) and sodium borocaptate (BSH), have been used clinically [4,5], and these studies demonstrated that 4-BPA was therapeutically more effective than BSH [6]. 4-BPA was discovered by Snyder et al. in 1958 [7], and Mishima et al. first succeeded in treating malignant melanoma with 4-BPA BNCT in 1989 [8]. Currently, 4-BPA is the most widely used boronoagent for BNCT [9–11]. In Japan, after positive results were shown in two clinical trials, 4-BPA was marketed under the name Borofalan (Steboronine<sup>®</sup>) in May 2020 for locally advanced or locally recurrent unresectable head and neck cancer [12]. As 4-BPA is taken up in cancer cells by L-type/large neutral amino acid transporter 1 (LAT1, SLC7A5) [13,14], a positron emission tomography (PET) scan with 2- $^{18}\text{F}$ fluoro-4-borono-L-phenylalanine, a LAT1 imaging probe, can noninvasively predict the applicability of 4-BPA BNCT [15]. Since LAT1 expression on plasma membrane has been reported to be cancer-specific [16], the agent with high LAT1 recognition ability can be expected to exhibit tumor-specific accumulation.

In clinical BNCT settings, the intratumor boron concentration must be maintained at a high level (>20 ppm) [17] for a 3 h treatment period because the therapeutic effect is directly proportional to the intratumor boron concentration. It is necessary to administer a large amount of boron; thus, high tumor targetability with high water solubility are prerequisites for a useful boronoagent. However, 4-BPA has extremely poor water solubility under neutral conditions (0.6–0.7 g/L), as mentioned in the Borofalan interview form; thus, it

is solubilized by complex formation with sugars, such as fructose [18] and sorbitol [19], before administration. In particular, in the case of a patient with 60 kg body weight, 30 g 4-BPA, solubilized with 31.5 g D-sorbitol in 1000 mL administration solvent, is infused intravenously for treatment. Such a high load on the patient would have side effects. For example, hypoglycemia and liver and kidney failures could occur in patients with hereditary fructose intolerance due to fructose arising from D-sorbitol metabolism [20], and hematuria could also be a side effect due to the crystallization of 4-BPA in the urine resulting from its insolubility [12,21]. Thus, a critical drawback of 4-BPA is its low water solubility. However, it is quite challenging to develop boronoagents with high tumor targetability and high water solubility because the transmembrane transport system which is applicable for intracellular targeting of such a water-soluble boronoagent with an inferior passive intracellular penetration property to the high boron concentration levels required for BNCT is limited [3]. To date, no small molecular boronoagent other than 4-BPA and BSH has been tested in clinical trials [6].

We hypothesized that 3-borono-L-phenylalanine (3-BPA), a *meta* isomer of 4-BPA (Figure 1), has higher water solubility than 4-BPA, focusing on previous findings that *meta*-substituents show higher water solubility than *para*-substituents of the benzene ring due to asymmetric conformation and structural folding [22–24]. Furthermore, recent structure–activity relationship studies have shown that *meta*-substituted phenylalanine derivatives are transported more efficiently into cells by LAT1 than *para*-substituted derivatives [25,26]. Thus, 3-BPA would have improved water solubility and LAT1 recognition ability compared with 4-BPA. Although 3-BPA had been evaluated and concluded to be slightly inferior to 4-BPA in terms of accumulation in mouse melanoma in the 1990s [27,28], intraperitoneal administration had been adopted in these experiments targeting mouse melanoma regardless of LAT1 expression levels. Besides, the researchers added solubilizer sugar to the tested compounds, such as 2-, 3-, and 4-BPA, without estimating solubility in every experiment. Therefore, in this study, we carefully re-evaluated 3-BPA compared with 4-BPA *in vitro* and *in vivo*, focusing on water solubility and uptake through LAT1, and consequently found a significant superiority of 3-BPA as a promising lead compound of next-generation boronoagents in future BNCT.



**Figure 1.** Chemical structure of 4-borono-L-phenylalanine (4-BPA, (a)) and 3-borono-L-phenylalanine (3-BPA, (b)).

## 2. Materials and Methods

### 2.1. General

All reagents were obtained commercially and used without further purification unless otherwise noted. 4-BPA ( $^{10}\text{B}$ ) was supplied by Stella Pharma Corp. (Osaka, Japan). Milli-Q water (Merck Millipore, Burlington, MA, USA) was used in all experiments.

## 2.2. Synthesis of 3-BPA

The synthesis of 3-BPA was performed according to previous reports [25,29–31]. The synthetic scheme is shown in Supplementary Figure S1, and the details are described in the Supplementary Methods. 3-BPA was purified and characterized using an RP-HPLC system equipped with a C18 reversed-phase column (COSMOSIL 5C18-AR-II 10 ID × 250 mm; Nacalai Tesque, Kyoto, Japan). The mobile phase was a mixture of water and acetonitrile (95:5, *v/v*) at a flow rate of 5.0 mL/min. This condition was also used for 4-BPA. The purified 3-BPA was lyophilized to obtain fluffy white crystals and characterized by ESI-MS and <sup>1</sup>H and <sup>13</sup>C-NMR (Supplementary Figures S2 and S3).

## 2.3. Evaluation of the Physicochemical Properties of 3-BPA and 4-BPA

### 2.3.1. Water Solubility

3-BPA or 4-BPA (40 mg) were suspended in 200 µL water and stirred at 25 °C for 24 h. After stirring, the solution was centrifuged at 5000 rpm for 10 min, and the amount of boron in the supernatant solution was measured by 8800 triple quadrupole ICP-MS (Agilent, Santa Clara, CA, USA). The experiment was repeated twice with *n* = 3.

### 2.3.2. Log *p* Measurement

After dissolving 3-BPA or 4-BPA in water (0.2 mg/mL), 1-octanol was added to compose a water:1-octanol (1:1, *v/v*) mixture. The mixture was shaken for 5 min and then centrifuged at 5000 rpm for 10 min. The amount of boron was measured for each liquid phase using ICP-MS, and log *p* was calculated from the concentration ratio of each liquid phase. The experiment was repeated twice with *n* = 6.

## 2.4. In Vitro Experiments

### 2.4.1. Cell Lines

B16F10 mouse melanoma cells (RCB2630) and T3M-4 human pancreatic adenocarcinoma cells (RCB1021) were provided by the RIKEN BRC (Ibaraki, Japan). U-87MG human glioblastoma cells were provided by Prof. Magata (Hamamatsu University School of Medicine, Hamamatsu, Japan), and A549 human lung carcinoma cells (CCL-185) were obtained from ATCC (Manassas, VA, USA). Cells were cultured in growth medium RPMI 1640 for B16F10 and T3M-4 and DMEM for A549 and U-87MG, containing 10% fetal bovine serum at 37 °C in a humidified atmosphere of 5% CO<sub>2</sub>.

### 2.4.2. Western Blotting

Cultured cells lysed in Passive Lysis Buffer (Promega, Madison, WI, USA) were homogenized by sonication, centrifuged to remove debris, and subsequently diluted in 2-mercaptoethanol containing sample buffer (70 mM Tris, 1% SDS, 11% glycerol, 0.005% bromophenol blue). Samples (10 µL, 1.0 mg/mL) were then loaded, and Western blotting was performed using anti-LAT1 (KE026, 0.1 µg/mL) (Medicinal Chemistry Pharmaceutical, Sapporo, Japan) as a primary antibody and horseradish peroxidase-conjugated mAb as a secondary antibody (1:3000 dilution, HAF008, R&D Systems, Minneapolis, MN, USA). β-Actin levels were used to control protein loading in samples and were measured with anti-β-actin antibody (1:5000 dilution, NB600-505SS, Novus Biologicals, Littleton, CO, USA). Immunoreactive bands were visualized using Chemi-Lumi One L (Nacalai Tesque). The FastGene Bluestar prestained protein marker (NIPPON Genetics, Tokyo, Japan) was used as a molecular weight marker to estimate molecular weights. An Amersham Imager 600 (GE Healthcare Japan, Tokyo, Japan) was used to visualize bands. After ImageJ quantified the bands, the LAT1 expression levels among tumor cells were compared as the LAT1/β-actin ratio (*n* = 3).

### 2.4.3. Cell Staining

The cells were fixed with 4% paraformaldehyde, permeabilized with 0.2% Triton X100, and incubated with Blocking One Histo (Nacalai Tesque) for 10 min, followed by

incubation for 2 h at room temperature with an anti-LAT1 antibody (KE026, 0.1 µg/mL) as the primary antibody. The cells were then rinsed with PBS(-) and incubated for 30 min at room temperature with a CF555-labeled antibody (SAB4600068, 2 µg/mL, Sigma-Aldrich, St. Louis, MO, USA). For nuclear staining, the cells were incubated with Hoechst 33342 (5 µg/mL, Nacalai Tesque) for 10 min at room temperature. Fluorescence images were acquired with a BZ-X810 instrument (Keyence Japan Co., Osaka, Japan) and visualized by BZ-X800 Analyzer (Keyence Japan Co.).

#### 2.4.4. Cellular Uptake Study

Cells were cultured in six-well plates 2 days before the experiment. After medium removal, cells were washed twice with choline buffer (140 mM choline chloride, 2 mM potassium chloride, 1 mM magnesium chloride, 1 mM calcium chloride, 1 M Tris) [25] and preincubated with 900 µL of choline buffer containing/not containing 10 µM of the LAT1-specific inhibitor JPH203 [32,33] (Selleck Biotech, Tokyo, Japan) at 37 °C for 5 min. After incubation, 100 µL of 3-BPA or 4-BPA mixed with fructose (0.5 mg/mL, 0.11 *w/v*% Fru, pH 7.4) was added and incubated at 37 °C for 1, 5, and 30 min. After washing three times with choline buffer, 400 µL of 0.2 M NaOH was added to lyse the cells. After the amount of cell protein was measured using the BCA method (Thermo Fisher Scientific, Tokyo, Japan) and the mixture was ashed with nitric acid, the amount of boron was measured using ICP-MS. The accumulation rate was calculated as % dose/mg protein from the quantified dose of boron in added 3-BPA and 4-BPA, respectively (n = 3).

### 2.5. *In Vivo* Experiment

#### 2.5.1. Animal Preparation

Male BALB/c mice (4 weeks old, Japan SLC, Shizuoka, Japan, n = 35) and BALB/c nu-nu mice (4 weeks old, Japan SLC, n = 18) were housed under a 12 h light/12 h dark cycle and given free access to food and water. Animal experiments were conducted according to the institutional guidelines for animal experiments. The study protocol was approved by the institutional Experimental Animal Committee (Permission Number: 19-76 and 20-76). Tumor-bearing mice were prepared by subcutaneous inoculation of B16F10 cells ( $5 \times 10^5$  cells/mouse) suspended in PBS (-) solution (100 µL) into the right hind legs of BALB/c mice or T3M-4 cells ( $2.5 \times 10^6$  cells/mouse) suspended in PBS (-):Matrigel = 1:1 solution (100 µL) into the right hind legs of BALB/c nu-nu mice. The treatments were performed under 3–5% isoflurane anesthesia to reduce pain in the mice. Animals with a tumor of approximately 10 mm in diameter at 5 weeks after inoculation of cells were assigned for *in vivo* biodistribution studies so that tumor size was not biased between groups. Mice without viable T3M-4 tumors (n = 5) were euthanized by isoflurane inhalation overdose.

#### 2.5.2. *In Vivo* Biodistribution Study

B16F10-bearing mice were intravenously injected with 3-BPA or 4-BPA mixed with fructose (3-BPA-Fru, 4-BPA-Fru, 1 mg/100 µL PBS (-), 2.2 *w/v*% Fru, pH 7.4), and sacrificed 10, 30, 60, or 120 min after administration. Samples of the plasma and the tissues of interest were excised, weighed, and ashed by nitric acid, followed by ICP-MS measurements of the boron amount. The accumulation rate was calculated as the % injected dose/g (%ID/g) of the quantified dose of boron in the administrated solution.

LAT1-positive T3M-4 xenograft mice were intravenously injected with 3-BPA-Fru, 4-BPA-Fru (1 mg/100 µL PBS (-), 2.2 *w/v*% Fru, pH 7.4), or fructose-free 3-BPA (1 mg/100 µL PBS (-)) and sacrificed 60 min later, followed by boron amount measurement in the same manner. The details of the preparation of 3-BPA-Fru and 4-BPA-Fru and measurement of  $^{11}\text{B}$ -NMR (DD2 NMR Spectrometer, Agilent, Santa Clara, CA, USA, 600 MHz) to confirm the formation of the complex with fructose are described in Supplementary Methods.

## 2.6. Statistics

Data are presented as means  $\pm$  standard deviations. Statistical analyses were performed using Tukey's multiple comparison tests or an unpaired *t*-test with GraphPad Prism 8. Differences at the 95% confidence level ( $p < 0.05$ ) were considered significant unless otherwise noted.

## 3. Results

### 3.1. Properties of the 3-BPA and 4-BPA

The physicochemical properties of 3-BPA and 4-BPA are summarized in Table 1.

Notably, the solubility of 3-BPA in water was  $125 \pm 12$  g/L, which is more than 100 times higher than that of 4-BPA ( $0.72 \pm 0.13$  g/L) ( $n = 4$ , each). 3-BPA has a significantly higher  $\log p$  value ( $n = 6$ ) and a longer RP-HPLC retention time than 4-BPA.

**Table 1.** Physicochemical properties of 3-BPA and 4-BPA.

	3-BPA	4-BPA
Solubility (in water, 25 °C, $n = 6$ )	* $125 \pm 12$ (g/L)	$0.72 \pm 0.13$ (g/L)
Log <i>p</i> ( $n = 12$ )	<sup>†</sup> $-1.59 \pm 0.03$	$-1.80 \pm 0.04$
RP-HPLC Retention time	4.5 (min)	3.7 (min)

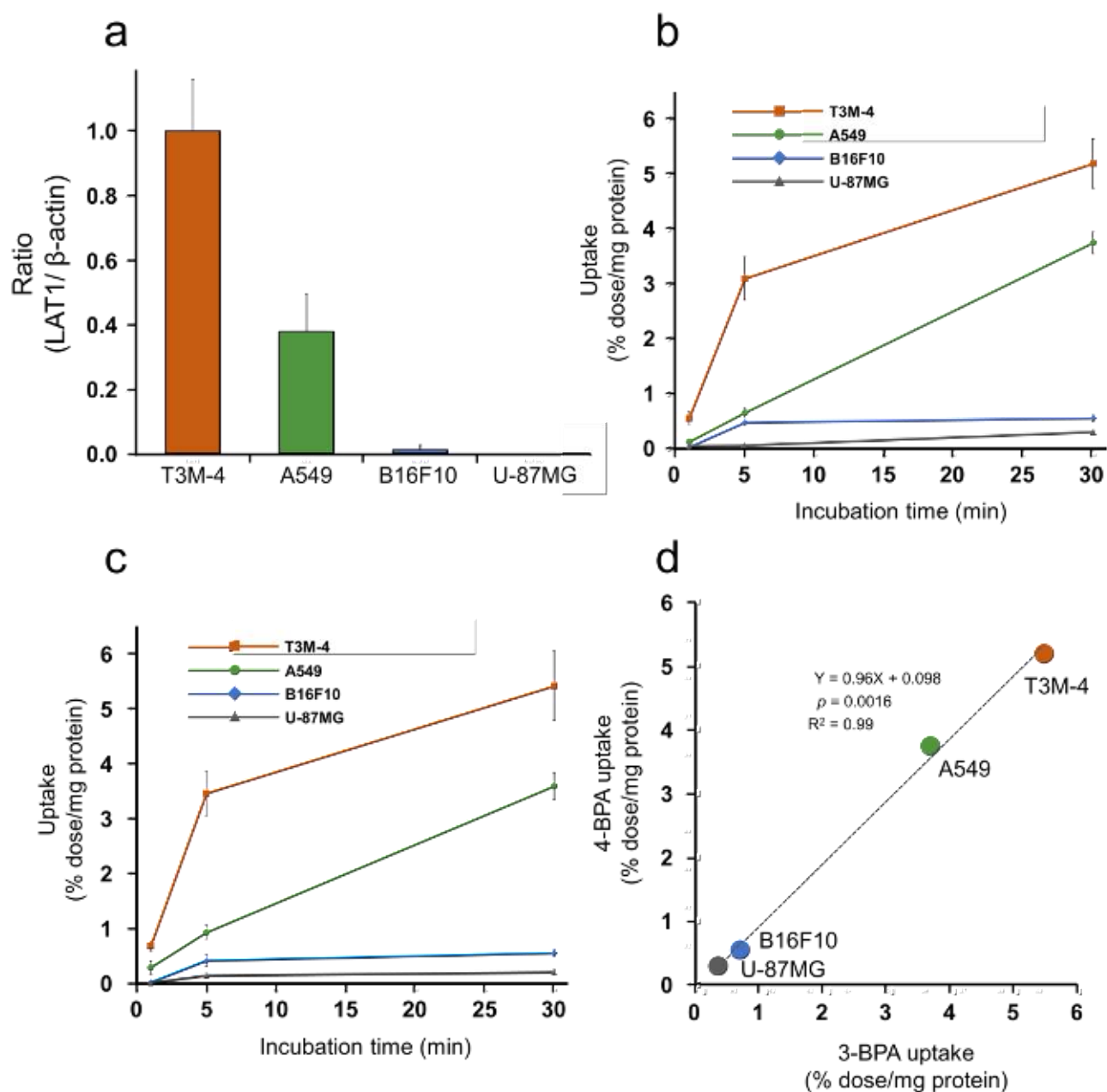
\*  $p < 0.0001$  vs. 4-BPA by unpaired *t*-test.  $t = 24.24$ ,  $df = 10$ . <sup>†</sup>  $p < 0.0001$  vs. 4-BPA by unpaired *t*-test.  $t = 15.41$ ,  $df = 22$ .

### 3.2. Cellular Uptake Study

Representative bands from Western blotting of T3M-4, A549, U-87MG, and B16F10 cells and the intensity ratio to the  $\beta$ -actin band are shown in Supplementary Figure S4 and Figure 2a, respectively. Representative images of cellular immunofluorescence staining are shown in Supplementary Figure S5. These results indicated that the LAT1 expression levels were decreased in each cell type in the following order: T3M-4, A549, B16F10, and U-87MG cells. Boron uptakes in each cell line after 3-BPA and 4-BPA additions are summarized in Supplementary Tables S1 and S2, showing significant inhibition of boron uptake by LAT1 inhibitor treatment in all cell groups. The LAT1-specific boron uptake calculated from the difference in accumulations between the inhibitor and noninhibitor groups is plotted with time in Figure 2b,c. LAT1-specific boron uptake after the addition of 3-BPA and 4-BPA was correlated with the expression level of LAT1 (Figure 2a), which was confirmed by statistical analysis (Supplementary Tables S3 and S4). Further, simple linear regression (Figure 2d) and Tukey's multiple comparison tests (Supplementary Table S5) showed substantial equivalence between the LAT1-specific boron uptakes of 3-BPA and 4-BPA in vitro.

### 3.3. Biodistribution Study

<sup>11</sup>B-NMR analysis of 3-BPA-Fru, 4-BPA-Fru, and 3-BPA showed chemical shifts of <sup>11</sup>B atoms in 9.9, 10.1, and 30.6 ppm, respectively (Supplementary Figures S6–S8). It indicated a change in electron density around <sup>11</sup>B atoms due to fructose complex formation in 3-BPA-Fru and 4-BPA-Fru solutions. Biodistributions after intravenous administration of 3-BPA-Fru and 4-BPA-Fru to B16F10 melanoma-bearing mice are summarized in Tables 2 and 3, and significant differences between 3-BPA-Fru and 4-BPA-Fru in boron accumulations are summarized in Supplementary Table S6. Both exhibited high accumulation in the pancreas, which is a high LAT1-expressing organ [34], whereas 3-BPA-Fru showed a significantly higher boron level in the kidneys than 4-BPA-Fru. The boron levels in the melanoma and plasma and the melanoma to plasma ratios were not significantly different between 3-BPA-Fru and 4-BPA-Fru groups over time (Figure 3).



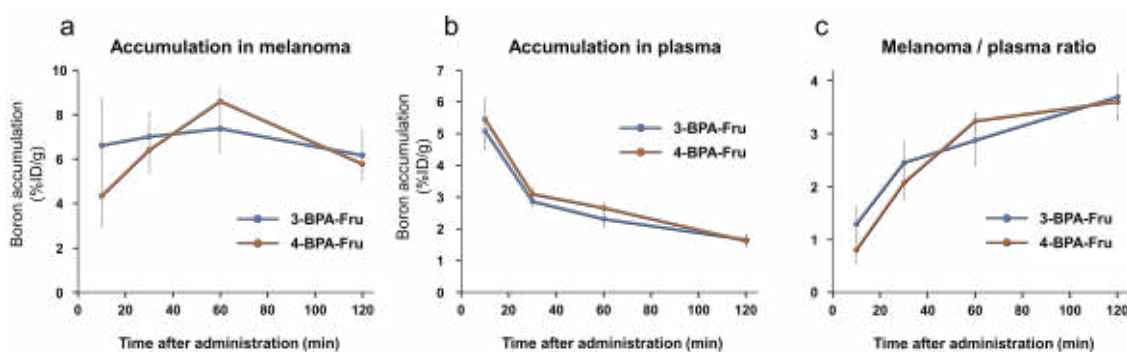
**Figure 2.** In vitro cell uptake of 3-BPA and 4-BPA in cancer cells with various LAT1-expression. (a) The LAT1/ $\beta$ -actin ratio of each cell calculated from the expression levels of LAT1 and  $\beta$ -actin obtained by Western blotting and standardized to a value of 1 for T3M-4. (b,c) LAT1-specific accumulation (the difference in accumulation between the inhibitor group and the noninhibitor group) in T3M-4, A549, B16F10, and U-87MG cells after 1, 5, and 30 min incubation with 3-BPA (b) and 4-BPA (c). (d) The relationship between the uptake (% dose/mg protein) of 3-BPA and 4-BPA at 30 min incubation with a simple linear regression. Statistical analyses of LAT1-specific accumulation of 3-BPA (b) and 4-BPA (c) were shown in Supplementary Tables S3 and S4, respectively.

**Table 2.** Biodistribution of boron concentration after administration of 3-BPA-Fru in melanoma-bearing mice (%ID/g, n = 19).

	Time after Administration (min)			
	10 (n = 4)	30 (n = 4)	60 (n = 7)	120 (n = 4)
Plasma	5.1 ± 0.6	2.9 ± 0.2	2.3 ± 0.3	1.7 ± 0.1
Liver	8.4 ± 0.6	4.6 ± 0.4	3.5 ± 0.9	2.6 ± 0.3
Kidneys	58.3 ± 11.3	53.6 ± 7.1	36.4 ± 8.4	23.0 ± 1.9
Pancreas	52.5 ± 4.9	50.2 ± 4.5	33.1 ± 8.5	34.4 ± 2.9
Brain	2.6 ± 0.3	3.0 ± 0.1	3.0 ± 0.9	3.4 ± 0.5
Skin	5.3 ± 0.4	4.2 ± 0.5	3.4 ± 0.5	2.7 ± 0.6
Muscle	4.5 ± 0.8	5.1 ± 0.3	4.6 ± 0.5	4.4 ± 0.5
B16F10 melanoma	6.6 ± 2.1	7.0 ± 1.1	7.4 ± 1.0	6.2 ± 1.1
Tumor/Plasma	1.3 ± 0.3	2.4 ± 0.4	2.9 ± 0.5	3.7 ± 0.4

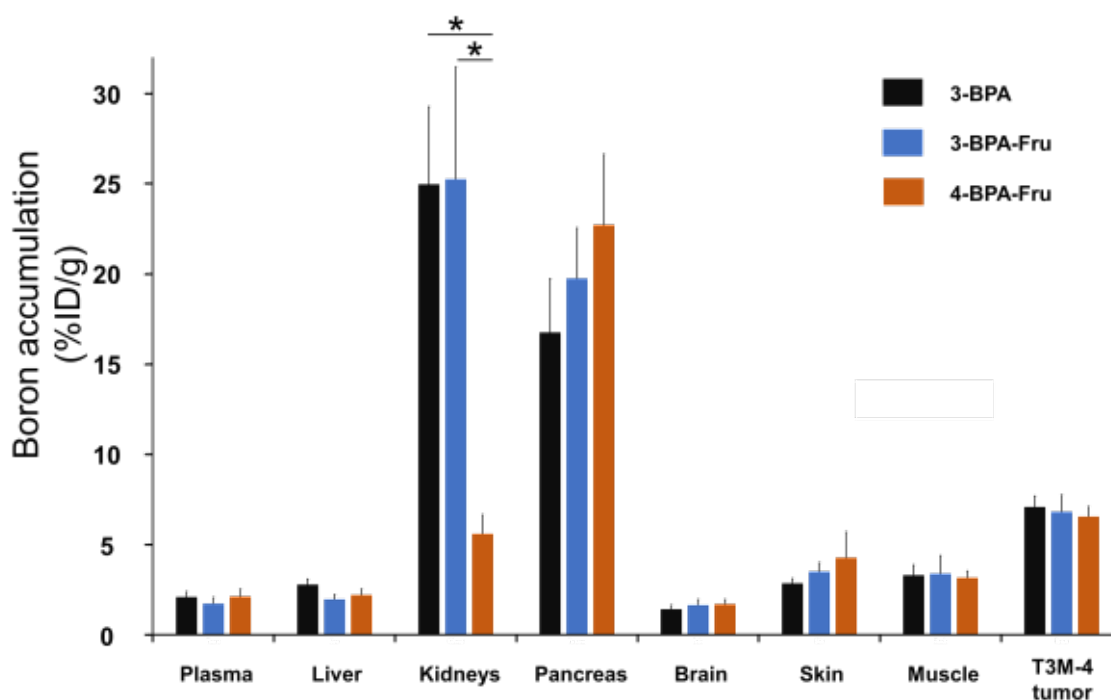
**Table 3.** Biodistribution of boron concentration after administration of 4-BPA-Fru in melanoma-bearing mice (%ID/g, n = 16).

	Time after Administration (min)			
	10 (n = 4)	30 (n = 4)	60 (n = 4)	120 (n = 4)
Plasma	5.5 ± 0.7	3.1 ± 0.2	2.7 ± 0.2	1.6 ± 0.2
Liver	7.4 ± 0.7	4.2 ± 0.2	2.9 ± 0.3	2.0 ± 0.1
Kidneys	16.9 ± 2.5	10.8 ± 1.6	8.4 ± 3.7	4.7 ± 0.6
Pancreas	44.1 ± 7.0	44.8 ± 5.7	33.9 ± 6.5	12.9 ± 1.4
Brain	1.3 ± 0.1	2.5 ± 0.2	3.0 ± 0.3	2.2 ± 0.2
Skin	5.2 ± 0.7	4.4 ± 0.5	5.0 ± 0.9	2.5 ± 0.3
Muscle	3.1 ± 0.7	4.2 ± 0.4	4.4 ± 0.3	2.8 ± 0.3
B16F10 melanoma	4.3 ± 1.4	6.4 ± 1.0	8.6 ± 0.6	5.8 ± 0.4
Tumor/Plasma	0.8 ± 0.3	2.1 ± 0.3	3.2 ± 0.1	3.6 ± 0.4

**Figure 3.** Boron accumulation in B16F10 melanoma (a) and plasma (b), and melanoma to plasma ratio of boron accumulation (c) of 3-BPA-Fru and 4-BPA-Fru at 10, 30, 60, and 120 min after administration.

Biodistributions 60 min after intravenous administration of 3-BPA-Fru, 4-BPA-Fru, and 3-BPA to LAT1-positive T3M-4-bearing mice are summarized in Figure 4 and Supplementary Table S7. Similar to the above results, there were no significant differences among groups in boron accumulation levels in the organs, except for the kidneys. Note that 3-BPA and 3-BPA-Fru showed similar boron levels in all evaluated organs, indicating no additive function of fructose on drug pharmacokinetics.





**Figure 4.** Boron accumulation in T3M-4 tumor, plasma, liver, kidneys, and the tissues surrounding the tumor at 60 min after administration of 3-BPA, 3-BPA-Fru, and 4-BPA-Fru into BALB/c nu-nu mice. \*  $p < 0.001$  by Tukey's multiple comparison tests.

#### 4. Discussion

As 4-BPA has a low water solubility that can cause side effects in patients with BNCT, this study aimed to develop an alternative boronoagent and re-evaluated 3-BPA compared with 4-BPA in water solubility and tumor targetability through LAT1. We found that 3-BPA is highly soluble in water, more than 100 times higher than 4-BPA. As 3-BPA and 4-BPA have similar acid dissociation constants (3-BPA:  $pK_{a1} = 2.26$ ,  $pK_{a2} = 8.46$ ,  $pK_{a3} = 9.95$ ; 4-BPA:  $pK_{a1} = 2.35$ ,  $pK_{a2} = 8.45$ ,  $pK_{a3} = 9.67$ ) [35], both would exist in similar charge states in the neutral solution. The  $\log p$  values and retention times in RP-HPLC suggest a slightly higher tendency of 3-BPA toward the organic layer than 4-BPA. Although this would appear contradictory to the solubility result, a relationship between tyrosine and phenylalanine is similar to this case. Tyrosine shows a lower  $\log p$  value but a lower water solubility than phenylalanine ( $\log p$  value,  $-2.26$  [36] vs.  $-1.38$  [36]; water solubility,  $0.47$  g/L [37] vs.  $12.0$  g/L [38]), indicating that the hydroxyl group present at the *para*-position of phenylalanine contributes to a decrease in water solubility. Similarly, 4-BPA shows a lower  $\log p$  value and water solubility than phenylalanine. In addition, to clarify the substituent position effect, we measured and compared the water solubility of DL-*meta*-tyrosine and DL-tyrosine (Supplementary Table S8). The results showed more than 25 times higher water solubility of DL-*meta*-tyrosine than DL-tyrosine, confirming that introducing a substituent at *meta*-position improves water solubility. The improved water solubility of 3-BPA may be attributed to the difference in thermodynamically stable conformations from 4-BPA, leading to increased intermolecular interactions with the surrounding water molecules and decreased  $\pi$ - $\pi$  interaction within boron agents, but further studies are required to understand the detailed mechanism.

In *in vitro* experiments, we initially used B16F10 cells as a positive control following past BNCT studies [28,39,40]. Surprisingly, we still found low LAT1 expression and boron accumulation after 3-BPA and 4-BPA addition compared with other LAT1-expressing cell groups. In the past, research was focused on melanoma, which was the primary target disease of BNCT at that time, and no further evaluation was conducted when slightly less accumulation of 3-BPA was observed in melanoma cells [27]. Nevertheless, in the present

experiments using high LAT1 expressing cells, we have succeeded in demonstrating a LAT1-dependent accumulation profile of 3-BPA statistically equivalent to that of 4-BPA, which supports our decision to re-evaluate.

In clinical BNCT, the boron accumulations in the tumor and surrounding normal tissues are both considered because neutron exposure to the surrounding tissues is inevitable during neutron irradiation and can have side effects [41,42]. This study evaluated the amount of boron accumulation in the brain, skin, and muscle as peripheral tissues in addition to the tumor. 3-BPA-Fru and 4-BPA-Fru showed equivalent biodistribution profiles in the tumor and peripheral tissues in conventional melanoma mice, suggesting similar effectiveness of 3-BPA-Fru as a boronoagent in BNCT. A significant boron accumulation observed in the kidneys after 3-BPA-Fru injection could come from a possible recognition difference in renal transporter systems, but it could not cause crystallization and hematuria due to the improved solubility. The mechanism of the accumulation difference in the kidneys remains unclear, and further studies are needed to determine the associated effects. Interestingly, *in vitro* and *in vivo* tumor boron accumulation after 3-BPA-Fru administration was perfectly similar to the level obtained by 4-BPA-Fru, unlike our prediction based on the previous reports showing the superiority of *meta*-substituted phenylalanine in LAT1 recognition [25,26]. Since these studies did not include boronic acid substitution [25,26], further research on the structure–activity relationship of compounds with boronic acid substitution using 3-BPA as a lead compound will contribute to BNCT agent development.

We evaluated the biodistribution of 3-BPA without fructose solubilization due to highly improved solubility. The boron concentration in the administration solution was more than 10 times higher than the solubility of 4-BPA. The biodistribution of 3-BPA was comparable to that of 3-BPA-Fru, indicating that there was no need for fructose addition in the preparation. In a tentative estimate, for a patient with 60 kg of body weight, 250 mL or less of 3-BPA solution is required without solubilizer addition, in contrast to the case of 4-BPA, which includes 31.5 g D-sorbitol in 1000 mL solution. Details of Borofalan marketization that fructose was changed to D-sorbitol due to unsuitability for long-term storage by the Maillard reaction [43], may support that 3-BPA prepared without solubilizer addition has advantages in terms of quality control. In the clinical settings, 4-BPA would cause crystalluria and hematuria because the solubility is lower than the possible urinary concentration level excreted from the body [44], but the solubility of 3-BPA is much higher than the estimated urinary concentration level, thus eliminating such related side effects. Next, 3-[<sup>10</sup>B]BPA synthesized by an optimized synthetic scheme needs to be assessed using the intravenous infusion method before its application in clinical settings. The tumor targetability of 3-BPA should also be evaluated at clinical doses in the future, with reference to the report that transporters other than LAT1 contribute to tumor uptake at clinical doses of 4-BPA [14]. As 4-BPA was initially developed to target melanoma [8,45], 4-BPA was designed according to the structure of tyrosine, the precursor of melanin. Since then, 4-BPA has been promoted for clinical use, and several agents based on the 4-BPA structure have been developed [46,47]. As the *meta*-substituent improved water solubility and sustained tumor targetability, 3-BPA can replace 4-BPA as the lead compound for future drug design of boronoagents.

In summary, although future verification for clinical use is needed, this study demonstrated that 3-BPA is highly water-soluble, enables solubilizer elimination unlike 4-BPA, and has a biodistribution property comparable to 4-BPA. Therefore, 3-BPA is a promising BNCT agent that surpasses the currently marketed 4-BPA.

**Supplementary Materials:** The following supporting information can be downloaded at: <https://www.mdpi.com/article/10.3390/pharmaceutics14051106/s1>, Figure S1: Synthetic scheme of 3-BPA, Figure S2: <sup>1</sup>H-NMR spectrum of 3-BPA, Figure S3: <sup>13</sup>C-NMR spectrum of 3-BPA, Figure S4: Representative western blot bands (LAT1 and β-actin) of cell lysate, Figure S5: Representative images of fluorescence immunostaining of LAT1 and nuclear staining in cells, Figure S6: <sup>11</sup>B-NMR spectrum of 3-BPA in PBS(-), Figure S7: <sup>11</sup>B-NMR spectrum of 3-BPA-Fru in PBS(-), Figure S8: <sup>11</sup>B-NMR spectrum of 4-BPA-Fru in PBS(-); Table S1: Boron uptake in cancer cells after incubation with 3-BPA,

Table S2: Boron uptake in cancer cells after incubation with 4-BPA, Table S3: Statistical analysis of specific uptake between each cell after addition of 3-BPA, Table S4: Statistical analysis of specific uptake between each cell after addition of 4-BPA, Table S5: Statistical analysis of specific uptake between 3-BPA and 4-BPA in each cell, Table S6: Significant difference between 3-BPA-Fru and 4-BPA-Fru in boron accumulation in each tissue after administration into melanoma-bearing mice, Table S7: Biodistribution of boron concentration at 60 min after injection of 3-BPA, 3-BPA-Fru, and 4-BPA-Fru in T3M-4 tumor-bearing mice, Table S8: Water solubility of phenylalanine, tyrosine, and meta-tyrosine; Supplementary Methods.

**Author Contributions:** Conceptualization, N.K. and T.T.; Methodology, N.K.; Validation, N.K. and F.H.; Formal Analysis, N.K. and T.T.; Investigation, N.K. and F.H.; Resources, N.K. and F.H.; Data Curation, N.K. and T.T.; Writing—Original Draft Preparation, N.K. and T.T.; Writing—Review and Editing, N.K., F.H. and T.T.; Visualization, N.K.; Supervision, T.T.; Project Administration, N.K. and T.T. All authors have read and agreed to the published version of the manuscript.

**Funding:** This research received no external funding.

**Institutional Review Board Statement:** Animal experiments were carried out according to the guidelines for animal experiments from the Osaka University of Pharmaceutical Sciences. The study protocol was approved by the Experimental Animal Committee at Osaka University of Pharmaceutical Sciences (Permission Number: 19-76, date of approval: 31 March 2019; and Permission Number: 20-76, date of approval: 31 March 2020).

**Informed Consent Statement:** Not applicable.

**Data Availability Statement:** The data supporting the results and findings of this study are available within the paper and the Supplementary Information files. Additional raw data are available from the corresponding author upon request.

**Acknowledgments:** The authors thank Katsuhiko Minoura for experimental support of NMR measurement, and Rio Tamae for experimental assistance of in vitro experiments.

**Conflicts of Interest:** The authors have no conflict of interest.

## References







1. Moss, R.L. Critical review, with an optimistic outlook, on boron neutron capture therapy (BNCT). *Appl. Radiat. Isot.* **2014**, *88*, 2–11. [CrossRef]
2. Nedunchezian, K.; Aswath, N.; Thiruppathy, M.; Thirugnanamurthy, S. Boron neutron capture therapy—A literature review. *J. Clin. Diagn. Res.* **2016**, *10*, ZE01–ZE04. [CrossRef]
3. Barth, R.F.; Coderre, J.A.; Vicente, M.G.; Blue, T.E. Boron neutron capture therapy of cancer: Current status and future prospects. *Clin. Cancer Res.* **2005**, *11*, 3987–4002. [CrossRef]
4. Vos, M.J.; Turowski, B.; Zanella, F.E.; Paquis, P.; Siefert, A.; Hideghety, K.; Haselsberger, K.; Grochulla, F.; Postma, T.J.; Wittig, A.; et al. Radiologic findings in patients treated with boron neutron capture therapy for glioblastoma multiforme within EORTC trial 11961. *Int. J. Radiat. Oncol. Biol. Phys.* **2005**, *61*, 392–399. [CrossRef]
5. Skold, K.; Gorlia, T.; Pellettieri, L.; Giusti, V.; H-Stenstam, B.; Hopewell, J.W. Boron neutron capture therapy for newly diagnosed glioblastoma multiforme: An assessment of clinical potential. *Br. J. Radiol.* **2010**, *83*, 596–603. [CrossRef]
6. Barth, R.F.; Mi, P.; Yang, W. Boron delivery agents for neutron capture therapy of cancer. *Cancer Commun.* **2018**, *38*, 35. [CrossRef]
7. Snyder, H.R.; Reedy, A.J.; Lennarz, W.J. Synthesis of aromatic boronic acids. aldehydo boronic acids and a boronic acid analog of tyrosine1. *J. Am. Chem. Soc.* **2002**, *80*, 835–838. [CrossRef]
8. Mishima, Y.; Ichihashi, M.; Hatta, S.; Honda, C.; Yamamura, K.; Nakagawa, T. New thermal neutron capture therapy for malignant melanoma: Melanogenesis-seeking  $^{10}\text{B}$  molecule-melanoma cell interaction from in vitro to first clinical trial. *Pigment Cell Res.* **1989**, *2*, 226–234. [CrossRef]
9. Elowitz, E.H.; Bergland, R.M.; Coderre, J.A.; Joel, D.D.; Chadha, M.; Chanana, A.D. Biodistribution of p-boronophenylalanine in patients with glioblastoma multiforme for use in boron neutron capture therapy. *Neurosurgery* **1998**, *42*, 463–468, discussion 468–469. [CrossRef]
10. Chanana, A.D.; Capala, J.; Chadha, M.; Coderre, J.A.; Diaz, A.Z.; Elowitz, E.H.; Iwai, J.; Joel, D.D.; Liu, H.B.; Ma, R.; et al. Boron neutron capture therapy for glioblastoma multiforme: Interim results from the phase I/II dose-escalation studies. *Neurosurgery* **1999**, *44*, 1182–1192, discussion 1192–1183. [CrossRef]
11. Kato, I.; Ono, K.; Sakurai, Y.; Ohmae, M.; Maruhashi, A.; Imahori, Y.; Kirihata, M.; Nakazawa, M.; Yura, Y. Effectiveness of BNCT for recurrent head and neck malignancies. *Appl. Radiat. Isot.* **2004**, *61*, 1069–1073. [CrossRef] [PubMed]

12. Kanno, H.; Nagata, H.; Ishiguro, A.; Tsuzuranuki, S.; Nakano, S.; Nonaka, T.; Kiyohara, K.; Kimura, T.; Sugawara, A.; Okazaki, Y.; et al. Designation products: Boron neutron capture therapy for head and neck carcinoma. *Oncologist* **2021**, *26*, e1250–e1255. [CrossRef] [PubMed]
13. Detta, A.; Cruickshank, G.S. L-amino acid transporter-1 and boronophenylalanine-based boron neutron capture therapy of human brain tumors. *Cancer Res.* **2009**, *69*, 2126–2132. [CrossRef] [PubMed]
14. Wongthai, P.; Hagiwara, K.; Miyoshi, Y.; Wiriyasermkul, P.; Wei, L.; Ohgaki, R.; Kato, I.; Hamase, K.; Nagamori, S.; Kanai, Y. Boronophenylalanine, a boron delivery agent for boron neutron capture therapy, is transported by ATB0+, LAT1 and LAT2. *Cancer Sci.* **2015**, *106*, 279–286. [CrossRef] [PubMed]
15. Ishiwata, K. 4-Borono-2-<sup>18</sup>F-fluoro-L-phenylalanine PET for boron neutron capture therapy-oriented diagnosis: Overview of a quarter century of research. *Ann. Nucl. Med.* **2019**, *33*, 223–236. [CrossRef] [PubMed]
16. Kanai, Y. Amino acid transporter LAT1 (SLC7A5) as a molecular target for cancer diagnosis and therapeutics. *Pharmacol. Ther.* **2022**, *230*, 107964. [CrossRef]
17. Soloway, A.H.; Tjarks, W.; Barnum, B.A.; Rong, F.G.; Barth, R.F.; Codogni, I.M.; Wilson, J.G. The chemistry of neutron capture therapy. *Chem. Rev.* **1998**, *98*, 1515–1562. [CrossRef]
18. Mori, Y.; Suzuki, A.; Yoshino, K.; Kakihana, H. Complex formation of p-boronophenylalanine with some monosaccharides. *Pigment. Cell Res.* **1989**, *2*, 273–277. [CrossRef]
19. Wada, Y.; Hirose, K.; Harada, T.; Sato, M.; Watanabe, T.; Anbai, A.; Hashimoto, M.; Takai, Y. Impact of oxygen status on <sup>10</sup>B-BPA uptake into human glioblastoma cells, referring to significance in boron neutron capture therapy. *J. Radiat. Res.* **2018**, *59*, 122–128. [CrossRef]
20. Laakso, J.; Ruokonen, I.; Lapatto, R.; Kallio, M. Inborn errors in metabolism and 4-boronophenylalanine-fructose-based boron neutron capture therapy. *Radiat. Res.* **2003**, *160*, 606–609. [CrossRef]
21. Henriksson, R.; Capala, J.; Michanek, A.; Lindahl, S.A.; Salford, L.G.; Franzen, L.; Blomquist, E.; Westlin, J.E.; Bergenheim, A.T.; Swedish Brain Tumour Study Group. Boron neutron capture therapy (BNCT) for glioblastoma multiforme: A phase II study evaluating a prolonged high-dose of boronophenylalanine (BPA). *Radiother. Oncol.* **2008**, *88*, 183–191. [CrossRef] [PubMed]
22. Morimoto, J.; Miyamoto, K.; Ichikawa, Y.; Uchiyama, M.; Makishima, M.; Hashimoto, Y.; Ishikawa, M. Improvement in aqueous solubility of achiral symmetric cyclofenil by modification to a chiral asymmetric analog. *Sci. Rep.* **2021**, *11*, 12697. [CrossRef] [PubMed]
23. Hiramatsu, M.; Ichikawa, Y.; Tomoshige, S.; Makishima, M.; Muranaka, A.; Uchiyama, M.; Yamaguchi, T.; Hashimoto, Y.; Ishikawa, M. Improvement in aqueous solubility of retinoic acid receptor (RAR) agonists by bending the molecular structure. *Chem. Asian J.* **2016**, *11*, 2210–2217. [CrossRef] [PubMed]
24. Ichikawa, Y.; Hiramatsu, M.; Mita, Y.; Makishima, M.; Matsumoto, Y.; Masumoto, Y.; Muranaka, A.; Uchiyama, M.; Hashimoto, Y.; Ishikawa, M. Meta-non-flat substituents: A novel molecular design to improve aqueous solubility in small molecule drug discovery. *Org. Biomol. Chem.* **2021**, *19*, 446–456. [CrossRef] [PubMed]
25. Chien, H.C.; Colas, C.; Finke, K.; Springer, S.; Stoner, L.; Zur, A.A.; Venteicher, B.; Campbell, J.; Hall, C.; Flint, A.; et al. Reevaluating the substrate specificity of the L-type amino acid transporter (LAT1). *J. Med. Chem.* **2018**, *61*, 7358–7373. [CrossRef]
26. Singh, N.; Ecker, G.F. Insights into the structure, function, and ligand discovery of the large neutral amino acid transporter 1, LAT1. *Int. J. Mol. Sci.* **2018**, *19*, 1278. [CrossRef]
27. Hiratsuka, J.; Yoshino, K.; Kondoh, H.; Imajo, Y.; Mishima, Y. Biodistribution of boron concentration on melanoma-bearing hamsters after administration of p-, m-, o-boronophenylalanine. *Jpn. J. Cancer Res.* **2000**, *91*, 446–450. [CrossRef]
28. Hiratsuka, J.; Kondoh, H.; Tsuboi, T.; Yoshino, K.; Imajo, Y.; Mishima, Y. Selective uptake of para-boronophenylalanine increases in amelanotic melanoma cells transfected by the tyrosinase gene. *Melanoma Res.* **2000**, *10*, 297–302. [CrossRef]
29. Ahn, S.-J.; Lee, C.-Y.; Cheon, C.-H. General methods for synthesis of N-methyliminodiacetic acid boronates from unstable ortho-phenolboronic acids. *Adv. Synth. Catal.* **2014**, *356*, 1767–1772. [CrossRef]
30. Craig, W.; Chen, J.; Richardson, D.; Thorpe, R.; Yuan, Y. A Highly stereoselective and scalable synthesis of L-allo-enduracididine. *Org. Lett.* **2015**, *17*, 4620–4623. [CrossRef]
31. Colgin, N.; Flinn, T.; Cobb, S.L. Synthesis and properties of MIDA boronate containing aromatic amino acids: New peptide building blocks. *Org. Biomol. Chem.* **2011**, *9*, 1864. [CrossRef] [PubMed]
32. Okunushi, K.; Furihata, T.; Morio, H.; Muto, Y.; Higuchi, K.; Kaneko, M.; Otsuka, Y.; Ohno, Y.; Watanabe, Y.; Reien, Y.; et al. JPH203, a newly developed anti-cancer drug, shows a preincubation inhibitory effect on L-type amino acid transporter 1 function. *J. Pharmacol. Sci.* **2020**, *144*, 16–22. [CrossRef] [PubMed]
33. Hafliger, P.; Graff, J.; Rubin, M.; Stooss, A.; Dettmer, M.S.; Altmann, K.H.; Gertsch, J.; Charles, R.P. The LAT1 inhibitor JPH203 reduces growth of thyroid carcinoma in a fully immunocompetent mouse model. *J. Exp. Clin. Cancer Res.* **2018**, *37*, 234. [CrossRef] [PubMed]
34. Kobayashi, N.; Okazaki, S.; Sampetean, O.; Irie, J.; Itoh, H.; Saya, H. CD44 variant inhibits insulin secretion in pancreatic beta cells by attenuating LAT1-mediated amino acid uptake. *Sci. Rep.* **2018**, *8*, 2785. [CrossRef] [PubMed]
35. Yoshino, K.; Watanabe, N.; Takahashi, H.; Watanabe, S.; Ichihashi, M.; Kakihana, H.; Mishima, Y. Chemical properties of p-, m-, o-boronophenylalanine. In *Cancer Neutron Capture Therapy*; Springer: Boston, MA, USA, 1996; pp. 91–97. [CrossRef]

36. Nie, W.; Cai, K.Z.; Li, Y.Z.; Zhang, S.; Wang, Y.; Guo, J.; Chen, C.G.; Xu, B.C. Small molecular weight aldose (d-Glucose) and basic amino acids (L-Lysine, L-Arginine) Increase the occurrence of PAHs in grilled pork sausages. *Molecules* **2018**, *23*, 3377. [CrossRef] [PubMed]
37. Hitchcock, D.I. The solubility of tyrosine in acid and in alkali. *J. Gen. Physiol.* **1924**, *6*, 747–757. [CrossRef] [PubMed]
38. Hossain, A.; Roy, S.; Ghosh, S.; Mondal, S.; Dolui, B.K. Solubility of dl-serine and dl-phenylalanine in aqueous mixtures of dimethyl sulfoxide and solvation thermodynamics. *RSC Adv.* **2015**, *5*, 69839–69847. [CrossRef]
39. Tsuboi, T.; Kondoh, H.; Hiratsuka, J.; Mishima, Y. Enhanced melanogenesis induced by tyrosinase gene-transfer increases boron-uptake and killing effect of boron neutron capture therapy for amelanotic melanoma. *Pigment Cell Res.* **1998**, *11*, 275–282. [CrossRef]
40. Kubota, R.; Yamada, S.; Ishiwata, K.; Tada, M.; Ido, T.; Kubota, K. Cellular accumulation of <sup>18</sup>F-labelled boronophenylalanine depending on DNA synthesis and melanin incorporation: A double-tracer microautoradiographic study of B16 melanomas in vivo. *Br. J. Cancer* **1993**, *67*, 701–705. [CrossRef]
41. Aihara, T.; Morita, N.; Kamitani, N.; Kumada, H.; Ono, K.; Hiratsuka, J.; Harada, T. Boron neutron capture therapy for advanced salivary gland carcinoma in head and neck. *Int. J. Clin. Oncol.* **2014**, *19*, 437–444. [CrossRef]
42. Watabe, T.; Hanaoka, K.; Naka, S.; Kanai, Y.; Ikeda, H.; Aoki, M.; Shimosegawa, E.; Kirihata, M.; Hatazawa, J. Practical calculation method to estimate the absolute boron concentration in tissues using <sup>18</sup>F-FBPA PET. *Ann. Nucl. Med.* **2017**, *31*, 481–485. [CrossRef] [PubMed]
43. Heikkinen, S.; Savolainen, S.; Melkko, P. In vitro studies on stability of L-p-boronophenylalanine-fructose complex (BPA-F). *J. Radiat. Res.* **2011**, *52*, 360–364. [CrossRef] [PubMed]
44. Svantesson, E.; Capala, J.; Markides, K.E.; Pettersson, J. Determination of boron-containing compounds in urine and blood plasma from boron neutron capture therapy patients. The importance of using coupled techniques. *Anal. Chem.* **2002**, *74*, 5358–5363. [CrossRef] [PubMed]
45. Ichihashi, M.; Nakanishi, T.; Mishima, Y. Specific killing effect of <sup>10</sup>B1-para-boronophenylalanine in thermal neutron capture therapy of malignant melanoma: In vitro radiobiological evaluation. *J. Investig. Dermatol.* **1982**, *78*, 215–218. [CrossRef] [PubMed]
46. Nomoto, T.; Inoue, Y.; Yao, Y.; Suzuki, M.; Kanamori, K.; Takemoto, H.; Matsui, M.; Tomoda, K.; Nishiyama, N. Poly(vinyl alcohol) boosting therapeutic potential of p-boronophenylalanine in neutron capture therapy by modulating metabolism. *Sci. Adv.* **2020**, *6*, eaaz1722. [CrossRef] [PubMed]
47. Li, J.; Shi, Y.; Zhang, Z.; Liu, H.; Lang, L.; Liu, T.; Chen, X.; Liu, Z. A metabolically stable boron-derived tyrosine serves as a theranostic agent for positron emission tomography guided boron neutron capture therapy. *Bioconjug. Chem.* **2019**, *30*, 2870–2878. [CrossRef] [PubMed]

## Article

# Tuning the Cytotoxicity of Bis-Phosphino-Amines Ruthenium(II) Para-Cymene Complexes for Clinical Development in Breast Cancer

Elena Domínguez-Jurado <sup>1,2,†</sup>, Francisco J. Cimas <sup>3,†</sup>, José Antonio Castro-Osma <sup>1,2</sup> , Alberto Juan <sup>1,2</sup> , Agustín Lara-Sánchez <sup>4</sup> , Antonio Rodríguez-Diéguez <sup>5</sup> , Alexandr Shafir <sup>6</sup>, Alberto Ocaña <sup>7,\*</sup>  and Carlos Alonso-Moreno <sup>1,2,\*</sup> 

- <sup>1</sup> Centro Regional de Investigaciones Biomédicas, Unidad NanoCRIB, 02008 Albacete, Spain; elena.dominguez@uclm.es (E.D.-J.); joseantonio.castro@uclm.es (J.A.C.-O.); alberto.juan@uclm.es (A.J.)
- <sup>2</sup> Facultad de Farmacia de Albacete, Universidad de Castilla-La Mancha, 02008 Albacete, Spain
- <sup>3</sup> Oncología Traslacional, Unidad de Investigación del Complejo Hospitalario Universitario de Albacete, 02008 Albacete, Spain; franciscojose.cimas@uclm.es
- <sup>4</sup> Facultad de Ciencias y Tecnologías Químicas, Universidad de Castilla-La Mancha, 13005 Ciudad Real, Spain; Agustin.Lara@uclm.es
- <sup>5</sup> Departamento de Química Inorgánica, Facultad de Ciencias, Universidad de Granada, Avda de Fuentenueva s/n, 18071 Granada, Spain; antonio5@ugr.es
- <sup>6</sup> Department of Biological Chemistry, Institute of Advanced Chemistry of Catalonia, IQAC-CSIC, c/Jordi Girona 18-26, 08034 Barcelona, Spain; ashafir@icq.es
- <sup>7</sup> Experimental Therapeutics Unit, Hospital Clínico San Carlos, IdISSC and CIBERONC, 28040 Madrid, Spain
- \* Correspondence: alberto.ocana@salud.madrid.org (A.O.); Carlos.amoreno@uclm.es (C.A.-M.); Tel.: +34-6356-81806 (A.O.); +34-9675-99200 (C.A.-M.)
- † These authors contributed equally to this work.

**Citation:** Domínguez-Jurado, E.; Cimas, F.J.; Castro-Osma, J.A.; Juan, A.; Lara-Sánchez, A.; Rodríguez-Diéguez, A.; Shafir, A.; Ocaña, A.; Alonso-Moreno, C. Tuning the Cytotoxicity of Bis-Phosphino-Amines Ruthenium(II) Para-Cymene Complexes for Clinical Development in Breast Cancer. *Pharmaceutics* **2021**, *13*, 1559. <https://doi.org/10.3390/pharmaceutics13101559>

Academic Editor: Tomáš Etrych

Received: 14 July 2021

Accepted: 22 September 2021

Published: 26 September 2021

**Publisher's Note:** MDPI stays neutral with regard to jurisdictional claims in published maps and institutional affiliations.



**Copyright:** © 2021 by the authors. Licensee MDPI, Basel, Switzerland. This article is an open access article distributed under the terms and conditions of the Creative Commons Attribution (CC BY) license (<https://creativecommons.org/licenses/by/4.0/>).

**Abstract:** Despite some limitations such as long-term side effects or the potential presence of intrinsic or acquired resistance, platinum compounds are key therapeutic components for the treatment of several solid tumors. To overcome these limitations, maintaining the same efficacy, organometallic ruthenium(II) compounds have been proposed as a viable alternative to platinum agents as they have a more favorable toxicity profile and represent an ideal template for both, high-throughput and rational drug design. To support the preclinical development of bis-phosphino-amine ruthenium compounds in the treatment of breast cancer, we carried out chemical modifications in the structure of these derivatives with the aim of designing less toxic and more efficient therapeutic agents. We report new bis-phosphino-amine ligands and the synthesis of their ruthenium counterparts. The novel ligands and compounds were fully characterized, water stability analyzed, and their in vitro cytotoxicity against a panel of tumor cell lines representative of different breast cancer subtypes was evaluated. The mechanism of action of the lead compound of the series was explored. In vivo toxicity was also assessed. The results obtained in this article might pave the way for the clinical development of these compounds in breast cancer therapy.

**Keywords:** breast cancer; metallodrugs; RAPTA derivatives; phosphino-amine ligands

## 1. Introduction

Cancer is one of the most devastating diseases in the world and particularly breast cancer is a leading cause of death in women [1]. Classical treatments for this disease include chemotherapy, hormonotherapy, and targeted agents such as anti-HER2 treatments [1]. However, it is a global concern that many patients harbor an inherent resistance to these drugs, and even for those that respond, progression after a specific period of time becomes frequent [2,3].

Breast cancer can be divided into three different subtypes based on their genomic/transcriptomic profile, the HER2 enriched, the basal-like, and the luminal breast [4,5]. The

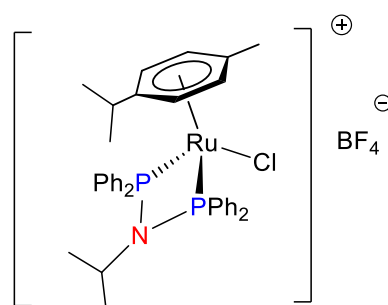
triple-negative breast cancer subtype mimics the basal-like subgroup and is termed in that way due to the lack of HER2 and estrogen receptor expression, representing 15% of breast tumors. It also harbors a more aggressive behavior along with a limited number of efficient therapeutic options [5]. In this regard, the identification of novel targets with potential for druggability, the optimization of those that are currently in clinical use, or the development of new compounds with higher efficacy and a safer toxicity profile, is the main objective.

Platinum-based therapies including carboplatin and cisplatin have been the standard treatment of care as a chemotherapy backbone, in many solid tumors, such as in triple-negative and HER2 positive breast cancer [6–8]. Platinum agents are highly cytotoxic and unspecific, therefore, they can produce severe undesired side effects [9]. In addition, some tumors express an inherent resistance to these agents and others acquired secondary resistance after being exposed to these agents for a period of time [2]. In this context, other metallic compounds with better biological and pharmacological properties are needed. Rutheniums have emerged as a novel and promising anticancer family of agents [10,11]. Ruthenium-based therapy might overcome platinum resistance, and improve the narrow therapeutic window of ‘the platinum family of agents’ [12,13]. In addition, ruthenium compounds have been shown to mediate their biological effect through a combination of anti-proliferative activity, anti-angiogenic action, and an anti-metastatic property which can clearly improve the action of current platinum derivatives [14–16].

To date, there have been several ruthenium compounds in clinical trials [17]. NAMI-A was the first ruthenium agent that eventually reached the clinical stage giving rise to high expectations for this new class of metal-based anticancer drugs [15,18]. KP1019 and its sodium salt KP1339 were the following compounds to be evaluated [19]. NAMI-A and KP compounds were tested in animal models demonstrating activity. Phase II combination studies of NAMI-A along with gemcitabine against lung cancer reported moderate clinical activity limiting their further evaluation [20]. Phase I clinical investigation of KP1019 for patients with advanced solid tumors showed a moderate antitumor activity [21]. The ruthenium compound TLD1433 completed phase I clinical trials for intravesical photodynamic therapy in patients with a non-muscle invasive bladder tumor and is currently recruiting patients in a phase II study [22,23].

Organometallic ruthenium compounds such as RAPTA-C [24] and RM175 [25,26] are in advanced preclinical studies. In this regard, a very high number of new organometallic ruthenium agents have been reported as potential candidates for clinical translation. Many examples of the screening of mono-, di-, and poly-nuclear ruthenium compounds with biologically inactive and active auxiliary ligands to give chiral and achiral complexes have been reported by advanced biological methods to understand their mechanism of action [27–34]. In this context, successful ruthenium complexes have been reported for the treatment of breast cancer [35]. In this regard, we proposed bis-phosphino-amines as versatile auxiliary ligands for a direct and simple generation of RAPTA-C derivatives [36]. The cytotoxicity of the novel ruthenium compounds was studied in a panel of tumoral cells to exploit them as a promising family of therapeutic agents. In addition, the lead compound of the series was selected for further evaluation (Figure 1). In a second study, we focused our efforts on understanding its mode of action, pharmacokinetic and biodistribution parameters and proposed plausible targets to improve subsequent designs [37].

Herein, a new family of ligands was synthesized and characterized to generate their ruthenium counterparts. The novel ruthenium agents were evaluated against a panel of breast tumoral cells representative of the three described breast cancer subtypes and were also compared to platinum agents. From this work, a new lead complex was obtained, and its mechanism of action was studied in depth. Finally, *in vivo* toxicity of the lead compound and its versatility against other tumor cells overexpressing HER2+ was performed.



**Figure 1.** Chemical structure of the lead bis-phosphino-amine compound for breast cancer therapy.

## 2. Materials and Methods

### 2.1. General Procedure

Synthesis reactions were performed using standard Schlenk and glove-box techniques under an atmosphere of dry nitrogen.  $\text{CH}_2\text{Cl}_2$  and hexane were pre-dried over  $\text{CaCl}_2$  and sodium wire, respectively, and distilled under nitrogen from sodium-potassium alloy (hexane), and  $\text{CaCl}_2$  ( $\text{CH}_2\text{Cl}_2$ ).  $\text{CDCl}_3$ ,  $\text{DMSO-d}_6$ , and  $\text{D}_2\text{O}$  were stored over activated 4 Å molecular sieves and degassed by several freeze-thaw cycles. All NMR experiments were conducted in deuterated solvents at 297 K in a Varian FT-400 spectrometer (VARIAN Inc., Palo Alto, California, USA) equipped with a 4 nucleus ASW PFG  $^1\text{H}/^{19}\text{F}/^{13}\text{C}/\{^{15}\text{N}-^{31}\text{P}\}$ . The  $^1\text{H}$   $\pi/2$  pulse length was adjusted for each sample.  $^1\text{H}$ - and  $^{13}\text{C}\{^1\text{H}\}$ -NMR chemical shifts ( $\delta$ ) are given in ppm relative to TMS.  $^{31}\text{P}\{^1\text{H}\}$ -NMR chemical shifts are given in ppm relative to  $\text{H}_3\text{PO}_4$  (85%). Coupling constants ( $J$ ) are documented in Hz. The solvent signals were used as references and chemical shifts converted to the TMS scale. IR experiments were conducted on an FT/IR-4000 Series Jasco Instruments (Jasco Analytics, Madrid, Spain). The UV-Vis absorption spectra were recorded at room temperature using a Cary 100 spectrophotometer (Agilent, Madrid, Spain) using a slit width of 0.4 nm and a scan rate of 600 nm/min. Elemental Analysis was performed at the Unidad de Análisis Químico Elemental, University Complutense, Madrid (Spain) using an Elementary Chemical Analyzer LECO CHNS-932. Mass spectroscopy was performed at the Unidad de Espectrometría de Masas, University Complutense, Madrid (Spain) using a MAXXIS II Bruker spectrometer.

### 2.2. Synthesis and Characterization of Ligands L1–L10

To a solution of chlorodiphenylphosphine (0.54 mL, 2.92 mmol) in toluene (15 mL) at 0 °C were added dropwise triethylamine (0.45 mL, 3.22 mmol) and the corresponding amine (1.45 mmol). After a 30 min stirring time, the ice bath was removed, and the stirring continued. Monitoring by NMR showed all starting materials to have been consumed within 5 h; at this point, the solution was filtered to remove the  $\text{Et}_3\text{NHCl}$  formed. On removing all volatiles under reduced pressure, the resultant white solid was repeatedly washed with degassed MeCN until no  $\text{Ph}_2\text{PP}(\text{O})\text{Ph}_2$  impurity could be detected by  $^{31}\text{P}\{^1\text{H}\}$ -NMR.

*N-tert-butyl-N-(diphenylphosphanyl)-1,1-diphenylphosphanamine (L1)*: After extracting in toluene, L1 was recovered as a white solid with a yield of 86%.  $^1\text{H}$  NMR (400 MHz,  $\text{CDCl}_3$ )  $\delta$  7.88–7.17 (m, 20 H, Ar), 1.43 (s,  $J = 7.9$  Hz, 9 H,  $\text{CH}_3$ ).  $^{13}\text{C}\{^1\text{H}\}$ -NMR (101 MHz,  $\text{CDCl}_3$ )  $\delta$  140.74 (4 C, Ar quaternary ( $\text{PPh}_2$ )), 132.81 (8 C, *o*-Ar CH ( $\text{PPh}_2$ )), 128.23 (8 C, *m*-Ar CH ( $\text{PPh}_2$ )), 127.91 (4 C, *p*-Ar CH ( $\text{PPh}_2$ )), 63.8 (1 C,  $\text{C}-(\text{CH}_3)_3$ ), 32.75 (3 C,  $\text{CH}_3$ ).  $^{31}\text{P}$  NMR (162 MHz,  $\text{CDCl}_3$ )  $\delta$  21.39. UV-vis: maximum absorbance at 288 nm. IR:  $2961\text{ cm}^{-1}$  ( $\text{C}-\text{H}$   $\text{sp}^3$  stretching),  $1476\text{--}1431\text{ cm}^{-1}$  (two bands  $\text{C}=\text{C}$  aromatic stretching),  $1174\text{ cm}^{-1}$  ( $\text{C}-\text{N}$  stretching),  $1087\text{ cm}^{-1}$  ( $\text{C}-\text{P}$  stretching). Elemental analysis calcd (%) for  $\text{C}_{28}\text{H}_{29}\text{NP}_2$ : C, 76.17; H, 6.62; N, 3.17; P, 14.03; found: C, 76.12; H, 6.52; N, 3.31.

*N-(diphenylphosphanyl)-1,1-diphenyl-N-propylphosphanamine (L2)*: After extracting in toluene, L3 was recovered as a white solid with a yield of 84%.  $^1\text{H}$  NMR (400 MHz,  $\text{CDCl}_3$ )  $\delta$  7.40–7.33 (m, 8H, *o*-Ar), 7.30–7.24 (m, 12H, *m*- and *p*-Ar), 3.20–3.09 (m, 2H,  $-\text{CH}_2-\text{CH}_2-\text{CH}_3$ ), 1.11–0.95 (m, 2H,  $-\text{CH}_2-\text{CH}_2-\text{CH}_3$ ), 0.45 (t,  $J = 7.3$  Hz, 3H,  $-\text{CH}_2-\text{CH}_2-\text{CH}_3$ ).  $^{13}\text{C}\{^1\text{H}\}$ -NMR



(101 MHz,  $\text{CDCl}_3$ )  $\delta$  139.66 (4 C, Ar quaternary ( $\text{PPh}_2$ )), 132.65 (8 C, *o*-Ar CH ( $\text{PPh}_2$ )), 128.65 (6 C, *m*- and *p*-Ar CH ( $\text{PPh}_2$ )), 127.95 (6 C, *m*- and *p*-Ar CH ( $\text{PPh}_2$ )), 54.65 (2 C,  $-\text{CH}_2-\text{CH}_2-\text{CH}_3$ ), 24.60 (2 C,  $-\text{CH}_2-\text{CH}_2-\text{CH}_3$ ), 10.94 (3 C,  $-\text{CH}_2-\text{CH}_2-\text{CH}_3$ ). UV-vis: maximum absorbance at 284 nm. IR:  $2957\text{ cm}^{-1}$  (C-H  $\text{sp}^3$  stretching),  $1478\text{--}1433\text{ cm}^{-1}$  (two bands C=C aromatic stretching),  $1090\text{ cm}^{-1}$  (C-P stretching),  $1057\text{ cm}^{-1}$  (C-N stretching). Elemental analysis calcd (%) for  $\text{C}_{27}\text{H}_{27}\text{NP}_2$ : C, 75.86; H, 6.37; N, 3.28; found: C, 75.69; H, 6.52; N, 3.39.

*N*-cyclohexyl-*N*-(diphenylphosphanyl)-1,1-diphenylphosphanamine (L3): After extracting in toluene, L3 was recovered as a white solid with a yield of 82%.  $^1\text{H}$  NMR (400 MHz,  $\text{CDCl}_3$ )  $\delta$  7.24 (m, 20H, Ar), 3.29–3.11 (m, 1H, cyclohexyl CH), 1.93–1.74 (m, 2H, cyclohexyl  $\text{CH}_2$ ), 1.64–1.30 (m, 4H, cyclohexyl  $\text{CH}_2$ ), 1.12–0.89 (m, 4H, cyclohexyl  $\text{CH}_2$ ).  $^{13}\text{C}\{^1\text{H}\}$ -NMR (101 MHz,  $\text{CDCl}_3$ )  $\delta$  140.00 (4C, Ar quaternary ( $\text{PPh}_2$ )), 132.64 (8C, *o*-Ar CH ( $\text{PPh}_2$ )), 128.48 (8C, *m*-Ar CH ( $\text{PPh}_2$ )), 127.96 (4 C, *p*-Ar CH ( $\text{PPh}_2$ )), 60.33 (1 C, cyclohexyl CH), 34.89 (1 C, cyclohexyl  $\text{CH}_2$ ), 26.12 (2C, cyclohexyl  $\text{CH}_2$ ), 25.47 (2C, cyclohexyl  $\text{CH}_2$ ).  $^{31}\text{P}$  NMR (162 MHz,  $\text{CDCl}_3$ )  $\delta$  55.78. UV-vis: maximum absorbance at 276 nm. IR:  $2927\text{ cm}^{-1}$  (C-H  $\text{sp}^3$  stretching),  $1449\text{--}1433\text{ cm}^{-1}$  (two bands C=C aromatic stretching),  $1091\text{ cm}^{-1}$  (C-P stretching),  $1056\text{ cm}^{-1}$  (C-N stretching). Elemental analysis calcd (%) for  $\text{C}_{30}\text{H}_{31}\text{NP}_2$ : C, 77.07; H, 6.68; N, 3.00; found: C, 76.84; H, 6.88; N, 3.31.

*N*-(diphenylphosphanyl)-*N*,1,1-triphenylphosphanamine (L4): After extracting in toluene, L4 was recovered as a white solid with a yield of 91%.  $^1\text{H}$  NMR (400 MHz,  $\text{CDCl}_3$ )  $\delta$  7.40–7.21 (m, 20H), 6.99–6.88 (m, 3H), 6.64 (d,  $J = 6.2$  Hz, 2H).  $^{13}\text{C}\{^1\text{H}\}$ -NMR (101 MHz,  $\text{CDCl}_3$ )  $\delta$  159.32 (2C, *o*-Ar quaternary (*o*-Ph)), 158.02 (1C, Ar quaternary (*o*-Ph)), 140.28 (4C, Ar quaternary ( $\text{PPh}_2$ )), 132.32 (8C, *o*-Ar CH ( $\text{PPh}_2$ )), 128.03 (2C, *m*-Ar (*o*-Ph)), 127.65 (8C, *m*-Ar CH ( $\text{PPh}_2$ )), 126.92 (4C, *p*-Ar CH ( $\text{PPh}_2$ )), 122.03 (2C, *o*-Ar (*o*-Ph)), 117.22 (1C, *p*-Ar (*o*-Ph)).  $^{31}\text{P}$  NMR (162 MHz,  $\text{CDCl}_3$ )  $\delta$  68.46. UV-vis: maximum absorbance at 280 nm. IR:  $3057\text{ cm}^{-1}$  (C-H  $\text{sp}^2$  stretching),  $1488\text{--}1431\text{ cm}^{-1}$  (two bands C=C aromatic stretching),  $1172\text{ cm}^{-1}$  (C-N stretching),  $1091\text{ cm}^{-1}$  (C-P stretching). Elemental analysis calcd (%) for  $\text{C}_{30}\text{H}_{25}\text{NP}_2$ : C, 78.08; H, 5.46; N, 3.04; found: C, 78.12; H, 5.54; N, 3.30.

*N*-(diphenylphosphanyl)-*N*-(2-fluorophenyl)-1,1-diphenylphosphanamine (L5): After extracting in toluene, L5 was recovered as a white solid with a yield of 80%.  $^1\text{H}$  NMR (400 MHz,  $\text{CDCl}_3$ )  $\delta$  7.40–7.18 (m, 20 H, Ar ( $\text{PPh}_2$ )), 7.04–6.96 (m, 1H, *o*-Ar (*o*-FPh)), 6.87–6.77 (m, 1H, *p*-Ar (*o*-FPh)), 6.76–6.62 (m, 2H, *m*-Ar (*o*-FPh)).  $^{13}\text{C}\{^1\text{H}\}$ -NMR (101 MHz,  $\text{CDCl}_3$ )  $\delta$  160.47 (1C, *o*-Ar quaternary (*o*-FPh)), 158.02 (1C, Ar quaternary (*o*-FPh)), 139.18 (4C, Ar quaternary ( $\text{PPh}_2$ )), 133.39 (8C, *o*-Ar CH ( $\text{PPh}_2$ )), 131.43 (1C, *m*-Ar (*o*-FPh)), 129.05 (8C, *m*-Ar CH ( $\text{PPh}_2$ )), 127.97 (4C, *p*-Ar CH ( $\text{PPh}_2$ )), 127.08 (1C, *o*-Ar (*o*-FPh)), 123.59 (1C, *m*-Ar (*o*-FPh)), 116.21 (1C, *p*-Ar (*o*-FPh)). UV-vis: maximum absorbance at 280 nm. IR:  $3057\text{ cm}^{-1}$  (C-H  $\text{sp}^2$  stretching),  $1479\text{--}1432\text{ cm}^{-1}$  (two bands C=C aromatic stretching),  $1245\text{ cm}^{-1}$  (C-F stretching),  $1181\text{ cm}^{-1}$  (C-N stretching),  $1089\text{ cm}^{-1}$  (C-P stretching). Elemental analysis calcd (%) for  $\text{C}_{30}\text{H}_{24}\text{FNP}_2$ : C, 75.15; H, 5.05; N, 2.92; found: C, 74.92; H, 5.11; N, 3.18.

*N*-(diphenylphosphanyl)-*N*-(4-fluorophenyl)-1,1-diphenylphosphanamine (L6): After extracting in toluene, L6 was recovered as a white solid with a yield of 86%.  $^1\text{H}$  NMR (400 MHz,  $\text{CDCl}_3$ )  $\delta$  7.38–7.19 (m, 20H, Ar), 6.58 (t,  $J = 8.7$  Hz, 2H, *m*-Ar (*p*-FPh)), 6.48 (dd,  $J = 8.9, 5.1$  Hz, 2H, *o*-Ar (*p*-FPh)).  $^{13}\text{C}\{^1\text{H}\}$ -NMR (101 MHz,  $\text{CDCl}_3$ )  $\delta$  161.44 (1C, *p*-Ar quaternary (*p*-FPh)), 159.01 (1C, Ar quaternary (*p*-FPh)), 138.93 (4C, Ar quaternary ( $\text{PPh}_2$ )), 133.20 (8C, *o*-Ar CH ( $\text{PPh}_2$ )), 130.67 (2C, *m*-Ar CH (*p*-FPh)), 129.11 (8C, *m*-Ar CH ( $\text{PPh}_2$ )), 128.00 (4C, *p*-Ar CH ( $\text{PPh}_2$ )), 114.79 (2C, *o*-Ar CH (*p*-FPh)). UV-vis: maximum absorbance at 278 nm. IR:  $3056\text{ cm}^{-1}$  (C-H  $\text{sp}^2$  stretching),  $1496\text{--}1430\text{ cm}^{-1}$  (two bands C=C aromatic stretching),  $1202\text{ cm}^{-1}$  (C-F stretching),  $1151\text{ cm}^{-1}$  (C-N stretching),  $1091\text{ cm}^{-1}$  (C-P stretching). Elemental analysis calcd (%) for  $\text{C}_{30}\text{H}_{24}\text{FNP}_2$ : C, 75.15; H, 5.05; N, 2.92; found: C, 75.33; H, 5.27; N, 3.11.

*N*-(3-bromophenyl)-*N*-(diphenylphosphanyl)-1,1-diphenylphosphanamine (L7): After extracting in toluene, L7 was recovered as a white solid with a yield of 92%.  $^1\text{H}$  NMR (400 MHz,  $\text{CDCl}_3$ )  $\delta$  7.40–7.19 (m, 20H, Ar ( $\text{PPh}_2$ )), 7.08 (d,  $J = 8.2$  Hz, 1H, *o*-Ar (*m*-BrPh)), 6.81 (t,  $J = 8.0$  Hz, 1H, *m*-Ar (*m*-BrPh)), 6.68 (s, 1H, *o'*-Ar (*m*-BrPh)), 6.62 (d,  $J = 8.0$  Hz, 1H, *p*-Ar (*m*-

BrPh)).  $^{13}\text{C}\{^1\text{H}\}$ -NMR (101 MHz,  $\text{CDCl}_3$ )  $\delta$  148.66 (4C, Ar quaternary (*m*-BrPh)), 138.57 (2C, *m'*-Ar quaternary (*m*-BrPh) and Ar quaternary ( $\text{PPh}_2$ )), 133.13 (8C, *o*-Ar CH ( $\text{PPh}_2$ )), 131.95 (1C, *p*-Ar (*m*-BrPh)), 129.20 (8C, *m*-Ar CH ( $\text{PPh}_2$ )), 128.04 (4C, *p*-Ar CH ( $\text{PPh}_2$ )), 127.43 (2C, *o*-Ar (*m*-BrPh)), 121.36 (1C, *m*-Ar (*m*-BrPh)).  $^{31}\text{P}$  NMR (162 MHz,  $\text{CDCl}_3$ )  $\delta$  68.65. UV-vis: maximum absorbance at 282 nm. IR:  $3072\text{ cm}^{-1}$  (C–H  $\text{sp}^2$  stretching),  $1465\text{--}1432\text{ cm}^{-1}$  (two bands C=C aromatic stretching),  $1203\text{ cm}^{-1}$  (C–N stretching),  $1091\text{ cm}^{-1}$  (C–P stretching),  $690\text{ cm}^{-1}$  (C–Br stretching). Elemental analysis calcd (%) for  $\text{C}_{30}\text{H}_{24}\text{BrNP}_2$ : C, 66.68; H, 4.48; N, 2.59; found: C, 66.92; H, 4.53; N, 2.75.

*N*-(4-chlorophenyl)-*N*-(diphenylphosphanyl)-1,1-diphenylphosphanamine (L8): After extracting in toluene, L8 was recovered as a white solid with a yield of 90%.  $^1\text{H}$  NMR (400 MHz,  $\text{CDCl}_3$ )  $\delta$  7.36–7.19 (m, 20H, Ar ( $\text{PPh}_2$ )), 6.85 (d,  $J = 8.7\text{ Hz}$ , 2H, *m*-Ar CH (*p*-ClPh)), 6.48 (d,  $J = 8.8\text{ Hz}$ , 2H, *o*-Ar CH(*p*-ClPh)).  $^{13}\text{C}\{^1\text{H}\}$ -NMR (101 MHz,  $\text{CDCl}_3$ )  $\delta$  145.62 (1C, Ar quaternary (*p*-ClPh)), 138.72 (5C, *p*-Ar quaternary(*p*-ClPh) and Ar quaternary ( $\text{PPh}_2$ )), 133.15 (8C, *o*-Ar CH ( $\text{PPh}_2$ )), 130.22 (2C, *m*-Ar CH (*p*-ClPh)), 129.15 (8C, *m*-Ar CH ( $\text{PPh}_2$ )), 128.17 (2C, *o*-Ar CH (*p*-ClPh)), 128.06 (4C, *p*-Ar CH ( $\text{PPh}_2$ )).  $^{31}\text{P}$  NMR (162 MHz,  $\text{cdcl}_3$ )  $\delta$  69.64. UV-vis: maximum absorbance at 282 nm. IR:  $3036\text{ cm}^{-1}$  (C–H  $\text{sp}^2$  stretching),  $1477\text{--}1431\text{ cm}^{-1}$  (two bands C=C aromatic stretching),  $1211\text{ cm}^{-1}$  (C–N stretching),  $1092\text{ cm}^{-1}$  (C–P stretching),  $901\text{ cm}^{-1}$  (C–Cl stretching). Elemental analysis calcd (%) for  $\text{C}_{30}\text{H}_{24}\text{ClNP}_2$ : C, 72.66; H, 4.88; N, 2.82; found: C, 72.45; H, 4.46; N, 2.62.

*N,N*-bis(diphenylphosphanyl)quinolin-6-amine (L9): After extracting in toluene, L9 was recovered as a yellow solid with a yield of 78%.  $^1\text{H}$  NMR (400 MHz,  $\text{CDCl}_3$ )  $\delta$  8.73 (dd,  $J = 4.2, 1.7\text{ Hz}$ , 1H, Ar CH8 (quinoline)), 7.67 (t,  $J = 9.6\text{ Hz}$ , 2H, Ar CH9 and Ar CH10 (quinoline)), 7.41–7.32 (m, 8H, *o*-Ar ( $\text{PPh}_2$ )), 7.33–7.23 (m, 12H, *m*-Ar and *p*-Ar ( $\text{PPh}_2$ )), 7.20 (dd,  $J = 8.3, 4.3\text{ Hz}$ , 1H, Ar CH3 (quinoline)), 7.10 (d,  $J = 9.0\text{ Hz}$ , 1H, Ar CH2 (quinoline)), 6.93 (s, 1H, Ar CH6 (quinoline)).  $^{13}\text{C}\{^1\text{H}\}$ -NMR (101 MHz,  $\text{CDCl}_3$ )  $\delta$  149.65 (1 C, C8 (quinoline)), 145.95 (1 C, C1 (quinoline)), 145.66 (1 C, C4 (quinoline)), 138.75 (4 C, Ar quaternary ( $\text{PPh}_2$ )), 135.66 (1 C, C10 (quinoline)), 133.17 (8 C, *o*-Ar CH ( $\text{PPh}_2$ )), 131.77 (1 C, C5 (quinoline)), 129.19 (8 C, *m*-Ar CH ( $\text{PPh}_2$ )), 129.12 (1 C, C2 (quinoline)), 128.10 (1 C, C3 (quinoline)), 127.94 (4 C, *p*-Ar CH ( $\text{PPh}_2$ )), 125.90 (1 C, C6 (quinoline)), 120.89 (1 C, C9 (quinoline)).  $^{31}\text{P}$  NMR (162 MHz,  $\text{cdcl}_3$ )  $\delta$  68.73. UV-vis: maximum absorbance at 282 nm. IR:  $3047\text{ cm}^{-1}$  (C–H  $\text{sp}^2$  stretching),  $1492\text{--}1431\text{ cm}^{-1}$  (two bands C=C aromatic stretching),  $1210\text{ cm}^{-1}$  (C–N stretching),  $1094\text{ cm}^{-1}$  (C–P stretching). Elemental analysis calcd (%) for  $\text{C}_{33}\text{H}_{26}\text{N}_2\text{P}$ : C, 77.33; H, 5.11; N, 5.47; found: C, 77.22; H, 5.32; N, 5.81.

(*E*)-*N*-(diphenylphosphanyl)-1,1-diphenyl-*N*-(4-(phenyldiazenyl)phenyl)phosphanamine (L10): After extracting in toluene, L10 was recovered as a yellow solid with a yield of 79%.  $^1\text{H}$  NMR (400 MHz,  $\text{CDCl}_3$ )  $\delta$  7.82 (d,  $J = 6.9\text{ Hz}$ , 2H, H3 and H5 (azobenzene)), 7.53 (d,  $J = 8.8\text{ Hz}$ , 2H, H10 and H14 (azobenzene)), 7.45 (d,  $J = 7.5\text{ Hz}$ , 2H, H11 and H13 (azobenzene)), 7.42–7.38 (m, 8H, *o*-Ar ( $\text{PPh}_2$ )), 7.34 (t,  $J = 1.5\text{ Hz}$ , 1H, H12 (azobenzene)), 7.33–7.23 (m, 12H, *m*-Ar and *p*-Ar (azobenzene)), 6.81 (d,  $J = 8.8\text{ Hz}$ , 2H, H2 and H6 (azobenzene)).  $^{13}\text{C}\{^1\text{H}\}$ -NMR (101 MHz,  $\text{CDCl}_3$ )  $\delta$  152.59 (1 C, C9 (azobenzene)), 150.47 (1 C, C1 (azobenzene)), 149.38 (1 C, C4 (azobenzene)), 138.55 (4 C, Ar quaternary ( $\text{PPh}_2$ )), 133.15 (8 C, *o*-Ar CH ( $\text{PPh}_2$ )), 130.72 (2 C, C3 and C5 (azobenzene)), 129.19 (8 C, *m*-Ar CH ( $\text{PPh}_2$ )), 129.02 (2 C, C11 and C13 (azobenzene)), 128.83 (2 C, C10 and C14 (azobenzene)), 128.12 (4 C, *p*-Ar CH ( $\text{PPh}_2$ )), 122.82 (1 C, C2 (azobenzene)), 122.66 (1 C, C6 (azobenzene)). UV-vis: maximum absorbance at 358 nm. IR:  $3047\text{ cm}^{-1}$  (C–H  $\text{sp}^2$  stretching),  $1492\text{ cm}^{-1}$  (N=N stretching),  $1478\text{--}1434\text{ cm}^{-1}$  (two bands C=C aromatic stretching),  $1214\text{ cm}^{-1}$  (C–N stretching),  $1091\text{ cm}^{-1}$  (C–P stretching). Elemental analysis calcd (%) for  $\text{C}_{36}\text{H}_{29}\text{N}_3\text{P}_2$ : C, 76.45; H, 5.17; N, 7.43; found: C, 76.71; H, 5.32; N, 7.75.

### 2.3. Synthesis and Characterization of Ruthenium Compounds Ru1–Ru10

To a mixture of ligand (0.07 mmol),  $[\text{RuCl}_2(\text{p-cym})]_2$  (0.023 g, 0.037 mmol) and  $\text{NaBF}_4$  (0.010 g, 0.091 mmol) was added methanol (3 mL) and the mixture was allowed to stir for 4 h at room temperature. After this time, a white precipitate appeared. The complexes were isolated as orange solids after filtration.

$[RuCl(p-cym)(Ph_2P)_2N(C_4H_9)][BF_4]$  (Ru1). Yield: 46.32 mg, 0.064 mmol, 85%.  $^1H$  NMR (400 MHz,  $CDCl_3$ )  $\delta$  8.23–8.10 (d,  $J = 6.6$  Hz, 8 H, *o*-Ar), 7.85 (t,  $J = 7.4$  Hz, 4 H, *p*-Ar), 7.67 (t,  $J = 7.3$  Hz, 8 H, *m*-Ar), 5.88 (d,  $J = 6.4$  Hz, 2 H, cym), 5.85 (d,  $J = 6.5$  Hz, 2 H, cym), 2.60–2.49 (m, 1 H,  $CH_3-CH-CH_3$ ), 1.95 (d,  $J = 5.9$  Hz, 3 H,  $CH_3$ ), 0.96 (d,  $J = 6.9$  Hz, 6 H,  $CH_3-CH-CH_3$ ), 0.71 (s, 9 H,  $CH_3$ ).  $^{13}C\{^1H\}$ -NMR (101 MHz,  $CDCl_3$ )  $\delta$  135.36 (8 C, *o*-Ar CH ( $PPh_2$ )), 132.64 (8 C, *m*-Ar CH ( $PPh_2$ )), 130.22 (4 C, *p*-Ar CH ( $PPh_2$ )), 98.50 (4 C, cym), 31.82 (1 C,  $CH-CH_3$ ), 31.18 (3 C,  $CH_3$ ), 22.81 (2 C,  $CH_3-CH$ ), 18.62 (1 C,  $CH_3$ ). Quaternary carbons were not found.  $^{31}P$  NMR (162 MHz,  $CDCl_3$ )  $\delta$  79.91. UV-vis: maximum absorbance at 280 nm. IR: 2963  $cm^{-1}$  (C–H  $sp^3$  stretching), 1474–1436  $cm^{-1}$  (two bands C=C aromatic stretching), 1090  $cm^{-1}$  (C–N stretching), 1053  $cm^{-1}$  (C–P stretching), 701  $cm^{-1}$  (Ru–Cl stretching). Elemental analysis calcd (%) for  $C_{38}H_{43}BClF_4NP_2Ru$ : C, 57.12; H, 5.42; N, 1.75; found: C, 57.93; H, 5.15; N, 1.97. MS (ESI)  $m/z$  for  $[C_{38}H_{43}ClNP_2Ru]^+$ : 712.16 (100%).

$[RuCl(p-cym)(Ph_2P)_2N(C_3H_7)][BF_4]$  (Ru2). Yield: 49.41 mg, 0.070 mmol, 93%.  $^1H$  NMR (400 MHz,  $CDCl_3$ )  $\delta$  7.54 (dd,  $J = 61.7, 29.3$  Hz, 20 H, Ar), 6.05 (s, 2 H, cym), 5.79 (s, 2 H, cym), 2.75 (t,  $J = 4.3$  Hz, 2 H,  $CH_2-CH_2-CH_3$ ), 2.55 (s, 1 H,  $CH_3-CH-CH_3$ ), 1.79 (s, 3 H,  $CH_3$ ), 1.10–0.94 (m, 2 H,  $CH_2-CH_2-CH_3$ ), 1.06 (d,  $J = 6.8$  Hz, 6 H,  $CH_3-CH-CH_3$ ), 0.40 (s, 3 H,  $CH_2-CH_2-CH_3$ ).  $^{13}C\{^1H\}$ -NMR (101 MHz,  $CDCl_3$ )  $\delta$  133.55 (4 C, Ar quaternary ( $PPh_2$ )), 132.65 (8 C, *m*-Ar CH ( $PPh_2$ )), 130.07 (8 C, *o*-Ar CH ( $PPh_2$ )), 127.95 (4 C, *p*-Ar CH ( $PPh_2$ )), 117.87 (1 C, cym quaternary), 111.04 (1 C, cym quaternary) 95.95 (2 C, cym), 90.19 (2 C, cym), 52.26 (1 C,  $CH_2-CH_2-CH_3$ ), 31.77 (1 C,  $CH-CH_3$ ), 23.46 (1 C,  $CH_2-CH_2-CH_3$ ), 22.79 (2 C,  $CH_3-CH$ ), 18.85 (1 C,  $CH_3$ ), 11.15 (1 C,  $CH_2-CH_2-CH_3$ ).  $^{31}P$  NMR (162 MHz,  $CDCl_3$ )  $\delta$  76.56. UV-vis: maximum absorbance at 276 nm. IR: 2966  $cm^{-1}$  (C–H  $sp^3$  stretching), 1477–1435  $cm^{-1}$  (two bands C=C aromatic stretching), 1091  $cm^{-1}$  (C–N stretching), 1050  $cm^{-1}$  (C–P stretching), 695  $cm^{-1}$  (Ru–Cl stretching). Elemental analysis calcd (%) for  $C_{37}H_{41}BClF_4NP_2Ru$ : C, 56.61; H, 5.26; N, 1.78; found: C, 56.68; H, 5.48; N, 1.87. MS (ESI)  $m/z$  for  $[C_{37}H_{41}ClNP_2Ru]^+$ : 698.14 (100%).

$[RuCl(p-cym)(Ph_2P)_2N(C_6H_{11})][BF_4]$  (Ru3). Yield: 53.11 mg, 0.072 mmol, 92%.  $^1H$  NMR (400 MHz,  $CDCl_3$ )  $\delta$  7.89–7.42 (m, 20 H, Ar), 5.99 (t,  $J = 6.8$  Hz, 2 H, cym), 5.95 (d,  $J = 6.2$  Hz, 2 H, cym), 2.66–2.53 (m, 1 H,  $CH_3-CH-CH_3$ ), 2.03 (s, 3 H,  $CH_3$ ), 1.23 (t,  $J = 16.6$  Hz, 4 H, cyclohexyl  $CH_2$ ), 1.11 (d,  $J = 11.5$  Hz, 2 H, cyclohexyl  $CH_2$ ), 1.02 (d,  $J = 6.9$  Hz, 6 H,  $CH_3-CH-CH_3$ ), 0.63 (t,  $J = 13.1$  Hz, 1 H, cyclohexyl CH), 0.55–0.40 (m, 4 H, cyclohexyl  $CH_2$ ).  $^{13}C\{^1H\}$ -NMR (101 MHz,  $CDCl_3$ )  $\delta$  134.33 (8 C, *o*-Ar CH ( $PPh_2$ )), 133.71 (4 C, Ar quaternary ( $PPh_2$ )) 132.36 (8 C, *m*-Ar CH ( $PPh_2$ )), 130.03 (4 C, *p*-Ar CH ( $PPh_2$ )), 116.76 (1 C, cym quaternary), 112.54 (1 C, cym quaternary), 96.29 (2 C, cym), 89.63 (2 C, cym), 33.19–32.77 (2 C, cyclohexyl  $CH_2$ ), 31.73 (1 C,  $CH-CH_3$ ), 25.95 (2 C, cyclohexyl  $CH_2$ ), 24.51 (2 C, cyclohexyl  $CH_2$  and cyclohexyl CH), 22.83 (2 C,  $CH_3-CH$ ), 19.01 (1 C,  $CH_3$ ).  $^{31}P$  NMR (162 MHz,  $CDCl_3$ )  $\delta$  75.97. UV-vis: maximum absorbance at 276 nm. IR: 2941  $cm^{-1}$  (C–H  $sp^3$  stretching), 1478–1434  $cm^{-1}$  (two bands C=C aromatic stretching), 1075  $cm^{-1}$  (C–N stretching), 1046  $cm^{-1}$  (C–P stretching), 699  $cm^{-1}$  (Ru–Cl stretching). Elemental analysis calcd (%) for  $C_{40}H_{45}BClF_4NP_2Ru$ : C, 58.23; H, 5.50; N, 1.70; found: C, 58.42; H, 5.39; N, 1.61. MS (ESI)  $m/z$  for  $[C_{40}H_{45}ClNP_2Ru]^+$ : 731.18 (100%).

$[RuCl(p-cym)(Ph_2P)_2N(C_6H_5)][BF_4]$  (Ru4). Yield: 51.31 mg, 0.070 mmol, 92%.  $^1H$  NMR (400 MHz,  $CDCl_3$ )  $\delta$  7.68–7.56 (m, 8 H, *o*-Ar ( $PPh_2$ )), 7.54–7.43 (m, 8 H, *m*-Ar ( $PPh_2$ )), 7.35 (t,  $J = 7.6$  Hz, 4 H, *p*-Ar ( $PPh_2$ )), 7.04 (t,  $J = 7.3$  Hz, 1 H, *p*-phenyl), 6.96 (t,  $J = 7.7$  Hz, 2 H, *m*-phenyl), 6.54 (d, 2 H, *o*-phenyl), 6.06 (d,  $J = 6.3$  Hz, 2 H, cym), 5.83 (d,  $J = 6.3$  Hz, 2 H, cym), 2.57–2.47 (m,  $J = 13.8, 6.8$  Hz, 1 H,  $CH_3-CH-CH_3$ ), 1.68 (s, 3 H,  $CH_3$ ), 1.09 (d,  $J = 6.9$  Hz, 6 H,  $CH_3-CH-CH_3$ ).  $^{13}C\{^1H\}$ -NMR (101 MHz,  $CDCl_3$ )  $\delta$  139.66 (1 C, phenyl quaternary), 133.41 (8 C, *o*-Ar CH ( $PPh_2$ )), 132.79 (4 C, Ar quaternary ( $PPh_2$ )), 129.82 (8 C, *m*-Ar CH ( $PPh_2$ )), 128.97 (2 C, phenyl *m*-Ar CH), 127.83 (4 C, *p*-Ar CH ( $PPh_2$ )), 126.73 (1 C, phenyl *p*-Ar CH), 126.51 (2 C, phenyl *o*-Ar CH), 120.58 (1 C, cym quaternary), 109.01 (1 C, cym quaternary), 94.69–93.57 (2 C, cym), 92.19 (2 C, cym), 31.44 (1 C,  $CH-(CH_3)_2$ ), 22.49 (2 C,  $CH_3-CH$ ), 18.00 (1 C,  $CH_3$ ).  $^{31}P$  NMR (162 MHz,  $CDCl_3$ )  $\delta$  79.01. UV-vis: maximum absorbance at 276 nm. IR: 2962  $cm^{-1}$  (C–H  $sp^3$  stretching), 1482–1435  $cm^{-1}$  (two bands C=C aromatic stretching), 1089  $cm^{-1}$  (C–N stretching), 1031  $cm^{-1}$  (C–P stretching), 691

$\text{cm}^{-1}$  (Ru–Cl stretching). Elemental analysis calcd (%) for  $\text{C}_{40}\text{H}_{39}\text{BClF}_4\text{NP}_2\text{Ru}$ : C, 58.66; H, 4.80; N, 1.71; found: C, 58.79; H, 4.48; N, 1.97. MS (ESI)  $m/z$  for  $[\text{C}_{40}\text{H}_{38}\text{ClFNP}_2\text{Ru}^+]$ : 731.18 (100%).

$[\text{RuCl}(p\text{-cym})(\text{Ph}_2\text{P})_2\text{N}(\text{C}_6\text{H}_4\text{F})][\text{BF}_4]$  (Ru5). Yield: 50.19 mg, 0.067 mmol, 89%.  $^1\text{H}$  NMR (400 MHz,  $\text{CDCl}_3$ )  $\delta$  7.57 (s, 8 H, *o*-Ar (PPh<sub>2</sub>)), 7.50–7.39 (m, 8 H, *m*-Ar (PPh<sub>2</sub>)), 7.29 (t,  $J = 7.5$  Hz, 4 H, *p*-Ar (PPh<sub>2</sub>)), 7.14 (t,  $J = 10.2$  Hz, 1 H, *p*-Ar (*o*-FPh)), 6.97 (t,  $J = 9.1$  Hz, 1 H, *m'*-Ar (*o*-FPh)), 6.62 (t,  $J = 7.6$  Hz, 1 H, *m*-Ar (*o*-FPh)), 6.17 (d,  $J = 6.2$  Hz, 2 H, *cym*), 6.08 (t,  $J = 7.6$  Hz, 1 H, *o*-Ar (*o*-FPh)), 5.90 (d,  $J = 6.0$  Hz, 2 H, *cym*), 2.60–2.47 (m, 1 H,  $\text{CH}_3\text{-CH-CH}_3$ ), 1.69 (s, 3 H,  $\text{CH}_3$ ), 1.11 (d,  $J = 6.9$  Hz, 6 H,  $\text{CH}_3\text{-CH-CH}_3$ ).  $^{13}\text{C}\{^1\text{H}\}$ -NMR (101 MHz,  $\text{CDCl}_3$ )  $\delta$  134.15 (1 C, *o'*-Ar quaternary (*o*-FPh)), 134.00 (1 C, *o*-Ar (*o*-FPh)), 132.94 (8 C, *m*-Ar CH (PPh<sub>2</sub>)), 131.94 (4 C, Ar quaternary (PPh<sub>2</sub>)), 130.53 (1 C, *p*-Ar (*o*-FPh)), 129.43 (8 C, *o*-Ar CH (PPh<sub>2</sub>)), 128.12 (1 C, Ar quaternary (*o*-FPh)), 127.69 (4 C, *p*-Ar CH (PPh<sub>2</sub>)), 124.25 (1 C, *m*-Ar (*o*-FPh)), 120.59 (1 C, *cym* quaternary), 116.96 (1 C, *m'*-Ar (*o*-FPh)), 108.09 (1 C, *cym* quaternary), 93.89 (2 C, *cym*), 92.57 (2 C, *cym*), 31.31 (1 C,  $\text{CH-(CH}_3)_2$ ), 22.47 (2 C,  $\text{CH}_3\text{-CH}$ ), 17.99–16.94 (1 C,  $\text{CH}_3$ ).  $^{31}\text{P}$  NMR (162 MHz,  $\text{CDCl}_3$ )  $\delta$  84.21. UV-vis: maximum absorbance at 272 nm. IR: 3065  $\text{cm}^{-1}$  (C–H  $\text{sp}^2$  stretching), 2968  $\text{cm}^{-1}$  (C–H  $\text{sp}^3$  stretching), 1485–1435  $\text{cm}^{-1}$  (two bands C=C aromatic stretching), 1257  $\text{cm}^{-1}$  (C–F stretching), 1097  $\text{cm}^{-1}$  (C–N stretching), 1050  $\text{cm}^{-1}$  (C–P stretching), 691  $\text{cm}^{-1}$  (Ru–Cl stretching). Elemental analysis calcd (%) for  $\text{C}_{40}\text{H}_{38}\text{BClF}_5\text{NP}_2\text{Ru}$ : C, 57.40; H, 4.58; N, 1.67; found: C, 57.72; H, 4.32; N, 1.83. MS (ESI)  $m/z$  for  $[\text{C}_{40}\text{H}_{38}\text{ClFNP}_2\text{Ru}^+]$ : 750.12 (100%).

$[\text{RuCl}(p\text{-cym})(\text{Ph}_2\text{P})_2\text{N}(\text{C}_6\text{H}_4\text{F})][\text{BF}_4]$  (Ru6). Yield: 51.40 mg, 0.068 mmol, 90%.  $^1\text{H}$  NMR (400 MHz,  $\text{CDCl}_3$ )  $\delta$  7.67–7.32 (m, 20 H, Ar (PPh<sub>2</sub>)), 6.71–6.63 (t, 2 H, *o*-Ar (*p*-FPh)), 6.52–6.45 (m, 2 H, *m*-Ar (*p*-FPh)), 6.15 (d,  $J = 6.3$  Hz, 2 H, *cym*), 5.90 (d,  $J = 6.2$  Hz, 2 H, *cym*), 2.60–2.50 (m, 1 H,  $\text{CH}_3\text{-CH-CH}_3$ ), 1.74 (s, 3 H,  $\text{CH}_3$ ), 1.09 (d,  $J = 6.9$  Hz, 6 H,  $\text{CH}_3\text{-CH-CH}_3$ ).  $^{13}\text{C}\{^1\text{H}\}$ -NMR (101 MHz,  $\text{CDCl}_3$ )  $\delta$  133.62 (1 C, *p*-Ar quaternary (*p*-FPh)), 133.38 (4 C, Ar quaternary (PPh<sub>2</sub>)), 133.22 (8 C, Ar CH (PPh<sub>2</sub>)), 131.94 (1 C, Ar quaternary (*p*-FPh)), 130.11 (2 C, *m*-Ar CH (*p*-FPh)), 129.83 (8 C, Ar CH (PPh<sub>2</sub>)), 127.81 (4 C, Ar CH (PPh<sub>2</sub>)), 119.96 (1 C, *cym* quaternary), 115.83 (2 C, *o*-Ar CH (*p*-FPh)), 110.03 (1 C, *cym* quaternary), 94.94 (2 C, *cym*), 91.74 (2 C, *cym*), 31.59 (1 C,  $\text{CH-(CH}_3)_2$ ), 22.61 (2 C,  $\text{CH}_3\text{-CH}$ ), 18.26 (1 C,  $\text{CH}_3$ ).  $^{31}\text{P}$  NMR (162 MHz,  $\text{CDCl}_3$ )  $\delta$  81.02. UV-vis: maximum absorbance at 274 nm. IR: 3071  $\text{cm}^{-1}$  (C–H  $\text{sp}^2$  stretching), 2965  $\text{cm}^{-1}$  (C–H  $\text{sp}^3$  stretching), 1503–1434  $\text{cm}^{-1}$  (two bands C=C aromatic stretching), 1212  $\text{cm}^{-1}$  (C–F stretching), 1093  $\text{cm}^{-1}$  (C–N stretching), 1050  $\text{cm}^{-1}$  (C–P stretching), 691  $\text{cm}^{-1}$  (Ru–Cl stretching). Elemental analysis calcd (%) for  $\text{C}_{40}\text{H}_{38}\text{BClF}_5\text{NP}_2\text{Ru}$ : C, 57.40; H, 4.58; N, 1.67; found: C, 57.51; H, 4.61; N, 1.88. MS (ESI)  $m/z$  for  $[\text{C}_{40}\text{H}_{38}\text{BrClNP}_2\text{Ru}^+]$ : 810.04 (100%).

$[\text{RuCl}(p\text{-cym})(\text{Ph}_2\text{P})_2\text{N}(\text{C}_6\text{H}_4\text{Br})][\text{BF}_4]$  (Ru7). Yield: 56.04 mg, 0.069 mmol, 92%.  $^1\text{H}$  NMR (400 MHz,  $\text{CDCl}_3$ )  $\delta$  7.74–7.33 (m,  $J = 51.1, 40.4, 17.9$  Hz, 22 H, Ar (PPh<sub>2</sub>)), *o*-Ar CH (*m*-BrPh) and *m*-Ar CH (*m*-BrPh), 6.93 (d,  $J = 8.7$  Hz, 1 H, *p*-Ar CH (*m*-BrPh)), 6.44 (d,  $J = 8.7$  Hz, 1 H, *o*-Ar CH (*m*-BrPh)), 6.12 (d, 2 H, *cym*), 5.91 (d, 2 H, *cym*), 2.59–2.49 (m, 1 H,  $\text{CH}_3\text{-CH-CH}_3$ ), 1.74 (s, 3 H,  $\text{CH}_3$ ), 1.09 (d,  $J = 6.6$  Hz, 6 H,  $\text{CH}_3\text{-CH-CH}_3$ ).  $^{13}\text{C}\{^1\text{H}\}$ -NMR (101 MHz,  $\text{CDCl}_3$ )  $\delta$  133.66 (1 C, *m'*-Ar quaternary (*m*-BrPh)), 133.26 (4 C, Ar quaternary (PPh<sub>2</sub>)), 132.04 (8 C, Ar CH (PPh<sub>2</sub>)), 130.09 (1 C, Ar quaternary (*m*-BrPh)), 129.81 (1 C, *m*-Ar CH (*m*-BrPh)), 129.57 (8 C, Ar CH (PPh<sub>2</sub>)), 128.02 (4 C, Ar CH (PPh<sub>2</sub>)), 127.61 (1 C, *o'*-Ar CH (*m*-BrPh)), 124.81 (1 C, *o*-Ar CH (*m*-BrPh)), 122.31 (1 C, *p*-Ar CH (*m*-BrPh)), 110.18 (1 C, *cym* quaternary), 109.26 (1 C, *cym* quaternary), 95.47 (2 C, *cym*), 92.17 (2 C, *cym*), 31.62 (1 C,  $\text{CH-(CH}_3)_2$ ), 22.64 (2 C,  $\text{CH}_3\text{-CH}$ ), 18.35 (1 C,  $\text{CH}_3$ ).  $^{31}\text{P}$  NMR (162 MHz,  $\text{CDCl}_3$ )  $\delta$  81.21. UV-vis: maximum absorbance at 257 nm. IR: 3053  $\text{cm}^{-1}$  (C–H  $\text{sp}^2$  stretching), 2968  $\text{cm}^{-1}$  (C–H  $\text{sp}^3$  stretching), 1475–1435  $\text{cm}^{-1}$  (two bands C=C aromatic stretching), 1092  $\text{cm}^{-1}$  (C–N stretching), 1050  $\text{cm}^{-1}$  (C–P stretching), 700  $\text{cm}^{-1}$  (Ru–Cl stretching). Elemental analysis calcd (%) for  $\text{C}_{40}\text{H}_{38}\text{BBrClF}_4\text{NP}_2\text{Ru}$ : C, 53.51; H, 4.27; N, 1.56; found: C, 54.19; H, 4.59; N, 1.34. MS (ESI)  $m/z$  for  $[\text{C}_{40}\text{H}_{38}\text{BrClNP}_2\text{Ru}^+]$ : 810.04 (100%).

$[\text{RuCl}(p\text{-cym})(\text{Ph}_2\text{P})_2\text{N}(\text{C}_6\text{H}_4\text{Cl})][\text{BF}_4]$  (Ru8). Yield: 51.09 mg, 0.066 mmol, 88%.  $^1\text{H}$  NMR (400 MHz,  $\text{CDCl}_3$ )  $\delta$  7.66 (d,  $J = 29.2$  Hz, 8 H, *o*-Ar (PPh<sub>2</sub>)), 7.49 (t,  $J = 8.1$ , 8 H, *m*-Ar (PPh<sub>2</sub>)), 7.39 (t,  $J = 6.8$  Hz, 4 H, *p*-Ar (PPh<sub>2</sub>)), 6.93 (d,  $J = 8.6$  Hz, 2 H, *o*-Ar (*p*-ClPh)), 6.45

(d,  $J = 8.6$  Hz, 2 H, *m*-Ar (*p*-ClPh)), 6.12 (d, 2 H, cym), 5.90 (d, 2 H, cym, 2.59–2.49 (m, 1 H, CH<sub>3</sub>–CH–CH<sub>3</sub>), 1.75 (s, 3 H, CH<sub>3</sub>), 1.09 (d,  $J = 5.7$  Hz, 6 H, CH<sub>3</sub>–CH–CH<sub>3</sub>). <sup>13</sup>C{<sup>1</sup>H}-NMR (101 MHz, CDCl<sub>3</sub>) δ 138.13 (1 C, *p*-Ar quaternary (*p*-ClPh)), 133.53 (1 C, Ar quaternary (*p*-ClPh)), 133.40 (8 C, *o*-Ar CH (PPh<sub>2</sub>)), 133.17 (8 C, *m*-Ar CH (PPh<sub>2</sub>)), 132.01 (4 C, Ar quaternary (PPh<sub>2</sub>)), 129.18 (2 C, Ar CH (*p*-ClPh)), 128.10 (2 C, Ar CH (*p*-ClPh)), 127.98 (4 C, *p*-Ar CH (PPh<sub>2</sub>)), 120.44 (1 C, cym quaternary), 109.75 (1 C, cym quaternary), 95.20 (2 C, cym), 92.12 (2 C, cym), 31.58 (1 C, CH–(CH<sub>3</sub>)<sub>2</sub>), 22.60 (2 C, CH<sub>3</sub>–CH), 18.23 (1 C, CH<sub>3</sub>). <sup>31</sup>P NMR (162 MHz, CDCl<sub>3</sub>) δ 80.65. UV-vis: maximum absorbance at 272 nm. IR: 3065 cm<sup>−1</sup> (C–H sp<sup>2</sup> stretching), 2969 cm<sup>−1</sup> (C–H sp<sup>3</sup> stretching), 1474–1434 cm<sup>−1</sup> (two bands C=C aromatic stretching), 1094 cm<sup>−1</sup> (C–N stretching), 1051 cm<sup>−1</sup> (C–P stretching), 890 cm<sup>−1</sup> (C–Cl stretching), 696 cm<sup>−1</sup> (Ru–Cl stretching). Elemental analysis calcd (%) for C<sub>40</sub>H<sub>38</sub>BCl<sub>2</sub>F<sub>4</sub>NP<sub>2</sub>Ru: C, 56.29; H, 4.49; N, 1.64; found: C, 56.45; H, 4.26; N, 1.98. MS (ESI) *m/z* for [C<sub>40</sub>H<sub>38</sub>Cl<sub>2</sub>NP<sub>2</sub>Ru<sup>+</sup>]: 766.09 (100%).

[RuCl(*p*-cym)(Ph<sub>2</sub>P)<sub>2</sub>N(C<sub>9</sub>H<sub>6</sub>N)] [BF<sub>4</sub>] (Ru9). Yield: 53.20 mg, 0.068 mmol, 90%. <sup>1</sup>H NMR (400 MHz, CDCl<sub>3</sub>) δ 7.76–7.32 (m, 24 H, Ar (PPh<sub>2</sub>) and Ar CH<sub>3</sub>, CH<sub>8</sub>, CH<sub>9</sub> and CH<sub>10</sub> (quinoline)), 7.03–6.98 (m, 1 H, Ar CH<sub>2</sub> (quinoline)), 6.76 (d,  $J = 1.5$  Hz, 1 H, Ar CH<sub>6</sub> (quinoline)), 6.12 (d,  $J = 6.2$  Hz, 2 H, cym), 5.90 (d,  $J = 6.5$  Hz, 2 H, cym), 2.61–2.52 (m, 1 H, CH<sub>3</sub>–CH–CH<sub>3</sub>), 1.76 (s, 3 H, CH<sub>3</sub>), 1.12 (d,  $J = 6.9$  Hz, 6 H, CH<sub>3</sub>–CH–CH<sub>3</sub>). <sup>13</sup>C{<sup>1</sup>H}-NMR (101 MHz, CDCl<sub>3</sub>) δ 133.51 (1 C, C<sub>8</sub> (quinoline)), 133.36 (8 C, *o*-Ar CH (PPh<sub>2</sub>)), 133.10 (1 C, C<sub>10</sub> (quinoline)), 132.00 (8 C, *m*-Ar CH (PPh<sub>2</sub>)), 130.01 (1 C, C<sub>3</sub> (quinoline)), 128.18 (1 C, C<sub>2</sub> (quinoline)), 127.98 (4 C, *p*-Ar CH (PPh<sub>2</sub>)), 125.00 (1 C, C<sub>6</sub> (quinoline)), 122.00 (1 C, C<sub>9</sub> (quinoline)), 95.07 (2 C, cym), 92.19 (2 C, cym), 31.55 (1 C, CH–(CH<sub>3</sub>)<sub>2</sub>), 22.58 (2 C, CH<sub>3</sub>–CH), 18.20 (1 C, CH<sub>3</sub>). Quaternary carbons were not found. <sup>31</sup>P NMR (162 MHz, CDCl<sub>3</sub>) δ 80.87. UV-vis: maximum absorbance at 257 nm. IR: 3057 cm<sup>−1</sup> (C–H sp<sup>2</sup> stretching), 2954 cm<sup>−1</sup> (C–H sp<sup>3</sup> stretching), 1498–1480 cm<sup>−1</sup> (two bands C=C aromatic stretching), 1093 cm<sup>−1</sup> (C–N stretching), 1046 cm<sup>−1</sup> (C–P stretching), 693 cm<sup>−1</sup> (Ru–Cl stretching). Elemental analysis calcd (%) for C<sub>43</sub>H<sub>40</sub>BClF<sub>4</sub>N<sub>2</sub>P<sub>2</sub>Ru: C, 59.36; H, 4.63; N, 3.22; found: C, 59.39; H, 4.66; N, 3.00. MS (ESI) *m/z* for [C<sub>43</sub>H<sub>40</sub>ClN<sub>2</sub>P<sub>2</sub>Ru<sup>+</sup>]: 783.14 (100%).

[RuCl(*p*-cym)(Ph<sub>2</sub>P)<sub>2</sub>N(C<sub>12</sub>H<sub>9</sub>N<sub>2</sub>)] [BF<sub>4</sub>] (Ru10). Yield: 57.18 mg, 0.068 mmol, 91%. <sup>1</sup>H NMR (400 MHz, CDCl<sub>3</sub>) δ 8.84–8.30 (m,  $J = 35.6, 14.9$  Hz, 27 H, Ar (PPh<sub>2</sub>) and Ar CH<sub>3</sub>, CH<sub>5</sub>, CH<sub>10</sub>, CH<sub>11</sub>, CH<sub>12</sub>, CH<sub>13</sub> and CH<sub>14</sub> (azobenzene)), 7.71 (d,  $J = 8.0$  Hz, 2 H, Ar CH<sub>2</sub> and CH<sub>6</sub> (azobenzene)), 7.08 (s, 2 H, cym), 6.88 (s, 2 H, cym), 3.65–3.45 (m, 1 H, CH–(CH<sub>3</sub>)<sub>2</sub>), 2.69 (s, 3 H, CH<sub>3</sub>), 2.13 (d,  $J = 6.8$  Hz, 6 H, CH<sub>3</sub>–CH–CH<sub>3</sub>). <sup>13</sup>C{<sup>1</sup>H}-NMR (101 MHz, CDCl<sub>3</sub>) δ 147.44 (1 C, C<sub>9</sub> (quaternary azobenzene)), 134.38 (1 C, C<sub>1</sub> (quaternary azobenzene)), 133.89 (1 C, Ar quaternary (PPh<sub>2</sub>)), 132.76 (8 C, Ar CH (PPh<sub>2</sub>)), 132.20 (1 C, C<sub>4</sub> (quaternary azobenzene)), 130.96 (8 C, Ar CH (PPh<sub>2</sub>)), 129.94 (5 C, *p*-Ar CH (PPh<sub>2</sub>) and C<sub>12</sub> (azobenzene)), 128.91 (2 C, C<sub>3</sub> and C<sub>5</sub> (azobenzene)), 126.22 (2 C, C<sub>11</sub> and C<sub>13</sub> (azobenzene)), 124.18 (2 C, C<sub>10</sub> and C<sub>14</sub> (azobenzene)), 123.60 (2 C, C<sub>2</sub> and C<sub>6</sub> (azobenzene)), 120.87 (1 C, cym quaternary), 109.99 (1 C, cym quaternary), 96.12 (2 C, cym), 93.32 (2 C, cym), 32.28 (1 C, CH–(CH<sub>3</sub>)<sub>2</sub>), 23.31 (2 C, CH<sub>3</sub>–CH), 18.84 (1 C, CH<sub>3</sub>). <sup>31</sup>P NMR (162 MHz, CDCl<sub>3</sub>) δ 80.39. UV-vis: maximum absorbance at 348 nm. IR: 3065 cm<sup>−1</sup> (C–H sp<sup>2</sup> stretching), 2944 cm<sup>−1</sup> (C–H sp<sup>3</sup> stretching), 1493 cm<sup>−1</sup> (N=N stretching), 1482–1435 cm<sup>−1</sup> (two bands C=C aromatic stretching), 1093 cm<sup>−1</sup> (C–N stretching), 1042 cm<sup>−1</sup> (C–P stretching), 690 cm<sup>−1</sup> (Ru–Cl stretching). Elemental analysis calcd (%) for C<sub>46</sub>H<sub>43</sub>BClF<sub>4</sub>N<sub>3</sub>P<sub>2</sub>Ru: C, 59.85; H, 4.70; N, 4.55; found: C, 60.12; H, 4.53; N, 4.42. MS (ESI) *m/z* for [C<sub>46</sub>H<sub>43</sub>ClN<sub>3</sub>P<sub>2</sub>Ru<sup>+</sup>]: 836.17 (100%).

#### 2.4. X-ray Crystallography

Prismatic crystal for Ru3 was mounted on a glass fiber and used for data collection on a Bruker D8 Venture with a Photon detector equipped with graphite monochromated MoK $\alpha$  radiation ( $\lambda = 0.71073$  Å) (Bruker Apex2, Bruker AXS Inc., Madison, WI, USA, 2004). The data reduction was performed with the APEX2 software and corrected for absorption using SADABS [38]. Crystal structures were solved by direct methods using the SIR97 program [39] and refined by full-matrix least-squares on  $F^2$  including all reflections using anisotropic displacement parameters by means of the WINGX crystallographic

package [40,41]. Generally, anisotropic temperature factors were assigned to all atoms except for C2 and hydrogen atoms, which are riding their parent atoms with an isotropic temperature factor arbitrarily chosen as 1.2 times that of the respective parent. Several crystals of *Ru3* were measured and the structure was solved from the best data we were able to collect, due to the fact that the crystals diffracted very little. Final  $R(F)$ ,  $wR(F^2)$ , and goodness of fit agreement factors, details on the data collection and analysis can be found in Table S1. CCDC 2,076,579 contain the supplementary crystallographic data for *Ru3*. These data can be obtained free of charge from The Cambridge Crystallographic Data Centre via [www.ccdc.cam.ac.uk/data\\_request/cif](http://www.ccdc.cam.ac.uk/data_request/cif), accessed on 11 April 2021.

### 2.5. HSA Binding Studies by Steady-State Fluorescence Spectroscopy

Three milliliters of protein solution (5  $\mu\text{M}$ ) was titrated by successive addition of a metallodrug stock solution. The excitation wavelength was 283 nm HSA, whereas the emission fluorescence intensities were collected at 372 nm. The excitation and emission slits were fixed at 5 nm. The step and dwell time was 0.1 s. For the inner filter effect fluorescence was corrected through:

$$F_{corr} = F_{obs} 10^{\frac{(A_{exc} + A_{em})}{2}}$$

where  $F_{corr}$  and  $F_{obs}$  are the corrected and observed fluorescence intensities, and  $A_{exc}$  and  $A_{em}$  are the absorbances of the system at excitation and emission wavelengths. Temperature was controlled at 300 K by a temperature-controlled cuvette holder, TC 125 (Quantum Northwest), and the experiment was repeated three times.

The Stern–Volmer equation was then used to evaluate the quenching constant  $K_{SV}$  of the studied drug–protein systems:

$$\frac{F_0}{F} = 1 + K_{SV}[Q]$$

where  $F_0$  and  $F$  are the emission intensities in the absence and the presence of the quencher, respectively,  $[Q]$  is the concentration of the quencher (metallodrug), and  $K_{SV}$  is the Stern–Volmer constant [42].

For static quenching, the relationship between fluorescence intensity and the quencher concentration,  $[Q]$ , is described by the following equation:

$$\log\left(\frac{F_0 - F}{F}\right) = \log K_a + n \log[Q]$$

where  $F_0$  corresponds to the fluorescence intensity of the protein in absence of quencher,  $n$  and  $K_a$  are the number of binding sites and binding constant, respectively [43,44].

### 2.6. Biological Assays

The compounds were dissolved in dimethyl sulfoxide (DMSO) before performing each experiment. The maximal concentration used was 50  $\mu\text{M}$ , due to limited water solubility; cisplatin was tested up to 100  $\mu\text{M}$  [45]. The same volume of solvent was added to control conditions and did not exceed 0.25% *v/v*.

*Cell culture studies.* The cell lines T47D, MCF7, BT474, SKBR3, BT549, HS578T, OV-CAR8, and SKOV3 and the immortalized non-transformed keratinocyte cell line HACAT was kindly provided by Drs. J. Losada and A. Balmain or acquired in ATCC. All lines were grown in DMEM containing 10% fetal bovine serum (FBS) and were supplemented with 100 U/mL penicillin, 5 mM L-glutamine, 100  $\mu\text{g}/\text{mL}$  streptomycin at 37  $^\circ\text{C}$  and 5%  $\text{CO}_2$  (Sigma-Aldrich, St. Louis, MO, USA). Carboplatin and cisplatin were purchased from Accord Healthcare (the United Kingdom, MA).

*MTT metabolization assays.* For viability assessment, cell proliferation was assayed by MTT (3-(4, 5-dimethylthiazol-2-yl)-2, 5 diphenyltetrazolium bromide) (Sigma Aldrich). Cell lines were plated at 10,000 cells per well in 48-multiwell plates. 24 h later, the cells were treated at correspondent doses of the drugs for 72 h. After that, the medium was

aspirated and phenol red-free DMEM with MTT 0.5 mg/mL was added for 60 min in growth conditions. The medium was removed and MTT crystals were solubilized with 0.5 mL of dimethylsulfoxide (DMSO) (Sigma-Aldrich) and evaluated at an absorbance of 555 nm in a multiwell plate reader.

*Cell cycle and apoptosis assay.* For cell cycle analyses, cell lines were plated at 100,000 cells per well in 6-multiwell plates. 24 h later, wells were treated with an  $IC_{50}$  dose of *Ru3* for 24 h. In order to fix the cells, the cells were incubated for 15 min in 70% ethanol. After that, pellets were washed in 2% BSA in PBS and were stained with Propidium iodide/RNase staining solution for 1 h at 4 °C in dark conditions (Immunostep S.L., Salamanca, Spain).

For apoptosis analysis, the same number of cells were treated for 48 h. Then, adherent and floating cells were washed with PBS and incubated in Annexin V binding buffer (Immunostep S.L.) for 1 h in the dark with Annexin V and PI staining solution (Immunostep S.L.). Percentage of dead cells was determined considering early apoptotic (Annexin V-positive, PI-negative), late apoptotic (Annexin V-positive and PI-positive), and residual necrotic (Annexin V-negative, PI-positive) cells which were included as dead cells in the analysis.

Flow cytometry assays were evaluated in a FACSCanto II flow cytometer (BD Biosciences).

*In vivo studies.* For in vivo toxicity analysis, 12 female BALB/c nu/nu mice of 5 weeks old were treated and weighted twice a week intraperitoneally with *Ru3* or cDDP at a fixed dose of 5mg/kg for up to four treatments. Mice were humanely sacrificed by CO<sub>2</sub> inhalation in an appropriated chamber. This study was performed under the supervision of the Ethics Committee and veterinary staff of Complejo Hospitalario Universitario de Albacete. Mice were monitored and managed at the animal facility following local legal guidelines.

### 2.7. Statistical Analysis

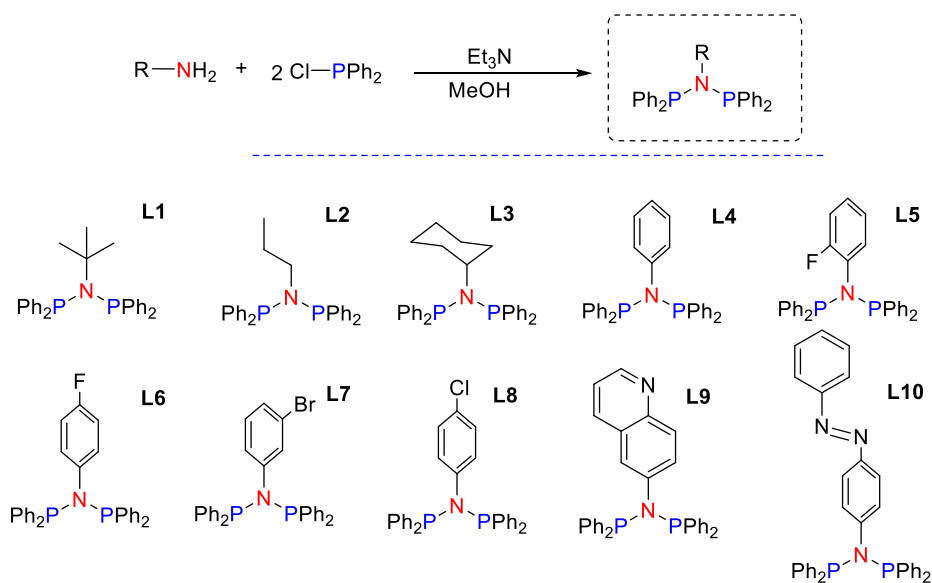
The in vitro experiments data are the average of three independent experiments performed in triplicate, with error bars showing the standard deviation of the triplicates. To determine significant statistical differences, equal variances Tukey's test was used with ANOVA, respectively, and to compare the media of experimental groups, Student's *t*-test was used. The values for the statistical analyses are: \*,  $p \leq 0.05$ ; \*\*,  $p \leq 0.01$ ; \*\*\*,  $p \leq 0.001$ .

## 3. Results

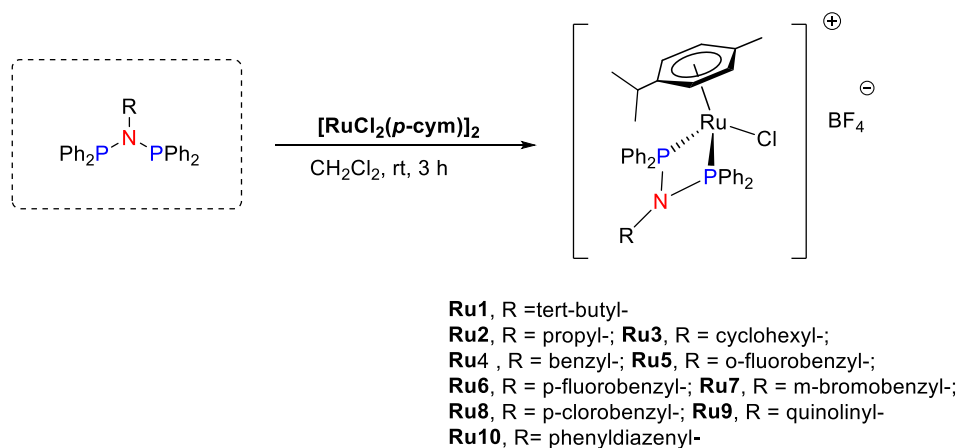
### 3.1. Synthesis and Characterization of Precursor Ligands and Ruthenium Compounds

At the outset, a new family of bis-phosphino-amines (PNP) ligands was synthesized. The new PNP ligands were obtained to expand the structure space previously covered and with the aim to generate new ruthenium therapeutic agents [36]. The PNP ligands (*L1–L10*) were directly obtained by condensing chlorophosphine with the corresponding amine in the presence of Et<sub>3</sub>N (Figure 2). Due to the abundance of commercial amines and phosphines, this methodology is very versatile to expand ligand sets for different purposes. To optimize the synthetic protocol, the reaction was monitored by <sup>31</sup>P-NMR. The ligands *L1–L10* were obtained in very good yields upon extraction with toluene. Even though PNP ligands are wide-angle bidentate ligands, mononuclear ruthenium compounds *Ru1–Ru10* were obtained after exposing the corresponding ligand to [RuCl<sub>2</sub>(*p*-cymene)]<sub>2</sub> in MeOH (Figure 2). Within a 30 min reaction time, an orange solution was observed and found to contain the mononuclear ruthenium derivative at a very good yield. *Ru0* was obtained following a procedure previously reported [36].

## Synthesis of precursor ligands



## Synthesis of Ruthenium compounds



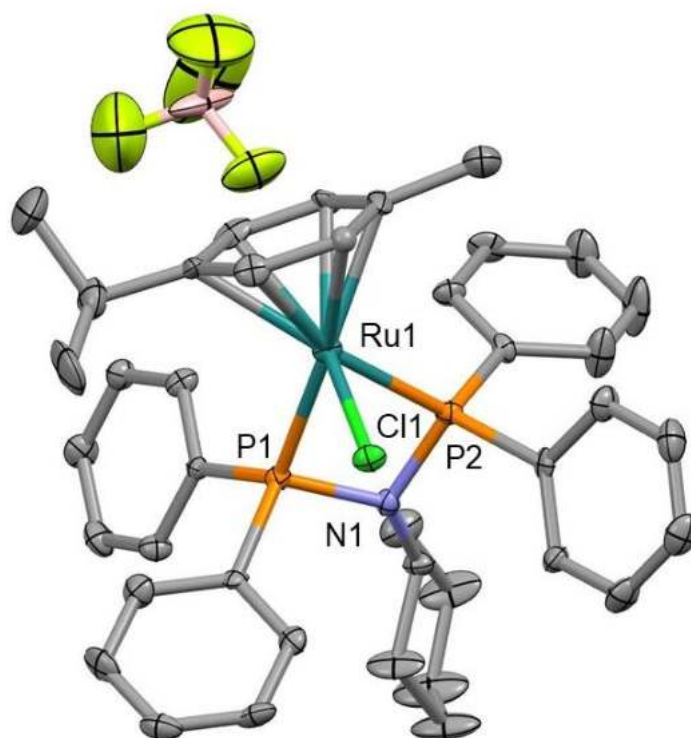
**Figure 2.** Synthesis of precursor ligands *L1–L10* and ruthenium compounds *Ru1–Ru10*.

The characterization of *L1–L10* and *Ru1–Ru10* were carried out by analytical methods, infrared (IR), ultraviolet-visible (UV-Vis), and nuclear magnetic resonance (NMR) spectroscopy. Structural elucidation is depicted in the experimental section and illustrated as representative examples of ligands and compounds in Figures S1–S5 in the Supporting Information. In the IR spectrum of *L1–L10* (solid state), the amine group manifested itself with a broad band around 1020–1250  $\text{cm}^{-1}$ , while a strong absorption around 1090  $\text{cm}^{-1}$  was attributed to the stretching vibration of the P–C moiety. The presence of two signals at 5.7–7.1 ppm and at 90–120 ppm in the  $^1\text{H}$  and  $^{13}\text{C}\{^1\text{H}\}$  NMR spectra of the ruthenium complexes, respectively, confirmed the presence of the *p*-cymene ligand in the coordination sphere. As expected, upon coordination to ruthenium, the peaks corresponding to the phenyl rings of the  $\text{PPh}_2$  moiety shifted downfield, as noted in the  $^1\text{H}$  NMR spectrum of complexes *Ru1–Ru10*. Explicitly, the characteristic signals for *L1–L10* in the complexes were downfield-shifted in all cases with regard to those of the free ligands. Moreover, the NMR patterns of the arene resonances supported the asymmetric nature of the resulting complexes. Indeed, the expected ABCD spin system for the *p*-cymene resonances was observed. The IR spectra of *Ru1–Ru10* exhibited a broad band around 300  $\text{cm}^{-1}$  for the



Ru–Cl [46,47], while a strong absorption in the range 1030–1050  $\text{cm}^{-1}$  was attributed to the stretching vibration of the P–C moiety. The UV-Vis absorption spectra of *L1–L10* and *Ru1–Ru10* were recorded in DMSO solutions ( $10^{-5}$  M) at 25 °C. *L1–L9* presented broad absorption bands centered at 278–290 nm, while *L10* presented intense and well-defined characteristic bands of quinoline moieties at 358 nm. The absorption spectra of the *Ru1–Ru10* compounds featured a very intense band attributed to  $\pi-\pi^*$  electronic transitions corresponding to the Ru-(*p*-cymene) moiety ( $\lambda = 250\text{--}304$  nm). A weak band is attributable to metal to ligand charge transfer transitions (MLCT) from Ru d orbitals to the  $\pi^*$  orbitals of the ligands (304–364 nm), and a shoulder assigned to d–d transitions (364–574 nm) [46].

Single crystals suitable for X-ray diffraction were obtained by slow evaporation of solutions of *Ru3* in  $\text{CH}_2\text{Cl}_2$ . Selected bond lengths and angles with estimated standard deviations are compiled in Table S1 and crystallographic refinement parameters are given in Table S2 in the Supporting Information. Figure 3 shows the ORTEP view of *Ru3* as a representative complex of the series. The structure shows the characteristic “three-legged piano-stool” conformation around the Ru center with a  $\eta^6$ -coordinated *p*-cymene ring [48,49]. Its solid-state structure revealed a distorted tetrahedral geometry with a P–Ru–P chelate angle of  $68.42(13)^\circ$ . The Ru–centroid distance for the *Ru3* complex has a value of 1.770 Å (Figure S7) and is standard compared to similar complexes [36]. The bond distance and angle values are comparable to those reported in the literature for ruthenium analogs [50].



**Figure 3.** MERCURY plot for the structure of complex *Ru3*. Thermal ellipsoids are given at the 30% probability level. Hydrogen atoms have been omitted for clarity. Selected bond distances (Å), Ru1–Cl1: 2.383(3) Å, Ru1–P1: 2.343(3) Å, Ru1–P2: 2.296(4) Å, N1–P1: 1.717(11) Å, N1–P2: 1.703(11) Å.

### 3.2. Stability of the Ruthenium Complexes in Solution

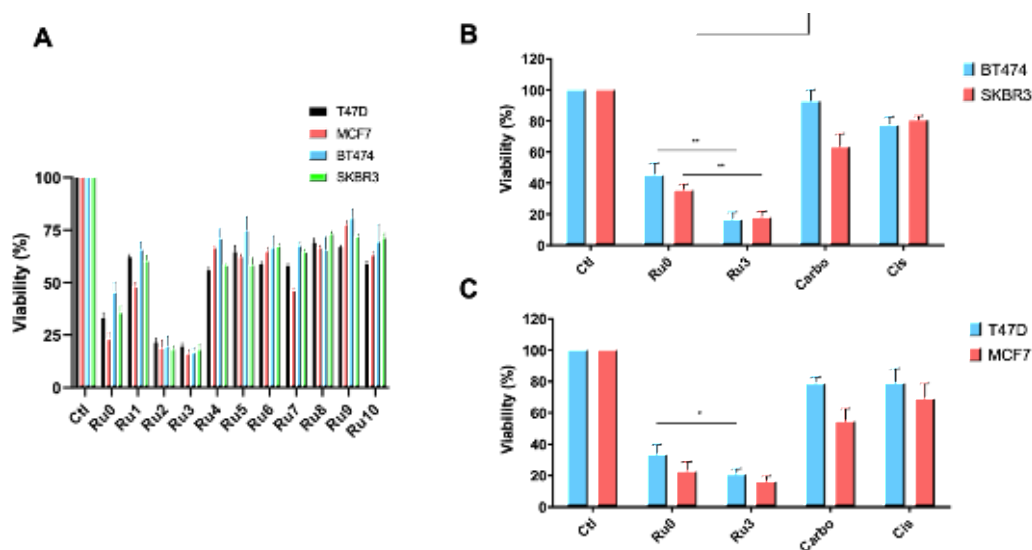
The ligands *L1–L10* were not soluble in water. *Ru1–Ru10* were air stable and soluble in chlorinated solvents, but not indefinitely stable upon air contact. According to NMR experiments, and as a representative example, *Ru3* completely degraded in chloroform after two weeks, with the orange/yellow solutions progressively turning to green and affording a complicated mixture of species. Qualitative tests determined that *Ru4–Ru8* are slightly soluble in water and very soluble in other polar solvents such as methanol and ethanol. *Ru9–Ru10* were sparingly soluble in water, but very soluble in some organic

solvents such as dichloromethane and dimethyl sulfoxide. The enhanced solubility of ruthenium compounds relative to the free ligands could be attributable to the blocking of the hydrogen-bonding acceptor atoms of the ligands after coordination. Regarding the PNP ligand influence, the non-aromatic derivatives gave better solubilities than the aromatic analogs because of the lower hydrophobicity. In any event, *Ru1–Ru10* were soluble enough to enable biological studies in aqueous media and circumvent hypothetical administration problems.

As it happens to many metallodrugs, the ruthenium compounds needed to be dissolved in a mixture of H<sub>2</sub>O:DMSO to perform biological assays which in any case did not exceed 0.25% *v/v* of DMSO. Therefore, the stability of the ruthenium compounds in DMSO-d<sup>6</sup> and DMSO-d<sup>6</sup>:D<sub>2</sub>O was carried out by NMR monitoring. The set of signals belonging to the starting ruthenium complex did not persist throughout the stability experiments carried out in DMSO-d<sup>6</sup> (25 °C). Partial release in different extents of the *p*-cymene ligand from *Ru1–Ru10* was observed due to the disruptive effect of DMSO (see Table S3 and Figure S6 as a representative example in the Supporting Information). However, this progressive dissociation is dismissed in the presence of water (Figure S7). The molar ratio between them remained constant in spectra recorded after one week in all the samples. In addition, the respective single set of resonances for the *p*-cymene ligand in the ruthenium compounds were not modified upon the addition of 0.15 mM NaCl. The existence of only one pattern for the ruthenium derivatives suggested ruling out fast chloride dissociation from *Ru1–Ru10*, analogously to that found for RAPTA-C [51]. The mechanism of action of RAPTA-C and its derivatives remains to be fully understood [52]. Although it is assumed that DNA is the target for metallodrugs, evidence suggests that, for certain compounds, proteins are likely involved in the therapeutic effect. It is well known that noncationic complexes underwent aquation to a notable extent, depending on the counterion and the chemical structure of the auxiliary ligand [53]. It is expected for *Ru0–Ru10* the formation of the more reactive aqua derivatives from their respective chloride precursors as the activation step for subsequent interaction with the biological targets.

### 3.3. Antiproliferative Efficacy of New Synthesized Ruthenium Compounds Compared to *Ru0* and Platins

In a previous study, we reported *Ru0* as the lead PNP-Ru compound by preliminary biochemical and biological studies in different breast cancer subtypes [37]. The results showed that complex *Ru0* is much more effective in promoting in vitro cytotoxic effect on HER2+ and RH+/HER2– breast cancer cell lines than the reference metallodrugs cisplatin, carboplatin, or RAPTA-C [35]. Therefore, a pharmacologic screening using *Ru1–Ru10* were performed in a panel of representative tumor cell lines of each subtype: luminal (RH+/HER2–: T47D and MCF7) and HER2+ (BT474 and SKBR3) (Figure 4A). As can be seen in Figure 4B,C, most ruthenium compounds showed better antiproliferative effects than platinum agents used as controls in all the cancer cell lines evaluated. *Ru2* and *Ru3* showed the highest cytotoxic activity, being *Ru3* the most active compound of all analyzed (see IC<sub>50</sub> values for T47D, MCF7, BT474, and SKBR3 cells of the most active ruthenium compounds *Ru0*, *Ru2*, and *Ru3* in Table 1). Ligands *L1–L10* did not show significant cytotoxicity with IC<sub>50</sub> > 1000 (see Table S5 in the Supporting Information). Importantly, *Ru3* displayed high cytotoxicity with IC<sub>50</sub> values lower than 1 μM, and was significantly more cytotoxic than cisplatin and carboplatin in the cancer cell lines studied. Notably, *Ru3* was found to be highly cytotoxic in both HER2+ and luminal breast cancer cell lines, suggesting a mode of action independent of the receptor status of the cells. The IC<sub>50</sub> values observed for *Ru3* were in the range for the most cytotoxic ruthenium complexes reported to date [35,54]. *Ru3* reports very low IC<sub>50</sub> values, confirming its high potential for breast cancer treatment (see IC<sub>50</sub> values of *Ru3* for all cell lines in Table 1). Otherwise, those ruthenium compounds with aromatic rings in the PNP moiety (*Ru4–Ru10*) did not reduce the cell viability by more than 50% at the concentration tested (Figure 4 and data not shown). These results clearly indicate that the substitution in the PNP moiety can lead to a significant increase in the cytotoxicity of the resulting complexes.



**Figure 4.** Impact in cell viability of ruthenium compounds at 1  $\mu\text{M}$ . (A) Screening of several ruthenium compounds by exploring cell viability in BT474, SKBR3, T47D, and MCF7 breast cancer cell lines for 72 h evaluated using MTTs. *Ru3* displayed the most anti-proliferative activity. The cytotoxic activity was evaluated at 1  $\mu\text{M}$  for 72 h by MTT metabolism between *Ru0*, carboplatin, and cisplatin in HER2+ (B) and luminal (C) cell lines. Data are the average  $\pm$  standard deviation (SD) of three independent experiments performed in triplicate. To determine significant statistical differences, Student's *t*-test was used. The values for the statistical analyses are: \*  $p \leq 0.05$ ; \*\*  $p \leq 0.01$ .

**Table 1.**  $\text{IC}_{50}$  values of the most active compounds in the different cell lines.

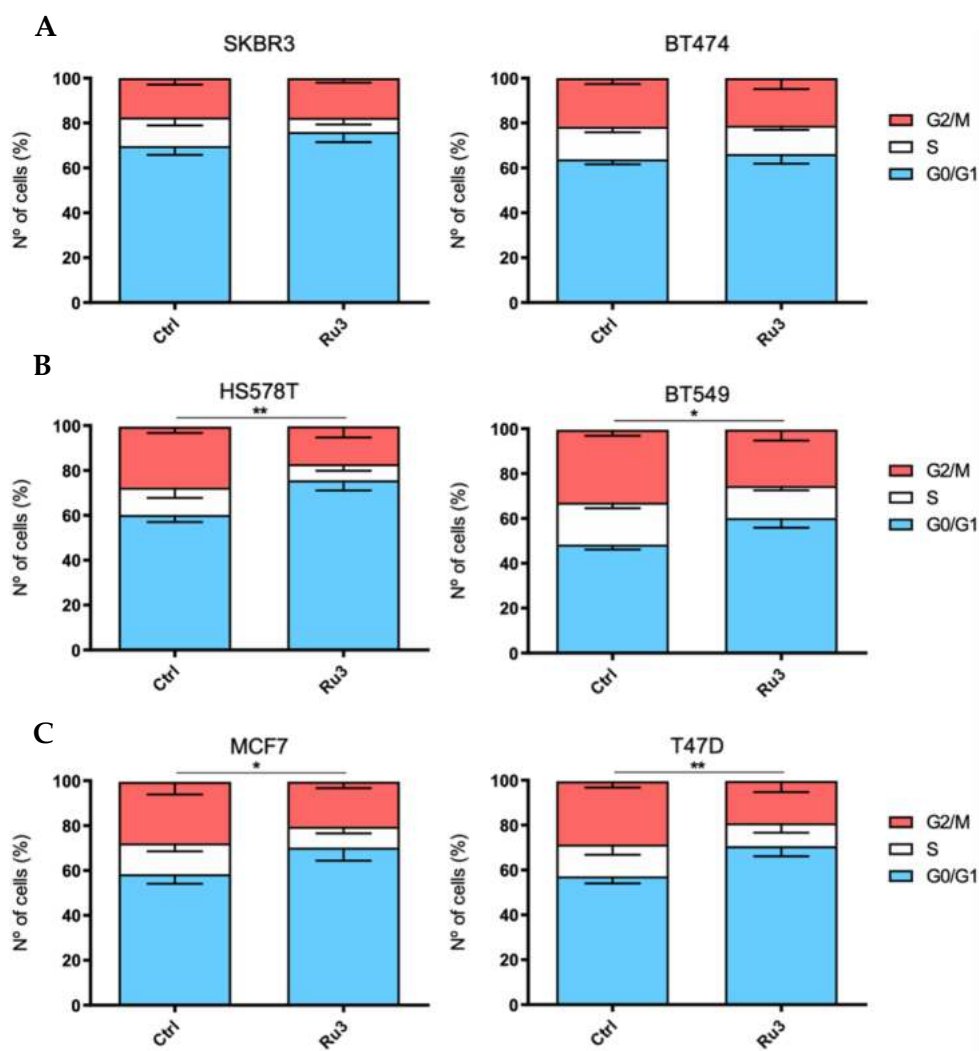
Cell Line	$\text{IC}_{50}$ (nM)		
	<i>Ru0</i>	<i>Ru2</i>	<i>Ru3</i>
HACAT	-	-	350
MCF7	300	45	15
T47D	450	60	10
HS578T	-	-	250
BT549	-	-	45
SKBR3	700	80	60
BT474	800	180	120
OVCAR8	-	-	300
SKOV3	-	-	170

Many factors could be involved in the cytotoxicity of the new ruthenium derivatives such as physical and chemical properties, target affinity, or even plausible interaction with other biomacromolecules. The relatively high activity exhibited by *Ru3* could be somehow related to the stability of the ruthenium complexes in biological media. Table S3 in the supporting information showed the high stability of these compounds in water which rule out any potential relationship between stability and cytotoxicity. On the other hand, the variability in the pharmacological profiles observed might depend on the ability of these compounds to penetrate biological membranes, which in turn is mainly dependent on lipophilicity factors [53]. In this context, calculated logarithmic octanol/water partition coefficients ( $\text{clogP}$ ) for *Ru1*–*Ru10* were obtained using the software Molinspiration. The variability of the substitution in the PNP moiety may explain the observed lipophilicity pattern. Figure S8 in the supporting information depicts the  $\text{logP}$  versus %MTTs transformed. A general trend in which the cytotoxicity could correlate with lipophilicity was not observed for these derivatives. In an effort to find a correlation between activity and affinity to proteins, the affinity to HSA of the most active compound of the series, *Ru3*, one of the less active, *Ru8*, and *Ru0* for comparison were obtained by UV-Vis absorption spectroscopy studies (see Table S4 in the Supporting Information). Unfortunately, a significant difference

in the  $K_a$  values was not observed between species which did not facilitate the discovery of any structure–activity relationship.

### 3.4. *Ru3* Exerts a G2/M Arrest in Breast Cancer Cell Lines

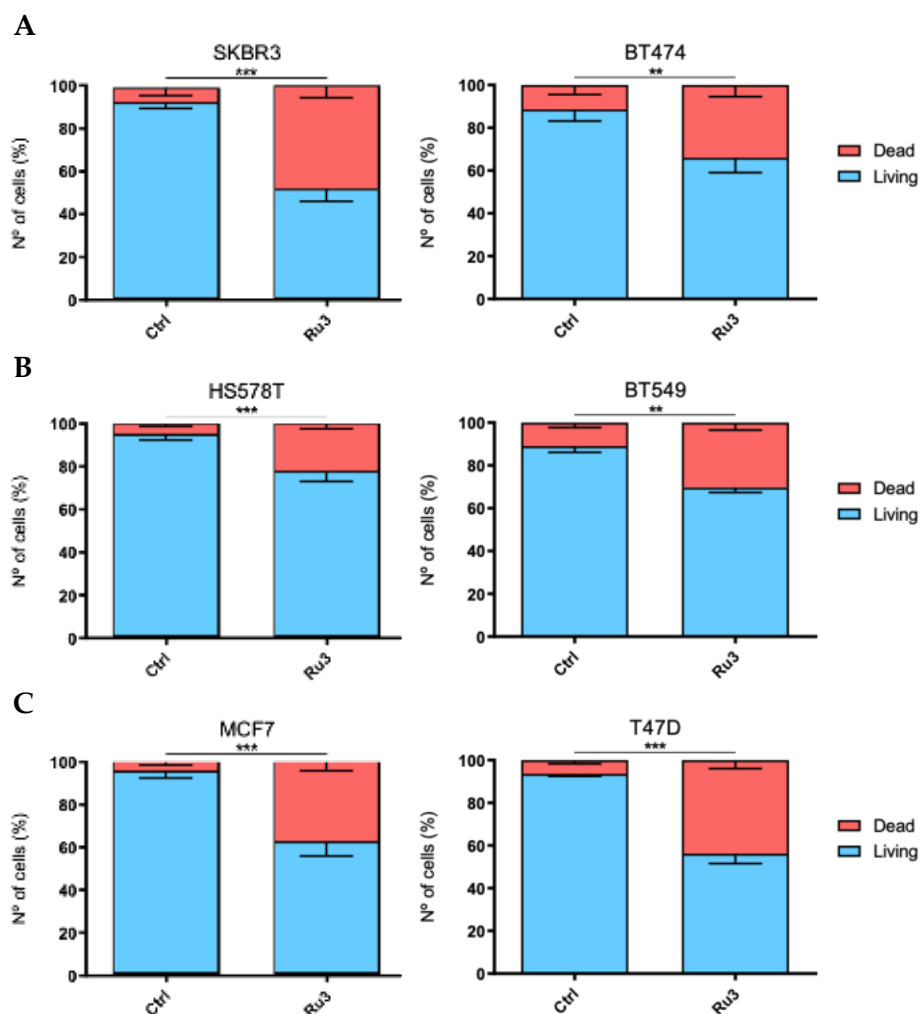
To further explore the effect of *Ru3* on cell viability, cell cycle analysis after a 24 h incubation period with *Ru3*-IC<sub>50</sub> was performed (Figure 5) (see representative FACS plots for cell cycle and apoptosis in Figure S9 in the Supporting Information). Due to the promising cytotoxicity results in luminal and HER2+ cell lines, we expanded our research to the three breast cancer subgroups, including the basal-like subtype. As a result, six cell lines (BT474 and SKBR3 as HER2+, T47D and MCF7 as luminal and HS578T, and BT549 as basal-like) were treated with either the vehicle or *Ru3* for 24 h and stained with propidium iodide/RNase solution. As shown in Figure 5, *Ru3* blocked cell cycle progression at the G0/G1 phases in all of the cell lines evaluated except for the HER2-positive subgroup (SKBR3 and BT474).



**Figure 5.** Evaluation of cell cycle impact exerted by *Ru3* in several breast cancer cell line models. Cell cycle progression was evaluated in HER2+ (A), basal (B), and luminal (C) cell lines by propidium iodide staining and cytometer evaluation after 24 h of IC<sub>50</sub> *Ru3* dose treatment for each cell line. Data are the average  $\pm$  standard deviation (SD) of three independent experiments performed in triplicate. To determine significant statistical differences between G0/G1 phase averages, Student's *t*-test was used. The values for the statistical analyses are: \*,  $p \leq 0.05$ ; \*\*,  $p \leq 0.01$ .

### 3.5. Ru3 Exerts Apoptotic-Based Cell Death in TNBC

On the basis of the cytotoxic results of *Ru3* in breast cancer cell lines, the mechanism of cell death induction was evaluated. We analyzed *Ru3* ability to induce apoptosis by flow cytometry as previously described [37,53,55–57]. The experiments were performed using an incubation time of 48 h, and *Ru3* concentrations corresponding to their respective  $IC_{50}$  value. Treatment with *Ru3* was able to significantly increase apoptosis in all the cell lines analyzed, (Figure 6), suggesting that the lead compound clearly induces cell death by apoptosis in a wide range of breast cancer cell lines.

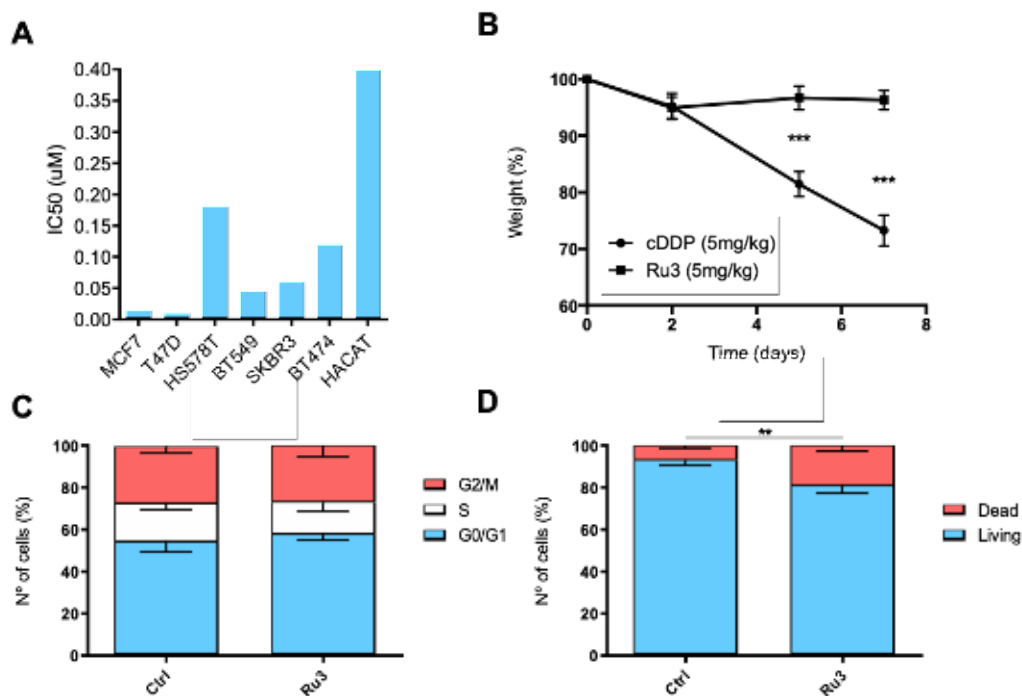


**Figure 6.** Evaluation of cell death mechanism exerted by *Ru3* in several breast cancer cell line models. Cell death was evaluated in HER2+ (A), basal (B), and luminal (C) cell lines by Annexin V/propidium iodide staining and cytometer evaluation after 48 h using the  $IC_{50}$  *Ru3* dose treatment specific each cell line. Data are the average  $\pm$  standard deviation (SD) of three independent experiments performed in triplicate. To determine significant statistical differences between living cells groups, Student's *t*-test was used. The values for the statistical analyses are: \*,  $p \leq 0.05$ ; \*\*,  $p \leq 0.01$ ; \*\*\*,  $p \leq 0.001$ .

### 3.6. Ru3 Is Less Toxic Than Cisplatin Using In Vitro and in In Vivo Studies

We next evaluated the in vitro effect of *Ru3* on the viability of non-tumoral cells. To this end, we used the non-transformed but immortalized keratinocytes cell line HACAT. Interestingly, *Ru3*, the most potent compound of the series, did not display significant toxicity in non-tumoral cells, showing  $IC_{50}$  values which doubled one of the transformed cell lines (Figure 7A and Table 1). The in vivo toxicity of *Ru3* and cisplatin was evaluated

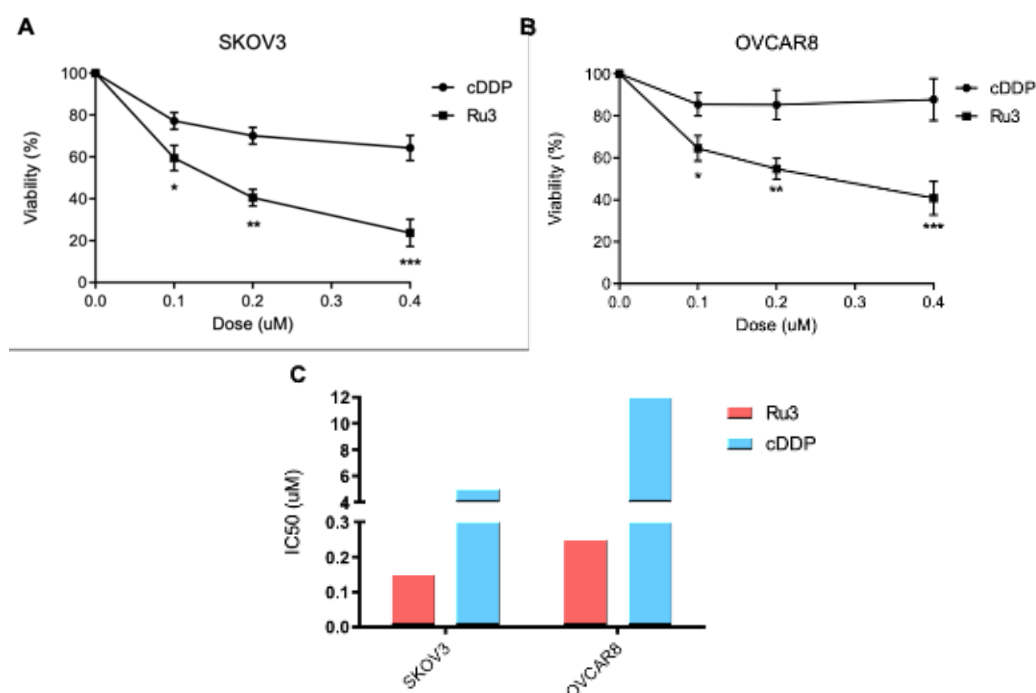
by measuring the animal body weight and their behavior. Treatment with *Ru3* and cisplatin was performed using 5 mg/kg intraperitoneal (IP) doses for seven consecutive days. As displayed in Figure 7B, *Ru3* did not induce significant weight loss compared with cisplatin where a 30% weight reduction was observed. No lethality was reported after seven days of treatment with both compounds. This data suggests that a repeated dose of *Ru3* is much better tolerated than cisplatin. On the other hand, in the HACAT cell line, the effects over cell cycle distribution were almost undetectable after 24 h at a 200 nM (Figure 7C), a treatment dose that would cause high toxicity on breast cancer cell lines. Moreover, the effect of that dose over cell death was weaker than the one caused to breast cancer cell lines, despite being statistically significant (Figure 7D).



**Figure 7.** *Ru3* displays less toxicity in non-transformed cells. (A) IC<sub>50</sub> comparison, measured by MTT metabolism, between breast cancer cell lines and HACAT, showing that the IC<sub>50</sub> of the non-transformed cell line at least doubles the value of the transformed cell lines. (B) *Ru3* shows lower toxicity in vivo than platinum compounds. Toxicity was evaluated after 7 days of IP treatment with 5 mg kg<sup>-1</sup> twice a week. *Ru3* (N = 6) exerted significantly less toxicity than cDDP (N = 6) at the 5 mg kg<sup>-1</sup> with a treatment schedule of two administrations a week. (C) The effect of *Ru3* in HACAT cell lines in terms of cell cycle arrest, demonstrating no modifications in any cell cycle phase. (D) Cell death was evaluated, and weaker effects were observed when compared to breast cancer cell lines at the dose of 200 nM. Data are the average ± standard deviation (SD) of three independent experiments performed in triplicate. To determine significant statistical differences between the averages of treatment groups, G0/G1 or living cells groups respectively, Student's *t*-test was used. The values for the statistical analyses are: \*,  $p \leq 0.05$ ; \*\*,  $p \leq 0.01$ ; \*\*\*,  $p \leq 0.001$ .

### 3.7. *Ru3* Is Also a Therapeutic Alternative in Ovarian Cancer

TNBC share many biological similarities with ovarian cancer including that both tumors display a high grade of antitumor sensitivity to platinum agents. In this context, we aimed to evaluate the activity of this agent in two well-characterized ovarian cancer cell lines, SKOV3 and OVCAR8, in comparison to cisplatin (cDDP) (Figure 8A,B). To detect differences, we used doses of cisplatin below their IC<sub>50</sub> (Figure 8C). As can be seen in Figure 8, cisplatin showed modest activity and the action of *Ru3* was much potent at the low doses used.



**Figure 8.** *Ru3* is a putative therapeutic candidate for ovarian cancer treatment. Viability of two ovarian cancer cell lines, OVCAR8 and SKOV3, was assayed by MTT metabolization after 72 h treatment with *Ru3* and cDDP, as a control, showing that *Ru3* developed more toxicity in both cell line models (A) and (B), as IC<sub>50</sub> values demonstrate (C). Data are the average  $\pm$  standard deviation (SD) of three independent experiments performed in triplicate. To determine significant statistical differences, Student's *t*-test was used. The values for the statistical analyses are: \*,  $p \leq 0.05$ ; \*\*,  $p \leq 0.01$ ; \*\*\*,  $p \leq 0.001$ .

#### 4. Discussion

Breast cancer is a heterogeneous disease where some genomic and clinical characteristics have classified this cancer into several subgroups. Among them, the triple-negative subtype harbors more aggressive behavior, and more therapeutic options are needed due to poor clinical outcomes. In addition, this tumor shares many similarities with ovarian cancer, such as the high grade of genomic instability or the special sensibility to DNA damaging agents including platinum compounds [58]. However, in both cases, after a specific period of time receiving treatment with platinum agents, progression is observed, and additional therapeutic options are needed.

In this context, the rapid development of drug-based metals other than platinum has placed organometallic ruthenium (II) complexes in the spotlight of interest for many drug designers over the last decade. The development of novel compounds in this scenario should fulfill two criteria, first, they must have an optimized toxicity profile, and secondly, their antitumoral activity should remain similar or improved compared with classical platinum agents such as

Cisplatin. In our case, both characteristics are included in the family of new agents described in this report.

Our previous studies allow us to validate PNP-Ru compounds as anticancer drugs for breast cancer therapy establishing a proof of concept for further optimization and characterization of novel agents. In this case, further rational modifications of the molecular structure were required to improve the pharmacological profile of these derivatives. A set of novel PNP ligands was designed to prepare an ample series of ruthenium(II) arene complexes, with the aim of fine-tuning the cytotoxic properties of these types of promising anticancer drugs. Our results suggest that slight modifications in the molecular structure of the PNP-Ru compounds is decisive for tuning its antitumoral activity.

In our work, we position *Ru3* as the lead compound of the series. Three reasons justify this approach: (1) *Ru3* is the most potent antitumoral compound of the series, able to induce

cell death without affecting non-transformed cells; (2) its antitumoral action is related to the activation of the intrinsic apoptotic pathway and displays a pharmacological profile that is maintained in cisplatin-resistant cells; (3) it shows less acute toxicity in vitro and in vivo than the reference metallodrug cisplatin and supporting its evaluation in different solid tumors where DNA-damaging agents have a role.

An interesting finding was the fact that *Ru3* induced a profound anti-tumoral effect in TNBC and ovarian cancer cell lines, and that the mechanism of action was mainly mediated by apoptotic cell death. Of note, only a slight increase in G0/G1 was detected, suggesting that the compound is cytotoxic rather than cytostatic. The relevant induction of apoptosis is shared by other metallodrugs such as platinum agents although our drug displayed a safer toxicity profile with a more antitumoral activity [9]. On the other hand, when compared with cisplatin, *Ru3* was less toxic in non-transformed cells and did not induce weight loss in animals after a maintenance dose administration. These findings, in addition to the clear antitumoral activity in vitro of *Ru3* compared with cisplatin or carboplatin, position this compound as a future alternative for clinical development. In addition, *Ru3* displayed a significant antitumoral activity in ovarian cancer, which suggests that these agents can cover a wide range of clinical necessities.

On the other hand, we acknowledge that the full mechanism of action of the compound has not been evaluated in this first study. We could speculate that induction of DNA could be one of those mechanisms, but not the principal, considering the significant induction of cell death observed after its administration. In this context, as an apoptotic inducer agent, combination with other agents acting on complementary molecular vulnerabilities could be exploited, such as the combination with anti-HER2 therapies. Our previous experience reinforces this approach.

## 5. Conclusions

In conclusion, the structure of *Ru3* might serve as the basis for the design of more active and less toxic antitumoral compounds and pave the way for the clinical development of these compounds as alternatives for the treatment of tumors. The simple accessible synthesis of this compound and its biological activity makes *Ru3* a good candidate for further evaluation in vivo as a potential chemotherapeutic agent against breast cancer.

**Supplementary Materials:** The following are available online at <https://www.mdpi.com/article/10.3390/pharmaceutics13101559/s1>, Figure S1:  $^1\text{H}$  NMR (400 MHz) spectrum of Ligands L3 ( $(\text{Ph}_2\text{P})_2\text{N}\{\text{C}_6\text{H}_{11}\}$ ), L6 ( $(\text{Ph}_2\text{P})_2\text{N}\{\text{C}_6\text{H}_4\text{F}\}$ ) and L9 ( $(\text{Ph}_2\text{P})_2\text{N}\{\text{C}_9\text{H}_6\text{N}\}$ ) in  $\text{CDCl}_3$ , Figure S2:  $^{13}\text{C}$  NMR (100 MHz) spectrum of Ligands L3 ( $(\text{Ph}_2\text{P})_2\text{N}\{\text{C}_6\text{H}_{11}\}$ ), L6 ( $(\text{Ph}_2\text{P})_2\text{N}\{\text{C}_6\text{H}_4\text{F}\}$ ) and L9 ( $(\text{Ph}_2\text{P})_2\text{N}\{\text{C}_9\text{H}_6\text{N}\}$ ) in  $\text{CDCl}_3$ , Figure S3:  $^1\text{H}$  NMR (400 MHz) spectrum of Complexes *Ru3* ( $[\text{RuCl}(\text{p-cym})\{(\text{Ph}_2\text{P})_2\text{N}\{\text{C}_6\text{H}_{11}\}\}][\text{BF}_4]$ ), *Ru6* ( $[\text{RuCl}(\text{p-cym})\{(\text{Ph}_2\text{P})_2\text{N}\{\text{C}_6\text{H}_4\text{F}\}\}][\text{BF}_4]$ ) and *Ru9* ( $[\text{RuCl}(\text{p-cym})\{(\text{Ph}_2\text{P})_2\text{N}\{\text{C}_9\text{H}_6\text{N}\}\}][\text{BF}_4]$ ) in  $\text{CDCl}_3$ , Figure S4:  $^{13}\text{C}$  NMR (100 MHz) spectrum of Complexes *Ru3* ( $[\text{RuCl}(\text{p-cym})\{(\text{Ph}_2\text{P})_2\text{N}\{\text{C}_6\text{H}_{11}\}\}][\text{BF}_4]$ ), *Ru6* ( $[\text{RuCl}(\text{p-cym})\{(\text{Ph}_2\text{P})_2\text{N}\{\text{C}_6\text{H}_4\text{F}\}\}][\text{BF}_4]$ ) and *Ru9* ( $[\text{RuCl}(\text{p-cym})\{(\text{Ph}_2\text{P})_2\text{N}\{\text{C}_9\text{H}_6\text{N}\}\}][\text{BF}_4]$ ) in  $\text{CDCl}_3$ , Figure S5: MS(ESI) spectra for *Ru1* ( $[\text{RuCl}(\text{p-cym})\{(\text{Ph}_2\text{P})_2\text{N}\{\text{C}_4\text{H}_9\}\}][\text{BF}_4]$ ) (*Ru1*), *Ru2* ( $[\text{RuCl}(\text{p-cym})\{(\text{Ph}_2\text{P})_2\text{N}\{\text{C}_3\text{H}_7\}\}][\text{BF}_4]$ ), and *Ru3* ( $[\text{RuCl}(\text{p-cym})\{(\text{Ph}_2\text{P})_2\text{N}\{\text{C}_6\text{H}_{11}\}\}][\text{BF}_4]$ ), Figure S6: Selected  $^1\text{H}$  spectra at different time of Complex *Ru3* ( $[\text{RuCl}(\text{p-cym})\{(\text{Ph}_2\text{P})_2\text{N}\{\text{C}_6\text{H}_{11}\}\}][\text{BF}_4]$ ) in  $\text{DMSO-d}_6$ . Selected region for aromatic and aliphatic, respectively, at different time of complex *Ru3*, Figure S7: Selected  $^1\text{H}$  spectra at different time of Complex *Ru3* ( $[\text{RuCl}(\text{p-cym})\{(\text{Ph}_2\text{P})_2\text{N}\{\text{C}_6\text{H}_{11}\}\}][\text{BF}_4]$ ) in  $\text{DMSO-d}_6$ : $\text{D}_2\text{O}$  / 1:3, Figure S8: Graph of %viability obtained from the MTT experiment vs  $\log P$ , Figure S9: FAC Plot for HS578T and BT549, Table S1: Principal bond distances and angles for compound *Ru3*, Table S2: Crystal data and structure refinement for compound *Ru3*, Table S3: Stability of *Ru1-Ru10* in  $\text{DMSO-d}_6$  monitoring by  $^1\text{H}$ -NMR, Table S4: Binding parameters ( $\pm 2\sigma$ ) obtained for the interaction of *Ru3* and *Ru8* with HSA compared to *Ru0*, Table S5:  $\text{IC}_{50}$  values for the most active compounds *Ru0*, *Ru2* and *Ru3*, and the ligands in every cell line used.

**Author Contributions:** Conceptualization, C.A.-M. and A.O.; methodology, F.J.C. and E.D.-J.; investigation, A.S., A.J., A.R.-D., F.J.C., E.D.-J. and J.A.C.-O.; resources, A.S., A.O. and A.L.-S.; writing—original draft preparation, C.A.-M. and A.J.; writing—review and editing, A.L.-S. and A.O.; supervi-



sion, C.A.-M., A.J. and J.A.C.-O. All authors have read and agreed to the published version of the manuscript.

**Funding:** We gratefully acknowledge the financial support from the Ministerio de Ciencia e Innovación y Agencia Estatal de la Investigación, Spain (Grant Nos. PID2020-117788RB-I00, PID2020-113661GB-I00, CTQ2017-84131-R and RED2018-102387-T Programa Redes Consolider), and Instituto de Salud Carlos III grant number PI16/01121. Alberto Ocaña's lab is supported by the Instituto de Salud Carlos III (ISCIII, PI19/00808); CRIS Cancer Foundation, ACEPAIN, and Diputación de Albacete.

**Institutional Review Board Statement:** Not applicable.

**Informed Consent Statement:** Not applicable.

**Acknowledgments:** A.J. and F.J.C. acknowledge ACEPAIN Cancer Foundation for the fellowships. E.D.-J. acknowledges University of Castilla-La Mancha for the fellowship.

**Conflicts of Interest:** The authors declare no conflict of interest. The funders had no role in the design of the study; in the collection, analyses, or interpretation of data; in the writing of the manuscript, or in the decision to publish the results.

## References

- Baliu-Piqué, M.; Pandiella, A.; Ocana, A. Breast Cancer Heterogeneity and Response to Novel Therapeutics. *Cancers* **2020**, *12*, 3271. [CrossRef]
- Aldea, M.; Andre, F.; Marabelle, A.; Dogan, S.; Barlesi, F.; Soria, J.-C. Overcoming Resistance to Tumor-Targeted and Immune-Targeted Therapies. *Cancer Discov.* **2021**, *11*, 874–899. [CrossRef]
- García-Alonso, S.; Ocaña, A.; Pandiella, A. *Trastuzumab Emtansine: Mechanisms of Action and Resistance, Clinical Progress, and Beyond*; Cell Press: Cambridge, MA, USA, 2020; Volume 6.
- Perou, C.M.; Børresen-Dale, A.-L. Systems Biology and Genomics of Breast Cancer. *Cold Spring Harb. Perspect. Biol.* **2011**, *3*, a003293. [CrossRef]
- Ocaña, A.; Pandiella, A. Identifying Breast Cancer Druggable Oncogenic Alterations: Lessons Learned and Future Targeted Options. *Clin. Cancer Res.* **2008**, *14*, 961–970. [CrossRef] [PubMed]
- Ocana, A.; Pandiella, A. Targeting Oncogenic Vulnerabilities in Triple Negative Breast Cancer: Biological Bases and Ongoing Clinical Studies. *Oncotarget* **2017**, *8*, 22218–22234. [CrossRef] [PubMed]
- Schneider, B.P.; Winer, E.P.; Foulkes, W.D.; Garber, J.; Perou, C.M.; Richardson, A.; Sledge, G.W.; Carey, L.A. Triple-Negative Breast Cancer: Risk Factors to Potential Targets. *Clin. Cancer Res.* **2008**, *14*, 8010–8018. [CrossRef] [PubMed]
- Tutt, A.; Tovey, H.; Cheang, M.C.U.; Kernaghan, S.; Kilburn, L.; Gazinska, P.; Owen, J.; Abraham, J.; Barrett, S.; Barrett-Lee, P.; et al. Carboplatin in BRCA1/2-Mutated and Triple-Negative Breast Cancer BRCAness Subgroups: The TNT Trial. *Nat. Med.* **2018**, *24*, 628–637. [CrossRef]
- Tchounwou, P.B.; Dasari, S.; Noubissi, F.K.; Ray, P.; Kumar, S. Advances in Our Understanding of the Molecular Mechanisms of Action of Cisplatin in Cancer Therapy. *J. Exp. Pharmacol.* **2021**, *13*, 303–328. [CrossRef]
- Murray, B.S.; Dyson, P.J. Recent Progress in the Development of Organometallics for the Treatment of Cancer. *Curr. Opin. Chem. Biol.* **2020**, *56*, 28–34. [CrossRef]
- Yousuf, I.; Bashir, M.; Arjmand, F.; Tabassum, S. Advancement of Metal Compounds as Therapeutic and Diagnostic Metallodrugs: Current Frontiers and Future Perspectives. *Coord. Chem. Rev.* **2021**, *445*, 214104. [CrossRef]
- Chang, L.; Ruiz, P.; Ito, T.; Sellers, W.R. Targeting Pan-Essential Genes in Cancer: Challenges and Opportunities. *Cancer Cell* **2021**, *39*, 466–479. [CrossRef] [PubMed]
- Anthony, E.J.; Bolitho, E.M.; Bridgewater, H.E.; Carter, O.W.L.; Donnelly, J.M.; Imberti, C.; Lant, E.C.; Lermyte, F.; Needham, R.J.; Palau, M.; et al. Metallodrugs Are Unique: Opportunities and Challenges of Discovery and Development. *Chem. Sci.* **2020**, *11*, 12888–12917. [CrossRef] [PubMed]
- Santi, M.; Mapanao, A.K.; Biancalana, L.; Marchetti, F.; Voliani, V. Ruthenium Arene Complexes in the Treatment of 3D Models of Head and Neck Squamous Cell Carcinomas. *Eur. J. Med. Chem.* **2021**, *212*, 113143. [CrossRef] [PubMed]
- Thota, S.; Rodrigues, D.A.; Crans, D.C.; Barreiro, E.J. Ru(II) Compounds: Next-Generation Anticancer Metallotherapeutics? *J. Med. Chem.* **2018**, *61*, 5805–5821. [CrossRef] [PubMed]
- Rausch, M.; Dyson, P.J.; Nowak-Sliwinska, P. Recent Considerations in the Application of RAPTA-C for Cancer Treatment and Perspectives for Its Combination with Immunotherapies. *Adv. Ther.* **2019**, *2*, 1900042. [CrossRef]
- Elsayed, S.A.; Harrypersad, S.; Sahyon, H.A.; El-Magd, M.A.; Walsby, C.J. Ruthenium(II)/(III) DMSO-Based Complexes of 2-Aminophenyl Benzimidazole with In Vitro and In Vivo Anticancer Activity. *Molecules* **2020**, *25*, 4284. [CrossRef]
- Alessio, E.; Messori, L. NAMI-A and KP1019/1339, Two Iconic Ruthenium Anticancer Drug Candidates Face-to-Face: A Case Story in Medicinal Inorganic Chemistry. *Molecules* **2019**, *24*, 1995. [CrossRef]

19. Trondl, R.; Heffeter, P.; Kowol, C.R.; Jakupec, M.A.; Berger, W.; Keppler, B.K. NKP-1339, the First Ruthenium-Based Anticancer Drug on the Edge to Clinical Application. *Chem. Sci.* **2014**, *5*, 2925–2932. [CrossRef]
20. Leijen, S.; Burgers, S.A.; Baas, P.; Pluim, D.; Tibben, M.; van Werkhoven, E.; Alessio, E.; Sava, G.; Beijnen, J.H.; Schellens, J.H.M. Phase I/II Study with Ruthenium Compound NAMI-A and Gemcitabine in Patients with Non-Small Cell Lung Cancer after First Line Therapy. *Investig. New Drugs* **2015**, *33*, 201–214. [CrossRef]
21. Dittrich, C.; Scheulen, M.E.; Jaehde, U.; Kynast, B.; Gneist, M.; Richly, H.; Schaad, S.; Arion, V.; Keppler, B.K. Phase I and Pharmacokinetic Study of Sodium Trans-[Tetrachlorobis(1H-Indazole)Ruthenate(III)]/Indazolehydrochloride (1:1.1) (FFC14A, KP1019) in Patients with Solid Tumors—A Study of the CESAR Central European Society for Anticancer Drug Research—EW. *Cancer Res.* **2005**, *65*, 110.
22. Chamberlain, S.; Cole, H.D.; Roque, J.; Bellnier, D.; McFarland, S.A.; Shafirstein, G. TLD1433-Mediated Photodynamic Therapy with an Optical Surface Applicator in the Treatment of Lung Cancer Cells In Vitro. *Pharmaceutics* **2020**, *13*, 137. [CrossRef] [PubMed]
23. Theralase Inc. A Phase II Clinical Study of Intravesical Photodynamic Therapy in Patients With BCG-Unresponsive Non-Muscle Invasive Bladder Cancer (“NMIBC”) Or Patients Who Are Intolerant to BCG Therapy (“Study”). 2021. Available online: <https://Clinicaltrials.gov> (accessed on 17 June 2021).
24. Gasser, G.; Ott, I.; Metzler-Nolte, N. Organometallic Anticancer Compounds. *J. Med. Chem.* **2011**, *54*, 3–25. [CrossRef] [PubMed]
25. Bergamo, A.; Masi, A.; Peacock, A.F.A.; Habtemariam, A.; Sadler, P.J.; Sava, G. In Vivo Tumour and Metastasis Reduction and in Vitro Effects on Invasion Assays of the Ruthenium RM175 and Osmium AFAP51 Organometallics in the Mammary Cancer Model. *J. Inorg. Biochem.* **2010**, *104*, 79–86. [CrossRef] [PubMed]
26. Morris, R.E.; Aird, R.E.; Murdoch, P.D.S.; Chen, H.; Cummings, J.; Hughes, N.D.; Parsons, S.; Parkin, A.; Boyd, G.; Jodrell, D.I.; et al. Inhibition of Cancer Cell Growth by Ruthenium(II) Arene Complexes. *J. Med. Chem.* **2001**, *44*, 3616–3621. [CrossRef] [PubMed]
27. Murray, B.S.; Babak, M.V.; Hartinger, C.G.; Dyson, P.J. The Development of RAPTA Compounds for the Treatment of Tumors. *Coord. Chem. Rev.* **2016**, *306*, 86–114. [CrossRef]
28. Steel, T.R.; Walsh, F.; Wieczorek-Błauż, A.; Hanif, M.; Hartinger, C.G. Monodentately-Coordinated Bioactive Moieties in Multimodal Half-Sandwich Organoruthenium Anticancer Agents. *Coord. Chem. Rev.* **2021**, *439*, 213890. [CrossRef]
29. Małecka, M.; Skoczyńska, A.; Goodman, D.M.; Hartinger, C.G.; Budzisz, E. Biological Properties of Ruthenium(II)/(III) Complexes with Flavonoids as Ligands. *Coord. Chem. Rev.* **2021**, *436*, 213849. [CrossRef]
30. Swaminathan, S.; Haribabu, J.; Kalagatur, N.K.; Nikhil, M.; Balakrishnan, N.; Bhuvanesh, N.S.P.; Kadirvelu, K.; Kolandaivel, P.; Karvembu, R. Tunable Anticancer Activity of Furoylthiourea-Based RuII–Arene Complexes and Their Mechanism of Action. *Chem. A Eur. J.* **2021**, *27*, 7418–7433. [CrossRef]
31. Maji, M.; Acharya, S.; Maji, S.; Purkait, K.; Gupta, A.; Mukherjee, A. Differences in Stability, Cytotoxicity, and Mechanism of Action of Ru(II) and Pt(II) Complexes of a Bidentate N,O Donor Ligand. *Inorg. Chem.* **2020**, *59*, 10262–10274. [CrossRef]
32. Mukherjee, A.; Acharya, S.; Purkait, K.; Chakraborty, K.; Bhattacharjee, A.; Mukherjee, A. Effect of N,N Coordination and RuII Halide Bond in Enhancing Selective Toxicity of a Tyramine-Based RuII (p-Cymene) Complex. *Inorg. Chem.* **2020**, *59*, 6581–6594. [CrossRef]
33. Song, L.; Bai, H.; Liu, C.; Gong, W.; Wang, A.; Wang, L.; Zhao, Y.; Zhao, X.; Wang, H. Synthesis, Biomacromolecular Interactions, Photodynamic NO Releasing and Cellular Imaging of Two [RuCl(Qn)(Lbpy)(NO)]X Complexes. *Molecules* **2021**, *26*, 2545. [CrossRef]
34. Munteanu, A.-C.; Notaro, A.; Jakubaszek, M.; Cowell, J.; Tharaud, M.; Goud, B.; Uivarosi, V.; Gasser, G. Synthesis, Characterization, Cytotoxic Activity, and Metabolic Studies of Ruthenium(II) Polypyridyl Complexes Containing Flavonoid Ligands. *Inorg. Chem.* **2020**, *59*, 4424–4434. [CrossRef]
35. Golbaghi, G.; Castonguay, A. Rationally Designed Ruthenium Complexes for Breast Cancer Therapy. *Molecules* **2020**, *25*, 265. [CrossRef]
36. Broomfield, L.M.; Alonso-Moreno, C.; Martin, E.; Shafir, A.; Posadas, I.; Ceña, V.; Castro-Osma, J.A. Aminophosphine Ligands as a Privileged Platform for Development of Antitumoral Ruthenium(II) Arene Complexes. *Dalton Trans.* **2017**. [CrossRef]
37. Corrales Sanchez, V.; Nieto-Jiménez, C.; Castro-Osma, J.A.; De Andrés, F.; Pacheco-Liñán, P.J.; Bravo, I.; Rodríguez Farinas, N.; Niza, E.; Domínguez-Jurado, E.; Lara-Sánchez, A. Screening and Preliminary Biochemical and Biological Studies of [RuCl(p-Cymene)(N, N-Bis(Diphenylphosphino)-Isopropylamine)][BF<sub>4</sub>] in Breast Cancer Models. *ACS Omega* **2019**, *4*, 13005–13014. [CrossRef]
38. Sheldrick, G. *Sadabs, Program for Empirical Absorption Correction of Area Detector Data*; University of Göttingen: Göttingen, Germany, 1996; undefined.
39. Altomare, A.; Burla, M.C.; Camalli, M.; Cascarano, G.L.; Giacovazzo, C.; Guagliardi, A.; Moliterni, A.G.G.; Polidori, G.; Spagna, R. SIR97: A New Tool for Crystal Structure Determination and Refinement. *J. Appl. Cryst.* **1999**, *32*, 115–119. [CrossRef]
40. Farrugia, L.J. WinGX Suite for Small-Molecule Single-Crystal Crystallography. *J. Appl. Crystallogr.* **1999**, *32*, 837–838. [CrossRef]
41. Sheldrick, G.M. Crystal Structure Refinement with SHELXL. *Acta Cryst. C* **2015**, *71*, 3–8. [CrossRef] [PubMed]
42. Lakowicz, J.R. *Principles of Fluorescence Spectroscopy*, 3rd ed.; Springer: New York, NY, USA; ISBN ISBN 978-0-387-31278-1.
43. Zhang, M.; Lv, Q.; Yue, N.; Wang, H. Study of Fluorescence Quenching Mechanism between Quercetin and Tyrosine-H<sub>2</sub>O<sub>2</sub>-Enzyme Catalyzed Product. *Spectrochim. Acta A Mol. Biomol. Spectrosc.* **2009**, *72*, 572–576. [CrossRef] [PubMed]

44. Feng, X.Z.; Lin, Z.; Yang, L.J.; Wang, C.; Bai, C.L. Investigation of the Interaction between Acridine Orange and Bovine Serum Albumin. *Talanta* **1998**, *47*, 1223–1229. [CrossRef]
45. Rimoldi, I.; Facchetti, G.; Lucchini, G.; Castiglioni, E.; Marchianò, S.; Ferri, N. In Vitro Anticancer Activity Evaluation of New Cationic Platinum(II) Complexes Based on Imidazole Moiety. *Bioorg. Med. Chem.* **2017**, *25*, 1907–1913. [CrossRef] [PubMed]
46. Guimarães, I.D.L.; Marszaukowski, F.; Ribeiro, R.; de Lazaro, S.R.; de Oliveira, K.M.; Batista, A.A.; Castellen, P.; Wrobel, E.; Garcia, J.R.; Boéré, R.T.; et al. Synthesis and Characterization of H6-p-Cymene Ruthenium(II) Complexes Containing Alkyl- and Methoxy-Substituted Triarylphosphines. *J. Organomet. Chem.* **2021**, *931*, 121599. [CrossRef]
47. Higuera-Padilla, A.R.; Batista, A.A.; Colina-Vegas, L.; Villarreal, W.; Colnago, L.A. Synthesis of the [(H6-p-Cymene)Ru(Dppb)Cl]PF<sub>6</sub> Complex and Catalytic Activity in the Transfer Hydrogenation of Ketones. *J. Coord. Chem.* **2017**, *70*, 3541–3551. [CrossRef]
48. Sari, O.; Schüttler, A.; Lönnecke, P.; Bednarski, P.J.; Hey-Hawkins, E.; Karakus, M. Synthesis, Structure and in Vitro Anticancer Activity of Ruthenium(II) and Platinum(II) Complexes with Chiral Aminophosphine Ligands. *Transit. Met. Chem.* **2021**, *46*, 299–305. [CrossRef]
49. Diaz, A.A.; Young, J.D.; Khan, M.A.; Wehmschulte, R.J. Facile Synthesis of Unsymmetrical 9-Phospha- and 9-Arsafluorenes. *Inorg. Chem.* **2006**, *45*, 5568–5575. [CrossRef]
50. Mazzeo, P.P.; Bacchi, A.; Pelagatti, P. Crystal Engineering Guidelines for Ruthenium Based Wheel-and-Axle Compounds. *Coord. Chem. Rev.* **2020**, *414*, 213302. [CrossRef]
51. Biancalana, L.; Zacchini, S.; Ferri, N.; Lupo, M.G.; Pampaloni, G.; Marchetti, F. Tuning the Cytotoxicity of Ruthenium(II) Para-Cymene Complexes by Mono-Substitution at a Triphenylphosphine/Phenoxydiphenylphosphine Ligand. *Dalton Trans.* **2017**, *46*, 16589–16604. [CrossRef]
52. Adhireksan, Z.; Davey, G.E.; Campomanes, P.; Groessel, M.; Clavel, C.M.; Yu, H.; Nazarov, A.A.; Yeo, C.H.F.; Ang, W.H.; Dröge, P.; et al. Ligand Substitutions between Ruthenium-Cymene Compounds Can Control Protein versus DNA Targeting and Anticancer Activity. *Nat. Commun.* **2014**, *5*, 3462. [CrossRef]
53. Martínez-Alonso, M.; Busto, N.; Jalón, F.A.; Manzano, B.R.; Leal, J.M.; Rodríguez, A.M.; García, B.; Espino, G. Derivation of Structure-Activity Relationships from the Anticancer Properties of Ruthenium(II) Arene Complexes with 2-Aryldiazole Ligands. *Inorg. Chem.* **2014**, *53*, 11274–11288. [CrossRef]
54. Pettinari, R.; Marchetti, F.; Condello, F.; Pettinari, C.; Lupidi, G.; Scopelliti, R.; Mukhopadhyay, S.; Riedel, T.; Dyson, P.J. Ruthenium(II)-Arene RAPTA Type Complexes Containing Curcumin and Bisdemethoxycurcumin Display Potent and Selective Anticancer Activity. *Organometallics* **2014**, *33*, 3709–3715. [CrossRef]
55. Cimas, F.J.; Niza, E.; Juan, A.; Noblejas-López, M.D.M.; Bravo, I.; Lara-Sanchez, A.; Alonso-Moreno, C.; Ocaña, A. Controlled Delivery of BET-PROTACs: In Vitro Evaluation of MZ1-Loaded Polymeric Antibody Conjugated Nanoparticles in Breast Cancer. *Pharmaceutics* **2020**, *12*, 986. [CrossRef] [PubMed]
56. Niza, E.; Noblejas-López, M.D.M.; Bravo, I.; Nieto-jiménez, C.; Castro-osma, J.A.; Canales-vázquez, J.; Lara-sanchez, A.; Moya, E.M.G.; Burgos, M.; Ocaña, A.; et al. Trastuzumab-Targeted Biodegradable Nanoparticles for Enhanced Delivery of Dasatinib in HER2+ Metastatic Breast Cancer. *Nanomaterials* **2019**, *9*, 1793. [CrossRef] [PubMed]
57. Niza, E.; Nieto-Jiménez, C.; Noblejas-López, M.D.M.; Bravo, I.; Castro-Osma, J.A.; De La Cruz-Martínez, F.; Martínez de Sarasa Buchaca, M.; Posadas, I.; Canales-Vázquez, J.; Lara-Sanchez, A. Poly (Cyclohexene Phthalate) Nanoparticles for Controlled Dasatinib Delivery in Breast Cancer Therapy. *Nanomaterials* **2019**, *9*, 1208. [CrossRef] [PubMed]
58. Manzano, A.; Ocaña, A. Antibody-Drug Conjugates: A Promising Novel Therapy for the Treatment of Ovarian Cancer. *Cancers* **2020**, *12*, 2223. [CrossRef]



Review

# A Review of Repurposed Cancer Drugs in Clinical Trials for Potential Treatment of COVID-19

Bárbara Costa <sup>1,2</sup> and Nuno Vale <sup>1,2,\*</sup>

<sup>1</sup> OncoPharma Research Group, Center for Health Technology and Services Research (CINTESIS), Rua Dr. Plácido da Costa, 4200-450 Porto, Portugal; b.c.211297@gmail.com

<sup>2</sup> Department of Community Medicine, Health Information and Decision (MEDCIDS), Faculty of Medicine, University of Porto, Al. Prof. Hernâni Monteiro, 4200-319 Porto, Portugal

\* Correspondence: nunovale@med.up.pt; Tel.: +351-225-513-622

**Abstract:** The pandemic of the coronavirus disease 2019 (COVID-19) represents an unprecedented challenge to identify effective drugs for prevention and treatment. While the world's attention is focused on news of COVID-19 vaccine updates, clinical management still requires improvement. Due to the similarity of cancer-induced inflammation, immune dysfunction, and coagulopathy to COVID-19, anticancer drugs, such as Interferon, Pembrolizumab or Bicalutamide, are already being tested in clinical trials for repurposing, alone or in combination. Given the rapid pace of scientific discovery and clinical data generated by the large number of people rapidly infected, clinicians need effective medical treatments for this infection.

**Keywords:** drug repurposing; COVID-19; cancer; pandemic; vaccination

**Citation:** Costa, B.; Vale, N. A Review of Repurposed Cancer Drugs in Clinical Trials for Potential Treatment of COVID-19. *Pharmaceutics* **2021**, *13*, 815. <https://doi.org/10.3390/pharmaceutics13060815>

Academic Editor: Hassan Bousbaa

Received: 28 April 2021

Accepted: 28 May 2021

Published: 30 May 2021

**Publisher's Note:** MDPI stays neutral with regard to jurisdictional claims in published maps and institutional affiliations.



**Copyright:** © 2021 by the authors. Licensee MDPI, Basel, Switzerland. This article is an open access article distributed under the terms and conditions of the Creative Commons Attribution (CC BY) license (<https://creativecommons.org/licenses/by/4.0/>).

## 1. Introduction

The coronavirus disease 2019 (COVID-19) pandemic, caused by the severe acute respiratory syndrome coronavirus-2 (SARS-CoV-2), has caused catastrophic damage to human life. Since December 2019, the pandemic has spread worldwide and still is ongoing. SARS-CoV-2 primarily infects the upper and lower respiratory tract; however, it can also affect other vital organs. Most people recover from the acute phase of the disease, but some people continue to experience a range of effects for months after recovery. Clinical management is currently focused on supportive care and prevention and control of complications such as acute respiratory distress syndrome (ARDS) [1].

Although the world's attention is understandably centred on reports of COVID-19 vaccine updates, from supply to administration, the need for treatments cannot be overlooked, as vaccination cannot protect everybody and as infection overwhelms hospitals and nursing homes. When we compare COVID-19 to the common flu, which is routinely targeted and has readily available and effective vaccines, we can see that no vaccine is ideal. Therefore, flu medications are still in high demand to avoid hospitalization and save lives. While the rise of new variants of COVID-19 threatens the efficacy of the available vaccines, it is critical that we must continue researching therapies to minimize hospitalization and cure COVID-19. The world health organization created (WHO) guidelines on using vaccines and antivirals during influenza pandemics to address the shortage of vaccines and antivirals [2]. Demonstrating that with therapy, people can live longer and gain control over the pandemic's curse, as the likelihood of people becoming ill and spreading the disease decreases. Therapeutics also can be used as prophylactics to prevent hospitalizations and severe cases of the disease.

The food and drug administration (FDA) granted emergency use authorization to two monoclonal antibody treatments for non-hospitalized adults and children over the age of 12 who have mild to moderate COVID-19 symptoms, who are at risk for developing severe COVID-19 or being hospitalized for it. Regeneron's casirivimab and imdevimab combo and

Eli Lilly's bamlanivimab and etesevimab combination are the two treatments. Prior approval for the single use of bamlanivimab to treat COVID-19 was withdrawn in April 2021 due to new data revealing minimal efficacy [3]. While these medications can be beneficial, the need for intravenous administration (IV) requires a visit to a clinic or hospital immediately after symptoms appear, which limits their use.

Consequently, effective therapies, which are available to anyone who needs them, must work with various populations and ensure that the responses to the pandemic are globally successful and inclusive. Having both important tools in our arsenal would ensure that most of the population is shielded from the severe effects of COVID-19. However, the development of novel antiviral drugs needs long-term investigation in clinical trials. Therefore, the benefit of repurposing drugs to justify off-label usage is linked to the established safety profile. However, it may vary depending on the disease and the consolidated data on pharmacodynamics, pharmacokinetics and efficacy in phase I–IV trials [4,5]. Some host cell targets that interfere with the viral growth cycle, such as kinases, are commonly shared in the mechanisms of multiple viral infections and other conditions such as cancer, indicating the possibility of translating information through medical disciplines and disease models [6].

Several anticancer compounds were investigated as possible future drugs for COVID-19, among the thousands of coronavirus drugs studied. This article includes anticancer drugs that have already been approved or are being fast-tracked by regulatory authorities, supported by published evidence and used to treat the treatment of cancer patients. In times of crisis, such as COVID-19, drug repurposing is a valuable technique because it provides quick access to agents with not only accessible safety data but also defined manufacturing lines and supply chains, which facilitates the process of discovery. The major limitation of the use of repurposed therapeutics is associated with dosage regimens. Most of the time, effective concentrations needed for antiviral activity are often higher than those clinically attainable under the approved regimens [7].

Drug repurposing is not a reason for designing low-quality clinical trials or emphasizing the bias of early outcomes and uncontrolled cohorts, and it is desirable to use molecules with a specified safety profile. In addition, these therapies have early- and late-phase data on toxicity and complications management, which are especially helpful in the setting of a pandemic versus novel therapies. Several antineoplastic agents have the potential to improve COVID-19 outcomes by using the exact mechanisms and targets used in cancer treatment [8]. These targets are primarily associated with inhibiting cell division, regulating inflammation, and modulating the host-tumor microenvironment.

## 2. Materials and Methods

Using the OpenData Portal [9] was possible to research COVID-19-related drug repurposing data and experiments for all approved drugs. From this portal were only selected the anticancer drugs tested. Then was searched on the database of clinicaltrials.gov [10], the list of anticancer drugs tested on COVID-19 to see which were listed in clinical trials (20 May 2021). Additionally, searching through the site of European Pharmaceutical Review [11], in the news section, we were able to find more information about repurposed drugs and clinical trials for COVID-19. In the end, it was possible to formulate an updated list of anticancer drug candidates for COVID-19 treatment.

## 3. Viral, Host and Immune Targets in COVID-19

Antiviral therapy and prevention approaches are focused on (a) inhibiting the replication of the viral genome by either preventing the virus from entering the host cells or suppressing one or more phases of replication; (b) boosting the immune system and producing a type of antiviral memory via vaccination; (c) injection of antiviral antibodies generated in the plasma [12].

SARS-CoV-2 replicates similarly to other Coronaviridae viruses. Coronaviruses can infect the host through both endosomal and non-endosomal (cell surface) routes. The viral

protein kinases and their associated signaling cascades have now been targeted in order to reduce coronavirus replication, particularly SARS-CoV-2. The virus can enter the cells via endocytosis or plasma membrane fusion through the interaction between the Spike (S) protein of the virus and angiotensin-converting enzyme 2 (ACE2) and transmembrane protease serine 2 (TMPRSS2) at the target cell [12,13].

After receptor-mediated endocytosis of the virus into the host cells, the virus releases the viral genome (single-stranded positive RNA) and uses the host ribosome to translate into viral polyproteins. Viral proteinases 3CLpro and PLpro cleave viral polyproteins into effector proteins (see Appendix A). RNA-dependent RNA polymerase, in turn, synthesizes a full-length negative-strand RNA template, which is used to make more viral genomic RNA. The viral genome then is synthesized by genomic replication, and four essential structural viral proteins (nucleocapsid (N), spike (S), membrane (M) and envelope (E)) are produced by transcription and translation [14]. The N protein binds genomic RNA, while S, M and E proteins are integrated into the membrane of the endoplasmic reticulum (ER), forming ERGIC—endoplasmic reticulum-Golgi intermediate compartment (also referred to as a vesicular-tubular cluster). The assembled nucleocapsid with helical twisted RNA is encapsulated into the ER lumen, viral progeny is transported by the ERGIC toward the plasma membrane of the host cell, and finally, the daughter virus is released by exocytosis [15].

The SARS-CoV-2 infection activates both innate and adaptive immune responses in the host. Patients with severe COVID-19 have a lower number of natural killer (NK) cells and a higher level of the C-reactive protein. The early failure of antiviral immunity during SARS-CoV-2 infection is correlated with a significant decrease in total T cells and NK cells [16].

Exploring potential clinical targets for COVID-19 attenuation is critical for long-term COVID-19 treatment.

#### 4. Similarities of Cancer Immune Response and COVID-19

Cancer treatment is still a major challenge, but tremendous progress in anticancer drug discovery and development has occurred in the last few decades. The spent decades developing drugs for cancer-induced inflammation, immune dysfunction, and vascularization provided us with a number of drug options that could be useful in the treatment of other diseases.

Patients affected by COVID-19 also display inflammation, immune dysfunction and vascular syndrome dysfunction [17].

Evidence suggests that the immune response to SARS-CoV-2 can play different roles: dysregulated immune responses in critically ill patients with COVID-19 is reflected by lymphopenia, mainly affecting CD4<sup>+</sup> T cells, including effector, memory, and regulatory T cells, and decreased IFN- $\gamma$  expression in CD4<sup>+</sup> T cells. Exhaustion of cytotoxic T lymphocytes, activation of macrophages, and a low human leukocyte antigen-DR expression on CD14 monocytes has been noted in patients with COVID-19 [18]. These similarities led scientists to consider anticancer therapy for the management of COVID-19 [8].

Furthermore, the homeostasis maintained by the vascular endothelium in health is affected by COVID-19 infection. In clinical studies, patients with COVID-19 have higher levels of fibrinogen, fibrin degradation products, and D-dimer, which appear to be related to disease severity and thrombotic risk [17]. Since the susceptibility to thrombotic events tends to be, at least in part, linked to inflammation and activation of the innate immune system that can cause systemic coagulation pathways. Therefore, the counterparts between the mechanisms of immunotherapy-related toxicities and the COVID-19 cytokine storm must be well considered in order not to affect the efficiency of the reused drug and increase the risk of the disease.

## 5. Repurposing Anticancer Drugs against COVID-19

The drug repurposing approach puts the drug discovery process on a fast track. COVID-19 researchers' attention to its potential growth is wider in a range of different scientific fields. Due to the availability of in-vitro and in-vivo screening data, chemical optimization, toxicity studies, bulk manufacturing, formulation development and pharmacokinetic profiles of FDA-approved drugs, drug development cycles are shortened as all these critical steps can be bypassed [7,8]. In addition, there is no need for larger investments and repurposed drugs are proven to be safe in preclinical models, thus lowering the attrition rates as well. The main advantage of drug repurposing is associated with the established safety of the known candidate compounds. The development time frame and costs are substantially reduced when advancing a candidate into a clinical trial, which is possible without neglecting the comorbidities already associated with certain medications not to aggravate the patient condition provoked by the viral infection [6].

Several drugs that have been approved for cancer indication by the US FDA are now in COVID-19 clinical trials to test their efficiency in reducing mortality and speed up recovery. The following Tables 1–6 represent anticancer drugs in clinical trials for COVID-19. In this review, we explore according to different categories of therapies which drugs represent more or fewer advantages for COVID-19. Appendix A is an updated list of all the anticancer drugs we could find or drugs used for the best supportive cancer care, which are being tested on their effectiveness to treat patients with mild to severe SARS-CoV-2.

**Table 1.** Anticancer drugs in clinical trials for COVID-19: Interferon-based therapies.

Anticancer Drug	Viral—Host Targets	Mechanism of Action	Combination	Primary End-Point	Source (20 May 2021)
IFN	Jak1 and Tyk2	Jak1 and Tyk2	-	Negative SARS-CoV-2 RNA on a nasopharyngeal swab	[10]
	Jak1 and Tyk2	Jak1 and Tyk2	-		
IFN-B1A	Jak1 and Tyk2	Jak1 and Tyk2	-	Clinical Improvement	[10]
		Jak1 and Tyk2	Lopinavir, ritonavir	Percentage of subjects reporting severity	
			Hydroxychloroquine, lopinavir, ritonavir	Reduce Mortality	
			Hydroxychloroquine, lopinavir, ritonavir, umifenovir	Time to clinical improvement	
IFN beta 1b	Jak1 and Tyk2	Jak1 and Tyk2	Remdesivir	Clinical improvement	[10]
			ribavirin	Reduce hospitalisation	
IFN-A2B	activate two Jak (Janus kinase) tyrosine kinases (Jak1 and Tyk2)	activate two Jak (Janus kinase) tyrosine kinases (Jak1 and Tyk2)	-	Improvement in FMTVDM Measurement with nuclear imaging	[10]
			-	Incidence of adverse events	
IFN-B1A/B	Jak1 and Tyk2	Jak1 and Tyk2	Hydroxychloroquine, lopinavir, ritonavir	Time to clinical improvement	[10]
IFN-B1B	Jak1 and Tyk2	Jak1 and Tyk2	Hydroxychloroquine, lopinavir, ritonavir	Time to negative NPS viral load	[10]
	Jak1 and Tyk2	Jak1 and Tyk2	Ribavirin, lopinavir, ritonavir	Time to negative NPS	

**Table 2.** Anticancer drugs in clinical trials for COVID-19: Anti-cytokine agents.

Anticancer Drug	Viral—Host Targets	Mechanism of Action	Combination	Primary End-Point	Source (20 May 2021)
Thalido-mide	Inhibition of inflammatory cytokine production	Inhibit the producti-on of interleukin (IL)-6	-	Time to clinical recovery	[10]
Siltuximab	Interleukin-6	Interleukin-6	-	The proportion of patients Requiring ICU admission at any time	[11]
			-	Mortality in siltuximab treated patients	
			Anakinra	Time to clinical improvement	
			tocilizumab	Ventilator-free days	

**Table 3.** Anticancer drugs in clinical trials for COVID-19: Immune-checkpoint inhibitors.

Anticancer Drug	Viral—Host Targets	Mechanism of Action	Combination	Primary End-Point	Source (20 May 2021)
PD-1 blocking antibody	PD-1	Can prevent the tumor cell from binding PD-1	-	Lung injury score	[10]
Nivolumab	PD-1/PD-L1 pathway blockade	Immune homeostasis restoration	-	Time to clinical improvement	[10]
			-	Efficacy and safety	[10]
			-	Viral clearance kinetics	[10]
			Tocilizumab	Percentage of patients with the normalisation of SpO <sub>2</sub> ≥96% in room air	[10]

**Table 4.** Anticancer drugs in clinical trials for COVID-19: Hormone therapy.

Anticancer Drug	Viral—Host Targets	Mechanism of Action	Combination	Primary End-Point	Source (6 February 2021)
Bicalutami-de	Downregulates TMPRSS2	Binding of androgen receptor	-	COVID-19 symptom relief	[9]
			Camostat	Reduce number of participants requiring hospitalization	
Enzalutami-de	Reduce androgen driven morbidity in COVID-19	Competitive binder of androgens	-	Time to worsening of disease	[9]
Toremifene	Interaction with coronavirus proteins	Inhibition of viral membranes fusion with Host cell endosomes	Melatonin	Clinical improvement	[10]
Tamoxifen	Decreased the PGE2 production	Compete with 17β-estradiol (E <sub>2</sub> ) at the receptor site	-	Lung injury score	[9]



**Table 5.** Anticancer drugs in clinical trials for COVID-19: The inhibitor of elongation factor 1A and the eukaryotic initiation factor 4A.

Anticancer Drug	Viral—Host Targets	Mechanism of Action	Combination	Primary End-Point	Source (20 May 2021)
Plitidepsin	Blockade of eEF1A	Interference with the viral cycle	-	Frequency of occurrence of Grade 3 or higher AEs	[10]
Zotatifin	Blockade of eIF4A	Inhibition of protein biogenesis	-	-	[10]

**Table 6.** Anticancer drugs in clinical trials for COVID-19: Blockade of kinase cascades.

Anticancer Drug	Viral—Host Targets	Mechanism of Action	Combination	Primary End-Point	Source (20 May 2021)
Duvelisib	PI3K inhibition	Immune homeostasis restoration and viral replication inhibition	-	Overall survival	[10]
			-	Reduce overall necessity of ventilation	
Zanubrutinib	Inhibition of the Bruton tyrosine kinase	Protection against immune, lethal and sepsis-induced pulmonary injuries	-	The respiratory failure-free survival rate	[10]
Carrimycin	Inhibit the replication of SARS-CoV-2 in the cells	Inhibits mTOR pathway	-	Fever to normal time	[11]
			-	Percentage of patients alive without the need for supplemental oxygen and ongoing in patient-medical care	
Ibrutinib	Inhibition of the Bruton tyrosine kinase	Protection against immune-induced lung injury	-	The respiratory failure-free survival rate, overall survival	[10]
			-	Patients with diminished respiratory failure and death	

### 5.1. Interferon-Based Therapies

The homeostasis maintained by the vascular endothelium in health is affected by COVID-19 infection. In clinical studies, patients with COVID-19 have higher levels of fibrinogen, fibrin degradation products, and D-dimer, which appear to be related to disease severity and thrombotic risk [19].

SARS-CoV-2 compromises the type 1 interferon antiviral response; therefore, IFN administration seemed a promising approach to stimulate macrophages, which engulf antigens and natural killer cells (NK cells). IFN might be able to strengthen the immune system by activating dormant components [20]. Clinical trials are running to test its effectiveness either alone or in combination with other drugs.

Ribavirin, lopinavir/ritonavir, remdesivir or hydroxychloroquine are some of the drugs tested in combination with IFNs in clinical trials (see Table 1). The study by Hung IF-N et al. demonstrated that early treatment with interferon beta-1b, lopinavir-ritonavir, and ribavirin is safe and highly effective in shortening the duration of the virus shedding, decreasing cytokine responses and allowing patients with mild to moderate disease to be discharged COVID-19 [21].

The problem is that when interferons boost the immune system, COVID-19 are likely to worsen before they improve. Giving anyone an interferon-based drug if they are still on a ventilator and their symptoms are about to overtake them may be fatal. This is why, in the case of viral infections, interferon therapies are usually only used as a last resort [22].

Nonetheless, interferon has already shown success against the antiviral activity, due to their ability to modulate the immune response, which is considered a “standard of care” in suppressing Hepatitis C and B infections [20].

### 5.2. Anticytokine Agents

The current COVID-19 infection is linked to elevated cytokine levels or hypercytokinemia. Patients who develop cytokine storms quickly experience cardiovascular collapse, multiple organ dysfunction and death [23]. The marked elevation of serum cytokines, especially tumor necrosis factor-alpha, interleukin 17 (IL-17), interleukin 8 (IL-8) and interleukin 6 (IL-6), is seen in patients with COVID-19 who go through pneumonia and hypoxia [24] (Table 2).

The administration of IL-6 blocking agents, such as tocilizumab and siltuximab, has been shown to be effective [25]. Repurposing tocilizumab would be interesting for the prevention or treatment of lung injury caused by COVID-19 since there is currently no effective antiviral therapy. In prospective studies, tocilizumab was linked to a lower relative risk of mortality, but the effects on other outcomes were inconclusive.

The drug siltuximab is a chimeric monoclonal antibody that binds to interleukin-6 (IL-6), preventing binding to soluble and membrane-bound interleukin-6 receptors. Current evidence showed that siltuximab led to a reduced mortality rate from COVID-19 promising to be a possible therapy; however, more studies are necessary [25].

### 5.3. Immune-Checkpoint Inhibitors

Immune checkpoints are regulatory molecules that are found on the surface of immune cells. When proteins on the surface of immune cells called T cells recognize and bind to partner proteins on other cells, such as tumor cells, immune checkpoints are activated. The T cells receive an “off” signal which may prevent cancer from being destroyed by the immune system. Therefore, immune checkpoint inhibitors are immunotherapy drugs that work by preventing checkpoint proteins from binding to their partner proteins. As a result, the “off” signal is not sent, allowing T cells to kill cancer cells [26,27].

The same principle can be applied for COVID-19 as a potential therapeutic approach (see Table 3). Evidence from preclinical models suggests that blocking programmed death receptor 1 (PD1) protects against RNA virus infections. Among the ICIs, antibodies capable of blocking the pathway of programmed death 1 (PD 1)/PD ligand-1 (PD L1) are promising. PD-1 expression levels on NK cells and T-cells were found to be highly upregulated in COVID-19 patients. When treated with anti-PD 1 and anti-PD L1 antibodies, they regain their T cell competence and effectively counteract viral infection [26,28]. Nivolumab and Pembrolizumab are ICIs that were successfully introduced into the management of various solid cancers, particularly for melanoma [24]. Currently, there is a phase II to trial to access efficacy for COVID-19. Pembrolizumab was tested in combination with tocilizumab [26].

### 5.4. Hormone Therapy

Androgen deprivation therapy (ADT), also known as androgen suppression therapy, is an antihormone therapy used to treat prostate cancer. Increasing evidence suggests that androgen has the potential to regulate the cellular TMPRSS2 expression and ACE2 [29].

TMPRSS2 is a membrane protease necessary for COVID pathogenesis, which is regulated by androgens. Blocking TMPRSS2 with bicalutamide can reduce viral replication and improve clinical outcomes. These agents may down-regulate TMPRSS2 mRNA and expression resulting in less entry of SARS-CoV-2 entry into cells and thus could arise as promising therapeutic tools in early SARS-CoV-2 infection and COVID-19 [30], see Table 4. A combination of bicalutamide in combination with camostat has the potential to reduce hospitalizations.

Toremifene used in the treatment of advanced breast cancer in postmenopausal women is a first-generation nonsteroidal-selective estrogen receptor modulator. It displays potential effects in blocking various viral infections, including MERS-CoV, SARS-CoV and

Ebola virus. Prevents fusion between the viral and endosomal membrane by interacting with and destabilizing the virus membrane glycoprotein and eventually inhibiting viral replication [31]. Moreover, a preliminary study reveals a high potential for the synergistic effects of melatonin and toremifene to reduce viral infection and replication [32].

#### 5.5. Inhibitor of Elongation Factor 1A and the Eukaryotic Initiation Factor 4A

Other molecules revealed potent pre-clinical efficacy against SARS-CoV-2 by inhibiting replication. In the life cycle of SARS-CoV-2, many host proteins play a role, and some are required for viral replication and translation. Drugs that target viral proteins are usually the focus of research, but a complementary approach is to target the required host proteins (Table 5).

Plitidepsin is an inhibitor of elongation factor 1A (eEF1A) and is an authorized drug in Australia for the treatment of multiple myeloma. Antiviral activity of plitidepsin has been analyzed in a human hepatoma cell line infected with the HCoV-229E-GFP virus, a virus similar to the SARS-CoV-2 virus [33]. Clinical studies using this drug are already taking place to assess safety and toxicity profile in patients with COVID-19 who require hospital admission, being the main goal is to select the recommended dose levels of plitidepsin for future phase 2/3 efficacy studies.

Another promising drug being tested in clinical trials is Zotatfin to assess its safety and tolerability. Zotatfin is a selective small-molecule inhibiting the eukaryotic initiation factor 4A (eIF4A), a powerful anti-proliferative target found at the intersection of the RAS and PI3K signaling pathways [34].

#### 5.6. Blockade of Kinase Cascades

To test the hypothesis that PI3K blockade could hamper immune system hyperactivation and thus reduce lung inflammation and interfere with the viral cycle, researchers used one of the most successful targeted strategies in cancer treatment: kinase cascade blockade [35]. In a randomized placebo-controlled phase 2 study, Duvelisib, an orally bioavailable phosphatidylinositol 3-kinase (PI3K) selective inhibitor, is being evaluated for its ability to reduce inflammation in the lungs of patients with severe acute respiratory syndrome coronavirus 2 infections. As has been demonstrated repeatedly for multiple compounds in this pharmacological class, PI3K inhibitors, including the drug duvelisib, can cause lung inflammation and increase the risk of infections, and special caution is required during clinical trials using this class of molecules (Table 6).

On the other hand, Zanubrutinib is an irreversible Bruton tyrosine kinase inhibitor. The aberrant activation of the Bruton tyrosine kinase has a key role in the tumorigenesis of B-cell lymphoma. For COVID-19 evidence suggesting protective effects, a phase II trial is ongoing, aiming to reduce the disease-related immune dysregulation and hyperinflammation [35].

#### 5.7. Radiation and Prophylactic Vitamin D

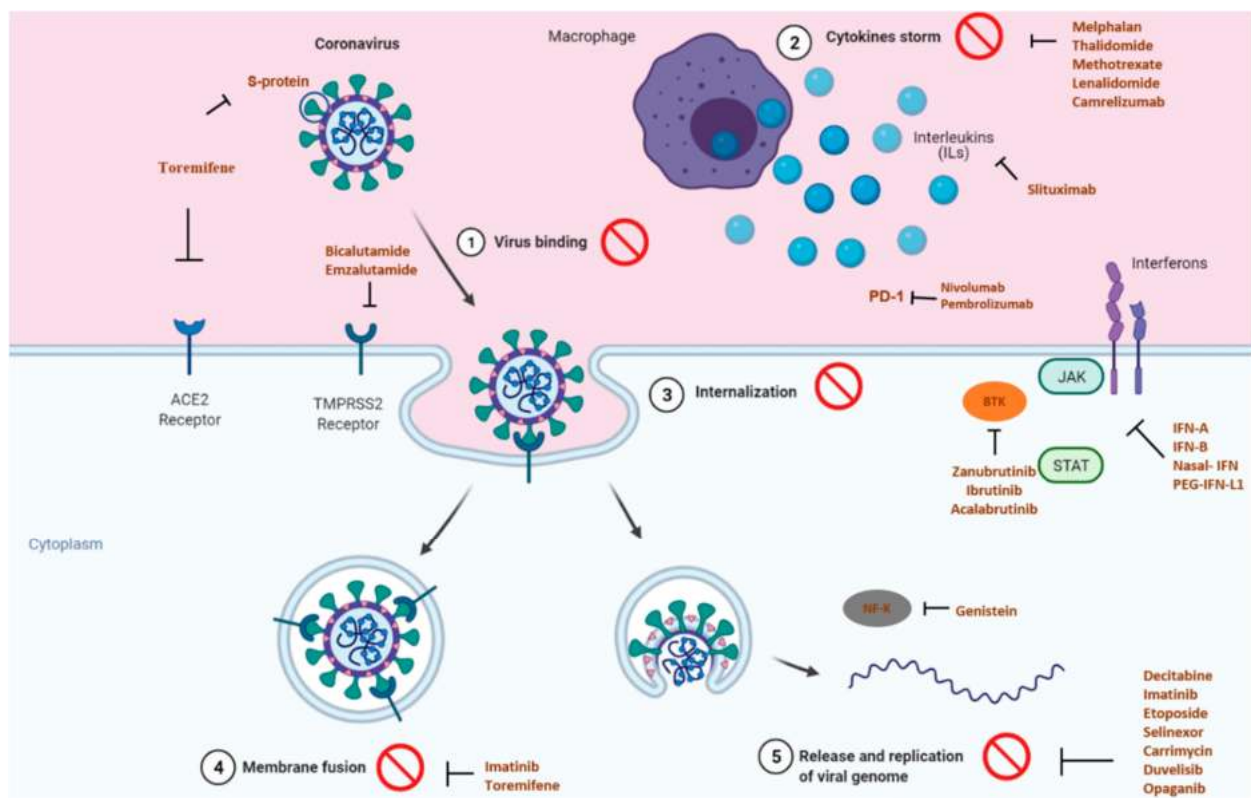
Low-dose thoracic irradiation strategies with anti-inflammatory or prophylactic vitamin D have shown antiviral potential. However, there is a lack of direct pre-clinical and clinical evidence for COVID-19 and other therapeutics that may be more accessible, less risky, and less complicated for treatment [36].

Recently, we have acquired an unparalleled knowledge of the molecular processes and immune tolerance mechanisms regulating the occurrence and severity of human neoplasms, contributing to a wide variety of targeted anticancer and immunotherapy treatments [37]. Despite their specificity, however, small-molecule inhibitors and antibody-based therapies cause both on- and off-target effects, including immune-related pneumonia and diabetes, among other conditions, which need to be addressed when translating COVID-19 anticancer therapy. Now it is necessary to continue with clinical trials to overcome the uncertainties about the risks of certain therapeutics and understand which

could be more beneficial in a time where vaccines are already available. Therapeutics along with immunization are the key to getting rid of the pandemic.

## 6. Conclusions

The COVID-19 pandemic has swiftly swept through the world, resulting in huge morbidity and significant mortality. While the news of vaccination brings the promise to the end of the pandemic, the importance of medicines must not be forgotten since it helps to limit the spread of disease and allows both prevention and treatment. Either using repurposed drugs, alone or in combination or even new molecules, the pandemic provides an opportunity to create new models for evaluating novel therapeutic approaches quickly. Due to similarities between cancer and COVID-19, anticancer drugs are repurposed in clinical trials to test their efficacy in targeting inflammation, immune dysfunction, and coagulopathy. Figure 1 illustrates the principal targets of anticancer drugs repurposed in clinical trials for COVID-19.



**Figure 1.** Principal targets of the anticancer drugs or drugs used for breast cancer supportive care, repurposed in clinical trials for COVID-19, adapted from BioRender templates [38].

Finally, the management of the SARS-CoV-2 pandemic includes multidisciplinary collaboration to identify suitable treatment options for everyone, including and especially countries with limited access to vaccines and people already hospitalized. From the evidence reviewed here, several anticancer drugs seem to retain a promising activity to treat patients with COVID-19.

**Author Contributions:** B.C. contributed to the conception of the review; the collection, analysis and interpretation of the information included within; the drafting of the review; and critically revising the review for important intellectual content. N.V. contributed to the conception of the review; the collection, analysis and interpretation of the information included within; the drafting of the review; and critically revising the review for important intellectual content; Supervision, N.V.; project administration, N.V.; funding acquisition, N.V. Both authors have read and agreed to the published version of the manuscript.

**Funding:** This work was supported by “Fundação para a Ciência e Tecnologia” (FCT, Portugal and FEDER—Fundo Europeu de Desenvolvimento Regional funds through the COMPETE 2020—Operacional Programme for Competitiveness and Internationalisation (POCI), Portugal 2020, in the framework of the project IF/00092/2014/CP1255/CT0004.

**Institutional Review Board Statement:** Not applicable.

**Informed Consent Statement:** Not applicable.

**Data Availability Statement:** Not applicable.

**Acknowledgments:** N.V. thanks Fundação para a Ciência e a Tecnologia (FCT, Portugal) for supporting these studies through a project from the National Funds, within CINTESIS, R&D Unit (reference UIDB/4255/2020). The contents of this report are solely the responsibility of the authors and do not necessarily represent the official view of the FCT.

**Conflicts of Interest:** The authors declare no conflict of interest.

### Abbreviations

Coronavirus disease 2019 (COVID-19); severe acute respiratory syndrome coronavirus-2 (SARS-CoV-2); acute respiratory distress syndrome (ARDS); world health organization (WHO); the food and drug administration (FDA); interferons (IFNs); transmembrane-serine-protease-2 (TMPRSS2); angiotensin-converting enzyme 2 (ACE2); phosphatidylinositol 3-kinase (PI3K); elongation factor 1A (eEF1A); eukaryotic initiation factor 4A; the eukaryotic initiation factor 4A (eIF4A); programmed death receptor 1 (PD1); programmed death ligand-1 (PD L1); immune-checkpoint inhibitors (ICIs); tumor necrosis factor alpha (TNF- $\alpha$ ); interleukin 17 (IL-17); interleukin 8 (IL-8); interleukin 6 (IL-6); Janus kinase (Jak); tyrosine kinases (Tyk); nucleocapsid (N); spike (S); membrane (M); envelope (E); endoplasmic reticulum (ER); endoplasmic reticulum-Golgi intermediate compartment (ERGIC); natural killer (NK)

Appendix A

Table A1. List of drugs with anticancer effects or used for best supportive cancer care, in clinical studies for the treatment of COVID-19.

Anticancer Drug	Viral—Host Targets	Mechanism of Action	Tested in Clinical Trials	NCT Identifier	Combination	Status	Phase	Eligible Population	Primary End-Point	Source (20 May 2021)
Acalabrutinib	BTK	Inhibits the activity of BTK and prevents the activation of the B-cell antigen receptor	United states Several locations	NCT04380688 NCT04346199	- -	Completed Completed	Phase 2 Phase 2	COVID-19 infection COVID-19 infection	Occurrence of Adverse Events and Serious Adverse Events Subject alive and free of respiratory failure	[10]
Bevacizumab	VEGF	Vascular permeability inhibition	Yes (France and China)	NCT04275414 NCT04344782	- -	Completed Not yet recruiting	Phase 2 Phase 2	Severe lung disease or critical disease Severe lung disease	Change of PaO <sub>2</sub> to FiO <sub>2</sub> ratio Number of patients who avoid mechanical-ventilation	[10]
Bicalutamide	Downregulates TMPRSS2	Binding of androgen receptor	Yes	NCT04305106 NCT04509999	- -	Recruiting Recruiting	Not applicable Phase 3	Disease requiring O <sub>2</sub> -support COVID-19 infection, confirmed	Time to clinical improvement COVID-19 symptom relief	[9]
Camrelizumab	Immune homeostasis	PD-1/PD-L1 pathway Blockade	Yes (China)	ChiCTR2000029806	-	Recruiting	Not applicable	COVID-19 infection	Proportion of patients with a lung injury score reduction	[10]

Table A1. Cont.

Anticancer Drug	Viral—Host Targets	Mechanism of Action	Tested in Clinical Trials	NCT Identifier	Combination	Status	Phase	Eligible Population	Primary End-Point	Source (20 May 2021)
Carrimycin	Inhibit the replication of SARS-CoV-2 in the <math>T</math>-cells	Inhibits mTOR pathway	Not provided	NCT04286503	-	Not yet recruiting	Phase 4	COVID-19 infection	Fever to normal time	[11]
				NCT04672564	-	Recruiting	Phase 3	Patient with SARS-CoV-2 infection	Percentage of patients alive without need for supplemental oxygen and ongoing in patient-medical care	
Decitabine	Nucleic Acid Synthesis Inhibitor	Nucleic acid synthesis inhibitor	Yes (USA)	NCT04482621	-	Recruiting	Phase 2	COVID infection	Clinical improvement	[9]
Duvelisib	PI3K inhibition	Immune homeostasis restoration and viral replication inhibition	Yes (USA)	NCT04372602	-	Recruiting	Phase 2	Critical disease severe COVID-19 who do not require mechanical ventilation	Overall survival	[10]
Ensifentrine	High selectivity for PDE3 and PDE4 over other enzymes and receptors to minimize off-target effects	Dual inhibitor of phosphodiesterase 3 (PDE3) and 4 (PDE4)	United states	NCT04527471	None	Active, not recruiting	Phase 2	SARS-CoV-2 infection	Proportion of patients with recovery	[11]
Enzalutamide	reduce androgen driven morbidity in COVID-19	Competitive binder of androgens	Sweden	NCT04475601	-	Recruiting	Phase 2	SARS-CoV-2 infection	Time to worsening of disease	[9]

Table A1. Cont.

Anticancer Drug	Viral—Host Targets	Mechanism of Action	Tested in Clinical Trials	NCT Identifier	Combination	Status	Phase	Eligible Population	Primary End-Point	Source (20 May 2021)
Etoposide	Topoisomerase II	Inhibits DNA synthesis by forming a complex with topoisomerase II and DNA	United states	NCT04356690	-	Active, not yet Recruiting	Phase 2	Confirmed COVID-19 infection	Change in pulmonary status	[9]
FN-B1A	Jak1 and Tyk2	Jak1 and Tyk2	UK	NCT04385095	-	Recruiting	Phase 2	COVID-19 infection	Clinical Improvement	[10]
		Jak1 and Tyk2	Several locations	NCT04315948	Lopinavir, ritonavir	Active, not yet Recruiting	Phase 3	COVID-19 infection	Percentage of subjects reporting severity	
		-	Iran	NCT04350671	Hydroxychloroquine, lopinavir, ritonavir	Enrolling by invitation	Phase 4	COVID-19 infection	Reduce Mortality	
		-	Irna	NCT04350684	Hydroxychloroquine, lopinavir, ritonavir, umifenovir	Enrolling by invitation	Phase 4	COVID-19 infection	Time to clinical improvement	
Genistein	Inhibition of <math>I\kappa B</math>/>both nuclear transcription factor- $\kappa B$ (NF- $\kappa B$ ) activation and chemokine-8 secretion	Triggers the ER stress through upregulation of glucose-regulated protein 78 (GRP78) expression	Several locations	NCT02735707	Multifactorial	Recruiting	Phase 4	COVID-19 infection	All-cause mortality	[9]
			United states	NCT04482595	-	Recruiting	Phase 2	Patients hospitalized for COVID-19	Change in Diffusing capacity of the lungs for carbon monoxide	
Ibrutinib	Inhibition of the Bruton tyrosine kinase	Protection against immune-induced lung injury	Yes (USA)	NCT04375397	-	Active, not yet Recruiting	Phase 2	Hospitalised patients with severe pneumonia	Respiratory failure-free survival rate, overall survival	[10]
			Several locations	NCT04439006	-	Recruiting	Phase 2	Patients Requiring Hospitalization	Patients with diminished respiratory failure and death	



Table A1. Cont.

Anticancer Drug	Viral—Host Targets	Mechanism of Action	Tested in Clinical Trials	NCT Identifier	Combination	Status	Phase	Eligible Population	Primary End-Point	Source (20 May 2021)
IFN	Jak1 and Tyk2	Jak1 and Tyk2	Canada	NCT04354259	-	Recruiting	Phase 2	COVID-19 infection	Negative SARS-CoV-2 RNA on nasopharyngeal swab	[10]
	Jak1 and Tyk2	Jak1 and Tyk2	China	NCT04331899	-	Active, Not yet recruiting	Phase 2	COVID-19 infection	Clinical improvement	[10]
IFN beta 1b	Jak1 and Tyk2	Jak1 and Tyk2	Hong kong	NCT04647695	Remdesivir	Recruiting	Phase 2	high risk of clinical deterioration	Reduce hospitalisation	[10]
	Jak1 and Tyk2	Jak1 and Tyk2	Hong kong	NCT04494399	ribavirin	Recruiting	Phase 2	COVID-19 infection	Reduce hospitalisation	[10]
IFN-A2B	activate two Jak (Janus kinase) tyrosine kinases (Jak1 and Tyk2)	activate two Jak (Janus kinase) tyrosine kinases (Jak1 and Tyk2)	United States	NCT04349410	-	Completed	Phase 2/3	CoVid-19 infection	Improvement in FMIVDM Measurement with nuclear imaging	[10]
IFN-B1A/B	Jak1 and Tyk2	Jak1 and Tyk2	Iran	NCT04343768	Hydroxychloroquine, lopinavir, ritonavir	Completed	Phase 2	COVID-19 infection	Time to clinical improvement	[10]
IFN-B1B	Jak1 and Tyk2	Jak1 and Tyk2	Hong kong	NCT04350281	Hydroxychloroquine, lopinavir, ritonavir	Completed	Phase 2	COVID-19 infection	Time to negative NPS viral load	[10]
	Jak1 and Tyk2	Jak1 and Tyk2	Hong kong	NCT04276688	Ribavirin, lopinavir, ritonavir	Completed	Phase 2	COVID-19 infection	Time to negative NPS	[10]
Imatinib	BCR/ABL kinase inhibition	Blockade of cell entry and endosomal trafficking	Yes (France, Spain and USA)	NCT04357613	-	Not yet Recruiting	Phase 2	Hospitalised patients	Rate of prevented severe disease worsening	[10]
Interferon	Jak1 and Tyk2	Jak1 and Tyk2	China	NCT04291729	Danoprevir, ritonavir	Completed	Phase 4	COVID-19 infectio	Rate of composite adverse outcome	[10]

Table A1. Cont.

Anticancer Drug	Viral—Host Targets	Mechanism of Action	Tested in Clinical Trials	NCT Identifier	Combination	Status	Phase	Eligible Population	Primary End-Point	Source (20 May 2021)
Lenalidomide	Immunomodulatory agent	substrate specificity of the CRL4 <sup>CRBN</sup> E3 ubiquitin ligase	Spain	NCT04361643	-	Not yet recruiting	Phase 4	COVID-19 infection	Clinical improvement	[10]
Leronlimab	Disruption of the CCL5/RANTES-CCR5 pathway	Immune homeostasis restoration	Yes (USA)	NCT04343651	-	Active, not recruiting	Phase 2	Mild/moderate disease	Clinical improvement	[10]
				NCT04347239	-	Recruiting	Phase 2	Severe lung disease or critical disease	Overall survival	[10]
Masitinib	directly binds to the active site of 3CLpro	Tyrosine kinase inhibitor	Yes (France)	NCT04622865	Isoquercetin	Recruiting	Phase 2	COVID 19 diagnosis	Clinical status of patients at day-15	[9]
Melfalhan	anti-inflammatory response	Inhibition of DNA and RNA synthesis by realizing an alkylating peptide	Yes (Russian Federation)	NCT04380376	-	Recruiting	Phase 2	COVID 19 diagnosis	The changes of COVID Ordinal Outcomes Scale	[9]
Methotrexate	Immunomodulatory agent	inhibition of folate dependent pathways leading to inhibition of DNA synthesis	France	NCT04481633	Hydroxychloroquine	Recruiting	Not applicable	COVID-19 infection	Rate of patients with positive anti-COVID19 serology	[10]
Nasal IFN- $\alpha$ 1B	Jak1 and Tyk2	Jak1 and Tyk2	China	NCT04320238	Anti-thymosin	Recruiting	Phase 3	Formally serving medical staff in Taihe Hospital	new-onset COVID-19	[10]

Table A1. Cont.

Anticancer Drug	Viral—Host Targets	Mechanism of Action	Tested in Clinical Trials	NCT Identifier	Combination	Status	Phase	Eligible Population	Primary End-Point	Source (20 May 2021)
Nivolumab	PD-1/PD-L1 pathway blockade	Immune homeostasis restoration	Yes (France and China)	NCT04343144	-	Not yet recruiting	Phase 2	Disease requiring O <sub>2</sub> -support	Time to clinical improvement	[10]
				NCT04413838	-	Not yet recruiting	Phase 2	Obese individuals	Efficacy and safety	[10]
				NCT04356508	-	Not yet recruiting	Phase 2	Clinically stable patients with mild or moderate disease and asymptomatic patients	Viral clearance kinetics	[10]
Opaganib	Inhibition of sphingosine kinase-2	Anti-inflammatory and antiviral properties	Yes (Israel)	NCT04414618	-	Completed	Phase 2	Disease requiring O <sub>2</sub> -support	Measurement of the daily O <sub>2</sub> requirements	[10]
				NCT04467840	-	Recruiting	Phase 2 and 3	Disease requiring O <sub>2</sub> -support	Reduce Intubation and mechanical ventilation	
				NCT04435106	-	Completed	-	severe COVID-19 who required oxygen support via high-flow nasal cannula	Measure the time to weaning from high-flow nasal cannula and Measure the time to breathing ambient	
PD-1 blocking antibody	PD-1	Can prevent the tumor cell from binding PD-1	Not provided	NCT04502069	-	Withdrawn (To be replaced with a randomized placebo-controlled study.)	Phase 1 and 2	Pneumonia Requiring Oxygen	Time to breathing room air	[10]
				NCT04268537	-	Not yet recruiting	Phase 2	COVID-19 infection	lung injury score	

Table A1. Cont.

Anticancer Drug	Viral—Host Targets	Mechanism of Action	Tested in Clinical Trials	NCT Identifier	Combination	Status	Phase	Eligible Population	Primary End-Point	Source (20 May 2021)
Peg-IFN-L1	Jak1 and Tyk2	Jak1 and Tyk2	United states	NCT04343976	-	Enrolling by invitation	Phase 2	COVID-19 infectio	Negative SARS-CoV-2 RNA on nasopharyngeal swab	[10]
						Withdrawn (Due to the number of competing trials at their site, the study team has closed enrollment and withdrawn this trial.)				
Peg-IFN-L1A	Jak1 and Tyk2	Jak1 and Tyk2	United states	NCT04388709	-		Phase 2	COVID-19 infection	Number of participants with resolution of hypoxia	[10]
						Not yet recruiting	Phase 2	COVID-19 infection	Proportion of participants with no evidence of SARS-CoV-2 infection	
			United states	NCT04344600	-					
Pembrolizumab	PD-1/PD-L1 pathway blockade	Immune homeostasis restoration	Yes (Spain)	NCT04335305	Tocilizumab	Recruiting	Phase 2	Severe lung disease or critical disease	Percentage of patients with normalisation of SpO <sub>2</sub> ≥ 96% on room air	[10]
Plitidepsin	Blockade of eEF1A	Interference with the viral cycle	Yes (Spain)	NCT04382066	-	Completed	Phase 1	Hospitalised patients	Frequency of occurrence of Grade 3 or higher AEs	[10]

Table A1. Cont.

Anticancer Drug	Viral—Host Targets	Mechanism of Action	Tested in Clinical Trials	NCT Identifier	Combination	Status	Phase	Eligible Population	Primary End-Point	Source (20 May 2021)
Selinexor	Blockade of nucleocytoplasmic transport	Antiviral and anti-inflammatory properties	Yes (USA, France, Austria, Spain and United Kingdom)	NCT04355676	-	Withdrawn (No participants enrolled)	Phase 2	Hospitalised patients with moderate or severe disease	Percentage of participants with at least a two-point improvement in the ordinal scale	[10]
				NCT04349098	-	Completed	Phase 2	Hospitalised patients with severe disease	Improvement	
				NCT04534725	-	Recruiting	Phase 3	received cancer related treatment	COVID-19 Prevention and Treatment in Cancer	
SFX-01	up-regulates the Nrf2 pathway	Up-regulates the Nrf2 pathway	UK + Evgen Pharma	-	-	Enrolment begins in July (results are expected in 2021)	Phase 2/3	-	Efficacy at treating ARDS	[11]
Siltuximab	Interleukin-6	Interleukin-6	Spain	NCT04329650	-	Recruiting	Phase 2	Hospitalized patient	Proportion of patients requiring ICU admission at any time	[11]
				NCT04322188	-	Completed	-	COVID-19 infection	mortality in siltuximab treated patients	
				NCT04330638	Anakinra	Active, not recruiting	Phase 3	COVID-19 infection	Time to Clinical Improvement	
				NCT04486521	tocilizumab	Recruiting	-	COVID-19 infection	Ventilator-Free Days	
Tamoxifen	Decreased the PGE2 production	Compete with 17 $\beta$ -estradiol (E <sub>2</sub> ) at the receptor site	Egypt	NCT04568096	-	Not yet recruiting	Phase 2	Adult SARI patients with COVID-19 infection	Lung injury score	[9]

Table A1. Cont.

Anticancer Drug	Viral—Host Targets	Mechanism of Action	Tested in Clinical Trials	NCT Identifier	Combination	Status	Phase	Eligible Population	Primary End-Point	Source (20 May 2021)
Tetrandrine	Ability to block the two-pore channel 2 (TPC2)	Checkpoint inhibitor of the cell cycle	China	NCT04308317	-	Enrolling by invitation	Phase 4	COVID-19 infection	Survival rate	[10]
Thalidomide	inhibition of inflammatory cytokine production	Inhibit the production of interleukin (IL)-6,	China	NCT04273529	-	Not yet recruiting	Phase 2	COVID-19 infection	Time to Clinical recovery	[10]
Toremifene	Interaction with coronavirus proteins	Inhibition of viral membranes fusion with host cell endosomes	? (Not provided)	NCT04531748	Melatonin	Withdrawn (Funding)	Phase 2	-	Clinical improvement	[10]
Zanubrutinib	Inhibition of the Bruton tyrosine kinase	Protection against immune, lethal and sepsis-induced pulmonary injuries	Yes (USA)	NCT04382586	-	Completed	Phase 2	Disease requiring O <sub>2</sub> -support	Respiratory failure-free survival rate	[10]
Zotatifin	Blockade of eIF4A	Inhibition of protein biogenesis	No	NCT04632381	-	Not yet recruiting	Phase 1	-	-	[10]

## References

- Zheng, J. SARS-CoV-2: An Emerging Coronavirus that Causes a Global Threat. *Int J Biol Sci.* **2020**, *16*, 1678–1685, Published 15 March 2020. [CrossRef] [PubMed]
- Drinka, P.J. Influenza vaccination and antiviral therapy: Is there a role for concurrent administration in the institutionalised elderly? *Drugs Aging* **2003**, *20*, 165–174. [CrossRef] [PubMed]
- Deb, P.; Molla, M.A.; Saif-Ur-Rahman, K. An update to monoclonal antibody as therapeutic option against COVID-19. *Biosaf. Health* **2021**. [CrossRef] [PubMed]
- Pushpakom, S.; Iorio, F.; Eyers, P.A.; Escott, K.J.; Hopper, S.; Wells, A.; Doig, A.; Williams, T.; Latimer, J.; McNamee, C.; et al. Drug repurposing: Progress, challenges and recommendations. *Nat. Rev. Drug Discov.* **2019**, *18*, 41–58. [CrossRef]
- Hernandez, J.J.; Pryszyk, M.; Smith, L.; Yanchus, C.; Kurji, N.; Shahani, V.M.; Molinski, S.V. Giving Drugs a Second Chance: Overcoming Regulatory and Financial Hurdles in Repurposing Approved Drugs As Cancer Therapeutics. *Front Oncol.* **2017**, *7*, 273. [CrossRef]
- Sultana, J.; Crisafulli, S.; Gabbay, F.; Lynn, E.; Shakir, S.; Trifirò, G. Challenges for drug repurposing in the COVID-19 pandemic era. *Front. Pharmacol.* **2020**, *11*, 1657. [CrossRef]
- Parvathaneni, V.; Gupta, V. Utilizing drug repurposing against COVID-19—Efficacy, limitations, and challenges. *Life Sci.* **2020**, *259*, 118275. [CrossRef] [PubMed]
- Saini, K.S.; Lanza, C.; Romano, M.; De Azambuja, E.; Cortes, J.; Heras, B.D.L.; De Castro, J.; Saini, M.L.; Loibl, S.; Curigliano, G.; et al. Repurposing anticancer drugs for COVID-19-induced inflammation, immune dysfunction, and coagulopathy. *Br. J. Cancer* **2020**, *123*, 694–697. [CrossRef]
- National Center for Advancing Translational Sciences | OpenData Portal. Available online: <https://opendata.ncats.nih.gov/covid19/databrowser> (accessed on 6 February 2021).
- ClinicalTrials.gov. Available online: <https://www.clinicaltrials.gov/ct2/home> (accessed on 6 February 2021).
- European Pharmaceutical Review | News. Available online: <https://www.europeanpharmaceuticalreview.com/> (accessed on 6 February 2021).
- Richman, D.D.; Nathanson, N. Antiviral Therapy. *Viral Pathog.* **2016**, 271–287. [CrossRef]
- Fehr, A.R.; Perlman, S. Coronaviruses: An overview of their replication and pathogenesis. *Methods Mol. Biol.* **2015**, *1282*, 1–23. [CrossRef]
- Astuti, I.; Ysrafil. Severe Acute Respiratory Syndrome Coronavirus 2 (SARS-CoV-2): An overview of viral structure and host response. *Diabetes Metab. Syndr.* **2020**, *14*, 407–412. [CrossRef]
- Romano, M.; Ruggiero, A.; Squeglia, F.; Maga, G.; Berisio, R.A. Structural View of SARS-CoV-2 RNA Replication Machinery: RNA Synthesis, Proofreading and Final Capping. *Cells* **2020**, *9*, 1267. [CrossRef]
- Zingaropoli, M.A.; Perri, V.; Pasculli, P.; Dezza, F.C.; Nijhawan, P.; Savelloni, G.; La Torre, G.; D’Agostino, C.; Mengoni, F.; Lichtner, M.; et al. Major reduction of NKT cells in patients with severe COVID-19 pneumonia. *Clin. Immunol.* **2021**, *222*, 108630. [CrossRef]
- Jin, Y.; Ji, W.; Yang, H.; Chen, S.; Zhang, W.; Duan, G. Endothelial activation and dysfunction in COVID-19: From basic mechanisms to potential therapeutic approaches. *Signal. Transduct. Target. Ther.* **2020**, *5*, 1–13. [CrossRef] [PubMed]
- Boechat, J.L.; Chora, I.; Morais, A.; Delgado, L. The immune response to SARS-CoV-2 and COVID-19 immunopathology—current perspectives. *Pulmonology* **2021**. [CrossRef] [PubMed]
- Minn, A.J. Interferons and the immunogenic effects of cancer therapy. *Trends Immunol.* **2015**, *36*, 725–737. [CrossRef] [PubMed]
- Lin, F.C.; Young, H.A. Interferons: Success in anti-viral immunotherapy. *Cytokine Growth Factor Rev.* **2014**, *25*, 369–376. [CrossRef]
- Hung, I.F.-N.; Lung, K.-C.; Tso, E.Y.-K.; Liu, R.; Chung, T.W.-H.; Chu, M.-Y.; Ng, Y.-Y.; Lo, J.; Chan, J.; Tam, A.R.; et al. Triple combination of interferon beta-1b, lopinavir–ritonavir, and ribavirin in the treatment of patients admitted to hospital with COVID-19: An open-label, randomised, phase 2 trial. *Lancet* **2020**, *395*, 1695–1704. [CrossRef]
- Abdolvahab, M.H.; Moradi-Kalbolandi, S.; Zarei, M.; Bose, D.; Majidzadeh, -A.K.; Farahmand, L. Potential role of interferons in treating COVID-19 patients. *Int. Immunopharmacol.* **2021**, *90*, 107171. [CrossRef]
- Costela-Ruiz, V.J.; Illescas-Montes, R.; Puerta-Puerta, J.M.; Ruiz, C.; Melguizo-Rodríguez, L. SARS-CoV-2 infection: The role of cytokines in COVID-19 disease. *Cytokine Growth Factor Rev.* **2020**, *54*, 62–75. [CrossRef]
- Lacroix, M.; Rousseau, F.; Guilhot, F.; Malinge, P.; Magistrelli, G.; Herren, S.; Jones, S.A.; Jones, G.W.; Scheller, J.; Lissilaa, R.; et al. Novel Insights into Interleukin 6 (IL-6) Cis- and Trans-signaling Pathways by Differentially Manipulating the Assembly of the IL-6 Signaling Complex. *J. Biol. Chem.* **2020**, *290*, 26943–26953. [CrossRef] [PubMed]
- Khan, F.A.; Stewart, I.; Fabbri, L.; Moss, S.; Robinson, K.; Smyth, A.R.; Jenkins, G. Systematic review and meta-analysis of anakinra, sarilumab, siltuximab and tocilizumab for COVID-19. *Thorax* **2021**. [CrossRef]
- Sullivan, R.J.; Johnson, D.B.; Rini, B.; Neilan, T.G.; Lovly, C.M.; Moslehi, J.J.; Reynolds, K.L. COVID-19 and immune checkpoint inhibitors: Initial considerations. *J. Immunother. Cancer* **2020**, *8*. [CrossRef]
- Chen, Z.; Wherry, E.J. T cell responses in patients with COVID-19. *Nat. Rev. Immunol.* **2020**, *20*, 529–536. [CrossRef]
- Saito, N.; Yoshida, K.; Okamoto, M.; Sasaki, J.; Kuroda, C.; Ishida, H.; Ueda, K.; Ideta, H.; Kamanaka, T.; Sobajima, A.; et al. Anti-PD-1 antibody decreases tumour-infiltrating regulatory T cells. *BMC Cancer* **2019**, *20*. [CrossRef]
- Mollica, V.; Rizzo, A.; Massari, F. The pivotal role of TMPRSS2 in coronavirus disease 2019 and prostate cancer. *Future Oncol.* **2020**, *16*, 2029–2033. [CrossRef]

30. Chakravarty, D.; Nair, S.S.; Hammouda, N.; Ratnani, P.; Gharib, Y.; Wagaskar, V.; Mohamed, N.; Lundon, D.; Dovey, Z.; Kyprianou, N.; et al. Sex differences in SARS-CoV-2 infection rates and the potential link to prostate cancer. *Commun. Biol.* **2020**, *3*, 1–12. [CrossRef]
31. Martin, W.R.; Cheng, F. Repurposing of FDA-Approved Toremifene to Treat COVID-19 by Blocking the Spike Glycoprotein and NSP14 of SARS-CoV-2. *J. Proteome Res.* **2020**, *19*, 4670–4677. [CrossRef]
32. Cheng, F.; Rao, S.; Mehra, R. COVID-19 treatment: Combining anti-inflammatory and antiviral therapeutics using a network-based approach. *Cleve Clin. J. Med.* **2020**. [CrossRef] [PubMed]
33. White, K.M.; Rosales, R.; Yildiz, S.; Kehrer, T.; Miorin, L.; Moreno, E.; Jangra, S.; Uccellini, M.B.; Rathnasinghe, R.; Coughlan, L.; et al. Plitidepsin has potent preclinical efficacy against SARS-CoV-2 by targeting the host protein eEF1A. *Science* **2021**, 926–931. [CrossRef] [PubMed]
34. Nebigil, C.G.; Moog, C.; Vagner, S.; Benkirane-Jessel, N.; Smith, D.R.; Désaubry, L. Flavaglines as natural products targeting eIF4A and prohibitins: From traditional Chinese medicine to antiviral activity against coronaviruses. *Eur. J. Med. Chem.* **2020**, *203*, 112653. [CrossRef] [PubMed]
35. Sriskantharajah, S.; Hamblin, N.; Worsley, S.; Calver, A.R.; Hessel, E.M.; Amour, A. Targeting phosphoinositide 3-kinase  $\delta$  for the treatment of respiratory diseases. *Ann. N. Y. Acad. Sci.* **2013**, *1280*, 35–39. [CrossRef] [PubMed]
36. Murdaca, G.; Pioggia, G.; Negrini, S. Vitamin D and Covid-19: An update on evidence and potential therapeutic implications. *Clin. Mol. Allergy* **2020**, *18*, 1–8. [CrossRef]
37. Gordon, D.E.; Jang, G.M.; Bouhaddou, M.; Xu, J.; Obernier, K.; White, K.M.; O'Meara, M.J.; Rezelj, V.V.; Guo, J.Z.; Swaney, D.L.; et al. A SARS-CoV-2 protein interaction map reveals targets for drug repurposing. *Nature* **2020**, *583*, 459–468. [CrossRef] [PubMed]
38. Repurposed Drugs with Broad-Spectrum Antiviral Activity, by BioRender.com. Available online: <https://app.biorender.com/biorender-templates> (accessed on 3 January 2020).





## Article

# Growth Inhibitory Effects of Ester Derivatives of Menahydroquinone-4, the Reduced Form of Vitamin K<sub>2(20)</sub>, on All-Trans Retinoic Acid-Resistant HL60 Cell Line

Hirofumi Yamakawa, Shuichi Setoguchi, Shotaro Goto, Daisuke Watase, Kazuki Terada, Nami Nagata-Akaho, Erina Toki, Mitsuhisa Koga, Kazuhisa Matsunaga, Yoshiharu Karube and Jiro Takata \*

Faculty of Pharmaceutical Sciences, Fukuoka University, Nanakuma, Jonan-ku, Fukuoka 814-0180, Japan; hyamakawa@adm.fukuoka-u.ac.jp (H.Y.); ssetoguchi@fukuoka-u.ac.jp (S.S.); sgoto@fukuoka-u.ac.jp (S.G.); watase@fukuoka-u.ac.jp (D.W.); kterada@fukuoka-u.ac.jp (K.T.); nanohana\_73@jewel.ocn.ne.jp (N.N.-A.); pd191005@cis.fukuoka-u.ac.jp (E.T.); kogami@fukuoka-u.ac.jp (M.K.); k-matsu@fukuoka-u.ac.jp (K.M.); karube@fukuoka-u.ac.jp (Y.K.)

\* Correspondence: jtakata@fukuoka-u.ac.jp; Tel.: +81-92-871-6631 (ext. 6662)

**Abstract:** The first-choice drug for acute promyelocytic leukemia (APL), all-trans retinoic acid (ATRA), frequently causes drug-resistance and some adverse effects. Thus, an effective and safe agent for ATRA-resistant APL is needed. Menaquinone-4 (MK-4, vitamin K<sub>2(20)</sub>), used for osteoporosis treatment, does not have serious adverse effects. It has been reported that MK-4 has growth-inhibitory effects on HL60 cells by inducing apoptosis via the activation of Bcl-2 antagonist killer 1 (BAK). However, the effect of MK-4 on ATRA-resistant APL has not been reported. Here, we show that ester derivatives of menahydroquinone-4 (MKH; a reduced form of MK-4), MKH 1,4-bis-*N,N*-dimethylglycinate (MKH-DMG) and MKH 1,4-bis-hemi-succinate (MKH-SUC), exerted strong growth-inhibitory effects even on ATRA-resistant HL60 (HL-60R) cells compared with ATRA and MK-4. MKH delivery after MKH-SUC treatment was higher than that after MK-4 treatment, and the results indicated apoptosis induced by BAK activation. In contrast, for MKH-DMG, reversion to MKH was slow and apoptosis was not observed. We suggest that the ester forms, including monoesters of MKH-DMG, exhibit another mechanism independent of apoptosis. In conclusion, the MKH derivatives (MKH-SUC and MKH-DMG) inhibited not only HL60 cells but also HL-60R cells, indicating a potential to overcome ATRA resistance.

**Keywords:** drug delivery; HL60; leukemia; prodrug; resistance; retinoic acid; vitamin K

**Citation:** Yamakawa, H.; Setoguchi, S.; Goto, S.; Watase, D.; Terada, K.; Nagata-Akaho, N.; Toki, E.; Koga, M.; Matsunaga, K.; Karube, Y.; et al. Growth Inhibitory Effects of Ester Derivatives of Menahydroquinone-4, the Reduced Form of Vitamin K<sub>2(20)</sub>, on All-Trans Retinoic Acid-Resistant HL60 Cell Line. *Pharmaceutics* **2021**, *13*, 758. <https://doi.org/10.3390/pharmaceutics13050758>

Academic Editor: Hassan Bousbaa

Received: 14 January 2021

Accepted: 19 May 2021

Published: 20 May 2021

**Publisher's Note:** MDPI stays neutral with regard to jurisdictional claims in published maps and institutional affiliations.



**Copyright:** © 2021 by the authors. Licensee MDPI, Basel, Switzerland. This article is an open access article distributed under the terms and conditions of the Creative Commons Attribution (CC BY) license (<https://creativecommons.org/licenses/by/4.0/>).

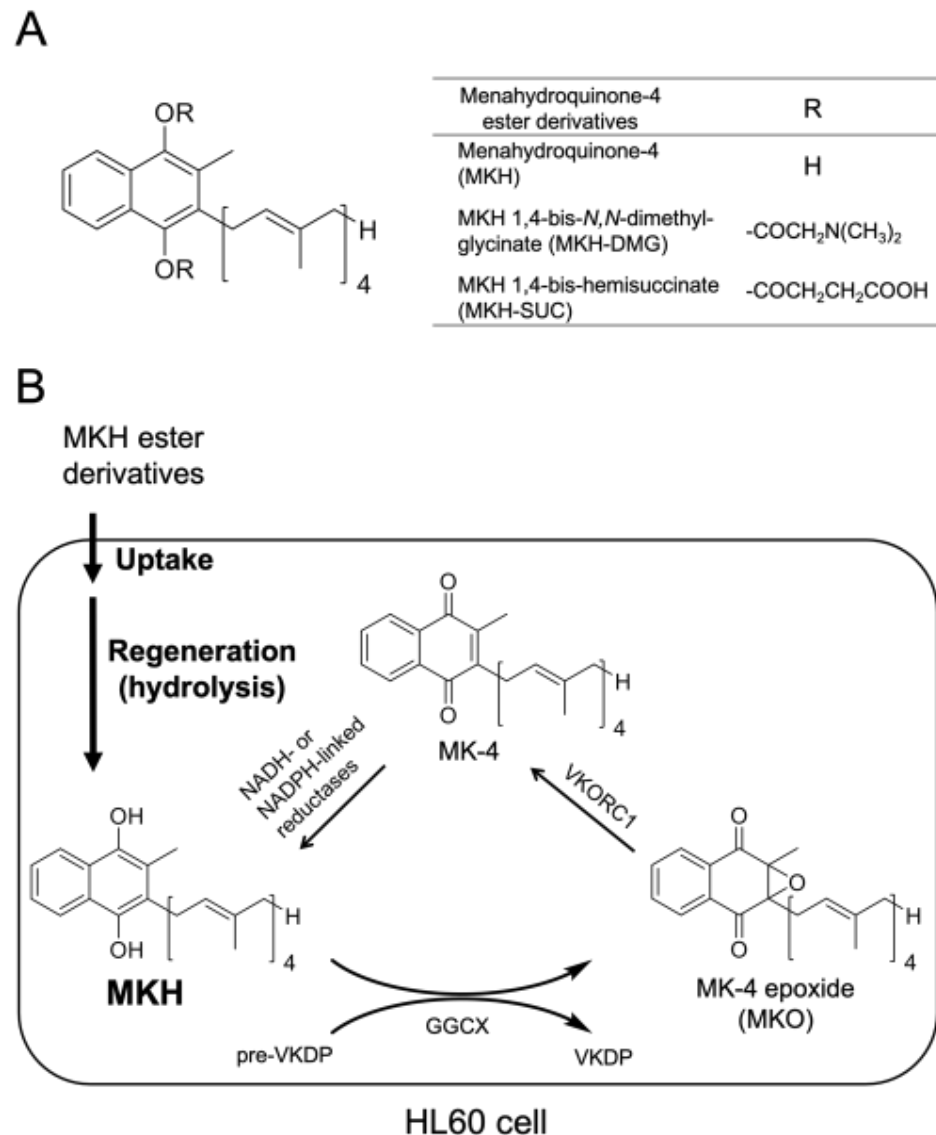
## 1. Introduction

Acute promyelocytic leukemia (APL) is a unique subtype of acute myeloid leukemia (AML). All-trans retinoic acid (ATRA), also known as tretinoin, a molecularly targeted drug, has been used for the initial (induction) treatment of APL in combination with anthracyclines. The cure rate associated with this general treatment approach is 80–90%. However, it has been reported that approximately 15–20% of patients relapse and most of them acquire ATRA resistance [1–5]. Thus, there is a demand for effective and safe agents for ATRA-resistant APL. HL60 was initially classified as an APL cell line, and ATRA was found to induce its differentiation; this discovery led to numerous studies [6,7]. HL60 was later reclassified as a non-APL cell line [8]. As mentioned below, because the aim of this study was to discover drug candidates that potentially overcome ATRA resistance, we used HL60 and HL-60R (ATRA-resistant HL60) as ATRA-responsive cell lines.

It has been reported that menaquinone-4 (MK-4, vitamin K<sub>2(20)</sub>) induces apoptosis in leukemia cell lines and primary cultured leukemia cells. MK-4 shows greater inhibitory effects on myeloid cells such as myeloblasts, which are abnormal promyelocytes, than on lymphoid cells. Therefore, MK-4 may exert selective effects against APL cells without any adverse effects on normal bone marrow cells in patients with APL [9–16]. MK-4 has been

used to treat osteoporosis, especially in postmenopausal women, and its long-term safety has been established. Thus, MK-4 has the potential to be an alternative chemotherapeutic agent for ATRA. However, the effect of MK-4 against ATRA-resistant APL has not been reported.

MK-4 is reduced to menahydroquinone-4 (MKH) via the vitamin K cycle in cells. MKH is a cofactor of  $\gamma$ -glutamyl carboxylase (GGCX), which converts glutamic acid residues into  $\gamma$ -carboxyglutamic acid residues of vitamin K-dependent proteins. In other words, the post-translational modification of vitamin K-dependent proteins depends on the supplied MKH. When MKH acts as a cofactor, it is stoichiometrically converted to MK-4 epoxide (MKO), which is further reduced to MK-4 for reuse (Figure 1B).



**Figure 1.** Chemical structure of MKH derivatives (A). The activation step for MKH derivatives, and the vitamin K cycle in HL60 cells (B). MKH, menahydroquinone-4; MK-4, menaquinone-4; MKO, menaquinone-4 epoxide; VKR, vitamin K reductase; VKOR, vitamin K epoxide reductase; VKDP, vitamin K-dependent proteins; GGCX,  $\gamma$ -glutamyl carboxylase.

It has been reported that MK-4 induces apoptosis via the activation of BAK, a member of the Bcl-2 family of apoptosis-promoting proteins, indicating an interaction between MKO and BAK [12]. Previously, we reported that the MKH ester derivatives 1,4-bis-*N,N*-dimethylglycinate (MKH-DMG) and 1,4-bis-hemi-succinate (MKH-SUC) (Figure 1A) act as prodrugs for hepatocellular carcinoma (HCC) cells, and exhibit strong antitumor effects compared with MK-4 [17,18]. As MKH is the active form of MK-4, in terms of the physiological effects, such as blood coagulation and bone formation, MKH may contribute to the inhibitory effect of MK-4. In this study, we investigated the efficacy of MKH ester derivatives against ATRA-responsive HL60 and ATRA-resistant HL60 (HL-60R) cells, the delivery of MKH by these derivatives, and the underlying mechanisms.

## 2. Materials and Methods

### 2.1. Chemicals

MK-4 and MKO were kindly provided by Eisai (Tokyo, Japan). MKH-DMG and MKH-SUC were synthesized in our laboratory, and the nuclear magnetic resonance (NMR) spectra and mass spectra for MKH-DMG and MKH-SUC have been reported previously [18–20]. ATRA and other chemicals were purchased from FUJIFILM Wako Pure Chemical (Osaka, Japan) unless otherwise specified.

### 2.2. Cell Lines

Human promyelocytic cell lines HL60 (RCB0041) and ATRA-resistant HL-60R (RCB1550, derived from RCB0041) were provided by RIKEN BRC (Ibaraki, Japan) [21]. The cell lines were maintained in RPMI 1640 (FUJIFILM Wako Pure Chemical) supplemented with 10% fetal bovine serum (Nichirei Biosciences, Tokyo, Japan) and 1% penicillin/streptomycin (Life Technologies, Carlsbad, CA, USA) at 37 °C under an atmosphere of 5% CO<sub>2</sub>.

### 2.3. Cell Viability Assay

HL60 and HL-60R cells were seeded at  $3.0 \times 10^3$  cells/well in 96-well plates and incubated for 24 h. ATRA, MK-4, MKH-DMG, and MKH-SUC were initially dissolved in ethanol. Stock solutions (15 mM) of each drug were diluted to the intended final concentrations with medium. Cells were exposed to a medium containing ATRA, MK-4, MKH-DMG, or MKH-SUC for 72 h, and cell viability was measured using the CellTiter-Glo 2.0 Luminescent Cell Viability Assay kit (Promega, Madison, WI, USA), according to the manufacturer's instructions. The CellTiter-Glo assay detects intracellular ATP, thereby enabling identification of living cells. The doubling times of the HL60 and HL-60R cells using CellTiter-Glo were  $24.9 \pm 3.68$  and  $26.2 \pm 2.69$  h, respectively. These values were almost consistent with the number of cells counted by staining them with trypan blue after each subculturing. The IC<sub>50</sub> values were determined using a log (drug) vs. normalized response-variable slope analysis with GraphPad Prism, version 6.0 (GraphPad Software, San Diego, CA, USA). Resistance index was calculated using the following equation:

$$\text{Resistance index} = \text{IC}_{50} \text{ to HL-60R} / \text{IC}_{50} \text{ to HL60} \quad (1)$$

### 2.4. Determination of Intracellular MK-4 and MKO Levels after Drug Treatment

HL60 and HL-60R cells were seeded at  $3.0 \times 10^5$  cells/well in six-well plates and incubated for 24 h. The cells were cultured in a medium containing MK-4, MKH-DMG, or MKH-SUC for the indicated time. After drug exposure, the medium was removed, and the cells were washed twice with PBS. Intracellular drug extraction was performed as previously described [22], and cell protein concentration was determined using a BCA protein assay kit (Thermo Fisher Scientific, Waltham, MA, USA). Curve fitting was performed using a Michaelis–Menten slope analysis with GraphPad Prism, version 6.0 (GraphPad Software).

## 2.5. LC-MS/MS

The LC-MS/MS system and conditions were set as previously described [22]. Briefly, LC-MS/MS was performed using an LCMS-8050 and Shimadzu UFLC System (Shimadzu, Kyoto, Japan) with a CAPCELL PAK C18 UG120 column (3  $\mu$ m, 2.0 mm  $\times$  100 mm; Shiseido Co., Ltd., Tokyo, Japan) and mobile phase of 10 mM ammonium acetate and 0.1% acetic acid in methanol and water (97:3) at a flow rate of 0.4 mL/min. Identification and quantitation were performed in the MS/MS-multiple reaction monitoring (MRM) mode with positive electrospray ionization. During MRM,  $m/z$  was 445 $\rightarrow$ 187 for the  $[M + H]^+$  MK-4 adduct and 461 $\rightarrow$ 81 for the  $[M + H]^+$  MKO adduct. The retention times were 3.3 min for MK-4 and 2.5 min for MKO.

## 2.6. Cell Cycle Analysis

HL60 and HL-60R cells were seeded at  $3.0 \times 10^5$  cells/dish in 100 mm dishes and incubated for 24 h. The cells were then exposed to medium containing ATRA, MK-4, MKH-DMG, or MKH-SUC for 72 h. The medium was removed, and the cells were washed with PBS and fixed in 70% ethanol at  $-20^\circ\text{C}$  overnight. The supernatant was removed after centrifugation, and the cell pellet was resuspended in 500  $\mu$ L of RNase (0.25 mg/mL; Sigma Aldrich, St. Louis, MO, USA) and incubated for 30 min at  $37^\circ\text{C}$ . The suspension was treated with 10  $\mu$ L of propidium iodide (PI, 1 mg/mL) on ice for 20 min. Cell populations and cell cycle phases were analyzed using a JSAN flow cytometer (Bay Bioscience, Kobe, Japan) and FlowJo software (Becton Dickinson, Franklin Lakes, NJ, USA).

## 2.7. Apoptosis Detection

HL60 and HL-60R cells were seeded at  $3.0 \times 10^5$  cells/dish in 100 mm dishes and incubated for 24 h. The cells were exposed to a medium containing MK-4, MKH-DMG, or MKH-SUC for 72 h. Apoptotic cells were detected using an Annexin V-FITC Apoptosis Detection kit (Medical & Biological Laboratories, Aichi, Japan) according to the manufacturer's instructions. The percentage of apoptotic cells to total cell population in each sample was determined using a JSAN flow cytometer (Bay Bioscience). Cells simultaneously stained negative for Annexin V-FITC and PI were considered live cells. Cells stained positive for Annexin V-FITC were considered apoptotic cells, and PI-negative and -positive cells were considered to be early- and late-stage apoptotic, respectively.

## 2.8. Mitochondrial Membrane Potential

HL60 and HL-60R cells were seeded at  $1.0 \times 10^5$  cells/well in 12-well plates and incubated for 24 h. The cells were exposed to a medium containing MK-4, MKH-DMG, or MKH-SUC for 48 h. Mitochondrial membrane potential was detected using the lipophilic cationic probe JC-1 (DOJINDO, Tokyo, Japan). The cells were washed with culture medium, and then incubated in culture medium containing 2  $\mu$ M JC-1 for 30 min at room temperature in the dark. Next, the cells were washed twice with the imaging buffer provided in the JC-1 package, and the mitochondrial membrane potential was determined using a JSAN flow cytometer (Bay Bioscience).

## 2.9. Determination of Cytochrome C in Mitochondrial and Cytosolic Fractions

HL60 and HL-60R cells were seeded at  $1.0 \times 10^5$  cells/well in six-well plates and incubated for 24 h. Next, the cells were treated with or without 10  $\mu$ M MK-4, MKH-DMG, or MKH-SUC for 48 h. The cells were washed three times with ice-cold PBS, resuspended in isotonic buffer A (10 mM HEPES, 0.3 M mannitol, and 0.1% BSA) with 0.1 mM digitonin, left on ice for 5 min, and centrifuged at  $8500 \times g$  for 5 min at  $4^\circ\text{C}$ . The supernatant was used as the cytosolic fraction. The pellet was resuspended in sonication buffer (50 mM Tris-HCl, pH 7.4, 150 mM NaCl, 2 mM EDTA, 1 mM PMSF, and 0.5% Tween 20), sonicated twice on ice, and centrifuged at  $10,000 \times g$  for 30 min at  $4^\circ\text{C}$ . The supernatant was used as the mitochondrial fraction. The amount of cytochrome c in the mitochondrial and cytosolic fractions was measured using the cytochrome c ELISA kit (R&D Systems, Minneapolis,

MN, USA) according to the manufacturer's instructions. The cell protein concentration was determined using a BCA protein assay kit.

#### 2.10. Western Blotting

HL60 and HL-60R cells were seeded at a density of  $1.5 \times 10^5$  cells/well in six-well plates for 36 h. Next, the cells were treated with or without 10  $\mu$ M MK-4, MKH-DMG, or MKH-SUC for 24, 48, or 72 h. The cells were washed with PBS after removing the drug-containing medium and lysed with RIPA buffer (0.5% NP-40, 0.25% sodium deoxycholate, 0.05% SDS, 150 mM NaCl, and 50 mM HEPES, pH 7.4) containing a protease inhibitor cocktail (Nacalai Tesque, Kyoto, Japan). Each cell lysate was combined with sample loading buffer (Nacalai Tesque), separated on 15% SDS-PAGE gels (SuperSep Ace, FUJIFILM Wako), and transferred onto PVDF membranes (BIO-RAD, Hercules, CA, USA). After blocking, the membranes were incubated with the following primary antibodies: anti-pro/p17-caspase-3, anti-cleaved PARP1 (1:2000) (ab136812; Abcam, Cambridge, UK), rabbit anti-Bak (1:2000) (#12105; Cell Signaling Technology, Danvers, MA, USA), and mouse anti-GAPDH antibody (1:2000) (G8795; Sigma-Aldrich, St. Louis, MO, USA). After washing, the membranes were treated with appropriate secondary antibodies and visualized using Immunostar LD or Immunostar Zeta (FUJIFILM Wako).

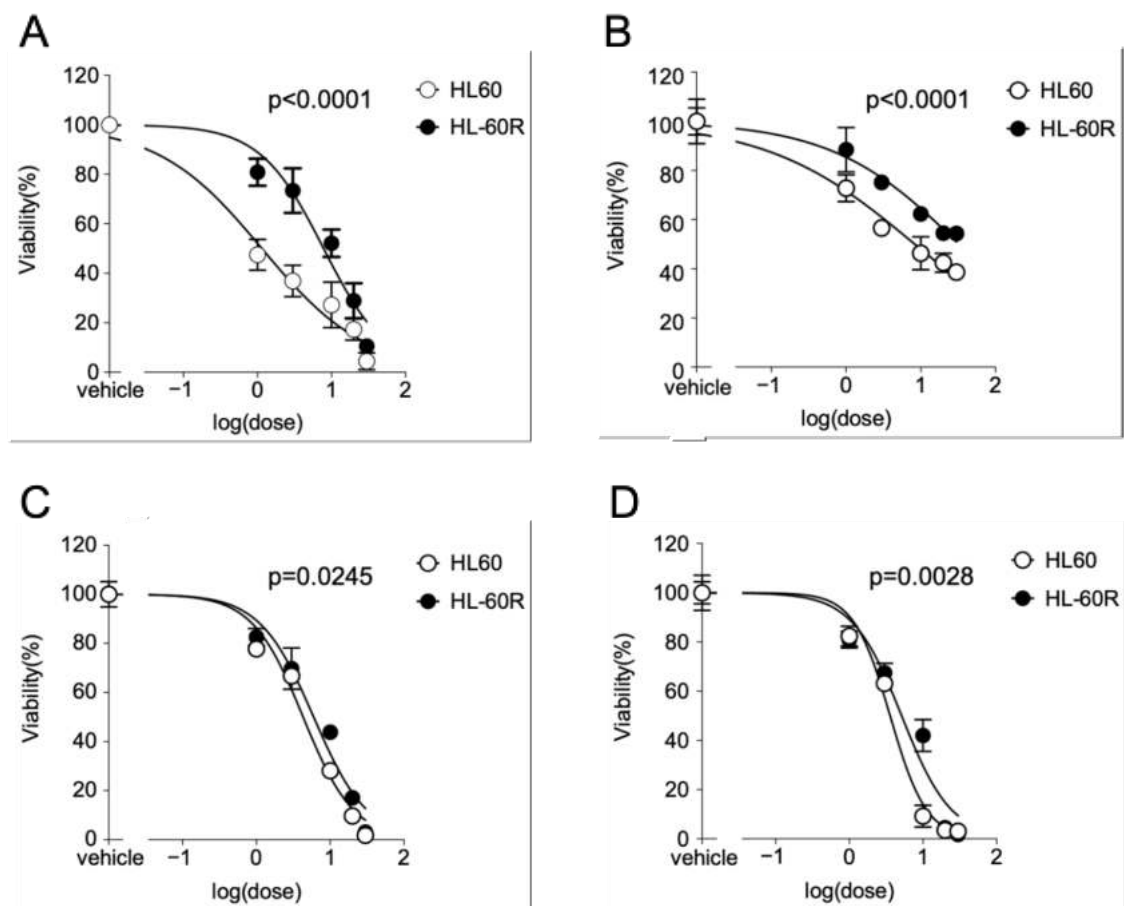
#### 2.11. Statistical Analysis

The statistical significance of the results in Section 3.1 was determined using the extra sum-of-squares F test, and that of the results in the other sections was determined using Dunnett's test. All analyses were carried out using GraphPad Prism 6 (GraphPad Software, San Diego, CA, USA); results with  $p < 0.05$  were considered significant.

### 3. Results

#### 3.1. Growth-Inhibitory Effects of MKH Derivatives on HL60 and HL-60R Cells

To assess the growth inhibitory effects of MKH derivatives (MKH-DMG and MKH-SUC) on HL60 and HL-60R cell lines, a dose–cell viability plot at 72 h after treatment with the test drugs was generated (Figure 2). The curves of viable HL60 and HL60R cells after drug treatment were compared using the extra sum-of-squares F test. All test drugs reduced the viability of both cell lines in a dose-dependent manner. The  $IC_{50}$  values and resistance indexes are summarized in Table 1. As the integrities of the curves from the MK-4 treatments are insufficient to determine  $IC_{50}$  values, the obtained  $p$  values and  $IC_{50}$  values for MK-4 were only used for reference. For ATRA treatment, the viability curve of the HL-60R cells shifted towards the higher doses represented on the HL60 cell curve (Figure 2A). Similarly, for the MK-4 treatment, the curve of the HL-60R cells shifted towards the higher doses for HL60 cells (Figure 2B). In contrast, the MKH-DMG and MKH-SUC treatments strongly inhibited the growth of both cell lines in a dose-dependent manner compared with MK-4 (Figure 2C,D). The resistance index values of MKH-DMG and MKH-SUC were considerably lower than those of ATRA and MK-4 and were close to 1 (Table 1). Similarly, to assess the growth-inhibitory effect of MKH-DMG and MKH-SUC on the APL cell line NB-4, a dose–cell viability plot at 72 h after treatment with the test drugs was generated (Supplementary Figure S1). MKH-DMG and MKH-SUC decreased the viability of cells in a dose-dependent manner. The  $IC_{50}$  value for MKH-DMG was 16.9  $\mu$ M (95% CI: 14.4–20.0) and that for MKH-SUC was 10.2  $\mu$ M (95% CI: 9.50–10.9).



**Figure 2.** Inhibitory effects of ATRA, MK-4, and MKH derivatives on the viability of HL60 and HL-60R cells. Cells were treated with 1–30  $\mu$ M ATRA (A), MK-4 (B), MKH-DMG (C), or MKH-SUC (D) for 72 h. Plotted values are mean  $\pm$  SD ( $n = 3$ ).  $p$  values were analyzed using the extra sum-of-squares F test.

**Table 1.**  $IC_{50}$  values of ATRA, MK-4, and MKH-ester derivatives in HL60 or HL-60R cells after 72 h.

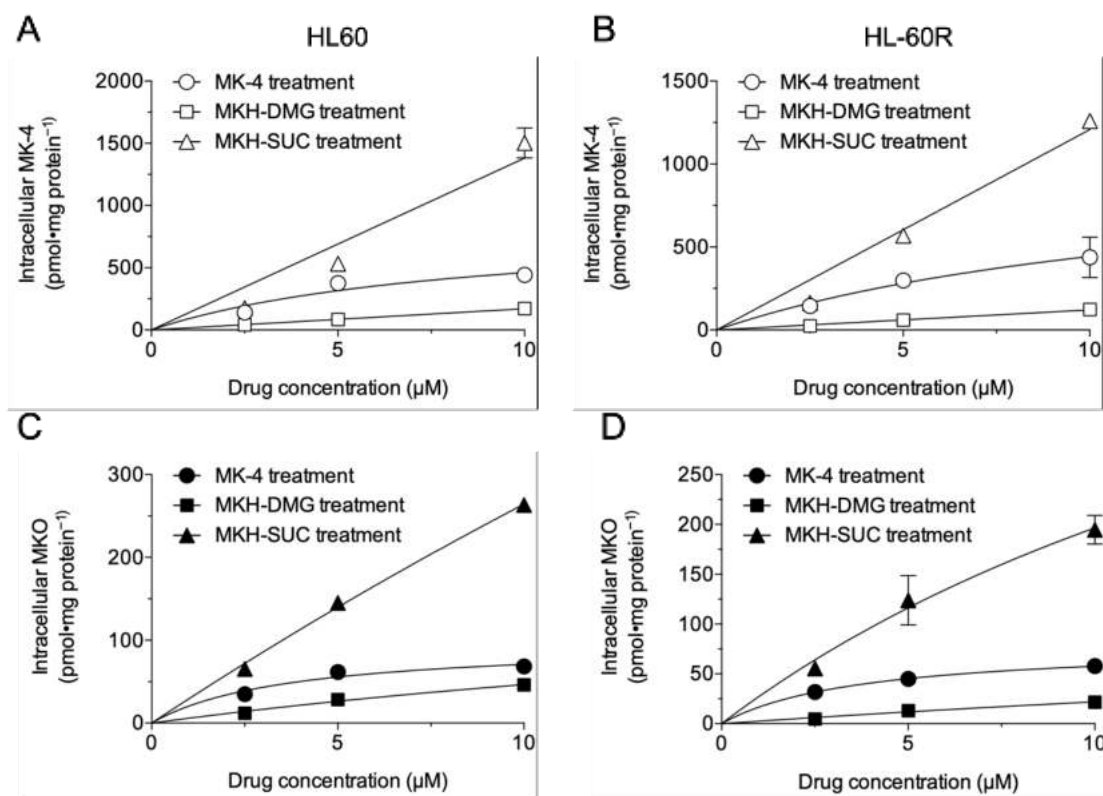
Compound	$IC_{50}$ ( $\mu$ M) (95% CI <sup>a</sup> )		Resistance Index <sup>b</sup>
	HL60 Cells	HL-60R Cells	
ATRA	1.15 (0.416–2.52)	7.83 (4.72–13.0)	6.79
MK-4	8.33 <sup>c</sup> (5.25–13.2)	32.5 <sup>c</sup> (20.2–52.3)	3.94
MKH-DMG	4.30 (2.89–6.40)	5.97 (3.74–9.53)	1.39
MKH-SUC	3.58 (2.66–4.83)	5.14 (2.81–9.40)	1.44

<sup>a</sup> 95% Confidence interval. <sup>b</sup> Resistance index =  $IC_{50}$  for HL-60R/ $IC_{50}$  for HL60. <sup>c</sup>  $IC_{50}$  values for MK-4 were considered just for reference.

### 3.2. Intracellular Drug Levels in HL60 and HL-60R Cells Treated with MK-4 and MKH Derivatives

To determine the intracellular drug levels corresponding to the growth inhibitory effects, cells treated with the test drugs were evaluated by LC-MS/MS (Figure 3). The intracellular levels of MK-4 and MKO in HL60 and HL-60R cells after 24 h of treatment with 2.5–10  $\mu$ M MK-4, MKH-DMG, or MKH-SUC are shown in Figure 3. Each dose–intracellular drug concentration plot is presented with curve fitting using the Michaelis–Menten model. When quantifying intracellular MKH levels, intracellular MKH was detected as MK-4, the oxidized reactant of MKH (reduced form), and intracellular MKO reflected the amount of MKH delivered, as MKH is stoichiometrically converted to MKO when it functions as a cofactor for GGCX (Figure 1B). Thus, both intracellular MK-4 and MKO levels after treatment with MK-4 or MKH derivatives were regarded as indicators of MKH delivery. All test drugs increased the intracellular MK-4 and MKO levels in a dose-dependent manner

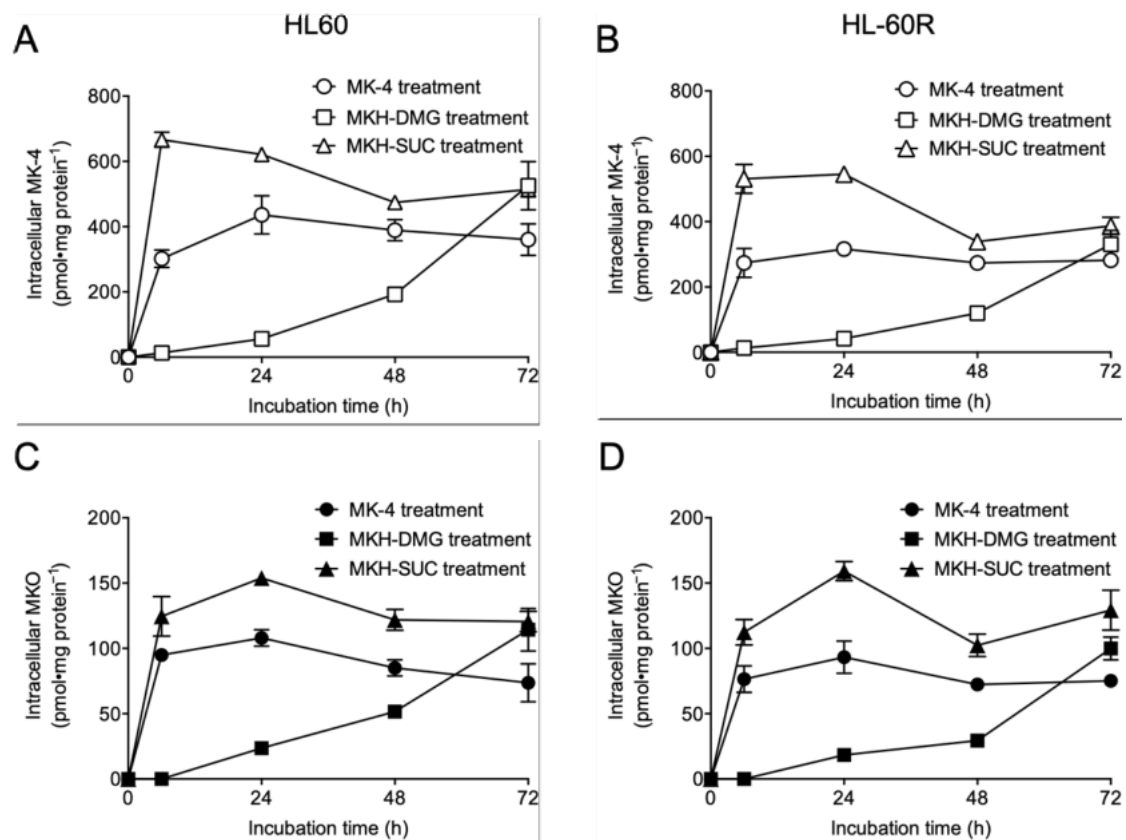
in both HL60 and HL-60R cell lines (Figure 3A–D). The intracellular MK-4 (Figure 3A,B) and MKO (Figure 3C,D) levels in cells treated with MK-4 reached a plateau at 5  $\mu\text{M}$  in both cell lines. In contrast, the saturation of the intracellular MK-4 (Figure 3A,B) and MKO (Figure 3C,D) levels in cells treated with MKH-DMG or MKH-SUC was not observed, and these levels increased in a dose-dependent manner in this dose range (2.5–10  $\mu\text{M}$ ). The intracellular MK-4 and MKO levels after MKH-SUC treatment were higher than those after MK-4 treatment. In contrast, the intracellular MK-4 and MKO levels after MKH-DMG treatment were lower than those after MK-4 treatment.



**Figure 3.** Intracellular level of MK-4 and MKO in HL60 and HL-60R cells treated with MK-4 or MKH derivatives. Intracellular MK-4 in HL60 (A) and HL-60R (B) cells treated with 2.5–10  $\mu\text{M}$  MK-4, MKH-DMG, or MKH-SUC for 24 h, and intracellular MKO in HL60 (C) and HL-60R (D) cells treated with 2.5–10  $\mu\text{M}$  MK-4, MKH-DMG, or MKH-SUC for 24 h. Plotted values are mean  $\pm$  SD ( $n = 3$ ).

The time course of intracellular MK-4 and MKO levels up to 72 h of treatment with 5  $\mu\text{M}$  of each drug is shown in Figure 4. The drug concentration was set at 5  $\mu\text{M}$ , which is an approximation of the  $\text{IC}_{50}$  values of the MKH derivatives given in Table 1. The intracellular MK-4 (Figure 4A,B) and MKO (Figure 4C,D) levels after MK-4 or MKH-SUC treatment rapidly increased and reached a plateau at 24 h. The intracellular MK-4 and MKO levels after MKH-SUC treatment were higher than those after MK-4 treatment at earlier time points, and the  $\text{AUC}_{0-72\text{h}}$  for MK-4 or MKO after MKH-SUC treatment was approximately 1.5-fold higher than that for MK-4 in both cell lines (Table 2). In contrast, the intracellular MK-4 and MKO levels after MKH-DMG treatment steadily increased in a time-dependent manner and surpassed those of MK-4 at 72 h. The  $\text{AUC}_{0-72\text{h}}$  for MK-4 or MKO after MKH-DMG treatment was approximately half that after MK-4 treatment in both cell lines (Table 2). However, the intracellular MKH-DMG level after MKH-DMG treatment increased rapidly in both cell lines, reaching a peak at 24 h. Furthermore, the sequential hydrolysis reaction of MKH-DMG was observed, indicating the elimination of bis-ester and the generation of the corresponding monoesters in a time-dependent manner (Supplementary Figure S2).





**Figure 4.** Intracellular concentration of MK-4 and MKO in HL60 and HL-60R cells treated with MK-4 or MKH derivatives. Intracellular MK-4 levels in HL60 (A) and HL-60R (B) cells treated with 5  $\mu$ M MK-4, MKH-DMG, or MKH-SUC up to 72 h, and intracellular MKO levels in HL60 (C) and HL-60R (D) cells treated with 5  $\mu$ M MK-4, MKH-DMG, or MKH-SUC up to 72 h. Plotted values are mean  $\pm$  SD (n = 3).

**Table 2.** Area under the curve over 72 h ( $AUC_{0-72h}$ ) of intracellular concentrations of MK-4 and MKO in HL60 and HL-60R cells treated with 5  $\mu$ M MK-4, MKH-DMG, or MKH-SUC.

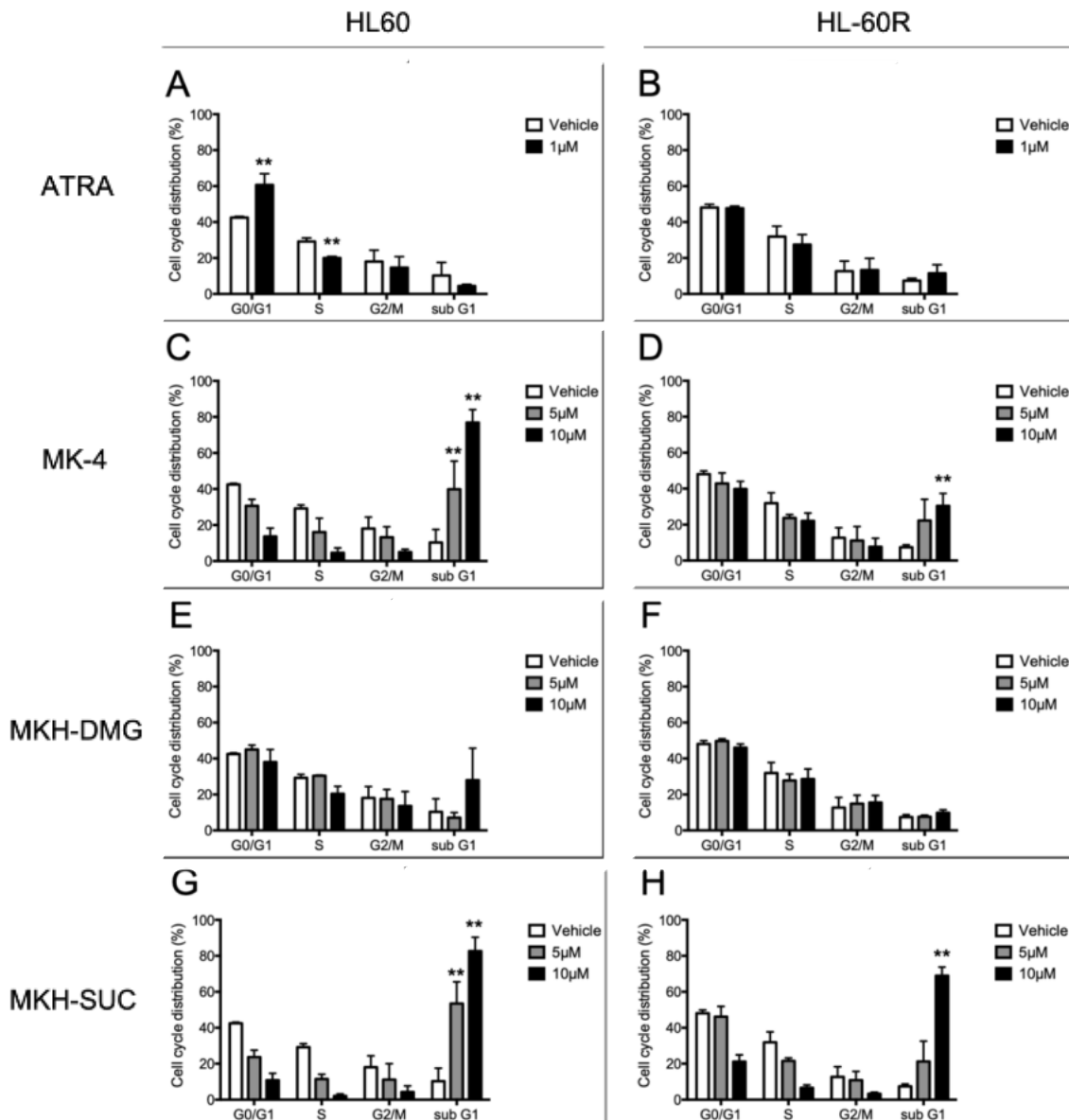
Compound	$AUC_{0-72h}$ <sup>a</sup> (nmol·h·mg Protein <sup>-1</sup> ) in HL60 Cells		$AUC_{0-72h}$ <sup>a</sup> (nmol·h·mg Protein <sup>-1</sup> ) in HL-60R Cells	
	MK-4	MKO	MK-4	MKO
MK-4	26.4 $\pm$ 0.80	6.33 $\pm$ 0.32	19.9 $\pm$ 0.40	5.52 $\pm$ 0.03
MKH-DMG	12.3 $\pm$ 1.29	3.11 $\pm$ 0.36	7.90 $\pm$ 0.66	2.29 $\pm$ 0.15
MKH-SUC	38.6 $\pm$ 0.50	9.10 $\pm$ 0.22	30.6 $\pm$ 1.24	8.70 $\pm$ 0.46

<sup>a</sup> Values are shown as mean  $\pm$  SD (n = 3).

### 3.3. Effects of MKH Derivatives on the Cell Cycle of HL60 and HL-60R Cells

To determine the effects of the test drugs on the cell cycle, we performed flow cytometry with PI staining (Figure 5). The distributions at each cell cycle phase in HL60 and HL-60R cells treated with 1  $\mu$ M ATRA, the pharmacological dose, for 72 h are shown in Figure 5A,B, respectively. The percentage of ATRA-treated HL60 cells in the G<sub>0</sub>/G<sub>1</sub> phase significantly increased, whereas that in the S phase decreased, indicating G<sub>1</sub> arrest. In contrast, G<sub>1</sub> arrest was not observed in HL-60R cells treated with ATRA (Figure 5B). The distributions at each cell cycle phase in HL60 and HL-60R cells treated with 5 and 10  $\mu$ M MK-4 or MKH derivatives for 72 h are shown in Figure 5C–H. In the MK-4 treatment, G<sub>1</sub> arrest was not observed in either cell line. The percentage of HL60 cells in the sub-G<sub>1</sub> phase, which indicates DNA fragmentation by apoptosis, significantly increased (Figure 5C). On the other hand, the percentage of HL-60R cells in the sub-G<sub>1</sub> phase slightly increased compared with that of the HL60 cells (Figure 5D). In the MKH-DMG treatment, there was no change in cell distribution at either the G<sub>0</sub>/G<sub>1</sub>–S or the sub-G<sub>1</sub> phase in either cell

line (Figure 5E,F). Under the MKH-SUC treatment, G<sub>1</sub> arrest was not observed, but the sub-G<sub>1</sub> cell distribution in both cell lines significantly increased (Figure 5G,H), similarly to that under the MK-4 treatment. The percentage of HL-60R cells in the sub-G<sub>1</sub> phase was considerably higher under the 10  $\mu$ M MKH-SUC treatment than under the 10  $\mu$ M MK-4 treatment (Figure 5D,H).

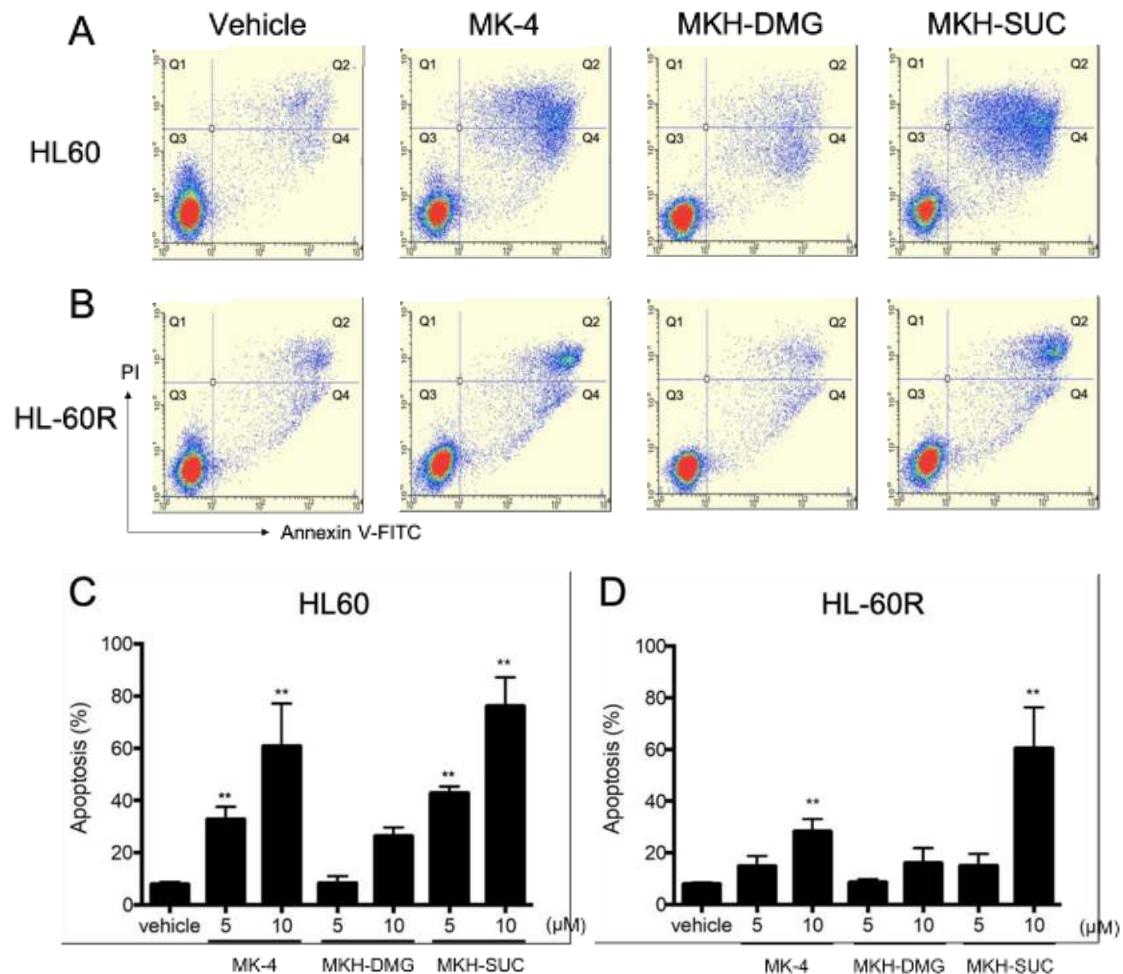


**Figure 5.** Effects of ATRA, MK-4, and MKH derivatives on the cell cycle distribution of HL60 and HL-60R cells. HL60 (A,C,E,G) and HL-60R (B,D,F,H) cells were treated with 1  $\mu$ M ATRA (A,B), 5 or 10  $\mu$ M MK-4 (C,D), 5 or 10  $\mu$ M MKH-DMG (E,F), or 5 or 10  $\mu$ M MKH-SUC (G,H) for 72 h. Cell cycle distribution was analyzed by flow cytometry after PI staining. Data are shown as mean  $\pm$  SD from triplicate experiments. \*\*  $p < 0.01$  by Dunnett's test.

### 3.4. Effects of MKH Derivatives on the Cell Apoptosis of HL60 and HL-60R Cells

To assess the cell apoptosis involved in the growth inhibitory effect of MKH derivatives on HL60 and HL-60R cells, apoptotic cells were detected using flow cytometry with Annexin V/PI staining (Figure 6). The typical flow cytograms for HL60 and HL-60R cells are shown in Figure 6A,B, respectively. Following treatment with MK-4 or MKH-SUC, the number of apoptotic HL60 (Figure 6C) and HL-60R (Figure 6D) cells increased in a dose-dependent manner. Under the MKH-DMG treatment, apoptotic cells tended to

increase at 10  $\mu\text{M}$ , but not at 5  $\mu\text{M}$  (Figure 6C,D). Ten micromolar of MKH-SUC induced strong apoptosis in both cell lines (Figure 6C,D).



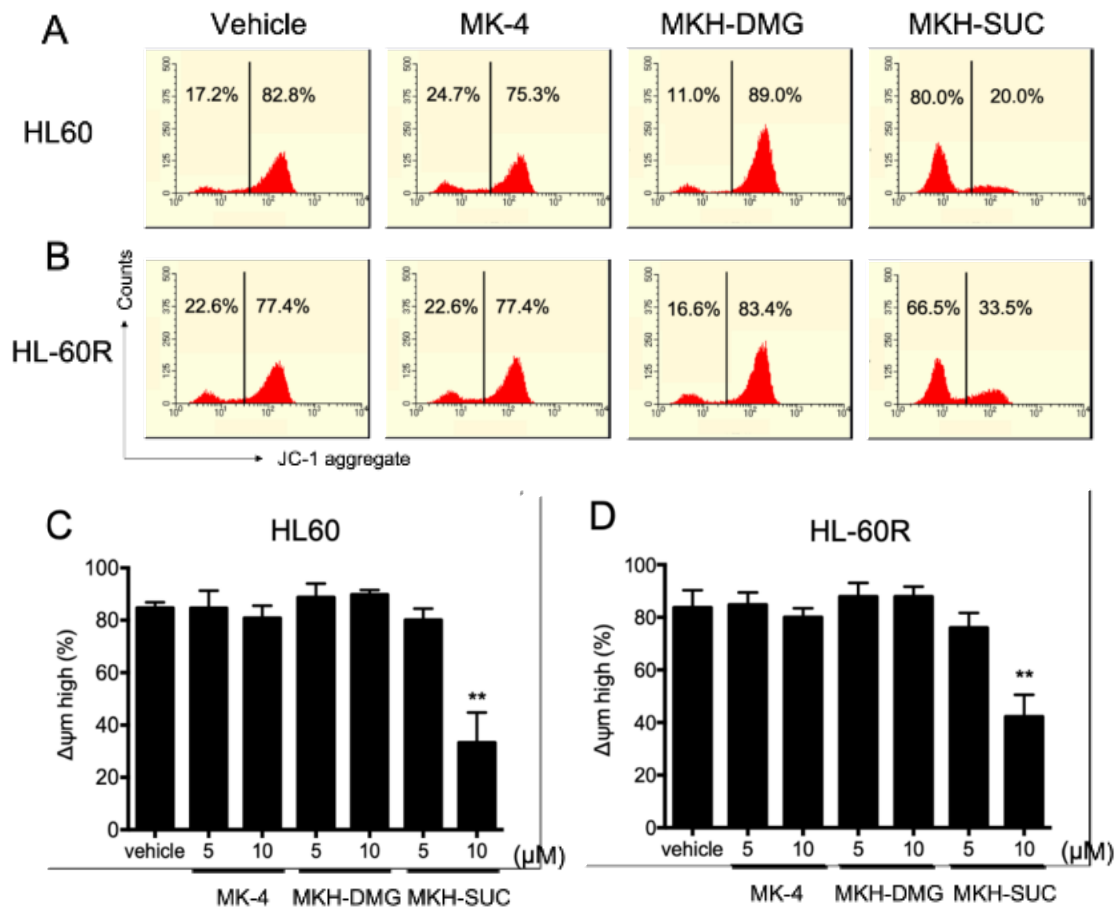
**Figure 6.** Effects of MK-4 and MKH derivatives on the apoptosis in HL60 and HL-60R cells. Typical flow cytograms of HL60 (A) and HL-60R (B) cells treated with the test drugs at 5  $\mu\text{M}$  for 72 h are shown, with percentages of apoptotic HL60 (C) and HL-60R (D) cells treated with 5 or 10  $\mu\text{M}$  MK-4, MKH-DMG, or MKH-SUC for 72 h. Apoptotic cells were determined using flow cytometry after Annexin V/PI staining. Data are shown as mean  $\pm$  SD from triplicate experiments. \*\*  $p < 0.01$  vs. vehicle by Dunnett's test.

### 3.5. Effect of MKH Derivatives on Mitochondrial Apoptotic Pathway

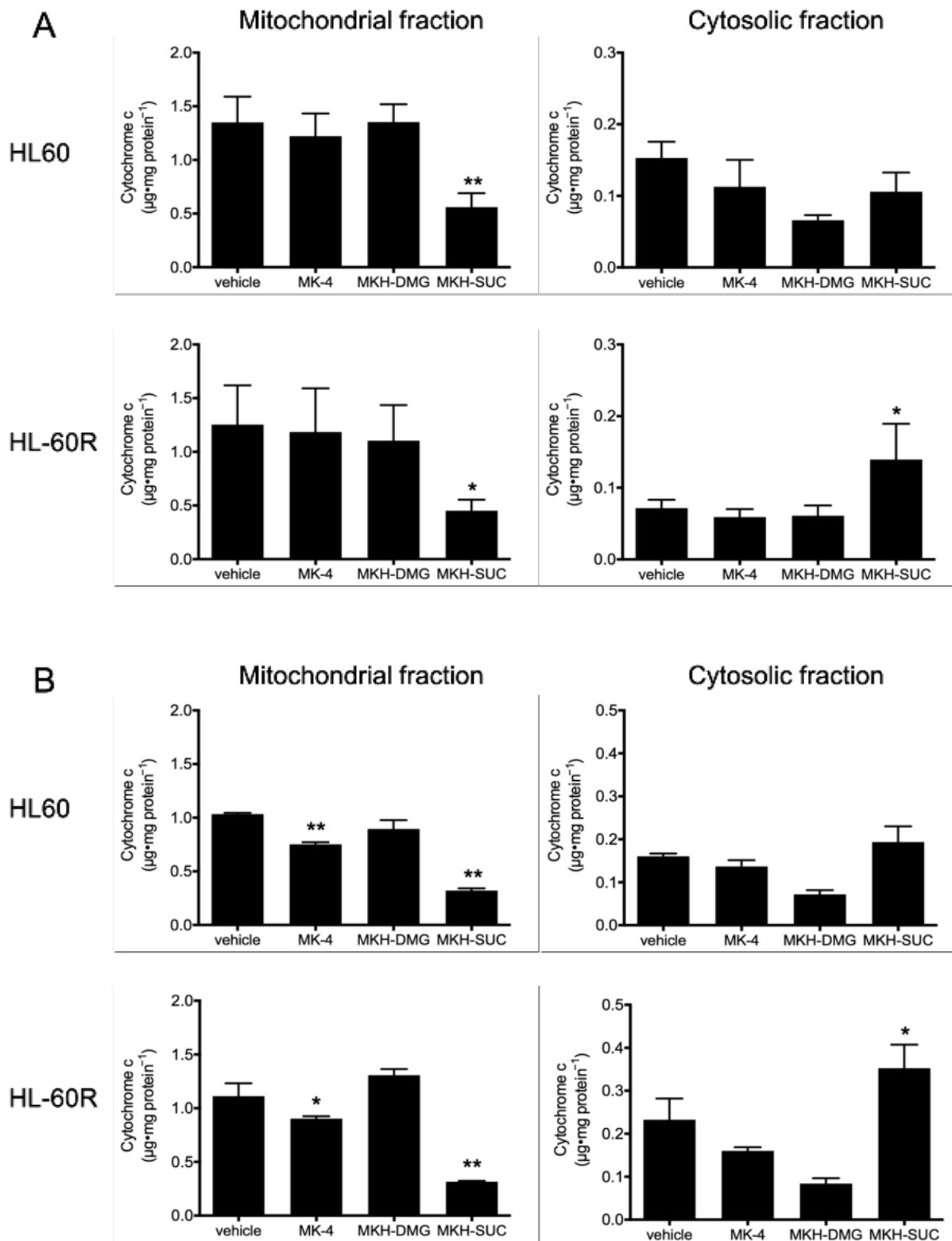
To confirm whether the apoptosis of cells induced by the MKH derivatives involves the mitochondrial pathway, mitochondrial membrane potential, cytochrome c release, and expression of apoptosis-related proteins (pro-/cleaved caspase-3, cleaved PARP, and BAK) were analyzed using flow cytometry with JC-1 staining, ELISA, and Western blotting, respectively.

The mitochondrial membrane potential of both cell lines treated with 10  $\mu\text{M}$  MK-4 and 5  $\mu\text{M}$  MKH-SUC for 48 h tended to decrease slightly compared with that under treatment with the vehicle, and that of cells treated with 10  $\mu\text{M}$  MKH-SUC strongly decreased (Figure 7C,D). In contrast, the MKH-DMG treatment did not affect the potentials in either cell line (Figure 7C,D). The level of mitochondrial cytochrome c in both cell lines treated with 10  $\mu\text{M}$  MK-4 decreased at 48 h and those in cells treated with MKH-SUC decreased at both 48 and 72 h (Figure 8). In the cytosolic fraction, the cytochrome c level after MK-4 treatment did not increase, whereas that in HL-60R cells significantly increased after MKH-SUC treatment for 72 h (Figure 8). In contrast, MKH-DMG did not promote the release of

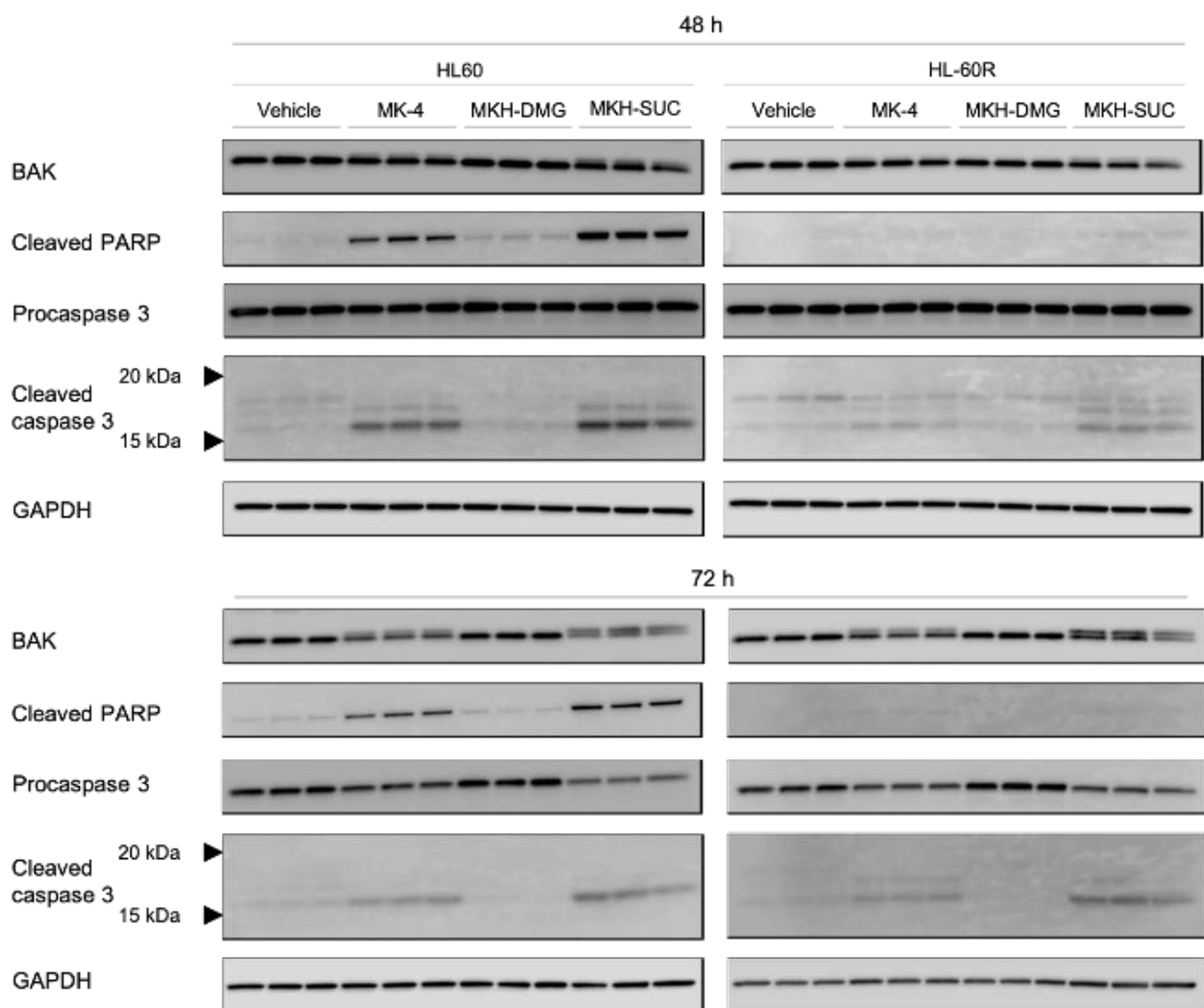
cytochrome c from the mitochondria to the cytosol (Figure 8). The Western blotting analysis showed that the bands of modified BAK protein in both cell lines treated with 10  $\mu$ M MK-4 and MKH-SUC for 48 h migrated at a slightly higher molecular weight than the bands of free BAK. Moreover, this doublet was clearly observed following MK-4 and MKH-SUC treatments for 72 h (Figure 9). The MK-4 and MKH-SUC treatments also induced cleaved caspase-3 and PARP at 48 h, and pro-caspase 3 decreased at 72 h (Figure 9). The expression of cleaved PARP was lower in HL-60R cells than in HL60 cells (Figure 9). The MKH-DMG treatment did not affect the levels of these proteins (Figure 9).



**Figure 7.** Effects of MK-4 and MKH derivatives on the mitochondrial membrane potentials of HL60 and HL-60R cells. Typical flow cytograms of HL60 (A) and HL-60R (B) cells treated with the test drugs at 10  $\mu$ M for 48 h. Percentages of  $\Delta\Psi_m$ -high cells among HL60 (C) and HL-60R (D) cells treated with 5 or 10  $\mu$ M MK-4, MKH-DMG, or MKH-SUC for 48 h. The mitochondrial membrane potentials were determined using flow cytometry after JC-1 staining. Data are shown as mean  $\pm$  SD from triplicate experiments. \*\*  $p < 0.01$  vs. vehicle by Dunnett's test.



**Figure 8.** Release of cytochrome c in HL60 and HL-60R cells treated with MK-4 and MKH derivatives. HL60 and HL-60R cells treated with the test drugs at 10 μM for 48 h (A) or 72 h (B). The cytochrome c level in the mitochondrial or cytosolic fractions was determined using ELISA. Data are shown as mean ± SD from at least 3 replicates. \*  $p < 0.05$ , \*\*  $p < 0.01$  vs. vehicle by Dunnett's test.



**Figure 9.** Effects of MK-4 and MKH derivatives on the expression of apoptosis-related proteins in HL60 and HL-60R cells. HL60 and HL-60R cells were treated with 10  $\mu$ M MK-4, MKH-DMG, or MKH-SUC for 48 and 72 h. The expression of BAK, cleaved PARP, and pro/cleaved caspase-3 was analyzed by Western blotting.

#### 4. Discussion

MK-4 is used to treat osteoporosis at a dose of 45 mg/day in Japan, and in this dosage regimen, the maximum blood level of MK-4 is 1  $\mu$ M [23]. In distribution studies using rats and dogs, the levels of MK-4 in the bone marrow were approximately 20 and 2–3 times greater than in plasma, respectively [24,25]. The level of MK-4 in the bone marrow was comparable with the  $IC_{50}$  values of MKH-DMG and MKH-SUC in HL60 or HL-60R cells (Table 1). In addition, treatment with MKH derivatives would be safer because they are eliminated through a metabolic pathway, the vitamin K cycle, similar to MK-4 administration following MKH delivery. Thus, it is strongly suggested that MKH-DMG and MKH-SUC could act as chemotherapeutic agents with a long-term safety profile. Furthermore, MK-4 is practically insoluble, or insoluble in water, according to the monograph of Japanese Pharmacopoeia 17th edition, whereas MKH derivatives are highly water-soluble. Thus, MKH derivatives are injectable intravascularly and intrathecally without surfactants.

First, we examined the growth-inhibitory effects of the MKH derivatives MKH-DMG and MKH-SUC on HL60 and HL-60R cells (Figure 2B,D and Table 1) and determined intracellular MKO and MK-4 levels. Both MKH-DMG and MKH-SUC were effective on not only HL60 but also HL-60R cells, and their effects were more potent than those of MK-4.

Although the curves between cells treated with each drug were significantly different at a significance level of 0.05, the resistance index values of the MKH derivatives were close to 1 and considerably lower than those of ATRA and MK-4 (Table 1), indicating the potential to overcome ATRA resistance. In addition, MKH-DMG and MKH-SUC exhibited similar effects on the APL cell line NB-4 (Supplementary Figure S1). Therefore, MKH-DMG and MKH-SUC are potentially effective against ATRA-resistant APL, and it is necessary to evaluate their efficacy against ATRA-resistant APL cell lines. Moreover, it is important to clarify the non-specificity to HL60 by observing the effect of MKH derivatives on multiple hematological cancer cells. Under the MK-4 treatment, the saturation of intracellular MKO and MK-4 levels was observed in both cell lines (Figure 3A–D). Thus, the phenomenon may limit its inhibitory effects (Figure 2B). In contrast, because MKH-SUC efficiently delivered MKH to both cell lines without any saturation (Figures 3A–D and 4A–D), MKH-SUC may exert strong growth-inhibitory effects against both cell lines (Figure 2D) compared with the MK-4 treatment (Figure 2B). Interestingly, although MKH delivery (intracellular MKO and MK-4 levels) after MKH-DMG treatment was lower than that after MK-4 treatment (Figure 4A–D and Table 2), MKH-DMG showed a strong growth-inhibitory effect against both cell lines (Figure 2C). Intracellular ester forms containing monoesters (1-mono and 4-mono) and 1,4-bis-ester (Supplementary Figure S2) probably affect MKH-DMG-mediated inhibition because the rate of intracellular hydrolysis of MKH-DMG must be lower than that of MKH-SUC, similar to the findings of our previous studies using different cell types [18,22]. For intracellular drug extraction, the cells were centrifuged in PBS and washed twice. Consequently, well-fragmented cells may be removed; however, damaged/dying cells may remain in the cell sample used for drug extraction. As the inhibitory effects of MKH derivatives were not observed until after 48 h, the irregular behavior of intracellular MK-4 and MKO from 48 h to 72 h after treatment with MKH-SUC and MKH-DMG may have been affected by cell toxicity (Figure 4A–D).

It has been demonstrated that ATRA induces apoptosis and cell cycle arrest along with cell differentiation [7,21,26,27]. In the present study, G<sub>1</sub> arrest was observed in HL60 cells treated with ATRA (Figure 5A); however, this arrest may have been masked by ATRA resistance in the HL-60R cells (Figure 5B). It has also been reported that MK-4 induces apoptosis, cell cycle arrest with differentiation, and autophagic cell death against APL-derived cell lines [9,11–16]. Nevertheless, in this study, both MK-4 and MKH derivatives did not affect cell cycle arrest (Figure 5C–H). Miyazawa et al. demonstrated, in HL60 cells overexpressing Bcl-2, an apoptosis-inhibitory protein, that the primary growth-inhibitory effect of MK-4 is the induction of apoptosis rather than differentiation [13]. Similar to previous reports, the MK-4 and MKH-SUC treatments led to an increase in the number of cells in the sub-G<sub>1</sub> phase (Figure 5C,D,G,H), along with increasing annexin V-positive cells (Figure 6C,D). Based on these results, we conclude that MK-4 and MKH-SUC exert a growth-inhibitory effect by inducing apoptosis and masking these effects on the cell cycle. Furthermore, Karasawa et al. demonstrated that MK-4-induced apoptosis is dependent on covalently bound MKO and BAK [12]. In the present study, the MK-4 and MKH-SUC treatments induced BAK protein modification and activated caspase-3 (Figure 9). These results indicate that apoptosis induced by MK-4 and MKH-SUC is mitochondrially mediated through BAK modification. As we did not isolate MKO from the shifted BAK protein band, it is unclear whether MKO is covalently bound to BAK. Further studies are therefore needed to clarify this issue. Moreover, a decrease in mitochondrial membrane potential caused by MK-4 and MKH-SUC was observed (Figure 7). Mitochondrial cytochrome c was released from the mitochondria to the cytosol by MKH-SUC treatment (Figure 8). However, the cytosolic cytochrome c level was not increased by MK-4 (Figure 8). It is speculated that cytosolic cytochrome c may have been consumed because it was bound to apoptosis protease-activating factor 1 (APAF-1) to promote apoptotic signaling [28,29]. Although MKH-DMG showed a strong growth-inhibitory effect similar to MKH-SUC, it induced a small percentage of sub-G<sub>1</sub> stage cells (Figure 5E,F), few apoptotic cells (Figure 6C,D), and no mitochondria-mediated apoptosis through BAK activation (Figures 7–9), suggesting

the involvement of another mechanism independent of apoptosis. As mentioned earlier, because MK-4 induces autophagic cell death [15], the inhibitory effect of MKH-DMG may involve autophagy. Further clarification of the mechanisms underlying the inhibitory effects of MKH derivatives, including the mechanism of how MKH derivatives avoid ATRA resistance, is needed.

## 5. Conclusions

The MKH derivatives (MKH-SUC and MKH-DMG) showed potential to be developed as APL therapeutic drugs that overcome ATRA resistance. Although MKH-SUC enhanced MKH delivery to cells compared with MK-4, MKH-DMG exerted an inhibitory effect owing to the intracellular delivery of ester forms (bis-ester and/or monoesters) rather than efficient MKH delivery, suggesting another unique mechanism independent of apoptosis. To develop a novel and safe chemotherapeutic agent effective against ATRA-resistant cell lines using MKH derivatives, further assessment of the mechanisms underlying the growth-inhibitory effect of MKH derivatives involved in ATRA resistance and in vivo pharmacological studies are required.

**Supplementary Materials:** The following are available online at <https://www.mdpi.com/article/10.3390/pharmaceutics13050758/s1>, Figure S1: Inhibitory effects of MKH derivatives on the viability of NB-4 cells; Figure S2: Intracellular concentration of MKH-esters in HL60 and HL-60R treated with MKH-DMG; Table S1: Area under the curve over 72 h (AUC<sub>0-72h</sub>) of intracellular concentrations of MKH-esters in HL60 and HL-60R cells treated with 5 µM MKH-DMG.

**Author Contributions:** Conceptualization, H.Y., S.S. and J.T.; methodology, H.Y. and S.S.; validation, H.Y. and S.S.; formal analysis, H.Y. and S.S.; investigation, H.Y., S.S., S.G., D.W., K.T., N.N.-A. and E.T.; resources, H.Y., S.S. and J.T.; data curation, H.Y. and S.S.; writing—original draft preparation, H.Y., S.S. and J.T.; writing—review and editing, H.Y., S.S. and J.T.; visualization, H.Y. and S.S.; supervision, K.M. and J.T.; project administration, M.K., K.M. and J.T.; funding acquisition, Y.K. and J.T. All authors have read and agreed to the published version of the manuscript.

**Funding:** This research received no external funding.

**Institutional Review Board Statement:** Not applicable.

**Informed Consent Statement:** Not applicable.

**Data Availability Statement:** The data that support the findings of this study are available from the corresponding author upon reasonable request.

**Acknowledgments:** We thank Shuji Hara and Taichi Matsumoto of the Faculty of Pharmaceutical Sciences of Fukuoka University for their valuable advice on this study, and Takafumi Kobayashi and Keisuke Nishiyama, who are students in our laboratory, for providing support with the execution of experiments in this study.

**Conflicts of Interest:** The authors declare no conflict of interest.

## References

1. Thomas, X. Acute Promyelocytic Leukemia: A History over 60 Years—From the Most Malignant to the most Curable Form of Acute Leukemia. *Oncol. Ther.* **2019**, *7*, 33–65. [CrossRef] [PubMed]
2. Huang, M.E.; Ye, Y.C.; Chen, S.R.; Chai, J.R.; Lu, J.X.; Zhao, L.; Gu, L.J.; Wang, Z.Y. Use of all-trans retinoic acid in the treatment of acute promyelocytic leukemia. *Blood* **1988**, *72*, 567–572. [CrossRef] [PubMed]
3. Masue, I. Molecular Mechanism of the Leukemogenesis and Differentiation-Induction in Acute Promyelocytic Leukemia. *Jpn. J. Pediatr. Hematol.* **2002**, *16*, 50–61.
4. Kimitaka, T.; Hiroshi, T. Pharmacokinetics of all-trans retinoic acid in Japanese patients with acute promyelocytic leukemia. *Vitamins* **2011**, *85*, 631–644.
5. Tomita, A.; Kiyoi, H.; Naoe, T. Mechanisms of action and resistance to all-trans retinoic acid (ATRA) and arsenic trioxide (As<sub>2</sub>O<sub>3</sub>) in acute promyelocytic leukemia. *Int. J. Hematol.* **2013**, *97*, 717–725. [CrossRef]
6. Honma, Y.; Takenaga, K.; Kasukabe, T.; Hozumi, M. Induction of differentiation of cultured human promyelocytic leukemia cells by retinoids. *Biochem. Biophys. Res. Commun.* **1980**, *95*, 507–512. [CrossRef]
7. Breitman, T.R.; Selonick, S.E.; Collins, S.J. Induction of differentiation of the human promyelocytic leukemia cell line (HL-60) by retinoic acid. *Proc. Natl. Acad. Sci. USA* **1980**, *77*, 2936–2940. [CrossRef]



8. Dalton, W.T.; Ahearn, J.M.; McCredie, K.B.; Freireich, E.J.; Stass, S.A.; Trujillo, J.M. HL-60 cell line was derived from a patient with FAB-M2 and not FAB-M3. *Blood* **1988**, *71*, 242–247. [CrossRef]
9. Yaguchi, M.; Miyazawa, K.; Katagiri, T.; Nishimaki, J.; Kizaki, M.; Tohyama, K. Vitamin K<sub>2</sub> and its derivatives induce apoptosis in leukemia cells and enhance the effect of all-trans retinoic acid. *Leukemia* **1997**, *11*, 779–787. [CrossRef]
10. Yaguchi, M.; Miyazawa, K.; Otawa, M.; Katagiri, T.; Nishimaki, J.; Uchida, Y.; Iwase, O.; Gotoh, A.; Kawanishi, Y.; Toyama, K. Vitamin K<sub>2</sub> selectively induces apoptosis of blastic cells in myelodysplastic syndrome: Flow cytometric detection of apoptotic cells using APO2.7 monoclonal antibody. *Leukemia* **1998**, *12*, 1392–1397. [CrossRef]
11. Sakai, I.; Hashimoto, S.; Yoda, M.; Hida, T.; Ohsawa, S.; Nakajo, S.; Nakaya, K. Novel Role of Vitamin K<sub>2</sub>: A Potent Inducer of Differentiation of Various Human Myeloid Leukemia Cell Lines. *Biochem. Biophys. Res. Commun.* **1994**, *205*, 1305–1310. [CrossRef]
12. Karasawa, S.; Azuma, M.; Kasama, T.; Sakamoto, S.; Kabe, Y.; Imai, T.; Yamaguchi, Y.; Miyazawa, K.; Handa, H. Vitamin K<sub>2</sub> Covalently Binds to Bak and Induces Bak-Mediated Apoptosis. *Mol. Pharmacol.* **2012**, *83*, 613–620. [CrossRef] [PubMed]
13. Miyazawa, K.; Yaguchi, M.; Funato, K.; Gotoh, A.; Kawanishi, Y.; Nishizawa, Y.; Yuo, A.; Ohyashiki, K. Apoptosis/differentiation-inducing effects of vitamin K<sub>2</sub> on HL-60 cells: Dichotomous nature of vitamin K<sub>2</sub> in leukemia cells. *Leukemia* **2001**, *15*, 1111–1117. [CrossRef]
14. Miyazawa, S.; Moriya, S.; Kokuba, H.; Hino, H.; Takano, N.; Miyazawa, K. Vitamin K<sub>2</sub> induces non-apoptotic cell death along with autophagosome formation in breast cancer cell lines. *Breast Cancer* **2020**, *27*, 225–235. [CrossRef] [PubMed]
15. Yokoyama, T.; Miyazawa, K.; Naito, M.; Toyotake, J.; Tauchi, T.; Itoh, M.; Yuo, A.; Hayashi, Y.; Georgescu, M.-M.; Kondo, Y.; et al. Vitamin K<sub>2</sub> induces autophagy and apoptosis simultaneously in leukemia cells. *Autophagy* **2008**, *4*, 629–640. [CrossRef]
16. Funato, K.; Miyazawa, K.; Yaguchi, M.; Gotoh, A.; Ohyashiki, K. Combination of 22-oxa-1,25-dihydroxyvitamin D<sub>3</sub>, a vitamin D<sub>3</sub> derivative, with vitamin K<sub>2</sub> (VK<sub>2</sub>) synergistically enhances cell differentiation but suppresses VK<sub>2</sub>-inducing apoptosis in HL-60 cells. *Leukemia* **2002**, *16*, 1519–1527. [CrossRef] [PubMed]
17. Setoguchi, S.; Watase, D.; Matsunaga, K.; Matsubara, M.; Kubo, Y.; Kusuda, M.; Nagata-Akaho, N.; Enjoji, M.; Nakashima, M.; Takeshita, M.; et al. Enhanced Antitumor Effects of Novel Intracellular Delivery of an Active Form of Menaquinone-4, Menahydroquinone-4, into Hepatocellular Carcinoma. *Cancer Prev. Res.* **2015**, *8*, 129–138. [CrossRef] [PubMed]
18. Setoguchi, S.; Watase, D.; Matsunaga, K.; Yamakawa, H.; Goto, S.; Terada, K.; Ohe, K.; Enjoji, M.; Karube, Y.; Takata, J. Antitumor Effects and Delivery Profiles of Menahydroquinone-4 Prodrugs with Ionic or Nonionic Promoiety to Hepatocellular Carcinoma Cells. *Molecules* **2018**, *23*, 1738. [CrossRef]
19. Takata, J.; Karube, Y.; Hanada, M.; Matsunaga, K.; Matsushima, Y.; Sendo, T.; Aoyama, T. Vitamin K Prodrugs: 1. Synthesis of Amino Acid Esters of Menahydroquinone-4 and Enzymatic Reconversion to an Active Form. *Pharm. Res.* **1995**, *12*, 18–23. [CrossRef]
20. Takata, J.; Karube, Y.; Hanada, M.; Matsunaga, K.; Matsushima, Y.; Sendo, T.; Oishi, R. Vitamin K Prodrugs: 2. Water-Soluble Prodrugs of Menahydroquinone-4 for Systemic Site-Specific Delivery. *Pharm. Res.* **1995**, *12*, 1973–1979. [CrossRef]
21. Mori, J.; Suzuki, S.; Hara, M.; Kaneko, A.; Yamashita, K.; Kumagai, M.; Sakuma, T.; Kakizawa, T.; Yamazaki, M.; Takeda, T.; et al. Characterization of Two Novel Retinoic Acid-resistant Cell Lines Derived from HL-60 Cells Following Long-term Culture with all-trans-Retinoic Acid. *Jpn. J. Cancer Res.* **1999**, *90*, 660–668. [CrossRef]
22. Goto, S.; Setoguchi, S.; Yamakawa, H.; Watase, D.; Terada, K.; Matsunaga, K.; Karube, Y.; Takata, J. Prodrugs for Skin Delivery of Menahydroquinone-4, an Active Form of Vitamin K<sub>2(20)</sub>, Could Overcome the Photoinstability and Phototoxicity of Vitamin K<sub>2(20)</sub>. *Int. J. Mol. Sci.* **2019**, *20*, 2548. [CrossRef]
23. Ishii, M.; Shimomura, M.; Hasegawa, J.; Asano, Y.; Yamato, Y. Multiple dose pharmacokinetic study of soft gelatin capsule of menatetrenone (Ea-0167) in elderly and young volunteers. *Jpn. Pharmacol. Ther.* **1995**, *23*, 2637–2642.
24. Sano, Y.; Tadano, K.; Kaneko, K.; Kikuchi, K.; Yuzuriha, T. Distribution of menaquinone-4, a therapeutic agent for osteoporosis, in bone and other tissues of rats. *J. Nutr. Sci. Vitaminol.* **1995**, *41*, 499–514. [CrossRef] [PubMed]
25. Sano, Y.; Tadano, K.; Kaneko, K.; Kikuchi, K.; Yuzuriha, T. Metabolic Fate of Menaquinone-4 in Dogs. (I). Absorption, Distribution, Metabolism and Excretion after a Single Oral Administration. *Drug Metab. Pharmacokinet.* **1997**, *12*, 48–57. [CrossRef]
26. Sun, H.; Wang, Y. Apoptosis of human leukemic HL-60 cells induced to differentiate by treatment with RA or DMSO. *Cell Res.* **1995**, *5*, 181–186. [CrossRef]
27. Dimberg, A.; Bahram, F.; Karlberg, I.; Larsson, L.-G.; Nilsson, K.; Öberg, F. Retinoic acid-induced cell cycle arrest of human myeloid cell lines is associated with sequential down-regulation of c-Myc and cyclin E and posttranscriptional up-regulation of p27Kip1. *Blood* **2002**, *99*, 2199–2206. [CrossRef] [PubMed]
28. Elmore, S. Apoptosis: A review of programmed cell death. *Toxicol. Pathol.* **2007**, *35*, 495–516. [CrossRef]
29. Ouyang, L.; Shi, Z.; Zhao, S.; Wang, F.-T.; Zhou, T.-T.; Liu, B.; Bao, J.-K. Programmed cell death pathways in cancer: A review of apoptosis, autophagy and programmed necrosis. *Cell Prolif.* **2012**, *45*, 487–498. [CrossRef]



Review

# Circulating Tumour Cells (CTCs) in NSCLC: From Prognosis to Therapy Design

Zdeněk Kejík<sup>1,2,3</sup>, Robert Kaplánek<sup>1,2,3</sup> , Petr Dytrych<sup>4</sup>, Michal Masařík<sup>1,2</sup>, Kateřina Veselá<sup>1,2,3</sup>, Nikita Abramenko<sup>1</sup> , David Hoskovec<sup>4</sup>, Martina Vašáková<sup>5</sup>, Jarmila Králová<sup>6</sup>, Pavel Martásek<sup>1</sup> and Milan Jakubek<sup>1,2,3,\*</sup>

- <sup>1</sup> Department of Paediatrics and Inherited Metabolic Disorders, First Faculty of Medicine, Charles University and General University Hospital, 128 08 Prague, Czech Republic
- <sup>2</sup> BIOCEV, First Faculty of Medicine, Charles University, 252 50 Vestec, Czech Republic
- <sup>3</sup> Department of Analytical Chemistry, Faculty of Chemical Engineering, University of Chemistry and Technology, 166 28 Prague, Czech Republic
- <sup>4</sup> 1st Department of Surgery-Department of Abdominal, Thoracic Surgery and Traumatology, First Faculty of Medicine, Charles University and General University Hospital, 121 08 Prague, Czech Republic
- <sup>5</sup> Department of Respiratory Medicine, First Faculty of Medicine, Charles University and Thomayer Hospital, 140 59 Prague, Czech Republic
- <sup>6</sup> Institute of Molecular Genetics, Czech Academy of Sciences, 142 20 Prague, Czech Republic
- \* Correspondence: Milan.Jakubek@lf1.cuni.cz

**Citation:** Kejík, Z.; Kaplánek, R.; Dytrych, P.; Masařík, M.; Veselá, K.; Abramenko, N.; Hoskovec, D.; Vašáková, M.; Králová, J.; Martásek, P.; et al. Circulating Tumour Cells (CTCs) in NSCLC: From Prognosis to Therapy Design. *Pharmaceutics* **2021**, *13*, 1879. <https://doi.org/10.3390/pharmaceutics13111879>

Academic Editor: Hassan Bousbaa

Received: 27 September 2021

Accepted: 30 October 2021

Published: 5 November 2021

**Publisher's Note:** MDPI stays neutral with regard to jurisdictional claims in published maps and institutional affiliations.



**Copyright:** © 2021 by the authors. Licensee MDPI, Basel, Switzerland. This article is an open access article distributed under the terms and conditions of the Creative Commons Attribution (CC BY) license (<https://creativecommons.org/licenses/by/4.0/>).

**Abstract:** Designing optimal (neo)adjuvant therapy is a crucial aspect of the treatment of non-small-cell lung carcinoma (NSCLC). Standard methods of chemotherapy, radiotherapy, and immunotherapy represent effective strategies for treatment. However, in some cases with high metastatic activity and high levels of circulating tumour cells (CTCs), the efficacy of standard treatment methods is insufficient and results in treatment failure and reduced patient survival. CTCs are seen not only as an isolated phenomenon but also a key inherent part of the formation of metastasis and a key factor in cancer death. This review discusses the impact of NSCLC therapy strategies based on a meta-analysis of clinical studies. In addition, possible therapeutic strategies for repression when standard methods fail, such as the administration of low-toxicity natural anticancer agents targeting these phenomena (curcumin and flavonoids), are also discussed. These strategies are presented in the context of key mechanisms of tumour biology with a strong influence on CTC spread and metastasis (mechanisms related to tumour-associated and -infiltrating cells, epithelial-mesenchymal transition, and migration of cancer cells).

**Keywords:** CTCs; NSCLCs; metastasis suppression; curcumin; flavonoids

## 1. Introduction

Lung cancer is a harmful and dangerous oncological disease responsible for frequent cancer-related deaths [1,2]. Non-small-cell lung cancer (NSCLC) is the most common type of lung cancer, accounting for 85% of those deaths. A significant proportion of NSCLC patients (~40%) have metastatic disease (stage IV) with a poor prognosis (low overall survival (OS) and progression-free survival (PFS)) [3–5]. It is well known that the majority of deaths of oncology patients, including those with NSCLC, are not caused by the primary tumour but by metastasis [5]. One of the most potent metastatic factors is circulating tumour cells (CTCs) [6].

The role of CTCs in NSCLC metastasis is briefly described below. Section 2 discusses the influence of CTC count on chemotherapeutic efficiency. Section 3 describes the potential of CTC analysis to improve therapeutic prognosis mainly in terms of programmed cell death protein ligand 1 (PD-L1) expression and epidermal growth factor receptor (EGFR) genotyping. Section 4 is focused on the mechanisms supporting the spread of CTCs, such

as tumour-associated and -infiltrating cells, epithelial–mesenchymal transition (EMT), and cellular migration, and discusses the ability of natural agents to suppress them.

CTCs were first observed by Asworth in 1869 [7]. They are released by primary tumours into the bloodstream or lymphatic system and have the potential to form micrometastatic deposits in distant sites [8]. Over time, many patients develop local recurrence or distant metastases. Therefore, the importance of CTCs in NSCLC pathology appears to be very significant. For example, Sienel et al. found that disseminated cancer cells are detectable in approximately 20% of patients with operable NSCLC who have poor clinical outcomes [9]. This finding implies that determining CTC levels can provide useful information about the efficacy of surgery and predict the need for adjuvant therapy. Yoon et al. showed that determining post-surgery CTC levels can help predict the risk of disease progression. CTCs expressing thyroid transcription factor-1 and/or cytokeratin 19 (CK19) were found to be strongly associated with disease progression and PFS [10]. It was shown that 40% of patients (10/25) developed disease progression after surgery when CTCs expressed these markers, and only 4.5% (1/22) had disease progression when these markers were not expressed. Numerous studies have demonstrated that surgical manipulation can promote the dissemination of tumour cells into circulation [11–13]. The risk of tumour cell dissemination can also be reduced by suitable operation techniques. Substituting an artery-first group with a vein-first group led to a reduction in incremental CTC change by half [14]. Five-year OS (disease-free survival) was significantly higher for patients who underwent a vein-first operation than for patients who underwent an artery-first operation. In agreement with the strong implications of numerous high-impact clinical studies, a higher CTC level correlated with a higher risk of metastasis and shorter OS [15–17]. However, clear cut-offs for such parameters are not yet known.

Due to the different techniques used for CTC isolation and enumeration and the heterogeneous and often small cohorts of patients, guidelines and standards are difficult to establish [18,19]. Examples of published thresholds are shown in Table 1. However, changes in CTC counts during therapy also represent an important marker for modulating cancer treatment.

The CTC count was approximately twice as high for NSCLC patients as for patients with benign lung diseases (pneumonia, pulmonary tuberculosis, bronchiectasis, or pneumothorax) or healthy subjects [20]. The counts for all controls (healthy subjects and patients with other lung diseases) were under the designated limit. In such cases, detection of CTCs is most likely a false positive result due to the extremely large numbers of blood cells in the samples [21,22]. On the other hand, Illie et al. found that CTC-positive patients with tobacco-induced chronic obstructive pulmonary disease may have developed lung cancer [23]. This suggests that cancer patients in the early stages of lung cancer could display high metastatic activity, such as higher CTC counts and formation of CTC clusters (a highly metastatic and aggressive form of CTC) [24–26].

Nevertheless, some trials imply that significant CTC levels should be seen only at a late stage of the late/metastatic stages. Chen et al. did not find a significant difference between subjects with benign diseases and healthy subjects [20]. The obtained values were not dependent on age ( $\leq 60$  years versus  $>60$  years), sex (male versus female), smoking status (former versus current smoker), or pathology type (adenocarcinoma versus squamous cell carcinoma and others). However, the observed CTC counts were significantly lower for patients with stage I or II disease than for those with stage III or IV disease. The difference between patients with stage III and patients with stage IV disease was not significant. In addition, Krebs et al. found that disease progression (from stage IIIa to IV) significantly increased the CTC count associated with metastatic activity [17]. Numerous clinical trials have shown that higher CTC counts correlate with poor therapeutic prognosis (shorter OS and PFS) [16,17,27,28]. Similarly, Wendel et al. observed a correlation between NSCLC development and CTC count [29]. On the other hand, NSCLC patients (early stage) with higher CTC count ( $\geq 5/\text{mL}$ ) display significantly higher radiotherapy failure and cancer

recurrence. [26] However, our knowledge is still limited, and other clinical trials are much needed for better understanding of this phenomenon.

Due to the importance of CTCs in tumour pathology, assessing CTC count can significantly improve cancer prognosis. For example, assessment of CTC count in combination with a panel of plasma tumour markers (carcinoembryonic antigen, neuron-specific enolase, and Cyfra21–1) led to a significant increase in the diagnostic efficacy of the panel [20]. Clinically valuable information can be obtained by CTC-based genotyping. This robust approach can analyse numerous cancer biomarkers. This strategy effectively enables the determination of tumour properties, mainly metastatic activity and drug resistance, and significantly increases the clinical potential of CTC count.

In short, we can say that CTC count and analysis represent revolutionary approaches in diagnostic methods. Whereas the utility of solid biopsy is strongly limited because of tumour heterogeneity, repeated tissue sampling is associated with a significant burden on patients. Liquid biopsies can dynamically and noninvasively interrogate the whole molecular landscape of tumours.

## 2. Influence of CTC Count on Chemotherapeutic Efficacy

Numerous studies have shown a strong association between CTC count and the clinical efficacy of chemotherapy. The CTC count data discussed in this chapter were determined with CellSearch and with 7.5 mL of blood, unless otherwise stated. Zhang et al. found an inverse correlation between the effects of cisplatin doublet therapy and CTC count for NSCLC patients (stage IIIB or IV) [28]. A CTC count of 8 (in 3.2 mL of peripheral blood) or more (15.2% patients) was clinically manifested by decreased PFS (7.4 vs. 5.3 months) and OS (23.1 vs. 9.0 months).

Similarly, Krebs et al. observed that patients (stage IIIA to IV) with CTC counts lower than 5 had more than double the PFS and OS of patients with higher counts [17]. Nevertheless, a change in the number during chemotherapy can have significantly higher prognostic importance than a single count. Patients with decreased CTC counts sometimes had higher OS and PFS than patients with unchanged CTC counts.

In summary, the CTC level is a strong biomarker for the prediction of NSCLC chemotherapy response. However, some works question its clinical application. For example, Zhang et al. did not find any correlation between CTC count and tumour size [28]. Similarly, Hirose did not observe any correlation between the presence of CTCs (one or more) and the number of metastatic sites, tumour burden, or serum levels of lactate dehydrogenase or albumin in NSCLC patients (metastatic stage IV) [30]. The correlation between response to chemotherapy (gemcitabine and carboplatin) and CTC count was found to be statistically insignificant. On the other hand, disease progression was significantly higher in CTC-positive patients (66.7%) than in CTC-negative patients (23.8%). The proportion of patients with stable disease and partial response was significantly higher in the CTC-negative group.

Juan et al. reported that 24% of patients with advanced NSCLC (stage IIIB with pleural effusion or stage IV) before the third cycle of chemotherapy displayed higher CTC counts (two or more) [31]. However, this pattern was not associated with significantly lower OS but with an insignificant improvement in OS. Nevertheless, a reduction in CTCs during chemotherapy led to a better prognosis. Findings regarding the influence of CTCs on chemotherapy are shown in Table 1.

The above implies that baseline CTCs can be used as markers for chemotherapy response; however, determination of CTC count during and after chemotherapy can lead to a better prognosis. Nevertheless, two points limit the utility of CTC count. CTCs, even obtained from a single patient at the same time, may show strong heterogeneity (see Section 3) and thereby varied metastatic potential. In addition, CTCs can exist in clusters (very strong metastatic factors) that can significantly influence cancer development [24].

**Table 1.** Influence of circulating tumour cell (CTC) count on non-small-cell lung cancer (NSCLC) chemotherapy.

Patient Characteristics	Clinical Finding	Ref.
101 patients with stage IIIA, IIIB, or IV disease; platinum doublet chemotherapy (United Kingdom)	CTC count <sup>1</sup> for prediction <sup>2</sup> (baseline): $\geq 5$ ; PFS (6.8 vs. 2.4) and OS (8.1 vs. 4.3) CTC count for prediction (after therapy): $\geq 5$ ; PFS (7.6 vs. 2.4) and OS (8.8 vs. 4.3)	[17]
21 patients with stage IV disease; previous chemotherapy with belagenpumatucel-L, 16 months (USA)	CTC count for prediction: $\geq 2$ ; OS (20 vs. 5)	[27]
37 patients with stage IIIB disease with pleural effusion or stage IV disease with bidimensionally measurable lesions in a previously irradiated field; docetaxel plus gemcitabine, 28 days <sup>4</sup> (Spain)	CTC distribution: $\geq 1$ (58%) <sup>3</sup> , $\geq 2$ (32%), and $\geq 5$ (8%) CTC count for prediction (baseline): $\geq 2$ (nonsignificant); OS (8.1 vs. 12.2) and PFS (9.4 vs. 4.3) CTC count for prediction (after therapy): $\leq 1$ ; OS (10.1 vs. X <sup>5</sup> )	[31]
46 patients with stage IIIB or IV disease; platinum doublet therapy (China)	CTC distribution: $\geq 1$ (87), $\geq 3$ (63), $\geq 5$ (37) and $\geq 8$ (15) CTC count for prediction (baseline): $\geq 8$ ; OS (21.3 vs. 9.0) and PFS (7.4 vs. 5.3))	[28]

<sup>1</sup> The CTC counts discussed in this table were determined with CellSearch and with 7.5 mL of blood. <sup>2</sup> Overall survival (OS) and progression-free survival (PFS) shown in months. <sup>3</sup> Proportion of patients with a given number of CTCs. <sup>4</sup> Length of chemotherapy. <sup>5</sup> Study time too short for determination.

Nevertheless, observing the CTC level during and after therapy can provide valuable information about the patient's response to therapy. As CTCs are an inherent marker of metastatic activity, their increase during therapy strongly indicates a high risk of metastases [32]. In the case of an increasing number of CTCs, alternative chemotherapy may be used; nevertheless, the efficiency of this strategy is limited [33].

It is well known that chemotherapy or radiotherapy failure is associated with not only drug efficiency but also the induction of new aggressive and metastatic forms of oncological diseases [34–36]. For example, Shah et al. found that cisplatin application induced EMT (one of the key steps in the mechanism of CTC spreading) via induction of endoplasmic reticulum (ER) stress [34]. The authors observed that following removal of stress, some characteristics of EMT, such as increased vimentin expression, persisted, indicating that the ER stress that induced these phenomena is a long-term effect. Wang et al. found that celecoxib (a selective inhibitor of cyclooxygenase 2 (COX-2)) induces EMT of NSCLC cells via upregulation of MEK-ERK signalling. [37] This fact could explain the failure of celecoxib in clinical trials [38–40]. The RAS–Raf–MEK (mitogen-activated protein kinase (MAPK))–extracellular signal-regulated kinase (ERK) pathway is a key signalling pathway that regulates a wide variety of cellular processes, including proliferation, differentiation, apoptosis, and stress responses. MAPKs and ERKs play a crucial role in the survival and development of tumour cells [41,42]. For example, resistance to third-generation EGFR tyrosine kinase inhibitors can be caused by activation of MEK/ERK signalling [43].

Dea et al. reported that doxorubicin treatment can support lung metastasis via suppression of MSDS exosomes in a mouse model [44]. Bhattacharya et al. found that paclitaxel-treated macrophages support angiogenesis and display a higher proportion of M2 macrophages [45].

The abovementioned studies strongly imply that mechanisms responsible for chemoresistance are at least partially responsible for CTC spreading. For example, Atjanasuppat et al. reported that nonadherent H460 cells (an NSCLC cell line) have significantly higher paclitaxel sensitivity than the original line. Both of these phenomena were caused by upregulation of ERK signalling [46]. Lee et al. reported that the hypoxia-related phenotype of A549 cells (an NSCLC cell line) and the hypoxic microenvironment in cancer tissue from NSCLC patients were associated with cisplatin resistance [47]. Similarly, in a breast cancer model, intratumour hypoxia led to the formation of CTC clusters with high metastatic ability [48].

As such, a new therapeutic strategy based on the application of antimetastatic compounds such as migrastatics has been considered [49,50]. These agents are not designed to kill cancer cells, as cytostatics are, but to block cell migration and thus metastatic spread. However, many developed and studied anticancer agents display antimetastatic effects. For example, the Food and Drug Administration (FDA) approved some compounds designed to delay metastatic prostate cancer [51]. In NSCLC, tyrosine kinase inhibitor, immune checkpoint inhibitors, and antibodies against interleukin 6 receptor (IL-6R) have shown antimetastatic effects [52–54]. Nevertheless, NSCLC is associated with high heterogeneity; therefore, we recommend the application of multifunctional agents. A higher CTC count or its increase during therapy may be a suitable predictive biomarker for the incorporation of such agents into therapy. Curcuminoids and flavonoids are agents with low toxicity that can target CTCs by various independent mechanisms (see Section 4), and they are potent antimetastatic adjuvant agents [55]. In the future, strategies employing such compounds could lead to earlier adjustment of therapy and increase treatment efficacy.

### 3. CTC Analysis in the Determination of Therapy Prognosis

CTC analysis has potential for the determination and dynamic observation of changes in tumour properties in oncology patients from various perspectives (genomic, transcriptomic, proteomic, and metabolomic) [56]. Such analysis seems to provide critical information for predicting therapeutic response and designing/redesigning optimal therapies for patients.

CTC detection can be based on physical CTC properties (e.g., size, density, and electromechanical characteristics) or tumour-specific epitopes, or CTCs can be detected by high-throughput imaging of unpurified blood cell preparations [57]. CTC analyses are mostly conducted using the FDA-approved EpCAM kit (positive and negative sorting based on epithelial cell adhesion molecule (EpCAM) and the protein tyrosine phosphatase (CD45) receptor, respectively) [32]. However, some obstacles (extremely low CTC numbers and CTC heterogeneity) can limit the promising potential of this approach. CTCs are strongly outnumbered by normal blood cells by a billion-fold, and in obtained clinical samples, there are only a few CTCs.

In addition, CTCs are heterogeneous, and their analysis can provide valuable information for diagnosis [58]. Brung et al. reported that CTC lines (UWG01CTC and UWG02CTC) from patients with gastroesophageal cancer demonstrated rapid tumourigenic growth in immunodeficient mice, and their genotypic and phenotypic profiles were consistent with those of the original tumours [59]. Nevertheless, UWG02CTC cells (EpCAM<sup>+</sup>, cytokeratin<sup>+</sup>, CD44<sup>+</sup>) were much more sensitive to carboplatin, paclitaxel, 5-fluorouracil, doxorubicin, and epoxide than were UWG01CTC cells (EpCAM<sup>-</sup>, low cytokeratin). CTCs are unlikely to be representative of all cancer cells; rather, they correspond to cells with more aggressive metastatic phenotypes [60,61]. On the other hand, CTCs can display high heterogeneity, and their potential for metastasis formation may be very different [62]. Analysis of other CTC phenotypes or the expression and DNA mutation profiles of CTCs may lead to more robust therapeutic prognosis prediction and determination of appropriate therapy.

For example, CTCs expressing programmed death-ligand 1 (PD-L1) constitute a promising biomarker for the design and management of immune checkpoint inhibitor (ICI) therapy. High PD-L1 expression is usually related to a higher histological grade, metastatic activity, and poor prognosis [63]. Satelli et al. reported that PD-L1 expression in the nucleus of CTCs but not the CTC count itself was associated with shorter OS in colorectal and prostate cancer patients [64]. Moreover, the number of CTCs was positively correlated with PD-L1 and cell surface vimentin expression in gastric cancer patients, and higher values were significantly associated with a shorter survival duration and poorer therapeutic response [65]. NSCLC CTCs can display higher levels of PD-L1 than original tumour tissue. For example, He et al. reported that 27% of biopsy samples obtained from lung cancer patients (stage I or II) displayed high expression of PD-L1, while this expression profile was found in the 40% of CTC samples [66]. Dong et al. reported a

positive correlation between PD-L1 expression in pulmonary venous CTCs and that in biopsy samples obtained from NSCLC patients (stages I–IV) [67]. However, Janing et al. found strong differences between results from biopsies and CTCs [68]. This finding was most likely caused by tumour heterogeneity and sampling of multiple tumour sites. Most patients in the study had metastatic disease (96%,  $n = 122$ ). Nevertheless, a correlation between higher CTC counts and poor prognosis was confirmed.

Another strategy is to analyse EGFR gene mutations. Hanssen et al. found that NSCLC patients with an altered EGFR genotype displayed higher CTC counts and metastatic activity than patients with EGFR wild-type tumours [69]. Lindsay et al. also observed that NSCLC patients with NG\_007726.3 EGFR mutation had higher CTC counts, including a vimentin<sup>+</sup> CTC (a marker of EMT) phenotype [70]. For example, the proportion of samples with a low CTC count ( $> 2$ ) with EGFR mutation was only 15%, but 34% of patients with a high CTC count (2 or more) had EGFR mutation. However, this finding is not consistent with studies of tumour samples obtained by biopsy. Nevertheless, the correlations between the mutation and expression profiles in tumours and those in CTCs may increase as the CTC count increases [32].

Importantly, Jiang et al. found high agreement (approximately 90%) between whole-genome sequencing data from DNA samples from primary biopsies and CTCs for oncology patients with pancreatic cancer [71]. Similarly, Heitzer et al. found that patients with stage IV colorectal carcinoma displayed good agreement in the mutation profile (e.g., APC, KRAS, or PIK3CA mutation) [61]. Mutations found in the primary tumour and metastatic tumour were also detected in the corresponding CTCs. However, some mutations were observed only in the DNA obtained from CTCs (hereinafter referred to as CTC DNA). More detailed analysis revealed that these mutations were mostly present at the subclonal level in primary tumours and metastases from the same patients. Similarly, the multiple myeloma frequency of TP53 R273C, BRAF G469A, and NRAS G13D mutations was higher in CTCs than in single cells isolated from tumours with the same aberrant malignant phenotype (CD138<sup>+</sup> and CD45<sup>-</sup>) with the same procedure [72].

Yanagita et al. published that higher CTC counts were observed in NSCLC patients with detectable oncogenic mutations in either EGFR ( $p = 0.062$ ) or KRAS ( $p = 0.065$ ) than in patients without mutations in these genes in either archival tissue or cell-free DNA [73]. Similarly, oncology patients with a higher number of CTCs were found to have marked changes in ESR1 ( $p < 0.005$ ) and GATA3 ( $p < 0.05$ ) [74].

Relevant clinical information can also be obtained by analysis of the methylation of tumour suppressor genes in CTC DNA or CTC cluster formation. Chimonidou et al. published that the BRMS1 promoter was methylated in CTC samples obtained from oncology patients [75]. This phenomenon was associated with shortened OS and PFS. Yang et al. found that NSCLC patients with a smoking history were more likely to have methylation of BRMS1 [76]. In contrast, patients with high levels of BRMS1 RNA (with a nonmethylated gene promoter) displayed significantly better therapeutic prognoses. Similarly, Schneck et al. observed heterogeneity in the mutation of phosphoinositide-3-kinase (PI3K; e.g., exon 9/E545K or exon 20/H1047R) in CTC DNA obtained from patients with metastatic breast cancer [77]. Because these mutations can significantly decrease the effectiveness of therapy targeting HER2 (EGFR), their analysis provides important insights for the improvement of anticancer therapy.

An important marker strongly associated with the metastatic activity of CTC clusters is plakoglobin (a component of cell junctions). Aceto et al. reported that CTC clusters obtained from oncology patients displayed plakoglobin overexpression (more than 200-fold) compared to single CTCs [78]. CTC clusters are derived from multicellular groupings of primary tumour cells held together through plakoglobin-dependent intracellular adhesion, and although rare compared to CTCs, these clusters greatly contribute to the metastatic spread of CTCs. Patients with at least one and at least three detected CTC clusters were found to have shorter OS and PFS, respectively. Similarly, knockdown of plakoglobin expression in a mouse model suppressed CTC cluster formation and reduced metastatic spread.

Some studies imply that analysing only one factor may not be relevant for determining therapeutic prognosis. One possible solution could be to identify more biomarkers. For example, Sher et al. designed and tested a gene panel (KRT19, ubiquitin thiolesterase, highly similar to HSFIB1 for the assessment of human fibronectin and TRIM28 mRNA) in Taiwanese NSCLC patients (stage IIIB or IV with operable cancer) [79]. The detection rate of this panel was higher (72%) than that of individual genes (41%, 11%, 39%, and 11%, respectively). The detection rate for the CK19 marker was 41%. Patients with higher scores had poor therapeutic responses and worse prognosis (e.g., shorter OS). Other suitable gene panels can be designed based on clinical data obtained from patients bearing other oncological diseases. In patients with breast cancer, co-expression of EpCAM, CD44, CD47, and MET was strongly associated with short OS and a higher number of metastatic sites [80].

The two most frequently studied approaches in NSCLC diagnosis are analysis of PD-L1 expression and EGFR genotyping in CTCs. Dong et al. found that 40.4% and 48.4% of tissue samples from NSCLC patients (stages I-III, after surgery) had EGFR mutations and PD-L1 expression in CTC, respectively [67]. Both of these characteristics are associated with immune checkpoint inhibitor (ICI) and tyrosine kinase inhibitor (TKI) resistance and higher metastatic activity. As such, analysis of CTC PD-L1 and EGFR expression could be used as a predictive strategy for the incorporation of curcuminoids and flavonoids into therapeutic regimens, as these agents target EGFR-related factors, including the T790M mutation and EGFR signalling, via various mechanisms and lower PD-L1 expression and signalling (see Section 4.3).

Both approaches are described and discussed in detail in the next subsections.

### 3.1. PD-L1 in CTCs

Numerous clinical trials have confirmed a strong correlation between PD-L1 expression and the OS and PFS of NSCLC patients [63,68,81–85], which is deeply associated with tumour immunoresistance [86].

For example, the transmembrane protein PD-1 is expressed on immune cells (e.g., B cells, T cells, natural killer (NK) cells, dendritic cells, and regulatory T (Treg) cells) [87]. Interferon gamma (IFN- $\gamma$ ; produced during the immune response) induces overexpression of PD-L1 to protect expressing cells. PD-L1 inhibits inflammatory signalling pathways, suppresses T cells, and prevents autoimmune attack. Nevertheless, tumour tissue protects cancer cells and tumour-associated cells from the immune system. In addition, the expression of these markers in CTCs and CTC clusters is expected to protect them from the immune system and thereby support metastatic spread [88].

On the other hand, anti-PD-1 and -PD-L1 antibodies reactivate the immune system of patients to subsequently eradicate tumours [86].

Tammaing et al. observed a strong influence of CTC level on the efficacy of therapies (mostly nivolumab therapy, 85% of patients) for patients with advanced NSCLC (stage IIIB or IV) [89]. For example, patients with at least one CTC displayed half the durable response rate of patients without CTCs at baseline. In addition, the durable response rate of patients with increased CTC counts was one-sixth that of patients with decreased counts. Similarly, higher CTC levels led to significantly shorter PFS and OS.

In addition, CTC genotyping can increase the utility of PD-L1 expression in NSCLC diagnosis, especially in advanced metastatic tumours. Ilie et al. reported that PD-L1 expression in tumour cells and infiltrating immune cells displayed high agreement with CTC (93%) and white blood cell (73%) counts [90]. Higher PD-L1 expression in strongly correlated with worse OS and PFS. Boffa et al. found that NSCLC patients with higher PD-L1-expressing CTC counts had worse OS (2 years, 31.2% vs. 78.8%,  $p = 0.00159$ ) [91]. According to Dhar et al., the presence of CTCs and the presence of PD-L1-expressing CTCs was negatively correlated with NSCLC patient survival (after treatment with anti-PD-L1 therapy) [92].



Similarly, Janning et al. found that responding NSCLC patients (mostly those with metastatic disease) exhibited either a decrease or no change in their total CTC counts after three or five cycles of therapy (anti-PD-L1 antibody), and primarily resistant patients had an increase in their CTC counts. [68] In contrast, all patients showed an increase in PD-L1-expressing CTCs at progression. A relationship between a higher PD-L1-expressing CTC count (at baseline) and nivolumab resistance for NSCLC patients (mostly after previous chemotherapy) was also reported by Guibert et al. [93].

Nevertheless, a high-impact clinical study published by Nicolazzo et al. revealed a more complicated relationship between PD-L1-expressing CTC count and the prediction of therapy response. PD-L1-expressing CTC counts were determined at baseline and at 3 and 6 months after starting therapy and correlated with outcome [84]. At baseline, 83% of patients (those with metastatic NSCLC previously treated with therapy, most of whom were smokers) displayed PD-L1-expressing CTCs. Overall, 70% of patients with PD-L1-expressing CTCs experienced disease progression or death, while 25% had stable disease or a partial response at the second follow-up time (6 months after starting nivolumab treatment). After three months of treatment, every CTC-positive patient had PD-L1-expressing CTCs. However, no significant difference in therapy prognosis between patients with low and high frequencies of PD-L1-expressing CTCs was found. Conversely, although CTCs were found in all patients after 6 months of treatment, patients could be dichotomised into two groups based on PD-L1 expression in CTCs. Only half of the patients had CTCs that expressed PD-L1, and these patients experienced disease progression, while patients with PD-L1-negative CTCs displayed stable disease or a partial response. This finding implies that 3 months of treatment may not be enough for the activation of the immune system to eliminate PD-L1-expressing CTCs; as such, assessment of PD-L1-expressing CTCs at this time point might not be able to provide relevant therapeutic predictions.

Patients with nonmetastatic NSCLC treated with radiotherapy and chemoradiotherapy showed a small influence of baseline CTC count on therapy prognosis indicators, such as PFS [94]. No significant difference in PFS was found between patients with a high number of CTCs ( $\geq 14$  CTCs/mL; median PFS 7.4 months) and those with a low number of CTCs (median PFS 9.6 months). In the case of PD-L1-expressing CTCs, a stronger correlation between therapeutic prognosis and CTC count was observed. In chemo-naïve stage IV NSCLC patients, a higher CTC count ( $>5$ ) at baseline predicted shortened PFS [82].

However, Kulasinghe et al. did not find any correlation between PD-L1-expressing CTC count and disease development in NSCLC patients [95]. This finding implies that PD-L1 expression may not always be a decisive factor in tumour development and metastatic activity. Manjuth et al. found that assessing other factors, such as the expression of mesenchymal markers (e.g., vimentin and N-cadherin), in PD-L1-expressing CTCs can lead to significantly better predictions [96]. Similarly, Schehr et al. found that neutrophils (insignificantly expressing CD45 and expressing PD-L1) can interfere with the assessment of PD-L1-expressing CTCs. The number of CD11b+ cells (CD11b is a neutrophil marker) misidentified as CTCs varied among patients, accounting for 33–100% of traditionally identified CTCs [97]. Another limitation of classical determination of PD-L1-expressing CTC count was shown by Zhang et al. [98]. The authors observed that detection of PD-L1-expressing CTC was not associated with significantly worse prognosis (e.g., PFS). Nevertheless, during nivolumab treatment, the PD-L1 levels sometimes decreased in patients with advanced NSCLC. On the other hand, an increase in the number of therapeutic cycles (four or more) could lead to the detection of aneuploid endothelial CTCs with PD-L1 expression. These cells were associated with disease progression and shorter PFS (5 versus 8 months).

### 3.2. EGFR Genotyping

EGFR (part of the ErbB family) has tyrosine kinase activity [99]. After ligand binding via autophosphorylation, it actively stimulates cellular growth and proliferation. Mutations in its gene can lead to ligand-independent activation, a common occurrence in NSCLC that

correlates with poor prognosis. In addition, mutations in lung tumour tissues have also been identified in the CTCs. Marchetti et al. used ultradeep next-generation sequencing to find that 84% of NSCLC patients (stage IIIB or IV) harbouring EGFR mutations in primary tumour tissue also displayed these mutations in CTCs [100], and 13% of patients displayed multiple EGFR mutations (a possible indicator of CTC heterogeneity). No EGFR mutations were observed in the control group.

These mutations can be targeted by TKIs. At present, TKIs represent a promising tool for NSCLC treatment. However, their clinical efficiency can be limited by some EGFR chemoresistance mutations, such as T790M [101,102], whose identification in CTCs represents another strategy that can aid therapeutic design and management. Sundaresan et al. reported that the T790M mutation of EGFR in CTCs correlated with TKI resistance [103]. The agreement between CTCs and tumour biopsies was 74%.

For the treatment of patients with TKI resistance, third-generation TKIs (e.g., AZD9291) have been developed [101]; their efficacy inversely correlates with the CTC level. Yang et al. reported that higher CTC counts predicted poor therapeutic response for NSCLC patients (stage IIIB or IV with the EGFR T790M mutation and TKI treatment failure) [104]. Similarly, the combined effect of erlotinib and pertuzumab was inversely correlated with CTC count, and a decreased CTC count was associated with an approximately two-fold longer PFS [105]. The fact that gene mutations in either EGFR or KRAS have been found to be associated with a higher CTC count could confirm the hypothesis that CTCs represent a more dangerous (aggressive or metastatic) subpopulation of cancer cells.

KRAS (a small GTPase and member of the RAS protein family) transmits signals from transmembrane receptors such as EGFR into cells [106]. It participates in many critical cellular processes, such as proliferation, differentiation and survival. Approximately one-third of patients with NSCLC have a mutation in KRAS. Some studies have found an association between KRAS mutations and higher metastatic activity [107,108]. Oncogenic KRAS mutations constitutively activate downstream signalling pathways (e.g., the MAPK/ERK and PI3K pathways) [109,110].

On the other hand, patients with EGFR DelEx19 mutation showed a good response to therapy (strong decreases in CTC counts associated with increased PFS and stable disease). These findings were provided by a study by Breitenbuecher et al., who reported that 40% of patients lost the EGFR DelEx19 mutation in CTCs during therapy [111]. This loss was associated with better therapy prognosis, as it prolonged the median time to therapy failure from 116 to 355 days.

High level of circulating tumour DNA (ctDNA) is a strong marker of bad prognosis [112]. Unlike CTC, very low concentrations of free DNA (5–10 ng/mL) can be observed in the plasma of healthy subjects [113]. Nevertheless, during tumour development (from beginning to advanced), its amount is significantly increased, and it is called ctDNA [114]. ctDNA display higher similarity with DNA obtained from the tissue biopsy sample than CTC DNA [73]. CT contains specific mutations identical to those found in the primary tumour and its metastases [115]. Yanagita et al. reported that CTCs displayed no T790M EGFR mutation despite the mutation being present in tissue biopsy and circulating tumour DNA samples from erlotinib-treated patients (with advanced NSCLC) [73]. A correlation between CTC count and PFS was not observed. However, Sundaresan et al. reported that a combination of CTC genotyping and circulating tumour DNA assessment displayed a higher sensitivity than tissue biopsy assessment [103]; 35% of patients with negative or indeterminate biopsy results had positive results with the combination.

These findings suggest that analysing the EGFR gene in CTCs represents a promising method for the design and management of NSCLC therapy, especially in the case of TKI therapy (Table 2). Nevertheless, resistance to TKIs can also be caused by factors other than mutations in the EGFR gene (e.g., mutations in KRAS and lymphoma-like 11 (BIM)) [104,116]. BIM deletion polymorphisms, such as those producing BIM- $\gamma$ , are associated with TKI resistance in NSCLC patients harbouring EGFR-activating mutations [117]. Isoibe et al. reported that the expression of BIM- $\gamma$  in CTCs (after therapy) was negatively

correlated with both the response of NSCLC patients with EGFR mutations (exon 19 deletion or the L858R mutation) to osimertinib therapy and their PFS [116]. A clinical response was achieved in 27% and 73% of patients with high and low BIM- $\gamma$  expression, respectively, while 60% and 40% of patients with high and low EGFR expression showed a clinical response. Therefore, more clinical trials are needed for better validation and understanding of this phenomenon and optimization of therapeutic regimens.

**Table 2.** Analysis of CTC count in patients treated with agents targeting programmed cell death protein ligand 1 (PD-L1) and epidermal growth factor receptor (EGFR). TKI, tyrosine kinase inhibitor.

Patient Characteristics	Clinical Finding	Ref.
104 patients with stage IIIB or IV disease; agents targeting PD-L1 or PD-1, 6 weeks (The Netherlands)	$\geq 1$ (32%) <sup>1</sup> CTC count for prediction <sup>2</sup> (baseline): $\geq 1$ ; OS (12.1 vs. 4.5) and PFS (4.8 vs. 1.4)	[89]
7.5 mL, CellSearch (Veridex LLC, Raritan, NJ, USA)		
68 patients with stage IIIB or IV disease; first-line TKI treatment failure, EGFR-T790M (China)	CTC distribution: $\geq 5$ (75%) CTC count for prediction (baseline): $\geq 5$ ; PFS (9.3 vs. 6.5)	[104]
7.5 mL, CellSearch (Veridex LLC, Raritan, NJ, USA)		
107 patients with stage IIIB (ineligible for sequential radiotherapy or concurrent chemo/radiotherapy) or stage IV disease; erlotinib/gefitinib therapy, 28 days <sup>3</sup> (China)	CTC distribution: $\geq 2$ (44%) and $\geq 5$ (15%) CTC count for prediction (baseline): $\geq 5$ ; PFS (11.1 vs. 6.8)	[118]
7.5 mL, CellSearch (Veridex LLC, Raritan, NJ, USA)		
41 relapsed or refractory NSCLC patients; erlotinib/pertuzumab, 3 weeks (USA)	CTC distribution: $\geq 1$ (78%) and $\geq 5$ (42%) Agreement (cDNA, tumour biopsy) of EGFR and KRAS mutations was not observed between CTCs and tumour tissues	[105]
CellSearch; EGFR status was determined by immunofluorescence; mutations in EGFR, KRAS, PIK3CA, BRAF, NRAS, and AKT1 were assessed by DxS kits and TaqMan genotyping assays (Qiagen, Venlo, Netherlands)		
37 patients with stage IIIB or IV disease; no previous chemotherapy, EGFR mutations (Italy)	CTC distribution: $\geq 1$ (13%) 84% <sup>4</sup> had EGFR mutations, 81% had in-frame deletions (exon 19), 19% had point mutations (exon 21), 13% had multiple mutations, 94% had mutations in tumour tissue	[100]
7.5 mL of peripheral blood was used for CellSearch analysis, PCR amplification (MIDs), and next-generation sequencing (massively parallel pyrosequencing)		
40 patients with stage III recurrent disease following locoregional treatment who developed resistance to a primary EGFR TKI, 30 days (USA)	76% were suitable for genotyping, 57% of CTC samples had T790M mutation, 74% had biopsy agreement (CTC and tumour biopsy agreement)	[103]
10 mL of blood was used for HbCTC-Chip (EpCAM) assessment of specific T790M amplification		
10 patients with the EGFR DelEx19 mutation (Germany)	Low mutation burden (40% of patients) delayed treatment failure (116 vs. 355 days)	[111]
20 mL of peripheral blood was used for assessment with anti-EpCAM (CD326, positive) and anti-CD45 (negative) microbeads (Miltenyi Biotech, Bergisch Gladbach, Germany), real time-PCR, and melting curve analysis		

<sup>1</sup> Proportion of patients with a given number of CTCs. <sup>2</sup> OS and PFS shown in months. <sup>3</sup> Length of the therapy. <sup>4</sup> Proportion of CTC samples/patients.

#### 4. Flavonoids and Curcuminoids for Suppressing the Spread of CTCs

For most cancer patients, metastases are the leading cause of death. Therefore, mi-grastatics have been developed, and their administration does not lead to shrinkage of tumours but to suppression of CTC spreading and thus metastatic activity [49]. Some

high-impact studies have shown the low toxicity of polyphenols such as curcumin and flavonoids (Figure 1), suggesting that they are very promising agents for this purpose.

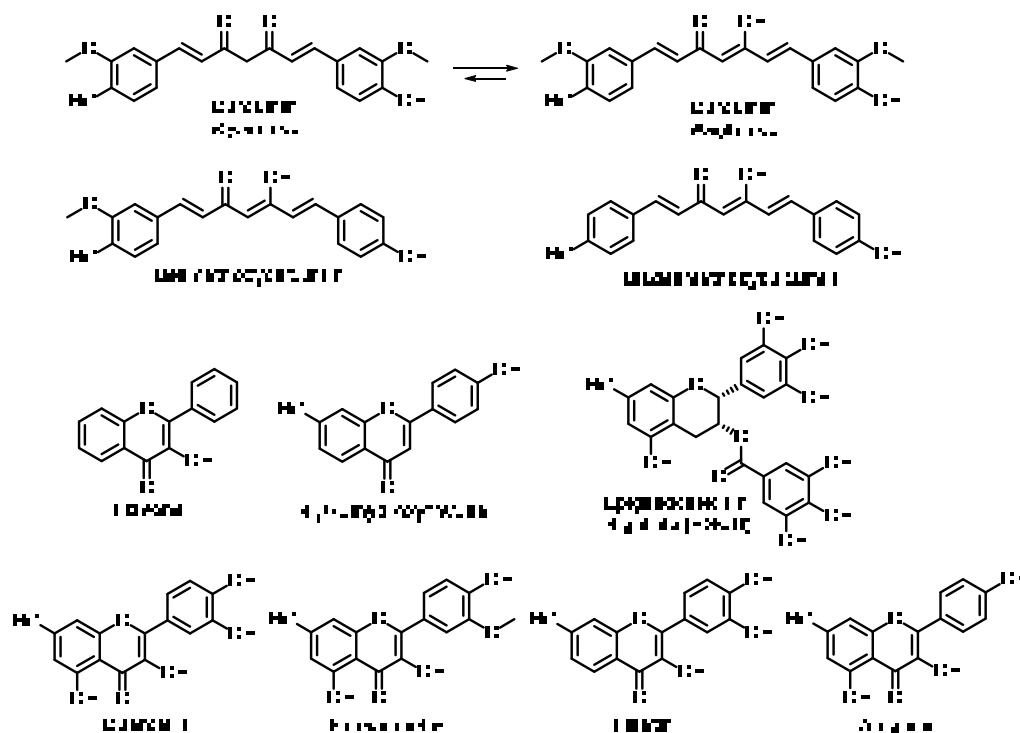


Figure 1. Structure of curcuminoids and flavonoids tested for suppression of NSCLC metastasis.

Curcumin and other curcuminoids are derived from turmeric (*Curcumin longa*) and have various anticancer effects. Their incorporation in the treatment of lung cancer (chemotherapy and radiotherapy) has led to significant improvement of patient quality of life [119]. Curcumin is one of the most studied agents used for the treatment of various cancers, and antimetastatic effects have also been observed for other natural and synthetic derivatives [120–128], implying high potential for incorporation into therapeutic regimens for NSCLC treatment.

Flavonoids are low-toxicity polyphenols that are usually obtained from fruits and vegetables and have great prospects for the treatment of lung cancer. For example, the results published by Sun et al. indicated that daily flavonoid intake could decrease metastatic activity and increase survival in NSCLC patients (stage IIIB or IV) [129]. The use of agents such as epigallocatechin-3-gallate (EGCG) is feasible and safe even at high concentrations, [130] and they have potential for incorporation into radiotherapy regimens. Zhao et al. reported that EGCG can effectively alleviate acute radiation oesophagitis in patients with advanced lung cancer without obvious side effects [131].

In addition, curcuminoids, flavonoids and other agents have the potential to be radiosensitisers, thus increasing the therapeutic efficacy of radiotherapy [132–134]. Furthermore, chemotherapy may improve the effectiveness of cytostatics by affecting mechanisms of resistance, tumour cell migration and the stem cell phenotype [123,133,135–137].

These results imply, in accordance with many high-impact studies, that curcuminoids and flavonoids have a strong ability to suppress metastasis. Based on their effects on cancer cells and tumour tissues, possible therapeutic strategies implementing curcuminoids and flavonoids can be developed for the repression of NSCLC metastasis, normalization of the tumour microenvironment, repression of EMT, and targeting of migrating cancer cells. The effects of curcumin and flavonoids on these phenomena are described in detail in the following subsections.

#### 4.1. Effects of Curcumin and Flavonoids on Tumour-Associated and -Infiltrating Cells: Suppression of CTC Support

The tumour microenvironment contains tumour support/tumour-associated cells, such as macrophages, lymphocytes, fibroblasts, and endothelial cells, and an extracellular matrix with signalling molecules [138,139]. While “healthy” stromal cells can repress carcinogenesis, interactions of cancer cells with the tumour stroma have a strong effect on tumour development, progression, and resistance. In addition, it was observed that CTCs cannot migrate on their own and rather migrate in clusters with tumour-supporting/tumour-associated cells, the metastatic activity of which is an order of magnitude higher than that of CTCs alone [8,24,140]. Therefore, targeting this circulating microenvironment [60] is an intensively studied method of cancer treatment.

The fact that curcumin administration in patients with cancer, including lung cancer, is strongly associated with a decreased level of inflammatory factors (interleukin 6 (IL-6), interleukin 8 (IL-8), and tumour necrosis factor alpha (TNF- $\alpha$ )) implies its strong potential for metastasis suppression [119]. High IL-6 activity is correlated with poor prognosis and lung-cancer-related symptoms such as fatigue, thromboembolism, cachexia, and anaemia [141]. In lung cancer, high IL-6 activity is associated with overactivated signal transducer and activator of transcription 3 (STAT3) signalling (one mechanism of TKI resistance) [142,143], which can lead to IL-6 overproduction and inflammation associated with tumour resistance and development [144]. Tumour inflammation is induced by reciprocal interactions of tumour cells and tumour-associated macrophages (TAMs, the most abundant immune cells in NSCLC), followed by stimulation of TAM polarization to the M2 phenotype and repression of the M1 phenotype [145]. The M1 (antitumour) TAM phenotype is associated with good prognosis, and the M2 phenotype (stimulated by IL-6, IL-8, and other inflammatory factors) is associated with shorter OS [146]. According to a study by Almatroodi et al., the expression of M2 markers (CD68 and CD163) was increased in NSCLC tumour tissue compared to a control (non-tumour tissue from the same patient) [147]. However, expression of M1 markers was decreased in patients with adenocarcinoma and squamous carcinoma; serum levels of interleukin 1 beta (IL-1 $\beta$ ), interleukin 4 (IL-4), IL-6, and IL-8 were higher in patients with large-cell carcinoma than in healthy controls.

Some studies imply that the anticancer effect of curcumin may be associated with repression of the M2 TAM phenotype [148–150]. For example, a sublethal dose of nanoformulated curcumin ( $c_{\max}$  0.61  $\mu\text{mol/l}$  in mouse plasma) or curcumin combined with epicatechin gallate and resveratrol can revert the M2 TAM phenotype to a tumouricidal phenotype with a potent immune antitumour response, leading to tumour eradication [148]. The decreased levels of inflammatory factors (IL-6, IL-8, and TNF- $\alpha$ ) strongly associated with curcumin administration (180 mg/day;  $\sim c_{\max}$  0.5  $\mu\text{mol/l}$  in human plasma [151]) in patients with cancer, including those with lung cancer [119], imply a possible reduction of the M2 TAM phenotype. Higher levels inflammatory factors can increase the M2 TAM phenotype [152,153]. Reduction of their levels in a mouse model of lung cancer led to upregulation of the M1 TAM phenotype [152]. Zou et al. reported that curcumin application to patients with lung cancer leads to a transformation of Treg cells into Th1 cells and an increase in IFN- $\gamma$  [154]. It is known that the secretion of IFN- $\gamma$  by Th1 cells leads to macrophage polarization into the M1 phenotype [155]. Nevertheless, the effect of curcumin on the macrophage phenotype in NSCLC patients must be evaluated in other clinical studies.

Myeloid-derived suppressor cells (MDSCs) are cells of the immune system that can play important roles in metastatic spread [156]. Activated MDSCs (e.g., activated by vascular endothelial growth factor (VEGF) or IL-6) induce suppression of innate and adaptive immune systems and thereby the host antitumour response. The blood level of MDSCs is a predictive marker. For example, Augustyn et al. reported that serum levels of cancer-associated macrophage-like cells (CAMLs; multinuclear myeloid cells) can significantly influence the treatment outcome of NSCLC patients (those with advanced

cancer treated with chemoradiotherapy and atezolizumab) [157]. The authors found that the levels after the chemoradiotherapy cycle correlated with the metastatic disease status and survival.

Interestingly, curcumin administration in a mouse model of carcinoma led to the maturation of MDSCs (loss of immunosuppressive effects) in spleen and tumour tissues [158]. Additionally, the levels of CD4+ and CD8+ T cells were restored. In MDSCs, this effect was associated with suppression of reactive oxygen species (ROS), arginase (Arg-1), and inducible nitric oxide synthase (iNOS). Lio reported that curcumin could support anticancer immunity by repressing the expression of PD-L1 in cancer cells [159].

An important immunosuppressive effect of MDSCs is the induction of CD4+ T cell differentiation to Treg cells. Via cytokines (e.g., transforming growth factor beta 1 (TGF- $\beta$ 1)), Treg cells suppress cancer-specific effector immune cells (CD8+ T cells) and decrease the antitumour capacity of the host [160]. According to a study by Zou et al., patients with lung cancer have significantly higher Treg cell levels [154]. Curcumin administration at 1.5 g per day significantly decreased Treg cells and increased Th1 cells in the peripheral system. An *in vitro* study showed that curcumin converted Treg cells obtained from patients into Th1 cells (which induce cancer cell apoptosis) [161] via repression of FOXP3. Experiments in a mouse model with lung metastasis suggested that this strategy could prolong the survival of patients with metastatic disease [162].

Cancer-associated fibroblasts (CAFs) constitute a major portion of the reactive tumour stroma and play a crucial role in tumour progression [163]. They initiate angiogenesis (via overproduction of VEGF), promote tumour progression, and support invasiveness [164]. In addition, some studies suggest that there is an association between CAFs and characteristics of the stem-cell-like phenotypes of NSCLC cells, such as chemoresistance and overproduction of inflammatory factors [165–167]. Sung et al. reported that netrin-1 secretion by CAFs leads to overexpression of IL-6 and IL-8 by cancer cells [168]. In a mouse model, administration of the netrin-1 antibody significantly repressed tumour growth. On the other hand, solid tumours after radiotherapy can display increased CAFs [169]. Cho et al. found that the survival of quiescent cancer cells induced via oncogenic signalling factors (e.g., IL-1 $\beta$ , IL-8, TGF- $\beta$ 1, and epidermal growth factor (EGF)) stimulated fibroblast migration to cancer cells and their transformation into CAFs [170]. Some studies imply that CAF metastatic effects could also be associated with CTC migration and survival [135,171,172]. Otero et al. observed CAF–CTC clusters in blood samples from patients with metastatic cancers such as NSCLC [171]. The interaction of such clusters with cancer cells via direct contact or signalling factors can induce drug resistance and cell proliferation and thereby enhance their metastatic potential [135].

Ba et al. reported that the administration of 10  $\mu$ M curcumin modulated the phenotype of CAFs into one of peritumour fibroblast-like cells via downregulation of the expression of alpha smooth muscle actin ( $\alpha$ -SMA), a marker of the CAF phenotype [173]. This transformation led to inhibition of the secretion of procarcinogenic cytokines, including TGF- $\beta$ 1, matrix metalloproteinase 2 (MMP-2), and stromal-cell-derived factor-1 (SDF-1). In accordance with the above findings, Wang et al. showed that curcumin-treated CAFs lost the ability to induce the metastatic potential of cancer cells (a primary cell line derived from patients with oral squamous cell carcinoma) compared to nontreated CAFs [174]. Their ability to interact with cancer cells via gap junctions was also reduced. Another study indicating that curcumin suppresses CAF communication with cancer cells was published by Kreutz et al. [175]. They found that administration of curcumin (30  $\mu$ M) in coculture with CAFs and cancer cells suppressed TNF- $\alpha$  signalling and survival pathways. However, in single-cell-type cultures, these effects were not observed. Luo et al. reported that CAFs obtained from NSCLC patients (stages I–III) induced EMT of NSCLC cells (A549 and H1299) [176]. This pattern was associated with a metabolic transition of NSCLC cells to aerobic glycolysis in association with the connexin 43 gap junction. Subsequently, overactivation of PI3K/protein kinase B (Akt) and MAPK/ERK signalling and increased mobility and invasiveness of cancer cells were observed. The expression of CAF markers

in tumour tissue ( $\alpha$ -SMA, lactate dehydrogenase isoform B, and connexin 43) was also strongly correlated ( $p < 0.0001$ ) with poor prognosis, and sometimes shorter OS and PFS.

Tumour endothelial cells (TECs) support nutritional transport to tumour tissue by inducing angiogenesis (via VEGF) and assist in leukocyte infiltration [177]. Higher levels of TECs can lead to chemoresistance and higher metastatic activity. In a mouse NSCLC model, targeting the vascular endothelial growth factor receptor (VEGFR) and EGFR pathways overcame TKI resistance and suppressed angiogenesis [178,179]. Similarly, Lee et al. showed that targeting TECs could repress the paclitaxel resistance of NSCLC brain metastases [180]. Unlike normal cells, TECs display wide and leaky junctions, multiple transendothelial channels, and abnormal shunts, which contribute to the high permeability of the tumour vasculature. This phenotype transition is stimulated by VEGF [181,182].

High levels of B cell lymphoma 2 (Bcl-2), a key antiapoptotic protein, were shown to promote [181,182] tumour cell proliferation and invasion [181,183]. A study in a mouse model indicated that this ability is not dependent on the tumour mass. Another important metastatic TEC function was reported by Yadav et al. [184]. They found that endothelial cells overexpressing Bcl-2 (EC-Bcl-2) can display a higher affinity for cancer cells via overexpressed E-selectin and can decrease the apoptosis of CTCs. In the mouse model, coadministration of cancer cells with EC-Bcl-2 led to significantly higher metastatic activity. This implies that tumour-associated endothelial cells can enhance the survival of tumour cells in the blood and chaperone them to distant sites. However, their function can be significantly repressed by curcumin, and more effectively repressed by curcumin in combination with flavonoids, such as EGCG [185]. Such applications can lead to repression of angiogenesis via decreased VEGF production [186–188], blocking monocyte binding via downregulation of nuclear factor kappa-light-chain-enhancer of activated B cells (NF- $\kappa$ B) signalling [189]. A model of the therapeutic effects of curcumin and flavonoids on the tumour microenvironment and tumour development is shown in Figure 2.

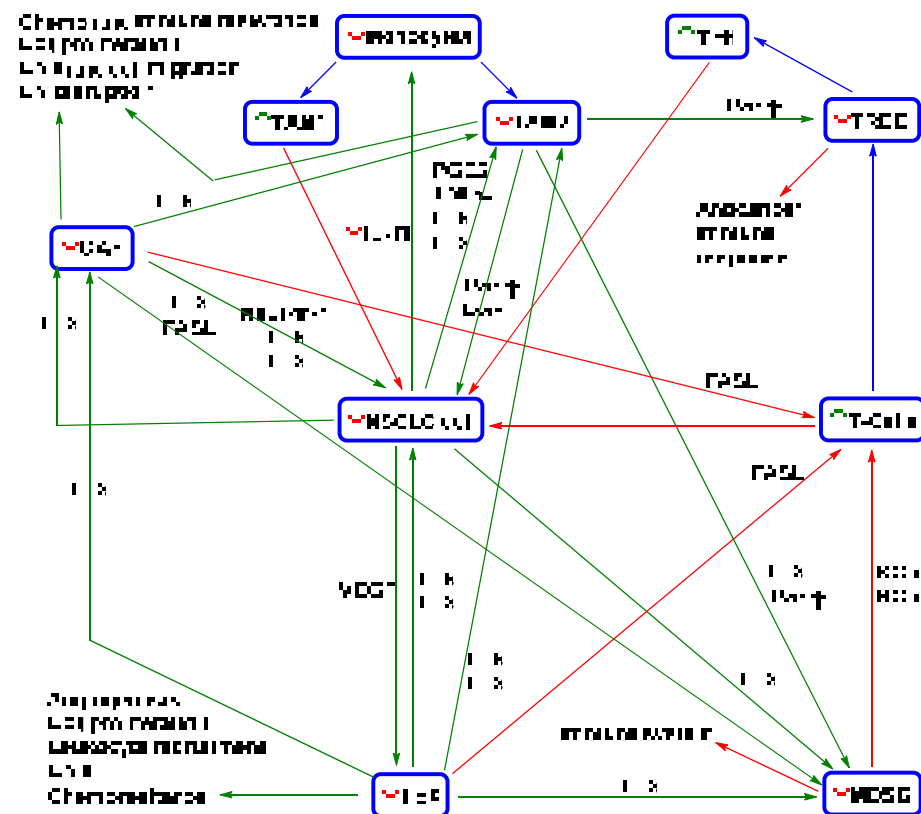


Figure 2. Simplified model of curcumin and flavonoids effects on the NSCLC microenvironment [83,119,148,158,159,162,168,170,174,175,186–196]. A necessary part of igenesis and CTC spreading is the interaction of NSCLC cells with tumour-associated cells. NSCLC cells recruit monocytes via IL-17

into tumour tissue. Signalling factors (e.g., IL-6, IL-8, TNF- $\alpha$ , and PGE2) produced in the tumour microenvironment stimulate monocyte differentiation into TAM2 (which support NSCLC cell proliferation, EMT, chemoresistance and immune resistance, and EM disruption). MDSCs recruited via IL-8 and TGF- $\beta$ 1 repress the cytotoxic effects of T cells against NSCLC cells and induce their differentiation into Treg cells that are responsible for the suppression of the host immune response. VEGF-recruited TECs affect EMT, chemoresistance, and the proliferation of NSCLC cells, recruit MDSCs and induce angiogenesis. IL-8-activated CAFs decrease the anticancer immune response (with the support of TAM2 and MDSCs) and repress T cells. CAFs stimulate EMT and induce NSCLC cell proliferation, migration, and drug resistance. Tumour-associated cells help sustain the tumour microenvironment and aggressive metastatic phenotype. TAM2, CAFs, and TECs are co-inducers of EMT and thereby CTC spreading, chemoresistance, and immune resistance. MDSCs and Treg cells repress the host immune response and thereby support CTC survival in the blood. Nevertheless, the anticancer effect of curcuminoids and flavonoids is not dependent on targeting of NSCLC cells, as they repress other important parts of the complex tumour ecosystem. The application of such agents is associated with stimulation of the immune system (higher levels of TAM1 and T cells; lower levels of Th1 cells, TAM2, and Treg cells; and lower recruitment of monocytes and MDSCs). Curcuminoids and flavonoids also decrease the levels of CAFs and TECs and repress their interaction with NSCLC cells. In addition, the application of curcuminoids and flavonoids leads to a decrease in the proliferation, survival, chemoresistance, immunoresistance, and migration ability of NSCLC cells. CAF, cancer-associated fibroblast; EM, extracellular matrix; EMT, epithelial–mesenchymal transition; EGF, endothelial growth factor; FasL, Fas ligand; IL-1 $\beta$ , interleukin 1 $\beta$ ; IL-6, interleukin 6; IL-8, interleukin 8; PGE2, prostaglandin E2; NOS, nitric oxide species; ROS, reactive oxygen species; TAM1, tumour-associated macrophage M1; TAM2, tumour-associated macrophage M2; TEC, tumour endothelial cell; TGF- $\beta$ 1, transforming growth factor beta 1; Th1, T helper 1; Treg, regulatory T; TNF- $\alpha$ , tumour necrosis factor alpha; VEGF, vascular endothelial growth factor. Green arrow = induction/activation of factor/phenomenon/cell; red arrow = repression/inhibition of factor/phenomenon/cell; blue arrow = differentiation of immune cells;  $\uparrow$  = curcumin/flavonoids activation/induction;  $\downarrow$  = curcumin/flavonoids repression/inhibition.

CTC spreading from tumours is not an isolated phenomenon but a central part of the complex process underlying the development of metastases. Tumour-associated cells can support CTC metastatic activity in several ways. As part of the tumour microenvironment, they can induce an aggressive metastatic phenotype with high production of CTCs (e.g., an EMT phenotype), protect CTCs in the bloodstream, and assist in metastasis formation (see the next subchapter). These phenomena suggest that repressing tumour-associated cells could be an important part of CTC targeting. For example, higher lymphocyte infiltration in breast cancer patients was associated with higher CTC counts and metastatic relapse [197]. Additionally, higher Treg cell levels and neutrophil-to-lymphocyte ratios can induce CTC spreading [198,199]. CTCs in clusters with CAFs display higher survival in the bloodstream [135]. Osmundski et al. found that TAM-associated macrophages can stimulate an aggressive phenotype of prostrate CTCs, including high adherence and plasticity [200]. In breast cancer, a decrease in CD8+ T cells and IFN- $\gamma$  can lead to an increase in the CTC count [201]. On the other hand, activated NK cells can repress metastasis via CTC killing [202].

In addition, the application of curcuminoids and flavonoids can significantly lower CTC counts [203,204]. Because these agents are multifunctional, their effects on tumour-associated cells should also be considered; these are shown in Table 3.



**Table 3.** Effects of curcuminoids and flavonoids on tumour-associated cells.

Agents	Model	Effects	Lit.
Phytosomal curcumin	Immune-competent syngeneic C57BL6 mice with orthotopically implanted mouse GL261 (GBM) cells	TAM phenotype ( $\downarrow$ STAT3 $\downarrow$ IL10, $\uparrow$ IL12, $\uparrow$ STAT1, $\downarrow$ ARG1 and $\uparrow$ MCP-1), $\uparrow$ NK recruitment and $\uparrow$ TAM repolarization from M2 to M1	[149]
TriCurin	Mice implanted with UMSCC47 (HNSCC) cells	TAM phenotype ( $\downarrow$ ARG1, $\downarrow$ IL10, $\uparrow$ iNOS, $\uparrow$ IL12, $\downarrow$ STAT3, $\uparrow$ STAT1 and $\uparrow$ NF-KB), $\uparrow$ NK recruitment and $\uparrow$ TAM repolarization from M2 to M1	[150]
Curcumin	Mice implanted with GL261 (GBM) cells	Microglia phenotype ( $\uparrow$ iNOS, $\downarrow$ ARG2 and $\uparrow$ NF-kB)	[205]
Pro-EGCG	Mice implanted with AN3CA and RL95-2 (EC) cells	$\downarrow$ VEGFA $\downarrow$ HIF1 $\alpha$ , $\downarrow$ SDF1 and $\downarrow$ TAM infiltration	[206]
EGCG exosomes	Mice implanted with 4T1 (BC) cells	TAM phenotype ( $\downarrow$ IL-6, $\downarrow$ TGF- $\beta$ , and $\uparrow$ TNF- $\alpha$ ), $\downarrow$ CSF-1, $\downarrow$ CCL-2, $\downarrow$ tumour growth and $\uparrow$ TAM repolarization from M2 to M1	[207]
Curcumin	Mice implanted with HepG2 (HC) cells	(MDSC inducers ( $\downarrow$ GM-CSF and $\downarrow$ G-CSF), $\downarrow$ MSDC phenotype ( $\downarrow$ TLR4/NF- $\kappa$ B), $\downarrow$ IL-6, $\downarrow$ IL-1 $\beta$ , $\downarrow$ PGE2, $\downarrow$ COX-2, $\downarrow$ VEGF and CAF marker ( $\downarrow$ CD31 and $\downarrow$ $\alpha$ SMC)	[208]
Curcumin	Mice implanted with Lewis lung carcinoma cells	$\downarrow$ IL-6 and $\downarrow$ MDSCs	[158]
Curcumin	Mice implanted with 4T1 (BC) cells	$\downarrow$ G-MDSC and $\uparrow$ M-MDSC polarization to M1 TAMs, $\uparrow$ CD4+ T cells and $\uparrow$ CD8+ T cells	[209]
Curcumin–PEG conjugate	Mice implanted with B16F10 (melanoma) cells	$\downarrow$ Treg cells $\downarrow$ MDSC and CAF markers ( $\downarrow$ $\alpha$ -SMA and $\downarrow$ CD31)	[210]
Lipid-based Trp2 peptide combination vaccine		$\uparrow$ CD4+ T cells and $\uparrow$ CD8+ T cells	
Curcumin	Mice implanted with OSCC (induced by 4NQO) cells	$\uparrow$ CD8+ T cells, $\downarrow$ Treg cells and $\downarrow$ MDSCs	[159]
Bisdemethoxycurcumin	Immunocompetent mice implanted with subcutaneous or lung metastasised MB79 (bladder cancer) cells	$\uparrow$ CD8+ T cells, $\downarrow$ Treg cells and $\uparrow$ IFN- $\gamma$	[162]
$\alpha$ -PD-L1 antibody combination		$\downarrow$ MDSCs and CD8+ T cells ( $\uparrow$ IFN- $\gamma$ , $\uparrow$ granzyme B, $\uparrow$ perforin and $\downarrow$ exhaustion)	
Quercetin	Human and mouse G-MDSCs	$\uparrow$ ESR/STAT3, $\uparrow$ NOS2 and prolonged MDSC survival in mice	[211]
EGCG	M-MDSCs	$\downarrow$ Arg-1/iNOS/Nox2/NF- $\kappa$ B/STAT3, $\downarrow$ IL-6, $\downarrow$ IL-10, $\downarrow$ TGF- $\beta$ , $\downarrow$ GM-CSF, and $\uparrow$ apoptosis	[212]
	Mice implanted with 4T1 (BC) cells	$\downarrow$ MDSCs $\uparrow$ CD4+ T cells $\uparrow$ CD8+ T cells	
Polyphenon E	Transgenic TH-MYCN mice	$\downarrow$ MDDCs	[213]
	NOD/SCID mice implanted with SHSY5Y (neuroblastoma) cells	0MDSCs	
	A/J mice implanted with syngeneic Neuro 2A (neuroblastoma) cells	$\downarrow$ MDSCs	
	MDSCs	$\uparrow$ G-CSF, $\uparrow$ IL-6, $\downarrow$ Treg cell induction	
Curcumin	Coculture of a primary BC line + T cells	$\downarrow$ TGF- $\beta$ , $\downarrow$ Treg cell phenotype induction (IL-2R $\alpha$ , IL-6, and FoxP3) in CD4+ T cells	[214]
	Mice implanted with 4T1 cells	$\downarrow$ Treg cell phenotype (CD4+, CD25+, and FoxP3+)	

Table 3. Cont.

Agents	Model	Effects	Lit.
Curcumin	HNSCC tissue	↓CCL22 (Treg cell mobility)	[215]
Curcumin	Patients with colon cancer	↑Conversion of Treg cells into Th1 cells and ↑induction of a Th1 cell phenotype (↓FoxP3 and ↑IFN-γ)	[216]
Curcumin	Patients with lung cancer	↑Conversion of Treg cell into Th1 cells and ↑induction of a Th1 cell phenotype (↓FoxP3 and ↑IFN-γ)	[154]
Curcumin	Primary TSCC CAFs	↓α-SMA, ↓TGF-β1, ↓SDF-1, ↓MMP-2, ↓SMAD2/3, ↓Cal27, and ↓proliferation	[173]
Curcumin	Mice implanted with Cal 27 (TSCC) cells	↓α-SMA and ↓Ki67	
Curcumin	CAFs cocultured with Capan-1 and Panc-1 (pancreatic carcinoma) cells	↓CAF phenotype (↓α-SMA and ↓vimentin), ↑E-cadherin, ↓EMT and ↓cancer cell migration	[174]
	nu/nu nude mice implanted with Panc-1 tumour cells	↓Lung metastasis	
Curcumin	CAFs cultured with prostate cancer pC-3 cells	↓ROS, ↓IL-6, ↓CXCR4 and ↓MAOA/mTOR/HIF-1α	[217]
Curcumin	Primary breast CAFs	↓α-SMA, ↓JAK2/STAT3, ↓SDF-1, ↓IL-6, ↓MMP-2 and ↓MMP-9, ↓TGF-β and ↓migration ability	[218]
Curcumin	TNF-α-activated ECs	↓NF-κB, ↓adhesion molecules (↓ICAM-1 and ↓VCAM-1) and ↓monocyte adhesion	[189]
Curcumin and EGCG or both agents combined	Coculture of ECs with SW620, HCT116, and HT-29 (CC) cells	↓TEC transition, ↓TEC phenotype (↓JAK, ↓STAT3, ↓IL-8, ↓TEM1, ↓TEM8 and ↓VEGFR2) and ↓TEC migration	[185]
	Mice implanted with patient-derived CCs	↓JAK, ↓STAT3 and ↓IL-8	

α-SMA, alpha-smooth muscle actin; ARG1, arginase 1; ARG2, arginase 2; CD31, a platelet endothelial cell adhesion molecule; COX-2, cyclooxygenase-2; G-CSF, granulocyte colony-stimulating factor; ESR, oestrogen signalling receptor; GM-CSF, granulocyte–macrophage colony-stimulating factor; iNOS, inducible nitric oxide synthase; IL-1β, interleukin 1β; IL-2Ra, interleukin 2 receptor alpha; IL-6, interleukin 6; IL-8, interleukin 8; IL-10, interleukin 10; IL-12, interleukin 12; ICAM-1, intercellular adhesion molecule 1; JAK, Janus tyrosine kinase; HIF-1α, hypoxia-inducible factor 1α; NOS2, NADPH oxidase 2; nitric oxide synthase 2; PGE2, prostaglandin E2; ROS, reactive oxygen species; TGF-β, transforming growth factor beta; TEM1, tumour endothelial marker 1; TEM8, tumour endothelial marker 1; TLR4, Toll-like receptor 4; STAT3, signal transducer and activator of transcription 3; SDF-1, stromal-cell-derived factor 1; VCAM-1, vascular cell adhesion molecule 1; VEGF, vascular endothelial growth factor; VEGFR2, vascular endothelial growth factor receptor 2; 4NQO 4-nitroquinoline-1-oxide; G-MDSCs, granulocytic MDSCs; M-MDSCs, monocytic MDSCs; BC, breast carcinoma; CC, colorectal carcinoma; EC, endometrial carcinoma; GBM, glioblastoma; HC, hepatocellular carcinoma; HNSCC, head and neck squamous cell carcinoma; OSCC, oral cavity squamous cell carcinoma; TSCC, the squamous cell carcinoma. ↑ curcuminoids/flavonoids activation/induction; ↓ = curcuminoids/flavonoid repression/inhibition; 0 = without change.

The above results show that curcuminoids and flavonoids repress CTC spreading induced by the tumour microenvironment and metastatic activity by targeting tumour-associated cells, including circulating cells. Relevant in vivo clinical trials show that the application of curcuminoids and flavonoids could greatly enhance NSCLC treatment [119,131,219]. However, the above data were mostly obtained from animal models of various oncological diseases. Therefore, more clinical trials are required to design therapeutic applications.

#### 4.2. Effect of Curcumin and Flavonoid Applications on EMT and Metastasis Formation

Two important phenomena that are strongly associated with CTC spreading in lung cancer are EMT and mesenchymal–epithelial transition. First, EMT (induction of the TAM M2 phenotype, CAFs, and TECs) causes polarity loss and cell/matrix adhesion of cancer cells, aids digestion of the extracellular matrix, and supports migratory properties (e.g., actin polymerization) [220]. In the next step, cancer cells are taken up in the bloodstream

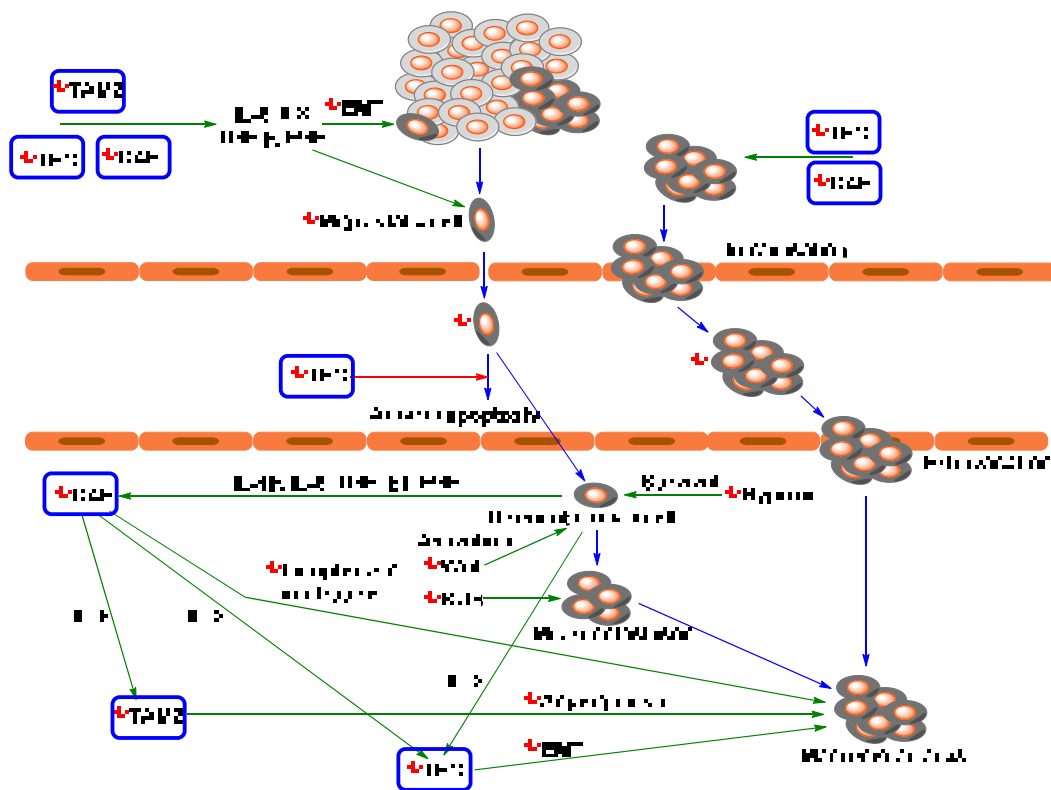
and become CTCs. CTCs are expected to undergo transitions. In the metastatic site or in the bloodstream, CTCs undergo mesenchymal–epithelial reverting transition (MErT) and obtain increased cell adhesion, and the most aggressive of them can form metastatic tumours [221]. CTC spreading can also be stimulated by macrophages, which provide immunoprotection and growth promotion for the formation of metastases [144]. Manjunath et al. found that a higher number of CTCs with expression of PD-L1 and mesenchymal markers (vimentin and N-cadherin) was significantly associated with reduction of PFS [96]. Another important role of EMT in metastatic spread could be stimulation of resistance of CTCs to treatment. For example, PD-L1-expressing CTCs obtained from NSCLC patients displayed spindle-like elongated morphology, which corresponded to EMT-associated nivolumab resistance [84,222]. PD-L1-negative CTCs were mostly small and regularly shaped (round). Raimondi et al. reported the coexpression of vimentin with PD-L1 in these cells [222].

Relevant studies imply that curcumin and flavonoids can repress the mesenchymal phenotype. Liang et al. reported that curcumin administration (100 mg/kg) reversed tobacco-smoke-induced EMT alterations in a mouse model [223]. This process was associated with increased expression of epithelial markers (E-cadherin) and decreased expression of mesenchymal markers (vimentin and N-cadherin). Similarly, Chang et al. found that quercetin repression of EMT via Akt downregulation was strongly associated with a reduction in bone metastasis in an NSCLC mouse model [224].

Knowledge about MErT is still limited. Several studies suggest that E-cadherin overexpression, which enables CTCs to adhere to target tissue and survive within ectopic metastatic microenvironments, is key in the MErT process [221,225–227]. MErT can also be significantly influenced by the presence of TAMs. Yang et al. reported that the M1 TAM phenotype can support MErT by stimulating E-cadherin expression and thereby enhance cancer cell colonization [228]. Infiltrating cancer cells that penetrate healthy tissues can likely survive in the dormant state even with a lower metabolic load. Their eradication is complicated.

Survival of dormant cancer cells can occur through induction of the hypoxia phenotype and NRF2 and their activation by Wnt/ $\beta$ -catenin signalling [229,230]. In the case of micrometastasis, cancer cell development and survival are strongly dependent on higher ROS levels [231]. Curcuminoids and flavonoids can repress oxidative stress and inflammatory factors in healthy tissues and cells [232–235] and are potent inhibitors of Wnt/ $\beta$ -catenin signalling [236,237]. For example, Tabasum et al. reported that fisetin (10  $\mu$ mol/L) inhibited the expression of  $\beta$ -catenin, NF- $\kappa$ B, EGFR, and STAT3 and decreased stem cell phenotype markers (CD44 and CD133) and TKI resistance in NSCLC cell lines (A549 and H1299) [236]. Targeting STAT3 was found to block TEC activation by cancer cells in metastatic brain sites and thereby suppress metastasis formation [238]. In addition, curcumin and flavonoid administration (apigenin, flavone, and 4',7-dihydroxyflavone) can modulate the hypoxic phenotype of NSCLC cells [239,240].

Importantly, the iron chelation ability of flavonoids may play a significant role in repressing micrometastasis. Fryknäs et al. reported that iron chelators are potent agents for targeting quiescent cancer cells [241]. The suppressive effects of curcumin and flavonoids on metastatic spread and development are shown in Figure 3.



**Figure 3.** Simplified model of curcumin and flavonoids action on NSCLC metastasis [83,190,223,224,229–231,236–240,242–249]. 1. NSCLC cells with a mesenchymal phenotype partially induced by TAM2, TECs, and CAFs migrate from tissue into blood vessels. 2. CTCs are transported (via passive transport) to distant metastatic site(s), and TECs can serve as guardians against anoikis apoptosis. 3. Infiltrating NSCLC cells revert to an epithelial phenotype via MER1 (which possibly occurs in blood). 4. Dormant cancer cells activated by Wnt signalling start recruiting CAFs and TECs and form micrometastases. 5 Micrometastases stabilised by oxidative stress recruit tumour-associated cells to form macrometastases, at which point metastatic NSCLC can be diagnosed in patients. TECs and CAFs can support the formation of highly aggressive and metastatic CTC clusters. CAF, cancer-associated fibroblast; EMT, epithelial–mesenchymal transition; EGF, endothelial growth factor; IL-1 $\beta$ , interleukin 1 $\beta$ ; IL-6, interleukin 6; IL-8, interleukin 8; PGE2, prostaglandin E2; ROS, reactive oxygen species; TAM2, tumour-associated macrophage M2 phenotype; TEC, tumour endothelial cell; TGF- $\beta$ 1, transforming growth factor beta 1; VEGF, vascular endothelial growth factor. Green arrow = induction/activation of factor/phenomenon; red arrow = repression/inhibition of factor/phenomenon; blue arrow = transition between individual steps of metastatic spread;  $\downarrow$  = curcumin/flavonoids repression/inhibition.

In this process, in addition to targeting signalling pathways of NSCLC cells, curcumin can modulate processes in tumour-associated cells. The presence of TAM2 in the tumour microenvironment of lung adenocarcinoma contributes to an invasive phenotype and induces the expression of EMT-related markers [250]. Zhang et al. reported that curcuminoids are able to reverse the macrophage phenotype from TAM2 to TAM1 by inhibiting STAT3 signalling [251]. In glioblastoma, curcumin treatment elicited activation of antitumour STAT1 signalling and the expression of iNOS in TAMs [149]. Mukherjee et al. found that a sublethal dose of TriCurin (curcumin in combination with resveratrol and epicatechin gallate; ~ nM concentration in plasma) in a mouse model changed TAMs to the M1 phenotype and was associated with strong repression of tumour growth [150]. Nevertheless, Murakami et al. found that curcumin inhibited lipopolysaccharide-induced expression of inducible forms of both nitric oxide synthase and cyclooxygenase in RAW 264.7 cells (murine macrophages) [252]. This finding could mean that curcumin could also target micrometastases by lowering inflammatory processes and oxidative stress.

Zeng et al. found that curcumin induces endoplasmic reticulum stress, loss of mitochondrial potential, cell cycle arrest at the G2–M transition, and apoptosis in prostate

CAFs. The sensitivity of natural fibroblasts was approximately three times lower than that in treated CAFs [253]. Ba et al. reported that a sublethal curcumin dose (10  $\mu$ M) decreased the expression of  $\alpha$ -SMA, MMP-2, SDF-1, and TGF- $\beta$ 1, and Smad2/3 phosphorylation/activation by approximately half [173]. Curcumin can also suppress CAF-induced EMT of cancer cells. Du et al. found that in CAFs, monoamine oxidase A (a mitochondrial enzyme) induces mammalian target of rapamycin (mTOR)/hypoxia-inducible factor 1 alpha (HIF-1 $\alpha$ ) signalling [217]. In prostate cancer cells, this CAF phenotype can induce ROS production and C-X-C motif chemokine receptor 4 (CXCR4) and IL-6 receptor expression and thereby cell migration and invasion. Nevertheless, curcumin application suppresses the activation of HIF-1 $\alpha$  signalling and subsequently suppresses EMT in cancer cells. In a mouse model of pancreatic cancer, it was observed that curcumin-induced EMT suppression via CAF targeting could repress cancer metastasis [174].

Recruitment of TECs by cancer cells is associated with activation of JAK/STAT3 signalling via IL-8. Nevertheless, application of curcumin in combination with EGCG (50 mg/kg per day) in a mouse model of colorectal carcinoma led to suppression of JAK/STAT3 signalling in endothelial cells and thereby their recruitment by cancer cells [185]. Similarly, the therapeutic effect of curcumin in glioblastoma also causes a reduction in TEC recruitment [254]. TEC presence was found to correlate with EMT and metastasis in various cancer models [255–257]. These effects, however, may be due to recruitment of leukocytes by TECs. NSCLC patients can have significantly increased blood levels of TNF- $\alpha$  [258]. Kumar et al. reported that endothelial cells induced TNF- $\alpha$  expression via activation of products of NF- $\kappa$ B signalling (adhesion factors; e.g., intracellular adhesion molecule-1 (ICAM-1), vascular cell adhesion molecule-1, and endothelial leukocyte adhesion molecule-1) [189]. Nevertheless, curcumin can effectively revert this phenotype of endothelial cells and subsequently monocyte adhesion.

In addition, some studies suggest that curcumin also repressed cluster formation. Tafta et al. reported that depletion of ICAM-1 in a mouse patient-derived xenograft (PDX) model of triple-negative breast cancer significantly inhibited cluster formation, tumour cell transendothelial migration, and lung metastasis [259]. Yang et al. found that curcumin inhibited the IL-6/STAT3 pathway in NCI-H446 and NCI-1688 small carcinoma cells, leading to suppression of VEGF, MMP-2, MMP-7, and ICAM-1 [260]. Nevertheless, in A549 cells, IL-1 $\beta$  can induce ICAM-1 expression via the NF- $\kappa$ B and Src/PDGFR/PI3K/Akt pathways [261,262]. However, in the presence of curcumin, ICAM-1 expression is repressed [262].

One of the key factors that control CTC acceptance and possible micrometastasis formation is induction and stimulation of the supportive microenvironment (called pre-metastatic niche [263]) in distant organs by primary tumour [264]. Tumour cells display an ability to selectively modify the microenvironment of distant organs via extracellular vesicles (e.g., exosomes). They are nano-sized membranous structures liberated from cells into extracellular space [265]. Exosomes transport proteins, RNA, DNA, miRNA, and lipids. Exosomes can mediate communication between different cell types from various tissue and organs.

Numerous high-impact studies imply that tumour exosomes strongly support tumour-growth and metastatic formation [264]. Ma et al. reported that exosomes isolated from NSCLC patients displayed significantly higher levels of some miRNAs (e.g., miR-3157-3p, miR-3613-5p, and miR-3921) against healthy controls [266]. In addition, metastatic patients have higher expression of miR-3157-3p (exosomes and tumour tissues) than comparative nonmetastatic ones. A549 cells with transferred miR-3157-3p display an increase in protein levels of VEGF, MMP2, and MMP9, and their exosomes can induce vascular permeability of endothelial cells and angiogenesis. In the mice model, exosomes with miR-3157-3p stimulate higher microvessel density and larger tumour tissue.

It was proven that curcuminoids and flavonoids are potent suppressor of MMPs activities and VEGF signalling [267,268]. This suggests that they could suppress the role of exosomes in the formation of the metastases. Kaplan et al. found that bone-marrow-derived

haematopoietic progenitor cells (BMDCs) with expression of vascular endothelial growth factor receptor 1 (VEGFR1) significantly participate in the formation of pre-metastatic sites in mice with Lewis lung carcinoma [263]. VEGFR1 repression by specific antibody suppresses BMDCs clusterisation and prevents tumour metastasis. Their cluster formation in the pre-metastatic site was associated with MMP9 induction. Nevertheless, their effect on tumour-derived exosomes was much more complicated. It was observed that curcumin-exposed cancer cells liberated exosomes. It has been shown that treatment of cancer cells with different doses of curcumin leads to the release of exosomes containing curcumin [269].

Unlike classical tumour exomes, curcumin-induced exosomes display anticancer effects in recipient cells and reduce tumour growth. For example, exosomes produced by H1299 cells (10  $\mu$ M curcumin for 48 h) display upregulation of the transcription factor 21 (TCF21) via downregulation of DNA Methyltransferase 1 [270]. The level of the TCF21 mRNA is inversely correlated with poor prognosis in patients with lung adenocarcinoma [271] and the aggressivity of NSCLC cell lines [270]. In the presence of exosomes derived from curcumin-pre-treated H1299 cells, BEAS-2B cells displayed a significant decrease in proliferation, colony formation, and migration.

Exosomes derived from K562 leukemic cells increase production of IL8 and VCAM1 in endothelial cells; nevertheless, after curcumin treatment (20  $\mu$ M for 24 h), the obtained exosomes displayed opposite effects and inhibited tube formation and vascular permeability in the endothelial cells [272]. In K562 cells, curcumin caused a decrease of cellular miR-21, while it increased miR-21 selective packaging in exosomes. Its decrease can induce PTEN expression (target of miRNA-21) [273]. In the endothelial cells, higher levels of miR-21 can suppress their angiogenic capacity, directly targeting RhoB, a critical regulator of actin dynamics [274].

Exosomes derived from the TS/A cell line (murine mammary adenocarcinoma) displayed a strong inhibition effect on cytotoxicity of the IL-2 activated NK cells [275]. Nevertheless, exosomes isolated from the cells pre-treated with polyphenols (curcumin, baicalin, or genistein, 1  $\mu$ M for 36 h) cause a significant reduction of immunosuppression of NK cells and increase their cytotoxicity against cancer cells. Other polyphenols, including biochanin A and quercetin, had no significant effects.

The cited studies prove that curcuminoids and flavonoids are effective agents for the repression of CTC spreading because they target EMT in primary tumours. We can assume that they also suppress macrometastasis formation by targeting the activation and survival of dormant cancer cells. In addition, the formation of macroscopic metastasis is accompanied by a second EMT event [229,247], which is a possible target for curcuminoids and flavonoids. However, knowledge of this phenomenon is very limited, and the presented model of metastasis formation needs to be validated in NSCLC.

#### 4.3. Effect of Curcumin and Flavonoids on the Migration of Cancer Cells

Another discussed strategy for metastasis suppression is targeting the mobility of cancer cells. At present, some high-impact studies strongly recommend targeting cytoskeletal dynamics as an optimal method to suppress metastatic activity [49].

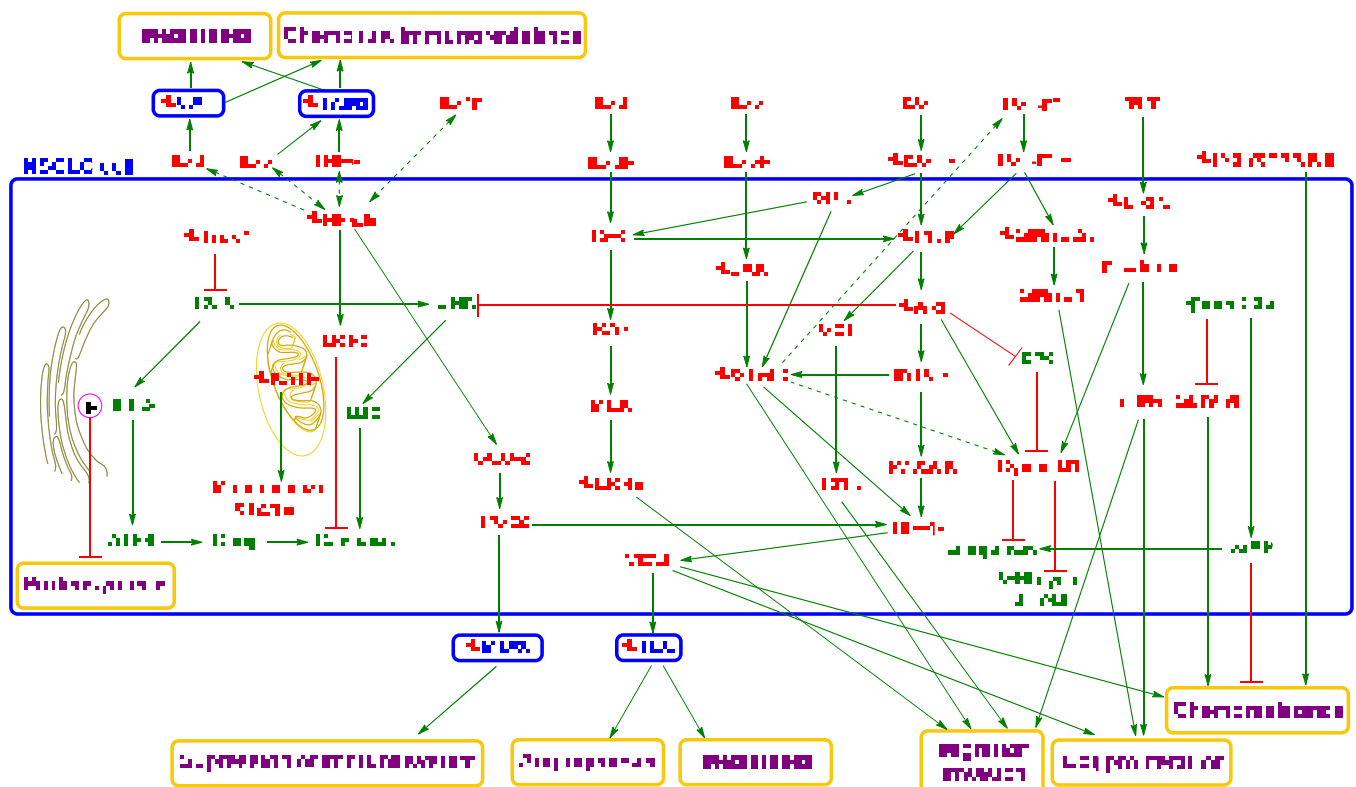
Chen et al. reported that curcumin administration to the 801D (human large-cell lung carcinoma) cell line led to significant inhibition of EGF- or TGF- $\beta$ 1-induced lung cancer cell migration and invasion [276]. These inhibitory effects of curcumin were related to the inhibition of Rac1/PAK1 signalling pathways, MMP-2/9 expression, and actin cytoskeleton rearrangement. In a mouse model, curcumin (60 mg/kg) displayed a comparable effect on tumour volume and metastatic potential to cisplatin (8 mg/kg).

Flavonoid administration could lead to repression of cancer cell mobility. Incubation of A549 cells with quercetin resulted in dose-dependent disorganization of the actin cytoskeleton [277].

The incorporation of curcumin in cancer treatment regimens aimed at erasing primary tumours may aid targeting and suppress metastases. High-impact studies of animal models strongly imply a high potential of this approach. For example, the combination of cisplatin

and curcumin led to a significant reduction in lymph node metastasis and primary tumour size [248]. Application of isorhamnetin in combination with cisplatin and carboplatin led to inhibition of cancer cell migration [278]. This effect was associated with the induction of microtubule depolymerization by isorhamnetin.

In addition to suppressing cancer metastasis, curcumin also has a cytostatic effect. For example, Mirza et al. reported that curcumin administration could lead to specific killing of circulating metastatic cells [249]. The authors reported that cancer cells obtained from peripheral blood of patients with lung adenocarcinoma displayed a cancer-stem-cell-related phenotype (expression of P-glycoprotein 1 (CD44), prominin-1 (CD133), and aldehyde dehydrogenase). These cells also had strong chemoresistance; for example, gemcitabine, even at concentrations higher than 100 µM, did not cause any significant cytotoxicity. Treated cells showed a high response to a low concentration of nanoformulated curcumin (IC<sub>50</sub> = 10 µM). This effect was coupled with inhibition of the DNA repair mechanism and DNA damage. In contrast, the cytotoxic effect against healthy cells (peripheral blood mononuclear cells) was lower. Possible effects of curcumin on NSCLC cells are shown in Figure 4.



**Figure 4.** Simplified model of the effects of curcumin on NSCLC cells [128,196,242–245,248,249,276,279–284]. NSCLC is associated with dysregulation of numerous signalling and regulatory pathways. Some signalling factors (e.g., IL-6, IL-8, EGF, TGF-β1, and Wnt) produced by cancer or tumour-associated cells can induce migration and invasion phenotypes of NSCLC cells and thereby support CTC spreading. These pathways are interconnected, and dysregulation of one can induce dysregulation of another and modulate therapeutic targeting. Nevertheless, curcumin targets multiple signalling pathways to repress this phenomenon. Its effect is associated with repression of ERK2, JAK, STAT3, EGFR, PI3K, Akt, SMAD 2/3, and β-catenin. In addition, curcumin induces oxidative stress in the endoplasmic reticulum by inhibiting TrxR1 and mitochondrial-dependent and mitochondrial-independent apoptotic pathways and repressing drug resistance. Reduced levels of signalling factors produced by NSCLC cells, such as IL-6, 8, VEGF, and PGE2, lead to decreased activity of tumour-associated/tumour-infiltrating cells and thereby decreased support of NSCLC cell metastasis, proliferation, and survival in the tumour microenvironment. Curcumin’s effects on the tumour microenvironment also include activation of the immune system and suppression of angiogenesis and chemoresistance and immune resistance. Akt, protein kinase B;

Bcl-2, B cell lymphoma 2; CAF, cancer-associated fibroblast; COX-2, cyclooxygenase-2; EGF, endothelial growth factor; EGFR, endothelial growth factor receptor; ERK2, extracellular signal-regulated kinase 2; GEF, guanine nucleotide exchange factor; HIF-1 $\alpha$ , hypoxia-inducible factor 1 $\alpha$ ; JAK, Janus tyrosine kinase; JNK, c-Jun N-terminal kinase; IL-1 $\beta$ , interleukin 1 $\beta$ ; IL-6, interleukin 6; IL-6R, interleukin 6 receptor; IL-8, interleukin 8; IL-8R, interleukin 8 receptor; KATP, ATP-sensitive potassium channel; LRP-6, low-density lipoprotein receptor-related protein 6; MAPK, mitogen-activated protein kinase; MDSC, myeloid-derived suppressor cell; mTOR, mammalian target of rapamycin; NF- $\kappa$ B, nuclear factor kappa-light-chain-enhancer of activated B cells; P70S6K, ribosomal protein S6 kinase beta-1; p-eIF2 $\alpha$ , phosphorylated eukaryotic translation initiation factor 2 subunit 1; PGE2, prostaglandin E2; PI3K, phosphoinositide 3-kinase; ROS, reactive oxygen species; STAT3, signal transducer and activator of transcription 3; SRC, intracytoplasmic tyrosine kinase; TAM2, tumour-associated macrophage M2 phenotype; TEC, tumour endothelial cell; TGF- $\beta$ , transforming growth factor beta; TGF- $\beta$ 1R, transforming growth factor beta 1 receptor; TNF- $\alpha$ , tumour necrosis factor alpha; Trx1, thioredoxin reductase 1; VEGF, vascular endothelial growth factor;  $\Delta\Psi$ m, mitochondrial membrane potential. Green arrow = induction/activation of factor/phenomenon/cell, dotted (indirect); red arrow = repression/inhibition of factor/phenomenon/tumour-supporting cell; green factor = anticarcinogenic factor; red factor = carcinogenic factor;  $\uparrow$  = curcumin activation/induction;  $\downarrow$  = curcumin repression/inhibition.

In NSCLC, curcumin represses some important signalling pathways. It inhibits the activation/phosphorylation of JAK and STAT3 (part of the EGF and IL-6 signalling pathways) [285]. STAT3 is constitutively activated in approximately 50% of NSCLC primary tumours and NSCLC cell lines and is associated with poor prognosis [286–288]. Jiang et al. reported that in A549 cells, curcumin application led to not only decreased EGFR expression but also reduced EGFR activity via induction of ubiquitin-activating enzyme E1-like [289]. In human samples (NSCLC tumour tissues and adjacent tissues from NSCLC patients (stages I–IIIa)), there was an inverse correlation between curcumin administration and the activity of the EGFR/AKT/NF- $\kappa$ B pathway.

In athymic nude mice bearing NCI-H460 tumours, curcumin-induced inhibition of JAK and STAT3 phosphorylation led to reduced tumour weight and improved the survival rate of mice. In addition, STAT3-regulated promoter activation of VEGF, Bcl-xL, and cyclin D1 was also repressed after treatment [285]. Targeting STAT3 thus represents another promising approach for reducing CTC counts. Zhang et al. reported that suppression of the JAK/STAT3 pathway reduced CTC seeding in primary tumours (with a nude mouse model of human osteosarcoma) [290]. Mautsaka et al. found that the CTC EGFR expression relative to baseline was strongly associated with regorafenib resistance in patients with refractory metastatic colorectal cancer [291].

One of key factors of NSCLC pathogenesis is NF- $\kappa$ B. Details on its role were described by Dimitrakopoulos et al. [292]. NF- $\kappa$ B has been found to control inflammation, proliferation, survival, apoptosis, angiogenesis, EMT, metastasis, stemness, metabolism, and therapy resistance [293,294]. For example, Sun et al. reported that activation of the PI3K/Akt/NF- $\kappa$ B/tyrosine kinase B (TrkB) pathway led to resistance of cancer cells to anoikis and thereby higher metastatic activity in a mouse model of hepatocellular carcinoma [295].

An interesting approach is using microRNAs (miRNAs) as therapeutics. The striking advantage of miRNAs is that a single miRNA has the potential to simultaneously suppress several oncogenic pathways because it can target multiple genes. Naidu et al. reported targeting of the miR-23b cluster, or miR-125a-5p, which silenced KRAS and NF- $\kappa$ B signalling and resulted in significant repression of the tumorigenicity of CTCs from NSCLC patients in a mouse model [296]. Similarly, Lin et al. showed that TNF- $\alpha$ -stimulated degradation of I $\kappa$ B $\alpha$  and translocation of NF- $\kappa$ B into the nucleus subsequently induce MMP-9 expression in A549 cells [297]. Nevertheless, curcumin application led to the suppression of I $\kappa$ B $\alpha$  phosphorylation and thereby NF- $\kappa$ B activation [298]. Lee et al. reported that interferon alpha (IFN- $\alpha$ )-induced activation of NF- $\kappa$ B and COX-2 was inhibited by curcumin in A549 cells [299]. Accordingly, curcumin inhibition of the migratory and invasive abilities of NSCLC cells seems to be mediated through the NF- $\kappa$ B/MPP pathway according to studies in a mouse model [300,301].



On the other hand, CTC survival can be associated with deacetylase sirtuin 1 (SIRT1) expression, which leads to suppression of NF- $\kappa$ B and ROS activity in some oncological diseases, such as breast cancer [85]. However, the role of SIRT1 expression is not clear, as it can have oncogenic and antitumour effects. For example, repression of cancer cell migration and angiogenesis via activation of both intrinsic (caspase-9) and extrinsic (caspase-8) apoptotic pathways was found to be associated with SIRT1 activation by curcumin in squamous cell carcinoma of the head and neck [302]. Nevertheless, in human colon cancer cells, the repressive effect of curcumin on cell viability and migration caused inactivation of SIRT1 via covalent modification of the cysteine 67 residue [303].

A great benefit of curcumin application is its targeting of hypoxia-related metabolism in NSCLC. Cancer cells, which are located further from blood vessels due to their faster metabolism, have lower oxygen levels. Therefore, hypoxic tumours display significantly lower oxygen pressure (10 mmHg or less) [304]. Hypoxia-activated HIF-1 $\alpha$  can stimulate carcinogenesis via induction of numerous signalling pathways (TGF- $\beta$ 1, EGF, Wnt, and Notch), transcription factors (Snail, Slug, Twist, and Zeb1/2) and other factors [305,306]. These effects lead to the induction of a cancer stem cell phenotype with features such as immune and drug resistance, a mesenchymal phenotype, and metastatic activity. In metastases, HIF-1 $\alpha$  levels have been found to be significantly increased compared with those in primary breast tumours [307]. This finding suggests the importance of HIF-1 $\alpha$  levels in CTC spreading.

Hypoxic CTCs have a greater chance of survival in the bloodstream because of their PD-L1 expression [308]. Nevertheless, the influence of hypoxia on CTC metastatic activity is complicated. Donato et al. reported that in a breast cancer model under hypoxic conditions, liberated CTC clusters contained cells with a hypoxic phenotype [48]. In contrast, in normoxia, liberated tumour cells have a normoxic phenotype. However, knockout of HIF-1 $\alpha$  did not repress cluster formation. Moreover, knockout of VEGF (an angiogenic factor induced by HIF-1 $\alpha$ ) led to tumour shrinkage but also supported cluster formation.

It has been proven that curcuminoids could represent suitable structural motifs for targeting HIF-1 $\alpha$  hypoxia-related signalling. For example, Li et al. reported that curcumin significantly decreased the expression of HIF-1 $\alpha$  and VEGF in a mouse model of lung cancer (A549 cells) [301]. Ye et al. reported curcumin-induced repression of HIF-1 $\alpha$ , which led to downregulation of P-glycoprotein expression and increased chemosensitivity of A549 cells [309]. Similarly, Fan et al. observed decreased levels of HIF1 $\alpha$ , p-mTOR/mTOR, VEGF, and VEGFR in a mouse model of Lewis lung carcinoma [310].

An important anticancer effect of curcumin could be its repression of Smad 2/3 phosphorylation. Datta et al. reported that curcumin represses Smad 2/3 phosphorylation in TGF- $\beta$ 1-dependent H358 and A549 (NSCLC) cell lines [311]. However, no difference in curcumin-induced toxicity or changes in tumourigenicity were reported between the TGF- $\beta$ 1-dependent cells and ACC-LC-176 cells (an NSCLC line independent of TGF- $\beta$ 1). Nevertheless, some results obtained from studies of other cancer types imply that curcumin can inhibit TGF- $\beta$ 1-induced EMT, invasion, and IL-6 expression, and thereby cancer metastasis [242,312–316].

Targeting the Wnt/ $\beta$ -catenin pathway is an intensively studied method in cancer treatment. Wang found that the suppressive effect of curcumin on  $\beta$ -catenin expression was mostly caused by the induction of oxidative stress in NSCLC cells (A549) [237]. Lu et al. reported that administration of curcumin to NSCLC cells (95D and A549) reduced the overexpression of metastasis-associated protein 1, which caused a decrease in Wnt/ $\beta$ -catenin signalling (downregulation of  $\beta$ -catenin, cyclin D1, and MMP-7) [317]. Wen et al. reported that targeting Wnt/ $\beta$ -catenin signalling could lead to a reduction in CTC counts in oncology patients [318].

Flavonoids represent potent agents for the suppression of cancer spreading. They can decrease the activity and expression of numerous factors associated with NSCLC metastatic activity, such as NF- $\kappa$ B, STAT3, Akt,  $\beta$ -catenin, VEGF, HIF-1 $\alpha$ , EGFR, and mTOR. For example, QSAR modelling strongly implies that EGCG is a potent EGFR binder [319].

Minnelli et al. reported that the interaction energies were 98, 54, and 75 kcal/mol for wild-type EGFR, T790M/L858R-mutated EGFR, and ELREA (EGFR with deletion of five amino acids in exon 19), respectively [320]. For comparison, the obtained values for erlotinib were 71 (wild-type EGFR), 39 (T790M/L858R-mutated EGFR), and 97 kcal/mol (ELREA). Liu et al. found that EGCG is a dual inhibitor of PI3K $\alpha$  (IC<sub>50</sub> = 0.69  $\mu$ M) and mTOR (IC<sub>50</sub> = 0.12  $\mu$ M), an inhibitor of EMT, and can overcome gefitinib resistance [321]. Zhang et al. found that EGCG not only reduces the active form of NF- $\kappa$ B but also directly impacts this factor (K<sub>D</sub> = 4.8  $\times$  10<sup>-5</sup> M) [322]. Rawangkan et al. reported that EGCG pretreatment of Lu99 cells (an NSCLC cell line) strongly decreased PD-L1 expression and induction by EGF and IFN- $\gamma$  [323].

Both EGFR mutations and PD-L1 overexpression enhance CTC and metastatic cell spreading in NSCLC. CTCs with EGFR mutations and PD-L1-expressing CTCs have been shown to correlate with shortened OS, disease progression, formation of metastases, and therapeutic failure (Sections 3.1 and 3.2). As such, agents with low toxicity, such as flavonoids, could represent promising tools for decreasing CTC counts and thereby suppress metastasis.

The application of flavonoids can, via various independent mechanisms, repress NSCLC cell survival, proliferation (e.g., modulation of cyclin-dependent kinases, caspase induction, activation of apoptotic factors, and repression of survival) and migration; for example, flavonoids can inhibit MMPs. Suzuki et al. described EGCG binding with the  $\beta$ - and  $\gamma$ -chains of fibrinogen, which represses fibrinogen interaction with NSCLC cancer cells (e.g., LL2-Lu3 cells) and thereby impairs their metastatic spread [324]. More details regarding the effects of flavonoids on NSCLC and lung cancer models are described in Table 4.

**Table 4.** Examples of flavonoid effects on NSCLC models.

Flavonoid	Model	Effects	Ref.
Atalantraflavone	A549 and 95D cells	↓Vimentin, ↓N-cadherin ↑E-cadherin, ↓Twist1, ↓cell migration, ↓colony formation and ↑cisplatin sensitivity	[325]
Quercetin	A549 cells	↓Vimentin, ↓N-cadherin and ↓microtubular network	[277]
Quercetin-3 orutinoside	BALB/c nude mic -bearing A549 tumours	↓Akt, ↓mTOR and ↓VEGF	[326]
Hyperoside	A549 cells	↑ERK/1/2, ↓LC3-I and ↑LC3-II ↓Akt, ↓mTOR, ↓p70S6K and ↓4E-BP1	[327]
Hyperoside	A549 cells	↑AMPK, ↑HO-1, ↓survival and ↓proliferation of cells with a hypoxia phenotype	[328]
Quercetin	A549 and H460 cells	↓Akt, ↑DR 5, ↓survivin and ↑TRAIL sensitization	[329]
Quercetin	A549 cells	↓NF- $\kappa$ B and ↓STAT3	[330]
Quercetin	HCC827 cells	↓IL-6-induced activation of NF- $\kappa$ B and STAT3, ↓colony formation, ↓migration and ↓invasion	
Quercetin	Mice implanted with HCC827 cells	↑E-cadherin, ↓N-cadherin and ↓tumour growth	[331]
Quercetin	1299 and H460 cells	↓NF- $\kappa$ B, IKK $\alpha$ , ↑I $\kappa$ B $\alpha$ , ↑FAS, ↑TRAILR, ↑MEKK1, ↑MEK4, ↑JNK, ↑GAD45 and ↑p21 <sup>CYP</sup>	[332]
Quercetin	A549 and HCC827 cells	↑E-cadherin, ↓N-cadherin, ↓vimentin (↓Snail, ↓Slug, and ↓Twist), ↓MMP-1, ↓MMP-2, ↓MMP-7, ↓MMP-9 and ↓MMP-12	[224]
Rhamnetin	NCI-H1299 and NCI-H460 cells	↑miR-34a ↓Notch1, ↓NF- $\kappa$ B, ↓vimentin, ↓N-cadherin, ↓survivin, ↓cIAP1, ↓cellular migration and ↑radiosensitivity	[333]

Table 4. Cont.

Flavonoid	Model	Effects	Ref.
Isorhamnetin	A549 cells	↓LC3-I and ↑LC3-II protein	[334]
Fisetin	A549 cells	↓COX-2, ↓MMP-2/9, ↑CDKN1A/B, ↑CDKN2D, ↑E-cadherin, ↓c-myc, ↓cyclin-D1 and ↓CXCR-4	[335]
Fisetin	A549 and H1299 cells	↑E-cadherin, ↓vimentin, ↓N-cadherin, (H1299), ↓ZO-1 (H1299) ↓MMP-2, stemness markers (↓CD44 and ↓CD133), ↓β-catenin, ↓NF-κB, ↓EGFR, ↓STAT3 and ↑erlotinib (a TKI) sensitivity	[236]
Fisetin	A549 cells	↓Akt, ↓mTOR, ↓p70S6K1, eIF-4E, 4E-BP1, ↓mTOR signalling molecules (↓Rictor, ↓Raptor, ↓GβL and ↓PRAS40), ↑AMPKα, ↑pTSC2, ↓p85 and ↓p110	[336]
Fisetin	HCC827 and HCC827-ER cells	↓Akt, ↓pMAPK, ↑caspase 3/8, ↑cytochrome C, ↓AXL, ↓Snail, ↑E-cadherin and ↑erlotinib sensitivity	[337]
Fisetin	A549 cells	↓NF-κB, ↓c-Fos, ↓c-Jun, ↓ERK1/2, ↓MMP-2/9, ↓u-PA, ↓adhesion, ↓invasion and ↓migration,	[338]
EGCG	A549 and H1299 sphere cells	↓β-catenin, ↓CLOCK (↓CD133, ↓CD44, Sox2, ↓Nanog, and ↓Oct4 protein) and ↓sphere formation	[81]
	Mice implanted with A549 sphere cells	↓CLOCK (↓CD133, ↓CD44, Sox2, ↓Nanog, and ↓Oct4 protein) and ↓Ki-67	
EGCG	A549 and H1299 cells	↓NF-κB (↓BCL2, ↓BCL-XL, ↓COX-2, ↓TNF-α, ↓cyclinD1, ↓C-↓MYC, ↓TWIST1, and ↓MMP-2)	[322]
	Balb/c athymic nude mice implanted with resected patient tumour cells	↓NF-κB, ↓tumour volume, ↓Ki-67, ↓EMT	
EGCG	HCC827-Gef cells	↓PI3Kα and ↓mTOR, ↓EMT, ↓colony formation and ↑gefitinib sensitivity	[321]
EGCG	H1299 and A549 cells	↑LKB-1, ↑AMPK (↓mTOR, ↓P70, and ↓4EBP1) and ↓cell migration	[339]
EGCG	AXL-high population of H1299 spheres	↓AXL receptor tyrosine kinase, ↓ALDH1A1 and ↓Slug	[340]
	Mice implanted with an AXL-high clone of spheres	↓p-AXL, ↓ALDH1A1, ↓Slug, and ↓tumour volume	
EGCG	A549 and NCI-H460 cells	↑ROS, ↓ERK1/2, ↑CTR1 and ↑NEAT1	[341]
EGCG	A549 xenografts	↓CD31, ↓αSMA, ↓collagen IV, ↓tumour hypoxia	[342]
EGCG	Lu99 cells	↓EGF and IFN-γ-induced PD-L1 expression, ↓JAK, ↓STAT1 and ↓Akt	[323]
	A/J mice implanted with NNK-induced tumour cells	↓PD-L1, ↑IL-2 expression by tumour-specific CD3+ T lymphocytes and ↓tumour volume	
EGCG	A549 cells	↑Nrf2, ↓Keap1, ↑HO-1, ↑ROS, ↑RNS, ↓Bcl-2, ↑Bax, ↑Bak, ↑Bim ↑Puma, ↓ΔΨ <sub>m</sub> , and ↓EMT	[343]
EGCG	Tumour spheres (from A549, 460, and 1299 cells)	↓NEAT1, ↑CTR1 ↓CD44+ Sox2, ↓Nanog, and ↓Oct4 protein	[344]
EGCG	A549 cells	↓Nicotine-induced effects (↓HIF-1α, ↓VEGF, ↓COX-2, ↓Akt, ↓ERK1/2, ↓vimentin, and ↑E-cadherin)	[345]
EGCG	Mice implanted with A549 cells	↓HIF-1α and ↓VEGF,	
EGCG	A549 cells	↓TGF-β1 induced activation of Smad2 and Smad3, ↑E-cadherin, ↓N-cadherin, ↓vimentin, ↓HAT, ↓EMT and ↓cell migration	[346]

Table 4. Cont.

Flavonoid	Model	Effects	Ref.
EGCG	A549 and NCI-H460 cells	↓HIF-1 $\alpha$ , ↓HPV-16 E6 and E7 oncoproteins, ↓VEGF, ↓IL-8, ↓Akt and ↓CD31	[347]
EGCG	Mice implanted with A549 cells	↓HIF-1 $\alpha$ , ↓VEGF, ↓HPV-16 E6 and ↓E7 oncoproteins and ↓CD31	
EGCG	A549 cells	↓IGF-1 induced expression of HIF-1 $\alpha$ and VEGF	[348]

4E-BP1, translation repressor protein; ALDH1A1, aldehyde dehydrogenase 1; AMPK, AMP-activated protein kinase; Akt, protein kinase B; Bcl-2, B cell lymphoma 2; Bcl-xL, B cell lymphoma-extra large; CTR1, copper transporter 1; Bim, Bcl-2-interacting mediator of cell death; COX-2, cyclooxygenase-2; DR5, death receptor 5; FAS, fatty acid synthase; GADD45, cell cycle inhibition growth arrest and DNA-damage-inducible 45; IAP1, cellular inhibitor of apoptosis protein-1; CDK1/AB, cyclin-dependent kinase inhibitor 1 A/B; CDK2D, cyclin-dependent kinase inhibitor; CLOCK, clock circadian regulator; eIF2 $\alpha$ , eukaryotic translation initiation factor 2 subunit 1; CXCR-4, C-X-C chemokine receptor type 4; EGFR, endothelial growth factor receptor; ERK1/2, extracellular signal-regulated kinase 1/2; HIF-1 $\alpha$ , hypoxia-inducible factor 1 $\alpha$ ; HAT, histone acetyl transferase; HO-1, haeme oxygenase 1; I $\kappa$ B $\alpha$ , inhibitor of kappa B alpha; IKK $\alpha$ , I $\kappa$ B kinase  $\alpha$ ; IFN- $\gamma$ , interferon gamma; IGF-1, insulin-like growth factor-1; JAK, Janus tyrosine kinase; JNK, c-Jun NH2-terminal kinase; LC3-I/II, microtubule-associated protein 1A/1B-light chain 3 I/II; Keap1, Kelch-like ECH-associated protein 1; mTOR, mammalian target of rapamycin; MEKK1, mitogen-activated protein kinase kinase kinase 1; MMP, matrix metalloproteinase; NEAT1, nuclear paraspeckle assembly transcript; 1 NF- $\kappa$ B, nuclear factor kappa-light-chain-enhancer of activated B cells; Notch 1, Notch homologue 1; Nrf2, nuclear factor erythroid 2-related factor 2; P70S6K, ribosomal protein S6 kinase beta-1; PRAS40, proline-rich Akt substrate of 40 kDa; Puma, p53 upregulated modulator of apoptosis; RNS, reactive nitrogen species; ROS, reactive oxygen species; STAT3, signal transducer and activator of transcription 3; TNF- $\alpha$ , tumour necrosis factor alpha; TRAILR, tumour-necrosis-factor-related apoptosis-inducing ligand receptor; TWIST1, Twist-related protein 1; uPA, urokinase plasminogen activator; VEGF, vascular endothelial growth factor;  $\alpha$ SMA,  $\alpha$ -smooth muscle actin;  $\Delta\Psi$ m, mitochondrial membrane potential;  $\uparrow$  = flavonoids activation/induction;  $\downarrow$  = flavonoids repression/inhibition.

Although curcumin and flavonoids display various toxic effects on cancer cells, they are surprisingly less toxic to normal cells. A possible explanation could be their effect on the redox homeostasis of cells [349]. Higher ROS levels are strongly associated with characteristics of carcinogenesis, such as increased mutations and dysregulation of signalling cascades (MAPK, PI3K/Akt, Nrf2, AP-1, NF- $\kappa$ B, STAT3, and p53) [350,351]. Curcumin and flavonoids are potent antioxidants and can protect normal cells against the carcinogenesis and apoptosis induced by ROS. On the other hand, ROS generation is part of numerous therapeutic strategies [351,352], and the application of antioxidants can be counterproductive. Some clinical trials have found that  $\beta$ -carotene and retinol can promote tumour growth and metastasis in cancer patients [353,354]. Godman et al. found that their application is associated with a higher risk of NSCLC in female patients [354].

However, hypermetabolism of cancer cells results in higher production of ROS and antioxidant capacity. Curcumin dysregulates redox balance by disrupting mitochondrial homeostasis via oxidative stress. It causes opening of the mitochondrial permeability transition pore, mitochondrial swelling, loss of mitochondrial membrane potential, and inhibition of ATP synthesis [355,356]. Curcumin can also supports the mitochondrial apoptotic pathway by inducing overexpression of pro-apoptotic Bax protein and reduced expression of Bcl-2 in NSCLC cells [357]. Moreover, the cytotoxic effect of curcumin or its analogues can be detected via the accumulation of curcuminoids in the ER and the upregulation of the ER stress-related unfolded protein response, which leads to inhibition of protein synthesis and cell cycle arrest [357,358]. In addition, curcuminoid application leads to increased intracellular ROS levels and increased SOD and  $\gamma$ -GCS activity [237]. Additionally, flavonoids such as fisetin can induce oxidative stress in cancer cells [336].

Another possible explanation for the high cell selectivity of curcuminoids and flavonoids is their effects on cellular hypoxia. These agents can significantly induce higher toxicity in hypoxic cancer cells [359,360]. However, in the case of normal cells, their application has protective effects and leads to restoration of normal metabolism [360,361]. For example, in ischaemic muscles (which have a decrease in oxygen level due loss of blood flow), curcumin helps tissue restoration [310].

Cancer cells have higher concentrations of and need iron ions [362]. Targeting iron homeostasis with flavonoid chelators such as quercetin has been intensively studied in anticancer treatment and is usually highly specific for cancer cells [363]. The anticancer effects of curcuminoids are also associated with iron chelation [364,365]. Nevertheless,

higher levels of transition metal ions can lead to higher levels of flavonoids and curcumin metal complexes. These complexes also likely have their own biological/anticancer activities [366]. For example, Tan et al. found that the anticancer effect of iron–flavonoid complexes is associated with DNA targeting [367]. Chen et al. reported that hyperoside activity against hypoxic A549 cells was significantly higher in the presence of iron ions [328]. Similarly, iron–curcumin complexes ( $IC_{50} = 8 \mu M$ ) displayed higher cytotoxicity against MDA-MB-231 breast cancer cells than curcumin ( $IC_{50} = 24 \mu M$ ) [368].

In addition, antimetastatic effects can be achieved by using a noncytotoxic dose [236,369]. Tabasum et al. observed that fisetin (10  $\mu M$ ) decreased the expression of NF- $\kappa B$ , STAT3, and  $\beta$ -catenin, and repressed EMT in A549 and H1299 cells [236].

The above findings imply that curcumin and flavonoids are prospective agents for incorporation in NSCLC therapy with effective targeting against cancer cell migration. However, oncogenic signalling pathways display strong redundancy; therefore, inhibiting one signalling pathway may not be enough. Incorporating multiple targeted agents, such as curcuminoids, flavonoids, or their combination, in therapeutic regimens could effectively avoid this phenomenon. This strategy could control the growth of tumours or shrink their volume with a reduced risk of metastasis. Many high-impact studies have shown that these compounds are potential agents for combination therapy [370–374]. Their application can significantly increase the efficiency of classically used therapies (e.g., chemotherapy, TKIs, immunotherapy, and radiotherapy) and repress tumour resistance. However, the anticancer effects of curcuminoids and flavonoids discussed above were mostly seen in *in vivo* and *in vitro* studies. A meaningful assessment of their potential therapeutic effects is not possible without other clinical trials.

## 5. Future Directions

CTCs are strong markers for disease development and prognosis and can be used in the design of anticancer regimens, especially in combination with proteomic, transcriptomic, and genomic profiling of metastatic CTCs [32,60]. However, the spread of CTCs is not an isolated phenomenon and is influenced by numerous factors, such as tumour-associated cells (e.g., M2 TAMs, MDSCs, Treg cells, CAFs, and TECs) [138,139]. Therefore, determining the CTC level or better analysing circulating tumour-associated cells that can strongly boost CTC metastatic ability or drug resistance could provide more precise information for future therapeutic development and design. Some clinical studies have shown that higher levels of tumour-associated cells are associated with worse therapy prognoses [146,153,157,176,200]. Clusters of CTCs in combination with tumour-associated cells, and not single CTCs, are likely associated with increased risk [8,140]. In accordance with this hypothesis, CTC clusters have been observed in NSCLC patients [95,375]. However, new analytical methods that are significantly easier and cheaper and have higher sensitivity are needed. For example, Watanabe developed the On-chip Sort method (22/30; median 5; range 0–18 cells/5 mL blood), which demonstrated significantly higher CTC-capturing ability for patients with metastatic NSCLC than CellSearch (9/30; median 0; range 0–12 cells/7.5 mL) ( $p < 0.01$ ) [376]. Hosokawa et al. also developed a microcavity assay (MCA) system that could isolate more CTCs and CTC clusters from NSCLC patients than the CellSearch system (Veridex LLC, Raritan, NJ, USA) [375].

CTC clusters are very strong metastatic forms of CTCs, implying their importance for clinical diagnosis [8,24,140]. Nevertheless, and despite unquestionable progress in this field, their identification and analysis remain a great challenge. Hasan et al. reported that CTC clusters from a mouse model of prostate cancer have cells with an epithelial surface phenotype and mesenchymal core phenotype [377]. In addition, CTCs can also form heterotopic clusters with tumour-associated cells, such as CAFs, which induce higher survival in the bloodstream [135]. On the other hand, although the determination of CTC count or CTC phenotype is complicated, an FDA-approved system for the determination of CTC count is already being used. Therefore, at present, determination of CTC count and CTC analysis have high utility in clinical diagnosis.

EpCAM is robust, reliable, reproducible standardised kit, which enables semiautomated processing and stain with one further antibody [378,379]. At present, it is FDA-approved for diagnostics in breast, prostate, and colorectal cancer. On the other hand, some limitation regarding its application in routine diagnostics can be noted. EPCAM is very expensive, has a low capture of CTC without epithelial markers (e.g., undergone EMT), and numbers of CTCs detected in the blood sample of NSCLC patients are sometimes lower than other kits (e.g., ISET) and cannot be used for the detection of CTC clusters [379]. ISET is less expensive and enables determination of CTC clusters; however, it captures small CTC (under 8  $\mu$ M) poorly, and manual processing limits its robustness, although it has potential for automatization.

Due to their importance in tumour metastasis, CTCs are valuable targets in anticancer therapy. Curcuminoids and flavonoids are promising agents for decreasing CTCs, as well as CTC clusters and support cells, in NSCLC therapy. In addition to their own highly selective cytostatic effects, these agents display strong potential for the repression of metastatic spread by various independent mechanisms [139]. However, their efficacy, especially curcumin, can be strongly limited by low solubility and biostability [380]. Nevertheless, this type of problem can be effectively solved by drug delivery systems [381–383]. In the case of curcuminoids and flavonoids, various nanoparticles or curcumin nanofibres have showed high efficacy in tumour targeting and metastatic suppression [370,384,385]. For example, Su et al., using a mouse model of lung cancer, designed and tested curcumin-modified silica nanoparticles for inhalation therapy [386]. The anticancer efficacy of a strategy inducing IL-6 and metastatic suppression was significantly higher than that of curcumin alone.

Incorporating these novel agents in therapy could lead to new neoadjuvant and adjuvant strategies. Classical neoadjuvant therapeutic regimens aim to shrink tumours using drugs that target cancer cells (mainly cytostatic drugs) and only indirectly affect metastasis-initiating cells [6]. However, the *in vitro*-determined drug sensitivity of CTCs suggests that agents related to CTCs have potential to optimise therapy [387]. Most deaths from cancer, including NSCLC, are not caused by primary tumours but by metastasis. [5] Therefore, a new therapeutic method that focuses on inhibiting metastasis formation via the use of migrastatic drugs (inhibitors of cell migration) instead of reducing the tumour mass has been proposed [49,50]. For example, some androgen receptor inhibitors (e.g., apalutamide, enzalutamide, and darolutamide) can delay metastases in high-risk nonmetastatic castration-resistant prostate cancer [51]. In NSCLC, the application of TKIs or ICIs and antibodies against IL-6R can suppress metastasis formation [52–54]. Nevertheless, NSCLC displays high heterogeneity, and multifunctional agents have a better chance of avoiding the development of resistance. In addition, potential therapeutic strategies and agents are still lacking.

Incorporating low-toxicity agents such as curcuminoids and flavonoids into chemotherapy regimens could effectively combine cytostatic and migrastatic effects to form a new migrastatic and cytostatic (MICY) combination strategy. The basic philosophy of the MICY combination (isolation and destruction) is to reduce the tumour mass and block the spread of CTCs and other circulating tumour-associated cells (Figure 5). MICY could also be applied after surgical eradication of primary tumours to target micrometastases.

Curcuminoids and flavonoids can be recommended for this purpose for several reasons. They have low toxicity and are part of daily dietary uptake [388]. Therefore, they should be able to be used daily and long-term, perhaps for the entire life of the patient. These agents repress the activation (Wnt/ $\beta$ -catenin signalling [236,237]) and survival (hypoxia [239,240]) of dormant cancer cells. They are potent antioxidants [232–235] and EMT inhibitors [223,224] and therefore can also suppress micrometastasis survival and macrometastasis formation [234,236,252]. Their administration can repress the recruitment and activation of tumour-associated cells that strongly support metastasis formation and development [150,154,158,159,173–175,185,189]. They are multifunctional agents; therefore, their risk of resistance is significantly lower. Additionally, combination can significantly

improve their efficacy (e.g., by reducing multidrug resistance) [185,389–395]. These potential benefits have led to the administration of combined rather than single agents, and we expect that this approach will lead to a significantly lower risk of resistance.

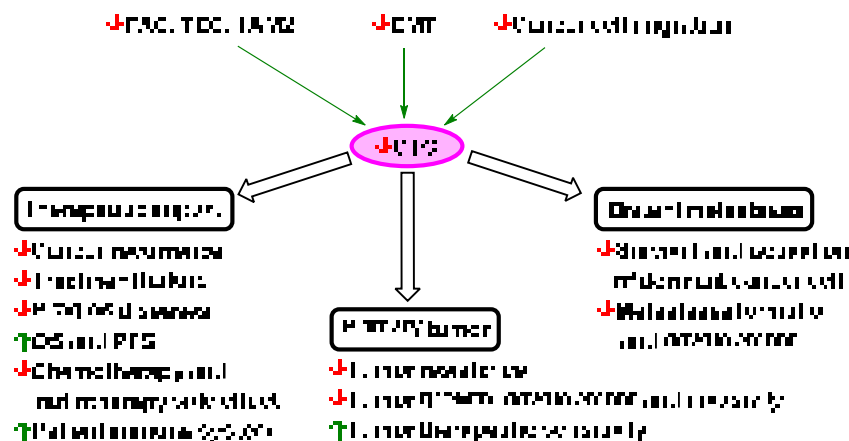


Figure 5. Curcuminoids and flavonoids in migrastatic and cytostatic (MICY) therapy. Green arrow = induction/activation of CTC; ↑ = curcuminoids/flavonoids activation/induction; ↓ = curcuminoids/flavonoids repression/inhibition.

The high potential of these agents in anticancer therapy has also been shown in numerous clinical trials (see Table 5). Their incorporation into therapeutic regimens led to a decrease in oxidative and inflammatory stress, a decrease in the level of metastatic factors, suppression of therapy side effects, and improvement of patient quality of life. In addition, some of the studies imply that such applications can have protective effects for subjects with higher cancer risk. The above clinical trials include various limitations and used various therapeutic regimens; as such, the usability of the acquired knowledge in the treatment of lung cancer may be limited. Therefore, other clinical trials are highly awaited to determine the therapeutic effects of these strategies in NSCLC patients.

Table 5. Curcuminoids and flavonoids in clinical trials.

Agents/Doses	Subjects	Clinical Findings	Ref.
Meriva (Thorne Research Inc., Dover, ID, USA; curcuminoid, 180 mg/day), 8 weeks	Oncological patients (solid tumours)	↑QoL, ↓TNF-α, ↓TGF-β, ↓IL-6, ↓substance P, ↓hs-CRP, ↓CGRP, ↓MCP-1, ↓IL-8 (placebo was more effective), negative correlation between QoL and TGF-β	[119]
Capsule curcuminoid powder (1440 mg/day), six months	Prostate cancer patients treated with intermittent androgen deprivation therapy	↓Progression (10.3% vs. 30.2%), 0PSA, 0testosterone level, 0HRQOL, ↓adverse drug reaction	[396]
Meriva (Thorne Research Inc., Dover, ID, USA; curcuminoid, 100 mg/day), 60 days (between the 4th and 16th weeks from surgery)	Oncological patients treated with chemotherapy or radiotherapy	↓Side effects	[397]
Micronised curcumin powder (2 g or 4 g per day) 30 days	Subjects with a smoking history (3 years or more)	↓Aberrant crypt foci (40% reduction, only 4 g), 0PGE2, 05-HETE, 0Ki-67	[398]
Curcumin (360 mg/day, capsule), 20 days	Colorectal cancer patients	Tumour tissue ↑p53, ↑Bax, ↓Bcl-2, and ↑cell apoptosis; serum ↓TNF-α; and ↑body weight	[399]
Isoflavones (40 mg/day, 66% daidzein, 24% glycitin, and 10% genistin) and curcumin (100 md) 6 months	Prostate cancer patients	↓PSA (patients with serum level higher 10 ng/mL)	[400]

Table 5. Cont.

Agents/Doses	Subjects	Clinical Findings	Ref.
Polyphenol combination (curcumin 150 mg, resveratrol 75 mg, EGCG 150 mg and soy isoflavone 125 mg each day), 2 weeks	Healthy human volunteers	↓TNF- $\alpha$ activation NF-kB in lymphocytes	[401]
Cur plus capsules (Indsaff LTD, Punjab, India; curcumin 475 mg, piperidin 25 mg)	Subjects with chronic arsenic exposure	↓ROS, ↓DNA damage, ↓lipid peroxidation, ↓protein carbonyl content and ↑antioxidant capacity (↑CAT, ↑SOD and ↓GSH)	[402]
Oxy-Q tablets (Farr Laboratories, Santa Clarita, CA, USA; curcumin 480 mg and quercetin 20 each day), 6 months	FAP patients	↓Polyp number (~half) and size (~third)	[403]
Curcumin tablet (500–8000 mg, gradually increased each day), 6 months	Patients with a high risk of premalignant lesions	Histological improvement in high-risk premalignant lesions	[404]
Curcumin (6 g/d for 7 days every 3 weeks), 6 months	mCRPC patients treated with docetaxel therapy	No positive results	[405]
CurcuRouge™ (Robertet, Grasse, France; 2 × 90 curcumin mg/d), 4 weeks	Elderly subjects (age > 60 years) with higher NLR	↓Neutrophil count and ratios, ↑lymphocyte ratios, ↓neutrophil/lymphocyte ratio, ↓eosinophil count and ratios	[406]
Nanoparticle curcumin powder (3 × curcumin 1 g/10 mL olive oil per day), 7 days, mouthwash without drinking	Radiotherapy patients with squamous cell carcinoma of the head and neck	↓Radiation-induced oral mucositis	[407]
Meriva (Thorne Research Inc., Dover, ID, USA; curcuminoid, 50 mg/day), 8 weeks	NAFLD patients	↓Mismatched base pairs in DNA and ↓methylation in the MLH1 and MSH2 promoters	[408]
Green tea extract (800 mg/day, topical and systematic) and curcumin (950 mg/day, topical and systematic), 3 months	OPMD patients	Tumour tissue: ↓p53 (mutant type), ↓Ki67, and ↓cyclin D1 (synergic effect)	[409]
APG-157 (Aveta Biomics, Bedford, MA, USA), capsule (3 × 100 or 3 × 200 mg, unfractionated turmeric extract)	Patients with oral cancer	Saliva: ↓IL-1 $\beta$ , ↓IL-6, and ↓IL-8; tumour tissue: ↑CD4+ T cells and ↑CD8+ T cells	[410]
Capsule (500 mg curcuminoid and 5 mg piperine), 8 weeks	NAFLD patients	↓TNF- $\alpha$ , ↓MCP-1, ↓EGF, the cytokine level did not change and ↑NAFLD severity	[411]
SinaCurcumin®80 (Nanotechnology ResearchCenter, Mashhad University of Medical Sciences, Mashhad Iran; 80 mg nanoformulation of curcumin/day), 42 days	HNC patients treated with radiotherapy	↓Oral mucositis (one-third) without obvious oral and systemic side effects	[412]
Meriva® (Thorne Research Inc., Dover, ID, USA; curcuminoid, 4 × 100 mg), 28 days	Pancreatic cancer patients treated with gemcitabine therapy	↑OS (10.2 vs. 6.7 month), 0toxicity	[413]
BCM95 (3 × 1.2 g/day, curcumin), 6 months	Patients with oral leukoplakia	↑Clinical and histologic response	[414]
3 × 15 mL EGCG solution (440 $\mu$ M/L physiological solution), 6 weeks after radiotherapy	Chemotherapy and radiotherapy patients with oesophageal cancers	↓ARIE and ↓RTOG score	[415]
3 × 15 mL EGCG solution (440 $\mu$ M/L physiological solution), 5 weeks after radiotherapy	Chemotherapy and radiotherapy patients with stage III lung cancer	↑Response rate, ↓pain score	[219]



Table 5. Cont.

Agents/Doses	Subjects	Clinical Findings	Ref.
2 × 10 mL EGCG (µM/L physiological solution), 5 weeks	Chemoradiotherapy patients with stage III NSCLC or limited-stage small-cell lung cancer	↓Maximum oesophagitis grade, ↓pain score and ↓dysphagia score	[131]
Green tea extract (800 mg EGCG/day), 6 weeks	Subjects with a high risk of colorectal cancer	↓NF-κB and ↓DNMT1	[416]
Polyphenon E™ (Mitsui Norin Co., Ltd., Shizuoka, Japan; 400 mg EGCG/day), 12 months	Subjects with a high risk of prostate cancer	↓HGPIN, ↓ASAP and ↓PSA	[417]
Polyphenon E ((Polyphenon E International, Inc., NY, USA; 2 × 2000 mg EGCG/day) administered twice daily, 6 months	CLL patients (early-stage)	↓Absolute lymphocyte count and ↓lymphadenopathy	[418]
Six capsules of green tea extract (189 mg EGCG and 97.5 mg caffeine), 6 months	CLL patients	↓Lymphocytosis, ↓absolute number of circulating Treg cells, ↓IL-10 and ↓TGF-β	[419]
2.5% w/w EGCG in a silicone in water emulsion, 6 weeks	Healthy volunteers with significant erythema and telangiectasia on the face	↓VEGF and ↓HIF-1α	[420]
Polyphenon E™ (Mitsui Norin Co., Ltd., Shizuoka, Japan; 800 mg EGCG/day), 6 weeks	Prostate cancer patients (stage I-III)	↓HGF, ↓VEGF, ↓PSA, ↓IGF-I, ↓IGFBP-3 and ↓IGF-I/IGFBP-3	[421]
Isoquercetin (500 mg (A), or 1000 mg (B) per day), 56 days	Cancer patients (with pancreatic cancer, NSCLC or colorectal malignancies) at high risk for thrombosis	↓Extracellular protein disulfide isomerase activity (median decrease in D-dimer +9.9 (A), −22% (B)), ↓P selectin (−0.3 (A), −58% (B)) and ↓platelet-dependent thrombin generation	[422]
Quercetin (2000 mg/day), 1 day	Symptomatic sarcoidosis patients	↑TEAC ↓MDA, ↓TNF-α and ↓IL-8	[423]
Novusetin™ (Bioriginal, Anaheim, CA, USA; fisetin, 100 mg/day), 7 weeks	CRC patients (stage II-III) treated with chemotherapy	↓IL-8 and ↓Hs-CRP	[424]

ARIE, acute radiation-induced oesophagitis; ASAP, atypical small acinar proliferation; Bax, Bcl-2-associated X protein; Bcl-2, B cell lymphoma protein 2; CAT, catalase; CGRP, calcitonin gene-related peptide; CLL, chronic lymphocytic leukaemia; DNMT1, DNA (cytosine-5)-methyltransferase 1; EGF, endothelial growing factor; FAP, familial adenomatous polyposis; GSH, non-enzymatic antioxidant-like glutathione; HGF, hepatocyte growth factor; HIF-1α, hypoxia-inducible factor 1α; HGPIN, high-grade prostatic intraepithelial neoplasia; HRQOL, health-related quality of life; IGF-1, insulin-like growth factor-1; IGFBP-3, insulin-like growth factor binding protein 3; IL-1β, interleukin 1 beta; IL-6, interleukin 6; IL-8, interleukin 8; IL-10, interleukin 10; TGF-β, transforming growth factor-β; hs-CRP, high-sensitivity C-reactive protein; MDA, malondialdehyde; MCP-1, monocyte chemotactic protein-1; MLH1, MutL homologue 1; MSH2, mismatch repair MutS homologue 2; NAFLD, non-alcoholic fatty liver disease; NF-κB, nuclear factor kappa-light-chain-enhancer of activated B cells; NLR neutrophil/lymphocyte ratio; OPMD, oral potentially malignant disorders; PGE2, prostaglandin E2; PSA, prostate-specific antigen; ROS, reactive oxygen species; RTOG, Radiation Therapy Oncology Group; SOD, superoxide dismutase; TEAC, total plasma antioxidant capacity; TNF-α, tumour necrosis factor alpha; VEGF, vascular endothelial growth factor; QoL, quality of life; 5-HETE, 5-hydroxyeicosatetraenoic acid; ↑ = curcuminoids/flavonoids activation/induction; ↓ = curcuminoids/flavonoids repression/inhibition; 0 without change.

The question is whether the reduction of CTCs, as well as CTC clusters, and thereby cancer metastasis in NSCLC, has utility. Some factors (e.g., TGF-β, EGF, IL-6, IL-8, and IL-1β) that are decreased by curcuminoid or flavonoid application have been found to play a significant role in CTC formation and metastatic activity (Section 4.3).

Some studies imply that these agents have promising potential to reduce CTCs. Ried et al. reported that the application of a nutrient combination (curcumin, garlic, green tea, grape seed extract, modified citrus pectin, and medicinal mushroom) decreased the CTC count in patients with oncological diseases [203]. Similarly, Pang et al. found in a mouse breast cancer model that the application of hesperidin (30 mg/day) decreased the metastasis number and CTC count by approximately half [204].

In addition, the decrease in d-dimer (a product of fibrin degradation and the end product of coagulation activation) and thrombin (conversion of fibrinogen to fibrin) generation induced by isoquercetin [422] also suggest an effect against CTCs. Kirwan et al. reported that in metastatic breast cancer, hypercoagulability markers (d-dimer) are associated with higher lethality (44% versus 19%; 1 year after the start of the study) for patients with CTCs ( $> 1$ ) [425]. In breast cancer and glioblastoma cell lines, thrombin induces higher proliferation, expression of angiogenetic proteins (Twist and Gro- $\alpha$ ), and migration [426]. Levitan et al. found that thromboembolic diseases are strongly associated with malignancy (in 90% of patients with metastasis) [427].

Another consideration is the effects of curcuminoids and flavonoids on the immune system. Basak et al. reported that the application of turmeric extracts (curcuminoids) led to an increase in CD4+ T and CD8+ T cells in the tumour tissue of patients with oral cancer [410]. Similarly, curcumin was found to induce the conversion of Treg cells into Th1 cells and increase IFN- $\gamma$  in patients with lung or colon cancer [154,216]. In breast cancer patients, higher Treg cell levels were associated with higher CTC abundance, and higher CD8+ T cell and IFN- $\gamma$  levels negatively correlated with CTC count [199,201].

The above results suggest that curcuminoids and flavonoids are potential agents for targeting CTC spread and metastasis formation. Nevertheless, MICY therapy design is still in the preliminary stages, and numerous animal and clinical studies are needed for its evaluation.

## 6. Conclusions

CTCs are a potential biomarker for NSCLC diagnosis and play key roles in tumour spread. Numerous clinical studies have shown a negative correlation between the level of CTCs in blood and therapeutic prognosis indicators (mainly OS and PFS). This review shows the potential utility of CTC parameters for obtaining information, such as protein expression and gene mutations (PD-L1 and EGFR, respectively), about primary tumours and metastases and the applicability of such information for the management and design of therapy. The effects of these promising, low-toxicity natural agents (curcuminoids, mainly curcumin and flavonoids) with mechanisms affecting the genesis and spread of cancers were presented and discussed. The cited high-impact studies imply high potential and applicability of CTC targeting in NSCLC treatment.

**Author Contributions:** Z.K. wrote Section 4.1 and unified the contributions of individual authors. R.K. designed and made Figures 1–5 and Tables 1–5. He also participated in the writing of Section 5 and supervised the writing of the manuscript. P.D. wrote Section 1 of the manuscript and the introductory part of Section 4. K.V. wrote Section 2 (regarding CTC count as a biomarker of cytostatic effects) and Section 3.2 (regarding EGFR genotyping). N.A. wrote the introductory part of Section 3 and participated in editing the manuscript. M.V. offered an overview of current therapeutic modalities for NSCLC and discussed the state of CTCs targeting and the effects of curcumin and flavonoids. D.H. wrote Section 3.1 (regarding PD-L1-expressing CTCs) and supervised the writing of the manuscript. M.M. wrote Section 4.3 (regarding the effect of curcumin and flavonoids on migrating cancer cells) and described and discussed the model of metastasis formation and its suppression by curcumin and flavonoids. J.K. described and discussed the selectivity of curcumin and flavonoids for cancer cells and supervised the writing of the manuscript. P.M. chose the topic, designed the outline of the manuscript, and supervised the writing of the manuscript. M.J. wrote the Abstract, Sections 5 and 6, and supervised the writing of the manuscript. All authors have read and agreed to the published version of the manuscript.

**Funding:** This work was supported by the Charles University in Prague (SVV260521; UNCE 204064; Progress Q26/LF1 and Q27/LF1). This work was also supported by Ministry of Education, Youth and Sports grant no. LM2018133 (EATRIS-CZ). The authors acknowledge support from the Ministry of Health of the Czech Republic (grant, no. RVO-VFN-64165/2012). The research was funded by the Technology Agency of the Czech Republic within projects TN01000013 and FW02020128 and the Ministry of Health of the Czech Republic (grant no. NU21-08-00407). The authors also thank Operational Programme Research, Development and Education, within the project Center for Tumor

Ecology—Research of the Cancer Microenvironment Supporting Cancer Growth and Spread (reg. no. CZ.02.1.01/0.0/0.0/16\_019/0000785).

**Conflicts of Interest:** All authors declare no conflict of interest. The funders had no role in the review topic choice, writing of the manuscript, or decision to publish the results.

## References

1. Torre, L.A.; Siegel, R.L.; Jemal, A. Lung Cancer Statistics. *Adv. Exp. Med. Biol.* **2016**, *893*, 1–19. [CrossRef] [PubMed]
2. Alberg, A.J.; Brock, M.V.; Ford, J.G.; Samet, J.M.; Spivack, S.D. Epidemiology of lung cancer: Diagnosis and management of lung cancer, 3rd ed: American College of Chest Physicians evidence-based clinical practice guidelines. *Chest* **2013**, *143*, e1S–e29S. [CrossRef] [PubMed]
3. Zappa, C.; Mousa, S.A. Non-small cell lung cancer: Current treatment and future advances. *Transl. Lung Cancer Res.* **2016**, *5*, 288–300. [CrossRef] [PubMed]
4. Postmus, P.E.; Kerr, K.M.; Oudkerk, M.; Senan, S.; Waller, D.A.; Vansteenkiste, J.; Escriu, C.; Peters, S. Early and locally advanced non-small-cell lung cancer (NSCLC): ESMO Clinical Practice Guidelines for diagnosis, treatment and follow-up. *Ann. Oncol.* **2017**, *28*, iv1–iv21. [CrossRef]
5. Scheff, R.J.; Schneider, B.J. Non-small-cell lung cancer: Treatment of late stage disease: Chemotherapeutics and new frontiers. *Semin. Interv. Radiol.* **2013**, *30*, 191–198. [CrossRef]
6. Menyailo, M.E.; Bokova, U.A.; Ivanyuk, E.E.; Khozyainova, A.A.; Denisov, E.V. Metastasis Prevention: Focus on Metastatic Circulating Tumor Cells. *Mol. Diagn. Ther.* **2021**, *25*, 549–562. [CrossRef]
7. Ashworth, T.R. A Case of Cancer in Which Cells Similar to Those in the Tumours Were Seen in the Blood after Death. *Med. J. Aust.* **1869**, *14*, 2.
8. Fabisiwicz, A.; Grzybowska, E. CTC clusters in cancer progression and metastasis. *Med. Oncol.* **2017**, *34*, 12. [CrossRef]
9. Siemel, W.; Seen-Hibler, R.; Mutschler, W.; Pantel, K.; Passlick, B. Tumour cells in the tumour draining vein of patients with non-small cell lung cancer: Detection rate and clinical significance. *Eur. J. Cardiothorac. Surg.* **2003**, *23*, 451–456. [CrossRef]
10. Yoon, S.O.; Kim, Y.T.; Jung, K.C.; Jeon, Y.K.; Kim, B.H.; Kim, C.W. TTF-1 mRNA-positive circulating tumor cells in the peripheral blood predict poor prognosis in surgically resected non-small cell lung cancer patients. *Lung Cancer* **2011**, *71*, 209–216. [CrossRef]
11. Kirschbaum, A.; Mirow, N. Infiltration of Cardiac Vessels by Lung Cancer: Incidence, Classification, Operative Technique with Heart Lung Bypass, and Results. *Zent. Fur Chir.* **2017**, *142*, 96–103. [CrossRef]
12. Gall, T.M.; Jacob, J.; Frampton, A.E.; Krell, J.; Kyriakides, C.; Castellano, L.; Stebbing, J.; Jiao, L.R. Reduced dissemination of circulating tumor cells with no-touch isolation surgical technique in patients with pancreatic cancer. *JAMA Surg.* **2014**, *149*, 482–485. [CrossRef]
13. Chen, Z.; Zhang, P.; Xu, Y.; Yan, J.; Liu, Z.; Lau, W.B.; Lau, B.; Li, Y.; Zhao, X.; Wei, Y.; et al. Surgical stress and cancer progression: The twisted tango. *Mol. Cancer* **2019**, *18*, 132. [CrossRef]
14. Wei, S.; Guo, C.; He, J.; Tan, Q.; Mei, J.; Yang, Z.; Liu, C.; Pu, Q.; Ma, L.; Yuan, Y.; et al. Effect of Vein-First vs Artery-First Surgical Technique on Circulating Tumor Cells and Survival in Patients With Non-Small Cell Lung Cancer: A Randomized Clinical Trial and Registry-Based Propensity Score Matching Analysis. *JAMA Surg.* **2019**, *154*, e190972. [CrossRef]
15. Nieva, J.; Wendel, M.; Lutgen, M.S.; Marrinucci, D.; Bazhenova, L.; Kolatkar, A.; Santala, R.; Whittenberger, B.; Burke, J.; Torrey, M.; et al. High-definition imaging of circulating tumor cells and associated cellular events in non-small cell lung cancer patients: A longitudinal analysis. *Phys. Biol.* **2012**, *9*, 016004. [CrossRef]
16. Wang, J.; Wang, K.; Xu, J.; Huang, J.; Zhang, T. Prognostic significance of circulating tumor cells in non-small-cell lung cancer patients: A meta-analysis. *PLoS ONE* **2013**, *8*, e78070. [CrossRef]
17. Krebs, M.G.; Sloane, R.; Priest, L.; Lancashire, L.; Hou, J.M.; Greystoke, A.; Ward, T.H.; Ferraldeschi, R.; Hughes, A.; Clack, G.; et al. Evaluation and prognostic significance of circulating tumor cells in patients with non-small-cell lung cancer. *J. Clin. Oncol.* **2011**, *29*, 1556–1563. [CrossRef]
18. Gallo, M.; De Luca, A.; Maiello, M.R.; D'Alessio, A.; Esposito, C.; Chicchinelli, N.; Forgione, L.; Piccirillo, M.C.; Rocco, G.; Morabito, A.; et al. Clinical utility of circulating tumor cells in patients with non-small-cell lung cancer. *Transl. Lung Cancer Res.* **2017**, *6*, 486–498. [CrossRef]
19. Gallo, M.; De Luca, A.; Frezzetti, D.; Passaro, V.; Maiello, M.R.; Normanno, N. The potential of monitoring treatment response in non-small cell lung cancer using circulating tumour cells. *Expert Rev. Mol. Diagn.* **2019**, *19*, 683–694. [CrossRef]
20. Chen, X.; Zhou, F.; Li, X.; Yang, G.; Zhang, L.; Ren, S.; Zhao, C.; Deng, Q.; Li, W.; Gao, G.; et al. Folate Receptor-Positive Circulating Tumor Cell Detected by LT-PCR-Based Method as a Diagnostic Biomarker for Non-Small-Cell Lung Cancer. *J. Thorac. Oncol.* **2015**, *10*, 1163–1171. [CrossRef]
21. Pantel, K.; Denève, E.; Nocca, D.; Coffy, A.; Vendrell, J.P.; Maudelonde, T.; Riethdorf, S.; Alix-Panabières, C. Circulating epithelial cells in patients with benign colon diseases. *Clin. Chem.* **2012**, *58*, 936–940. [CrossRef]
22. Hogan, B.V.; Peter, M.B.; Shenoy, H.; Horgan, K.; Hughes, T.A. Circulating tumour cells in breast cancer: Prognostic indicators, metastatic intermediates, or irrelevant bystanders? (Review). *Mol. Med. Rep.* **2008**, *1*, 775–779. [CrossRef]
23. Ilie, M.; Hofman, V.; Long-Mira, E.; Selva, E.; Vignaud, J.-M.; Padovani, B.; Mouroux, J.; Marquette, C.-H.; Hofman, P. “Sentinel” circulating tumor cells allow early diagnosis of lung cancer in patients with chronic obstructive pulmonary disease. *PLoS ONE* **2014**, *9*, e111597. [CrossRef]

24. Schuster, E.; Taftaf, R.; Reduzzi, C.; Albert, M.K.; Romero-Calvo, I.; Liu, H. Better together: Circulating tumor cell clustering in metastatic cancer. *Trends Cancer* **2021**, *7*, 1020–1032. [CrossRef]
25. Murlidhar, V.; Reddy, R.M.; Fouladdel, S.; Zhao, L.; Ishikawa, M.K.; Grabauskienė, S.; Zhang, Z.; Lin, J.; Chang, A.C.; Carrott, P.; et al. Poor Prognosis Indicated by Venous Circulating Tumor Cell Clusters in Early-Stage Lung Cancers. *Cancer Res.* **2017**, *77*, 5194–5206. [CrossRef]
26. Frick, M.A.; Feigenberg, S.J.; Jean-Baptiste, S.R.; Aguarin, L.A.; Mendes, A.; Chinniah, C.; Swisher-McClure, S.; Berman, A.; Levin, W.; Cengel, K.A.; et al. Circulating Tumor Cells Are Associated with Recurrent Disease in Patients with Early-Stage Non-Small Cell Lung Cancer Treated with Stereotactic Body Radiotherapy. *Clin. Cancer Res.* **2020**, *26*, 2372–2380. [CrossRef]
27. Nemunaitis, J.; Nemunaitis, M.; Senzer, N.; Snitz, P.; Bedell, C.; Kumar, P.; Pappen, B.; Maples, P.B.; Shawler, D.; Fakhrai, H. Phase II trial of Belagenpumatucel-L, a TGF-beta2 antisense gene modified allogeneic tumor vaccine in advanced non small cell lung cancer (NSCLC) patients. *Cancer Gene Ther.* **2009**, *16*, 620–624. [CrossRef]
28. Zhang, Z.; Xiao, Y.; Zhao, J.; Chen, M.; Xu, Y.; Zhong, W.; Xing, J.; Wang, M. Relationship between circulating tumour cell count and prognosis following chemotherapy in patients with advanced non-small-cell lung cancer. *Respirology* **2016**, *21*, 519–525. [CrossRef] [PubMed]
29. Wendel, M.; Bazhenova, L.; Boshuizen, R.; Kolatkar, A.; Honnatti, M.; Cho, E.H.; Marrinucci, D.; Sandhu, A.; Perricone, A.; Thistlethwaite, P.; et al. Fluid biopsy for circulating tumor cell identification in patients with early-and late-stage non-small cell lung cancer: A glimpse into lung cancer biology. *Phys. Biol.* **2012**, *9*, 016005. [CrossRef] [PubMed]
30. Hirose, T.; Murata, Y.; Oki, Y.; Sugiyama, T.; Kusumoto, S.; Ishida, H.; Shirai, T.; Nakashima, M.; Yamaoka, T.; Okuda, K.; et al. Relationship of circulating tumor cells to the effectiveness of cytotoxic chemotherapy in patients with metastatic non-small-cell lung cancer. *Oncol. Res.* **2012**, *20*, 131–137. [CrossRef] [PubMed]
31. Juan, O.; Vidal, J.; Gisbert, R.; Munoz, J.; Macia, S.; Gomez-Codina, J. Prognostic significance of circulating tumor cells in advanced non-small cell lung cancer patients treated with docetaxel and gemcitabine. *Clin. Transl. Oncol.* **2014**, *16*, 637–643. [CrossRef]
32. Cabel, L.; Proudhon, C.; Gortais, H.; Loirat, D.; Coussy, F.; Pierga, J.Y.; Bidard, F.C. Circulating tumor cells: Clinical validity and utility. *Int. J. Clin. Oncol.* **2017**, *22*, 421–430. [CrossRef]
33. Smerage, J.B.; Barlow, W.E.; Hortobagyi, G.N.; Winer, E.P.; Leyland-Jones, B.; Srkalovic, G.; Tejwani, S.; Schott, A.F.; O'Rourke, M.A.; Lew, D.L.; et al. Circulating tumor cells and response to chemotherapy in metastatic breast cancer: SWOG S0500. *J. Clin. Oncol.* **2014**, *32*, 3483–3489. [CrossRef]
34. Shah, P.P.; Dupre, T.V.; Siskind, L.J.; Beverly, L.J. Common cytotoxic chemotherapeutics induce epithelial-mesenchymal transition (EMT) downstream of ER stress. *Oncotarget* **2017**, *8*, 22625–22639. [CrossRef]
35. Yin, J.; Zhao, J.; Hu, W.; Yang, G.; Yu, H.; Wang, R.; Wang, L.; Zhang, G.; Fu, W.; Dai, L.; et al. Disturbance of the let-7/LIN28 double-negative feedback loop is associated with radio- and chemo-resistance in non-small cell lung cancer. *PLoS ONE* **2017**, *12*, e0172787. [CrossRef]
36. Lobb, R.J.; van Amerongen, R.; Wiegmans, A.; Ham, S.; Larsen, J.E.; Möller, A. Exosomes derived from mesenchymal non-small cell lung cancer cells promote chemoresistance. *Int. J. Cancer* **2017**, *141*, 614–620. [CrossRef]
37. Wang, Z.L.; Fan, Z.Q.; Jiang, H.D.; Qu, J.M. Selective Cox-2 inhibitor celecoxib induces epithelial-mesenchymal transition in human lung cancer cells via activating MEK-ERK signaling. *Carcinogenesis* **2013**, *34*, 638–646. [CrossRef]
38. Gadgeel, S.M.; Ruckdeschel, J.C.; Heath, E.I.; Heilbrun, L.K.; Venkatramanamoorthy, R.; Wozniak, A. Phase II study of gefitinib, an epidermal growth factor receptor tyrosine kinase inhibitor (EGFR-TKI), and celecoxib, a cyclooxygenase-2 (COX-2) inhibitor, in patients with platinum refractory non-small cell lung cancer (NSCLC). *J. Thorac. Oncol.* **2007**, *2*, 299–305. [CrossRef]
39. Agarwala, A.; Fisher, W.; Bruetman, D.; McClean, J.; Taber, D.; Titzer, M.; Juliar, B.; Yu, M.; Breen, T.; Einhorn, L.H.; et al. Gefitinib plus celecoxib in chemotherapy-naïve patients with stage IIIB/IV non-small cell lung cancer: A phase II study from the Hoosier Oncology Group. *J. Thorac. Oncol.* **2008**, *3*, 374–379. [CrossRef]
40. Koch, A.; Bergman, B.; Holmberg, E.; Sederholm, C.; Ek, L.; Kosieradzki, J.; Lamberg, K.; Thaning, L.; Ydreborg, S.O.; Sörenson, S. Effect of celecoxib on survival in patients with advanced non-small cell lung cancer: A double blind randomised clinical phase III trial (CYCLUS study) by the Swedish Lung Cancer Study Group. *Eur. J. Cancer* **2011**, *47*, 1546–1555. [CrossRef]
41. Abdel-Rahman, O. Targeting the MEK signaling pathway in non-small cell lung cancer (NSCLC) patients with RAS aberrations. *Therap. Adv. Respir Dis* **2016**, *10*, 265–274. [CrossRef]
42. Guo, Y.J.; Pan, W.W.; Liu, S.B.; Shen, Z.F.; Xu, Y.; Hu, L.L. ERK/MAPK signalling pathway and tumorigenesis. *Exp. Therap. Med.* **2020**, *19*, 1997–2007. [CrossRef]
43. Yu, D.; Zhao, W.; Vallega, K.A.; Sun, S.Y. Managing Acquired Resistance to Third-Generation EGFR Tyrosine Kinase Inhibitors Through Co-Targeting MEK/ERK Signaling. *Lung Cancer* **2021**, *12*, 1–10. [CrossRef]
44. Deng, Z.; Rong, Y.; Teng, Y.; Zhuang, X.; Samykutty, A.; Mu, J.; Zhang, L.; Cao, P.; Yan, J.; Miller, D.; et al. Exosomes miR-126a released from MDSC induced by DOX treatment promotes lung metastasis. *Oncogene* **2017**, *36*, 639–651. [CrossRef]
45. Bhattacharya, U.; Gutter-Kapon, L.; Kan, T.; Boyango, I.; Barash, U.; Yang, S.M.; Liu, J.; Gross-Cohen, M.; Sanderson, R.D.; Shaked, Y.; et al. Heparanase and Chemotherapy Synergize to Drive Macrophage Activation and Enhance Tumor Growth. *Cancer Res.* **2020**, *80*, 57–68. [CrossRef]
46. Atjanasuppat, K.; Lirdprapamongkol, K.; Jantaree, P.; Svasti, J. Non-adherent culture induces paclitaxel resistance in H460 lung cancer cells via ERK-mediated up-regulation of  $\beta$ IVa-tubulin. *Biochem. Biophys. Res. Commun.* **2015**, *466*, 493–498. [CrossRef]

47. Lee, J.G.; Shin, J.H.; Shim, H.S.; Lee, C.Y.; Kim, D.J.; Kim, Y.S.; Chung, K.Y. Autophagy contributes to the chemo-resistance of non-small cell lung cancer in hypoxic conditions. *Respir. Res.* **2015**, *16*, 138. [CrossRef]
48. Donato, C.; Kunz, L.; Castro-Giner, F.; Paasinen-Sohns, A.; Strittmatter, K.; Szczerba, B.M.; Scherrer, R.; Di Maggio, N.; Heusermann, W.; Biehlmaier, O.; et al. Hypoxia Triggers the Intravasation of Clustered Circulating Tumor Cells. *Cell Rep.* **2020**, *32*, 108105. [CrossRef]
49. Gandalovičová, A.; Rosel, D.; Fernandes, M.; Veselý, P.; Heneberg, P.; Čermák, V.; Petruželka, L.; Kumar, S.; Sanz-Moreno, V.; Brábek, J. Migrastatics-Anti-metastatic and Anti-invasion Drugs: Promises and Challenges. *Trends Cancer* **2017**, *3*, 391–406. [CrossRef]
50. Rosel, D.; Fernandes, M.; Sanz-Moreno, V.; Brábek, J. Migrastatics: Redirecting R&D in Solid Cancer towards Metastasis? *Trends Cancer* **2019**, *5*, 755–756. [CrossRef]
51. Chung, D.Y.; Ha, J.S.; Cho, K.S. Novel Treatment Strategy Using Second-Generation Androgen Receptor Inhibitors for Non-Metastatic Castration-Resistant Prostate Cancer. *Biomedicines* **2021**, *9*, 661. [CrossRef] [PubMed]
52. Sheng, J.; Yu, X.; Li, H.; Fan, Y. Progress of Immunotherapy Mechanisms and Current Evidence of PD-1/PD-L1 Checkpoint Inhibitors for Non-small Cell Lung Cancer with Brain Metastasis. *Zhongguo Fei Ai Za Zhi* **2020**, *23*, 976–982. [CrossRef] [PubMed]
53. He, J.; Zhou, Z.; Sun, X.; Yang, Z.; Zheng, P.; Xu, S.; Zhu, W. The new opportunities in medicinal chemistry of fourth-generation EGFR inhibitors to overcome C797S mutation. *Eur. J. Med. Chem.* **2021**, *210*, 112995. [CrossRef] [PubMed]
54. Brábek, J.; Jakubek, M.; Vellieux, F.; Novotný, J.; Kolář, M.; Lacina, L.; Szabo, P.; Strnadová, K.; Rösel, D.; Dvořánková, B.; et al. Interleukin-6: Molecule in the Intersection of Cancer, Ageing and COVID-19. *Int. J. Mol. Sci.* **2020**, *21*, 7937. [CrossRef]
55. Pan, P.; Huang, Y.W.; Oshima, K.; Yearsley, M.; Zhang, J.; Arnold, M.; Yu, J.; Wang, L.S. The immunomodulatory potential of natural compounds in tumor-bearing mice and humans. *Crit. Rev. Food Sci. Nutr.* **2019**, *59*, 992–1007. [CrossRef]
56. Keller, L.; Pantel, K. Unravelling tumour heterogeneity by single-cell profiling of circulating tumour cells. *Nat. Rev. Cancer* **2019**, *19*, 553–567. [CrossRef]
57. Yu, M.; Stott, S.; Toner, M.; Maheswaran, S.; Haber, D.A. Circulating tumor cells: Approaches to isolation and characterization. *J. Cell Biol.* **2011**, *192*, 373–382. [CrossRef]
58. Agnoletto, C.; Corrà, F.; Minotti, L.; Baldassari, F.; Crudele, F.; Cook, W.J.J.; Di Leva, G.; d’Adamo, A.P.; Gasparini, P.; Volinia, S. Heterogeneity in Circulating Tumor Cells: The Relevance of the Stem-Cell Subset. *Cancers* **2019**, *11*, 483. [CrossRef]
59. Brungs, D.; Minaei, E.; Piper, A.-K.; Perry, J.; Splitt, A.; Carolan, M.; Ryan, S.; Wu, X.J.; Corde, S.; Tehei, M.; et al. Establishment of novel long-term cultures from EpCAM positive and negative circulating tumour cells from patients with metastatic gastroesophageal cancer. *Sci. Rep.* **2020**, *10*, 539. [CrossRef]
60. Cortés-Hernández, L.E.; Eslami, S.Z.; Alix-Panabières, C. Circulating tumor cell as the functional aspect of liquid biopsy to understand the metastatic cascade in solid cancer. *Mol. Asp. Med.* **2020**, *72*, 100816. [CrossRef]
61. Heitzer, E.; Auer, M.; Gasch, C.; Pichler, M.; Ulz, P.; Hoffmann, E.M.; Lax, S.; Waldispuehl-Geigl, J.; Mauermann, O.; Lackner, C.; et al. Complex tumor genomes inferred from single circulating tumor cells by array-CGH and next-generation sequencing. *Cancer Res.* **2013**, *73*, 2965–2975. [CrossRef]
62. Sharma, S.; Zhuang, R.; Long, M.; Pavlovic, M.; Kang, Y.; Ilyas, A.; Asghar, W. Circulating tumor cell isolation, culture, and downstream molecular analysis. *Biotechnol. Adv.* **2018**, *36*, 1063–1078. [CrossRef]
63. Brody, R.; Zhang, Y.; Ballas, M.; Siddiqui, M.K.; Gupta, P.; Barker, C.; Midha, A.; Walker, J. PD-L1 expression in advanced NSCLC: Insights into risk stratification and treatment selection from a systematic literature review. *Lung Cancer* **2017**, *112*, 200–215. [CrossRef] [PubMed]
64. Satelli, A.; Batth, I.S.; Brownlee, Z.; Rojas, C.; Meng, Q.H.; Kopetz, S.; Li, S. Potential role of nuclear PD-L1 expression in cell-surface vimentin positive circulating tumor cells as a prognostic marker in cancer patients. *Sci. Rep.* **2016**, *6*, 28910. [CrossRef]
65. Liu, M.; Wang, R.; Sun, X.; Liu, Y.; Wang, Z.; Yan, J.; Kong, X.; Liang, S.; Liu, Q.; Zhao, T.; et al. Prognostic significance of PD-L1 expression on cell-surface vimentin-positive circulating tumor cells in gastric cancer patients. *Mol. Oncol.* **2020**, *14*, 865–881. [CrossRef]
66. He, Y.; Shi, J.; Schmidt, B.; Liu, Q.; Shi, G.; Xu, X.; Liu, C.; Gao, Z.; Guo, T.; Shan, B. Circulating Tumor Cells as a Biomarker to Assist Molecular Diagnosis for Early Stage Non-Small Cell Lung Cancer. *Cancer Manag. Res.* **2020**, *12*, 841–854. [CrossRef]
67. Dong, J.; Zhu, D.; Tang, X.; Lu, D.; Qiu, X.; Li, B.; Lin, D.; Li, L.; Liu, J.; Zhou, Q. Circulating tumor cells in pulmonary vein and peripheral arterial provide a metric for PD-L1 diagnosis and prognosis of patients with non-small cell lung cancer. *PLoS ONE* **2019**, *14*, e0220306. [CrossRef]
68. Janning, M.; Kobus, F.; Babayan, A.; Wikman, H.; Velthaus, J.-L.; Bergmann, S.; Schatz, S.; Falk, M.; Berger, L.-A.; Böttcher, L.-M.; et al. Determination of PD-L1 Expression in Circulating Tumor Cells of NSCLC Patients and Correlation with Response to PD-1/PD-L1 Inhibitors. *Cancers* **2019**, *11*, 835. [CrossRef]
69. Hanssen, A.; Wagner, J.; Gorges, T.M.; Taenzer, A.; Uzunoglu, F.G.; Driemel, C.; Stoecklein, N.H.; Knoefel, W.T.; Angenendt, S.; Hauch, S.; et al. Characterization of different CTC subpopulations in non-small cell lung cancer. *Sci. Rep.* **2016**, *6*, 28010. [CrossRef] [PubMed]
70. Lindsay, C.R.; Faugeroux, V.; Michiels, S.; Pailler, E.; Facchinetti, F.; Ou, D.; Bluthgen, M.V.; Pannet, C.; Ngo-Camus, M.; Bescher, G.; et al. A prospective examination of circulating tumor cell profiles in non-small-cell lung cancer molecular subgroups. *Ann. Oncol. Off. J. Eur. Soc. Med. Oncol.* **2017**, *28*, 1523–1531. [CrossRef]

71. Jiang, R.; Lu, Y.T.; Ho, H.; Li, B.; Chen, J.F.; Lin, M.; Li, F.; Wu, K.; Wu, H.; Lichterman, J.; et al. A comparison of isolated circulating tumor cells and tissue biopsies using whole-genome sequencing in prostate cancer. *Oncotarget* **2015**, *6*, 44781–44793. [CrossRef] [PubMed]
72. Lohr, J.G.; Kim, S.; Gould, J.; Knoechel, B.; Drier, Y.; Cotton, M.J.; Gray, D.; Birrer, N.; Wong, B.; Ha, G.; et al. Genetic interrogation of circulating multiple myeloma cells at single-cell resolution. *Sci. Transl. Med.* **2016**, *8*, 363ra147. [CrossRef] [PubMed]
73. Yanagita, M.; Redig, A.J.; Paweletz, C.P.; Dahlberg, S.E.; O’Connell, A.; Feeney, N.; Taibi, M.; Boucher, D.; Oxnard, G.R.; Johnson, B.E.; et al. A Prospective Evaluation of Circulating Tumor Cells and Cell-Free DNA in EGFR-Mutant Non-Small Cell Lung Cancer Patients Treated with Erlotinib on a Phase II Trial. *Clin. Cancer Res. Off. J. Am. Assoc. Cancer Res.* **2016**, *22*, 6010–6020. [CrossRef] [PubMed]
74. Davis, A.A.; Zhang, Q.; Gerratana, L.; Shah, A.N.; Zhan, Y.; Qiang, W.; Finkelman, B.S.; Flaum, L.; Behdad, A.; Gradishar, W.J.; et al. Association of a novel circulating tumor DNA next-generation sequencing platform with circulating tumor cells (CTCs) and CTC clusters in metastatic breast cancer. *Breast Cancer Res.* **2019**, *21*, 137. [CrossRef]
75. Chimonidou, M.; Kallergi, G.; Georgoulis, V.; Welch, D.R.; Lianidou, E.S. Breast Cancer Metastasis Suppressor-1 Promoter Methylation in Primary Breast Tumors and Corresponding Circulating Tumor Cells. *Mol. Cancer Res.* **2013**, *11*, 1248. [CrossRef]
76. Yang, J.; Shen, Y.; Liu, B.; Tong, Y. Promoter methylation of BRMS1 correlates with smoking history and poor survival in non-small cell lung cancer patients. *Lung Cancer* **2011**, *74*, 305–309. [CrossRef]
77. Schneck, H.; Blassl, C.; Meier-Stiegen, F.; Neves, R.P.; Janni, W.; Fehm, T.; Neubauer, H. Analysing the mutational status of PIK3CA in circulating tumor cells from metastatic breast cancer patients. *Mol. Oncol.* **2013**, *7*, 976–986. [CrossRef]
78. Aceto, N.; Bardia, A.; Miyamoto, D.T.; Donaldson, M.C.; Wittner, B.S.; Spencer, J.A.; Yu, M.; Pely, A.; Engstrom, A.; Zhu, H.; et al. Circulating Tumor Cell Clusters Are Oligoclonal Precursors of Breast Cancer Metastasis. *Cell* **2014**, *158*, 1110–1122. [CrossRef]
79. Sher, Y.P.; Shih, J.Y.; Yang, P.C.; Roffler, S.R.; Chu, Y.W.; Wu, C.W.; Yu, C.L.; Peck, K. Prognosis of non-small cell lung cancer patients by detecting circulating cancer cells in the peripheral blood with multiple marker genes. *Clin. Cancer Res. Off. J. Am. Assoc. Cancer Res.* **2005**, *11*, 173–179.
80. Baccelli, I.; Schneeweiss, A.; Riethdorf, S.; Stenzinger, A.; Schillert, A.; Vogel, V.; Klein, C.; Saini, M.; Bäuerle, T.; Wallwiener, M.; et al. Identification of a population of blood circulating tumor cells from breast cancer patients that initiates metastasis in a xenograft assay. *Nat. Biotechnol.* **2013**, *31*, 539–544. [CrossRef]
81. Jiang, P.; Xu, C.; Zhang, P.; Ren, J.; Mageed, F.; Wu, X.; Chen, L.; Zeb, F.; Feng, Q.; Li, S. Epigallocatechin-3-gallate inhibits self-renewal ability of lung cancer stem-like cells through inhibition of CLOCK. *Int. J. Mol. Med.* **2020**, *46*, 2216–2224. [CrossRef]
82. Kallergi, G.; Vetsika, E.K.; Aggouraki, D.; Lagoudaki, E.; Koutsopoulos, A.; Koinis, F.; Katsarlinos, P.; Trypaki, M.; Messaritakis, I.; Stournaras, C.; et al. Evaluation of PD-L1/PD-1 on circulating tumor cells in patients with advanced non-small cell lung cancer. *Ther. Adv. Med. Oncol.* **2018**, *10*, 1758834017750121. [CrossRef]
83. Lee, S.O.; Yang, X.; Duan, S.; Tsai, Y.; Strojny, L.R.; Keng, P.; Chen, Y. IL-6 promotes growth and epithelial-mesenchymal transition of CD133+ cells of non-small cell lung cancer. *Oncotarget* **2016**, *7*, 6626–6638. [CrossRef]
84. Nicolazzo, C.; Raimondi, C.; Mancini, M.; Caponnetto, S.; Gradilone, A.; Gandini, O.; Mastromartino, M.; Del Bene, G.; Prete, A.; Longo, F.; et al. Monitoring PD-L1 positive circulating tumor cells in non-small cell lung cancer patients treated with the PD-1 inhibitor Nivolumab. *Sci. Rep.* **2016**, *6*, 31726. [CrossRef]
85. Park, J.Y.; Han, S.; Ka, H.I.; Joo, H.J.; Soh, S.J.; Yoo, K.H.; Yang, Y. Silent mating-type information regulation 2 homolog 1 overexpression is an important strategy for the survival of adapted suspension tumor cells. *Cancer Sci* **2019**, *110*, 2773–2782. [CrossRef]
86. Kloten, V.; Lampignano, R.; Krahn, T.; Schlange, T. Circulating Tumor Cell PD-L1 Expression as Biomarker for Therapeutic Efficacy of Immune Checkpoint Inhibition in NSCLC. *Cells* **2019**, *8*, 809. [CrossRef]
87. Tsoukalas, N.; Kiakou, M.; Tsapakidis, K.; Tolia, M.; Aravantinou-Fatorou, E.; Baxevanos, P.; Kyrgias, G.; Theocharis, S. PD-1 and PD-L1 as immunotherapy targets and biomarkers in non-small cell lung cancer. *J. BUON* **2019**, *24*, 883–888.
88. Wang, X.; Sun, Q.; Liu, Q.; Wang, C.; Yao, R.; Wang, Y. CTC immune escape mediated by PD-L1. *Med. Hypotheses* **2016**, *93*, 138–139. [CrossRef]
89. Tamminga, M.; de Wit, S.; Hiltermann, T.J.N.; Timens, W.; Schuurin, E.; Terstappen, L.; Groen, H.J.M. Circulating tumor cells in advanced non-small cell lung cancer patients are associated with worse tumor response to checkpoint inhibitors. *J. Immunother. Cancer* **2019**, *7*, 173. [CrossRef]
90. Ilić, M.; Szafer-Glusman, E.; Hofman, V.; Chamorey, E.; Lalvée, S.; Selva, E.; Leroy, S.; Marquette, C.H.; Kowanetz, M.; Hedge, P.; et al. Detection of PD-L1 in circulating tumor cells and white blood cells from patients with advanced non-small-cell lung cancer. *Ann. Oncol.* **2018**, *29*, 193–199. [CrossRef]
91. Boffa, D.J.; Graf, R.P.; Salazar, M.C.; Hoag, J.; Lu, D.; Krupa, R.; Louw, J.; Dugan, L.; Wang, Y.; Landers, M.; et al. Cellular Expression of PD-L1 in the Peripheral Blood of Lung Cancer Patients is Associated with Worse Survival. *Cancer Epidemiol. Biomark. Prev. Publ. Am. Assoc. Cancer Res. Cosponsored Am. Soc. Prev. Oncol.* **2017**, *26*, 1139–1145. [CrossRef] [PubMed]
92. Dhar, M.; Wong, J.; Che, J.; Matsumoto, M.; Grogan, T.; Elashoff, D.; Garon, E.B.; Goldman, J.W.; Sollier Christen, E.; Di Carlo, D.; et al. Evaluation of PD-L1 expression on vortex-isolated circulating tumor cells in metastatic lung cancer. *Sci. Rep.* **2018**, *8*, 2592. [CrossRef] [PubMed]

93. Guibert, N.; Delaunay, M.; Lusque, A.; Boubekour, N.; Rouquette, I.; Clermont, E.; Mourlanette, J.; Gouin, S.; Dormoy, I.; Favre, G.; et al. PD-L1 expression in circulating tumor cells of advanced non-small cell lung cancer patients treated with nivolumab. *Lung Cancer* **2018**, *120*, 108–112. [CrossRef] [PubMed]
94. Wang, Y.; Kim, T.H.; Fouladdel, S.; Zhang, Z.; Soni, P.; Qin, A.; Zhao, L.; Azizi, E.; Lawrence, T.S.; Ramnath, N.; et al. PD-L1 Expression in Circulating Tumor Cells Increases during Radio(chemo)therapy and Indicates Poor Prognosis in Non-small Cell Lung Cancer. *Sci. Rep.* **2019**, *9*, 566. [CrossRef]
95. Kulasinghe, A.; Kapeleris, J.; Kimberley, R.; Mattarollo, S.R.; Thompson, E.W.; Thiery, J.-P.; Kenny, L.; O'Byrne, K.; Panyadeera, C. The prognostic significance of circulating tumor cells in head and neck and non-small-cell lung cancer. *Cancer Med.* **2018**, *7*, 5910–5919. [CrossRef]
96. Manjunath, Y.; Upparahalli, S.V.; Avella, D.M.; Deroche, C.B.; Kimchi, E.T.; Staveley-O'Carroll, K.F.; Smith, C.J.; Li, G.; Kaifi, J.T. PD-L1 Expression with Epithelial Mesenchymal Transition of Circulating Tumor Cells Is Associated with Poor Survival in Curatively Resected Non-Small Cell Lung Cancer. *Cancers* **2019**, *11*, 806. [CrossRef]
97. Schehr, J.L.; Schultz, Z.D.; Warrick, J.W.; Guckenberger, D.J.; Pezzi, H.M.; Sperger, J.M.; Heninger, E.; Saeed, A.; Leal, T.; Mattox, K.; et al. High Specificity in Circulating Tumor Cell Identification Is Required for Accurate Evaluation of Programmed Death-Ligand 1. *PLoS ONE* **2016**, *11*, e0159397. [CrossRef]
98. Zhang, L.; Zhang, X.; Liu, Y.; Zhang, T.; Wang, Z.; Gu, M.; Li, Y.; Wang, D.D.; Li, W.; Lin, P.P. PD-L1(+) aneuploid circulating tumor endothelial cells (CTECs) exhibit resistance to the checkpoint blockade immunotherapy in advanced NSCLC patients. *Cancer Lett.* **2020**, *469*, 355–366. [CrossRef]
99. da Cunha Santos, G.; Shepherd, F.A.; Tsao, M.S. EGFR mutations and lung cancer. *Annu. Rev. Pathol.* **2011**, *6*, 49–69. [CrossRef]
100. Marchetti, A.; Del Gramastro, M.; Felicioni, L.; Malatesta, S.; Filice, G.; Centi, I.; De Pas, T.; Santoro, A.; Chella, A.; Brandes, A.A.; et al. Assessment of EGFR mutations in circulating tumor cell preparations from NSCLC patients by next generation sequencing: Toward a real-time liquid biopsy for treatment. *PLoS ONE* **2014**, *9*, e103883. [CrossRef]
101. Tan, C.S.; Kumarakulasinghe, N.B.; Huang, Y.Q.; Ang, Y.L.E.; Choo, J.R.; Goh, B.C.; Soo, R.A. Third generation EGFR TKIs: Current data and future directions. *Mol. Cancer* **2018**, *17*, 29. [CrossRef]
102. Wang, S.; Song, Y.; Liu, D. EAI045: The fourth-generation EGFR inhibitor overcoming T790M and C797S resistance. *Cancer Lett.* **2017**, *385*, 51–54. [CrossRef]
103. Sundaresan, T.K.; Sequist, L.V.; Heymach, J.V.; Riely, G.J.; Janne, P.A.; Koch, W.H.; Sullivan, J.P.; Fox, D.B.; Maher, R.; Muzikansky, A.; et al. Detection of T790M, the Acquired Resistance EGFR Mutation, by Tumor Biopsy versus Noninvasive Blood-Based Analyses. *Clin. Cancer Res. Off. J. Am. Assoc. Cancer Res.* **2016**, *22*, 1103–1110. [CrossRef]
104. Yang, B.; Zheng, D.; Zeng, U.; Qin, A.; Gao, J.; Yu, G. Circulating tumor cells predict prognosis following secondline AZD 9291 treatment in EGFR-T790M mutant non-small cell lung cancer patients. *J. BUON* **2018**, *23*, 1077–1081.
105. Punnoose, E.A.; Atwal, S.; Liu, W.; Raja, R.; Fine, B.M.; Hughes, B.G.; Hicks, R.J.; Hampton, G.M.; Amler, L.C.; Pirzkall, A.; et al. Evaluation of circulating tumor cells and circulating tumor DNA in non-small cell lung cancer: Association with clinical endpoints in a phase II clinical trial of pertuzumab and erlotinib. *Clin. Cancer Res. Off. J. Am. Assoc. Cancer Res.* **2012**, *18*, 2391–2401. [CrossRef]
106. Lindsay, C.R.; Garassino, M.C.; Nadal, E.; Öhrling, K.; Scheffler, M.; Mazières, J. On target: Rational approaches to KRAS inhibition for treatment of non-small cell lung carcinoma. *Lung Cancer* **2021**, *160*, 152–165. [CrossRef]
107. Aggarwal, S.; Whipple, S.; Hsu, H.; Tu, H.; Carrigan, G.; Wang, X.; Ngarmchamnanrith, G.; Chia, V. 1339P Clinicopathological characteristics and treatment patterns observed in real-world care in patients with advanced non-small cell lung cancer (NSCLC) and KRAS G12C mutations in the Flatiron Health (FH)-Foundation Medicine (FMI) Clinico-Genomic Database (CGDB). *Ann. Oncol.* **2020**, *31*, S860. [CrossRef]
108. Renaud, S.; Seitlinger, J.; Falcoz, P.-E.; Schaeffer, M.; Voegeli, A.-C.; Legrain, M.; Beau-Faller, M.; Massard, G. Specific KRAS amino acid substitutions and EGFR mutations predict site-specific recurrence and metastasis following non-small-cell lung cancer surgery. *Br. J. Cancer* **2016**, *115*, 346–353. [CrossRef]
109. Ferrer, I.; Zugazagoitia, J.; Herberitz, S.; John, W.; Paz-Ares, L.; Schmid-Bindert, G. KRAS-Mutant non-small cell lung cancer: From biology to therapy. *Lung Cancer* **2018**, *124*, 53–64. [CrossRef]
110. Friedlaender, A.; Drilon, A.; Weiss, G.J.; Banna, G.L.; Addeo, A. KRAS as a druggable target in NSCLC: Rising like a phoenix after decades of development failures. *Cancer Treat. Rev.* **2020**, *85*, 101978. [CrossRef]
111. Breitenbuecher, F.; Hoffarth, S.; Worm, K.; Cortes-Incio, D.; Gauler, T.C.; Kohler, J.; Herold, T.; Schmid, K.W.; Freitag, L.; Kasper, S.; et al. Development of a highly sensitive and specific method for detection of circulating tumor cells harboring somatic mutations in non-small-cell lung cancer patients. *PLoS ONE* **2014**, *9*, e85350. [CrossRef] [PubMed]
112. Cargnin, S.; Canonico, P.L.; Genazzani, A.A.; Terrazzino, S. Quantitative Analysis of Circulating Cell-Free DNA for Correlation with Lung Cancer Survival: A Systematic Review and Meta-Analysis. *J. Thorac. Oncol.* **2017**, *12*, 43–53. [CrossRef] [PubMed]
113. Meddeb, R.; Dache, Z.A.A.; Thezenas, S.; Otandault, A.; Tanos, R.; Pastor, B.; Sanchez, C.; Azzi, J.; Tusch, G.; Azan, S.; et al. Quantifying circulating cell-free DNA in humans. *Sci. Rep.* **2019**, *9*, 5220. [CrossRef] [PubMed]
114. Indini, A.; Rijavec, E.; Grossi, F. Circulating Biomarkers of Response and Toxicity of Immunotherapy in Advanced Non-Small Cell Lung Cancer (NSCLC): A Comprehensive Review. *Cancers* **2021**, *13*, 1794. [CrossRef]
115. Chang, Y.; Tolani, B.; Nie, X.; Zhi, X.; Hu, M.; He, B. Review of the clinical applications and technological advances of circulating tumor DNA in cancer monitoring. *Clin. Risk Manag.* **2017**, *13*, 1363–1374. [CrossRef]

116. Isobe, K.; Yoshizawa, T.; Sekiya, M.; Miyoshi, S.; Nakamura, Y.; Urabe, N.; Isshiki, T.; Sakamoto, S.; Takai, Y.; Tomida, T.; et al. Quantification of BIM mRNA in circulating tumor cells of osimertinib-treated patients with EGFR mutation-positive lung cancer. *Respir. Investig.* **2021**, *59*, 535–544. [CrossRef]
117. Isobe, K.; Kakimoto, A.; Mikami, T.; Kaburaki, K.; Kobayashi, H.; Yoshizawa, T.; Makino, T.; Otsuka, H.; Sano, G.; Sugino, K.; et al. Association of BIM Deletion Polymorphism and BIM- $\gamma$  RNA Expression in NSCLC with EGFR Mutation. *Cancer Genom. Proteom.* **2016**, *13*, 475–482. [CrossRef]
118. Yang, B.; Qin, A.; Zhang, K.; Ren, H.; Liu, S.; Liu, X.; Pan, X.; Yu, G. Circulating Tumor Cells Predict Prognosis Following Tyrosine Kinase Inhibitor Treatment in EGFR-Mutant Non-Small Cell Lung Cancer Patients. *Oncol. Res.* **2017**, *25*, 1601–1606. [CrossRef]
119. Panahi, Y.; Saadat, A.; Beiraghdar, F.; Sahebkar, A. Adjuvant Therapy with Bioavailability-Boosted Curcuminoids Suppresses Systemic Inflammation and Improves Quality of Life in Patients with Solid Tumors: A Randomized Double-Blind Placebo-Controlled Trial. *Phytother. Res.* **2014**, *28*, 1461–1467. [CrossRef]
120. Shafiee, M.; Mohamadzade, E.; ShahidSales, S.; Khakpouri, S.; Maftouh, M.; Parizadeh, S.A.; Hasanian, S.M.; Avan, A. Current Status and Perspectives Regarding the Therapeutic Potential of Targeting EGFR Pathway by Curcumin in Lung Cancer. *Curr. Pharm. Des.* **2017**, *23*, 2002–2008. [CrossRef]
121. Ryskalin, L.; Biagioni, F.; Busceti, C.L.; Lazzeri, G.; Frati, A.; Fornai, F. The Multi-Faceted Effect of Curcumin in Glioblastoma from Rescuing Cell Clearance to Autophagy-Independent Effects. *Molecules* **2020**, *25*, 4839. [CrossRef]
122. Grammatikopoulou, M.G.; Gkiouras, K.; Papageorgiou, S.; Myrogiannis, I.; Mykoniatis, I.; Papamitsou, T.; Bogdanos, D.P.; Goulis, D.G. Dietary Factors and Supplements Influencing Prostate Specific-Antigen (PSA) Concentrations in Men with Prostate Cancer and Increased Cancer Risk: An Evidence Analysis Review Based on Randomized Controlled Trials. *Nutrients* **2020**, *12*, 2985. [CrossRef]
123. Yan, Y.B.; Tian, Q.; Zhang, J.F.; Xiang, Y. Antitumor effects and molecular mechanisms of action of natural products in ovarian cancer. *Oncol. Lett.* **2020**, *20*, 141. [CrossRef]
124. Ávila-Gálvez, M.; Giménez-Bastida, J.A.; Espín, J.C.; González-Sarrías, A. Dietary Phenolics against Breast Cancer. A Critical Evidence-Based Review and Future Perspectives. *Int. J. Mol. Sci.* **2020**, *21*, 5718. [CrossRef]
125. Jakubek, M.; Kejik, Z.; Kapláneek, R.; Hromádka, R.; Šandriková, V.; Sýkora, D.; Antonyová, V.; Urban, M.; Dytrych, P.; Mikula, I.; et al. Strategy for improved therapeutic efficiency of curcumin in the treatment of gastric cancer. *Biomed. Pharmacother.* **2019**, *118*, 109278. [CrossRef]
126. Lai, C.S.; Ho, C.T.; Pan, M.H. The Cancer Chemopreventive and Therapeutic Potential of Tetrahydrocurcumin. *Biomolecules* **2020**, *10*, 831. [CrossRef]
127. Piwowarczyk, L.; Stawny, M.; Mlynarczyk, D.T.; Muszalska-Kolos, I.; Goslinski, T.; Jelińska, A. Role of Curcumin and (–)-Epigallocatechin-3-O-Gallate in Bladder Cancer Treatment: A Review. *Cancers* **2020**, *12*, 1801. [CrossRef]
128. Wan Mohd Tajuddin, W.N.B.; Lajis, N.H.; Abas, F.; Othman, I.; Naidu, R. Mechanistic Understanding of Curcumin's Therapeutic Effects in Lung Cancer. *Nutrients* **2019**, *11*, 2989. [CrossRef]
129. Sun, A.S.; Yeh, H.C.; Wang, L.H.; Huang, Y.P.; Maeda, H.; Pivazyan, A.; Hsu, C.; Lewis, E.R.; Bruckner, H.W.; Fasy, T.M. Pilot study of a specific dietary supplement in tumor-bearing mice and in stage IIIB and IV non-small cell lung cancer patients. *Nutr. Cancer* **2001**, *39*, 85–95. [CrossRef]
130. Zhao, H.; Zhu, W.; Xie, P.; Li, H.; Zhang, X.; Sun, X.; Yu, J.; Xing, L. A phase I study of concurrent chemotherapy and thoracic radiotherapy with oral epigallocatechin-3-gallate protection in patients with locally advanced stage III non-small-cell lung cancer. *Radiother. Oncol. J. Eur. Soc. Ther. Radiol. Oncol.* **2014**, *110*, 132–136. [CrossRef]
131. Zhao, H.; Jia, L.; Chen, G.; Li, X.; Meng, X.; Zhao, X.; Xing, L.; Zhu, W. A prospective, three-arm, randomized trial of EGCG for preventing radiation-induced esophagitis in lung cancer patients receiving radiotherapy. *Radiother. Oncol. J. Eur. Soc. Ther. Radiol. Oncol.* **2019**, *137*, 186–191. [CrossRef]
132. Kuo, W.-T.; Tsai, Y.-C.; Wu, H.-C.; Ho, Y.-J.; Chen, Y.-S.; Yao, C.-H.; Yao, C.-H. Radiosensitization of non-small cell lung cancer by kaempferol. *Oncol. Rep.* **2015**, *34*, 2351–2356. [CrossRef]
133. Farhood, B.; Mortezaee, K.; Goradel, N.H.; Khanlarkhani, N.; Salehi, E.; Nashtaei, M.S.; Najafi, M.; Sahebkar, A. Curcumin as an anti-inflammatory agent: Implications to radiotherapy and chemotherapy. *J. Cell. Physiol.* **2019**, *234*, 5728–5740. [CrossRef]
134. Momtazi-Borojeni, A.A.; Mosafer, J.; Nikfar, B.; Ekhlasi-Hundrieser, M.; Chaichian, S.; Mehdizadehkashi, A.; Vaezi, A. Curcumin in Advancing Treatment for Gynecological Cancers with Developed Drug- and Radiotherapy-Associated Resistance. *Rev. Physiol. Biochem. Pharmacol.* **2019**, *176*, 107–129. [CrossRef]
135. Ortiz-Otero, N.; Clinch, A.B.; Hope, J.; Wang, W.; Reinhart-King, C.A.; King, M.R. Cancer associated fibroblasts confer shear resistance to circulating tumor cells during prostate cancer metastatic progression. *Oncotarget* **2020**, *11*, 1037–1050. [CrossRef]
136. You, J.; Cheng, J.; Yu, B.; Duan, C.; Peng, J. Baicalin, a Chinese Herbal Medicine, Inhibits the Proliferation and Migration of Human Non-Small Cell Lung Carcinoma (NSCLC) Cells, A549 and H1299, by Activating the SIRT1/AMPK Signaling Pathway. *Med. Sci. Monit. Int. Med. J. Exp. Clin. Res.* **2018**, *24*, 2126–2133. [CrossRef]
137. Wang, H.W.; Lin, C.P.; Chiu, J.H.; Chow, K.C.; Kuo, K.T.; Lin, C.S.; Wang, L.S. Reversal of inflammation-associated dihydrodiol dehydrogenases (AKR1C1 and AKR1C2) overexpression and drug resistance in nonsmall cell lung cancer cells by wogonin and chrysin. *Int. J. Cancer* **2007**, *120*, 2019–2027. [CrossRef]
138. Wood, S.L.; Pernemalm, M.; Crosbie, P.A.; Whetton, A.D. The role of the tumor-microenvironment in lung cancer-metastasis and its relationship to potential therapeutic targets. *Cancer Treat. Rev.* **2014**, *40*, 558–566. [CrossRef]



139. Park, C.R.; Lee, J.S.; Son, C.G.; Lee, N.H. A survey of herbal medicines as tumor microenvironment-modulating agents. *Phytother. Res. PTR* **2020**. [CrossRef]
140. Wrenn, E.; Huang, Y.; Cheung, K. Collective metastasis: Coordinating the multicellular voyage. *Clin. Exp. Metastasis* **2021**, *38*, 373–399. [CrossRef]
141. Yao, X.; Huang, J.; Zhong, H.; Shen, N.; Faggioni, R.; Fung, M.; Yao, Y. Targeting interleukin-6 in inflammatory autoimmune diseases and cancers. *Pharmacol. Ther.* **2014**, *141*, 125–139. [CrossRef] [PubMed]
142. Tamura, T.; Kato, Y.; Ohashi, K.; Ninomiya, K.; Makimoto, G.; Gotoda, H.; Kubo, T.; Ichihara, E.; Tanaka, T.; Ichimura, K.; et al. Potential influence of interleukin-6 on the therapeutic effect of gefitinib in patients with advanced non-small cell lung cancer harbouring EGFR mutations. *Biochem. Biophys. Res. Commun.* **2018**, *495*, 360–367. [CrossRef] [PubMed]
143. Kim, S.M.; Kwon, O.J.; Hong, Y.K.; Kim, J.H.; Solca, F.; Ha, S.J.; Soo, R.A.; Christensen, J.G.; Lee, J.H.; Cho, B.C. Activation of IL-6R/JAK1/STAT3 signaling induces de novo resistance to irreversible EGFR inhibitors in non-small cell lung cancer with T790M resistance mutation. *Mol. Cancer Ther.* **2012**, *11*, 2254–2264. [CrossRef] [PubMed]
144. Hamilton, G.; Rath, B. Smoking, inflammation and small cell lung cancer: Recent developments. *Wiener Medizinische Wochenschrift (1946)* **2015**, *165*, 379–386. [CrossRef] [PubMed]
145. Sedighzadeh, S.S.; Khoshbin, A.P.; Razi, S.; Keshavarz-Fathi, M.; Rezaei, N. A narrative review of tumor-associated macrophages in lung cancer: Regulation of macrophage polarization and therapeutic implications. *Transl. Lung Cancer Res.* **2021**, *10*, 1889–1916. [CrossRef]
146. Becker, M.; Müller, C.B.; De Bastiani, M.A.; Klamt, F. The prognostic impact of tumor-associated macrophages and intra-tumoral apoptosis in non-small cell lung cancer. *Histol. Histopathol.* **2014**, *29*, 21–31. [CrossRef]
147. Almatroodi, S.A.; McDonald, C.F.; Darby, I.A.; Pouniotis, D.S. Characterization of M1/M2 Tumour-Associated Macrophages (TAMs) and Th1/Th2 Cytokine Profiles in Patients with NSCLC. *Cancer Microenviron. Off. J. Int. Cancer Microenviron. Soc.* **2016**, *9*, 1–11. [CrossRef]
148. Mukherjee, S.; Baidoo, J.N.E.; Sampat, S.; Mancuso, A.; David, L.; Cohen, L.S.; Zhou, S.; Banerjee, P. Liposomal TriCurin, A Synergistic Combination of Curcumin, Epicatechin Gallate and Resveratrol, Repolarizes Tumor-Associated Microglia/Macrophages, and Eliminates Glioblastoma (GBM) and GBM Stem Cells. *Molecules* **2018**, *23*, 201. [CrossRef]
149. Mukherjee, S.; Fried, A.; Hussaini, R.; White, R.; Baidoo, J.; Yalamanchi, S.; Banerjee, P. Phytosomal curcumin causes natural killer cell-dependent repolarization of glioblastoma (GBM) tumor-associated microglia/macrophages and elimination of GBM and GBM stem cells. *J. Exp. Clin. Cancer Res.* **2018**, *37*, 168. [CrossRef]
150. Mukherjee, S.; Hussaini, R.; White, R.; Atwi, D.; Fried, A.; Sampat, S.; Piao, L.; Pan, Q.; Banerjee, P. TriCurin, a synergistic formulation of curcumin, resveratrol, and epicatechin gallate, repolarizes tumor-associated macrophages and triggers an immune response to cause suppression of HPV+ tumors. *Cancer Immunol. Immunother.* **2018**, *67*, 761–774. [CrossRef]
151. Cuomo, J.; Appendino, G.; Dern, A.S.; Schneider, E.; McKinnon, T.P.; Brown, M.J.; Togni, S.; Dixon, B.M. Comparative Absorption of a Standardized Curcuminoid Mixture and Its Lecithin Formulation. *J. Nat. Prod.* **2011**, *74*, 664–669. [CrossRef]
152. Liang, J.; Liu, X.; Xie, Q.; Chen, G.; Li, X.; Jia, Y.; Yin, B.; Qu, X.; Li, Y. Endostatin enhances antitumor effect of tumor antigen-pulsed dendritic cell therapy in mouse xenograft model of lung carcinoma. *Chin. J. Cancer Res.* **2016**, *28*, 452–460. [CrossRef]
153. Chen, R.; Lu, X.; Li, Z.; Sun, Y.; He, Z.; Li, X. Dihydroartemisinin Prevents Progression and Metastasis of Head and Neck Squamous Cell Carcinoma by Inhibiting Polarization of Macrophages in Tumor Microenvironment. *Onco Targets Ther.* **2020**, *13*, 3375–3387. [CrossRef]
154. Zou, J.Y.; Su, C.H.; Luo, H.H.; Lei, Y.Y.; Zeng, B.; Zhu, H.S.; Chen, Z.G. Curcumin converts Foxp3+ regulatory T cells to T helper 1 cells in patients with lung cancer. *J. Cell Biochem.* **2018**, *119*, 1420–1428. [CrossRef]
155. Shirabe, K.; Mano, Y.; Muto, J.; Matono, R.; Motomura, T.; Tushima, T.; Takeishi, K.; Uchiyama, H.; Yoshizumi, T.; Taketomi, A.; et al. Role of tumor-associated macrophages in the progression of hepatocellular carcinoma. *Surg. Today* **2012**, *42*, 1–7. [CrossRef]
156. Gabrilovich, D.I.; Nagaraj, S. Myeloid-derived suppressor cells as regulators of the immune system. *Nat. Rev. Immunol.* **2009**, *9*, 162–174. [CrossRef]
157. Augustyn, A.; Adams, D.; He, J.; Qiao, Y.; Liao, Z.; Tang, C.-M.; Heymach, J.; Tsao, A.; Lin, S. Giant Circulating Cancer-Associated Macrophage-like Cells Are Associated with Disease Recurrence and Survival in Non-Small-Cell Lung Cancer Treated with Chemoradiation and Atezolizumab. *Clin. Lung Cancer* **2020**, *22*, e451–e465. [CrossRef]
158. Liu, D.; You, M.; Xu, Y.; Li, F.; Zhang, D.; Li, X.; Hou, Y. Inhibition of curcumin on myeloid-derived suppressor cells is requisite for controlling lung cancer. *Int. Immunopharmacol.* **2016**, *39*, 265–272. [CrossRef]
159. Liao, F.; Liu, L.; Luo, E.; Hu, J. Curcumin enhances anti-tumor immune response in tongue squamous cell carcinoma. *Arch. Oral Biol.* **2018**, *92*, 32–37. [CrossRef]
160. Donkor, M.; Sarkar, A.; Li, M. Tgf- $\beta$ 1 produced by activated CD4 T Cells Antagonizes T Cell Surveillance of Tumor Development. *Oncoimmunology* **2012**, *1*, 162–171. [CrossRef]
161. Kennedy, R.; Celis, E. Multiple roles for CD4+ T cells in anti-tumor immune responses. *Immunol. Rev.* **2008**, *222*, 129–144. [CrossRef]
162. Shao, Y.; Zhu, W.; Da, J.; Xu, M.; Wang, Y.; Zhou, J.; Wang, Z. Bisdemethoxycurcumin in combination with  $\alpha$ -PD-L1 antibody boosts immune response against bladder cancer. *Onco Targets Ther.* **2017**, *10*, 2675–2683. [CrossRef]

163. Bremnes, R.M.; Dønnem, T.; Al-Saad, S.; Al-Shibli, K.; Andersen, S.; Sirera, R.; Camps, C.; Marinez, I.; Busund, L.T. The role of tumor stroma in cancer progression and prognosis: Emphasis on carcinoma-associated fibroblasts and non-small cell lung cancer. *J. Thorac. Oncol.* **2011**, *6*, 209–217. [CrossRef]
164. Kim, S.H.; Choe, C.; Shin, Y.S.; Jeon, M.J.; Choi, S.J.; Lee, J.; Bae, G.Y.; Cha, H.J.; Kim, J. Human lung cancer-associated fibroblasts enhance motility of non-small cell lung cancer cells in co-culture. *Anticancer Res.* **2013**, *33*, 2001–2009. [PubMed]
165. Shien, K.; Papadimitrakopoulou, V.A.; Ruder, D.; Behrens, C.; Shen, L.; Kalhor, N.; Song, J.; Lee, J.J.; Wang, J.; Tang, X.; et al. JAK1/STAT3 Activation through a Proinflammatory Cytokine Pathway Leads to Resistance to Molecularly Targeted Therapy in Non-Small Cell Lung Cancer. *Mol. Cancer Ther.* **2017**, *16*, 2234–2245. [CrossRef] [PubMed]
166. Zhang, Q.; Yang, J.; Bai, J.; Ren, J. Reverse of non-small cell lung cancer drug resistance induced by cancer-associated fibroblasts via a paracrine pathway. *Cancer Sci.* **2018**, *109*, 944–955. [CrossRef] [PubMed]
167. Kanzaki, R.; Naito, H.; Kise, K.; Takara, K.; Eino, D.; Minami, M.; Shintani, Y.; Funaki, S.; Kawamura, T.; Kimura, T.; et al. Gas6 derived from cancer-associated fibroblasts promotes migration of Axl-expressing lung cancer cells during chemotherapy. *Sci. Rep.* **2017**, *7*, 10613. [CrossRef] [PubMed]
168. Sung, P.J.; Rama, N.; Imbach, J.; Fiore, S.; Ducarouge, B.; Neves, D.; Chen, H.W.; Bernard, D.; Yang, P.C.; Bernet, A.; et al. Cancer-Associated Fibroblasts Produce Netrin-1 to Control Cancer Cell Plasticity. *Cancer Res.* **2019**, *79*, 3651–3661. [CrossRef]
169. Wang, Z.; Tang, Y.; Tan, Y.; Wei, Q.; Yu, W. Cancer-associated fibroblasts in radiotherapy: Challenges and new opportunities. *Cell Commun. Signal.* **2019**, *17*, 47. [CrossRef]
170. Cho, J.; Lee, H.J.; Hwang, S.J.; Min, H.Y.; Kang, H.N.; Park, A.Y.; Hyun, S.Y.; Sim, J.Y.; Lee, H.J.; Jang, H.J.; et al. The Interplay between Slow-Cycling, Chemoresistant Cancer Cells and Fibroblasts Creates a Proinflammatory Niche for Tumor Progression. *Cancer Res.* **2020**, *80*, 2257–2272. [CrossRef]
171. Ortiz-Otero, N.; Marshall, J.R.; Lash, B.; King, M.R. Chemotherapy-induced release of circulating-tumor cells into the bloodstream in collective migration units with cancer-associated fibroblasts in metastatic cancer patients. *BMC Cancer* **2020**, *20*, 873. [CrossRef]
172. Ao, Z.; Shah, S.H.; Machlin, L.M.; Parajuli, R.; Miller, P.C.; Rawal, S.; Williams, A.J.; Cote, R.J.; Lippman, M.E.; Datar, R.H.; et al. Identification of Cancer-Associated Fibroblasts in Circulating Blood from Patients with Metastatic Breast Cancer. *Cancer Res.* **2015**, *75*, 4681–4687. [CrossRef]
173. Ba, P.; Xu, M.; Yu, M.; Li, L.; Duan, X.; Lv, S.; Fu, G.; Yang, J.; Yang, P.; Yang, C.; et al. Curcumin suppresses the proliferation and tumorigenicity of Cal27 by modulating cancer associated fibroblasts of TSCC. *Oral Dis.* **2020**, *26*, 1375–1383. [CrossRef]
174. Wang, Q.; Qu, C.; Xie, F.; Chen, L.; Liu, L.; Liang, X.; Wu, X.; Wang, P.; Meng, Z. Curcumin suppresses epithelial-to-mesenchymal transition and metastasis of pancreatic cancer cells by inhibiting cancer-associated fibroblasts. *Am. J. Cancer Res.* **2017**, *7*, 125–133.
175. Kreutz, D.; Sinthuvanich, C.; Bileck, A.; Janker, L.; Muqaku, B.; Slany, A.; Gerner, C. Curcumin exerts its antitumor effects in a context dependent fashion. *J. Proteom.* **2018**, *182*, 65–72. [CrossRef]
176. Luo, M.; Luo, Y.; Mao, N.; Huang, G.; Teng, C.; Wang, H.; Wu, J.; Liao, X.; Yang, J. Cancer-Associated Fibroblasts Accelerate Malignant Progression of Non-Small Cell Lung Cancer via Connexin 43-Formed Unidirectional Gap Junctional Intercellular Communication. *Cell. Physiol. Biochem. Int. J. Exp. Cell. Physiol. Biochem. Pharmacol.* **2018**, *51*, 315–336. [CrossRef]
177. Chouaib, S.; Kieda, C.; Benlalam, H.; Noman, M.Z.; Mami-Chouaib, F.; Rüegg, C. Endothelial cells as key determinants of the tumor microenvironment: Interaction with tumor cells, extracellular matrix and immune killer cells. *Crit. Rev. Immunol.* **2010**, *30*, 529–545. [CrossRef]
178. Ito, K.; Semba, T.; Uenaka, T.; Wakabayashi, T.; Asada, M.; Funahashi, Y. Enhanced anti-angiogenic effect of E7820 in combination with erlotinib in epidermal growth factor receptor-tyrosine kinase inhibitor-resistant non-small-cell lung cancer xenograft models. *Cancer Sci.* **2014**, *105*, 1023–1031. [CrossRef]
179. Wu, W.; Onn, A.; Isobe, T.; Itasaka, S.; Langley, R.R.; Shitani, T.; Shibuya, K.; Komaki, R.; Ryan, A.J.; Fidler, I.J.; et al. Targeted therapy of orthotopic human lung cancer by combined vascular endothelial growth factor and epidermal growth factor receptor signaling blockade. *Mol. Cancer Ther.* **2007**, *6*, 471–483. [CrossRef]
180. Lee, H.J.; Hanibuchi, M.; Kim, S.J.; Yu, H.; Kim, M.S.; He, J.; Langley, R.R.; Lehembre, F.; Regenass, U.; Fidler, I.J. Treatment of experimental human breast cancer and lung cancer brain metastases in mice by macitentan, a dual antagonist of endothelin receptors, combined with paclitaxel. *Neuro-Oncology* **2016**, *18*, 486–496. [CrossRef]
181. Kumar, P.; Ning, Y.; Polverini, P.J. Endothelial cells expressing Bcl-2 promotes tumor metastasis by enhancing tumor angiogenesis, blood vessel leakiness and tumor invasion. *Lab. Investig. J. Technol. Methods Pathol.* **2008**, *88*, 740–749. [CrossRef]
182. Kaneko, T.; Zhang, Z.; Mantellini, M.G.; Karl, E.; Zeitlin, B.; Verhaegen, M.; Soengas, M.S.; Lingen, M.; Strieter, R.M.; Nunez, G.; et al. Bcl-2 orchestrates a cross-talk between endothelial and tumor cells that promotes tumor growth. *Cancer Res.* **2007**, *67*, 9685–9693. [CrossRef]
183. Nör, J.E.; Christensen, J.; Liu, J.; Peters, M.; Mooney, D.J.; Strieter, R.M.; Polverini, P.J. Up-Regulation of Bcl-2 in microvascular endothelial cells enhances intratumoral angiogenesis and accelerates tumor growth. *Cancer Res.* **2001**, *61*, 2183–2188.
184. Yadav, A.; Kumar, B.; Yu, J.G.; Old, M.; Teknos, T.N.; Kumar, P. Tumor-Associated Endothelial Cells Promote Tumor Metastasis by Chaperoning Circulating Tumor Cells and Protecting Them from Anoikis. *PLoS ONE* **2015**, *10*, e0141602. [CrossRef]
185. Jin, G.; Yang, Y.; Liu, K.; Zhao, J.; Chen, X.; Liu, H.; Bai, R.; Li, X.; Jiang, Y.; Zhang, X.; et al. Combination curcumin and (-)-epigallocatechin-3-gallate inhibits colorectal carcinoma microenvironment-induced angiogenesis by JAK/STAT3/IL-8 pathway. *Oncogenesis* **2017**, *6*, e384. [CrossRef]

186. Zhang, Z.; Li, C.; Tan, Q.; Xie, C.; Yang, Y.; Zhan, W.; Han, F.; Sharma, H.S.; Sharma, A. Curcumin Suppresses Tumor Growth and Angiogenesis in Human Glioma Cells Through Modulation of Vascular Endothelial Growth Factor/ Angiopoietin-2/Thrombospondin-1 Signaling. *CNS Neurol. Disord. Drug Targets* **2017**, *16*, 346–350. [CrossRef]
187. Mondal, G.; Barui, S.; Saha, S.; Chaudhuri, A. Tumor growth inhibition through targeting liposomally bound curcumin to tumor vasculature. *J. Control. Release Off. J. Control. Release Soc.* **2013**, *172*, 832–840. [CrossRef] [PubMed]
188. Barui, S.; Saha, S.; Yakati, V.; Chaudhuri, A. Systemic Codelivery of a Homoserine Derived Ceramide Analogue and Curcumin to Tumor Vasculature Inhibits Mouse Tumor Growth. *Mol. Pharm.* **2016**, *13*, 404–419. [CrossRef] [PubMed]
189. Kumar, A.; Dhawan, S.; Hardegen, N.J.; Aggarwal, B.B. Curcumin (Diferuloylmethane) inhibition of tumor necrosis factor (TNF)-mediated adhesion of monocytes to endothelial cells by suppression of cell surface expression of adhesion molecules and of nuclear factor-kappaB activation. *Biochem. Pharmacol.* **1998**, *55*, 775–783. [CrossRef]
190. Cho, H.; Seo, Y.; Loke, K.M.; Kim, S.W.; Oh, S.M.; Kim, J.H.; Soh, J.; Kim, H.S.; Lee, H.; Kim, J.; et al. Cancer-Stimulated CAFs Enhance Monocyte Differentiation and Protumoral TAM Activation via IL6 and GM-CSF Secretion. *Clin. Cancer Res. Off. J. Am. Assoc. Cancer Res.* **2018**, *24*, 5407–5421. [CrossRef] [PubMed]
191. Yuan, R.; Li, S.; Geng, H.; Wang, X.; Guan, Q.; Li, X.; Ren, C.; Yuan, X. Reversing the polarization of tumor-associated macrophages inhibits tumor metastasis. *Int. Immunopharmacol.* **2017**, *49*, 30–37. [CrossRef]
192. Liu, L.; Ge, D.; Ma, L.; Mei, J.; Liu, S.; Zhang, Q.; Ren, F.; Liao, H.; Pu, Q.; Wang, T.; et al. Interleukin-17 and prostaglandin E2 are involved in formation of an M2 macrophage-dominant microenvironment in lung cancer. *J. Thorac. Oncol. Off. Publ. Int. Assoc. Study Lung Cancer* **2012**, *7*, 1091–1100. [CrossRef]
193. Jeong, S.K.; Kim, J.S.; Lee, C.G.; Park, Y.S.; Kim, S.D.; Yoon, S.O.; Han, D.H.; Lee, K.Y.; Jeong, M.H.; Jo, W.S. Tumor associated macrophages provide the survival resistance of tumor cells to hypoxic microenvironmental condition through IL-6 receptor-mediated signals. *Immunobiology* **2017**, *222*, 55–65. [CrossRef]
194. Alfaro, C.; Sanmamed, M.F.; Rodríguez-Ruiz, M.E.; Teijeira, Á.; Oñate, C.; González, Á.; Ponz, M.; Schalper, K.A.; Pérez-Gracia, J.L.; Melero, I. Interleukin-8 in cancer pathogenesis, treatment and follow-up. *Cancer Treat. Rev.* **2017**, *60*, 24–31. [CrossRef] [PubMed]
195. Khan, M.N.; Wang, B.; Wei, J.; Zhang, Y.; Li, Q.; Luan, X.; Cheng, J.W.; Gordon, J.R.; Li, F.; Liu, H. CXCR1/2 antagonism with CXCL8/Interleukin-8 analogue CXCL8(3-72)K11R/G31P restricts lung cancer growth by inhibiting tumor cell proliferation and suppressing angiogenesis. *Oncotarget* **2015**, *6*, 21315–21327. [CrossRef]
196. Saidi, A.; Kasabova, M.; Vanderlynden, L.; Wartenberg, M.; Kara-Ali, G.H.; Marc, D.; Lecaille, F.; Lalmanach, G. Curcumin inhibits the TGF- $\beta$ 1-dependent differentiation of lung fibroblasts via PPAR $\gamma$ -driven upregulation of cathepsins B and L. *Sci. Rep.* **2019**, *9*, 491. [CrossRef]
197. Liu, J.; Xu, Y.; Yu, M.; Liu, Z.; Xu, Y.; Ma, G.; Zhou, W.; Kong, P.; Ling, L.; Wang, S.; et al. Increased Stromal Infiltrating Lymphocytes are Associated with Circulating Tumor Cells and Metastatic Relapse in Breast Cancer Patients After Neoadjuvant Chemotherapy. *Cancer Manag. Res.* **2019**, *11*, 10791–10800. [CrossRef]
198. Smolkova, B.; Cierna, Z.; Kalavska, K.; Miklikova, S.; Plava, J.; Minarik, G.; Sedlackova, T.; Cholujova, D.; Gronesova, P.; Cihova, M.; et al. Increased Stromal Infiltrating Lymphocytes Are Associated with the Risk of Disease Progression in Mesenchymal Circulating Tumor Cell-Positive Primary Breast Cancer Patients. *Int. J. Mol. Sci.* **2020**, *21*, 9460. [CrossRef]
199. Xue, D.; Xia, T.; Wang, J.; Chong, M.; Wang, S.; Zhang, C. Role of regulatory T cells and CD8(+) T lymphocytes in the dissemination of circulating tumor cells in primary invasive breast cancer. *Oncol. Lett.* **2018**, *16*, 3045–3053. [CrossRef]
200. Osmulski, P.A.; Cunsolo, A.; Chen, M.; Qian, Y.; Lin, C.L.; Hung, C.N.; Mahalingam, D.; Kirma, N.B.; Chen, C.L.; Taverna, J.A.; et al. Contacts with Macrophages Promote an Aggressive Nanomechanical Phenotype of Circulating Tumor Cells in Prostate Cancer. *Cancer Res.* **2021**, *81*, 4110–4123. [CrossRef]
201. Mego, M.; Gao, H.; Cohen, E.N.; Anfossi, S.; Giordano, A.; Sanda, T.; Fouad, T.M.; De Giorgi, U.; Giuliano, M.; Woodward, W.A.; et al. Circulating Tumor Cells (CTC) Are Associated with Defects in Adaptive Immunity in Patients with Inflammatory Breast Cancer. *J. Cancer* **2016**, *7*, 1095–1104. [CrossRef] [PubMed]
202. Dianat-Moghadam, H.; Mahari, A.; Heidarifard, M.; Parnianfard, N.; Pourmousavi-Kh, L.; Rahbarghazi, R.; Amoozgar, Z. NK cells-directed therapies target circulating tumor cells and metastasis. *Cancer Lett.* **2021**, *497*, 41–53. [CrossRef] [PubMed]
203. Ried, K.; Eng, P.; Sali, A. Screening for Circulating Tumour Cells Allows Early Detection of Cancer and Monitoring of Treatment Effectiveness: An Observational Study. *Asian Pac. J. Cancer Prev.* **2017**, *18*, 2275–2285. [CrossRef] [PubMed]
204. Pang, S.; Jia, M.; Gao, J.; Liu, X.; Guo, W.; Zhang, H. Effects of dietary patterns combined with dietary phytochemicals on breast cancer metastasis. *Life Sci.* **2021**, *264*, 118720. [CrossRef]
205. Mukherjee, S.; Baidoo, J.; Fried, A.; Atwi, D.; Dolai, S.; Boockvar, J.; Symons, M.; Ruggieri, R.; Raja, K.; Banerjee, P. Curcumin changes the polarity of tumor-associated microglia and eliminates glioblastoma. *Int. J. Cancer* **2016**, *139*, 2838–2849. [CrossRef]
206. Wang, J.; Man, G.C.W.; Chan, T.H.; Kwong, J.; Wang, C.C. A prodrug of green tea polyphenol (–)-epigallocatechin-3-gallate (Pro-EGCG) serves as a novel angiogenesis inhibitor in endometrial cancer. *Cancer Lett.* **2018**, *412*, 10–20. [CrossRef]
207. Jang, J.Y.; Lee, J.K.; Jeon, Y.K.; Kim, C.W. Exosome derived from epigallocatechin gallate treated breast cancer cells suppresses tumor growth by inhibiting tumor-associated macrophage infiltration and M2 polarization. *BMC Cancer* **2013**, *13*, 421. [CrossRef]
208. Tian, S.; Liao, L.; Zhou, Q.; Huang, X.; Zheng, P.; Guo, Y.; Deng, T.; Tian, X. Curcumin inhibits the growth of liver cancer by impairing myeloid-derived suppressor cells in murine tumor tissues. *Oncol. Lett.* **2021**, *21*, 286. [CrossRef]

209. Zhou, J.; Donatelli, S.S.; Gilvary, D.L.; Tejera, M.M.; Eksioglu, E.A.; Chen, X.; Coppola, D.; Wei, S.; Djeu, J.Y. Therapeutic targeting of myeloid-derived suppressor cells involves a novel mechanism mediated by clusterin. *Sci. Rep.* **2016**, *6*, 29521. [CrossRef]
210. Lu, Y.; Miao, L.; Wang, Y.; Xu, Z.; Zhao, Y.; Shen, Y.; Xiang, G.; Huang, L. Curcumin Micelles Remodel Tumor Microenvironment and Enhance Vaccine Activity in an Advanced Melanoma Model. *Mol. Ther.* **2016**, *24*, 364–374. [CrossRef]
211. Ma, Z.; Xia, Y.; Hu, C.; Yu, M.; Yi, H. Quercetin promotes the survival of granulocytic myeloid-derived suppressor cells via the ESR2/STAT3 signaling pathway. *Biomed. Pharmacother.* **2020**, *125*, 109922. [CrossRef]
212. Xu, P.; Yan, F.; Zhao, Y.; Chen, X.; Sun, S.; Wang, Y.; Ying, L. Green Tea Polyphenol EGCG Attenuates MDSCs-Mediated Immunosuppression through Canonical and Non-Canonical Pathways in a 4T1 Murine Breast Cancer Model. *Nutrients* **2020**, *12*, 1042. [CrossRef]
213. Santilli, G.; Piotrowska, I.; Cantilena, S.; Chayka, O.; D'Alicarnasso, M.; Morgenstern, D.A.; Himoudi, N.; Pearson, K.; Anderson, J.; Thrasher, A.J.; et al. Polyphenon [corrected] E enhances the antitumor immune response in neuroblastoma by inactivating myeloid suppressor cells. *Clin. Cancer Res. Off. J. Am. Assoc. Cancer Res.* **2013**, *19*, 1116–1125. [CrossRef]
214. Hossain, D.M.S.; Panda, A.K.; Chakrabarty, S.; Bhattacharjee, P.; Kajal, K.; Mohanty, S.; Sarkar, I.; Sarkar, D.K.; Kar, S.K.; Sa, G. MEK inhibition prevents tumour-shed transforming growth factor- $\beta$ -induced T-regulatory cell augmentation in tumour milieu. *Immunology* **2015**, *144*, 561–573. [CrossRef]
215. Kötting, C.; Hofmann, L.; Lotfi, R.; Engelhardt, D.; Laban, S.; Schuler, P.J.; Hoffmann, T.K.; Brunner, C.; Theodoraki, M.N. Immune-Stimulatory Effects of Curcumin on the Tumor Microenvironment in Head and Neck Squamous Cell Carcinoma. *Cancers* **2021**, *13*, 1335. [CrossRef]
216. Xu, B.; Yu, L.; Zhao, L.Z. Curcumin up regulates T helper 1 cells in patients with colon cancer. *Am. J. Transl. Res.* **2017**, *9*, 1866–1875.
217. Du, Y.; Long, Q.; Zhang, L.; Shi, Y.; Liu, X.; Li, X.; Guan, B.; Tian, Y.; Wang, X.; Li, L.; et al. Curcumin inhibits cancer-associated fibroblast-driven prostate cancer invasion through MAOA/mTOR/HIF-1 $\alpha$  signaling. *Int J. Oncol.* **2015**, *47*, 2064–2072. [CrossRef]
218. Hendrayani, S.F.; Al-Khalaf, H.H.; Abousekhra, A. Curcumin triggers p16-dependent senescence in active breast cancer-associated fibroblasts and suppresses their paracrine procarcinogenic effects. *Neoplasia* **2013**, *15*, 631–640. [CrossRef]
219. Zhao, H.; Xie, P.; Li, X.; Zhu, W.; Sun, X.; Sun, X.; Chen, X.; Xing, L.; Yu, J. A prospective phase II trial of EGCG in treatment of acute radiation-induced esophagitis for stage III lung cancer. *Radiother. Oncol. J. Eur. Soc. Ther. Radiol. Oncol.* **2015**, *114*, 351–356. [CrossRef]
220. Hamilton, G.; Rath, B. Mesenchymal-Epithelial Transition and Circulating Tumor Cells in Small Cell Lung Cancer. *Adv. Exp. Med. Biol.* **2017**, *994*, 229–245. [CrossRef]
221. Wells, A.; Yates, C.; Shepard, C.R. E-cadherin as an indicator of mesenchymal to epithelial reverting transitions during the metastatic seeding of disseminated carcinomas. *Clin. Exp. Metastasis* **2008**, *25*, 621–628. [CrossRef]
222. Raimondi, C.; Carpino, G.; Nicolazzo, C.; Gradilone, A.; Gianni, W.; Gelibter, A.; Gaudio, E.; Cortesi, E.; Gazzaniga, P. PD-L1 and epithelial-mesenchymal transition in circulating tumor cells from non-small cell lung cancer patients: A molecular shield to evade immune system? *Oncoimmunology* **2017**, *6*, e1315488. [CrossRef]
223. Liang, Z.; Wu, R.; Xie, W.; Zhu, M.; Xie, C.; Li, X.; Zhu, J.; Zhu, W.; Wu, J.; Geng, S.; et al. Curcumin reverses tobacco smoke-induced epithelial-mesenchymal transition by suppressing the MAPK pathway in the lungs of mice. *Mol. Med. Rep.* **2018**, *17*, 2019–2025. [CrossRef]
224. Chang, J.H.; Lai, S.L.; Chen, W.S.; Hung, W.Y.; Chow, J.M.; Hsiao, M.; Lee, W.J.; Chien, M.H. Quercetin suppresses the metastatic ability of lung cancer through inhibiting Snail-dependent Akt activation and Snail-independent ADAM9 expression pathways. *Biochim. Biophys. Acta Mol. Cell Res.* **2017**, *1864*, 1746–1758. [CrossRef]
225. Furukawa, M.; Wheeler, S.; Clark, A.M.; Wells, A. Lung epithelial cells induce both phenotype alteration and senescence in breast cancer cells. *PLoS ONE* **2015**, *10*, e0118060. [CrossRef]
226. Chao, Y.; Wu, Q.; Shepard, C.; Wells, A. Hepatocyte induced re-expression of E-cadherin in breast and prostate cancer cells increases chemoresistance. *Clin. Exp. Metastasis* **2012**, *29*, 39–50. [CrossRef]
227. Taylor, D.P.; Clark, A.; Wheeler, S.; Wells, A. Hepatic nonparenchymal cells drive metastatic breast cancer outgrowth and partial epithelial to mesenchymal transition. *Breast Cancer Res. Treat.* **2014**, *144*, 551–560. [CrossRef]
228. Yang, M.; Ma, B.; Shao, H.; Clark, A.M.; Wells, A. Macrophage phenotypic subtypes diametrically regulate epithelial-mesenchymal plasticity in breast cancer cells. *BMC Cancer* **2016**, *16*, 419. [CrossRef]
229. Giancotti, F.G. Mechanisms governing metastatic dormancy and reactivation. *Cell* **2013**, *155*, 750–764. [CrossRef]
230. Butturini, E.; Carcereri de Prati, A.; Boriero, D.; Mariotto, S. Tumor Dormancy and Interplay with Hypoxic Tumor Microenvironment. *Int. J. Mol. Sci.* **2019**, *20*, 4305. [CrossRef]
231. Hyoudou, K.; Nishikawa, M.; Kobayashi, Y.; Ikemura, M.; Yamashita, F.; Hashida, M. SOD derivatives prevent metastatic tumor growth aggravated by tumor removal. *Clin. Exp. Metastasis* **2008**, *25*, 531–536. [CrossRef] [PubMed]
232. Farzaei, M.H.; Zobeiri, M.; Parvizi, F.; El-Senduny, F.F.; Marmouzi, I.; Coy-Barrera, E.; Naseri, R.; Nabavi, S.M.; Rahimi, R.; Abdollahi, M. Curcumin in Liver Diseases: A Systematic Review of the Cellular Mechanisms of Oxidative Stress and Clinical Perspective. *Nutrients* **2018**, *10*, 855. [CrossRef] [PubMed]
233. Wojcik, M.; Krawczyk, M.; Wojcik, P.; Cypryk, K.; Wozniak, L.A. Molecular Mechanisms Underlying Curcumin-Mediated Therapeutic Effects in Type 2 Diabetes and Cancer. *Oxidative Med. Cell. Longev.* **2018**, *2018*, 9698258. [CrossRef] [PubMed]
234. Xu, D.; Hu, M.J.; Wang, Y.Q.; Cui, Y.L. Antioxidant Activities of Quercetin and Its Complexes for Medicinal Application. *Molecules* **2019**, *24*, 1123. [CrossRef]

235. Bernatoniene, J.; Kopustinskiene, D.M. The Role of Catechins in Cellular Responses to Oxidative Stress. *Molecules* **2018**, *23*, 965. [CrossRef]
236. Tabasum, S.; Singh, R.P. Fisetin suppresses migration, invasion and stem-cell-like phenotype of human non-small cell lung carcinoma cells via attenuation of epithelial to mesenchymal transition. *Chem. Biol. Interact.* **2019**, *303*, 14–21. [CrossRef]
237. Wang, J.Y.; Wang, X.; Wang, X.J.; Zheng, B.Z.; Wang, Y.; Wang, X.; Liang, B. Curcumin inhibits the growth via Wnt/ $\beta$ -catenin pathway in non-small-cell lung cancer cells. *Eur. Rev. Med. Pharmacol. Sci.* **2018**, *22*, 7492–7499. [CrossRef]
238. Lee, H.-T.; Xue, J.; Chou, P.-C.; Zhou, A.; Yang, P.; Conrad, C.A.; Aldape, K.D.; Priebe, W.; Patterson, C.; Sawaya, R.; et al. Stat3 orchestrates interaction between endothelial and tumor cells and inhibition of Stat3 suppresses brain metastasis of breast cancer cells. *Oncotarget* **2015**, *6*, 10016–10029. [CrossRef]
239. Ansó, E.; Zuazo, A.; Irigoyen, M.; Urdaci, M.C.; Rouzaut, A.; Martínez-Irujo, J.J. Flavonoids inhibit hypoxia-induced vascular endothelial growth factor expression by a HIF-1 independent mechanism. *Biochem. Pharmacol.* **2010**, *79*, 1600–1609. [CrossRef]
240. Khan, M.N.; Haggag, Y.A.; Lane, M.E.; McCarron, P.A.; Tambuwala, M.M. Polymeric Nano-Encapsulation of Curcumin Enhances its Anti-Cancer Activity in Breast (MDA-MB231) and Lung (A549) Cancer Cells Through Reduction in Expression of HIF-1 $\alpha$  and Nuclear p65 (Rel A). *Curr. Drug Deliv.* **2018**, *15*, 286–295. [CrossRef]
241. Fryknäs, M.; Zhang, X.; Bremberg, U.; Senkowski, W.; Olofsson, M.H.; Brandt, P.; Persson, I.; D’Arcy, P.; Gullbo, J.; Nygren, P.; et al. Iron chelators target both proliferating and quiescent cancer cells. *Sci. Rep.* **2016**, *6*, 38343. [CrossRef]
242. Bahrami, A.; Majeed, M.; Sahebkar, A. Curcumin: A potent agent to reverse epithelial-to-mesenchymal transition. *Cell. Oncol.* **2019**, *42*, 405–421. [CrossRef]
243. Tyagi, N.; Singh, D.K.; Dash, D.; Singh, R. Curcumin Modulates Paraquat-Induced Epithelial to Mesenchymal Transition by Regulating Transforming Growth Factor- $\beta$  (TGF- $\beta$ ) in A549 Cells. *Inflammation* **2019**, *42*, 1441–1455. [CrossRef]
244. Chen, Q.Y.; Jiao, D.M.; Yao, Q.H.; Yan, J.; Song, J.; Chen, F.Y.; Lu, G.H.; Zhou, J.Y. Expression analysis of Cdc42 in lung cancer and modulation of its expression by curcumin in lung cancer cell lines. *Int. J. Oncol.* **2012**, *40*, 1561–1568. [CrossRef]
245. Zhan, J.W.; Jiao, D.M.; Wang, Y.; Song, J.; Wu, J.H.; Wu, L.J.; Chen, Q.Y.; Ma, S.L. Integrated microRNA and gene expression profiling reveals the crucial miRNAs in curcumin anti-lung cancer cell invasion. *Thorac. Cancer* **2017**, *8*, 461–470. [CrossRef]
246. Fox, D.B.; Garcia, N.M.G.; McKinney, B.J.; Lupo, R.; Noteware, L.C.; Newcomb, R.; Liu, J.; Locasale, J.W.; Hirschey, M.D.; Alvarez, J.V. NRF2 activation promotes the recurrence of dormant tumour cells through regulation of redox and nucleotide metabolism. *Nat. Metab.* **2020**, *2*, 318–334. [CrossRef]
247. Chao, Y.L.; Shepard, C.R.; Wells, A. Breast carcinoma cells re-express E-cadherin during mesenchymal to epithelial reverting transition. *Mol. Cancer* **2010**, *9*, 179. [CrossRef]
248. Ichiki, K.; Mitani, N.; Doki, Y.; Hara, H.; Misaki, T.; Saiki, I. Regulation of activator protein-1 activity in the mediastinal lymph node metastasis of lung cancer. *Clin. Exp. Metastasis* **2000**, *18*, 539–545. [CrossRef]
249. Mirza, S.; Vasaiya, A.; Vora, H.; Jain, N.; Rawal, R. Curcumin Targets Circulating Cancer Stem Cells by Inhibiting Self-Renewal Efficacy in Non-Small Cell Lung Carcinoma. *Anti-Cancer Agents Med. Chem.* **2017**, *17*, 859–864. [CrossRef]
250. Alonso-Nocelo, M.; Raimondo, T.M.; Vining, K.H.; López-López, R.; de la Fuente, M.; Mooney, D.J. Matrix stiffness and tumor-associated macrophages modulate epithelial to mesenchymal transition of human adenocarcinoma cells. *Biofabrication* **2018**, *10*, 035004. [CrossRef]
251. Zhang, X.; Tian, W.; Cai, X.; Wang, X.; Dang, W.; Tang, H.; Cao, H.; Wang, L.; Chen, T. Hydrazinocurcumin Encapsulated nanoparticles “re-educate” tumor-associated macrophages and exhibit anti-tumor effects on breast cancer following STAT3 suppression. *PLoS ONE* **2013**, *8*, e65896. [CrossRef] [PubMed]
252. Murakami, A.; Furukawa, I.; Miyamoto, S.; Tanaka, T.; Ohigashi, H. Curcumin combined with turmerones, essential oil components of turmeric, abolishes inflammation-associated mouse colon carcinogenesis. *BioFactors* **2013**, *39*, 221–232. [CrossRef] [PubMed]
253. Zeng, Y.; Du, Q.; Zhang, Z.; Ma, J.; Han, L.; Wang, Y.; Yang, L.; Tao, N.; Qin, Z. Curcumin promotes cancer-associated fibroblasts apoptosis via ROS-mediated endoplasmic reticulum stress. *Arch. Biochem. Biophys.* **2020**, *694*, 108613. [CrossRef] [PubMed]
254. Perry, M.-C.; Demeule, M.; Régina, A.; Moumdjian, R.; Béliveau, R. Curcumin inhibits tumor growth and angiogenesis in glioblastoma xenografts. *Mol. Nutr. Food Res.* **2010**, *54*, 1192–1201. [CrossRef]
255. Zhang, W.; Xu, J.; Fang, H.; Tang, L.; Chen, W.; Sun, Q.; Zhang, Q.; Yang, F.; Sun, Z.; Cao, L.; et al. Endothelial cells promote triple-negative breast cancer cell metastasis via PAI-1 and CCL5 signaling. *FASEB J. Off. Publ. Fed. Am. Soc. Exp. Biol.* **2018**, *32*, 276–288. [CrossRef]
256. Plantureux, L.; Mège, D.; Crescence, L.; Carminita, E.; Robert, S.; Cointe, S.; Brouilly, N.; Ezzedine, W.; Dignat-George, F.; Dubois, C.; et al. The Interaction of Platelets with Colorectal Cancer Cells Inhibits Tumor Growth but Promotes Metastasis. *Cancer Res.* **2020**, *80*, 291–303. [CrossRef]
257. Sigurdsson, V.; Hilmarsdottir, B.; Sigmundsdottir, H.; Fridriksdottir, A.J.; Ringnér, M.; Villadsen, R.; Borg, A.; Agnarsson, B.A.; Petersen, O.W.; Magnusson, M.K.; et al. Endothelial induced EMT in breast epithelial cells with stem cell properties. *PLoS ONE* **2011**, *6*, e23833. [CrossRef]
258. Scagliotti, G.; Gatti, E.; Ferrari, G.; Mutti, L.; Pozzi, E. Tnp-alpha determination in serum and pleural effusion in patients with lung-cancer. *Int. J. Oncol.* **1995**, *6*, 147–151. [CrossRef]

259. Taftaf, R.; Liu, X.; Singh, S.; Jia, Y.; Dashzeveg, N.K.; Hoffmann, A.D.; El-Shennawy, L.; Ramos, E.K.; Adorno-Cruz, V.; Schuster, E.J.; et al. ICAM1 initiates CTC cluster formation and trans-endothelial migration in lung metastasis of breast cancer. *Nat. Commun.* **2021**, *12*, 4867. [CrossRef]
260. Yang, C.L.; Liu, Y.Y.; Ma, Y.G.; Xue, Y.X.; Liu, D.G.; Ren, Y.; Liu, X.B.; Li, Y.; Li, Z. Curcumin blocks small cell lung cancer cells migration, invasion, angiogenesis, cell cycle and neoplasia through Janus kinase-STAT3 signalling pathway. *PLoS ONE* **2012**, *7*, e37960. [CrossRef]
261. Lin, F.S.; Lin, C.C.; Chien, C.S.; Luo, S.F.; Yang, C.M. Involvement of p42/p44 MAPK, JNK, and NF-kappaB in IL-1beta-induced ICAM-1 expression in human pulmonary epithelial cells. *J. Cell. Physiol.* **2005**, *202*, 464–473. [CrossRef]
262. Lin, C.-C.; Lee, C.-W.; Chu, T.-H.; Cheng, C.-Y.; Luo, S.-F.; Hsiao, L.-D.; Yang, C.-M. Transactivation of Src, PDGF receptor, and Akt is involved in IL-1 $\beta$ -induced ICAM-1 expression in A549 cells. *J. Cell. Physiol.* **2007**, *211*, 771–780. [CrossRef]
263. Kaplan, R.N.; Riba, R.D.; Zacharoulis, S.; Bramley, A.H.; Vincent, L.; Costa, C.; MacDonald, D.D.; Jin, D.K.; Shido, K.; Kerns, S.A.; et al. VEGFR1-positive haematopoietic bone marrow progenitors initiate the pre-metastatic niche. *Nature* **2005**, *438*, 820–827. [CrossRef]
264. Dong, Q.; Liu, X.; Cheng, K.; Sheng, J.; Kong, J.; Liu, T. Pre-metastatic Niche Formation in Different Organs Induced by Tumor Extracellular Vesicles. *Front. Cell Dev. Biol.* **2021**, *9*, 733627. [CrossRef]
265. Colombo, M.; Raposo, G.; Théry, C. Biogenesis, secretion, and intercellular interactions of exosomes and other extracellular vesicles. *Annu. Rev. Cell Dev. Biol.* **2014**, *30*, 255–289. [CrossRef]
266. Ma, Z.; Wei, K.; Yang, F.; Guo, Z.; Pan, C.; He, Y.; Wang, J.; Li, Z.; Chen, L.; Chen, Y.; et al. Tumor-derived exosomal miR-3157-3p promotes angiogenesis, vascular permeability and metastasis by targeting TIMP/KLF2 in non-small cell lung cancer. *Cell Death Dis.* **2021**, *12*, 840. [CrossRef]
267. Cao, H.H.; Tse, A.K.; Kwan, H.Y.; Yu, H.; Cheng, C.Y.; Su, T.; Fong, W.F.; Yu, Z.L. Quercetin exerts anti-melanoma activities and inhibits STAT3 signaling. *Biochem. Pharmacol.* **2014**, *87*, 424–434. [CrossRef]
268. Mu, Y.T.; Feng, H.H.; Yu, J.Q.; Liu, Z.K.; Wang, Y.; Shao, J.; Li, R.H.; Li, D.K. Curcumin suppressed proliferation and migration of human retinoblastoma cells through modulating NF- $\kappa$ B pathway. *Int. Ophthalmol.* **2020**, *40*, 2435–2440. [CrossRef]
269. Mirzaei, H.; Masoudifar, A.; Sahebkar, A.; Zare, N.; Sadri Nahand, J.; Rashidi, B.; Mehrabian, E.; Mohammadi, M.; Mirzaei, H.R.; Jaafari, M.R. MicroRNA: A novel target of curcumin in cancer therapy. *J. Cell. Physiol.* **2018**, *233*, 3004–3015. [CrossRef]
270. Wu, H.; Zhou, J.; Zeng, C.; Wu, D.; Mu, Z.; Chen, B.; Xie, Y.; Ye, Y.; Liu, J. Curcumin increases exosomal TCF21 thus suppressing exosome-induced lung cancer. *Oncotarget* **2016**, *7*, 87081–87090. [CrossRef]
271. Xiao, J.; Liu, A.; Lu, X.; Chen, X.; Li, W.; He, S.; He, B.; Chen, Q. Prognostic significance of TCF21 mRNA expression in patients with lung adenocarcinoma. *Sci. Rep.* **2017**, *7*, 2027. [CrossRef] [PubMed]
272. Taverna, S.; Fontana, S.; Monteleone, F.; Pucci, M.; Saieva, L.; Caro, V.D.; Cardinale, V.G.; Giallombardo, M.; Vicario, E.; Rolfo, C.; et al. Curcumin modulates chronic myelogenous leukemia exosomes composition and affects angiogenic phenotype via exosomal miR-21. *Oncotarget* **2016**, *7*, 30420. [CrossRef] [PubMed]
273. Taverna, S.; Giallombardo, M.; Pucci, M.; Flugy, A.; Manno, M.; Raccosta, S.; Rolfo, C.; De Leo, G.; Alessandro, R. Curcumin inhibits in vitro and in vivo chronic myelogenous leukemia cells growth: A possible role for exosomal disposal of miR-21. *Oncotarget* **2015**, *6*, 21918–21933. [CrossRef] [PubMed]
274. Sabatel, C.; Malvaux, L.; Bovy, N.; Deroanne, C.; Lambert, V.; Gonzalez, M.L.; Colige, A.; Rakic, J.M.; Noël, A.; Martial, J.A.; et al. MicroRNA-21 exhibits antiangiogenic function by targeting RhoB expression in endothelial cells. *PLoS ONE* **2011**, *6*, e16979. [CrossRef]
275. Zhang, H.-G.; Kim, H.; Liu, C.; Yu, S.; Wang, J.; Grizzle, W.E.; Kimberly, R.P.; Barnes, S. Curcumin reverses breast tumor exosomes mediated immune suppression of NK cell tumor cytotoxicity. *Biochim. Biophys. Acta (BBA) Mol. Cell Res.* **2007**, *1773*, 1116–1123. [CrossRef]
276. Chen, Q.Y.; Zheng, Y.; Jiao, D.M.; Chen, F.Y.; Hu, H.Z.; Wu, Y.Q.; Song, J.; Yan, J.; Wu, L.J.; Lv, G.Y. Curcumin inhibits lung cancer cell migration and invasion through Rac1-dependent signaling pathway. *J. Nutr. Biochem.* **2014**, *25*, 177–185. [CrossRef]
277. Klimaszewska-Wiśniewska, A.; Hałas-Wiśniewska, M.; Izdebska, M.; Gagat, M.; Grzanka, A.; Grzanka, D. Antiproliferative and antimetastatic action of quercetin on A549 non-small cell lung cancer cells through its effect on the cytoskeleton. *Acta Histochem.* **2017**, *119*, 99–112. [CrossRef]
278. Zhang, B.-Y.; Wang, Y.-M.; Gong, H.; Zhao, H.; Lv, X.-Y.; Yuan, G.-H.; Han, S.-R. Isorhamnetin flavonoid synergistically enhances the anticancer activity and apoptosis induction by cis-platin and carboplatin in non-small cell lung carcinoma (NSCLC). *Int. J. Clin. Exp. Pathol.* **2015**, *8*, 25–37.
279. Yuquan, B.; Hexiao, T.; Laiyi, W.; Gaofeng, P.; Xuefeng, Z.; Ming, X.; Yanhong, W.; Li, Z.; Jinping, Z. Interaction between epidermal growth factor receptor and interleukin-6 receptor in NSCLC progression. *J. Cell. Biochem.* **2019**, *120*, 872–881. [CrossRef]
280. Xu, X.; Zhou, X.; Gao, C.; Cao, L.; Zhang, Y.; Hu, X.; Cui, Y. Nodal promotes the malignancy of non-small cell lung cancer (NSCLC) cells via activation of NF- $\kappa$ B/IL-6 signals. *Biol. Chem.* **2019**, *400*, 777–785. [CrossRef]
281. Zulkifli, A.A.; Tan, F.H.; Putoczki, T.L.; Stylli, S.S.; Luwor, R.B. STAT3 signaling mediates tumour resistance to EGFR targeted therapeutics. *Mol. Cell. Endocrinol.* **2017**, *451*, 15–23. [CrossRef]
282. Lee, J.-Y.; Lee, Y.-M.; Chang, G.-C.; Yu, S.-L.; Hsieh, W.-Y.; Chen, J.J.W.; Chen, H.-W.; Yang, P.-C. Curcumin induces EGFR degradation in lung adenocarcinoma and modulates p38 activation in intestine: The versatile adjuvant for gefitinib therapy. *PLoS ONE* **2011**, *6*, e23756. [CrossRef]

283. Liu, R.-Y.; Zeng, Y.; Lei, Z.; Wang, L.; Yang, H.; Liu, Z.; Zhao, J.; Zhang, H.-T. JAK/STAT3 signaling is required for TGF- $\beta$ -induced epithelial-mesenchymal transition in lung cancer cells. *Int. J. Oncol.* **2014**, *44*, 1643–1651. [CrossRef]
284. Jin, H.; Qiao, F.; Wang, Y.; Xu, Y.; Shang, Y. Curcumin inhibits cell proliferation and induces apoptosis of human non-small cell lung cancer cells through the upregulation of miR-192-5p and suppression of PI3K/Akt signaling pathway. *Oncol. Rep.* **2015**, *34*, 2782–2789. [CrossRef]
285. Xu, X.; Zhu, Y. Curcumin inhibits human non-small cell lung cancer xenografts by targeting STAT3 pathway. *Am. J. Transl. Res.* **2017**, *9*, 3633–3641.
286. Mukohara, T.; Kudoh, S.; Yamauchi, S.; Kimura, T.; Yoshimura, N.; Kanazawa, H.; Hirata, K.; Wanibuchi, H.; Fukushima, S.; Inoue, K.; et al. Expression of epidermal growth factor receptor (EGFR) and downstream-activated peptides in surgically excised non-small-cell lung cancer (NSCLC). *Lung Cancer* **2003**, *41*, 123–130. [CrossRef]
287. Haura, E.B.; Zheng, Z.; Song, L.; Cantor, A.; Bepler, G. Activated epidermal growth factor receptor-Stat-3 signaling promotes tumor survival in vivo in non-small cell lung cancer. *Clin. Cancer Res. Off. J. Am. Assoc. Cancer Res.* **2005**, *11*, 8288–8294. [CrossRef]
288. Gao, S.P.; Mark, K.G.; Leslie, K.; Pao, W.; Motoi, N.; Gerald, W.L.; Travis, W.D.; Bornmann, W.; Veach, D.; Clarkson, B.; et al. Mutations in the EGFR kinase domain mediate STAT3 activation via IL-6 production in human lung adenocarcinomas. *J. Clin. Investig.* **2007**, *117*, 3846–3856. [CrossRef]
289. Jiang, A.P.; Zhou, D.H.; Meng, X.L.; Zhang, A.P.; Zhang, C.; Li, X.T.; Feng, Q. Down-regulation of epidermal growth factor receptor by curcumin-induced UBE1L in human bronchial epithelial cells. *J. Nutr. Biochem.* **2014**, *25*, 241–249. [CrossRef]
290. Zhang, Y.; Ma, Q.; Liu, T.; Guan, G.; Zhang, K.; Chen, J.; Jia, N.; Yan, S.; Chen, G.; Liu, S.; et al. Interleukin-6 suppression reduces tumour self-seeding by circulating tumour cells in a human osteosarcoma nude mouse model. *Oncotarget* **2016**, *7*, 446–458. [CrossRef]
291. Matsusaka, S.; Hanna, D.L.; Ning, Y.; Yang, D.; Cao, S.; Berger, M.D.; Miyamoto, Y.; Suenaga, M.; Dan, S.; Mashima, T.; et al. Epidermal growth factor receptor mRNA expression: A potential molecular escape mechanism from regorafenib. *Cancer Sci.* **2020**, *111*, 441–450. [CrossRef]
292. Dimitrakopoulos, F.-I.; Kottorou, A.; Kalofonou, M.; Kalofonos, H. The Fire Within: NF- $\kappa$ B involvement in Non-Small Cell Lung Cancer. *Cancer Res.* **2020**, *80*, canres.3578.2019. [CrossRef]
293. Chen, W.; Li, Z.; Bai, L.; Lin, Y. NF-kappaB in lung cancer, a carcinogenesis mediator and a prevention and therapy target. *Front. Biosci. (Landmark Ed.)* **2011**, *16*, 1172–1185. [CrossRef]
294. Min, C.; Eddy, S.F.; Sherr, D.H.; Sonenshein, G.E. NF-kappaB and epithelial to mesenchymal transition of cancer. *J. Cell Biochem.* **2008**, *104*, 733–744. [CrossRef]
295. Sun, B.; Hu, C.; Yang, Z.; Zhang, X.; Zhao, L.; Xiong, J.; Ma, J.; Chen, L.; Qian, H.; Luo, X.; et al. Midkine promotes hepatocellular carcinoma metastasis by elevating anoikis resistance of circulating tumor cells. *Oncotarget* **2017**, *8*, 32523–32535. [CrossRef] [PubMed]
296. Naidu, S.; Shi, L.; Magee, P.; Middleton, J.D.; Laganá, A.; Sahoo, S.; Leong, H.S.; Galvin, M.; Frese, K.; Dive, C.; et al. PDGFR-modulated miR-23b cluster and miR-125a-5p suppress lung tumorigenesis by targeting multiple components of KRAS and NF- $\kappa$ B pathways. *Sci. Rep.* **2017**, *7*, 15441. [CrossRef]
297. Lin, C.C.; Tseng, H.W.; Hsieh, H.L.; Lee, C.W.; Wu, C.Y.; Cheng, C.Y.; Yang, C.M. Tumor necrosis factor-alpha induces MMP-9 expression via p42/p44 MAPK, JNK, and nuclear factor-kappaB in A549 cells. *Toxicol. Appl. Pharmacol.* **2008**, *229*, 386–398. [CrossRef]
298. Puliappadamba, V.T.; Thulasidasan, A.K.T.; Vijayakurup, V.; Antony, J.; Bava, S.V.; Anwar, S.; Sundaram, S.; Anto, R.J. Curcumin inhibits B[a]P/PDE-induced procarcinogenic signals in lung cancer cells, and curbs B[a]P-induced mutagenesis and lung carcinogenesis. *BioFactors* **2015**, *41*, 431–442. [CrossRef]
299. Lee, J.; Im, Y.H.; Jung, H.H.; Kim, J.H.; Park, J.O.; Kim, K.; Kim, W.S.; Ahn, J.S.; Jung, C.W.; Park, Y.S.; et al. Curcumin inhibits interferon-alpha induced NF-kappaB and COX-2 in human A549 non-small cell lung cancer cells. *Biochem. Biophys. Res. Commun.* **2005**, *334*, 313–318. [CrossRef]
300. Tsai, J.R.; Liu, P.L.; Chen, Y.H.; Chou, S.H.; Cheng, Y.J.; Hwang, J.-J.; Chong, I.-W. Curcumin Inhibits Non-Small Cell Lung Cancer Cells Metastasis through the Adiponectin/NF-kb/MMPs Signaling Pathway. *PLoS ONE* **2015**, *10*, e0144462. [CrossRef] [PubMed]
301. Li, X.; Ma, S.; Yang, P.; Sun, B.; Zhang, Y.; Sun, Y.; Hao, M.; Mou, R.; Jia, Y. Anticancer effects of curcumin on nude mice bearing lung cancer A549 cell subsets SP and NSP cells. *Oncol. Lett.* **2018**, *16*, 6756–6762. [CrossRef] [PubMed]
302. Hu, A.; Huang, J.J.; Li, R.L.; Lu, Z.Y.; Duan, J.L.; Xu, W.H.; Chen, X.P.; Fan, J.P. Curcumin as therapeutics for the treatment of head and neck squamous cell carcinoma by activating SIRT1. *Sci. Rep.* **2015**, *5*, 13429. [CrossRef] [PubMed]
303. Lee, Y.H.; Song, N.Y.; Kim, D.H.; Na, H.K.; Surh, Y.J. Abstract 1250: Curcumin inhibits migration and growth of human colon cancer cells through covalent modification of oncogenic SIRT1: Cysteine 67 as a potential binding site. *Cancer Res.* **2017**, *77*, 1250. [CrossRef]
304. Bernauer, C.; Man, Y.K.S.; Chisholm, J.C.; Lepicard, E.Y.; Robinson, S.P.; Shipley, J.M. Hypoxia and its therapeutic possibilities in paediatric cancers. *Br. J. Cancer* **2021**, *124*, 539–551. [CrossRef]
305. Noman, M.Z.; Messai, Y.; Muret, J.; Hasmim, M.; Chouaib, S. Crosstalk between CTC, Immune System and Hypoxic Tumor Microenvironment. *Cancer Microenviron. Off. J. Int. Cancer Microenviron. Soc.* **2014**, *7*, 153–160. [CrossRef]
306. Salem, A.; Asselin, M.C.; Reymen, B.; Jackson, A.; Lambin, P.; West, C.M.L.; O'Connor, J.P.B.; Faivre-Finn, C. Targeting Hypoxia to Improve Non-Small Cell Lung Cancer Outcome. *J. Natl. Cancer Inst.* **2018**, *110*, 14–30. [CrossRef]

307. Ebright, R.Y.; Zachariah, M.A.; Micalizzi, D.S.; Wittner, B.S.; Niederhoffer, K.L.; Nieman, L.T.; Chirn, B.; Wiley, D.F.; Wesley, B.; Shaw, B.; et al. HIF1A signaling selectively supports proliferation of breast cancer in the brain. *Nat. Commun.* **2020**, *11*, 6311. [CrossRef]
308. Bartkowiak, K.; Koch, C.; Gärtner, S.; Andreas, A.; Gorges, T.M.; Pantel, K. In Vitro Modeling of Reoxygenation Effects on mRNA and Protein Levels in Hypoxic Tumor Cells upon Entry into the Bloodstream. *Cells* **2020**, *9*, 1316. [CrossRef]
309. Ye, M.X.; Zhao, Y.L.; Li, Y.; Miao, Q.; Li, Z.K.; Ren, X.L.; Song, L.Q.; Yin, H.; Zhang, J. Curcumin reverses cis-platin resistance and promotes human lung adenocarcinoma A549/DDP cell apoptosis through HIF-1 $\alpha$  and caspase-3 mechanisms. *Phytomedicine* **2012**, *19*, 779–787. [CrossRef]
310. Fan, S.; Xu, Y.; Li, X.; Tie, L.; Pan, Y.; Li, X. Opposite angiogenic outcome of curcumin against ischemia and Lewis lung cancer models: In silico, in vitro and in vivo studies. *Biochim. Biophys. Acta (BBA) Mol. Basis Dis.* **2014**, *1842*, 1742–1754. [CrossRef]
311. Datta, R.; Halder, S.K.; Zhang, B. Role of TGF- $\beta$  signaling in curcumin-mediated inhibition of tumorigenicity of human lung cancer cells. *J. Cancer Res. Clin. Oncol.* **2013**, *139*, 563–572. [CrossRef]
312. Santibañez, J.F.; Quintanilla, M.; Martínez, J. Genistein and curcumin block TGF-beta 1-induced u-PA expression and migratory and invasive phenotype in mouse epidermal keratinocytes. *Nutr. Cancer* **2000**, *37*, 49–54. [CrossRef]
313. Park, J.I.; Lee, M.G.; Cho, K.; Park, B.J.; Chae, K.S.; Byun, D.S.; Ryu, B.K.; Park, Y.K.; Chi, S.G. Transforming growth factor-beta1 activates interleukin-6 expression in prostate cancer cells through the synergistic collaboration of the Smad2, p38-NF-kappaB, JNK, and Ras signaling pathways. *Oncogene* **2003**, *22*, 4314–4332. [CrossRef]
314. Tanaka, Y.; Kobayashi, H.; Suzuki, M.; Kanayama, N.; Terao, T. Transforming growth factor-beta1-dependent urokinase up-regulation and promotion of invasion are involved in Src-MAPK-dependent signaling in human ovarian cancer cells. *J. Biol. Chem.* **2004**, *279*, 8567–8576. [CrossRef]
315. Mo, N.; Li, Z.Q.; Li, J.; Cao, Y.D. Curcumin inhibits TGF- $\beta$ 1-induced MMP-9 and invasion through ERK and Smad signaling in breast cancer MDA-MB-231 cells. *Asian Pac. J. Cancer Prev.* **2012**, *13*, 5709–5714. [CrossRef]
316. Wright, L.E.; Frye, J.B.; Lukefahr, A.L.; Timmermann, B.N.; Mohammad, K.S.; Guise, T.A.; Funk, J.L. Curcuminoids block TGF- $\beta$  signaling in human breast cancer cells and limit osteolysis in a murine model of breast cancer bone metastasis. *J. Nat. Prod.* **2013**, *76*, 316–321. [CrossRef] [PubMed]
317. Lu, Y.; Wei, C.; Xi, Z. Curcumin suppresses proliferation and invasion in non-small cell lung cancer by modulation of MTA1-mediated Wnt/ $\beta$ -catenin pathway. *Vitr. Cell. Dev. Biol. Anim.* **2014**, *50*, 840–850. [CrossRef] [PubMed]
318. Wen, Z.; Li, Z.; Yong, P.; Liang, D.; Xie, D.; Chen, H.; Yang, Y.; Wu, S.; Li, C.; Cheng, Z. Detection and clinical significance of circulating tumor cells in patients with nasopharyngeal carcinoma. *Oncol. Lett.* **2019**, *18*, 2537–2547. [CrossRef] [PubMed]
319. Bommur, U.D.; Konidala, K.K.; Pabbaraju, N.; Yeguvapalli, S. QSAR modeling, pharmacophore-based virtual screening, and ensemble docking insights into predicting potential epigallocatechin gallate (EGCG) analogs against epidermal growth factor receptor. *J. Recept. Signal. Transduct. Res.* **2019**, *39*, 18–27. [CrossRef] [PubMed]
320. Minnelli, C.; Laudadio, E.; Mobbili, G.; Galeazzi, R. Conformational Insight on WT- and Mutated-EGFR Receptor Activation and Inhibition by Epigallocatechin-3-Gallate: Over a Rational Basis for the Design of Selective Non-Small-Cell Lung Anticancer Agents. *Int. J. Mol. Sci.* **2020**, *21*, 1721. [CrossRef]
321. Liu, J.; Zhong, T.; Yi, P.; Fan, C.; Zhang, Z.; Liang, G.; Xu, Y.; Fan, Y. A new epigallocatechin gallate derivative isolated from Anhua dark tea sensitizes the chemosensitivity of gefitinib via the suppression of PI3K/mTOR and epithelial-mesenchymal transition. *Fitoterapia* **2020**, *143*, 104590. [CrossRef]
322. Zhang, L.; Chen, W.; Tu, G.; Chen, X.; Lu, Y.; Wu, L.; Zheng, D. Enhanced Chemotherapeutic Efficacy of PLGA-Encapsulated Epigallocatechin Gallate (EGCG) Against Human Lung Cancer. *Int. J. Nanomed.* **2020**, *15*, 4417–4429. [CrossRef]
323. Rawangkan, A.; Wongsirisin, P.; Namiki, K.; Iida, K.; Kobayashi, Y.; Shimizu, Y.; Fujiki, H.; Suganuma, M. Green Tea Catechin Is an Alternative Immune Checkpoint Inhibitor that Inhibits PD-L1 Expression and Lung Tumor Growth. *Molecules* **2018**, *23*, 2071. [CrossRef]
324. Suzuki, Y.; Isemura, M. Binding interaction between (-)-epigallocatechin gallate causes impaired spreading of cancer cells on fibrinogen. *Biomed. Res.* **2013**, *34*, 301–308. [CrossRef]
325. Yuan, T.; Ling, F.; Wang, Y.; Teng, Y. A natural product atalantoflavone inhibits non-small cell lung cancer progression via destabilizing Twist1. *Fitoterapia* **2019**, *137*, 104275. [CrossRef]
326. Li, Y.; Feng, X.; Zhang, Y.; Wang, Y.; Yu, X.; Jia, R.; Yu, T.; Zheng, X.; Chu, Q. Dietary flavone from the *Tetragium hemsleyanum* vine triggers human lung adenocarcinoma apoptosis via autophagy. *Food Funct.* **2020**, *11*, 9776–9788. [CrossRef]
327. Fu, T.; Wang, L.; Jin, X.N.; Sui, H.J.; Liu, Z.; Jin, Y. Hyperoside induces both autophagy and apoptosis in non-small cell lung cancer cells in vitro. *Acta Pharmacol. Sin.* **2016**, *37*, 505–518. [CrossRef]
328. Chen, D.; Wu, Y.X.; Qiu, Y.B.; Wan, B.B.; Liu, G.; Chen, J.L.; Lu, M.D.; Pang, Q.F. Hyperoside suppresses hypoxia-induced A549 survival and proliferation through ferrous accumulation via AMPK/HO-1 axis. *Phytomedicine* **2020**, *67*, 153138. [CrossRef]
329. Chen, W.; Wang, X.; Zhuang, J.; Zhang, L.; Lin, Y. Induction of death receptor 5 and suppression of survivin contribute to sensitization of TRAIL-induced cytotoxicity by quercetin in non-small cell lung cancer cells. *Carcinogenesis* **2007**, *28*, 2114–2121. [CrossRef]
330. Mukherjee, A.; Khuda-Bukhsh, A.R. Quercetin Down-regulates IL-6/STAT-3 Signals to Induce Mitochondrial-mediated Apoptosis in a Non-small-cell Lung-cancer Cell Line, A549. *J. Pharmacopunct.* **2015**, *18*, 19–26. [CrossRef]



331. Dong, Y.; Yang, J.; Yang, L.; Li, P. Quercetin Inhibits the Proliferation and Metastasis of Human Non-Small Cell Lung Cancer Cell Line: The Key Role of Src-Mediated Fibroblast Growth Factor-Inducible 14 (Fn14)/ Nuclear Factor kappa B (NF- $\kappa$ B) pathway. *Med. Sci. Monit. Int. Med. J. Exp. Clin. Res.* **2020**, *26*, e920537. [CrossRef]
332. Youn, H.; Jeong, J.C.; Jeong, Y.S.; Kim, E.J.; Um, S.J. Quercetin potentiates apoptosis by inhibiting nuclear factor-kappaB signaling in H460 lung cancer cells. *Biol. Pharm. Bull.* **2013**, *36*, 944–951. [CrossRef]
333. Kang, J.; Kim, E.; Kim, W.; Seong, K.M.; Youn, H.; Kim, J.W.; Kim, J.; Youn, B. Rhamnetin and cirsiolol induce radiosensitization and inhibition of epithelial-mesenchymal transition (EMT) by miR-34a-mediated suppression of Notch-1 expression in non-small cell lung cancer cell lines. *J. Biol. Chem.* **2013**, *288*, 27343–27357. [CrossRef]
334. Ruan, Y.; Hu, K.; Chen, H. Autophagy inhibition enhances isorhamnetin-induced mitochondria-dependent apoptosis in non-small cell lung cancer cells. *Mol. Med. Rep.* **2015**, *12*, 5796–5806. [CrossRef]
335. Wang, J.; Huang, S. Fisetin inhibits the growth and migration in the A549 human lung cancer cell line via the ERK1/2 pathway. *Exp. Ther. Med.* **2018**, *15*, 2667–2673. [CrossRef]
336. Khan, N.; Afaq, F.; Khusro, F.H.; Mustafa Adhami, V.; Suh, Y.; Mukhtar, H. Dual inhibition of phosphatidylinositol 3-kinase/Akt and mammalian target of rapamycin signaling in human nonsmall cell lung cancer cells by a dietary flavonoid fisetin. *Int. J. Cancer* **2012**, *130*, 1695–1705. [CrossRef]
337. Zhang, L.; Huang, Y.; Zhuo, W.; Zhu, Y.; Zhu, B.; Chen, Z. Fisetin, a dietary phytochemical, overcomes Erlotinib-resistance of lung adenocarcinoma cells through inhibition of MAPK and AKT pathways. *Am. J. Transl. Res.* **2016**, *8*, 4857–4868.
338. Liao, Y.C.; Shih, Y.W.; Chao, C.H.; Lee, X.Y.; Chiang, T.A. Involvement of the ERK Signaling Pathway in Fisetin Reduces Invasion and Migration in the Human Lung Cancer Cell Line A549. *J. Agric. Food Chem.* **2009**, *57*, 8933–8941. [CrossRef] [PubMed]
339. Chen, B.H.; Hsieh, C.H.; Tsai, S.Y.; Wang, C.Y.; Wang, C.-C. Anticancer effects of epigallocatechin-3-gallate nanoemulsion on lung cancer cells through the activation of AMP-activated protein kinase signaling pathway. *Sci. Rep.* **2020**, *10*, 5163. [CrossRef] [PubMed]
340. Namiki, K.; Wongsirisin, P.; Yokoyama, S.; Sato, M.; Rawangkan, A.; Sakai, R.; Iida, K.; Suganuma, M. (-)-Epigallocatechin gallate inhibits stemness and tumorigenicity stimulated by AXL receptor tyrosine kinase in human lung cancer cells. *Sci. Rep.* **2020**, *10*, 2444. [CrossRef] [PubMed]
341. Chen, A.; Jiang, P.; Zeb, F.; Wu, X.; Xu, C.; Chen, L.; Feng, Q. EGCG regulates CTR1 expression through its pro-oxidative property in non-small-cell lung cancer cells. *J. Cell. Physiol.* **2020**, *235*, 7970–7981. [CrossRef]
342. Deng, P.; Hu, C.; Xiong, Z.; Li, Y.; Jiang, J.; Yang, H.; Tang, Y.; Cao, L.; Lu, R. Epigallocatechin-3-gallate-induced vascular normalization in A549-cell xenograft-bearing nude mice: Therapeutic efficacy in combination with chemotherapy. *Cancer Manag. Res.* **2019**, *11*, 2425–2439. [CrossRef]
343. Velavan, B.; Divya, T.; Sureshkumar, A.; Sudhandiran, G. Nano-chemotherapeutic efficacy of (-)-epigallocatechin 3-gallate mediating apoptosis in A549 cells: Involvement of reactive oxygen species mediated Nrf2/Keap1 signaling. *Biochem. Biophys. Res. Commun.* **2018**, *503*, 1723–1731. [CrossRef]
344. Jiang, P.; Chen, A.; Wu, X.; Zhou, M.; ul Haq, I.; Mariyam, Z.; Feng, Q. NEAT1 acts as an inducer of cancer stem cell-like phenotypes in NSCLC by inhibiting EGCG-upregulated CTR1. *J. Cell. Physiol.* **2018**, *233*, 4852–4863. [CrossRef]
345. Shi, J.; Liu, F.; Zhang, W.; Liu, X.; Lin, B.; Tang, X. Epigallocatechin-3-gallate inhibits nicotine-induced migration and invasion by the suppression of angiogenesis and epithelial-mesenchymal transition in non-small cell lung cancer cells. *Oncol. Rep.* **2015**, *33*, 2972–2980. [CrossRef]
346. Ko, H.; So, Y.; Jeon, H.; Jeong, M.H.; Choi, H.K.; Ryu, S.H.; Lee, S.W.; Yoon, H.G.; Choi, K.C. TGF- $\beta$ 1-induced epithelial-mesenchymal transition and acetylation of Smad2 and Smad3 are negatively regulated by EGCG in Human A549 lung cancer cells. *Cancer Lett.* **2013**, *335*, 205–213. [CrossRef]
347. He, L.; Zhang, E.; Shi, J.; Li, X.; Zhou, K.; Zhang, Q.; Le, A.D.; Tang, X. (-)-Epigallocatechin-3-gallate inhibits human papillomavirus (HPV)-16 oncoprotein-induced angiogenesis in non-small cell lung cancer cells by targeting HIF-1 $\alpha$ . *Cancer Chemother. Pharmacol.* **2013**, *71*, 713–725. [CrossRef]
348. Li, X.; Feng, Y.; Liu, J.; Feng, X.; Zhou, K.; Tang, X. Epigallocatechin-3-Gallate Inhibits IGF-I-Stimulated Lung Cancer Angiogenesis through Downregulation of HIF-1 $\alpha$  and VEGF Expression. *Lifestyle Genom.* **2013**, *6*, 169–178. [CrossRef]
349. Gupta, N.; Verma, K.; Nalla, S.; Kulshreshtha, A.; Lall, R.; Prasad, S. Free Radicals as a Double-Edged Sword: The Cancer Preventive and Therapeutic Roles of Curcumin. *Molecules* **2020**, *25*, 5390. [CrossRef]
350. Seifermann, M.; Epe, B. Oxidatively generated base modifications in DNA: Not only carcinogenic risk factor but also regulatory mark? *Free Radic. Biol. Med.* **2017**, *107*, 258–265. [CrossRef]
351. Moldogazieva, N.T.; Lutsenko, S.V.; Terentiev, A.A. Reactive Oxygen and Nitrogen Species-Induced Protein Modifications: Implication in Carcinogenesis and Anticancer Therapy. *Cancer Res.* **2018**, *78*, 6040–6047. [CrossRef]
352. Sinha, B.K. Free radicals in anticancer drug pharmacology. *Chem. Biol. Interact.* **1989**, *69*, 293–317. [CrossRef]
353. Neuhouser, M.L.; Barnett, M.J.; Kristal, A.R.; Ambrosone, C.B.; King, I.B.; Thornquist, M.; Goodman, G.G. Dietary supplement use and prostate cancer risk in the Carotene and Retinol Efficacy Trial. *Cancer Epidemiol. Biomark. Prev. Publ. Am. Assoc. Cancer Res. Cosponsored Am. Soc. Prev. Oncol.* **2009**, *18*, 2202–2206. [CrossRef]
354. Goodman, G.E.; Thornquist, M.D.; Balmes, J.; Cullen, M.R.; Meyskens, F.L., Jr.; Omenn, G.S.; Valanis, B.; Williams, J.H., Jr. The Beta-Carotene and Retinol Efficacy Trial: Incidence of lung cancer and cardiovascular disease mortality during 6-year follow-up after stopping beta-carotene and retinol supplements. *J. Natl. Cancer Inst.* **2004**, *96*, 1743–1750. [CrossRef]

355. Morin, D.; Barthélémy, S.; Zini, R.; Labidalle, S.; Tillement, J.P. Curcumin induces the mitochondrial permeability transition pore mediated by membrane protein thiol oxidation. *FEBS Lett.* **2001**, *495*, 131–136. [CrossRef]
356. Wang, C.; Song, X.; Shang, M.; Zou, W.; Zhang, M.; Wei, H.; Shao, H. Curcumin exerts cytotoxicity dependent on reactive oxygen species accumulation in non-small-cell lung cancer cells. *Future Oncol.* **2019**, *15*, 1243–1253. [CrossRef]
357. Li, Y.; Zhang, S.; Geng, J.X.; Hu, X.Y. Curcumin inhibits human non-small cell lung cancer A549 cell proliferation through regulation of Bcl-2/Bax and cytochrome C. *Asian Pac. J. Cancer Prev.* **2013**, *14*, 4599–4602. [CrossRef]
358. Szebeni, G.J.; Balázs, Á.; Madarász, I.; Pócz, G.; Ayaydin, F.; Kanizsai, I.; Fajka-Boja, R.; Alföldi, R.; Hackler, L., Jr.; Puskás, L.G. Achiral Mannich-Base Curcumin Analogs Induce Unfolded Protein Response and Mitochondrial Membrane Depolarization in PANC-1 Cells. *Int. J. Mol. Sci.* **2017**, *18*, 2105. [CrossRef]
359. Mielczarek-Putna, M.; Chrzanowska, A.; Otto-Ślusarczyk, D.; Graboń, W.; Barańczyk-Kuźma, A. Effect of antioxidants on human primary and metastatic colon cancer cells at hypoxia and normoxia. *Wiad. Lek.* **2017**, *70*, 946–952.
360. Du, G.; Lin, H.; Wang, M.; Zhang, S.; Wu, X.; Lu, L.; Ji, L.; Yu, L. Quercetin greatly improved therapeutic index of doxorubicin against 4T1 breast cancer by its opposing effects on HIF-1 $\alpha$  in tumor and normal cells. *Cancer Chemother. Pharm.* **2010**, *65*, 277–287. [CrossRef]
361. Chiş, I.C.; Baltaru, D.; Dumitrovici, A.; Coseriu, A.; Radu, B.C.; Moldovan, R.; Mureşan, A. Protective effects of quercetin from oxidative/nitrosative stress under intermittent hypobaric hypoxia exposure in the rat's heart. *Physiol. Int.* **2018**, *105*, 233–246. [CrossRef] [PubMed]
362. Kuang, Y.; Wang, Q. Iron and lung cancer. *Cancer Lett.* **2019**, *464*, 56–61. [CrossRef] [PubMed]
363. Yin, M.; Liu, Y.; Chen, Y. Iron metabolism: An emerging therapeutic target underlying the anti-cancer effect of quercetin. *Free Radic. Res.* **2021**, *55*, 296–303. [CrossRef] [PubMed]
364. Prasad, S.; DuBourdieu, D.; Srivastava, A.; Kumar, P.; Lall, R. Metal-Curcumin Complexes in Therapeutics: An Approach to Enhance Pharmacological Effects of Curcumin. *Int. J. Mol. Sci.* **2021**, *22*, 7094. [CrossRef]
365. Yang, C.; Ma, X.; Wang, Z.; Zeng, X.; Hu, Z.; Ye, Z.; Shen, G. Curcumin induces apoptosis and protective autophagy in castration-resistant prostate cancer cells through iron chelation. *Drug Des. Dev. Ther.* **2017**, *11*, 431–439. [CrossRef]
366. Kejik, Z.; Kapláneek, R.; Masařík, M.; Babula, P.; Matkowski, A.; Filipenský, P.; Veselá, K.; Gburek, J.; Sýkora, D.; Martásek, P.; et al. Iron Complexes of Flavonoids-Antioxidant Capacity and Beyond. *Int. J. Mol. Sci.* **2021**, *22*, 646. [CrossRef]
367. Tan, J.; Wang, B.; Zhu, L. DNA binding, cytotoxicity, apoptotic inducing activity, and molecular modeling study of quercetin zinc(II) complex. *Bioorg. Med. Chem.* **2009**, *17*, 614–620. [CrossRef]
368. Mohammed, F.; Rashid-Doubell, F.; Taha, S.; Cassidy, S.; Fredericks, S. Effects of curcumin complexes on MDA-MB-231 breast cancer cell proliferation. *Int. J. Oncol.* **2020**, *57*, 445–455. [CrossRef]
369. Chiaem, K.; Lirdprapamongkol, K.; Keeratichamroen, S.; Surarit, R.; Svasti, J. Curcumin Suppresses Vasculogenic Mimicry Capacity of Hepatocellular Carcinoma Cells through STAT3 and PI3K/AKT Inhibition. *Anticancer Res.* **2014**, *34*, 1857–1864.
370. Salehi, M.; Movahedpour, A.; Tayarani, A.; Shabaninejad, Z.; Pourhanifeh, M.H.; Mortezaipoor, E.; Nickdasti, A.; Mottaghi, R.; Davoodabadi, A.; Khan, H.; et al. Therapeutic potentials of curcumin in the treatment of non-small-cell lung carcinoma. *Phytother. Res. PTR* **2020**, *34*, 2557–2576. [CrossRef]
371. Suresh, R.; Ali, S.; Ahmad, A.; Philip, P.A.; Sarkar, F.H. The Role of Cancer Stem Cells in Recurrent and Drug-Resistant Lung Cancer. *Adv. Exp. Med. Biol.* **2016**, *890*, 57–74. [CrossRef]
372. Kashyap, D.; Garg, V.K.; Tuli, H.S.; Yerer, M.B.; Sak, K.; Sharma, A.K.; Kumar, M.; Aggarwal, V.; Sandhu, S.S. Fisetin and Quercetin: Promising Flavonoids with Chemopreventive Potential. *Biomolecules* **2019**, *9*, 174. [CrossRef]
373. Dhatwalia, S.K.; Kumar, M.; Dhawan, D.K. Role of EGCG in Containing the Progression of Lung Tumorigenesis—A Multistage Targeting Approach. *Nutr. Cancer* **2018**, *70*, 334–349. [CrossRef]
374. Suganuma, M.; Saha, A.; Fujiki, H. New cancer treatment strategy using combination of green tea catechins and anticancer drugs. *Cancer Sci.* **2011**, *102*, 317–323. [CrossRef]
375. Hosokawa, M.; Kenmotsu, H.; Koh, Y.; Yoshino, T.; Yoshikawa, T.; Naito, T.; Takahashi, T.; Murakami, H.; Nakamura, Y.; Tsuya, A.; et al. Size-based isolation of circulating tumor cells in lung cancer patients using a microcavity array system. *PLoS ONE* **2013**, *8*, e67466. [CrossRef]
376. Watanabe, M.; Kenmotsu, H.; Ko, R.; Wakuda, K.; Ono, A.; Imai, H.; Taira, T.; Naito, T.; Murakami, H.; Abe, M.; et al. Isolation and molecular analysis of circulating tumor cells from lung cancer patients using a microfluidic chip type cell sorter. *Cancer Sci.* **2018**, *109*, 2539–2548. [CrossRef]
377. Hassan, S.; Blick, T.; Thompson, E.W.; Williams, E.D. Diversity of Epithelial-Mesenchymal Phenotypes in Circulating Tumour Cells from Prostate Cancer Patient-Derived Xenograft Models. *Cancers* **2021**, *13*, 2750. [CrossRef]
378. Chmi, F.; Mohan, S.; Brady, G. Circulating Tumour Cells in Lung Cancer. *Recent Results Cancer Res.* **2020**, *215*, 105–125. [CrossRef]
379. Krebs, M.G.; Hou, J.M.; Sloane, R.; Lancashire, L.; Priest, L.; Nonaka, D.; Ward, T.H.; Backen, A.; Clack, G.; Hughes, A.; et al. Analysis of Circulating Tumor Cells in Patients with Non-small Cell Lung Cancer Using Epithelial Marker-Dependent and -Independent Approaches. *J. Thorac. Oncol.* **2012**, *7*, 306–315. [CrossRef]
380. Hassanzadeh, K.; Buccarello, L.; Dragotto, J.; Mohammadi, A.; Corbo, M.; Feligioni, M. Obstacles against the Marketing of Curcumin as a Drug. *Int. J. Mol. Sci.* **2020**, *21*, 6619. [CrossRef]
381. de Lázaro, I.; Mooney, D.J. Obstacles and opportunities in a forward vision for cancer nanomedicine. *Nat. Mater.* **2021**, *20*, 1469–1479. [CrossRef]

382. Kral, V.; Sotola, J.; Neuwirth, P.; Kejik, Z.; Zaruba, K.; Martasek, P. Nanomedicine—Current status and perspectives: A big potential or just a catchword? *Chem. Listy* **1997**, *100*, 4–9.
383. Chiang, C.L.; Cheng, M.H.; Lin, C.H. From Nanoparticles to Cancer Nanomedicine: Old Problems with New Solutions. *Nanomaterials* **2021**, *11*, 1727. [CrossRef]
384. Dobrzynska, M.; Napierala, M.; Florek, E. Flavonoid Nanoparticles: A Promising Approach for Cancer Therapy. *Biomolecules* **2020**, *10*, 1268. [CrossRef]
385. Ciurana, J.; Rodríguez, C.A. Trends in Nanomaterials and Processing for Drug Delivery of Polyphenols in the Treatment of Cancer and Other Therapies. *Curr. Drug Targets* **2017**, *18*, 135–146. [CrossRef]
386. Su, W.; Wei, T.; Lu, M.; Meng, Z.; Chen, X.; Jing, J.; Li, J.; Yao, W.; Zhu, H.; Fu, T. Treatment of metastatic lung cancer via inhalation administration of curcumin composite particles based on mesoporous silica. *Eur. J. Pharm. Sci.* **2019**, *134*, 246–255. [CrossRef]
387. Smit, D.J.; Pantel, K.; Jücker, M. Circulating tumor cells as a promising target for individualized drug susceptibility tests in cancer therapy. *Biochem. Pharmacol.* **2021**, *188*, 114589. [CrossRef]
388. Mitra, T.; Bhattacharya, R. Phytochemicals modulate cancer aggressiveness: A review depicting the anticancer efficacy of dietary polyphenols and their combinations. *J. Cell. Physiol.* **2020**, *235*, 7696–7708. [CrossRef]
389. Zhang, P.; Zhang, X. Stimulatory effects of curcumin and quercetin on posttranslational modifications of p53 during lung carcinogenesis. *Hum. Exp. Toxicol.* **2018**, *37*, 618–625. [CrossRef]
390. Niedzwiecki, A.; Roomi, M.W.; Kalinovsky, T.; Rath, M. Anticancer Efficacy of Polyphenols and Their Combinations. *Nutrients* **2016**, *8*, 552. [CrossRef]
391. Liu, Y.; Wu, Y.M.; Zhang, P.Y. Protective effects of curcumin and quercetin during benzo(a)pyrene induced lung carcinogenesis in mice. *Eur. Rev. Med. Pharmacol. Sci.* **2015**, *19*, 1736–1743. [PubMed]
392. Nair, P.; Malhotra, A.; Dhawan, D.K. Curcumin and quercetin trigger apoptosis during benzo(a)pyrene-induced lung carcinogenesis. *Mol. Cell. Biochem.* **2015**, *400*, 51–56. [CrossRef] [PubMed]
393. Zhou, D.H.; Wang, X.; Yang, M.; Shi, X.; Huang, W.; Feng, Q. Combination of low concentration of (-)-epigallocatechin gallate (EGCG) and curcumin strongly suppresses the growth of non-small cell lung cancer in vitro and in vivo through causing cell cycle arrest. *Int. J. Mol. Sci.* **2013**, *14*, 12023–12036. [CrossRef] [PubMed]
394. Choudhury, D.; Ganguli, A.; Dastidar, D.G.; Acharya, B.R.; Das, A.; Chakrabarti, G. Apigenin shows synergistic anticancer activity with curcumin by binding at different sites of tubulin. *Biochimie* **2013**, *95*, 1297–1309. [CrossRef] [PubMed]
395. Saha, A.; Kuzuhara, T.; Echigo, N.; Suganuma, M.; Fujiki, H. New role of (-)-epicatechin in enhancing the induction of growth inhibition and apoptosis in human lung cancer cells by curcumin. *Cancer Prev. Res.* **2010**, *3*, 953–962. [CrossRef]
396. Choi, Y.H.; Han, D.H.; Kim, S.W.; Kim, M.J.; Sung, H.H.; Jeon, H.G.; Jeong, B.C.; Seo, S.I.; Jeon, S.S.; Lee, H.M.; et al. A randomized, double-blind, placebo-controlled trial to evaluate the role of curcumin in prostate cancer patients with intermittent androgen deprivation. *Prostate* **2019**, *79*, 614–621. [CrossRef]
397. Belcaro, G.; Hosoi, M.; Pellegrini, L.; Appendino, G.; Ippolito, E.; Ricci, A.; Ledda, A.; Dugall, M.; Cesarone, M.R.; Maione, C.; et al. A Controlled Study of a Lecithinized Delivery System of Curcumin (Meriva®) to Alleviate the Adverse Effects of Cancer Treatment. *Phytother. Res.* **2014**, *28*, 444–450. [CrossRef]
398. Carroll, R.E.; Benya, R.V.; Turgeon, D.K.; Vareed, S.; Neuman, M.; Rodriguez, L.; Kakarala, M.; Carpenter, P.M.; McLaren, C.; Meyskens, F.L., Jr.; et al. Phase IIa clinical trial of curcumin for the prevention of colorectal neoplasia. *Cancer Prev. Res.* **2011**, *4*, 354–364. [CrossRef]
399. He, Z.Y.; Shi, C.B.; Wen, H.; Li, F.L.; Wang, B.L.; Wang, J. Upregulation of p53 Expression in Patients with Colorectal Cancer by Administration of Curcumin. *Cancer Investig.* **2011**, *29*, 208–213. [CrossRef]
400. Ide, H.; Tokiwa, S.; Sakamaki, K.; Nishio, K.; Isotani, S.; Muto, S.; Hama, T.; Masuda, H.; Horie, S. Combined inhibitory effects of soy isoflavones and curcumin on the production of prostate-specific antigen. *Prostate* **2010**, *70*, 1127–1133. [CrossRef]
401. Dominiak, K.; McKinney, J.; Heilbrun, L.K.; Sarkar, F.H. Critical need for clinical trials: An example of a pilot human intervention trial of a mixture of natural agents protecting lymphocytes against TNF-alpha induced activation of NF-kappaB. *Pharm. Res.* **2010**, *27*, 1061–1065. [CrossRef]
402. Biswas, J.; Sinha, D.; Mukherjee, S.; Roy, S.; Siddiqi, M.; Roy, M. Curcumin protects DNA damage in a chronically arsenic-exposed population of West Bengal. *Hum. Exp. Toxicol.* **2010**, *29*, 513–524. [CrossRef]
403. Cruz-Correa, M.; Shoskes, D.A.; Sanchez, P.; Zhao, R.; Hyland, L.M.; Wexner, S.D.; Giardiello, F.M. Combination treatment with curcumin and quercetin of adenomas in familial adenomatous polyposis. *Clin. Gastroenterol. Hepatol.* **2006**, *4*, 1035–1038. [CrossRef]
404. Cheng, A.L.; Hsu, C.H.; Lin, J.K.; Hsu, M.M.; Ho, Y.F.; Shen, T.S.; Ko, J.Y.; Lin, J.T.; Lin, B.R.; Ming-Shiang, W.; et al. Phase I clinical trial of curcumin, a chemopreventive agent, in patients with high-risk or pre-malignant lesions. *Anticancer Res.* **2001**, *21*, 2895–2900.
405. Passildas-Jahanmohan, J.; Eymard, J.C.; Pouget, M.; Kwiatkowski, F.; Van Praagh, I.; Savareux, L.; Atger, M.; Durando, X.; Abrial, C.; Richard, D.; et al. Multicenter randomized phase II study comparing docetaxel plus curcumin versus docetaxel plus placebo in first-line treatment of metastatic castration-resistant prostate cancer. *Cancer Med.* **2021**, *10*, 2332–2340. [CrossRef]
406. Kishimoto, A.; Imaizumi, A.; Wada, H.; Yamakage, H.; Satoh-Asahara, N.; Hashimoto, T.; Hasegawa, K. Newly Developed Highly Bioavailable Curcumin Formulation, curcuRouge™, Reduces Neutrophil/Lymphocyte Ratio in the Elderly: A Double-Blind, Placebo-Controlled Clinical Trial. *J. Nutr. Sci. Vitaminol.* **2021**, *67*, 249–252. [CrossRef]

407. Shah, S.; Rath, H.; Sharma, G.; Senapati, S.; Mishra, E. Effectiveness of curcumin mouthwash on radiation-induced oral mucositis among head and neck cancer patients: A triple-blind, pilot randomised controlled trial. *Indian J. Dent. Res.* **2020**, *31*, 718–727. [CrossRef]
408. Hariri, M.; Gholami, A.; Mirhafez, S.R.; Bidkhorji, M.; Sahebkar, A. A pilot study of the effect of curcumin on epigenetic changes and DNA damage among patients with non-alcoholic fatty liver disease: A randomized, double-blind, placebo-controlled, clinical trial. *Complement. Ther. Med.* **2020**, *51*, 102447. [CrossRef]
409. Neetha, M.C.; Panchaksharappa, M.G.; Pattabhiramasasthy, S.; Shivaprasad, N.V.; Venkatesh, U.G. Chemopreventive Synergism between Green Tea Extract and Curcumin in Patients with Potentially Malignant Oral Disorders: A Double-blind, Randomized Preliminary Study. *J. Contemp. Dent. Pr.* **2020**, *21*, 521–531. [CrossRef]
410. Basak, S.K.; Bera, A.; Yoon, A.J.; Morselli, M.; Jeong, C.; Tosevska, A.; Dong, T.S.; Eklund, M.; Russ, E.; Nasser, H.; et al. A randomized, phase 1, placebo-controlled trial of APG-157 in oral cancer demonstrates systemic absorption and an inhibitory effect on cytokines and tumor-associated microbes. *Cancer* **2020**, *126*, 1668–1682. [CrossRef]
411. Saberi-Karimian, M.; Keshvari, M.; Ghayour-Mobarhan, M.; Salehizadeh, L.; Rahmani, S.; Behnam, B.; Jamialahmadi, T.; Asgary, S.; Sahebkar, A. Effects of curcuminoids on inflammatory status in patients with non-alcoholic fatty liver disease: A randomized controlled trial. *Complement. Ther. Med.* **2020**, *49*, 102322. [CrossRef] [PubMed]
412. Delavarian, Z.; Pakfetrat, A.; Ghazi, A.; Jaafari, M.R.; Homaei Shandiz, F.; Dalirsani, Z.; Mohammadpour, A.H.; Rahimi, H.R. Oral administration of nanomicelle curcumin in the prevention of radiotherapy-induced mucositis in head and neck cancers. *Spec. Care Dent.* **2019**, *39*, 166–172. [CrossRef] [PubMed]
413. Pastorelli, D.; Fabricio, A.S.C.; Giovanis, P.; D'Ippolito, S.; Fiduccia, P.; Soldà, C.; Buda, A.; Sperti, C.; Bardini, R.; Da Dalt, G.; et al. Phytosome complex of curcumin as complementary therapy of advanced pancreatic cancer improves safety and efficacy of gemcitabine: Results of a prospective phase II trial. *Pharmacol. Res.* **2018**, *132*, 72–79. [CrossRef] [PubMed]
414. Kuriakose, M.A.; Ramdas, K.; Dey, B.; Iyer, S.; Rajan, G.; Elango, K.K.; Suresh, A.; Ravindran, D.; Kumar, R.R.; Prathiba, R.; et al. A Randomized Double-Blind Placebo-Controlled Phase IIB Trial of Curcumin in Oral Leukoplakia. *Cancer Prev. Res.* **2016**, *9*, 683–691. [CrossRef]
415. Li, X.; Xing, L.; Zhang, Y.; Xie, P.; Zhu, W.; Meng, X.; Wang, Y.; Kong, L.; Zhao, H.; Yu, J. Phase II Trial of Epigallocatechin-3-Gallate in Acute Radiation-Induced Esophagitis for Esophagus Cancer. *J. Med. Food* **2020**, *23*, 43–49. [CrossRef]
416. Hu, Y.; McIntosh, G.H.; Le Leu, R.K.; Somashekar, R.; Meng, X.Q.; Gopalsamy, G.; Bambaca, L.; McKinnon, R.A.; Young, G.P. Supplementation with Brazil nuts and green tea extract regulates targeted biomarkers related to colorectal cancer risk in humans. *Br. J. Nutr.* **2016**, *116*, 1901–1911. [CrossRef]
417. Kumar, N.B.; Pow-Sang, J.; Egan, K.M.; Spiess, P.E.; Dickinson, S.; Salup, R.; Helal, M.; McLarty, J.; Williams, C.R.; Schreiber, F.; et al. Randomized, Placebo-Controlled Trial of Green Tea Catechins for Prostate Cancer Prevention. *Cancer Prev. Res.* **2015**, *8*, 879–887. [CrossRef]
418. Shanafelt, T.D.; Call, T.G.; Zent, C.S.; Leis, J.F.; LaPlant, B.; Bowen, D.A.; Roos, M.; Laumann, K.; Ghosh, A.K.; Lesnick, C.; et al. Phase 2 trial of daily, oral Polyphenon E in patients with asymptomatic, Rai stage 0 to II chronic lymphocytic leukemia. *Cancer* **2013**, *119*, 363–370. [CrossRef]
419. D'Arena, G.; Simeon, V.; De Martino, L.; Statuto, T.; D'Auria, F.; Volpe, S.; Deaglio, S.; Maidecchi, A.; Mattoli, L.; Mercati, V.; et al. Regulatory T-cell modulation by green tea in chronic lymphocytic leukemia. *Int. J. Immunopathol. Pharm.* **2013**, *26*, 117–125. [CrossRef]
420. Domingo, D.S.; Camouse, M.M.; Hsia, A.H.; Matsui, M.; Maes, D.; Ward, N.L.; Cooper, K.D.; Baron, E.D. Anti-angiogenic effects of epigallocatechin-3-gallate in human skin. *Int. J. Clin. Exp. Pathol.* **2010**, *3*, 705–709.
421. McLarty, J.; Bigelow, R.L.H.; Smith, M.; Elmajian, D.; Ankem, M.; Cardelli, J.A. Tea Polyphenols Decrease Serum Levels of Prostate-Specific Antigen, Hepatocyte Growth Factor, and Vascular Endothelial Growth Factor in Prostate Cancer Patients and Inhibit Production of Hepatocyte Growth Factor and Vascular Endothelial Growth Factor In vitro. *Cancer Prev. Res.* **2009**, *2*, 673–682. [CrossRef]
422. Zwicker, J.I.; Schlechter, B.L.; Stopa, J.D.; Liebman, H.A.; Aggarwal, A.; Puligandla, M.; Caughey, T.; Bauer, K.A.; Kuemmerle, N.; Wong, E.; et al. Targeting protein disulfide isomerase with the flavonoid isoquercetin to improve hypercoagulability in advanced cancer. *JCI Insight* **2019**, *4*, e125851. [CrossRef]
423. Boots, A.W.; Drent, M.; de Boer, V.C.; Bast, A.; Haenen, G.R. Quercetin reduces markers of oxidative stress and inflammation in sarcoidosis. *Clin. Nutr.* **2011**, *30*, 506–512. [CrossRef]
424. Farsad-Naeimi, A.; Alizadeh, M.; Esfahani, A.; Darvish Aminabad, E. Effect of fisetin supplementation on inflammatory factors and matrix metalloproteinase enzymes in colorectal cancer patients. *Food Funct.* **2018**, *9*, 2025–2031. [CrossRef]
425. Kirwan, C.C.; Descamps, T.; Castle, J. Circulating tumour cells and hypercoagulability: A lethal relationship in metastatic breast cancer. *Clin. Transl. Oncol.* **2020**, *22*, 870–877. [CrossRef]
426. Vianello, F.; Sambado, L.; Goss, A.; Fabris, F.; Prandoni, P. Dabigatran antagonizes growth, cell-cycle progression, migration, and endothelial tube formation induced by thrombin in breast and glioblastoma cell lines. *Cancer Med.* **2016**, *5*, 2886–2898. [CrossRef]
427. Levitan, N.; Dowlati, A.; Remick, S.C.; Tahsildar, H.I.; Sivinski, L.D.; Beyth, R.; Rimm, A.A. Rates of initial and recurrent thromboembolic disease among patients with malignancy versus those without malignancy. Risk analysis using Medicare claims data. *Medicine* **1999**, *78*, 285–291. [CrossRef]



## Article

# Investigation on the Composition of Agarose–Collagen I Blended Hydrogels as Matrices for the Growth of Spheroids from Breast Cancer Cell Lines

Alessandra Quarta <sup>1,\*</sup> , Nunzia Gallo <sup>2</sup> , Daniele Vergara <sup>3</sup> , Luca Salvatore <sup>2</sup> , Concetta Nobile <sup>1</sup>,  
Andrea Ragusa <sup>1,3</sup>  and Antonio Gaballo <sup>1,\*</sup> 

<sup>1</sup> CNR Nanotec, Institute of Nanotechnology, via Monteroni, 73100 Lecce, Italy; concetta.nobile@nanotec.cnr.it (C.N.); andrea.ragusa@unisalento.it (A.R.)

<sup>2</sup> Department of Engineering for Innovation, University of Salento, via Monteroni, 73100 Lecce, Italy; nunzia.gallo@unisalento.it (N.G.); luca.salvatore@unisalento.it (L.S.)

<sup>3</sup> Department of Biological and Environmental Sciences and Technologies, University of Salento, via Monteroni, 73100 Lecce, Italy; daniele.vergara@unisalento.it

\* Correspondence: alessandra.quarta@nanotec.cnr.it (A.Q.); antonio.gaballo@nanotec.cnr.it (A.G.)

**Abstract:** Three-dimensional (3D) cell culture systems mimic the structural complexity of the tissue microenvironment and are gaining increasing importance as they resemble the extracellular matrix (ECM)–cell and cell–cell physical interactions occurring in vivo. Several scaffold-based culture systems have been already proposed as valuable tools for large-scale production of spheroids, but they often suffer of poor reproducibility or high costs of production. In this work, we present a reliable 3D culture system based on collagen I-blended agarose hydrogels and show how the variation in the agarose percentage affects the physical and mechanical properties of the resulting hydrogel. The influence of the different physical and mechanical properties of the blended hydrogels on the growth, size, morphology, and cell motility of the spheroids obtained by culturing three different breast cancer cell lines (MCF-7, MDA-MB-361, and MDA-MB-231) was also evaluated. As proof of concept, the cisplatin penetration and its cytotoxic effect on the tumor spheroids as function of the hydrogel stiffness were also investigated. Noteworthy, the possibility to recover the spheroids from the hydrogels for further processing and other biological studies has been considered. This feature, in addition to the ease of preparation, the lack of cross-linking chemistry and the high reproducibility, makes this hydrogel a reliable biomimetic matrix for the growth of 3D cell structures.

**Keywords:** spheroids; tumoroids; hydrogel; collagen; agarose; mammary spheroids; tissue engineering; breast cancer; cisplatin; cancer therapy

**Citation:** Quarta, A.; Gallo, N.; Vergara, D.; Salvatore, L.; Nobile, C.; Ragusa, A.; Gaballo, A. Investigation on the Composition of Agarose–Collagen I Blended Hydrogels as Matrices for the Growth of Spheroids from Breast Cancer Cell Lines. *Pharmaceutics* **2021**, *13*, 963. <https://doi.org/10.3390/pharmaceutics13070963>

Academic Editor: Hassan Bousbaa

Received: 19 May 2021

Accepted: 23 June 2021

Published: 26 June 2021

**Publisher's Note:** MDPI stays neutral with regard to jurisdictional claims in published maps and institutional affiliations.



**Copyright:** © 2021 by the authors. Licensee MDPI, Basel, Switzerland. This article is an open access article distributed under the terms and conditions of the Creative Commons Attribution (CC BY) license (<https://creativecommons.org/licenses/by/4.0/>).

## 1. Introduction

Three-dimensional (3D) cell culture models, such as multicellular spheroids and organoids, have been demonstrated to mimic several biological processes in vitro much better than monolayer cell cultures [1,2]. There are essentially two methods to produce uniform-size multicellular spheroids: scaffold free, in which cells are prevented from adhering to the substrate but not to each other, thus forming spheroids, and scaffold- or matrix-based, in which cells are embedded into a three-dimensional biomaterial, such as a hydrogel [3]. The latter has the advantage of providing a physical structure comparable, in terms of stiffness and viscoelasticity, to the in vivo extracellular matrix (ECM), thus being able to reproduce not only cell–cell interactions, but also cell–matrix interplays directly related to phenomena associated with cell growth (cell fate), such as cytoskeletal organization, gene expression, nutrients diffusion, pH, and hypoxia [4]. This makes matrix-based spheroids extremely important for studying solid tumors microenvironment and their response to drug treatments [5].

Among 3D biomaterials, hydrogels of complex biological origin have been used in many studies [6–8]. The most common are Matrigel™, derived from Engelbreth-Holm-Swarm mouse tumor sarcoma, and other basement membrane-rich matrices. These hydrogels contain matrix membrane proteins, hormones, and soluble growth factors whose composition may vary among different batches. This aspect limits severely their use because, although they allow for the growth of spheroids, the batch-to-batch variability can alter cell culture systems and experimental results. Thus, simpler hydrogels, without hormones and growth factors, able to maximize reproducibility and offering the possibility to tune biochemical as well as mechanical properties, have been considered for growing spheroids. Hydrogels with these features are made of natural, synthetic, or hybrid materials, such as alginate, agarose, collagen, hyaluronic acid, and polyethylene glycol [1,9].

Among them, agarose is an inert, inexpensive, and easily available linear polysaccharide derived from red marine algae and consisting of alternating units of D-galactose and 3,6-anhydro- $\alpha$ -L-galactopyranose joined by  $\alpha$ -1,3- and  $\beta$ -1,4-linkages. It possesses excellent biocompatibility, optimal gelling features, and tuneable mechanical properties that boosted its use as biomaterial for the manufacturing of tissue engineering scaffolds [10,11]. In addition, thanks to the ease of preparation, it has been recently exploited as non-adhesive and micromolded substrate for the growth of tumor spheroids based on multicellular aggregation [12,13]. Nevertheless, due to its poor bioadhesivity, its use as ECM-mimicking material is very limited.

On the other hand, type I collagen is the main protein component of the ECM in mammals. The presence of cellular binding sites (e.g., the “RGD” and “GxOGER” sequence, where “R” is arginine, “G” is glycine, “D” is aspartate, “O” is hydroxyproline, “E” is glutamate, and “x” is a hydrophobic amino acid) that promote cell adhesion, proliferation, and signalling makes collagen highly bioactive and suitable for the development of biocompatible hydrogels [14–17]. In addition, collagen plays a crucial role in tumor progression and invasion [18]. Nevertheless, it suffers of poor mechanical properties, limited stability over time, and high costs [19]. In this sense, blended hydrogels composed of agarose and collagen combine the mechanical properties of the former and the biomimetic nature of the latter.

As far as we know, only one study described the use of hydrogels containing agarose and collagen, as well as alginate, as matrices for producing tumor spheroids and their viability was monitored up to 14 days [20]. In addition, two studies described the use of agarose–collagen blended hydrogels to unravel the effects of biophysical cues on cellular mechanobiology of 2D intervertebral disc cells [21] and previously prepared glioblastoma spheroids [22]. Both works highlighted the crucial role of the hydrogel stiffness and adhesivity as driving forces that modulate the cell plasticity and connect the biological functionality to the surrounding physical stimuli. In living tissues, the stiffness ranges from few tens of Pa in intestinal mucus to GPa in bones, and variations of the mechanical properties are typically associated with cancer development and other diseases [23]. In the case of breast cancer, the stiffness has been shown to increase from hundreds of Pa to a few kPa when the normal tissue undergoes tumor transformation, due to the remodeling of the ECM [24].

Therefore, artificial matrices mimicking the physical properties of the naïve tumor environment can facilitate the study of the behaviour of 3D tumors *in vitro* and predict their response to modifications of the mechanical cues or to drug treatments, as it occurs during cancer progression and metastasis [4].

In this work, we developed collagen hydrogels blended with variable amounts of agarose (from 0.5% to 0.125%) and we investigated the possibility to grow within them tumor spheroids of three different breast cancer cell lines, i.e., the luminal estrogen receptor positive cells, MCF-7 and MDA-MB-361, and the triple negative model, MDA-MB-231. The physical properties of the matrices were analyzed in detail and the morphological characteristics of the spheroids were correlated over time to the hydrogel features. Prelim-

inary drug testing studies with cisplatin and the possibility to recover the spheroids for additional studies were also evaluated.

## 2. Materials and Methods

Soluble type I collagen from calf skin was purchased from Symatase (Chaponost, France). Agarose,  $\beta$ -agarase from *Pseudomonas atlantica*, FITC-labeled hyaluronic acid, transferrin-TRITC, cisplatin, Dulbecco's Modified Eagle Medium high glucose (DMEM), fetal bovine serum (FBS), penicillin and streptomycin were purchased from Sigma–Aldrich (Milan, Italy). Live/dead assay and MitoTracker Red CMXRos were purchased from Thermo Fisher (Rodano, Italy). Ultrapure grade water with a conductivity of 18.2 M $\Omega$  cm was used in all experiments. All chemicals were used as received.

### 2.1. Preparation of the Hydrogels

Agarose was dissolved in sterile phosphate-buffered saline (PBS, pH 7.4) to obtain a 1% (*w/v*) stock solution by heating on a hot plate. An aqueous suspension of 0.1% (*w/v*) type I collagen was obtained by slowly hydrating collagen flakes in distilled water for 3 h, under magnetic stirring at 4 °C. The blended hydrogels were prepared inside the wells of a 24 well plate, and each well was loaded to a final volume of 1 mL. In detail, the warm agarose solution (at around 45 °C, the gel point is at 36 °C) was added to the collagen suspension to obtain 3 different final concentrations, 0.5%, 0.25%, and 0.125%. The starting collagen solution was always diluted to 0.02% in the final blend. The mixture in each well was gently stirred with a glass rod and allowed to gel at room temperature. The gelation time varied from 30 s, in the case of hydrogels containing 0.5% agarose, up to 10 min, for those with 0.125% agarose. The gelation time was longer (up to 20 min) when the cells were embedded into the hydrogel, as all the preparation steps were carried out at 37 °C. All the glassware was sterilized in an autoclave before use, and the preparation of the hydrogels was carried out under a laminar flow hood. The preparation scheme is summarized in Figure S1.

### 2.2. Characterization of the Hydrogels

#### 2.2.1. Scanning Electron Microscopy (SEM)

Surface morphology and porosity of the hydrogels were investigated by using SEM imaging techniques. SEM images were recorded with a Carl Zeiss–Merlin field emission scanning electron microscope (Carl Zeiss, Oberkochen, Germany) equipped with a Gemini column and integrated with high efficiency in-lens and SE2 detectors, for high spatial/depth-of-field resolution secondary electrons (SE) imaging of surface structure and topography. The microscope was used in high vacuum and high-resolution acquisition mode and the images were recorded at an accelerating voltage of 5 kV and a few seconds frame-integration time, in order to minimize charging effects and sample damage. The hydrogels were cut, frozen, and lyophilized before imaging. The pore size was determined by measuring 50 random pores followed by statistical analysis using ImageJ software (NIH, Bethesda, MD, USA).

#### 2.2.2. Stability Test

The analysis was carried out keeping the hydrogels at 37 °C either in PBS or DMEM, and the samples were weighted at determined time points (up to 14 days). The stability of the hydrogels was then calculated as residual weight percentage:

$$Rw\% = \frac{w - w_0}{w_0} \times 100\%$$

where  $w_0$  is the starting weight of the hydrogel at  $t = 0$ , and  $w$  is the weight at each time point.



### 2.2.3. Swelling Behavior

The swelling property of the hydrogels was determined by using a conventional gravimetric method [25]. Briefly, the dry weight of hydrogels was recorded before soaking them in PBS at 37 °C. The swelled weight of hydrogels was then measured at various time points, up to 48 h. The swelling behaviour was estimated as the percentage of the swelling ratio using the following equation:

$$Sr\% = \frac{w_s - w_d}{w_d} \times 100\%$$

where  $w_d$  is the dry weight of the hydrogel and  $w_s$  is the wet weight after hydration in PBS.

### 2.2.4. Collagen Release

The agarose–collagen (A-C) hydrogels were kept in PBS at 37 °C and the volume of buffer (equal to 1 mL) was collected at determined time intervals to estimate the protein content via bicinchoninic acid (BCA) assay [26]. A calibration curve was set using collagen solutions at known concentrations. For each time interval, a blank sample (i.e., the PBS collected from agarose hydrogels prepared without collagen) was also measured.

### 2.2.5. Fourier-Transform Infrared (FTIR) Spectroscopy

FT-IR spectra were recorded in transmittance mode on a Jasco 6300 spectrometer (Jasco Corp., Tokyo, Japan) between 4000 and 500  $\text{cm}^{-1}$  with 40 scans and a resolution of 4  $\text{cm}^{-1}$  and analyzed with the Spectra Manager software (Jasco). The measurements were performed by directly depositing the hydrogels onto the ATR crystal. The spectrum of each sample was acquired against a background obtained with the crystal without any sample. All analyses were carried out at room temperature.

### 2.2.6. Mechanical Compression Test

The effect of the agarose concentration on the Young's modulus of the A-C hydrogels was evaluated by uniaxial compression test. The correlation with time and temperature was also investigated. Briefly, the samples were incubated in PBS at 37 °C in a humidified atmosphere with 5%  $\text{CO}_2$ . Cylinders of 8 mm were punched out and loaded into the testing chamber at fixed time points (0, 1, 4, and 8 days). All tests were performed with a universal ZwickiLine (Zwick Roell, Ulm, Germany) testing machine fitted with 10 N load cell. Loaded samples were hydrated in PBS at 37 °C and subjected to compression with a displacement rate of 0.01 mm/s, until 80% strain [27,28]. The compressive modulus was calculated by linear fitting between 2% and 10% of strain of the stress-strain curve. The test was performed in triplicate for each sample type and time point.

### 2.2.7. Diffusion Test

PBS solutions containing either FITC-labeled hyaluronic acid (10 kDa molecular weight) or transferrin-TRITC (80 kDa molecular weight) at known concentration were prepared and deposited over the A-C hydrogels. The photoluminescence signal of the loaded solutions was recorded over time and the resulting concentration was extrapolated from the calibration curve of the corresponding standard staining solution. The diffusivity of the two molecules within the hydrogels was assessed determining the ratio between the concentration of the fluorescent molecule (either hyaluronic acid or transferrin) at the analyzed time point and that measured in free PBS.

### 2.2.8. Drug Diffusion Test

1 mL of cisplatin solution (100  $\mu\text{M}$  in PBS) was loaded above 1 mL of either 0.25–0.02% or 0.125–0.025% A-C hydrogels. Five time points (1, 2, 4, 8, and 24 h) were set and three duplicates for each time point and type of hydrogel were defined. The hydrogels were incubated at 37 °C. The cisplatin solution was withdrawn at the determined time points and the hydrogel was frozen before being lyophilized. Soon after, the samples were digested

overnight in 65% nitric acid and the amount of Pt was estimated via elemental analysis using an Inductively Coupled Plasma Atomic Emission Spectrometer (ICP-AES) Varian 720-ES (Santa Clara, CA, USA).

### 2.3. Tumor Spheroid Preparation and Characterization

Human tumor cells were purchased from the American Type Culture Collection (ATCC). The human breast cancer cell lines, i.e., MCF-7, MDA-MB-361, and MDA-MB-231, and the human neuroblastoma SH-SY5Y cells were cultured as 2D monolayers in DMEM medium (4500 mg/L glucose) supplemented with 10% FBS, 100 U/mL penicillin, and 100 µg/mL streptomycin at 37 °C in an atmosphere of 5% CO<sub>2</sub>.

The cells were trypsinized, counted and added to the hydrogels at a density of  $2.5 \times 10^4$  cells/mL in complete growth medium. The cell suspension containing agarose and collagen was let to gel into the well plate. As an example, to prepare 1 mL of 0.25–0.02% A-C hydrogel, 250 µL of 1% agarose solution in PBS was added to 750 µL of a cellular suspension containing 200 µL of 0.1% collagen solution. After gelation, 1 mL of DMEM was added over the cell-embedded hydrogels before transferring the plate into the incubator. The medium was changed every 4 days.

### Morphological Analysis of the Tumor Spheroids

The morphological characteristics of spheroids, including their diameter and shape, were determined by optical analysis using a EVOS XL Cell Imaging System microscope (Thermo Fisher, Waltham, MA, USA). The progressively developing spheroids were observed at 24 h intervals. The mean diameter of the 3D structures was calculated by using ImageJ Software (1.48 v).

For the SEM imaging, the tumor spheroids embedded within the hydrogels were fixed overnight with glutaraldehyde (2.5%) in cacodylate buffer (0.1 M) at 4 °C. The fixed specimens were washed three times with PBS and then 1% osmium tetroxide in a cacodylate buffer was added. After 6 h, the samples were washed three times with PBS, cut and lyophilized. Finally, the as-prepared samples were transferred to the SEM microscope for imaging. The operating conditions of the microscope were the same as those used for imaging the hydrogels.

### 2.4. Cellular Assays

#### 2.4.1. Live/Dead Assay

Viability of spheroids was investigated by using a live/dead assay kit (Thermo Fisher Scientific Inc., Waltham, MA, USA). Briefly, the activity of intracellular esterase induces non-fluorescent, cell-permeant calcein acetoxymethyl ester to become fluorescent after hydrolysis, giving a green fluorescence to the viable spheroids. On the other hand, ethidium homodimer enters and binds to nucleic acids only into damaged cells, producing a red fluorescence that indicates dead cells. The assay was performed at three time points to monitor the viability of the spheroids during their growth. In detail, the medium was removed from the plates containing the spheroids-embedded hydrogels and the samples were washed twice with PBS. A phosphate buffer solution containing calcein and ethidium homodimer was then added, and the plate was kept in incubation at 37 °C for 1 h. Finally, the solution was replaced with fresh PBS before imaging the samples under a Fluorescence Microscope (EVOS FLoid Cell Imaging Station, ThermoFisher, Waltham, MA, USA).

#### 2.4.2. Mitochondria Toxicity Assay

MitoTracker Red from Life Technologies was dissolved in PBS and added to the hydrogel containing the spheroids at the 5th day of growth (working concentration: 250 nM). The samples were kept in incubation for 1 h at 37 °C and then imaged under a Fluorescence Microscope (EVOS FLoid Cell Imaging Station, ThermoFisher, Waltham, MA, USA).

#### 2.4.3. Cisplatin Treatment

MCF-7 spheroids were grown in 0.25–0.02% and 0.125–0.02% A-C hydrogels up to 12 days. A DMSO solution of cisplatin was then added to the spheroids-embedded hydrogels to reach a final concentration of 100  $\mu$ M. After 24 h incubation, the medium was removed and the hydrogels were carefully rinsed with fresh medium before performing the live/dead assay (ThermoFisher), as already reported.

#### 2.5. Immunofluorescence Microscopy Analysis

After 5 days of growth within the hydrogels, the spheroids were fixed with ice-cold 4% paraformaldehyde for 30 min. Then, the spheroids were washed twice with PBS and incubated overnight with a mouse anti-E-cadherin (E-cad; Santa Cruz, sc-8426) antibody, according to the manufacturer's protocol (1:1000 dilution in PBS). Subsequently, the samples were incubated with an anti-mouse Alexa Fluor 488 (AF488) conjugated secondary antibody (Cell Signaling). The images of fluorescently labeled proteins were captured using a fluorescence microscope (Leica LMD7000, Mannheim, Germany).

#### 2.6. Enzymatic Digestion of Agarose for Spheroids Recovery

0.25–0.02% and 0.125–0.02% A-C hydrogels containing MCF-7 spheroids at different days of growth were incubated with 40 U of  $\beta$ -agarase from *Pseudomonas atlantica* and incubated overnight at 37 °C. The supernatant was then collected and observed under an optical microscope to visualize the presence of floating spheroids. Soon after, the spheroids were fixed with 4% paraformaldehyde and stained with 4',6-diamidino-2-phenylindole (DAPI). The labeled structures were imaged under a fluorescence microscope (EVOS FLoid Cell Imaging Station, ThermoFisher, Waltham, MA, USA).

#### 2.7. Ultrastructural Analysis of the Recovered Spheroids

The spheroids recovered from the hydrogels were fixed with glutaraldehyde (2.5%) in cacodylate buffer (0.1 M) at 4 °C for 1 h. The fixed specimens were washed three times with the same buffer, and 1% osmium tetroxide in a cacodylate buffer was added for 1 h. The cells were then washed again and dehydrated with 25%, 50%, 75%, and 100% acetone. Two steps of infiltration in a mixture of resin/acetone (1/1 and 2/1 ratios) were performed, and then the specimens were embedded in 100% resin at 60 °C for 48 h. Ultrathin sections (70 nm thick) were cut with an Ultramicrotome and then stained with lead citrate. TEM images were recorded on a JEOL Jem1011 microscope operating at an accelerating voltage of 100 kV (Tokyo, Japan).

#### 2.8. Statistical Analysis

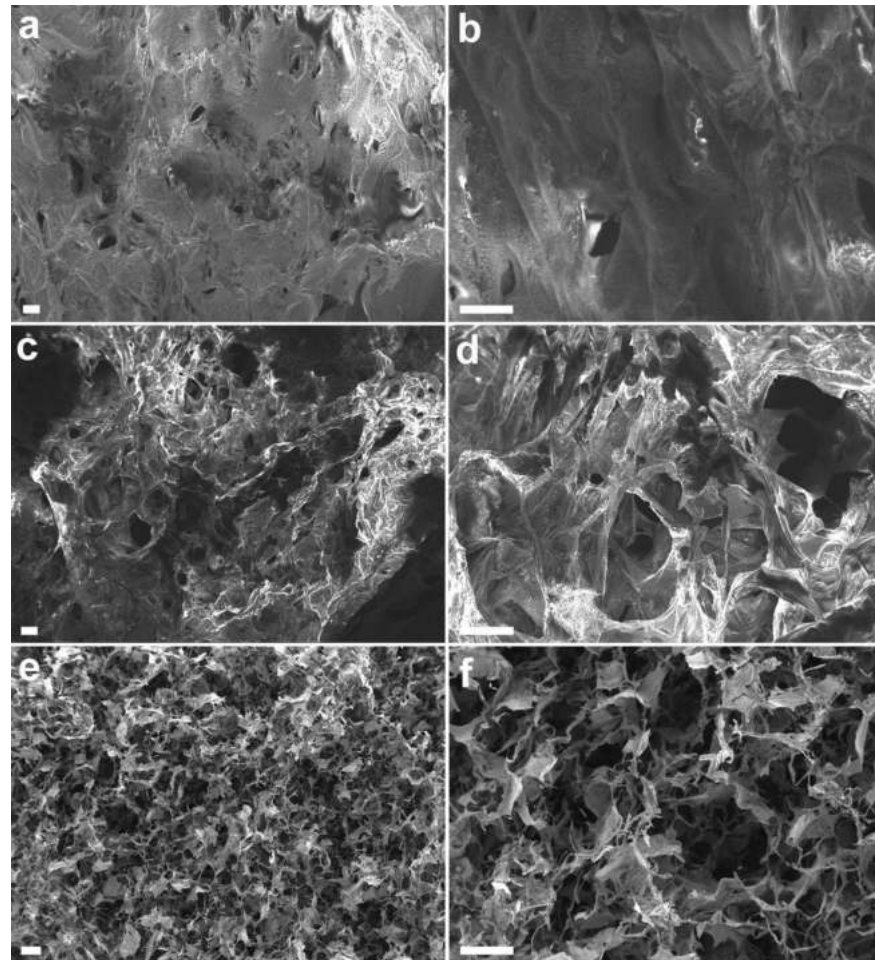
All data represent the average value of at least three independent experiments, unless otherwise specified. Normally distributed data was compared with a two-tailed Student's *t*-test.

### 3. Results

#### 3.1. Agarose–Collagen Hydrogels: Preparation and Characterization

Three agarose–collagen (A-C) hydrogels with different weight ratios were tested in this study. The collagen amount was kept constant to 0.02% in all the hydrogel formulations because it was already proven to be sufficient to provide enough anchoring sites to the embedded cells [22]. On the other hand, the amount of agarose, that confers the structural support, was varied from 0.5% to 0.125% to evaluate its impact on the biophysical properties of the hydrogel and, consequently, its effect on the cellular spheroids development. To prepare the hydrogels without denaturing the collagen and causing cell death, the agarose solution was first heated until boiling (100 °C) to dissolve the polysaccharide, and then cooled down to 45 °C. At this point, since gelation of pure agarose occurs at around 36 °C, it was rapidly mixed with collagen and the cell suspension (Figure S1).

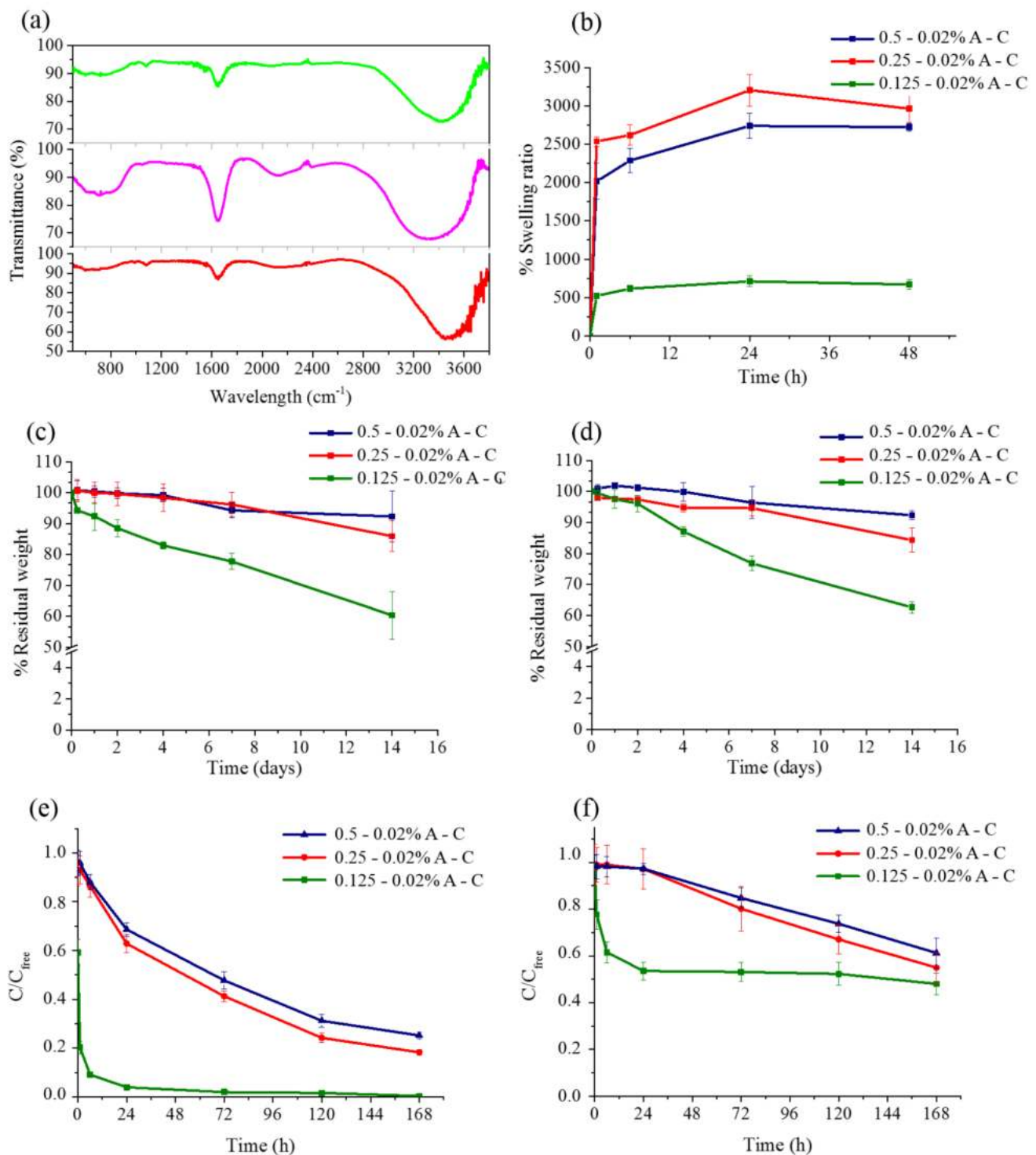
The SEM images of the resulting hydrogels showed that, by decreasing the agarose percentage, the porosity of the structure increases significantly, also appearing less compact (Figure 1).



**Figure 1.** SEM images at lower (a,c,e) and higher (b,d,f) magnification of the A-C hydrogels with different agarose concentration: (a,b) 0.5%; (c,d) 0.25%; (e,f) 0.125%, respectively. Type I collagen is always 0.02%. Scale bar is 100  $\mu\text{m}$ .

In fact, the higher percentage of water in the 0.125–0.02% A-C hydrogel makes the dry structure very brittle, displaying pores with a mean size of  $71 \pm 14 \mu\text{m}$  that are quite uniform and interconnected (Figure 1e,f). Although the measure of the pore size of a dry structure cannot be considered realistic, it still provides a good estimation of the 3D organization of the hydrogels. The number of pores is smaller in the 0.25–0.02% and 0.5–0.02% A-C hydrogels, while the average pore size appears to be slightly larger ( $81 \pm 21$  and  $87 \pm 25 \mu\text{m}$ , respectively, Figure 1a–d). The higher turgidity and compactness of the hydrogels with higher percentage of agarose is also evident at a macroscopic level, where the 0.25–0.02% and 0.5–0.02% A-C hydrogels appeared self-standing, while that with 0.125% agarose did not (bottom panel of Figure S1).

FTIR spectroscopy was performed on the hydrogels to investigate whether collagen, despite the low percentage amount used, was detectable on the outer surface of the hydrogels. To this aim, the analysis was performed directly on the synthesized hydrogels deposited on the ATR crystal, without any further manipulation (Figure 2a).



**Figure 2.** (a) FTIR spectra of agarose (green curve), collagen (pink curve), and 0.25–0.02% A-C (red curve) hydrogels. (b) Swelling behavior of the A-C hydrogels kept for 2 days in PBS at 37 °C. (c,d) Degradation curves up to 2 weeks of the A-C hydrogels either in PBS (c) or in DMEM (d). Diffusion tests performed up to one week with hyaluronic acid-FITC (e) and transferrin-TRITC (f).

Pure agarose hydrogel (0.25% *w/v*) was recorded as reference (light green line in Figure 2a), showing the typical signals at 988 and 1076 cm<sup>-1</sup>, relative to the C–H bending and to the C–O stretching of the glycosidic bonds, and two broad peaks at 1656 and 3421 cm<sup>-1</sup>, characteristic of the stretching of the H–O–H bound water and of the O–H hydrogen bonded carbohydrate hydroxylic groups, respectively [29]. Two broad peaks

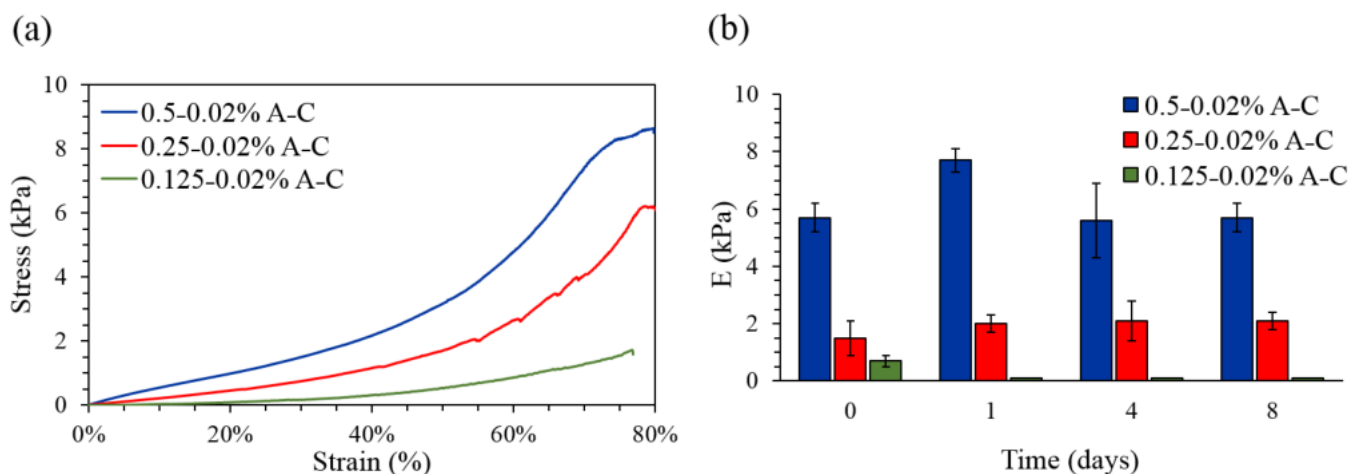
were also observed in the pure collagen hydrogel at about 3328 and 1645  $\text{cm}^{-1}$  for the amide C=O and N–H stretching, respectively (pink line in Figure 2a). Additional smaller signals were detected at 1051  $\text{cm}^{-1}$  for the C–OH stretching vibrations of carbohydrate moieties attached to the protein [30]. The FTIR spectrum of the blend 0.25–0.02% A–C hydrogel (red curve of Figure 2a) showed all the peaks characteristic of the pure compounds, i.e., smaller signals at 989 and 1079  $\text{cm}^{-1}$ , with a small side-bump at 1045  $\text{cm}^{-1}$ , and much broader peaks at 1649 and 3464  $\text{cm}^{-1}$ . Interestingly, while the last two peaks had similar intensity in pure collagen, a much higher intensity of the signal at lower frequencies was observed in pure agarose as well as in the blend hydrogel. As expected, no significant differences were observed in the spectra of the other two blend hydrogels (data not shown).

A critical feature of polymeric hydrogel is their capability to absorb and retain water, i.e., their swelling behavior. This property depends on many factors, such as network density, solvent used, and non-covalent interactions among all the components. In this case, the hydrogels containing 0.5% and 0.25% agarose showed a similar trend with a swelling ratio of about 20 and 25 times at  $t_0$  and a maximum swelling of about 27 and 30 times after 24 h in PBS, respectively (Figure 2b). These data are in accordance with those reported in the literature [31]. On the other hand, the ability to absorb water of the hydrogel with 0.125% agarose was considerably lower, with a swelling ratio of about 5 times at  $t_0$  and 7 after 24 h. Thus, there appears to be a critical threshold of agarose percentage below which the physical properties of the hydrogel are dramatically altered.

The stability over time of the three formulations was also investigated by measuring the percentage residual weight at 37 °C up to two weeks. The 0.5–0.02% and 0.25–0.02% A–C hydrogels were shown to be quite stable and lost around 10% and 15% of their weight after 14 days of incubation in PBS (Figure 2c) and DMEM (Figure 2d), respectively. On the other hand, the 0.125–0.02% A–C hydrogel showed a maximum of degradation close to 40% after 2 weeks in both incubation media. In parallel, the amount of collagen potentially released was estimated through the BCA assay (Figure S2). To this aim, the A–C hydrogels were kept in PBS at 37 °C and the volume of solvent collected and renewed every 24 h up to 14 days. Some collagen release was detected in all hydrogels, although to a higher extent and with a quicker trend in those with a lower agarose content. The overall percentage amount of collagen leaked after 2 weeks was equal to 50%, 27%, and 8% of the whole collagen present in the hydrogels containing 0.125%, 0.25%, and 0.5% agarose, respectively. This loss, together with the less compact texture of the 0.125–0.02% A–C hydrogel, would explain the higher degradation of this matrix.

A further parameter that deserves investigation is the capability of a hydrogel to allow the diffusion throughout the matrix of biomolecules and nutrients, such as growth factors and serum proteins having molecular weight of several tens of kDa. To this aim, a diffusion test was performed by using two fluorescent probes, FITC-conjugated hyaluronic acid and transferrin-TRITC, with a MW of around 10 and 80 kDa, respectively. Once loaded onto the three hydrogel formulations, the variation of concentration of the feeding solution was monitored over time and reported versus the diffusion in pure PBS. Hyaluronic acid diffused rapidly into the softest hydrogel, reaching 100% diffusion after 72 h (Figure 2e). The other two hydrogels performed similarly but with a more gradual diffusion that decreased by increasing the percentage of agarose, reaching a maximum of 82% and 75% after one week, respectively. On the other hand, transferrin-TRITC spread much more slowly, reaching after 24 h a diffusion value of almost 48% in the case of the 0.125–0.02% A–C hydrogel, while it was close to 10% in the case of the other two blends (Figure 2f). Noteworthy, after one week the diffusivity did not exceed 50% even in the softest matrix.

The structural properties of the A–C samples were also evaluated by mean of compression test under physiological-like conditions showing how the agarose concentration deeply affects the hydrogels' mechanical properties (Figure 3a).



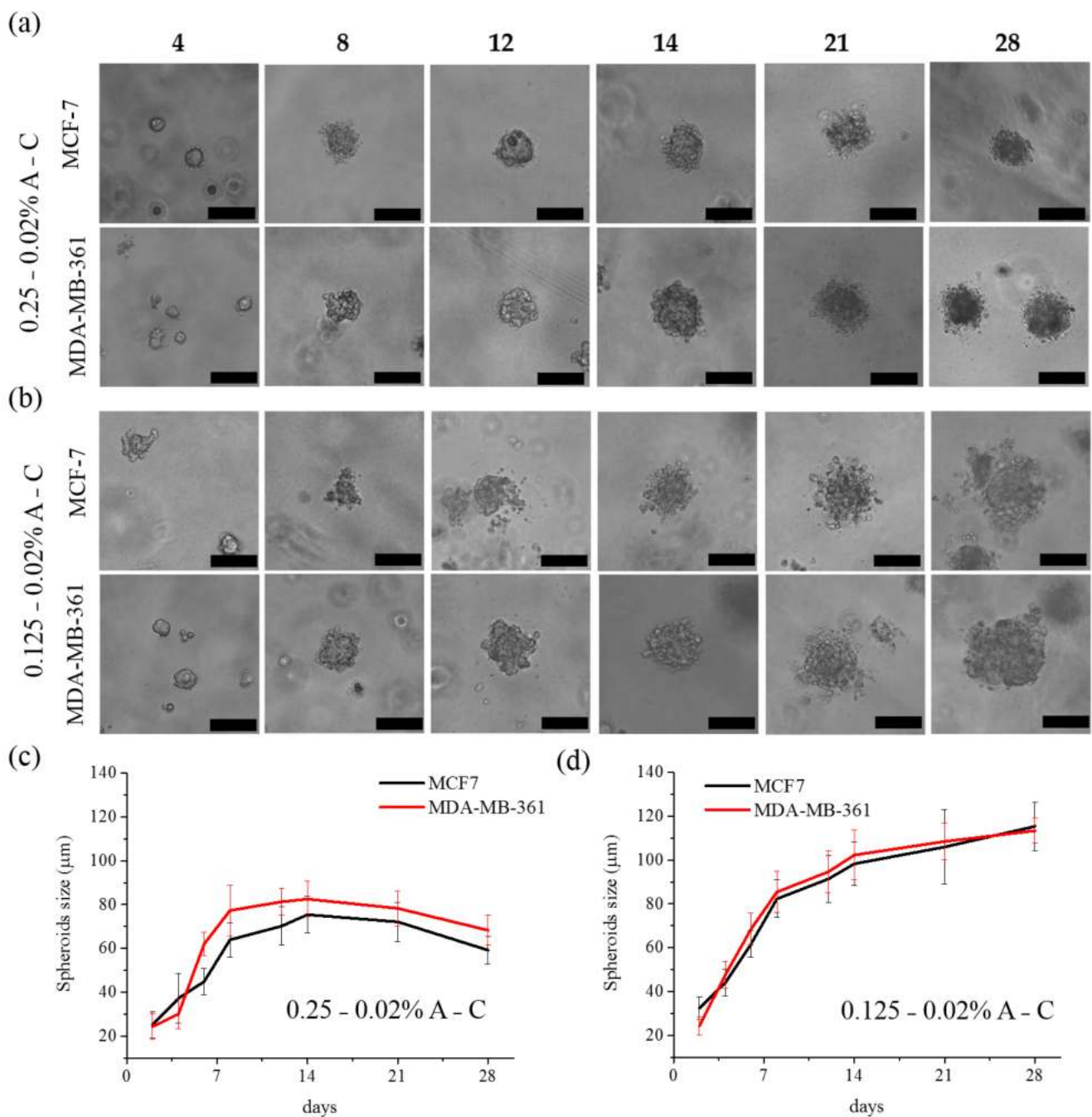
**Figure 3.** (a) Representative stress-strain curves of the A-C hydrogels subjected to unconfined compression with a displacement rate of 0.01 mm/s, until 80% strain. (b) Compressive moduli of the A-C hydrogels after 0, 1, 4, and 8 days of incubation in PBS at 37 °C, in humidified atmosphere with 5% CO<sub>2</sub>.

In fact, an increase in the agarose concentration corresponded to an increase in the compressibility modulus. As expected, the 0.5–0.02% ratio showed the highest E modulus ( $5.7 \pm 0.5$  kPa), followed by the 0.25–0.02% ( $1.6 \pm 0.4$  kPa) ( $p = 0.0004$ ) and the 0.125–0.02% ( $0.7 \pm 0.2$  kPa) ( $p = 0.0001$ ) ones. A minor but still significant difference was found between the 0.25–0.02% and the 0.125–0.02% ratios ( $p = 0.03$ ). In order to correlate degradation resistance to structural stability over time, the mechanical performances of the hydrogels were evaluated after 0, 1, 4, and 8 days of incubation in physiological-like conditions (PBS at pH 7.4, 37 °C, humidified atmosphere with 5% CO<sub>2</sub>). While the 0.125–0.02% hydrogel could not be tested over time due to its low consistence, the 0.5–0.02% and the 0.25–0.02% blends retained their structural integrity until the 8th day of measure. As shown in Figure 3b, no significant changes in the E modulus were registered in the case of the 0.5–0.02% and the 0.25–0.02% hydrogels. These data are in accordance with those obtained by the degradation tests, in which a minimum weight loss was recorded.

### 3.2. Growth of Mammary Spheroids in A-C Hydrogels

One of the major advantages of hydrogels is their ability to provide more realistic 3D models for in vitro studies. In this study, we generated mammary spheroids from three different breast cancer cell lines, i.e., two luminal estrogen receptor positive cells (MCF-7 and MDA-MB-361) and a triple negative model (MDA-MB-231) for comparative analysis. The cells were seeded at the density of  $2.5 \times 10^4$  per mL inside the three types of hydrogels and time course studies (up to 14 days) were performed to monitor the process of multicellular spheroid formation. MCF-7 and MDA-MB-361 successfully formed spheroids in all the three types of hydrogels. On the other hand, MDA-MB-231 cells replicated during the first days, but they were not able to reach a defined 3D organization, thus not forming spheroids in any of the hydrogel conditions (Figure S3). It is worth to report that no multicellular spheroid formation was observed by culturing the three cell lines in 0.02% pure collagen, while the spheroids started to grow in the case of pure agarose hydrogel, but they underwent senescence after few days (data not shown).

As reported, MCF-7 and MDA-MB-361 cells formed spheroids in the three blends, but the size and the morphology of the 3D structures were different depending on the experimental conditions. In particular, the spheroids grown in the stiffest hydrogel were spherical but smaller (Figure S4) than those grown in softer conditions (Figure 4), especially in the case of MDA-MB-361 cells.



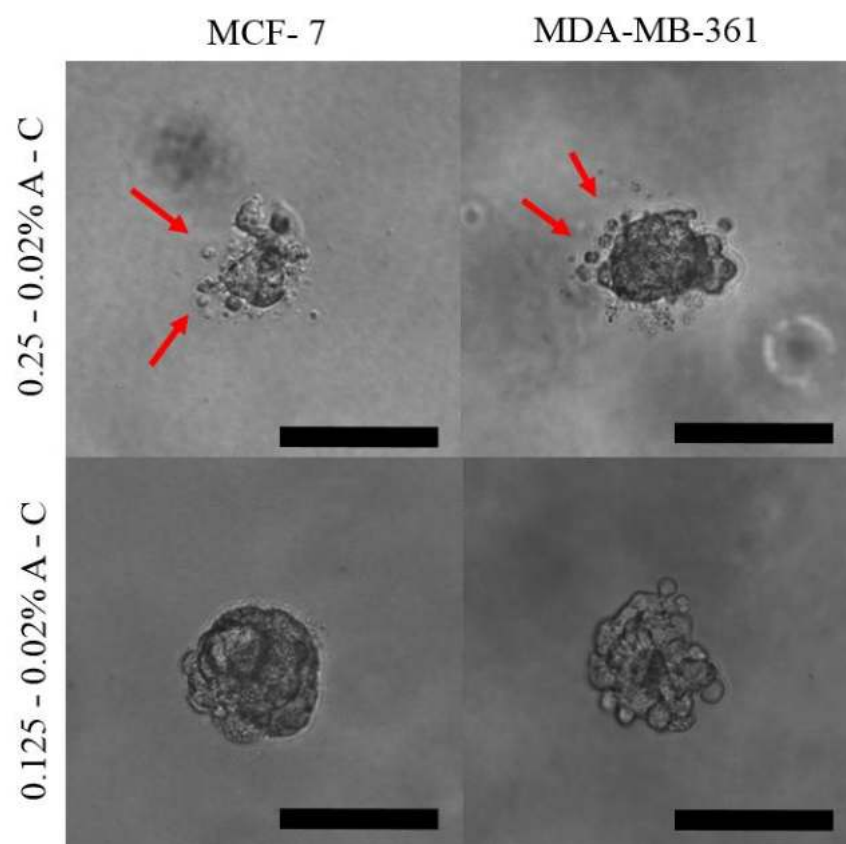
**Figure 4.** Optical images (a,b) and average size (c,d) of the spheroids obtained with MCF-7 and MDA-MB-361 cells grown up to 14 days either in 0.25–0.02% (a,c) or 0.125–0.02% (b,d) A-C hydrogels. Scale bar is 100  $\mu\text{m}$ .

This effect is more evident as the 3D structure progressively grows over time: the average size of MDA-MB-361 derived spheroids after 12 days grown in hydrogels with 0.5% agarose was around  $63.1 \pm 7.8 \mu\text{m}$ , while it reached  $81.3 \pm 6.3 \mu\text{m}$  and  $94.7 \pm 9.5 \mu\text{m}$  in 0.25–0.02% and 0.125–0.02% A-C hydrogels, respectively (Table S1). In the case of MCF-7 cells, the size gap was of about 7 and 27  $\mu\text{m}$  respectively, being the spheroids in the hydrogels with 0.5% agarose about 64  $\mu\text{m}$  large after 12 days, while they reached a diameter of about 70  $\mu\text{m}$  in the 0.25–0.02% A-C hydrogel and about 91  $\mu\text{m}$  in the softest one (Table S1). The images in Figure 4 clearly evidence how the 3D structures evolved over time from a single cell to more complex aggregates, but the growth curves showed that while the spheroids in the hydrogel with 0.25% agarose reached a growth plateau after 14 days, they still displayed a positive growth trend in the softest environment. In



fact, the spheroids in the softest matrix continued to grow exceeding the 100  $\mu\text{m}$  diameter in both cell lines after 28 days. On the other hand, the spheroids in the 0.25–0.02% A-C hydrogel stopped their growth and, after 2 weeks, they started to shrink and exhibited a dark intracellular substance. In this sense, it appears that the softest hydrogel is capable of sustaining the spheroids' growth for longer time although, especially in the case of MCF-7, they displayed irregular contours and looser structure [32,33]. As a general consideration, we observed that MCF-7 cells could tolerate stiffer environments as compared to MDA-MB-361, as confirmed by the fact that they also generated small spheroids in hydrogels with 1% agarose (Figure S5), while MDA-MB-361 did not.

In conclusion, the hydrogel stiffness and the matrix composition regulated the spheroids growth and morphology and, more interestingly, they affected the local migration of the outer cells. In fact, only the softest matrix was able to induce protrusion of cells from the outer layer and their local dissemination (Figure 5).



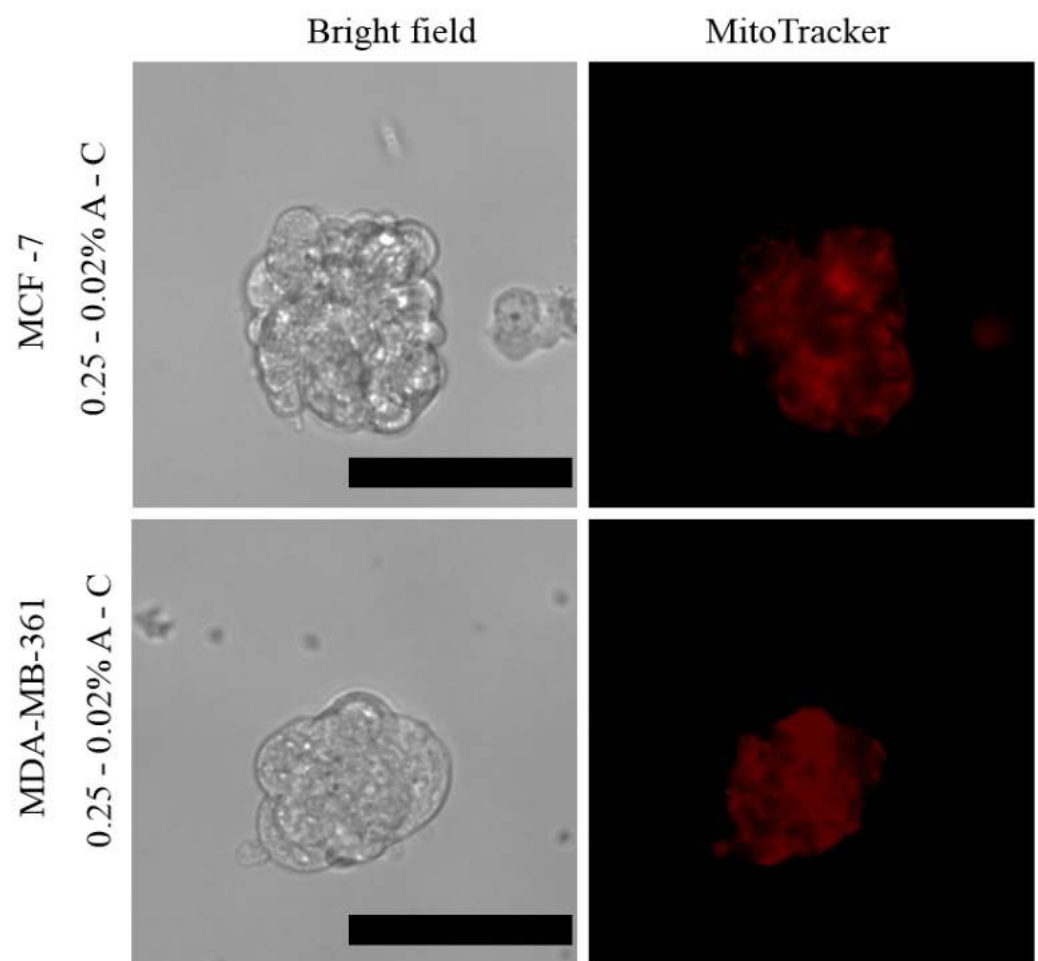
**Figure 5.** Optical images of the tumor spheroids obtained by MCF-7 and MDA-MB-361 cells after growing for 8 days in either 0.125–0.02% (**top**) or 0.25–0.02% A-C hydrogels (**bottom**). The red arrows point to the cells disseminated by the spheroids grown in the soft matrix. Scale bar is 100  $\mu\text{m}$ .

As already stated, the motility of these cells depends on the interaction with the microenvironment, mainly with collagen [21,34]. It is likely that the less dense hydrogel facilitates the protrusive behavior, also facilitating contact with the collagen anchoring points for the spatial dissemination of the cells. On the other hand, the reduced migration of the outer cells in the hydrogels with 0.25% agarose should be related to the tighter pressure that the matrix exerts on the cells, leading, as already described, to more compact spheroids.

Based on these observations and with the aim to study the effects of the mechanical features of the environment on the tumoroids features, the following analyses were carried out comparing the two conditions (0.25% and 0.125% agarose-based hydrogels) in which both cell lines were able to form healthy and stable spheroids up to two weeks.

### 3.3. Mammary Spheroids Viability and Epithelial Markers Expression

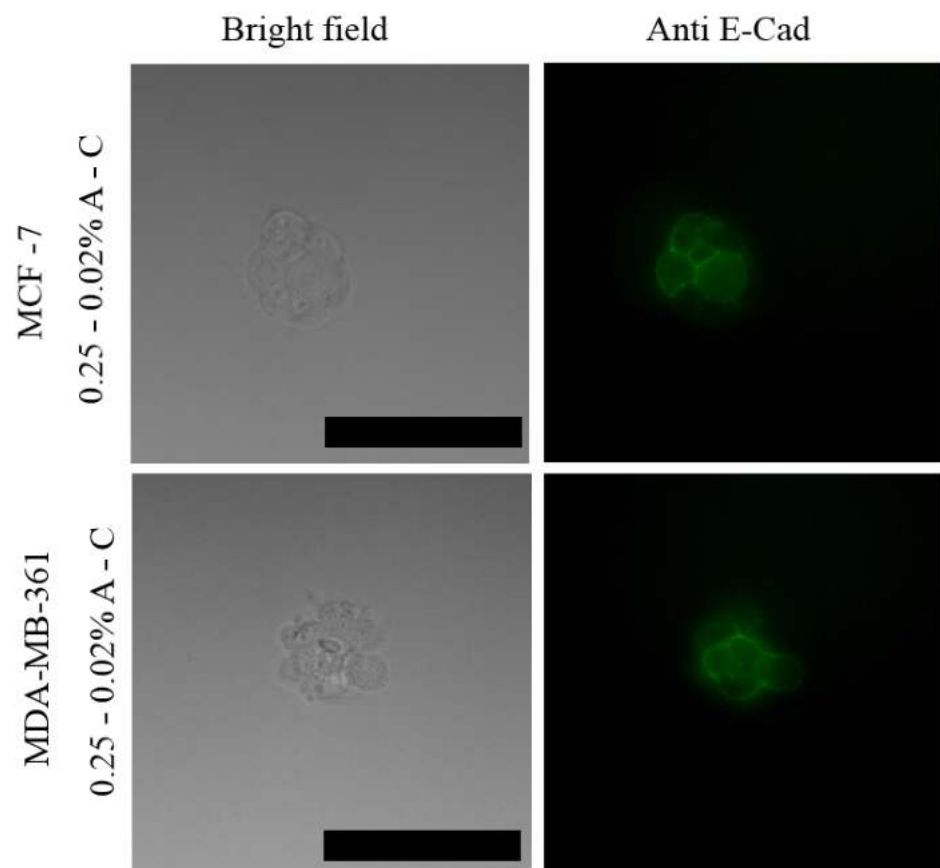
The viability of the spheroids obtained from the MCF-7 and MDA-MB-361 cell lines in both type of hydrogels was investigated through a live/dead fluorescence assay (Figure S6). The homogeneous green fluorescence evidenced that all the cells in the spheroids were viable after 8 days; while few red spots were already visible after 14 days in the 3D structure grown in the matrix with 0.25% agarose, showing their initial aging. On the other hand, the spheroids embedded in the 0.125–0.02% A-C hydrogel resulted absolutely viable. These data are in accordance with the previous analysis of the growth curves of the 3D structures in the two systems (Figure 4). To further confirm this trend, the assay was also performed after 28 days. Notably, while the spheroids grown in the 0.125% agarose-based hydrogels were still viable, those prepared in the stiffer matrix were dead. Furthermore, MitoTracker red, an indicator of mitochondrial membrane potential able to selectively stain active mitochondria, was used to gain information on the mitochondrial function (Figure 6).



**Figure 6.** Mitochondrial labeling with MitoTracker red of living spheroids of MCF-7 and MBA-MB-361 cells after 5 days of growth. Scale bar is 50  $\mu$ m.

MitoTracker staining showed the presence of active mitochondria in the periphery as well as in the center of the spheroids.

The expression of E-cadherin, a typical epithelial marker in 3D spheroids, was then determined by immunofluorescence, clearly showing that the mammary spheroids maintained the expression of the transmembrane glycoprotein and evidencing the presence of tight cell–cell interactions, both typical features of an epithelial phenotype (Figure 7). Similar results were obtained with the 0.125–0.02% A-C hydrogel for both MitoTracker and E-cadherin staining (data not shown).



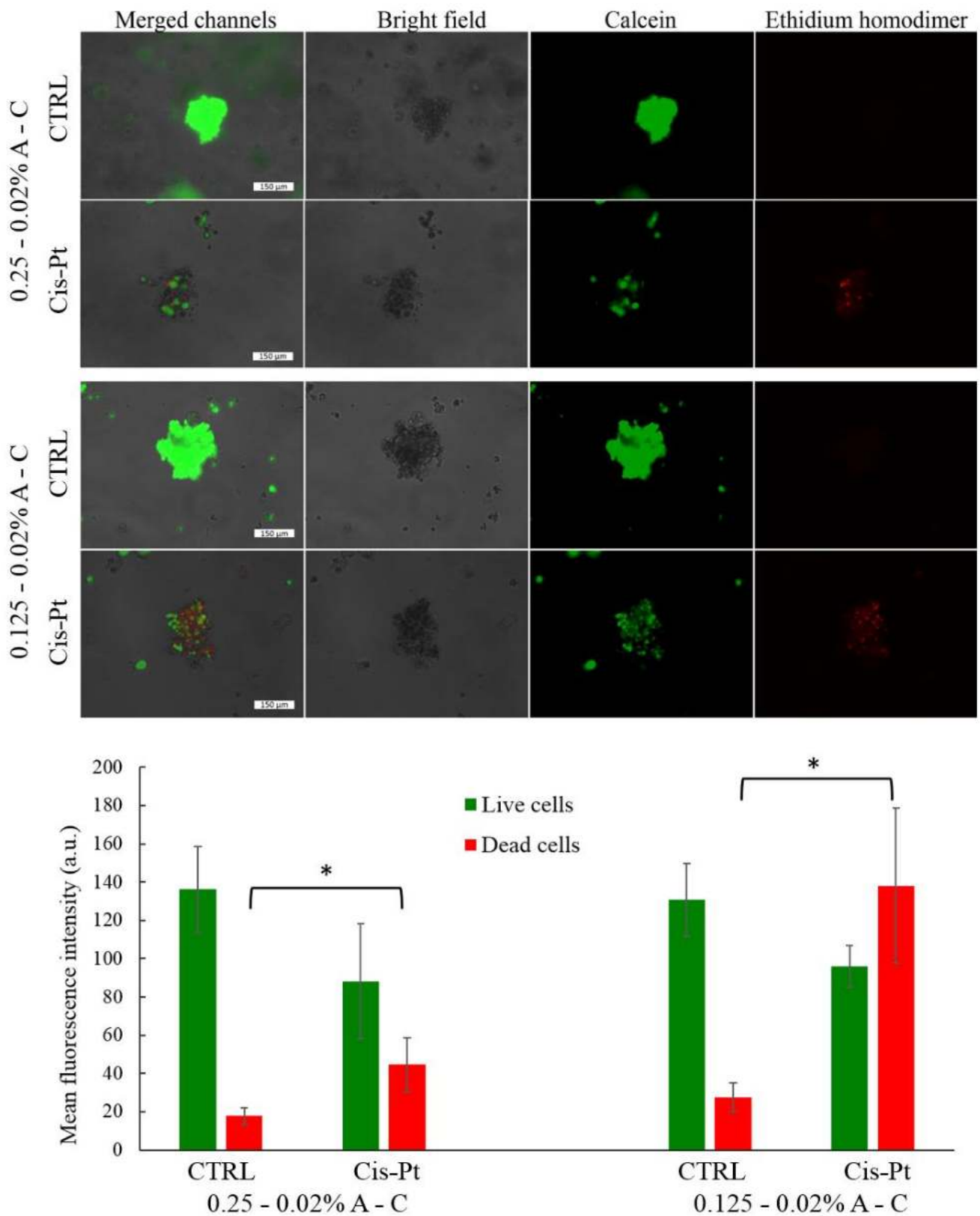
**Figure 7.** Staining of E-cadherin in cellular spheroids of MCF-7 and MBA-MB-361 after 5 days of growth in A-C hydrogels. Scale bars correspond to 58  $\mu\text{m}$ .

The morphology of the MCF-7 spheroids grown for 12 days and their arrangement into the 0.25–0.02% A-C hydrogel was also investigated by ultrastructural analysis, showing a 3D structure wrapped into the hydrogel matrix (Figure S7). The protrusion of the spheroids from the hydrogel can be clearly appreciated and they can be compared to cocoons anchored to a branch.

Overall, these data suggest that this type of hydrogel is a suitable approach for the generation and growth of mammary spheroids.

### 3.4. Cisplatin Delivery to the Embedded Spheroids

To evaluate the exploitation of these 3D systems as a drug-screening platform, the MCF-7 spheroids embedded either in the 0.25–0.02% or 0.125–0.02% A-C hydrogels were treated with 100  $\mu\text{M}$  cisplatin. This concentration was chosen in accordance with recently published studies in which the drug response of hydrogel-embedded spheroids was assayed [35–37]. In a preliminary experiment the diffusion time of cisplatin into the hydrogels (without the spheroids) was determined via elemental analysis. As shown in Figure S8, the drug diffusion was faster in the softer hydrogel, reaching a 100% rate (concentration at the equilibrium) already after 2 h incubation at 37  $^{\circ}\text{C}$ . In the case of the 0.25–0.02% A-C hydrogel, the maximum diffusion was detected after 8 h of incubation. Based on these findings the incubation time of the spheroids with the drug was set at 24 h. After drug treatment, the cell mortality was estimated by the live/dead assay: dead cells were detected in the hydrogels administered with cisplatin, while control samples were brightly green fluorescent (Figure 8).



**Figure 8.** Live/dead assay performed with the MCF-7 spheroids embedded into the 0.25–0.02% (a) and 0.125–0.02% A-C hydrogels (b) after 24 h incubation with 100  $\mu$ M cisplatin. (c) Mean fluorescent intensity detected in the 0.25–0.02% (left) and 0.125–0.02% (right) A-C hydrogels. Green bars correspond to the fluorescence signal of calcein, while red bars to ethidium homodimer, respectively. (\* indicates  $p < 0.01$  when comparing CTRL spheroids with cisplatin-treated spheroids in both types of hydrogel. Statistical significance was assessed by  $t$ -test).

The analysis of the distribution of the fluorescent pixels performed on 25 spheroids for each type of sample evidenced that the difference between the number of dead cells of the control and those of the drug-treated samples is statistically significant ( $p < 0.01$ ) (Figure 8, lower panel). This assay confirmed that the drug diffusion depends on the agarose percentage amount, as the number of dead cells was higher in the hydrogel containing 0.125% agarose. Interestingly, the structure of the spheroids was dramatically altered if the samples, after 24 h incubation with the drug, were kept in fresh medium for additional 5 days. A large number of dead cells detached from the spheroids and many cellular debris were scattered in the matrix, while small residues of the 3D structures were still visible (Figure S9). This effect was observed in both types of hydrogels after 5 days post drug treatment.

### 3.5. Enzymatic Digestion of Agarose for Spheroids Recovery

To evaluate the possibility to recover the spheroids from the hydrogels for additional processing and/or other biological studies, the blends with 0.25% and 0.125% agarose containing MCF-7 spheroids at different days of growth were incubated with  $\beta$ -agarase from *Pseudomonas atlantica* [38,39]. However, only the spheroids located in the outer layer of the 0.25–0.02% A-C hydrogel were recovered after overnight incubation at 37 °C with the enzyme (upper panels in Figure S10). Most of the hydrogel remained intact and the spheroids continued to grow inside it as in control hydrogels not treated with agarase. On the other hand, the overnight enzymatic treatment completely dissolved the hydrogel containing 0.125% agarose, and all the spheroids could be recovered (lower panels of Figure S10). Noteworthy, the stability test (Figure 2) already showed a higher degree of spontaneous degradation of the hydrogel with 0.125% agarose compared to that higher amount. Thus, the addition of agarase boosted the degradation process, leading to the complete dissolution of the softer matrix. The morphology of the spheroids collected from both types of hydrogels after agarase treatment was preserved even at different times of growth, up to 12 days (Figure S10). The vitality of the recovered spheroids was also confirmed by the live/dead assay (Figure S11) as well as by DAPI staining (Figure 9), showing their suitability for further processing and study. Only a few free individual cells could be observed, probably detached from the surface of the spheroids during the centrifugation steps required by the staining protocol.

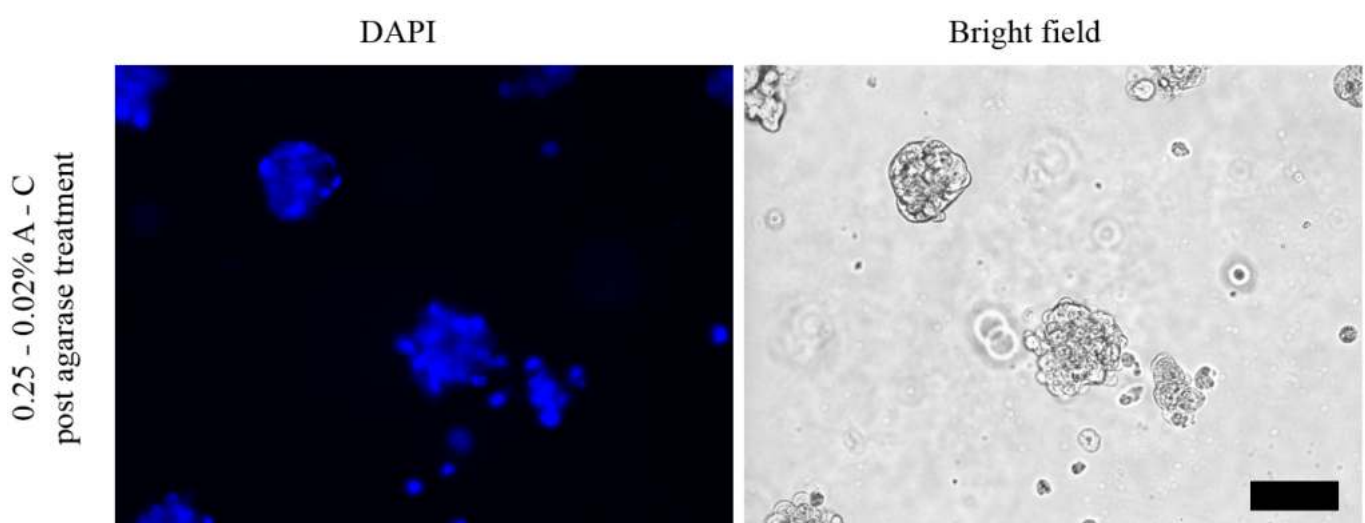
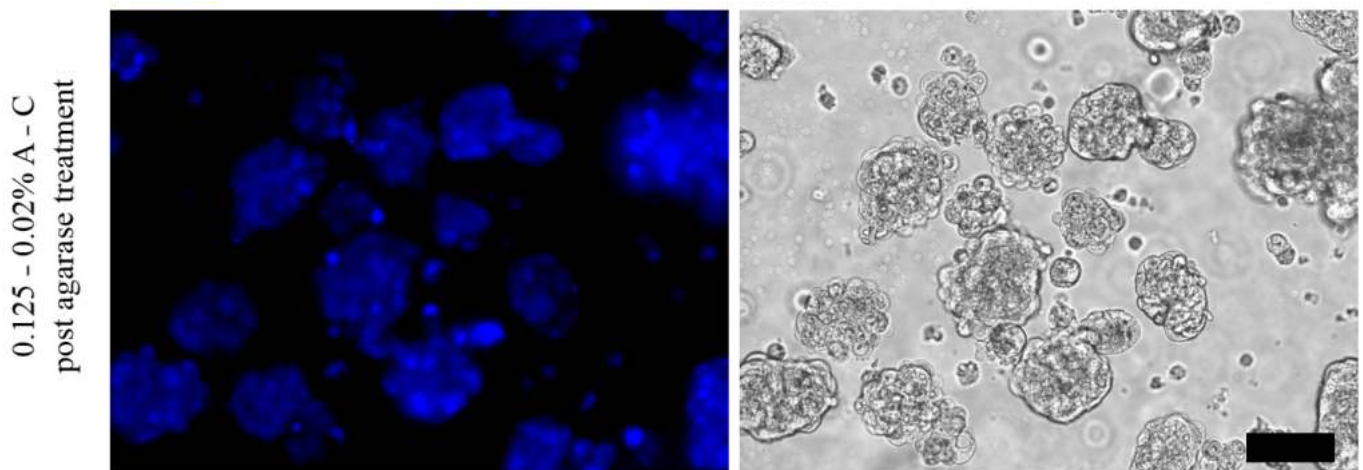


Figure 9. Cont.



**Figure 9.** Optical images of MCF-7 spheroids grown in the 0.25–0.02% (upper panels) and 0.125–0.02% (lower panels) A-C hydrogels, recovered after agarase treatment, fixed and stained with DAPI. Scale bars correspond to 100  $\mu\text{m}$ .

Nevertheless, the spheroids preserved their shape, morphology, and vitality characteristics, confirming their suitability for subsequent biological studies (Figure S11).

As proof of concept of the applicative potential of the recovered spheroids, they were processed for ultrastructural imaging. The TEM images of Figure S12 show neighbouring cells tightly connected through cellular junctions and cellular organelles typical of metabolically active cells.

#### 4. Discussion

In this work blended hydrogels composed of agarose (variable weight amount from 0.125% to 0.5%) and collagen (fixed weight amount equal to 0.02%) were prepared as enabling matrices for the growth of 3D cellular structures. These hydrogels combine the biomechanical properties of agarose and the bioadhesivity of collagen. The amount of collagen is 6.25-, 12.5-, and 25-times lower than that of agarose, and the formation of the hydrogel is probably to be ascribed mainly to agarose. In fact, although the self-assembling capability of collagen molecules *in vitro* under physiological conditions is well known, reconstituted collagen fibrils, that are held together by non-covalent interactions (hydrogen bonding, hydrophobic and electrostatic interactions) are free to slide and do not form a stable 3D network [40–42]. In addition, in preliminary experiments we have observed that collagen itself does not go into the gel state under the same experimental conditions we used to obtain the A-C hydrogels (data not shown). Thus, the gelation likely depends upon the formation of intra- and inter-molecular hydrogen bonds in the agarose backbone at a temperature lower than  $<40\text{ }^{\circ}\text{C}$ , as elsewhere reported [43].

Although agarose and collagen have already been used to prepare hydrogels, they still represent valuable candidates for creating and exploiting viable hydrogels because of their biocompatibility and low cost. More complex hydrogel composed of expensive polymers have been also developed for growing spheroids, but they suffer of limited availability and high costs of the products. Furthermore, it is worth reminding that agarose gelation does not require chemical crosslinking (whose residues would have effects on cell viability) and occurs at temperatures compatible with cell growing conditions.

Here we suppose that the A-C hydrogel formulations combine the mechanical support for 3D cell growth on the one hand, and the biomimetic component on the other. In this sense, agarose acts as the structural backbone of the matrix while collagen provides biological fingerprints for the growing 3D structures [20,32].

As expected, the characterization of the hydrogels evidenced that the agarose percentage governs the morphological, structural, and mechanical features of the matrix. Reasonably, the greater the amount of agarose, the stiffer the hydrogel resulted. On the other hand, the lowest agarose amount corresponded to the fastest hydrogel degradation

and diffusion of the molecules through the matrix. The higher degree of degradation of the softest hydrogel was also associated to a higher release of collagen. Thus, it can be expected that a less compact hydrogel facilitates the release of collagen, as determined by the protein quantification assay.

Similarly, the entry and movement of biomolecules through the blended hydrogels appears to be associated to the agarose percentage. The bigger the biomolecule and the stronger the type of non-covalent interactions it can establish with the matrix, the slower they are and the lesser the total amount of molecules that may reach the cells embedded into the matrix. In this sense, the hydrogel could act as a physical barrier to the diffusive transport of specific nutrients and drugs to the spheroid, similarly to what occurs *in vivo* [44].

The hydrogels were exploited for growing tumoroids from three breast cancer cell lines, namely MCF-7, MDA-MB-361, and MDA-MB-231 cells. However, while MCF-7 and MDA-MB-361 cells formed nice 3D structures, MDA-MB-231 cells, a triple negative breast cell line, did not organize into any three-dimensional arrangement, in accordance with previous findings [45,46], probably because of their lack of adherens junctions.

The spheroids generated by MCF-7 and MDA-MB-361 cells presented size and compactness strictly related to the stiffness of the surrounding matrix, and thus to the percentage of agarose. Apparently, both breast cancer cells prefer hydrogels with a stiffness from about 1.5 to 0.7 kPa, i.e., with a percentage of agarose equal or below 0.25%, while stiffer matrices, such as that with 0.5% agarose, did not result suitable to support the growth of the spheroids. A different tissue-specific tropism of the cellular models probably contributes to this result. In fact, MCF-7 cells have a low metastatic potential and are not tissue-specific, while MDA-MB-361 cells were derived from a brain metastasis and their growth on a softer hydrogel could match their *in vivo* metastatic microenvironment. With the intent to partially confirm this hypothesis, the 3D growth of a neural cell model was examined. SH-SY5Y neuroblastoma cells generated spheroids in the 0.125–0.02% A-C hydrogel, while in the stiffer matrix after a slow cellular duplication, the structures did not grow further over time (Figure S13). As a general remark, SH-SY5Y spheroids reached larger diameters ( $121.7 \pm 14.2 \mu\text{m}$ ) than those obtained with MCF-7 and MDA-MB-361 cells grown for 14 days in the same matrix (i.e.,  $98.3 \pm 10.0$  and  $101.3 \pm 11.4 \mu\text{m}$ , respectively), and this heterogeneity could be probably related to the different origin of the cell line.

The live/dead assay and the mitochondrial staining showed that the spheroids are viable up to 14 days in both types of hydrogels. Notably, the 3D cultures were monitored for up to one-month, evidencing a continued growth of the spheroids in the softer hydrogel, reaching an average size larger than 100  $\mu\text{m}$ . On the other hand, the spheroids in the 0.25–0.02% A-C hydrogel stopped their growth after 2 weeks, resulting completely dead after 4 weeks. This different behavior might be related to the tighter interactions between the cells and the surrounding environment as the 3D structures grow over time, i.e., the limited degradation and capability of the stiffer hydrogel to accommodate the spheroids induced their slow aging and death.

These results confirm that soft agarose–collagen hydrogels allow for long-term spheroid growth although cells derived from different tissues sense the change in stiffness of the substrate and significantly modify their behavior. In this respect, it has been shown that cells respond to ECM environment by regulating a plethora of transcription factors and other signals that affect cytoskeleton, cellular uptake, and cell cycle, that in turn determine their morphology, proliferation, differentiation, tumor invasion and metastasis [47–50]. Among them, it is worth mentioning the transmembrane glycoprotein E-cadherin that is expressed in epithelial cells and connect them through lateral adherent junctions. It has been demonstrated that the level of expression of E-cadherin represents a crucial feature in cancer progression as it is involved in the epithelial-mesenchymal transition [51]. Loss of E-cadherin expression is generally associated to a lack of intercellular contacts and to an increased tumor cell invasiveness through the activation of signaling pathways that regulate metastatic progression [52]. E-cadherin expression is also associated to the formation

of multicellular tumor spheroids, as already demonstrated [1]. Expression of E-cadherin was also observed in the spheroids derived from MCF-7 and MDA-MB-361 cells, as shown in Figure 7, confirming its importance in tumor development and progression, and the suitability of these spheroids for mimicking natural tissues. This was also demonstrated by successfully delivering a common chemotherapy drug, i.e., cisplatin, through the matrix.

In conclusion, as a general consideration from all the experiments performed, softer hydrogels allowed for the establishment of long-term culture of large and irregular breast tumor spheroids, while stiffer environmental conditions favored the growth of small and compact 3D cell structures viable for shorter periods (Figure S14). Finally, the possibility to recover the tumoroids was demonstrated by treating the hydrogels with agarase. The yield of the recovery process was quantitative and highly reproducible in the softest gel, that already underwent partial spontaneous degradation, while in the matrix with 0.25% agarose only a small percentage of 3D structures could be successfully recovered for additional biological and biomolecular studies.

## 5. Conclusions

A simple (no crosslinking steps are required), cost-effective, and highly reproducible method for the generation of tumor spheroids has been reported. The optical transparency of the matrix facilitates the daily monitoring of the cellular growth and the morphological variations due to drug testing. The procedure consists in wrapping individual tumor cells in agarose hydrogels (with either 0.25% or 0.125% weight percentage) blended with 0.02% collagen, where agarose reproduces the biomechanical features of the ECM, while collagen provides the anchoring sites for the membrane proteins. The growth of tumoroids deriving from three breast cancer cells lines was investigated in detail and compared. Interestingly, one cell line, MDA-MB-231 did not form spheroids in any of the conditions employed, while the other two lines, MCF-7 and MDA-MB-361, displayed quite similar behavior.

The variation in the agarose amount affected the physical and mechanical features of the resulting hydrogel and the growth of the spheroids. In fact, the stiffer the hydrogel, the more compact and slightly smaller the tumoroids resulted. Therefore, depending on the type of tumoroids to be prepared and studied, the composition of the hydrogel can be easily tuned. The growth of the spheroids was monitored for up to 2 weeks and the qualitative analysis of their viability evidenced few dead cells only after 14 days.

Preliminary studies of drug testing with cisplatin showed that the blended hydrogels allow for tracking the response of the spheroids to the drug administration. This aspect makes the system potentially useful for routine drug screening.

Finally, the degradability of the hydrogels upon enzymatic treatment was demonstrated, leading to complete recovery of the tumoroids in the case of the softest hydrogels, while to a partial recovery in the hydrogel with 0.25% agarose. The possibility to recover the spheroids is of a paramount importance as it enables further biomolecular studies on the collected samples, showing the full potential of this cheap and easily scalable biomimetic hydrogel.

**Supplementary Materials:** The following are available online at <https://www.mdpi.com/article/10.3390/pharmaceutics13070963/s1>, Figure S1: schematic drawing of hydrogels' preparation and pictures of the obtained hydrogels, Figure S2: BCA assay, Figure S3: optical images of MDA-MB-231 spheroids grown in the 0.25–0.02% A-C hydrogel after 2, 4, 6, and 8 days, Figure S4: optical images of MCF-7 and MDA-MB-361 spheroids grown in the 0.5–0.02% A-C hydrogel after 6, 8, and 12 days, Table S1: average size of the tumor spheroids after 12 days, Figure S5: optical images of MCF-7 spheroids grown in the 1–0.02% A-C hydrogel after 6, 8, and 12 days, Figure S6: live/dead assay performed with the cellular spheroids embedded into the A-C hydrogels at 8, 14, and 28 days, Figure S7: SEM images of MCF-7 spheroids embedded in the 0.25–0.02% A-C hydrogel after 12 days of growth, Figure S8: cisplatin diffusion in 0.25–0.02% and 0.125–0.02% A-C hydrogels estimated via elemental analysis, Figure S9: optical images of MCF-7 spheroids grown in 0.125–0.02% A-C hydrogel after 24 h cisplatin treatment and additional 5 days of incubation with fresh medium, Figure S10: optical images of MCF-7 spheroids grown in 0.25–0.02% and 0.125–0.02% A-C hydrogel and recovered



after incubation of the hydrogels with agarose, Figure S11: live/dead assay performed with the MCF-7 spheroids grown for 8 days in the 0.125–0.02% A-C hydrogel and recovered after agarose treatment, Figure S12: a–d) TEM images of MCF-7 spheroids grown for 8 days in the 0.125–0.02% A-C hydrogel, Figure S13: optical images of SH-SY5Y spheroids grown in the 0.125–0.02% and 0.25–0.02% A-C hydrogels up to 14 and 6 days, respectively, Figure S14: sketch depicting the effects over time of the hydrogel stiffness on the size and viability of breast tumor spheroids derived from MCF-7 and MDA-MB-361 cells.

**Author Contributions:** Conceptualization, A.Q. and A.G.; methodology, A.G., A.Q., A.R., L.S., N.G. and C.N.; validation, A.Q. and A.G.; formal analysis, A.R.; investigation, A.Q., A.G. and D.V.; resources, A.G., A.Q. and L.S.; data curation, A.Q., A.G., L.S. and N.G.; writing—original draft preparation, A.G. and A.Q.; writing—review and editing, A.G., A.Q., A.R. and D.V.; visualization, A.Q., A.G. and L.S.; supervision, A.Q., A.G., L.S., A.R. and D.V.; project administration, A.Q. and A.G.; funding acquisition, A.Q. and A.G. All authors have read and agreed to the published version of the manuscript.

**Funding:** This research was funded by the Italian project “Lab on a Swab” (cod. OTHZY54).

**Acknowledgments:** The authors would like to acknowledge the support of the following Italian projects: “Tecnopolo per la medicina di precisione” (TecnoMed Puglia)—Regione Puglia: DGR n. 2117 del 21/11/2018 (CUP: B84I18000540002), and “Tecnopolo di Nanotecnologia e Fotonica per la medicina di precisione” (TECNOMED)—FISR/MIUR-CNR: delibera CIPE n. 3449 del 7-08-2017 (CUP: B83B17000010001).

**Conflicts of Interest:** The authors declare no conflict of interest.

## References

- Cui, X.; Hartanto, Y.; Zhang, H. Advances in multicellular spheroids formation. *J. R. Soc. Interface* **2017**, *14*, 20160877. [CrossRef]
- Jensen, C.; Teng, Y. Is It Time to Start Transitioning From 2D to 3D Cell Culture? *Front. Mol. Biosci.* **2020**, *7*, 33. [CrossRef]
- Thakuri, P.S.; Liu, C.; Luker, G.D.; Tavana, H. Biomaterials-Based Approaches to Tumor Spheroid and Organoid Modeling. *Adv. Healthc. Mater.* **2018**, *7*, e1700980. [CrossRef] [PubMed]
- Singh, A.; Brito, I.; Lammerding, J. Beyond Tissue Stiffness and Bioadhesivity: Advanced Biomaterials to Model Tumor Microenvironments and Drug Resistance. *Trends Cancer* **2018**, *4*, 281–291. [CrossRef]
- Nath, S.; Devi, G.R. Three-dimensional culture systems in cancer research: Focus on tumor spheroid model. *Pharmacol. Ther.* **2016**, *163*, 94–108. [CrossRef] [PubMed]
- Athukorala, S.S.; Tran, T.S.; Balu, R.; Truong, V.K.; Chapman, J.; Dutta, N.K.; Roy Choudhury, N. 3D Printable Electrically Conductive Hydrogel Scaffolds for Biomedical Applications: A Review. *Polymers* **2021**, *13*, 474. [CrossRef] [PubMed]
- Zeshan, M.; Dilshad, M.R.; Islam, A.; Iqbal, S.S.; Akram, M.S.; Mehmood, F.; Gull, N.; Khan, R.U. Synergistic effect of silane cross-linker (APTEOS) on PVA/gelatin blend films for packaging applications. *High Perform. Polym.* **2021**, 0954008321994659. [CrossRef]
- Jiang, Z.; Liu, H.; He, H.; Ribbe, A.E.; Thayumanavan, S. Blended Assemblies of Amphiphilic Random and Block Copolymers for Tunable Encapsulation and Release of Hydrophobic Guest Molecules. *Macromolecules* **2020**, *53*, 2713–2723. [CrossRef]
- Teruki, N.; Kimiko, M.; Yasuhiko, T. Three-Dimensional Culture System of Cancer Cells Combined with Biomaterials for Drug Screening. *Cancers* **2020**, *12*, 2754. [CrossRef]
- Anderson, D.E.; Johnstone, B. Dynamic Mechanical Compression of Chondrocytes for Tissue Engineering: A Critical Review. *Front. Bioeng. Biotechnol.* **2017**, *5*, 76. [CrossRef] [PubMed]
- López-Marcial, G.R.; Zeng, A.Y.; Osuna, C.; Dennis, J.; García, J.M.; O’Connell, G.D. Agarose-Based Hydrogels as Suitable Bioprinting Materials for Tissue Engineering. *ACS Biomater. Sci. Eng.* **2018**, *4*, 3610–3616. [CrossRef]
- Tang, Y.; Liu, J.; Chen, Y. Agarose multi-wells for tumour spheroid formation and anti-cancer drug test. *Microelectron. Eng.* **2016**, *158*, 41–45. [CrossRef]
- Napolitano, A.P.; Dean, D.M.; Man, A.J.; Youssef, J.; Ho, D.N.; Rago, A.P.; Lech, M.P.; Morgan, J.R. Scaffold-free three-dimensional cell culture utilizing micromolded nonadhesive hydrogels. *Biotechniques* **2007**, *43*, 494–500. [CrossRef] [PubMed]
- Davidenko, N.; Schuster, C.F.; Bax, D.V.; Farndale, R.W.; Hamaia, S.; Best, S.M.; Cameron, R.E. Evaluation of cell binding to collagen and gelatin: A study of the effect of 2D and 3D architecture and surface chemistry. *J. Mater. Sci. Mater. Med.* **2016**, *27*, 148. [CrossRef] [PubMed]
- Davidenko, N.; Hamaia, S.; Bax, D.V.; Malcor, J.D.; Schuster, C.F.; Gullberg, D.; Farndale, R.W.; Best, S.M.; Cameron, R.E. Selecting the correct cellular model for assessing of the biological response of collagen-based biomaterials. *Acta Biomater.* **2018**, *65*, 88–101. [CrossRef] [PubMed]
- Hamaia, S.; Farndale, R.W. Integrin recognition motifs in the human collagens. *Adv. Exp. Med. Biol.* **2014**, *819*, 127–142. [CrossRef]
- Tibbitt, M.W.; Anseth, K.S. Hydrogels as extracellular matrix mimics for 3D cell culture. *Biotechnol. Bioeng.* **2009**, *103*, 655–663. [CrossRef]

18. Li, Y.; Kumacheva, E. Hydrogel microenvironments for cancer spheroid growth and drug screening. *Sci. Adv.* **2018**, *4*, eaas8998. [CrossRef]
19. Caliarì, S.R.; Burdick, J.A. A practical guide to hydrogels for cell culture. *Nat. Methods* **2016**, *13*, 405–414. [CrossRef]
20. Shin, S.; Ikram, M.; Subhan, F.; Kang, H.Y.; Lim, Y.; Lee, R.; Jin, S.; Jeong, Y.H.; Kwak, J.-Y.; Na, Y.-J.; et al. Alginate–marine collagen–agarose composite hydrogels as matrices for biomimetic 3D cell spheroid formation. *RSC Adv.* **2016**, *6*, 46952–46965. [CrossRef]
21. Cambria, E.; Brunner, S.; Heusser, S.; Fisch, P.; Hitzl, W.; Ferguson, S.J.; Wuertz-Kozak, K. Cell-Laden Agarose-Collagen Composite Hydrogels for Mechanotransduction Studies. *Front. Bioeng. Biotechnol.* **2020**, *8*, 346. [CrossRef]
22. Ulrich, T.A.; Jain, A.; Tanner, K.; MacKay, J.L.; Kumar, S. Probing cellular mechanobiology in three-dimensional culture with collagen-agarose matrices. *Biomaterials* **2010**, *31*, 1875–1884. [CrossRef]
23. Guimarães, C.F.; Gasperini, L.; Marques, A.P.; Reis, R.L. The stiffness of living tissues and its implications for tissue engineering. *Nat. Rev. Mater.* **2020**, *5*, 351–370. [CrossRef]
24. Butcher, D.T.; Alliston, T.; Weaver, V.M. A tense situation: Forcing tumour progression. *Nat. Rev. Cancer* **2009**, *9*, 108–122. [CrossRef]
25. Gallo, N.; Lunetti, P.; Bettini, S.; Barca, A.; Madaghiele, M.; Valli, L.; Capobianco, L.; Sannino, A.; Salvatore, L. Assessment of physico-chemical and biological properties of sericin-collagen substrates for PNS regeneration. *Int. J. Polym. Mater.* **2020**, *70*, 403–413. [CrossRef]
26. Terzi, A.; Storelli, E.; Bettini, S.; Sibillano, T.; Altamura, D.; Salvatore, L.; Madaghiele, M.; Romano, A.; Siliqi, D.; Ladisa, M.; et al. Effects of processing on structural, mechanical and biological properties of collagen-based substrates for regenerative medicine. *Sci. Rep.* **2018**, *8*, 1429. [CrossRef]
27. Gallo, L.C.; Madaghiele, M.; Salvatore, L.; Barca, A.; Scialla, S.; Bettini, S.; Valli, L.; Verri, T.; Bucalá, V.; Sannino, A. Integration of PLGA Microparticles in Collagen-Based Matrices: Tunable Scaffold Properties and Interaction Between Microparticles and Human Epithelial-Like Cells. *Int. J. Polym. Mater.* **2020**, *69*, 137–147. [CrossRef]
28. Monaco, G.; Cholas, R.; Salvatore, L.; Madaghiele, M.; Sannino, A. Sterilization of collagen scaffolds designed for peripheral nerve regeneration: Effect on microstructure, degradation and cellular colonization. *Mater. Sci. Eng. C Mater. Biol. Appl.* **2017**, *71*, 335–344. [CrossRef] [PubMed]
29. Oza, M.D.; Prasad, K.; Siddhanta, A.K. One-pot synthesis of fluorescent polysaccharides: Adenine grafted agarose and carageenan. *Carbohydr. Res.* **2012**, *357*, 23–31. [CrossRef] [PubMed]
30. Petibois, C.; Gouspillou, G.; Wehbe, K.; Delage, J.P.; Déléris, G. Analysis of type I and IV collagens by FT-IR spectroscopy and imaging for a molecular investigation of skeletal muscle connective tissue. *Anal. Bioanal. Chem.* **2006**, *386*, 1961–1966. [CrossRef] [PubMed]
31. Singh, Y.P.; Bhardwaj, N.; Mandal, B.B. Potential of Agarose/Silk Fibroin Blended Hydrogel for in Vitro Cartilage Tissue Engineering. *ACS Appl. Mater. Interfaces* **2016**, *8*, 21236–21249. [CrossRef]
32. Li, Y.; Khuu, N.; Prince, E.; Tao, H.; Zhang, N.; Chen, Z.; Gevorkian, A.; McGuigan, A.P.; Kumacheva, E. Matrix Stiffness-Regulated Growth of Breast Tumor Spheroids and Their Response to Chemotherapy. *Biomacromolecules* **2021**, *22*, 419–429. [CrossRef]
33. Kalli, M.; Stylianopoulos, T. Defining the Role of Solid Stress and Matrix Stiffness in Cancer Cell Proliferation and Metastasis. *Front. Oncol.* **2018**, *8*, 55. [CrossRef] [PubMed]
34. Nguyen-Ngoc, K.V.; Cheung, K.J.; Brenot, A.; Shamir, E.R.; Gray, R.S.; Hines, W.C.; Yaswen, P.; Werb, Z.; Ewald, A.J. ECM microenvironment regulates collective migration and local dissemination in normal and malignant mammary epithelium. *Proc. Natl. Acad. Sci. USA* **2012**, *109*, E2595–E2604. [CrossRef] [PubMed]
35. Antunes, J.; Gaspar, V.M.; Ferreira, L.; Monteiro, M.; Henrique, R.; Jerónimo, C.; Mano, J.F. In-air production of 3D co-culture tumor spheroid hydrogels for expedited drug screening. *Acta Biomater.* **2019**, *94*, 392–409. [CrossRef]
36. Song, H.; Cai, G.-H.; Liang, J.; Ao, D.-S.; Wang, H.; Yang, Z.-H. Three-dimensional culture and clinical drug responses of a highly metastatic human ovarian cancer HO-8910PM cells in nanofibrous microenvironments of three hydrogel biomaterials. *J. Nanobiotechnology* **2020**, *18*, 90. [CrossRef] [PubMed]
37. Flores-Torres, S.; Peza-Chavez, O.; Kuasne, H.; Munguia-Lopez, J.G.; Kort-Mascort, J.; Ferri, L.; Jiang, T.; Rajadurai, C.V.; Park, M.; Sangwan, V.; et al. Alginate–gelatin–Matrigel hydrogels enable the development and multigenerational passaging of patient-derived 3D bioprinted cancer spheroid models. *Biofabrication* **2021**, *13*, 025001. [CrossRef] [PubMed]
38. Malmqvist, M. Degradation of agarose gels and solutions by bacterial agarase. *Carbohydr. Res.* **1978**, *62*, 337–348. [CrossRef]
39. Fu, X.T.; Kim, S.M. Agarase: Review of major sources, categories, purification method, enzyme characteristics and applications. *Mar. Drugs* **2010**, *8*, 200–218. [CrossRef]
40. Tian, Z.; Liu, W.; Li, G. The microstructure and stability of collagen hydrogel cross-linked by glutaraldehyde. *Polym. Degrad. Stab.* **2016**, *130*, 264–270. [CrossRef]
41. Griffanti, G.; Nazhat, S.N. Dense fibrillar collagen-based hydrogels as functional osteoid-mimicking scaffolds. *Int. Mater. Rev.* **2020**, *65*, 502–521. [CrossRef]
42. Walimbe, T.; Panitch, A. Best of Both Hydrogel Worlds: Harnessing Bioactivity and Tunability by Incorporating Glycosaminoglycans in Collagen Hydrogels. *Bioengineering* **2020**, *7*, 156. [CrossRef] [PubMed]
43. Tako, M.; Nakamura, S. Gelation mechanism of agarose. *Carbohydr. Res.* **1988**, *180*, 277–284. [CrossRef]
44. Monteiro, M.V.; Gaspar, V.M.; Ferreira, L.P.; Mano, J.F. Hydrogel 3D in vitro tumor models for screening cell aggregation mediated drug response. *Biomater. Sci.* **2020**, *8*, 1855–1864. [CrossRef]

45. Iglesias, M.J.; Beloqui, I.; Garcia-Garcia, F.; Leis, O.; Vazquez-Martin, A.; Eguiara, A.; Cufi, S.; Pavon, A.; Menendez, J.A.; Dopazo, J.; et al. Mammosphere formation in breast carcinoma cell lines depends upon expression of E-cadherin. *PLoS ONE* **2013**, *8*, e77281. [CrossRef]
46. Tasdemir, N.; Bossart, E.A.; Li, Z.; Zhu, L. Comprehensive Phenotypic Characterization of Human Invasive Lobular Carcinoma Cell Lines in 2D and 3D Cultures. *Cancer Res.* **2018**, *78*, 6209–6222. [CrossRef]
47. Kruger, T.M.; Bell, K.J.; Lansakara, T.I.; Tivanski, A.V.; Doorn, J.A.; Stevens, L.L. Reduced Extracellular Matrix Stiffness Prompts SH-SY5Y Cell Softening and Actin Turnover To Selectively Increase A $\beta$ (1–42) Endocytosis. *ACS Chem. Neurosci.* **2019**, *10*, 1284–1293. [CrossRef]
48. Ranamukhaarachchi, S.K.; Modi, R.N.; Han, A.; Velez, D.O.; Kumar, A.; Engler, A.J.; Fraley, S.I. Macromolecular crowding tunes 3D collagen architecture and cell morphogenesis. *Biomater. Sci.* **2019**, *7*, 618–633. [CrossRef]
49. Trappmann, B.; Gautrot, J.E.; Connelly, J.T.; Strange, D.G.; Li, Y.; Oyen, M.L.; Cohen Stuart, M.A.; Boehm, H.; Li, B.; Vogel, V.; et al. Extracellular-matrix tethering regulates stem-cell fate. *Nat. Mater.* **2012**, *11*, 642–649. [CrossRef]
50. Wang, Y.; Gong, T.; Zhang, Z.R.; Fu, Y. Matrix Stiffness Differentially Regulates Cellular Uptake Behavior of Nanoparticles in Two Breast Cancer Cell Lines. *ACS Appl. Mater. Interfaces* **2017**, *9*, 25915–25928. [CrossRef] [PubMed]
51. Wong, S.H.M.; Fang, C.M.; Chuah, L.H.; Leong, C.O.; Ngai, S.C. E-cadherin: Its dysregulation in carcinogenesis and clinical implications. *Crit. Rev. Oncol. Hematol.* **2018**, *121*, 11–22. [CrossRef] [PubMed]
52. Vergara, D.; Simeone, P.; Franck, J.; Trerotola, M.; Giudetti, A.; Capobianco, L.; Tinelli, A.; Bellomo, C.; Fournier, I.; Gaballo, A.; et al. Translating epithelial mesenchymal transition markers into the clinic: Novel insights from proteomics. *EuPA Open Proteom.* **2016**, *10*, 31–41. [CrossRef] [PubMed]

MDPI  
St. Alban-Anlage 66  
4052 Basel  
Switzerland  
Tel. +41 61 683 77 34  
Fax +41 61 302 89 18  
[www.mdpi.com](http://www.mdpi.com)

*Pharmaceutics* Editorial Office  
E-mail: [pharmaceutics@mdpi.com](mailto:pharmaceutics@mdpi.com)  
[www.mdpi.com/journal/pharmaceutics](http://www.mdpi.com/journal/pharmaceutics)





MDPI  
St. Alban-Anlage 66  
4052 Basel  
Switzerland  
Tel: +41 61 683 77 34  
[www.mdpi.com](http://www.mdpi.com)



ISBN 978-3-0365-7032-7